ELI - Extreme Light Infrastructure

WHITEBOOK

Science and Technology with Ultra-Intense Lasers

editors:

Gérard A. Mourou Georg Korn Wolfgang Sandner John L. Collier

We acknowledge the support of this work from ELI-PP contract number 21 21 05.

Executive Editor
Georg Korn
ELI PP Deputy Coordinator

ELI PP Publications
Patrizio Antici

CNRS
1, place Aristide-Briand
92195 Meudon Cedex
France

Publisher
Andreas Thoss

The ELI Whitebook is produced for ELI by
THOSS Media GmbH
Wolfshagener Str. 56
13187 Berlin
Germany
www.thoss-media.com

Cover picture: Courtesy of Thomas Metzger
(Max-Planck-Institut für Quantenoptik/Ludwig-Maximilians-Universität München)

Copyright © 2011 CNRS

Contents

Authors vii

Executive Summary 1
1 Introduction and Objectives . . . 1
2 ELI in the international context of high intensity laser facilities . . . 2
3 Scientific and technological mission . . . 4
4 General Layout and performance goals of the facilities . . . 5
5 Phasing of the institutional and legal implementation of ELI . . . 12
6 Financial requirements and funding scheme . . . 12
7 Time schedule . . . 14

I ELI: Introduction and Vision

1 Introduction 17
1.1 ELI: A Science Federator in an Integrated Infrastructure . . . 18
1.2 ELI: A Technology Booster . . . 18
1.3 ELI: First European Laser Infrastructure and Geopolitical Science Attractor . . . 19
1.4 ELI's Long Term Vision . . . 20

II ELI Science

2 The quest for extreme light 25
2.1 Investigation of Vacuum Structure – Towards Schwinger Fields . . . 25
2.1.1 QED effects . . . 25
2.1.2 Particle physics at ELI . . . 42
2.1.3 Refractive QED processes at ELI and future exprimental considerations at ultrahigh intensities . . . 53
2.1.4 Search for axion-like particles by two laser beam crossing . . . 57
2.1.5 Search for a candidate of Dark Energy by quasi-parallel laser beam focusing 58
2.1.6 Testing radiation backreaction at super-high intensities . . . 58
2.2 Electron Acceleration . . . 61
2.2.1 Introduction . . . 61
2.2.2 Experimental progress and State-of-the-art on laser-plasma electron accelerators . . . 62
2.2.3 Future research directions . . . 67
2.2.4 Prospects for electron acceleration with ELI . . . 68
2.3 Ion sources . . . 71
2.3.1 Ion beams produced in laser matter interaction: introduction . . . 71
2.3.2 State of the art . . . 71
2.3.3 Scientific program . . . 73
2.3.4 Potential for business and technology transfer . . . 75
2.3.5 Conclusion . . . 77
2.4 Neutron sources . . . 79
2.4.1 Introduction . . . 79

2.4.2 State of the art neutron sources . . . 79
2.4.3 Neutron beams produced via neutron halo isomers . . . 81
2.4.4 Applications . . . 82
2.5 Terahertz sources . . . 85
2.5.1 Introduction . . . 85
2.5.2 Table-top terahertz sources . . . 86
2.5.3 Accelerator based terahertz sources . . . 86
2.5.4 Terahertz generation using laser-plasma techniques . . . 87
2.5.5 Applications . . . 88
2.6 Ultrafast-laser driven X-ray sources . . . 91
2.6.1 Current Status of X-ray Source Development and Applications . . . 92
2.6.2 Directions of implementation at ELI . . . 98
2.6.3 Source Development and Advanced Source Use . . . 100
2.6.4 Potential for Applications, Business and Technology Transfer . . . 102
2.7 Attophysics . . . 106
2.7.1 State of the art . . . 106
2.7.2 Recent results . . . 108
2.7.3 Predicted evolution . . . 110
2.7.4 Tested applications . . . 111
2.7.5 Potential applications . . . 115
2.7.6 Requirements from the users . . . 121
2.8 ELI Nuclear Physics . . . 125
2.8.1 Stand-alone High Power Laser Experiments . . . 125
2.8.2 Stand-alone γ/e^- Facility for Nuclear Spectroscopy . . . 134
2.8.3 Stand-alone γ/e^- Facility for Astrophysics . . . 142
2.9 Physics of dense plasmas . . . 145
2.9.1 Introduction . . . 145
2.9.2 State of the art . . . 145
2.9.3 Directions of plasma, HEDP and interaction studies at ELI . . . 146
2.9.4 Potential for Applications and Technology Transfer . . . 150
2.9.5 Conclusions . . . 151
2.10 Laboratory Astrophysics . . . 152
2.10.1 Modeling of astrophysics phenomena under the terrestrial laboratory conditions: general aspects . . . 152
2.10.2 Principle of qualitative scaling . . . 152
2.10.3 Cosmic-ray acceleration mechanisms . . . 154
2.10.4 Collisionless shock waves . . . 156
2.10.5 Reconnection of magnetic-field lines and vortex patterns in laser plasmas 157
2.10.6 Mechanisms of magnetic-field generation in relativistic plasmas . . . 161
2.10.7 Modeling of pulsar magnetosphere (oblique magnetic rotator) with relativistic EM solitons . . . 162
2.10.8 Conclusion . . . 163

3 Applications in multidisciplinary sciences 167
3.1 Biomedical imaging with laser-driven brilliant compact X-ray sources . . . 167
3.2 Material sciences . . . 175
3.2.1 Attosecond electron dynamics . . . 175
3.2.2 Materials behaviour at intense electromagnetic fields . . . 177
3.3 Biological imaging with ELI's intense and ultra-short X-ray pulses . . . 179
3.4 Life Sciences . . . 186
3.4.1 Ion Beam Therapy . . . 186

3.4.2 Medical Radioisotopes produced by γ Beams . . . 198
3.5 Industrial Applications for the Management of Nuclear Materials . . . 200
3.5.1 Non-destructive detection and assay of nuclear materials by using high-brightness γ-rays . . . 200
3.5.2 Management of radioactive wastes . . . 200
3.5.3 Nuclear material accounting and safeguards . . . 202
3.5.4 Summary . . . 204
3.6 Ultrafast molecular dynamics . . . 206

4 Theory and numerical simulations 213

III ELI Technology

5 Technological basis for the primary sources 221
5.1 General laser layout . . . 221
5.2 Operation Principles . . . 225
5.2.1 Femtosecond Laser Oscillators . . . 225
5.2.2 Amplification in laser media . . . 227
5.2.3 Optical Parametric Amplification . . . 230
5.2.4 Dispersion management of high intensity short pulse lasers . . . 235
5.2.5 Beam propagation and focusing . . . 238
5.3 Diagnostics of Laser Parameters . . . 242
5.3.1 Duration and spectral phase . . . 242
5.3.2 CEP measurement and stabilization . . . 245
5.3.3 Temporal contrast . . . 248
5.4 Pump sources . . . 254
5.4.1 Flash-lamp pumped lasers. . . . 254
5.4.2 Diode pumped disk lasers . . . 256
5.4.3 Diode pumped slab lasers . . . 260
5.5 Nonlinear frequency conversion . . . 264
5.5.1 Bandwidth broadening techniques . . . 264
5.5.2 XPW for pulse cleaning . . . 266
5.5.3 SHG for pump lasers . . . 268
5.6 Materials and coatings . . . 270
5.6.1 High damage threshold mirrors for broad bandwidth and dispersion control . . . 270
5.6.2 Gratings . . . 271
5.6.3 Optical metrology . . . 273
5.7 Laser Control . . . 278
5.7.1 Computer System and Network . . . 278
5.7.2 Laser Control and Alignment . . . 279
5.7.3 ELI Laser Safety Control . . . 279

6 Technological basis for the secondary sources 281
6.1 Attosecond pulse generation . . . 281
6.1.1 Source based on High Harmonic Generation in gases . . . 281
6.1.2 Source based on surface harmonic . . . 284
6.1.3 Source diagnostics . . . 292
6.1.4 Measurement of the spectrum . . . 302
6.1.5 On-line measurement of the intensity . . . 303

6.2 Charged Particle Beamlines . . . 311
6.2.1 Electron beamlines . . . 311
6.2.2 Proton-ion beamlines . . . 323
6.3 A brilliant Neutron Beam produced via Neuton Halo Isomers . . . 335
6.4 X-ray Generation . . . 337
6.4.1 The ELI Plasma Wiggler Beamline . . . 337
6.4.2 XFEL-beamline . . . 349
6.4.3 Relativistic Flying Mirrors . . . 351
6.5 Infrastructure Producing High Intensity Gamma Rays . . . 363
6.5.1 Introduction . . . 363
6.5.2 First stage warm linac in X-band RF plus 532 nm laser . . . 364
6.5.3 Second stage 100 mA Energy Recovery Linac . . . 372
6.5.4 Conclusions . . . 373
6.6 Terahertz source . . . 375
6.6.1 Introduction . . . 375
6.6.2 Source design . . . 375
6.6.3 Target area design . . . 378
6.7 System Control . . . 380
6.7.1 Computer System and Network . . . 380
6.7.2 Target Area Control Systems . . . 380
6.7.3 Data Acquisition System . . . 380

IV Implementation Strategy

7 Risks analysis and synergies with other projects 385
7.1 Risks and risk reduction . . . 385
7.2 National programmes . . . 389
7.2.1 Apollon at Institute Lumiere Extreme (ILE), France . . . 389
7.2.2 Astra-Gemini at Central Laser Facility, RAL, U.K. . . . 390
7.2.3 HiLASE: New lasers for industry and research . . . 392
7.2.4 Petawatt Field Synthesizer at MPQ Garching, Germany . . . 397
7.2.5 VULCAN 10 PW at Central Laser Facility, RAL, U.K. . . . 400
7.2.6 Texas Petawatt Laser and 10 PW upgrade . . . 403
7.3 European Programmes . . . 416
7.3.1 The European X-ray Free-Electron Laser Facility in Hamburg . . . 416
7.3.2 ELI-Beamlines Synergy with the HiPER Project . . . 418

8 Safety 419
8.1 Laser and other hazards . . . 419
8.1.1 Laser safety . . . 419
8.1.2 Non-laser-related hazards . . . 420
8.1.3 Impact of non-radiation risks on the environment . . . 424
8.2 Radioprotection safety . . . 425
8.2.1 Pre-definition of the radiation source term for 1 PW, 10 PW and 100 PW lasers . . . 425
8.2.2 Shielding . . . 433
8.2.3 Activation . . . 446
8.2.4 Monitoring . . . 446
8.3 Law . . . 448

8.3.1 Advisory Agencies . . . 448
8.3.2 Regulatory Agency . . . 449
8.3.3 ELI license . . . 449
8.4 Operative rules . . . 452
8.4.1 Basic concepts of the laser safety procedure at ELI . . . 452
8.4.2 The laser-based accelerator safety system . . . 455
8.4.3 Access to experimental areas and material-transportation rules . . . 456

9 ELI Facilities 459
9.1 Site decision process . . . 459
9.1.1 Organisation of the site decision process . . . 459
9.1.2 Terms and milestones of the decision on the conditions of implementation of ELI . . . 460
9.1.3 Rationale of the distributed implementation of ELI . . . 461
9.1.4 Elements on the sites of the three first ELI facilities . . . 462
9.2 ELI-Beamlines in the Czech Republic . . . 463
9.2.1 Beamline scheme . . . 463
9.2.2 Site and building . . . 468
9.2.3 Budget and timeline . . . 477
9.3 ELI-ALPS in Hungary . . . 480
9.3.1 Beamline scheme . . . 480
9.3.2 Site and building . . . 484
9.3.3 Budget and timeline . . . 488
9.4 ELI-NP in Romania . . . 490
9.4.1 Beamlines Scheme . . . 490
9.4.2 Site and building . . . 494
9.4.3 Planned budget and timeline . . . 496
9.5 Regional facilities . . . 498
9.5.1 The Attosecond science and technology RPF, Greece . . . 499
9.5.2 High Field Computational Sciences RPF, Portugal . . . 503
9.5.3 Ultrashort, Ultraintense Pulsed Laser Center, Spain . . . 504

10 Institutional and legal implementation of ELI 507
10.1 Genesis and terms of the decision on the implementation of ELI . . . 509
10.1.1 Path to the decision . . . 509
10.1.2 Resolutions of the ELI-PP Steering Committee on the implementation of ELI . . . 509
10.2 Institutional arrangements in the three host countries . . . 512
10.2.1 Elements on the EU Regional Policy . . . 512
10.2.2 Application process in the three host countries . . . 512
10.3 Objectives and organisation of the ELI Delivery Consortium . . . 514
10.3.1 Establishment and missions of the ELI Delivery Consortium . . . 514
10.3.2 Organisation of the ELI Delivery Consortium . . . 514
10.3.3 Work plan of the ELI Delivery Consortium . . . 516
10.4 Prospective structure and missions of the ELI European Research Infrastructure Consortium . . . 517
10.4.1 Elements of understanding on the ERIC legal form . . . 517
10.4.2 Prospective structure of the ELI-ERIC . . . 519
10.4.3 Distribution of tasks between the ELI-ERIC and the local ELI facilities . . . 520
10.4.4 Memorandum of Understanding on the Establishment and Operation of the Extreme Light Infrastructure (ELI) . . . 521

Authors

M. M. Aléonard
M. Altarelli
P. Antici
A. Apolonskiy
P. Audebert
A. Bartnik
C. P. J. Barty
A. Bernstein
J. Biegert
P. Böni
N. Booth
M. Borghesi
D. Bote
S. V. Bulanov
R. Butkus
L. Cardoso
J. P. Chambaret
D. Charambilidis
G. Cheriaux
R. Clarke
J. Collier
L. Cramer
A. Czitrovszky
E. d'Humières
A. Di Piazza
B. Dietz
T. Ditmire
P. Dombi
A. Dorobantu
G. Dyer
R. Ernstorfer
K. Ertel
E. Esarey
T. Zh. Esirkepov
A. Esposito
M. Fajardo
A. Fedotov
C. Fenic
F. Fernandez
A. Ferrari
I. B. Földes
C. Frederickson
J. Fuchs
J. A. Fülöp
Z. Fülöp
M. Galimberti
E. Gaul
H. Gies
A. Giulietti
D. Giulietti
L. Gizzi
F. Gliksohn
E. Goulielmakis
W. Grigsby
M. Gross
F. Grüner
D. Habs
J. Hajdu
R. Hajima
Z. Harman
K. Z. Hatsagortsyan
J. Hebling
T. Heinzl
A. Henig
K. Homma
R. Hörlein
A. Ilderton
D. A. Jaroszynski
M. P. Kalashnikov
C. Kalpouzos
S. Karsch
C. H. Keitel
D. Kiefer
R. Kienberger
M. Kling
S. Kneip
G. Korn
U. Köster
A. P. Kovács
M. Kozlova
G. Kraft
S. Kraft
F. Krausz
K. L. Lancaster
C. Le Blanc
B. Le Garrec
W. Leemans
M. Lenner
J. Limpouch
T. Lippenyi
N. C. Lopes
R. Lopez-Martens
W. Ma
Z. Major
D. Margarone
K. Markey
M. Marklund
M. Marti
M. Martinez
P. Mason
F. Mathieu
T. Metzger
T. Mocek
M. Molls
G. Mourou
S. D. Moustaizis
C. Müller
C. D. Murphy
I. Musgrave
N. B. Narozhny
N. Naumova
D. Neely
F. Negoita
P. V. Nickles
M. Nisoli
E. Oliva
K. Osvay
J. L. Paillard
D. Pepler
F. Pegoraro
V. Pervak
V. Petrillo
F. Pfeiffer
N. Pietralla
A. Piskarksas
I. Ploumistakis
L. Poleto
G. Priebe
C. Rodríguez Tajes
K. Rohlena
M. Roth
H. Ruhl
C. Ruiz
B. Rus
R. Ruth
V. Růžička
W. Sandner
G. Sansone
D. Savran
J. Schreiber
R. Schützhold
L. Serafini
L. Silva
S. De Silvestri
K. Sonnabend
C. Stehle
D. R. Symes
G. Szabo
T. Tajima
G. Tempea
P. G. Thirolf
A. G.R. Thomas
V. Tikhonchuk
G. D. Tsakiris
I. Tsohantjis
P. Tzallas
E. Urruti
D. Ursescu
K. Varjú
L. Veisz
M. Vrakking
H. A. Weidenmüller
W. White
J. J. Wilkens
I. Will
T. Winstone
T. Wittmann
N. Woolsey
G. Wormser
X. Q. Yan
N. V. Zamfir
M. Zepf

Executive Summary

1 Introduction and Objectives

The first laser shot rang in the Hughes Aircraft Laboratory in 1960. It was a copernican event that touched all parts of science and technology. In science, the laser has been extremely effective to improve our understanding of the molecular and atomic structure of matter and the associated dynamical events. However it was quite inefficient in probing the subjacent strata formed by the nucleons and their components the quarks or to dissociate the vacuum in its elements. Nor the laser photon energy or its electric field were large enough or its pulse duration sufficiently short to conceive decisive experiments. A few years ago, a new type of large scale laser infrastructure specifically designed to produce the highest peak power and focused intensity was heralded by the European Community: the Extreme Light Infrastructure, ELI. ELI was designed to be the first exawatt class laser, equivalent to 1000 times the National Ignition Facility (NIF) power. This gargantuan power will be obtained by producing kJ of power over 10 fs. Focussing this power over a micrometer size spot, will bring forth the highest intensity. By producing, firstly, the highest electric field, secondly the shortest pulse of high energy radiations in the femto-zeptosecond regime and thirdly, electrons and particles with ultrarelativistic energy in the GeV regime, the laser signals its entry into Nuclear Physics, High Energy Physics, Vacuum Physics and in the future Cosmology and Extradimension Physics.

More precisely, ELI will be the first infrastructure dedicated to the fundamental study of laser-matter interaction in the ultra-relativistic regime ($I > 10^{24}\,W/cm^2$). In practice, The infrastructure will serve to investigate a new generation of compact accelerators delivering energetic particle and radiation beams of femtosecond (10^{-15} s) to attosecond (10^{-18} s) duration. Relativistic compression offers the potential of intensities exceeding $I_L > 10^{25}\,W/cm^2$, which will challenge the vacuum critical field as well as provide a new avenue to ultrafast attosecond to zeptosecond (10^{-21} s) studies of laser-matter interaction. ELI will afford wide benefits to society ranging from improvement of oncology treatment, medical and biomedical imaging, fast electronics and our understanding of aging nuclear reactor materials to development of new methods of nuclear waste processing.

The report contains the description of the science, the technology basis and the implementation of a new international scientific infrastructure the Extreme Light Infrastructure (ELI). The ultra-intense ELI laser user facilities will be built within the ESFRI process in the Czech Republic (Southwest of Prague), Romania (Magurele, South of Bucharest) and Hungary (Szeged, East Hungary). The purposes of the facilities is to design, develop and build ultra-high-power lasers with focusable intensities and average powers reaching far beyond the existing laser systems and organize them as international user facilities for new up to now unconceivable revolutionary experiments in different scientific disciplines as well as in technology and medicine. The laser science and technology developments in the facilities will pave the way to intensities above the ultra-relativistic regime. This will open new frontiers in fundamental science. Depending on the expertise in the countries the ELI facilities will concentrate on different science and technology topics covering at the same time the main topics defined by the science case: The Beamline-Facility (Czech Republic) focuses on short pulse X-ray generation and acceleration of particles and their applications, the Attosecond facility (Hungary) on generation and application of super-short (Attosecond-range) pulses with very high repetition rates, whereas the facility in Romania will use ultra-intense optical and gamma ray pulses mainly for investigations of fundamental problems in the field of nuclear physics and their practical applications.

The baseline laser technology is chirped pulse amplification of femtosecond optical pulses in broadband solid state laser materials and (or) nonlinear crystals. The maximum single laser beam peak-power will exceed 10 PW (1 PW = 10^{15} W). Nonlinear and relativistic compression as well as phasing of high power laser beams will push the peak power by more than one order of

magnitude to above 100 PW. Diode pumping will increase the repetition rate (10 Hz–1 kHz) up to the peak-power level of PW (Petawatt) (Hungary, Czech Republic). The planned overall 10 interaction areas (Cz: 4, Hu 4; Ro 2) will have 20 photon and particle beamlines equipped with numerous state of the art experimental stations for an efficient user facility mode of operation enabling multi parallel use and exploitation.

The implementation of ELI helps strengthening the leading European position in high-intensity laser research and will give new additional opportunities to the European photonic industry.

The localization of the ELI facilities in central and Eastern Europe utilizes the scientific and technological potentials of the involved new EU-member countries, accelerates the European integration process and will lead to immense improvements of their research infrastructures. ELI will provide new educational and training perspectives for the younger generation of students and scientists in the field of lasers, laser-matter interaction and photonics.

The unique possibility of using infrastructural funds of those countries secures the financial needs for building ELI.

2 ELI in the international context of high intensity laser facilities

Today's top specifications of high power laser systems are characterized by a peak power between one and two petawatts at very low (sub Hz) repetition rates, this being unchanged over more than one decade now. The majority of high power systems, however, still rests at the 100 TW level. ELI and its national predecessor projects like ILE and Vulcan-10 PW will boost the peak power of single lasers (modules) into the 10 PW or multi-10 PW regime at much higher repetition rates, constituting an evolution of more than one order of magnitude in both of these parameters. In addition, the high intensity pillar of ELI aims at another order of magnitude in peak power, into the 100 PW regime, by coherent combination of several such modules. With these parameters ELI will certainly lead the international high power laser scenario. The interesting questions to be asked are: Why now? And why here (in Europe)?

The answers to these questions appear to be strongly correlated. They both lie in the observation that *ELI will be the first laser research infrastructure which is the result of a co-ordinated effort of a multi-national scientific laser community.* Other communities (high energy physics, synchrotrons, astronomy etc.) have long standing traditions in the operation of international user facilities. Lasers, having evolved 50 years ago from small table-top devices, are only now at the edge of such mode of operation, and ELI is the first installation world-wide to make that step.

In this context it is illustrative to view the global distribution of high-power laser systems beyond 100 TW peak power, and its temporal evolution, particularly in Europe. Figure 1 shows the world map of high intensity systems in 2006 and the current situation in Europe, Russia and India by the end of 2010. The left part of the figure shows that high power lasers are pre-dominantly located in three global regions at moderate northern latitudes: North America (US and Canada), Europe (including Russia), and the Asian-Pacific region (including India). This general feature has not changed since 2006 except that now (in 2010) the overall number of such systems has considerably increased (c.f. www.icuil.org). The increase, however, was most dramatic in Europe (c.f. right part of figure 1).

Perhaps not surprisingly, the recent increase in European high-power laser systems parallels the increase in national laser laboratories within the EC-funded European network LASERLAB-EUROPE (www.laserlab-europe.net), now comprising 27 of Europe's most important laser research infrastructures from 19 EU countries. It shows (and this is part of the answer to the above questions) that the European nations and the European Commission both pay particular attention to the scientific field of lasers, optics and photonics. In fact, besides operating a multitude of national laser research infrastructures several European nations have large funding

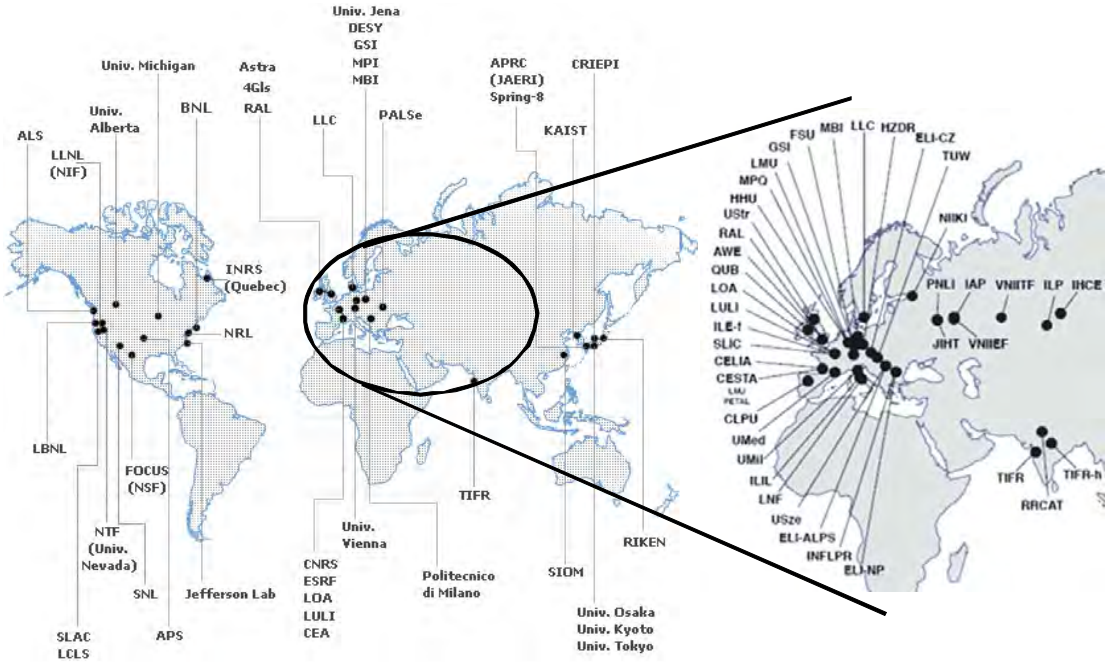

Figure 1: World map of high intensity systems in 2006 (left) and the current situation in Europe, Russia and India by the end of 2010 (right). Taken from the "International Committee on Ultra-High Intensity Lasers" (ICUIL, www.icuil.org).

programs in optics and photonics. The EC has recently counted optics and photonics as one of the 5 key enbaling technologies to tackle the Grand Societal Challenges of the 21^{st} century.

Hence, Europe appears as a particularly fertile ground for laser technologies, laser development and laser applications at the national level. ELI, however, goes beyond the national capabilities of most countries. Here it helps that the European Commission has, over more than a decade now, established and funded networks of large national research infrastructures with three essential elements: 1) Joint Research Activities (including device development), 2) Transnational Access to the benefit of a broad user community, and 3) Networking among national infrastructures. In laser science the relevant network is LASERLAB-EUROPE which, during its current funding period, is concentrating its research activities among others on the development of high-power lasers (including those with high average powers), attosecond physics and applications. There is a coordinated approach to meet these challenges by investigation of new techniques as for example the development of high average power diode pumped solid state laser, parametric conversion to high peak power and coherent multiple aperture beam combination. While this research was mostly carried by the top national laboratories with their individual funding it was the co-ordination through LASERLAB-EUROPE which added considerable value to these efforts and lifted them beyond the national level. Hence, the ground was laid for revolutionary new laser projects like ELI and HiPER when the European nations, as the final ingredient to the process leading to ELI, called for proposals for Pan-European Research Infrastructures in the context of the ESFRI process.

In summary, ELI seems to have evolved from a lucky coincidence of a particularly fruitful environment of European nations paying considerable attention to optics, photonics and lasers, and sustaining very productive scientific communities in these areas on the one hand, and from international coordination, funded or triggered by the EC, of existing national research infrastructures and of the creation of new Pan-European Infrastructures on the other.

What is ELI's future within this international context? Given the dynamic evolution of European and global national laser facilities as shown in fig. 1 it is not surprising that they continue to develop top-of-the-line laser facilities themselves. Fig. 2 shows the European state projects (already under development) towards the PW regime; similar projects exist in the other global regions. The following conclusions may be drawn from this observation: 1) the top-of-the-line in high power lasers is slowly, but steadily shifting from the 100 TW to the 1 PW level, while singular projects (especially the ELI predecessor projects) attain similar powers as the ELI 10 PW modules. ELI's multi-100 PW facility seems to remain largely unchallenged in the near future. 2) Such a development, although tending to close the gap between ELI and its national companions and competitors, is much more of an opportunity than a threat. Without the availability of a large number of comparable high-power systems (even if an order of magnitude less powerful) the international user community could not be sustained which is necessary to exploit all the new physics that ELI provides. 3) The only threat, however, may lie in the lack of human resources needed to complete all these projects in time. This is why ELI, together with LASERLAB-EUROPE and other allies (HiPER, EOS, Photonics21) is actively working to develop the international community of laser scientists, engineers and technicians.

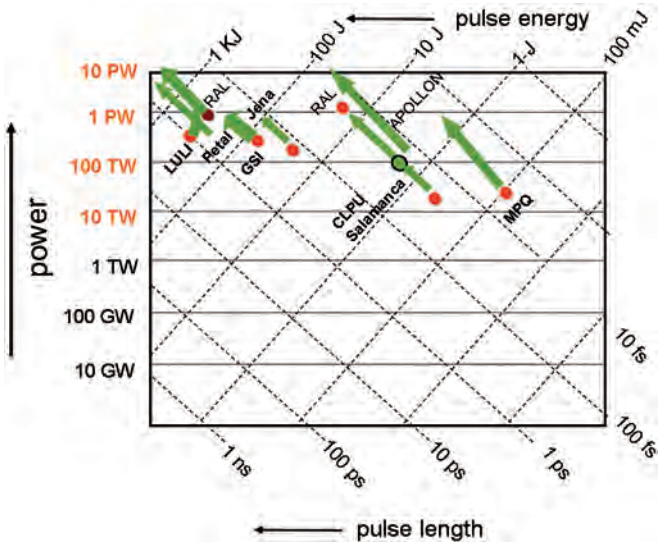

Figure 2: European state projects (already under development) towards the PW regime.

3 Scientific and technological mission

ELI will extend the field of laser-matter interaction, now limited to the relativistic regime ($a_0 \sim$ 1–10, which corresponds to intensities 10^{18} W/cm^2–10^{20} W/cm^2), into the ultra-relativistic regime $a_0 \sim 10^2$–10^4. By means of relativistic effects, these extreme intensities will provide access to extremely short pulse durations in the attosecond or zeptosecond regime. ELI will comprise 4 branches: **Ultra-High-Field Science** centred on direct physics of the unprecedented laser field strength, **Attosecond Laser Science**, which will capitalize on new regimes of time resolution, **High-Energy Beam Facility**, responsible for development and use of ultra-short pulses of high-energy particles and radiation stemming from relativistic and ultrarelativistic interaction, and **Nuclear Physics Facility** with ultra-intense laser and brilliant gamma beams (up to 19 MeV) enabling also brilliant neutron beam generation with a largely controlled variety of energies.

By relativistic pulse compression, the femtosecond high energy pulses could be further compressed to the attosecond range and the laser power boosted accordingly. ELI will open the possibility of taking snap-shots in the attosecond or zeptosecond scale of the electron dynamics in atoms, molecules, plasmas and solids. ELI will afford new investigations in particle physics, nuclear physics, gravitational physics, nonlinear field theory, ultrahigh-pressure physics, astrophysics and cosmology. Besides its fundamental physics mission, a paramount objective of ELI will be to provide ultra-short energetic particle (10–100 GeV) and radiation (up to few MeV) beams produced from compact laser plasma accelerators. ELI will mate its scientific, engineering and medical missions for the benefit of industry and society. For instance, the secondary sources expected in the project will provide X-ray technologies to clarify the complete time history of reactions such as protein activity and protein folding, radiolysis, monitoring of chemical bonds and catalysis processes. This will lead to a better understanding and control of key events during chemical bond formation and destruction. A high impact on society and on new technologies for industry is then expected since these processes will play a major role in creating new drugs or in improving their efficiency. The new Gamma source to be built within the ELI Nuclear Physics branch will help to produce new medical radioisotopes to determine the efficiency of chemotherapy for tumors and the optimum dose by nuclear imaging. New 'matched pairs' of isotopes of the same element become available, one for diagnostics, the other for therapy, allowing to contol and optimize the transport of the isotope by the bioconjugate to the tumor. Emitters of low-energy Auger electrons for highly efficient targeted tumor therapy may be generated for clinical use. Investigations in this "medical technology direction" will open up absolutely new important perspectives for the society.

In collaboration with medical doctors, laser driven ion beam therapy will be developed with this novel source. In material science ELI helps to clarify the mechanisms leading to defect creation and aging of materials in nuclear reactors. It should be emphasised that the optical, X-ray and particle beams provided by ELI-lasers will be perfectly synchronized due to their way of generation from the high power optical laser pulses.This enables pump-probe investigations in a very broad range of energies for the photon (eV–MeV) and particle beams (eV–GeV) with very high accuracy.

4 General Layout and performance goals of the facilities

Attosecond Light Pulse Source (Szeged, Hungary)

The primary mission of the ELI Attosecond Light Pulse Source (ALPS) (Fig. 3) is to provide the international scientific community a broad range of ultrafast light sources, especially with coherent XUV and X-ray radiation, including single attosecond pulses, to enable temporal investigations of electron dynamics in atoms, molecules, plasmas and solids on femtosecond and attosecond time scales. The secondary purpose is to contribute to the scientific and technological development towards generating 200 PW pulses, being the ultimate goal of the ELI project. ELI-ALPS will be operated also as a user facility and hence serves basic and applied research in physical, chemical, material and biomedical sciences as well as industrial applications.

To fulfil the primary mission of ELI-ALPS, PW-class driving lasers providing few-cycle, carrier-envelope phase (CEP) stabilised laser pulses are necessary to be operated at unprecedentedly high repetition rate. These pulses enable the utilization and scaling of all known methods of attosecond pulse generation. i) The well-established method of high harmonic generation in rare gases (GHHG) will be pushed to its ultimate limits by a loose focusing geometry, aiming at producing attosecond pulses with tens of μJ pulse energy. ii) It is anticipated that much more energetic and shorter attosecond pulses can be generated on solid surfaces (SHHG) reaching the X-ray domain. This method is not yet fully explored, so research will also be directed for the full exploitation of the technique. These two methods are offering complementary parameters to

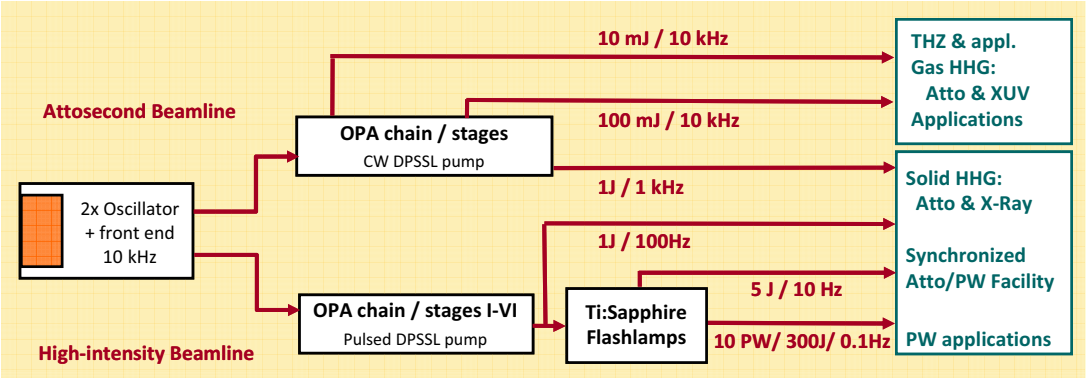

Figure 3: Current schematics of the laser systems of the ELI-ALPS Research Infrastructure with a list of secondary sources and applications.

deliver a versatile atto-source for users. New methods of attosecond pulse generation utilizing field enhancement at nanostructured surfaces or dc-like external fields will be tested to enhance the harmonic generation process. Partly for this purpose, intense, synchronized THz pulses will be generated and their use for atto pulse generation will be implemented.

The high-intensity, multi-PW beamline will serve as a testbed for scientific and technological researches towards the 200 PW laser and also as a driver source for versatile radiation and particle secondary sources. The unique feature of these sources will be their broad spectrum in terms of available photon and particle energy.

In order to satisfy all the basic design criteria driven by applications, the scheme in Fig. 3 is proposed. A separate channel is devoted to user facility experiments, primarily based on CEP-stabilized, few-cycle laser pulses in near-IR and mid-IR domains at 10 kHz repetition rate to drive the GHHG source. The laser beamlines has identical early front ends, so that synchronisation will be ensured. The optical parametric (chirped pulse) amplifier stages are pumped with diode-

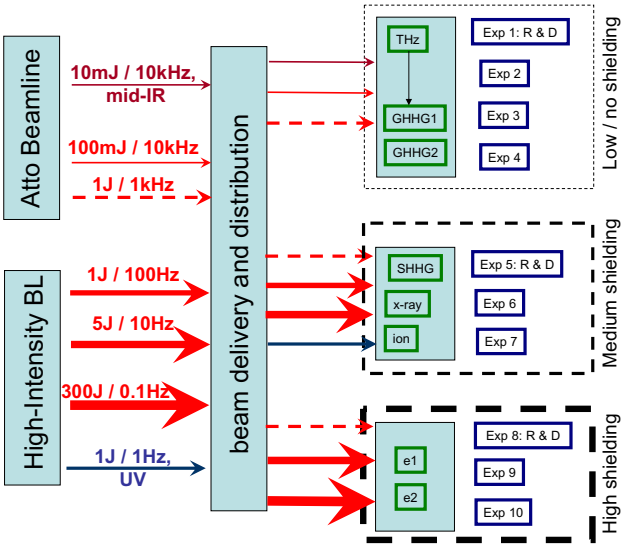

Figure 4: Layout of the target areas. The indicated laser parameters are compatible with the laser scheme in figure 3.

pumped solid-state lasers, while the duty end of the high intensity beamline may retain flashlamp pumped Ti:S amplifiers. The workhorse of the attosecond beamline will provide 1 J, CEP-stabilized few-cycle laser pulses at 1 kHz with two outputs.

A target area (TA) layout corresponding to the laser system described above is shown in figure 4. According to the expected radiation dose and the required shielding, three groups of target areas are planned. In each group of TAs one of the experimental areas is devoted to source development supporting future updates of the secondary sources and the implementation of new technologies.

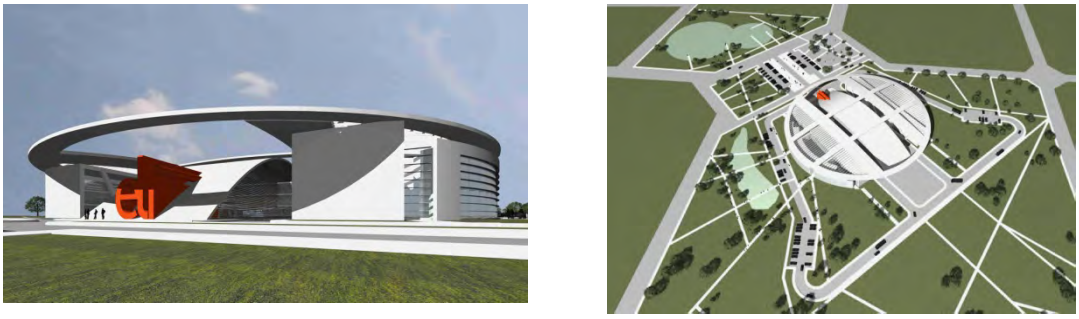

Figure 5: Conceptual building plan and the close neighbourhood.

Figure 6: Site plan of ELI-ALPS.

High Energy Beam-Line Facilitiy (Prague, Czech Republic)

General Considerations and beamline architecture

The beamline facility will exploit the PFS technology in the front end up to a few 100 mJ and will use amplification techniques exploiting repetition-rate pumping (especially cryogenic multislab pump systems) to provide ultrashort petawatt-class pulses with up to 50 J of energy, at a repetition rate of up to 10 Hz. As emphasized by the ELI-PP consortium, ideally all the beamlines should run at 10 Hz repetition rate, in order to enable ELI to become, amongst other, a highly competitive source of extremely short pulse X-rays, accelerated electrons, or protons for applications.

The contribution of ELI-Beamlines to the development of high-intensity facility will consist in two laser blocks providing each 10 PW. The design options for laser high-intensity systems, as well as techniques of coherent combination of their pulses, will be prototyped and tested at ELI-Beamlines.

Laser Layout

The schematic layout of the ELI beamline facility is shown in Fig. 7. The laser consists of:

- Front end including the oscillator section and the three booster amplifiers;
- Beamlines with output energy 10 J, including pulse compressors;
- Beamlines with output energy 50 J, including pulse compressors;
- High intensity 2×10 PW section, including pulse compressors.

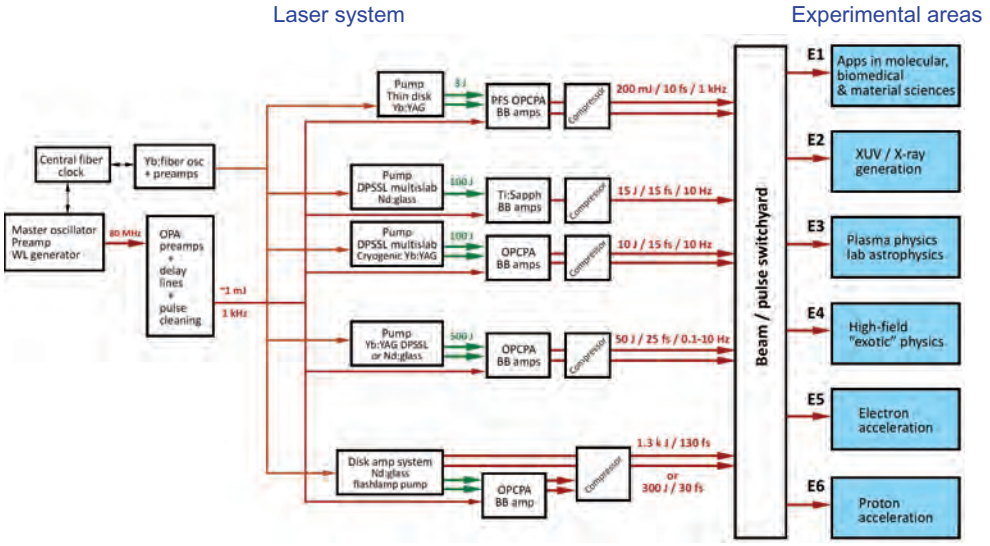

Figure 7: Schematic layout of laser chains of ELI-Beamlines. Its primary mission will be to deliver repetition-rate ultrashort pulses with up to 50 J of energy, and contribute to development of the high-intensity systems. The two 10-PW laser blocks will serve to development and testing of selected technologies (OPCPA and/or Ti:Sapphire). Pulse compressors are not represented.

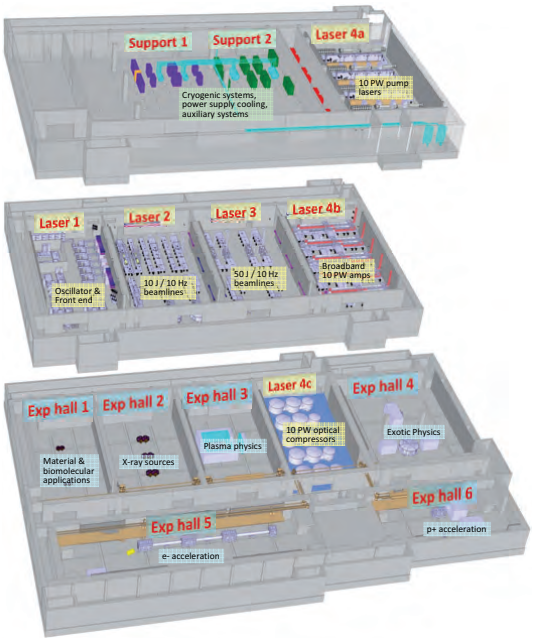

Figure 8: Proposed layout of the internal structure of ELI-Beamlines facility.

The designed facility features six Experimental Halls (E1 to E6).

Laser systems L1 (oscillator and booster amplifiers), L2 (diode-pumped 10 J/10 Hz beamlines) and L3 (diode-pumped 50 J/10 Hz beamlines) are placed in the ground floor, whereas the 10-PW laser units spreads over the three floors (pump system on the first floor (4a), broadband amplifiers on the ground floor (4b) and optical compressors in the basement(4c)).

Support technology systems located in the first floor include heat exchangers of the cryogenic circuits, capacitor banks, and power supplies for the diode-pumped repetition laser blocks L2 and L3.

Figure 9: Map with the location of the Czech ELI beamline facility south of Prague.

Figure 10: Artist impressions of the high energy beam line facility near Prague.

Nuclear Physics Facility (Magurele, Romania)

The ELI-NP facility will generate laser and gamma beams with unique characteristics suited to perform frontier laser, nuclear and fundamental research. The core of the facility is a double multi-PW chain laser system. In order to perform cutting edge photo-nuclear physics experiments, a complementary high brilliance gamma beam, very performant low bandwidth, energies

in the 15 MeV range, will be generated via the laser interaction with a brilliant bunched electron beam. Thus ELI-NP will allow either combined experiments using the high power laser beams and the γ beam or stand-alone experiments. The design of the facility is modular, reserving the space for further extension of the laser system and allowing the extension later of the experimental area, according to the needs.

The basic objectives of the ELI-RO Nuclear Physics (NP) pillar are:

- precise diagnosis of the laser beam interaction with matter using nuclear methods and techniques.
- photonuclear reactions for nuclear structure studies and for applications
- exotic nuclear physics and astrophysics.
- frontier fundamental physics based on high intensity laser and very brilliant γ beams.

The ELI-NP high power laser system, consists essentially in two 10 PW class Apollon-type lasers coherently added to the high intensity of 10^{23}–10^{24} W/cm^2 or electrical fields of 10^{15} V/m. Its main parameters are presented in Fig. 11. Higher repetition 100 TW and 1 PW laser pulses will be also available for experiments.

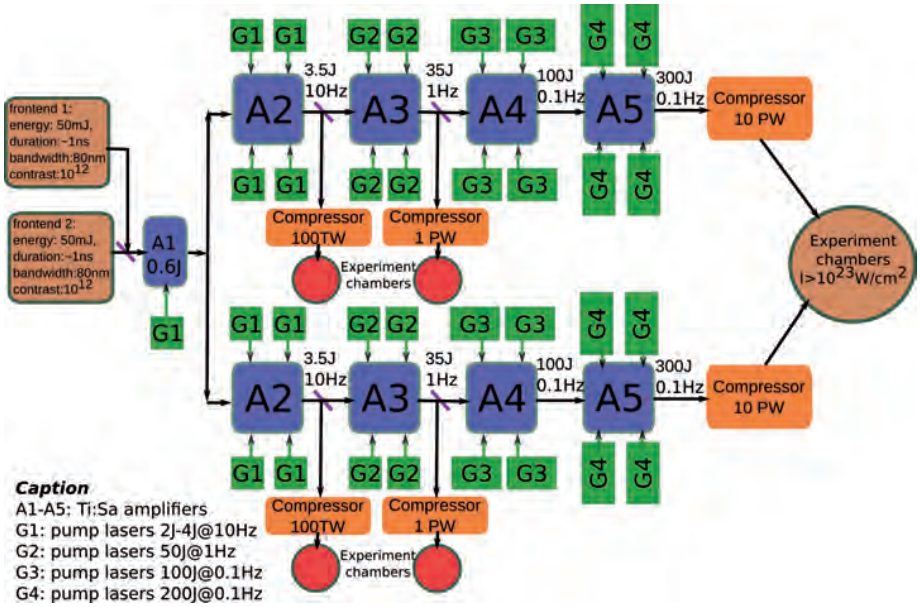

Figure 11: The ELI-NP multi-PW laser system conceptual design: FE1, FE2 – Font-End based on OPCPA. A1–A5 – Ti:sapphire amplifiers.

Concerning the gamma beam part, the scientific community decided that the gamma beam should be generated by a X-band 'warm' LINAC coupled to a 10 J/120 Hz diode pumped solid state laser system This choice ensures that ELI-NP will be the world-leading gamma beam facility at the time of its start of operation. A laser pulse recirculation system synchronized to a train of electron bunches allows to increase by a factor of 100 the effective gamma pulse rate up to 12 kHz. The characteristics of these systems are adapted to produce gamma beams with variable energy up to 19 MeV, 10^{-3} energetic width, 10^{13} photons/second total flux and a peak brilliance larger than 10^{21} photons/sec/mm^2/mrad^2/0.1%BW. After a first stage of acceleration up to 400 MeV, a similar laser-electrons interaction system is installed such that intermediary energies gamma beams are available in two additional experimental halls increasing the experiments preparation flexibility and, consequently, the total beam time effectively used.

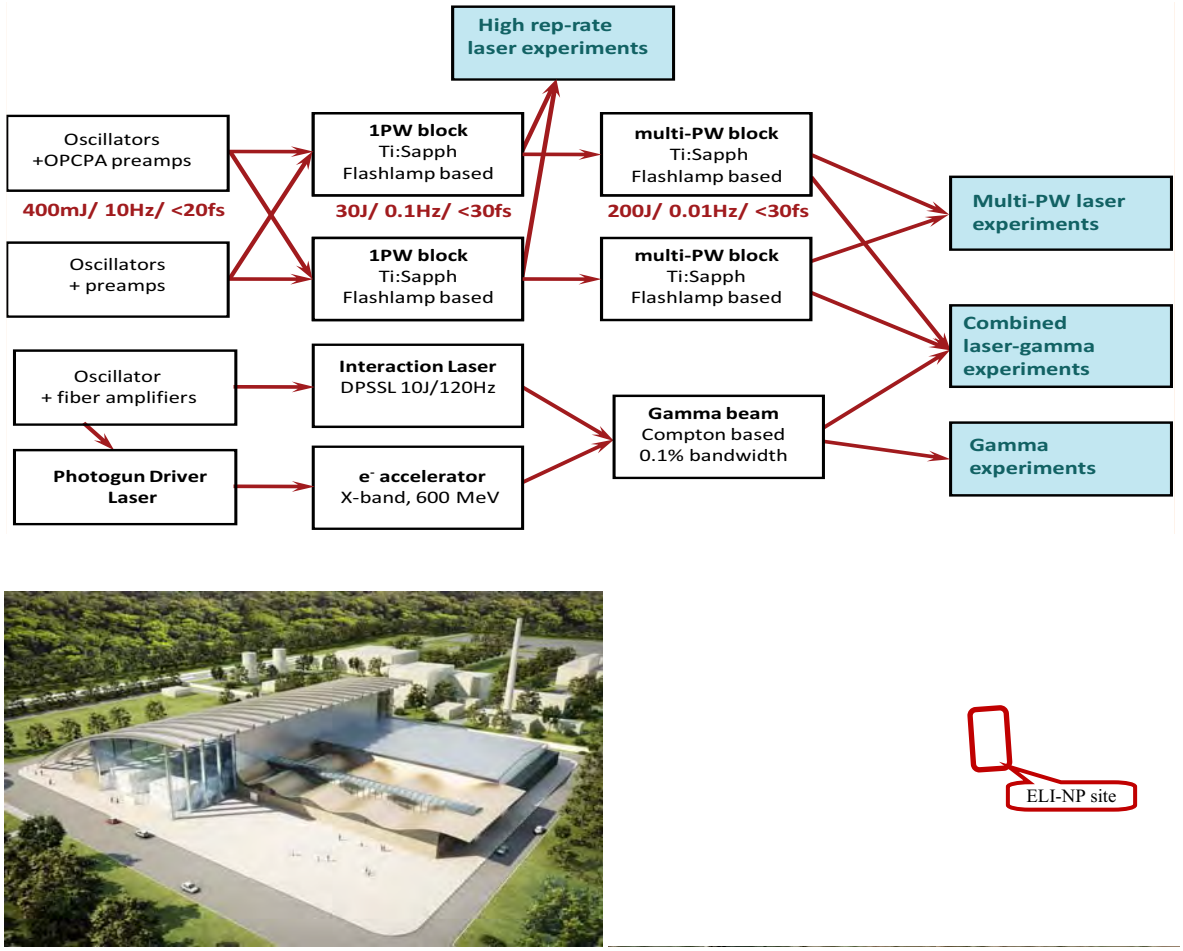

Figure 12: The schematic layout of ELI-NP facility. left: general architectural concept; right: satellite view of site with the forest ring around existing IFIN-HH facilities.

Coupling a high power laser with a gamma beam will confer ELI-NP facility a truly unique character in the world. Indeed, none of the many existing new projects, lasers with powers similar to those proposed for ELI-NP, will not be able to benefit from the gamma beams synergy proposed here. Technically, the temporal and spatial superposition of ultra-short laser and gamma pulses will be for the first time implemented and demonstrated at ELI-NP.

The general architectural concept of the facility is presented in Fig. 12. Experiments will be distributed in eight experimental halls, reconfigurable due to the use of movable concrete blocks, having main primarily thematic assignment as follows:

- E1 – laser induced nuclear reactions;
- E2 – nuclear resonance fluorescence and applications;
- E3 – positrons source and experiments;
- E4/E5 – accelerated beams induced by high repetition 100 TW/1 PW pulses;
- E6 – intense electron and gamma beams induced by high power laser beams;
- E7 – experiments with combined laser and gamma beams;
- E8 – nuclear reactions induced by high energy gamma beams.

ELI-NP will be built at Magurele, Ilfov County, at 15 km Southwest of the center of Bucharest,

on the premises of the "Horia Hulubei" National Institute of Research and Development in Physics and Nuclear Engineering (IFIN-HH).

5 Phasing of the institutional and legal implementation of ELI

In order to promote the pan-European character of ELI and ensure consistency between the three project teams during the implementation phase, the three hosting countries have established an interim organisation, the *ELI Delivery Consortium*, entitled with two essential responsibilities. On the one hand, the ELI Delivery Consortium will be in charge of defining a single delivery plan for the whole project making optimal and coordinated use of the expertise and financial and human resources available in Europe. On the other hand, the Consortium will negotiate and submit to the European Commission the application for establishing the ELI-ERIC on the basis of a detailed definition of the governance and financial scheme of the future infrastructure. For that purpose, the hosting countries have invited all funding agencies represented in the ELI Preparatory Phase Consortium to join the Delivery Consortium.

The consortium is currently established as a structure with no legal personality on the basis of a Memorandum of Understanding signed in April 2010 by the Czech, Hungarian and Romanian plenipotentiaries for ELI.

6 Financial requirements and funding scheme

Implementation phase

Implementation budget

The implementation costs of each of the three first ELI facilities have been evaluated by the local implementation teams in the three hosting countries on the basis of the specifications described in this White Book and expert studies performed in relation with the building designs. They represent the best estimates as of December 2010. We provide here only total figures, the breakdown being still subject to negotiation with the funding authorities. All figures below cover preparation costs (additional to those already covered by the preparatory phase of ELI and covered from other sources[1]), construction and commissioning of the three first ELI facilities.

As shown in the two tables below, the budget of the three ELI facilities have a fairly similar scale, ranging from € 243.7 million to € 341 million (including VAT).

Table 1 shows the distribution of the total costs according to these categories. Items 1 to 5 do not include value-added tax. At this stage, contingencies have not yet been evaluated in Hungary. It should be noted that those figures are still subject to negotiations with the Managing authorities and European Commission (see following section for more details).

The cost estimates presented here do not include the investment costs related to the implementation of the ultra-high intensity pillar of ELI, as the location and technological specifications of this fourth facility are yet to be decided. Yet, part of the technological developments that will be undertaken in the three host countries are meant to contribute to the future implementation of the fourth pillar.

[1] This includes in particular the whole or part of the costs related to the preparation of the applications for structural funds in the three host countries and to the detailed design of the facilities and equipment based on the work already carried out during the Preparatory Phase of ELI. The Preparatory Phase of ELI, started in November 2007 and ended in December 2010, benefited from a € 6-million grant financed by the European Commission (FP7).

Table 1: Detailed implementation costs of ELI (in € million and in % of total).

	Consolidated implementation budget	ELI-ALPS	ELI-Beamlines	ELI-NP
1	Site acquisition	1,8	10,4	0,0
2	Building costs (including planning and design fees)	45,6	60,4	65,5
3	Plant and machinery	123,9	141,2	169,3
4	Contigencies	0,0	5,7	14,0
5	Techncal assistance / Start-up grant, including:	28,0	32,5	31,2
	Payroll	20,0	21,7	23,0
6	VAT	44,4	40,2	61,1
T1	TOTAL (excluding VAT)	199,3	250,2	280,0
T2	TOTAL (including VAT)	243,7	290,4	341,1

Elements on the funding scheme of the implementation phase of ELI

The three facilities located in the Czech Republic, Hungary and Romania will be funded using structural funds. Funds are allocated on the basis of a strategic plan defined by each member state in cooperation with the European Commission and translated into specialised 'operational programmes'.

The three ELI facilities will be funded under three different "Operational Programmes" co-funded by the European Regional Development Fund (ERDF)[2]:

- The Operational Programme "Research and Development for Innovations" (OP RDI) in the Czech Republic[3]
- The Operational Programme "Economic Development" (EDOP) in Hungary[4]
- The Sectoral Operational Programme "Increase of Economic Competitiveness" (SOP-IEC) in Romania[5]

A specific evaluation process organised by the relevant national Managing Authority decides on the allocation of funding in each of these Operational Programmes. Given the level of funding – over € 50 million – the three facilities are considered *major projects* and have to be approved by the European Commission under the conditions set in the applicable European Regulation. The three Operational Programmes are neither synchronised nor interdependent. They are managed by three national Managing Authorities: the Ministry of Education, Youth and Sports for the OP RDI in the Czech Republic, the General Directorate of the National Development Agency for the EDOP in Hungary, and the National Authority for Scientific Research (as an "Intermediate Body") for the SOP-IEC in Romania.

Grants are co-funded by ERDF (up to 85%) and by national budgets. They cover almost all of the items of cost listed above and funds are eligible until December 2015. The rules conditioning the use of the European Regional Development Fund in the three host countries exclude the possibility of having a non-national entity as the applicant for funding or beneficiary of the grant. This precluded in particular having an international Consortium or even the ELI-ERIC as the applicant or direct beneficiary of the funds. In the three hosting countries, national entities – existing entities or *ad-hoc* legal vehicles – will be in charge of preparing the application

[2] In all three countries, part of the investment is co-funded by national financial resources (approximately 15% in each of the three countries).

[3] For more information, see: http://www.strukturalni-fondy.cz/Programy-2007-2013/Tematicke-operacni-programy/OP-Vyzkum-a-vyvoj-pro-inovace

[4] For more information, see http://www.nfu.hu/new_hungary_development_plan

[5] See http://amposcce.minind.ro/ for more information.

and managing all activities related to the implementation of the ELI Project (all activities of implementation and coordination linked to the construction, research and development, setting-up, assembling, testing and commissioning of the three ELI facilities until December 2015):

- The Institute of Physics of the Academy of Sciences[6] in the Czech Republic
- The ELI-Hungary Limited Liability Company in Hungary, an *ad-hoc* not-for-profit public company owned by the town of Szeged, the municipality of Szeged the National Office for Research and Technology
- The Horia Hulubei National Institute of Physics and Nuclear Engineering[7], in Romania, in partnership with two other Institutes located in Magurele, namely the National Institute for Laser, Plasma and Radiation Physics and the National Institute for Research and Development for Material Physics.

Operational phase

The three hosting countries are currently working on a detailed evaluation of the running costs of each of the three facilities. This evaluation will be finalised under the aegis of the ELI Delivery Consortium in order to ensure the consistency of all assumptions and clarify the financial aspects of the governance model of the operational phase (in particular the exact distribution of tasks between the ELI-ERIC and the three local institutions that are currently in charge of the implementation).

At this stage, the annual operational costs have been estimated as follows:

- € 22 million for the ELI-ALPS facility
- € 21 million for the EL-Beamlines facility
- € 29 million for the ELI-NP facility.

Those figures represent the average[8] annual funding requirements of each facility and include re-investments. In practice, re-investment costs will vary over time and each facility will have its own re-investment profile. Here, re-investment costs have been taken into account on the basis of an annual average over the whole operational period.

The three hosting countries will most certainly contribute significantly to the operational costs as founding members of the future ELI-ERIC. They expect additional contributions from partners already involved in the Preparatory Phase Consortium and from other countries showing interest in the project. Negotiations on the establishment of the ELI-ERIC and therefore on contributions to the operational costs will be coordinated by the ELI Delivery Consortium under conditions that are still under discussion.

7 Time schedule

The overview of the implementation schedules of the three first ELI facilities is given in the white book and in the national applications for structural funds. As indicated above, in the three cases, the implementation phase is due to come to its end by 31 December 2015, in compliance with the rules pertaining to the use of structural funds.

[6] See http://www.fzu.cz/ and http://www.eli-beams.eu/

[7] See http://www.nipne.ro/ and http://www.eli-np.ro/

[8] Operational costs are expected to gradually increase in the first few years of operation and reach a plateau by 2019–2021.

Part I

ELI: Introduction and Vision

1 Introduction

Since the laser's first demonstration in 1960, we have seen a relentless pursuit toward large scale laser national infrastructures with the main motivation to fuse nuclei on earth for energy production. In this category the most advanced are the NIF at Livermore and the Laser Megajoule in France. The NIF for instance delivers a MJ in few nanoseconds, corresponding to a peak power of 0.5 PW.

A few years ago, was proposed the Extreme Light Infrastructure, ELI under the aegis of the ESFRI (European Strategy Forum for Research Infrastructure). It was largely inspired by a paper by T. Tajima and G. Mourou [1]. It was a new type of infrastructure designed to produce the highest peak power possible in the sub-exawatt regime or about 1000 times the NIF or The Laser Megajoule power. These gargantuan powers are obtained by packing the laser energy in extremely short pulses measured in femtoseconds or few optical periods. When focused to a spot size of about the size of the laser wavelength, i.e. few micrometers, extraordinarily large intensities will be produced, in the 10^{25} W/cm^2 range. Figure 1.1 sketches the laser focused intensity evolution over the years These intensities represent a formidable leap of 3–4 orders of magnitude over today's performance. They are called ultra relativistic intensities because of their capability to accelerate not only electrons but also ions to the speed of light.

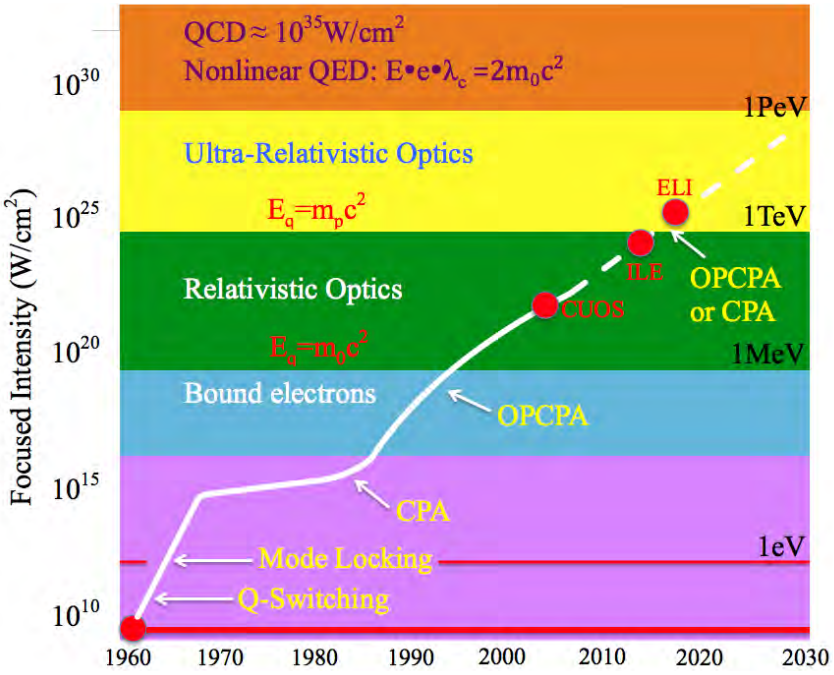

Figure 1.1: Sketches of the laser intensity over the years. It shows ILE/Apollon that is ELI one beam prototype. ELI will include 10 ELI/Apollon-type beams. It shows also that zetawatt and 10^{28} W/cm^2 level could be reached by harnessing megajoule systems like the National Ignition Facility and the Laser Megajoule.

They are the gateway of a new type of interaction that will make possible for the first time the possibility to penetrate beyond the stratum of atomic physics to explore subsequent matter strata relevant to nuclear physics, particle high energy physics, astrophysics, field traditionally studied with high energy particle accelerators. ELI may bring a completely new approach to the investigation of fundamental physics where massive and charged particle; electron, ion are

replaced by the massless and chargeless photon, announcing a shift from the traditional paradigm based on momentum to one based on energy.

The laser ultra-relativistic intensity is ELI's quintessence. It underpins the following features that form its foundation. In particular it leads to:
1) the highest electromagnetic field,
2) the possibility for light to move matter, electrons and ions at relativistic velocity.
3) The generation of coherent or incoherent high energy radiation, X or γ,
4) the possibility to produce much shorter pulse than the initial one in the zeptosecond-yoctosecond range.

These four unique features alone or combined offer a new set of powerful structural dynamic tools. They define the adopted ELI's four-pillar architecture.

1.1 ELI: A Science Federator in an Integrated Infrastructure

The initial plan called ELI to be under one roof in one location, while the final design is to build ELI as a distributed Pan-European Infrastructure with four pillars. After careful consideration and discussion it was found that although more expensive such solution would have a considerably stronger impact on the structure of European research infrastructures and on the development of local scientific and industrial communities than if ELI were built on a single site. Analysis of user statistics within LASERLAB-EUROPE seems to imply that the existence of large research infrastructures within a country are indispensable for the creation of a productive national scientific community. On the educational and technology transfer ground, it is expected that it will be more effective in attracting students and creating spinoff companies. This is the more important as optics and photonics is considered as one of the five key enabling technologies (KET) by the European Commission. The four pillars will be under one unified governance and specialized according to the selected themes.

- ***the Attosecond Science facility in Hungary:*** attosecond pulses are naturally delivered during laser-matter interaction at ultrahigh intensities, Figure 1.2. It will provide a way to take snap-shots in the attosecond and may be in zeptosecond time scale, of the electron dynamics in atoms, molecules, plasmas and solids. Its site will be located at Szeged, Hungary.
- ***High Energy beam facility in Czech Republic:*** ELI will provide energetic particles ($> 10\,\mathrm{GeV}$) and radiations (up to few MeV) beams with ultrashort time structure produced from compact laser plasma accelerators. The site will be in Prague, Czech Rep.
- ***Nuclear Physics facility in Romania:*** In its first fifty years the laser revolutionized the atomic physics but the electric field was too weak to probe the nucleus. With ELI the ultra high field combined with short time-duration γ-ray, will provide a way to interrogate the nucleus structure and dynamics. Its site will be Magurele, Romania.
- ***The Ultra High Field Science (site to be decided in 2012):*** In this pillar, ultra high intensity will be applied to Nonlinear Field theory, Nonlinear QED, Vacuum Physics, High Energy Particle Physics and Gravitational physics. The site and ultra high intensity technology will be decided in 2012.

The three first infrastructures are scheduled to deliver their first light in by the end of 2015, whereas the high field infrastructure should be ready for experiments in 2017.

1.2 ELI: A Technology Booster

The ELI program is scientifically ambitious and demands the most challenging technical specifications. In particular it will require the highest peak power, in the 200 PW range necessary to produce the highest single shot signal. However, we will need the highest average power or repetition rate to maximize signal-to-noise ratio.

Sub-exawatt can not be reached by a single beam. Therefore, the current design calls for the development of beams of 10 PW peak power. This power could be produced by Ti: Sapphire (Apollon) but also by OPCPA (Optical Parametric Chirped Pulse Amplification). The power will be produced by 300 J delivered in 10–30 fs. The pulses must be immaculate in time with an excellent intensity contrast greater than 10^{15} for solid target experiments. The final decision between the two technologies will be done in 2012. The ultrahigh peak power pillar will require the phasing of at least 10 beams of 10 Petawatts. This challenge has never been attempted. It will require an excellent mechanical stability and optical pump stablity (1%). The 10 optical arms have to be maintained within $\lambda/20$ accuracy to provide the sought after coherent addition.

If we can produce easily extremely high peak power, it is still difficult to produce large average power above the 100 W. This is due in large part by the overall mediocre laser efficiency in the 1% range. A large effort largely based on solid state diode pumped lasers is undertaken in Czech Republic, Germany and United Kingdom to bring the efficiency to the 10% level.

The CPA (chirped pulse amplification) approach requires large Ti:sapphire crystals of around 20 cm diameter. Because of the ELI program, an American company has been already able to produce high quality crystals of this dimension and is trying to grow it to 25 cm diameter.

The most important hurdle in getting ultrahigh peak power is improving the diffraction grating optical damage threshold. At the moment diffraction gratings have a damage threshold at least 10 times less than other system components. A higher damage threshold would reduce the surface grating area and will reduce overall system cost and size. The ELI program is working on new grating designs that will lead to a large improvement in grating damage size and cost.

1.3 ELI: First European Laser Infrastructure and Geopolitical Science Attractor

Immediately after its announcement by ESFRI, ELI aroused scientist's and technologist's interest as a laser that would deliver the most powerful burst of energy with the capability to federate a number of scientific and technological disciplines, combined with a tantalizing societal application offering, in material science and medicine.

The numerous meetings among the 13 countries partners held during the Preparatory Phase have led to the inception of ELI and contributed to shape and unify the European science and technology landscape. The ELI Preparatory Phase of three years, culminated by the astonishing choice of three countries, Czech Republic, Hungary, and Romania that did not have an history to work together as the site of the first three pillars. Now they have been given the considerable challenge of establishing, in the central-eastern part of Europe not only the first ESFRI infrastructure, but also the first and largest civilian laser infrastructure.

However, the ELI's construction activity won't take place only in these three countries alone. It will spill over all the partner's countries expected to bring a considerable contribution by lending expertise, workforce and equipment. ELI by its science but also by its pan European character is becoming a recognized model and a beacon for the rest of the world. Today, because of ELI, the ultra relativistic interaction and Exawatt systems are on the agenda of most scientifically inclined countries, especially USA, Russia, China, Japan, India.. The fact that Europe is leading this development may be the result of a long-standing tradition in networking among national laser laboratories within the EC-funded network LASERLAB-EUROPE. It has prepared the laser community to segue from university size systems to large scale infrastructure so new scientific challenges can be addressed. ELI, the world's first truly international laser research infrastructure, appears as the natural culmination of this development.

ELI will also be the first large scale infrastructure that will propel the laser beyond the atomic physics frontier which has been hitherto, the laser privileged domain to penetrate into the deeper strata of nuclear physics and vacuum physics. This will be ELI's primary goal.

Having with ELI such a control of space, time, amplitude and polarization, nuclear reaction, nonlinear QED interaction could be produced and studied with minute accuracy as it is the case today in photochemistry or solid state physics. ELI will make possible to scout a field that could only be explored until now using pertubative theory.

1.4 ELI's Long Term Vision

Already now it appears as if ELI during its preparatory phase has created "new physics" in many areas, most notably in those which did not use lasers before. Examples which are already foreseen are nonlinear QED in strong laser field, laser-particle acceleration, and new ways to produce ultra-short wave length radiation in the hard x-ray or gamma-ray regime, frequently associated with ultra-short pulse durations. Other examples will inevitably arise from experiments once ELI goes into operation. ELI's long term vision certainly is to become the world's first and the world's best user facility to utilize the power of today's most advanced lasers for the advancement of fundamental science and applications in many areas of societal relevance, including the Grand Challenges of the 21st century.

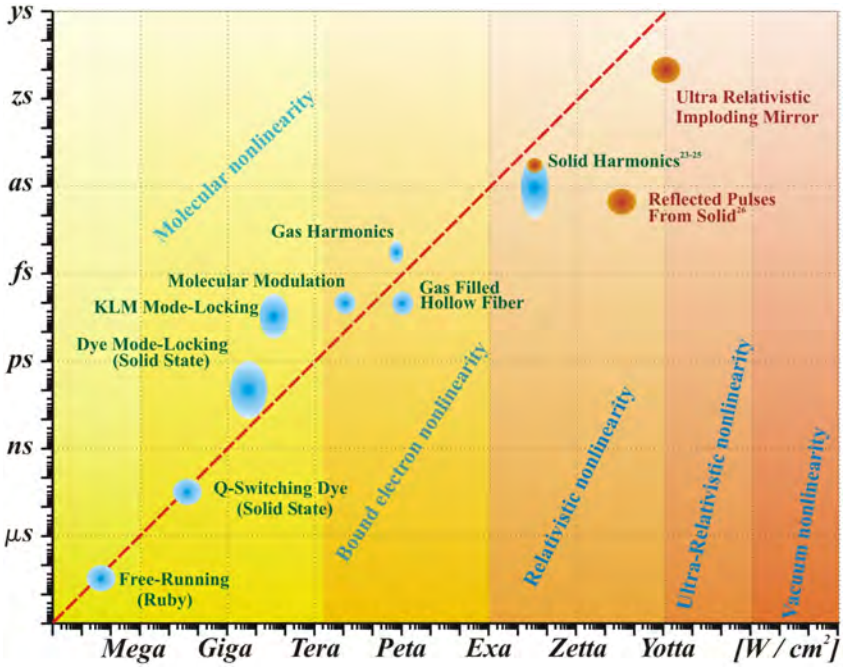

Figure 1.2: The Pulse Intensity-Duration Conjecture is shown. An inverse linear dependence exists between the pulse duration of coherent light emission and its intensity of the laser driver in the generation volume over 18 orders of magnitude. These entries encompass different underlying physical regimes, whose nonlinearities are arising from molecular, bound atomic electron, relativistic plasma, and ultra-relativistic, and further eventually from vacuum nature. The blue patches are from the experiments, while the red from the simulation or theory.

In addition, if ELI as an exawatt machine turns out to be an effective tool to address fundamental physics, it would help us to plan experiments at much higher peak power in the zettawatt regime. This type of power could, for instance, be obtained by harnessing already built megajoule systems. Figure 1.1 shows the evolution of the laser intensity over the years. There seems to be the possibility to go beyond the exawatt using already built megajoule large scale systems like the National Ignition Facility, NIF and soon The Megajoule. These machines

could become available for basic science within 10 to 20 years, once the campaign to demonstrate inertial fusion is concluded. If that were the case a new life could be given to these machines, for the benefit of science, by providing Schwinger size fields from the laser directly. In addition using Figure 1.2, describing the relationship between input intensity and output pulse duration [2], extremely short duration pulse below the zeptosecond regime could be produced.

This, however, may only be one of many ways to achieve the next level of laser powers, others may arise due to new and unexpected progress in laser technology as we have seen it frequently during the last decades. In any case, the next level of high power laser infrastructures beyond ELI could deliver simultaneously extremely high field with Schwinger magnitude, particles with PeV energy, and coherent bursts of gamma radiation with zeptosecond pulse duration tying the three distinct disciplines of science, i.e. ultrafast science, high field science, and large-energy laser science together with a single stroke.

Bibliography

[1] T. Tajima, G. A. Mourou, *Phys. Rev. STAB* **5**, 031301 (2002).
[2] G. A. Mourou and T. Tajima, *Science* **331**, 41 (2011).

Part II

ELI Science

2 The quest for extreme light

2.1 Investigation of Vacuum Structure – Towards Schwinger Fields: QED effects and Particle Physics at ELI

2.1.1 QED effects

Summary

An overview of QED and particle physics effects relevant for the fundamental physics potential of the Extreme Light Infrastructure (ELI) project is presented. This includes processes at tree level such as nonlinear Compton scattering and Unruh radiation as well as loop effects associated with strong-field vacuum polarisation. The latter come in two classes, dispersive and absorptive, as described by the real and imaginary parts of the vacuum polarisation tensor, respectively. Dispersive effects comprise modifications of photon propagation in strong laser fields due to vacuum birefrigence and diffraction. Absorption implies the 'disappearance' of photons due to pair production. We discuss a variety of pair creation processes differing in their characteristic energies and intensities and/or the presence or absence of stimulating probes. In contrast to standard weak field vacuum polarisation effects (Lamb shift, $g-2$) the processes discussed here are nonperturbative: they either involve an infinite number of diagrams to be summed or do not have a perturbative expansion at all. Examples are spontaneous vacuum pair creation via the Schwinger mechanism and laser photon merging in laser-proton collision. Moreover, we give a brief overview of the particle physics potential of the ELI facility. This includes the concept of a laser-driven collider and physics beyond the Standard Model, i.e. potential discovery of new particles such as axion-like and minicharged particles.

QED Physics: Introduction

The unprecedented laser intensities available at ELI allow, for the first time, to test the predictions of Quantum Electrodynamics (QED) in strong external laser fields [1]. The field amplitudes typical for strong field QED are of the order of the so-called critical field [2–6], $E_{cr} = m^2/e = 1.3 \times 10^{16}$ V/cm and $B_{cr} = m^2/e = 4.41 \times 10^{13}$ G (m here is the electron mass, $-e < 0$ its charge and natural units with $\hbar = c = 1$ are used throughout this chapter). These field amplitudes correspond to the laser intensity $I_{cr} = E_{cr}^2/8\pi = 2.3 \times 10^{29}$ W/cm^2. In general, QED predicts electron-positron pair creation from the vacuum in the presence of electromagnetic fields with an amplitude of the order of the critical fields. Intuitively, one may view this process as a break-up of the virtual e^e 'dipoles' that are omnipresent as fluctuations of the vacuum. Collectively, they produce what is known as vacuum polarization. Even for weak fields, this has observable consequences such as the Lamb shift and the electron and muon anomalous magnetic moment. The realm of strong fields (of order E_{cr}), however, has never been explored, in particular in the optical regime, and thus remains an uncharted region of the Standard Model. It should also be noted that one of the most important questions of contemporary physics is 'why do vacuum fluctuations not gravitate?' Thus, investigating these fluctuations in a new and rather 'extreme' environment may shed some new light on this possibly most difficult question of 'vacuum physics'.

In terms of Feynman diagrams, vacuum polarization is represented by a fermion loop. One can associate a mathematical expression with this graph which, above threshold, develops an imaginary part signaling the creation of real electron-positron pairs. As in this case photons 'disappear', pair creation is called an *absorptive* process. The real part of the fermion loop Feynman diagram, on the other hand, describes how virtual pairs polarizing the vacuum affect the propagation of probe photons and thus govern all *dispersive* effects. Schematically, the

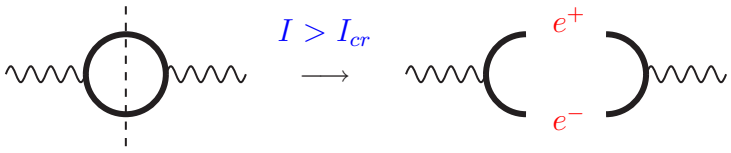

Figure 2.1: Pair production via 'break-up' of vacuum polarisation. Wiggly lines denote probe photons, the fat lines represent electrons and positrons 'quivering' in a strong laser background.

situation is depicted in Fig. 2.1 which shows how the vacuum polarisation loop involving *virtual* pairs 'breaks up' into *real* pairs for supercritical intensities, $I > I_{cr}$.

Technically, Fig. 2.1 is an illustration of the optical theorem (or a Kramers-Kronig relation) which states that the imaginary part of the vacuum polarisation loop (left-hand side) is proportional to the total pair creation probability on the right-hand side. Note that this provides a connection between a loop diagram and tree-level diagrams. Crossing the latter one obtains diagrams describing strong-field Compton scattering and photon annihilation.

In the following, we present an overview of the processes involved and the prospects of observing them at ELI. We begin discussing nonlinear Compton scattering and the Unruh effect. The next section describes several variants of pair production followed by a presentation of dispersive effects. QED cascade processes observable at ELI are discussed in subsequent section. Finally, the experimental requirements are briefly listed before we conclude.

Nonlinear Compton scattering, Single-photon emission

The process in question is the collision of an electron and a high intensity laser beam such that a photon γ is scattered out of the beam. In terms of dressed electrons this is depicted on the left-hand side of Fig. 2.2 which, when expanded in the number of laser photons involved, becomes a sum of diagrams of the type shown on the right-hand side representing the processes

$$e + n\gamma_L \to e' + \gamma \,. \tag{2.1}$$

Here, the electron absorbs an arbitrary number n of laser photons ($\omega_L \simeq 1$ eV) before emitting a single photon of energy ω'.

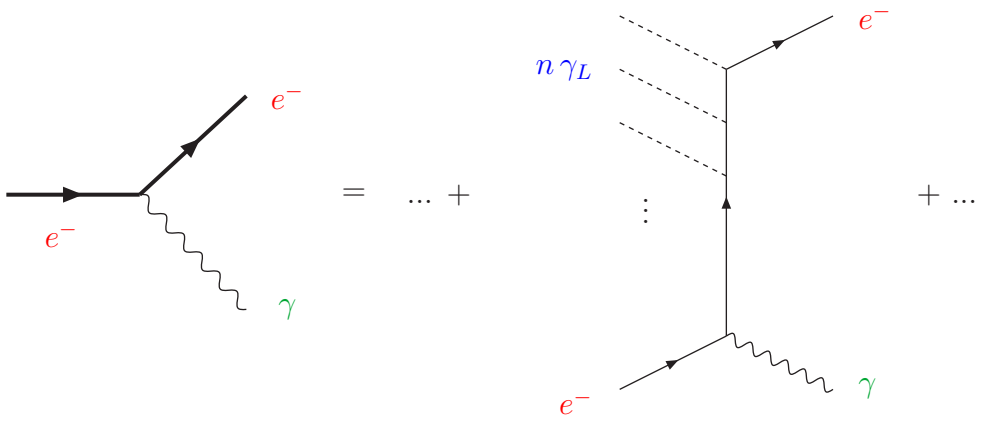

Figure 2.2: Feynman diagrams for nonlinear Compton scattering.

Note that the tree-level diagrams involved have a classical limit which is a good description of the process when the electron mass m is the dominant energy scale. This classical limit is

referred to as Thomson scattering. In terms of lab quantities, for the latter to be valid, one requires $\gamma \ll m/\omega_L \simeq 10^5 \ldots 10^6$ where $\gamma \equiv /m$ is the γ-factor of the electrons[1]. It is important to emphasise that the processes (2.1) are not suppressed by any threshold effect. Thus, one can study intensity effects at arbitrarily low centre-of-mass energies both for photons and electrons. This is quite a unique feature of nonlinear Thomson/Compton scattering and singles out this process from a particle physics point of view.

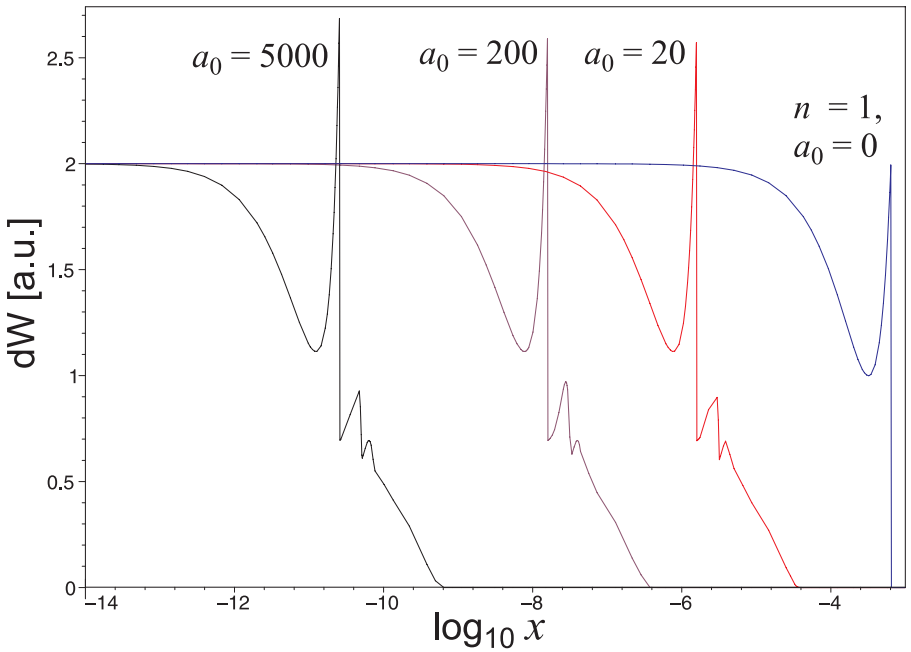

Figure 2.3: Shift of the (linear) Compton edge as a function of the Lorentz invariant x, for electron energy $E_p = 40$ MeV and different intensities a_0.

In Fig. 2.3 we show the photon emission rates as a function of a suitably chosen Lorentz invariant, x, which basically measures the energy of the scattered photons in any chosen reference frame. The peak at the very right corresponds to standard ($n = 1$) low intensity ($a_0 \simeq 0$) Compton back scattering of laser photons colliding with a 40 MeV electron beam. Using a *polarised* laser beam this may be used to produce polarised high energy photons of an energy given by the linear Compton edge value, $\omega'_{max} \simeq 4\gamma^2\omega_L$ [7, 8]. Note that, in the lab frame, substantial energy is transferred from electrons to the scattered photons (blue-shift). In an astrophysical context such a process is referred to as 'inverse Compton scattering'. This is to be contrasted with 'normal' Compton scattering (Compton's original experiment) where the electrons are at rest in the lab and one observes a red-shift of the photon frequency ω_L. Employing the inverse Thomson/Compton up-shift new facilities are currently under way for producing brilliant hard X-rays, see e.g. [9, 10].

To study intensity effects one uses the (quantum) theory for high-intensity Compton scattering, developed in the 1960's. This is based on Volkov electrons as asymptotic scattering states [11–14] and may be found in the textbook [15] (for a recent review emphasizing lab frame signatures see [16]). The most striking experimental signal is a red-shift of the linear Compton edge, from $4\gamma^2\omega_L$ to $4\gamma_*^2\omega_L$ with $\gamma_*^2 \equiv \gamma^2/(1 + a_0^2)$. This may be understood in terms of the

[1]The precise invariant statement is $p \cdot k \ll m^2$ where p and k are the 4-momenta of incoming electrons and photons, respectively. Note that k is of order $\hbar k = \hbar(\omega_L/c, \mathbf{k})$ upon reinstating $\hbar$ and c.

electron mass shift [17, 18] mentioned earlier,

$$m_* = m\sqrt{1+a_0^2}\,. \tag{2.2}$$

As the electron 'gains weight' ($m \to m_*$) it will recoil less, reducing the energy transfer to the final state photon, hence the red-shift in the maximum photon energy[2]. This effect is illustrated in the photon spectrum of Fig. 2.3 for $a_0 = 20$, 200 and 5000, the latter value expected for ELI. It is interesting to consider what one would observe in the lab frame. We have seen that backscattering off high-energy electrons ($\gamma \gg 1$) produces a blue-shift ('inverse' Compton). On the other hand, high intensity ($a_0 \gg 1$) produces a red-shift, hence works in the opposite direction. It turns out that there is exact balance in the centre-of-mass frame of the Volkov electrons and the n laser photons, that is when $4\gamma_*^2 \simeq 1$. This can obviously be achieved by fine-tuning γ and a_0: for 40 MeV electrons the associated a_0 is about $2\gamma \simeq 160$. Hence, for a_0 of this order or larger one expects an overall red-shift, $\omega' < \omega_L$, as the Volkov electron has become so heavy that it appears almost 'static' from the photons' point of view. For ELI intensities the Compton backscattered photons will always be red-shifted unless the electron energy exceeds 1 GeV.

The dominant spikes in Fig. 2.3 correspond to single-photon absorption, $n = 1$ in (2.1). However, these spectra also show further peaks corresponding to absorption of $n = 2, 3, \ldots$ laser photons, i.e. higher harmonic generation. Their identification will depend crucially on the size of the background noise which may wash out the signals of higher harmonics. Similar effects are expected as a result of finite beam duration [19]. It will hence be important to simulate the scattering process numerically using realistic beam pulse shapes.

Nonlinear Compton scattering (2.1) has been observed and analysed in the SLAC E-144 experiment [20, 21] using 47 GeV electrons from the SLAC beam and a Terawatt laser with $a_0 \simeq 0.4$. This was a high energy ($\gamma \simeq 10^5$) and low intensity ($a_0 < 1$) experiment (hence deep in the 'inverse' Compton regime). Photon spectra were not recorded and hence no red-shift was observed [22]. We reemphasize that this easily accessible process should be studied to a high precision with high-power optical lasers as a first step in exploring the uncharted region of low energy and high intensity QED. Also, note that radiation reaction effects can be measured in Compton and Thomson scattering [23].

Nonlinear Compton scattering, Entangled photon pairs and the Unruh effect

Electrons in a laser field undergo an oscillatory motion and are thus strongly accelerated. As every accelerated charge, they emit Larmor radiation, which can be understood as Thomson (or Compton) backscattering of the laser photons. In terms of Feynman diagrams, this process corresponds to the emission of single independent photons. However, there are also further (higher-order) Feynman diagrams corresponding to the emission of two entangled photons. This process cannot be explained within classical electrodynamics and is a pure quantum effect. Transforming to the accelerated frame comoving with the electrons, it can be understood as a signature of the Unruh effect – which states that a (uniformly) accelerated observer experiences the usual Minkowski vacuum as a thermal state. (The analogy is not quite perfect since the electron is not uniformly accelerated etc., but this main idea remains, see, e.g., [24–26]). This quantum effect might be detectable with ELI: Using a thin carbon foil (with a thickness of a few nm) and pushing out the electrons with a strong laser beam, one may obtain a thin sheet of electrons moving perpendicular to the plane with relativistic velocity $\gamma = \mathcal{O}(10)$. Illuminating the electron sheet with a counterpropagating optical laser beam with a laser parameter of order one, the electrons would see a frequency around $\mathcal{O}(10\,\mathrm{eV})$ and thus the laser wavelength in the

[2]Hence, if one is interested in a large energy up-shift one should rather use low intensity beams ($a_0 < 1$) to scatter off from the electrons.

rest frame of the electrons would exceed the thickness of the sheet, i.e., the electrons would act coherently. After a few hundred laser cycles, the probability that *one* electron emits a classical (Larmor) photon is of order one, while the probability for a quantum (Unruh) pair is much smaller $\mathcal{O}(10^{-14})$. However, the sheet contains $N_e = \mathcal{O}(10^9)$ or more electrons (depending on the lateral dimensions etc.), which act coherently – and thus we obtain (in the ideal case) a huge number $\mathcal{O}(N_e^2)$ of classical (Larmor) photons, but also many $\mathcal{O}(10^4)$ pairs of entangled (Unruh) photons [26]. Since the classical (Larmor) radiation and the entangled (quantum) pairs are emitted in different directions with different energies and polarizations, it should in principle be possible to distinguish them. Apart from detecting the quantum effect, a refined setup might even serve as a source for entangled photon pairs in the energy range $\mathcal{O}(100\,\mathrm{eV})$.

Absorptive vacuum polarization effects

In this section we will discuss absorptive vacuum polarization effects, namely electron-positron pair creation from vacuum in the presence of strong laser fields as available at ELI. A pictorial overview in terms of Feynman graphs is given in Fig. 2.4 (adopted from the review [27]).

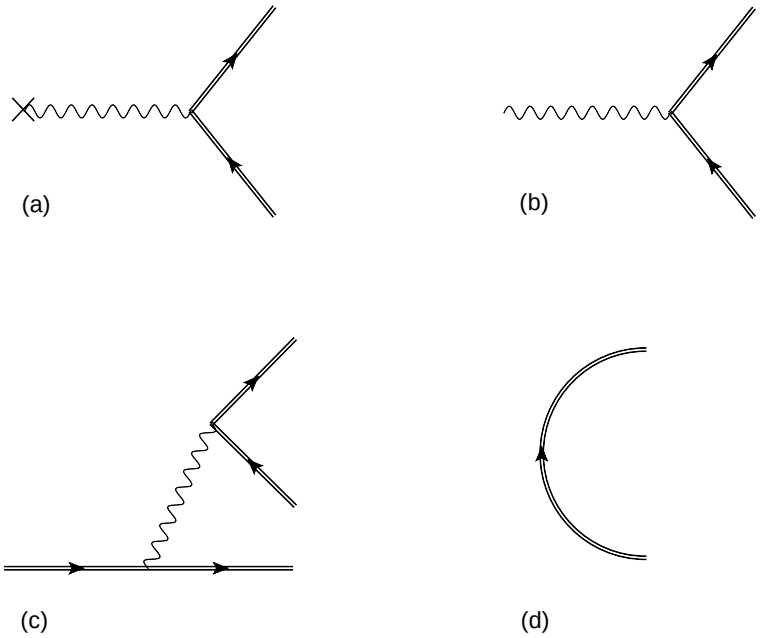

Figure 2.4: Variants of pair production processes in the presence of a strong laser field. Double lines denote electrons/positrons dressed by the laser field, wiggly lines represent probe or virtual photons. (a) Pair production in the presence of a Coulomb field (denoted by $\times$), (b) multiphoton Breit-Wheeler pair production, (c) trident process, (d) 'spontaneous' pair production via the Schwinger mechanism ('vacuum breakdown').

The strong-field trident process has been addressed in the context of SLAC E-144 and, quite recently in [29, 30].

Breakdown of QED vacuum in strong focused laser beams

The process of e^+e^- pair creation by a single and by two colliding focused laser pulses in vacuum is considered here (see Fig. 2.4(d)). Pair production by a laser pulse in vacuum strongly depends on the geometry of the electromagnetic field at the focus. Here, we use the field model

developed in [31]. In this model, the laser field contains nonvanishing longitudinal components of the electric and magnetic fields in the focal region. There are two types of waves with either electric or magnetic transverse vectors (e- or h-polarized waves, respectively). The model is based on an exact solution of the Maxwell's equations and reproduces certain properties of the laser pulse that are common for all focused waves in vacuum.

Unfortunately, there is no exact solution to Dirac's equation for an electron interacting with such a field. However, it was shown by A. I. Nikishov [32] that the formation length for the process of pair creation by a constant electric field E in vacuum is $l_f \sim \lambda_c(E_{cr}/E)^{3/2}$ if $E E_{cr}$, where $\lambda_c = 1/m = 3.86 \cdot 10^{-11}$cm is the electron Compton length. Therefore l_f is much less than the laser wavelength λ when the peak field strength of the laser pulse E_0 satisfies the condition $E_0 \gg E_{cr}(\lambda_c/\lambda)^{2/3}$. Physically, this means that to calculate the number of created pairs per unit volume and unit time, we can use the formulas derived for the case of the constant field and then obtain the total number of created pairs as an integral over the volume and duration of the laser pulse. The same arguments are also valid for the effect of harmonic generation in a laser pulse in vacuum.

The probability of pair production by a single laser pulse turns out to be significantly different for different polarization types [33]. In our model, pairs are most efficiently produced by an e-polarized pulse. In this case, the number of pairs produced by a single pulse strongly depends on the focusing parameter $\Delta = \lambda/2\pi\sigma$, where σ is the radius of the focal spot. The number of pairs decreases sharply when $\Delta \to 0$, whereas such a dependence is not observed for two colliding pulses. In the model under consideration, a single e-polarized pulse with wavelength $\lambda = 1$ μm, duration $\tau = 10$ fs, and focusing parameter $\Delta = 0.1$ produces one pair at the intensity that is almost two orders of magnitude lower than I_{cr}. This is because the effective volume of the laser pulse where pairs are efficiently produced is much larger than the Compton volume. Owing to the exponential dependence of the probability of pair production on the peak strength E_0 of the electric field in the pulse, the number of pairs increases sharply with E_0. The increase is so sharp that at $I \sim I_{cr}$ the total energy of created pairs becomes comparable with the energy of the pulse itself. Thus, the effect of pair creation leads to a collapse of the laser pulse and hence sets the natural limit for attainable focused laser pulse intensity. The limiting intensity is of the order of $0.3\, I_{cr}$ for the pulse with the parameters as indicated above.

The efficiency of the process in the field of two colliding pulses is much higher than that in the field of a single pulse. For the case of two colliding laser pulses the effect of pair creation becomes observable at the intensity of $I \sim 10^{26}$ W/cm^2 of both pulses, which is very close to the value which is planned to be obtained at ELI. Hence, in the case of colliding pulses the back reaction of the effect of pair production on the field producing them should be taken into account for intensities that are one to two orders of magnitude lower than the attainable maximum value.

Pair creation in combined laser and Coulomb fields

In relativistic collisions of charged particles with intense laser beams electron-positron pairs can be generated. This was demonstrated in the multiphoton regime ($a_0 = eE_0/m\omega_0 \ll 1$, with ω_0 and E_0 being the laser photon energy and the laser electric field amplitude, respectively) ten years ago at SLAC with a 46 GeV electron beam [28]. Electron-positron pair production in the tunneling regime ($a_0 \gg 1$) could be realized at ELI within an all-optical setup where the relativistic electron beam (of ~ 1 GeV) is produced via laser wake-field acceleration. At 10^{22} W/cm^2, the production rate can be estimated as $\sim 10^{12}$ sec^{-1} per projectile electron. While in the SLAC experiment the pairs were predominantly produced indirectly by a Compton-backscattered high-energy γ-photon (Breit-Wheeler process, Fig. 2.4(b)), in the ELI experiment a significant contribution would arise from the direct production channel of laser photon absorption in the Coulomb field (Bethe-Heitler process, Fig. 2.4(a)).

Almost pure Bethe-Heitler pair creation occurs in collisions of laser fields with heavy projectiles like protons or ions where the Compton channel is strongly suppressed. Analytical formulas for the corresponding total production rates in various asymptotic regimes can be found, for example, in [34]. In laser-ion collisions bound-free pair production can also happen, where the electron is created in a bound atomic state of the projectile nucleus [35]. For high nuclear charges the bound-free channel can compete with the usual free pair creation.

Very recently, muon pair creation has also been considered in relativistic laser-ion collisions. It may occur in a two-step process [36] where first an electron-positron pair is created via tunneling in a powerful low-frequency laser field which is then driven into an annihilating recollision to produce the muons (see also [37]). Another possibility is the direct production of muon pairs through few-photon absorption in ultrarelativistic ion collisions with x-ray laser pulses [38].

Dynamically assisted Schwinger mechanism

One of the main reasons why the Schwinger mechanism is very interesting from a fundamental point of view lies in the fact that it is of purely nonperturbative nature. In order to explain this statement in more detail, one has to specify the meaning of "nonperturbative". Given some perturbative expansion, one might call parameters within the radius of convergence of this expansion the perturbative regime, while the rest is nonperturbative. However, the Dyson argument shows that the radius of convergence of the perturbative expansion in powers of α_{QED} is actually zero, such that this notion cannot be applied here. In order to gain some insight, let us consider the Volkov solutions describing an electron in a laser field, which is treated as a classical plane wave

$$\psi_p(x) = u_p[1 + q\, f_p] \exp\left\{-ip\cdot x + q\, g_p(x) + q^2\, h_p(x)\right\}\,, \tag{2.3}$$

Where $f_p, g_p(x)$, and $h_p(x)$ depend on the laser field, but not on the electron charge (i.e., coupling constant) q. If the Keldysh (adiabaticity) parameter (which is the inverse of the laser parameter a_0)

$$\gamma = \frac{m\omega}{qE} \tag{2.4}$$

is large, one may Taylor expand Eq. (2.3) and just keep the terms to lowest order in q. On the other hand, if γ is small, the lowest-order terms are not enough and one has to include all the terms up to a very large order q^n with $n \gg 1$. In terms of Feynman diagrams, one has to sum over diagrams with many ($n \gg 1$) external field lines describing the laser. Since the perturbative expansion of QED is expected to diverge at large orders $n = \mathcal{O}(1/\alpha_{\mathrm{QED}}) = \mathcal{O}(137)$, one might call these processes nonperturbative.

However, there is still a crucial difference to the Schwinger mechanism: Here, pair creation occurs via a tunneling process and thus the rate scales with

$$P_{e^+e^-} \propto \exp\left\{-\pi\,\frac{m^2}{qE}\right\} \tag{2.5}$$

In contrast to Eq. (2.3), this form contains an essential singularity in q (and E) and hence it can *never* be obtained by a perturbation (i.e., Taylor) expansion in q up to arbitrarily large (finite) order n. Therefore, this process is purely nonperturbative. In QCD, such nonperturbative effects are very important. For example, the gluon condensate is explained in the instanton picture via a ongoing tunnelling events whose rate scales with $\exp\left\{-4\pi/g^2\right\}$. Of course, the coupling strength g in QCD (which is the analogue of the charge q in QED) is rather large and thus there is ample experimental evidence for these purely nonperturbative effects. In QED, experimental access is far more difficult due to the smallness of α_{QED}, but with ultra-strong lasers, it might become possible.

With an electric field corresponding to a peak intensity of $10^{27}\,\mathrm{W/cm^2}$, the Schwinger exponent $\exp\{-m^2/(qE)\}$ yields a suppression of $\mathcal{O}(10^{-20})$ which can be compensated by the comparably large four-volume of the focal spot of the laser $(\lambda_{\mathrm{laser}}/\lambda_c)^4 \approx 10^{22}$, i.e., pair creation should be observable. For a peak intensity of $10^{26}\,\mathrm{W/cm^2}$, one the other hand, we have $\exp\{-m^2/(qE)\} = \mathcal{O}(10^{-61})$, which renders an observation very difficult. In this case, however, one might employ the dynamically assisted Schwinger mechanism: Superimposing the strong optical laser by a suitably chosen weaker x-ray pulse, one may help the (virtual) electron-positron pairs to partially bridge the energy gap of $2mc^2$. Then the effective way to tunnel is reduced and the pair-creation probability is enhanced to [39]

$$P_{e^+e^-} \propto \exp\left\{-\pi\,\frac{m^2}{qE}\,f(\omega)\right\}\,, \tag{2.6}$$

where $f(\omega) \leq 1$ is a function of the frequency ω of the x-ray pulse (and the pulse shape etc.). Even for frequencies ω well below the energy gap of $2mc^2 \approx 1$ MeV, $f(\omega)$ decreases significantly – which might facilitate the observation of this effect for $10^{26}\,\mathrm{W/cm^2}$. Note that Eq. (2.6) clearly shows that we are still in the purely nonperturbative regime, i.e., the tunneling picture still applies. Finally, for a peak intensity of $10^{25}\,\mathrm{W/cm^2}$, we have $\exp\{-m^2/(qE)\} = \mathcal{O}(10^{-193})$ and thus it will probably be extremely hard to observe pair creation without going to very large frequencies $\omega \gg 1$ MeV, where the classification as purely nonperturbative tunnelling will be difficult.

Another setup of assisted electron-positron pair creation in which a high-energy photon and a strong laser field collide with an ultrarelativistic proton has been proposed in [40].

Enhanced pair creation from multiphoton laser-vacuum breakdown

Electron-positron pair production from vacuum in the presence of strong electromagnetic fields has been an area of rich theoretical and phenomenological investigation [2–6, 41–46], especially in recent years [47–52]. As laser technology develops rapidly, an experimental verification of this phenomenon is becoming feasible [53–55] especially at ultra-intense laser facilities such as ELI [56] and XFEL [57]. Electron-positron pair creation has been observed at SLAC (E-144 experiment) [28] (Fig. 2.4(b)). This work aims at presenting experimental configurations and relative numerical estimates for multiphoton pair production from vacuum in the presence of strong electromagnetic fields as those expected to be provided by the ELI laser facility in the exawatt or even zettawatt regime. The approximations used are the imaginary time method [44, 47, 48] and the two-level-on-resonance multiphoton approximation [58–61].

An ELI oriented E-144 experiment for pair creation would consist of a configuration where in a first step a high-intensity, ultra short ($\tau \sim$ 20–25 fs) laser beam of laser photon energy $\omega = 1$ eV is used to produce and accelerate an electron beam to the relativistic energy regime of a few tens of GeV (theoretical estimates for the ELI system allow up to 100 GeV) (see also Subsection 3.2). In a second step the electron beam collides head-on with the same focused laser beam. In the electron's frame the photons have energy $\omega^* = 2\gamma_L\omega$ where $\gamma_L = E_{e-beam}/m$ is the Lorenz factor and E_{e-beam} is the energy of the electron beam. The electric field strength in that frame is $E^* = 2\gamma_L E$ leading to a subsequent increase of the intensity. It is shown that, within the range of applicability of the two-level-on-resonance approximation, electron beam energies up to 50 GeV can result in an increase of intensity up to 10^{27} W/cm^2 in the beam frame and an increase of the electric field strength up to 10^{16} V/cm. The two-level-on-resonance approximation then predicts up to 10^{14} pairs to be created in a 4-volume $V\tau \sim \sigma^3\tau$ (laser spot size $\sigma \sim 20$ μm) for quite low multiphoton orders. On the other hand it is shown that the tunneling regime of the imaginary time method gives very promising pair production efficiencies when the ELI laser facility is built in the exawatt or even zettawatt regime. It is demonstrated that electron beam energies up to 100 GeV can result in an increase of the electric field strength

up to 10^{18} V/cm in the electron beam frame. The nth-order probability per 4-Compton volume then reaches values up to $\sim 10^{54}$ m^{-3}s^{-1}, for n close to the threshold multiphoton order. For a realistic interaction 4-volume of 10^{-49} m^{3}s, the imaginary time method predicts up to 10^5 pairs per shot.

Finally, pair creation using a laser-based XFEL system is proposed and investigated by using the two level on resonance approximation. This table top XFEL utilizes a relativistic electron beam produced and accelerated by a high-intensity ($10^{22} - 10^{23}$ W/cm^2) ultrashort laser beam. The electron beam propagates through a wiggler system and an X-ray beam is produced. The X-ray photons have wavelength $\lambda = \lambda_u/2\gamma_L^2$, where λ_u is the undulator period. For an electron beam energy up to 1 GeV, X-ray pulse duration $\tau = 100$ fs, spot size $\sigma = 100$ nm and an estimated 5% conversion efficiency, the number of pairs created in $V \sim \sigma^3\tau$ rise up to 10^{11}.

We point out that there is a controversy among the authors about the results of this paragraph. The experimental test of these results by employing ELI is, for this reason, even more in demand.

QED cascades in intense laser fields

It is well known that an ultrarelativistic electron colliding with an intense laser pulse will emit a hard photon which in turn can create a relativistic e^-e^+ pair. This can result in origination of a chain of sequential acts of photon radiation and pair production, or an electromagnetic cascade. This effect, besides being interesting *per se*, will accompany any act of interaction of high energy particles with an intensive laser field both in vacuum, and in plasma, and thus is of crucial importance for physics of extreme light-matter interaction.

The intensity $I \geq 10^{24}$W/cm^2 will be obtained at ELI with very short and tightly focused laser pulses. Nevertheless, at such intensities the length of formation for elementary processes is all the same much less than the characteristic length of variation of the laser field. Therefore such field can be treated locally as a constant homogeneous field, compare Sec. 2.2.1.

Interaction of a single particle with a constant field is controlled by three parameters: two field invariants

$$\mathcal{F} = \frac{\vec{E}^2 - \vec{H}^2}{E_{cr}^2}\,, \quad \mathcal{G} = \frac{\vec{E}\vec{H}}{E_{cr}^2}\,, \tag{2.7}$$

and the dynamical parameter

$$\chi = \frac{e}{m^3}\sqrt{-(F_{\mu\nu}p^\nu)^2} = \frac{\sqrt{(\varepsilon\vec{E} + \vec{p}\times\vec{H})^2 - (\vec{E}\cdot\vec{p})^2}}{mE_{cr}}. \tag{2.8}$$

If χ is the largest parameter among these three, any constant field looks as a crossed one ($\mathcal{F} = \mathcal{G} = 0$) [11, 63]. The probabilities of the elementary processes in a crossed field were studied in [11, 63] and are well known, see also [64, 65]. Note that, if $\chi_e \geq 1$, recoil in the process of photon emission becomes essential, while pair creation by a photon becomes possible if $\chi_\gamma \geq 1$.

To estimate multiplicities of e^-e^+ pairs and photons for a cascade initiated by a high-energy electron or photon colliding with a laser pulse 1D master equations for electron, positron and photon occupation numbers have been used. The results, $N_{ee} \sim 2\chi_e$, $N_\gamma \sim 10^2\chi_e$ per half-period of the laser, are in good agreement with the E144 SLAC experiment [28] ($\chi_e \sim 0.1$), where the effect of pair creation by hard photons in a laser field was observed for the first time. With ELI facility, long cascades can be realized even at the first stage. For example, in a head-on collision of an electron beam of 10^6 electrons with energy ~ 50GeV and a laser beam of intensity 10^{23}W/cm^2 about 10^9 e^-e^+ pairs and 50 billions of photons per shot will be produced. The outgoing particles will be of relatively small energy of about 50MeV.

In agreement with [29], we expect that at laser intensities higher than 10^{24}W/cm^2 the cascades will be initiated even by initially slow electrons, because at such intensities the electrons will be accelerated by the laser field itself and will acquire high enough energy for the time small as compared with the pulse duration. To illustrate this possibility qualitatively, consider a toy model of an electron placed initially at rest in the uniformly rotating electric field. Let E_0 and Ω be the strength of the field and the frequency of its rotation. At $t \ll 2\pi/\Omega$ the growth of the electron energy can be estimated as $\varepsilon \sim eE_0t$. An important point is that the angle between the directions of the field strength and the momentum of an electron also increases, but as $\theta = \Omega t/2$. As a result, the parameter χ_e increases as $\chi_e = eE_0\varepsilon\theta/m^3 \sim e^2E_0^2\Omega t^2/2m^3$ and may become of the order of unity at $t \sim t_{acc} = E_{cr}/E_0\sqrt{m\Omega}$ if $t_{acc} \ll 2\pi/\Omega$, i.e. if $E_0 > E_{cr}\sqrt{\Omega/m} \sim 10^{-3}E_{cr}$. On the other hand, the probability of photon emission at $\chi_e \ll 1$ can be estimated by it's quasiclassical expression $W_{rad} = 1.44\alpha m^2\chi_e/\varepsilon$. It is easy to see that if $E_0 > E_* = \alpha E_{cr} \sim 10^{-2}E_{cr}$, then the total probability P_{rad} of radiation during the period t_{acc} is less then unity. This indicates that emission of hard photons with $\chi_\gamma \sim 1$ is quite probable if $E > E_*$. Such photons can produce a pair, however the resulting electron and positron will be much slower than the initial one. But they can be accelerated again by the field as discussed above, so that the cascade can proceed until either all the charged particles will be pushed out of the focus by the ponderomotive potential or considerable depletion of the incoming laser pulse will occur.

The results of preliminary numerical simulations are summarized in the Table 2.1. As it is seen from the Table 2.1, the cascades are expected to arise at the intensity level of 10^{24}W/cm^2 and that at the intensity of about 10^{26}W/cm^2 they will lead to depletion of laser pulse. The spontaneous pair creation from vacuum which can occur in the common focus of two collided pulses with total intensity $\sim 10^{27}$ W/cm^2 [27] seems to be the natural mechanism of injection of slow electrons in the center of the focus. In such set-up it will be possible to observe the substantial transformation of the energy of collided laser pulses into macroscopic jets of lepton plasma and photons.

Table 2.1: Multiplicity of self-developed cascades initiated by a slow electron versus laser intensity.

I, W/cm^2	N_{ee}
$2.7 \cdot 10^{23}$	negligible and depends on initial conditions
$6.7 \cdot 10^{24}$	15
$2.7 \cdot 10^{25}$	7800
$1.1 \cdot 10^{26}$	$1.6 \cdot 10^{10}$
$6.7 \cdot 10^{26}$	$3.6 \cdot 10^{30}$

Dispersive vacuum polarization effects

In this section we discuss different dispersive vacuum polarization effects that are theoretically predicted to be observed at ELI.

QED effects in laser-proton collisions

In this paragraph we investigate the vacuum polarization effects arising from the head-on collision of a high-energy proton and a strong laser beam [62]. In fact, the virtual electron-positron pairs surrounding the proton can absorb many photons from the laser field and emit after annihilating only one high-energy photon (laser photon merging). Below, we present the results of

our numerical simulations for an all-optical setup that can in principle be realized at ELI. The proton beam could be produced in the so-called laser-piston regime by shooting an ultra-strong laser beam onto a plasma slab [66]. According to the simulations of the latter, proton energies E_p of about 50 GeV can be envisaged. The other relevant proton beam parameters are: number of protons in the bunch 2×10^{12}, bunch transversal radius 5 μm and bunch duration 20 fs. We point out that the dominance of the process of laser photon merging with respect to multiphoton Thomson scattering requires $(E_p[\mathrm{GeV}]\omega_0\ [\mathrm{KeV}])^4 1.5 \times 10^4$, with ω_0 being the laser photon energy. The relatively low proton energy can be compensated by employing a strong attosecond pulse of extreme ultraviolet (XUV) radiation (see [67]): intensity of $I_0 = 1.4 \times 10^{24}$ W/cm^2, photon energy of 200 eV and pulse duration of 38 as. This XUV pulse, according to [67], can be produced by the reflection from a plasma surface of an ultra-strong laser pulse of 5 fs duration, intensity 2.5×10^{24} W/cm^2, focused onto a spot-radius of 5 μm which assumes a conversion efficiency of 4×10^{-3} (we have extrapolated the values of the conversion efficiency that in [67] are available for initial laser intensities up to about 10^{22} W/cm^2; however, the conversion efficiency weakly depends on the laser intensity at high relativistic intensities). We obtain that in one shot 6.9 photons are produced via 2-photon Thomson scattering, 5.2 photons via 2-laser photon merging only and 12.1 photons via the two processes together. In conclusion, in the described setup laser photon merging is in principle measurable. Moreover, by employing the maximum intensity envisaged at ELI of the order of 10^{26} W/cm^2 and by assuming that the results in [67] can be still be extrapolated to such high intensities, even nonperturbative refractive vacuum polarization effects and the merging of multiple laser photon pairs can be in principle observed [62].

Vacuum birefringence at ELI

A particularly important dispersive effect is vacuum birefringence as first discussed in Toll's thesis [68]. The polarized vacuum acts as a medium with preferred directions dictated by the external fields which we assume to be generated by a high-power laser of frequency ω_0. Accordingly, there are two different refractive indices for electromagnetic probe beams of different polarization states. These are

$$n_\pm = 1 + \frac{\alpha\varepsilon^2}{45\pi}\left\{11 \pm 3 + \mathcal{O}(\varepsilon^2\nu^2)\right\}\left\{1 + \mathcal{O}(\alpha\varepsilon^2)\right\}\ , \tag{2.9}$$

to the lowest order in (dimensionless) laser intensity$\varepsilon^2 \equiv I_0/I_{cr} \simeq (a_0\omega_0/m)^2$ and probe frequency $\nu \equiv \omega_p/m$. Here, $a_0 \equiv eE_0/m\omega_0$ is the dimensionless laser amplitude, a Lorentz and gauge invariant measure of laser intensity [69] which for ELI is estimated to be $a_0 \simeq 5 \times 10^3$ for $I_0 \simeq 10^{26}$ W/cm^2. Adopting this magnitude and an X-ray probe of $\omega_p = 5$ keV, one may achieve values of $\varepsilon \simeq \nu \simeq 10^{-2}$.

The experimental proposal [70] is to send a linearly polarized probe beam of sufficiently large frequency ω_p into a high-intensity region of extension d generated by one laser beam (or two counter-propagating laser beams) and measure the ellipticity signal, $\delta^2 \sim \omega_p^2(n_- n_)^2$ caused by a phase retardation of one of the polarization directions, see Fig. 2.5.

To the leading order in probe frequency ν and intensity parameter a_0^2, assuming a laser photon energy $\omega_0 = 1$ eV, one finds a signal of the size

$$\delta^2 = 1.1 \times 10^{-17}\left(\frac{d}{\mu\mathrm{m}\, a_0^2\,\nu}\right)^2 \tag{2.10}$$

Which grows quadratically with the dimensionless parameters ν and a_0^2 as well as the spot size d (taken to be the Rayleigh length). For ELI one expects a maximal value of $\delta^2 \simeq 10^{-4}$, assuming $\nu = 10^{-2}$, $a_0 = 5 \times 10^3$ and $d = 10$ μm. X-ray polarimetry (required when $\nu = 10^{-2}$) is

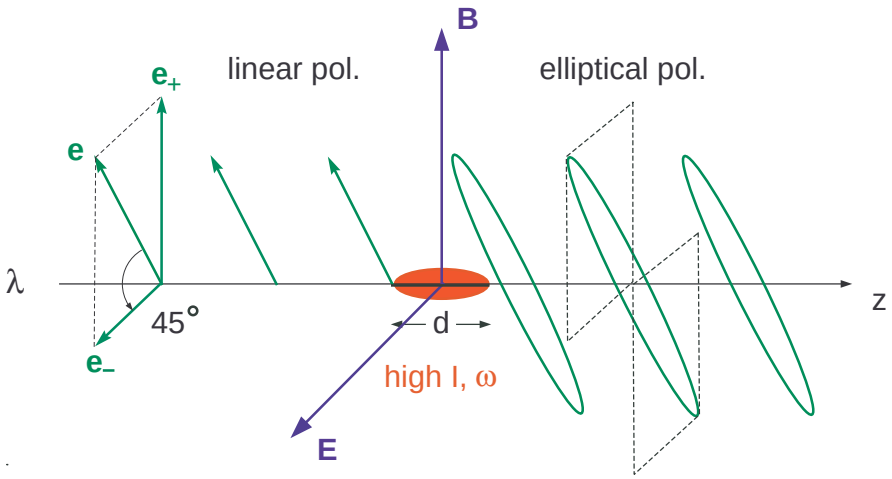

Figure 2.5: Schematic experimental setup to measure vacuum birefringence via an ellipticity signal.

currently sensitive to ellipticities of just about 10^{-4}. So one indeed requires intensities in the upper range of ELI specifications (10^{26} W/cm^2). However, the situation changes if one could produce polarized photon beams of MeV energies. Then the signal should increase significantly (with an expansion in $\varepsilon\nu = \mathcal{O}(1)$ no longer possible). Photon sources of this type can be obtained via Thomson or Compton backscattering off an electron beam generated, i. e., via laser wake field acceleration. Backscattering a probe laser (with$a_0 < 1$) off 3 Gev electrons, for instance, would yield 50 MeV γ-rays, hence $\nu \simeq 10^2$ compensating the 'small' $\varepsilon \simeq 10^{-2}$. In this case one becomes sensitive to the frequency dependence of the refractive indices in a regime where a Kramers-Kronig relation is expected between real and imaginary parts, the presence of the latter being tied to anomalous dispersion, $\partial n/\partial\nu < 0$ [71]. This would be an alternative signal for vacuum pair production [72], see Fig. 2.6.

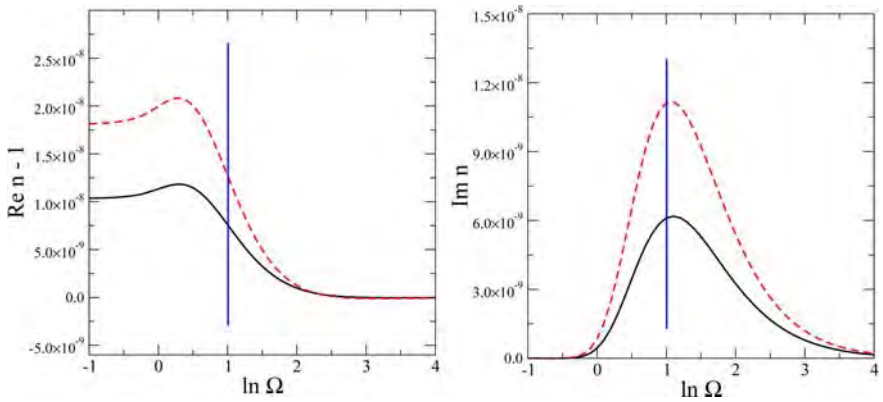

Figure 2.6: Real and imaginary parts of the QED refractive indices as a function of $\ln\Omega \equiv \ln\varepsilon\nu$. Dashed line: n_+, full line: n_-, vertical line: $\ln\Omega = 1$, achieved for photons backscattered off 3 GeV electrons.

Diffraction effects in laser-laser collision

QED predicts that electromagnetic waves interact in vacuum due to the presence of virtual electron-positron pairs. In a typical experimental setup one strong electromagnetic field polarizes the vacuum and another; usually weak field probes the induced vacuum polarization. Already in [68] it was pointed out that the polarized vacuum behaves like a dielectric medium. In [73] we have shown that the tight spot generated by a strong, focused laser field acts as a microscopic piece of matter that diffuses the probe field. This diffusion or diffraction alters the polarization state of the probe and if the probe initially is linearly polarized, then after the interaction it results elliptically polarized, with the main axis of the ellipse rotated with respect to the initial polarization direction (note that including laser's tight focusing reduces the effect of vacuum polarization of about one order of magnitude with respect to the results obtained by describing the laser field as an infinite plane wave [73]). The two observable quantities, the polarization rotation angle ψ and the ellipticity ε, can be written as

$$\psi + i\varepsilon = \frac{\omega_p}{8\pi}\frac{3\alpha}{45\pi}\frac{I_0}{I_{cr}}\frac{\omega_p V}{2y_d}\sin 2\theta. \tag{2.11}$$

In this expression $\alpha = e^2/4\pi \approx 1/137$ is the fine-structure constant, ω_p is the probe frequency, $I_0 = E_0^2/8\pi$ is the strong laser intensity, y_d is the observation distance from the interaction region, θ is the angle between the initial probe polarization and the strong field polarization and V is a complex quantity depending on the fields' parameters and on the observation distance (see [73]). We show below two numerical examples where, if the strong field is generated by ELI, the obtained values of the polarization rotation angle ψ and of the ellipticity ε are in principle measurable. In the first example the probe field is an X-ray beam and in the second one it is an optical beam. In both cases we set $\theta = \pi/4$, such that vacuum effects are maximal and we consider a strong optical laser beam with wavelength $\lambda_0 = 2\pi/\omega_0 = 0.745$ μm, spot radius $w_0 = 5$ μm and intensity $I_0 = 10^{25}$ W/cm^2. In the first example, we assume an X-ray probe with wavelength $\lambda_p = 2\pi/\omega_p = 0.4$ nm and waist size $w_p = 8$ μm. At $y_d = 20$ cm we find $\psi = \varepsilon \approx 3.5 \times 10^{-5}$ rad. These values of ellipticity and polarization are more than one order of magnitude larger than those in principle measurable in the X-ray regime [74]. In the next example, we consider an all-optical setup with a probe field wavelength $\lambda_p = 0.745$ μm and waist size $w_p = 300$ μm. We find that at $y_d = 20$ cm, then $\psi \approx 6.5 \times 10^{-10}$ rad and $\varepsilon \approx 3.5 \times 10^{-10}$ rad. In the optical regime values of ellipticities of the order of 10^{-10} rad can be measured nowadays [75]. The advantage of this second setup is, of course, that one does not need an additional X-ray source.

Elastic scattering between real photons

Direct observation of elastic photon–photon scattering among real photons would be an important benchmark test of laser-based QED experiments. Deviations from the expected scattering rate would indicate new physics in the low-energy regime. Throughout the last decades, several suggestions on how to detect elastic photon–photon scattering, using laser assisted schemes, have been put forward. Crossing electromagnetic waves can interact and yield new modes of different frequencies. One of the most prominent modes in such a mechanism is given by the four-wave interaction mediated mode satisfying the resonance condition between the frequencies and wave vectors (i.e. photon energy and momentum conservation) [76]. It is therefore not a surprise, given the evolution of laser powers and frequencies, that the search for photon–photon scattering using resonant four-wave interactions has caught the attention of researchers in this area. This approach has progressed furthest in the experimental attempts to detect elastic scattering among photons [77–82].

Using the resonance conditions $\omega_4 = \omega_1 + \omega_2 - \omega_3$ and $\mathbf{k}_4 = \mathbf{k}_1 + \mathbf{k}_2 - \mathbf{k}_3$, between the vacuum generated photons and the laser pump sources, respectively, one may derive a set of wave interaction equations for slowly varying amplitudes a_i, $i = 1, \ldots, 4$, of the form [83]

$$\frac{da_i}{dt} = C a_j a_k a_l^*, \tag{2.12}$$

given any type of media through which the waves may interact. Here the coupling constants C depend on the interaction in question, as well as on the physical parameters of the system around which the waves are modulated.

The coupling constants may be interpreted in terms of the nonlinear susceptibility of the vacuum. Moulin & Bernard [79] considered the interaction of three crossing waves, characterized by their respective electric field vectors $\mathbf{E}_i$, which produce a fourth wave E_4. Starting from the Maxwell's equations with the usual weak-field limit Heisenberg–Euler third order nonlinear corrections, they derive the nonlinear Schrödinger equation (see also Ref. [84] for similar results in a different setting)

$$i\left(\frac{\partial}{\partial t} + \frac{\partial}{\partial z}\right) E_4 + \frac{1}{2\omega_4}\nabla_\perp^2 E_4 = -\frac{\omega_4}{2}\chi^{(3)} E_1 E_2 E_3^* \tag{2.13}$$

for the driven wave amplitude E_4, where the overall harmonic time dependence $\exp(-i\omega t)$ has been factored out. Here $\chi^{(3)}$ is the third order nonlinear susceptibility given by

$$\chi^{(3)} = \frac{\alpha}{45\pi}\frac{K}{E_{cr}^2} \approx 3 \times 10^{-41} \times K \frac{m^2}{V^2}, \tag{2.14}$$

where K is a dimensionless form factor of the order of unity. The value of K depends on the polarization and propagation directions of the pump modes, and reaches a maximum of $K = 14$ for degenerate four-wave mixing [79]. Refs. [81] and [82] presented experiments on four-wave mixing in vacuum, improving previous attempts by nine orders of magnitude, although no direct detection of photon–photon scattering was achieved.

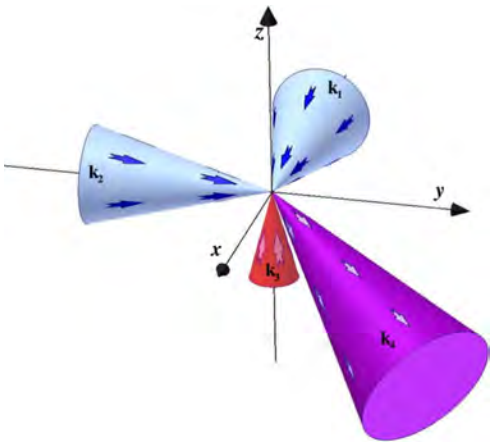

Figure 2.7: Configuration of the incoming laser beams (represented by the wave vectors k_1, k_2 and k_3) and the direction of the scattered wave (with wave vector k_4).

There are more recent proposals for the detection of photon–photon scattering by using four-wave interactions. In [85,86] more detailed calculations concerning experimental constraints have been done, showing the feasibility of such an experiment. Using a proposed setup according to Fig. 2.7, the number of photons generated through a four-wave mixing process was determined. For simplicity, in the 3D case the interaction region will be modelled by a cube with a side b, existing during a time L/c (more precise numerical estimates can easily be derived by using

more accurate laser pulse profiles, but the result does not differ significantly from the one given below). The estimated number of scattered photons per shot is found to be (see Fig. 2.8 and Table 2.2)

$$N_{3d} = 1.31\eta^2 G_{3d}^2 \left(\frac{1\,\mu\mathrm{m}}{\lambda_4}\right)^3 \left(\frac{L}{1\,\mu\mathrm{m}}\right) \left(\frac{P_1 P_2 P_3}{1\ \mathrm{PW}^3}\right), \tag{2.15}$$

where G_{3d} is a geometric factor capturing the polarization dependence, P_j is the power of the incoming pulses, λ_4 the generated wavelength determined by the resonance conditions and the pump laser parameters, and η^2 can be found in [86]. Here we assume the same focal spot size, independent of the beam power. For further discussion on noise sources and their treatment, see Ref. [86].

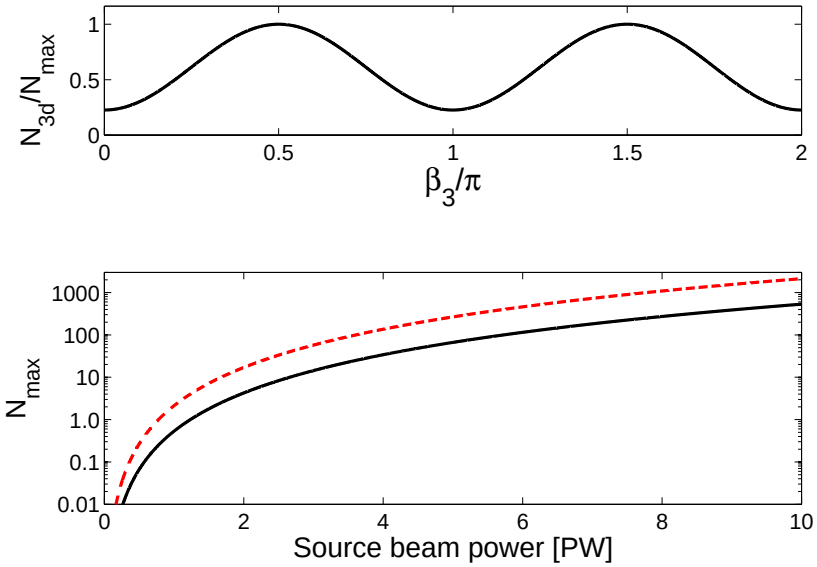

Figure 2.8: The upper panel shows the number of scattered photons N_{3d} per shot, normalized by the number of photons $N_{\max}$ per shot for an optimal choice of polarization, as a function of the polarization angle β_3 of the wave with direction $\hat{\mathbf{k}}_3$. The lower panel shows $N_{\max}$ predicted by Eq. 2.4 when increasing the laser power while the beam width is kept constant at $b = 1.6$ μm, for a system where two source beams are used and one of the beams is split into two (solid line) and where three source beams are used (dashed line), hence no beam splitting is required.

Experiments along the same lines as described for four-wave mixing above can also be used for a large number of other, non-QED tests, such as axion[3] searches [80, 88, 89]. Thus, progress of low-energy QED experiments could also prove to be useful for e.g. dark matter searches.

Vacuum harmonic generation in the collision of two strong laser fields

The process of elastic scattering between real photons can be seen as the absorption of two laser photons by a virtual electron-positron pair and the successive emission of two other photons. In this paragraph we study a generalization of this effect in which during the collision of two strong laser beams many photons are absorbed by a virtual pair and only two high-energy photons are emitted [90]. We consider two counterpropagating waves with the same angular frequency ω_0 and electric field amplitude $E_0/2$. If the emitted frequencies we are interested in are such that

[3] Axions are bosons which were introduced in order to explain the absence of CP symmetry breaking in QCD [87], and the axion is still to be detected.

$\omega \gg \omega_0$, then the resulting standing laser wave can be approximated by the oscillating electric field. In these approximations, since the external electric field is uniform, the photons produced are emitted with opposite momentum. Moreover, since in the process only two photons are created with the same energy, they are emitted with a frequency multiple of the laser frequency ω_0. In conclusion, each final photon has exactly half of the energy of all the photons initially absorbed by the virtual electron-positron pair. Nowadays, the most realistic regime from an experimental point of view is that of laser electric field amplitudes E_0 which are much smaller than E_{cr}. In this regime, it can be seen that the harmonic yield decreases monotonically as the harmonic order increases. As it is expected from general considerations, if $E_0 \ll E_{cr}$, the production of high harmonics is very unlikely. Instead, in the strong field regime $\rho_L \gg 1$ it can be shown that the vacuum high-harmonic generation spectra show the presence of a *plateau* as in atomic high-order harmonic generation. The *plateau* is followed by a rapid cut-off approximately at photon energies $\sim \sqrt{eE_0}$ [90].

Vacuum harmonic generation in a focused laser field

In this paragraph another vacuum polarization effect is considered, namely generation of odd harmonics by a super-strong focused laser beam in the vacuum [91]. The process occurs due to the plural light-by-light scattering effect. We have shown that for the laser pulse with $\lambda \sim 1$ μm and $\Delta = 0.1$ (see the notation in Par. 1.1), the number of generated photons reaches the value of one photon per period at intensity $I \approx 5 \cdot 10^{27}$ W/cm^2 $\approx 10^{-2} I_{cr}$. The corresponding peak value of the electric field is one order of magnitude lower than the characteristic QED field E_{cr}. As in the case of electron-positron pair creation, this is explained by a very large value of the effective focal region as compared to the characteristic Compton 4-volume. It is very important that the rates of photon generation for e- and h-polarized waves are similar and reach an observable level at $\vartheta = \Delta E_0/E_{cr} \approx 10^{-2}$. The effect of pair creation by a focused e-polarized laser pulse arises at the same values of ϑ, while in an h-polarized wave production of pairs it occurs noticeably later. This means that in an h-polarized wave we will not have the background of secondary photons radiated by created particles. Therefore, just these waves should be employed for the observation of the effect of harmonics generation by a focused laser pulse in vacuum.

Experimental considerations

The high field science (HFS) described in this report requires a versatile target area with multiple high intensity beams available as well as various secondary sources. Most of the experiments are based on a configuration of two counterpropagating fundamental beams focussed to the highest possible intensity. Experiments which rely on the most extreme intensities ($\sim 10^{26}$ W/cm^2) will need the coherent combination of up to 10 beams of power exceeding 50 PW. It must also be possible to arrange laser beams along three orthogonal directions in order to perform the four wave mixing experiment 4.4.

The laser repetition rate required to generate sufficient signal levels in a reasonable amount of time needs to be estimated for each individual experiment but is likely to be of the order 1 minute. The laser beams need to have polarisation control and for one experiment (4.4) frequency conversion to the second harmonic is necessary. For large aperture ultra-short pulses neither of these actions is trivial and significant effort must be given to developing techniques for achieving them.

The secondary source requirements are highly demanding. It must be possible to align these sources either counterpropagating or transverse to the main laser beam. Ideal parameters are as follows: an electron beam with energy up to 50 GeV (3.4), a proton beam with energy up to 50 GeV (4.1), an extreme ultraviolet attosecond pulse (4.1), a 5 keV polarised x-ray beam (4.2) and a 50 MeV γ-ray beam (4.2). The facility must accommodate transport of sources from the dedicated secondary source development areas to the HFS area. The more extreme

Table 2.2: The table shows more precise values for the number of scattered photons in Fig. 2.8, for different laser powers. N_a is the number of scattered photons for a system where two source beams are used and N_b is the number when three source beams are used (i.e. without beam-splitting). We see that for a system like ELI a very large fraction of photons will be generated through the nonlinear quantum vacuum.

Source beam power [PW]	N_a	N_b
0.5	0.066	0.27
2.5	8.3	33
5	66	266
10	5.3×10^2	2.1×10^3
25	8.3×10^3	3.3×10^4
50	6.6×10^4	2.7×10^5
100	—	2.2×10^6
1000	—	2.2×10^9

energy particles and radiation would be generated locally to the HFS chamber through processes such as Compton backscattering and laser-piston acceleration. In these cases, shielding will be essential to prevent particles and radiation from the source interaction reaching the HFS detectors. Likewise, it will be necessary to dump the secondary source in some manner which does not impact on the experiment.

The high field science interaction chamber must be evacuated to the lowest pressure achievable. A poor vacuum will lead to generation of particles and radiation from the intense lasers irradiating the residual gas in the chamber. The background signal from these interactions is likely to overwhelm the very small signals expected from vacuum effects. The pressure requirement can be relaxed somewhat by using a second intense pulse arriving before the main pulse. This will clear the focal volume of particles through the action of the ponderomotive force and the detectors can be gated in such a way that they are blind to any signal from this earlier interaction.

The detectors required for these experiments are, in general, standard for high intensity plasma interaction facilities and will be common to the requirements of the other work packages. The notable exception is the need for x-ray (4.2, 4.3) and optical (4.3) polarimetry with sensitivity at the limit of what is currently achievable.

Conclusions

We have given an overview of the ELI physics potential in the context of strong-field QED. The processes under consideration are typically characterised by two parameters, one being the dimensionless laser amplitude, a_0, the other the energy ω_p of an incoming probe electron, proton or photon[4]. Nonlinear Compton scattering and Unruh radiation in principle take place at arbitrary low intensities but to safely observe signatures one certainly would prefer to have $a_0 > 1$. However, it is worth noting that one does not have to overcome energy thresholds. The situation is different for vacuum polarisation effects, in particular for the absorptive ones, i.e. pair production. For those, one would generally have as high intensity as possible. As this is determined by the technological frontier the crucial question then is: what is the minimum intensity to see an effect? An overview of the current best estimates is given in the frequency-intensity plot below (Fig. 2.9).

[4]These lab frame quantities can all be given an invariant meaning, [12, 92].

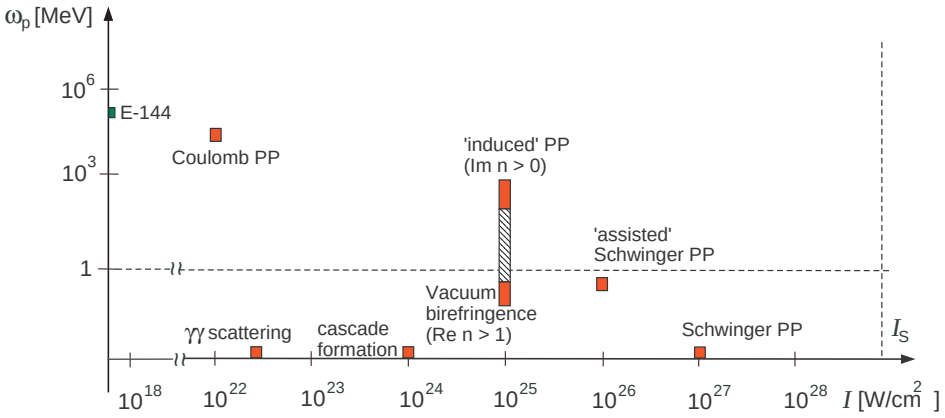

Figure 2.9: Sketch of the opportunities for detecting fundamental physics effects with ELI for the pure light scenario. Horizontal axis and vertical axes correspond to the peak intensity I of the optical laser focus and the energy ω_p of the (weak) probe photons, respectively. The dashed lines denote the Schwinger critical field strength $I_{cr}E_{cr}^2/\pi$ and the e^+e^--pair creation threshold, $2m_e$, respectively. For the different processes, see the main text.

Employing strong laser and Coulomb fields one may study a 'tunneling version' of the SLAC E-144 pair creation experiment. Here, stimulation by high energy electrons yields pairs at currently existing energies. Dispersive effects such as $\gamma\gamma$ scattering (i. e. vacuum four-wave mixing), laser photon merging, vacuum birefringence and diffraction are generally rather tiny and require sufficiently large intensities between 10^{23} and 10^{25} W/cm^2. Absorption of probe photons is signalled by an imaginary part of the vacuum refractive indices and arises upon going sufficiently above energy threshold with probe energy, say $\omega_p 100$ MeV, inducing pair creation. An interesting recent work [29] has suggested cascade formation of pairs by a combination of Bethe-Heitler and trident processes and may occur already at 10^{24} W/cm^2. At these or even slightly lower intensities multi-photon resonance production of pairs may occur though this claim remains controversial for the time being. Going to higher intensities, but staying below energy threshold, one should be able to detect pairs produced via the assisted Schwinger mechanism ($I = 10^{26}$ W/cm^2). Finally, by 'switching off' the probe, the proper Schwinger mechanism will sufficiently 'boil the vacuum' even below the critical field, $I_{cr} = E_{cr}^2/8\pi$, where a large pre-exponential factor compensates the exponential suppression due to the tunneling factor. This cancellation is expected to take place at 10^{27} W/cm^2.

2.1.2 Particle physics at ELI

Introduction

The technological breakthrough of chirped pulse amplification [93] has opened the door to unprecedented laser intensities, the current state of the art being about 10^{22} W/cm^2. The next generation of high power lasers will increase this number by orders of magnitude culminating in the ELI facility, an exawatt laser expected to reach 10^{26} W/cm^2. At intensities of this order charged particles traversing a laser wavelength gain huge electromagnetic energies such that even protons become relativistic. It is therefore reasonable to assess the particle physics opportunities that arise in the strong-field environment provided by the ELI ultra-high intensity laser. This is the central topic of this contribution. In the following section we discuss a coherent GeV collider scheme based on extremely strong laser pulses of the ELI class rather than traditional large

scale accelerators. We then move on to physics questions beyond genuine quantum electrodynamics (QED) which will be covered elsewhere. First we briefly consider possible modifications of low energy QED including Born-Infeld theory and Lorentz violating terms. The main part of our discussion is given later on searching and detecting new weakly interacting light particles. Finally, we briefly address the strongly interacting sector. Units with $\hbar = c = 1$ are used in this chapter.

GeV energy recollisions for particle physics

A collider scheme based on ELI could be accomplished to realize particle reactions with high-power lasers. Separate from the way of improving plasma-based laser accelerator schemes, this goal can be achieved via laser-driven electron-positron coherent recollisions of GeV energy, employing a gas of positronium (Ps) atoms [37]. The latter combines acceleration, focusing and collision in a single stage in counterpropagating laser fields. The recollision-based laser-driven collider can yield high luminosity, compared to conventional laser accelerators because here the electron and positron stem from a Ps atom with the initial coordinates being confined within the range of the Bohr radius. They are driven coherently by the laser field (the relativistic drift in the laser propagation direction is the same for the electron as for the positron [94]) and recollide with a mean impact parameter of the order of the electron wave packet size. Consequently, the luminosity is substantially enhanced due to its coherent component. In a setup of counter-propagating laser beams, the electron wave packet size at the recollision moment is only a few times larger than the initial wave packet size [37].

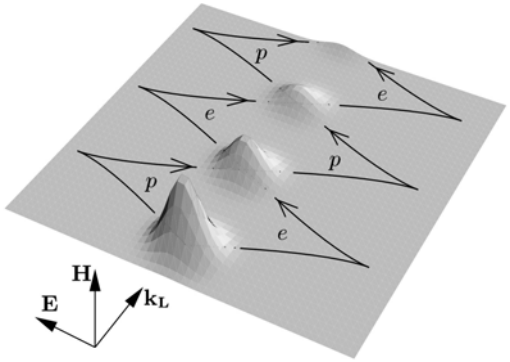

Figure 2.10: High energy laser driven recollision scheme with positronium atoms.

The simplest particle reaction which could be observed in this setup is the muon pair production from a Ps gas in a strong laser field [37]. The threshold laser field for muon pair production from an e^+e^- pair is $\xi \approx M/m \approx 200$, where $\xi = eE/m_e\omega$, e and m_e are the absolute value of the electron charge and mass, respectively, E and ω the laser field and frequency, respectively and M the muon mass. The number of reaction events per laser pulse via coherent collisions with counter-propagating laser pulses can be estimated to reach up to a value of 10^{-4}, taking into account the recent progress and perspectives in the technique of the production, accumulation and trapping of Ps atoms [95–97]. Then, the observation of coherent muon pair production from laser-driven Ps becomes feasible at a high laser repetition frequency of several kHz with a laser intensity of 4×10^{22} W/cm^2.

Beyond (Strong-Field) QED

At particle energies small compared to the electron mass, $\ll m_e$, fermionic degrees may be integrated out from the QED partition function yielding the Heisenberg-Euler (HE) effective action [4, 98]. It describes the nonlinear self-interaction of the electromagnetic field via fermion

loops which, however, are not resolved but rather encoded in an infinite number of effective couplings multiplying purely photonic vertices of increasing mass dimension. In a somewhat generalised form this old idea has become a cornerstone of modern particle physics under the label of 'effective field theory'. For low-energy QED, it is most useful to define the bilinear invariants, $\mathcal{S} \equiv (E^2 - B^2)/2$ and $\mathcal{P} \equiv E \cdot B$. In terms of these the HE addition $\mathcal{L}_{EH}$to Maxwell theory ($\mathcal{L}_{Max} \equiv \mathcal{S}$) may be written schematically and to lowest order,

$$\mathcal{L}_{EH} = \kappa \left(\mathcal{S}^2 + \lambda \mathcal{P}^2\right) , \tag{2.16}$$

with $\kappa \equiv 8\alpha^2/45m_e^4$ and $\lambda = 7/4$, where $\alpha = 1/137$ denotes the fine structure constant as usual. It is important to note that the effects induced by (2.18) are tiny, their typical magnitude (relative to the Maxwell term) being $\delta \sim \alpha E^2/E_{cr}^2$. Here, $E_{cr} \equiv m_e^2/e \simeq 1.3\times\ 10^{18}$ V/m denotes the critical electric field where the vacuum starts to 'break down' and spontaneous pair creation sets in [3, 6]. For ELI intensities one expects a maximum $\delta \simeq 10^{-5}$.

There is an alternative version of nonlinear electrodynamics, introduced in 1934 by Born and Infeld [99, 100] in an attempt to solve the self-energy problem of the electron. The idea then was to introduce a maximal electric field in analogy with the relativistic point particle and its limiting velocity, c. This approach lay dormant after the successes of renormalisation but has been resurrected within string theory after the Born-Infeld (BI) Lagrangian was rediscovered as a low-energy limit in the electromagnetic sector [101, 102]. To leading order the theory formally coincides with (2.16). However, while the BI version of the parameter κ remains undetermined theoretically (hence needs to be measured), λ is known to be unity such that $\mathcal{S}^2$ and $\mathcal{P}^2$ contribute with equal weight. This gives a special status to BI nonlinear electrodynamics, the most striking prediction being the absence of vacuum birefringence [103, 104]. Recall that (2.16) with HE parameters implies a difference in vacuum refractive indices, $\Delta n \sim \delta$, which should be measurable at ELI intensities [70]. Further tests of HE vs. BI would be light-by-light scattering [98, 105] using laser beams [85], and photon splitting in strong magnetic fields [106]. One should also reassess the light-by-light scattering contribution to the anomalous magnetic moment to infer bounds on the size of the HE or BI parameters.

In the same vein one may be able to address the size of Lorentz violations which are another (hypothetical) source of modifications to Maxwell theory. They imply effects similar to those stemming from the nonlinear terms such as vacuum birefringence, photon splitting and vacuum Cherenkov radiation [107]. High-precision laser experiments may very well be able to supplement or improve the existing cosmological bounds on the Lorentz violating parameters.

ELI's particle discovery potential

The study of nonlinear self-interactions of strong electromagnetic fields in vacuum is also an investigation of the field content of fluctuating particles in the quantum vacuum. If so far unknow particles couple to photons they can mediate apparent photon self-interactions in a manner similar to electron-positron fluctuations which generate the HE Lagrangian (2.16). Moreover, such hypothetical particles could even be created from strong fields. As ELI will substantially push the frontier of strong fields available in a laboratory, it has the potential to search for new fundamental particles.

As the scale set by the ELI peak field strength is expected to be of order $\mathcal{O}$(100keV) in particle-mass/energy units, a typical strong-field experiment will be sensitive to particle masses up to this scale and particularly to much lower scales. On the other hand, the high field strength together with modern optical techniques provides for a strong handle on very weakly coupled particles. With this particular sensitivity to potentially light but weakly coupled degrees of freedom, strong-field experiments are complementary to accelerator searches for new particles [108].

Indeed a number of extensions of the Standard Model of particle physics predict the existence of weakly interacting sub-eV particles (WISPs) which couple to the electromagnetic sector. A popular candidate is the axion [87] which provides for a possible solution of the strong CP problem; more generally, we can think of axion-like particles (ALPs) as an uncharged scalar or pseudo-scalar degree of freedom with a coupling to two photons. Further candidates are mini-charged particles (MCPs), i.e., matter fields with charge εe and $\varepsilon \ll 1$, which arise naturally in scenarios with gauge-kinetic mixing [109] or extra-dimensional scenarios [110]. More generally, many Standard-Model extensions not only involve but often require – for reasons of consistency – a hidden sector, i.e., a set of so far unobserved degrees of freedom very weakly coupled to the Standard Model. Hence, a discovery of hidden-sector properties could decisively single out the relevant theoretical fundament.

Low-energy effective actions

From a bottom-up viewpoint, many Standard-Model extensions lead to similar consequences for low-energy laboratory experiments, parameterizable by effective couplings between photons and the new effective degrees of freedom. The first example is given above in Eq. (2.16): the HE or BI action. As already mentioned, HE-type effective actions predict vacuum birefringence in a strong field. For instance, for a probe beam counter-propagating in a strong beam with intensity I, the refractive index difference for the two eigenmodes $(\parallel, \perp)$ with mutually orthogonal polarization is given by $\Delta n = (\lambda - 1)\kappa I/E_{cr}^2$. As an observable, an initially linearly polarized probe laser can pick up an *ellipticity* by traversing the strong beam. The ellipticity angle ψ is given by $\psi = (\omega/2)L\Delta n \sin 2\theta$, where θ is the angle between the probe polarization and the fast eigenmode's polarization, and L is the path length inside the strong field.

Another optical observable can be important: any effect which modifies the amplitudes of the $\parallel$ or $\perp$ components in a polarization-dependent manner but leaves the phase relations invariant will induce a *rotation* angle $\Delta\theta$. Since amplitude modifications involve an imaginary part for the index of refraction, rotation from a microscopic viewpoint is related to particle production or annihilation. In QED below threshold $\omega < 2m$, electron-positron pair production by an incident laser is excluded. Further possibly rotation inducing effects such as photon splitting [106] or neutrino-pair production [112] in a strong field are severly suppressed for typical laboratory parameters. Therefore, a sizeable signal for vacuum rotation $\Delta\theta$ in a strong-field experiment would be a signature for new fundamental physics.

Axion-Like Particle (ALP)

As a first example, we consider a new neutral scalar φ or pseudo-scalar degree of freedom φ^- (such as an axion) which is coupled to the photon by,

$$\mathcal{L}_{\rm ALP} = \left\{ -\frac{g}{4}\varphi^{(-)} F^{\mu\nu} \overset{(\sim)}{F}_{\mu\nu} - \frac{1}{2}(\partial\varphi^{(-)})^2 - \frac{1}{2}\, {m_\varphi}^2\, \varphi^{(-)2} \right\}, \tag{2.17}$$

parameterized by the mass m_φ of this axion-like particle (ALP) and the dimensionful coupling g. In optical experiments in strong fields, ALPs can induce both ellipticity and rotation [113], since only one polarization mode couples to the ALP and the strong field. For instance, coherent photon-ALP conversion causes a depletion of one photon mode, implying rotation. In order to make contact with the literature, we approximate the strong field by a homogeneous magnetic field B as may be provided by a slowly beating standing wave formed from counter-propagating laser beams. We stress that detailed studies employing all relevant properties of the field provided by systems such as ELI still need to be performed. From the equations of motion for

the photon-ALP system for the pseudo-scalar case, the induced ellipticity and rotation can be calculated:

$$\Delta\theta^- = \left(\tfrac{gB\omega}{m_\varphi^2}\right)^2 \sin^2\left(\tfrac{Lm_\varphi^2}{4\omega}\right)\sin 2\theta,\;\; \psi^- = \frac{1}{2}\left(\tfrac{gB\omega}{m_\varphi^2}\right)^2 \left(\tfrac{Lm_\varphi^2}{2\omega} - \sin\left(\tfrac{Lm_\varphi^2}{2\omega}\right)\right)\sin 2\theta, \tag{2.18}$$

for single passes of a probe beam through a strong B field of length L. For the scalar, we have $\Delta\theta = -\Delta\theta^-$, $\psi = -\psi^-$. Measuring ellipticity and rotation signals uniquely determines the two model parameters, ALP mass m_φ and ALP-photon coupling g. Measuring the signs of $\Delta\theta$ and ψ can even resolve the parity of the involved particle.

The effective interaction (2.17) is representative for various underlying particle scenarios. In the axion case, only the weak coupling to the photon is relevant and all other potential matter couplings are negligible. This facilitates the interesting experimental option to shine the ALP component through a wall which blocks all photons. Behind the wall, a second strong field can induce the reverse process and photons can be regenerated out of the ALP beam [114]. The regeneration rate is

$$n_{\rm out} = n_{\rm in}\,\frac{1}{16}\,(gBL\cos\theta)^4 \left[\sin\left(\frac{Lm_\varphi^2}{4\omega}\right)\Big/\frac{Lm_\varphi^2}{4\omega}\right]^4, \tag{2.19}$$

where $n_{\rm in}$ is the initial photon rate, and the fields B and its extension L are assumed to be identical on both sides of the wall.

In other models, such as those with a chameleon mechanism which have been developed in the context of cosmological scalar fields and the fifth-force problem [115], the ALP cannot penetrate the end caps of the vacuum chamber but gets reflected back. Whereas this has no influence on the formulas for ψ and $\Delta\theta$ in Eq. (2.18), a new detection mechanism arises: synchronizing a short laser probe pulse with the strong pulse, chameleons can be created inside the vacuum chamber and stored in a parallel cavity. By a synchronized second strong pulse, the chameleons can be re-converted into photons again inside the strong field; this would result in an afterglow phenomenon which is characteristic for a chameleonic ALP [116]. In the parameter range where $gB/m_\varphi \ll 1$, the number of photons in the first afterglow pulse $n_{\rm out}$ is again given by Eq. (2.19) where this time $n_{\rm in}$ is the number of photons in the synchronized probe pulse initially generating the chameleons.

Minicharged Particle (MCP)

The fluctuations of minicharged particles with mass m_ε and charge εe, $\varepsilon \ll 1$ induce photon self-interactions in the same way as electrons do. However, the weak-field HE Lagrangian (2.16) is not sufficient to describe the physics of MCPs properly, as the expansion parameters $\varepsilon eB/m_\varepsilon^2$ and ω/m_ε in a strong field B varying with ω are not necessarily small. As an interesting consequence, the probe laser frequency can be above the pair-production threshold $\omega > 2m_\varepsilon$ such that a rotation signal in addition to birefringence-induced ellipticity becomes possible [117].

All relevant information is encoded in the polarization tensor which is well known from QED [68, 118, 119]. Explicit results are available in asymptotic limits, e.g., for the rotation signal induced by a Dirac-fermionic MCP,

$$\Delta\theta \simeq \frac{1}{12}\frac{\pi}{\Gamma(\frac{1}{6})\Gamma(\frac{13}{6})}\left(\frac{2}{3}\right)^{\frac{1}{3}}\varepsilon^2\alpha(m_\varepsilon L)\left(\frac{m_\varepsilon}{\omega}\right)^{\frac{1}{3}}\left(\frac{\varepsilon eB}{{m_\varepsilon}^2}\right)^{\frac{2}{3}}, \quad \text{for } \frac{3}{2}\frac{\omega}{m_\varepsilon}\frac{\varepsilon eB}{m_\varepsilon^2} \gg 1, \tag{2.20}$$

which is valid above threshold and for a high number of allowed MCP Landau levels. Similar formulas exist for ellipticity or the case of spin-0 MCPs [120]. Note that this rotation appears to become independent of m_ε in the small-mass limit. In practice, once the associated Compton

wavelength $\sim 1/m_\varepsilon$ becomes larger than the size of the strong field, the field size acts as a cutoff reducing the effect. Precise predictions then require computations of polarization tensors in inhomogeneous fields which is a challenge for standard methods and remains an interesting question for future research.

ELI's sensitivity scales

In order to put the capabilities of ELI's particle-physics potential into a greater context, let us draw a comparison with other currently performed optical experiments, such as PVLAS [121], BMV [122], ALPS [123], LIPSS [124], OSQAR [125], GammeV [126, 127]. In these experiments, optical probe lasers traverse a magnetic field of $\mathcal{O}(1-10\,\text{Tesla})$ and length $\mathcal{O}(1-10\,\text{m})$. Whereas the reachable field strengths are comparatively small, e.g., if measured in units of the QED critical field strength of $B_{cr} \simeq 4\times 10^9$ Tesla, the length of the interaction region is macroscopic. The latter can even be enhanced by placing the field into a high-finesse cavity such that the signal is increased by a factor N_{pass} counting the number of passes of the probe laser inside the cavity.

By contrast, high-intensity laser systems provide for an interaction region only of the order of $\mathcal{O}(10-100\,\mu\text{m})$; also cavities are of no use, since pulse durations on the femtosecond scale are far too short compared to the time scale for a multiple pass. Nevertheless, the extreme intensity can compensate for these disadvantages. In the ALP scenarios, the relevant parameter in the limit $Lm_\varphi^2/\omega \ll 1$ (sub-eV particle masses) is gBL. For instance, for PVLAS this parameter is $gBL|_{\text{PVLAS}} \simeq 5\times(g/\text{GeV}^{-1})$. The corresponding ELI parameters are expected to give

$$gBL|_{\text{ELI}} = 3.3\times 10^3 (g/\text{GeV}^{-1})[L/(50\,\mu\text{m})], \tag{2.21}$$

exceeding that of macroscopic optical experiments by up to 3 orders of magnitude.

However, this improvement does not directly translate into a comparable increase of sensitivity, due to the lack of cavity enhancements and the necessity of pulse-probe synchronization. As an example estimate, let us consider a regeneration or afterglow experiment (2.4), using a probe laser of the petawatt class delivering $\sim 10^{21}$ photons per shot. Assuming single-photon detection behind the wall or in the afterglow, the sensitivity range includes coupling values $g3\times 10^{-9}$ GeV^{-1} for ALP masses in the sub-eV range. This should be compared with the current best laboratory bounds excluding ALP couplings of $g10^{-6}$ GeV^{-1} or chameleonic couplings $g2.5\times 10^{-7}$ GeV^{-1}. Also ALP rotation and ellipticity signals could be enhanced in comparison with standard optical experiments, but the potential improvement of ALP parameter bounds might not be as dramatic as from regeneration or afterglow experiments. In any case, we conclude that ELI has the potential to significantly improve existing laboratory bounds for Standard Model extensions involving ALPs.

In the MCP case, ELI parameters yield a maximum rotation (at $\theta = \pi/2$) of

$$\delta\theta = 4.1\times 10^8 \varepsilon^{8/3}(\text{eV}/\omega)^{1/3}[L/(50\,\mu\text{m})]. \tag{2.22}$$

Assuming a detection sensitivity of $\delta\theta|_{\text{sens}} \simeq 10$nrad, ELI will be sensitive to minicharge couplings down to $\varepsilon O(10^{-7})$ for optical probe lasers and sub-eV MCP masses. This is of the same order of magnitude as the current best laboratory bounds from PVLAS [121] and in the same ball park as cosmological observations [128].

It is worthwhile to emphasise, however, that optical experiments typically test a regime characterised by momentum transfers below the eV scale. This clearly distinguishes them from experiments looking for astrophysical bounds. Nevertheless, astrophysical observations in combination with energy-loss arguments impose strong constraints, e.g., on the ALP coupling $g10^{-10}$ GeV^{-1} for ALP masses in the eV range and below [129], or on MCP couplings $\varepsilon \leq 2\times 10^{-14}$ for m_ε below a few keV [130]. However, since the underlying solar physics involves

keV momentum transfer scales, these bounds apply to laboratory transfer scales ($\sim \mu$eV) only if the coupling values are extrapolated over these many orders of magnitude [131]. It is precisely this assumption which has been put into question by various models [132–115, 135, 136] and which can be checked or falsified by a particle discovery at strong-field experiments such as ELI. Indeed, current strong-field laboratory experiments begin to enter the parameter regime which has previously been accessible only to cosmological and astrophysical considerations [137].

In case of a positive signal, ELI could not only discover a new particle but also contribute to the particle's identification. Whereas the field stength, length and frequency dependence can distinguish between ALPs or MCPs, the signs of ellipticity and rotation are characteristic for spin and parity [120]. Light-shining-through-wall or afterglow experiments are indicative for additional matter couplings. Further experiments have been suggested such as Schwinger-type MCP pair production [138] or hidden-photon searches [139] which may also become realizable at ELI.

To conclude this section we stress that all the above estimates are based on various approximations. In particular, the homogeneous-field assumption is questionable as the typical variation scale of the strong field can be of the same order of magnitude as the new particle's Compton wavelength. More detailed theoretical analyses are certainly required for precise estimates, and new unknown effects may arise from this equality of scales.

Strong interactions in external electromagnetic fields

At ELI intensities the pion, the lightest strongly interacting particle ($m_\pi = 140$ MeV), will become relativistic. It is hence reasonable to address the effects of ultra-intense lasers within the context of strong interactions. The relevant theory is then quantum chromodynamics (QCD) which describes the microscopic interactions of quarks and gluons. The ELI laser will provide an electromagnetic extreme-field environment for these particles. Of course, a direct influence will only be exerted on quarks as the only carriers of electromagnetic charge in QCD. (The gluons exclusively couple to colour charge and hence are blind against electromagnetism).

A well known effect of external electromagnetic fields is their influence on chiral symmetry (and its breaking). The latter is probably the most important (approximate) symmetry of low-energy QCD as it governs the dynamics in this sector to a large extent. The pion, for instance, is best described as the Goldstone boson associated with the spontaneous breakdown of chiral symmetry, its mass being due to the small but finite masses of up and down quarks. The order parameter of the symmetry breaking is the quark condensate, $< 0|\bar{\psi}\psi|0 > \simeq 1.8$ fm^{-3} (for zero external fields) which measures the vacuum density of virtual quark-antiquark pairs. It is not directly measurable as a physical observable but determines, for example, the pion mass via the Gell-Mann-Oakes-Renner relation [140]. From a theoretical point of view the condensate is the derivative of effective Lagrangians like (2.16) with respect to the fermion mass. Hence, it is an alternative tool to investigate the quantum vacuum, both its 'persistence' and 'breakdown'.

It is known that external magnetic (electric) fields increase (decrease) the value of the condensate [141]. A plane wave field, on the other hand, has no influence as the effective action in this case vanishes together with the invariants $\mathcal{S}$ and $\mathcal{P}$. One would therefore expect the largest effect on the condensate near the antinodes of a standing wave formed from two counter-propagating laser beams. It would be most interesting to see how a modification of the condensate in extreme fields affects the pion mass. In a strong interaction (QCD) context, one naively expects electromagnetic effects to become relevant for field strengths about five orders of magnitude above the Sauter/Schwinger limit E_{cr}. However, as the pion mass splitting of approximately 5 MeV is mostly electromagnetic in nature one may envision measurable effects already below. In addition, the fermion condensate can also be discussed for QED where 'magnetic catalysis' may lead to QED versions of chiral symmetry breaking and dynamical mass generation [142, 143]. This

may open up an avenue to studying external field mass shifts of a purely quantum nature to be added to their classical counterparts [14, 17].

Concluding Remarks

Experiments employing ultra-strong electromagnetic fields provide many new routes to asking and answering fundamental physics questions. From a field theoretical, as we as particle physics, perspective, new optical probing techniques of high precision allow for testing QED as well as extensions thereof together with modifications of the standard model in a hitherto uncharted high-intensity, low energy regime. Particularly promising seems 1) the possibilities for subcritical nonperturbative effects, such as all-optical pair production and 2) the search for new light degrees of freedom which interact weakly at momentum scales much below the eV scale. Moving on to higher energy scales seems feasible, for instance by utilising new laser-based accelerator concepts such as the electron positron collider discussed above. Alternatively, high-power lasers may be combined with conventional accelerators. These ideas even open up the possibility to experimentally address modifications of quark-gluon dynamics in electromagnetic fields.

Bibliography

[1] V. I. Ritus, J. Sov. Laser Res., 497 (1985).
[2] O. Klein, Z. Phys., 157 (1929).
[3] F. Sauter, Z. Phys., 742 (1931).
[4] W. Heisenberg and H. Euler, Z. Phys., 714 (1936).
[5] V. Weisskopf, K. Dan. Vidensk. Selsk. Mat. Fys. Medd., 1 (1936).
[6] J. Schwinger, Phys. Rev., 664 (1951).
[7] R. H. Milburn, Phys. Rev. Lett., 75 (1963).
[8] J. Ballam *et al.*, Phys. Rev. Lett., 498 (1969).
[9] F. V. Hartemann *et al.*, Proceedings of Particle Accelerator Conference (PAC 07), Albuquerque, New Mexico, 25-29 Jun 2007, pp 1245; Phys. Rev. E, 016501 (2001); Phys. Rev. St. Accel. Beam, 100702 (2005); Phys. Rev. St. Accel. Beam, 011301 (2007).
[10] G. Priebe *et. al.*, Laser and Particle Beams, 649 (2008).
[11] A. I. Nikishov and V. I. Ritus, *Zh. Eksp. Teor. Fiz.* (1963) 776–796. [Sov. Phys. JETP, 529 (1964)]; A. I. Nikishov and V. I. Ritus, *Zh. Eksp. Teor. Fiz.* (1964) 1768–1781. [Sov. Phys. JETP, 1191 (1964)].
[12] N. B. Narozhnyi, A. Nikishov, and V. Ritus, *Zh. Eksp. Teor. Fiz.* (1964) 930. [Sov. Phys. JETP, 622 (1965)];
[13] I. I. Goldman, Phys. Lett., 103 (1964).
[14] L. S. Brown and T. W. B. Kibble, Phys. Rev., A705 (1964).
[15] V. Berestetskii, E. Lifshitz, and L. Pitaevskii, *Quantum Electrodynamics (Course of Theoretical Physics)* (Butterworth-Heinemann, 1982).
[16] C. Harvey, T. Heinzl and A. Ilderton, arXiv:0903.4151 [hep-ph].
[17] N. Sengupta, Bull. Math. Soc. (Calcutta), 187 (1949).
[18] N. Sengupta, Bull. Math. Soc. (Calcutta) (1952) 175–180.
[19] G. A. Krafft, Phys. Rev. Lett. 204802 (2004).
[20] C. Bula *et al.*, Phys. Rev. Lett, 3116 (1996).
[21] C. Bamber *et al.*, Phys. Rev. D, 092004 (1999).
[22] K. T. McDonald, Prepared for Conference on Probing Luminous and Dark Matter: Adrian Fest, Rochester, New York, 24-25 Sep 1999; available as http://viper.princeton.edu/mcdonald/e144/adrianfestdoc.pdf.
[23] A. Di Piazza, K. Z. Hatsagortsyan, and C. H. Keitel, Phys. Rev. Lett. accepted for publication. See also arXiv:0810.1703.
[24] R. Schützhold, C. Maia, to appear in Eur. J. Phys. (2009).

[25] R. Schützhold, G. Schaller, and D. Habs, Phys. Rev. Lett., 121302 (2006).
[26] R. Schützhold, G. Schaller, and D. Habs, Phys. Rev. Lett., 091301 (2008).
[27] W. Becker, Laser and Particle Beams, 603 (1991).
[28] D. Burke *et al.*, Phys. Rev. Lett., 1626 (1997).
[29] A. R. Bell and J. G. Kirk, Phys. Rev. Lett., 200403 (2008).
[30] J. G. Kirk, A. R. Bell and I. Arka, arXiv:0905.0987 [hep-ph].
[31] N. B. Narozhny and M. S. Fofanov, JETP, 753 (2000).
[32] A. I. Nikishov, Zh. Eksp. Teor. Fiz., 1210 (1969).
[33] S. S. Bulanov, N. B. Narozhny, V. D. Mur, and V. S. Popov JETP, 9 (2006).
[34] A. I. Milstein, C. Müller, U. D. Jentschura, K. Z. Hatsagortsyan, and C. H. Keitel, Phys. Rev. A, 062106 (2006).
[35] C. Müller, A. B. Voitkiv, and N. Grün, Phys. Rev. Lett., 223601 (2003).
[36] M. Yu. Kuchiev, Phys. Rev. Lett., 130404 (2007).
[37] K. Z. Hatsagortsyan, C. Müller, and C. H. Keitel, Europhys. Lett., 29 (2006); C. Müller, K. Z. Hatsagortsyan, and C. H. Keitel, Phys. Lett. B, 209 (2008).
[38] C. Müller, C. Deneke, and C. H. Keitel, Phys. Rev. Lett., 060402 (2008).
[39] R. Schützhold, H. Gies, and G. Dunne, Phys. Rev. Lett., 130404 (2008).
[40] A. Di Piazza, E. Lotstedt, A. I. Milstein, C. H. Keitel, arXiv:0906.0726.
[41] E. Brezin and C. Itzykson, Phys. Rev. D, 1191 (1970).
[42] G.J. Troup and H.S. Perlman, Phys. Rev. D, 2299 (1972).
[43] W. Greiner, B. Muller, J. Rafelski, 'Quantum Electrodynamics of Strong Fields', Springer – Verlag, Berlin, 1985; E. S. Fradkin, D. M. Gitman, and S. M. Shvartsman, 'Quantum Electrodynamics', Springer – Verlag, Berlin, 1991; A. A. Grib, S. G. Mamayev, and V. M. Mostepaneko, 'Vacuum Quantum Effects in Strong Fields', Friedmann Laboratory Publishing, St. Petersburg, 1994.
[44] V.S. Popov, JETP Lett., 185 (1971); Sov. Phys. JETP, 709 (1972); Sov. Phys. JETP, 659 (1972); V.S. Popov and M. S. Marinov, Sov. J. Nucl. Phys., 449 (1973) ; JETP Lett., 255 (1974); Sov. J. Nucl. Phys., 584 (1974).
[45] A. I. Nikishov, Nucl. Phys. B, 346 (1970).
[46] N.B. Narozhnyi and A. I. Nikishov, Sov. J. Nucl. Phys., 596 (1970); Sov. Phys. JETP, 427 (1974).
[47] A. Ringwald, Phys. Let. B, 107 (2001).
[48] V.S. Popov, JETP Lett., 133 (2001); Phys. Lett. A, 83 (2002).
[49] S. S. Bulanov, N. B. Narozhny, V. D. Mur, and V. S. Popov, Phys. Lett. A, 1 (2004).
[50] A. Di Piazza, Phys. Rev. D, 053013 (2004).
[51] D. B. Blaschke, A.V. Prozorkevich, C. D. Roberts, S. M. Schmidt and S. A. Smolyansky, Phys. Rev. Lett., 140402 (2006).
[52] M. Ruf et al., Phys. Rev. Lett., 080402 (2009).
[53] M. Perry and G. Mourou, Science, 917 (1994)
[54] P. Chen and C. Pellegrini, in Quantum Aspects of Beam Physics, Proc.15th Advanced ICFA Beam Dynamics Workshop, Monterey, Cal., 4-9 Jan 1998 (World Scientific, Singapore, 1998) p. 571.
[55] P. Chen and T. Tajima, Phys. Rev. Lett., 256 (1999).
[56] T. Tajima and G. Mourou, Phys. Rev. ST. Accel. Beams, 031301 (2002).
[57] XFEL-Technical Disign Report (2006) Publisher: DESY XFEL Project Group, European XFEL Project Team, Deutsches Elektronen-Synchrotron, Member of the Helmholtz Association, Notkestrasse 85, 22607 Hamburg, Germany ISBN 3-935702-17-5.
[58] H. K. Avetissian, A. K. Avetissian, G. F. Mkrtchian and Kh. V. Sedrakian, Phys. Rev. E, 016502 (2002).

[59] C. Kaberidis, I. Tsohantjis and S. Moustaizis in 'Frontiers of Foundamental and Computational Physics' Udine, Italy, 26-29 September 2004, Sidharth B.G, Honsell F., de Angelis A. (Eds.) 2005 pp. 279-283.
[60] I. Tsohantjis, S. Moustaizis and I. Ploumistakis, Phys. Lett. B, 249 (2007).
[61] I. Ploumistakis, I. Tsohantjis and S. Moustaizis, "New approaches on Laser Vacuum Breakdown for Pair Creation", poster presented at the 35th EPS Plasma Physics Conference, 9-13 June 2008 Hersonissos, Crete, Greece.
[62] A. Di Piazza, K. Z. Hatsagortsyan, and C. H. Keitel, Phys. Rev. Lett., 010403 (2008); Phys. Rev. A, 062109 (2008).
[63] A. I. Nikishov and V. I. Ritus, Sov. Phys. JETP, 757 (1965); , 1135 (1967).
[64] V. I. Ritus, in Issues in Intense-Field Quantum Electrodynamics, ed. by V. L. Ginzburg (Nova Science, Commack, 1987).
[65] V. B. Berestetskii, L. P. Pitaevskii, E. M. Lifshitz, Quantum Electrodynamics, Second Edition: Vol.4 (Oxford: Butterworth-Heinemann, 1982).
[66] T. Esirkepov, *et al.*, Phys. Rev. Lett., 175003 (2004).
[67] G. Tsakiris, *et al.*, New J. Phys., 19 (2006).
[68] J. Toll, (1952), PhD thesis, Princeton, 1952.
[69] T. Heinzl and A. Ilderton, Opt. Commun., 1879 (2009), arXiv:0807.1841.
[70] T. Heinzl *et al.*, Opt. Commun., 318 (2006), hep-ph/0601076.
[71] T. Heinzl and O. Schröder, J. Phys. A39, 11623 (2006), hep-th/0605130.
[72] T. Heinzl and A. Ilderton, Eur. Phys. J. D (2009)
[73] A. Di Piazza, K. Z. Hatsagortsyan, and C. H. Keitel, Phys. Rev. Lett., 083603 (2006).
[74] E. E. Alp, W. Sturhahn, and T. S. Toellner, Hyperfine Interact., 45 (2000).
[75] K. Muroo, *et al.*, J. Opt. Soc. Am. B, 2249 (2003).
[76] N. N. Rozanov, Zh. Eksp. Teor. Fiz., 1996 (1993) [JETP, 991 (1993)].
[77] F. Moulin, D. Bernard, and F. Amiranoff, Z. Phys. C, 607 (1996).
[78] D. Bernard, Experiments on Photon–Photon Scattering, in *Frontier Tests of QED and Physics of the Vacuum*, eds. E. Zavattini, D. Bakalov, and C. Rizzo (Heron Press, Sofia, Hungary, 1998).
[79] F. Moulin, and D. Bernard, Opt. Comm., 137 (1999).
[80] D. Bernard, Nucl. Phys. B (Proc. Suppl.), 201 (1999).
[81] D. Bernard et al., Eur. Phys. J. D, 141 (2000).
[82] D. Bernard, Nucl. Phys. B (Proc. Suppl.), 439 (2000).
[83] M. Marklund and P. K. Shukla, Rev. Mod. Phys., 591 (2006).
[84] M. Marklund, G. Brodin, and L. Stenflo, Phys. Rev. Lett., 163601 (2003).
[85] E. Lundström et al., Phys. Rev. Lett., 083602 (2006);
[86] J. Lundin et al., Phys. Rev. A, 043821 (2006).
[87] R. D. Peccei and H. R. Quinn, Phys. Rev. Lett., 1440 (1977); Phys. Rev. D, 1791 (1977); S. Weinberg, Phys. Rev. Lett., 223 (1978); F. Wilczek, Phys. Rev. Lett., 279 (1978).
[88] A. Dupays, C. Rizzo, M. Roncadelli, and G. F. Bignami, Phys. Rev. Lett., 211302 (2005).
[89] R. Bradley et al., Rev. Mod. Phys., 777 (2003).
[90] A. Di Piazza, K. Z. Hatsagortsyan, and C. H. Keitel, Phys. Rev. D, 85005 (2005).
[91] A. M. Fedotov, N. B. Narozhny, Phys. Lett. A, 1 (2007).
[92] T. Heinzl and A. Ilderton, Opt. Commun., 1879 (2009), arXiv:0807.1841.
[93] D. Strickland and G. Mourou, Opt. Commun., 212 (1985).
[94] B. Henrich, K. Z. Hatsagortsyan and C.H. Keitel, Phys. Rev. Lett., 013601 (2004).
[95] C. M. Surko and R. G. Greaves, Phys. Plasmas, 2333 (2004).
[96] A.P. Mills Jr., Nucl. Instrum. Meth. Phys. Res. B, 107 (2002); D. B. Cassidy *et al.*, Phys. Rev. Lett., 195006 (2005); D. B. Cassidy and A. P. Mills Jr., Nature, 195 (2007).
[97] J. Estrada et al., Phys. Rev. Lett., 859 (2000); P. Perez and A. Rosowsky, Nucl. Instrum. Meth. Phys. Res. A, 523 (2004); ibid. 545, 20 (2005); L. V. Jørgensen *et al.*, Phys. Rev.

Lett., 025002 (2005); S. C. Wilks, *et al.*, Astroph. Space Sci., 347 2005; R. Funakoshi *et al.*, Phys. Rev. A, 012713 (2007).
[98] H. Euler, Ann. Phys. (Leipzig), 398 (1936).
[99] M. Born and L. Infeld, Proc. R. Soc. London Ser. A, 522 (1934).
[100] M. Born and L. Infeld, Proc. R. Soc. London Ser. A, 141 (1935).
[101] E. S. Fradkin and A. A. Tseytlin, Phys. Lett. B163, 123 (1985).
[102] A. A. Tseytlin, (1999), hep-th/9908105.
[103] G. Boillat, J. Math. Phys., 941 (1970).
[104] J. Plebanski, (1970), *Lecture Notes on Nonlinear Electrodynamics*, NORDITA, 1970.
[105] A. I. Akhiezer, Phys. Z. Sowjetunion, 263 (1937).
[106] S. L. Adler, Annals Phys., 599 (1971).
[107] V. A. Kostelecky and M. Mewes, Phys. Rev. D66, 056005 (2002), hep-ph/0205211.
[108] H. Gies, J. Phys. A, 164039 (2008) [arXiv:0711.1337 [hep-ph]].
[109] B. Holdom, Phys. Lett. B (1986) 196.
[110] B. Batell and T. Gherghetta, Phys. Rev. D, 045016 (2006) [arXiv:hep-ph/0512356].
[111] S.L. Adler, Annals Phys. (1971) 599.
[112] H. Gies and R. Shaisultanov, Phys. Lett. B, 129 (2000) [arXiv:hep-ph/0009342].
[113] L. Maiani, R. Petronzio and E. Zavattini, Phys. Lett. B, 359 (1986); G. Raffelt and L. Stodolsky, Phys. Rev. D, 1237 (1988).
[114] P. Sikivie, Phys. Rev. Lett. (1983) 1415 [Erratum-ibid. (1984) 695]; A. A. Anselm, Yad. Fiz. (1985) 1480; M. Gasperini, Phys. Rev. Lett. (1987) 396; K. Van Bibber, N. R. Dagdeviren, S. E. Koonin, A. Kerman, and H. N. Nelson, Phys. Rev. Lett., 759 (1987).
[115] J. Khoury and A. Weltman, Phys. Rev. D, 044026 (2004); Phys. Rev. Lett., 171104 (2004); D. F. Mota and D. J. Shaw, Phys. Rev. D, 063501 (2007); Phys. Rev. Lett., 151102 (2006); P. Brax *et al.*, Phys. Rev. D, 085010 (2007).
[116] H. Gies, D. F. Mota and D. J. Shaw, arXiv:0710.1556 [hep-ph]; M. Ahlers, A. Lindner, A. Ringwald, L. Schrempp and C. Weniger, arXiv:0710.1555 [hep-ph].
[117] H. Gies, J. Jaeckel and A. Ringwald, Phys. Rev. Lett., 140402 (2006) [arXiv:hep-ph/0607118].
[118] V. Baier and V. Katkov, Zh. Eksp. Teor. Fiz., 1478 (1967); W.-y. Tsai and T. Erber, Phys. Rev. D12, 1132 (1975); Phys. Rev. D10, 492 (1974); J.K. Daugherty and A.K. Harding, Astrophys. J., 761 (1983); H. Gies, Phys. Rev. D, 085021 (2000); C. Schubert, Nucl. Phys. B, 407 (2000).
[119] W. Dittrich and H. Gies, Springer Tracts Mod. Phys., 1 (2000).
[120] M. Ahlers, H. Gies, J. Jaeckel and A. Ringwald, Phys. Rev. D , 035011 (2007).
[121] E. Zavattini *et al.* [PVLAS Collaboration], Phys. Rev. D, 032006 (2008) [arXiv:0706.3419 [hep-ex]].
[122] C. Robilliard *et al.*, A. M. Sautivet, F. Amiranoff and C. Rizzo, Phys. Rev. Lett., 190403 (2007); M. Fouche *et al.*, Phys. Rev. D, 032013 (2008) [arXiv:0808.2800 [hep-ex]].
[123] K. Ehret *et al.*, arXiv:hep-ex/0702023.
[124] A. V. Afanasev, O. K. Baker and K. W. McFarlane, arXiv:hep-ph/0605250; A. Afanasev *et al.*, arXiv:0806.2631 [hep-ex].
[125] P. Pugnat *et al.*, CERN-SPSC-2006-035;
see http://graybook.cern.ch/programmes/experiments/OSQAR.html; P. Pugnat *et al.* [OSQAR Collaboration], arXiv:0712.3362 [hep-ex].
[126] A. S. Chou *et al.* [GammeV (T-969) Collaboration], Phys. Rev. Lett., 080402 (2008) [arXiv:0710.3783 [hep-ex]].
[127] A. S. Chou *et al.*, arXiv:0806.2438 [hep-ex].
[128] A. Melchiorri, A. Polosa and A. Strumia, Phys. Lett. B, 416 (2007) [arXiv:hep-ph/0703144].

[129] G. G. Raffelt, arXiv:hep-ph/0611350; S. Andriamonje *et al.* [CAST Collaboration], JCAP, 010 (2007) [arXiv:hep-ex/0702006].
[130] S. Davidson, S. Hannestad and G. Raffelt, JHEP, 003 (2000) [arXiv:hep-ph/0001179].
[131] J. Jaeckel, E. Masso, J. Redondo, A. Ringwald and F. Takahashi, Phys. Rev. D, 013004 (2007); arXiv:hep-ph/0605313.
[132] E. Masso and J. Redondo, Phys. Rev. Lett., 151802 (2006) [arXiv:hep-ph/0606163].
[133] R. N. Mohapatra and S. Nasri, Phys. Rev. Lett. (2007) 050402 [arXiv:hep-ph/0610068].
[134] P. Jain and S. Stokes, arXiv:hep-ph/0611006.
[135] R. Foot and A. Kobakhidze, Phys. Lett. B (2007) 46 [arXiv:hep-ph/0702125].
[136] I. Antoniadis, A. Boyarsky and O. Ruchayskiy, Nucl. Phys. B, 246 (2008) [arXiv:0708.3001 [hep-ph]].
[137] M. Ahlers, H. Gies, J. Jaeckel, J. Redondo and A. Ringwald, Phys. Rev. D, 095001 (2008) [arXiv:0711.4991 [hep-ph]].
[138] H. Gies, J. Jaeckel and A. Ringwald, Europhys. Lett., 794 (2006) [arXiv:hep-ph/0608238].
[139] M. Ahlers, H. Gies, J. Jaeckel, J. Redondo and A. Ringwald, Phys. Rev. D, 115005 (2007) [arXiv:0706.2836 [hep-ph]].
[140] M. Gell-Mann, R. J. Oakes, and B. Renner, Phys. Rev., 2195 (1968).
[141] T. D. Cohen, D. A. McGady, and E. S. Werbos, Phys. Rev. C76, 055201 (2007), 0706.3208.
[142] V. P. Gusynin, V. A. Miransky, and I. A. Shovkovy, Phys. Rev. D52, 4747 (1995), hep-ph/9501304.
[143] V. P. Gusynin, V. A. Miransky, and I. A. Shovkovy, Nucl. Phys. **B462**, 249 (1996), hep-ph/9509320.

2.1.3 Refractive QED processes at ELI and future exprimental considerations at ultrahigh intensities

Diffraction effects in laser-laser collision

Due to quantum vacuum polarization effects (VPEs) a strong laser beam can change the polarization of a probe field that passes through it (see Fig. 2.11) [1].

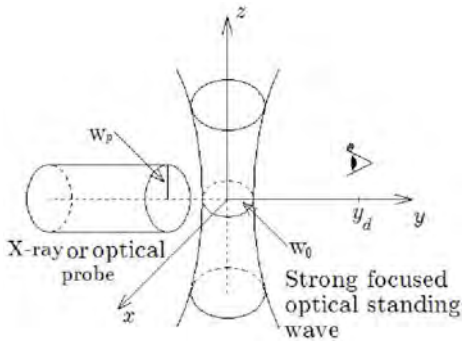

Figure 2.11: Schematic setup for observing light-by-light diffraction.

Setup 1

The strong field has the following parameters: wavelength $\lambda_0 = 0.745$ μm, spot radius $w_0 = 5$ μm and intensity $I_0 = 10^{25}$ W/cm^2. The probe beam is an X-ray probe with wavelength $\lambda_p = 0.4$ nm. and waist size $w_p = 8$ μm. The probe acquires an ellipticity of the order of 10^{-5} rad. Such values of ellipticity and polarization are nowadays measurable in the X-ray regime [2].

Setup 2

The strong field parameters are the same as before but the probe field is optical: wavelength $\lambda_p = 0.745$ μm and waist size $w_p = 300$ μm. In this case values of ellipticities of the order of 10^{-10}–10^{-9} rad are obtained that, again, can be measured nowadays [3].

Note: as compared to estimations within a plane-wave approximation, the diffraction effects due to the spatial confinement of the strong laser beam decrease the ellipticity of the probe by an order of magnitude and induce a rotation of the polarization main axis of the same order of the ellipticity.

Laser photon merging in proton-laser collision

In the head-on collision of a high-energy proton and a strong laser beam photons from the laser merge into one high-energy photon by interacting with the electromagnetic field of the proton (see Fig. 2.12) [4].

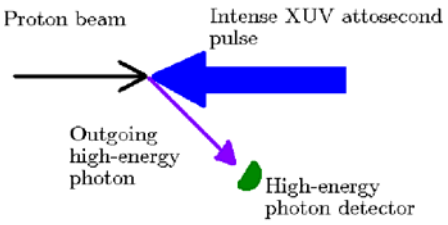

Figure 2.12: Schematic setup for observing laser photon merging.

Setup

The proton beam parameters are obtained from the simulations in [5]. They show that envisaged proton beams with the following characteristic can be obtained in the so-called laser-piston regime by employing an Exawatt laser like ELI: proton energy $E_p = 50$ GeV, number of protons per beam 2×10^{12}, beam transversal radius 5 μm and beam duration 20 fs. Rather high laser photon energies are needed to suppress background processes. By extrapolating the results of the simulations in [6] it can be envisaged that strong extreme ultraviolet (XUV) attosecond pulses with the following characteristics can be produced by the reflection of an ultra-strong laser pulse (intensity of 2.5×10^{24} W/cm^2, spot-radius of 5 μm and duration of 5 fs) from a plasma surface: intensity of 1.4×10^{24} W/cm^2, photon energy of 200 eV, pulse duration of 38 as. An energy conversion efficiency of 4×10^{-3} is assumed. With the above parameters about five photons per shot are produced due to laser photon merging.

Note 1: the simulations performed in [5, 6] have been done for laser intensities much smaller than those available at ELI. If the results can be scaled to intensities of the order of 10^{25} W/cm^2 like those available at ELI, much larger rates can easily be obtained and one can even expect that non-perturbative, multiphoton (merging of more than two laser photons) VPEs could be observable.

Note 2: if ELI could be combined with a large-scale proton accelerator much high photon yields can be obtained.

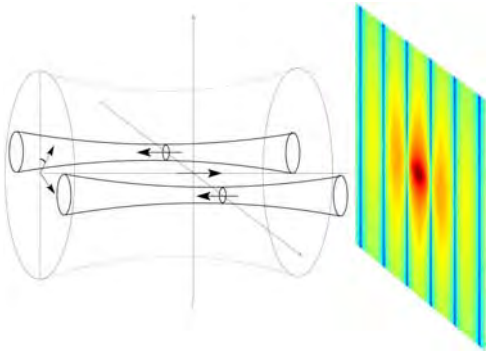

Figure 2.13: A matterless-double-slit setup.

A matterless double-slit

The quantum interaction among photons in the vacuum mediated by virtual electron-positron pairs can be exploited to put forward a matterless double-slit consisting only of light (see Fig. 2.13) [7].

In the proposed scenario two separated, parallel Gaussian laser beams form the "slits" that are probed by a third Gaussian laser beam which is diffracted to generate an interference pattern (see Fig. 2.13, where the strong beams come from the right and the probe beam is counterpropagating to them). In Fig. 2.13 a typical interference pattern is shown, where typical alternating maxima and minima are visible.

Setup

The strong laser beams parameters are: wavelength $\lambda_0 = 0.8$ μm, spot radius $w_0 = 0.8$ μm, intensity $I_0 = 5 \times 10^{24}$ W/cm^2 and pulse duration $\tau_0 = 30$ fs. The probe beam parameters are: wavelength $\lambda_p = 0.5$ nm and intensity $I_p = 4 \times 10^{16}$ W/cm^2. With these parameters about four diffracted photons are produced per laser shot. By assuming a repetition rate of the strong laser field of one shot per minute, the interference pattern is expected to be visible in about four hours of operation [7].

Absorptive QED and related issues

Pair creation can also be realized well below the critical values in combination with high frequency photons [8] or employing accelerated electrons [9] even employing ELI parameters at the initial phase. At the onset of ELI the laser pulses need also be characterized, especially with respect to intensity via highly charged ions [10] or the carrier envelope phase via injecting fast electrons [11]. Finally focussed ELI pulses may serve to accelerate ions for medical applications [12].

Probing nonlinear QED and beyond by phase contrast imaging of vacuum

Quantum electrodynamics (QED) predicts that intense electromagnetic fields cause birefringence in vacuum with the intrinsic dispersive nature. The dispersion relation from IR ($\omega \sim 0$) to UV ($\omega \sim \infty$) frequency is theoretically known only in the case of QED fields [13]. However, there has never been data even in IR frequencies to date. It is important, therefore, for experiments to quantitatively verify or disprove the QED prediction. We propose to use the phase contrast imaging to measure birefringence of vacuum under intense laser fields.

We focus on the measurement of birefringence in the optical frequency domain. As illustrated in Fig. 2.14 phase velocity shift of an optical probe laser pulse traversing a wireshaped area of a tightly focused intense laser pulse (target) is the observable we propose [15]. While the target

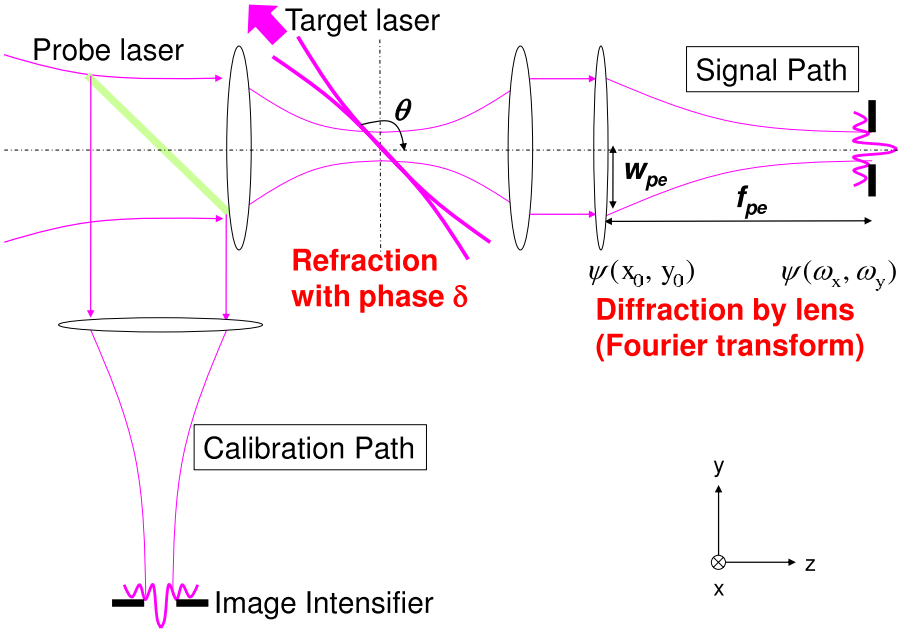

Figure 2.14: Conceptual experimental setup for the suggested phase contrast Fourier imaging.

laser is tightly focused to increase the local refractive index shift in vacuum, the probe laser has a larger transverse profile than that of the target laser. This condition produces the phase contrast inside the probe laser profile. The phase contrast is efficiently measurable by adding a conceptual lens component with a finite focal length. The added phase of the lens produces the Fourier transform of the shape of the contrast on the focal plane. Owing to the characteristic Fourier image which widely spreads from the focal point, we can separate the intensity profile caused by the interference due to the phase shift from the most intense pedestal part of the focal spot. This method is found to be similar to but distinct from the idea in [14]. We use the refractive feature of vacuum rather than diffractive one as discussed by [14].

By choosing the combination of the linear polarizations between the target and probe laser pulses we directly measure the birefringence from the photon yield found in the characteristic Fourier image on the focal plane. The nonlinear QED effect predicts the ratio between the parallel and orthogonal cases as 4 to 7. This measurement may provide the first important data in IR frequency domain to quantitatively discuss the QED dispersion relation in vacuum. If we could observe a statistically significant deviation from the prediction, that is an indication of the unexpected nature of vacuum such as QED-QCD interference and something beyond the standard model.

The change of refractive index is proportional to energy density of a pulse. In the case of a tightly focused target laser with the beam waist of 1 μm and the 0.1 kJ pulse energy, the local refractive index shift may be order of 10^{-10} with 10 fs duration time, if we assume only the nonlinear QED effect. If higher energy like several kJ is available, the phase contrast Fourier imaging may be sensitive to the amount of phase shift on the shot-by-shot basis in the ideal calculation given the equal pulse energy for the probe pulse as well. (see Table I, Fig. 5 and Fig. 6 in [15] in detail).

Bibliography

[1] A. Di Piazza, K. Z. Hatsagortsyan, and C. H. Keitel, Phys. Rev. Lett. 97, 083603 (2006).

[2] E. E. Alp, W. Sturhahn, and T. S. Toellner, Hyperfine Interact. 125, 45 (2000).
[3] K. Muroo, *et al.*, J. Opt. Soc. Am. B 20, 2249 (2003).
[4] A. Di Piazza, K. Z. Hatsagortsyan, and C. H. Keitel, Phys. Rev. Lett. 100, 010403 (2008); A. Di Piazza, K. Z. Hatsagortsyan, and C. H. Keitel, Phys. Rev. A 78, 062109 (2008).
[5] T. Esirkepov, *et al.*, Phys. Rev. Lett. 92, 175003 (2004).
[6] G. Tsakiris, *et al.*, New J. Phys. 8, 19 (2006).
[7] B. King, A. Di Piazza and C. H. Keitel, Nature Photon. 4, 92 (2010).
[8] A. Di Piazza, E. Lötstedt, A. I. Milstein, C. H. Keitel, Phys. Rev. Lett. 103, 170403 (2009).
[9] H. Hu, C. Müller, C.H. Keitel, Phys. Rev. Lett. 105, 080401 (2010).
[10] H. G. Hetzheim, C. H. Keitel, Phys. Rev. Lett. 102, 083003 (2009).
[11] F. Mackenroth, A. Di Piazza, C. H. Keitel, Phys. Rev. Lett. 105, 063903 (2010).
[12] Y. I. Salamin, Z. Harman, C. H. Keitel, Phys. Rev. Lett. 100, 155004 (2008).
[13] G. M. Shore, Nucl. Phys. B 778, 219 (2007) [arXiv:hep-th/0701185].
[14] B. King, A. Di Piazza and C. H. Keitel, Nature Photonics 4 (2010), 92.
[15] K. Homma, D. Habs and T. Tajima, [arXiv:1006.4533 [quant-ph]].

2.1.4 Search for axion-like particles by two laser beam crossing

Dark Matter is needed for explaining galactic dynamics and other astronomical observations. Axion-like particles are to explain it among possible candidates [1–5]. It is supposed that these particles have evaded all of laboratory searches so far, because they only weakly couple to matter. The high intense laser field of ELI should serve as a unique facility to test the coupling to laser photons in much weaker domains of coupling strength. We aim at the simultaneous production and decay within the crossing region of two laser beams. We utilize the frequency upshift of photons as the signature of the decay of axion-like particles by requiring the proper combinations of the linear polarizations of the two incident beams. We cover mass ranges of axion-like particles below 1 eV by changing the crossing angle.

We focus on the resonance production of axion-like particles(ALP) and their decay into two photons within the focal region where two laser beams overlap. We search for the frequency upshift of decayed photons emitted around the axis defined by a half of the angle between incident directions of the two laser beams. The production of ALP requires the initial linear polarization state of two laser beams to be orthogonal each other. The decayed photon must also satisfy the same condition. This is a feature of pseudoscalar field [6]. The mass of ALP can be scanned by changing the crossing angle of the incident two laser beams. The head-on crossing provides the center of mass energy of $2\omega_{opt}\bar{h}$ where ω_{opt} is the frequency of optical laser beam, while possible small incident angles between two beams provide the lower mass ranges. The pulse energy is a key issue to the sensitivity of detection. If 10 kJ energy is available, with a single shot we can improve the coupling limit by several orders of magnitude smaller than what is obtained in other laboratory experiments. However, alternatively, a stable high repetition rate like 1 kHz may be able to provide equivalent or higher event rate, even if we use 0.1 kJ per pulse.

Bibliography

[1] See section for *Axions and other similar particles* in C. Amsler et al. (Particle Data Group), Phy. Lett. B 667, 1 (2008) and 2009 partial update for the 2010 edition.
[2] B. Holdom, Phys. Lett. B 166, 196 (1986).
[3] B. Batell and T. Gherghetta, Phys. Rev. D 73, 045016 (2006) [arXiv:hep-ph/0512356].
[4] S. A. Abel, J. Jaeckel, V. V. Khoze and A. Ringwald, Phys. Lett. B 666, 66 (2008) [arXiv:hepph/0608248].

[5] H. Gies, J. Jaeckel and A. Ringwald, Phys. Rev. Lett. 97, 140402 (2006) [arXiv:hepph/0607118].
[6] K. Homma, D. Habs and T. Tajima, arXiv:1006.4533 [quant-ph].

2.1.5 Search for a candidate of Dark Energy by quasi-parallel laser beam focusing

Cosmological observations suggest the presence of Dark Energy. This may be attributable to undiscovered fields of small mass below 1 eV [1, 2]. Since these fields weakly couple to matter, they have evaded our effort to detect them in laboratory. The high intense laser field in ELI may open up a new window for probing these fields via the coupling to laser photons with its huge statistics per pulse. We search for these fields by observing second harmonic generation of photons in the quasi-parallel colliding system by focusing a single laser beam.

We look for higher harmonic generation of photons out of vacuum in the quasi-parallel colliding system. In order to access to ranges of small mass in the search of dark energy fields, it is essential to introduce small energies in the center of mass systems (CMS) between incoming two photons which couple to unknown fields via resonances [3]. By introducing small incident angle, we can change the CMS energy by several orders of magnitude even with the optical laser photons. We achieve small incident angles by focusing a single laser beam with long focal lengths. In this special geometry photon-photon interaction can be observed similar to second harmonic generation in the direction of the laser propagation [4]. Frank et al. applied this to the measurement of second harmonic generation in the quartz crystal [6]. The sensitive mass range depends on how small incident angle we can achieve. If we could introduce 100 m as the focal length, we can discuss mass ranges well below 10 MeV. The pulse energy is a very important factor to the sensitivity of detection. If 10 kJ energy is available, with a single shot we can improve the coupling limit by many orders of magnitude smaller than what is obtained in other laboratory experiments performed so far. Even if we use 0.1 kJ per pulse, a high repetition rate like 1 kHz which is stable over a longer run period can overcome the reduction of the event rate.

Bibliography

[1] Y. F. Cai, E. N. Saridakis, M. R. Setare and J. Q. Xia, arXiv:0909.2776 [hep-th]; S. Tsujikawa, arXiv:1004.1493 [astro-ph.CO].
[2] Y. Fujii and K. Maeda, *The Scalar-Tensor Theory of Gravitation* (Cambridge Univ. Press, 2003).
[3] Y. Fujii and K. Homma, arXiv:1006.1762 [gr-qc].
[4] K. Homma, D. Habs and T. Tajima, arXiv:1006.4533 [quant-ph].
[5] A. Afanasev *et al.*, Phys. Rev. Lett. 101, 120401 (2008) [arXiv:0806.2631 [hep-ex]].
[6] P. Franken, A. E. Hill, C. W. Peters, and G. Weinreich, Phys. Rev. Lett. 7, 118 (1961).

2.1.6 Testing radiation backreaction at super-high intensities

When laser pulses of intensities exceeding $I = 10^{22}$ W/cm^2 interact with plasmas they produce accelerated electron beams that can be directed toward the incident pulse. Another scheme to produce such interaction is an acceleration of electrons by a moderate laser pulse toward the second pulse of superstrong intensity. During such an interaction a large portion of electron energy is converted to photons of MeV energy.

Expected photon energy for such laser-beam interaction can be estimated using parameter χ, which value may be conveniently expressed in terms of the local instantaneous intensity I of the laser wave, and energy E_{el} of counter-propagating electron beam (see Ref. [1]):

$$\chi \approx 2.7 \times 10^{-3} E_{el}\ [\mathrm{MeV}] \sqrt{I/10^{23}\ [\mathrm{W/cm^2}]}.$$

For example, for $I = 10^{24}$ W/cm^2 and 1-GeV electron beam, according to Fig. 2.15, we obtain $\chi \approx 10$. According to Sokolov et al. [1], photons of $\sim 15\%$ of electron beam energy can be generated efficiently for the values of χ in the range between 1 and 10. It means that ~ 150-MeV photons are expected for 1-GeV electron beam. It is necessary to note that ~ 100-MeV electrons are easily generated during the interaction of such an intense laser pulse with bulk plasmas, what leads to production of ~ 15-MeV photons.

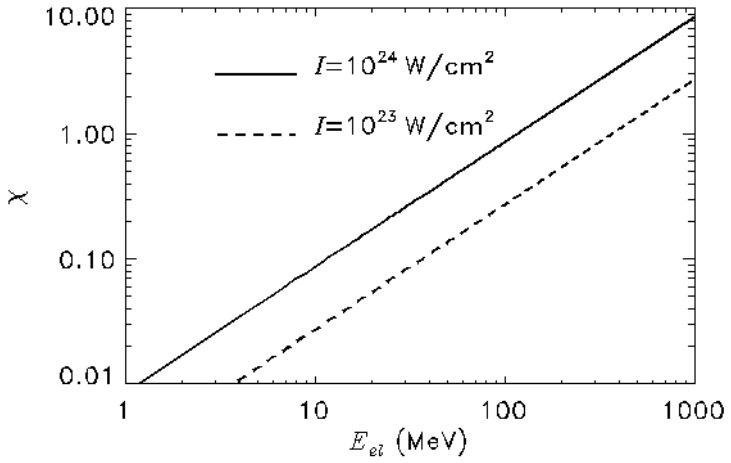

Figure 2.15: Dependence of parameter χ on the electron beam energy, counterpropagating to laser pulses of intensity I.

The radiation losses in their turn change the electron dynamics and general plasma behavior, they need to be taken into account in a self-consistent way in simulations. Such scheme has been developed in papers by Sokolov et al. [1–3], which allows considering plasma dynamics from the regime with classical radiation losses up to the one when QED effects come into play. This scheme has been extensively used to study hole-boring at super-high intensities [4–6]. It has been found that super-high intensities improve laser penetration into the target having an additional benefit of electron cooling. Half of the laser pulse energy can be converted to MeV photons.

It is necessary to note, that for parameters χ exceeding 0.1 the behavior cannot be considered as classical anymore. Corresponding changes need to be done in radiation losses spectrum and intensity. For example, Fig. 2 and Fig. 3 of Ref. [1] show these changes in transition to QED regime. Angular and frequency distributions of high-frequency radiation may as well be extracted from simulations, what allows planning future experiments and their diagnostics in greater detail.

When χ exceeds unity, electron–positron pairs can be easily produced in such interactions. Sokolov et al. [7] derived the system of integrodifferential kinetic equations for electrons, positrons and γ photons, which can be easily solved numerically. In the examples presented in Ref. [7] it is shown that laser pulses of intensity only $I = 5 \times 10^{22}$ W/cm^2 interacting with multi-GeV electron beams can produce several electron–positron pairs per beam electron. This scheme can be used for producing a pair plasma, or can be employed to deactivate electron beams, reducing the radiation hazard.

Bibliography

[1] I. V. Sokolov, J. A. Nees, V.P. Yanovsky, N. M. Naumova, and G. A. Mourou, Phys. Rev. E 81, 036412 (2010).

[2] I.V. Sokolov, JETP 109, 207 (2009).
[3] I. V. Sokolov, N. M. Naumova, J. A. Nees, G. A. Mourou, V. P. Yanovsky, Phys. Plasmas 16, 093115 (2009).
[4] T. Schlegel, N. Naumova, V.T. Tikhonchuk, C. Labaune, I.V. Sokolov, G. Mourou, Phys. Plasmas 16, 083103 (2009).
[5] N. Naumova, T. Schlegel, V.T. Tikhonchuk, C. Labaune, I. V. Sokolov, G. Mourou, Phys. Rev. Lett. 102, 025002 (2009).
[6] N. Naumova, T. Schlegel, V.T. Tikhonchuk, C. Labaune, I. V. Sokolov, G. Mourou, *Eur. Phys. J. D* 55, 383 (2009).
[7] I. V. Sokolov, N. M. Naumova, J. A. Nees and G. A. Mourou, Phys. Rev. Lett. 105, 195005 (2010).

2.2 Electron Acceleration

2.2.1 Introduction

Extreme Light Infrastructure (ELI) will be the ideal harbor for a development program of laser-plasma electron accelerators including the use of the current state-of-the-art acceleration techniques in new applications such as the generation of coherent XUV radiation in a compact free-electron-laser, electron cancer therapy or electron radiography, as well as the development of new acceleration techniques to improve this source to the level required by many present and future applications.

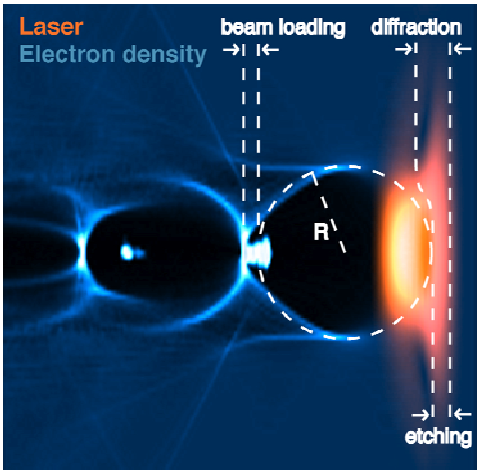

Figure 2.16: Laser-plasma acceleration: A high-intensity short duration laser pulse (orange) propagates in a plasma (blue) creating a relativistic acceleration structure in its wake. The high density electron regions inside the "bubbles" are electron bunches injected into the wakes and being accelerated.

The concept of laser-plasma wake-field electron accelerator was proposed in 1979 by T. Tajima and J. M. Dawson [1]. In a laser-plasma accelerator (LPA), a plasma medium (e.g., fully stripped helium or hydrogen ions surrounded by free moving electrons) is used to transform electromagnetic energy from a laser pulse into kinetic energy of accelerated electrons by exciting high amplitude plasma density waves. An intense laser pulse causes the plasma electrons to move out of its path through the "photon pressure". The much heavier ions barely move and as a consequence are left unshielded. Some distance behind the laser pulse, the electrostatic force exerted by the ions on the electrons pulls them back to the axis, creating an electron density peak. The pattern of alternating positive and negative charges is referred to as a plasma wave or laser wake and supports an electric field. The wave oscillates at the plasma frequency, which scales as the square root of the plasma density, and has a wavelength typically around 10 to 100 μm. This is several orders of magnitude shorter than the typical RF period used in conventional accelerators. The amplitude of the plasma wave or strength of the electric field is proportional to the square root of the plasma density (number of free electrons per unit volume) and proportional to the laser intensity (for intensities $\geq 10^{18}$W/cm^2). For typical densities (10^{18}–10^{19} electrons/cm^3) used in experiments, fields ranging from 10–100 GV/m are produced, three orders of magnitude greater than with conventional technology. The wave's phase velocity is near the speed of light and electrons injected at the proper phase can be accelerated to high energies. To reach the same particle energy, plasma accelerators can then, in principle, be three orders of magnitude shorter than their conventional counterparts.

The wavelength of the plasma waves is also around three orders of magnitude smaller than the wavelength of the radiofrequency used in conventional accelerators. The generation of low energy dispersion electron bunches requires that the length of the bunch to be a small fraction of these wavelengths and/or the use of complex techniques only compatible with a large facility. In the case of plasma accelerators this condition implies the use of electron bunches shorter than

10 fs to get an energy dispersion bellow 10% typically. So far these short pulses were produced by controlling the wavebreaking of the plasma waves or by using laser beam collision in the acceleration zone to produce a strongly localized injection.

The present state-of-the-art of laser-plasma accelerators combined with a stable laser system and a well engineered facility allows to start an experimental program of beam time for users requiring the advantages of laser-plasma accelerators (short pulse duration, high current, synchronization with intense laser pulses or other laser secondary sources) and tolerating the present limitations (high energy dispersion, low repetition rate, reproducibility, moderate bunch charge). However, since the specifications of the ELI lasers are a major leap in the laser landscape new developments on the laser-plasma accelerator are needed to take advantage of this type of lasers. These developments include long plasma channels with adequate plasma profiles to guide the laser beam during the acceleration length overcoming the diffraction, robust techniques to inject short electron bunches into the accelerating plasma structure leading to mono-energetic and usable electron beams, multiple acceleration stages to reduce the length of the accelerator and improve the energy dispersion, robust and practical laser beam coupling to the plasma channels, radiation protection and adequate diagnostics.

Bibliography

[1] T. Tajima and J. M. Dawson, Phys. Rev. Lett. **43**, 267 (1979).

2.2.2 Experimental progress and State-of-the-art on laser-plasma electron accelerators

The ability for plasmas to support very large electric fields had been demonstrated more than two decades ago at UCLA under the leadership of Chan Joshi [1]. It was not until 2004, however, that three independent groups demonstrated that, under the right conditions, laser plasma accelerators can produce narrow energy spread e-beams, an essential requirement for the broad usability of the e-beam [2–4]. The highest energy seen to date of such a high quality e-beam from a laser-driven accelerator is $\sim$ 1 GeV from a 3-cm long plasma structure [5] In the groundbreaking 2004 LPA experiments, low energy spread and low divergence e-beams were produced at the 100 MeV. A powerful laser was focused into either a gas jet or a preformed plasma. Under the right conditions, all electrons were blown out in the vicinity of the laser pulse. The electric field in this highly nonlinear wake is extremely strong, and plasma electrons become self-trapped in the back of the blown-out region and accelerated to high energy. Energy spreads on the order of a few to 10% were observed using plasma densities $\sim$ few 10^{19} cm^{-3}. Two groups, one from Imperial College/Rutherford Appleton Laboratory (UK) [3] and one from at the Laboratoire d'Optique Appliquée (LOA) in France [4], used a gas jet and focused the laser beam to a large spot size of about 20-25 mm. As a result, the distance over which the laser beam remained at high intensity was of the order of the gas jet length. The third group, the LOASIS Group at LBNL [2], made a laser produced, preformed plasma channel in the plume of a gas jet. This acted like an optical fiber for the drive laser pulse, which was guided at high intensity with a spot size $\sim$ 8 microns. An example of the measured e-beam spectra is shown in Fig. 2.17(a). To obtain low energy spread bunches, all three groups adjusted plasma density so that the accelerator length matched the dephasing distance. Modeling the experiments with particle-in-cell codes confirmed that formation of high quality e-beams with nearly all electrons at the same energy was indeed found to rely on a critical matching of the acceleration and dephasing distances, controlled by the plasma and laser parameters.

In 2006, the LOASIS group at LBNL, through a collaboration with Simon Hooker from Oxford University, subsequently demonstrated the production of high quality (low energy spread and low divergence) e-beams with energies up to 1 GeV [5], see Fig. 2.17(b). This was done using

a channel-guided LPA with laser peak powers similar to those that produced order 100–200 MeV in experiments without preformed plasma channels. A capacitor-based capillary discharge system was used to produce a 3-cm-long plasma channel with density $\sim 3 \times 10^{18}$ cm^{-3}, lower by nearly an order of magnitude than the laser-produced channels, for guiding a 40-TW peak-power laser pulse. The lower density allows for higher electron energies at dephasing.

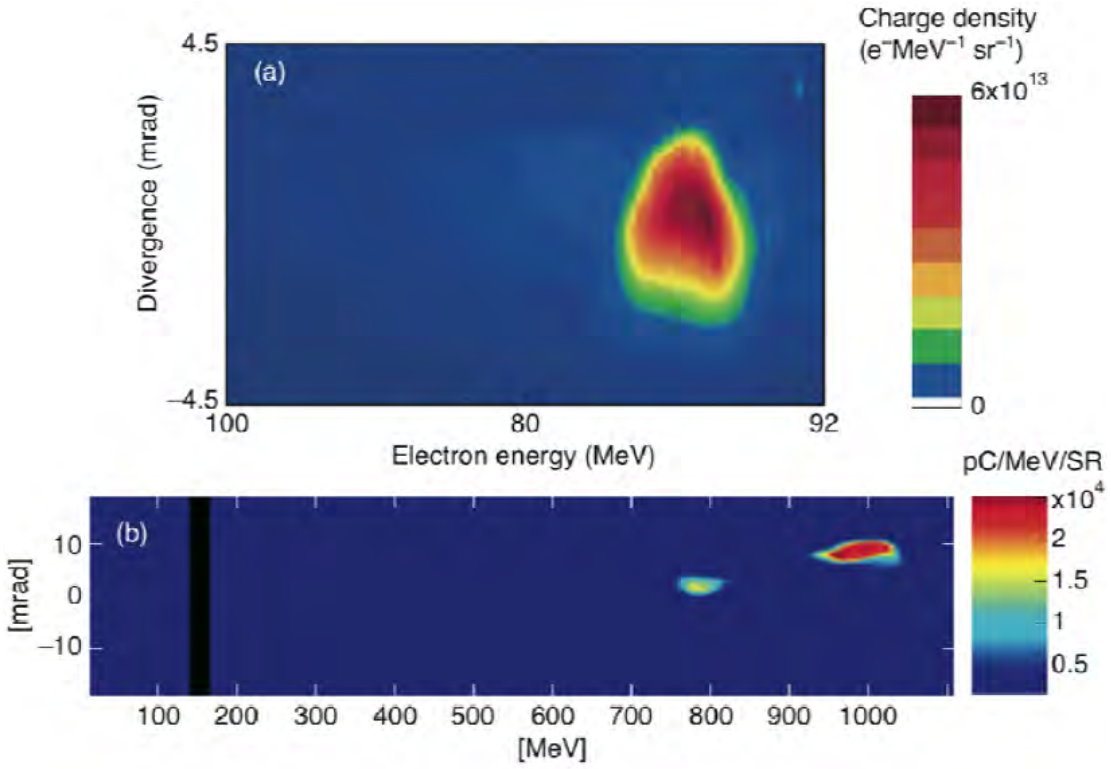

Figure 2.17: Electron energy spectra as measured with a dipole magnet and phospor screen. The charge density (electrons per MeV per unit solid angle, color scale) is shown versus divergence (mrad, vertical axis) and energy (MeV, horizontal axis). (a-top) 86 MeV e-beam containing 2×10^9 electrons with an energy spread of 4% FWHM and a 3 mrad FWHM divergence using a 9 TW laser in a 2×10^{19} cm^{-3}, 2 mm wide gas-jet plasma, within which was a laser-generated plasma channel. (b-bottom) 1 GeV e-beam containing $\sim$30 pC with an RMS energy spread of 2.5% and a 1.6 mrad RMS divergence using a 40 TW laser in a 4.3×10^{18} cm^{-3}, 33 mm long capillary discharge plasma.

On the theoretical side significant progress was achieved with the establishment of scaling laws for laser-plasma electron accelerators [6] that, in agreement with previous experimental results, allow to optimize the parameters of an accelerator (plasma density, plasma length, focal spot size, laser pulse duration) as a function of the energy available in the laser pulse. Following these scaling laws an ultra-compact accelerator using a few-cycle laser pulse with an energy of only 40 mJ was able to produce mononenergetic electron bunches with energies around 20 MeV and charges of 20 pC [7]. Later on, by introducing a controllable modulation in the plasma density the energy spread of the was improved and the electron bunch energy was controlled between 10 and 20 MeV [8] opening the way to the use of this electron beam in experiments.

In nearly all experiments to date, the accelerated electrons are plasma electrons that get trapped, from the background sea of electrons, in large-amplitude plasma wakes. Similar to ocean waves that approach the beach to break and project ocean spray forward, plasma wakes

can break and produce trapped and accelerated electrons. This is akin to a tsunami grabbing anything in its path: things move forward but without much real control. Techniques that are being developed to control this trapping or injection process are key to applicability of plasma accelerators.

Many spectacular results have been obtained in the past few years using modest lasers by today's standards (order 100 TW, 10 Hz repetition rate), providing compact sources of high energy (few hundred MeV to GeV) e-beams. This has prompted research on novel, hyperspectral radiation sources: femtosecond x-rays, coherent terahertz and infrared radiation, spanning six decades in the electromagnetic spectrum, all from the same source. Preliminary demonstration FEL experiments using a LPA are in progress at the University of Jena in Germany in collaboration with Strathclyde University, at the Max Planck Institute for Quantum Optics in Germany, and at LBNL. The most challenging applications, however – intense FEL-based radiation sources and multi-TeV particle colliders – will require exquisite e-beam quality and stability, with relative energy spreads at least an order of magnitude better than currently achieved.

Electron injection methods:

One method for controlling injection and e-beam quality in laser-plasma accelerators is colliding pulse injection [9]. In colliding pulse injection, two counterpropagating laser pulses intersect at a predetermined location in the wake. The overlapping laser pulses produce an interference or electromagnetic beat pattern with slow phase velocity (zero if the colliding laser pulses have the same wavelength). This slow-moving beat pattern can interact strongly with the slow-moving plasma electrons and, for sufficiently high pulse intensities, can boost the plasma electron velocity in the direction of the wake to trigger trapping. Colliding pulse injection, using a simplified two-pulse configuration [10], has been experimentally demonstrated at LOA in France [11]. In these experiments, a laser pulse drove a wake in a 2-mm long gas jet plasma. A second counterpropagating pulse was used to inject electrons when it overlapped with the trailing edge of the first pulse. A quasimonoenergetic e-beam containing about 20 pC was produced with about 10% energy spread.

Another method for injecting electrons into the wake is to use a density down ramp [12]. In down-ramp injection, an intense laser pulse is focused on the exit side of a gas jet plume, where the plasma density is longitudinally decreasing. As the laser pulse travels through the decreasing density, it generates a wake with an increasing wavelength. This gives the effect of "stretching" the wake behind the laser pulse, that is, the phase velocity of the wake is less than the velocity of the laser pulse. The wake's phase velocity can be tuned by adjusting the rate at which the plasma density decreases, to the point at which localized trapping readily occurs. Downramp injection has been experimentally demonstrated at LBNL [13]. A 10-TW, 50-fs laser was focused on the back edge of a 750-micron-long gas jet and generated stable low energy (order one MeV/c) e-beams, with a charge of a few hundred pC and just 170 keV/c momentum spread. Although the initial relative momentum spread is high ($> 10\%$), simulations indicate that by injecting this e-beam into a plasma channel acceleration stage, energetic ebeams at the GeV level or greater can be produced with very low energy spread (~ 100 keV).

Using one of the above injection or trapping methods to produce a high quality e-beam as the first stage, then coupling this e-beam into a second acceleration stage consisting of a plasma channel, should generate high-energy, high-quality e-beams for a variety of applications. Theory and simulation indicate that the absolute energy spread of the e-beam should be nearly preserved as the e-beam is accelerated through subsequent stages. For example, if a 1 MeV absolute energy-spread e-beam is accelerated up to a level of 10 GeV, this could result in an e-beam with a 10^{-4} energy spread, sufficient to drive a free-electron-laser in the x-ray regime. It is also essential that the second stage operates with fields that do not self-trap electrons again, i.e., "dark-current free" in conventional accelerator terminology.

Channeling methods:

The production of a multi-GeV transportable and focusable electron beam in a laser-plasma accelerator requires the use of a plasma channel. A plasma channel consists in a cylindrically symmetric plasma with a radial parabolic density profile with the minimum density coincident with the laser beam propagation axis. In this way, the plasma channel provides the required plasma density for the electron accelerator and behaves like an index graded optical fiber keeping the laser focused to high intensity. In a channel the plasma needs to have a high degree of ionization, i. e. the intense laser pulse should not produce significant additional ionization or the guiding profile will be compromised. Therefore, the plasma channel is normally produced in a background of a light gas such as hydrogen or helium where total ionization is possible. The use of plasma channels and ELI laser beams (50 J) has the potential to produce electron bunches up to 15 GeV in a 1 meter acceleration stage.

A plasma channel is typically produced by the fast release of energy in a low diameter plasma cylinder of the background gas. The expansion of the column and the fast cooling of its external layers will result in the required parabolic profile.

The fastest mechanism for releasing the necessary energy to create the channel consists in using one or more laser pulses [14, 15] in an adequate geometry. However, these techniques are difficult to scale above the few centimeters level. An alternative is to use an electric discharge. Electric discharges have been used with success to guide intense laser beams and accelerate electrons up to 3 cm and 1 GeV [5]. In these experiment the discharge was produced inside a small diameter dielectric capillary filled with hydrogen and the interaction of the plasma with the capillary walls result in the required channel profile.

Another discharge based technique consists in produce a discharge in free space (not confined by a capillary) between to sharp electrodes with apertures for laser coupling and decoupling [16]. In this case a higher-voltage (typically 50 kV/cm) is required to produce a straight plasma channel. Using this setup a current around 1 kA in a 100 ns pulse can produce the required plasma profile for plasma channels with an electron density of 10^{18} cm^{-3} on the channel axis. This technique was scaled to a length of 2 cm producing highly reproducible plasma channels [17].

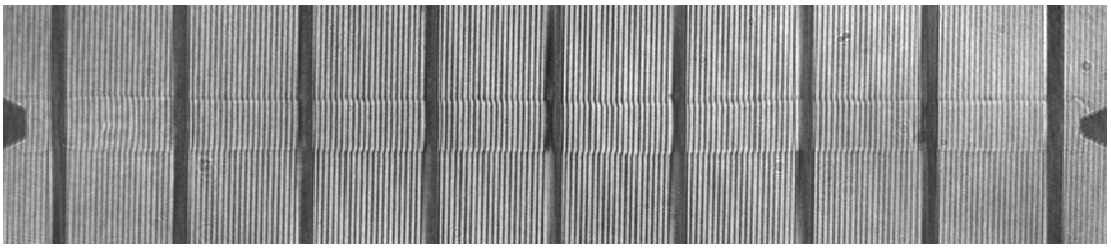

Figure 2.18: Interferometry picture of a 2 cm long plasma channel produced inside a gas cell [17]. A plasma line is produced between the to conical electrodes. The vertical dark lines are the shadow of 250 micron thick dielectric plates with 300 micron diameter apertures coincident with the optical axis defined by the electrodes. The cylindrical shock wave is clearly seen in the image. These plasma channels present an acceptance aperture around 50 micron (for near infrared) and the axial plasma density close to 10^{17} cm^{-3}. The ideal length of this channel is around 10 cm leading to a potential energy gain around 4 GeV for electron acceleration.

Numerical laser-plasma experiments with massively parallel simulations:

In addition to theoretical and experimental studies, numerical modeling plays an important role in the LWFA research, by helping to target and to optimize the experimental parameter ranges, and also by providing insights on the physical processes underlying the experiments. Although

several physical regimes are possible for the same laser pulse energy, the scalings predicted by the theoretical models indicate that a next generation of LWFAs, at the Petawatt range, will involve the propagation of a moderate intensity (10^{18}–10^{19} W/cm^2) laser pulse through a plasma column of several meters, with the output of a high energy beam with tens of GeV.

In a fully kinetic three-dimensional particle-in-cell (PIC) simulation [18] the Maxwell equations are resolved on a numerical grid, while the particles move freely in space. The smallest structure to be resolved is the laser wavelength, typically on the order of 1 micron, which contrasts with the length of the plasma column at the meter scale. This constitutes the main challenge for LWFA numerical modeling. The several orders of magnitude that separate the laser wavelength from the plasma length may lead to over a million of simulation iterations for the modeling of future experiments. This constitutes a challenge to the accuracy of the numerical algorithms, and is extremely computationally intensive. Therefore, and while it is possible to simulate a few centimeters of plasma, a fully kinetic three-dimensional simulation of a meter scale accelerator is currently unpractical, even with the large computational facilities available (e.g., [19–21]). One alternative currently employed is the use of reduced codes that leverage on physical assumptions to simplify the numerical algorithms. For instance, QuickPIC [22] uses the quasi-static approximation to separate the (long) laser and the (short) plasma evolutions, and thus reach computational gains that can go above three orders of magnitude. These approximations, however, limit the application of the code and particular regimes/conditions cannot be fully modeled. Examples may include the self-injection process or the laser evolution close to the depletion length. The fully kinetic algorithms are therefore required for the thorough modeling of LWFA experiments.

OSIRIS [23] and VORPAL [31] are two examples of fully relativistic, electromagnetic, and massivelly parallel PIC codes that have been extensively used in LWFA simulations [2, 24–26]. Recent developments have focused on optimizing the code scalability on large supercomputers and on improving the overall computing performance. For example for the code OSIRIS, strong scaling benchmarks were performed from 256 cores up to 65,536 cores in Jugene [19], with a final efficiency of 75%. The efficiency is ensured with a spatial domain composition where the field solver is local, with communication minimization, and with dynamic load balancing (node boundary adjustment as the simulation progresses). To increase the performance of the code, we have written the core algorithm sections, namely the current deposition and the particle pusher, to use the vector units of state-ofthe-art processors. For the hardware currently available, this implies running in single precision, and allows for computational gains of 2-3 times. We have also developed advanced diagnostics, like particle tracking [27] and radiation emission [28], together with an advanced visualization infrastructure for quick data display, analysis, and post-processing [27]. Despite the advances in code scalability and performance, the simulations for the next generation of laser systems are still challenging, in particular if large parameter scans are to be performed. It was recently shown that, in the modeling of two distinct spatial scales, the computational requirements may be strongly reduced by performing the simulation in a relativistic moving frame [29]. Standard LWFA simulations are done in the laboratory frame, where the plasma is at rest. As mentioned above, this implies resolving the laser wavelength of 1 micron over the plasma length, that can reach several meters. If we move to a frame that travels relativistically in the direction of the laser, the plasma will contract and the laser will stretch, thus reducing the scale gap and the disparity of lengths to be simulated. This transformation enables computational gains that can go above three orders of magnitude, with equivalent quantitative outputs.

The application of this scheme enables not only the ultra-fast simulation of current experiments where plasma lengths of a few cm are typically used, but also allows the first time, fully kinetic, three-dimensional study of the next generation of laser systems where plasma lengths can reach several meters. This study was performed with OSIRIS for three different regimes of a 250 J laser [30], confirming the predictions from the phenomenological models that energy

frontier beams will be possible with these advanced systems.

Modeling the next generation of LWFA experiments poses a challenge to code developers due to the long plasma distances to be simulated, while still resolving the laser wavelength. This thus implies extreme scale simulations in the largest supercomputers available. The most recent upgrades of the OSIRIS framework have been depicted, in particular the strong scalability benchmarks, optimized algorithms, and sophisticated diagnostics. By performing the simulations in a boosted frame, computational requirements can be reduced by several orders of magnitude, which enables ultra-fast modeling of current experiments and first-time modeling of the future LWFA's. First simulations already indicate the possibility to reach output beams at the energy frontier.

Bibliography

[1] C.E. Clayton et al., Phys. Rev. Lett. 54, 2343 (1985).
[2] C.G.R. Geddes et al., Nature 431, 538 (2004).
[3] S.P.D. Mangles et al., Nature 431, 535 (2004).
[4] J. Faure et al., Nature 431, 541 (2004).
[5] W.P. Leemans et al., Nature Phys. 2, 696 (2006).
[6] W. Lu, et al., Phys. Rev. ST Accel. Beams 10, 061301 (2007).
[7] K. Schmid, et al., Phys. Rev. Lett. 102, 124801 (2009).
[8] K. Schmid, et al., Phys. Rev. ST Accel. Beams 13, 091301 (2010).
[9] E. Esarey et al., Phys. Rev. Lett. 79, 2683 (1997).
[10] G. Fubiani et al., Phys. Rev. E 70, 016402 (2004).
[11] J. Faure et al., Nature 444, 737 (2006).
[12] S.V. Bulanov et al., Phys. Rev. E 58, R5257 (1998).
[13] C.G.R. Geddes et al., Phys. Rev. Lett. 100, 215004 (2008).
[14] C. G Durfee and H. M. Milchberg, Phys Rev. Lett. 71, 2409 (1993).
[15] P. volfbeyn et al., Phys Plasmas, 6, 2269, (1999).
[16] R. Bendoyro et al., IEEE Trans. Plasma Sci. 36, 1728 (2008).
[17] C. Russo et al. to be published.
[18] Birdsall, C. K.& Langdon, A.B., Plasma Physics via Computer Simulations, Adam Hilger, NY (1991).
[19] Julich Supercomputing Centre (www.fz-juelich.de/jsc/ibm-bgl).
[20] Argonne National Laboratory (www.anl.gov).
[21] National Energy Research Scientific Computing Center (www.nersc.gov).
[22] Huang, C. et al., J. Comp. Phys. 217, 658-679 (2006).
[23] Fonseca, R. A. et al., in P.M.A. Sloot et al., editors, ICCS 2002, LNCS.
[24] Tsung, F. et al., Phys. Rev. Lett. 93, 185002 (2004).
[25] Pak, A. et al., accepted for publication in Phys. Rev. Lett.
[26] Froula, D. H. et al., accepted for publication in Phys. Rev. Lett.
[27] Fonseca, R. A. et al., Plasma Physics and Controlled Fusion 50, 124034 (2008).
[28] Martins, J. L., Martins, S. F., Fonseca, R. A., Silva, L. O., in SPIE Conf. Ser., 7359 (2009).
[29] Vay, J.-L., Phys. Rev. Lett. 98, 130405 (2007).
[30] Martins, S. F. et al., submitted for publication
[31] C. Nieter, J. R. Cary, J. Comput. Phys. 162, 448 (2004).

2.2.3 Future research directions

Laser-plasma accelerators can be developed in different directions. In the short term it will be possible to install small permanent facilities able to deliver electron bunches in the sub-GeV, sub

100 pC ranges with energy spreads bellow 10%. Such a program can use a commercial state-of-the-art CPA laser system, but it will require a considerable size facilities. These permanent laser-plasma electron accelerators are an essential step in order to start growing a community of beam users with capability to develop or adapt applications taking advantage of the parameters of these sources.

The other main research direction would be the development of the laser-plasma acceleration technology and diagnostics making it compatible with ELI type laser beams. For pulse energies around 50 J (ELI specification for 10 Hz repetition rate) the optimum length of a plasma accelerator is close to 1 meter. Probably the more challenging and innovative developments required in the field would be the development of the plasma channels for 1 meter length acceleration stages and a beam loading technique to produce a low energy dispersion (better than 1%) beam in the first acceleration stage. An extensive experimental and numerical development would be necessary to produce electron beams with quality for efficient transport and focusing in demanding applications such as free-electron-lasers. These developments, due to their complexity, will require dedicated permanent facilities and teams. ELI can be a major step in this strategy.

2.2.4 Prospects for electron acceleration with ELI

The ELI laser is uniquely suited to explore electron acceleration in plasmas in that it can span all parameter regimes of interest. This includes the quasi-linear wakefield regime, typically characterized by laser intensities on the order of 10^{18}–10^{19} W/cm^2, and the highly nonlinear blowout (or bubble) regime, typically characterized by intensities greater than 10^{19} W/cm^2. The quasi-linear regime has the advantage of being nearly symmetrical for acceleration of both electrons and positrons, since the wakefield is nearly sinusoidal. The highly nonlinear bubble regime has the advantage of extremely large accelerating fields, but due to the highly nonlinear structure, the wake is highly asymmetric, with a small phase region available for positron acceleration. The ELI laser could explore electron acceleration to 100 GeV in a single stage or in multiple stages. In addition, ELI could explore a quasi-1D wakefield regime, by using large spot sizes (and large powers), which would have the advantage of greater amounts of accelerated charge.

The general physics issues that could be explored with ELI include study of the quasi-linear, blowout, and quasi-1D wakefield regimes, the maximum charge that could be accelerated in the wake, beam loading (the effect of the accelerated charge on the wake structure), the quality (energy spread and emittance) of the accelerate bunch, pump depletion (loss of laser pulse energy to the wake), dephasing (the accelerated particles outrunning the wake and laser pulse), electron injection techniques, stability of the both the laser pulse and electron bunch within the plasma (hosing instabilities), and the efficiency of the acceleration process.

Several approaches to achieving 100 GeV energy gains can be envisioned, including:

Approach 1: Acceleration in the quasi-linear regime using a single-stage plasma channel. This would require a laser pulse with a normalized field strength of $a = 1$–2 (here, $a = 0.85 \times 10^{-9}\, l$ [mm] $I1/2$ [W/cm^2], with l the laser wavelength and I the laser intensity), a laser pulse energy on the order of 1 kJ, a laser pulse duration on the order of 300 fs, a plasma density on the order of 10^{16} cm^{-3}, and plasma channel length on the order of 20 m. Issues include the production of long plasma channels (current state-ofthe-art is tens of cm) and the possibility of using magnetic fields to lower the on-axis plasma density.

Approach 2: Acceleration in the blowout regime using a single-stage uniform plasma. This would require a laser pulse with a normalized field strength of $a = 5$–10, a laser pulse energy on the order of 10 kJ, a laser pulse duration on the order of 300 fs, a plasma density on the order of 10^{16} cm^{-3}, and plasma length on the order of 5 m. Issues include the self-focusing and self-guiding of high power $P \gg Pc$ (here $Pc = 17\, lp^2/l2$ GW is the critical power for relativistic

self-focusing with lp the plasma wavelength), and the transverse stability of such pulses. The short pulse length (<lp) should help in reducing instabilities.

Approach 3: Acceleration using multiple stages. One possibility is to reach 100 GeV by using 10 stages, each providing 10 GeV energy gain. Each stage would use a laser pulse on the order of 40 J, 100 fs, propagating within a plasma channel with density on the order of 10^{17} cm^{-3} with a length on the order of 1 m. Issues include the coupling of the laser to the channel, staging and synchronization, and novel focusing optics to couple the laser pulse to the plasma channel over short distances.

Approach 4: Acceleration using extremely nonlinear bubble regime wakefields. This regime would use very high laser intensities with $a \sim 100$ in uniform plasmas. The advantage of this regime would be extremely large accelerating fields, but the energy gain in a single stage may be limited due to rapid depletion of the laser pulse energy. The experiments could explore the scaling laws in this regime, since theoretical studies in this regime are less extensive than in the regimes of more modest laser intensity. Experiments could also explore the bunch quality, which is likely to be worst than in regimes of more modest intensity. Proof-of-principle experiments on the trapping and acceleration of protons in these very highly nonlinear wakes can also be explored.

Electron acceleration from solid targets: It also possible to accelerate electrons using an intense laser pulse interaction with a thin solid target. When an intense laser pulse impacts a thin, overdense target (that remains overdense), the ponderomotive force accelerates electrons through the target. If the target is thin enough, the electrons can emerge from the back side. However, a strong electrostatic field quickly develops on the back side of the target that inhibits electron acceleration to high energies. This electrostatic force is also responsible for the acceleration of ions from the back side of the target (Target Normal Sheath Acceleration). For lasers impinging on the target surface at an angle, electrons can be accelerated to modest energies in the direction of the reflected laser pulse. For extremely large laser intensities with normal incidence on a very thin target, the target can appear underdense to the laser pulse due to relativistic effects. The laser pulse can then propagate completely through the very thin target, and all of the electrons in the path of the laser pulse can be accelerated by the ponderomotive force of the laser. In this regime the ponderomotive force is much greater than the space charge force and acceleration can continue as both the laser pulse and the electrons propagate away from the back of the target. This can result in the production of a dense sheet of relativistic electrons (a "flying mirror"). This mechanism requires very high laser intensities ($a \sim 20$–100), very high laser contrast (to avoid pre-ionization of the target, the pre-pulse should be $< 10^{15}$ W/cm^2), and very thin targets (as thin as a few nm). Circular polarization is also beneficial. Issues include production of circularly polarized laser pulses with very high intensities and very high contrast, and production of very thin targets and targets with densities lower than typical solid density.

Applications of laser accelerated electron bunches:

Some of the unique properties of laser accelerated electron bunches include ultrashort bunch duration (< laser pulse duration) and intrinsic synchronization with the laser pulse. This can enable a variety of applications in the field of ultra-fast science (pump-probe measurements). Broadband incoherent x-rays can be generated due to the transverse (betatron) oscillations of the electrons in the laser wakefield. Narrow bandwidth, incoherent gamma-rays can be generated by backscattering a laser pulse off the relativistic electron bunch. Coherent THz radiation can be generated when the bunch exits the plasma or passes through a thin foil. Incoherent narrow bandwidth x-rays can be generated by passing the bunch through an undulator magnet (synchrotron radiation). Coherent x-rays can be generated by passing the bunch through an undulator magnet via the free electron laser (FEL) mechanism, provided the bunch quality is sufficiently high (low emittance and low energy spread). Production of "flying mirrors" (dense

relativistic electron sheets from the interaction of ultra-intense pulses with very thin targets), which can be used to generate ultrashort coherent x-rays pulses by reflection of a short laser pulse. Production of positrons by the interaction of the bunch with a solid target, the direct interaction of the laser pulse with a solid target, or with the interaction of an ultra-relativistic bunch with a counterpropagating laser pulse. Ultrafast x-rays can also be produced from laser interactions with thick solid targets. High energy density physics studies and astrophysical studies (gamma ray bursts) with intense laser-solid interactions. Production of ultra-relativistic bunches for high energy physics (electron-positron colliders) and studies in nonlinear QED (with the interaction of a counterpropagating intense laser pulse).

2.3 Ion sources

2.3.1 Ion beams produced in laser matter interaction: introduction

By directing a high power ultra-short laser pulse onto a thin target, it has been found in 2000 that beams of high-energy ions and protons could be produced. These beams have intrinsic, unique, qualities (extreme laminarity [~ 0.0025 mm.mrad for a current $\sim$ kA], ultra-short duration [ps] and high particle number per bunch [10^{11}–10^{13}]) that distinguish them from beams produced by conventional sources (e. g. accelerators) and that have already lead to innovative applications of these beams. Moreover, these sources are extremely compact (the acceleration occurs over a distance of about tens of microns). Fast recent progress, both experimental and theoretical (studying new interaction regimes), has hinted that the extreme parameters of ELI will allow the production of ultra-high energy ions (GeV and beyond). This will open the door to future unique applications like time and space resolved radiography of dense matter, injectors study for medical applications, for ion beam physics, spallation, or transmutation. The multi-beam capability of ELI will be moreover in a position to grasp the opportunities for pomp probe experiment offered by combining the produced ion beams with the range of other ELI-based radiation sources (e. g. X-rays, electrons, high harmonics).

2.3.2 State of the art

Status as of 2010

Using present-day common laser facilities in the 100 TW range, low-emittance [1] protons are routinely accelerated up to 20–30 MeV energies from thin ($\sim 20\,\mu$m) solid metallic target. Record level in terms of kinetic energy was first set by the early Nova 1 PW laser facility at LLNL which had produced up to 56 MeV protons [2] but was recently improved at the Trident laser facility, which has produced up to 59 MeV [3] using special cone-flat targets, and at the Sandia 100 TW laser facility, which has produced up to 65 MeV protons [4] using reduced-mass targets. These beams can be refocused and energy selected [5, 6]. In standard conditions, protons contained in a surface layer (~ 20 Å thick) of hydrocarbon contaminants are preferentially accelerated due to their lowest q/m ratio. Heating of the target prior to the experiment eliminates these hydrogen contaminants and allows acceleration of heavier ions [7]. By simply changing the substrate, laser-acceleration can therefore produce a versatile, easy to modify source of ions. Up to a few % conversion efficiency have been measured from laser energy to proton energy integrated in the spectrum from 10% to 100% of the cut-off energy.

Basic regimes and acceleration mechanisms

Several mechanisms have been demonstrated to induce proton and ion acceleration, namely target sheath normal acceleration (TNSA) [8], front-surface acceleration [9], shock acceleration [10, 11] and collective acceleration [12, 13], the TNSA mechanism being the one, with presently accessible highest laser intensities that produces highest energy ions. Acceleration takes place at the target-vacuum interfaces where laser-accelerated relativistic electrons form a dense electron plasma sheath (field $\sim$ TV/m) that ionizes surface atoms and accelerates ions in the target normal. High laminarity of the ion beam requires acceleration from an initially cold surface (i. e. that has a sharp vacuum interface). Usually, this is ensured only at the target non-irradiated rear surface. Using very high temporal contrast laser pulses (i. e. contrast $> 10^{10}$), laminar acceleration is also possible from the target front that is in this case also unperturbed by the low-level laser pedestal [14]. Enhancing the laser temporal contrast also allows using extremely thin targets (in the nm range) which have been shown to yield higher energy ions with increased efficiency [14–16], due to a combination of increased laser absorption and electron recirculation. Very recently, first experimental demonstrations of Radiation Pressure Acceleration, which do

not rely, on the contrary of TNSA, on hot electrons, were obtained [17, 18]. Simulations by Esirkepov and Macchi [19, 20] show that in this regime, the whole volume of the target can steadily gain energy from the laser, as the target is exposed to the radiation pressure of the laser that quasi-balances the restoring force given by the ion-electron charge separation field. A signature of this regime is that all particle species are accelerated to similar velocity, resulting in a monochromatic spectrum. If stable acceleration can be ensured, the process, particularly in its so-called "light-sail" implementation employing ultrathin foils [21–23], should lead to very high conversion efficiencies and ion energies scaling linearly with laser intensity.

Ion beam manipulation

Refocusing of the naturally divergent beam (due to the curvature of the electron sheath) is possible using curved targets [24] or optics, either conventional [6, 25] or plasma-based [5]. Monochromaticity in the TNSA regime is made possible either by accelerating only a monolayer of elements (all ions then experience the same electric field and are accelerated to the same energies) deposited on a foil made of higher-Z material [7], by using the specific electron distribution on the surface of isolated microdroplets [26] or by selecting differentially focused spectral components [5,27]. TNSA acceleration has been tested using low-density plasmas [28,29] and has been shown to be also efficient. Although it produces beams of lower quality than from solids, it offers the advantage of being compatible with a high-repetition rate for the laser source.

A review of the maximum energy and proton number obtained in various experiments is shown in Fig. 2.19. It shows clearly that the maximum proton energy increases with the laser pulse duration (see experiments inset box). It has also been shown that the efficiency of the acceleration process also increases with the laser pulse duration and the laser irradiance.

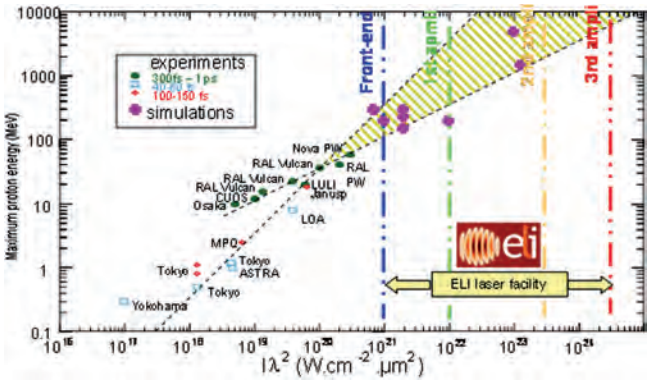

Figure 2.19: Review of cut-off maximum proton beam energy, as a function of laser intensity, as reported from published data. Experimentally measured data are small dots, boxes and crosses corresponding to three pulse duration ranges shown. Simulations performed at higher laser intensities planned for ELI are reported as big purple dots. Note that, as experimentally proven up to 10^{20} W.cm^{-2}, the maximum proton energy for the extreme short pulses is $\sim$I, whereas for the longer pulses $\sim$I$^{1/2}$.

Directions for evolution (2015)

ELI, in its various stages, will allow exploring new, efficient, ion acceleration regimes that have been observed in numerical simulations. As a result, and as shown in Fig. 2.19, several hundred MeV up to a few GeV protons could be achievable with the planned on-target intensities within reach of ELI in its final stage (i. e. on target intensities of up to 10^{25} W/cm^2). Supposing that the proton number would be similar to what obtained currently ($\sim 10^{10}$) on existing facilities

and considering a higher repetition rate (e. g. 10 Hz), we could then obtain currents of up to a few tens of nA, comparable with a conventional accelerator.

According to simulations, the predominant ion acceleration regime should be, when increasing the laser intensity, first (i) shock accelerated at the target front surface or in its interior for $I > 10^{21}$ W.cm^{-2} [10], followed by (ii) radiation pressure acceleration (RPA), when $I \sim 10^{23}$ W.cm^{-2}. In the latter case, at such high intensities, the electromagnetic wave is directly converted into ion energy via the space-charge force related to the displacement of all electrons in a thin (nm scale) foil, allowing to reach GeV-scale energies . As mentioned above, this regime can be already explored at more moderate intensities ($\sim 10^{20}$–10^{21} W/cm^2). For this, TNSA is intentionally suppressed by using circularly polarized laser light in order to avoid producing hot electrons [23].

Multiple stage acceleration using stacked foils [30] would offer the additional prospect of further energy increase of the ion maximum energy. However, further simulations and benchmarking experiments are necessary in order to investigate the influence of radiation losses appearing at such ultrahigh intensities. RPA would impose constraints on the facility, namely an extremely high temporal contrast for the laser pulse and circular polarization for the wave interacting with the plasma. At a similar intensity regime, other simulations have also shown that ions could be accelerated to > 10 GeV in the "bubble" regime of wakefield acceleration using near-critical density plasmas and mixed ions [31]. Such underdense plasma targets would have the benefit of allowing high repetition rate operation. ELI will thus offer the prospect of producing and study a versatile ions source, at high repetition rate, while enhancing simultaneously the high-energy end of the spectrum, the beam monochromatization and the laser-to-ions conversion efficiency, all of which being crucial points for the development of applications in various areas. The possibility to vary the pulse duration of the ELI laser beam lines offer also a way to create proton/ion bunches of different durations, offering a way to adapt the emission optimal to the various envisioned applications.

2.3.3 Scientific program

Current applications

Laser-accelerated ion beams are currently mainly used in two applicative areas: (i) warm dense plasma generation and (ii) probing of matter and/or electric and magnetic fields but have potentially very close parameters to other significant applications.

At the boundary between condensed matter and plasma physics, the study of matter in the warm dense matter (WDM), i. e. of dense matter (1–10 g/cm^3) at high temperature (1–100 eV) [32], is essential as this class of states of matter is relevant to a wide range of disciplines. Indeed, the matter in this state is found not only in astrophysical objects but also in the transition from solid density matter to the plasma state found in numerous plasma generators and in the initial low-adiabatic compression phase of indirectly driven inertial fusion experiments. Accurate modeling of inertial plasmas requires physical data, equation of states, stopping power and transport coefficients in this WDM regime where classical theories such as plasma kinetic theory and condensed matter theory fail, as WDM is defined by ion-ion correlation and Fermi degeneracy parameters that are both on the order of the unity or greater. Using high currents of laser-accelerated ions presents a significant advantage over other techniques to produce WDM [24]. Indeed, ions have intrinsically in-depth energy deposition capability. Moreover, being produced in a very short time (few ps) the ions can also deposit energy potentially in a shorter time scale than the expansion time of matter heated to a few eV. This technique allows one to produce sufficiently large volumes of WDM to permit quantitative observations, thus opening the way for measurements of WDM parameters [33], stopping power, equation of state and others. Protons are also relevant as a diagnostic tool for fusion science, they are e. g. employed

in experiments that study laser-plasma or hydrodynamic instabilities or as a tool to diagnose target compression.

ELI, by producing a high number of ions at high energy in a compact manner and in a short time-scale, will offer a decisive advantage when producing such WDM by allowing to increase the volume of heated matter and to push the achieved temperatures up to 10 keV range, as required for e. g. laboratory astrophysics. This will be complementary with very large scale international projects like FAIR at GSI (Germany) which share the same goal but with much longer bunch duration.

Short, low-emittance ion sources produced by laser-acceleration are already used to perform pump/probe ps-resolved and μm-resolved experiments to probe electric and magnetic fields in plasmas [34]. This technique has proved to be an essential tool, yielding the discovery of entirely new phenomena by diagnosing previously inaccessible observables [35]. Besides the possibility to take 2D snapshots of electric and magnetic field structures in plasmas the usually broader energy distribution of protons in combinations with their time of flight effects allow also to track the whole dynamics of field evolution in plasmas [36,37]. Due to the relatively modest ion energies achieved up to now, this technique is however limited to probing fields in low-density media. For the same reason, dense matter (e. g. shocked matter) probing is also possible using this technique in order to retrieve density (and not field) information, but is presently limited to very thin samples.

At relatively modest energies, that should be within reach of its first, but still higher than presently available ($\sim$ 100–200 MeV), ELI will allow extending the range of such field/matter probing application. It will then allow studying e. g. electron transport in dense matter (as required for the optimization of secondary X-rays or of nuclear reactions within dense materials to produce positrons or γ-rays) or shocks in compressed material for laboratory astrophysics and geophysics [38]. Higher ion energies (up to 800 MeV), will allow to radiograph very dense and thick objects (e. g. matter at 50 g/cm^2). Here, compared to conventional accelerators (e. g. the LANSCE 800 MeV proton accelerator found at LANL for dense matter probing), the excellent emittance of an ELI ion source in combination with its short pulse duration will be a significant advantage, allowing unprecedented spatial and temporal resolution.

Potential future applications

Bio-chemistry

A first potential area of application for ion sources produced by ELI lies within the area of bio-chemistry helped by ion beam irradiation for conditioning materials (using radicals, e. g. hydroxyl radical yields in the tracks of high energy C6+ and Ar18+ ions in liquid water) to steer reactions. For this, ELI will offer interesting complementary prospects with cyclotron facility like GANIL as, again, the ion beams will be produced with the possibility of offering simultaneously other sources of companion radiation to work with (e. g. X-rays, electrons, etc).

High quality collimated ion beams for nuclear reactions and hadron-therapy

High yield medical applications can also be investigated using ELI-based ion sources. For medicine, two main applications can be considered: first, proton therapy assisted by lasers [39,40]. Here, the proton energies ought to be within the therapeutic window: between 70 and 250 MeV with a $\sim$ nA current (10^{10} part/s) with spectral and spatial beam shaping. Not only protons, but also other ion beams, such as carbon or lithium beams, will also be produced in this prospect, as they appear nowadays to be of major interest for hadron therapy. Another potential advantage of such a source is that the energy and quantity of the ions could be adapted from shot to shot (i. e. during the treatment time), which allows a more modular form of treatment compared to conventional accelerators. By fostering development of such technique, ELI would help promoting proton source for hospitals to treat cancer tumors. ELI will allow estimation of the cost and optimization of the source through the guidance of radiotherapists. Moreover,

electron and proton beams with a pulse length in the ps or fs time scale will provide a unique opportunity to study new and important biological radiation effects (small/high dose irradiation). Here are, as a reference, the required energies for proton and ion therapy in the case of a "mobile arm" treatment (i. e. the proton beam is moved around the treatment position in order to irradiate the concerned parts of the body):

Ions	p	3He2+	12C6	16O8+
energies (MeV/u)	48	72	88	102
beam spot size	4–10 mm (2d-gaussian)			

ELI could also be used for time-resolved biology studies. There is a fundamental difference between the impact of a heavy ion and a proton or electron beam. The difference in the delta electron density caused by the impacting ion results in biological effects, which are not known below a microsecond timescale. It manifests itself in certain tumors which are resistant to proton therapy, but not to e. g. Carbon therapy. Increasing the dose rate, but keeping the total dose constant could lead to higher biological effectiveness and would allow proton therapy to new types of cancer not applicable today. Here basic research is required to investigate dose dependent effects, like water radiolysis close to cell DNA or multiple impacts within the chemical recombination timescales. Short proton and ion bunches from ELI would increase the accessible range of particle energy and flux by orders of magnitude from the present status. Higher particle energies could also stretch the range for radiobiological research from solar cosmic radiation to the realm of interstellar radiation background experiments.

Nuclear physics applications: Towards highest ion energy and high luminosity (Extreme Light Hadron Collider, ELHC)

Reaching extremely high ion energies, in the GeV range, would allow using ELI in another extremely attractive area, namely as a source for spallation. This opens all the downstream study of neutron beams, or as a source for the transmutation of radio-nucleides. Currently there is only one very costly facility (Spallation Neutron Source (SNS), recently completed at ORNL, USA) that is able to perform transmutation of nuclear waste, moreover, conventional neutron sources are currently not very flexible and are of low brillance. Here ELI would again offer a complementary tool to conventional sources like the SNS to probe matter but in a time-resolved manner that is not possible at the SNS. Indeed, the neutron, produced through D–D monochromatic reactions, should be bunched and keep the short duration of the initial ion source.

One should also note all the works proceeding for Accelerator Driven System (ADS) for waste disposal and future power plants suported by the IAEA, Vienna [41] as well as C. Rubbia's proposals needing ~ 2 GeV proton beams [42].

Finally, proton beams with energies $>$ GeV could be used for laser-driven heavy-ion collider experiments with about 1 million events per laser shot [19]. For this, beams containing about 10^{12} protons in the 5–6 GeV range, as predicted in [43] could be suitable. Pair creation through laser-proton collisions [44] would also be a unique application allowed by ELI when using both the high-field laser beams and the extremely high energy proton beams both produced by the facility.

2.3.4 Potential for business and technology transfer

The laser accelerated ion beams provided by ELI facility will potentially find a wide area of applications, e. g. hadron therapy for tumour treatment, PET isotope production, bio-chemistry

to steer reactions, spallation, pair creation through laser-proton collisions, etc. In particular, laser-driven proton therapy could find itself suitable for shallow tumours of several centimetres in depth: ocular disease, nasal tumours, thyroid cancer, laryngeal cancer, skin cancer, etc.

A strong advantage of laser-driven accelerators could lie in the compactness and huge reduction of size as compared to conventional accelerator facilities, resulting in substantial reduction in costs. Moreover, the laser-produced ion beam characteristics offer complementary advantages over classical accelerator beams, especially in medical and nuclear application fields. For example, while the conventional sources for spallation do not offer the possibility of time-resolved probing of matter, a laser facility apparently does offer this option.

The potential for drastic cost reduction of particle accelerators for cancer treatment is potentially extremely important for medical business. The interest is that, by utilizing laser accelerated protons, the generating laser beams can be transported close to the Gantry-like set-up where the protons are produced close to the patients. Therefore no expensive measures for radiation protection of the proton beam transport as in conventional facilities are required. This arrangement makes also easier to vary the proton dose in terms of energy spectra and pulse duration. If realized, this scheme could stimulate a large market of photo-medical industry with huge investment leverage. In fact, current limitation of particle beam therapy with the conventional accelerators is its high cost. Thus, small laser accelerators could lead to a revolutionary change in the cancer therapy scenery and thus open a vast photo-medical industrial market.

Currently there are about 30 conventional proton or heavy ion therapy facilities in operation worldwide: e. g. Loma Linda University in California, USA (http://www.protons.com), PSI (Paul Scherrer Institut) in Villigen, Switzerland (http://www.psi.ch), HIMAC (Heavy Ion Medical Accelerator) in Chiba, Japan (http://www.nirs.go.jp), Institut Curie in Orsay, France (http://protontherapie.curie.info), NPTC-MGH (Northeast Proton Therapy Center - Massachussets General Hospital) in Boston, USA (http://www.massgeneral.org). Thousands of patients per year are treated in the existing facilities. The average cost of a conventional proton therapy facility is 70–100 M USD consisting of 40 M for building and radiation shielding, 15–30 M for accelerator itself, and 15–30 M for gantries and other related costs. The cost for a carbon therapy facility is about 2–3 times higher. On the other hand, the best estimate for a laser-based proton facility is currently 4.5–7.5 M USD consisting of 0.5 M for building/shielding, 3–5 M for accelerator (laser + target), and 1–2 M for gantries/others. The main advantage is evidently the drastic decrease in the cost of building and shielding (about 100 times), which could permit rapid spread of commercial proton facilities around the world.

The ELI facility can provide a major contribution for the development of future high-quality and low-cost proton sources for cancer therapy. In particular, ELI can first optimize the ion source, and then in collaboration with industrial partners design and test the prototypes. In particular, shielding and beam transport design will concern magnet systems for electron stopping and ion energy selection, beam stoppers, collimators. The sources to be considered will be primary protons/electrons, secondary photons and neutrons, implying different shielding materials (lead, tungsten, copper, steel, polyethylene, heavy concrete). Thus the radiation protection, extremely important for practical implementation in therapeutic facilities, can be verified.

Co-operation with companies working in the field of conventional accelerators, such as HITACHI, IBA, VARIAN, SIEMENS or ACCSYS is anticipated. In fact these companies can also transfer their know-how and suggest the way to fit conventional techniques to the small laser accelerator machines. Thus, an efficient technology transfer towards commercial sector and back is expected, e. g. in terms of accelerator and gantry coupling, beam transport, particle selection, collimation, monochromaticity, scanning beam systems, etc.

Besides the medical applications, MeV protons are used in a variety of industrial applications, ranging from radiography of paintings and art objects to colouring of precious stones. It is therefore likely that a facility, offering high-precision, high luminescence protons beam, better and cheaper than conventional proton facilities, will soon attract industries for their po-

tential applications. However, since the characteristics of the achieved proton beams are still to be refined, a precise definition of the technology transfer between industry and ELI is still premature.

2.3.5 Conclusion

In summary, ELI offers a versatile proton/ion source emitting in an unprecedented energy range but moreover it is worth to note that the facility with its unique variability in the parameter range given by the optional different laser beam parameters would not exclusively be interesting for basic science studies. The proton/ion "beam lines" with the concomitant environment (diagnostics, radiation protection etc) would also allow to accomplish more technically relevant applications, which are already in the focus of present day activities. ELI will be a demonstrator of these possibilities and prepare integrated designs of specific lasers facilities for many applications ranging from medical to industrial ones.

Bibliography

[1] T. E. Cowan et al., Phys. Rev. Lett. **92**, 204801 (2004).
[2] R. A. Snavely et al., Phys. Rev. Lett. **85**, 2945 (2000).
[3] K. A. Flippo et al., Phys Plasmas **15**, 056709 (2008).
[4] M. Schollmeier et al., Bull Am Phys Soc **55**, 377 (2010).
[5] T. Toncian et al., Science **312**, 410 (2006).
[6] M. Schollmeier et al., Phys. Rev. Lett. **101**, 055004 (2008).
[7] B. M. Hegelich et al., Phys. Plasmas **7**, 2076 (2000).
[8] S. P. Hatchett, C. G. Brown, T. E. Cowan, E. A. Henry, J. S. Johnson, M. H. Key, J. A. Koch, A. B. Langdon, B. F. Lasinski, R. W. Lee, A. J. Mackinnon, D. M. Pennington, M. D. Perry, T. W. Phillips, M. Roth, T. C. Sangster, M. S. Singh, R. A. Snavely, M. A. Stoyer, S. C. Wilks and K. Yasuike, Phys Plasmas 7, 2076 (2000).
[9] K. Nemoto et al., Appl. Phys. Lett. **78**, 595 (2001).
[10] L. O. Silva et al., Phys. Rev. Lett. **92**, 015002 (2004).
[11] A. Henig et al., Phys. Rev. Lett. **102**, 095002 (2009).
[12] A. Henig et al., Phys. Rev. Lett. **103**, 045002 (2009).
[13] S. Steinke et al., Laser and Particle Beams **28**, 215 (2010).
[14] T. Ceccotti et al., Phys. Rev. Lett. **99**, 185002 (2007).
[15] P. Antici et al., Phys Plasmas **14**, (2007).
[16] S. J. Gitomer et al., Phys. Fluids **29**, 2679 (1986).
[17] A. Henig et al., Phys. Rev. Lett. **103**, 245003 (2009).
[18] M. Borghesi, Bull. Am. Phys. Soc. **55**, 194 (2010).
[19] T. Esirkepov et al., Phys. Rev. Lett. **92**, 175003 (2004).
[20] A. Macchi et al., Phys. Rev. Lett. **94**, 165003 (2005).
[21] A. Macchi, S. Veghini and F. Pegoraro, Phys. Rev. Lett. **103**, 085003 (2009).
[22] A. P. L. Robinson et al., New J. Phys. **10**, 013021 (2008).
[23] B. Qiao et al., Phys. Rev. Lett. **102**, 145002 (2009).
[24] P. K. Patel et al., Phys. Rev. Lett. **91**, 125004 (2003).
[25] S. Ter-Avetisyan et al., Laser and Particle Beams **26**, 637 (2008).
[26] S. Ter-Avetisyan et al., Phys. Rev. Lett. **96**, 145006 (2006).
[27] E. Fourkal, J. Li, M. Ding, T. Tajima, and C. Ma, Med. Phys. **29**, 1326 (2002).
[28] L. Willingale et al., Phys. Rev. Lett. **96**, 245002 (2006).
[29] P. Antici et al., New J. Phys. **11**, 023038 (2009).
[30] S. M. Pfotenhauer et al., New J. Phys. **12**, 103009 (2010).
[31] B. Shen, Y. Li, M. Y. Yu, and J. Cary, Phys. Rev. E **76**, 055402 (2007).

[32] S. Ichimaru, Rev. Mod. Phys. **54**, 1017 (1982).
[33] A. Mancic et al., Phys. Rev. Lett. **104**, 035002 (2010).
[34] M. Borghesi et al., Phys. Plasmas **9**, 2214 (2002).
[35] L. Romagnani et al., Phys. Rev. Lett. **105**, 175002 (2010).
[36] L. Romagnani et al., Phys. Rev. Lett. **95**, 195001 (2005).
[37] T. Sokollik et al., Appl. Phys. Lett. **92**, 091503 (2008).
[38] A. Ravasio et al., Phys. Rev. E **82**, 016407 (2010).
[39] V. Malka et al., Med. Phys. **31**, 1587 (2004).
[40] S. V. Bulanov, V. S. Khoroshkov, Plasma Phys. Rep. **28**, 453 (2002).
[41] A. Stanculescu, Nuclear Reaction Data and Nuclear Reactors: Physics, Design and Safety, Nos 1 and 2, Vol. 5, p. 561 (2001).
[42] C. Rubbia, J. A. Rubio, *A tentative programme toward full scale energy amplifier*, European Organisation for Nuclear Research, CERN/LHC/96-11(EET)).
[43] A. Pukhov, Reports on Progress in Physics **66**, 47 (2003).
[44] A. Di Piazza, K. Z. Hatsagortsyan and C. H. Keitel, Phys. Rev. Lett. **100**, 010403 (2008).

2.4 Neutron sources

2.4.1 Introduction

Neutron beamlines at ELI will enable a broad range of both fundamental and applied science. Thermal neutron sources ($\sim$ meV–eV) are widely used for diffraction and spectroscopy experiments, (see e. g. Ref. [1]) and fast neutrons ($\sim$ MeV) can be applied to radiography, medicine and material damage studies [2]. Laser generated sources of neutrons hold the advantages of a small source size and pulse duration and synchronicity with other secondary sources at ELI. Imaging using combined sources can yield information about the composition of materials as well as their density [3]. The intense source of γ-radiation planned at ELI-NP also opens up the possibility of a revolutionary thermal neutron source generated through neutron halo isomers. This scheme avoids the need for moderation of the neutron energy and is predicted to generate neutron fluxes orders of magnitude higher than at existing spallation sources [4].

2.4.2 State of the art neutron sources

(a) Non-laser based sources

Intense neutron fluxes can be generated at ion accelerators through a secondary reaction in a solid density converter. Any ions transiting the converter are deflected and the neutrons pass through a shielded collimator into the experimental area. Quasi-monoenergetic sources use a thin, low-Z target and D(d,n), T(d,n) or ^{7}Li(p,n) reactions [2, 5]. Numerous facilities provide neutron energies up to 300 MeV in fluxes exceeding 10^5 n cm^{-2}s^{-1}. When the target used is a thick, high-Z material neutrons are generated through spallation as the high energy ion beam strikes the converter. This leads to the emission of a broad spectrum of fast neutrons (MeV–GeV), typically following a $1/E_n$ dependence, commonly termed *white beams* [2]. Large-scale accelerator based neutron facilities offer very high neutron fluxes of order 10^{16}–10^{17} n cm^{-2}s^{-1}. For many applications, low-Z moderators (e. g. heavy water) slow the neutrons to the thermal or cold energy range (MeV–eV) [1].

Other methods to create high fluxes of neutrons are from nuclear fission reactors giving of order 10^{15} n cm^{-2}s^{-1} (see e. g. the discussion in Ref. [4]) and photonuclear reactions (γ,n) driven by bremsstrahlung from relativistic electron beams giving $\sim 10^{13}$ n s^{-1} [6]. Compact portable devices based on DD and DT reactions at 2.5 MeV and 14 MeV are commercially available with a strength $\sim 10^9$ n s^{-1} [7].

(b) Laser based sources

Laser-driven neutron sources are based on DD or DT fusion and (p,n) and (γ,n) reactions. There are two approaches: reactions between ions within a single laser-heated deuterium target or conversion in a secondary target of a laser driven ion or γ ray beam.

Single target scheme

Neutrons can be generated by irradiating thick solid deuterated plastic targets with intense lasers. A series of experiments with 1–100 TW lasers demonstrated yields up to 10^7–10^8 n sr^{-1} per shot [8–12]. Highly energetic deuterons heated directly by the laser at the front surface stream into the target and so initiate 'beam-target' fusion reactions with cold deuterons within the bulk of the solid. The angular distribution of the neutrons is closely related to that of the accelerated ions and is predominantly in the forward direction for short scale-length plasmas [9, 13]. Particle in cell code modeling of this mechanism (Fig. 2.20) was in good agreement with these experimental results and identified laser and plasma parameters, which lead to the production of an energy tuneable, quasi-mono-energetic forward-directed fast neutron beam [13].

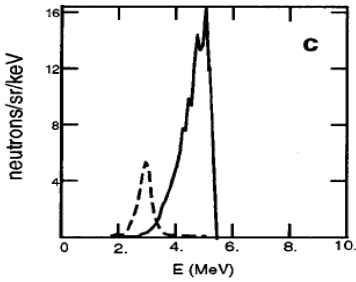

Figure 2.20: Quasi-monoenergetic neutron spectrum simulated from [13].

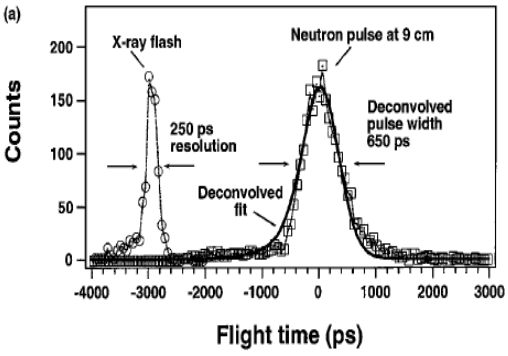

Figure 2.21: Sub-nanosecond neutron pulse from cluster fusion [16].

Fusion reactions can also be initiated in gases [14–18] or a mist of sub-micron droplets [19] produced using pulsed gas jets. The presence of solid-density clusters or droplets dramatically increases the absorption efficiency of short pulse intense irradiation, which can exceed 90% of a petawatt-class laser pulse [20]. Because the interaction is with an extended target several millimeters in length, 'beam–beam' reactions can occur between hot deuterons within the plasma as well as 'beam–target' reactions with the surrounding medium. If the emission is dominated by the thermonuclear process, then the duration of the neutron burst is limited to less than a nanosecond (Fig. 2.21) because the ions rapidly traverse the laser-heated volume [16]. These experiments have been performed using D_2, CD_4 or D_2O and in principle can use a mixture of the tritiated forms of these materials. There are some indications of a weak anisotropy, but these sources are generally considered isotropic. The flux scales strongly with laser energy and has been measured as $\sim 5 \times 10^4$ n sr^{-1} when driven with a 10 J laser pulse [17].

Double target scheme

In 'pitcher-catcher' experiments a primary target (pitcher) is irradiated with an intense laser pulse to generate an ion beam from the rear surface. The catcher is a slab of material which acts as a neutron converter in the same way as they are used on accelerator facility neutron sources.

DD fusion in deuterated plastic catcher targets yielding $\sim 10^4$ neutrons per shot has been demonstrated using liquid droplets as the laser interaction target (20 μm diameter D_2O) enabling a high repetition rate [21,22]. Ions were accelerated from the droplet through similar mechanisms to those seen in planar solids. A two-peaked distribution of (DD) fusion neutrons was detected indicating neutron production both within the droplet and from sheath accelerated deuterons striking the catcher target. When scaled to petawatt class lasers, the yield from this process is expected to reach 10^{10} neutrons per shot [7].

Several experiments have been performed to measure neutron fluxes generated through (p,n) reactions in a catcher target from intense laser interactions [7, 23–25]. Beams of protons were generated in a primary foil target and directed onto lithium, boron, zinc and lead samples

yielding up to 10^9 n sr^{-1} per shot using petawatt class lasers. In these experiments the targets are relatively thick, producing a broad distribution of proton energies and a correspondingly broad neutron spectrum. With control of the properties of the proton beam it should be possible to generate a quasi-monoenergetic neutron source following the same principle as the linear accelerator based ^{7}Li(p,n) schemes [5].

The same arrangement can employ the large fluxes of γ rays produced in intense laser plasma interactions to initiate (γ,n) reactions in the catcher sample [22,26,27] (these reactions also take place within the target itself [28]). These photoneutrons are usually measured to diagnose the interaction rather than being optimised to investigate their potential as a source and so yields tend to be low ($\sim$ 100 neutrons per shot [27]). In the next section we discuss a preferable option for generating neutrons using γ beams.

2.4.3 Neutron beams produced via neutron halo isomers

The intense sources of γ-rays available in the near future will enable a unique neutron source based on neutron halo isomers. The proposed scheme (Fig. 2.22) has been described in detail in a recent publication [4]. At the ELI-NP facility high intensity, small bandwidth (<0.1%) γ-beams will be produced through Compton scattering a laser beam from an electron beam energized by a linear accelerator. These 6–8 MeV γ beams can populate neutron halo isomers in stable nuclei with mass numbers of about A = 140–180 and A = 40–60, where the $4s_{1/2}$ or $3s_{1/2}$ neutron shell model state reaches zero binding energy. Irradiation from a second photon source subsequently releases the neutron, providing a bright polarized beam of low energy neutrons. The second source is either at an optical or an x-ray wavelength depending on the separation energy of the isomer.

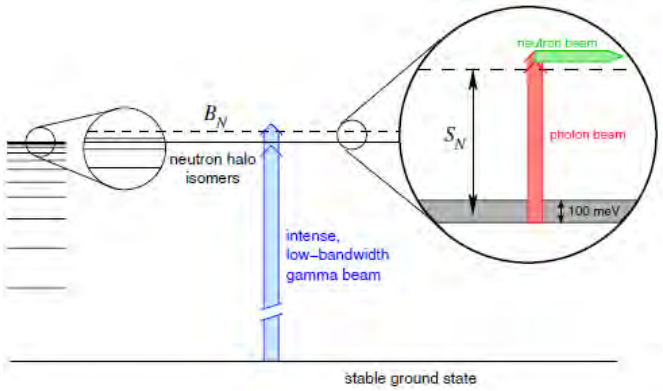

Figure 2.22: Schematic picture of the neutron production scheme [4].

If successful, the brightness of this new neutron facility will be orders of magnitude higher than existing sources. The average brilliance is estimated to be about 100 times greater than the best performance of reactors and because it will be pulsed with a duration of order a microsecond, the peak brilliance will reach a value of 10^{11} / [(mm mrad)^2 0.1% BW s] (see Fig. 2.23). Further optimization of the source could lead to nanosecond neutron bunch durations. If the isomers have a low binding energy ($\sim$ eV), the neutron beams can be launched with an optical laser. This might lead to directed neutron emission along the laser polarization direction increasing the flux and also polarizing the neutron beams. The most optimistic estimates for the brilliance of the neutron beams are thus 10^8 times better even than those shown in Fig. 2.23.

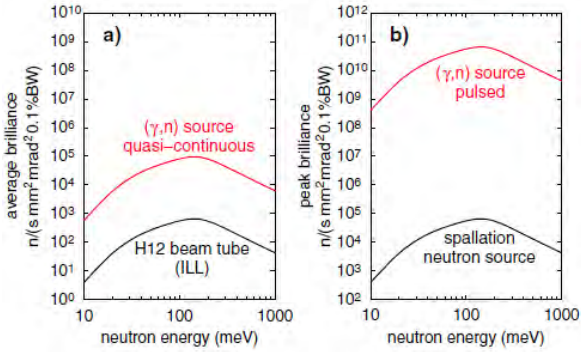

Figure 2.23: (a) Average brilliance of continuous neutron sources and (b) peak brilliance of pulsed neutron sources as a function of neutron energy [4].

2.4.4 Applications

At ELI-NP the source produced using neutron halo isomers will provide unprecedented fluxes of polarized thermal neutrons. There is a wealth of scientific applications for these beams as evidenced by the extensive programs pursued by researchers at current facilities (e. g. Ref. [1]). These areas include studies of soft condensed matter, including polymer structure, surface adsorption and intermolecular interaction. Neutron sources are also used in solid state chemistry, to probe material structure and magnetic ordering within solids and also in Earth Sciences and Engineering.

The availability at ELI-Beamlines of a short pulse (<nanosecond) laser-driven fast neutron source inherently synchronized to other high quality radiation and particle beams will be ideal for pump-probe type experiments. Spectral and spatial control will offer access to regions of warm dense matter, high energy density plasmas and shocked materials not achievable by other means. There are also applications for fast neutron beams which address some key societal issues in security, medicine and energy [2].

Single event effect testing

Soft errors occur in electronic equipment as a result of bombardment from neutrons produced as a secondary effect of cosmic rays impinging on the atmosphere. The neutron flux increases with altitude so is of particular concern for aircraft. Intense neutron sources are used to perform *single event effect* tests to determine the response of electrical equipment to the neutron flux. The fast neutron spectrum obtained from a white beam spallation source is very similar to that encountered in the atmosphere [29].

Security screening

Neutrons are a very useful tool for radiography, since they are complementary to x-ray sources because neutrons are attenuated by low-Z materials, whereas x-rays are attenuated by high-Z. Using either source independently gives a map of the density of the sample, but combining γ and neutron beams provides an image of the *composition* of the sample as well as its density. The ratio of the attenuation factor of the two gives a ratio which can be attributed to a certain material and shown in false colour [3].

Material and detector testing

With realistic plans in place for a demonstration nuclear fusion reactor within the next 20 years, it is imperative to study the effects of neutron bombardment on the materials which will be used for these devices [30]. The damage processes occur on a sub-nanosecond timescale, so to perform pump-probe experiments requires a short-pulse neutron source synchronized to a sampling secondary source. A laser-based facility would thus be ideal for this application. There must also be a concurrent program to build and test the many detectors needed to operate such reactors.

nTOF experiments for cross-section data

Obtaining cross-section data for neutron capture and neutron induced fission reactions is crucial for exploring options for alternative nuclear fission reactor designs and for radioactive waste management. Many of these cross-sections are poorly known at high incident neutron energy. Currently these experiments take place at the n_TOF facility at CERN which uses a 20 GeV proton beam to generate a white spectrum from 1 eV to 250 MeV [31].

Neutron cancer therapy

Neutron sources also offer certain advantages for cancer therapy treatments and the technology for patient treatment is well established [32]. Some tumours can be treated with neutrons, which would be either resistant to or would reoccur with conventional therapy. The biological effectiveness of neutrons is high (they have a high rather than a low linear energy transfer) and so the required tumour dose is lower than with photons, electrons or protons.

Bibliography

[1] http://www.isis.stfc.ac.uk.
[2] J. Blomgren, Proceedings of Science (FNDA 2006) 022.
[3] J. Rynes *et al.*, Nucl. Instrum. Meth. A **422**, 895 (1999).
[4] D. Habs, M. Gross, P. G. Thirolf and P. Böni, Appl. Phys. B (accepted 2010).
[5] M. Baba, Proceedings of Science (FNDA 2006) 086.
[6] W. Mondelaers and P. Schillebeeckx, Notiziario neutron e luce di sincrotrone **11**, 19 (2006).
[7] T. Zagar *et al*, New J. Phys. **7**, 253 (2005).
[8] G. Pretzler *et al.*, Phys. Rev. E **58**, 1165 (1998).
[9] L. Disdier *et al.*, Phys. Rev. Lett. **82**, 1454 (1999).
[10] D. Hilscher *et al.*, Phys. Rev. E **64**, 016414 (2001).
[11] P. A. Norreys *et al*, Plasma Phys. Contr. F. **40**, 175 (1998).
[12] N. Izumi *et al.*, Phys. Rev. E **65**, 036413 (2002).
[13] C. Toupin *et al.*, Phys. Plasmas **8**, 1011 (2001).
[14] S. Fritzler *et al.*, Phys. Rev. Lett. **89**, 165004 (2002).
[15] T. Ditmire *et al.*, Nature (London) **398**, 489 (1999).
[16] J. Zweiback *et al.*, Phys. Rev. Lett. **85**, 3640 (2000).
[17] K. W. Madison *et al.*, Phys. Plasmas **11**, 270 (2004).
[18] G. Grillon *et al.*, Phys. Rev. Lett. **89**, 065005 (2002).
[19] S. Ter-Avetisyan *et al.*, Phys. Plasmas **12**, 012702 (2005).
[20] E.T. Gumbrell *et al*, New. J. Phys. **10**, 123011 (2008).
[21] S. Karsch *et al.*, Phys. Rev. Lett. **91**, 015001 (2003).
[22] F. Ewald *et al.*, Plasma Phys. Control. Fusion **45**, A83 (2003).
[23] K. L. Lancaster *et al.*, Phys. Plasmas **11**, 3404 (2004).
[24] J.M. Yang *et al.*, J. App. Phys. **96**, 6912 (2004).

[25] P. McKenna *et al.*, Phys. Rev. Lett. **94**, 084801 (2005).
[26] K. W. D. Ledingham *et al.*, Phys. Rev. Lett. **84**, 899 (2000).
[27] H. Schwoerer *et al.*, Phys. Rev. Lett. **86**, 2317 (2001).
[28] T.E. Cowen *et al.*, Phys. Rev. Lett. **84**, 903 (2000).
[29] C. Slayman, Proceedings of the SELSE6 conference, paper 16 (2010).
[30] D. Ridikas and X. Ledoux, Proceedings of Science (FNDA 2006) 021.
[31] P. F. Mastinu *et al.*, J. Phys.: Conf. Ser. **41**, 352 (2006).
[32] http://www-bd.fnal.gov/ntf/index.html.

2.5 Terahertz sources

2.5.1 Introduction

There is huge potential for ELI to generate intense sources of terahertz radiation (0.1–10 THz, 30–3000 μm, 3.3–333 cm^{-1}) through laser-driven processes. Because this frequency range lies above the capabilities of traditional electronics but below the range of optical and infrared generators, bright THz sources of any kind have only become available in recent years in an attempt to cover the "terahertz gap" [1, 2].

a) Terahertz applications

This range of frequencies has many scientific applications because it contains, for example, the rotation frequency of large molecules and the characteristic frequencies of high temperature superconductors. The THz absorption spectra of important biological molecules are sensitive to the conformation of these molecules. In the last two decades THz pulses were used in a vast number of spectral measurements. Since the penetration depth of THz radiation is relatively high for insulators, semiconductor structures, plants and biological tissues, an important application of this radiation is imaging. Many applications of THz pulses exist, since (in contradiction to the visible electromagnetic pulses) not only the temporal shape of their intensity, but the temporal shape of its electric field strength can be measured by (for example) electro-optic sampling [3]. Using time domain spectroscopy it is possible for example to measure simultaneously the real and the imaginary part of the dielectric constant of materials in the far-infrared range. Because of these applications it is important to explore this spectral range. However, at room temperature the maximum of the blackbody radiation is at about 4 THz. To suppress the strong background noise, intense coherent THz sources are needed.

b) Terahertz sources

The interest in such radiation has led to the design and construction of numerous large-scale facilities optimized specifically for high power THz operation [4–7]. Synchrotrons are the leading sources of high average power THz radiation ($\sim$ 100 W) because of the very high repetition rate ($\sim$ GHz) whereas the highest peak powers ($\sim$ 100 MW) have been obtained using linear accelerators [8] and free electron lasers [6]. High THz pulse energies up to 100 μJ have been produced using coherent transition radiation from a linear accelerator [8]. High demand and high cost limits the available access to such large machines and laser based sources offer an attractive alternative.

Although generation of THz pulses by photoconductive switches with useful spectral content in the 1–20 THz range has also been reported [9], no data are available concerning the THz pulse energy, which is expected to be small because of the small area between the electrodes of the used switch. Recently, ultrashort THz pulses up to 5 μJ energy have been generated from two-color-pumped plasma sources driven by femtosecond lasers. Another table-top method is optical rectification of femtosecond pulses. By using the tilted-pulse-front pumping technique in $LiNbO_3$ ultrashort THz pulses with energies in the 10 μJ range (up to 50 μJ) have been demonstrated [10, 11].

In high power laser interaction research, emission in the THz region is less well characterized than is short wavelength radiation (x-rays and γ-rays). Unlike other secondary sources there is also a lack of a strong theoretical and numerical basis for the expected scaling of THz parameters using the next generation of intense lasers. In Chapter 2.6.7 we detail various options for producing intense THz sources using petawatt class lasers. These consist of harvesting radiation from relativistic electron beams, driving solid surface plasma process and direct conversion of the laser light through optical rectification. We discuss the scalability of the THz emission and are confident that ELI has the capability for highest energy THz pulses so far available.

2.5.2 Table-top terahertz sources

Commercial laser-pumped THz sources use a high repetition rate (>kHz) Ti:Sapphire laser to induce THz emission in electro-optic crystals and photoconductive antenna but generally the power is rather limited [2].

Several THz generation techniques are available which utilize moderate intensity laser pulses ($\sim 10^{14}$ Wcm^{-2}) and could potentially be scaled to higher laser energies. One method is to focus a fundamental and second harmonic beam together into ambient air [2, 12, 13]. These drive a four wave mixing process in which the envelope of the laser pulse creates a "rectified field" which drives a single cycle THz pulse. Similar intensities have been used to form long ($\sim$ 1 m) filaments in air which emit terahertz radiation through a "transition-Cerenkov" process [14].

Optical rectification can also be activated in electro-optic crystals. The maximum pump intensity is limited by either material damage or saturation and so for high energy conversion a large aperture crystal is required. Terahertz pulses of 1.5 μJ were generated with a 40mm diameter laser beam in 75 mm diameter ZnTe crystals [15]. Materials such as $LiNbO_3$ with a higher non-linearity can be used in the tilted-pulse-front pumping (TPFP) scheme [16]. Pulse energies up to 30 μJ have been measured [10,11] which are comparable to the large scale facility sources discussed below. The scaling of this process with laser energy may lead to THz conversion to Joule-level energies [17] and is discussed in Chapter 2.6.7.

2.5.3 Accelerator based terahertz sources

The highest power THz sources to date have been produced by manipulating picosecond duration bunches of relativistic electrons. These can generate THz radiation in a variety of ways, the main mechanisms being coherent synchrotron radiation (CSR), coherent transition radiation (CTR), the free-electron laser (FEL) and coherent emission through the Smith-Purcell effect (SPR).

a) Coherent synchrotron radiation

Synchrotron radiation is emitted when electrons follow a curved path. In electron storage rings this covers a wide wavelength range from far infrared to x-radiation. The emission is usually incoherent but coherent synchrotron radiation (CSR) can be emitted when the electron bunch length is shorter than the wavelength of the emission. Sub-picosecond electron bunches can be accelerated in "ultra-stable" modes generating a bright broadband source in the region of about 0.3–1.2 THz [18,19]. This can be complemented by "femtoslicing" the electron bunches so that they emit in the range from a few THz to $\sim$ 0.5 THz [20].

CSR has also been demonstrated using a linear accelerator to provide the relativistic electron bunch [21] and in a cavity as a driver of a free-electron laser [22]. Because of the high repetition rate of these sources the average CSR power is of order 100 W.

b) Coherent transition radiation

Coherent transition radiation (CTR) is emitted when relativistic electrons cross a boundary between two different media. The highest energy THz pulses to date were generated from 1 nC, 1 ps, 120 MeV electron bunches accelerated using a linear accelerator striking an aluminium mirror [8]. The emitted THz radiation was measured to be a single-cycle with energy of $\sim$ 100 μJ and was focused to a $\sim$3 mm spot to reach field strengths of $\sim$ 1 MV/cm. This method thus achieves high peak power of $\sim$ 1 MW but the average power was limited by the 2.5 Hz repetition rate. Using the same method, a CTR beamline has recently been installed on the FLASH facility providing 10 μJ pulses tuneable from 0.2–20 THz [7].

c) Free-electron lasers

Free-electron laser (FEL) facilities operating in the THz regime are a well-established technology and several powerful systems exist [23]. One example is the FELIX facility [6] which injects 25 MeV electron bunches into an undulator with 65 mm spacing. The output is in the range 1–100 THz (4–250 μm) with sub-picosecond micropulses of energy 1–50 μJ [24]. The repetition rate of macropulses is 10 Hz within which the micropulses arrive at 25 MHz or 1 GHz giving a high peak power of 100 MW.

d) Smith-Purcell effect

Another attractive method for generating THz is to use the Smith-Purcell effect. Smith-Purcell Radiation (SPR) is emitted when an electron bunch passes close to a grating structure and so is entirely non-invasive for the electron beam. Its use as an electron bunch duration diagnostic has recently been demonstrated at SLAC [25] and theoretical calculations predict that the flux will be significantly increased if the SPR is frequency locked [26].

2.5.4 Terahertz generation using laser-plasma techniques

Research regarding terahertz generation from high power laser interactions is not as well-established as that into other secondary sources such as x-ray emission. Current measurements indicate that the parameters compare favorably to existing high power THz facilities but it is difficult to predict how plasma processes will scale on larger laser systems. We expect the peak power from a laser-based source to reach $\sim$ 100 MW and would aim to cover the same wavelength range as next generation accelerator sources.

a) Terahertz from laser driven electron beams

The rapid improvement in the quality of laser-driven electron beams from wakefield acceleration has enabled them to be applied to THz generation [27–31]. Electrons energized through the laser wakefield acceleration process encounter a plasma-vacuum boundary as they reach the rear of the gas jet. A foil can also be placed into the path of the electron beam in the same way as used on accelerator CTR beamlines. As the electrons change medium, they emit a powerful burst of THz CTR with pulse duration similar to that of the electron bunch (<100 fs). Indeed this correlation has enabled the THz emission to be used as an effective diagnostic of the properties of the electron bunch. It is estimated that pulse energies of 100 μJ should be achievable using this technique.

Along with the transition radiation at the exit of the plasma, THz radiation could originate within the wakefield itself, explaining a double pulse temporal structure in the measured emission [30, 32]. If the plasma frequency is matched the oscillations of the background plasma electrons in the wakefield will also emit in the THz range. This is usually weak compared to THz from the other processes but could possibly be enhanced by introducing clusters which drastically increase the absorption of the laser light by the gas [33].

b) Intense laser irradiation of solid targets

Terahertz emission from high intensity solid target interactions shows strong potential although few experiments have been performed [34–37]. The seminal work performed at the Lawrence Berkeley National Laboratory in the early 1990s [34] achieved THz emission with a peak power comparable to current THz facilities. In a plasma with a rising density gradient the laser reaches a density at which the pulse envelope duration matches the plasma period and so the ponderomotive force drives a resonant electron oscillation. For $\sim$100 fs pulses focused to $\sim 10^{19}$ Wcm^{-2}, this process can emit $\sim$μJ THz pulses in a sub-picosecond burst leading to peak powers of

$\sim$ 1 MW and field strengths of 100 MVcm^{-1} [34]. Because this needs a region of underdense plasma before the critical surface, precise control over a preparation pulse arriving before the main pulse is required.

Another process giving rise to THz is the "antenna mechanism" in which relativistic electrons are driven along the surface of the target. On leaving the edge of the sample a burst of radiation is emitted with a frequency depending on the target size. This was measured with a moderate laser intensity of $\sim 10^{17}$ Wcm^{-2} to yield $\sim$ 5 μJ assuming an isotropic emission. The spectral peak at 0.2 THz corresponded to the time taken for a relativistic electron to traverse their sample size of 5 mm [35]. Recent experiments have measured 50 μJ sr^{-1} of polarized THz emission from solid targets. This corresponds to a conversion efficiency higher than 10^{-4} from their 150 mJ laser pulse [37]. If the conversion efficiency is maintained as the laser energy is increased to $\sim$ 100 J, the THz pulse energy should reach levels of >30 mJ sr^{-1}, orders of magnitude larger than the present state of the art.

2.5.5 Applications

a) Linear and nonlinear THz spectroscopy

High intensity ultrashort THz sources allow new types of spectroscopic studies. THz time-domain spectroscopy is conventionally carried out with rather weak sources. By using intense sources the technique can be combined with imaging techniques and, for example, large samples can be studied using 2D electro-optic sampling, without the need for time-consuming scanning over the sample surface.

Driven by the recent advance in THz generation techniques, time resolved studies could be carried out in the THz range with techniques known previously for the optical domain only. This includes THz pump–THz probe studies, where intense THz pulses are used to initiate changes in the sample as well as for detecting these changes. One important application is the study of carrier dynamics in semiconductors. Picosecond carrier dynamics in indium antimonide (InSb) following excitation by below band gap broadband far-infrared radiation was investigated [38]. Using a THz-pump/THz-probe scheme with pump THz fields of 100 kV/cm and an intensity of 100 MW/cm^2, carrier heating and impact ionization dynamics was observed. THz pump–THz probe measurements also revealed the strong saturation of the free-carrier absorption in n-type semiconductors in the THz frequency range when single-cycle pulses with intensities up to 150 MW/cm^2 were used [39]. The recovery of the free-carrier absorption was monitored by time-resolved THz pump–THz probe measurements. Ultrafast high-field transport of electrons was studied in n-type GaAs with ultrashort terahertz (THz) pulses of an electric field amplitude of up to 300 kV/cm [40]. Another recent example is the study of the interaction of excitons with THz electric fields in ZnSe/ZnMgSSe multiple quantum wells with THz-pump and optical-probe spectroscopy [41]. The dependence of the excitonic absorption resonance energy on the THz field was observed to follows the Stark effect for smaller THz fields, while for larger THz fields, the interaction enters the nonperturbative regime.

Further increasing the THz field in spectroscopic applications allows to enter the regime of extreme nonlinear optics also in the THz frequency range, which will allow new insight into the behavior of materials under the influence of extremely high fields as well as new engineering tools.

b) THz-assisted attosecond pulse generation

A recently proposed scheme for attosecond pulse generation relies on HHG in presence of a strong dc or quasi-static electric field [42–44]. The applied field increases the asymmetry between subsequent half optical cycles of a few-cycle laser pulse thereby enables the generation of higher-order harmonics, and as a consequence, attosecond pulse shortening. For a pronounced effect

the electric field vector of the applied quasi-static field has to be extremely strong, on the order of 10 MV/cm (or several tens of MV/cm). The tremendous progress of the last few years in the generation of intense ultrafast THz pulses driven by femtosecond laser pulses has opened up the way towards achieving such extremely high field strengths.

Experimental realization of a THz-assisted attosecond pulse generation stage will require dedicated attosecond source with a synchronized high-intensity THz source. Optimized high-intensity THz sources based on optical rectification will require infrared pump wavelengths in the range of 1.5–2 μm or even longer. In order to facilitate experiments requiring extremely high THz field strength on the one hand, and to allow to utilize the advantageous scaling properties of HHG with increasing wavelength on the other hand, an IR driver source together with HHG and THz generation stages are required. An attached R&D experimental tage will allow to explore additional novel applications of intense THz fields in high-field physics.

c) Investigation of material properties and processes under the influence of (extremely) high quasi-static (THz) fields

The extremely high THz field strengths achievable nowadays in the tens-of-THz frequency range and in the near future also in the 1-THz range will allow new types of fundamental investigations with far-reaching consequences for applied multidisciplinary research. New type of insight into the dynamical properties of molecules, clusters, nanostructured as well as bulk materials will be gained by investigating such materials and the physical, chemical and biological processes they are involved in under the influence of strong external fields in the THz frequency range. For example, time-resolved studies of biomolecules in various conformational states will be enabled by combining THz fields with optical pulses. Alignment of (induced or permanent) polar molecules by the strong external quasi-dc field will allow studies of novel types of coherent or collective phenomena. Combined with the various sources available at ELI from x-ray to infrared wavelengths and the ultrashort pulse durations will enable an unprecedented variety of studies.

d) Multispectral single-shot imaging

Terahertz time-domain spectroscopic (THz-TDS) imaging is an interesting new tool for nondestructive testing and other applications. However, the current speed of image acquisition is relatively low, making it difficult to use e.g. for moving objects [45]. THz spectroscopic imaging system based on two-dimensional electro-optic sampling was used for recording the spatial patterns of chemicals extracted from the THz multispectral images [46].

Single-shot multispectral imaging will require high-intensity and high-average-power THz sources. Intense THz radiation can be used for nondestructive testing, security screening, and biomedical applications, where the analysis of the chemical composition of the test object is also important besides visualizing the geometrical shapes of its internal structures. Since many materials indicate spectral fingerprints in the THz region, the spectroscopic analysis in this region has received interests as a new tool for material characterizations.

Bibliography

[1] G. P. Williams, Rep. Prog. Phys. **69**, 301 (2006).
[2] K. Reimann, Rep. Prog. Phys. **70**, 1597 (2007).
[3] Q. Wu and X.-C. Zhang, Appl. Phys. Lett. **71**, 1285 (1997).
[4] J. M. Byrd *et al.*, ICFA Beam Dynamics Newsletter **35**, 71 (2004).
[5] F. Sannibale, A. Marcelli, and P. Innocenzi, J. Synchrotron Rad. **15**, 655 (2008).
[6] A. F. G. Van der Meer, Nucl. Instrum. Meth. Phys. Res. A **528**, 8 (2004).
[7] S. Casalbuoni *et al.*, Phys. Rev. ST Accel. Beams **12**, 030705 (2009).

[8] Y. Shen *et al.*, Phys. Rev. Lett. **99**, 043901 (2007).
[9] Y. C. Shen, P. C. Upadhya, E. H. Linfield, H. E. Beere, and A. G. Davies, Appl. Phys. Lett. **83**, 3117 (2003).
[10] K.-L. Yeh, M. C. Hoffmann, J. Hebling, and K. A. Nelson, Appl Phys Lett. **90**, 171121 (2007).
[11] A. Stepanov, L. Bonacina, S. V. Chekalin and J-P. Wolf, Opt. Lett. **33**, 2497 (2008).
[12] X. Xie, J. Dai and X.-C. Zhang, Phys. Rev. Lett. **96**, 075005 (2006).
[13] J. Dai, X. Xie and X.-C. Zhang Appl. Phys. Lett. **91**, 211102 (2007).
[14] C. D'amico *et al.*, Phys. Rev. Lett. **98**, 235002 (2007).
[15] F. Blanchard *et al.*, Opt. Express **15**, 13213 (2007).
[16] J. Hebling, G. Almasi, I. Kozma and J. Kuhl, Opt. Express **10**, 1161 (2002).
[17] J. A. Fülöp, L. Pálfalvi, G. Almási and J. Hebling, Opt. Express **18**, 12311 (2010).
[18] M. Abo-Bakr *et al.*, Phys. Rev. Lett. **90**, 094801 (2003).
[19] F. Sannibale *et al.*, Phys. Rev. Lett. **93**, 094801 (2004).
[20] J. M. Byrd *et al.*, Phys. Rev. Lett. **96**, 164801 (2006).
[21] G. L. Carr *et al.*, Nature **420**, 153 (2002).
[22] D. A. Jaroszynski *et al.* Phys. Rev. Lett. **71**, 3798 (1993).
[23] www.lightsources.org
[24] D. A. Jaroszynski *et al.*, Phys. Rev. Lett. **78**, 1699 (1997).
[25] V. Blackmore *et al.*, Phys. Rev. ST Accel. Beams **12**, 032803 (2009).
[26] S. E. Korbly *et al.*, Phys. Rev. Lett. **94**, 054803 (2005).
[27] W. P. Leemans *et al.*, Phys. Rev. Lett. **91**, 074802 (2003).
[28] J. van Tilborg *et al.*, Phys. Rev. Lett. **96**, 014801 (2006).
[29] J. van Tilborg *et al.*, Opt. Lett. **33**, 1186 (2008).
[30] J. van Tilborg et al., Phys. Plasmas **13**, 056704 (2006).
[31] A. D. Debus *et al.*, Phys. Rev. Lett. **104**, 084802 (2010).
[32] R. A. Bosch, Phys. Plasmas **13**, 113107 (2006).
[33] T. Nagashima *et al.*, Opt. Express **17**, 8807 (2009).
[34] H. Hamster *et al.*, Phys. Rev. Lett. **71**, 2725 (1993).
[35] A. Sagisaka *et al.*, Appl. Phys. B **90**, 373 (2008).
[36] Y. Gao, T. Drake, Z. Chen and M. F. DeCamp, Opt. Lett. **33**, 2776 (2008).
[37] Y. T. Li *et al.*, private communication
[38] M. C. Hoffmann, J. Hebling, H. Y. Hwang, K.-L. Yeh, and K. A. Nelson, Phys. Rev. B **79**, 161201 (2009).
[39] J. Hebling, M. C. Hoffmann, H. Y. Hwang, K.-L. Yeh, and K. A. Nelson, Phys. Rev. B **81**, 035201 (2010).
[40] W. Kuehn, P. Gaal, K. Reimann, M. Woerner, T. Elsaesser, and R. Hey, Phys. Rev. B **82**, 075204 (2010).
[41] H. Hirori, M. Nagai, and K. Tanaka, Phys. Rev. B **81**, 081305R (2010).
[42] Weiyi Hong, Peixiang Lu, Pengfei Lan, Qingbin Zhang, and Xinbing Wang, Opt. Express **17**, 5139 (2009).
[43] C. Serrat and J. Biegert, Phys. Rev. Lett. **104**, 073901 (2010).
[44] E. Balogh, J. A. Fülöp, J. Hebling, P. Dombi, G. Farkas, and K. Varjú, "Attosecond pulse generation in noble gases in the presence of extreme high intensity THz pulses", 31st European Conference on Laser Interaction with Matter (XXXI ECLIM), 6-10 September 2010, Budapest, Hungary.
[45] Takeshi Yasui, Ken-ichi Sawanaka, Atsushi Ihara, Emmanuel Abraham, Mamoru Hashimoto, and Tsutomu Araki, Opt. Express **16**, 1208 (2008).
[46] M. Usami, M. Yamashita, K. Fukushima, C. Otani, and K. Kawase, Appl. Phys. Lett. **86**, 141109 (2005).

2.6 Ultrafast-laser driven X-ray sources

Introduction

One of the main goals within the ELI scientific community is to produce ultrashort X-ray beamlines, both coherent as well as non-coherent, paving the way towards imaging nature with atomic resolution both in space and time – with university-lab sized devices. In fact, the discovery of X-rays by W.C. Roentgen in 1895 [1] has been one of the most important driving forces to push forward understanding and knowledge in many kinds of scientific areas. Applications range from structure analysis in solid-state, atomic physics and molecular chemistry via imaging applications in medicine and the life sciences to the discovery of the basic building blocks of life, in particular the DNA, and more generally the structure of proteins and other macromolecules. Having access to the spatial resolution of molecular structure and electron orbitals is only one side of the coin to be explored by X-rays. It took about one century to flip the coin to the other side showing the temporal resolution of the atomic and molecular motion, making it possible to monitor the dynamics of molecules and electrons on their natural time scale, which is now in the attosecond range. The early X-ray generation devices and techniques such as X-ray tubes, electrical discharges or the first synchrotron sources have not been able to deliver X-ray pulses that had durations of less than several nanoseconds and thus could not be used to gather both types of information, spatial and temporal, simultaneously. An insight into the temporal dynamics of quantum systems was first gained by using probes of much larger wavelength than the one of X-rays: namely infrared (IR), visible (VIS) and ultraviolet (UV) laser pulses. Today, the fundamental limit of ultrashort laser pulses is one single optical cycle, lasting about 1 fs in the UV to several femtoseconds in the IR spectral region [2, 3]. Having at hand the possibility of monitoring molecular and electronic motion, unfortunately it is not possible to use these lasers to directly image molecular structure at atomic resolution due to the large wavelength of the laser photons. The principal solution to this problem is to transform the coherent long-wavelength laser pulses into coherent/incoherent X-ray pulses via several techniques to be explored within ELI. These laser-based sources have, in contrast to large-scale facilities such as third-generation synchrotrons or X-ray Free-Electron-Lasers (XFELs), the great perspective of having only university-lab size and can, thus, offer a much broader accessibility as only few large-scale facilities exist world-wide. Another added value besides reduction in size and costs is the intrinsic synchronization between the (optical) driver laser and the generated X-ray pulses as well as the spectrum of different X-ray sources each delivering another specific feature – from single attosecond spikes to coherent X-ray bursts with peak brilliances competitive with large-scale XFELs.

For transforming optical driver laser pulses into brilliant bursts of X-rays four paths will be developed within this ELI research area: X-ray plasma lasers, laser-driven XFELs, Thomson backscattering, betatron radiation, and, to some extent, K_α sources. The pre-requisite for this research branch is ELI's pursuit of high-energy/high-peak power lasers with high repetition rate and high average power.

X-ray lasers can be realized through the production of very short lived, high temperature laser plasma. Such X-ray bursts may be used to study ultrafast structural dynamics in solids and complex molecules like proteins. In fact, intense attosecond X-ray pulses will enable study of the movement of electrons in an atom or molecule as it undergoes a quantum or chemical transition. In particular, coherent X-rays present a very important secondary source perfectly suitable for the nano-scale metrology due to its very short wavelength combined with coherence. X-ray interferometry with X-ray lasers can be an excellent method to measure the surface properties with nm-scale resolution, thanks to the fact that X-ray lasers are extremely monochromatic sources. Possible applications thus include X-ray holography, coherent imaging or measurement

of fine structures on any solid surface. It may be also used for inspection of defects in lithography masks having thus great impact on the industry.

Recent advances in laser wakefield accelerators have allowed the production of electron beams with energies ranging from tens of MeV to more than 1 GeV within a centimeter scale, and with an intrinsic pulse duration of few femtoseconds only. The enormous progress in improving the beam quality and stability makes them serious candidates for driving the next generation of compact light sources. The versatile laser-based radiation sources range from infrared to X-ray energies. They attract a large user community, because they are ultra-short, brilliant sources tunable up to keV photon energies with an intrinsic synchronization to the IR driver laser, making them useful for time-resolved structural analysis of matter with atomic resolution. The development of FELs has led to an enormous increase of brilliance and coherence. However, accelerator technology currently limits the pulse duration of synchrotron sources just under a picosecond and demands large and expensive facilities due to the accelerating field gradients of conventional accelerators, which are restricted to 20–100 MV/m by radiofrequency-cavity electrical breakdown. In contrast, a plasma, which is already fully broken down, can sustain electric fields that are 3–4 orders of magnitude higher, exceeding 100 GV/m.

Thomson backscattering of laser pulses from relativistic electron bunches is an alternative technique of producing high-energy incoherent X-ray pulses, with relatively broad spectral bandwidth and low efficiencies, using current Ti:sapphire lasers. A source of broad-bandwidth X-ray radiation is also the betatron-like wiggler radiation from electrons undergoing transverse motion in the accelerating potential of the wakefield. Both sources will be able to deliver the highest X-ray energies, even MeV photons.

2.6.1 Current Status of X-ray Source Development and Applications

X-ray lasers

Since the first demonstration of lasing action at optical frequencies in 1960 [4], there has been considerable theoretical and experimental effort aimed at the extension of lasing into the X-ray spectral region. To date, lasing at wavelengths between 3 nm and 50 nm has been observed in numerous ionic species [5] and X-ray lasers have the potential to extend current optical laser applications to much shorter space and timescales, while probing much deeper into the core of matter. X-ray time-resolved imaging of biological samples, nanolithography, or laboratory astrophysics is a typical example of applications that are recently starting to be explored as X-ray lasers become closer to reality. The use of X-ray lasers in these novel applications is obviously limited by the parameters of the driver creating population inversion. For the first X-ray laser demonstration nearly 20 years ago, kilojoules of laser pump energy were required to generate a laser at $\sim$ 20 nm [6]. However, year after year, the required pump energy has been dramatically reduced (nevertheless at the expense of output pulse energy) thanks to the improvement of plasma and X-ray laser dynamics. To date, the most energetic collisional X-ray laser [7] has been demonstrated at the kJ-class laser facility PALS [8] in the Czech Republic. It operates in a quasi steady state regime where the driving sequence consists of a weak prepulse followed by a strong main pulse, both being linearly focused on solid Zn target (Fig. 2.24). The double-pass zinc X-ray laser at 21.2 nm (58.5 eV) delivers up to 10 mJ (10^{15} photons), 150 ps pulses in a narrowly collimated beam with divergence of about 4×6 mrad^2.

To reduce the pumping energy and increase the repetition rate, a transient collisional excitation scheme was proposed and demonstrated [9]. In this scheme, a longer (ns) pulse, which generates plasma and the required closed-shell ionization balance, is followed by much shorter (ps) pulse, which rapidly heats the performed plasma and generates a transient population inversion. In 2005, an extension of the transient pumping scheme was demonstrated using a grazing-incidence angle for pumping (GRIP), achieving lasing at 18.9 nm close to saturation [10].

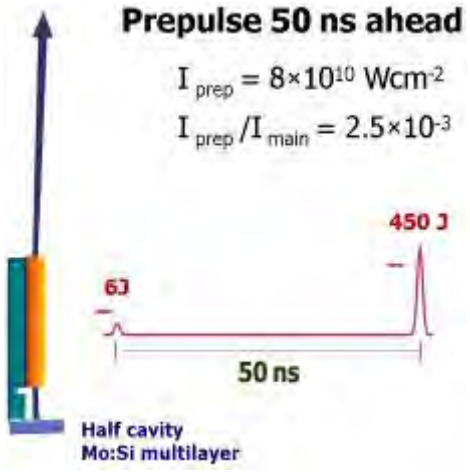

Figure 2.24: Typical geometry of quasi steady state X-ray laser using half cavity.

Similarly to the original prepulse pumping mentioned above, a long pulse (200–600 ps) producing 10^{12} to 10^{13} W cm^{-2} is first applied to the target, generating plasma with the required (Ni-like) ionization balance. Subsequently, a short pulse (1-5 ps) is injected into the plasma under a small angle, sampling a specific electron density region where it instantaneously raises the electron temperature and efficiently creates population inversion (Fig. 2.25). Using this approach, strong laser emission at wavelengths down to 10.9 nm was demonstrated [11].

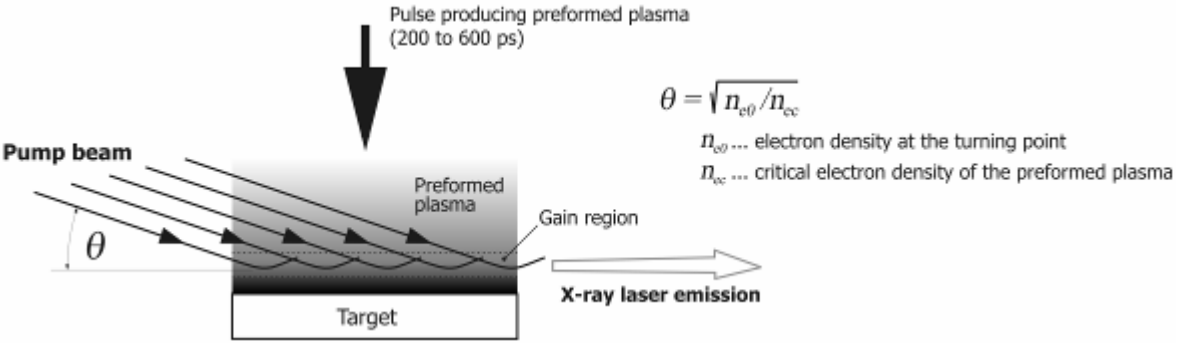

Figure 2.25: Generic scheme of the grazing incidence pumping.

In 2004, an optical field ionization X-ray laser amplifier produced by femtosecond laser excitation of a krypton gas cell was seeded with the 25th harmonic of a Ti:sapphire laser to generate saturated amplification in the 32.8 nm laser line of Ni-like krypton [12]. This seeded X-ray laser provides about 10^{11} (0.8 μJ) photons per pulse in a narrowly collimated beam with divergence of as low as 1 mrad. Also the amplification of 19th harmonic of a Ti:Sapphire laser in Pd-like xenon laser at 41.8 nm was demonstrated [13]. By further elaboration of this approach, the injection-seeded X-ray amplifier using a solid target (Ne-like Ti) was demonstrated at 32.6 nm in 2006 [14]. Using the same experimental setup, seeded X-ray lasers at wavelengths down to 13.2 nm [15] have been achieved so far, delivering coherent X-ray beams with excellent parameters (aberration-free, Fourier-limited, polarized), but still with low output pulse energy on a sub-microjoule level only.

The use of extremely powerful lasers to be developed at ELI as a driver for injection-seeded X-ray lasers presents an excellent opportunity to boost significantly the X-ray laser output up to the mJ level and even more using the concept of "slab amplifier" consisting in increasing

the active surface of the amplifier. This scheme is purely pump dependent, and so there is no principal limit for the output X-ray laser pulse energy. At ELI facility, the seeding technique will be extended down to the "water window" (2.2–4.4 nm) based on the understanding of pump energy scaling laws. In particular, energetic Ni-like Au X-ray laser at 3.6 nm operating at high repetition rate can finally become a reality, being an ideal source for X-ray imaging and holography of living cells (Fig. 2.26) as suggested long time ago [16].

Regarding X-ray applications, coherent radiation is necessary for interferometry, holography, diffractive imaging or nanopatterning. For such applications free electron lasers or plasma X-ray lasers are the best sources. For example, using a 46.9 nm wavelength EUV radiation from a capillary discharge laser a series of experiments was performed [17]. An interferometric lithographic technique was implemented using a Lloyd's mirror interferometer to pattern cone shaped, 58-nm FWHM diameter nano-dots over the area of $500 \times 500\,\mu m^2$ [18]. The scheme allows also to pattern lines, holes and oval shaped features in PMMA and HSQ photoresists. Holographic imaging in Gabor's in-line scheme was performed using 50–80 nm diameter carbon nanotubes CNTs as an object. After a numerical reconstruction of the hologram the images of CNTs were retrieved with the spatial resolution of 46 ± 2 nm, comparable to the illumination wavelength. Finally diffractive "lens-less" imaging with a spatial resolution of 70 nm was achieved by storing and processing a single diffraction pattern from the object using a phase-retrieval algorithm.

Apart from the above mentioned applications, sufficiently strong X-ray lasers are the only sources allowing for dense plasma probing and interferometry. X-ray laser interferometry can be used for measurements in material science, metrology, and especially dense plasma diagnostic. Two types of X-ray laser interferometry have been applied in practice: amplitude division interferometry (Mach-Zehnder interferometer [19]) and wavefront division interferometry (Fresnel double-mirror [20] or Lloyd's mirror [21]). Amplitude division interferometry requires high temporal coherence, while wavefront division interferometry requires high transverse coherence. Injection-seeded X-ray lasers elaborated at ELI facility will possess both of these features. X-ray laser holography offers the potential to obtain high-resolution 3-D images of biological and other specimens. High-resolution images can be obtained thanks to the high coherence combined with the high brightness of X-ray lasers that enables a single shot record. Exposure times can be reduced to < 1 ns, which eliminates motion blurring in biological samples as the dynamic processes in biology have time scales of typically 1 msec. Note that synchrotron X-ray holography and undulator X-ray holography typically needs about 1000 second exposure times from many shots. The first demonstration of X-ray laser holography was carried out using a Gabor in-line geometry and a hologram of a 3-D structure of a gold test pattern was recorded by using the Ne-like Se X-ray laser at 20.6 nm [22]. Since then, unfortunately no big progress has been done due to the lack of sufficiently strong X-ray laser. One of the challenging missions within ELI will be to revive this topic.

X-ray laser microscopy offers the opportunity to observe biological specimens in an aqueous environment [23]. The main goal here is to have lasing at wavelengths near or inside the water window (2.3–4.5 nm), where the high contrast in absorption cross section between carbon in biological specimens and oxygen in water can be obtained. However, as current X-ray lasers cannot be routinely produced at wavelengths much shorter than ~ 10 nm, until now other wavelength ranges have been employed for X-ray microscopy. The high brightness and short duration of X-ray lasers again enable the elimination of problems associated with motion blurring and radiation-induced chemical decomposition of any biological specimen. Researchers at LLNL demonstrated X-ray laser microscopy using a Fresnel zone plate lens and imaged a test pattern with resolution of 75 nm with a Ni-like Ta X-ray laser at the wavelength of 4.5 nm in 1992 [24], and subsequently rat sperm nuclei were also observed [25]. In this proof-of-principle experiment the X-ray laser had an energy of 10 μJ in 400 ps and structures with size of about 50 nm were resolved. Since then, not many demonstrations of X-ray laser microscopy have been reported until now. One reason is that no saturated X-ray laser at wavelength inside the water window

has been achieved. Moreover, in this particular case coherence characteristics of X-ray lasers are not so beneficial for microscopy because of the problem of fringes and/or speckle. To stimulate further progress in this field, X-ray laser saturation at a wavelength in the water window is required.

X-ray laser radiography is useful for measuring plasma parameters. The short pulse duration of X-ray laser is of the same scale as the hydrodynamic timescale of laser-produced plasma. The high brightness of X-ray lasers allows them to be used as a backlighter for the imaging bright sources such as high temperature plasmas. The very short wavelength enables the X-ray laser to probe large and near-solid density plasmas. Measurement of the early laser imprint and subsequent Rayleigh-Taylor instability is of great interest in studying direct drive inertial confinement fusion [26].

An important method to measure densities and temperature of plasmas is Thomson scattering. X-ray laser Thomson scattering has a great potential for probing plasmas at much higher density than optical probing, even above the solid density [27]. A laser entering a plasma is scattered by electrons. The temperature of plasma can be measured by observing the spectrum of scattered light and the density of plasma can be measured by observing the amount of scattered light. As the Thomson scattering cross-section is very small, it is difficult to gain a signal above the noise level caused by plasma emission. Because of this fact, X-ray laser Thomson scattering experiments have not succeeded in observing scattered spectrum so far. To improve the situation, X-ray lasers of higher brightness and at a shorter wavelength are absolutely necessary.

Another type of X-ray lasers is given in the form of laser-driven K-shell thermal and Kα sources, which are currently the most widely applied laser-plasma X-ray (defined as photons with energies that exceed 1 keV) sources. These sources are bright, short-lived, quasi-monochromatic and may be well synchronised to a laser. This fulfils the basic requirements for radiography and X-ray scattering, thus the area that has seen widest application for these sources is dense plasma physics. These sources are often used in point projection and area backlighter configurations. Kα sources are monochromatic ($\Delta\lambda/\lambda < 10^{-4}$) and available with photon energies between 1.48 keV to 68.8 keV from aluminium and gold targets respectively. The emission is fast electron driven. These fast electrons are created during the laser-target interaction, and propagate into the target material and slow rapidly through bremsstrahlung losses and collisions. Collisions result in atomic inner-shell ionisation and subsequent de-excitation can result in the emission of a Kα photon of specific and material dependent, wavelength. Bremsstrahlung losses results in continuum emission and ultimately degrade the contrast between the monochromatic source and background. The resulting X-ray pulse is short, lasting a few picoseconds longer than the laser pulse [28]. Sub-ps temporal resolution is readily achieved. The conversion efficiency from laser energy to Kα energy is good at around 10^{-4} albeit in to a solid angle of 4π. In general, higher laser intensity yields brighter K-alpha sources as more laser energy couples in to these non-thermal electrons. However, inner-shell ionization probability increases and then falls off as the energy of the fast electrons increases. Source optimisation is target material dependent and is possible by controlling laser intensity and prepulse characteristics.

X-ray free electron lasers (XFELs)

In 2006 Grüner et al. presented the first detailed scheme on driving an FEL by laser-plasma accelerators [29]. This first design consideration already included degrading effects, such as space-charge and resistive wall wakefields, and included also beam transport. The essential advantage of using Laser-Wakefield Accelerators (LWFAs) is twofold, their intrinsic ultra-high peak current far beyond the (non-relativistic) Alfvén current of 17 kA and their compactness of a few centimetres only. The first feature allows reducing the XFEL-undulator length from hundred meters down to few meters and the second point decreases the total length by shrinking also the accelerator.

The first combination of a laser-plasma wakefield accelerator (producing 55–75 MeV electron bunches) with an undulator in order to generate visible synchrotron radiation, has been successfully demonstrated [30]. Just one year later Grüner and co-workers realized the first laser-driven soft X-ray undulator source [31], shown in Fig. 2.26. The major breakthrough of this experiment was not only the extension of the produced wavelength range from visible to soft X-ray, but also the development of dedicated electron beam transport devices allowing to tune and stabilize this ultra-short radiation source. All future setups will be based on this first approach.

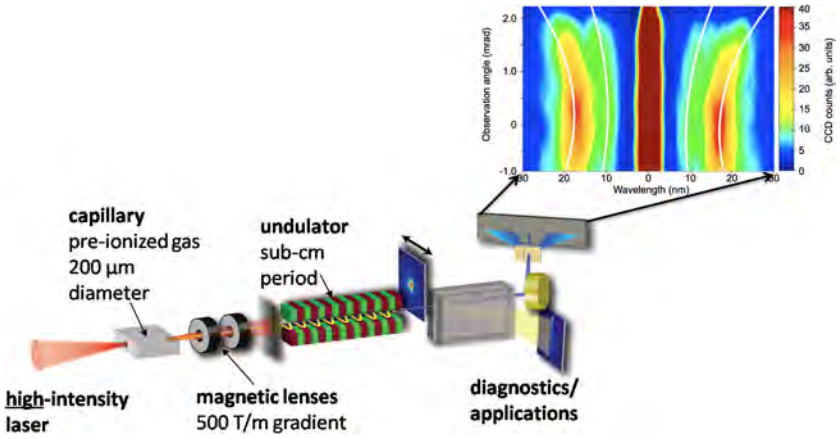

Figure 2.26: Basic scheme of laser-driven undulator X-ray source and spatially resolved spectrum.

XFELs based on laser-plasma accelerators could provide orders of magnitude brighter X-ray radiation than the already demonstrated incoherent undulator source. The expected number of photons (10^{12} photons/pulse/0.1%BW) and peak-brilliance (10^{30} photons/s/mm^2/mrad^2/0.1% BW) is competitive with large-scale XFELs, of which only few will exist world-wide due to their great size and costs.

In the laser-driven FEL scheme, the laser-accelerated electron beam undergoes micro-bunching in the undulator, causing the electrons to bunch in packets with a distance of the FEL wavelength in between – hence, these electrons emit their X-ray coherently. Owing to the high electron beam peak current intrinsically generated by laser-wakefield accelerators, FEL saturation lengths on the order of just a few meters can be obtained, offering the opportunity to develop very compact XFEL devices as the accelerator is just a few centimetres long and the driver high-power lasers fit on few laser tables. This is in contrast to the existing huge scale facilities world-wide, which are based on radiofrequency technology acceleration requiring hundred-meter-long undulators and kilometer-long accelerating lines.

The field of laser-plasma accelerators is relatively young: with the first seminal work by Dawson and Tajima in 1979 [32] and, due to lacking laser power, a very slow experimental progress thereafter, the breakthrough was initiated in 2000 by the work of Meyer-ter-Vehn at al. on the prediction of the so-called bubble regime [33]. Finally, in 2004, three independent experimental groups verified this bubble scheme [34] and launched an international ever increasing effort for reaching higher electron energies [35] and improved stability [36].

In the meanwhile, new schemes aiming at further substantially increased electron beam qualities arise, for instance, plasma downramp [37] and counter-propagating laser pulses [38]. These advanced concepts are necessary, because the current state-of-the-art would not allow the onset of the FEL-process, mainly due to unacceptedly large energy spreads. While in the bubble regime plasma electrons are mostly injected from transverse directions, the new schemes explore longitudinal trapping with the perspective of reduced emittance and lower energy spread.

ELI's new multi-PW class lasers will have several benefits: first of all, with such high intensities it is possible to accelerate much more charge, hence increasing the required peak current for driving the FEL. Secondly, one can use more advanced schemes which allow tailoring the injection mechanisms for increasing the beam quality in terms of energy spread and controlling the separation of the acceleration from the injection for preserving good beam qualities up to highest electron energies.

The key application for XFELs are found in all research areas, where ultra-high peak brilliances are mandatory, that is, a maximum on X-ray photons in ultra-short time-scales. The most prominent scientific case is single molecule imaging, where a single XFEL X-ray pulse is strong enough for recording a diffraction image behind a protein, before the molecule disintegrates through the X-ray induced Coulomb explosion. A single diffraction image is, of course, too little information for reproducing the entire atomic structure of the protein, but repeating this procedure with many independent proteins finally leads to entire map of all atomic positions. This would boost medicine, as most proteins cannot be studied with X-ray crystallography.

Another field of research is femtochemistry, aiming at imaging the transient states of chemical reactions – with atomic resolution in both space and time. This would allow studies of unknown reaction channels for deeper understanding and controlling of chemical processes. Circular polarized X-ray pulses (from a helical undulator) open the study of magnetic material on ultra-short time-scales, such as spin flips in thin films – answering the question on how fast data can be written on magnetic storage devices.

There are also ways of reducing the time-duration of the XFEL-pulse even further below the electron bunch length, hence paving the way towards so-called fifth-generation light sources. The latest generation of large-scale synchrotron sources is the third, with FELs being the fourth generation. An ultra-brilliant sub-femtosecond X-ray source would then be coined fifth generation. Laser-driven XFELs utilize ultra-compact electron bunches and their properties allow slicing out a fraction of the bunch such that only sub-femtosecond ranges undergo the FEL-instability.

A completely new application could be medical imaging with the spontaneous emission from the undulator source in combination with dedicated beam optics. The group of Grüner et al. currently calculates the reduction in applied dose for X-ray absorption imaging like in mammography. A very first pre-study holds promise that the dose can be much more reduced than by current detector technology improvements. For medical imaging, this Laser-driven Undulator X-ray (LUX) source relies on much higher electron energies and charge than what is available with today's laser. ELI's next generation high power lasers will allow generating sufficient X-ray flux in a narrow bandwidth for medical X-ray absorption imaging with suitable exposure times.

Thomson backscattering and Betatron radiation

As mentioned above both Thomson scattering of laser pulses from relativistic electrons and betatron radiation from a laser-plasma accelerator deliver the highest achievable photon energies. The reason is that basically both sources are undulator sources, where in the first case the undulator field is established by the laser field and in the betatron case by the plasma field. The undulator period is the laser wavelength and, for betatron radiation, it is the period of the betatron motion along the plasma channel in which electrons oscillate in the transverse electric field. Both effective undulator periods are much shorter than in any conventional undulator, hence the resulting photon wavelength is shorter as well – even when using less energetic electrons. This makes especially the Thomson source an interesting hard X-ray source, capable of delivering sufficient flux for medical imaging, when driven by a high repetition rate driver laser. The main advantage of the betatron source is its simplicity: it consists just of a laser-plasma accelerator. The drawback, however, is that its photon spectrum is very broad due to the variety of different electron energies and trajectories along the plasma channel leading to different betatron periods.

Compared to the X-ray plasma lasers and XFELs the two sources here will most likey remain incoherent sources. The reason is that their intrinsic features hinder the FEL-process. Nevertheless, they are very compact, reliable hard X-ray sources that complement the spectrum of ELI's laser-driven X-ray sources.

The first experimental realization of Thomson backscattering from laser-accelerated electrons was done in Jena [39], however, with a very poor signal to background ratio and electron beam qualities. Using ELI's powerful pump lasers, the flux of Thomson-scattered electrons can be substantially increased. Recently, a group at Rutherford has demonstrated phase-contrast imaging of a fish sample with betatron radiation [40].

2.6.2 Directions of implementation at ELI

X-ray lasers

Current X-ray lasers are mainly based on electron collisional pumping scheme. At the proposed ELI facility, in order to make the X-ray laser sources fully competitive with current and projected state-of-the-art XFELs, major effort will be devoted to improve the beam quality, shorten the pulse duration, and boost the output pulse energy. At this moment, the most promising way is to elaborate the concept of injection-seeded X-ray laser which ensures excellent beam quality in terms of spatial homogenity [41], aberration-free wavefront [42], high degree of coherence, polarization, and short pulse duration limited only by the laser transition bandwidth.

At ELI the community will start by investigating the physical phenomena constituting a base for understanding and development of novel X-ray lasers with a special emphasis on the medium excitation and the consecutive generation, amplification and propagation of the X-ray radiation. There are two possibilities of the amplifier architecture: normal incidence, and grazing incidence pumping geometry. In the normal incidence scheme, a weak long prepulse (ns, 100 mJ level) followed by a much shorter stronger pump pulse (ps, multi-J level) are sent perpendicularly onto a bulk solid target. In the GRIP scheme, only prepulse is sent at normal incidence to the target whilst the energetic pump beam is injected under an angle. The later case has an advantage of reduced pump beam energy. In both cases we will seed the X-ray laser plasma amplifier with a high-order harmonic beam to improve the output beam quality (divergence, coherence, photon number).

With a pulse of sufficiently high energy available at ELI facility, it will be possible to create a multi-stage X-ray laser chains (Fig. 2.27) that will deliver beams with excellent quality of wavefront and energy on the multi-mJ level in sub-ps pulses. Considering the nominal pump laser parameters (50 J/10 fs operating at 10 Hz), several X-ray laser beamlines at various wavelengths may be constructed, all of them being synchronized to each other. With appropriate focusing, X-ray intensities on the order of 10^{20} W cm^{-2} could be reached [12]. The high-energy, high-power ELI laser driver will allow to realize novel X-ray laser schemes in the "water window" region that are desired for investigation of biological species in their natural environment with a hundreds time higher resolution than with any existing optical microscope.

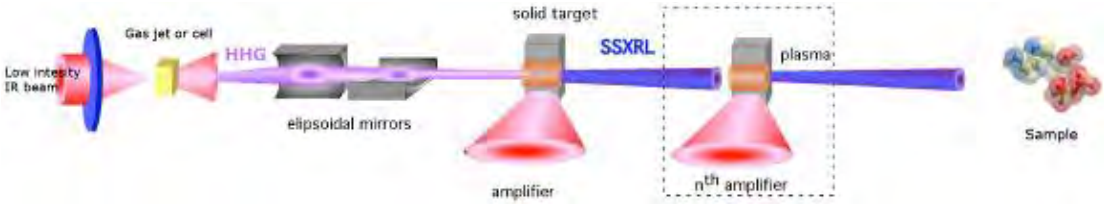

Figure 2.27: Principal scheme of the XRL beamline at ELI facility.

The alternative schemes such as "recombination scheme" and "inner-shell ionization scheme" will be also explored at ELI as they have inherent potential to overcome the wavelegth-limits of collisionally pumped X-ray lasers. Achieving high gain in a fast recombining plasma is a very desirable in the pursuit of X-ray lasers. Compared to collisional X-ray laser schemes, where a very high degree of ionization is needed, recombination schemes require relatively low pumping power. The idea of inner shell transition for lasing in sodium at 37 nm was first proposed about 40 years ago [43] but never realized. It is based on the fact that cross section for photo-ionization of atom or ion in deeper states can be larger than for more shallow states. More challenging experiments are expected for X-ray laser gain generations using several very innovative approaches to obtain lasing in inner shell transitions, which may be very attractive for wavelengths significantly below 1 nm. However, it will require pumping pulses of very high intensities and very short durations in the order of 100 as. With the advent of ELI project, such pulses are already on lasers "horizon".

The feature that distinguishes Kα sources from XFELs and potentially makes them unique are high divergence and high photon energy (68.8 keV). To attract the widest science base it is important to develop Kα sources with high-average and high-peak brightness sources at approximately 10 keV and above. Ultimately, this demands a source repetition rate of 100 Hz.

The next step in Kα source development should be to optimize the yield, enhance the source to background contrast, and reduce the source size from $\sim 10\,\mu$m down to $\sim 2\,\mu$m. Optimisation and contrast improvement are closely related. This work will require comprehensive experimental and computation studies to assess optimum laser wavelength, and acceptable laser contrast, optimal laser pulse duration and shape. A predictive capability is needed to determine optimal laser characteristics for materials of different atomic number. Progress demands the precise measurements using high-energy and high-performance laser systems.

Contrast and photon flux may be improved by using polycapillary micro-lenses, although these devices temporally stretch the X-ray pulse. The need for high throughput target manufacture, target and debris handling in high repetition sources is well known and needs to be addressed. As a part of this we should attempt to exploit the coherent properties of the Kα source. Spatial resolution is a major incentive to reduce the effective source size to and below the few micron scale.

XFEL

The ultimate goal of the Prague ELI-XFEL-beamline is to provide an installation which allows driving the new field of laser-driven XFELs towards future user facilities. This, of course, requires a series of basic research steps, just like large-scale facilities went through a long development process. The key point here is the demand for novel diagnostic methods, adressing the intrinsic properties of LWFA-beams, that is, their ultra-short bunch length and relatively large energy spread. Only when fundamental parameters, such as bunch profile, energy chirp, slice energy spread and emittance, can be measured and controlled, the high risk/high impact project of a laser-driven XFEL is feasible. We, therefore, propose to establish an explicit and direct cooperation with DESY (Hamburg, Germany), a renowned world-leading center for conventional/superconducting rf accelerators and beam diagnostics. In order to use directly the synergy between both rf and laser-driven accelerators, a beamline linked to an accelerator at DESY is of great profit for both sides. A common question to both schemes is the demand for few-femtosecond bunch diagnostics.

Once these diagnostic methods are developed and tested with well-defined beams, they can be established at the ELI beamline, boosting the XFEL-research substantially.

The grand goal for ELI is a 5-keV-XFEL and a spontaneous emission LUX source generating photon energies suitable for medical imaging (above 20 keV).

The very first step towards a laser-driven XFEL is, as stated above, the development of dedicated diagnostic and control methods for laser-driven electron beams. In combination with increasing the electron beam qualities in terms of energy spread and charge, the second step consists of a first FEL-demonstrator experiment. This stage aims at measuring the amplification of the spontaneous emission and/or of a seed (for instance, from surface higher harmonics). Once this stage of maturity is reached, the third step improves further the electron beam quality towards FEL-saturation, supposedly at rather long wavelengths. Consequently, a step-like increase in FEL-photon energy is pursued, until, in the long run, a 5-keV-XFEL is reached. Together with novel LWFA-schemes, currently developed, and ELI's high power lasers, it can be expected that the required beam parameters are reachable.

As the last step the XFEL will be run for user experiments.

Thomson and betatron sources

The major challenge for the Thomson backscatter beamline is the synchronization of the driver pulse for low-energy electron acceleration and the counter-propagating seed pulse, which is scattered off the electron bunch and frequency-upshifted. The overlap between the electron bunch and seed laser pulse needs to be established both in space and time. Moreover, in order to keep the bandwidth of the Thomson radiation as narrow as possible, both the energy spread of the electrons must be kept small as well as the variation of the laser amplitude with respect to transverse and longitudinal position along the interaction region.

Consequently, the first step consists of generating low-energy electrons with about 50 MeV and a maximum on charge. This implies that for fulfilling this constraint with the powerful lasers at ELI new schemes aiming mostly at increasing the charge, while maintaining low energy spread need to be developed. Secondly, the setup for the counter-propagating seed pulse needs to be developed in terms of optimal overlap with the electron bunch.

Apart from medical phase-contrast imaging, Thomson backscattering can also be used for radiation therapy, but then require higher electron energies for producing MeV-photons. Therefore, in a third step the LWFA-scheme is extended towards higher, but still moderate energies below 1 GeV. A detailed description of the laser driven Betatron source and its implementation is given in Sect. 6.4.

2.6.3 Source Development and Advanced Source Use

The basic driving force behind all X-ray source development at ELI is "4D imaging", that is, observing nature with atomic resolution both in space and time. As an international laser user facility, ELI will offer secondary X-ray sources with excellent parameters and complementary characteristics allowing an experimental setup which is not feasible in any other existing laser laboratory. In practice, it means enough flexibility in manipulation and timing of several X-ray pulses. Taking the advantage of inherent synchronization of all ELI lasers which originate from one master oscillator, it will be possible to perform pump-probe experiments with multiple, ultra-intense X-ray beams such as X-ray lasers, high-order harmonics, and/or non-coherent X-rays (e.g. K-alpha, Thomson, betatron, or spontaneous undulator radiation). This diversity will be a unique feature of ELI. Considering, for instance, a 50 J/10 fs laser operating at 10 Hz, a typical user at ELI may require 2–3 mutually synchronized energetic X-ray and/or ultrashort (e.g. high-order harmonic or IR driver laser) beams along with several high power, auxiliary NIR laser beamlines. This will enable complex investigations of fusion-relevant plasmas via X-ray laser Thomson scattering and X-ray interferometry at the same time, as well as various pump-probe configurations with multiple beams coming from different directions.

Femtochemistry will be one of the key applications of ELI's laser-driven X-ray sources for 4D imaging. Femtochemistry by pump-probe spectroscopy aims at real-time observation of transient molecular behaviours including the atomic positions, bond lengths and angles during

chemical reactions. As chemical reactions occur with timescales on the order of femtoseconds and structural changes occur on an atomic scale, high spatial and temporal atomic resolution are required to observe molecular motion in real time.

For sources with ultra-high peak brilliance, with the XFEL being the strongest candidate, even single molecule imaging should become feasible. This is especially interesting for medicine, as about 70% of all proteins that medical drugs address cannot be crystallized.

X-ray lasers

The possibility of using X-ray lasers in combination with microscopy and holography for the study of cell biology is very attractive even at 10 nm. Of course, X-ray lasers will have a much broader application potential in biology when they become operational in the "water window", where cells in their natural environment (water, atmospheric pressure) can be observed with a high resolution X-ray microscope. Structures of biomolecules such as protein with atomic resolution can be also determined by X-ray diffraction. The high brightness of X-ray lasers should produce enough scattering to record diffraction pattern of very small samples such as single particles of large macromolecular assemblies without the need for the sample to be crystalline, where large signals are obtained due to coherent addition of the electric field of the X-rays by Bragg reflection. Femtosecond pulses are short enough to avoid image blurring due to the vibrational motion of nuclei, thus atomic structure can be obtained without averaging over any periodic atomic motions. X-ray lasers will be suitable for observing biological specimens in their natural wet environment. Though radiation damage may become a problem, the very short period (femtosecond) can be expected to allow the collection of diffraction patterns before radiation damage that distorts or destroys the biomolecule structure occurs. A large degree of spatial coherence of an X-ray laser is just perfect to record a 3-D image by holographic technique. Imaging at the atomic scale can be obtained by advanced X-ray microscopy enabling to observe amorphous and disordered materials, including polymers, crystals with strains and defects, inorganic structures such as nanotubes, and bio-molecules that are difficult to crystallize.

The advanced X-ray lasers should have sufficient spatial and temporal resolution even for femtochemistry experiments. Even for such a short pulse, the photon flux per pulse can be enough to carry out spectroscopic observations with a single pulse. Short pulse X-ray lasers can provide an opportunity to observe various nanoscale dynamics spectroscopically, such as viscoelastic flow, protein folding, crystalline phase transitions, and magnetization dynamics of nanostructures over a wide range of time scales.

Finally, some fundamental scientific experiments that have not been able to be carried out so far with other light sources such as synchrotron radiation can be realized with an X-ray lasers at ELI. They include studying of plasma, warm dense matter and atomic physics, e.g. determination of energies, ionization cross sections, lifetimes and transition rates. The high X-ray intensity will enable to study nonlinear effects that lead to multiphoton processes in the keV region. Thanks to the expected high repetition rate of the source, X-ray lasers may be utilized to create controlled structures in the nanometre range which is a big challenge for the semiconductor industry (nanolithography).

X-ray free electron lasers

With future multi-petawatt lasers like ELI, ultra-high beam currents up to 100 kA within few femtoseconds can be expected, allowing a drastic reduction in the undulator length of free-electron lasers. A crucial parameter to be reached is the charge contained within a small electron energy bandwidth. For instance, 1 nC at 1 GeV electron energy and 0.1% energy spread will be required to produce an efficient XFEL lasing at 5 keV. FELs rely either on self-amplified spontaneous emission or seeding (for instance with surface higher-harmonics). Both schemes

depend on the current density of the electron beam, which could be very high for laser-wakefield accelerators.

In order for LWFAs becoming the optimal compact drivers of X-ray FELs, their current state of the art needs to be substantially improved. Besides pointing stability and fluctuations in electron energy and charge, the most decisive parameters for improvement are the charge and energy spread. So far, most experiments are run in sub-optimal ways, for instance because the lasers are too weak and, thus, need to undergo non-linear self-modulation before reaching intensities inside the plasma to drive wakefields. This is a major reason for instability. The second type of improvement consists of new advanced schemes, especially for the injection of the plasma electrons into the wakefields.

In 2006 Leemans et al., utilizing only 40-TW laser pulse of 38 fs duration and a gas density of 4.3×10^{18} cm^{-3}, clearly showed that 1 GeV electron beams can be produced by means of capillary discharge [35]. However, the measured charge of 30 pC is significantly below the goal of 1 nC. In order to further improve the resulting current and especially the energy spread, several alternative schemes have been proposed. In order to prevent a large initial emittance a predominantly longitudinal trapping of plasma electrons would be favourable. This can be done in the plasma downramp scheme, where the electrons are injected as the phase velocity of the wake tail is reduced effectively down to the level of the plasma fluid [37]. The trapped electrons are then accelerated at constant (low) plasma density in the subsequent plasma region. Another scheme explores beat waves of two counter-propagating laser pulses, which inject the plasma electrons directly into the acceleration buckets of the wakefield trailing the laser pulse [38]. Both these concepts will be studied with ELI's strong laser systems. The key goal is to deliver very low energy-spread beams with large amount of trapped charge. Only strong PW-class lasers will generate large enough plasma wakes, whose fields are strong enough to compensate for beam loading effects, which otherwise would increase the energy spread or effectively decrease the trapped charge.

Thomson backscattering and betatron source

In contrast to the beam quality required for the XFEL, the current state-of-the art of LWFA allows already the generation of electron bunches for usage as a Thomson backscattering source. Electron energies as well as energy spread and charge suffices, since medical phase-contrast imaging can be operated with few percent bandwidths. However, in order to reduce the exposure times significantly, a higher charge for increased flux is mandatory. Apart from this issue on the LWFA-side, the synchronization of the laser-driven electron bunch with the counter-propagating seed pulse needs to be developed. In order to generate a sufficient Thomson flux, the number of seed laser periods in the interaction region must be large enough, implying laser pulse lengths on the order of pump lasers, that is, picoseconds. The transverse and longitudinal laser profile needs to be as constant as possible along the interaction range of typically sub-millimeter. A deviation of the dimensionless laser amplitude a immediately causes a broadening of the Thomson radiation, equivalent to undulator radiation in an undulator with inhomogeneous magnetic field. Details of the laser driven Betatron source are given in Sect. 6.4.

2.6.4 Potential for Applications, Business and Technology Transfer

The development of the short wavelengths sources for the scientific and technological use in the next 30 years is absolutely crucial. In particular, the 2007 report of US Department of Energy explicitly states that: "*During the half-century since the laser was conceived, the use of coherent light has become an indispensable part of our world, with applications such as telecommunications and optical data storage playing a* ***trillion-dollar role in the global economy****. In today's world, the development of tools and techniques that use coherent light at ever-shorter wavelengths – in the extreme ultraviolet and soft X-ray regions of the spectrum – is assuming increasing*

importance". Considering the size and future needs of X-ray sources for research, academia and industry, it is not surprising, that huge effort is being devoted to develop these sources of coherent X-ray radiation as well as methods for their application.

The main advantages of ultrashort and intense X-ray sources are threefold: first, the spatial resolution of the information to be extracted from a system is proportional to the wavelength of the probing electromagnetic field. Sufficiently strong X-ray sources will greatly help science and technology to move from the micrometer to the nanometer range and finally to the atomic scale. Secondly, coherence and polarization of such sources tremendously improves the quality of the obtained information and opens research possibilities which are impossible for incoherent radiation. The intensity of X-ray sources to be developed at ELI, will reach the highest intensities ever at these wavelengths. As a consequence, transformations of matter can be initiated on a nanometer scale range in a controlled way with high resolution. Last but not least, probing with atomic resolution is extended into the time domain as well: the intrinsic time-scales of XFEL, Thomson, and betatron radiation is on the order of few femtoseconds only, the natural time-scale of chemical reactions. The XFEL source can even be advanced further into the sub-femtosecond time-domain, opening the accessibility of electronic motion within atoms.

ELI's light sources will provide a unique variety of ultrashort, brilliant X-ray beams, which are all complementary to each other, at one single site – hence providing users the possibility of addressing complex studies with different and well-synchronized probes. The X-ray lasers are coherent X-ray sources with high photon flux at moderate energies. XFELs are the most brilliant X-ray sources in the range of several keV photons and even sub-femtosecond time resolution. Thomson backscattering will yield the highest photon energies, even up into the MeV range. Among all sources, betatron radiation is the most compact one, it is incoherent, however, its flux can already be used for medical imaging.

The above aspects can specifically impact the following R&D areas with certain commercial potential:

1) **Material science,** where **nanotechnologies** are quickly developing: magnetism, phase transitions, smart materials, liquids and disordered systems, cluster vibrations and reactions, phase transitions and cluster melting, warm dense matter generation, and imaging plasmas are waiting for the ultra-high spatial resolution to be achieved with the advanced X-ray sources at ELI.
2) **Medical imaging** with laser-driven undulator and/or Thomson sources opens the possibility of performing mammography screens with a substantial reduction in the applied dose. This is due to the physical properties of the low-bandwidth and spatially highly peaked radiation cone, which helps reducing the distortion of X-ray absorption images by scatter radiation, and, finally, yielding the same contrast, but at much reduced dose. Another approach is to use these novel sources for medical phase-contrast imaging, aiming at early tumour detection, where tumours are still small and in a state, before metastases are developed. Both schemes could lead to a revolution in preventive medicine.
3) **Ultrafast radiation biology** aims at a better understanding of the primary processes involved in ion beam therapy and its optimization. Up to now, the so-called pre-chemical stage after ion impact is experimentally inaccessible, but is of essential importance when it comes to non-linearities: pulsed, highly dense ion beams are expected to have a greater biological effect, if their effective track radii overlap. On the other hand, radicals produced by ionization of the target material through the impinging ions, may start interacting with each other, which may lead to more recombination, and hence a lowering of the biological effectiveness. Laser-driven ion acceleration and probing with a well-synchronized laser-driven X-ray pulse would open a unique way of studying the physical and pre-chemical stage on time-scales from femto- to pico-seconds, where the radicals are generated.
4) **Single molecule imaging** requires ultra-brilliant X-ay sources in order to gain sufficient information about the structure of a protein, before it disintegrates due the Coulomb explo-

sion induced by the highly ionizing X-ray flash. Single molecule imaging could thus advance structure biology in making the structure of all such proteins accessible, which cannot be crystallized – which is in fact the case for the majority of all medically relevant proteins.

5) **Time-resolved studies** yield detailed insights into fundamental processes such as ionization dynamics of atoms, molecules, clusters and highly charged ions, multiple core hole formation, nonlinear effects in the X-ray domain, Coulomb explosion of clusters, generation of plasmas at solid density, hydrodynamic response to X-ray pulses, non-equilibrium plasmas generation and the study of materials under extreme conditions.
6) **High-resolution atomic physics**: excitation of highly charged ions, study of X-ray nonlinear effects, resonant elastic scattering, plasma spectroscopic time-resolved diagnosis, application of X-ray lasers in nuclear spectroscopy.

Laser-based accelerators imply a large reduction in infrastructure, and thus in size and cost. This would make this novel technology accessible to many more users at other labs as well, once ELI has put forward the basic developments. A purely laser-driven light source would, besides the reduction of infrastructure requirements, inherently produce ultrashort-duration pulses with a perfect temporal synchronization with the driving laser. Imaging of matter in both space and time with atomic resolution is then a natural application of these novel sources.

The advanced X-ray sources at ELI will be unique and complementary to existing large-scale facilities, as it combines many different sources with their specific parameters at one single site. In this sense ELI will advance the development of fifth-generation light sources with a broad and substantial impact on various fields of technology and research.

Bibliography

[1] W.C. Roentgen, Nature 53, 274 (1896).
[2] B. Schenkel et al., Opt. Lett. 28, 1987 (2003).
[3] K. Yamane et al., Opt. Lett. 28, 2258 (2003).
[4] T.H. Maiman, Nature 187, 493 (1960).
[5] H. Daido, Rep. Prog. Phys. 65, 1513 (2002).
[6] D.L. Matthews et al., Phys. Rev. Lett. 54, 110 (1985).
[7] B. Rus et al., Phys. Rev. A 66, 063806 (2002).
[8] K. Jungwirth et al., Phys. Plasmas 8, 2495 (2001).
[9] J. Dunn et al., Phys. Rev. Lett. 84, 4834 (2000).
[10] R. Keenan et al., Phys. Rev. Lett. 94,103901(2005).
[11] Y. Wang et al., Phys. Rev. A 72, 053807 (2005).
[12] Ph. Zeitoun et al., Nature 431, 426 (2004).
[13] T. Mocek et al., Phys. Rev. Lett. 95, 173902 (2005).
[14] Y.Wang et al., Phys. Rev. Lett. 97, 123901 (2006).
[15] Y. Wang et al., Nature Photonics 2, 94 (2008).
[16] P. Jaeglé, La Recherche 184, 16 (1987)
[17] S. Heinbuch et al., Opt. Express 13, 4050 (2005).
[18] P.W. Wachulak et al., Opt. Express 15, 3465 (2007).
[19] L.B. DaSilva et al., Phys. Rev. Lett. 74, 3991 (1995).
[20] F. Albert et al., Opt. Commun. 142, 184 (1997).
[21] J.J. Rocca et al., Opt. Lett. 24, 420 (1999).
[22] J.E. Trebes et al., Science 238, 517 (1987).
[23] S. Suckewer et al., Science 247, 1553 (1990).
[24] L.B. DaSilva et al., Opt. Lett. 17, 754 (1992).
[25] L.B. DaSilva et al., Science 258, 269 (1992).
[26] D.H. Kalantar et al., Phys. Rev. Lett. 76, 3574 (1996).
[27] H.A. Baldis et al., Rev. Sci. Instrum. 73, 4223 (2002).

[28] H.S. Park et al., Phys. Plasmas 13, 056309 (2006).
[29] F. Grüner et al., Appl. Phys. B 86, 431 (2007). and refs. therein
[30] H.P. Schlenvoigt et al., Nature Phys. 4, 130 (2008)
[31] M. Fuchs et al., Nature Physics 5, 826 (2009).
[32] T. Tajima and J. Dawson, Phys. Rev. Lett. 43, 267 (1979)
[33] A. Pukhov and J. Meyer-ter-Vehn, Appl. Phys. B74, 355 (2002).
[34] Mangles, S. et al., Nature 431, 535 (2004).
Geddes, C. G. R. et al., Nature 431, 538 (2004).
Faure, J. et al., Nature 431, 541 (2004).
[35] W. Leemans et al., Nature Phys. 2, 696 (2006).
[36] J. Osterhoff et al., Phys. Rev. Lett. 101, 085002 (2008).
[37] S. Bulanov et al., Phys. Rev. E **58**, R5257 (1998).
[38] E. Esarey et al., Phys. Rev. Lett. 79, 2682 (1997).
Faure, J. et al., Nature 444, 737 (2006).
[39] Schwoerer, H. et al., Phys. Rev. Lett. 96, 014802 (1967).
[40] S. Kneip et al., Nature Physis, 6, 980 (2010).
[41] F. Brunel et al., Phys. Rev. Lett. 59, 52 (1987).
[42] J.Ph. Goddet et al., Opt. Lett. 32, 1498 (2007).
[43] J.Ph. Goddet et al., Opt. Lett. 34, in press (2009).

2.7 Attophysics

2.7.1 State of the art

High photon energy, high brilliance radiation sources, such as synchrotron installations, have been proven instrumental in structural studies encompassing several disciplines including physics, chemistry, material sciences, biology and medicine. Recent pioneering developments in intense, coherent XUV/x-ray radiation sources, with ultra-short pulse duration are for the first time close to offering the possibility of complete four dimensional (4D) studies in light matter interactions, at the unprecedented $Å^3$ spatial and sub-fs temporal resolution. These sources may be classified in i) free electron laser (XFEL) based installations [1, 2] and ii) laser based sources utilizing non-linear laser frequency up-conversion processes, such as higher order harmonic generation (HOHG) in gas [3,4] or on solid surface [5–9] targets. XFEL and HOHG sources are at the moment complementary sources, with the XFEL providing today substantially higher brilliances, while HOHG sources hold by far the record in ultra-short pulse durations of 80 attoseconds (1 atto = 10^{-18}) [10]. Real time studies of dynamic processes involving electronic motion in all states of matter, from atoms and molecules to macromolecules, liquids or condense matter, require temporal precision of the scale of the atomic unit of time (24.1889 asec). Indeed, since few years, progress in the field of attoscience has culminated, for the first time, the direct observation of ultra-fast processes in atoms, molecules and condensed mater on the sub-femtosecond regime [11–13].

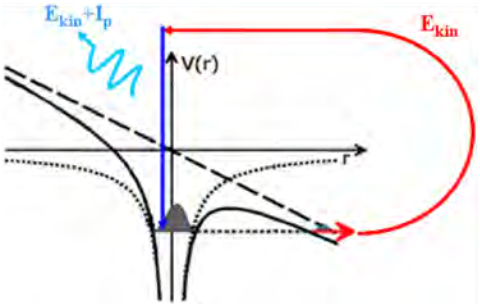

Figure 2.28: Atomic attosecond burst emission. An electron tunnels out, accelerated away, returns back and recombines emitting XUV radiation.

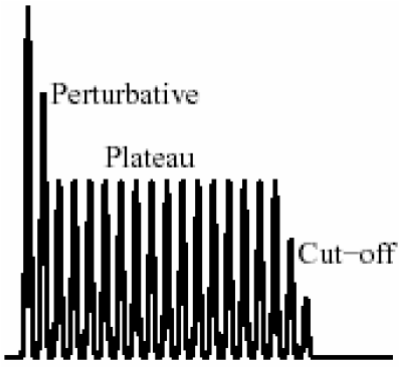

Figure 2.29: Harmonic spectrum.

Attosecond pulses are synthesized from XUV and/or x-ray waves, with HOHG in rare gases being so far the core process of the synthesizer. When an ultrashort laser pulse is focused into a rare gas, achieving intensities of the order of $10^{14} \sim 10^{15}$ W/cm^2, the atomic potential is considerably distorted, and electrons can tunnel out to the continuum. The free electron is then accelerated by the laser field first away from the nucleus, and after the electric field

changes sign, towards the nucleus. If the driving field is linearly polarised, there is a probability for the electron to be recaptured by the atom, in which case the kinetic energy gained from the laser field is emitted in the form of a high energy photon (Fig. 2.28). A typical harmonic spectrum, consisting of peaks separated by twice the laser frequency is shown in Fig. 2.29. It consists of a low-energy (perturbative) region with a characteristic rapid decrease in amplitude, followed by an extensive plateau of almost constant amplitudes that ends in an abrupt cut-off corresponding to the maximum energy that the electron can gain in the continuum. High-order harmonic generation (HHG) has become a tool for atomic physicists that provides insight into the fundamental physics of the interaction between an atom and a strong field. In addition, the generated extreme ultraviolet light inherits the driving laser's desirable properties, such as ultrashort duration, spatial and temporal coherence, directionality and high intensity over a very broad spectrum, enabling thus a wide range of applications in physical, chemical or biological sciences. It was realised shortly after the discovery of HHG, that the broad frequency range of the plateau harmonics would support pulses of sub-femtosecond duration. The periodic structure of the spectrum – when translated to the time domain – suggests, that a train of attosecond bursts, rather than a single pulse, might be produced, reflecting the process occurring in every half-cycle of the laser pulse (Fig. 2.30).

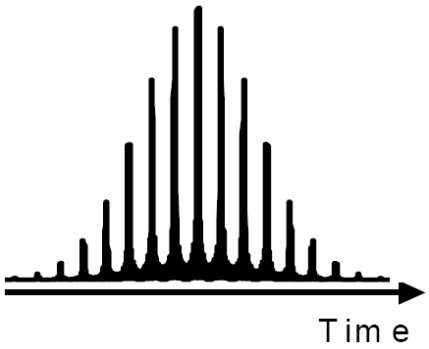

Figure 2.30: Train of asec pulses.

Isolating a single attosecond pulse from this pulse train is a challenge, as well as a necessity for clean analysis of pump-probe experiments. There are two methods proposed and demonstrated to meet this aim, i.e., to confine harmonic emission to a single half-cycle of the driving laser pulse. The first method is based on driving the process with a few-cycle driving pulse, and hence generation of the highest harmonics is naturally confined to the peak half-cycle. By spectral selection of these highest harmonics a single attosecond pulse is produced (Fig. 2.31). The other solution to the problem utilizes the fact that the efficiency of harmonic generation rapidly drops with increasing ellipticity of the driving field. Therefore the use a longer driving pulse with varying ellipticity in a way that the pulse is linearly polarized only during the central half-cycle may lead to the production of single attosecond pulses (Fig. 2.32). To increase the amount of the emitted high order harmonic radiation, one can turn on the generating laser intensity, or attempt an improvement of the generating efficiency. In both methods the stabilization of the relative phase between the driving carrier wave and its envelope, known as CEP (carrier-envelope phase) becomes an important issue. CEP stabilized pulses, through automated feed-back based technologies, have been recently achieved even for amplified pulses, albeit for few-cycle duration pulses only.

There is a limit to which the generating intensity can be increased imposed by ionization of the medium: beyond an intensity level there will be no atoms left to participate in the harmonic generation process. The efficiency of high order harmonic generation is to a large extent determined by whether phase matching can be achieved in the medium or not. Phase matching can be greatly enhanced either by making the phase variation in the medium low, or by

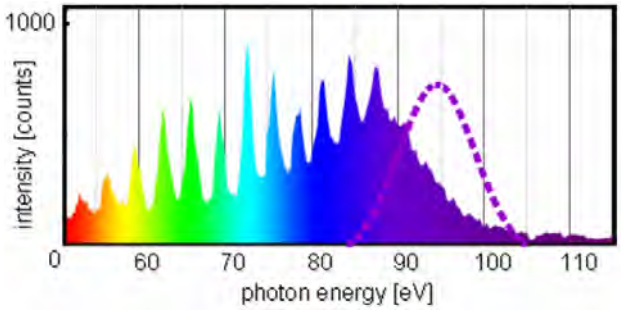

Figure 2.31: Spectral selection of the cut-off continuum region: Emission of isolated pulses.

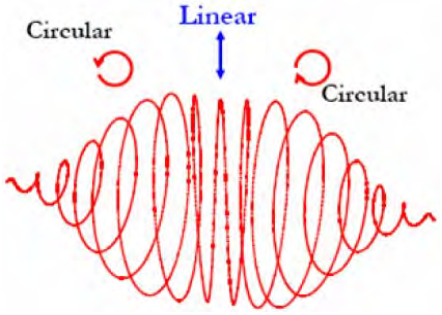

Figure 2.32: Polarization modulated pulse used in the polarization gating technique.

making different phase-variations balance each other. Both of these issues profit by applying a loose focusing geometry, the advantage of which was realised early. In case of loose focusing the ionization rate is strongly reduced, and both the geometrical phase shift and intensity (together with the dipole phase and the electron density) vary more slowly across the focus. Since the increase of the confocal parameter leads to a reduction in peak intensity and an increase of the number of the coherent emitters, the method can effectively be applied only, if an ample amount of laser energy is available.

Applying the above described approach, isolated pulses of limited power but of ultra-short duration (about 100 asec) have been synthesized utilizing few cycle CEP stabilized driving laser pulses [10, 14]. At somewhat longer durations (400–700 asec) trains of asec pulses, with substantial power have been generated, utilizing high peak power, many-cycle driving lasers. The focused XUV intensities of these trains reached 10^{14}W/cm^2 and have been successfully used in inducing two-XUV-photon processes.

2.7.2 Recent results

While the above discussed techniques are applied successfully in many laboratories, their scope of applications is limited mainly because the maximum achievable XUV energy is limited. Especially for XUV-pump and XUV-probe type experiments and imaging of single molecules [15] a higher photon flux is needed. The generation of coherent high harmonics from the interaction of an ultra-intense laser pulse with a solid density plasma surface has the potential of overcoming this limitation and producing attosecond pulses of unprecedented intensities [7] that could be applied to a wide range of experiments. Two distinct mechanisms for plasma surface high harmonic generation (SHHG) have been identified. For relativistic laser intensities, i.e., when $I\lambda^2 > 1.38 \times 10^{18}$ W/cm^{-2} μm^2, the dominant process is the frequency up-shifting of the incident laser light due to the reflection from the relativistically oscillating electron density surface, termed as the relativistic oscillating mirror (ROM). This process is explained in detail

by the theory of relativistic spikes of Baeva *et al.* [16]. For sub- and moderately relativistic intensities the dominant mechanism is the coherent wake emission (CWE) described by Quéré *et al.* [8]. Both these mechanisms are expected to generate coherent harmonics leading to temporal bunching and the generation of attosecond bursts of XUV radiation. Many recent experiments have increased our understanding for both SHHG mechanisms. In a series of measurements Dromey *et al.* have shown harmonic spectra extending up to the keV photon energy range (approximately the 2800^{th} order of the fundamental laser frequency) [17], and the generation of diffraction limited harmonic beams at 40 nm wavelength [18].

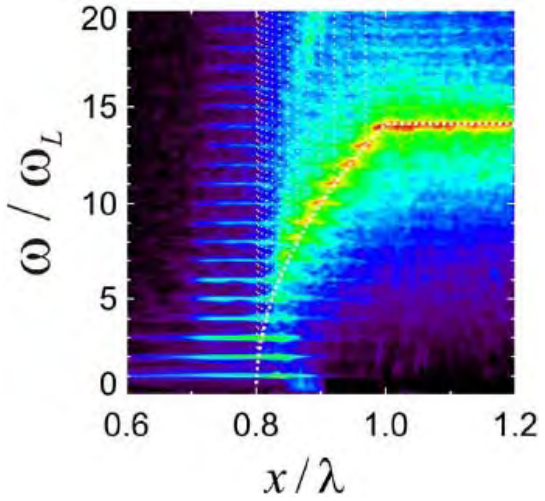

Figure 2.33: 1D PIC simulations elucidating the CWE generation The color plot shows current component J_x perpendicular to the target. From [25].

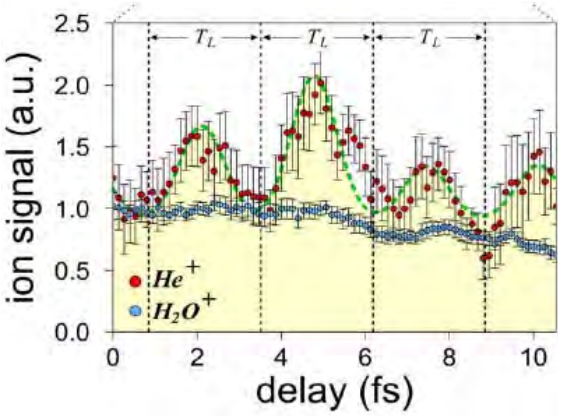

Figure 2.34: Measured non-linear volume AC traces for the harmonic composition comprising the 8th to 14th harmonic. A train of 900 asec pulses has revealed phase locking of SHHG.

Experiments have led to new insights into the CWE mechanism, proving that the spectrum has a sharp cut-off related to the maximum density of the target and the unequal temporal spacing of the individual emitted attosecond bursts [8, 19, 20]. In a very recent experiment, an order of magnitude higher conversion efficiency in SHHG than in gas HOHG was demonstrated. In this experiment it was further shown that the harmonic emission emanating from the interaction of intense laser pulses with solid surfaces indeed possesses the necessary properties to give rise to attosecond temporal bunching. Using the technique of the second-order volume autocorrelation [21, 22], a sub-femtosecond temporal structure has been observed [23]. Although all these experiments have led to a wealth of new insights into the generation mechanisms of

high harmonics from plasma surfaces, they have all, up to now, focused on characterizing the generated harmonics. If one wants to take surface harmonics to the next level, i.e., to use the generated radiation in a variety of applications, it becomes important to study issues such as transporting the beam, filtering the spectrum, suppressing the reflected infrared (IR) light from the target and increase the repetition rate to allow accumulation of many shots.

In the front of intense isolated attosecond pulses a recent development is the Interferometric Polarization Gating technique [24]. This technique allows for the application of the approach to many cycle pulses and thus to high peak power lasers. Through an interferometrically controlled ellipticity modulation of 50 fs long driving pulses we demonstrate broad continuum XUV emission [24]. Coherent broadband radiation down to 15 nm, capable to support synthesis of single pulses of 120 asec duration, and energy content in the sub-100 nJ range has been lately measured [25]. The present results open up excellent perspectives for intense asec pulse generation, either from gas targets or from relativistic laser–surface plasma interactions, for several existing high peak power many cycle laser installations.

2.7.3 Predicted evolution

Current and future efforts in attosecond pulse engineering are focusing on the progress in laser technology. Systems emitting pulses of few 100 of mJ and sub-10 fs durations are operational (e.g. the LWS 10 beam line at MPQ). The under construction PFS system at MPQ and the forefront laser system at ELI are challenging the few cycle pulse PW range (5 fs, 1-5 J). Utilizing such systems at intensities exceeding 10^{20} W/cm^2, intense attosecond pulses are predicted to reach the water window and beyond, while in the XUV region focused intensities of 10^{23} W/cm^2 may become achievable. Developments in the generation process are following two directions: I) Use of gas targets and highly loose focusing geometries (sub-20 m focal lengths) and II) Use of solid targets and ultra-high contrast laser beams. Such an evolution is subject to profound developments in short wavelength optics and filters mentioned in the previous section. Table 2.3 summarizes some specifications of current and future, including ELI, attosecond radiation sources.

Table 2.3: Specifications of current and future laser-based attosecond radiation sources.

Source	$\eta\omega$	τ	E (@ the source)	$I_{\max}$ (@ the target)
Gas HOHG single pulse	20–100 eV	$\sim$ 100 asec	$\leq$ 1 nJ	$<10^{11}$W/cm^2
Gas HOHG pulse trains	10–100 eV	$\geq$ 300 asec $\geq$ 10 fs envelope	$\leq$ 1 μJ	$<10^{14}$ W/cm^2
Surface HOHG (current)	10 s of eV –few keV	$\sim$ 900 asec $\sim$40 fs envelope	$\leq$ 1 μJ	$<10^{12}$ W/cm^2
Surface HOHG (future, i.e., ELI)	10 s of eV – few keV	100–5 asec	$\leq$ 100 mJ**	$<10^{23}$ W/cm^2 **

** Predictions based on PIC simulations.

Bibliography

[1] R.H. Pantell, Y. Soncini, and H. E. Putoff, IEEE Quantum Electronics **4**, 905 (1968).
[2] D.A.G. Deacon et al., Phys. Rev. Lett. **38**, 892 (1977).
[3] A. McPherson, G. Gibson, H. Jara, U. Johann, T.S. Luk, I. McIntyre, K. Boyer, and C. K. Rhodes, J. Opt. Soc. Am. B **4**, 595 (1987).
[4] M. Ferray, A. L' Huillier, F. X. Li, L. A. Lompré, G. Mainfray, and C. Manus, J. Phys. B **21**, L31 (1988).
[5] S. V. Bulanov, N.M. Naumova, and F. Pegoraro, Phys. Plasmas **1**, 745 (1994).
[6] R. Lichters, J. Meyer-ter-Vehn, and A. Pukhov, Phys. Plasmas **3**, 3425 (1996).
[7] G. Tsakiris, K. Eidmann, J. Meyer-ter-Vehn, and F. Krausz, New J. Phys. **8**, 19 (2006).
[8] F Quéré, C. Thaury, P. Monot, S. Dobosz, Ph. Martin, J.-P. Geindre, and P. Audebert, Phys. Rev. Lett. **96**, 125004 (2006).
[9] A. Dromey et al., Nat. Phys. **2**, 456 (2006).
[10] E. Goulielmakis et al., Science **320**, 1614 (2008).
[11] A. L. Cavalieri et al., Nature **449**, 1029 (2007).
[12] M. Uiberacker et al., Nature **446**, 627 (2007).
[13] M. Drescher, M. Hentschel, R. Kienberger, M. Uiberacker, V. Yakovlev, A. Scrinzi, Th. Westerwalbesloh, U. Kleineberg, U. Heinzmann, and F. Krausz, Nature, **419** 803 (2002).
[14] G. Sansone, E. Benedetti, F. Calegari, C. Vozzi, L Avaldi, R. Flammini, L. Poletto, P. Villoresi, C. Altucci, R. Velotta, S. Stagira, S. De Silvestri, and M. Nisoli, Science **314**, 443 (2006).
[15] H.N. Chapman et al., Nature **448,** 676 (2007).
[16] T. Baeva, S. Gordienko, and A Pukhov, Phys. Rev. E **74,** 046404 (2006).
[17] B. Dromey et al., Phys. Rev. Lett. **99,** 085001 (2007).
[18] B. Dromey, D. Adams, R. Härlein, Y. Nomura, S. G. Rykovanov, D. C. Carroll, P. S. Foster, S. Kar, K. Markey, P. McKenna, D. Neely, M. Geissler, G. D. Tsakiris, and M. Zepf, Nat. Phys. **5**, 146, (2009).
[19] C. Thaury et al., Nature Phys. **3**, 424 (2007).
[20] F. Quéré, C. Thaury, J-P Geindre, G. Bonnaud, P. Monot, and Ph. Martin, Phys. Rev. Lett. **100**, 095004 (2008).
[21] P. Tzallas, D. Charalambidis, N.A. Papadogiannis, K. Witte, and G. D. Tsakiris, Nature **426**, 267 (2003).
[22] L.A.A. Nikolopoulos, E.P. Benis, P. Tzallas, D. Charalambidis, K. Witte, and G.D. Tsakiris, Phys. Rev. Lett. **94**, 113905 (2005).
[23] Y. Nomura, R. Hörlein, P. Tzallas, B. Dromey, S. Rykovanov, S. Major, J. Osterhoff, S. Karsch, M. Zepf, D. Charalambidis, F. Krausz, and G.D. Tsakiris, Nat. Phys. **5**, 124 (2009).
[24] P. Tzallas, E. Skantzakis, C. Kalpouzos, E.P. Benis, G. D. Tsakiris, and D. Charalambidis, Nat. Phys. **3**, 846 (2007).
[25] P. Tzallas, E Skatzakis, G. Maravelias O. C. Kalpouzos, and D. Charalambidis Opt. Lett. **34**, 1732 (2009).

2.7.4 Tested applications

There are different options for probing electron dynamics with sub-femtosecond temporal resolution. An attosecond XUV pulse can trigger the electronic motion in an atom or molecule by exciting a valence or a core electron; the subsequent relaxation dynamics could be probed using the conventional pump-probe techniques, i.e., by a second attosecond XUV probe pulse. So far, such an experimental approach is not technically feasible due to the low energy of the currently available isolated attosecond pulses (limited to the nanojoule level) and to the low two-photon transition probability in the XUV and soft-X ray spectral region. It has been demonstrated that

a few-cycle infrared (IR) or visible pulse with controlled electric field, in combination with a highly nonlinear process, can replace the attosecond pulse either in probing or starting electron dynamics. Indeed, the electric field of an IR pulse, which changes its amplitude from zero to the maximum value in about 600 asec in the case of 750 nm pulses, can be used to probe, with attosecond resolution, the temporal evolution of electronic processes initiated by an attosecond pulse. It is worth pointing out that the harmonic generation process automatically leads to the production of attosecond pulses perfectly synchronized with the electric field of the IR driving pulse. This characteristic enables one to use attosecond pulses in combination with the driving pulses to investigate, with sub-femtosecond accuracy, the electron dynamics in atoms and molecules.

The first remarkable demonstration of such an experimental approach was offered by the introduction of the streak-camera technique for temporal characterization of attosecond pulses [1]. The basic idea of the measurement is the following: the attosecond pulse ionizes a gas, by single-photon absorption, thus generating an attosecond electron pulse, which, far from any resonance, is a perfect replica of the optical pulse. The conversion of the XUV pulse into an electron wavepacket occurs in the presence of a streaking IR pulse, whose electric field acts as an ultrafast phase modulator on the generated electron wavepacket. The evolution of the photoionization spectra as a function of the delay between the attosecond and the IR pulses allows one to retrieve the temporal intensity profile and phase of the XUV pulses and the electric field of the IR pulse. The presence of the streaking field maps the temporal profile of the electron emission, and therefore the temporal profile of the XUV pulse, into a distribution of final electron energies, from which it is possible to retrieve the XUV pulse duration.

The first experimental application of the streak-camera concept to the measurement of the duration of isolated XUV pulses was reported in 2001 by Hentschel *et al.* [2]. Isolated attosecond pulses have been produced by spectrally selecting the cutoff region of the harmonic spectrum generated in neon by 7 fs driving pulses. The XUV beam transmitted by a circular Zr filter, with a size matching the diameter of the harmonic beam, and the co-propagating annular IR beam were focused onto a second gas jet (krypton) by a concentric piezo-controlled double mirror unit. The central part of the mirror unit was a Mo/Si multilayer acting as a bandpass filter centered at 90 eV (bandwidth ~ 5 eV). Upon measuring the evolution of the width of the photoelectron spectrum as a function of the delay between the XUV and IR pulses it was possible to deduce an XUV pulse duration of ~ 650 asec. Using the same technique, pulses as short as 250 asec have been measured in 2004 [3]. Complete temporal characterization of isolated attosecond pulses has been reported in 2006 by Sansone *et al.* [4] and in 2008 by Goulielmakis *et al.* [5].

In the last few years, first experiments have been performed where attosecond laser pulses have been used to study time-resolved electron dynamics. The streaking technique can be used for probing inner atomic relaxation dynamics with sub-femtosecond resolution. In 2002 Drescher *et al.* [6] reported on the real-time observation of an atomic inner-shell process with attosecond accuracy, using a pump-probe experimental apparatus. In the experiment 0.9 fs soft-X-ray pulses have been used to excite krypton atoms and sub-7-fs IR pulses to probe electron emission. In this case the attosecond pulse creates a core hole, which is not stable; the system tends to minimize its energy by filling the vacancy with an electron from an outer shell. The excess energy is either carried away by fluorescence (emission of an XUV photon) or it is transferred via electrostatic forces to another (Auger) electron, which subsequently escapes from the atom, in the presence of a few-cycle IR streaking field. Upon measuring the temporal evolution of the spectrum of the Auger electrons as a function of the delay between the XUV and IR pulses it was possible to characterize the relaxation dynamics of the core hole. An Auger lifetime of 7.9 fs has been determined. In general, when the lifetime is much shorter than the period of the streaking field, the Auger electron maps out the oscillation of the IR field (as in the case of the photoelectrons directly generated by the attosecond pulse). In the case of lifetimes exceeding the optical period of the IR field, the energy spectrum shows the generation of sidebands spaced

by the IR photon energy. In this case the measurement of the core-hole dynamics does not rely on time-energy mapping. Rather, the sideband area as a function of pump-probe delay gives the temporal evolution of the Auger electrons.

More recently, the attosecond streaking technique has been extended to the investigation of electronic processes in condensed-matter systems [7]. Photoelectron emission from single-crystal tungsten has been probed, with attosecond resolution, revealing a 100 asec delay between the emission of photoelectrons that originate from localized core states of the metal and those that are freed from delocalized conduction-band states.

Another technique, which has been used so far to investigate electron dynamics with sub-femtosecond resolution, is based on XUV excitation of bound states followed by ionization by an intense IR field [8]. Energetic photo-excitations are commonly accompanied by electron transitions to unoccupied states via *shake-up*. A few-cycle, phase-stabilized IR pulse can now ionise the shake-up states in sub-femtosecond steps: this offers the possibility to probe the population of the shake-up states by measuring the number of ions resulting from the XUV pump, IR probe process. At the same time it is possible to investigate the temporal dynamics of strong-field ionization.

A very important aspect of attosecond technology is related to the fact that attosecond optical pulses produced by harmonic generation in gases are always associated with attosecond electron pulses. Indeed, XUV radiation is emitted by the oscillating dipole generated by the interference between the electron wavepacket (WP) bound to the atom (or molecule) and the electron WP freed in the continuum by tunnel ionization (the so called recollision electron wavepacket). Such attosecond electron pulses give access to spatial resolution. Indeed, the inter-atomic separation in matter and the typical structure size of valence electron orbitals are ~ 1 Å, which almost exactly matches the de Broglie wavelength of a typical recollision electron. Thus attosecond science can simultaneously control and measure structure and dynamics. Various techniques for molecular imaging have been proposed and partly experimentally implemented.

(i) *Laser-induced electron diffraction*: the recollision electron wave can diffract from its parent ion; by measuring the 3-D electron momentum of the scattered electrons it is possible to gain information required to reconstruct atomic positions within the molecule. In 2008 Meckel *et al.* [9] reported first experimental evidences of laser-induced electron diffraction from aligned O_2 and N_2 molecules. In order to obtain electron diffraction the de Broglie wavelength of the electron has to be of the order of the molecular size. Small diatomic molecules have a bond length of the order of 1 Å: an electron kinetic energy of 150 eV is required, which is easily obtainable. It has been demonstrated that the measured momentum distribution of the electrons extracted from the O_2 and N_2 molecules "carries the fingerprint of the highest occupied molecular orbital, whereas the elastically scattered electrons reveal the position of the nuclear components of the molecule. Thus the photoelectrons give detailed information about the electronic orbital and the position of the nuclei." [9].

(ii) *Tomographic imaging of molecular orbitals.* Since the harmonic emission is produced by the interference between the recolliding electron WP and the parent orbital, the harmonic spectrum contains the one-dimensional Fourier transform of the bound state orbital wave function. If we rotate the molecule in space we can take projections of the orbital shape from different directions and then build up its 3-D structure, as demonstrated by P. Corkum, D. Villeneuve and co-workers in the case of nitrogen molecule [10].

Trains of attosecond pulses, in combination with the use of ponderomotive streaking, have been used for complete characterization of electronic wavepackets [11]. The basic idea of the method is the following. If two attosecond pulses, separated by half optical cycle, are focused on a gas medium, two electron wavepackets are created in the continuum. Under the influence of a strong IR field, it is possible to modify the phase and/or the velocity of such electron wavepackets, thus allowing for the observation of interference patterns that contain information about the IR field and the electron wavepackets [12]. The proof-of-principle experiment has

been performed by using a train of attosecond pulses focused on Argon [11]. An interference pattern in the electron momentum space has been measured, whose characteristics depends on the temporal delay between the IR streaking field and the train of attosecond pulses. Although the reported measurements do not allow the recovery of the full momentum wave function, the experiment showed a promising new avenue for reconstructing the wavefunctions of atoms and molecules and for following the ultrafast dynamics of electronic wave packets.

A different class of applications of attosecond pulses to metrology and spectroscopy is based on the use of nonlinear effects, as in the case of femtosecond visible or near-infrared pulses. The extension of nonlinear optics to the XUV spectral region by using attosecond pulses, in the form of a train of pulses or of isolated pulses, has been so far limited by the low photon yield of the available attosecond sources and by the low nonlinear cross-section in the XUV spectral region. Various nonlinear processes have been used so far for the measurement of ultrashort XUV pulse duration: (i) two-photon above threshold ionization (ATI); (ii) two-photon absorption in atoms; (iii) two-photon double ionization; (iv) Coulomb explosion of diatomic molecules via two-photon double ionization [13].

In 2004 Sekikawa *et al.* reported on the temporal characterization of the ninth harmonic of sub-10 fs, 3.1 eV pulses by the autocorrelation technique, employing two-photon above-threshold ionization of helium [14, 15]. Upon measuring the number of photoelectrons with energy corresponding to the two-photon ATI peak (at 31.2 eV) as a function of the time delay between the two ninth-harmonic pulses, it was possible to measure the autocorrelation trace, with a minimum pulse duration of 950 ± 90 asec. More recently the temporal phase and intensity profile of the ninth harmonic pulses at 27.9 eV have been measured by using the Frequency Resolved Optical Gating (FROG) technique, based on two-photon ATI in He [16]. The measured shortest pulse duration was 860 asec implied by a flat spectral phase. In 2003, by using two-photon absorption (TPA) ionization of helium, Tzallas *et al.* demonstrated the first autocorrelation measurement of a train of attosecond pulses [17]. The He^+ yield induced by TPA was measured by a time-of-flight mass spectrometer as a function of the delay between two attosecond pulse train replicas, and provided the second-order autocorrelation signal. The measured ion yield exhibits a clear attosecond structure, with a periodicity twice that of the driving laser field, from which it was possible to obtain an estimate of 780 ± 80 asec for the average duration of the attosecond pulses in the train. The approach is extendable to shorter wavelengths utilizing an alternative non linear process in the XUV region, such as two-photon direct double ionization. Observation of the processes induced by a superposition of harmonics has been demonstrated in Kr and Ar atoms [18]. Coulomb explosion of diatomic molecules via two-photon double ionization has been recently proposed and used for the measurement of the interferometric autocorrelation of an attosecond pulse train [19], due to the larger nonlinear cross section with respect to rare-gas atoms. The integrated ion yield as a function of the temporal delay between the two XUV pulses displays clear bunches with a periodicity twice that of the driving laser field, which correspond to the interferometric autocorrelation trace of the train of attosecond pulses, with an estimated duration of the pulse bursts of 320 asec in full width at half maximum. Two-photon ATI is an additional alternative that has been used for an energy resolved autocorrelation measurement of an attosecond pulse train [20]. Second order autocorrelation applications have been very recently initiated [21] as well in surface plasma harmonics. Nomura *et al.* have observed a sub-fs pulse train of odd and even surface plasma harmonics generated at an increased conversion efficiency of 6×10^{-5}.

Bibliography

[1] J. Itatani, F. Quéré, G.L. Yudin, M.Yu. Ivanov, F. Krausz, P.B. Corkum, Phys. Rev. Lett. **88**, 173903 (2002).

[2] M. Hentschel, R. Kienberger, Ch. Spielmann, G.A. Reider, N. Milosevic, T. Brabec, P.B. Corkum, U. Heinzmann, M. Drescher, F. Krausz, Nature **414**, 509 (2001).
[3] R. Kienberger, E. Goulielmakis, M. Uiberacker, A. Baltuška, V. Yakovlev, F. Bammer, A. Scrinzi, Th. Westerwalbesloh, U. Kleineberg, U. Heinzmann, M. Drescher, F. Krausz, Nature **427**, 817 (2004).
[4] G. Sansone, E. Benedetti, F. Calegari, C. Vozzi, L. Avaldi, R. Flammini, L. Poletto, P. Villoresi, C. Altucci, R. Velotta, S. Stagira, S. De Silvestri, M. Nisoli, Science **314**, 443 (2006).
[5] E. Goulielmakis, M. Schultze, M. Hofstetter, V.S. Yakovlev, J. Gagnon, M. Uiberacker, A.L. Aquila, E.M. Gullikson, D.T. Attwood, R. Kienberger, F. Krausz, U. Kleineberg, Science **320**, 614 (2008).
[6] M. Drescher, M. Hentschel, R. Kienberger, M. Uiberacker, V. Yakovlev, A. Scrinzi, Th. Westerwalbesloh, U. Kleineberg, U. Heinzmann, F. Krausz, Nature **419**, 803 (2002).
[7] A.L. Cavalieri, N. Müller, Th. Uphues, V.S. Yakovlev, A. Baltuška, B. Horvath, B. Schmidt, L. Blümel, R. Holzwarth, S. Hendel, M. Drescher, U. Kleineberg, P.M. Echenique, R. Kienberger, F. Krausz, U. Heinzmann, Nature **449**, 1029 (2007).
[8] M. Uiberacker, Th. Uphues, M. Schultze, A.J. Verhoef, V. Yakovlev, M.F. Kling, J. Rauschenberger, N.M. Kabachnik, H. Schröder, M. Lezius, K.L. Kompa, H.-G. Muller, M.J.J. Vrakking, S. Hendel, U. Kleineberg, U. Heinzmann, M. Drescher, F. Krausz, Nature **336**, 627 (2007).
[9] M. Meckel, D. Comtois, D. Zeidler, A. Staudte, D. Pavièiæ, H.C. Bandulet, H. Pépin, J.C. Kieffer, R. Dörner, D.M. Villeneuve, P.B. Corkum, Science **320**, 1478 (2008).
[10] J. Itatani, J. Levesque1, D. Zeidler, H. Niikura, H. Pépin, J.C. Kieffer, P.B. Corkum, D.M. Villeneuve, Nature **432**, 867 (2004).
[11] T. Remetter, P. Johnsson, J. Mauritsson, K. Varjú, Y. Ni, F. Lépine, E. Gustafsson, M. Kling, J. Khan, R. López-Martens, K.J. Schafer, M.J.J. Vrakking, A. L'Huillier, Nat. Phys. **2**, 323 (2006).
[12] M.F. Kling, M.J.J. Vrakking, Annu. Rev. Phys. Chem. **59**, 463 (2008).
[13] K. Midorikawa, Y. Nabekawa, A. Suda, Progr. Quantum Electronics **32**, 43 (2008).
[14] T. Sekikawa, A. Kosuge, T. Kanai, S. Watanabe, Nature **432**, 605 (2004).
[15] N. Miyamoto, M. Kamei, D. Yoshitomi, T. Kanai, T. Sekikawa, T. Nakajima, S. Watanabe, Phys. Rev. Lett. **93**, 83903 (2004).
[16] A. Kosuge, T. Sekikawa, X. Zhou, T. Kanai, S. Adachi, S. Watanabe, Phys. Rev. Lett. **97**, 263901 (2006).
[17] P. Tzallas, D. Charalambidis, N.A. Papadogiannis, K. Witte, G.D. Tsakiris, Nature **426**, 267 (2003).
[18] E.P. Benis, D. Charalambidis, T. N. Kitsopoulos, G. D. Tsakiris and P. Tzallas Phys. Rev. A **74**, 051402 (R) (2006).
[19] Y. Nabekawa, T. Shimizu, T. Okino, K. Furusawa, H. Hasegawa, K. Yamanouchi, K. Midorikawa, Phys. Rev. Lett. **97**, 153904 (2006).
[20] A. Nabekawa et al., Phys. Rev. Lett. **96**, 083901 (2006).
[21] Y. Nomura, R. Hörlein, P. Tzallas, B. Dromey, S. Rykovanov, S. Major, J. Osterhoff, S. Karsch, M. Zepf, D. Charalambidis, F. Krausz, G.D. Tsakiris Nat. Phys. **5**, 124 (2009).

2.7.5 Potential applications

The prospects for attosecond science and for the study of ultrafast electron dynamics in all kinds of matter are greatly extended if brighter light sources with a wider wavelength range become available. Current sources of isolated attosecond pulses have restricted brightness ($\sim 10^6$ photons per pulse) and so essentially limit us to linear experiments, where there is single photon excitation by the ultrashort XUV pulse. Higher brightness sources ($>10^9$ photons per pulse)

available from HHG induced by high peak power laser pulses may enable nonlinear coupling to permit two-photon and higher order processes to be excited. Just as in the optical domain, where the reach of coherent nonlinear spectroscopy (e.g., four-wave mixing, photon echo, multi-dimensional approaches) has a greatly extended power over linear spectroscopy, so we would anticipate a more powerful probe of ultrafast electron dynamics if XUV ultrashort pulse nonlinear spectroscopy were possible. Pump/probe studies with attosecond pump/attosecond probe, as well as some (nonlinear) coherent control schemes require multiphoton absorption. Intense attosecond pulses will thus open an enormous range of processes that can be investigated. It will become possible to probe in a pricise way, with XUV radiation, molecular/cluster fragmentation induced by another ultrashort XUV pulse. More generally, the possibility to induce nonlinear processes using XUV or soft X-ray radiation opens a vast number of possible processes such as nonlinear frequency conversion into hard X-rays, wave mixing processes, advanced diagnostics etc. Intense attosecond pulses will be able to drive electros at very high frequencies. This will make possible electron bunching of interest for free electron laser coherent emission. The predicted unprecedented photon numbers per pulse (10^{16} in the VUV to $5{\cdot}10^{12}$ in the x-ray spectral region) to be emitted through relativistic laser-surface plasma interactions further boost the application spectrum towards fully unexplored research areas such as multi-photon, non-perturbative and relativistic inner-shell processes or exotic high XUV/X-ray field physics.

On a microscopic level, high field physics will be extended to the XUV and X-ray regime. One can envision to create a wavepacket with an attosecond pulse and to drive it with a second intense attosecond pulse, inducing a number of interesting new phenomena. One of these is the stabilization of atoms exposed to intense XUV light. Spatially coherent and intense attosecond pulses will also be of interest for temporally-resolved microscopic studies. This includes the very interesting topic of single molecule imaging by coherent diffraction techniques.

Multiple ionization/excitation of atoms and ions in XUV short fields

Strong field multiple ionization/excitation with several active electrons is a fundamental problem in atomic physics and a challenge for both experiment and theory. Because of the canonical importance of multiphoton processes in helium, a large number of theoretical studies have focused on two-photon excitation of auto-ionizing states (AIS) and two-photon double ionization (TPDI) in helium. Concerning auto-ionizing states, the lower $^1S^e$ and $^1D^e$ AIS series of He are excited from fundamental state through two-photon absorption with $\hbar\omega \cong 30$ eV [1, 2]. TPDI channel opens for photon energy close to 40 eV, a considerable amount of works have focused on this problem these last years, with large discrepancies between theoretical results. The difficulty of this problem is that the highly nonlinear field interaction is entangled with the few-body correlated dynamics. For photon energies ranging from 40 eV to 54.4 eV the two-photon double ionization process is direct, in this range there exists two clusters of results, separated by more than one order of magnitude (see [3], and references therein). One reason for such a discrepancy might be the different treatment of electron interaction in the final double continuum state. However, this clustering of theoretical data cannot be explained by categorizing them with respect to accounting or neglecting the electron interaction in final state. With photon energies larger than 54.4 eV and ultrashort pulses, TPDI electron spectrum reveals electron dynamics at the attosecond scale [4]. Morishita *et al.* have theoretically investigated the possibility to obtain a complete characterization of the time-dependent correlated motion of two electrons in helium by using attosecond-pump/attosecond-probe measurements [5]. In this case a broadband attosecond pump pulse generates an electron wavepacket by coherent superposition of states. A second attosecond pulse is used to doubly ionize the atom and the momentum vectors of the two ejected electrons must be measured in coincidence. As pointed out in Ref. [5], "for simple wave packets the stretching, the rotational, and the bending vibrational motion of the two electrons can be extracted from the measured momentum spectra when they are analyzed

in special coordinates".

The ELI project opens the perspective to pursue these studies with heavier atoms or ions and to explore the tunneling regime. Indeed, if we consider that the photon energy, time duration and intensity scale like ωZ^2, TZ^{-2} and IZ^6, respectively, with the nuclear charge Z, attosecond intense XUV fields are ideal to explore multielectron processes in heavy atoms and ions [6]. At contrast with femtosecond pulses, the atom or ion submitted to attosecond intense radiation will experience the maximum field intensity before it fully ionizes. This paves the way to studies of the relativistic effects and multiple ionization/excitation in the tunneling regime, which has received very little attention up to now [7].

Inner-shell processes are highly correlated processes than have only been studied in the linear regime. The ELI project will uniquely enable the study of multiphoton inner-shell effects. Utilizing any other "long pulse" source non-linear inner-shell processes will be overwhelmed by linear outer (or inner) shell interactions at any intensity below saturation. It has been estimated that due to the ultrashort duration of attosecond pulses there exist intensity regions prior to the depletion of the target in which two-photon inner shell processes become the dominant process of the interaction. Thus ELI will be a unique installation for the study of non-linear inner shell processes.

Attosecond nanoplasmonics

Synchronized waveform-controlled few-cycle visible and attosecond XUV pulses can be used to study collective electron dynamics (plasmons) in nanoscopic systems. Collective electron dynamics are of particular importance for the optical response of nanoparticles. Nano-structured materials, nanoparticles and clusters (with sizes between 1 and 1000 nm) are ideally suited to study collective electronic phenomena. These materials bridge the gap between atoms and molecules and the bulk materials. The motivation for studies on these materials is related to the possibility of tailoring their dynamical behavior on the basis of size and shape. They are of fundamental interest and have wide applications ranging from markers in medicine and biology over catalysts in chemistry to quantum computers. In a number of the important physical phenomena, the excitation and relaxation of electrons play a key role and collective electron excitations (Mie-plasmons) are typical signatures in the optical response of nanoparticles. While the spectral positions of plasmon excitations as a function of particle size, shape and dielectric properties are well understood, the ultrafast dynamics of collective electronic excitations, i.e., how they are formed and how the phase coherence is lost, is an open research field that can only now be explored in detail with attosecond spectroscopic tools.

In 2007 Stockman *et al.* proposed a new experimental method to measure the temporal dynamics of the collective electron oscillations in nanostructures with attosecond temporal resolution and nanometer-scale spatial resolution [8]. The proposed attosecond nanoplasmonic field (ANPF) microscope combines the temporal resolution of attosecond pulses with the spatial resolution of a photoelectron emission microscope (PEEM). The approach is based on the attosecond streak-camera method. The achievable temporal resolution of the proposed ANPF microscope is limited so far to ~ 100 asec, by the pulse duration of the available attosecond sources, not by the proposed measurement method. Spatial information can be obtained by imaging the excited nanoplasmonic system in a PEEM with energy resolution. The achievable spatial resolution is determined by the electron optics of the PEEM, and can be on the order of nanometers.

The ELI project opens the perspective to explore electron dynamics in isolated nanoparticles and nanoparticles on surfaces with sub-femtosecond time resolution. While first proof-of-principle studies on nanoparticles on surfaces with ultrahigh spatial (few tens of nanometer) and temporal (sub-100 asec) resolution may be implemented within the next years with state-of-the art table top attosecond setups, the studies on isolated nanoparticles are a great challenge as the expected count rate with current table-top sources is too low (estimated to be 0.1/s). An

ultrabright source can increase the count rate by several orders of magnitude and thus facilitate such explorations for the first time. The aim is to gain information on the collective electronic properties of nanostructured materials on a timescale on which they occur in nature. The work can have a huge impact on the development of nanoplasmonic devices, which may exceed the current speed of electronics by several orders of magnitude.

Plasma physics

In the field of dense plasma physics, in particular plasmas close to solid densities originating from the sudden heating of solid matter, the time scale of all plasma oscillations is set by the plasma frequency $\omega_p = 2\pi/T_p$. The period of these oscillations is given by $T_p/T_L = \sqrt{n_{\rm crit}/n_e}$, where the critical density is about $n_{\rm crit} \approx 10^{21}$ cm^{-3} for light of period $T_L \approx 3$ fs and the actual electron density $n_e \approx 10^{23}$–10^{24} cm^{-3}. This implies oscillation periods of 100–300 as, and time-resolved measurements will depend on even shorter attosecond pulses. Detailed investigations of plasma dynamics on these time scales will be crucial for a number of applications, such as laser-driven ion acceleration from thin solid targets and high harmonics generation from solid surfaces. Here Rayleigh-Taylor-type instability of laser-driven electron fronts may play a major role and need to be controlled. For fast ignition of inertial confinement fusion (ICF) targets, densities up to 1000 time solid density are required and the crucial question of electron energy transport to the highly compressed fuel core involves time scales down to a few attoseconds [9]. Here the beam transport involves currents of up to 1 GA, and filamentation instability on attosecond time scale needs to be resolved. All applications to high-field physics that are now discussed within the ELI project for even higher intensities (e.g. reaching the Schwinger limit, pair creation, generation of Unruh radiation, etc.) will depend on focusing the attosecond pulses. This will require curved plasma sheets, and time resolved control of how they form and propagate will be crucial for success.

Attosecond science in condensed matter

Beyond a broad range of electron dynamics in isolated atoms and molecules, a rich variety of ultrafast electronic motion, important for many ongoing and future developments, occur on surfaces and in solids.

(i) Strongly-correlated electron systems. Many condensed matter systems of current interest are characterized by electronic interactions with energy scales that exceed 1 eV. These are the so called strongly-correlated electron systems, where interaction between charge carriers greatly exceeds their kinetic energy. The response of these systems to external perturbations, such as a photo-excitation event, can teach us a great deal about the elementary interactions taking place. Furthermore, photo-control of such strongly-correlated electron solids may lead to new applications in ultrafast data processing and storage. Because the energy scale is so high, the rearrangements in the electronic system can only be followed by pulses of commensurate duration. In the copper oxides, that give rise to high-temperature superconductivity, the electron correlation energy is of order 2 eV, giving rise to important dynamics occurring in the attosecond regime.

(ii) Photo-electron spectroscopy. Elementary photo-electron spectroscopy rely on the assumption that the emission of the photo-electron is a prompt process. This "sudden approximation" underpins our ability to learn about the solid by looking at the energy distribution of the photo-electron. However, the exact escape time of photo-emitted electrons is finite and being able to follow the dynamics of the photo-emission process would revolutionize this kind of spectroscopy.

(iii) Electron diffraction. The ability to use UV radiation for photo-electron diffraction, in which the angular distribution of the photo-electrons carries information on the surface atomic and electronic structure, is one of the most interesting probes of surfaces. These are demanding experiments that may become possible with intense attosecond pulses. These probes, which are ideally understood as an "inverse LEED" technique, may give us structural information on a timescale that is faster than any internal rearrangement of a solid state system. Even geometric charge distributions could be probed in this way.

(iv) 4-dimensional microscopy of electron dynamics with nanometer resolution in space and attosecond resolution in time. Emphasis in surface science and nanotechnology is shifting towards complex architectures. These include layers of large organic molecules and biomolecules, self-assembly of monolayers and of supramolecular structures on surfaces and nanoparticle formation. In all applications, ranging from functionalized surfaces of nanoparticles to solar cells based on dyes on surfaces, bio sensors and molecular electronics, insight into electronic dynamics is a prerequisite for modeling and optimizing surface-based systems. In the field of semiconductor nanostructures, the realization of fully-quantized systems has allowed the development of optoelectronic devices that have true quantum mechanical functionality. Probing these systems with attosecond temporal resolution will provide direct access to the processes responsible for quantum state dephasing, the origin of which is ill-understood. Insight into the nature of such processes is essential to the development of solid-state coherent quantum devices such as hardware for utilization in quantum information technologies. Attosecond techniques will grant access to even the fastest electronic processes on surfaces and in solids, including those relating to the motion of electrons as well as their spin dynamics. Selecting its radiation at the highest photon energies ($\sim$ 1 keV) will offer attosecond temporal resolution combined with nanometer spatial resolution by means of attosecond soft-X-ray diffraction. This 4D microscopy will allow – for the first time –recording of movies of electronic dynamics in nanometer-scale molecular and solid-state structures with truly electronic attosecond time resolution.

Imaging with ultrashort light pulses

Theory predicts that with an extremely intense and ultrashort X-ray pulse, a diffraction pattern can be recorded from an object before it explodes [10]. Experiments performed at the FLASH soft X-Ray Free Electron Laser in Hamburg at DESY (Deusches Elektronen-Synchroton) have validated the principle of single-shot “flash diffraction imaging” of solid samples [11] and isolated, substrate-free particles in the gas-phase [12]. Femtosecond time-delay holography [13] and Laser-pump/X-ray probe experiments [14] have allowed the investigation of sample disintegration dynamics in response to energy deposited by X-ray and IR pulses, respectively. The development of massively parallel holography [15] employing uniformly redundant arrays allows the amplification of diffraction signals by several orders of magnitude. These techniques open novel opportunities for imaging biological samples ranging in size from entire living cells to viruses and potentially down to individual macromolecules. Bergh *et al.* have recently modelled the ideal laser pulse requirements for imaging biological cells [16]. While X-ray pulses of few tens of fs “kill” the sample, pulses at the few fs level or shorter allow for sharp diffraction images. The availability of ultra-short pulse X-ray lasers will enable these methods to reach their full potential.

Tailored electron dynamics and application to chemistry

With the development of attosecond pulses in the range of 5 to 15 eV energy per photon it will become possible to tailor the valence electron motion so as to direct the motion of the nuclei and chemical reactivity [17]. Examples of possible applications of isolated attosecond pulses in this energy range are the following: investigation of the electron dynamics in small peptides

ionized locally by an attosecond pulse [17, 18] and investigation of the electron dynamics of a coherent superposition of excited electronic states produced by an ultrashort attosecond pulse in LiH [19–21].

The small number of electrons in LiH makes it possible to use a time-dependent multi-configuration method with a large electronic basis set to compute the response of all the electrons to a few-cycle intense pump field followed by a probe pulse. The effect of the pulse is added to the electronic Hamiltonian of the system so that the treatment of electron correlation during and after the pulse is essentially exact. The motion of the electrons can be controlled by the parameters of the ultrashort pulse, i.e., intensity, duration, polarization and the carrier envelope phase (CEP) [19, 20]. For example, by shifting the CEP phase of the pulse the electrons can be driven towards the Li nucleus or away from it. The probing of the electronic wave packet by a probe pulse is included in the Hamiltonian and the resulting frequency dispersed spectrum computed.

For larger systems like the peptide cations, the almost exact treatment of the electron correlation that is possible in LiH is computationally intractable. An one-electron theory approach can be used in this case to follow the motion of the hole created by the ultrafast localized ionization. The formalisms that have been used up to now were developed for ultrashort time such that the nuclei are de facto frozen in their position. Such a theory could only describe the ultrafast electron dynamics that takes place before the nuclei start to move. Novel theoretical tools and concepts must be developed to explore the early time nuclear dynamics that is induced by the electronic motion. In particular, an understanding is needed on how to tailor the electron-nuclei coupling with the attosecond pulse in order to control the nuclear motion.

Bibliography

[1] I. Sánchez, H. Bachau, E. Cormier, J. Phys. B **28,** 2367 (1995).
[2] R. Hasbani, E. Cormier, H. Bachau, J. Phys. B **33**, 2101, (2000).
[3] E. Foumouo, Ph. Antoine, B. Piraux, L. Malegat, H. Bachau, R. Shakeshaft, J. Phys. B **41**, 051001 (2008).
[4] E. Foumouo, Ph. Antoine, H. Bachau, B. Piraux, New J. Phys. **10**, 025017 (2008).
[5] T. Morishita, S. Watanabe, C.D. Lin, Phys. Rev. Lett. **98**, 083003 (2007).
[6] S. Laulan et al., J. of Mod. Optics **50**, 353 (2003).
[7] J. Bauer and K. Rzazewski, J. Phys. B **29**, 3351 (1996).
[8] M.I. Stockman, M.F. Kling, U. Kleineberg, F. Krausz, Nat. Photon. **1**, 539 (2007).
[9] S. Atzeni, J. Meyer-ter-Vehn: The Physics of Inertial Fusion, Oxford University Press, 2004.
[10] R. Neutze, R. Wouts, D. van der Spoel, E. Weckert, J. Hajdu, Nature **406**, 752 (2000).
[11] H.N. Chapman, A. Barty, M.J. Bogan, S. Boutet, M. Frank, S.P. Hau-Riege, S. Marchesini, B.W. Woods, S. Bajt, H. Benner, R.A. London, E. Plonjes, M. Kuhlmann, R. Treusch, S. Dusterer, T. Tschentscher, J.R. Schneider, E. Spiller, T. Moller, C. Bostedt, M. Hoener, D.A. Shapiro, K.O. Hodgson, D. Van der Spoel, F. Burmeister, M. Bergh, C. Caleman, G. Huldt, M.M. Seibert, F. Maia, R.W. Lee, A. Szoke, N. Timneanu, J. Hajdu, Nat. Phys. **2**, 839 (2006).
[12] M.J. Bogan, W.H. Benner, S. Boutet, U. Rohner, M. Frank, A. Barty, M.M. Seibert, F. Maia, S. Marchesini, S. Bajt, B. Woods, V. Riot, S.P. Hau-Riege, M. Svenda, E. Marklund, E. Spiller, J. Hajdu, H.N. Chapman, Nano Letters **8**, 310 (2008).
[13] H.N. Chapman, S.P. Hau-Riege, M.J. Bogan, S. Bajt, A. Barty, S. Boutet, S. Marchesini, M. Frank, B.W. Woods, W.H. Benner, R.A. London, U. Rohner, A. Szoke, E. Spiller, T. Moller, C. Bostedt, D.A. Shapiro, M. Kuhlmann, R. Treusch, E. Plonjes, F. Burmeister, M. Bergh, C. Caleman, G. Huldt, M.M. Seibert, J. Hajdu, Nature **448**, 676 (2007).

[14] A. Barty, S. Boutet, M.J. Bogan, S. Hau-Riege, S. Marchesini, K. Sokolowski-Tinten, N. Stojanovic, R. Tobey, H. Ehrke, A. Cavalleri, S. Duesterer, M. Frank, S. Bajt, B.W. Woods, M.M. Seibert, J. Hajdu, R. Treusch, H.N. Chapman, Nature Photonics **2**, 415 (2008).
[15] S. Marchesini, S. Boutet, A. E. Sakdinawat, M.J. Bogan, S. Bajt, A. Barty, H.N. Chapman, M. Frank, S.P. Hau-Riege, A. Szoke, C. Cui, D.A. Shapiro, M.R. Howells, J.C.H. Spence, J.W. Shaevitz, J.Y. Lee, J. Hajdu, M.M. Seibert, Nature Photonics **2**, 560 (2008).
[16] M. Bergh, G. Huldt, N. Timneanu, F. Maia, J. Hajdu, Quarterly Reviews of Biophysics, in press.
[17] F. Remacle, R.D. Levine, Proc. Natl. Acad. Sci. USA **103**, 6793 (2006).
[18] F. Remacle, R.D. Levine, Z. Phys. Chem. **221**, 647 (2007).
[19] M. Nest, F. Remacle, and R. D. Levine, New J. Phys. **10**, 025019 (2008).
[20] F. Remacle, M. Nest, and R. D. Levine, Phys. Rev. Lett. **99**, 183902 (2007).
[21] F. Remacle, R. Kienberger, F. Krausz, and R. D. Levine, Chem. Phys. **338**, 342 (2007).

2.7.6 Requirements from the users

Since the source is dedicated to users, its specifications have to be user oriented. Thus a central parameter in defining specifications is the requirements set by users. The spectrum of users of such a source is very broad and the adjacent requirements rather diverse. On the other hand resources are limited and thus encompassing tendencies have to be avoided and optimal compromises have to be made.

User requirements have been identified during the preparatory phase of ELI through discussions during meetings of the WP7B-1 "attosecond source open for users" as well as through workshops and conferences that have been organized on attosecond science. These events have hosted talks by potential users of the Attosecond Light Source of ELI, presenting possible novel research projects to be conducted in this unique infrastructure giving special emphasis to the required source parameters Examples of such events are the joined ELI/X-HOMES Workshop on "Science with novel, user oriented intense attosecond radiation sources", organized in Heraklion in August 2008 or the International Conference on Non Linear Phenomena in Russia July, 2008 and the Attosecond workshop organized in Budapest in July 2010. But also in a number of regular conferences, symposia, schools and other scientific events examples of what could be done in the upcoming attosecond sources of the next generation European Research Infrastructures are more and more frequent part of the presentations.

The source parameters to be defined are the pulse duration, energy, central wavelength and spatio-tempotral coherence as well as the average power that directly relates to the repetition rate of the source and the beam divergence. Depending on the specific application the required specifications are diverse and often in partial conflict. Some examples that have been provided by potential users of the source are:

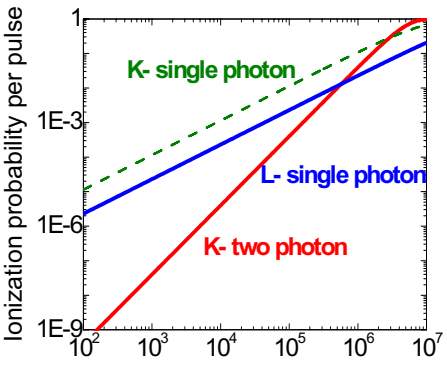

Figure 2.35: Estimated one- and two-photon K-shell and one-photon L-shell ionization probabilities for $Z = 5$.

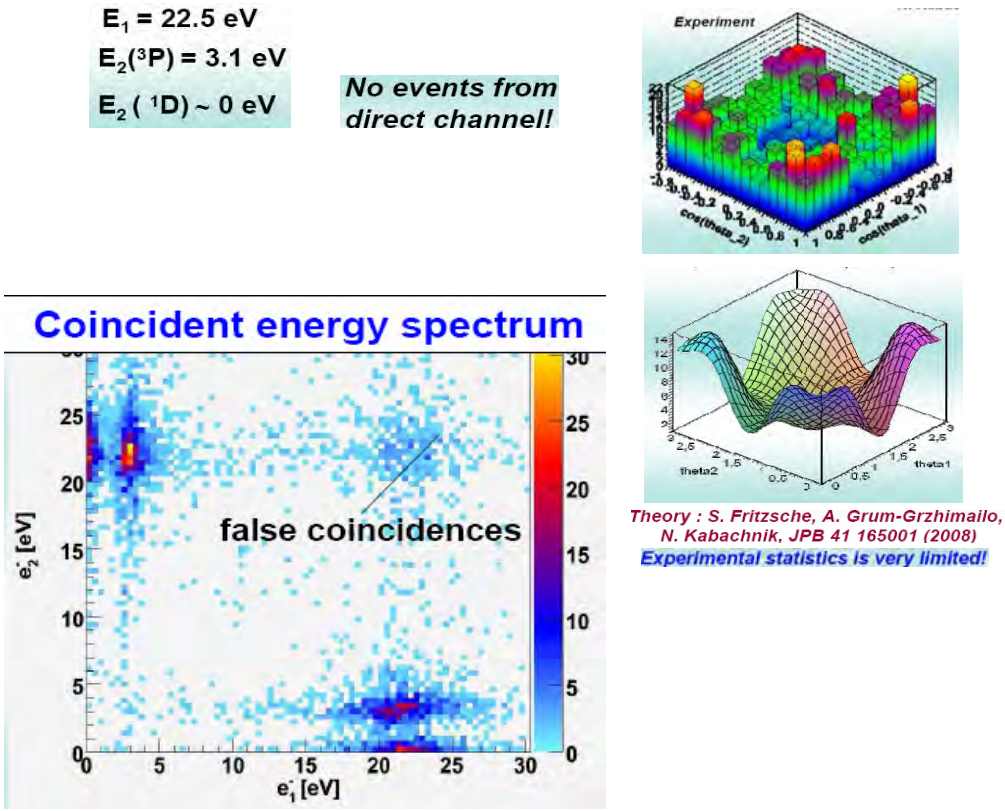

Figure 2.36: Coincidence measurements with fully differential data of sequential Two Photon Double Ionization of Ne (left) and correlated angular distribution data (right). In both data statistics are limited. For such an experiment a tunable source with photon energy 30–50 eV at intensities 10^{14}–10^{16} W/cm^2, no strict duration requirements and 1 kHz repetition rate is needed. (From the presentation of A. Rudenco at the ELI workshop on "XUV-High Order Harmonic Metrology Tools for Novel Spectroscopic Applications" August 2008, FORTH, Crete, Greece.

1) Many of the applications are based on non-linear and/or relativistic/ultra-relativistic XUV/x-ray processes for which peak intensity is a crucial parameter. Relativistic multi-photon inner shell processes, an entirely new research topic, is one representative paradigm of such applications. Fig. 2.35 shows estimated at FORTH-IESL two-photon K-shell ionization probabilities for $Z = 5$ (from the presentation of D. Charalambidis at the Paris ELI workshop). The process becomes dominant against other competing processes at relativistic intensities. In contrast "complete" experiments requiring coincidence detection of the radiation-matter interaction products seek for high repetition rates of the order of MHz or higher and thus high average power. Fig. 2.36 shows fully differential data of coincidence measurements of the sequential Two Photon Double Ionization (TPDI) of Ne (left) and experimental and theoretical data of correlated angular distribution data (right). In both experiments the statistics are very low. For this type of experiments intense (10^{14}–10^{16} W/cm^2) XUV pulses at repetition rates of 1 kHz are required.

2) Studies of ultra fast electron-electron correlations require ultra-short pulse duration, of up to some 10 asec, and not necessarily too high photon fluxes. Fig. 2.37 shows photoelectron spectra of the He atom double ionization in which electron-electron correlation effects may become visible if the atom is ionized with pulses of 400 asec duration.

In contrast, in diffraction experiments, aiming e.g. at the imaging of bio-molecules, the

required photon fluxes are very important and pulse duration short but not ultra short. Since the sample is destroyed within few fs upon irradiation (diffraction), imaging has to be completed in a single shot, and pulse duration of 1 fs would be sufficient. Fig. 2.38 shows the temporal evolution of the Coulomb explosion of lysozyme clusters after irradiation with x-rays. The estimated time for which an exploding protein molecule irradiated by x-rays remains "freezed" in its initial shape is few fs.

3) Diffraction experiments of nm scale objects require x-ray wavelengths, while for a large number of experiments aiming at the study of attosecond dynamics in all stages of matter XUV radiation is sufficient.

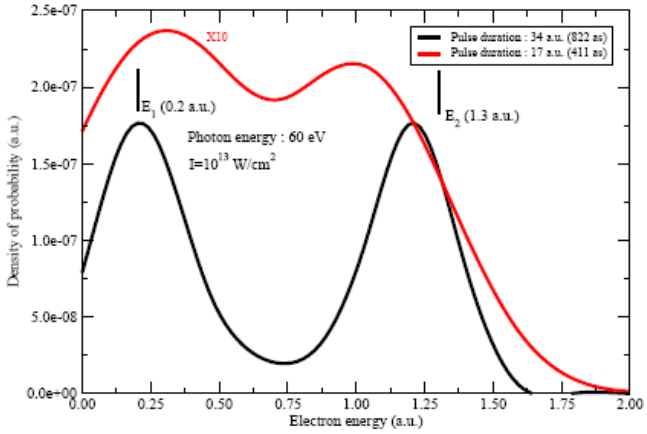

Figure 2.37: Photoelectron spectra obtained through two-photon double ionization of He at two different pulse durations, reviling the electron-electron correlation in the He ground state. The correlation time becomes time dependene during the ionization process.(From the presentation of H. Bachau at the ELI workshop on "XUV-High Order Harmonic Metrology Tools for Novel Spectroscopic Applications" August 2008, FORTH, Crete, Greece. See also Foumouo et al., New J. Phys. 10, 025017 (2008)).

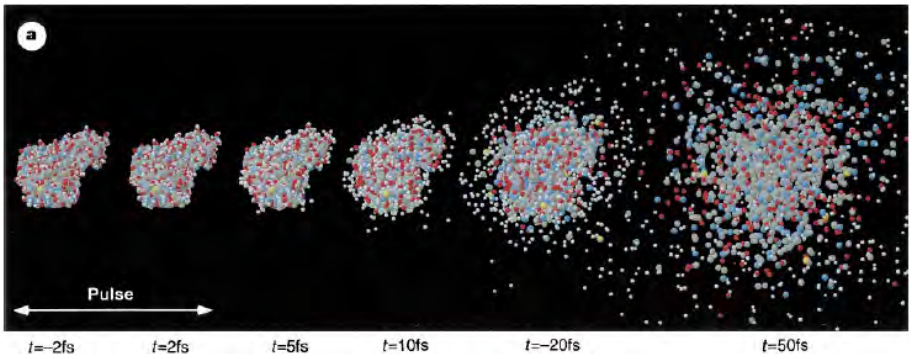

Figure 2.38: Explosion of T4 lysozyme (white, H; grey, C; blue, N; red, O; yellow, S) induced by radiation damage. The integrated X-ray intensity was 3×10^{12} (12 keV) photons per 100 nm diameter spot (3.8×10^6 photons per Å^2) in all cases. A protein exposed to an X-ray pulse with an FWHM of 2 fs, and disintegration followed in time. Atomic positions in the first two structures (before and after the pulse) are practically identical at this pulse length because of an inertial delay in the explosion. Rnucl = 3%, Relec = 11%. From [1].

4) High repetition rates are beneficial for attosecond material processing, while single shot radiography requires high photon fluxes.

An assessment of the user requirements in conjunction with the available technologies and the infrastructure scale has led to the following specifications:

Table 2.4: Attosecond source specifications.

Source target	1. Solid density plasma 2. Gas jet
Photon energy	10 eV–5 KeV
Pulse duration	300–10 asec
Photon flux	10^{16}- 10^{12} Photons/pulse
Repetition rate	1 kHz
M^2	1.5

Bibliography

[1] R. Neutze, R. Woutls, D. Van Der Spoel, E. Wecket and J. Hadju, Nature **406**, 752 (2000).

2.8 ELI Nuclear Physics

Introduction

For ELI-NP the extreme light is realized in a twofold way: by very high optical laser intensities of high power laser and by the very short wavelength beams with very high brilliance. This combination allows for three types of experiments: stand-alone high power laser experiments, stand-alone γ beam experiments and combined experiments of both facilities. Here the low repetition rate (1/min) of the high power laser requires the same low repetition rate for the γ beam in combined experiments. While the stand-alone γ beam will be used with typically 12 kHz the low repetition mode requires few very intense γ pulses.

2.8.1 Stand-alone High Power Laser Experiments

With the high power laser we do not plan to interact with nuclear dynamics directly, but we use the laser for ion acceleration or to produce relativistic electron mirrors by laser acceleration followed by a coherent reflection of a second laser beam in order to generate very brilliant X-ray or γ beams. We plan to use these beams later to produce exotic nuclei or to perform new γ spectroscopy experiments in the energy or time domain.

A Laser-Accelerated Th Beam is used to produce Neutron-Rich Nuclei around the $N = 126$ Waiting Point of the r-Process via the Fission-Fusion Reaction Mechanism

The origin of the heaviest elements (e.g. Gold, Platin, Thorium, Uranium) remains one of the 11 greatest unanswered questions of modern physics, according to a recent report by the US National Research Council of the National Academy of Science [1]. A recent paper accepted in Appl. Phys. B by D. Habs et al. [2] outlines in detail, how the dense laser-accelerated ion beams open up a new access to very neutron-rich nuclei, relevant to this element production. In this proposal we introduce the new 'fission-fusion' nuclear reaction process, which allows to produce the decisive extremely neutron-rich nuclei in the range of the astrophysical R-process (the rapid neutron-capture process) around the waiting point N=126 [3–5] by fissioning a dense laser-accelerated thorium ion bunch in a thorium target (covered by a polyethylene layer, CH_2), where the light fission fragments of the beam fuse with the light fission fragments of the target. So far the astrophysically relevant nuclei are about 15 neutrons away from the last known isotope and nothing is known about their nuclear properties. Via the 'hole-boring' (HB) mode of laser Radiation Pressure Acceleration (RPA) [6, 7] using a high-intensity, short pulse laser, very efficiently bunches of ^{232}Th with solid-state density can be generated from a Th layer (ca. 0.5 µm thick), placed on a deuterated diamond-like carbon foil (CD_2 with ca. 0.5 µm), forming the production target. Laser-accelerated Th ions with about 7 MeV/u will pass through a thin CH_2 layer placed in front of a thicker second Th foil (both forming the reaction target) closely behind the production target and disintegrate into light and heavy fission fragments. In addition, light ions (d,C) from the CD_2 backing of the Th layer will be accelerated as well, inducing the fission process of ^{232}Th also in the second Th layer. The laser-accelerated ion bunches with solid-state density, which are about 10^{14} times more dense than classically accelerated ion bunches, allow for a high probability that generated fission products can fuse again when the fragments from the thorium beam strike the Th layer of the reaction target.

In contrast to classical radioactive beam facilities, where intense but low-density radioactive beams of one ion species are merged with stable targets, the novel fission-fusion process draws on the fusion between neutron-rich, short-lived, light fission fragments both from beam and target. Moreover, the high ion beam density may lead to a strong collective modification of the stopping power in the target by 'snowplough-like' removal of target electrons, leading to significant range enhancement, thus allowing to use rather thick targets.

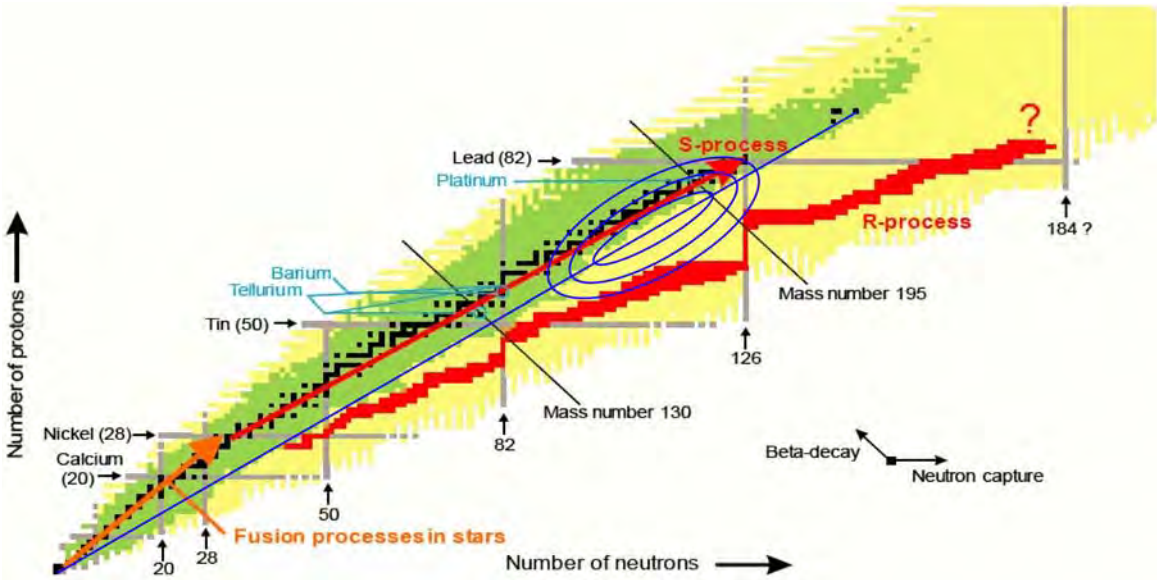

Figure 2.39: Nuclidic chart, showing the different nucleosynthesis processes like the R-process, the S-Process or the fusion processes in stars together with conture lines of the new fission-fusion process for producing very neutron-rich nuclei close to $N = 126$ waiting point of the R-process.

Using a high-intensity laser with 300 J and 32 fs pulse length, as, e.g., envisaged for the ELI-Nuclear Physics project in Bucharest (ELI-NP), order-of-magnitude estimates promise a fusion yield of about 10^3 ions per laser pulse in the mass range of $A = 180$–190, thus enabling to approach the R-process waiting point at $N = 126$. The produced nuclei from the fission-fusion process will be injected into a Penning trap (see Fig. 2.40) to measure their nuclear binding energy, a measure for shell quenching, with high accuracy. This information will narrow down possible sites for the astrophysical R-process decisively.

Bibliography

[1] E. Haseltine, http:discovermagazine.com2002febcover.
[2] D. Habs, P.G. Thirolf, M. Gross, K. Allinger, J. Bin, A. Henig, D. Kiefer, W. Ma, J. Schreiber, arXiv:1007.1251v2 [nucl-ex] 2010, accepted by Appl. Phys. B.
[3] K.L. Kratz, K. Farouqi, B. Pfeiffer, Prog. Part. Nucl. Phys. **59**, 147 (2007).
[4] M. Arnould, S. Goriely, K. Takahashi, Phys. Rep. **450**, 97 (2007).
[5] I.V Panov and H.-Th. Janka, Astr. Astroph. **494**, 829 (2009).
[6] A.P.L. Robinson, P. Gibbon, M. Zepf, S. Kar, R.G. Evans and C. Bellei, Plasma Phys. Control. Fusion **51**, 024004 (2009).
[7] A. Henig, S. Steinke, M. Schnürer, T. Sokollik, R. Hörlein, D. Kiefer, D. Jung, J. Schreiber, B.M. Hegelich, X.Q. Yan, J. Meyer-ter-Vehn, T. Tajima, P.V. Nickles, W. Sandner, and D. Habs, Phys. Rev. Lett. **103**, 245003 (2009).

From Radiation Pressure Acceleration (RPA) and Laser-Driven Ion Pistons to Direct Laser Acceleration of Protons at Intensities up to 10^{24} W/cm^2

Since the pioneering work that was carried out 10 years ago [1–4], the generation of highly energetic ion beams from laser-plasma interactions has been investigated in much detail in the regime of target normal sheath acceleration (TNSA) [5]. Creation of ion beams with small

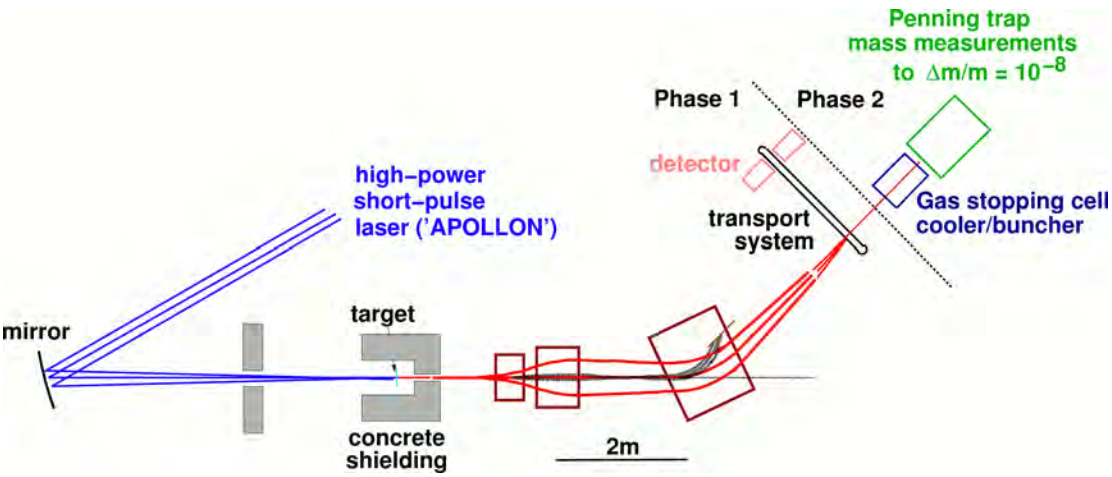

Figure 2.40: Experimental setup to produce the neutron-rich nuclei by laser acceleration, to separate them in a gas-filled separator and finally to measure their masses very accurately in a Penning trap.

longitudinal and transverse emittance and energies extending up to tens of MeV fueled visions of compact, laser-driven ion sources for applications such as ion beam therapy of tumors, fast ignition inertial confinement fusion or the generation of neutron-rich nuclei. However, new pathways are of crucial importance to push the current limits of laser-generated ion beams further towards parameters necessary for those applications.

To overcome the limitations of TNSA, a novel mechanism, which is referred to as Radiation Pressure Acceleration (RPA) was proposed [6–9]. Here, much thinner foil targets of only nanometers are used so that the laser transfers energy to all electrons located within the focal volume. While for TNSA the accelerating electric field that is generated by hot electrons is stationary and ion acceleration is spatially separated from laser absorption into electrons, in RPA a localized longitudinal field enhancement is present that co-propagates with the ions as the accompanying laser pulse pushes the electrons forward. By changing the laser polarization to circular, electron heating and expansion are efficiently suppressed, resulting in a phase-stable acceleration that is dominated by the laser radiation pressure and is maintained for an extended time. Thus, the whole target is accelerated ballistically as a quasi-neutral, dense plasma bunch like a light sail. Just recently, this novel acceleration process has been observed for the first time in an experiment at intensities of 5×10^{19} W/cm^2 [10, 11] and pulse energies below 1 J, generating a peaked spectrum of C^{6+} ions. Compared to quasi-monoenergetic ion beam generation within the TNSA regime [12], a more than 40 times increase in conversion efficiency was achieved.

A large number of theoretical studies lately predicted further improvement of the ion beam characteristics in terms of conversion efficiency as well as peak energy and monochromaticity when significantly higher laser pulse energies and intensities are used [13–17]. In particular, it is expected that the RPA process progresses much more stably when ions reach relativistic velocities already in the initial hole-boring phase before the whole target is set in motion (i.e., before the light sail stage). At intensities around 10^{23} W/cm^2, simulations show that protons become relativistic within one half-cycle of the laser pulse and acceleration by the laser radiation pressure is dominant even for linear polarization in what is referred to as the laser-piston regime [18, 19]. Here, the target can be viewed as a relativistic plasma mirror with Lorentz factor γ being propelled by the reflected laser and the laser-to-ion conversion efficiency $\eta = 1 - 1/4\gamma^2$ approaches unity in the ultrarelativistic limit.

In all ion acceleration mechanisms discussed so far, the laser energy was not directly trans-

fered to ions but mediated by electrons instead. For even higher laser intensities of 5×10^{24} W/cm^2 at a wavelength of 1 µm, protons can be driven to relativistic velocities directly by the laser field. This regime of direct ion acceleration has not been studied in simulations so far, since the new phenomenon of radiation damping strongly changes the laser-plasma interaction and is also expected to occur at 10^{24} W/cm^2, hence preventing the straightforward application of existing PIC codes [20,21]. Basically all theories of radiation damping suffer from more or less severe intrinsic inconsistencies [22] and only by comparison with experiment the proper theory can be established (see project 5.3: Radiation Damping at 10^{24} W/cm^2).

Employing the high power laser, unprecedented intensities on the order of 10^{24} W/cm^2 become available for experiments, allowing for improved RPA and for the first time study of the laser-piston regime as well as direct proton acceleration. According to theory, mono-energetic solid density ion bunches are expected at laser-to-ion conversion efficiencies approaching unity. Such a novel compact ion source could serve a wealth of experiments and applications, with an example being given by the production of neutron-rich nuclei around the $N = 126$ waiting point as described in project 4.1.

Bibliography

[1] E. L. Clark et al., Phys. Rev. Lett. **85**, 1654 (2000).
[2] A. Maksimchuk et al., Phys. Rev. Lett. **84**, 4108 (2000).
[3] R. A. Snavely et al., Phys. Rev. Lett. **85**, 2945 (2000).
[4] S. P. Hatchett et al., Phys. Plas. **7**, 2076 (2000).
[5] S.C. Wilks et al., Phys. Plasma **8**, 542 (2001).
[6] A. Macchi et al., Phys. Rev. Lett. **94**, 165003 (2005).
[7] O. Klimo et al., Phys. Rev. ST Accel. Beams **11**, 031301 (2008)
[8] A.P.L. Robinson et al., New J. Phys. **10**, 013021 (2008).
[9] X. Q. Yan et al., Phys. Rev. Lett. **100**, 135003 (2008).
[10] A. Henig et al., Phys. Rev. Lett. **103**, 245003 (2009).
[11] T. Tajima, D. Habs, X. Yan, RAST **2**, 221 (2009).
[12] B. M. Hegelich et al., Nature **439**, 441 (2006).
[13] X. Q. Yan et al., Phys. Rev. Lett. **103**, 135001 (2009).
[14] B. Qiao et al., Phys. Rev. Lett. **102**, 145002 (2009).
[15] A.P.L. Robinson et al., Plasma Phys. Control Fusion **51**, 024004 (2009).
[16] A. Macchi et al., Phys. Rev. Lett. **103**, 085003 (2009).
[17] A. Macchi et al., New J. Phys. (2010), in press.
[18] T. Esirkepov et al., Phys. Rev. Lett. **92**, 175003 (2004).
[19] F. Pegoraro and S.V. Bulanov, Phys. Pev. Lett. **99**, 065002 (2007).
[20] T. Schlegel et al., Phys. Plas. **16**, 083103 (2009).
[21] M. Chen et al., arXiv:0909.5144v1(2009).
[22] I.V. Sokolov, JETP **109**, 207 (2009).

Deceleration of Very Dense Electron and Ion Beams

In nuclear physics the Bethe-Bloch formula [2] is used to calculate the atomic stopping of energetic individual electrons [1] by ionization and atomic excitation:

$$-\left[\frac{dE}{dx}\right]_I = K \cdot z^2 \frac{Z}{A}\frac{1}{\beta^2}\left[\frac{0.5\ln\left(2m_e c^2\beta^2\gamma^2 T_{\max}\right)}{I^2} - \beta^2 - \frac{\delta}{2}\right] \tag{2.23}$$

and ions:

$$-\left[\frac{dE}{dx}\right] = 4\pi n_e \frac{Z_{eff}^2 e^4}{m_e v^2 \left(4\pi\varepsilon_0\right)^2}\left[\ln\left(\frac{2m_e v^2}{I\left(1-\beta^2\right)}\right) - \beta^2\right] \tag{2.24}$$

where I is the ionization potential, n_e the density of the electrons, m_e the mass of the electron, v is the ion velocity, $\beta = v/c$, T_{max} is the maximum kinetic energy which can be imparted to a single electron in a single collision, and Z_{eff} is the effective charge of the ions.

For relativistic electrons the other important energy loss is bremsstrahlung with:

$$-\left[\frac{dE}{dx}\right]_R = \frac{\left(\frac{4\pi n_e}{m_e c^2}\right) Z}{137\pi\left(\gamma - 1\right)\ln\left(183 Z^{-\frac{1}{3}}\right)} \tag{2.25}$$

The approximate ratio of the two loss processes [1] is:

$$\frac{-\left[\frac{dE}{dx}\right]_I}{-\left[\frac{dE}{dx}\right]_R} = \frac{EZ}{1600 mc^2} \tag{2.26}$$

Thus radiation loss is dominant for high energy electrons e.g. E $\geq$ 100 MeV and $Z = 10$. If, however (see below), the atomic stopping becomes orders of magnitude larger by collective effects, the radiation loss can be neglected.

For laser acceleration, the electron and ion bunch densities reach solid state densities, which are about 14 orders of magnitude larger compared to beams from classical accelerators. Here collective effects become important. One can decompose the Bethe-Bloch equation according to Ref. [3] into a first contribution describing binary collisions and a second term describing long range collective contributions:

$$-\frac{dE}{dx} = 4\pi n_e \frac{Z_{eff}^2 e^4}{m_e v^2 \left(4\pi\varepsilon_0\right)^2}\left[\ln\left(\frac{m_e v^2}{e^2 k_D}\right) + \ln\left(\frac{k_D v}{\omega_p}\right)\right] \tag{2.27}$$

Here k_D is the Debye wave number and ω_p is the plasma frequency of the electrons. Similar to bubble acceleration [4] but now with opposite phase for deceleration a strong collective field is built up by the blown-out electrons that decelerates them much faster than the processes that take effect for individual charged particles. Typical electric fields E are:

$$E = m_e \omega_p \cdot v \cdot \frac{nb}{n_e e} \tag{2.28}$$

where n_b is the charge density of the bunch. In Ref. [5] we discuss this mechanism of collective deceleration of a dense particle bunch in a thin plasma, where the particle bunch fits into part of the plasma oscillation and is decelerated 10^5–10^6 stronger than predicted by the classical Bethe-Bloch equation [2] due to the strong collective wakefield. For ion deceleration we want to use targets with suitable low density. These new laws of deceleration and stopping of charged particles have to be established to use them later in experiments in an optimum way.

We may also discuss the opposite effect with a strongly reduced atomic stopping power that occurs when sending an energetic, solid state density ion bunch into a solid target. For this target the plasma wavelength ($\lambda_p \approx 1$ nm) is much smaller than the ion bunch length (≈ 100 nm) and collective acceleration and deceleration effects cancel each other. Only the binary collisions are important. Hence, we may consider the dense ion bunch as consisting of 300 layers with Å distances. Here the first layers of the bunch will attract the electrons from the target and – like a snow plough – will take up the decelerating electron momenta. The predominant part of the ion bunch is screened from electrons and we expect a $\approx 10^2$ fold reduction in stopping power. The electron density n_e is strongly reduced in the channel, because many electrons are driven out by the ion bunch and the laser. Again all these effects have to be studied in detail.

Bibliography

[1] Particle Data Group, Phys. Rev. D **66**, 010001 (2002).
[2] S. Segrè, Nuclei and Particles, 2nd edition (W.A. Benjamin, RA, London, 1977).
[3] S. Ichimaru, Basic Principles of Plasma Physics: A Statistical Approach (Benjamin, Reading, MA, 1973).
[4] A. Pukhov and J. Meyer-ter-Vehn, Appl. Phys. B **74**, 355 (2002).
[5] H. -C. Wu et al., arXiv:0909.1530v1 [physics.plasm-ph] (2010).

A Relativistic Ultra-thin Electron Sheet used as a Relativistic Mirror for the Production of Brilliant, Intense Coherent γ-Rays

In Ref. [1] we have proposed the use of an intense laser to drive a very dense electron sheet out of an ultra-thin Diamond-Like-Carbon (DLC) foil. The sheet then surfs on the half-wave of the laser pulse and gains a relativistic energy characterized by $\gamma = \frac{1}{\sqrt{1-\beta^2}}$ with the total velocity $\beta = v/c$. We also introduce $\gamma_x = \frac{1}{\sqrt{1-\beta_x^2}}$ with the velocity $\beta_x = v_x/c$ normal to the electron sheet. This relativistic electron mirror is expected to allow the reflection of a second laser beam for very brilliant, very intense, coherent X ray and γ beams with many unique applications.

Kulagin et al. [2, 3] showed that the produced flat electron sheet stays together for some μm, having energies of $\gamma \approx a$, where a is the dimensionless laser intensity parameter. This γ is different from the $\gamma = 1 + a^2/2$ calculated for a single electron, which probably is too high for a dense electron sheet. We have experimentally observed this production of electron sheets for the first time at the Trident laser in Los Alamos for 500 fs laser pulses [4] and also at the laser of the Max-Born-Institute in Berlin with their 35 fs laser pulses [5].

If one would reflect optical photons of energy $E_0 = 1$ eV normally from this electron sheet with an energy characterized by γ_x, one naively would expect to obtain reflected γ photons of energy $E_\gamma = 4 \cdot \gamma_x^2 \cdot E_0$. However, Wu et al. [6, 7] showed that the electron sheet also acquires a transverse velocity component v_x from the transverse laser E-field. Only later the $\vec{v} \times \vec{B}$ force leads to the dominant forward acceleration. The transverse velocity causes a much smaller Doppler boost of the reflected γ photons of $E_\gamma = 4 \cdot \gamma_x^2 \cdot E_0 = 2 \cdot \gamma \cdot E_0$, where γ is the total γ. However, recently Wu et al. [8] showed that one should place a second foil of about 2 times the skin depth (15 nm) in a 1–2 μm distance behind the first target foil, where the accelerating laser pulse is reflected. The reflected laser pulse completely cancels the transverse velocity component v_x, but basically leaves the longitudinal velocity component unchanged. In this way the originally expected full Doppler boost of the γ photons with $E_\gamma = 4 \cdot \gamma^2 \cdot E_0$ is recovered. While the preliminary simulations of Wu et al. [8] are very impressive, more realistic ultrathin foils with much larger n_e/n_c for 1 nm foils are required. The present simulations correspond to independent individual electrons, while then collective effects like expansion of the foil become important.

We invented a special target design with ultra-thin DLC foils and a very low-density carbon nanotube target as a spacer inbetween, in order to realize such a target for a perfectly reflecting electron sheet. The dense electron sheet then traverses the reflector target and shortly behind the reflector is bombarded with the second laser pulse (split off from the high power laser with wavelength λ_0) to produce the γ photons with $\lambda_\gamma = \lambda_0/4\gamma^2$. The thickness d of the electron sheet determines up to which γ energy a coherent reflection occurs. In the inner rest frame of the electron sheet the photons have the wavelength $\lambda_i = \lambda_0/2\gamma$ before reflection. The requirement is $\lambda_i/ \leq d$. Possibly the electron sheet is compressed during acceleration and also by the interaction with the reflected laser, reducing the thickness d. It may even induce structured multilayers with much smaller thickness d. If we use $d = 1$ nm, $\lambda_0 = 1$ μm and $\gamma = 250$, we obtain reflected γ photons of ≈ 250 keV. These γ pulses would be coherent and would have a pulse length of a few zeptoseconds. Since we will have about $N \approx 10^9$–10^{10} coherently reflecting electrons, the

reflected amplitude is increased by N. If we assume a spot diameter of the reflected laser pulse of 3 μm, we obtain a large reflectivity (1%) and expect $\approx 10^{16}\gamma$/shot with $(6\,\mu\text{m})^2$, $(\approx 5$ mrad$)^2$, 10^{20} s and 0.1% BW. Thus a rough estimate of the peak brilliance is 10^{39}/[s (mm mrad)^2 0.1% BW]. With the high power laser we easily can realize $a = 250$, but require in addition a very high contrast of 10^{16} for the survival of ultrathin foils during the prepulse. In this context careful experimental studies have to be performed, aiming to characterize potential effects of reflectivity modifications by distortions of the reflecting mirror foil during the laser interactions.

In Ref. [9] we showed that a much larger reflecting force should occur, since the transition from the Lorentz force to the radiation damping force is strongly enhanced. While the Lorentz force scales with charge e, the radiation damping force or Landau-Lifshitz term scales with $\left(\frac{2}{3}\frac{e^3}{mc^3}\right)$ [10] and thus, if N electrons act coherently, the Lorentz force is proportional to N, while the Landau-Lifshitz force scales with N^2 and thus one obtains an acceleration due to radiation damping which is N fold enhanced. Thus 10^2 larger γ-energies may be reflected, reaching energies in the 25 MeV range. Here the ensemble of all electrons reflects like one macro-particle, which then takes up the recoil momentum as a whole. The electron sheet is trapped between the potential of the strongly reflecting laser and the Coulomb potential of the more backward layers of the electron sheet and may even be structured. This binding together of the electrons to a macroparticle is essential to result in a Mössbauer-like reflection scenario. If the Landau-Lifshitz force becomes dominant and higher order terms of the Landau-Lifshitz expansion series become important, even higher orders of N become relevant.

If these coherent intense γ pulses become available, many proposed experiments of ELI-NP with the incoherent γ beam like pair creation from the vacuum or excited multiple nuclear excitons will give orders of magnitude better results. Furthermore pump-probe experiments with two consecutive excitations of nuclei will become possible, which open a new field of studying highly excited states described by random matrix theory [11].

Bibliography

[1] D. Habs et al., Appl. Phys. B **93**, 349 (2008).
[2] V.V. Kulagin et al., Phys. Rev. Lett. **99**, 124801 (2007).
[3] V.V Kulagin et al., Phys. Rev. E **80**, 016404 (2009).
[4] D. Kiefer et al., Eur. Phys. J. D **55**, 427 (2009).
[5] D. Kiefer et al., to be published.
[6] H.-C. Wu and J. Meyer-ter-Vehn, Eur. Phys. J. D **55**, 443 (2009).
[7] J. Meyer-ter-Vehn and H.-C. Wu, Eur. Phys. J. D **55**, 433 (2009).
[8] H.-C. Wu et al., arXiv:1003.1739v2 (2010).
[9] D. Habs et al., Brasov Conference, AIP (2009).
[10] L.D. Landau and E.M. Lifschitz, Klassische Feldtheorie, Volume 2, (Verlag Harri Deutsch, 1992), chapter 76.
[11] J.Z. Gu and H.A. Weidenmüller, Nucl. Phys. A **690**, 382 (2001).

Nuclear Lifetime Measurements by Streaking Conversion Electrons with a Laser Field.

Nuclear levels have lifetimes down to the zeptosecond range once one reaches excitation energies beyond the particle emission threshold, while nuclear levels have lifetimes longer than typically 10 fs below the particle threshold [1]. We plan to study this drastic change in lifetime and predicted changes in decay laws for the first time. We modulate the energy of emitted conversion electrons in a phase-locked laser field and carry over the technique used to measure *as* lifetimes of atomic levels [2] to nuclear systems. Only for heavier nuclei we will get sufficiently large conversion coefficients. We will follow the modulated energies of the accompanying conversion

electrons of the particle decay. We induce the particle decay by the γ beam, which is locked to the high power laser or the γ's from the relativistiv mirror. Since we do not require the maximum laser fields, we may use laser light from an earlier amplifier state, which is delivered with higher repetition rate like 10 Hz. We want to induce the particle decay with very short γ-pulses, where we hopefully reach times below 1 as for the relativistic mirror. The emitted conversion electrons have energies, where the K binding energy is subtracted from the γ beam energy (typically 6–8 MeV). They can be observed in an electron spectrometer under angles where laser accelerated electrons from the target do not contribute.

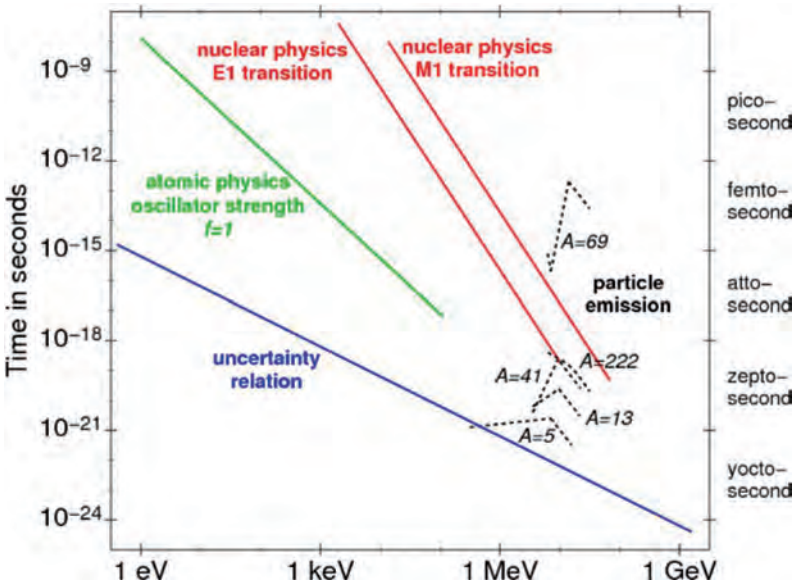

Figure 2.41: Correlation between nuclear lifetime and energy. The curve in green corresponds to atomic levels with oscillator strength $f = 1$, the red curves represent single particle estimates for nuclear E1 and M1 γ transitions, while the blue line denotes the limit given by the uncertainty relation for a single-cycle laser pulse. The dashed black lines indicate lifetimes of nuclear levels after particle emission for different mass numbers A.

Fig. 2.41 shows some nuclear lifetimes as a function of the excitation energy above the ground state for E1 and M1 transitions. In comparison also typical atomic lifetimes as a function of level energy are shown. Until now only time integrated particle spectra have been measured and it was not possible to measure the particle spectra as a function of the emission time. Typical particle emission times in the range of 10^{-20} s are obtained from statistical model calculations for higher excitation energies [4]. If it were possible to follow the emission spectra as a function of time, e.g. a much better understanding of dissipation and damping processes in the energy region of overlapping resonances above 15 MeV excitation energy could be obtained.

Experimental access to these ultrashort sub-attosecond lifetimes can be gained by exploiting the production technique for brilliant photon beams, where laser pulses are Compton-backscattered from a relativistic electron mirror, thus resulting in an energy boost by a factor of $4\gamma^2$, while the corresponding pulse duration is reduced by a factor $1/(4\gamma^2)$. For a single cycle pulse the energy versus time relation would be described by the uncertainty principle. This demonstrates that excitations with γ pulses much shorter than the expected lifetimes are possible. Though many experimental methods have been developed in different time ranges for different decay modes, transfering the well-established streaking technique of atomic physics to the regime of even shorter lifetimes in nuclear physics will enable to disentangle different chan-

nels of nuclear decay processes, where complex energy spectra could be followed as a function of time.

Properties of the Decay in Time of the Compound Nucleus

Ultrashort light pulses offer the possibility to study photonuclear reactions up to 10 or 15 MeV from a different and completely new perspective. The band width $\Delta E = h/\Delta t$ defined by the length (in time) Δt of the pulse may be large compared to the mean spacing d between adjacent levels of the same spin and parity. For medium-weight and heavy nuclei, d is typically 100 keV near the ground state and decreases exponentially with excitation energy, so that typically $d = 10$ eV at the neutron threshold, i.e. there are about 10^6 levels above the ground state. Below the neutron threshold, the average decay width Γ of nuclear levels is due to γ emission and has typical values of 10 meV. Right above the neutron threshold, particle decay increases Γ to typical values of about 1 eV. From here on Γ increases monotonically with excitation energy, until it reaches typical values of 50 or 100 keV (corresponding to a lifetime of 10^{-21} s) at the upper end of the energy interval here considered. Until now, photonuclear reactions were investigated with continuous beams of fairly poor energy resolution (measured in terms of the values of Γ and d discussed above) and have yielded only gross features of nuclear excitation functions, with the exception of the study of individual levels in the ground state domain. In particular, spectroscopic properties of levels in the energy range between several 100 keV of excitation energy and the neutron threshold are unknown. Neutron time-of-flight spectroscopy has offered a window to study spacing distributions and other statistical properties of levels (i.e. neutron resonances) right above the neutron threshold. The outstanding feature of that gross structure is the emergence of giant resonances, especially the giant dipole resonance, that were investigated in considerable detail.

With a band width $\Delta E > d$, several or even many nuclear states will be simultaneously excited. In that case, meaningful theoretical statements can be made only if $\Delta E \gg d$ or, if $\Gamma \gg d$, for $\Delta E \gg \Gamma$. Then the decay in time of the excited nucleus is determined by the Fourier transform of the photonuclear autocorrelation function. With S_{ab}(E) being the scattering amplitude leading from the incident photon channel to the final channel b, that function is defined as

$$S_{ab} = \int |g\,(E)|^2 S_{ab}\left(E + \frac{1}{2\varepsilon}\right) \cdot S^*_{ab}\left(E - \frac{1}{2\varepsilon}\right). \tag{2.29}$$

Here $|g\,(E)|^2$ describes the distribution in energy of the photon intensity and is centered at energy E_0 with width ΔE. The autocorrelation function is a running average over energy of the two scattering amplitudes with arguments separated by the energy ε. For the energy average to be representative, we must have $\Delta E \gg d, \Gamma$. At the same time, ΔE should be small in comparison with the characteristic energy scale of gross features of photonuclear excitations. For the giant dipole resonance that is the resonance width with typical values around several MeV. The numbers given above for d and Γ then define the desirable band width for short light pulses. It is given by $\Delta E = N_{\max}\,(d, \Gamma)$, where N determines the relative statistical accuracy $\frac{1}{\sqrt{N}}$ of the energy average. The spectroscopic data taken with neutron time-of-flight spectroscopy are consistent with a random matrix description and suggest that the compound nucleus is chaotic. It is probable that this feature prevails at lower excitation energies. The hallmark of that description is a non-exponential decay in time of the compound nucleus when few channels are open. Only for many open channels is the expected exponential decay attained (mean lifetimes are always defined in terms of the values of Γ that pertains to the energy interval of interest). Measurements on the decay in time of nuclei excited by short light pulses could confirm this theoretical expectation. In particular such data could cast light on hitherto unexplored properties of excited nuclear states above the neutron threshold.

H.A. Weidenmüller et al. [5] are studying the decay of such compound nuclear resonances within random-matrix theory [3] and find an exponential decay below the particle threshold, while they predict an exponential decay folded by a power law above the particle threshold. Weidenmüller et al. state that such measurements "comprise information on amplitude correlations in compound nucleus resonances, which cannot be obtained from other observables and that they would establish a new unambigous test of random-matrix theory for nuclear physics".

Streaking of Electrons

Experimental access to sub-attosecond nuclear lifetimes can be expected from an adaptation of the well-established streaking technique of atomic physics [5, 6] to decay processes in excited nuclei. Nuclear levels below the particle emission threshold ($\sim$6–8 MeV) not only decay by γ emission, but also are accompanied by prompt conversion electrons with a fraction given by the conversion coefficient. The dominant peaks in the conversion electron spectrum are the K-conversion lines. Now we excite a level of a stable nucleus with a γ beam of suitable energy. In parallel we superimpose a laser field to the nucleus with a tunable delay between the photonuclear excitation and the streaking field for the conversion electron. The energy modulation of the conversion electron should be in the range of 5 keV, requiring only moderate laser intensities of about $10^{14}/\mathrm{cm}^2$. With a magnetic transport and filter system ('Mini-Orange' spectrometer [7]) for conversion electrons we can choose the transmission curve to select a narrow range of the conversion electron spectrum with high efficiency, while fully suppressing all electrons being directly accelerated from atomic shells. By varying the delay of the streaking field, lifetimes in the range of 1–100 fs can be measured. For the release of the conversion electrons we need γ beams of 10 keV–5 MeV. Metallized tapes with stable target nuclei would be ideal targets. The measurements would allow to determine the spins and parities of the excited levels. From the transition matrix elements many properties of their wave functions could be deduced.

Bibliography

[1] D. Habs et al., Eur. Phys. J. D **55**, 279 (2009).
[2] E. Goulielmakis et al., Science **317**, 769 (2007).
[3] H.A. Weidenmüller and R. Dietz; *Photonuclear Reactions induced by Intense Short Laser Pulses*, to be published (2010).
[4] H.A. Weidenmüller and G.E. Mitchell, Rev. Mod. Phys. **81**, 539 (2009).
[5] J. Itatani et al., Phys. Rev. Lett. **88**, 173903 (2002).
[6] R. Kienberger et al., Nature **427**, 817 (2004).
[7] J. v. Klinken and K. Wisshak, Nucl. Instr. Meth. **98**, 1 (1972).

2.8.2 Stand-alone γ/e^- Facility for Nuclear Spectroscopy

Measuring Narrow Doorway States, embedded in Regions of High Level Density in the First Nuclear Minimum, which are identified by specific (γ, f), (γ, α), (γ, p), (γ, n) Reactions and allow to map out the Nuclear Potential Landscape

We want to make use of the unique high resolution of the γ beam to selectively identify doorway states with a small damping width via the (γ, x) reaction. A prototype example are states in the second or third potential minimum of actinide nuclei, which due to their tunneling through the inner barrier, show a small damping width. These transmission resonances can be uniquely identified by their fission decay. Due to the high level density in the first minimum, there are always states in the first minimum which completely mix with the states in the second and third minimum and can be nicely excited via the γ beam. This concept of weakly coupled doorway states in fission can be carried over to p,n or α decays, where strongly deformed halo states

again are particle unstable and we can identify them as rather sharp resonances in photonuclear reactions. We prefer to use odd target nuclei, because then we can populate several members of a rotational band with E1,M1 or E2 transitions.

The present photon energy resolution of the HIγS facility at 6–8 MeV with 300 keV does not allow to identify these resonances, while a few keV are equivalent to the resolution of particle-induced reactions, where we identified such resonances [1]. In this way vibrational and rotational bands in the second and third minimum can be identified [2]. From the rotational bands the moments of inertia can be determined for the states in the different minima.

We plan to employ multi-layer actinide targets, which allow to measure the fission fragment angular distributions for rather thick overall targets. From the rotational and vibrational states the potential landscape of the nuclei can de deduced. At higher excitation energies a reasonable transmission through the barrier exists and good yields can be expected. The spin and parity selectivity of the γ excitation is important. Also the damping width is an important parameter.

Bibliography

[1] P.G. Thirolf and D. Habs; Prog. Part. Nucl. Phys. **49**, 325 (2002).
[2] M. Hunyadi et al., Phys. Lett. B **505,** 27 (2001).

Precision Tests of Fluctuating Quantities in Nuclear Physics of Highly Excited Nuclear Levels in Comparison to Random-Matrix-Theory and Quantum Chaos

A very detailed theory of highly excited compound nuclear states has been developed over the last 70 years. It started with the compound nucleus picture of Bohr [1], where a nucleon collides with a nucleus and shares its energy with many nucleons and after many collisions the energy is concentrated again in a nucleon, which then is reemitted. This started the random-matrix theory by Wigner and Dyson [2] and finally led to the recent reviews on random matrices and chaos in nuclear physics [3, 4]. The theory represents a prototype for quantum chaos and leads to many generic predictions for fluctuating quantities, like Porter-Thomas distributions for decay widths or nearest-neighbor-spacing (NNS) level distributions of the Gaussian Orthogonal Ensemble (GOE). The phenomena of quantum chaos predominantly occur for systems with short range forces like in nuclear physics but do not occur for systems with long range Coulomb forces like in atomic and molecular physics. A special case with quantum chaos were hydrogen atoms in ultrahigh magnetic field.

The study of quantum chaos in nuclear physics requires a new type of spectroscopy: We have to measure a large number of nuclear levels very accurate including their spin and parity. Thus we have to use a largely automated computer appraoch to handle this big amount a data. For the spin and parity determination of neutron resonances we have to study the angular distribution to descriminate between weak s wave and strong p wave resonances. We want to carefully the fluctations around average values. Until now only smaller ensembles of quantities have been studied experimentally and seem to confirm this theory. Here we want to perform precision measurements for levels above the particle threshold with the new intense, brilliant γ facility. One example are precise measurements of the energy levels and their strength of (γ, n) resonances via a longer neutron flight path setup ($\approx$ 100 m). Here the high intensity of the γ beam, the very precise start signal (3 ps), the larger Breit-Wigner cross section and the good band width of the γ beam allow precision measurements with several orders of magnitude larger ensembles than obtained in earlier measurements.

It turned out that the Wigner-Dyson distrbutions of nearest neighbour level spacings are a much less sensitive measure for the occurance of quantum chaos than the $\Delta_3(L)$ statistics. With new measurements the question of the best measures to observe deviation from quantum chaos can be addressed. The pressent experimental data with about 50 levels were too small. Also new measures like autocorrelation functions between neighbouring energy regions as a function of

energy distance or S-matrix correlation functions may be studied [9]. If one Fourier transforms larger spectral regions one expects for quantum chaos that still large range periodic motion persists, a phenomena which has not been studied in nuclear physics until now. Furthermore we expect that other global parameters like nuclear deformation will have a strong influence on the occurance of quantum chaos. For spherical nuclei the transition to chaos should occur at lower excitation energies [10]. Other fluctuation measures, e.g. [8] may be used to describe this transition. Here the world of quantum chaos is somehow similar to classical thermodynamics, where general generic laws are predicted from a few general principles.

Thus we can test the generic predictions and perhaps additional refinements become necessary. E.g. deviations from the GOE description are expected, when the spreading time or equilibration time becomes comparable to the compound nucleus decay time [4]. At the same time many new predictions are being developped in much more detail within random-matrix theory and they can be tested in high resolution experiments in the energy or time domain.

The former studies of the double excitation of the giant dipole resonance [6, 7, 12] can be regarded as a first prototype of new pump-probe experiments with γ beams, exploring the interference of different amplitudes of states, populated by damping into other compound states and then excited a second time. If the expected higher flux for γ beams can be realized with the relativistic mirror approach, such pump-probe experiments become possible for the given Breit-Wigner resonance cross sections and more detailed time dependent studies of developments in quantum chaos.

Also the decay of these compound nucleur states in time frequently are not simple exponentials, but show power law components [5, 8]. Here new precision measurements in the *as* and *zs* time range (see project 5.4) will allow to test a rich new world of predictable decay patterns.

Another area of research are special doorway states, which are damped by their damping width $\Gamma^{\downarrow}$ into the compound levels. Here very weakly bound halo states with energies just below the binding energy may be of special interest, because their large spatial extensions may lead to new features like long lifetimes or low rotational excitation energies. Also new collective excitations, e.g. having more complex structures than the scissors mode may be explored at higher excitation energies. All these new doorway states at excitations energies below the particle binding energy can be addressed much better with the new γ beam facility.

A fourth class of experiments may explore the violation of symmetries and invariances [4]. An example are parity violating amplitudes in E1/M1 mixing (see also project 6.4), where close lying parity doublets will increase these amplitudes with increasing excitation energy, because more levels of opposite parity move closer and closer together.

Thus these precision experiments will lead to a deeper understanding of higher-lying nuclear levels and quantum chaos. We will be able to predict the strong component of the many very weak, unobservable transitions of the pygmy dipole resonance more accurately via the random matrix theory of this fluctuation strength, and obtain better predictions for the element production in astrophysics.

The measurement of the (γ,n) resonances also can have a large impact on the improved operation of the γ beam facility. Here we can measure the γ beam energy above ≈ 7 MeV with an accuracy of better than 10^{-7} by measuring the Time-Of-Flight (TOF) of the neutrons. By subtracting the large fixed neutron binding energy, by obtaining rather slow neutrons and having a very good start signal for the TOF, we get a very high resolution. Here the development of keV neutron TOF systems with good efficiency and resolution here is a major task. Thus we can measure the average γ energy and the width of the γ beam within ≈ 100 μs without perturbing the γ facility. This signal can be used in a feedback loop to stabilize the electron beam energy very accurately in the last cavity. In several measurements one wants to perform a controlled variation of the γ beam energy, which again becomes very easy.

For an improved γ beam band width other quantities have to be adjusted: One probably has to reduce the bunch charge to 1 pC and increase the repetition rate. It should not be a

problem to improve the band width of the super cavity, as we know from LIGO cavities. Thus the photons have more periods N and smaller angular divergence. It is clear that the emittance of the γ beam is a convolution of the emittance of the electron beam and the photon beam. Thus we need the best normalized emittance from the photo cathode of the electrons. One will use a larger spot size within the diffraction limit to get the best γ beam band width. Presently the high voltage ripple of the clystrons limits the achievable stability to $2 \cdot 10^{-5}$ of the cavities, and this is the area where further improvements have to focus on [11].

By using different photon energies in the super cavities for γ energy stabilization and for the γ experiments in parallel, the high resolution energy range can be extended significantly in γ energy.

This will open up a complete spectroscopy of 1^- and 1^+ levels up to 8 MeV excitation energy. In this way the vision in nuclear physics becomes possible, to study the transition from regular nuclear motion to chaotic motion for many nuclear species in detail. The change in nearest neighbour spacing of levels or changes in the γ strength distribution and its fluctuations can be studied with high accuracy.

Bibliography

[1] N. Bohr, Nature **137**, 344 (1936).
[2] C.E. Porter, Statistical Theories of Spectra: Fluctuations (Academic Press, New York, 1965).
[3] H.A. Weidenmüller and G.T. Mitchell, Rev. Mod. Phys. **81**, 539 (2009).
[4] G.E. Michell, A. Richter and H.A. Weidenmüller, arXiv:1001.2411v1[nucl-th]14 jan 2010.
[5] H.A. Weidenmüller and B. Dietz, *Photonuclear Reactions induced by Intense Short Laser pulses*, to be published (2010).
[6] J.Z. Gu and H.A. Weidenmüller, Nucl. Phys. A **690**, 382 (2001).
[7] H.A. Weidenmüller and G.T. Mitchell, Rev. Mod. Phys. **81**, 539 (2009).
[8] G.E. Michell, A. Richter and H.A. Weidenmüller, arXiv:1001.2411v1[nucl-th]14 jan 2010.
[9] B. Dietz et al., Phys. Rev. E in press (2010).
[10] V. Zelevinsky et al., Phys. Rep. **391**, 311 (2004).
[11] M. Liepe et al., ERL-09 workshop, pp. 49–52 (2009).
[12] H.A. Weidenmüller, Phys. Rev. Lett. (2011), in press.

Nuclear Transitions and Parity-violating Meson-Nucleon Coupling

In Ref. [1] light nuclei with known highly excited parity doublets in ^{14}C, ^{14}N, ^{15}O, ^{16}O, ^{18}F and ^{20}Ne are investigated theoretically for the enhancement of parity-mixing amplitudes of E1/M1 or E2/M2 transitions. According to first order perturbation theory calculations, the mixing is strongly enhanced, because the parity violating matrix element is divided by the small energy difference of the two levels of opposite parity. The doublet levels are at excitation energies between 5 MeV and 12 MeV and can be nicely reached with the high resolution γ beam facility, where $\Delta E_\gamma / E_\gamma \leq 10^{-3}$ is expected to be realized, but even extensions to 10^{-5} appear possible. Until now many nuclei with a possible E1/M1 mixing have been investigated like ^{19}F (1080 keV); ^{19}F (109.9 keV); ^{21}Ne (2789 keV); ^{175}Lu (396 keV); however, experimental accuracies were insufficient. With the ultra brilliant, tunable, polarized and monochromatic γ beams, the effect of parity non-conservation (PNC) will be studied at higher excitation energies. For circularly polarized γ beams a forward-backward asymmetry can be used to measure mixed parity transitions, where a high sensivity is reached by switching the sign of the circular polarisation. The experiments will allow to understand the fundamental role of the exchange processes of weakly interacting bosons in the nucleon-nucleon interaction [3–5]. Fig. 2.42 illustrates this exchange process.

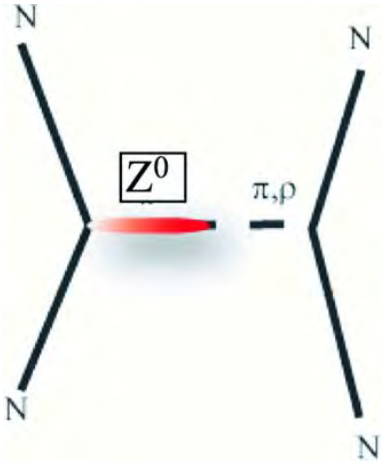

Figure 2.42: Parity-violating nucleon-nucleon interaction.

The results can also be compared with chiral perturbation theory, furthering the development of effective couplings between Z_0 and π, ρ and ω mesons.

Table 2.5: Candidate for PNC asymmetry in light nuclei.

Nucleus	Transition	E_{f1}	E_{f1}	Amplif. fac.
^{14}C	$(0+,1) \rightarrow (2^-,1)$	7340 keV	7010 keV	31 ± 6
^{14}N	$(1^+,0) \rightarrow (1^+,0)$	6203 keV	5691 keV	7.0 ±2.0
	$(1^+,0) \rightarrow (0^+,1)$	8624 keV	8776 keV	40 ±5
	$(1^+,0) \rightarrow (2^-,1)$	9509 keV	9172 keV	45 ±5
^{15}O	$(1/2^-,1/2) \rightarrow (1/2^-,1/2)$	11025 keV	10938 keV	37 ± 7
^{16}O	$(0^+,0) \rightarrow (2^-,0)$	8879 keV	6917 keV	18 ±2
^{18}F	$(1^+,0) \rightarrow (1^-,0+1)$	5605 keV	5603 keV	590 ± 110
^{20}Ne	$(0^+,0) \rightarrow (1^-,0)$	11270 keV	11262 keV	670 ± 7000

^{20}Ne seems to be most interesting case with largest enhancement. The two highly excited parity doublet levels where observed in particle-induced reactions and not in a (γ,γ') reaction. Their energies are quoted in the Nuclear Data Sheets as 11262.3(19) keV for the 1^+ state and 11270(5) keV for the 1^- state. Both states are assigned to be T=1 states and thus the isospin quantum number does not prevent their mixing. Their excitation energy difference is thus ΔE = 7.7(5.7) keV. If their total widths are comparable to their energy difference, then mixing due to the effects of the maximum parity-violating weak interaction must be expected. Observation of such a mixing effect would represent a rare precision test of the weak interaction on nuclear structure. Unfortunately, the current accuracy of the energy difference is insufficient for an estimate of the amount of parity mixing. The width of the 1^- is known to be smaller than 0.3 keV. The total width of the 1^+ state is unknown. Its ground state M_1 decay width is $\Gamma_0 = 11 \pm 2$ eV. Direct investigations in high-resolution (γ,γ') reactions with large-volume Germanium detectors are highly desirable. One would move the γ-energy across the 1^+ and 1^- and measure the E1/M1 mixing ratio. Hopefully the step upper energy edge of the γ beam will allow a better separation of the contributions from the two levels. Also the purity of the circular

polarisation of the γ beam has to be determined.

Bibliography

[1] A.I. Titov et al., J. Phys. G: Nucl. Part. Phys. **32**, 1097 (2006).
[2] U.E.G. Berg et al., Phys. Rev. C **27**, 2981 (1983).
[3] E. Adelberger et al., Nucl. Phys. A **396**, 221c (1983).
[4] E. Adelberger et al., Ann. Rev. Nucl. Sci. **35**, 501 (85).
[5] B. Desplanques., Phys. Rep. **297**, 1 (1998).
[6] R. Hajima et al., Nucl. Instr. Meth. A **608**, 557 (2009).

The Pygmy Dipole Resonance (PDR) of deformed nuclei

Phenomena in nuclear physics which have recently attracted great interest of experimentalists as well as theoreticians are collective electric dipole modes below the Giant Dipole Resonance, frequently denoted as Pygmy Dipole Resonances (PDR) [1, 2]. Evidence for such excitation modes has been found in many stable spherical nuclei below the particle separation energies [3–5]. In addition, above threshold energies a similar observation has been made recently in exotic nuclei with a large neutron excess [8,9]. The experiments are accompanied by intense theoretical investigations to explain the nature of this nuclear phenomenon, see e.g. [10] and references therein. Understanding the nature of the low-lying E1 strength will, e.g., help to constrain the symmetry energy in atomic nuclei [2, 8] and has an impact on reaction rates of astrophysical interest [12, 13] as well as on the photodisintegration of ultra-high-energy cosmic rays [14]. However, the experimental database is still scarce, especially for non-magic nuclei. Consequently the influence of deformation on the PDR strength has yet not been investigated experimentally, while recently first relativistic Random Phase Approximation (RPA) calculations of low-lying E1 strength in deformed nuclei became available [15, 16]. It is thus of mandatory importance to extend the experimental investigations towards deformed nuclei in order to provide the necessary test grounds for these modern calculations.

The method of choice for the investigation of low-lying E1 strength below the particle threshold in stable nuclei is the method of real photon scattering [1, 17]. It assures a clean excitation mechanism and allows a model independent extraction of quantum numbers such as multipolarities, absolute strengths, decay branching ratios, and parities. Up to now, nearly exclusively bremsstrahlung has been used as high energy photon source. However, the investigation of the E1 strength close to the particle thresholds in deformed nuclei has been hindered by the extremely high level densities. In addition, the determination of parities is mandatory for the clean identification of E1 strength in deformed nuclei, which is difficult to achieve with unpolarized bremsstrahlung. These drawbacks can be overcome by using Linear Compton Backscattered (LCB) photons, as has partly been shown in [5, 18]. The benefits of using a monoenergetic polarized LCB source is two-fold:

- The monoenergetic character of the beam will allow a energy dependent determination of the photon absorbtion cross sections even in the vicinity of very high level densities.
- The polarized character of the beam will allow for an unambiguous disentanglement of E1, M1 and E2 contributions to the photon absorption cross section.

Compared to the experiments using LCB photons performed in [7, 18], the superior properties of ELI will improve the sensitivity of the experiments by at least one order of magnitude and thus will allow the investigation of the PDR also in deformed nuclei.

Bibliography

[1] G. A. Bartholomew, E. D. Earl, A. J. Ferguson, J. W. Knowles, M. A. Lone, Adv. Nucl. Phys. **7** (1973) 229.

[2] U. Kneissl, N. Pietralla, A. Zilges, J. Phys. G **32** (2006) R217.
[3] K. Govaert, F. Bauwens, J. Bryssinck, D. De Frenne, E. Jacobs, W. Mondelaers, L. Govor, V. Y. Ponomarev, Phys. Rev. C **57** (1998) 2229.
[4] S. Volz, N. Tsoneva, M. Babilon, M. Elvers, J. Hasper, R.-D. Herzberg, H. Lenske, K. Lindenberg, D. Savran, A. Zilges, Nucl. Phys. **A779** (2006) 1.
[5] R. Schwengner, G. Rusev, N. Benouaret, R. Beyer, M. Erhard, E. Grosse, A. R. Junghans, J. Klug, K. Kosev, L. Kostov, C. Nair, N. Nankov, K. D. Schilling, A. Wagner, Phys. Rev. C **76** (2007) 034321.
[6] D. Savran, M. Fritzsche, J. Hasper, K. Lindenberg, S. Müller, V. Y. Ponomarev, K. Sonnabend, A. Zilges, Phys. Rev. Lett. **100** (2008) 232501.
[7] A. P. Tonchev, S. L. Hammond, J. H. Kelley, E. Kwan, H. Lenske, G. Rusev, W. Tornow, N. Tsoneva, Phys. Rev. Lett. **104** (2010) 072501.
[8] P. Adrich, A. Klimkiewicz, M. Fallot, K. Boretzky, T. Aumann, D. Cortina-Gil, U. Datta Pramanik, Th. W. Elze, H. Emling, H. Geissel, M. Hellström, K. L. Jones, J. V. Kratz, R. Kulessa, Y. Leifels, C. Nociforo, R. Palit, H. Simon, G. Surowka, K. Sümmerer, W. Walus, Phys. Rev. Lett. **95** (2005) 132501.
[9] A. Klimkiewicz, P. Adrich, K. Boretzky, M. Fallot, T. Aumann, D. Cortina-Gil, U. D. Pramanik, T. W. Elze, H. Emling, H. Geissel, M. Hellstroem, K. L. Jones, J. V. Kratz, R. Kulessa, Y. Leifels, C. Nociforo, R. Palit, H. Simon, G. Surowka, K. Suemmerer, S. Typel, W. Walus, Nucl. Phys. **788** (2007) 145.
[10] N. Paar, T. Niksic, D. Vretenar, P. Ring, Phys. Lett. B **606** (2005) 288.
[11] J. Piekarewicz, Phys. Rev. C **73** (2006) 044325.
[12] S. Goriely, Phys. Lett. B **436** (1998) 10.
[13] S. Goriely, E. Khan, M. Samyn, Nucl. Phys. **A739** (2004) 331.
[14] E. Khan, S. Goriely, D. Allard, E. Parizot, T. Suomijärvi, A. J. Koning, S. Hilaire, M. C. Duijvestijn, Astro. Phys. **23** (2005) 191.
[15] D. Pena Arteaga, P. Ring, Phys. Rev. C **77** (2008) 034317.
[16] D. Pena Arteaga, E. K. P. Ring, Phys. Rev. C **79** (2009) 034311.
[17] U. Kneissl, H. H. Pitz, A. Zilges, Prog. Part. Nucl. Phys. **37** (1996) 349.
[18] N. Pietralla, Z. B. V. N. Litvinenko, S. Hartman, F. F. Mikhailov, I. V. Pinayev, G. S. M. W. Ahmed, J. H. Kelley, S. O. Nelson, R. Prior, K. Sabourov, A. P. Tonchev, H. R. Weller, Phys. Rev. Lett. **88** (2001) 012502.

Fine-structure of Photo-response above the Particle Threshold

The excitation energy region around the particle separation threshold is of particular importance for nuclear physics. On one hand side this energy region is of interest for theoretical reasons because the coupling of bound quantum states to the continuum of unbound states requires an extended formalism, the mastering of which becomes extremely important for exotic nuclei near the drip-lines, where all structures are weakly bound [1]. Examples are the famous halo-nuclei like e.g. ^{11}Li [2]. On the other hand, this energy region covers the Gamow-window of thermally driven reactions of nucleons with heavy nuclei. Its understanding is a prerequisite for the modelling of nuclear reaction cascades in hot cosmic objects and thus for nucleosynthesis.

Below the threshold all excited resonances must decay by γ emission. They can be studied with the typical high energy resolution of semiconductor-detector technology (e.g., 5 keV at 8 MeV). The photo-response below the particle separation energy is currently investigated in nuclear resonance fluorescence experiments [1] at existing γ-beam facilities such as the bremsstrahlung facilities at the S-DALINAC electron accelerator in Darmstadt, Germany, [4] or at the High Intensity γ-ray Source (HIγS) at Duke Univ., Durham, NC, U.S.A [5].

Above the threshold the particle-decay channel opens up. Either no γ rays can be observed at all or their intensity cannot be used as a measure for the total electromagnetic excitation

strength to the resonance due to the unknown particle-decay branching ratio. Neutrons cannot be measured with a competitive energy resolution at acceptable solid-angle coverage.

An intense and high-energy resolving γ-ray beam from ELI-NP will open up new horizons for the investigation of the nuclear photo-response at and above the separation threshold. Alternatively to nuclear fluorescence, a photo-transmission experiment could be performed. A reduction in the photo transmission is directly proportional to the photo-excitation cross section. A measurement of the transmitted intensity is sensitive to the fine-structure in the energy window of the photon beam. A high-resolution γ-ray beam with energy width $dE/E \leq 10^{-3}$ will allow for the performance of transmission experiments with semiconductor-detector resolution even in the regime of unbound resonances. We expect a tremendous increase of insight into nuclear structure in the continuum and a deepened understanding of the structure of the nuclear Gamow-window.

Bibliography

[1] B. Jonson, Phys. Rep. **389** (2004) 1.
[2] J. Dobaczewski, I. Hamamoto, W. Nazarewicz, J.A. Sheikh, Phys. Rev. Lett. 72 (1994) 981.
[3] U. Kneissl, N. Pietralla, A. Zilges, J. Phys. G **32** (2006) R217.
[4] D. Savran, M. Fritzsche, J. Hasper, K. Lindenberg, S. Müller, V. Y. Ponomarev, K. Sonnabend, A. Zilges, Phys. Rev. Lett. **100** (2008) 232501.
[5] A. P. Tonchev, S. L. Hammond, J. H. Kelley, E. Kwan, H. Lenske, G. Rusev, W. Tornow, N. Tsoneva, Phys. Rev. Lett. **104** (2010) 072501.

Nuclear Resonance Fluorescence on Rare Isotopes and Isomers

Nuclear studies with the powerful experimental method of Resonance Fluorescence have been possible up to now only if sufficient amounts of (preferably isotopically enriched) target material on the order of about 1 g has been available. The production of such an amount of target material is not always possible at a reasonable cost (e.g., the worlds rarest naturally occuring isotope ^{180}Ta costs about $ 10,000 per mg at an enrichment of 5%). The advances in γ-ray beam brilliance at ELI will increase the sensitivity of NRF experiments by the same factor and thus it offers the opportunity to perform NRF studies on small target samples, whose amounts could be reduced with respect to todays NRF experiments by the same factor. This opens up an entire new area of applicability of the NRF method to materials that may be available only in quantities of a few mg.

The dipole response of the long-lived radioactive isotope ^{14}C, the basis of the radio-carbon dating method, will be accessible. These experiments will shed light on the neutron-spectroscopic factors for the *p*- and *sd*-shell orbitals in that mass region that nowadays is accessible to ab initio no-core shell models calculations.

Nuclear high-spin K isomers are known to be examples of highly-deformed nuclear structures. Due to their simple Nilsson-model wave function, they offer a unique laboratory for the study of very deformed nuclear systems. Nuclear spectroscopy experiments with hadronic probes have previously been performed on the long-lived K-isomer of ^{178}Hf. An investigation of the E_1 and M_1 response of the highly-deformed isomer using NRF on an enriched isomeric sample of a few mg will enable us to study the phenomenon of quadrupole-octupole coupling (E1) or the nuclear scissors mode (M1) at a nuclear deformation that has not been accessible for these types of investigations before.

Bibliography

[1] U. Kneissl, N. Pietralla, A. Zilges, J. Phys. G **32** (2006) R217.

2.8.3 Stand-alone γ/e^- Facility for Astrophysics

The production of heavy elements in the Universe, a central question of astrophysics, will be studied within ELI-NP in several experiments. While we want to address the s-process and p-process with the γ beam, we also plan to study the r-process at the $N = 126$ waiting point by producing these neutron-rich nuclei via fission-fusion reactions with the high power laser. This close interaction between nuclear physics and astropyhisics will be very productive.

Neutron Capture Cross Section of s-Process Branching Nuclei with Inverse Reactions

The heavy elements above the so-called iron peak are mainly produced in neutron capture processes: the r process (r: rapid neutron capture) deals with high neutron densities well above 10^{20} cm^{-3} and temperatures in the order of 2–3 $\cdot$ 10^9 K. It is thought to occur in explosive scenarios like *e. g.* supernovae [1, 2]. In contrast, the average neutron densities during s-process nucleosynthesis (s: slow neutron capture) are rather small ($n_n \approx 10^8$ cm^{-3}), *i. e.* the neutron capture rate λ_n is normally well below the β-decay rate λ_β and the reaction path is close to the valley of β stability [3–5]. However, during the peak neutron densities branchings occur at unstable isotopes with half-lives as low as several days. While the half-lives of these branching points are normally known with high accuracy at least under laboratory conditions and rely only on theory for the extrapolation to stellar temperatures [6], the neutron capture cross sections are only in special cases accessible to direct experiments. Besides the production of a sufficient amount of target material, the intrinsic activity of the target mainly hinders the experimental access especially in the case of the short-lived branching points.

However, the predictions in the Hauser-Feshbach model yield different results due to the underlying parameter sets. Additionally, the single studies on long-lived branching points (e. g. ^{147}Pm [7], ^{151}Sm [8. 9], ^{155}Eu [10]) showed that the recommended values of neutron capture cross sections in the Hauser-Feshbach statistical model [11] differ by up to 50% from the experimentally determined values. Thus, any experimental constraints on the theoretical predictions of these crucial values are welcome. Therefore, the inverse (γ, n) reaction could be used to decide for the most suitable parameter set and to predict a more reliable neutron capture cross section using these input values. This method has been applied to the branching nuclei ^{185}W and ^{95}Zr using a continuous-energy bremsstrahlung spectrum [12] and Laser-Compton backscattered photons [13].

In addition, data of the inverse (γ, n) reaction is also supposed to yield information for the calculation of Stellar Enhancement Factors (SEF) in some special cases like *e. g.* ^{151}Sm [14]. The inverse ^{152}Sm(γ, n) reaction only populates excited states in ^{151}Sm for energies close to the reaction threshold. Using the high resolution of ELI would allow measuring the matrix elements of the transitions to the particular states and, hence, measure the SEF which is the main source of uncertainty for the stellar cross section of ^{151}Sm(n, γ).

Bibliography

[1] K.-L. Kratz *et al.*, Astrophys. J. **403** (1993) 216.
[2] G. Wallerstein *et al.*, Rev. Mod. Phys. **69** (1997) 995.
[3] F. Käppeler, Prog. Part. Nucl. Phys. **43** (1999) 419.
[4] F. Käppeler, A. Mengoni, Nucl. Phys. A **777** (2006) 291.
[5] I. Dillmann, C. Domingo Pardo, F. Käppeler, A. Mengoni, K. Sonnabend, Publ. Astro. Soc. Australia **25** (2008) 18.
[6] K. Takahashi, K. Yokoi, Nucl. Phys. A **404** (1983) 578.
[7] R. Reifarth *et al.*, Astrophys. J. **582** (2003) 1251.
[8] U. Abbondanno *et al.*, Phys. Rev. Lett. **93** (2004) 161103.

[9] K. Wisshak *et al.*, Phys. Rev. C **73** (2006) 015802.
[10] S. Jaag, F. Käppeler, Phys. Rev. C **51** (1995) 3465.
[11] Z. Y. Bao *et al.*, At. Data Nucl. Data Tables **76** (2000) 70.
[12] K. Sonnabend *et al.*, Astrophys. J. **583** (2003) 506.
[13] K. Sonnabend *et al.*, AIP **1090** (2009) 481.
[14] A. Mengoni, AIP **769** (2005) 1209.

Measurements of (γ, p) and (γ, α) Reaction Cross Sections for p-Process Nucleosynthesis

Photodesintegration rates – like (γ, n), (γ, p), and (γ, α) – play an important role in the nucleosynthesis of the so-called p nuclei. These proton-rich, in general very low-abundant isotopes cannot be produced by neutron capture reactions. Complete network calculations on p-process nucleosynthesis include several hundred isotopes and the corresponding reaction rates. Therefore, theoretical predictions of the rates, normally in the framework of the Hauser-Feshbach theory, are necessary for the modelling. The reliability of these calculations should be tested experimentally for selected isotopes.

Different approaches are available and necessary to improve the experimental data base for the p process. While the (γ, n) cross sections in the energy regime of the Giant Dipole Resonance around 15 MeV have already been measured extensively several decades ago (see *e. g.* [1]), many efforts using continuous bremsstrahlung spectra have been made at the S–DALINAC at Darmstadt [2, 3] and the ELBE setup at Forschungszentrum Dresden [4] to determine the reaction rates without any assumptions on the shape of the cross section's energy dependence in the astrophysically relevant energy region close above the reaction threshold. A determination of the reaction rates by an absolute cross section measurement is also possible using monoenergetic photon beams produced by Laser Compton Backscattering [5].

In contrast, the experimental knowledge about the (γ, p) and (γ, α) reactions in the corresponding Gamow window is worse. In fact, the experimental data is based on the observation of the time reversal (p, γ) and (α, γ) cross sections, respectively [6–10] for the proton-rich nuclei with mass numbers around 100. Due to the difficulties concerning the experimental accessibility of the (γ, α) reaction rates a method using elastic α scattering has been established [11, 12].

Therefore, it would be a tremendous advance to measure these rates directly. However, the impact on the understanding of p-process nucleosynthesis would not be the measurement of one or two selected reactions but the development of a broad database. This is only possible if the time needed for one experiment is kept very short as it will be provided by the high intense γ beam of ELI.

Bibliography

[1] B. L. Berman, S. C. Fultz, Rev. Mod. Phys. **47** (1975) 713.
[2] K. Vogt, P. Mohr, M. Babilon, J. Enders, T. Hartmann, C. Hutter, T. Rauscher, S. Volz, A. Zilges, Phys. Rev. C **63** (2001) 055802.
[3] K. Sonnabend, K. Vogt, D. Galaviz, S. Müller, A. Zilges, Phys. Rev. C **70** (2004) 035802.
[4] M. Erhard, A.R. Junghans, R. Beyer, E. Grosse, J. Klug, K. Kosev, C. Nair, N. Nankov, G. Rusev, K.D. Schilling, R. Schwengner, A. Wagner, Eur. Phys. J. A **27** (2006) s01.135.
[5] H. Utsunomiya, H. Akimune, S. Goko, M. Ohta, H. Ueda, T. Yamagata, K. Yamasaki, H. Ohgaki, H. Toyokawa, Y.-W. Lui, T. Hayakawa, T. Shizuma, S. Goriely, Phys. Rev. C **67** (2003) 015807.
[6] T. Sauter, F. Käppeler, Phys. Rev. C **55** (1997) 3127.
[7] J. Bork, H. Schatz, F. Käppeler, T. Rauscher, Phys. Rev. C **58** (1998) 524.

[8] N. Özkan, A. S. J. Murphy, R. N. Boyd, A. L. Cole, M. Famiano, R. T. Güray, M. Howard, L. Sahin, J. J. Zach, R. deHaan, J. Görres, M. C. Wiescher, M. S. Islam, T. Rauscher, Nucl. Phys. A **710** (2002) 469.
[9] W. Rapp, M. Heil, D. Hentschel, F. Käppeler, R. Reifarth, H. J. Brede, H. Klein, T. Rauscher, Phys. Rev. C **66** (2002) 015803.
[10] G. Gyürky, Z. Fülöp, G. Kiss, Z. Máté, E. Somorjai, J. Görres, A. Palumbo, M. Wiescher, D. Galaviz, A. Kretschmer, K. Sonnabend, A. Zilges, T. Rauscher, Nucl. Phys. A **758** (2005) 517.
[11] Z. Fülöp, G. Gyürky, Z. Máté, E. Somorjai, L. Zolnai, D. Galaviz, M. Babilon, P. Mohr, A. Zilges, T. Rauscher, H. Oberhummer, G. Staudt, Phys. Rev. C **64** (2001) 065805.
[12] D. Galaviz, Z. Fülöp, G. Gyürky, Z. Máté, P. Mohr, T. Rauscher, E. Somorjai, A. Zilges, Phys. Rev. C (2005) in press.

2.9 Physics of dense plasmas

2.9.1 Introduction

The "Extreme Light Infrastructure" (ELI) will open a possibility to study previously inaccessible states of matter and interaction regimes of laser, X-ray and charged particle beams with various targets. The basic advantages of the ELI will be the unprecedented focused laser intensity and the synergy of laser and secondary sources. Additionally, repetition rate will be superior to the present high-power installations, as the ELI is proposed as a high repetition facility. On the other hand, relatively low laser energy due to a very short pulse may present a limitation for some types of experiments.

In the initial phase, the ELI will be built to the second stage which assumes 50 J laser pulses of the duration going down to 15 fs. The focused intensity may reach as high as 10^{23} W/cm^2 in an ideal case, while a focused intensity of a few times 10^{22} W/cm^2 seems to be realistic. At least 2 beamlines should run at the 10 Hz repetition rate. Later, when the third, high intensity stage is completed, ELI will achieve 3–5 kJ and over 200 PW. The focused intensity will reach 10^{24} W/cm^2 opening the era of new exotic physics experiments.

ELI will be a unique user facility and the experimental studies of plasma and interaction physics and of high energy density physics will be proposed and guided by user teams. Consequently, the research topics proposed here cannot be complete by any means, and they are not intended for setting any limitations on the future research. They can only serve as guidelines setting an insight that is required for the design conceptions of the interaction and diagnostic complex. The infrastructure ELI must provide very flexible environment that will enable very broad range of experimental set-ups.

Though studies of dense plasma physics on the ELI will be oriented mainly to gaining the knowledge of the interaction and properties of the studied systems, the results will find applications in various fields of science. First, the development of the secondary sources (X-ray and charged particle beams) of ELI will benefit from the research of laser-target interactions. There is still a vast space for an improvement of the existing schemes for X-ray sources and charged particle acceleration, and innovative schemes will be proposed based on the laser-plasma interaction research. Second, plasma is a suitable medium for parametric amplification and compression of laser pulses. It can sustain much higher intensities than any other medium and applications of stimulated Raman (SRS) and Brillouin (SBS) scattering are currently being explored experimentally. Third, the envisioned research will have impact on many other physics and science fields. For example, novel fusion schemes will be proposed and explored. High energy density systems will be formed with parameters near to or scalable to those important for astrophysics and thus the basic data for modeling certain astrophysical systems will be obtained. Laser-produced plasmas may be also utilized in the technology of the classical accelerators as ultraintense electric or magnetic lenses focusing intense particle beams (e.g. Large Hadron Collider) to a focal spot significantly narrower than via classical technology.

2.9.2 State of the art

Interactions of high-intensity lasers with targets have been studied since the early 1960ies, immediately after the invention of laser. The driving idea behind the largest lasers was the inertial confinement fusion (ICF). Nanosecond laser pulses were used and the interaction was non-relativistic, the maximum laser intensities were up to 10^{16} W/cm^2. Warm dense matter was produced near to the ablation surface and also by intense shock waves inside solid targets. Solid matter was compressed several times and temperature behind the shock wave reached up to 10 eV. The interaction physics was summarized in Ref. [1], the physics of laser-produced warm dense matter is described in Ref. [2]. With the invention of chirped pulse amplification (CPA), the studies of interactions of much shorter, femtosecond laser pulses with targets started in 1989

and the physical description of this new interaction regime was published soon together with an overview of its prospective applications [3].

Relativistic intensities were first reached at Los Alamos CO_2 laser Helios in 1978 [4]. Due to the long wavelength (10.6 μm) of the CO_2 laser, intensity of 10^{16} W/cm^2 was sufficient for the electrons to oscillate relativistically. However, the program of fusion with CO_2 lasers was abandoned soon, because the laser energy was predominantly transformed into fast electrons that preheat the fuel making fuel compression unfeasible. Relativistic intensities were reached again in the end of 1990ies by femtosecond solid state lasers, relativistic $\gamma \approx 25$ was achieved in 1999 in LLNL where one of the NOVA laser beams was converted to CPA femtosecond laser [5]. High-power femtosecond lasers are either high-energy, long-pulse ($\sim$ 500 fs), low-repetition rate (10^{-3}–10^{-4} Hz) Nd-glass-based lasers (Vulcan-PW, RAL, UK; FIREX-I, Osaka, Japan and Omega-EP, Rochester, USA), or lower-energy, short-pulse ($\sim$ 30 fs), higher repetition rate Ti:Sapphire lasers (Astra Gemini, UK; Texas Petawatt, USA). Extremely sharp focusing led to the record laser intensity of 2×10^{22} W/cm^2 at 300 TW-Ti:Sapphire laser Hercules at Univ. Michigan, USA. ELI will fully exploit the existing laser technologies and at the same time explore the emerging novel approaches such as diode-pumped solid-state lasers (DPSSL) to generate the extreme laser power and intensity.

Research of relativistic laser interactions with various targets is driven mainly by prospective applications. Laser propagation in long underdense plasmas is examined in connection with laser wakefield acceleration of electrons [6]. Laser interaction with thin foils is investigated in order to improve the ion acceleration process [7]. Limited-mass targets are used to diminish the undesirable lateral energy spread out of the focal spot [8], and thus to enhance the energy density. Cluster targets are used for the initialization of various nuclear reactions [9] as the reaction rate is increased due to the ion energy enhancement via Coulomb explosion. Strong shock and radiative blast waves in cluster media can also be scaled to astrophysical conditions [10]. Isochoric heating of thin foils by laser-accelerated protons was studied experimentally [11]. We have mentioned only a few important examples, as compilation and presentation of a complete list is beyond the scope of this text.

2.9.3 Directions of plasma, HEDP and interaction studies at ELI

We shall discuss here several important directions of plasma and high energy physics research at ELI. This list is far from being complete and even new topics may become more important in the forthcoming years. At present, it is impossible to foresee the evolution of this booming field in the next 5 years fully; and moreover the research topics will be selected from the user proposals. The research topics are organized into seven following subsections.

Nonlinear optics of plasmas and laser interactions with underdense plasmas

The propagation of high-intensity, coherent, electromagnetic radiation in plasmas, and the resulting modifications of the plasma state, is the subject of the nonlinear optics of plasmas. Coherent radiation can scatter from and decay into collective plasma modes and it can create radiation at new frequencies. Plasma oscillations may become self-organized, nonlinear, kinetic states. Simple modes that have linear and fluid limits can be strongly influenced by nonlinear kinetic modes, such kinetic electrostatic electron (KEEN) and ion (KEIN) non-linear waves. This subject is very exciting from theoretical, computational, and experimental points of view because of the myriad states made possible by the interaction of multimode fields, together with the wave-particle resonances and the non-locality of the self-consistent plasma-particle dynamics [12].

This topic includes wake formation behind the laser pulse and studies of the wake properties [13] that are important for electron acceleration. Presently, the interest is concentrated on the bubble regime [14] that leads to the formation of a monoenergetic beam of electrons

accelerated up to GeV energies. However, the limits of electron, positron and ion acceleration in the wakefields are not clear yet. Wakefields are multidimensional and the electron density in the wake may reach values orders of magnitude higher than the background density. The intensity of the ELI laser will be so high that ions could be trapped and accelerated in the wake. The optimum configuration of laser beams for a stable propagation over long distances in tenuous plasmas is not known now yet. The optimum regime for the electron acceleration at ultra-relativistic intensities may differ substantially from the present situation.

Parametric instabilities like SRS and SBS can influence propagation of laser beams and at high intensities they could create the conditions for trapping laser light and formation of relatively long-lived electromagnetic solitons [15]. These solitons have been observed in three-dimensional PIC simulations and more recently in the nonlinear stage of SBS evolution [16]. They can stay in the same place for a sufficiently long time (of about tens of ps) or slowly drift if the ambient plasma is inhomogeneous. Laser intensity can be even increased due to laser beam self-focusing and filamentation. SRS-induced non-linear KEEN wave has been observed in Vlasov simulations [17]. ELI will allow such structures to be manipulated, and used for the studies of long-term effects of extremely high electric and magnetic fields on isolated nuclei. Backward Raman and Brillouin scattering can also lead to laser pulse amplification and compression [18] that could be used in the interaction experiments or in the laser technology. ELI will allow studying this process at much higher intensities.

Relativistic HED plasmas

ELI will create plasmas with electron thermal energy significantly exceeding 100 keV. In these plasmas bremsstrahlung photons will have energy sufficient for creation of electron-positron pairs in a two-step process when the γ photon, generated in electron-ion collision, creates an e-p pair during its impact on an ion. This – already observed – process [19] is particularly efficient with high-Z target materials like gold. Creation of plasma with positron density comparable to the ion density will become possible with the next generation lasers like ELI. Understanding how these plasmas behave when either their directed flow or their average energy is relativistic is a fascinating area for research. This includes understanding how to create useful electron-positron plasmas in the laboratory. This topic is important in high energy astrophysics, in the development of compact photon and energetic-particle sources, and in extending the boundaries within which high energy density systems have been explored.

Laser interaction with solid targets and dense matter

When an intense laser as ELI is incident on a solid-density target, a complicated suite of phenomena occurs. The electric field in such lasers is orders of magnitude larger than the fields that bind the electrons to the atoms, single free electrons can oscillate with energies in excess of 100 MeV, and the radiation pressure can exceed 1 Tbar. The absorption of an intense laser at a dense plasma boundary is not completely understood because of the complexity of the electron-distribution function and fields (both electric and magnetic) at the interface. Investigation of radiation pressure effects on density steepening and consequently on electron spectrum and temperature is important. Research of laser interaction with solid foils is needed for the optimization of proton and ion acceleration for various applications, i.e. for the optimization of fast ion source at the ELI. One can use either portions of the few-cycle laser pulse itself as a probe beam or secondary electron, ion, or X-ray pulses of similar time duration or even much shorter, attosecond XUV pulses that can be generated by means of laser harmonics. Attosecond time scales govern electron motion not only in atoms and molecules, but also in metals and solid-density plasmas.

When the ELI laser will interact with the corona produced by a laser prepulse incident on a solid target, the laser beam will penetrate to the dense plasma region via relativistic transparency

and channel boring by the ponderomotive force. A recent theoretical paper [20] demonstrates that pulses with intensities exceeding 10^{22} W/cm^2 may penetrate deeply into the plasma as a result of efficient ponderomotive acceleration of ions in the forward direction. The penetration depth as big as hundreds of microns depends on the laser fluence, which has to exceed a few tens of GJ/cm^2. The fast ions, accelerated at the bottom of the channel with an efficiency of more than 20%, show a high directionality and may heat the precompressed target core to fusion conditions. With the ELI laser, the physics of channel boring and ion acceleration can be investigated in duration significantly shorter than in the fusion case.

Laser interactions with clusters and limited-mass targets

Atomic clusters have been shown to be very efficient absorbers of intense laser radiation. During Coulomb explosion of laser-heated clusters, high energy ions and hard X-rays are produced. New possibilities arose of applying clusters for various applications, such as tabletop nuclear fusion from exploding deuterium clusters and synchrotron radiation. Clusters were recently used to create high energy density plasmas that drive strong shocks (Mach >50) and radiative blast waves [10]. The plasma states generated can be described by magnetohydrodynamic equations that have a number of similarities. Careful application of these equations and similarities allow experiments to be scaled to astrophysical phenomena that have spatial and temporal scales that are greater by as much as 15–20 orders of magnitude. In this way, the radiative blast waves in the laboratory have been scaled to those experienced in supernova remnants and the physics governing their dynamics investigated under controlled conditions.

Limited-mass targets are used to limit the undesirable energy spread out of the laser focal spot. Thus, high energy density deposition is achieved. For example, the deposition of 1 J in a droplet of 10 μm in diameter would correspond to the deposition of about 10 keV for each particle. Since the expansion time of such a droplet is greater than 1 ps, one can study matter in a quite unusual state of very high density and temperature during this time period. The limited-mass targets made from transparent materials allow one to avoid negative effects associated with pre-pulses and they could be used in many applications, in particular for efficient ion acceleration to high energies [8].

Warm dense matter studies

With the ELI it will be possible to heat macroscopic amounts of solid density matter up to keV temperatures either directly by the laser or by the secondary sources. While direct heating by the laser uses heating by the hot electrons confined by self-generated electric and magnetic fields and shock waves launched at material interfaces [21], using ion or proton beam is very straightforward. Isochoric heating of 15 μm-thick Al foils by laser-accelerated protons up to 80 eV has already been demonstrated at the Gekko petawatt laser [22]. Equation of state, opacities and transport properties of warm dense matter are the key data for astrophysics that will be well measurable with ELI.

The proton beam generated by the ELI will unite the properties unreached so far by any laser generated proton beams: high energy combined with high intensity and focusability. This makes it an ideal instrument for a plasma generation. Since the ELI performance covers a broad interval of energies and intensities of the generated proton beam, it will be possible to generate plasmas ranging from a deeply non-ideal state (warm dense matter) to plasmas with high energy content, close to that formed in the tempers meant for the ion-driven inertial fusion. The warm dense matter is an object of physical interest in its own right, not to speak about the astrophysical relevance. Any relevant quantity, e.g. the optical properties like the opacity coefficient in the optical and X-ray region, emission spectra, measured on this exotic state of matter will be of interest for astrophysical purposes. On the high energy end, we are likely to obtain proton-beam-generated plasma in a high power density regime. If such a regime is reached

with the laser-generated proton beam of sufficiently high power density, the hot dense matter beam plasma would become available to the physical research and, moreover, a very interesting transition from a highly non-ideal to the ideal state could be traced by simply varying the properties of the ELI generated proton beam.

With the ELI, it will be possible to create high energy density plasmas and probe it with the secondary hard X-ray source. Thus, extremely important plasma opacities will be measured in this regime.

Stopping of proton beams in a pre-generated plasma

Plasma heating by proton beams is of interest for the fundamental research as well as for the particle beam driven fusion experiments. Experiments of this kind have been carried out for a long time using combined equipment of lasers to provide the stopping plasma and of accelerators to supply the proton beam. Unfortunately, just a very few laboratories can host experiments of this kind and they are mostly located on the accelerator sites. ELI will be the first purely laser laboratory, where the necessary proton beam could be generated by the ELI main laser beam. The stopping of charged particles in plasmas is a complex physical process [23], which can hardly be reduced to binary Coulomb collisions governed simply by the Coulomb logarithm. Even then, the Coulomb logarithm is a somewhat vaguely defined quantity and its determination is often provided by a hand-waving argument. Its measurement would thus shed more light on hitherto badly clarified questions of plasma kinetics, especially in non-ideal plasmas. But even in rarefied plasmas the stopping power is determined by other processes than binary collisions. The onset of collective phenomena is to be expected under the effect of the impinging proton beam, whose spontaneously created electric fields will add to the plasma stopping power. This phenomenon might show a resonant behavior, anomalous dependences on the beam energy and the plasma parameters. The expected flexibility of the ELI performance might help to map out broad regions of both the stopping plasma and the proton beam parameters not yet explored in the classical way. For the purpose of pre-forming the stopping plasma, a part of the ELI pumping beams will have to be diverted on the ps or even ns level.

Testing of advanced nuclear fusion schemes

ELI is not designed for complex inertial confinement fusion (ICF) experiments. However, many physical issues of advanced ICF schemes, such as fast ignition or shock ignition can be addressed at ELI.

First, the transport of high-current electron beams in dense plasmas is crucial for fast ignition via fuel heating by electrons (both for schemes using or avoiding a cone). The ELI laser pulses will drive relativistic electron currents of the order of gigaamperes in overdense plasma targets [24]. In vacuum, electron current transport is limited by $I_A = 17\beta\gamma$ kA due to magnetic self-interaction. But in the plasma the return current tends to suppress B-fields. The system of counter-propagating beam and plasma currents is, however, unstable and leads to beam filamentation and a host of secondary filament dynamics and merging events [25]. At present, it is unclear to what extent the beam energy can be transported to the compressed cores of fusion targets. The filamentation instability may be reduced by transverse beam heating and other effects. Again, the present predictions are based only on 3D simulations [26] and require experimental verification. The filamentary structures at the Extreme Light infrastructure evolve and change on the microscopic plasma time scale, which is in the attosecond regime at these densities.

Second, ELI will supply many important data for fast ignition by ion beams. Ion stopping data in dense plasma will be measured as described in the previous subsection, ion acceleration in channel formed by laser will be studied as described previously when laser interactions with solid targets were discussed.

Third, it will be possible to study the shock-ignition-relevant strong shock propagation in dense plasmas and the shock collision with a counter-propagating shock wave at ELI. The temporal visualization of this process is obviously important for the shock ignition feasibility and optimization. The vital temporal visualization of the colliding shocks inside the compressed fuel can be done with a hard X-ray or γ-ray imaging coming from the ELI main beam.

2.9.4 Potential for Applications and Technology Transfer

Experimental research in the plasma and high energy density physics at the ELI infrastructure will be mainly oriented to fundamental science. This will accumulate scientific knowledge of new regimes of laser and secondary sources interactions with targets and investigate unique states of matter that can be prepared only with the ELI infrastructure.

However, there is also a large application potential of the plasma and interaction physics investigated at ELI. First, the basic physics of laser-target interactions is essential for the optimization of the secondary sources. Generation of quasi-monoenergetic electron and ion beams is particularly novel in which field a fundamental breakthrough was achieved in 2004 for electrons and in 2006 for ions. New acceleration mechanisms are still being proposed and the acceleration process has not yet been optimized even for the intensities existing at present. Numerical simulations and the theory predict a possibility of significant improvements of the acceleration process at intensities achievable at the ELI but an extensive search for suitable experimental set-ups will be inevitable. The possible improvements in the parameters of the secondary sources would significantly enhance their application potential that is discussed in detail in the descriptions of the particular activities.

Interaction experiments will be directly used in the material science, for example for understanding the aging process in construction materials of nuclear power plants. One can carry out experiments when ultrafast processes induced in a material by the laser-accelerated ion beam will be detected by a synchronized ultrafast laser or X-ray probe. Indeed, the mechanisms leading to defect creation or phase transformation in materials subjected to low or high-energy ions involve as initial steps ultrafast processes whose elucidation is still a challenge: in the case of elastic scattering, collision cascades – at present observed only through atomistic simulations – or intense and short-lived electronic excitation in the case of high-energy ions – for which essentially two models were proposed long ago; and there is no clear answer yet concerning their respective validity. It is essential in both cases to obtain observations of the state of the target in the first few picoseconds after the passage of the particles, and only laser-based sources can make such observations possible. Additionally, ELI laser-target interactions will become an intense source of ultrashort neutron and γ-ray pulses, thus ultrafast response of materials on radiation damage could be probed by synchronized laser and X-ray pulses. Such experiments could bring essential progress to radiation physics that is vital for many major technologies.

By focusing the ELI laser on a high-Z material we shall be able to produce an intense pulse of γ-rays that can be used for nuclear transmutation of long-lived radioactive isotopes into less radioactive or short-lived products. This concept is being developed in the world for nuclear waste management. The primary risk isotope is long-lived iodine-129 with high radiotoxicity and mobility, and this may be transformed to iodine-128 that decays with a half-life of 25 minutes to stable inert xenon-128. The experiments may demonstrate the feasibility of the laser-induced transmutation process.

Laser produced plasmas can be used in the classical accelerator technology. Laser-ion accelerator can serve as an intense ion source for classical accelerators. Additionally, laser-produced plasmas may serve as ultrastrong lenses for the focusing of a classical accelerator beam as they can sustain quasistatic electric and magnetic fields higher than any other system. Recently, a micro-lens for focusing and energy selection of laser-accelerated MeV protons has been demonstrated [27]. It is anticipated that with a laser of the ELI scale it could be possible to develop

ultrastrong lenses that could narrow the focus of large accelerators like LHC (Large Hadron Collider) significantly, thus the beam intensity and the collision probabilities will be enhanced.

The above discussed technologies could be potentially transferred to industry in the future and could bring an important (incl. commercial) profit for the whole society.

2.9.5 Conclusions

In summary, ELI will be a versatile facility for dense plasma studies. It offers an unprecedented range of laser intensities together with a variety of secondary sources that can enable a variety of interaction and diagnostics set-ups. We have mentioned here only a few important research fields, but many others will be proposed by the facility users. It is worth to note that the facility with its unique variability in the parameter range given by the optional different laser beam parameters will not be exclusively used for basic science studies, but it will also allow accomplishing more technically relevant applications, which are already in the focus of present day activities.

Bibliography

[1] M.N. Rosenbluth, R.Z. Sagdeev, A. Rubenchik, S. Witkowski (eds.), Handbook of Plasma Physics vol 3 Physics of Laser Plasma (North-Holland, Amsterdam 1991).
[2] S. Eliezer, A. Ghatak, H. Hora, E. Teller, Fundamentals of Equations of State (World Scientific Singapore 2002).
[3] P. Gibbon, E. Förster, Plasma Phys. Control. Fusion **38** (1996) 769.
[4] R.L. Carlson *et al.*, IEEE J. Quantum Electronics **17** (1981) 1662.
[5] D.M. Pennington *et al.*, IEEE J. ST in Quantum Electronics **6** (2000) 676.
[6] B. Walton *et. al.*, Plasma Phys. Control. Fusion **48** (2006) 29.
[7] M. Borghesi *et al.*, Laser Part. Beams **20** (2002) 31.
[8] M. Schnürer *et al.*, Laser Part. Beams **23** (2005) 337.
[9] T. Ditmire *et al.*, Nature **398** (1999) 489.
[10] P.A. Norreys *et al.*, Phys. Plasmas 16 (2009) 041002.
[11] P. Antici *et al.*, J. Physique IV **133** (2006) 1077.
[12] *Advancing the Science of High Energy Density Laboratory Plasmas*, report of the Panel on High Energy Density Laboratory Plasmas (United States Department of Energy, January 2009).
[13] P. Dong *et al.*, New J. Phys. **12** (2010) 045016.
[14] J. Faure *et al.*, Nature **431** (2004) 541.
[15] G.A. Mourou, T. Tajima, S.V. Bulanov, Rev. Modern Phys. **78** (2006) 309.
[16] S. Weber *et al.*, Phys. Plasmas **12** (2005) 112107.
[17] A. Ghizzo *et al.*, Phys. Rev. E **74** (2006) 046407.
[18] A.A. Andreev *et al.*, Phys. Plasmas **13** (2006) 053110.
[19] H. Chen *et al.*, Phys. Rev. Let. **102** (2009) 105001.
[20] N. Naumova *et al.*, Phys. Rev. Lett. **102** (2009) 025002.
[21] Y. Sentoku *et al.*, Phys. Plasmas **14** (2007) 122701.
[22] R.A. Snavely *et al.*, Phys. Plasmas **14** (2007) 092703.
[23] R. Singleton, Phys. Plasmas **15** (2008) 056302.
[24] G. Mourou *et al.*, *Proposal for a European Extreme Light Infrastructure (ELI)*, Paris 2008.
[25] J. Meyer-ter-Vehn *et al.*, Plasma Phys. Control. Fusion **47** (2005) B807.
[26] J.J. Honrubia, J. Meyer-ter-Vehn, Plasma Phys. Control. Fusion **51** (2009) 014008.
[27] O. Willi et al., Laser Part. Beams **25** (2007) 71.

2.10 Laboratory Astrophysics

We discuss the prospects of using the ELI laser radiation interaction with plasmas in the laboratory relativistic astrophysics context.

2.10.1 Modeling of astrophysics phenomena under the terrestrial laboratory conditions: general aspects

Typically, in the course of laser irradiation of targets shock waves are generated; the target compression is accompanied by the Rayleigh–Taylor (RT) and Richtmayer–Meshkov (RM) instability development; collimated plasma jets are observed; the matter equation of state (EOS) acquires new properties under extreme pressure, density and temperature conditions; the laser plasma emits high-energy charged-particle beams and high- and low-frequency powerful electromagnetic radiation. Gathering of these facts principal for both space and laboratory physics has initiated work in laboratory astrophysics [1, 2] with the aim to model the processes of key importance for the space objects under laboratory conditions.

Interaction of radiation produced by the lasers with a long pulse of pico- and nanosecond duration was the first category developed for the purposes of inertial confinement fusion corresponds to the collisional hydrodynamics phenomena [3]. These are also called the high energy-density plasma (HEDLP) phenomena [4]. In the context of laboratory astrophysics they are used for experiments on shock waves, including the radiative shocks and RT & RM instability, the jet formation, the dense plasma optical properties, the nuclear physics, and the EOS studies. The ultrashort pulse lasers can produce extremely high power and relativistically high-intensity electromagnetic pulses the interaction of which with matter occurs in the relativistic and highly nonlinear regime. They can be used for the purposes of relativistic laboratory astrophysics.

If we address the problems of contemporary relativistic astrophysics, first questions on the mechanisms of the cosmic ray acceleration and on the properties of strong EMW interaction with relativistic plasmas attract our attention [5]. In space plasmas the basic mechanisms of charged particle acceleration are connected with the reconnection of magnetic-field lines, which is accompanied by the strong and regular electric-field generation (it occurs in the planet magnetospheres, in binary stellar systems, in accretion disks, in the magnetar magnetospheres, etc.) and with collisionless shock waves, at the fronts of which charged-particle acceleration occurs (this happens in interplanetary space, during supernova explosions, in colliding galaxies, etc.) [5, 6].

Tracing a relationship between astrophysics and laser physics, we see a number of publications devoted to the laboratory modeling of astrophysical processes (see [1, 2] and references therein). As is known there has been an interest in modeling space physics with laboratory experiments for many years. The first modeling of processes fundamental for space physics in terrestrial laboratories was done by Kristian Birkeland, who more than 100 years ago conducted the first experiments on studying the auroral regions in the Earth magnetosphere. Later, progress has been achieved in the laboratory modeling of various processes, including the magnetic-field reconnection, collisionless shock waves, etc., which provide mechanisms for charged-particle acceleration under various astrophysical conditions.

2.10.2 Principle of qualitative scaling

Laboratory experiments for studying astrophysical phenomena are of two types. The first type of experiments can be referred to as *configuration modeling*, which is aiming at simulating the actual configuration of a system, e.g. the whole Earth's magnetosphere or the solar active region. The second type of experiments corresponds to *process simulation*, i.e. they are aimed at studying the properties of physical processes relevant to astrophysical phenomena. There are a number of nonlinear plasma physical processes in space plasmas that require clarification.

Physical systems obey scaling laws, which can also be presented as similarity rules. In the theory of similarity and modeling the key role is played by dimensionless parameters that characterize the phenomena under consideration [7]. The principle requirement of the laboratory modeling is the equality of the key dimensionless parameters in the modeled processes. In cases of modeling astrophysical phenomena where this equality can hardly be respected, the *principle of limited similarity* (PLS) or *principle of qualitative scaling* has been formulated in [8]. According to the PLS those dimensionless parameters that are relevant in a certain context and that are much larger or smaller than unity under astrophysical conditions must retain this property (i.e. be much larger or smaller than unity) in the laboratory experiments modeling the astrophysical process. The dimensionless parameters that characterize the high-intensity electromagnetic wave (EMW) interaction with matter can be found in [2]. The key in the extreme field limit parameters are as follows:

1. Mach number, $M = u/v_{\rm s}$, is the local velocity of plasma (in our case a velocity of a shock wave or soliton) divided by the speed of sound (the speed of ion acoustic waves). It is a measure of the shock-wave amplitude.
2. Reynolds number, $\mathrm{Re} = uL/\nu$, is a ratio of the inertial force $\rho u^2/L$ to the viscous force $\mu u/L^2$ with L being the scale length and kinematic viscousity $\nu = \mu/\rho$.
3. Lundquist number, $Rm = v_{\rm A}L/\eta_{\rm m}$, gives a measure of dissipative effects in magnetohydrodynamics. It is important in studying the magnetic reconnection [9]. Here, $v_{\rm A} = B/(4\pi n m_{\rm p})^{1/2}$ is the Alfven speed in a plasma with the magnetic field B and $\eta_{\rm m} = c^2/4\pi\sigma$ is the magnetic diffusivity with σ being the electric conductivity.
4. The ratio of the pulse length, $l_{\rm las} = c\tau_{\rm las}$, to the radiation wavelength, λ_0. This ratio, $N_{\rm p} = l_{\rm p}/\lambda_0$, is equal to the number of wavelengths per pulse, and is Lorentz invariant.
5. Normalized dimensionless EM wave amplitude, $a_0 = eE_0/m_{\rm e}\omega_0 c = eE_0\lambda\!\!\!^{-}_0/m_{\rm e}c^2$, where $\lambda\!\!\!^{-}_0 = c/\omega_0$. At $a_0 = 1$ corresponding to the intensity $1.37 \times 10^{18}(1\,\mu\mathrm{m}/\lambda_0)^2$ W/cm^2, the laser electric field E_0 acting on the electric charge e produces a work equal to $m_{\rm e}c^2$ over the distance $\lambda\!\!\!^{-}_0$. The quiver electron energy becomes relativistic.
6. The parameter characterizing the electromagnetic emission by an electron is 2/3 of the ratio between the classical electron radius and the electromagnetic wavelength, $2r_{\rm e}/3\lambda\!\!\!^{-}_0 = e^2\omega_0^2/3\pi m_{\rm e}c^3$. The radiation effects are dominant at $a_0 > (3\lambda\!\!\!^{-}_0/2r_e)^{1/3}$, i.e. in the limit $I > 10^{23}(1\,\mu\mathrm{m}/\lambda_0)^2$ W/cm^2.
7. Quantum electrodynamics (QED) effects become important, when the energy of the photon generated by Compton scattering is of the order of the electron energy, i.e. $\hbar\omega_{\rm m} = \gamma_{\rm e}m_{\rm e}c^2$. An electron with energy $\gamma_{\rm e}m_{\rm e}c^2$ rotating with frequency ω_0 in a circularly polarized wave emits photons with energy $\hbar\omega_{\rm m} = \hbar\omega_0\gamma_{\rm e}^3$. The quantum effects come into play when $\gamma_{\rm e} > \gamma_{\rm Q} = \left(m_{\rm e}c^2/\hbar\omega_0\right)^{1/2} \approx 600\,(\lambda_0/1\,\mu\mathrm{m})^{1/2}$, i.e. when the laser normalized amplitude equals $a_{\rm Q} = 2e^2m_{\rm e}c/3\hbar^2\omega_0 = (2r_{\rm e}/3\lambda\!\!\!^{-}_{\rm C})(m_{\rm e}c^2/\hbar\omega_0)$, where $\lambda\!\!\!^{-}_{\rm C} = \hbar/m_{\rm e}c$.
8. The limit of the critical QED field, also called the Schwinger field, $E_{\rm S} = m_{\rm e}^2c^3/e\hbar = m_{\rm e}c^2/e\lambda\!\!\!^{-}_C$ corresponding to the intensity of 10^{29} W/cm^2, is characterized by the normalized laser amplitude $a_{\rm S} = m_{\rm e}c^2/\hbar\omega_0 \approx 5.1 \times 10^5\,(\lambda_0/1\,\mu\mathrm{m})$. The electric field $E_{\rm S}$ acting on the electric charge e produces a work equal to $m_{\rm e}c^2$ over the distance equal to the Compton wavelength $\lambda\!\!\!^{-}_{\rm C}$.
9. In QED the charged-particle interaction with EM fields is determined by relativistically and gauge invariant parameter $\chi_{\rm e} = \left((F^{\mu\nu}p_\nu)^2\right)^{1/2}/m_{\rm e}cE_{\rm S}$, where $F_{\mu\nu}$ is the EM field tensor. The parameter $\chi_{\rm e}$ characterizes the probability of the gamma-photon emission by the electron with Lorentz factor $\gamma_{\rm e}$. It is of the order of the ratio $E/E_{\rm S}$ in the electron rest frame of reference. Another parameter, $\chi_\gamma = \hbar\left((F_{\mu\nu}k_\nu)^2\right)^{1/2}/m_{\rm e}cE_{\rm S}$, is similar to $\chi_{\rm e}$ with the photon 4-momentum, $\hbar k_\nu$, instead of the electron 4-momentum, p_ν. It characterizes the probability of the electron-positron pair creation due to the collision between the high-energy photon and the EM field.

2.10.3 Cosmic-ray acceleration mechanisms

Shock waves in supernova remnants

The origin of cosmic rays (CR) is one of the most interesting problems in astroparticle physics [5]. The observation of ultrahigh-energy cosmic rays indicates that cosmic rays exist beyond 10^{19} eV energies about the GZK cutoff for the extragalactic sources due to the pionization loss of protons that decay by collision with cosmic microwave background photons. The Greizin, Zatsepin, Kuzmin (GZK) cutoff occurs due to the proton interaction with the 3 K cosmic background radiation [10]. The reactions $p + \gamma_{\mathrm{CBR}} \rightarrow p + \pi^0$ and $p + \gamma_{\mathrm{CBR}} \rightarrow n + \pi^+$ have the cross section $\sigma_\pi \approx 100\,\mu\mathrm{bn}$. For the cosmic background radiation photon density, $n_{\mathrm{CBR}} \approx 550$, this yields the mean path associated with this interaction about 50 Mpc at CR energy 5×10^{19} eV, i.e. CR with larger energy cannot be observed on the Earth.

The galactic CR spectra in the energy range above a few GeV and below $\mathcal{E} \approx 10^7$ GeV are power-laws with the total cosmic ray spectrum being $I_{\mathrm{CR}} = 1.8 \times \mathcal{E}^{-k}$ particles/cm^2 s st GeV in the energy range from a few GeV to 100 TeV with $k \approx 2.7$. Around 10^{15} eV (the *knee*), the slope steepens from $k \approx 2.7$ to $k \approx 3$. The energies 10^{18} eV correspond to the ultrahigh-energy cosmic rays (UHECR), the sources of which are associated with active galactic nuclei (AGNs) [11].

For the most advanced theoretical models of galactic cosmic-ray acceleration with the energy below 10^{17} eV the shock waves formed in the supernova explosions are most important. This process is related to the nature of collisionless shock waves [12].

During explosions of type-II supernovae an energy $\mathcal{E}_{SN}$ of the order of 10^{51} erg is released. The frequency of supernova explosions is about 1/30 per year. Estimates [5] show that approximately 2% of the energy of a supernova should be transferred into the cosmic-ray energy.

In the initial stage of the evolution of a supernova envelope a system of shocks is formed (Fig. 2.43). The matter ejected from a star is decelerated and compressed in the inner shock wave. Through the circumstellar gas a second shock wave propagates. The matter ejected from a star is separated from the circumstellar gas by a contact discontinuity, which is unstable with respect to a Rayleigh–Taylor instability. The RT instability leads to the relatively long-scale modulations of the gas density inside the supernova shells.

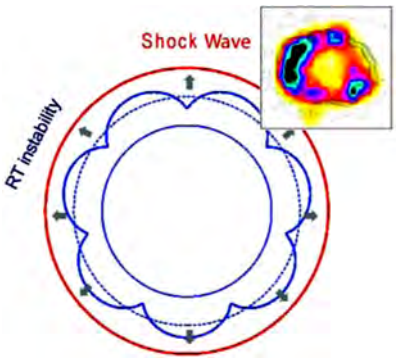

Figure 2.43: Schematic of magnetic reconnection the Earth magnetosphere. Schematic view of the shock waves and contact discontinuity in a supernova remnant. In the inset: X-ray and optical image of supernova remnant SNR 1987A [13].

When the mass of the swept interstellar gas becomes larger than the mass ejected from the star, the propagation of the outer shock in Fig. 2.43 is described by the Sedov–Taylor self-similar solution [7]. The radius of the shock, R_{SW}, as a function of time is related to the energy, $\mathcal{E}_{SN}$, released in the explosion and to the gas density ρ_0 by the expression $R_{\mathrm{SW}}(t) = 1.51(\mathcal{E}_{SN}/\rho_0)^{1/5}t^{2/5} = (5/2)u_{\mathrm{SW}}t$. The shock wave velocity, $u_{\mathrm{SW}}(t) \sim t^{-3/5}$, decreases with time. At a later time, when the radiation losses become important, the law of the supernova envelope expansion changes. The asymptotic time dependence of the SN envelope radius is given by $R_{\mathrm{SW}}(t) \sim t^{2/7}$ (see [5] and references therein).

Diffusive acceleration of cosmic rays at the shock wavefront

The charged-particle interaction with fluctuations of the electric and magnetic field in a turbulent plasma may result in particle scattering and diffusion. When the shock wave propagates in a turbulent medium, an average velocity of electromagnetic fluctuations is different in the regions ahead of and behind the shock front. The particle appears to move efficiently between semitransparent (due to diffusion) walls with a decreasing distance between them. A transport equation describing the particle convection, diffusion and acceleration has a form [5, 14, 15]: $\partial_t f + \nabla \cdot (\boldsymbol{u} f - D\nabla f) = p^{-2}\partial_p \left(p^3 f \nabla \cdot \boldsymbol{u}/3 - p^2 K(p) f\right)$, where $f(p, x, t)$ is the fast particle-distribution function, p, x and t the particle momentum, coordinate and time, $\boldsymbol{u}$ being the speed of the shock-wave propagation, and D is the diffusion coefficient. A term in the right-hand side describes regular acceleration or deceleration of the charged particles: $\dot{p} = -K(p) - p\nabla \cdot \boldsymbol{u}/3$. The function $K(p)$ corresponds to the energy losses. For the cosmic-ray electron component the Compton and synchrotron losses are important with $K(p) = -\beta_{\rm B} m_{\rm e} c^2 p^2$, where $\beta_{\rm B} = 8 \times 10^{-25}(B^2/8\pi + w_{\rm ph}) m_{\rm e} c^2 p^2$ eV^{-1} s^{-1}. An average change of the particle momentum proportional to $p\nabla \cdot \boldsymbol{u}$ occurs due to the particle bouncing between converging, $\nabla \cdot \boldsymbol{u} < 0$, or diverging, $\nabla \cdot \boldsymbol{u} > 0$, scattering centers.

The average particle bouncing between two reflecting plates with distance l as a function of time provides a simple example of a dynamic system with conservation of the longitudinal adiabatic invariant, $J_{||} = pl$. The phase plane shown in the inset to Fig. 2.44, illustrates the Fermi acceleration mechanism of the first type (type A according to [16]). By virtue of the longitudinal adiabatic invariant conservation, for decreasing distance between the plates, $\mathrm{d}l/\mathrm{d}t < 0$, the particle momentum grows, i.e. the particle acquires energy.

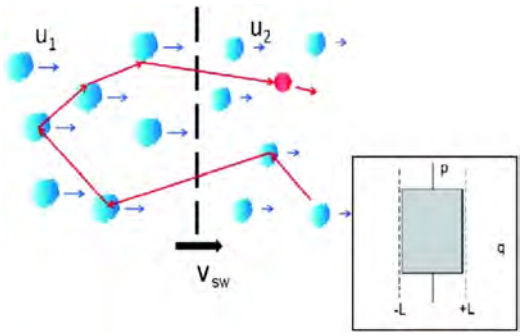

Figure 2.44: Particle diffusion at the front of a shock wave propagating in a turbulent plasma. Inset: the phase plane of the particle bouncing between two plates.

The velocity distribution in the vicinity of the front of an infinitely thin shock wave, propagating from left to right, has the form: $u(X) = u_1$ in the region $X < 0$, and $u(X) = u_2$ for $X > 0$. Here, $X = x - u_{\rm SW} t$. The velocities ahead of the shock front and behind it are related to each other as $u_2 = u_1(\kappa - 1)/(\kappa + 1)$. Here, κ is the polytropic index. For an infinitely thin shock wavefront the divergence of the velocity is equal to $\nabla \cdot \boldsymbol{u} = (u_2 - u_1)\delta(X)$. Using this expression we can obtain that in the limit, when the energy losses are negligibly small, the distribution function describes a power-law dependence $f \sim p^{-k}$ with the index $k = 3u_2/(u_2 - u_1)$ [14]. For $\kappa = 5/3$ the index equals $\kappa = 4$, i.e. $f \sim p^{-4}$, or the energy spectrum $\mathrm{d}N_{\rm CR}(\mathcal{E})/\mathrm{d}\mathcal{E} \sim \mathcal{E}^{-3}$ is close to the power-law index observed in the galactic cosmic-ray energy spectrum.

For the cosmic-ray electron component in the high-energy limit, at the energy when we cannot neglect the Compton and synchrotron losses, there is a cut off in the spectrum [15]. For typical parameters in supernova remnants, $D = 10^{25}$ cm^2 s^{-1}, $B = 10^{-4}$G, $u_2 = 10^8$ cm s^{-1}, the radiation losses limit the energy of ultrarelativistic electrons by values of the order of 10 TeV.

Under the conditions of typical timescales of the laser plasmas the synchrotron losses of ultrarelativistic electrons interacting with the self-generated magnetic field is of the order of $\tau_{\rm B} = 5\left(10^3/\gamma_{\rm e}\right)\left(10^9/B\right)^2$fs.

2.10.4 Collisionless shock waves

Phenomena taking place at shock-wavefronts play a key role in various astrophysical conditions. The characteristic dimensionless parameters that determine the shock- wave propagation are the Mach number, $M_{\rm A} = u_{\rm SW}/v_{\rm A}$, defined here as the ratio of the shock wavefront velocity, $u_{\rm SW}$, to the Alfven velocity, $v_{\rm A}$, the ratio of the gas pressure to the magnetic pressure, $\beta_{\rm B} = 8\pi nT/B^2$, and θ, the angle between the normal to the front and the magnetic field.

If the shock wave has a relatively small amplitude, $M_{\rm A} < M_1 \approx 1.5$ (the precise value depends on $\beta_{\rm B}$ and θ), then the front profile is laminar in structure and it is determined by a joint action of the dispersion and dissipation on the nonlinear wave propagation. These effects are described in the framework of the Korteweg–de Vries–Burgers equation: $\partial_t u + u\partial_x u - \nu\partial_{xx}u + \beta\partial_{xxx}u = 0$. The stationary wave propagating with constant velocity is described by a solution that shows the change of the amplitude of the wave from zero far ahead of the shock wavefront, to $u_2 = 2u_{\rm SW}$ far behind the shock wavefront. The collisionless shock wavefront has typically an oscillatory structure – the chain of solitons. The decay of the oscillation amplitude, with the coefficient equal to ν/β, results in the decrease of the amplitude of solitons, as shown in Fig. 2.45.

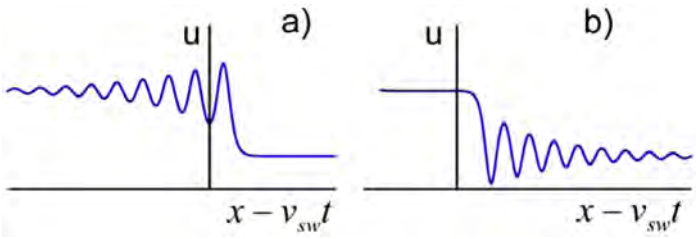

Figure 2.45: Structure of collisionless shock wavefront for $\beta > 0$ (a) and for $\beta < 0$ (b).

If dissipation effects are more important than the effects of dispersion, $\nu \gg (4\beta u_2)^{1/2}$, there are no oscillations at the shock wavefront and the wave has a monotonous structure. In the case of $\nu \ll \beta$, the dispersion effects are dominant and there are many well-seen solitons near the front. For $\beta > 0$ the oscillations are localized behind the front (Fig. 2.45a), while for $\beta < 0$ they are ahead of the front (Fig. 2.45b).

Dissipation, which determines the distance of the oscillation decay, can be due to anomalous resistance and anomalous viscosity arising from an excitation of the plasma instability, i.e. the Weibel instability of counterpenetrating plasmas. If the amplitude of the shock wave is large, $M_{\rm A} > 3$, a high level of turbulent fluctuations of electric and magnetic fields are excited ahead of and behind the wavefront.

In the laser-plasma physics context, the observation of collisionless shocks was reported by several authors [17,18], aiming to reproduce astrophysical phenomena in small-scale laboratories. In [18] the propagation in a rarefied plasma ($n_{\rm e} < 10^{15}$ cm^{-3}) of collisionless shock waves being excited following the interaction of a long $\tau_{\rm las} = 470$ ps) and intense ($I = 10^{15}$ W/cm^2) laser pulse with solid targets, has been investigated via proton-probing techniques [19]. The shocks' structures and related electric field distributions were reconstructed with high spatial and temporal resolution. The experimental results are described within the framework of the nonlinear wave description based on the Korteweg–deVries–Burgers equation (see Fig. 2.46).

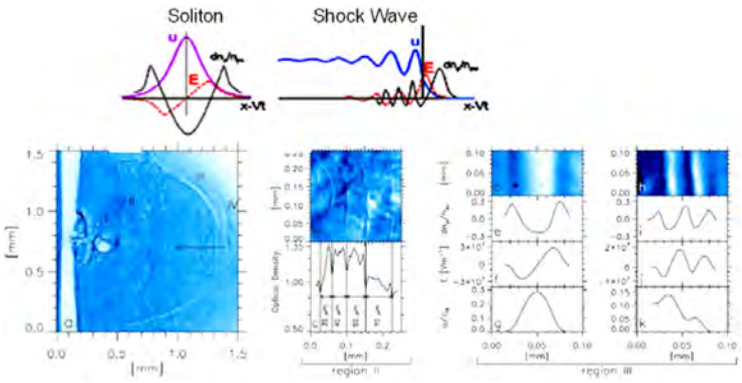

Figure 2.46: Collisionless shock waves observed in the laser–plasma interaction [18]. (a) Typical proton imaging data. The arrow indicates the laser beam direction. (b) and (c) Detail and RCF optical density lineout corresponding to the region II showing modulations associated with a train of solitons. (d)–(k) Details of the region III and correspondent lineouts of the probe proton density reconstructed electric field, and reconstructed normalized ion velocity in the case of an ion acoustic soliton (d)–(g) and of a collisionless shock wave (h)–(k). Inset: Theoretical ion velocity (purple and blue lines), electric field (red lines) and expected probe proton density modulation (black lines) for (a) an ion-acoustic soliton and (b) a collisionless shock wave.

2.10.5 Reconnection of magnetic-field lines and vortex patterns in laser plasmas

The term *magnetic-field line reconnection* refers to a broad range of problems that are of interest for space and laboratory plasmas with high Lundquist number, $Rm \gg 1$, [5, 9] (Fig. 2.47). As it concerns relativistic laser plasmas, earlier a conclusion was made in [20] about the important role of the generation of magnetic fields by fast electron currents and their reconnection in the relativistic laser–matter interaction regime. The experiments conducted in [21] revealed magnetic reconnection phenomena in laser plasmas, when two high-power laser beams irradiated a thin foil target (Fig. 2.48).

Processes of reconnection are accompanied by an ultrafast magnetic energy release, which is transformed into different forms, such as internal plasma energy, radiation and fast particles.

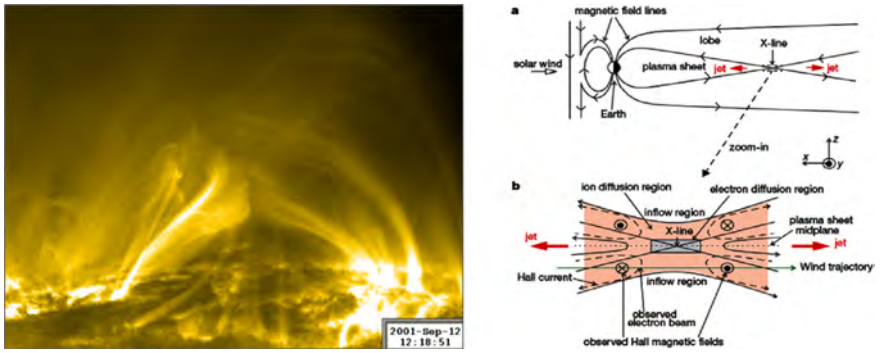

Figure 2.47: (left) Solar flare [Solar flare/12.09.2001(12:18:51]. (right) Schematic of magnetic reconnection of/to the Earth magnetosphere.

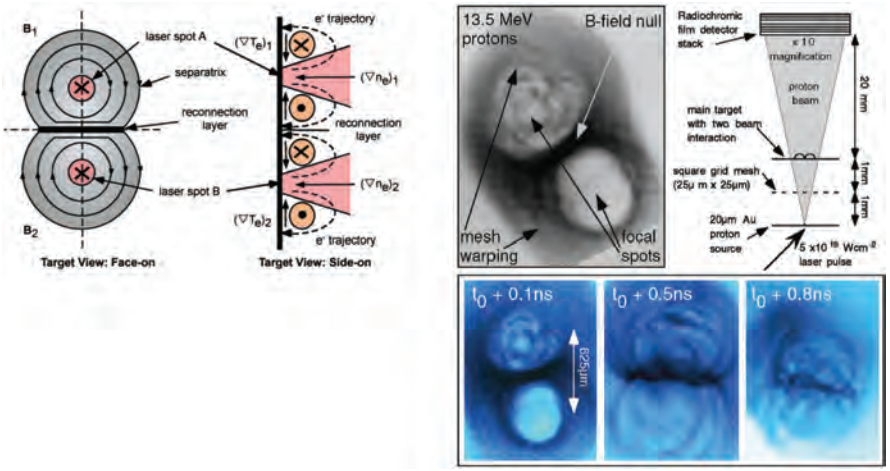

Figure 2.48: (left) Schematic of the experiment with two laser beams irradiating thin foil; target [21]. The current sheet observed with the proton imaging.

Current sheet

In a simple 2D configuration the current sheet is formed in the magnetic field described by a complex function $\boldsymbol{B}(x,y) = B_x - iB_y = h\zeta$ of a complex variable $\zeta = x + iy$. The magnetic field vanishes at the coordinate origin. The magnetic-field lines lie on the surfaces of constant vector potential, $A(x,y) = \Re\mathfrak{e}\{h\zeta^2\}/2$. They are hyperbolas, as can be seen in Fig. 2.49a). Under finite-amplitude perturbations the magnetic null-line evolves to the magnetic configurations of the form $\boldsymbol{B}(x,y) = h(\zeta^2 - b^2)^{1/2}$, which describes the magnetic field created by thin current sheet between two points $\pm b$ [22]. The magnetic field is shown in Fig. 2.49b. The width of the current layer b is determined by the total electric current J inside, and by the magnetic field gradient, h. It is equal to $b = (4J/hc)^{1/2}$. The current sheet thickness is determined by the dissipation [23]. Within the Parker–Sweet model is equal to $(\eta_\mathrm{m}/\Omega_\mathrm{A})^{1/2}$ with $\Omega_\mathrm{A} = h/(4\pi n m_\mathrm{p})^{1/2}$ [5].

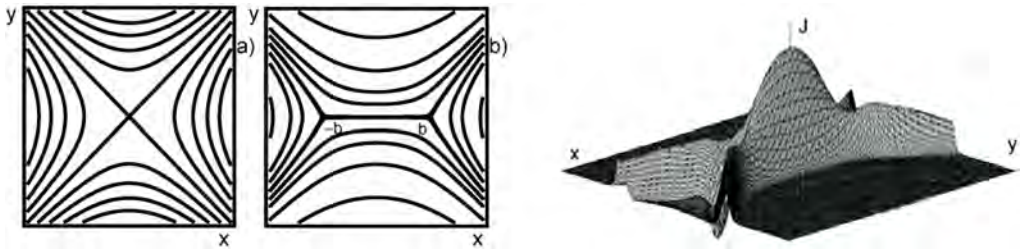

Figure 2.49: (left) Magnetic field pattern in the vicinity of the X-line (a). Current sheet formed in the vicinity of the X-line (b). (right) Electric current-density distribution inside the current sheet [24].

In the strongly nonlinear stage of the magnetic field and plasma evolution a quite complex pattern in the MHD flow in the nonadiabatic region near the critical point can be formed, with shock waves and current sheets. In Fig. 2.49 we show the results of the dissipative MHD simulations of the current sheet formation near the X-line [24].

Magnetic reconnection in collisionless plasmas

When the Hall effect is dominant, i.e. the electron inertia determines the relationship between the electric field and the electric current density carried by the electron component, the magnetic-

field evolution is described by the equation (see [2] and references therein) $\partial_t(\boldsymbol{B} - \Delta\boldsymbol{B}) = \nabla \times [(\nabla \times \boldsymbol{B}) \times (\boldsymbol{B} - \Delta\boldsymbol{B})]$, which corresponds to the condition of generalized vorticity, $\Omega = \boldsymbol{B} - \Delta\boldsymbol{B}$, being frozen into the electron component motion with the velocity $v_e = c\nabla \times \boldsymbol{B}/4\pi ne$. Here the space scale is chosen to be equal to the collisionless electron skin-depth, c/ω_{pe}, and the time unit is $\omega_{Be}^{-1} = m_e c/eB$. In the linear approximation this equation describes the propagation of whistler waves, for which the relationship between the wave frequency and the wavevector, is $\omega = |\boldsymbol{k}|(\boldsymbol{k} \cdot \boldsymbol{B}_0)/(1 + k^2)$. From this relationship it follows that in a weakly inhomogeneous magnetic field the critical points are the points and lines where $|\boldsymbol{B}_0| = 0$ or/and $(k \cdot \boldsymbol{B}_0) = 0$.

The electron-inertia effects make the reversed magnetic field configuration unstable against tearing modes, which result in magnetic-field-line reconnection. The slab equilibrium configuration with a magnetic field given by $\boldsymbol{B}_0 = B_{0z}\boldsymbol{e}_z + B_{0x}(y/L)\boldsymbol{e}_x$, where $B_{0x}(y/L)$ is the function that gives the current sheet magnetic field, is unstable with respect to perturbations of the form $f(y)\exp(\gamma t + ikx)$ with $kL < 1$. For this configuration one has $(\boldsymbol{k} \cdot \boldsymbol{B}_0) = 0$ at the surface $y = 0$. The growth rate of the tearing mode instability is $\gamma \approx (1 - kL)^2\Delta'^2/kL^2$.

In Fig. 2.50 the results of a numerical solution of equation for generalized vorticity in a 2D geometry with magnetic field $(\nabla \times \alpha) \times e_\perp + \beta e_{||}$ are shown. The unperturbed configuration is chosen to be a current sheet, infinite in the x-direction, that separates two regions with opposite magnetic field. Both the line pattern of generalized vorticity, $\Omega = \alpha - \Delta\alpha$, and of the magnetic field show the formation of quasi-one-dimensional singular distributions in the electric-current density and in the distribution of the generalized vorticity. The magnetic-field topology changes, as is seen from Fig. 2.50.

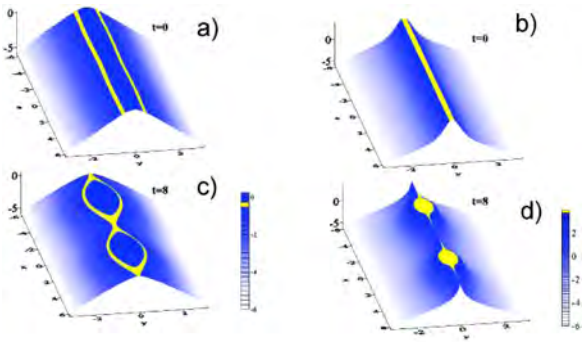

Figure 2.50: Nonlinear stage of the tearing mode development in a current sheet in collisonless plasma: (a) the magnetic field and (b) the generalized vorticity distribution at $t = 0$. The same functions at $t = 8$ in (c) and (d) [25].

Charged-particle acceleration

A fully developed tearing mode results in a current sheet break up into parts separated by a distance $2a(t)$, as is illustrated in Fig. 2.51a. Under the magnetic-field line tension the plasma is thrown out. The model magnetic field describing this configuration is given by the complex variable function $\boldsymbol{B}(x, y, t) = B_0\zeta/(a^2(t) - \zeta^2)^{1/2}$. The magnetic-field lines lie on the surfaces of constant vector potential, $A(x, y, t) = \Re\mathfrak{e}\{B_0(a^2(t) - \zeta^2)^{1/2}\}$. Due to a dependence of the function $a(t)$ on time the electric field parallel to the zzz-axis arises. It is given by $E(x, y, t) = -c^{-1}\partial_t A = -c^{-1}B_0 a(t)\dot{a}(t)/(a^2(t) - \zeta^2)^{1/2}$. In the vicinity of the null line we have a quadrupole structure of the magnetic $\boldsymbol{B}(x, y, t) \approx B_0\zeta/a(t)$ field and a locally homogeneous electric field, $E \approx B_0\dot{a}(t)/c$.

In the vicinity of critical points of magnetic configurations the standard approximations adopted to describe the plasma dynamics are no longer valid. In such regions the drift approximation,

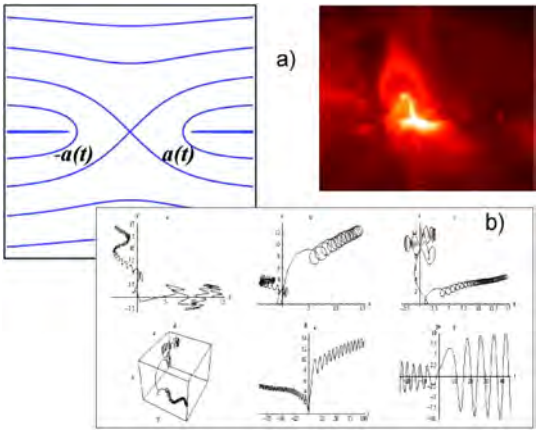

Figure 2.51: (a) The current sheet break up into two parts separated by the distance $2a(t)$. (b) The projections of the trajectory of charged particle accelerating in the vicinity of the magnetic X-line. Inset: The solar flare (YOHKOH image).

i.e. the assumption that the adiabatic invariants are constant, can no longer be applied. On the other hand, the particle spends only a finite time interval in the nonadiabatic region, since there its motion is unstable. After a finite time interval it gets out of the nonadiabatic region, and gets into the drift region as is seen in Fig. 2.51b. Matching the solution described by the particle trajectories in different regions, we can describe the particle motion and hence the acceleration near critical points of the magnetic configurations.

Under the conditions of space plasmas, the radiation losses during the charged particle acceleration in the magnetic reconnection processes are caused by the inverse Compton scattering and by synchrotron losses. A characteristic time of the synchrotron losses for the electron with energy $m_e c^2 \gamma_e$ is $\tau_B = 3m_e^3 c^5/2e^4 B^2 \gamma_e$. During solar flares this effect limits the ultrarelativistic electron energy to a value of about several tens of GeV [26].

Electron vortices in collisionless plasmas

The vortical fluid motion is well known to be widely present under Earth and space conditions. In laser plasmas, when an ultrashort and high-intensity EMW pulse propagates in the collisionless plasmas, it accelerates a copious number of relativistic electrons. The electric current of fast electrons produces a quasistatic magnetic field, whose evolution results in the formation of electron vortex structures. They naturally take the form of the vortex rows [27], as is shown in the LHS inset to Fig. 2.52. A strong magnetic field in the relativistic laser plasma has been detected experimentally [28].

The interacting vortices can be described within the framework of a two-dimensional theoretical model. By taking the $\boldsymbol{B}$ field to be along the z-axis ($\boldsymbol{B} = B\boldsymbol{e}_z$), and assuming all the quantities to depend on the x, y coordinates, we obtain from vector equations for generalized vorticity one equation $\partial_t(B - \Delta B) + \{B, (B - \Delta B)\} = 0$ for a scalar function $\boldsymbol{B}(x, y, t)$, where $\{f, g\} = \partial_x f \partial_y g - \partial_x g \partial_y f$ are the Poisson brackets. This equation is known as the Charney equation or the Hasegawa–Mima (HM) equation in the limit of zero drift velocity. Linear mode with the dispersion equation $\omega = |\boldsymbol{k}|(\boldsymbol{k} \cdot \boldsymbol{B}_0)/(1 + k^2)$ corresponds to the Rossby waves, the drift waves or to the whistler waves, respectively.

The equation for $B(x, y, t)$ has a discrete vortex solution, for which the magnetic field is a superposition of the magnetic fields created at isolated vortices localized at the coordinates $\boldsymbol{x}^\alpha(t)$: $B(\boldsymbol{x}, t) = -\sum_\alpha (\kappa_\alpha/2\pi) K_0(|\boldsymbol{x} - \boldsymbol{x}^\alpha(t)|)$ with $K_n(x)$ being the modified Bessel function.

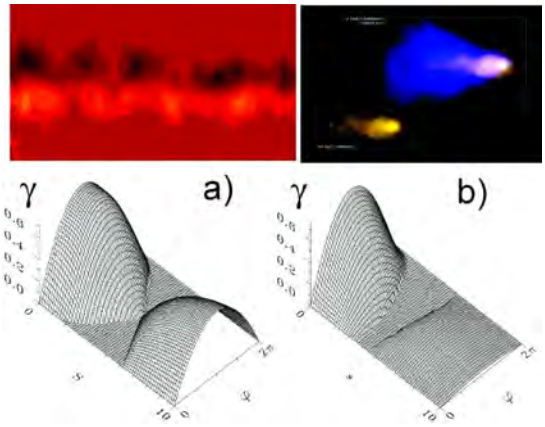

Figure 2.52: Instability growth rate on s and φ plane for the vortex row described within the framework of the Euler (a) and Hasegawa–Mima (b) approximations [27]. Left inset: The vortex row seen in the magnetic field patch distribution in a plasma behind the laser pulse. Right inset: The Mouse pulsar (NASA/CXC/SAO, Chandra image of G359.23-0.82 pulsar).

The curves $\boldsymbol{x}^\alpha(t)$ are determined by the Hamiltonian equations

$$\kappa_\alpha \dot{x}_i^\alpha = -J_{ij} \sum\nolimits_{\beta \neq \alpha} \left(\kappa_\alpha \kappa_\beta \left(x_i^\alpha - x_j^\beta \right) / 2\pi |x_i^\alpha - x_j^\beta|^2 \right) K_1(|x_i^\alpha - x_j^\beta|),$$

where J_{ij} is the antisymmetric unit matrix.

In the case of Euler hydrodynamics, a point vortex is described by $(\kappa_\alpha/2\pi)\ln(|\boldsymbol{x} - \boldsymbol{x}^\alpha(t)|)$, instead of the expression which involves the Bessel function $K_0(|\boldsymbol{x} - \boldsymbol{x}^\alpha(t)|)$. The latter results in the shielding of the interaction between vortices at large distances. A typical scale length of the problem under consideration is equal to the collisionless electron skin depth, $d_\mathrm{e} = c/\omega_\mathrm{pe}$.

Considering the problem of the stability of a double vortex chain we assume that the opposite vortices with intensity $\kappa_\alpha = \pm 1$ have coordinates: $x_j^0 = js + Ut, \quad y_j^0 = q/2, \quad -\infty < j < +\infty, \kappa_\alpha = -1$ for the upper chain, and $x_j^0 = (k+\sigma)s + Ut, \quad y_j^0 = -q/2, \quad -\infty < k < +\infty, \kappa_\alpha = +1$, for the lower chain. The symmetric row ($\sigma = 0$) is always unstable. As noted in Lamb's monograph [29], in Euler hydrodynamics the antisymmetrical von Karman's vortex row is stable for $q/s \approx 0.281$, where s and q give a distance between the vortices in the unperturbed vortex row along the x and y coordinates. A dependence of the instability growth rate on s and q for the vortex row described within the framework of the Euler hydrodynamics approximation is shown in Fig. 2.52a, where the perturbation wavelength is expressed via φ as $2\pi s/\varphi$. For large distance between neighboring vortices the antisymmetric vortex row is stable for $3s^2/4 > q > s/2$ (see Fig. 2.52b) [27]. We note here that in this domain the antisymmetric row is stable nonlinearly (in terms of the Lyapunov stability).

These results shed light on typical patterns in the self-generated magnetic field left in a wake behind the laser pulse propagating in underdense plasmas.

2.10.6 Mechanisms of magnetic-field generation in relativistic plasmas

As was above discussed the quasistatic magnetic-field generation in relativistic laser plasmas occurs due to the fast electron-beam interaction with the background plasma. It can also be understood in terms of the Weibel instability or in the generic case, in terms of the electromagnetic filamentation instability. When the fast electron beam propagates in the plasma, its electric current is compensated by the current carried by the plasma electrons. A repulsion of the oppositely directed electric currents results in electron-beam filamentation and in the

generation of a strong magnetic field [30]. An electromagnetic filamentation instability leads to the generation of a quasistatic magnetic field and is associated with many small-scale current filaments [31, 32]. Each filament consists of a direct and of a return electric current that repel each other (see Fig. 2.53). This produces a strong electric field, which accelerates the ions in the radial direction. In the long-term evolution, the successive coalescence of the small-scale current filaments forms a large-scale magnetic structure. This process is accompanied by the reconnection of the magnetic-field lines, by the formation of current sheets, and by strong ion acceleration inside these sheets [33].

The filamentation phenomena are of great interest for the explanation of the quasistatic magnetic field origin in laser plasmas irradiated by relativistically strong EMW [34]. Counterstreaming electric-current configurations naturally appear in space at the fronts of colliding electron–positron and electron–ion plasma clouds [35] as in the cases of the Galactic Gamma Ray Bursts and in shock waves in supernova remnants. The filamentation instability generates the magnetic field required by the theory of the synchrotron afterglow in GRB [36]. The Weibel instability has been invoked as a mechanism of the primordial magnetic-field generation by colliding electron clouds in cosmological plasmas [37].

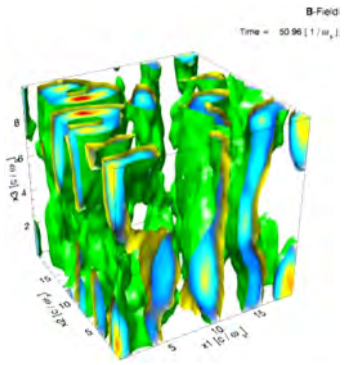

Figure 2.53: 3D PIC simulation of magnetic field generation during the Weibel instability development [32].

The filamentation instability developing in the vicinity of shock wavefronts together with other types of instabilities plays the role of the source of strong electromagnetic turbulence invoked in the theoretical models of the Fermi acceleration of cosmic rays [36, 38].

2.10.7 Modeling of pulsar magnetosphere (oblique magnetic rotator) with relativistic EM solitons

According to the antenna mechanism of the pulsar radiation emission [39] in the pulsar magnetosphere, which is an obliquely rotating magnetic dipole, the magnetic dipole interaction with a plasma at the magnetosphere periphery induces strong modulations of the electron density, an electron density lump. The phase velocity of the electron lump can be arbitrarily close to the speed of light in vacuum. It is directed along a circle as illustrated in Figure 2.54. As a result of the curvilinear acceleration, the electron lump emits radiation, the properties of which are similar to the synchrotron radiation [40].

In the context of relativistic laboratory astrophysics it is remarkable that the relativistic rotating dipole can naturally be formed in the laser plasma [2]: the high-power coherent synchrotron-like radiation can be generated by the relativistic charge density wave rotating self-consistently inside an electromagnetic-dipole solitary wave, dwelling in a laser plasma [41]. Figure 2.54 presents the structure of electric and magnetic fields inside the soliton [41]. The soliton resembles an oscillating or rotating electric dipole. The toroidal magnetic field, shown in Figure 2.54, indicates that, besides the strong electrostatic field, the soliton emits high-frequency EM radiation, whose frequency is much higher than the Langmuir frequency [41]. This radiation

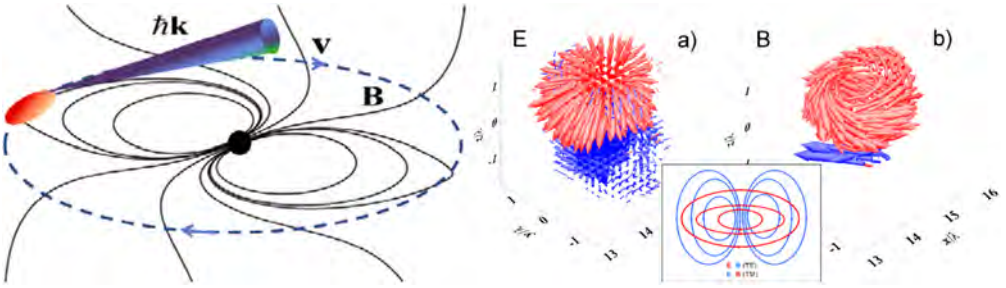

Figure 2.54: (left) Schematic pulsar magnetosphere, according to reference [39]. A rotating relativistic electron lump emits electromagnetic radiation by the antenna mechanism. (right) Structure of electric (a) and magnetic (b) fields inside the EM relativistic soliton. Inset: the magnetic and electric-field topology in the TE (with poloidal magnetic field and toroidal electric field) and in the TM (with poloidal electric field and toroidal magnetic field) solitons [41].

is emanated from the electron-density hump rotating in the wall of the soliton cavity, similar to coherent synchrotron-like emission. This radiation has the characteristics of a well-pronounced outgoing spiral EM wave, Fig. 2.55a. The emission of the spiral wave correlates to the rotation of the electron-density hump in the cavity wall, and it leads to the spiral modulations of the electron density (see Fig. 2.55b). The density hump gyrates in a circle, and the period of revolution is exactly equal to the soliton period. The polarization of the spiral wave corresponds to the well-known synchrotron radiation [40] and the density-hump emission is coherent.

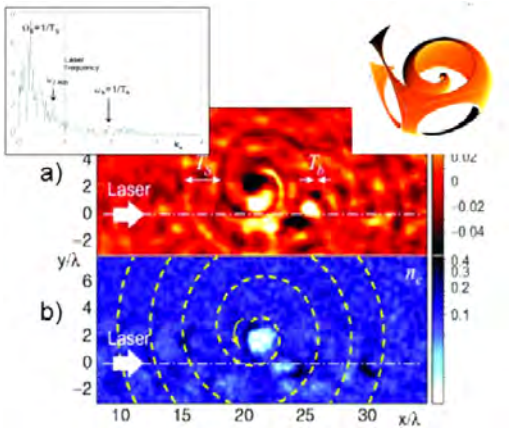

Figure 2.55: (a) Cross sections of the magnetic field component $eBz = m_e c$ in the plane x, y. (b) The electron-density distribution. Right inset: the EM field of the rotating electric charge. Left inset: a frequency spectrum of the emitted EM wave.

2.10.8 Conclusion

Finally, we note that the development of superintense lasers with parameters in the ELI range will provide the necessary conditions for experimental physics where it will become possible to study ultrarelativistic energy of accelerated charged particles, superhigh-intensity EM wave and the relativistic plasma dynamics. A fundamental property of the plasma to create nonlinear coherent structures, such as relativistic solitons and vortices, collisionless shock waves and high-energy particle beams, and to provide the conditions for relativistic regimes of the magnetic-field line reconnection, makes the area of relativistic laser plasmas attractive for modeling of processes of key importance for relativistic astrophysics.

Bibliography

[1] B. Remington, R. Drake, and D. Ryutov, Rev. Mod. Phys. **78**, 755 (2006).
[2] S. V. Bulanov, T. Zh. Esirkepov, D. Habs, F. Pegoraro, and T. Tajima, Eur. Phys. J. D **55**, 483 (2009).
[3] J. D. Lindl et al., Phys. Plasmas **11**, 339 (2004).
[4] Basic Research Needs for High Energy Density Laboratory Physics. Report of the Workshop on High Energy Density Laboratory Physics Research Needs, Nov. 15–18 (2009) US Dep. of Energy.
[5] V. S. Berezinskii, S. V. Bulanov, V. L. Ginzburg, V. A. Dogiel, and V. S. Ptuskin, Astrophysics of cosmic rays (North Holland Publishing Co. Elsevier Science Publishers, Amsterdam, 1990).
[6] F. A. Aharonian et al., Phys. Rev. D **66**, 023005 (2002); M. V. Medvedev, Phys. Rev. E **67**, 045401 (2003).
[7] L. I. Sedov, Similarity and dimensional methods in mechanics (Academic Press, New York, 1959); G. I. Barenblatt, Scaling, self-similarity, and intermediate asymptotics: dimensional analysis and intermediate asymptotics (Cambridge University Press, Cambridge, 1996).
[8] I. M. Podgorny and R. Z. Sagdeev, Sov. Phys. Uspekhi **98**, 445 (1970); C.-G. Falthammar, Space Sci. Rev. **15**, 803 (1974).
[9] E. Priest and T. Forbes, Magnetic reconnection: MHD theory and applications (Cambridge University Press, Cambridge, 2000); D. Biskamp, Magnetic reconnection in plasmas (Cambridge University Press, Cambridge, 2000).
[10] K. Greisen, Phys. Rev. Lett. **16**, 748 (1966); G.T. Zatsepin, V.A. Kuz'min, Sov. Phys. JETP. Lett. **4**, 78 (1966).
[11] J. Abraham (Pierre Auger Collaboration), Science **318**, 938 (2007); R. U. Abbasi, et al., Phys. Rev. Lett. **100**, 101101 (2008); J. Abraham, et al., Phys. Rev. Lett. **101**, 061101 (2008).
[12] D. A. Tidman and N. A. Krall, Shock waves in collisionless plasmas (Wiley-Interscience, New York, 1971).
[13] D. Burrows et al., Astrophys. J. **543**, L149 (2000).
[14] G. F. Krymskii, Sov. Phys. Dokl. **23** (1977); W. I. Axford, et al., Proc. 15th Int. Cosmic Ray Conf.(Plovdiv) **11**, 132 (1977); A. R. Bell, Month. Not. R. Astron. Soc. **182**, 147 (1978); R. D. Blandford and J. P. Ostriker, Astrophys. J. **221**, 29 (1978).
[15] S.V. Bulanov, V.A. Dogiel, Sov. Astron. J. Lett. **5**, 521 (1979).
[16] E. Fermi, Phys. Rev. **75**, 1169 (1949); E. Fermi, Astrophys. J. **119**, 1 (1954).
[17] D. W. Koopman and D. A. Tidman, Phys. Rev. Lett. **18**, 533 (1967); A. R. Bell et al., Phys. Rev. A **38**, 1363 (1988); N. C. Woolsey et al., Phys. Plasmas **8**, 2439 (2001); T. Morita, et al., Phys. Plasmas **17**, 122702 (2010).
[18] L. Romagnani, et al., Phys. Rev. Lett. **101**, 025004 (2008).
[19] M. Borghesi et al., Phys. Plasmas **9**, 2214 (2002).
[20] G. A. Askar'yan et al., Commun. Plasma Phys. Contr. Fusion **17**, 35 (1995).
[21] P. M. Nilson et al., Phys. Rev. Lett. **97**, 255001 (2006); C. K. Li et al., Phys. Rev. Lett. **99**, 055001 (2007); P. M. Nilson et al., Phys. Plasmas **15**, 092701 (2008); L. Willingale et al., Phys. Plasmas **17**, 043104 (2010).
[22] S. I. Syrovatskii, Ann. Rev. Astron. Astrophys. **19**, 163 (1981).
[23] P. A. Sweet, in Electromagnetic phenomena in cosmic physics, edited by B. Lehnert (Cambridge University Press, Cambridge, 1958), p. 122; E. Parker, Cosmical magnetic fields: their origin and their activity (Oxford University Press, New York, 1979).
[24] S. V. Bulanov et al., Phys. Lett. A **203**, 219 (1995).
[25] K. Avinash et al., Phys. Plasmas **5**, 2946 (1998).
[26] S. V. Bulanov et al., Sov. Astron. Lett. **11**, 159 (1985).

[27] M. Borghesi et al., Phys. Rev Lett. **80**, 5137 (1998); M. Tatarakis et al., Nature **415**, 280 (2002).
[28] S. V. Bulanov et al., in Reviews of plasma physics, edited by V. D. Shafranov (Kluwer Academic, Plenum Publishers, New York, 2001), Vol. 22, p. 227.
[29] H. Lamb, Hydrodynamics (Cambridge University Press, Cambridge, 1932).
[30] F. Califano et al., Phys. Rev. E **56**, 963 (1997).
[31] M. Honda et al., Phys. Plasmas **7**, 1302 (2000).
[32] L. O. Silva et al., Astrophys. J. 596, L121 (2003).
[33] J. I. Sakai et al., Phys. Plasmas **9**, 2959 (2002).
[34] V. Y. Bychenkov et al., Sov. Phys. JETP **71**, 709 (1990); G. A. Askar'yan et al., JETP Lett. **60**, 251 (1994).
[35] Y. Kazimura et al., Astrophys. J. 498, L**183** (1998).
[36] M. V. Medvedev and A. Loeb, Astrophys. J. **526**, 697 (1999); E. Waxman, Plasma Phys. Control. Fusion **48**, B137 (2006).
[37] J. I. Sakai, R. Schlickeiser, and P. Shukla, Phys. Lett. A **330**, 384 (2004).
[38] H. Takabe et al., Plasma Phys. Contr. Fusion **50**, 124057 (2008).
[39] V. L. Ginzburg and V. V. Zheleznyakov, Ann. Rev. Astron. Astrophys. **13**, 511 (1975).
[40] V. L. Ginzburg, Applications of electrodynamics in theoretical physics and astrophysics (Gordon and Breach, New York, 1989).
[41] T. Esirkepov et al., Phys. Rev. Lett. **89**, 275002 (2002).

3 Applications in multidisciplinary sciences

3.1 Biomedical imaging with laser-driven brilliant compact X-ray sources

Since its discovery more than a hundred years ago X-ray radiation has become an indispensable tool in medical diagnostics. Despite its invaluable contribution to patient care, for example in imaging bone structure, X-ray diagnostics ultimately reaches its limits in the examination of soft tissue, such as tumors embedded in healthy tissue. Modern X-ray imaging methods, which explicitly utilise the wave character of X-ray light, promise a significant improvement in image quality and reduction in patient-delivered dose over conventional, absorption-based approaches. The requirements on the X-ray beam brilliance mean, however, that presently the applications of such innovative methods are restricted to large-scale synchrotron facilities.

Introduction

Visible light microscopy is a standard and widely utilized tool with a broad range of applications in science, industry and everyday life. Besides standard bright-field imaging, many more contrast mechanisms have been developed, and dark-field imaging, phase-contrast, confocal and fluorescence microscopy are routine methods in today's light microscopy applications [1]. It is not surprising that this development has stimulated a similar progress in imaging applications with other forms of radiation. In electron microscopy, for example, where the initial electron microscope image was produced in the early thirties, dark-field imaging was introduced in the late thirties [2], and imaging based on phase contrast in the forties [3].

In X-ray microscopy, or more generally, X-ray imaging, the development of a similar range of contrast modalities proceeded much more slowly and is still a very active field of research. Despite the early pioneering work on X-ray interferometry by Bonse et al. in the sixties [4], the majority of phase-contrast imaging [5,6] and dark-field imaging [7–10] methods were introduced in the late nineties. The development of such advanced imaging methods is particularly difficult for hard X-rays (with energies in the multi-keV range), because of the lack of efficient X-ray optics. Most existing hard X-ray dark-field and phase-contrast imaging methods, for example, work best with a narrow energy band-width (typically between 0.01 and 1%) and a very small source size (typically between 10 an 100 μm) of the radiation [4, 7–18], and this effectively restricts their use to highly brilliant and well-collimated large-scale X-ray synchrotron sources. Medical imaging applications, on the other hand, would require a more compact and cost-effective solution, which could be integrated into a clinical environment.

ELI opportunities

A 'gap of opportunities' – in terms of novel X-ray sources – is illustrated in Fig. 3.1, which compares the brilliance (and price tags) of commercially available X-ray sources for medical diagnostics with that of large-scale synchrotron X-ray facilities. While equipment used in medical device technology typically offers a brilliance of around 10^8 ph/(sec mm^2 mrad^2 0.1% BW), large-scale synchrotron sources can presently deliver values of 10^{14} ph/(sec mm^2 mrad^2 0.1% BW) at bending magnets and up to 10^{22} ph/(sec mm^2 mrad^2 0.1% BW) at dedicated undulator beamlines. In terms of pricing, lab-based X-ray generators typically range in the few ten to hundred thousand Euro range. Large-scale facilities, on the other hand, usually are priced on the several hundred million Euro scale, which rules out widespread clinical applications.

If we now consider the requirements X-ray phase-contrast imaging applications, we can state that a brilliance of 3–4 orders above X-ray generators, i.e. in the range of 10^{11} to 10^{13} ph/(sec mm^2 mrad^2 0.1% BW) would be sufficient for most methods to work very well. Therefore state-of-the-art undulator brilliance values of 10^{22} ph/(sec mm^2 mrad^2 0.1% BW)

are not really required for advanced biomedical phase-contrast imaging applications, as they typically target only medium resolutions with pixel sizes in the several ten micron range at minimum.

From this discussion we conclude that there is a need for cost-effective X-ray sources in the 10^{11} to 10^{14} ph/(sec mm^2 mrad^2 0.1% BW) brilliance regime, and that this is currently not targeted by any existing technology of today. Laser-driven X-ray sources could potentially fill this gap and provide sources with brilliance values significantly above X-ray generators, but with a price tag significantly below large-scale synchrotron research facilities.

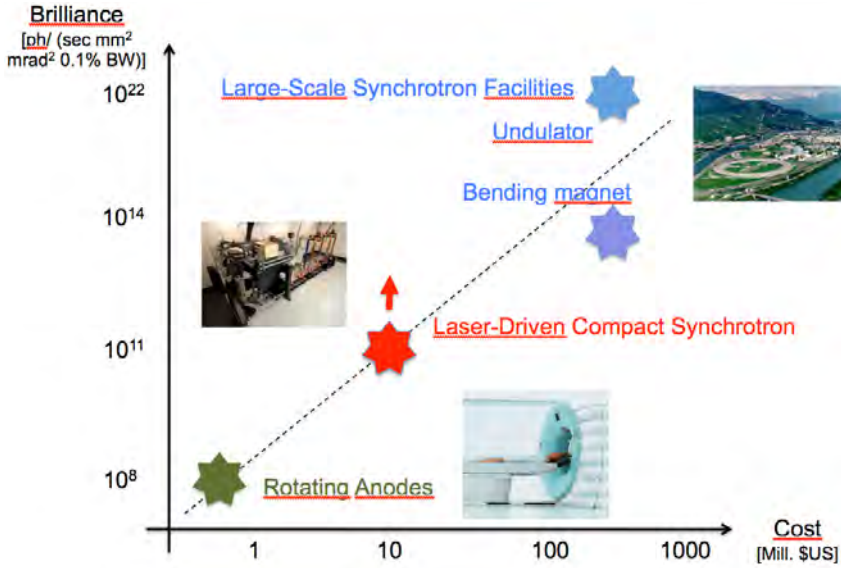

Figure 3.1: This viewgraph illustrates the 'gap of opportunities' – in terms of brilliance vs. cost ratio – of novel, laser-driven X-ray sources, with respect to existing low-cost/low-brilliance rotating anodes and high-cost/high-brilliance large-scale synchrotron X-ray facilities.

Laser-driven compact X-ray sources

A possible solution to this problem are novel compact, but yet brilliant, laser-driven synchrotron X-ray radiation sources. These sources are presently expected to deliver brilliance values of up to 10^{11} ph/(sec mm^2 mrad^2 0.1% BW), and fulfill the requirements of most phase-contrast imaging modalities, while keeping a moderate price envelope. The main concept of such compact, laser-driven synchrotron sources is based on head-on collision of high-power picosecond laser pulses and relativistic electron bunches circulating in a laser enhancement cavity and electron storage ring, respectively (see also Fig. 3.2).

Whereas the insertion devices such as undulators and wigglers on third-generation synchrotron radiation facilities are built with permanent magnets, BRIX produces X-rays in the field of an intense laser undulator (through a mechanism called 'Thomson or inverse Compton scattering', see [19]). The characteristic parameters for undulator radiation are γ (electron energy in units of rest mass) and λ_u (spatial period of the undulator). The fundamental wavelength of X-rays emitted from a magnetic undulator is $\lambda_u/2\gamma^2$, and for magnetic undulators λ_u is typically a few centimeters, so γ needs to be of the order of 10^4 to reach a fundamental wavelength in the Ångström range. The fundamental wavelength for a laser undulator is $\lambda_u/4\gamma^2$ [20], and as the laser undulator at BRIX has a wavelength of ~ 1 µm, we only need $\gamma \sim 50$ to obtain a fundamental wavelength in the Ångström range. For this reason the electron energy is two

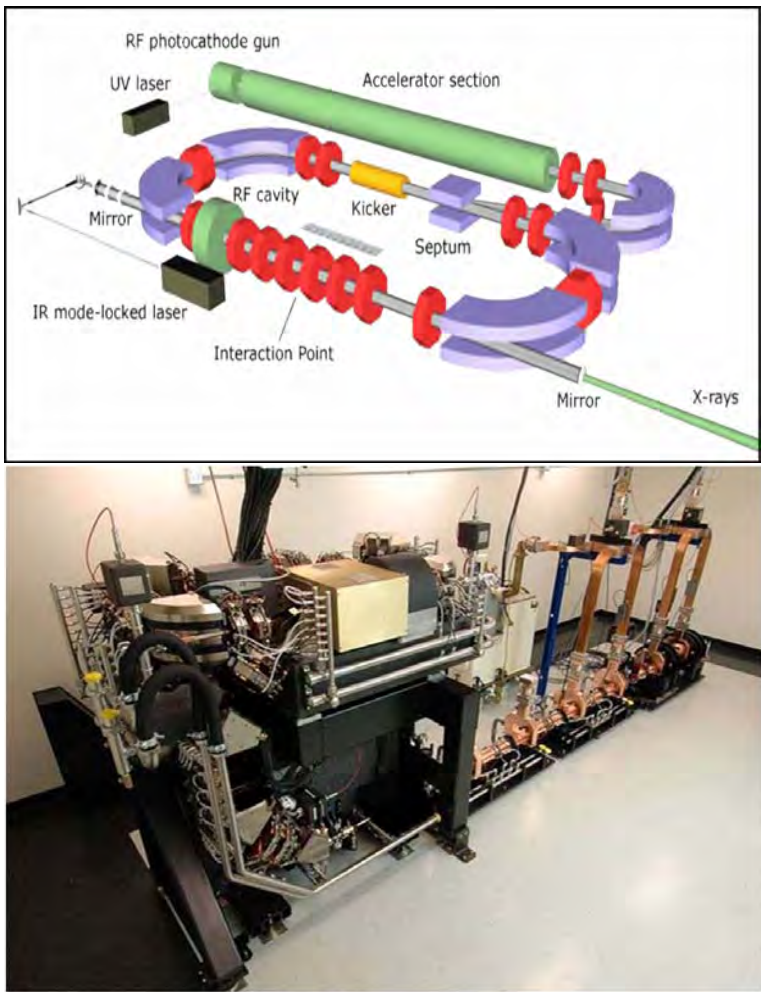

Figure 3.2: Top: Schematic layout of a compact, laser-driven, synchrotron X-ray source. Bottom: Photograph of the currently existing prototype at Lyncean Technologies/US. The main components are a linear electron accelerator, an electron storage ring, and a resonator laser cavity, in which X-rays are produced by a Thomson (or inverse Compton) scattering process of the electrons with the laser pulses.

orders of magnitude lower than that at large-scale synchrotron facilities. This allows the BRIX storage ring to be scaled down to a few meters in circumference, making it feasible for use in a conventional laboratory or for clinical use. The currently existing protoype (see Fig. 3.2) can be operated at an electron energy of up to 45 MeV, yielding X-ray energies of up to 35 keV with 3% energy bandwidth.

Phase-contrast X-ray imaging

Based on the availability of a first prototype source, we have carried several experimental campaigns during the last two years at the prototype test facility installed at Lyncean Techologies (CA, USA). While there exists a number of different phase-contrast imaging techniques (including propagation-based imaging, analyzer-based imaging, and crystal interferometry), we have focused specifically on a recently developed approach based on X-ray optical gratings [15–18]. This is mainly because this novel approach is the most promising method for use with both a

large field-of-view (> 10 cm) and with an X-ray bandwidth of 3–5%, as expected from compact synchrotron sources.

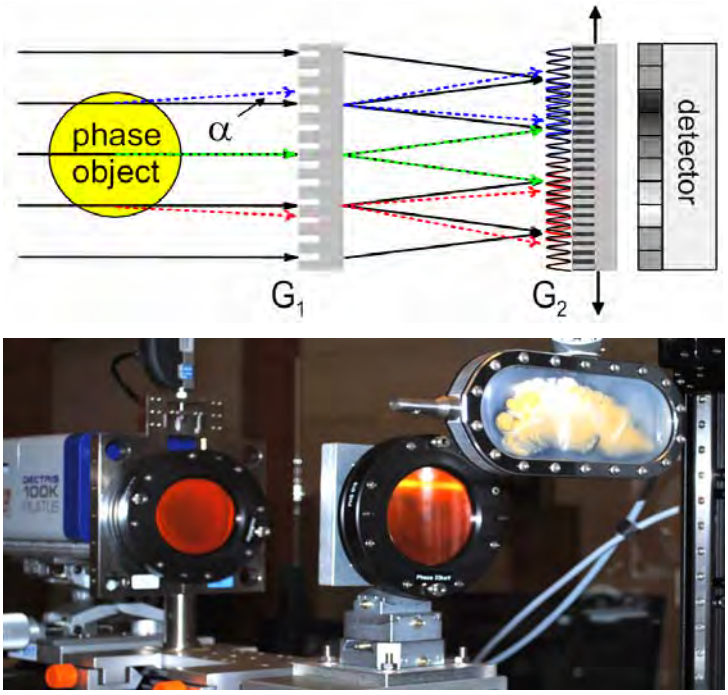

Figure 3.3: Top: Setup for differential phase-contrast imaging with a grating interferometer. Bottom: Photograph of an actual experiment, carried out at a compact synchrotron light source.

A setup for grating-based phase-contrast imaging essentially consists of a phase grating G_1 and an analyzer absorption grating G_2 (Fig. 3.3). The image formation process is similar to differential interference contrast (DIC) microscopy used in a visible light microscope. It essentially relies on the fact that a phase object placed in the X-ray beam path causes a slight refraction of the beam transmitted through the object. In our setup the measurement of the small deflection angles is achieved by the arrangement formed by G_1 and G_2. Most simply, it can be thought of as a multi-collimator translating the angular deviations into changes of the locally transmitted intensity, which can be detected with a standard imaging detector. In addition to phase-contrast images such a grating-based setup can be used to record X-ray dark-field images [18].

For the experiments described further below, we have used a grating system consisting of a phase grating G_1 with 3.96 µm pitch, and an absorption grating G_2 with 2.00 µm pitch. We used a distance of 22 mm between the two gratings, corresponding to the first fractional Talbot distance [21]. The distance of the setup from the source was $L = 8.65$ m. The protoype compact synchrotron light source was operated at an X-ray energy of 13.5 keV (Fig. 3.2) and 20 keV, with an rms energy spread of 2%. The angular divergence of the X-ray beam was limited to ±2 mrad by a cylindrical aperture. For each data set, nine phase steps were performed over two grating periods, yielding nine images from which the absorption, differential phase and dark field images were calculated (see [18] for more details). Each image was recorded with an exposure time of ~ 5 s, hence the total exposure time was 45 s per data set. All images were recorded on a MAR CCD detector with square pixels of 78×78 µm^2.

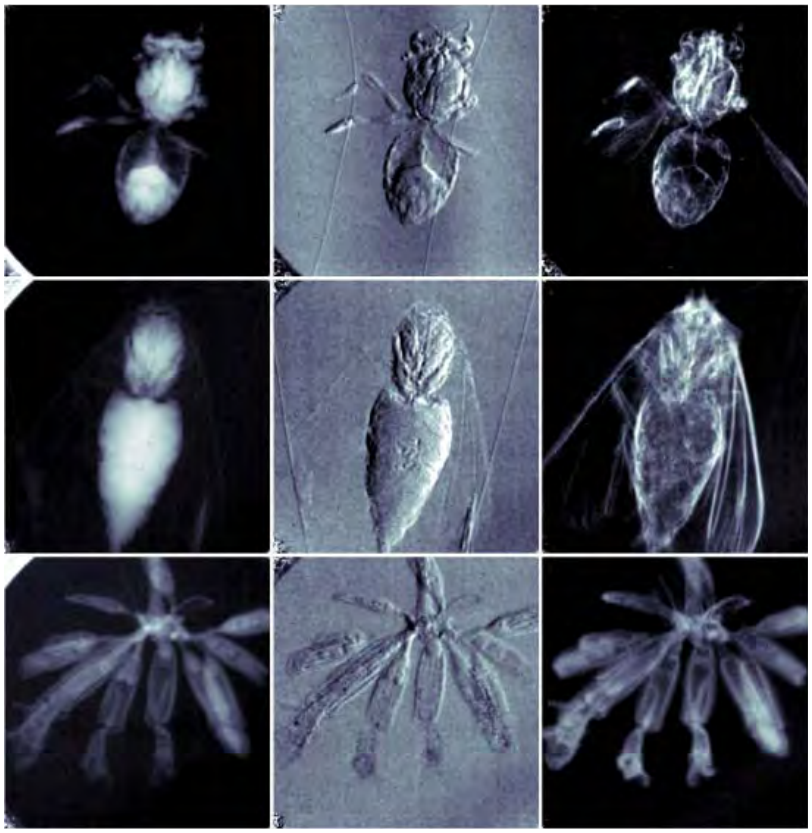

Figure 3.4: The first proof-of-principle X-ray images of several small test samples (top row: a bee, middle row: a moth, bottom row: a flower), recorded with a laser-driven, compact synchrotron prototype machine during an experiment at Lyncean Technologies/US in 2008. The conventional absorption image is shown on the left, the phase-contrast image in the centre, and the dark-field image on the right (see [21] for more details).

Experimental results

Figure 3.4 shows three types of images obtained from one raw data set for three different test samples (two insects and a flower): (a) absorption contrast, (b) differential phase-contrast and (c) dark-field image. We can clearly observe that the three types of contrast supplement each other well, as each image shows details different from the others.

Another example, which particularly highlights the potential of the method for future medical applications in clinical phase-contrast mammography is shown in Fig. 3.5. An American College of Radiology (ACR) mammographic accreditation phantom was imaged using absorption, phase contrast, and dark field imaging. The images in Fig. 3.5 show the tumor and spiculation models comparing absorption contrast to the other contrast mechanisms available using grating-based phase-contrast and dark-field imaging. The phantom consist of mainly three different types of features, namely nylon fibers (to simulate breast ducts), 'tumor like masses' (to simulate compact tumors), and 'specks' (to simulate micro-calcifications). While the 'specs' are nicely resolved in the absorption image (upper left panel), we interestingly learned that our dark-field imaging modality (upper right panel) highlights particularly the tumor-like masses. We hypothesize that this is essentially due to the fact that dark-field imaging measures the local integrated small-angle scattering power of the sample. The phase-contrast image (lower right

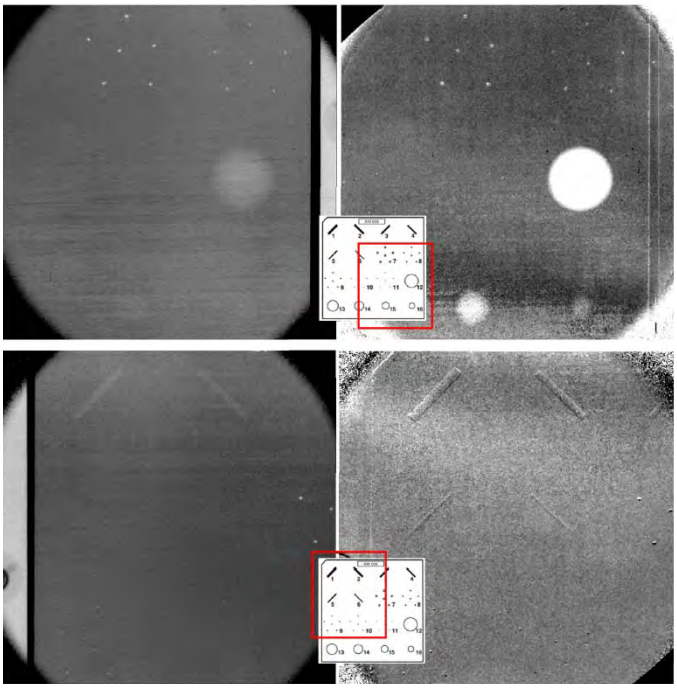

Figure 3.5: Mammography phantom imaged at a compact synchrotron source (GAMMEX 156). Top left: absorption image, top right: dark-field image: showing increased contrast for the so-called 'tumor-like masses'; lower left: absorption image; lower right: phase-contrast image, showing increased contrast of the nylon-fibres, simulating ducts in the breast.

panel), on the other hand, is superior to the conventional absorption image (lower left panel), when it comes to detecting the nylon fibers in the phantom. This can be explained by the fact that phase-contrast imaging enhances particularly high spatial frequencies, i.e., edges or boundaries of objects.

Finally, Fig. 3.6 reports the first micro-CT results obtained at a compact synchrotron source. The images show volume rendered images of the reconstructed CT data set, which was aquired

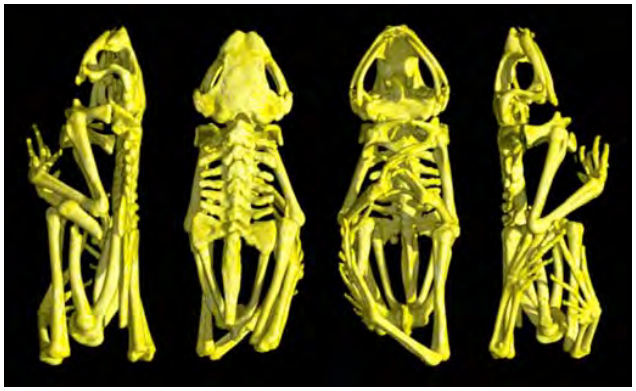

Figure 3.6: Three-dimensional renderings of a first reconstructed tomography data set recorded at the laser-driven compact synchrotron X-ray source.

by rotating the sample around 360 deg at interval angles of 1 deg. The raw projection images were pre-processed into quantitative projection images of the specimen and subsequently reconstructed into a 3D volume data set using an optimized filtered back-projection algorithm developed for grating-based CT [17].

Benchmarking

To further evaluate the potential of biomedical phase-contrast imaging with future compact sources of increased brilliance, we have performed benchmarking experiments using highly brilliant large-scale synchrotron sources (e.g. ESRF/Grenoble). One such result is displayed in Figs. 3.7 and 3.8, and concerns experiments on a rat brain bearing a gliosarcoma (see also [16]). Figure 3.7 shows several three dimensional renderings of the reconstructed phase-contrast volume data set, and cleary demonstrate the improved sensitivity of the method.

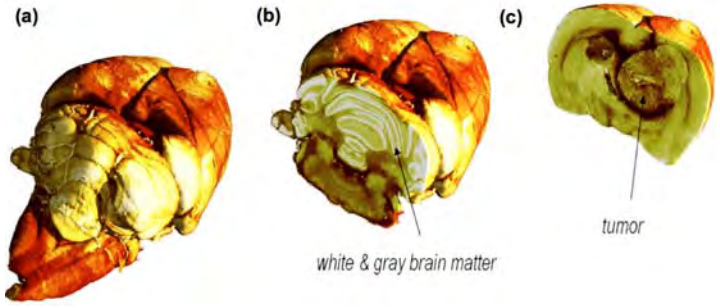

Figure 3.7: Phase-contrast micro-tomography images of a rat brain, recorded with a 3rd generation sycnchrotron source (ESRF/Grenoble). The sample was a formalin-fixated rat brain bearing a 9L gliosarcoma (see [16] for more details).

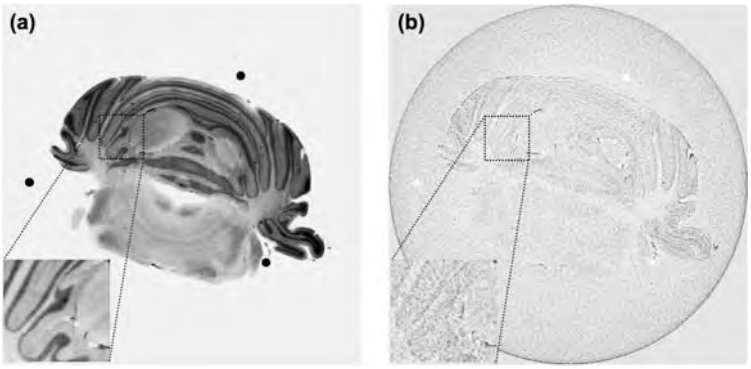

Figure 3.8: Comparison between absorption-contrast and phase-contrast micro-tomography results of a rat brain, recorded with 3rd generation sycnchrotron source (ESRF/Grenoble). (a) Phase-contrast micro-tomography slice through the rat's cerebellum showing a clear contrast between the white and gray brain matter and (b) corresponding slice through the absorption-based reconstruction of the specimen (see [16] for more details).

Figure 3.8 shows tomographic image slices through the brain region containing the rat's cerebellum. In the phase tomography reconstruction (Fig. 3.8a), we can clearly observe good contrast between the brain's white and gray matter, whereas this is hardly possible on the absortion data set (Fig. 3.8b).

Future

Following the initial exploitation of the exisiting prototype and its optimisation, further developments in the direction of MegaWatt laser resonator cavity systems and higher electron beam energy (> 100 MeV) in the storage ring could be anticipated in ELI. This would open the door to clinical diagnostics applications in the X-ray energy range of 80–150 keV and potentially even allow for advanced radiation treatment procedures, such as micro-beam radiation therapy using X-ray energies in the range of a few hundred keV.

Bibliography

[1] Murphy DB. Fundamentals of Light Microscopy and Electronic Imaging (Wiley John & Sons, New York, 2001).
[2] von Ardenne M., Z. tech. Phys 19:407–416 & Z Phys 1938;109:553–72.
[3] Ramberg EG., J Appl Phys 1949;20:441–4.
[4] Bonse U, Hart M., Appl Phys Lett 1965;6:155–6.
[5] Fitzgerald R., Physics Today 2000;53:23–7.
[6] Momose A., Jap J Appl Phys 2005;44:6267–355.
[7] Pagot E, Fiedler S, Cloetens P, Bravin A, Coan P, Fezzaa K, et al., Appl Phys Lett 2003;82:3421–3.
[8] Levine LE, Long GG., J Appl Cryst 2004;37:757–65.
[9] Ando M, Hashimoto E, Hashizume H, Hyodo K, Inoue H, Kunisada T, et al., Nucl Inst Meth A 2005;548:1–16.
[10] Shimao D, Sugiyama H, Kunisada T, Ando M., Appl Rad Isot 2006;64:868–74.
[11] Davis TJ, Gao D, Gureyev TE, Stevenson AW, Wilkins SW., Nature 1995;373:595–8.
[12] Ingal VN, Beliaevskaya EA., J Phys D 1995;28:2314–7.
[13] Chapman D, Thomlinson W, Johnston RE, Washburn D, Pisano E, Gmuer N, et al., Phys Med Biol 1997;42:2015–25.
[14] Beckmann F, Bonse U, Busch F, Gunnewig OJ., J Comput Assist Tomogr 1997;21:539–53.
[15] Pfeiffer F, Weitkamp T, Bunk O, David C., Nature Phys 2006;2:258–61.
[16] Pfeiffer F, Bunk O, David C, Bech M, Le Duc G, Bravin A, et al., Phys Med Biol 2007;52:6923–30.
[17] Pfeiffer F, Kottler C, Bunk O, David C., Phys Rev Lett 2007;98:108105.
[18] Pfeiffer F, Bech M, Bunk O, Kraft P, Eikenberry EF, Broennimann C, et al., Nature Mat 2008;7:134–7.
[19] Huang Z and Ruth RD., Phys Rev Lett 2998; 80: 976–979.
[20] Loewen RJ., A Compact Light Source: Design and Technical Feasibility Study of a Laser Electron Storage Ring X-ray Source, SLAC Report (Stanford University, USA, 2003), p. 632.
[21] Bech M, Bunk O, David C, Ruth R, Rifkin J, Loewen R, Feidenhans'l R, Pfeiffer F., J Sync Rad 2009; 16: 43–47.

3.2 Material sciences

Material sciences have come to extremes: while many static material properties are defined by the collective behaviour of electrons and atoms in a solid, on the ultrafast time scale, highly non-equilibrium conditions in condensed matter can be achieved. The primary response of materials to optical excitations is electron dynamics on the attosecond timescale. The subsequent structural response is driven and controlled by this transient, non-equilibrium electronic structure. The ultrashort and ultraintense light sources that will be available at ELI allow for unprecedented studies of primary attosecond electron dynamics as well as for the generation of controlled extremely short-lived states of matter, which will enable us to study the complex interplay between electronic and structural dynamics. Fundamental processes on these extreme timescales start to play a role in electronics and other applications of material sciences.

3.2.1 Attosecond electron dynamics

Fundamental electronic effects in condensed matter occur on the attosecond timescale. In the following, a few examples shall be given where intense attosecond extreme-ultraviolet and X-ray pulses will enable new insight into ultrafast material phenomena [1, 2].

Time-resolved view of many-body response in condensed matter

When comparing electron binding energies from stationary photoemission experiments on isolated atoms with one-electron energy levels of the unperturbed particle obtained from one-electron calculations, significant differences appear, in particular for localized initial states. This effect, known as intraatomic relaxation, is a manifestation of the many-body response to the creation of the vacancy and is caused by the rearrangement of the ion's electron distribution. As a result, the total energy of the ion is decreased and the kinetic energy of the photoelectron is increased. Coulombic and exchange energy also contribute to the observed increase in kinetic energy. For incomplete relaxation, part of the excess energy remains in the ion as a bound or continuum excitation, and additional shake-up or shake-off satellites are observed besides the main photoemission peaks. For molecules or solid compounds, this satellite structure can be very rich due to contributions of local and non-local excitations (e.g., plasmons), and charge transfer between the atomic constituents of the compound. How fast do these screening processes proceed? Calculations indicate that the dynamics can be divided into two parts: For *short* times, i.e., less than one half of a plasma frequency oscillation period, the electrons react ballistically as independent particles. For *long* times, collective oscillations with the plasma frequency are encountered [3]. For all metals these dynamics proceed in the sub-femtosecond regime due to their corresponding plasma frequencies. So far, time-resolved measurements have only been possible for semiconductors with very low electron density, small plasma frequency and correspondingly slow screening dynamics [4]. Intense attosecond light pulses with photon energies beyond 100 eV will allow direct time-resolved views on these fundamental many-body effects in condensed matter.

Charge transfer dynamics and resonant photoemission

Lifetimes of inner shell levels can be very short. For those with large binding energies or those decaying via Coster-Kronig or super-Coster-Kronig processes, lifetimes are well below one femtosecond. Lifetime-broadened maxima are observed in kinetic energy spectra for the photoelectrons as well as for the decay electrons. We note, however, that these homogeneous broadenings are correlated. For all decay processes with a final state of well-defined energy, e.g. the ground state of a doubly charged ion, and no further inelastic channels, energy conservation can only be violated for the (short) lifetime of the intermediate core-ionized state; it has to apply between initial (ground) and final (doubly ionized) state. In other words, a positive

energy shift ($+\Delta$E) of the photoelectron is compensated by $-\Delta$E of the decay electron. It has been convincingly demonstrated by coincidence experiments that excitation and de-excitation are coherent processes. Unfortunately, coincidence experiments are very difficult to carry out, due to the very large background counts from solids. It is much easier to start with a *bound* core *resonance* instead and excite it with narrow-band radiation. If the resonantly excited electron does not exchange energy with its environment during the lifetime of the core hole, the energy of the decay electron disperses linearly with the excitation energy. The decay electron spectrum resembles the off-resonant photoemission spectrum, with one-hole states and one-hole two-electron states, however with different relative amplitudes [5]. For molecules, which may be vibrationally excited in the intermediate as well as in the final state, this dispersion rule holds strictly only within one set of vibrational quanta; interesting redistribution processes among the vibrations are observed by detuning the initial excitation within the resonance. This coherent process, which is termed Resonant Photoemission or Auger Resonant Raman Effect, is a very powerful tool for investigations of ultrafast charge delocalization dynamics on surfaces. Particles bound to surfaces or other molecules are not isolated. They can exchange charge and energy. If the status of the resonantly excited electron is changed during the lifetime of the core hole by interaction with the environment, the coherence of excitation and de-excitation noted above is lost. Particularly, delocalization of the resonance electron into a continuum, e.g., into unoccupied electronic states of the substrate, converts the shape of the decay spectrum from resonant into normal Auger (see Fig. 3.9).

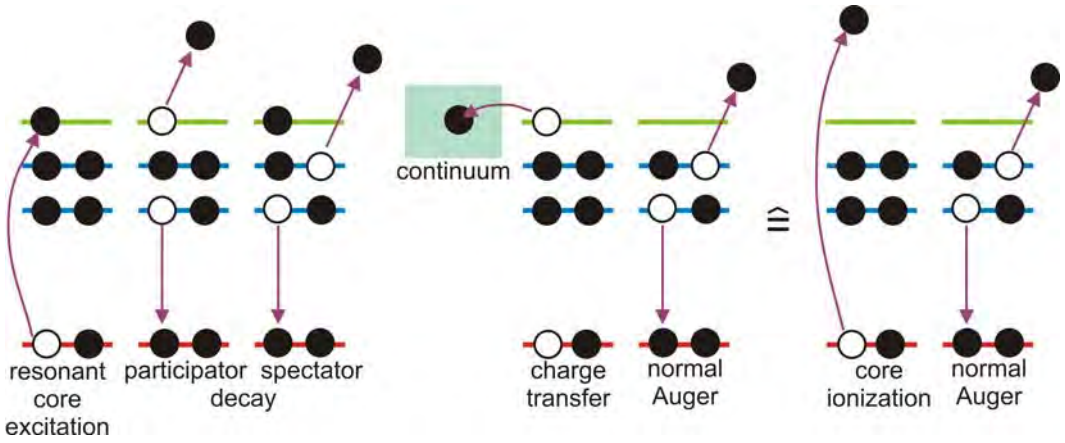

Figure 3.9: Principle of measuring charge delocalization by core-hole clock spectroscopy. Inner shell levels are indicated in red, occupied outer shell/valence levels in blue and unoccupied levels in green. Core excitons (right) decay via participator or spectator processes if the lifetime of the resonance is longer than the lifetime of the core hole. If the delocalization of the resonantly excited electron is faster than core decay, normal Auger is observed as for primary core ionization (left) [from [1]].

In many cases both contributions can be well separated. Combined with the known lifetime of the core hole, the ratio of the integrated intensities of these two channels yields the charge delocalization time. So far, the core-hole clock method is the only method making charge delocalization and transfer times in the attosecond range accessible [6], the time range characteristic for charge transfer between strongly coupled adsorbates and their substrates. However, the core-hole clock method has some disadvantages. Most severe is that core levels of appropriate lifetime may not be available for the surface particles of specific interest. Moreover, one has to keep in mind that core ionization increases the effective atomic number from Z to Z + 1 and therefore changes the chemical behaviour of the atom during the lifetime of the core hole. It should also be noted that the core-hole clock method provides an atomically localized probe of the dynamics

of valence electron wavepackets. In case of molecular adsorbates with spatially extended valence state wavefunctions, the core-hole clock method is not capable to distinguish intramolecular charge delocalization from heterogeneous electron transfer without further geometrical and/or energetic information.

Future experiments with attosecond pulses can overcome these limitations and provide direct information on the attosecond evolution of atomic and molecular charge distribution at surfaces.

Scattering experiments and dynamics of band structure build-up. Atomic and molecular orbitals of particles condensed into the solid state interact, forming energy bands with energy values depending on the electrons' momenta. However, as for the collective behaviour in the screening example, a few scattering events are necessary for the electrons to probe the structure of their environment in order to form bands. On a very short time scale, we can assume that the electrons "do not know" about the solid's structure or the corresponding electronic band structure. Theoretical investigations and experiments on charge transfer during scattering of fast ions at surfaces confirm this. Neutralization of negative ions probes the unoccupied, that of positive ions the occupied density of states at the surface. For crystalline materials, the density of states varies strongly with energy showing maxima, minima and gaps. As a result, charge transfer rates should vary depending on the energetic positions of the projectiles' ionization or affinity levels. Theory and experiment show that the signature of the band structure in the charge transfer rates vanishes for increasing particles energies, corresponding to decreasing interaction times. Future experiments with attosecond light pulses promise to provide a time-resolved view of these fundamental effects.

3.2.2 Materials behaviour at intense electromagnetic fields

Electromagnetic excitations may be broadly classified by their field strengths or intensity (field strength squared) and time duration and/or frequency. For materials, a useful reference is provided by the bonding "field" experienced by valence electrons, which is of the order of 1 V/atom, corresponding to a field strength of $\sim 10^{10}$ V/m. Characteristic time scales in solids are set by nuclear motions (> 100 fs) and valence electron motions (~ 1 fs). With our present and future capabilities to create electric fields that exceed the bonding fields and span a large frequency range from terahertz or picosecond fields to X-ray or attosecond fields we are entering new regimes of experiment and theory that go well beyond our present knowledge. This will require the development of new theoretical approaches that include dynamic field effects.

Femtosecond optical excitation of materials coupled with new probe sources capable of atomic-scale (attosecond) resolution opens up new possibilities for elucidating the fundamental structural and dynamical properties underlying nanoscale materials at extreme conditions, as illustrated in Figure 3.10.

Atomic-scale rearrangements and synthesis of new structural forms may be enabled by the ability to characterize and capture snapshots of the transient states induced by high temperature and/or high pressure. It is largely unknown how phase diagrams on the nanoscale are modified. Techniques are required for traversing and accessing new regions of the phase diagram that are impossible to reach with present steady-state methods. This may be achieved through direct optical excitation of materials as well as through the generation of shock waves that rapidly traverse the material to be studied, both requiring transient techniques to characterize the structural evolution. Such studies are also critical for discovering new pathways for synthesis of materials of enhanced stability and strength. Other key questions, with an eye on both fundamental and applied research, are: "How do complex phases involving spin-orbital-charge order respond to excitation with light? Why are strongly correlated electron systems so sensitive to photo-stimulation? How do these dynamic processes evolve in time? Can one put them to good use?"

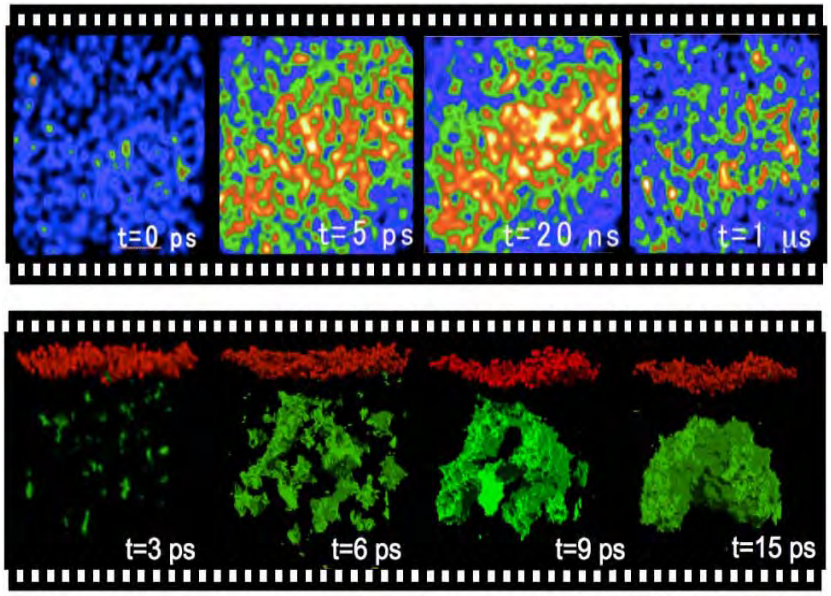

Figure 3.10: Top: Raw X-ray diffuse scattering measurements capturing the nucleation of nanoscale voids in optically excited semiconductors in real time. Bottom: molecular dynamics (MD) simulations showing the formation of nanoscale voids beneath the surface, supported by the experimental data. [Source: A. Lindenberg], reproduced from "Science and Technology of Future Light Sources a White Paper", 2008 editors Arthur L. Robinson (LBNL) and Brad Plummer (SLAC).

Insight into the fastest processes in materials will have a huge impact on the future developments in material sciences. For investigating and understanding these processes the attosecond time structure of the ELI light sources is highly desired and needed. Especially, attosecond pulses at photon energies in the keV range as will be provided by ELI are a key for future success in material sciences at the extremes.

Bibliography

[1] A.Cavalieri, F. Krausz, R. Ernstorfer, R. Kienberger, P. Feulner, J. Barth, D. Menzel, "Attosecond Time-Resolved Spectroscopy at Surfaces", in "Dynamics at Solid Surfaces and Interfaces, Vol.1", U. Bovensiepen, H. Petek, M. Wolf (eds.), (Wiley-VCH, 2010).
[2] A.L. Cavalieri et al., Nature **449**, 1029 (2007).
[3] A. Borisov, D. Sánchez-Portal, R. Díez Muiño, and P.M. Echenique, Chem. Phys. Lett. **397**, 95 (2004).
[4] R. Huber, F. Tauser, A. Brodschelm, M. Bichler, G. Abstreiter, and A. Leitensdorfer, Nature **414**, 286 (2001).
[5] E. Jensen, R.A. Bartynski, S.L. Hubert, E.D. Johnson, and R. Garrett, Phys. Rev. Lett. **62**, 71 (1989).
[6] W. Wurth and D. Menzel, Chem. Phys. **251**, 141 (2000).

3.3 Biological imaging with ELI's intense and ultra-short X-ray pulses

Theory predicts that with an ultra-short and very bright coherent X-ray pulse, a single diffraction pattern may be recorded from a large macromolecule, a virus, or a cell before the sample explodes and turns into a plasma. The over-sampled diffraction pattern permits phase retrieval and hence structure determination. The interaction of an intense X-ray pulse with matter is profoundly different from that of an optical pulse. A necessary goal at ELI is to explore photon-material interactions in strong X-ray fields. The aim in structural biology is to step beyond conventional damage limits and develop the science and technology required to enable high-resolution studies of single biological objects near the physical limits of imaging. Eligible targets include nanocrystals, cells, cell organelles, single virus particles and isolated macromolecules. The challenges engage an interdisciplinary approach, drawing upon structural sciences, biology, atomic and plasma physics, optics and mathematics. The potential for breakthrough science is great with impact not only in biology or physics but wherever dynamic structural information with high spatial and temporal resolution is valuable. The overall relevance of such a program at ELI extends beyond basic science, to technologies of essential importance to a future Europe.

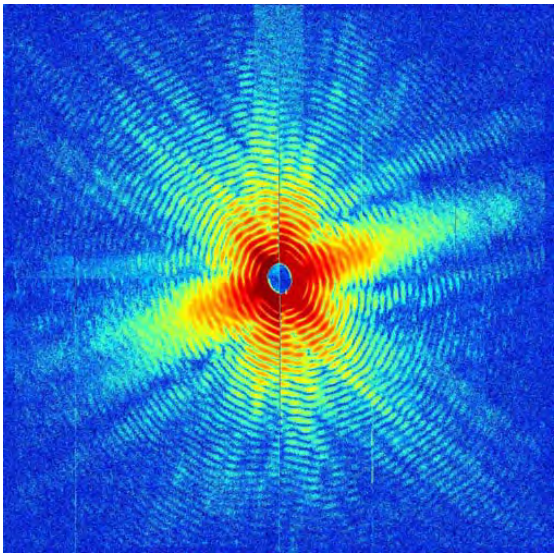

Figure 3.11: Diffraction pattern from a single mimivirus particle captured at the Linac Coherent Light Source with a single 60 fs long X-ray pulse at 2 keV photon energy.

Biological imaging at or near atomic resolution is probably the most challenging of all experiments that have been proposed for X-ray lasers, and it requires a detailed understanding of photon-material interactions on ultra-short time scales at very high X-ray intensities. *Radiation damage* limits the resolution in all imaging experiments. Damage is caused by energy deposited into the sample during exposure. Cooling can slow sample deterioration, but it cannot eliminate damage-induced sample movement during measurements. Theoretical studies and simulations based on molecular dynamics [1–3], hydrodynamic plasma models [4], and particle plasma models [5] agree with each other, and predict that with a very short and very intense coherent X-ray pulse, a single diffraction pattern may be recorded from a large macromolecule, a virus, or a cell [6, 7] without the need for crystalline periodicity in the sample. A recent algorithm by Quiney and Nugent [8] derived from optical coherence theory and quantum electrodynamics, model the damage in the image-forming processes and we can therefore allow the sample to sustain far more damage and still recover it's structure.

The coherent diffraction pattern of a non-periodic object is continuous, and in principle, there is a direct way to determine the phases from the pattern for image reconstruction by

"over-sampling" [9–12]. Figure 3.11 shows diffraction from a single mimivirus particle and was obtained with a single 60 fs-long pulse of 2 keV radiation at the LCLS (the Linac Coherent Light Source at Stanford). Resolution in single-particle experiments does not depend on sample quality in the same way as in conventional crystallography, but is a function of radiation intensity, pulse duration, and wavelength, which are factors controlling ionisation and sample movement during exposure. *A three-dimensional data set* can be assembled from such diffraction patterns when copies of a *reproducible sample* are exposed to the beam one by one in random orientations [13, 14]. Damage can be distributed over many copies of the sample in a similar manner as in "single-molecule" electron microscopy or in crystallography. Diffraction data from reproducible objects can be enhanced by merging redundant data, and this should be possible even from very weak individual shots [15, 16]. Averaging (in a redundant data set) reduces the error in the signal by the square root of the number of patterns that sample the same pixel. The limiting factors here are the accuracy of the orientation information and heterogeneity in the sample population, both of which will blur the reconstructed image [8, 17]. With a *non-reproducible object*, there is no chance of repeating the experiment to improve the signal, and this creates a resolution gap between structures for reproducible and non-reproducible objects. The highest possible resolution in a *single* shot is not necessarily at the shortest possible wavelength. For an analysis see [6]. Experimental strategies are, therefore, different for high-resolution studies on reproducible and non-reproducible objects.

The first demonstration of coherent flash diffraction with an extremely intense and very short photon pulse was performed on 1 February 2006 at the VUV-FEL free-electron laser in Hamburg [18]. The FEL pulse produced an interpretable diffraction pattern from a non-periodic object, before destroying it at 60,000 K. The reconstructed image, obtained directly from the coherent diffraction pattern by phase retrieval through over-sampling (on the spot at the beam line), shows no measurable damage. Significant damage occurred only about 2 ps after the 15 fs long pulse had left the sample [19]. These results validate the general concept of flash diffractive imaging. Over the past few years, experiments at the SPPS (Short Pulse Photon Source, Stanford), FLASH (Hamburg), ALS (Advanced Light Source, Berkeley), and recently also at the LCLS at Stanford have allowed us to refine our concepts, and to identify new research opportunities. We have amassed a great deal of experience on how to acquire low-noise diffraction data with ultra-short pulses from objects in the gas, liquid, and solid phases. For instance, in our first experiments at the LCLS [7, 20], background scattering in the vacuum chamber did not exceed the read-out noise of the detectors nor the noise of the diffuse photon background. This is quite remarkable, considering that the number of photons in the pulse was nearly 100 billion times higher than this background. We have also developed analysis tools to generate two- and three-dimensional images from coherent diffraction data [17, 21], and developed new concepts in phase retrieval and holography [22]. We have explored the limits of imaging biological materials under the conditions of long-wavelength X-ray pulses at FLASH [23], and at shorter wavelengths at the LCLS [7].

Research opportunities at ELI

1. Studies on photon-material interactions. The dominant interaction of hard X-rays with atoms is through K-shell photoionisation. Relaxation of the resulting hollow ions proceeds through the emission of Auger electrons in light elements. Shake-up and shake-off excitations, initial- and final-state configuration interactions and interference between decay channels will modulate this picture. Electrons ejected from atoms cause further ionisation by eliciting secondary electron cascades in condensed materials. The thermal equilibration of a single 12 keV photoelectron releases 400–500 cascade electrons over a period of about 10 fs in a macroscopic sample. Conventional X-ray crystallography lives with this. With very short X-ray pulses available from ELI, most of these processes will have no time to develop.

Primary and secondary ionisations: With the advent of high-brightness FELs, instantaneous heating of uniform targets to well controlled mono-energetic states will become possible. We will be able to heat and probe a plasma on a time scale faster than the collisional and thermalisation time-scale. Such studies are important in creating and probing extreme states of matter [24,25] and they are also relevant to biology experiments on micron-sized objects, like cells [6]. Experiments will be performed on gases, solids and micron-sized biological objects. No measurement of this type has been possible so far with hard X-rays. This is new physics that will validate predictions and guide the development of atomic and molecular sciences in intense photon fields and lead to new biology.

Time-dependent X-ray absorption and scattering: Can photoionisation be suppressed? First experiments with hard X-rays at the LCLS show a significant drop in the photoelectric cross section of hollow atoms [26]. This effect was predicted [1] but it is larger than expected, and can already be measured with LCLS pulses of 20–80 fs duration. Photo-absorption decreased 20-fold in hollow neon to equal the cross-section of coherent scattering [26]. Ions with double core holes had extended life times. Ejection of the 1s electrons at the beginning of an intense and short pulse could practically stop photo-ionisation without significantly changing the elastic cross-sections of outer-shell electrons. We will study this effect and explore this phenomenon to avoid (or reduce) photoinisation for the duration of an ultra-short X-ray pulse. We expect the conventional handicap of X-rays over electrons in imaging to be reversed with ultra short pulses and made into a net gain over a broad range of sample sizes. A further factor to consider in suppressing photoemission is the expected adiabatic stabilisation of atoms in extremely intense and very high-frequency photon fields.

Experiments at ultra high energy densities. In an extremely intense photon field, electrons can be stripped from atoms. At optical frequencies, high-field effects become significant with power densities exceeding 10^{14-15}W/cm^2, where some of the new atomic physics and plasma physics phenomena have been observed. The high-field regime is unexplored at X-ray frequencies. Various estimates suggest that field ionisation becomes measurable at around 10^{22-23} W/cm^2, and relativistic effects will dominate at around 10^{26} W/cm^2. Before reaching these extremes, an adiabatic stabilisation of atoms can be expected [27]. The electron wave function has its maxima at the outer turning points. At high photon frequencies, the electrons quiver, the life-time of the initial state increases, and the harder one hits the atom the less it will become ionised – at least in principle. There is no consensus if one can avoid the "valley of death" on the way to stabilisation (see Figure 1 in [27]. This area is simply unexplored. New focusing optics and the pulse structure of ELI will allow us to get into this regime. In a recent study, we achieved better than 1 μm focus at FLASH [25, 28, 29]. A focal spot of 7 nm diameter has recently been reported with 20 keV X-rays from a synchrotron [30]. Combination of such optics with FELs would bring us deep into the high-field regime with hard X-rays.

An imaging concept for utilizing every scattered photon and emitted particle: We discovered characteristic signatures in the fragmentation of small protein molecules, suggesting that key features of the explosion are reproducible. The results show that the smaller the molecule, the more reproducible the explosion. In very large macromolecules, the anisotropy of the explosion is washed out by thermal effects and by a transition from Coulomb explosion to hydrodynamic expansion. Large samples scatter X-rays well but smaller objects have a 'visibility problem'. It is in these systems, where the reproducibility of the explosion is high, and this could be exploited to derive relative sample orientations from fragmentation patterns, e.g. through velocity map imaging with single ion sensitivity. This idea separates the orientation problem from the problem of a weak scattering signal, and extends photon-based imaging to the smallest of molecules (perhaps as small as oligopeptides, glyco-conjugates, or water). Some of the necessary methodology is described in Chapter 3.6. There is a chance to explore the nanoworld beyond the current horizon by measuring every particle and scattered photon.

2. Coherent diffractive imaging with X-ray lasers.
Sample injection and manipulation. Samples have to be delivered in a controlled manner under conditions where structural integrity can be preserved for the duration of the experiment. A highly efficient aerosol injector has been developed in Uppsala. The injector introduces living cells, viruses or biomolecules at reduced pressure into a beam of X-rays or electrons. In a recent experiment at the LCLS (Jan/Feb 2011), a hit rate of 43% was achieved with the aerosol injector giving 1.2 million hits on viruses in 36 hours.

Another type of injector uses a focused liquid jet of micron-submicron dimensions [20, 31]. The liquid jet produced 3 million hits on nanocrystals over five days of beam time [20]. These are world records, but the ratio between the number of particles hit over the number of particles that went between the pulses was only about 1 in 10^6 in these studies. While this is fantastic for most studies (consider the Avogadro number), this ratio needs to be improved for studies on "non-abundant objects" like chromosomes or isolated cell organelles where less than 100,000 copies of the target may be available. While improvements to the injector methods are crucial, the high repetition rate of ELI alone may bring the current system to within the required specifications.

The biological studies will start with large objects (nanocrystals, giant viruses, living cells), and move on, as the source and the imaging techniques develop to study smaller virus particles, isolated cell organelles, and ultimately, single macromolecules and complexes. Single-shot diffractive imaging with a table-top femtosecond soft X-ray laser-harmonics source has already been demonstrated [32].

Femtosecond X-ray protein nanocrystallography [20,33] is an area where significant advances can be expected early in the operation of ELI. X-ray crystallography provides the vast majority of macromolecular structures, but the success of the method relies upon growing crystals of sufficient size. Many macromolecules yield poorly diffracting crystals, even after extensive efforts. In conventional measurements, the necessary increase in X-ray dose to record data from nanocrystals leads to extensive damage before a diffraction signal can be recorded. We mitigate the problem of radiation damage in such measurements by using pulses briefer than the timescale of most damage processes and use this method for the structure determination of target proteins that form nanocrystals. It is particularly challenging to obtain large well-diffracting crystals of membrane proteins, for which less than 300 unique structures have been determined.

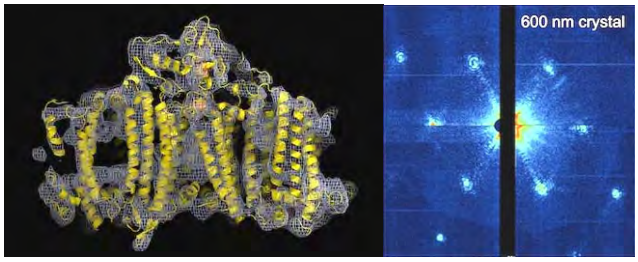

Figure 3.12: Electron density map of Photosystem I (left) derived from nanocrystals of this membrane protein (right). For more detail see text and reference [6].

We developed a method for structure determination where single-crystal X-ray diffraction "snapshots" are collected [20] from a fully hydrated stream of nanocrystals [31] using 70 femtosecond pulses from the LCLS. We tested this concept with nanocrystals of Photosystem I, a large membrane protein complex. Over 3 million diffraction patterns were collected in 5 days in this study, and a 3D data set was assembled from a subset of these exposures. The resulting structure is shown above [20]. Each nanocrystal was blown up by the pulse, but the data show no measurable damage and the structure is fully interpretable.

Structural studies on single non-crystalline objects [1, 23] (Figure 3.13). Mimivirus is one of the largest viruses and it is visible in an optical microscope. It is too big for a full three-

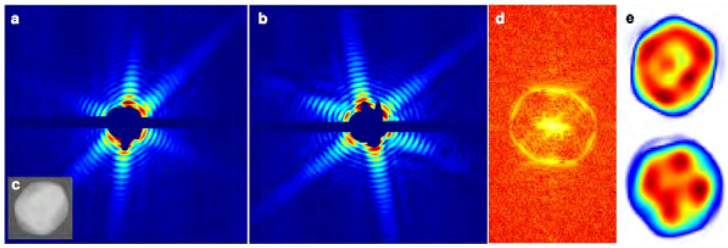

Figure 3.13: Diffraction patterns and reconstructed exit wave fronts (images) for mimivirus particles. For more detail see text and ref. [20].

dimensional reconstruction by electron microscopy [34], and its core is surrounded by fibrils, preventing crystallisation. Figure 3.13 shows diffraction patterns and the reconstructed exit wave front from two mimivirus particles injected into the FEL beam at the LCLS [7]. The diffraction patterns were recorded with 1.8 keV X-rays, 70 fs pulse length, 6.5×10^{15} W/cm^2 on the sample, and the patterns contained about 1.7 million scattered photons. (a,b) Diffraction patterns. (c) EM image. (d) Autocorrelation function for (a). (e) Reconstructions for (a,b). The reconstructions give a first glimpse at the structure of mimivirus in 2D projections [7]. In 36 hours of shooting time at the LCLS, running at 120 Hz, we obtained 1.2 million more hits on mimivirus recently. Some of the single shot exposures go out to 2 nm resolution. Signal averaging in a redundant data set will improve resolution further and a 3D reconstruction at high resolution may become possible.

Non-reproducible objects: Studies on living cells and cell organelles injected into the FEL beam

A Grand Challenge for the 21^{st} Century is molecular-level structural studies on a living cell, and a first step in this direction is to gain an understanding of key damage processes in micron-sized biological objects [6]. We have identified, selected and collected aquatic microorganisms of 0.5–2.0 micron size. Many of these are photosynthetic species from Arctic and Antarctic waters, *and have the same size as the giant mimivirus*. Tests show we can inject live cells into the vacuum chamber, and the cells remain viable.

We expect to reach sub-nanometer resolution with a pulse shorter than $\sim$ 10 fs, and ELI will be able to bring us there. Figure 3.14 shows a raw uncorrected diffraction pattern from a submicron-sized photosynthetic picoplankton injected into the LCLS recently. The middle of the picture is the pattern on the back-detectors and the left- and right-hand images are from

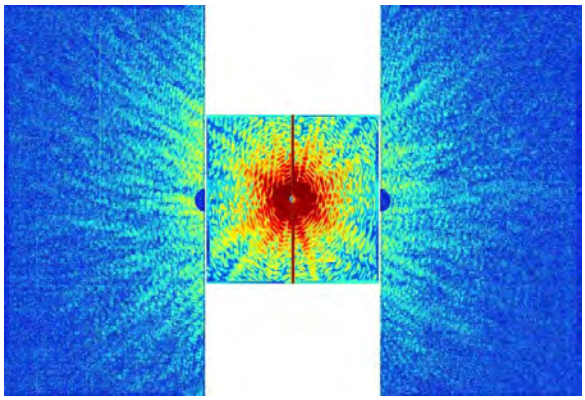

Figure 3.14: Diffraction patterns and reconstructed exit wave fronts (images) for mimivirus particles. For more detail see text and ref. [20].

the two front detectors where the signal extends to about 10–20 Å resolution. The cell was alive at the time it met the X-ray pulse.

From projection images to (almost) 3d structures Flash diffraction methods provide the highest possible resolution on a cell in a single shot. At X-ray wavelengths and at the scattering angles considered here, a single diffraction pattern contains depth information, and this information may be retrieved from the diffraction pattern by a numerical propagation of the complex-valued wave front [6,35–37]. Experimental procedures to gain depth information about the sample fall into two major categories: manipulating the wavelength, and manipulating the angle of illumination. ELI offers the possibility for both, including setting up simultaneous hits from two or three different directions, and this should be explored. Laser harmonics produce discrete-wavelength Laue diffraction, and this extends sampling.

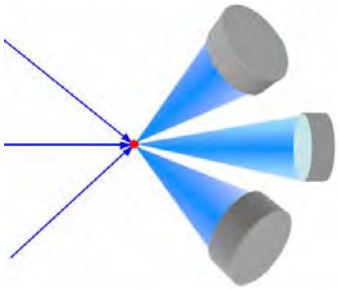

Figure 3.15: Simultaneaous illumination from three different directions. For details, see ref. [6].

Simultaneous illumination from multiple directions could provide a 3D view of the object and assure that significant damage does not develop during data collection. Methods have been proposed for obtaining three simultaneous projections of a target from a single radiation pulse [6]. ELI offers new possibilities here. Figure 3.15 shows 3 incident X-ray pulses illuminating the sample simultaneously. The timing of such pulses is a challenge, but not as critical as first thought: we know from our time-delay holographic measurements on sample explosions [19] that the explosion of micron-sized samples happens over a period of many picoseconds, following exposure to a 20 fs FEL pulse of 10^{14} W/cm^2. Timing of split X-ray pulses has already been achieved with better than 30 fs accuracy. While challenging, this approach is feasible. NIF brings together many more pulses onto a single target. In addition, the principal axes of a compact charge-density distribution can be derived from projections of its autocorrelation function, which is directly accessible from the individual diffraction patterns in this geometry. ELI offers possibilities for setting up simultaneous hits from three different directions. It can also provide laser harmonics for the extended sampling of the Fourier space.

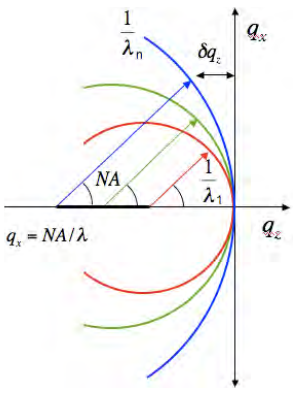

Figure 3.16: Laser harmonics can create discrete-wavelength Laue diffraction [6].

Laser harmonics and discrete-wavelength Laue diffraction for extended sampling. An additional avenue that can be explored to enhance the sampling of the reciprocal space is the possibility of using X-ray laser harmonics to create a "discrete-wavelength" Laue pattern (Figure 3.16). Following the first successful use of Laue diffraction in protein crystallography [38], the technique reached certain maturation. Developments in advanced detector technology (e.g. the pnCCD of [39]) allow the direct measurement of the energy distribution of the scattered radiation with good spatial- and energy-resolution.

Bibliography

[1] Neutze, R. et al., Nature 406, 752–757 (2000).
[2] Jurek et al., Eur. Phys. J. D, 29, 217–229 (2004).
[3] Jurek et al., Europhys. Lett., 65, 491–497 (2004).
[4] Hau-Riege et al., Phys. Rev. E 69, 051906, (2004).
[5] Timneanu, N., Caleman, C., Hajdu, J., van der Spoel, D., Chem. Phys. 299, 277–283 (2004)
[6] Bergh, M., et al, Quar. Rev. Biophys. 41, 181–204 (2008).
[7] Seibert, Ekeberg, Maia et al., Nature 470, 78–81 (2011).
[8] Quiney, H.M., Nugent, K.A., Nature Physics 7, 142–146 (2010).
[9] Bernal, J.D. et al., Nature 141, 523–524 (1938).
[10] Shannon, C. E., Proc. Inst. Radio Engineers 37, 10–21 (1949).
[11] Sayre, D., Acta Cryst. 5, 843 (1952).
[12] Fienup, J. R., Appl. Opt. 21, 2758–2769 (1982).
[13] Huldt, G., Szoke, A., Hajdu, J. Struct. Biol. 144, 219–227 (2003).
[14] Bortel G., Faigel G., J. Struct. Biol. 158, 10–18 (2007).
[15] Fung, R. et al., Nature Phys. 5, 64 (2009).
[16] Loh, N.T.D., Elser, V., Phys. Rev. E 80, 026705 (2009).
[17] Maia, F.R.N.C., et al., Phys. Rev. E 80, Article Number: 031905 (2009).
[18] Chapman, H. N., et al., Nature Physics 2, 839–843 (2006).
[19] Chapman, H.N. et al., Nature 448, 676–679 (2007).
[20] Chapman, H.N. et al., Nature 470, 73–77 (2011).
[21] http://xray.bmc.uu.se/hawk
[22] Marchesini, S., et al., Nature Photonics 2, 560–563 (2008).
[23] Seibert et al., J. Phys. B 43, Article Number: 194015 (2010).
[24] Nagler, B., Zastrau, U., Faustlin, R.R., et al., Nature Phys. 5, 693–696 (2009).
[25] Andreasson, J. et al., Phys. Rev. E 83, DOI: 10.1103/PhysRevE.83.016403 (2011).
[26] Young, L., et al., Nature 466, 56–U66 (2010).
[27] Pont, M., Gavrila, M., Phys. Rev. Lett. 65, 2362 (1990).
[28] Bajt, S. et al., Proc. SPIE 7361, 73610J1–10 (2009).
[29] Nelson, A. J. et al., Optics Express 17, 18271–18278 (2009).
[30] Mimura, H. et al., Nature Physics 6, 122–125 (2010).
[31] DePonte et al., J. Physics D-Appl. Phys. 41, 195505 (2008).
[32] Ravasio, A. et al., Phys. Rev. Lett. 103, 028104 (2009).
[33] Hajdu, J., et al., SSRL, SLAC, Stanford, USA, SLAC-R-611, (September 1, 2000).
[34] Xiao, C. et al., PLoS Biology 7, e1000092 (2009).
[35] Spence, J. C. H., Weierstall, U., Howells, M., Phil. Trans. R. Soc. Lond. A, 360, 875–895 (2002).
[36] Chapman, H. N. et al., J. Opt. Soc. Am. A 23, 1179–1200 (2006).
[37] Raines, K.S. et al., Nature 463, 214–217 (2010).
[38] Hajdu, J. et al., Nature, 329, 178–181 (1987).
[39] Struder, L. et al., Nucl. Instr. Meth. Phys. Res. A 614, 483–496 (2010).

3.4 Life Sciences

3.4.1 Ion Beam Therapy

Introduction

Besides surgery, radiation therapy is a key method for treating tumour patients with localized disease. Over the last years, advances in research and technology led to significant improvements in various fields of radiotherapy, resulting in higher cure rates and less side effects in normal tissue. The majority of radiation treatments for tumours in humans is currently done by ultra-hard X-ray beams generated by clinical linear electron accelerators. Within the last decade, the clinical interest in high-energy protons or heavier ions as a promising alternative has risen clearly (see for example [1–3]). Compared to the standard X-ray treatment, this particle or ion- beam therapy can deliver better dose distributions with less dose burden in normal, healthy tissue. The therapeutical use of ion beams was proposed by Wilson in 1946, and the first patients were irradiated in the 1950s and 1960s in the USA (Berkeley and Harvard), Sweden (Uppsala) and the former Soviet Union (Dubna and Moscow). Since then, more than 70 000 tumour patients have been treated with ions all over the world (85% with protons, 15% with heavier ions, mainly carbon). The number of ion beam facilities is increasing, and especially in the last few years several new hospital based ion accelerators started their operation (e. g. the Heidelberg Ion Beam Therapy Center HIT), while some more are under construction. Rather than the high energy physics laboratories, where the first patients were treated, these new therapy units are dedicated to medical applications only and provide a patient friendly environment, higher patient throughput and research facilities in the fields of oncology and medical physics. Turn-key solutions are available from several commercial vendors.

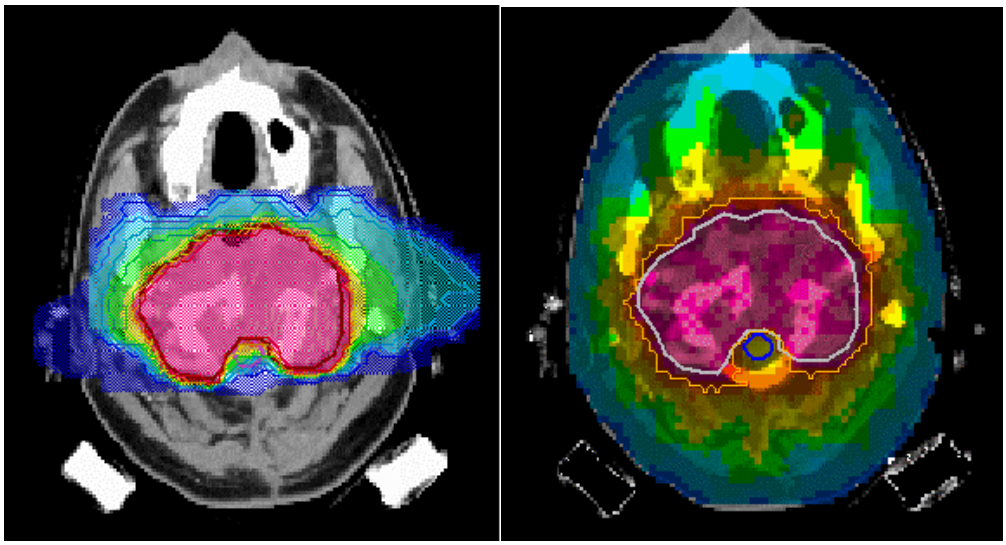

Figure 3.17: CT scan of a tumor in the head overlaid by a treatment plan giving the dose in a linear color-scale: a scanned carbon beam from two entrance ports (left) is compared to X-ray treatment plan using 9 entrance channels (right). In both cases a high tumor conformity can be achieved but ion beam treatment spares normal tissue to a larger extend.

Clinically, the main applications for low energy proton therapy are uveal melanoma and for high energy protons various paediatric tumours, chordomas and chondrosarcomas of the skull base and prostate tumors. Due to the lower integral dose in normal tissue, one could argue

that proton therapy (or ion therapy in general) is advantageous compared to photon irradiation in almost all situations (especially if the modern techniques of Intensity Modulated Particle Therapy IMPT are applied), although there are only very few clinical studies to confirm this. In any case, proton therapy has successfully been applied to many other tumour entities like those mentioned above as well as non-small-cell lung cancer, head-and-neck tumours and meningeomas. Heavier ions like carbon ions have the additional advantage of less lateral scattering and an increased biological effectiveness in the target volume compared to photons and protons. Up to now carbon ions were mainly used to treat chordomas and chondrosarcomas of the skull base, malignant salivary gland tumours and tumours in the lung, prostate, liver and soft tissue [7–9].

A major drawback of ion beam therapy is that the required technologies for ion acceleration (large scale cyclotrons or synchrotrons) and beam lines are complex and afford an investment of 100 to 200 Mio € for a therapy unit with four treatment rooms. As a consequence, this type of therapy is still limited to roughly 30 centres worldwide. Currently there are several approaches how to make this technology more compact and cost-efficient. Some commercial companies are working on compact, dedicated machines based on conventional accelerator technology, e. g. superconducting cyclotrons or compact synchrotrons for multi- or single-room therapy units. Alternative acceleration concepts are the so-called dielectric wall accelerator [10] and laser-based particle sources [11] as pursued by the ELI project. Compact laser-based therapy units could dramatically increase the availability of high-energy proton and carbon ion beams, and provide particle therapy to a broader range of patients. One huge advantage of laser based ion therapy units compared to conventional technology could be a compact gantry that does not need large and heavy bending magnets to deflect the ion beam. Instead, the laser beam would be guided by mirrors through a compact gantry structure to hit the target in the treatment room not too far from the patient.

At present, the achievable energies for laser-accelerated particles are not high enough for therapeutic applications, and the detailed properties (repetition-rates, fluxes, energy spectra, divergence etc.) of future beam are not precisely known yet. Therefore there are not even prototypes of such irradiation units available. Various groups (e. g. at the OncoRay centre in Dresden-Rossendorf/Germany, at the Munich-Centre for Advanced Photonics in Munich/Germany, and at the Photo-Medical Research Center in Japan) are currently investigating the required physical, technological and biological basis for laser-based radiation therapy with proton or carbon ion beams. Advanced treatment planning strategies were already developed to best utilize their specific properties (see e. g. [12]). A major milestone towards the therapeutic application of these new beams has been demonstrated by the first cell irradiations using laser-accelerated protons [13, 14]. With the progress on the physics side (e. g. the realization of the radiation pressure acceleration regime as an alternative to the target normal sheath acceleration mechanism), we expect higher energies being available soon. Here ELI can play a key role in providing high power lasers to explore the future potential of laser driven ion beams and their medical applications.

Ion beam therapy using conventional acceleration

Physical and biological characteristics

The main reason to use ion-beams for tumor therapy instead of photons is the inverse dose profile i.e. the increase of energy deposition with penetration depth up to a sharp maximum at the end of the particle range, the Bragg peak.

In the entrance channel corresponding to high energies the interaction of the projectile with the target atom and consequently the dose deposition is low. The maximum of interaction between projectile and target occurs near the end of range in the so-called Bragg maximum. In the Bragg maximum the ions have low energies at around 10–20 MeV/u and are still fully

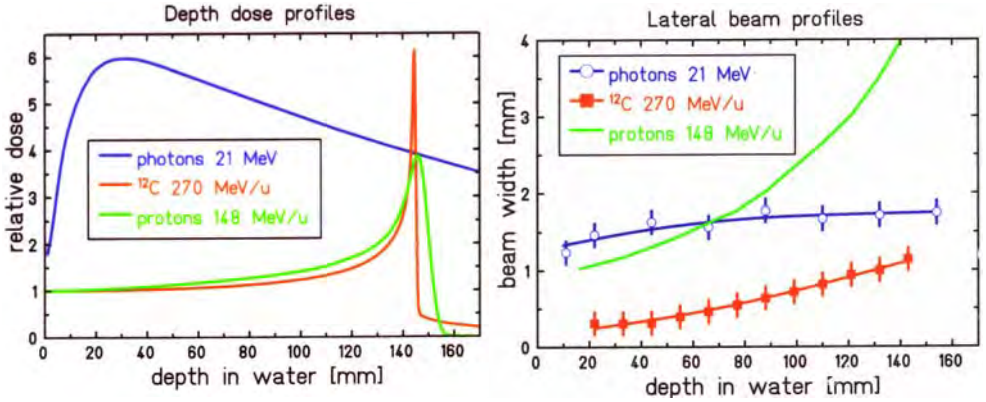

Figure 3.18: The measured dose as function of penetration depth is compared for photons, protons and carbon ions (left). The lateral scattering of these beams is given for the same penetration depth (right) [15, 16].

ionized but have a larger interaction time because of the low velocity. Then many electrons are liberated from the target atoms by the ions impact forming a very dense track with large local doses. This behavior is common to all ions but for the heavier ions the local doses in the Bragg maximum exceeds a level where by one ion track local clusters of double strand breaks are produced in the DNA. Then the quality of the biological lesion changes: for the heavier ions like carbon the production of double strand break clusters extends over the complete Bragg peak region. There the relative biological effectiveness (RBE) increases by a factor of 3–5 compared to the high energies in the entrance channel. In the clinical application, carbon ions have a 2–3 times greater biological effective dose in the target volume than protons but still a small effectiveness in the entrance channel. This larger RBE combined with a smaller straggling are the main reasons to use Carbon ions for therapy [17].

For the clinical application the lateral and longitudinal straggling parameters determine the overall conformity of the irradiated volume: The range-straggling broadens the individual Bragg curve and decreases the peak to plateau ratio. With increasing atomic number the Bragg peak becomes broader (Fig. 3.18), but the intrinsic width of the Bragg maxima is less important than the lateral scattering which translates into range uncertainties in the usually inhomogeneous target-volumes which are largest for proton beams [15].

In consequence the heavier beams like carbon produce the best overall confinement of the treated target volume compared to the planned target volume. Consequently the production not only of protons but also of the heavier carbon ions is still an important goal for any LDIA.

Passive beam spreading

Essential for the treatment-success is the conformity of the delivered dose to the target volume. The pristine beam from a synchrotron-accelerator has a small energy spread and a small divergence resulting in a beam spot of a few millimetres in diameter at the isocenter. These parameters are necessary for acceleration and transport but in order to cover an extended target volume of $100\,\mathrm{cm}^3$ or more the beam has to be enlarged, both in lateral and longitudinal direction. At present, most proton- and heavy ion-facilities use passive beam forming techniques which emerged from the dose shaping systems of the conventional X-ray therapy. In these techniques, the primary mono-energetic and sharp “pencil" beam is widened laterally by complex scattering systems that produce a beam having a flat top. Then using apertures the outer contours are shaped to the projected tumor-contours. In addition, the beam is modulated

in depth with ridge filters according to the maximum extension of the target volume: particles penetrating through the valleys between the ridges experience a smaller energy loss than particles that penetrate through the full ridge. In this way energy spread and consequently range variations are introduced to cover the target volume in depth with a homogenous dose distribution for protons or in case of carbon ions with a dose distribution shaped according to the RBE variation.

The shape of the wanted dose profile determines the shape of the ridge filter. So each filter covers not only a certain range variation but has also an intrinsic RBE acceptance.

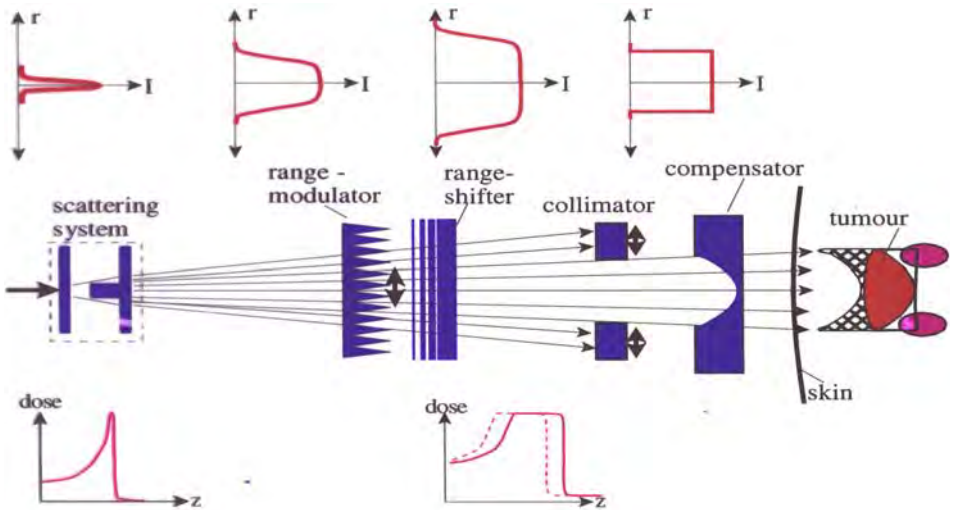

Figure 3.19: Principles of passive beam application: the pristine ion beam is widened laterally by a set of inhomogeneous foils that provide a flat top in the lateral profile. Range modulators produce the extension in depth. Collimators restrict the outer contours to the largest cross section of the target and compensators can be used to for the distal contours. A general review of passive beam shaping methods is given in [18].

Active beam delivery

Active shaping systems use the option of deflecting charged particles by applying magnetic fields and were introduced into clinical practice at PSI in Villigen for protons [19] and at GSI in Darmstadt for carbon ions [20].

The principles of active beam shaping are illustrated in Fig. 3.20. The target volume is dissected into layers of equal particle range: iso-energy layers. Using two deflecting magnets driven by fast power supplies, the "pencil beam" is scanned in a raster-like pattern over each layer, starting with the most distal one. After one layer has been painted, the energy of the beam and consequently the range is reduced and the next layer is treated. The beam may be delivered in discrete "spots" with minimal overlap along the raster path (PSI technique) or near-continuously in largely overlapping pixels as in a raster scan technique (GSI method). The intensity of the beam is monitored in 100 µsec intervals and the dose delivered at each location is controlled by monitors installed directly in front of the patient.

Although each layer has a different contour the shape of a target volume can be "filled" with high precision. In Fig. 3.21 a complete set of iso-energy slices of a patient treatment is shown: in the magnified panel the circles represent the calculated positions of the beam that are filled with the measured center of the beam. The beam diameter is larger than the circles and overlap

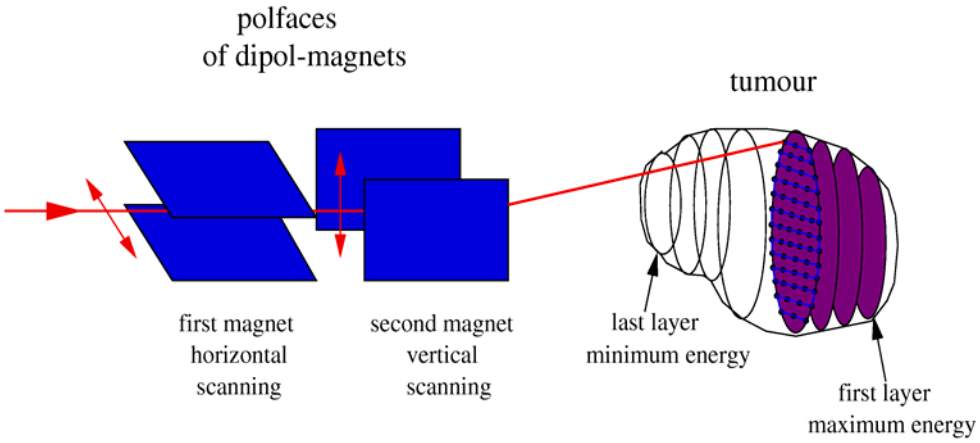

Figure 3.20: Principle of active scanning: the target volume is divided in layers of equal particle range and each layer is covered by a grid of individual pixels which are treated sequentially.

over many positions yielding a homogeneous distribution. The small slices of high or of low energy ions in the beginning and at the end of scanning are due to the density inhomogeneities of the tissue. Small areas of high density like bones have to be treated with higher energies to account for the small spots of higher energy irradiation. Vice versa, areas behind low density have to be filled with low energy particles.

Using cyclotrons, the energy variations have to be performed using passive degraders after which the beam has to be cleaned from the large energy spread. Then more than 95% of the primary beam is lost producing a large amount of neutrons. Using synchrotrons the energy can be requested step by step from the accelerator with the appropriate energy from pulse to pulse.

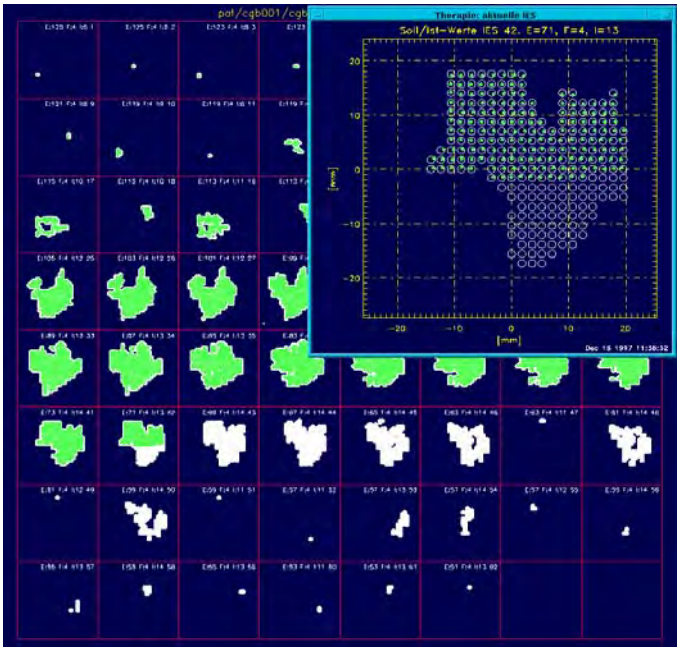

Figure 3.21: Compilation of the different range slices of a treatment volume.

In addition to accelerate the scanning procedure different intensities and beam diameters should be available pulse by pulse from the accelerator. In practice for an average target volume of 100 ccm 30–60 iso-energy layers are filled with 30–50 000 pixels which are painted with beam in 3–5 min. New developments at NIRS Japan could improve the total exposure time to $t < 20$ sec mainly by increasing the analysis time of the monitors in front of the patient. In the next step using an energy variable extraction from the synchrotron it seems possible to perform a complete exposure of one treatment field within less than 5 sec. This would be a very important achievement because it would allow treating targets subjected to motion e.g. from the lung. By using the usual "breath hold"technique of a few second these tumors could be treated with the extreme conformity like stationary targets. [36]

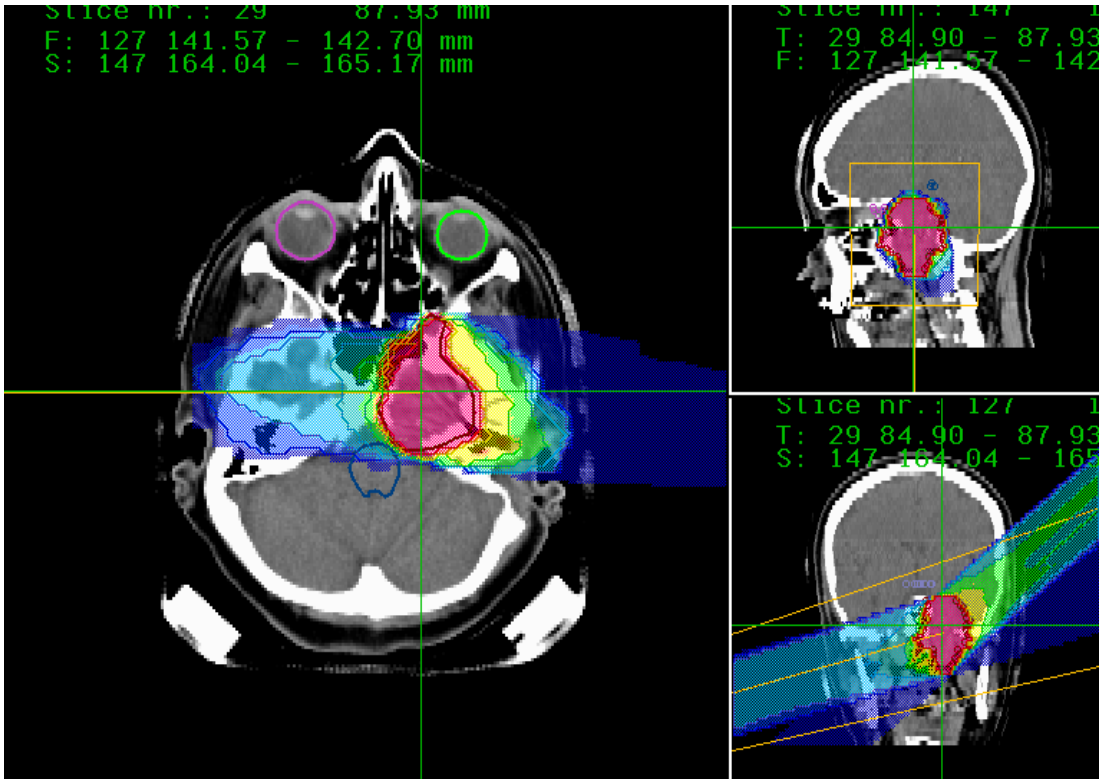

Figure 3.22: An optimized plan for a two field treatment is shown in three sections. A high conformity to the target volume is reached and simultaneously critical organs like the eye balls and brainstem are completely spared.

For this intensity modulated particle therapy (IMPT) the beam delivery, scanning and the accelerator form an interactive system, separate optimization of the individual components is not sufficient to get the system to the necessary performance; a fast interplay between all components from ion source to the scanning system has to be reached. Similar an LDIA based therapy system has to be regarded as one complex and it is not optimal to try to add a LDIA accelerator to an existing particle therapy unit as injector.

Parameters for a laser driven ion beam therapy unit

Laser accelerated ion beams have a quite different time and energy structure than conventional accelerators. Instead of trying to reproduce the energy and time structures of conventional

accelerators, one has to think of novel irradiation strategies for Laser Driven Ion Accelerators (LDIA)s. Until now, mainly continuous spectra with many low energetic protons and cut off energies up to 60 MeV have been measured. Although there is a very high bunch charge in every proton pulse, the repetition rate of the individual proton bunches is limited to the maximal laser pulse repetition rate and typically at most in the range of a few Hertz.

The maximum proton energy in the most established acceleration regime, the Target Normal Sheeth Acceleration (TNSA) [21] is linked to the laser intensity on target and scales with the square root of the intensity for laser pulses exceeding ≈ 150 fs (see Fig. 3.23 [23]). Extrapolating this to higher energies, the next generation of high power lasers exceeding the 1 PW level, should be capable of producing protons in a therapeutically relevant energy range of up to 200 MeV [22]. Proposed new schemes such as the Radiation Pressure Regime (RPA) [24, 25] and usage of under-dense plasma tragets [26], would boost the energies even higher.

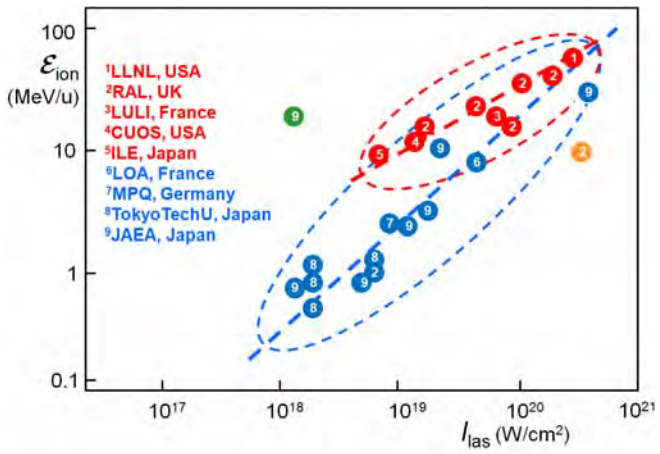

Figure 3.23: Collection of the maximum ion energies reached with different laser systems so far. Red circles correspond to long (ps), large scale ($E_{las} \gg$ J), single shot laser pulse irradiating thin foil solid targets. Blue circles correspond to short (fs), compact, high repetition rate laser pulse irradiating thin foil solid targets. The orange circle presents the results of a long-pulse, large scale ($E_{las} \approx$ J), single shot laser pulse irradiating a gas target [26]. The green circle presents results of short (fs), compact, high repetition rate laser pulse irradiating a gas-cluster target [38].

From Fig. 3.23 we see apparent advantage of using short pulse lasers due to their compactness and high repetition rate and more favourable ion energy versus laser intensity scaling compared to the long pulse lasers.

It is difficult to summarize the ion beam parameters required for ion beam therapy with LDIAs because these numbers depend very much on the type of beam application system like passive or active application. But in all cases the maximal energy should be of 250 MeV for protons and 430 MeV/u for Carbon ions. In order to treat a tumor of 250 ccm with a dose of 4 Gye particle fluences of 5×10^{10} for protons and 10^9 for Carbon ions are required.

The required particle flux, the repetition rate and dynamical range of control of the particle number per bunch depend on the dose delivery scheme: In the case of passive dose delivery, the repetition rate can be of the order of 0.1 Hz and the dynamical range of the particle number control of about 10. The energy spread of a 1–2% is sufficient because all the beam shaping will be done by absorbers. But at present, these passive devices produce a dose conformity which is worse than conventional X-ray IMRT. Because poor conformity increases the occurrence of severe side effect all the modern ion beam units are equipped with scanning systems.

For active dose delivery the situation is complex. In general, an energy spread of 1% and discrete energy steps of <5 MeV are required. The repetition rate is correlated with the extraction length: in the very unlikely case that a slow extraction over 1–10 sec can be achieved with LDIA , the many voxels of one iso-energy layer can be treated with one extraction pulse and a pulse rate of approx. 1 Hz would be sufficient. But when for each voxel a single beam pulse has to be requested than the repetition rate would amount to several kHz which seem to be difficult if not impossible for LDIA. But in any case the particle fluence per voxel has to be controlled within 3% and the dynamical controls are in a range factor of 10–100 which requires the appropriate control monitors in front of the patient.

Following the paradigm formulated in [11], application of high power lasers for ion therapy implies no (or minimum) magnetic systems for acceleration, transportation and manipulation of the high energy ions beams, using instead all optical schemes, such as the "optical gantries" are (see Fig. 3.24), and tailoring the targets for providing not only required ion energy but the energy spectrum, ion beam emittance and shape. To replace all application devices like scanning magnets not only the beam energy but also the beam direction and final location inside the patient has to be controlled better than 1 mm lateral and longitudinal. Fast beam controls for intensity and location have to be developed and implemented in order to guarantee the homogeneity and the conformity of the delivered dose.

In summary ,for the project of LDIA for therapy, the laser technology has to be developed together with a novel application and control systems as a requested by law with the final goal to produce a medical product.

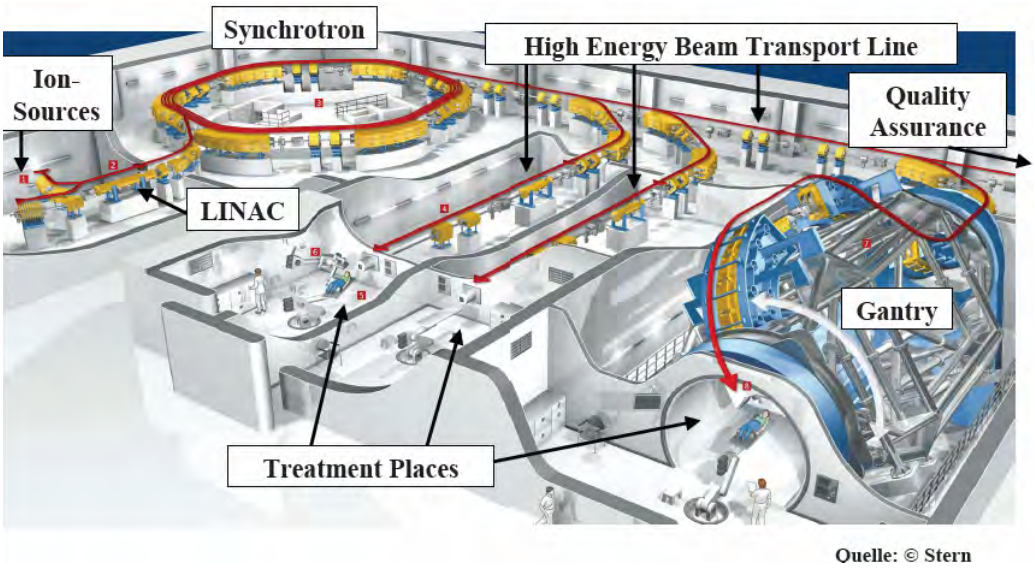

Figure 3.24: Lay out of the Heidelberg Ion-beam Therapy HIT showing the accelerating part at the left side and the treatment areas at the right side. The gantry in the right fore-front can rotate around the patient and deliver the beam from any direction. It has a diameter of 12 m, a length of 24 m and a weight of approx. 600 t.

New scanning concepts for LDIA

In order to make a laser generated beam useable for therapy lateral scanning seems to be inappropriate and new scanning concepts have to be investigated. A promising candidate is depth scanning, a method where the tumor volume is partitioned in several columns instead

of voxels (see Fig. 3.25). Each column could be addressed to by one ion bunch having an appropriate energy spectrum that reaches from the maximum energy to the minimum with an appropriate shape. Then one column can be filled with one laser pulse and hence the number of laser shots necessary is reduced dramatically: instead of some 10 000 voxels less than hundred columns are required.

For this technique, it is only necessary to produce a stable energy spectrum with sufficient energy. After the production of the ion beam, a passive beam shaping system would follow preparing the energy spectrum for every shot. This can be done e.g. by using a combination of collimators, dipole magnets in order to select different proton energies and absorbers which modify the individual components. In a first stage, a collimated beam is produced by passing the beam through an aperture. The directed beam is sent through a dipole magnet and split in its different energetic components. Now it is possible to attenuate and shift the different parts by an adjustable absorber and thus to produce any desired energy spectrum. After the absorber, the beam can be recombined by a second dipole magnet and led to the patient [37].

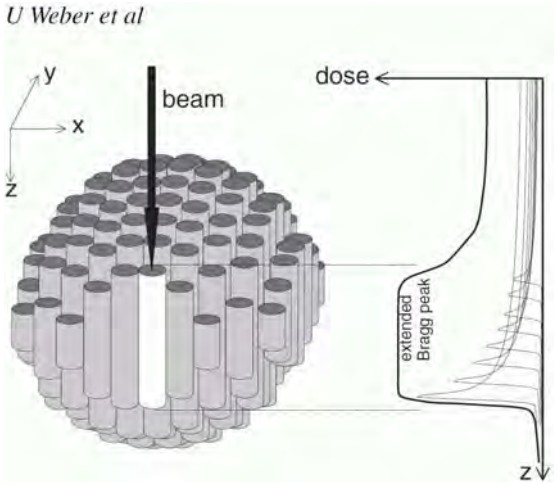

Figure 3.25: Principles of depth scanning: A target volume is not devided into distinct columns which are irradiated with one single laser pulse having an appropriate energy spectrum [25].

Directly in front of the patient the ions have to pass through a fast dosimetry device because the local dose has to be as accurate as plus-minus 3%. After an analysis of the actually delivered dose, the differences to the planned values can be corrected by a repainting of the volume in a following fraction.

In the clinical practice in ion-therapy the dose for one treatment fraction is delivery from two to three entrance ports which are optimized simultaneously. These two fields are frequently nearly opposing. The individual fields do not have to produce a homogeneous dose in the target, only the final superposition yields the planned homogeneous iso-dose. The advantage of this intensity modulated particle therapy IMPT is that critical targets can be spared to a larger extend and that the fluence distribution can be more homogenous. Normally high fluences are needed to fill the most distal edges of the field and only smaller fluences to fill the more proximal parts. This yield energy spectrum of the ions with a maximum at the high energy part which are quite different to the energy spectra obtained from laser acceleration having a pronounced low energy fraction.

For IMPT the spectrums form is a new parameter widely but not completely independent. Applying a new strategy of filling mostly the proximal and not the distal part of a target volume the energy spectrum can have the characteristics from the LDIA but with a sharp high energy

cut off. Such spectra could be generated using the energy filter system described before. Using two (or four) opposing fields it will be possible to achieve a target conform treatment even for the low repetition rate of LDIA.

Laser ion acceleration for ion beam therapy

As theory predicts, the existing and planned laser systems are potentially able to accelerate ions to an energy of hundreds of MeV required for ion beam therapy. In in Fig. 7 we see, although the highest experimentally achieved ion energy has been reached with single-shot multijoule picosecond pulse duration lasers, ultra-short pulse (tens of femtoseconds) lasers may prove to be more advantageous.

Several regimes are considered for ion acceleration from solid and gas targets. In laser interaction with a thin foil solid density target the ion acceleration occurs: i) due to target normal sheath acceleration (TNSA), through the sheath of hot electrons produced at the front of the target [21], ii) Coulomb explosion [30], through the charge separation electric field generated by the exploding ion core after the evacuation of all the electrons, and iii) the laser piston regime [24], through electromagnetic wave pressure. In recently proposed schemes the electromagnetic wave pressure is combined with the Coulomb explosion of accelerated ion slab in the so-called "Directed Coulomb Explosion" regime [31]. Lots of attention have also been paid to an ion acceleration from near-critical density plasmas which are considered to have an advantage of higher laser-plasma coupling (see also Fig. 3.23). In this regime the ions are accelerated at the rear surface of the moderate or near-critical density plasma slab by the sheath field [26] or sheath field with its extended lifetime due to a quasistatic magnetic field generation [32].

The mechanism of laser acceleration of ions (protons and other ions) is determined by the electric field set up by the space charge separation of hot or energetic electrons and the ions. Although the exact mechanisms, entering into the energy transfer from the fast electron to the ion energy, depend on the specific conditions of the laser-target interaction, the ion generation is always a direct consequence of an electron acceleration.

The typical energy spectrum of laser accelerated particles observed both in experiments and in computer simulations can be approximated by a quasi-thermal distribution with a cut-off at a maximum energy. There are different investigations showing the possibility for LDIA to generate proton beams with a sufficiently small energy spread using double-layer targets [11, 34]. This approach will be interesting for laser driven ion beam therapy with multikilohertz repetition rate high intensity lasers.

Results of computer simulations of various regimes of small energy spread ion beam generation using double layer targets (see Fig. 3.26)

We note that high quality laser accelerated ion beams with low energy spread can also be obtained with the use of micro-lens device as has been demonstrated in [35].

Here we discuss the possibility of ion acceleration up to the required for ion beam-therapy energy above 200 MeV with the usage of moderate intensity lasers. The electric field of the laser pulse, $E_{\rm las} = \sqrt{4\pi I/c}$, in order to expel almost all electrons from the focus region must be larger than the electric field that is formed here due to the electric charge separation, $E_0 = 2\pi e n_0 l$. Using the expression for the proton energy $\mathcal{E}_p = eE_0R$, where R is the focus radius, we find a relationship between the proton energy and the laser power $\mathcal{P}_{\rm las} = \pi R^2 I$. From these relationships we obtain

$$\mathcal{E}_p = \sqrt{4e^2\mathcal{P}_{\rm las}/c}. \tag{3.1}$$

As we see, for the proton energy $\mathcal{E}_p \approx 200\,\mathrm{MeV}$ one needs a Petawatt class laser system. An optimization of the acceleration regimes and use of the underdense plasma targets could allow to substantially lowering the power requirements [31, 32].

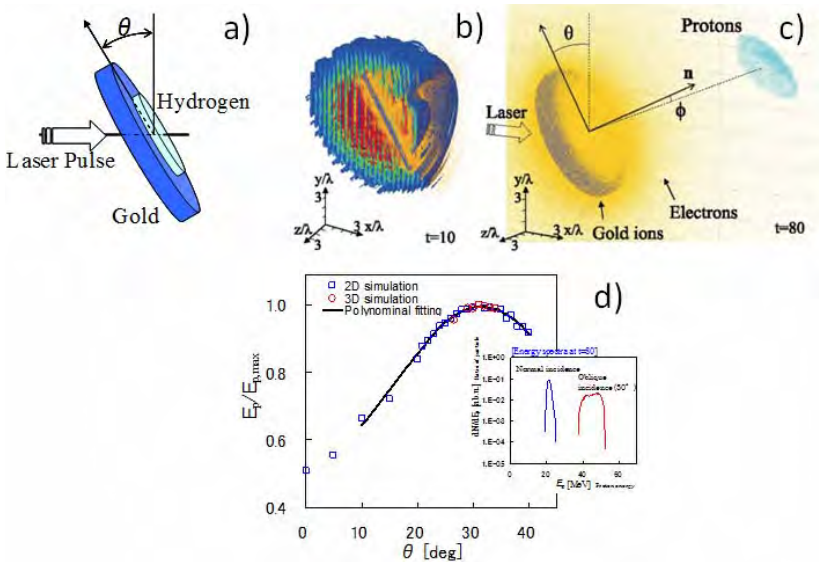

Figure 3.26: Proton acceleration driven by a laser pulse with oblique incidence on a double layer target (a) [39]. (b) Electric field distribution; half of the box is removed to reveal the internal structure. (c) Distribution of gold ions, electrons (yellow), and protons (light blue). (d) Proton energy, normalized by the maximum, vs the laser pulse incidence angle. In the inset: proton energy spectra, as obtained in 3D PIC simulation.

Eli contributions

The ELI high energy electron beamline (see Sect. 2.1 and Sect. 6.3) is designed for energies in the range of 10–15 GeV of the accelerated particles. The planned laser driver for this application is a 15–20 fs laser with a peak-power of 1 PW. The diode pumped frequency doubled pump laser will enable repetition rates in the range of 10 Hz–20 Hz depending on the required output energy or peak-power of the short pulse laser. The estimate given in (3.1) for the necessary driver laser power to generate protons in the range of 200–250 MeV shows that the laser (approximately 1 PW, 10 Hz) planned for ELI electron acceleration posses the necessary parameters for laser based ion beam therapy investigations. The high intensity interaction and ion irradiation investigations will be performed with an especially devoted beam line in the same shielded area as the electron acceleration experiments. Different kinds of renewable targets will be developed and investigated for LDIA at repetition rates between 1–10 Hz in the required therapy energy range. The short pulse CPA driver laser will allow changing the irradiation conditions of the targets for an efficient conversion of the laser energy in to ions with the necessary energy spectrum. It should also be mentioned that for applications in eye tumor therapy much lower proton energies in the order of 70 MeV are necessary due to the reduced penetration depth (24–25 mm, eye ball length) of the protons.

Conclusions

LDIA –technology offers a novel technical approach for ion beam therapy. By replacing the conventional particle accelerators by less spacey and expensive laser units. But the major challenge that should be addressed in the ELI project is not only to reach the required maximum energies of 200 MeV for protons and 400 MeV/ u for carbon. In addition the beam application system like the scanning system and the control monitors have to be adapted to the short beam

pulses expected by LDIA in order to achieve the required dose homogeneity and distribution. In the proposal new strategies are discussed for such an approach.

In the realization of the medical application of the ELI proposal several topics should be treated in parallel:

- Extension of the energy spectrum to 200 MeV for protons and 400 MeV/u for Carbon
- Production of a pencil beam having a defined diameter and direction
- Modulation of the energy spectra to achieve a variable energy cut offs towards higher and lower energies
- Production of a homogenous intensity between the two cut off points.
- Development of a fast monitor system to be used before the patient
- Development of new strategies for an adapted treatment planning for LDIA
- Prompt Gamma spectroscopy for range and energy determination of the protons inside the patient/target
- New concepts for high repetition rate renewable targets and debris handling

Acknowledgements

Supported by DFG Cluster of Excellence: Munich-Centre for Advanced Photonics The support by the BMBF contract 0S83355: Radiobiology Center Darmstadt is gratefully acknowledged by GK.

Bibliography

[1] Schulz-Ertner D., Jäkel O., Schlegel W., 2006 Semin. Radiat. Oncol. 16(4):249–59.
[2] De Laney TF, Kooy HM, 2007 Proton and Charged Particle Radiotherapy, Lippincott Williams & Wilkins, Philadelphia.
[3] Durante M, Loeffler JS, 2010 Nat Rev Clin Oncol. 7(1):37–43.
[4] Wilson RR, 1946 Radiology 47:487–491.
[5] Kraft G., *AIP Conference Proceedings*, **1099**(1):439–444 (2009).
[6] Elsaesser et al., *Int. J. Radiat. Oncol. Biol. Phys.*, (2010).
[7] Schulz-Ertner et al., 2006 Journal of clinical oncology 25. 963–964 (2007).
[8] Schulz-Ertner D., Tsujii, Journal of clinical oncology 25, 963–964 (2007).
[9] Debus J, Kraft G, Hug E, 2009 Hadronentherapie. In: Bamberg M, Molls M, Sack H (eds.) Radioonkologie – Band 1: Grundlagen (München: Zuckschwerdt) 95–108.
[10] Caporaso GJ et al., 2008 Phys. Med. 24(2):98–101.
[11] S. V. Bulanov, V. S. Khoroshkov, *Plasma Phys. Rep.* **28**, 453 (2002).
[12] Schell S, Wilkens JJ, 2010 Medical Physics 37(10):5330–40.
[13] Yogo A et al., 2009 Applied Physics Letters 94:181502
[14] Kraft SD et al., 2010 New Journal of Physics **12**, 085003.
[15] Weber U., Kraft G., *The Cancer Journal*, **15** (4): 325–332 (2009).
[16] Suit H., DeLaney et al., Radiotherapy & Oncology **95** (2010) 3–22.
[17] Elsässer Th., Weyrather W.K., et al., *Int. J. Radiat. Oncol. Biol. Phys.*, (2010).
[18] Chu W.T., B.A. Ludewigt and T.R. Renner, Rev. Sci. Instr. **64**, 2055–2122 (1993).
[19] Pedroni E. et al., Med. Phys. **22**, 37–53 (1995).
[20] Haberer Th., Becher W., Schardt D., Kraft G., Nucl. Instr. and Meth. in Phys. Res. A 330, 296–305 (1993).
[21] S. C. Wilks, et al., Phys. Plasmas **8**, 542 (2001).
[22] S. V. Bulanov, et al., AIP Conference Proceedings, **740**, 414–429 (2004).
[23] M. Borghesi, J. Fuchs, S. V. Bulanov, A. J. Mackinnon, P. Patel, M. Roth, Fusion Sci. Technol. **49**, 412 (2006).

[24] T. Esirkepov, M. Borghesi, S.V. Bulanov, G. Mourou, and T. Tajima, Phys. Rev. Lett. **92**, 175003 (2004).
[25] S. V. Bulanov, E. Yu. Echkina, T. Zh. Esirkepov, I. N. Inovenkov, M. Kando, F. Pegoraro, and G. Korn, *Phys. Rev. Lett.* **104**, 135003 (2010).
[26] L. Willingale et al., Phys. Rev. Lett. **96**, 245002 (2006).
[27] Weber U., Becher W., Kraft G., Phys Med Biol. **45**, 3627 (2000).
[28] Kraft G., Progr. Part. Nucl. Phys. **45**, 473 (2000).
[29] Kraft G., Kraft S.D., New J. Phys. 11:025001-(16pp) (2009) [DOI: 10.1088/1367-2630/11/2/025001].
[30] S. V. Bulanov, T. Zh. Esirkepov, V. S. Khoroshkov, A. V. Kuznetsov, and F. Pegoraro, Phys. Lett. A **299**, 240 (2002).
[31] S. S. Bulanov et al., Med. Phys. **35**, 1770 (2008).
[32] A.V. Kuznetsov et al., Plasma Phys. Rep. **27**, 211 (2001).
T. Nakamura et al., Phys. Rev. Lett. **105**, 135002 (2010).
[33] C. Schwoerer et al., Nature **439**, 445 (2006).
[34] T. Esirkepov et al., Phys. Rev. Lett. **89**, 175003 (2002).
[35] T. Toncian et al., Science **312**, 410 (2006).
[36] T. Furukawa et al., Med. Phys. 374874 (2010).
[37] Kraft G., Weber U., Kraft S. D., Kraft S. P., Energy filter device Patent Pub. US 2005 / 0029471n A 1 (2005).
[38] Y. Fukuda et al., Phys. Rev. Lett. **103**, 165002 (2009)
[39] T. Morita et al., Phys. Rev. Lett. **100**, 145001 (2008)

3.4.2 Medical Radioisotopes produced by γ Beams

In [1] about 50 radioisotopes are described, which can be produced much better by γ beams and are of interest to medicine for diagnostic and/or therapeutic purposes. With the small band width γ beams for many of the isotopes we will find specific gateway states or groups of resonant states where the production cross sections can be increases by 2–3 orders of magnitude compared to [1], making them even more interesting for large-scale industrial applications. Here we shell focus on some of the most interesting isotopes to give a flavour of the possibilities:

^{195m}Pt: Determining the efficiency of chemotherapy for tumours and the optimum dose by nuclear imaging

In chemotherapy of tumours most often platinum cytotoxic compounds like cisplatin or carbonplatin are used. We want to label these compounds with ^{195m}Pt for pharmacokinetic studies like tumour uptake and want to exclude "non-responding" patients from unnecessary chemotherapy and optimizing the dose of all chemotherapy. For such a diagnostics a large scale market can be foreseen, but it would also save many people from painful treatments. We estimated in Ref. [1] that several hundred patient-specific uptake measurements could be produced with a γ beam facility. However this probably may be increased to 10^5, if optimum gateway states are identified by scanning the isomer production with high γ beam resolution. ^{195m}Pt has a high $13/2^+$ spin isomer at 259 keV, half-life ($T_{1/2} = 4$ d) with SPECT transitions of 130 keV and 99 keV to the $1/2^-$ ground state.

^{117m}Sn: An emitter of low energy Auger electrons for tumour therapy

Auger electron therapy requires targeting into individual tumour cells, even into the nucleus or to DNA, due to short range below 1 µm of the Auger electrons; but there it is of high REB due to the shower of many 5–30 Auger electrons produced. On the other hand Auger radiation is of low toxicity, while being transported through the body. Thus Auger electron therapy needs

special tumour specific transport molecules like antibodies or peptides. Many of the low lying high spin isomers produced in (γ, γ') reactions have strongly converted transitions, which trigger these large showers of Auger cascades.

A ^{44}Ti → ^{44}Sc generator for the γ-PET isotope ^{44}Sc with much improved resolution in nuclear imaging

In recent years PET (Positron Emission Tomography) with typical spatial resolution of (3–10 mm) was supplemented by multi-slice X-ray CT (Computer Tomography) of much better resolution, leading to the novel technology of PET/CT. The coregistration and the reference frame of CT are very helpful for the interpretation of PET images. CT and PET require comparable dose. Looking at such images it is very apparent, that an order of magnitude improvement in the resolution of PET is highly desirable and might even make accompanying CT obsolete. ^{44}Sc is the best candidate to supply the two 511 keV annihilation quanta together with a strongly populated 1157 keV transition. By measuring the position and direction of this γ quantum accurately with a Compton spectrometer together with the two 511 keV quanta the location of the emitting nucleus can be located in 3 dimensions. In conventional PET the two collinear 511 keV quanta only allow to determine a 2-dimensional localization on a line. Thus a much better spatial resolution can be achieved for the same dose with γ-PET compared to PET. With ^{44}Ti (half life $T_{1/2} = 59$ a) the production with a very promising generator for ^{44}Sc ($T_{1/2} = 3.9$ h) becomes available with γ beams. Again a much stronger population via the fine structure of the Giant Dipole Resonance (GDR) in the ^{46}Ti(γ,2n)^{44}Ti is expected for the ^{44}Ti core consisting of the doubly magic ^{40}Ca and an α particle. The long half life of ^{44}Ti requires a large transmutation with an intense γ beam, but on the other hand leads to a very valuable, long-lived generator. The production of ^{44}Ti in the $(\gamma, 2n)$ reactions require rather large γ-energies of 23–24 MeV, and would require an increase of the maximum presently planned γ energy at ELI-NP of 19 MeV.

Many further new interesting medical radioisotopes can be produced (see Ref. [1]): "New matched pairs" of isotopes of the same element become available, one for diagnostics the other for therapy, allowing to control and optimize the transport of the isotope by the bioconjugate to the tumour. Also new therapy isotopes become available like ^{225}Ac, where 4 consecutive α decays can cause much more double strand breaking. Developing these techniques and applications is a promising task of ELI-NP with a strong socio-societal component.

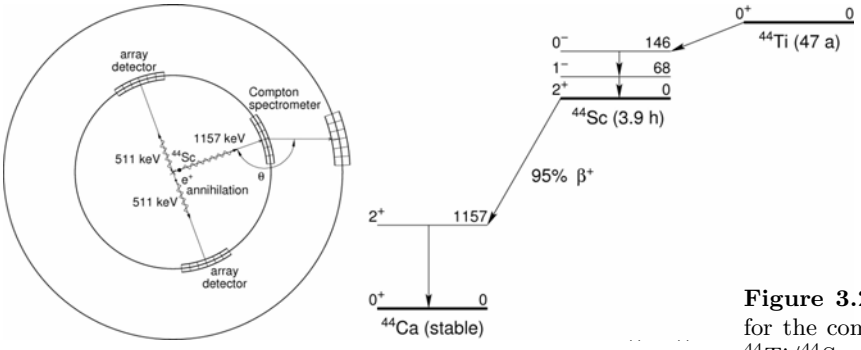

Figure 3.27: Schematic picture for the combined γ-PET and the ^{44}Ti/^{44}Sc generator.

Bibliography

[1] D. Habs and U. Köster, arXiv-1008.5336v1[physics.med-ph] 2010, submitted to Appl. Phys. B.

3.5 Industrial Applications for the Management of Nuclear Materials

3.5.1 Non-destructive detection and assay of nuclear materials by using high-brightness γ-rays

A resonant excitation of definite nuclear states of a nucleus occurs when the nucleus absorbs an electromagnetic radiation equal to the excitation energy (see Fig. 3.28). This excitation state instantaneously decays mainly to a lower state with re-emission of the radiation equivalent to the absorbed radiation. This process is nuclear resonance fluorescence (NRF). The energy width of resonance is determined by the lifetime of excited nuclear states, which is of the order of 10^{-10} second. The absorption and re-emission of electromagnetic radiation by nuclei occurs only at exact resonance with tiny energy width, typically $\Gamma \sim 10^{-5}$ eV. This resonant interaction is a unique property of NRF, while other nuclear absorption phenomena such as photo-nuclear reactions and the giant dipole resonance involve the continuum states of nuclei and show broad absorption spectra. Nuclear resonance fluorescence provides important information about the nuclear structure, the energies of the excited states, their lifetimes (equivalent to energy widths), their angular momenta and their parities, which are relevant to the fundamental forces between the nuclear constituents.

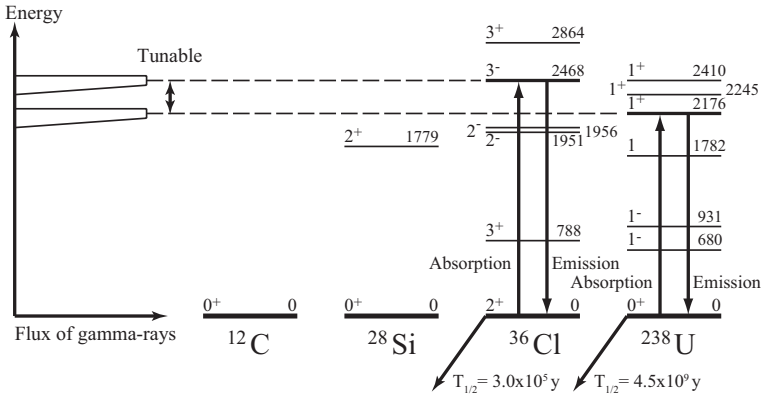

Figure 3.28: A schematic view of the non-destructive assay system based on nuclear resonance fluorescence. If the incident γ-ray energy is identical with the excitation energy of the nucleus of interest, the incident γ-ray is effectively absorbed in the nucleus. The excited nucleus subsequently de-excite and strongly emit the γ-ray whose energy is identical with the incident γ-ray energy.

Applications of NRF to non-destructive detection and assay of nuclear materials have been proposed [1,2]. In these proposals, laser Compton scattered (LCS) γ-ray sources are utilized because of their energy-tunabitity and monochromaticity. The proposed method has several advantages: (1) non-destructive identification of radioactive and stable nuclides is possible by detecting a fluorescence γ-ray, which is a unique fingerprint for each nuclide, (2) a quasi-monochromatic γ-ray tuned at a fluorescence energy is essential to improve signal-to-noise ratio in the energy-resolved γ-ray detection by separating the fluorescence γ-ray from back-ground noise, most of which is generated through Compton scattering of γ-rays in the object, (3) detecting many kind of nuclides is practically possible by scanning the γ-ray energy.

3.5.2 Management of radioactive wastes

Radioactive wastes are produced from a nuclear fuel cycle, decommission of nuclear facilities, and the use of radionuclides for research and medical purpose. At the final disposal, the radioactive wastes are segregated, according to the amount of the activity concentration of the radionuclides,

into categories - geological disposal, subsurface disposal, concrete pit disposal, trench disposal. Since the disposal cost depends on the disposal category, the appropriate classification of the radioactive waste by accurate measurements of the radioactivity concentration is a key issue for the efficient management of the radioactive waste.

The radionuclides are classified into easy-to-measure nuclides of high-energy γ-ray emitters, for example Co-60 and Cs-137, and difficult-to-measure nuclides such as alpha- and beta-ray emitters in viewpoint of the waste management. Radioactive wastes discharged from the nuclear fuel cycle contains many alpha- and beta-ray emitters, whose concentration dominates the process of the waste management. It is difficult to measure alpha- and beta-rays in the outside of the drum of the the radioactive waste and thus alternative methods should be developed.

The non-destructive assay based on the high-brightness γ-rays can be applied to the management of radioactive wastes. As described above, this method has advantages: (1) non-destructive identification of radioactive and stable nuclides is possible, (2) a quasi-monochromatic γ-ray tuned at a fluorescence energy improves signal-to-noise ratio in the energy-resolved γ-ray detection, (3) detecting many kind of nuclides is practically possible by scanning the γ-ray energy.

Figure 3.29 shows a schematic view of the non-destructive measurement of radionuclides in a radioactive waste drum, where a 200-litter drum (200-litter) is surrounded by an array of Germanium detectors (18 detectors) for detecting NRF signals.

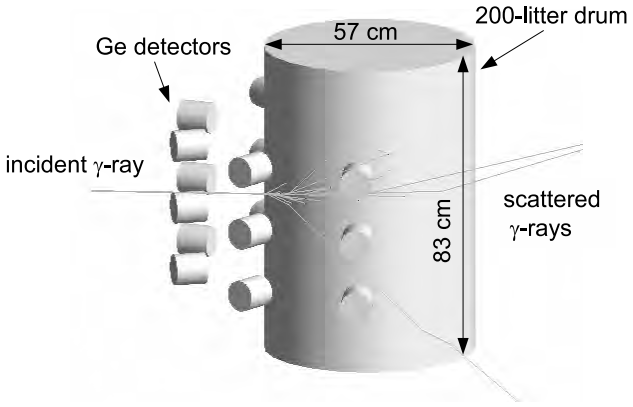

Figure 3.29: A schematic view for a non-destructive assay of U-238 in a drum. An array of Germanium detectors are located surrounding the drum (18 detectors).

In order to evaluate the performance of the non-destructive measurement, Monte Carlo simulations were conducted [3]. In the simulation, generation of γ-rays via Compton scattering of photons with high-energy electrons was calculated by `CAIN` [4] and interactions of the generated γ-rays with an object was simulated by `GEANT4` [5]. `GEANT4` is widely used in applications of high energy, nuclear and accelerator physics, as well as studies in medical and space science. However, nuclear resonance fluorescence is not supported in the original package of `GEANT4`. The JAEA group, therefore, modified `GEANT4` to calculate nuclear resonance fluorescence in cascade interactions of photons and particles triggered by incident γ-rays.

A 200-litter drum filled with concrete and homogeneously distributed U-238 was assumed and a resonance energy at 2.17 MeV was used for the NRF detection. The density of the concrete and the concentration of U-238 were 2 g/cm^3 and 1000 Bq/g, respectively. The geometry of a drum and detectors for the simulation was same as Fig. 3.29.

Figure 3.30 shows a γ-ray spectrum obtained from the simulation, which is a summation of incident γ-rays into the detectors. We can clearly see a peak of NRF signal in the spectrum,

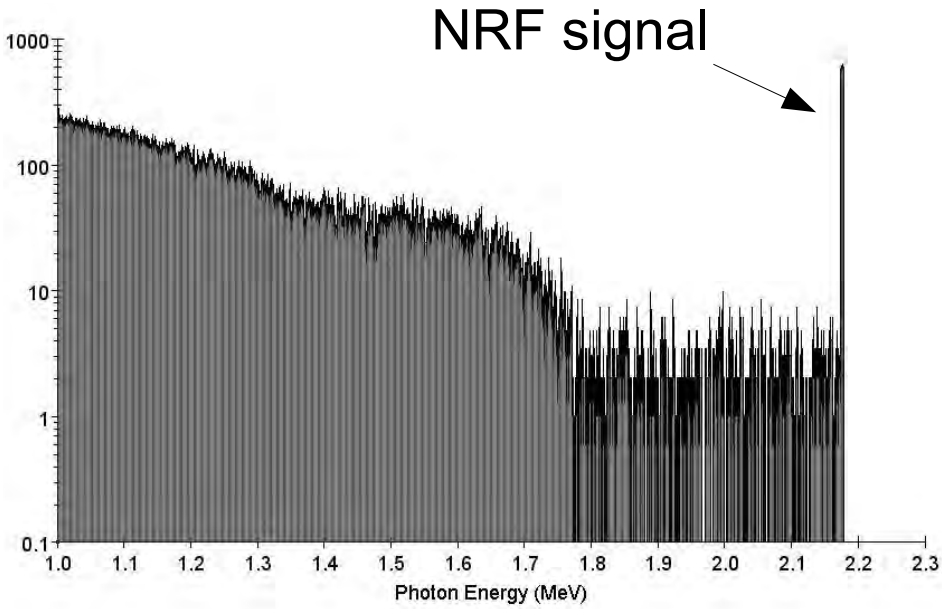

Figure 3.30: A result of `GEANT4` simulation. a γ-ray spectrum obtained at detectors is plotted. The sharp peak corresponds to the NRF signal from U-238.

and the number of NRF γ-ray is found to be $N_\gamma = 1200$ for two bins in total. In this simulation, the incident γ-ray has 10^9 photons within 1 keV energy spread.

If we assume a γ-ray flux of 10^{13}/s, corresponding to a spectral density of flux $\sim 10^{10}$/s/keV [6], the NRF signal shown in Fig. 3.30 can be obtained in 0.1 sec and even the lower concentration of U-238, 1 Bq/g, can be detected in a practical measurement time, ~ 100 s.

3.5.3 Nuclear material accounting and safeguards

In order to prevent transfer and proliferation of the fissile materials, the mass of plutonium in spent nuclear fuel assemblies must be quantified and the diversion of pins from them must be detected. For this purpose, both nuclear material accounting and nuclear safeguards are applied in reprocessing plants and once-through spent fuel repositories.

US-DOE-NNSA launched the Next Generation Safeguards Initiative (NGSI) to develop the policies, concepts, technologies, expertise, and infrastructure necessary to sustain the international safeguards system as its mission evolves over the next 25 years. In the NGSI program, non-destructive analysis (NDA) of plutonium in the spent nuclear fuel is the top priority in the technology development. For the Pu-NDA in the spent fuel, K X-ray resonance fluorescence, or differential die-away analysis with neutrons have been studied. However, the NDA of Pu-239 in the nuclear fuel assembly has not been well established yet. The first reason stems from the fact that high-Z element uranium in the nuclear fuel absorbs detection probes such as low-energy X-rays. Second we should not only detect elements but also analyze each isotope of interest. However, the non-destructive detection of such an isotope in heavy materials is generally difficult. Third the spent nuclear fuel is heated up due to the presence of the residual radioactivities. Thus, the spent fuel is often kept in a cooling water pool; the water absorbs or scatters neutrons and low energy X-rays.

The combination of a high-brightness γ-ray beam and NRF measurements can be applied to the NDA of Pu-239 in spent nuclear fuel located in a water pool [7]. This method has excellent advantages: we can detect isotopes of uranium, plutonium and minor actinides located deeply

in the nuclear fuel by measuring the NRF γ-rays since high energy γ-rays of several MeV are used as the probe. In addition, the spent fuel can be analyzed with keeping in water pool. This is important, in particular, in viewpoint of the nuclear material safeguards since anyone cannot easily access fissile nuclides through water and walls of the pool.

Figure 3.31 shows a schematic view of the detector system and a spent fuel assembly in a water pool. The γ-rays emitted from the spent fuel are measured with HPGe detectors. The resolution of the HPGe detectors is typically smaller than 0.2% (full width at half maximum (FWHM)). The spent fuel contains many radioactivities and becomes feverish. Thus, the spent fuel is stored in a water pool for cooling. The neutrons emitted from spontaneous fission of actinides in the nuclear fuel are absorbed by cooling water. The energy range of the incident LCS γ-ray beam is 1.9–2.3 MeV which is high enough to penetrate materials through shield water with a thickness of several ten centimeters. A result of Monte Carlo simulation is shown

Table 3.1: Excitation energy and Resonance width for important nuclides in spent nuclear fuel.

Nuclide	Excitation energy [keV]	Cross section [eV b]	Ref.
^{235}U	1733.60	29.8±3.9	[8]
	1769.16	4.4±1.0	[8]
	1815.31	9.7±1.7	[8]
	1827.54	6.7±1.2	[8]
	1862.31	9.6±1.7	[8]
	2003.32	9.7±1.7	[8]
	2006.19	4.7±1.6	[8]
^{238}U	1782	21.9±2.5	[9]
	1793	5.1±1.0	[9]
	1846	23.0±2.6	[9]
	2176	57.7±3.4 [a]	[10]
	2209	53.4±3.3 [a]	[10]
	2245	26.3±1.8 [a]	[10]
	2295	7.1±0.7 [a]	[10]
	2410	21.8±1.4 [a]	[10]
	2468	25.3±1.9 [a]	[10]
^{239}Pu	2040.25	8±2	[8]
	2046.89	5±2	[8]
	2135.56	4±2	[8]
	2143.56	13±2	[8]
	2150.98	5±2	[8]
	2289.02	8±2	[8]
	2423.48	10±2	[8]
	2431.66	9±3	[8]
	2454.37	9±3	[8]

[a] Calculated from experimental Γ^0/Γ.

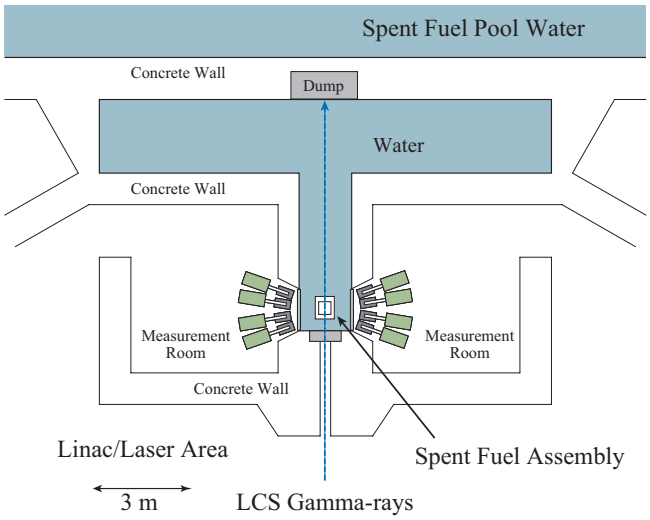

Figure 3.31: Schematic view of the non-destructive assay system based on nuclear resonance fluorescence with laser Compton scattering γ-ray source. If the incident γ-ray energy is identical with the excitation energy of the nucleus of interest, the incident γ-ray is effectively absorbed in the nucleus and subsequently the nucleus de-excites by γ-ray emission.

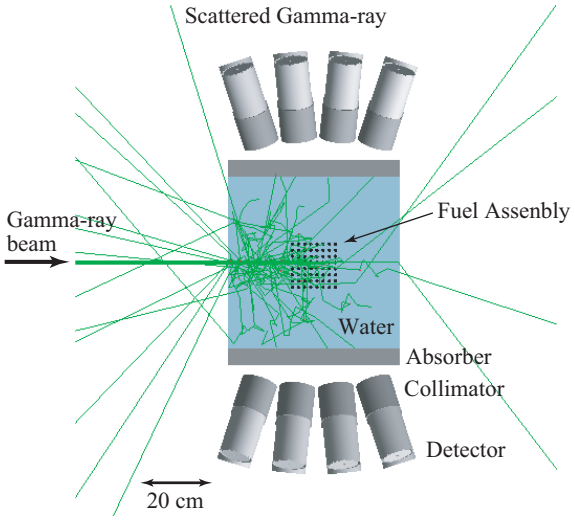

Figure 3.32: Result of simulation calculation. The solid lines are traces of γ-rays. The incident γ-rays are scattered by Compton scattering and NRF. The LCS γ-rays reach at the fuel dots located at the opposite side.

in Fig. 3.32, where traces of γ-rays in a water pool and a spent nuclear fuel assembly are plotted.

Table 3.1 shows the γ-ray energies emitted from the isotopes relevant to this application. The difference between energies of two any γ-rays are larger than 0.2% and thus we can identify the relevant isotopes in the spent fuel. The γ-ray to cover these energies can be generated by laser Compton scattering of 1-μm laser photons and 350-MeV electrons.

3.5.4 Summary

Generation of energy-tunable and quasi-monochromatic γ-rays via laser Compton scattering makes it possible to detect or measure radioactive nuclides in an object non-destructively, which

is a key technology for nuclear industrial applications such as management of radioactive wastes, nuclear material accounting and safeguards.

Bibliography

[1] J. Pruet et al., J. Appl. Phys., **99** (2006) 123102-1.
[2] R. Hajima et al., J. Nucl. Sci. and Tech., **45** (2008) 441.
[3] N. Kikuzawa et al., Proc. AccApp-07, p.1017 (2007).
[4] P. Chen et al., Nucl. Instrum. Meth., **A355** (1995) 107–110.
[5] S. Agostinelli et al., Nucl. Instrum. Meth., **A506** (2003) 250–303.
[6] R. Hajima et al., Nucl. Instrum. Meth. **A608** (2009) S57–S61.
[7] T. Hayakawa et al., Nucl. Instrum. Meth. **A621** (2010) 695–700.
[8] W. Bertozzi et al., Phys. Rev. C **78** (2008) 041601(R).
[9] A. Zilges et al., Phys. Rev. C **52** (1995) 468(R).
[10] R.D. Heil et al., Nucl. Phys. A **476** (1988) 39.

3.6 Ultrafast molecular dynamics

The ELI XUV/x-ray light sources allow to develop novel strategies for studying chemical reaction dynamics with the potential to significantly advance molecular physics. These novel strategies benefit from two characteristics of the ELI light sources, namely the unique *attosecond time-structure* and the unique *wavelength structure.*

The *attosecond time-structure* of the ELI light sources allows unprecedented access to the ultrafast electronic dynamics that constitutes the primary response of molecular systems to incident light. The coupling of this electronic response to the nuclear degrees of freedom sets the stage for studies of nuclear motion that have been pursued in the context of femtochemistry research, notably through the pioneering efforts of Ahmed Zewail [1]. Nuclear motion is always preceded by an electronic response, which not only couples to nuclear degrees of freedom, but to other electronic degrees of freedom as well. As has been recently predicted in several theoretical works, intense attosecond light sources allow to induce a purely electronic response in molecules [2,3]. This purely electronic response may lead to ultrafast electron transfer in extended systems on the attosecond or few-femtosecond timescale. Visualizing this electronic response should be one of the "holy grails" pursued at the ELI-HU facility. In addition to ultrafast intra-molecular electronic responses, ELI will allow to study inter-molecular electronic responses, such as in the ubiquitous ICD (interatomic Coulombic decay) process, that has recently been observed [4–6].

The *wavelength structure* of the ELI light source allows to develop completely novel strategies for probing nuclear motion that significantly go beyond the methods of femtochemistry. In femtochemical experiments, photo-absorption by a pump laser pulse induces nuclear motion that is typically probed by monitoring the evolution of photo-absorption spectra (either directly, or indirectly as part of a high-order non-linear optical scheme). Although proven to be powerful in smaller systems, these methods depend in an undesirable way on ones' ability to know, calculate or infer the dependence of the absorption spectrum on the instantaneous molecular structure. This implies that a time-resolved study of the molecular structure is only possible when it includes a detailed understanding of the electronic structure (including excited states) of the molecule. The ELI light sources allow to probe molecular structure without a prior knowledge of the electronic structure. With the short wavelengths offered by ELI, photoelectrons can be ejected from molecules that carry a de Broglie wavelength that is comparable to the internuclear distances that occur in the molecule, inducing diffractive structures in the photoelectron angular distributions that are reminiscent of the structures in the photoionization efficiency that are measured in EXAFS experiments [7, 8].

The main advance offered by the ELI-HU facility is that both of the advances described above can be pursued as part of one and the same experiment. With weaker attosecond light sources that are based on lab-scale femtosecond lasers, on the one hand, and with Free Electron Lasers like FLASH and LCLS on the other, the two aspects described above (i.e. inducing ultrafast electron dynamics by ionization, and probing molecular dynamics using XUV/x-ray ionization) have recently been separately pursued and demonstrated in two-color XUV+IR, resp. IR+XUV experiments. In the former first hints of the coupling of electronic and nuclear degrees of freedom, and of coupling of multiple electronic degrees of freedom have been observed [9], while in the latter, first indications of the manifestation of the molecular structure in the photoelectron angular distribution have been obtained [10]. Brief descriptions of these two experiments are given below.

A) Probing of ionization induced electron dynamics

In the framework of a large international collaboration involving, among others, MBI (Berlin), AMOLF (Amsterdam), INFM (Milano), the University of Lund and MPQ (Garching) a first molecular application of attosecond pump-probe spectroscopy was recently achieved [9]. In the

experiment, H_2 resp. D_2 molecules were ionized by an isolated attosecond laser pulse that was generated by means of high-harmonic generation including the use of a polarization gate. Dissociation of the molecule was induced/influenced by a time-delayed few-cycle infrared laser pulse, that induced an asymmetric ejection of the H^+ resp. D^+ formed, which depended with attosecond time-resolution on the delay between the isolated attosecond pulse and the IR pulse. An analysis of the mechanisms leading to the observed asymmetry revealed the presence of both phenomena discussed in the introduction to this section, namely the coupling of electronic and nuclear degrees of freedom and the coupling of multiple electronic degrees of freedom in auto-ionization.

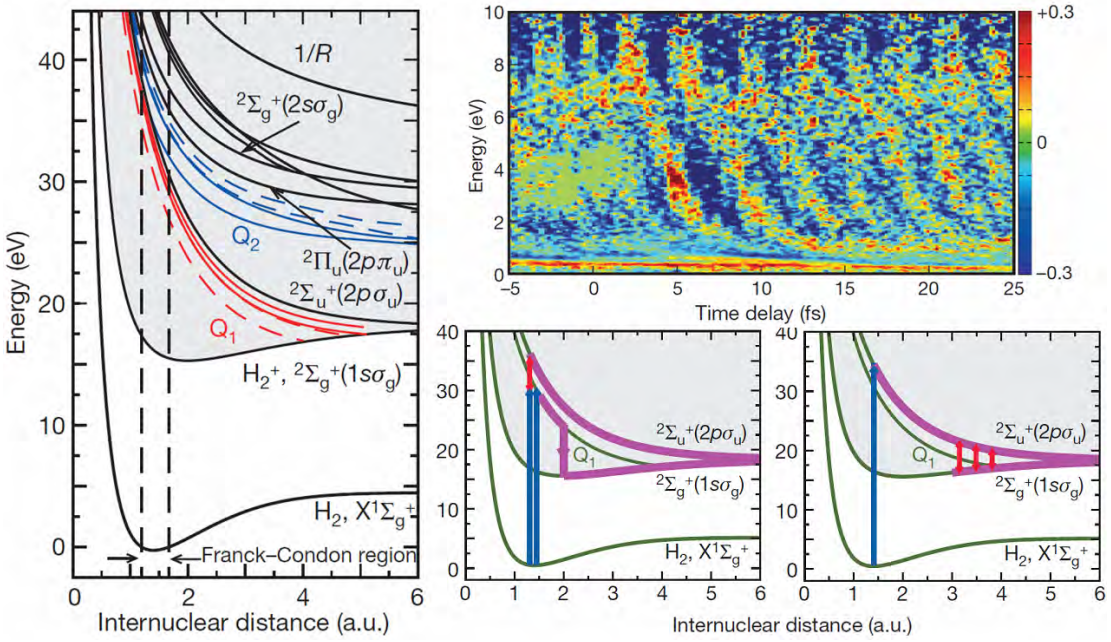

Figure 3.33: Asymmetric dissociation of D_2^+, obtained by exposing neutral D_2 molecules to the sequence of an isolated attosecond pulse and a few-cycle IR pulse. Two mechanisms lead to the observed normalized asymmetry shown in the contour plot on the upper right, as a function of the fragment kinetic energy and the XUV-IR time delay. These two mechanisms can be viewed as two-path interferences producing a coherent superposition of the $1s\sigma_g$ and $2p\sigma_u$ states, and rely on coupling of electronic degrees freedom in autoionization (left) and coupling of electronic and nuclear degrees of freedom during dissociation (right).

Although capable of revealing first insights into attosecond time-scale electron dynamics, the experiment introduced above leaves a lot to be desired. The contour plot shown in Figure 3.33 is a testament to the only marginally sufficient attosecond photon flux that was available for inducing the ionization process. In addition, the use of a few-cycle IR pulse for probing the electron dynamics is highly undesirable, as it introduces an ambiguity in the time at which the observation is made, similar to the ambiguity that the use of attosecond pulse trains induces in pump-probe experiments.

The approximate pulse energy of the attosecond source in the experiments shown in Figure 3.33 was 3 pJoule. Assuming a 10^{-4} cm^2 spot size and a 300 as pulse duration, this translates into a peak intensity of appr. 10^8 W/cm^2, i.e. about 5 orders of magnitude lower than what (based on experiments performed at FLASH) is required/desirable. With the ELI light sources the required isolated attosecond pulse intensities would be achievable.

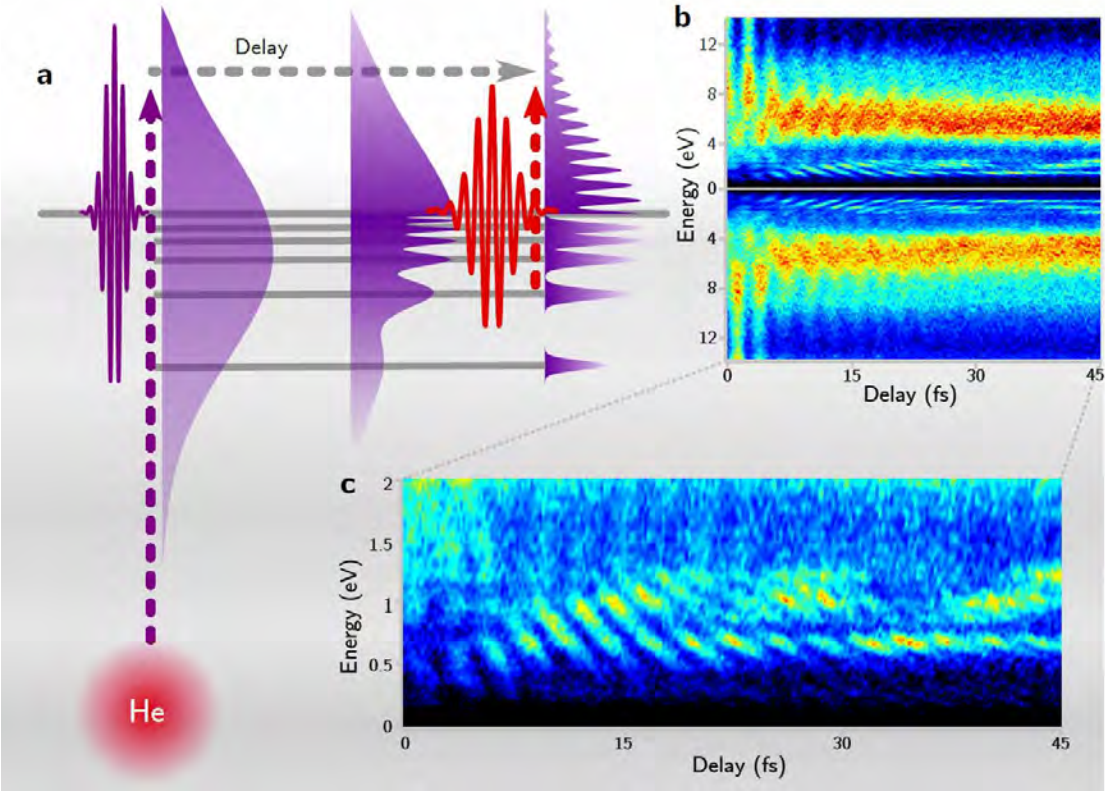

Figure 3.34: XUV-IR pump-probe experiments on the He atom, revealing the occurrence of holographic interference fringes in the energy- and angle-resolved photoelectron spectrum, that allow to fully characterize the energies, populations and relative phases of the states that are excited by the XUV pulse.

The availability of sufficiently intense XUV pulses would allow to perform experiments such as those presented in figure 3.33 (as well as similar experiments on considerably more complicated and more chemically/biologically relevant molecules) in XUV-XUV pump-probe schemes, where angle- and energy-resolved photoelectron spectroscopy is used to map out the time-dependent electronic response. A recent experiment performed by the same collaboration mentioned above reveals that under these conditions holographic information can be measured that fully encodes the ultrafast electron dynamics, the ultimate observable in an attosecond experiment [11]. In the experiment (see Figure 3.34) He atoms were ionized with an isolated attosecond pulse that was tuned to the ionization threshold (meaning that both bound states and the He^+ ionization continuum were excited). At a variable delay the bound state population was promoted into the continuum using a few-cycle IR laser, leading to interferences with the continuum wavepacket directly produced by the attosecond laser pulse. The interference revealed the energy, population and relative phase of the bound state wavepacket that the attosecond pulse had produced, in other words: a complete characterization. Of course, in this proof-in-principle experiment these quantities were also known ahead of time, however, none of this knowledge was required to arrive at this interpretation and the experiment could likewise be performed for systems where one would like to characterize fully unknown electron dynamics, such as Auger decay, shake-up, and – conceivably – electron transfer and localization processes in molecules.

B) Probing molecular dynamics using XUV/x-ray ionization

Probing molecular structure and dynamics with XUV/x-ray ionization offers important advantages over the use of IR/visible/UV that is customary in femtochemistry experiments. At moderate ionization energies, XUV ionization is a universal probe without 'dark states' that allows the measurement of angle- and energy-resolved photoelectron angular distributions that contain a wealth of information about molecular orbitals and dynamical processes that may be going on in a molecule. At higher ionization energies, it is primarily the molecular structure that gets encoded, in holographic geometries where the angle- and energy-resolved photoelectron angular distribution reveals the interference between 'reference' electron waves that are ejected from localized sites within a molecule and 'signal' electron waves that are also ejected from said sites, but scatter off one or more atoms within the molecule prior to reaching the detector [8].

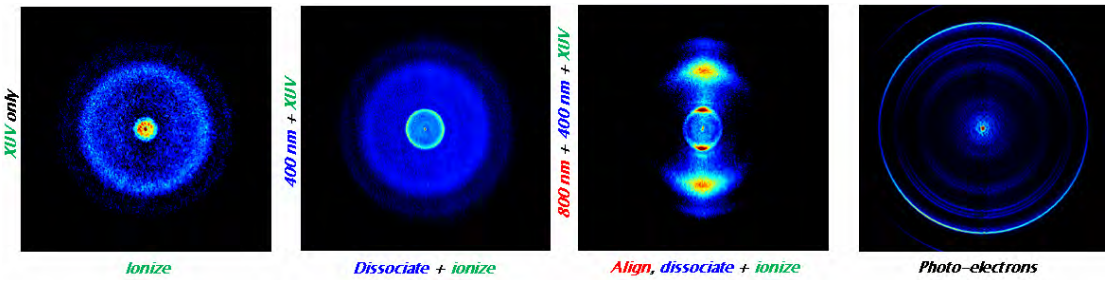

Figure 3.35: Dissociative ionization of Br_2 at the FLASH facility in Hamburg; the three left images reveal that it is possible to ionize Br_2, align it (using an 800 laser) and dissociate it (using a 400 nm laser); the right image is a photoelectron measurement obtained from the aligned molecules.

In the synchrotron community the use of XUV ionization to retrieve structural and dynamical information has a rich tradition, and is commonly carried out – of course, without time resolution - using coincident detection of photoelectrons and fragment photo-ions that allow a view of the photo-emission in the molecular frame. Coincidence techniques are ill-matched with the use of moderately low repetition rate light sources ($\leq$ 1 kHz) such as ELI. Rather, at a facility like ELI it would be preferred to carry out these experiments in adiabatically [12] or impulsively [13] aligned molecules. Recent experiments performed at the FLASH free electron laser and a lab-scale high-harmonic source have made significant progress towards the realization of the goal of using XUV/x-ray radiation as a probe of molecular dynamics.

At FLASH, experiments have been performed where Br_2 molecules were impulsively aligned (using 800 nm radiation), dissociated (using 400 nm radiation), and finally ionized using 13 nm radiation from the free electron laser [14]. Energy- and angle-resolved momentum maps were recorded both for Br^{2+} ions, revealing the dissociation and alignment, and photoelectrons. Unfortunately no time-dependence of the photo-electrons was thus far observed, largely owing to the challenge of laser synchronization that is encountered at free electron laser facilities. The availability of the ELI laser as a source where multi-color pump lasers and a powerful XUV/x-ray probe all derive from one and the same oscillator/amplifier system fully solves these problems and opens the path towards routine operation of experiments where molecular dynamics is probed using XUV/x-ray radiation.

The potential for such experiments was recently illustrated in experiments where a range of small molecules like CO_2, N_2, O_2 and CO were impulsively aligned and ionized using a high-harmonic frequency comb [10]. In these experiments, which did not yet include any photo-induced dynamics, the angle- and energy-resolved photoelectron spectra clearly indicated the involvement of multiple electronic orbitals in the ionization process. Due to the low photon energy available in the experiments (<45 eV) the amount of structural information that could

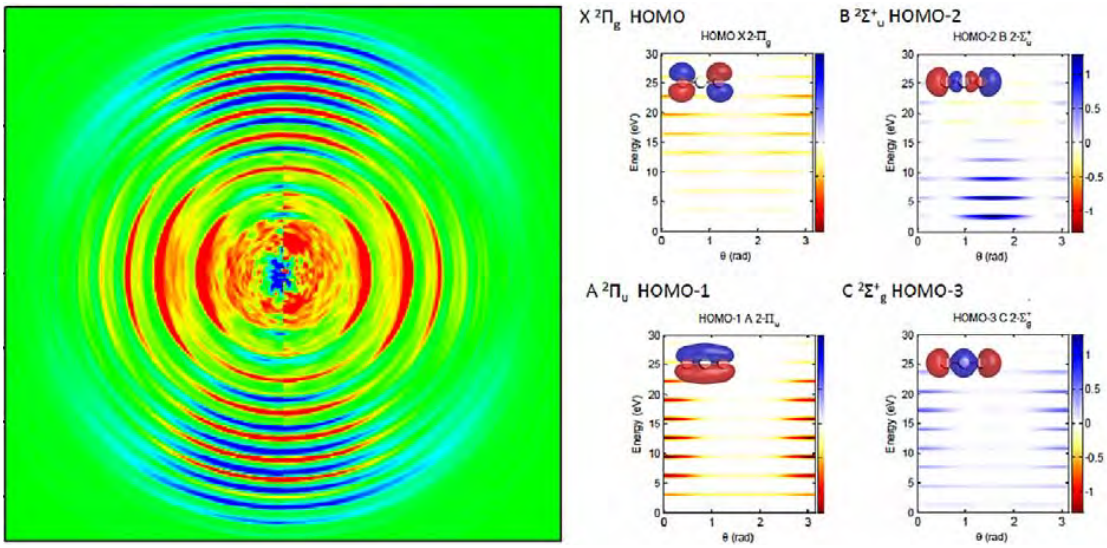

Figure 3.36: Photoelectron angular distributions obtained from aligned molecules with XUV radiation. The image on the left represents the difference between a measurement with aligned and anti-aligned molecules and reveals contributions from at least 4 molecular orbitals (see right).

be obtained in the experiments was thus far limited. When ELI is used to efficiently generate harmonics in the water window range (either directly, or indirectly, after converting the ELI light source to mid-infrared wavelengths) XUV/x-ray probing becomes possible in a regime where the angle- and energy-resolved photoelectron spectrum will directly reveal the molecular structure.

Velocity map imaging

A technique that has – in the last few years – become very popular in the attosecond science field is velocity map imaging [15]. In velocity map imaging, ions or electrons are formed at the crossing point of an atomic/molecular beam and one or more laser beams. The ions or electrons are accelerated towards a two-dimensional detector that usually consists of a dual micro-channel plate followed by a phosphor screen and a camera system. Since the extraction ion optics are designed as an immersion lens, the position on the camera is almost exclusively dependent on the velocity of the ion or electron, and hardly on the position where the ionization event took place. Hence, velocity map imaging measures a 2D projection of the 3D electron or ion velocity distribution that is formed in the experiment. If the experiment contains an axis of symmetry in the plane of the detector, as is usually the case, the 3D distribution can be retrieved from the 2D projection. Using velocity map imaging the duration of attosecond pulses that are part of a train has been characterized [16], a new type of electron interferometry as been developed [17], and the previously mentioned experiments on molecular electron dynamics [9], attosecond holography [11], and angle-resolved photo-emission [10] have been performed.

Velocity map imaging allows detection of fragment ions and electrons over an extremely wide range of photoelectron and -ion kinetic energies. As an illustration Figure 3.37 shows results for detection of 2.5 meV photoelectrons in threshold photoionization of Xe [18], and detection of 80 eV photoelectrons from Ne ionization at FLASH [19].

Advantages of velocity map imaging that make its prominent use at ELI very advantageous are

- the possibility to detect (fragment) ions and electrons with unit efficiency using a simple, electrostatic geometry that is easily accessible to (multiple) laser beams

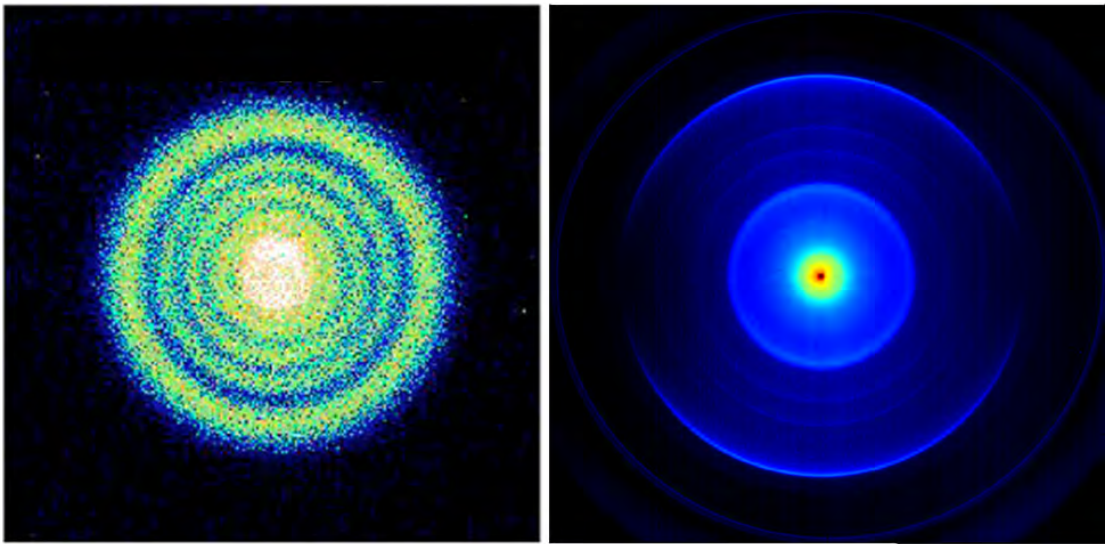

Figure 3.37: (left) Photoionization of Xe near the ionization threshold, producing threshold electrons that undergo extensive holographic interference en route to the velocity imaging detector.

- the possibility to achieve reasonable energy resolution (typically $\Delta E/E = 1$–2%) and excellent angular resolution over a wide range of kinetic energies, ranging from meV to (shortly) appr. 1 keV/charge.
- the ability to use geometries that allow high quality signal generation even under conditions where sample densities, photon fluxes and photoionization cross-sections are small.

In its simplest, and most commonly used form, velocity map imaging involves the use of a crossed atomic/molecular + laser beam geometry. Recent attosecond experiments have significantly benefitted from the use of an ion optics geometry where the target gas is injected by means of a (pulsed) gas injection system that is integrated in a specially shaped repeller electrode [20]. The spatially resolved recording of electrons or ions is performed using the combination of a set of microchannel plates, a phosphorscreen and a camera system. Such a detection system has a spatial resolution of 100–200 μm, and (use of in pulsed operation) a temporal resolution of 50–100 ns. Future improvements involving the use in vacuum pixel detectors are under investigation and show the promise of delivering considerably higher spatial resolution (35 μm is already demonstrated, and sub-10-μm is expected) and time resolution (sub-ns is expected).

Bibliography

[1] A. H. Zewail, Journal of Physical Chemistry A **104**, 5660 (2000).
[2] J. Breidbach and L. S. Cederbaum, Journal of Chemical Physics **118**, 3983 (2003).
[3] F. Remacle and R. D. Levine, Proceedings of the National Academy of Sciences of the United States of America **103**, 6793 (2006).
[4] R. Santra, J. Zobeley, L. S. Cederbaum, et al., Physical Review Letters **85**, 4490 (2000).
[5] M. Mucke, M. Braune, S. Barth, et al., Nature Physics **6**, 78 (2010).
[6] N. Sisourat, N. V. Kryzhevoi, P. Kolorenc, et al., Nature Physics **6**, 508 (2010).
[7] A. Landers, T. Weber, I. Ali, et al., Physical Review Letters **8701** (2001).
[8] F. Krasniqi, B. Najjari, L. Struder, et al., Physical Review A **81**, 033411 (2010).
[9] G. Sansone, F. Kelkensberg, J. F. Perez-Torres, et al., Nature, 763 (2010).
[10] F. Kelkensberg, A. Rouzee, W. Siu, et al., (2010 (in preparation)).
[11] J. Mauritsson, T. Remetter, M. Swoboda, et al., Physical Review Letters **105** (2010).

[12] J. J. Larsen, H. Sakai, C. P. Safvan, et al., Journal of Chemical Physics **111**, 7774 (1999).
[13] F. Rosca-Pruna and M. J. J. Vrakking, Physical Review Letters **8715** (2001).
[14] N. Berrah, J. Bozek, J. T. Costello, et al., Journal of Modern Optics **57**, 1015.
[15] A. T. J. B. Eppink and D. H. Parker, Review of Scientific Instruments **68**, 3477 (1997).
[16] S. A. Aseyev, Y. Ni, L. J. Frasinski, et al., Physical Review Letters **91**, 223902 (2003).
[17] T. Remetter, P. Johnsson, J. Mauritsson, et al., Nature Physics **2**, 323 (2006).
[18] F. Lepine, C. Bordas, C. Nicole, et al., Physical Review A **70** (2004).
[19] A. Rouzee, P. Johnsson, H. Fukuzawa, et al., (2010 (in preparation)).
[20] O. Ghafur, W. Siu, P. Johnsson, et al., Review of Scientific Instruments **80**, 033110 (2009).

4 Theory and numerical simulations

In the second half of the XX century physicists witnessed magnificent progress in elementary particle physics with the formulation of the standard model, and its experimental confirmation by the discoveries of the W and Z bosons, and in cosmology with the construction of the inflation theory and the evidence for the presence of dark matter and dark energy in the Universe. At the same time classical physics maintained its vigorous development which resulted in a novel understanding of collective phenomena in multiparticle systems, ranging from the scale of the Universe down to modelling socio-economic systems and in particular in the understanding of the nature of chaos in mechanical systems, thus providing a foundation for statistical mechanics and turbulence theory. Novel and fundamental developments also took place in our understanding of the physics of nonlinear systems and in particular in nonlinear wave theory with the discovery of the method of "inverse scattering" for solving nonlinear partial differential equations, thus confirming the old truth that there cannot be a fully complete area of science [1].

At the beginning of the XXI century a demand arose to understand the collective behaviour of relativistic quantum systems (such as quark-gluon plasmas) and to probe quantum vacuum. During the last decade it was realized that the experimental study of nonlinear collective quantum physics and vacuum probing are possible using high power lasers. The laser light interacts with matter under conditions that are well described by classical or by quantum electrodynamics, the parts of theoretical physics that were established at the end of the XIX century and in the '50s of the XX century, respectively.

In present experiments the interaction of ultra high intensity laser pulses with matter (which instantaneously becomes a plasma) takes place in physical regimes where the energy of the charged particles in the plasma becomes ultrarelativistic and is accompanied by the generation of high frequency electromagnetic radiation. This interaction leads to the generation of coherent structures such as wave-guiding channels that appear due to the relativistic self-focusing of the laser pulse, regular wake waves left behind by ultrashort laser pulses, collisionless shock waves, relativistic electromagnetic solitons and vortices. In order to describe such structures adequately we need to use our full arsenal of methods of nonlinear wave theory and particle dynamics. Focusing on an important problem for fundamental science and applications such as charged particle acceleration, in the frameworks of laser wake wave acceleration for electrons and of radiation pressure dominated acceleration for ions, one must expand this arsenal by the knowledge that has been built up in the field of standard accelerator physics. In addition, with extremely intense laser pulses a considerable portion of a charged particle energy acquired from the laser field is wasted by radiation, so that the dynamics of charged particles becomes dissipative due to radiation losses, which so far have been considered for processes typical for astrophysical conditions. Thus exchanging ideas and methods with theoretical astrophysics becomes imperative for a successful development of our field of science. Coming and future laser generations will provide physical conditions for light-matter interaction where the effects caused by the radiation friction force will completely change the main features of the propagation of electromagnetic waves in plasmas. In particular these effects can result in the generation of high power ultra-short gamma ray bursts whose interaction with matter will open up unexplored sides of material science.

The study of relativistic electrodynamics of continuous media is formidable due to strongly nonlinear relativistic dynamics of media, the importance of discrete nature of media and corresponding kinetic effects, and, in general, due to the high dimensionality and lack of symmetry of the problem.

Fortunately, powerful methods for investigating laser-matter interactions have become available through the development of applied mathematics and advent of modern supercomputers. In certain cases low dimensional, though pithy, analytic solutions can be found and these solutions act as paradigms for directing and interpreting numerical simulations of problems with

higher dimensionality and less symmetry. In three-dimensional modelling of ultrashort relativistically intense laser pulses propagating in collisionless plasmas, particle-in-cell codes provide a unique opportunity for properly describing the nonlinear wave dynamics, including nonlinear wave breaking, charged particle acceleration, and the generation of nonlinear coherent and turbulent structures such as collisionless shocks, solitons, self-focusing channels, etc. Computer simulations play an invaluable role in the analysis of "extreme" regimes which are outside the reach of most analytical methods. Simulations allow detailed analysis of physical processes and visualization techniques provide a spectacular presentation of the results.

Although simulation methods stem from the analytical theory and must be validated by known exact solutions, here they are not only used for extending analytical models, but play the more vital role of an investigative tool for discovering new phenomena. However the simulation analysis must be accompanied by the creation of an appropriate terminology and of an appropriate conceptual framework needed in order to describe the numerical results, and must be guided by an "a priori" understanding of the relevant range of parameters and their scaling. Both the conceptual framework and terminology and the parameter estimates can only be obtained from a physical understanding based on the extrapolation of simplified, lower dimensionality, analytical models.

As in the case of classical mechanics and of mechanics of continuous media 50 years ago, we expect to witness spectacular discoveries in the emerging discipline of quantum electrodynamics of continuous media. Increasing the laser intensity will lead us to encounter novel physical processes such as the radiation reaction dominated regimes and, at even higher intensities, the regime of the quantum electrodynamics (QED) processes. Near the intensity that corresponds to the QED critical electric field, light can generate electron-positron pairs from vacuum and vacuum begins to act as a nonlinear medium, leading, e.g., to the process of light-light scattering. These nonlinear QED effects reveal the nature of vacuum thus helping us to understand the properties of more general nonlinear quantum field theories.

The parameters characterising the nonlinear interaction depend on the laser wavelength λ and amplitude $E_{\rm las}$ and on the relativistic electron energy $m_e c^2 \gamma_e$ (see Fig. 4.1 and [1]). When the laser normalized amplitude, $a = eE_{\rm las}\lambda/m_e c^2$, reaches $\sim (\lambda/r_e)^{1/3} = 400$, where $r_e = e^2/m_e c^2$, i. e., the intensity of 10^{23} W/cm^2, we enter the radiation reaction dominated regime, which so far has not been studied in laser plasma experiments. The nonlinear QED processes come into full play when the parameter $\chi_e = (E/E_S)\gamma_e$ exceeds unity, where $E_S = m_e^2 c^3/e\hbar$ is the so called Schwinger field. This parameter shows how close is the electric field in the electron rest frame of reference to the Schwinger field which can create electron-positron pairs in vacuum. The corresponding intensity is 10^{29} W/cm^2. The first electron-positron pairs in the interaction of the laser pulse with ultrarelativistic electrons will be seen when the parameter χ_e is small but finite, being of the order of unity. If χ_e becomes substantially larger than unity, an avalanche type discharge with abundant electron-positron plasma generation will change the laser-plasma interaction and will result into a novel state of matter creation which can be called a "lepton-gamma-plasma" (LGP).

An adequate description of the QED processes in the electrodynamics of continuous media requires an adequate development of theoretical methods and computer codes. The new and fruitful investigation in the area of extremely high power electromagnetic fields causing macroscopic QED effects is only possible with the mutual interplay between analytical theory, computer simulation and experiment. However, we must keep in mind the cost of the experiments and of the simulations, the cost which have become an important factor in the development of scientific culture. With the growth of the cost of each shot of exawatt-and-higher-power lasers and of each run of petaflop-and-higher-performance supercomputers, developing adequate theoretical models becomes imperative. This situation is markedly different from the case with relatively lower power lasers which can operate in high repetition rate regimes, where a major part of the investigation of the physical processes can be performed experimentally by finding

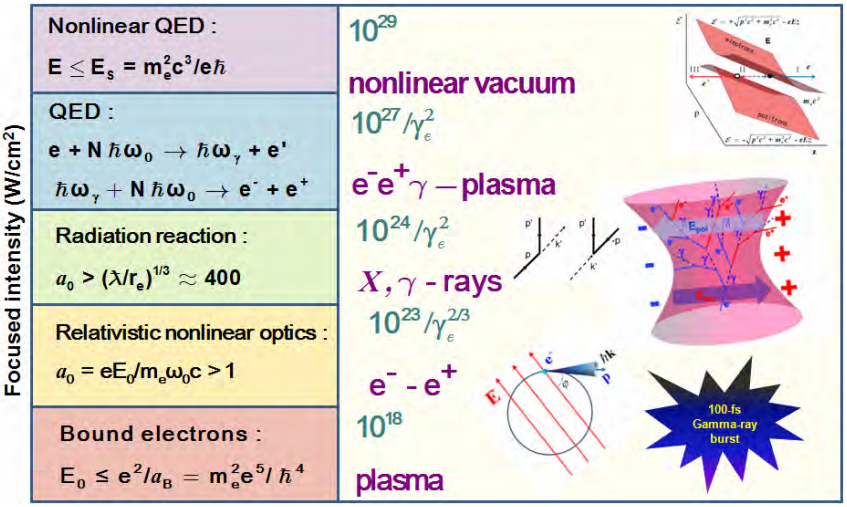

Figure 4.1: High intensity regimes of laser-plasma interaction (see discussions and literature cited in [2])

iteratively the proper conditions for revealing phenomena of interest.

The unprecedented power of the ELI facility evokes the investigation of new physics. This investigation necessitates an "extensive" use of supercomputers because the large spatio-temporal scales and the multitude of physical properties must be accounted for in multi-scale simulations which aim to prove the feasibility of the desired regimes and to reveal new effects. The parameters that are required for studying for example the Relativistic Flying Mirror [3] for a petaflop computer are presented in Fig. 4.2.

Within an "intensive" approach to supercomputer use, the key role belongs to multi-parametric simulations [4, 5], with the aim to provide optimization, to find scaling laws and to reveal new effects. In this technique, a series of N tasks with different sets of laser and target parameters is

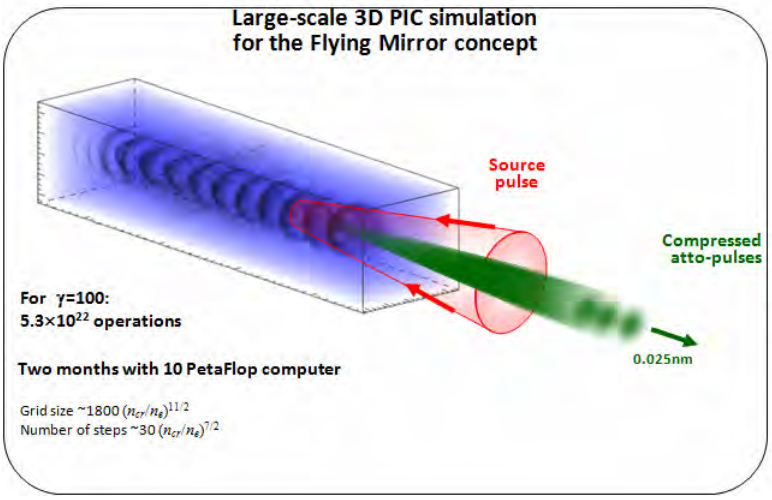

Figure 4.2: Large scale (10 PetaFlop Computer) 3D PIC simulations for the Relativistic Flying Mirror Concept.

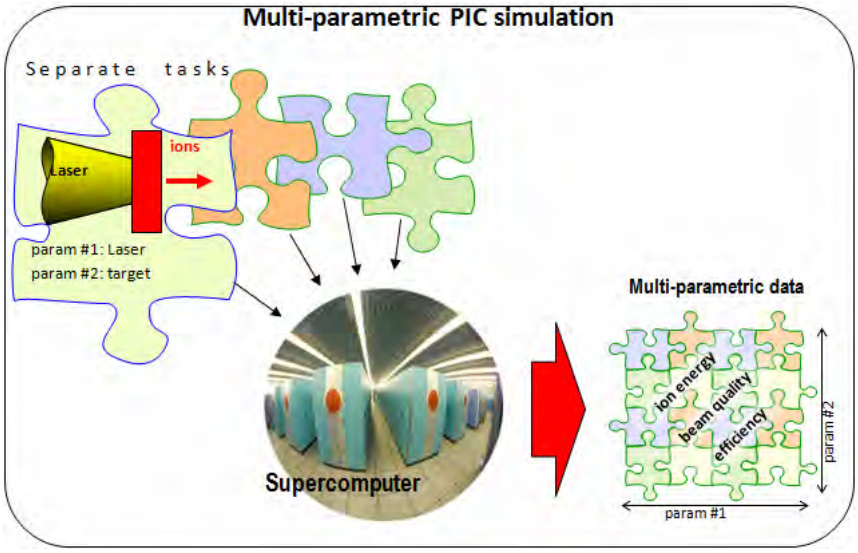

Figure 4.3: Multi-parametric simulation concept [4, 5].

performed simultaneously on the N processors of a multiprocessor supercomputer (see Fig. 4.3), using massively parallel and fully vectorized codes, such as, e.g., the REMP code based on the PIC method and the "density decomposition" scheme [6].

The required performance of a supercomputer should match the laser facility power: a petaflops scale supercomputer is required for a highly accurate simulation of physical processes induced by a petawatt laser due to necessarily high spatio-temporal resolution. A substantial part of the cost of such computers comes from operation costs (electricity, maintenance, etc.). The exawatt laser physics will require exaflop supercomputers with operating costs several orders of magnitude higher. In view of this, a realistic way of running the simulation centre devoted to ELI problems will require a direct high-speed connection to one or few EU supercomputer centres.The ELI simulation centre is expected to have a hundred teraflops computer facility aimed

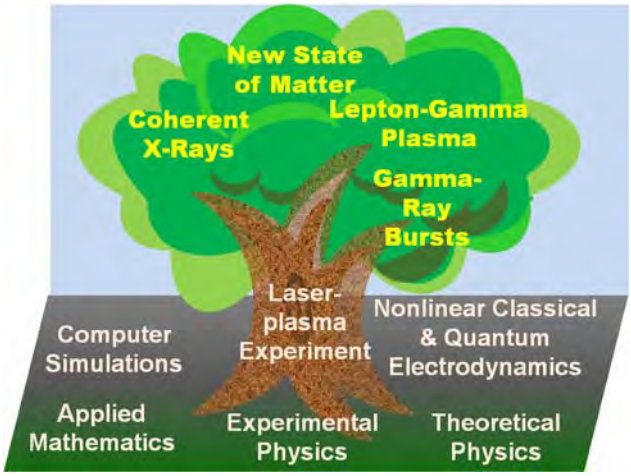

Figure 4.4: Multi-disciplinary nature of the ELI project.

at the theoretical support of experiments, parameter and optimization search, and preliminary studies of lepton-gamma-plasma (LGP) created in the focus of the ELI full-scale pulse.

In an organizational way, it is highly desirable to have at least two ELI centres completely devoted to theory and computer simulations: the goal of one of them would be the development of analytical theory and the aim of the other would be the elaboration of computer codes and their usage on supercomputers for simulations. It is important to provide conditions for their mutual independence combined with close cooperation. The optimum number of experts in each centre should be high enough in order to exceed the "critical mass" number required for productive generation of new ideas and for obtaining world highest level scientific results, for teaching and forming next generations of experts in theoretical physics and applied mathematics, which is only possible within a creative and free atmosphere. The multidisciplinary nature of the scientific studies within the framework of the ELI project (see Fig. 4.4) implies a multitude of approaches for reaching the goals that have already been formulated and the new goals which will inevitably come into being. For achieving these goals establishing theoretical and simulations ELI centres is crucially important.

Bibliography

[1] V. L. Ginzburg, Usp. Fiz. Nauk 80 (1963) 207.
[2] S. V. Bulanov, T. Zh. Esirkepov, Y. Hayashi, M. Kando, H. Kiriyama, J. K. Koga, K. Kondo, H. Kotaki, A. S. Pirozhkov, S. S. Bulanov, A. G. Zhidkov, P. Chen, D. Neely, Y. Kato, N. B. Narozhny, and G. Korn, [2011arXiv1101.2501B].
[3] S. V. Bulanov, T. Zh. Esirkepov, T. Tajima, Phys. Rev. Lett. 91 (2003) 085001.
[4] K. Matsukado et al., Phys. Rev. Lett. 91 (2003) 215001.
[5] T. Esirkepov, M. Yamagiwa, and T. Tajima, Phys. Rev. Lett. 96 (2006) 105001.
[6] T. Zh. Esirkepov, Comput. Phys. Commun. 135 (2001) 144.

Part III

ELI Technology

5 Technological basis for the primary sources

5.1 General laser layout

In order to reach the unprecedentedly high peak power for ELI, modern laser technology has to be pushed to its limits by both implementing many new concepts and optimizing tried state-of-the-art technology. In general, the desired peak powers require the creation of high-energy laser pulses with ultra-short duration. However, the direct amplification of short pulses to high energies is limited by constraints for size and damage threshold of the optical components in the laser. Moreover, owing to the nonlinear response of optical materials at high intensities, upon propagation in matter such as transparent optical components the laser pulse itself will experience spatial and temporal phase distortions, leading to a degradation of the beam quality and eventually a loss of coherence in both time and space. Therefore, safe direct amplification in a single amplifier without detrimental effects is only possible up to a maximum intensity of $\sim 1\,\mathrm{GW/cm^2}$ [1, 2]. If a laser chain is considered aiming for producing energetic short laser pulses, then the overall effect of the amplifier gain media, transmission optics and air has to be considered. Thus, the general rule of thumb in designing laser systems is that the so called break-up integral calculated (and first measured in [3]) for the entire laser system has to be kept below 1 to avoid considerable deterioration of the focused pulses.

To overcome the nonlinear effects in a high power laser chain, an obvious solution is to increase the beam diameter and also to multiply the pulses. These routes were, however, soon blocked by technological and economical constraints. The breakthrough came with the proposal to decrease the peak pulse power in the laser chain by stretching the pulse duration prior to amplification, and temporally compress the pulses again just before the target. The idea how to stretch and compress light pulses was inspired by radar technology and adopted into optics, is dubbed chirped pulse amplification (CPA) [4] and has been the key for the realization of a dramatic increase in laser power and focused intensity over the last 25 years. The basis of realization lays in the fact that short laser pulses consist not of a monochromatic wave, but a broad range of colors[1]. This provides a handle for stretching a short laser pulse into a long one (and vice versa) by sending the different colors in the pulse over different optical paths, hence dramatically lowering its peak power during amplification. It is schematically shown in Fig. 5.1. A low-energy ultra-short pulse is first stretched in time, then amplified and finally temporally compressed in an all-reflective setup to allow for an ultra-short, high-energy pulse.

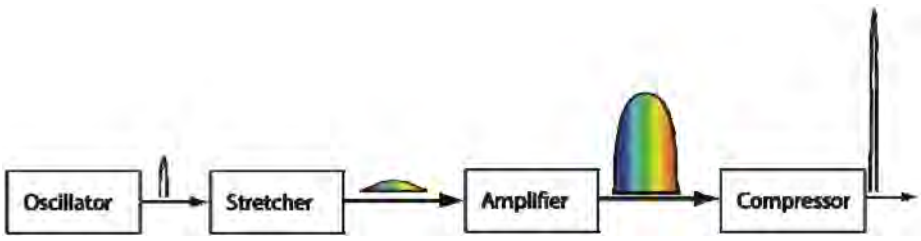

Figure 5.1: Principle of Chirped Pulse Aplification (CPA): An ultrashort laser pulse is temporally stretched, amplified at low peak intensity and temporally recompressed.

High-power lasers usually consist of a chain of separate amplifiers with increasing size and energy level. In the first amplifiers, the gain factor is very large (10^6), while the overall energy level is rather low (mJ). The architecture of such low-energy, high-gain amplifiers is particularly vulnerable to photon noise, prepulses from multiple passes, and phase or gain nonlinearities.

[1] This feature is in direct connection to the general phyisical law stating that short events in time are not well defined in energy, which can be eventually derived from Heisenberg's uncertainty principle.

These effects may lead to the emission of substantial amounts of light nanoseconds to picoseconds before the main pulse has reached its maximum power, hence lowering the "temporal contrast", i.e. the ratio of background light to peak power.

As solid targets become ionized above a threshold of around $10^{10}\,\mathrm{W/cm^2}$, in a laser system such as ELI, a high temporal contrast is of utmost importance for applications. Hence, with an envisioned peak focal intensity of $10^{24}\,\mathrm{W/cm^2}$, ELI calls for temporal contrast of greater than 10^{14} outside the last picosecond before the main pulse. Otherwise, solid targets would not stay solid for the main pulse, but expand into a low-density plasma, altering the interaction characteristics in an unpredictable manner. These high contrast values up to now cannot even be measured with state-of-the art devices.

Since all important contrast degradation effects occur in the first high gain amplifier stages (commonly dubbed "frontend"), it is necessary to clean the temporal shape of the pulses after these stages by filtering the pulses in the temporal domain. The so far most successful architectural solution is the double CPA (DCPA) scheme [5], where the pulses from the frontend are fully compressed and the prepulses cut away by an ultrafast optical "switch". Instantaneous effects triggered by the laser pulse itself and displaying strong intensity dependence, such as cross-polarized wave generation (XPW) [6, 7], are ideal for pulse cleaning. Afterwards, the clean, intermediate energy pulses are stretched again, amplified in low-gain, high-energy amplifiers with low distortions and finally compressed (see Fig. 5.2). To compensate for gain narrowing in laser materials and hence keep the eventual pulse duration from a DCPA laser the shortest, the scheme of negative and positive CPA (NPCPA) calls for opposite sign of chirping in the first and second CPA parts [8].

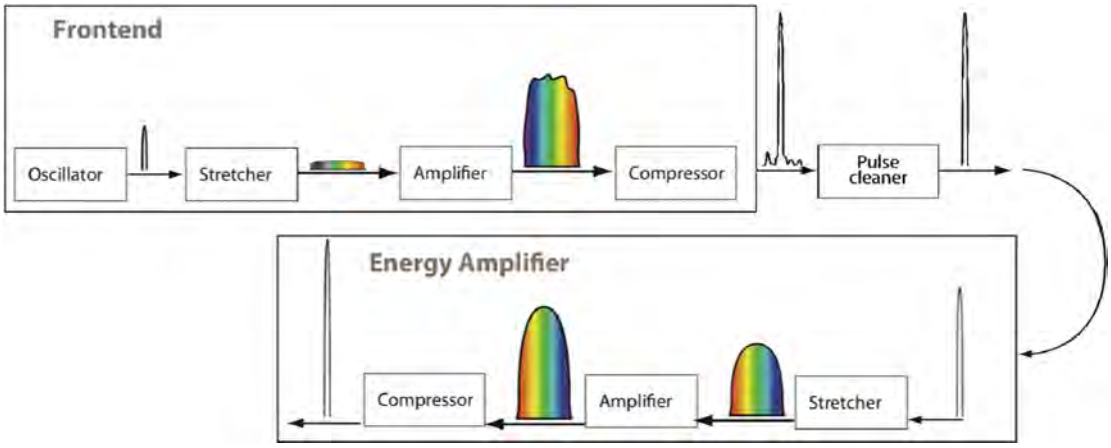

Figure 5.2: Double CPA Technique: In order to generate a temporally clean (i.e. high contrast) laser pulse, the pulses are temporally filtered at an intermediate energy level before being injected into the high-energy, low distortion amplifiers.

As a different approach to keep the bandwidth broad along the laser chain, optical parametric devices were suggested to replace some amplifiers in high power laser systems [9]. These optical parametric chirped pulse amplification (OPCPA) stages could be located either in the front end part where the gain is very high in order to reduce the gain narrowing, or in the power section where the available size of amplifier materials is the limiting parameter (KDP crystals exist in very large dimensions). In order to prevent from parametric superfluorescence in these OPCPA lasers, however, the pump sources shall be short (i.e. picosecond) pulsed lasers [10, 11], which circumvents most of the contrast problems inherent of high-gain, multiple-pass laser amplifiers by providing high, ultrabroadband gain in a single pass [12].

Ultimately, the output of a high-power laser reaches a technological limit through availability of large optics, in particular the laser crystals and pulse compression gratings. Recent progress in manufacturing appears to predict that limit to be somewhere around 10–20 PW for a single beam laser within the implementation of the ELI lasers at the three sites. This assumes that optics currently at the prototype stage can be commercialized within the next 2–3 years. However, for the ultimate goal of ELI to reach a level of 200 PW, a single beam laser will not be the most cost-effective solution. Combining multiple powerful laser beams onto a common target is not a new technology, but has become state-of-the-art for many fusion research facilities around the world since the 1970's. However, also in this field ELI will have to break new ground. In contrast to a fusion machine that aims at smoothly distributing a large amount of energy onto a target much larger than the light wavelength, ELI wants to concentrate the energy of multiple large-scale single-beam lasers onto a spot with a size on the order of one laser wavelength (see Fig. 5.3).

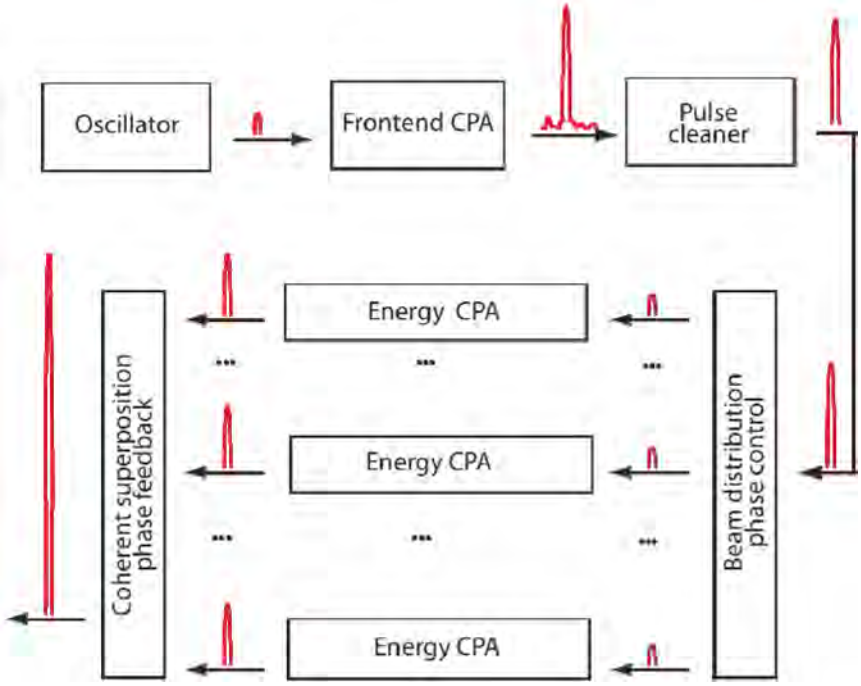

Figure 5.3: Beam multiplexing: A sophisticated real-time phase control loop has to stabilize the coherent superposition of up to ten 20 PW-laser beams, all derived from a common frontend.

This requires not only to overlap the individual beams, but to do so in a phase-coherent way, i.e. the optical path difference between the individual lasers in any part of the beam has to be below a fraction of a wavelength. Since even air turbulence or mechanical vibrations can easily lead to many wavelengths path difference, a sophisticated real-time phase monitoring and control system has to be implemented into each laser chain, complemented by ultra-stable mechanical engineering and installation of large parts of the laser chain in vacuum.

Bibliography

[1] S. Backus, C. G. Durfee III, M. M. Murnane, H. C. Kapteyn, Rev. Sci. Instr. **69**, 1207 (1998).
[2] G. A. Mourou, T. Tajima, and S. V. Bulanov, Rev. Mod. Phys. **78**, 309 (2006).
[3] D. Villate, N. Blanchot, C. Rouyer, Opt. Lett. **32**, 524 (2007).

[4] A. D. Strickland and G. Mourou, Opt. Commun. **56**, 212 (1985).
[5] M. P. Kalashnikov, E. Risse, H. Schönnagel, W. Sandner, Opt. Lett. **30**, 923 (2005).
[6] N. Minkovski, G. I. Petrov, S. M. Saltiel, O. Albert, J. Etchepare, J. Opt. Soc. Am. B **21,** 1659 (2004).
[7] A. Jullien, O. Albert, F. Burgy, G. Hamoniaux, J.-P. Rousseau, J.-P. Chambaret, F. Augé-Rochereau, G. Chériaux, J. Etchepare, N. Minkovski, S. M. Saltiel, Opt. Lett. **30**, 920 (2005).
[8] M. P. Kalashnikov, K. Osvay, I. M. Lachko, H. Schönnagel, W. Sandner, Appl. Phys. B **81**, 1059 (2005).
[9] I. N. Ross, P. Matousek, M. Towrie, A. J. Langley, and J. L. Collier, Opt. Commun. **144**, 125 (1997).
[10] G. Cerullo, S. DeSilvestri, Rev. Sci. Instr. **74**, 1 (2003).
[11] A. Dubietis, R. Butkus, A. P. Piskarskas, IEEE J. Sel. Top. Quantum Electron. **12**, 163 (2006).
[12] Z. Major, S. A. Trushin, I. Ahmad, M. Siebold, C. Wandt, S. Klingebiel, T. J. Wang, J. A. Fülöp, A. Henig, S. Kruber, R. Weingartner, A. Popp, J. Osterhoff, R. Hörlein, J. Hein, V. Pervak, A. Apolonski, F. Krausz, S. Karsch, Rev. Las. Eng. **36**, 431 (2009).

5.2 Operation Principles

5.2.1 Femtosecond Laser Oscillators

Femtosecond solid-state and fiber laser technology has been advancing tremendously in the past 20 years. To enable stable, broadband, mode-locked operation of femtosecond oscillators, several novel laser active materials have been tested including titanium-doped sapphire (Ti:sapphire) [1], various Cr [2] and Yb-doped bulk and thin disk crystals [3] and fibers [4]. The architecture of the laser cavity varies accordingly, depending on the type of active material, pumping, heat management, dispersion compensation solutions etc. Several novel mode locking methods have also been developed including Kerr-lens [5] and semiconductor saturable absorber based mode-locking [6, 7].

The construction of record breaking CPA/OPCPA chains necessitates the usage of a robust, reliable and broadband laser front end including a stable, turnkey femtosecond oscillator. The broad commercial availability of various Ti:sapphire oscillators delivering directly the wavelength range that can be used in high-intensity femtosecond amplifier chains indicates that these oscillators are the technology of choice. Therefore, the next sections will introduce key technological elements and state-of-the-art of Ti:sapphire oscillator technology.

Features of Ti:sapphire active material

The usage of Ti:sapphire as laser active material opened huge perspectives in femtosecond laser technology more than 20 years ago [1]. It enabled the reliable generation of unprecedentedly short femtosecond pulses from a simple cavity due to the unparalleled broad gain bandwidth of the crystal. The key figure for determining the relative bandwidth of the laser transition is $\Delta\nu/\nu_0$ where ν_0 is the central laser frequency and $\Delta\nu$ is the frequency bandwidth of the transition. The achievable minimum pulse width (in units of optical cycles) is inversely proportional to this figure. The value of $\Delta\nu/\nu_0$ for Ti:sapphire is 0.27 meaning that the gain spectrum could, in principle, support 4-fs pulses at the central wavelength of 800 nm. This value can be surpassed only by Cr:ZnS and Cr:ZnSe oscillators operating at 2400 nm featuring a $\Delta\nu/\nu_0$ of around 0.4 [2]. Owing to the properties of the host crystal, heat management issues can be handled relatively easily in standard Ti:sapphire oscillators pumped by up to 10 W of green light (typically with frequency doubled cw Nd:XX lasers at 532 nm) even though heat production is not insignificant due to the large difference between pump and laser wavelengths. The mechanical, thermal and spectroscopic properties of sapphire make it an ideal host crystal for applications where robust, turnkey laser operation is required.

Key technologies and state-of-the-art in Ti:sapphire oscillators

In addition to the active material, Ti:sapphire oscillators also feature several key features and technologies that play a crucial role in the build-up and stabilization of the femtosecond pulse inside the cavity. i) The so-called Kerr-lens mode-locking mechanism enabled by the nonlinearity of the crystal provides for the generation and stabilization of the mode-locked pulse train [5]. ii) In order to exploit the full gain bandwidth and achieve the shortest possible output pulses, accurate, broadband control of cavity dispersion is required up to the third or even fourth order. A slightly negative net group delay dispersion (GDD, or second order dispersion) in the cavity is a prerequisite for solitonically mode-locked pulse formation, therefore, optical elements with negative GDD are required to compensate for the dispersion of the active crystal and air. The first Ti:sapphire oscillators mostly employed various prism pairs for this purpose [8], as they have low losses and enable accurate compensation of the GDD at a given wavelength. However, they fail to provide control over higher order dispersion terms limiting the shortest achievable pulse duration to approximately 10 fs [8]. The invention of chirped mirrors [9] enabled tailoring

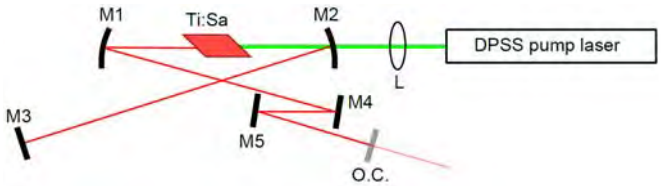

Figure 5.4: Typical setup of a compact, mirror-dispersion-controlled (MDC) Ti:sapphire oscillator. All mirrors involved (M1–M5) can be chirped mirrors. OC: output coupler, DPSS: diode-pumped solid-state pump laser.

the negative dispersion in the cavity resulting in sub-10-fs pulse generation directly from the oscillator [10] and also increased the compactness (and thus, the robustness) of these oscillators.

The breakthrough features enabled by the use of chirped mirror technology have been prompting active developments in this field, therefore, state-of-the art chirped mirror manufacturing is strongly related to oscillator development in many cases [11–13]. Dispersive mirrors providing high reflectance and accurate dispersion management over bandwidths of up to 150 THz in the visible and near infrared spectral ranges became routinely available. As a result, oscillators with 5 fs output can be obtained [11] (also commercially with sub-7-fs pulses [14]) for a number of applications including CPA/OPCPA seeding [15]).

Carrier-envelope phase stabilization of femtosecond oscillators

Another unique feature of femtosecond laser oscillators is the possibility to control the optical waveform of the output pulses. This means that it is not just the envelope of the laser pulses that is kept stable but also the underlying optical waveform can be stabilized by means of the carrier-envelope (CE) offset phase. This quantity can be actively locked with a technique called f-to-$2f$ interferometry [16, 17]. This technology has immense implications in optical frequency comb generation, too, and has revolutionized the field of frequency metrology [18]. All-chirped-mirror dispersion controlled oscillators are ideal candidates for CE phase stabilization owing to their inherent stability, whereas prism-based oscillators proved to be less effective for this application, since beam pointing fluctuations are transferred into phase-fluctuations via the prism pair. Novel amplifier chains also feature a CE phase stabilized front end and an additional "slow" feed-back loop that corrects for the phase fluctuations in the amplifier in order to produce controlled few-cycle optical waveforms for various light-matter interaction studies. This is a prerequisite if one intends to investigate few-cycle pulse-induced phenomena in the strong field and relativistic regimes with the amplifier chain, therefore the implementation of various CE phase stabilization techniques at the ELI facilities will be necessary, starting with the oscillator. In the past 5 years, several further significant advances were made in the field of CE phase stabilization. A monolithic stabilization scheme was developed [19], obviating the need for the construction of a separate f-to-$2f$ interferometer and resulting in higher stability. An alternative scheme is offered by a feed-forward technique based on an extracavity acousto-optic frequency shifter [20]. This method was demonstrated to surpass the precision of previous schemes by a factor of 5 [20]. CE phase stabilized oscillators in which these techniques are implemented are also available commercially [14, 21, 22]. Furthermore, complete CE phase stabilized single or double-stage front-end amplifiers are also commercially available [14, 22].

Bibliography

[1] Moulton P., J. Opt. Soc. Am. B **3**, 125 (1986).
[2] Deloach L. D., Page R. H., Wilke G. D., Payne S. A., Krupke W. F., IEEE J. Quant. El. **32**, 885 (1996).

[3] Giesen A., Hügel H., Voss A., Witting K., Brauch U., Opower H., Appl. Phys. B **58**, 365 (1994).
[4] Fermann M. E. and Hartl I., IEEE J. Sel. Top. Quant. El. **15**, 191 (2009) and references therein.
[5] Spence D. E., Kean P. N. and Sibbett W., Opt. Lett. **16**, 42 (1991).
[6] Keller U., Miller D. A. B., Boyd G. D., Chiu T. H., Ferguson J. F., Asom M. T., Opt. Lett. **17**, 505 (1992).
[7] Tsuda S., Knox W. H., de Souza E. A., Jan W. Y., and Cunningham J. E., Opt. Lett. **20**, 1406 (1995)
[8] Lemoff B. E. and Barty C. P. J., Opt. Lett. **18**, 57 (1993).
[9] Szipõcs R., Ferencz K., Spielmann C. and Krausz F., Opt. Lett. **19**, 201 (1994).
[10] Stingl A., Lenzner M., Spielmann C., Krausz F. and Szipõcs R., Opt. Lett. **20**, 602 (1995).
[11] Ell R. et al., Opt. Lett. **26**, 373 (2001).
[12] Baum P., Breuer M., Riedle E. and Steinmeyer G., Opt. Lett. **31**, 2220 (2006).
[13] Dombi P., Rácz P., Lenner M., Pervak V. and Krausz F., Opt. Express **17**, 20598 (2009).
[14] www.femtolasers.com
[15] Major Z. et al., Laser Rev. **37**, 431 (2009).
[16] Jones D. J. et al., Science **288**, 635 (2000).
[17] Apolonski A. et al., Phys. Rev. Lett. **85**, 740 (2000).
[18] Udem T., Holzwart R. and Hänsch T. W., Nature **416**, 233 (2002) and references therein.
[19] Fuji T. et al., Opt. Lett. **30**, 332 (2005).
[20] Koke S., Grebing C., Frei H., Anderson A., Assion A. and Steinmeyer G., Nature Phot. **4**, 462 (2010).
[21] www.menlosystems.com.
[22] www.kmlabs.com.

5.2.2 Amplification in laser media

Theory of pulse propagation in homogeneously broadened laser medium, with a fluorescence lifetime much longer than any pulse duration was developed by L.M. Frantz and J.S. Nodwick [1]. Thereafter the integrated amplification output fluence J_{out} can be written as:

$$J_{\text{out}} = J_{\text{sat}} \left[\ln(1 + G(\exp(J_{\text{in}}/J_{\text{sat}}) - 1))\right](1 - L) \tag{5.1}$$

$$G = \exp\left(J_p/J_{\text{sat}}\right) \tag{5.2}$$

$$J_{\text{sat}}(\nu) = h\nu_{\text{central}}/\sigma_g\left(\nu\right) \tag{5.3}$$

where J_{in} and J_{out} are respectively the input and output pulse fluence, J_{sat} is the saturation fluence, L the losses, G is the small signal gain, J_p is the fluence stored in the gain medium, ν_{central} is the transition frequency, h is Plank's constant. Active medium for ultra high intense lasers requires a set of specific parameters that make it capable to support short (after recompression) energetic pulses of high quality. It must be also commercially available in big volumes. As seen from [1] after amplification in laser media the output energy is limited by the saturation fluence J_{sat}, and by the size of the output stage of amplification, thus medium with higher saturation fluence is preferable. Since for ultrahigh intense lasers short pulses are required, another extremely important parameter is the bandwidth of amplification. This depends on the gain bandwidth of the active medium as well as on optical components used in the system. Because of their wide spectrum, short pulses can only be amplified without a loss of their bandwidth by materials with a gain width exceeding the bandwidth of the pulse.. Pumping band, spectral bandwidth and the upper-state radiative lifetime determine major pumping capabilities. Currently these major requirements are fulfilled by two types of solid-state laser materials. These are the Nd doped glasses and Titanium doped sapphire crystal.

The Nd:glass medium is one of the most old known laser media. It is commercially available in big volumes. The saturation fluence of the phosphate Nd:glass is ~ 4 J/cm^2 which is sufficiently high. The Nd:glas laser technology is advanced to support the energy up to a MJ level with laser-fusion installations [1, 2]. Typically the gain bandwidth of this medium allows pulses of ~ 1 ps duration. This makes more than a 10 Petawatt level available [3–9]. Different kinds of Nd:glasses have slightly spectrally shifted central wavelengths. For instance typically silicate ($\lambda_{\text{central}} \sim 1.06$ μm) and phosphate ($\lambda_{\text{central}} \sim 1.05$ μm) – bases types have spectral difference of $\Delta\lambda_{\text{central}} \sim 10$ nm. A combination of different types of Nd doped glasses allows pulses of duration shorter than 1 ps. Currently ~ 170 fs pulses were demonstrated with this technique at a Petawatt level [10], but with an OPCPA front end. Because of a relatively low thermal conductivity of the glass host, the technology of Nd:glass lasers is limited to low repetition rate, that depends on the output laser energy, from several shots/min for the output energy <100 J to few shots/hours for KJ and 1 shot/day for higher energy levels. This medium has a storage time in the range of 300–500 μs. It is well suited for both flash lamp and laser diode pumping.

Another and even more suitable for amplification of short pulses medium is the Titanium doped sapphire crystal (Ti:Sa). Ti:Sa lasers are the most widely spread short pulse and intense lasers. The progress of the Ti:Sa technology started from the publication of P. F. Moulton in 1983 [11]. Ti:Sa has several very desirable characteristics which make it ideal as a high-power amplifier material. The large saturation fluence (1 J/cm^2), long storage time (3 μs), a very high damage threshold ($\sim$8–10 J/cm^2) and a high thermal conductivity of $\sim$ 46 W/mK at 300 K make it an ideal amplifier gain material. It has a broad absorption band around 500 nm, that is especially suitable for laser pumping with frequency doubled pulses of Nd:YAG-lasers. It can easily support repetition rate of 10 Hz and higher. Moreover, Ti:Sa has the broadest gain bandwidth of any known laser material ($\sim$ 230 nm), thus it can support pulses of only several oscillations. High aperture crystals of Ti:sapphire are commercially available with a diameter up to ~ 175 mm, that is required for the recompressed power of $\sim$ 10 PW. Despite that development of high aperture Ti:Sa crystals is being strongly pushed by the Apollon-10P project, currently such crystals of sufficient optical quality are available only from the firm Crystal Systems Inc. [12].

The architecture of an ultra-high intense laser implements CPA technology, when amplification starts from a single stretched pulse of nearly a nanojoule energy. Thus to achieve required multijoule energy level, the total gain in access of 10^{10}–10^{11} is required. Amplification is accomplished in several stages that include the pre amplifier and power amplifiers. In the pre amplifier the pulse energy is being pushed to a level above a milijoule (total gain $\sim 10^6$–10^7). The power amplifiers are designed to efficiently extract the stored energy, thus run close to saturation. Despite that there are many variants thereof, the pre amplifiers are accomplished either with a regenerative [13–15] or a multipass (9–11 passes) schemes [16–17]. Currently most of the high intense lasers implement multipass amplifiers, because of lower losses they are not so strongly influenced by gain narrowing and are free of pre-pulses leaking through the Pockels cell as in the regenerative amplifier. The pre amplifier has the highest gain in the system ($\sim 10^7$), thus it determines the major characteristics of the pulse: bandwidth and ASE contrast (see 5.3.3). With stretched pulses, the amplification process significantly reshapes and shifts the spectrum of the pulse. This happens due to the finite gain bandwidth of the active medium. The gain cross section, $\sigma_g(\nu)$, appearing in the exponent in calculating the amplification factor (see [1–3]), through successive passes in the amplifier tends to narrow the amplified spectrum (gain narrowing). As the result, for the pre-amplifiers based on Ti:Sa even though the bandwidth of the gain cross section is very large, the total bandwidth of the pre amplifier without spectral corrections can not exceed ~ 47 nm [18]. The saturated amplification that mostly takes place in the power amplifiers, in addition to the gain narrowing, shifts the pulse spectrum [19]. For positively chirped pulses that are required for the diffraction grating based compressors, this leads to a red shift of the pulse spectrum and possible slight improvement of total bandwidth. There are

several ways to overcome the problem. First, accomplish spectral correction [20–24] that works better for regenerative amplifiers. Second, use the scheme with flipping the chirp sign during amplification (NPCPA [25]). This scheme allows separate preferable amplification of the blue in a first part and the red in a second part. This enables supporting substantially broader total bandwidth ($\sim$ 60 nm). Another solution consists in spatio-temporal CPA [26]. This solution has been demonstrated only in the mJ level regime. A last solution that is applicable for high energy pulses, is the recourse to spectral filtering before each power amplifier. The spectrum is shaped in such a way that the gain narrowing and spectral shifting are precompensated.

The power amplifiers of Ti:sapphire lasers use the multipass architecture, that allows efficient extraction of stored energy. The energy extraction efficiency of $\sim$40% can be reached after 3–4 passes through the active medium. The power multipass Ti:Sapphire amplifiers use a relatively thin (up to 3–4 cm) and normally with respect to the incident beam cut crystals, that is determined by technological limits of the crystal growth and high efficiency of amplification (good matching of pumping and amplifying modes). Then typical axial low signal gain at the power stages is $\sim$4–5. Taking into account that the diameter of the pump area can substantially exceed the crystal thickness, the total gain inside the crystal at an arbitrary angle to the incoming beam can substantially exceed the axial gain. This can lead to the internal self lasing of crystals thus reducing population inversion. If the doping of the crystal is not very high, so that the inversion is nearly uniformly distributed, then the highest gain corresponds to rays reflected at the angle of total reflection inside. One can easily estimate that the parasitic lasing starts when the ratio of the diameter of the pump region to the crystal thickness exceeds the value of $\sim$0.8–1. In this case being scattered at the crystal surface the rays come back to the pumped area thus closing the loop. To avoid this process the side surface of the crystal is being covered with index matching absorbing substances.

Bibliography

[1] D. Besnard, J. Phys. Conf. Ser. **112**, 012004 (2008).
C. Cavaillier et al, "Status of the LMJ program", Inertial Fusion Sciences and Applications 2003, pp. 523-528, edited by B. Hammel, D. Meyerhofer, J. Meyer-ter-Vehn and H. Azechi, ISBN 0-89448-686-1 (2004).

[2] C. A. Haynam, P. J. Wegner, J. M. Auerbach, M. W. Bowers, S. N. Dixit, G. V. Erbert, G. M. Heestand, M. A. Henesian, M. R. Hermann, K. S. Jancaitis, K. R. Manes, C. D. Marshall, N. C. Mehta, J. Menapace, E. Moses, J. R. Murray, M. C. Nostrand, C. D. Orth, R. Patterson, R. A. Sacks, M. J. Shaw, M. Spaeth, S. B. Sutton, W. H. Williams, C. C. Widmayer, R. K. White, S. T. Yang, and B. M. Van Wonterghem, Appl. Opt. **46**, 3276 (2007).

[3] M. D. Perry, D. Pennington, B. C. Stuart, G. Tietbohl, J. A. Britten, C. Brown, S. Herman, B. Golick, M. Kartz, J. Miller, H. T. Powell, M. Vergino, and V. Yanovsky, Opt. Lett. **24**, 160 (1999).

[4] J. D. Zuegel, S. Borneis, C. Barty, B. Le Garrec, C. Danson, N. Miyagana, P. K. Rambo, C. Le Blanc, T. J. Kessler, A. W. Schmid, L. J. Waxer, J. H. Kelly, B. Kruschwitz, R. Jungquist, E. Moses, J. Britten, I. Jovanovic, J. Dawson, and N. Blanchot, Fusion Sci. Technol. **49**, 453 (2006).

[5] L. J. Waxer, D. N. Maywar, J. H. Kelly, T. J. Kessler, B. E.Kruschwitz, S. J. Loucks, R. L. McCrory, D. D. Meyerhofer, S. F. B. Morse, C. Stoeckl, and J. D. Zuegel, Opt. Photonics News **16**, 30 (2005).

[6] C. P. J. Barty, M. Key, J. Britten, R. Beach, G. Beach, G. Beer, C. Brown, S. Bryan, J. Caird, T. Carlson, J. Dawson, A. C. Erlandson, D. Fittinghoff, M. Hermann, C. Hoaglan, A. Iyer, L. Jones II, I. Jovanovic, A. Komashko, O. Landen, Z. Liao, W. Molander, S. Mitchell, E. Moses, N. Nielsen, H.-H. Ngyuen, J. Nissen, S. Payne, D. Pennington, L. Risinger, M.

Rushford, K. Skulina, M. Spaeth, B. Stuart, G. Tietbohl, and B. Wattelier, Nucl. Fusion **44**, S266 (2004).
[7] C. Le Blanc, C. Felix, J. C. Lagron, N. Forget, Ph. Hollander, A. M. Sautivet, C. Sauteret, F. Amiranoff, and A. Migus, "The petawatt laser glass chain at LULI: from the diode-pumped front end to the new generation of compact compressors," in *Proceedings of Third International Conference on Inertial Fusion Sciences and Applications,* B. A. Hammel, D. D. Meyerhofer, J. Meyer ter Vehn, and H. Azechi, eds. (American Nuclear Society, 2004), pp. 608–611.
[8] C. N. Danson, P. A. Brummitt, R. J. Clarke, J. L. Collier, B. Fell, A. J. Frackiewicz, S. Hancock, S. Hawkes, C. Hernandez- Gomez, P. Holligan, M. H. R. Hutchinson, A. Kidd, W. J. Lester, I. O. Musgrave, D. Neely, D. R. Neville, P. A. Norreys, D. A. Pepler, C. J. Reason, W. Shaikh, T. B. Winstone, R. W. W. Wyatt, and B. E. Wyborn, Nucl. Fusion **44**, S239 (2004).
[9] K. Mima, H. Azechi, Y. Johzaki, Y. Kitagawa, R. Kodama, Y. Kozaki, N. Miyanaga, K. Nagai, H. Nagatomo, M. Nakai, H. Nishimura, T. Norimatsu, H. Shiraga, K. Tanaka, Y. Izawa, Y. Nakao, and H. Sakagami,, Fusion Sci. Technol. **47**, 662 (2005).
[10] E. W. Gaul, M. Martinez, J. Blakeney, A. Jochmann, M. Ringuette, D. Hammond, T. Borger, R. Escamilla, S. Douglas, W. Henderson, G. Dyer, A. Erlandson, R. Cross, J. Caird, C. Ebbers, T. Ditmire, Appl. Opt. **49**, 1676 (2010).
[11] P. F. Moulton, J. Opt. Soc. Am. B **3**, 125 (1986).
[12] http://www.crystalsystems.com/ti_sapphire_products.html.
[13] B. E. Lemoff and C. P. Barty, Opt. Lett. **17**, 1367 (1993).
[14] J. V. Rudd, G. Korn, S. Kane, J. Squier, and G. Mourou, Opt. Lett. **18**, 2044 (1993).
[15] H. Takada, M. Kakehata, K. Torizuka, Opt. Lett. **31**, 1145 (2006).
[16] J. P. Zhou, C. P. Huang, C. Shi, H. C. Kapteyn, and M. M. Murnane, Opt. Lett. **19,** 126 (1994).
[17] J. P. Chambaret, C. LeBlanc, G. Cheriaux, P. Curley, G. Darpentigny, P.Rousseau, G. Hamoniaux, A. Antonetti, and F. Salin, Opt. Lett. **21**, 1921 (1996).
[18] S.Backus, C.G. Durfee III, M.M. Murnane, H.C. Kapteyn, Rev. Sci.. Instr. **69**, 1207 (1998).
[19] Le Blanc, P. Curley, F. Salin, Opt. Comm. **31**, 391 (1996).
[20] C.P,J. Barry, G. Korn, F. Raski, C. Rose-Petruck, J. Squier, A.C. Tien, K.R. Wilson, V.V. Yakovlev and K. Yamakawa, Opt.Lett. **21**, 219 (1995).
[21] C. P. J. Barty, T. Guo, C. Le Blanc, F. Raksi, C. Rose-Petruck, J. Squier, K. R. Wilson, V. V. Yakovlev, and K. Yamakawa, Opt.Lett. **21**, 668 (1996).
[22] K. Yamakawa, M. Aoyama, S. Matsuoka, H. Takuma, C. P. J. Barty, D. Fittinghoff, Opt. Lett. **23**, 525 (1998).
[23] Pierre Tournois, Optics Commun. **140**, 245 (1997).
[24] http://www.photonic.saint-gobain.com/uploadedFiles/SGphotonic/Documents/Product-Specs-SF6040-SF6080.pdf
[25] M.P.Kalashnikov, K. Osvay, I.M. Lachko, H. Schönnagel, W.Sandner, Appl. Phys. B **81**, 1059 (2005).
[26] M. B. Danailov and I. P. Christov, Opt. Commun. **77**, 397 (1990).

5.2.3 Optical Parametric Amplification

Since the invention of the first solid state laser in early 1960s, the optical parametric amplifiers (OPA) closely followed the trends in development of lasers. Unlike the laser amplifiers, where transfer of population between the lasing energy levels gives rise to amplification through the stimulated emission, OPAs do not involve any real energy levels. In essence it is three-wave interactions mediated by the second-order nonlinearity in birefringent materials offering some unique possibilities for light amplification.

High peak-power pulses can not be amplified directly in laser amplifiers due to accumulating self-action effects. The chirped-pulse-amplification (CPA) technique, demonstrated in 1985, helps to overcome this limitation and is nowadays used in almost any ultrashort pulse powerful laser system. On the other hand, chirped signal pulses can also be amplified in an optical parametric amplifier (OPA) producing an idler wave with reversed frequency chirp [1]. The first proof-of-principle experiment on stretching, amplification and compression of chirped pulses in OPA was demonstrated in 1992 [2]. Later on, this technique was further elaborated and petawatt peak-powers using optical parametric chirped pulse amplification (OPCPA) were anticipated [3]. Since that time OPCPA became a recognized and rapidly developing amplification technology for high-power femtosecond pulse generation and is widely used either separately or in conjunction with laser amplifiers. The OPCPA concept maintains all the basic requisites as CPA, just with the laser amplifier being replaced by the OPA (Fig. 5.5).

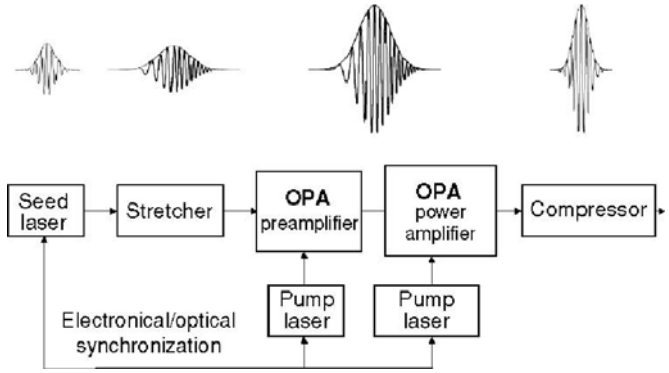

Figure 5.5: Principal scheme of chirped pulse parametric amplification.

OPCPA offer several significant advantages as compared with laser amplifiers: 1) high gain per single pass; 2) low thermal effects due to the fact that no population inversion is involved; 3) output signal wavelength tunability; 4) possibility to amplify ultra-broad bandwidth spectrum; 5) reduced amplified spontaneous emission along with high contrast ratio of the amplified pulses; 6) preservation of amplified signal phase and simultaneous production of phase-conjugated idler wave; 7) high amplified signal beam quality. Despite some disadvantages such as lack of pump energy accumulation, amplified parametric fluorescence, limited aperture of many available nonlinear crystals, requirements of precise pump and signal synchronization, and losses introduced by the idler wave, OPCPA remains an attractive approach to generate high-contrast, high-energy ultrashort pulses even at wavelengths not supported by conventional CPA-based laser amplifiers. Moreover, carrier envelope phase-stable seed for the OPCPA can be formed by means of parametric three wave mixing [4] and preservation of amplified signal carrier envelope phase was also demonstrated [5].

Broadband pulses in an OPA can only be amplified if all three interacting waves (pump, signal and idler) are phase matched. As a complete phase matching condition over a broad frequency range can hardly be satisfied in a given nonlinear medium, the broadest bandwidth is supported when wave-vectors mismatch is as close to zero as possible for the entire range of frequencies of interacting waves. If OPA is pumped by a monochromatic pump wave (as is usually the case) and group velocities of signal and idler pulses are equal, the supported bandwidth can already be converted to few-cycle output. In practice, this is achieved either in a collinear interaction at degeneracy or in a non-collinear geometry out of degeneracy. And going forward, for certain frequencies even broader bandwidths may be supported in a given nonlinear crystal by minimizing higher order terms of wave-vectors mismatch.

Due to inherently high-contrast output pulses, optical parametric amplifiers of chirped pulses are increasingly adopted as front-ends of ultra-high intensity lasers. OPCPAs are employed at nearly a dozen of existing and soon to be built (sub-)PW-level lasers. Relatively high-contrast pulses after parametric amplifiers are further amplified in either Nd:glass or Ti:sapphire up to ultra-high energies. A large portion of highest intensity lasers in Europe, US, Japan and China make use of chirped pulse parametric amplifiers for contrast enhancement.

However, stand-alone OPCPA systems have also been widely investigated and up to now, several tens unique OPCPA-based laser systems are demonstrated [6]. All-solid-state systems can produce up to 0.5 TW few-cycle pulses [7] or very high repetition rates [8]. Parametric amplification of white-light pulses in a non-collinear configuration and subsequent recompression yielded few-cycle pulses in the visible-NIR [9]. CEP-stabilized pulses with over 16 TW have also been demonstrated [10]. And flash-lamp pumped high-energy nanosecond lasers are used to amplify chirped pulses in a near-collinear configuration up to Joule level energies at 1 μm wavelength [11,12]. Several practical designs for OPCPA configurations enabling output powers of above 1 PW had been already offered in the past [3,13] and this is what is needed for ELI.

To obtain such high intensities with reasonably short pulse durations, one must use high-energy sources which inevitably provide large beams. Thus, nonlinear crystals with large apertures must be used and there are basically three potential candidates that can be grown in sufficient size: KDP, DKDP and YCOB. For the moment, DKDP crystal seems to be the only choice for parametric amplifiers pumped by the second harmonic of highest energy Nd:glass lasers due to its supported bandwidth, absorption, growth issues and availability in large sizes, while YCOB and probably even LBO would be attractive alternatives if growth technology is significantly advanced. A figure of merit has been derived to examine the impact of average power on OPA performance by estimating the thermal limiting power [14]. This takes into consideration the thermal conductivity of the crystal, the thermal sensitivity and the linear optical absorption at the pump wavelength. For DKDP, this figure has a value of 0.3 kW for a tentative figure of 600 J pump energy gives a limiting repetition rate of 0.5 Hz. The nonlinear crystal YCOB has been developed as an alternative for second harmonic generation for high average power systems and has even been used to demonstrate OPA at 1 μm. This has a thermal power limit over 40 times greater than that of DKDP leading to a potential increase in the repetition rate to 2 Hz at 600 J.

OPCPA requires high pump intensities to generate gain in reasonable crystal lengths. Thus, a significant challenge, and key to success, is the selection of an appropriate pump laser for the OPCPA process. Parameters that influence the choice for appropriate system are: pulse duration in relation to seed stretch factor and possible recompression, repetition rate and available energy, beam quality, synchronization and jitter, etc. For moderate energy systems, picosecond systems present a good compromise in terms of readily achieving pump pulse intensities for OPCPA whilst requiring moderate seed stretch factors and avoiding the complexity of CPA based pumps. A master-oscillator power-amplifier (MOPA) approach with picosecond duration is attractive since it can be directly seeded from a multi branch fibre system without any need for electronic synchronization or regenerative amplification.

In [15], a single Ti:Sapphire oscillator seeds both the pump laser and the OPCPA chain, while the pump pulse is amplified in a fibre laser ensuring a high stability pump output with excellent beam profile. The use of a single Ti:Sapphire oscillator ensures timing stability of the pump and seed pulses, removing a major source of fluctuations. In contrast, [16] uses a two-colour fibre laser oscillator to produce a mid-IR seed pulse, and an electronically synchronised solid-state pump laser to amplify this. This system benefits from passive CEP stabilisation of the seed pulse and an alignment-free oscillator. We believe the optimum configuration is a combination of the two systems, where the pump and seed pulses are generated from a single fibre oscillator, thus ensuring excellent timing stability, reliability and beam quality. Fibre systems producing a few hundred millijoules of energy have already been demonstrated [17], allowing the operation

of a single stage OPCPA system, while the fibre-based pump laser can be further amplified in free-space amplifiers to reach even higher energies.

For multi-petawatt OPCPA output very high energy pump lasers are needed and they generate nanosecond pulses. High energy Nd:glass lasers with sufficient energy to achieve the required pump power have been already developed and demonstrated, however with the current and projected technology have repetition rates on the minute timescales. However recent development of diode pumped Yb:host and even Nd:host lasers has made significant advances in laser pulse energy generation. At present they have been limited to the $\sim$ 100 J region but it is expected that with the added interest from other laser development programmes, laser systems will be designed that are capable of delivering 1 kJ of energy at the fundamental wavelength on a repetition rate measured in seconds or a fraction thereof.

A high energy but poor beam quality pump beam would have a detrimental effect on pump-to-signal conversion efficiency so the principle requirements of the pump beam are to have an approximately Top-Hat profile in the temporal and spatial domains within the non-linear crystal. To achieve the required temporal profile, it is now common practice on the large laser facilities to tailor the shape of a pulse and a number of schemes have been demonstrated. A simple scheme uses a CW source that is then modulated using a fibre optic modulator to generate the required temporal pulse shape. It is then amplified by the use of fibre amplifiers or direct injection into a regenerative amplifier.

Another challenge of OPCPA is the coupling of amplified seed energies not just to the pump intensity fluctuations, but also the temporal overlap between pump and seed pulses in an OPCPA amplifier. This challenge can be overcome, and recently highly stable OPCPA systems have been produced with RMS fluctuations of 1.5% [15] and even as low as 0.7% [16]. Both of these systems use fibre laser technology, which provides a template for the optimum design of an OPCPA front-end.

An important property of the OPA, which up to now has been quite rarely exploited, is that the OPA permits the use of multiple pump beams if each of them satisfies the phase-matching condition with a single signal beam. This possibility is pre-defined by the nature of the parametric amplification process; the phase difference between the pump and the signal pulses is transferred to the idler pulse, thus compensating for random differences between these two. Such pumping geometry allows energy combining from a number of pump beams to a single signal beam. Hence, a single high-energy but low repetition rate pump laser for OPA could be in principal substituted by a number of lower energy lasers of equivalent sum energy but running at higher repetition rate.

Energy combining by the use of multiple-beam pumped OPA was demonstrated and the amplified signal energy exceeded that of the single pump pulse, and almost 80% conversion efficiency has been reported with no impact on the pulse temporal profile [18]. It was also demonstrated that multiple pump beams used in a proper geometry could notably extend the amplification bandwidth in the case of the chirped broadband seed [19] and that a singe signal pulse can be amplified by two different pump wavelengths [20, 21]. Finally, two and even three-beam pumped optical parametric amplification of broadband chirped pulses was demonstrated recently with promising outlook on energy and average power scaling [22, 23].

A truly unique OPA feature is its great wavelength flexibility. The principle of chirped pulse parametric amplification can be adapted to any ultrashort pulse system operating in ultraviolet, visible, and infrared. The majority of experimentally demonstrated OPCPAs, including those of highest output peak powers, are concentrated in the vicinity of visible-NIR boundary. However there is a substantial amount of research put OPCPA based sources through the NIR and even to mid-IR wavelengths above 3 microns - a spectral range of interest for industrial, biological, medical research, as well as fundamental physics experiments that benefit from large ponderomotive energies [24]. Such OPCPA systems have already been realised at 2.1 μm [25] and in the mid-IR at 3.2 μm [16, 26]. These sources take advantage of the fact that OPCPA can work

efficiently as long as the relevant phase-matching conditions can be met. A major advantage of operating OPCPA at longer wavelengths is the fact that it is energetically more economic since doubling of typical near-IR pump lasers can be avoided and efficient (dielectric) grating become a possibility.

Theoretical studies for such OPCPA systems are extremely important since, especially in the case of ELI, never achieved parameters are sought for. Such extreme bandwidths and pulse energies demand multiple amplification stages with carefully tuned nonlinear media, pump profiles and temporal profiles etc. In other words: one needs to theoretically model OPCPA at extreme average power and/or peak intensity in full 3D plus time and include associated nonlinear and parasitic effects since those effects can significantly hamper estimated performance. The spatial as well as the temporal variation of the pump and seed profiles needs to be accounted for, as well as the effects of pump depletion on the spatial phase of the pulse. Due to the high intensities in the crystals various interactions can arise such as self and cross focusing, self and cross phase modulation and nonlinear change of the phase mismatch, all of which modify the gain spectrum of the OPA process. In a recent paper, it has been shown [27] that the effects of nonlinear refractive index can change the output of a petawatt scale OPCPA system by up to 16%. Such a decrease in output energy will, in the best case, mean that large investments in additional pump lasers and synchronization is required, it goes however hand in hand with a significant decrease in achievable Strehl ratio; a detrimental factor for experiments. These effects can be offset by careful design of the OPCPA system, a process which would be much relieved with the help of 3D full modeling.

Bibliography

[1] Piskarskas A. et al. Sov. Phys. Usp. **29**, 869 (1986).
[2] Dubietis A. et al. Opt. Commun. **88**, 437 (1992).
[3] Ross I. N. et al. Opt. Commun. **144**, 125 (1997).
[4] Baltuška A. et al. Phys. Rev. Lett. **88**, 133901, (2002).
[5] Hauri C. P. et al. Opt. Lett. **29**, 1369 (2004).
[6] Dubietis A. et al. IEEE J. Selec. Top. Quant. Electron. **12**, 163 (2006).
[7] Adachi S. et al. Opt. Express **16**, 14341, (2008).
[8] Rothhardt J. et al. Opt. Express **15**, 16729, (2007).
[9] Baltuška A. et al. Opt. Lett. **27**, 306 (2002).
[10] Herrmann D. et al. Opt. Lett. **34**, 2459, (2009).
[11] Lozhkarev V.V. et al. Laser Phys. Lett. **4**, 421, (2007).
[12] Chekhlov O. et al. Opt. Lett. **31**, 3665 (2006).
[13] Ross I. N. et al. Laser Part. Beams **17**, 331 (1999).
[14] Liao Z.M. et. al. Optics Letters **31**, 1277 (2006).
[15] Tavella F. et al. Opt. Express **18**, 4689, (2010).
[16] Chalus O. et al. Opt. Express **16**, 21297 (2008).
[17] Roser F. et al. Opt. Lett. **30**, 2754 (2005).
[18] Dubietis A. et al. J. Opt. Soc. Amer. B, Opt. Phys., **15**, 1135 (1998).
[19] Žeromskis E. et al. Opt. Commun. **203**, 435 (2002).
[20] Tamošauskas G. et al. Appl. Phys. B, **91**, 305 (2008).
[21] Herrmann D. et al. Opt. Express **18**, 18752 (2010).
[22] Herrmann D. et al. Opt. Express **18**, 4170 (2010).
[23] Ališauskas S. et al. Opt.Commun. **283**, 469 (2010).
[24] Erny C. et al. Appl. Phys. B **96**, 257 (2009).
[25] Fuji T. et al. Opt. Lett. **31**, 1103 (2006).
[26] Chalus O. et al. Opt. Lett. **35**, 3204 (2010).
[27] Thai A. et al. Opt. Lett. **35**, 3471 (2010).

5.2.4 Dispersion management of high intensity short pulse lasers

Current designs of the laser systems at the three sites involve high intensity laser systems up to 10 PW. Although these systems are different in bandwidth and hence pulse duration as well as in the amplifier medium (Ti:S or optical parametric crystal), but all are basically rely on chirped pulse amplification. Regarding the peak pulse power, they would need a robust stretcher- compressor system with reliable and accurate dispersion compensation.

Some of the designed systems will be based on double CPA principles. In this case the first stretcher-compressor system is relatively easy to handle and modify, as the required stretch ratio is relatively modest, and also active devices (AOPDF, SLM) are readily available. The second stretcher-compressor system is, however, much more challenging, as the 20-30 fs pulses have to be stretched over 10000 times. Moreover, the intense pulses are passing through considerable amount of gain material at a B-integral close to 1, so the high fidelity re-compression is a real challenge. Thus, here we describe the main designing considerations for the large scale stretcher-compressor system for such an ultra-short pulse duration and ultra-high-energy laser facility.

In order to keep the ultra-short duration and high contrast in the pulse, the spectral bandwidth is chosen to be 200 nm wide in the stretcher. The difficulty is to design the stretcher with low aberration through the whole spectrum. At the end of the laser chain, the vacuum compressor must be dimensioned for compressing a 300-J, 15-fs beam. We describe a possible design using four ultra-wide monolithic gratings and show the sensitivity on the alignment of such a big compressor. As an example we take the stretcher and the compressor design of the Apollon 10 PW laser facility [1].

Stretcher design

To minimize the introduction of residual chirp along the broad spectrum, the stretcher must exhibit low temporal and spatial aberration and high spectral acceptance. A way to achieve these characteristics is to base the stretcher on an all-reflective Öffner triplet [2]. Moreover, as we expect a large time-expansion ratio (13 ps/nm), and require a relatively compact system, we must design a double-pass stretcher.

We first studied a single-grating Öffner stretcher. As the Apollon10P compressor works with 1480 groove/mm gratings, we also use a 1480-groove/mm grating to match stretching and compression. The imaging system is composed of two spherical mirrors with the same center of curvature and a -1 expansion ratio. The stretching coefficient is achieved by placing the grating away from the center of curvature. By doing so, we introduce spherical aberrations in the system. To fully characterize the behavior of this design, using the ray tracing program *Zemax*, we observe the Fast Fourier Transform of the Point Spread Function and the spot diagram after a perfect lens at the output. The results show a bad Strehl ratio (≈ 0.015) due to aberrations on both lateral and vertical axes. To reduce the aberrations over the whole spectral bandwidth, we decided to build a stretcher using the same spherical mirrors but with two diffraction gratings (see Fig. 5.6).

One grating is placed on the center of curvature. We keep the same relative distance on the gratings which leads to a second grating over the convex mirror. The results show a better Strehl ratio of 0.91. The lateral and vertical aberrations observed after the perfect output lens are manageable.

Compressor design

The compressor is composed of four monolithic $910 \times 455\ \mathrm{mm}^2$ Livermore gold gratings. Because of the amount of energy carried by the beam, we expand it to Ø400 mm. For geometrical reasons, the angle of incidence is calculated to be 56 degrees.

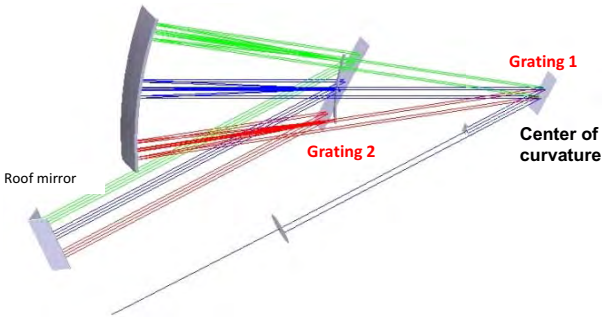

Figure 5.6: Two-grating Öffner triplet design for the Apollon 10P facility.

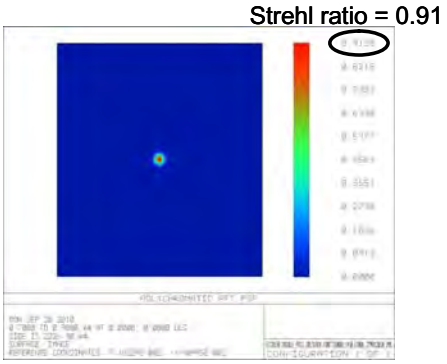

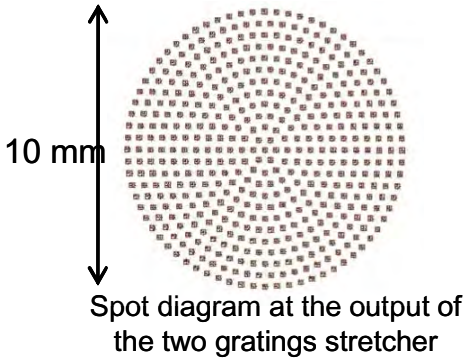

Figure 5.7: (left): Calculated Strehl ration of the beam after the stretcher, (Right) spot diagram at the output of the two grating stretcher. There is no visible chirp in the beam.

Here we have studied the sensitivity to misalignment [3–4] as we know that a four-grating compressor is more sensitive to tilt than a double pass. We underscored the influence of the misalignment on each grating and tilts on the input beam.

Spectral phase management of the stretcher/compressor and amplifier stages

The spectral chirp of the stretcher, amplification stages and compressor, have been also studied. Because the amplification stages introduce dispersion, we have to adapt several stretcher parameters to provide a near-transform-limited recompression. Since the compressor gratings have a fixed number of grooves (1480 gr/mm), we calculated the residual spectral phase for different numbers of grooves in the stretcher (between 1420 gr/mm and 1480 gr/mm) and show the best solution for our system.

Upon construction of the entire laser system, the stretcher and compressor system has to be perfectly aligned. The aligment procedure has to address the paralelism of the gratings,

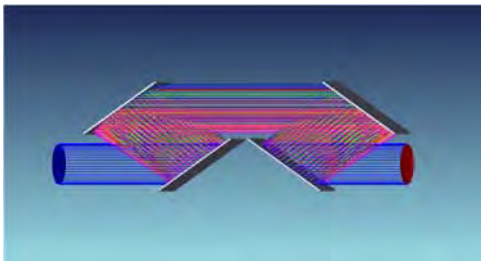

Figure 5.8: Four-grating compressor design (by zemax).

measurement and cancellation of residual angular dispersion of the entire system as well as minialization of the residual spectral phase.

There are three basic methods for the accurate alignment procedure. The one, useful especially for high power, relatively narrow bandwidth laser systems, is based on two different colour laser beams. The beams are sent into the system collinearly, and they have to leave also collinearly. The angular deviation of the two beams is hence directly proportional to the angular dispersion of the system.

The other group of alignment procedures are based on various versions of spectrally (and spatially) resolved interferometry and concerns mainly broadband, sub-50 fs systems [5–10]. In these measurements and alignment procedures the residual spectral phase can be absolute [5] or relative [6–7], that is, the performance of the stretcher-compressor system is aligned to the oscillator pulse. However, the residual angular dispersion of the system is measured as an absolute value [8–10].

In case of large scale, narrow band laser systems, the amount of stretch requires size of grating which is not yet available. The solution is to use a tiled grating compressor system, where two or more gratings are built together. It can be especially challenging to align and maintain the alignment of such many-grating systems. One of the common methods is the use of expanded cw laser sources and investigate the interference originating from diffraction of different gratings of the system [11–13], while the other one is based also on spectrally and spatially resolved interferometry [14].

Bibliography

[1] J.P. Chambaret, F. Canova, R. Lopez-Martens, G. Cheriaux, G. Mourou, A. Cotel, C. Le Blanc, F. Druon, P. Georges, N. Forget, F. Ple, M. Pittman, CLEO/QELS 2007 **1-5**, 2377 (2007).

[2] G. Cheriaux, P. Rousseau, F. Salin, J.P. Chambaret, B. Walker L.F. Dimauro: Opt. Lett. **21**, 414 (1996).

[3] C. Fiorini, S. Sauteret; C. Rouyer; N. Blanchot; S. Seznec; A. Migus, IEEE J. Quantum Electron. **30**, 1662 (1994).

[4] K.Osvay, I.N.Ross, Opt.Commun. **105,** 271 (1994).

[5] C. Dorrer, B. de Beauvoir, C. Le Blanc, J.P. Roussaeu, R. Ranc, P. Rousseau, J.P. Chambaret, F. Salin, Appl. Phys. B **70**, S77 (2000).

[6] D. Meshulach; D. Yelin; Y. Silberberg, IEEE J. Quantum Electron. **33,** 1969 (1997).

[7] A.P. Kovács, K. Osvay, G. Kurdi, M. Görbe, J. Klebniczki and Z. Bor, Appl. Phys. B **80,** 165 (2005).

[8] G. Pretzler, A. Kasper, K.J.Witte, Appl. Phys. B **70,** 1 (2000).

[9] K. Varjú, A.P. Kovács, G. Kurdi K. Osvay, Appl.Phys.B **74,** 259 (2002).

[10] K. Osvay, A.P. Kovacs, Z. Heiner, G. Kurdi, J. Klebniczki, M. Csatari, IEEE J.Sel.Top.Quant.Electr. **10,** 213 (2004).

[11] M. Hornung, R. Bödefeld, M. Siebold, M. Schnepp, J. Hein, R. Sauerbrey, M. C. Kaluza, Appl.Opt. **46,** 7432 (2007).

[12] A. Cotel, M. Castaing, P. Pichon, C. Le Blanc, Opt.Exp. **15,** 2742 (2007).

[13] J. Qiao, A. Kalb, M. J. Guardalben, G. King, D. Canning, J. H. Kelly, Opt.Exp. **15,** 9562 (2007).

[14] N. Blanchot, E. Bar, G. Behar, C. Bellet, D. Bigourd, F. Boubault, C. Chappuis, H. Coïc, C. Damiens-Dupont, O. Flour, O. Hartmann, L. Hilsz, E. Hugonnot, E. Lavastre, J. Luce, E. Mazataud, J. Neauport, S. Noailles, B. Remy, F. Sautarel, M. Sautet, C. Rouyer, Opt.Exp. **18,** 10088 (2010).

5.2.5 Beam propagation and focusing

Along the amplification chain, a broad range of aberrations can be present, perturbing the pulses propagation, the focusing, or producing back-reflections. Therefore, few basic rules have to be followed, and careful evaluation of the beam parameters has to be performed along the amplification chain, until the pulses reach the target and even after it.

Image relaying is the main approach to be used for beam transportation. It is a technique for preserving the transverse intensity profile of a high power beam as it propagates long distances through the laser system. Amplifier apertures can be filled more effectively, leading to an increase of fixed-aperture system performance [1]. Relay imaging is essential also for the reduction of the beam pointing fluctuations.

For large aperture beams, *reflective focusing optics* should be employed, in order to avoid the material dispersion introduced in the broadband spectrum of the pulses and further optical aberrations.

Care has to be taken in experiments to avoid back-reflections of the pulses in the amplification chain, especially in the experiments involving counter-propagating pulses and normal incidence pulses. Therefore, *optical isolation* should be implemented in the amplification chain, for example in the form of Pockels cells.

Evaluation of the *spatiotemporal distortion* of ultrashort pulses is an active field of research. Beam propagation for ultrashort pulses is usually described in a matrix formalism, known as Kostenbauder matrix formalism (KMF) [2, 3], which is an extension of the ABCD ray matrix formalism. There are versions of 4×4 matrices and also 6×6 matrices [4]. The formalism offers a first order series description of the pulse distortion. Moreover, in analogy with the complex Gaussian beam formalism, the Kostenbauder formalism was extended to Gaussian beams, using complex numbers representation [5]. The spatiotemporal distortion specific to the ultrashort pulses, described within KMF, are partial derivatives of the ray coordinates, as follows: Spatial Chirp ($\partial \mathrm{x}_{\mathrm{out}}/\partial \nu_{\mathrm{in}}$), Angular Chirp ($\partial \theta_{\mathrm{out}}/\partial \nu_{\mathrm{in}}$), Pulse-Front Tilt ($\partial \mathrm{t}_{\mathrm{out}}/\partial \mathrm{x}_{\mathrm{in}}$), Time vs Angle coupling ($\partial \mathrm{t}_{\mathrm{out}}/\partial \theta_{\mathrm{in}}$) and Group Delay Dispersion ($\partial \mathrm{t}_{\mathrm{out}}/\partial \nu_{\mathrm{in}}$). All these types of distortions should be well evaluated and controlled.

The KMF is a very versatile approach to follow the propagation of the pulses through the entire amplification chain. It offers a proper description of the ultrashort pulse evolution and also shows the entanglement of the specific parameters mentioned. It also allows a first-order analysis of the perturbation effects along the propagation path, coming from different sources. However, there are several issues to be considered, related to nonlinearities and further optical aberrations:

1) higher order terms are not included in the KMF. Such higher order terms are important in the description of ultrashort laser pulses. Some of them are analyzed in the "Dispersion management section" (5.2.4).

2) self phase modulation (SPM) process due to high peak power of the laser pulse has to be treated separately. The B-integral parameter which characterizes in SPM the nonlinear phase accumulation along the entire laser chain should be kept below a value of 1, otherwise strong perturbation of the ultra-short pulses electromagnetic field will be produced;

3) if optical aberration is present, it can also cause significant spatiotemporal distortion of ultra-short pulses in the focal region resulting in reduced intensity and spatiotemporal resolution. Therefore, it is important to study the effect of optical aberration theoretically and experimentally.

The shape of the pulse front distorted by chromatic aberration can be simply determined by geometrical optical ray tracing [6–10] as it was first pointed out by Bor [6, 7]. However, in the vicinity of the focal point, the validity of the geometrical optics breaks off, so a wave optical model is needed [11–15]. It was shown that the pulse front is delayed with respect to the phase front. The delay is proportional to the difference between the group and phase velocity

of the light in the lens material and also proportional to the path length of the ray in the lens material. Therefore it is a parabolic function of the distance from the optical axis. This effect may cause that the pulse front forms a loop in the vicinity of the focus. In this case the outer rays have already passed the focus, while the rays propagating along the optical axis have not reached it yet. This phenomenon results in significant temporal broadening of the pulse in the focal point. The parabolic delay between the pulse and phase fronts in a lens-based telescope was first demonstrated experimentally using time of light interferometry [16]. This effect can be avoided by applying an achromatic lens, since in this case the delay is constant across the cross-section of the lens [6, 7].

In high intensity lasers, lens-based telescopes are used for spatial filtering and magnifying the laser beam. Since the diameter of the lenses in the telescopes is large, singlet lenses are used instead of achromatic lenses. Therefore chromatic aberrations appear in the case of lens-based telescopes [15, 17]. Methods to compensate such chromatic aberrations were proposed [15, 17]. One straightforward approach would be the use of reflective mirrors (off axis parabolic mirrors) instead of lenses. Another solution may be the use of hybrid optics, a combination of a diffractive lens and a commercial lens [18, 19].

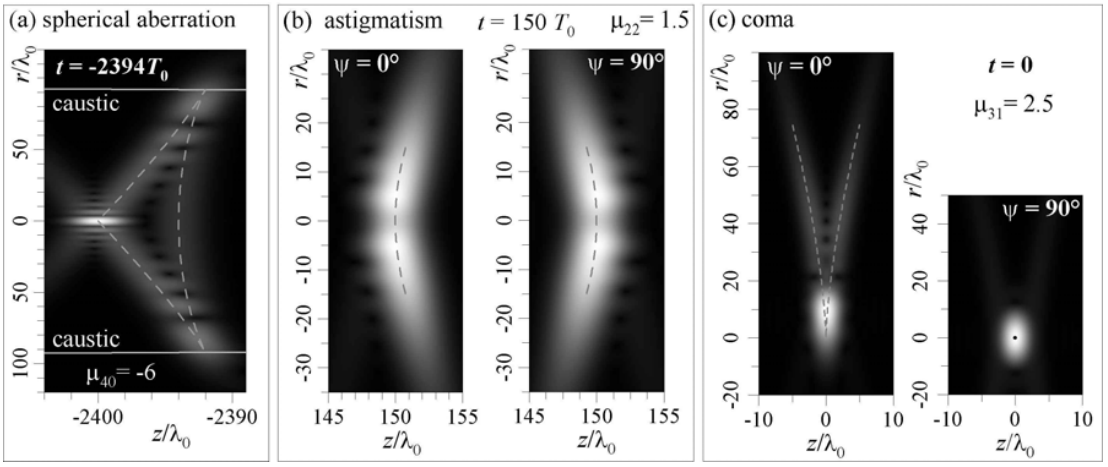

Figure 5.9: Intensity distribution of a spatially and temporally Gaussian pulse with temporal duration $\tau = 2T_0$ at the moment t in the presence of aberrations, where T_0 is the period of the vibration at $\lambda_0 = cT_0$ ($T_0 = 2.67$ fs, $\lambda_0 = 800$ nm). The amount of the aberrations are characterized by μ_{nm}. The angle $\psi = 0°$ and $\psi = 90°$ corresponds to the meridional and the sagital plane, respectively. The dashed line shows the pulse front predicted by the geometrical optics

Using large-aperture optics, we must take care of another type of optical aberration, the spherical aberration. To describe its effect on the pulse front, several models based on wave optics have been developed [13, 15, 20–23]. The calculations show that the spherical aberration leads to the formation of a Bessel-like, x-shaped pulse front (see Fig. 5.9a). There are some more aberrations, e. g. astigmatism and coma, the effect of which has been slightly studied so far [23, 24]. The theoretical and the experimental results show that astigmatism and coma, similarly to spherical aberration, do not introduce a significant pulse broadening but they cause a considerable distortion of the pulse front which leads to a significant loss of intensity (see Fig. 5.9b,c). The distorted pulse fronts calculated by geometrical optics ray tracing, are in good agreement with the shape obtained from the wave optical model [23].

To check the theoretical results on the effect of optical aberrations experimentally, several linear methods based on spectral interferometry [17, 24–30] and shifted-field autocorrelator [15], and non-linear methods based on the FROG technique [31, 32] have been developed recently.

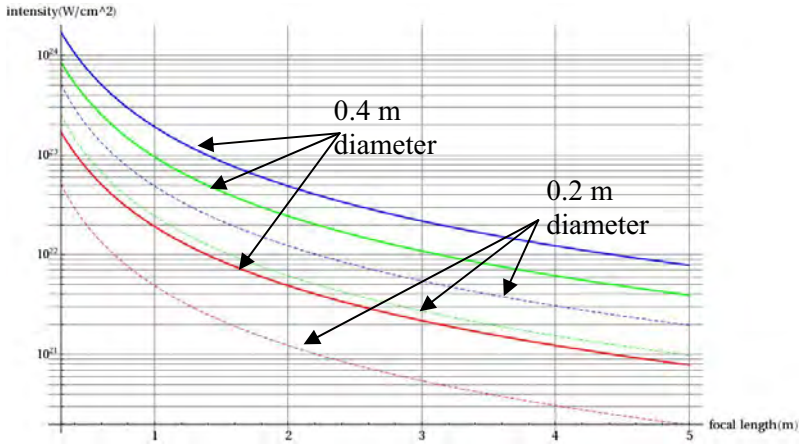

Figure 5.10: Peak intensity reached using 1 PW, 5 PW and 10 PW pulses for 0.2 m (dashed line) and 0.4 m (continuous line) as a function of focal distance of the optics used.

Not only the optical aberrations but also the angular dispersion caused by the non-parallel gratings in the pulse compressor may result in pulse broadening in the focal region. The front of the pulse reaching the lens is tilted because of angular dispersion. Therefore one side of the pulse front will reach the focal point sooner than the other side leading a significant time broadening [33].

Another interesting phenomenon may occur at focusing when the diameter of the pulse front is larger than the aperture of the focusing element. In this case the waves leaving the edge of the optical elements, the so-called boundary waves give constructive interference along the optical axis, which results in the boundary wave pulse [34–36]. If no aberrations are present, this pulse propagates behind the main pulse before the focal point, and they meet at the focal point, and then the boundary wave pulse propagates in front of the main pulse.

We have reviewed briefly the problems occurring during the propagation and focusing of ultrashort pulses. It can be seen that the phenomena are complicated. Therefore in addition to the numerical models mentioned so far, a number of software tools are available for ray-tracing the laser systems, with different approaches, such as Miro code [37], Lab2 package for LabView [38], Optica3 package for Mathematica [39], Zemax [40] and so on.

Special care should be taken when focusing multi-PW beams to high intensities. With an ideal spatial Gaussian beam and with ideal focusing optics one can get a simple estimate of the intensity in the focus. In the figure below are analyzed two beam diameter cases, namely 0.4 m (thick lines) and 0.2 m (dashed lines). For each case we represented on logarithmic scale the intensity for different peak powers, namely 10 PW (blue), 5 PW (green) and 1 PW (red). The conclusion is that the focal length of the focusing optics should be below 1.5 m for the large beam size and below 0.6 m for the small beam size in order to reach 10^{23} W/cm^2. More general, the f# for the focusing optics needed to reach 10^{24} W/cm^2 should be below 1.0, in an ideal gaussian pulse case. Such high quality optics remains a challenge. Besides, the typical spatial profile in the OPCPA or Ti:Sa laser systems are flat-top or super-gaussian. Such profiles tend to develop intensity modulations and to distort the field in the focus.

Bibliography

[1] J. T. Hunt, J. A. Glaze, W. W. Simmons, and P. A. Renard, Applied Optics **17**, 2053 (1978).

[2] O. E. Martinez, IEEE Journal Quantum Electronics **24**, 2530 (1988).

[3] A.G. Kostenbauder, IEEE Journal Quantum Electronics **26**, 1148 (1990).
[4] M. Seemann, in Doctoral Thesis at Universität Rostock, Germany (2005).
[5] Selcuk Akturk, Xun Gu, Pablo Gabolde and Rick Trebino, Opt. Express **13**, 8642 (2005).
[6] Z. Bor, J. Mod. Opt. **35**, 1907 (1988).
[7] Z. Bor, Opt. Lett. **14,** 119 (1988).
[8] S. Szatmari, G. Kühnle, Opt. Commun. **69,** 60 (1988).
[9] H. Staerk, J. Ihlemann, A Helmbold, Laser and Optoelektronik **20,** 34 (1988).
[10] J. Ihlemann, A. Helmbold, H. Staerk, Rev. Sci. Instrum. **59,** 2502 (1988).
[11] Zs. Bor and Z. L. Horváth, Opt. Commun. **94,** 249 (1992).
[12] Z. L. Horváth and Zs. Bor, Phys. Rev. E **63,** 26601 (2001).
[13] U. Fuchs, U.D. Zeitner, A. Tünnermann, Opt. Express **13**, 3852 (2005).
[14] M. Kempe, U. Stamm, B. Wilhelmi, W. Rudolph, J. Opt. Soc. Am. B **9,** 1158 (1992).
[15] H.-M. Heuck, P. Neumayer, T. Kuehl, and U. Wittrock, Appl. Phys. B **84**, 421 (2006).
[16] Zs. Bor, Z. Gogolák, and G. Szabó, Opt. Lett. **14,** 862 (1989).
[17] C. Rouyer, N. Blanchot, J. Neauport, C. Sauteret, Opt. Express **15,** 2019 (2007).
[18] U. Fuchs, U.D. Zeitner, A. Tünnermann, Opt. Lett. **31**, 1516 (2006).
[19] J. Néauport, N. Blanchot, C. Rouyer, C. Sauteret, Appl. Opt. **46**, 1568 (2007).
[20] M. Kempe and W. Rudolph, Opt. Lett. **18,** 137 (1993).
[21] M. Kempe and W. Rudolph, Phys. Rev. A **48,** 4721 (1993).
[22] G. O. Mattei, M. A. Gil, Appl. Opt. **38**, 1058 (1999).
[23] Z. L. Horváth, A. P. Kovács, and Zs. Bor, in Ultrafast Phenomena XV, Springer Series in Chemical Physics, eds P. Corkum, D. Jonas, R. J. D Miller, A. M. Weiner (Springer, Berlin, 2007) p. 220.
[24] K. Mecseki, A. P. Kovács, Z.L. Horváth, First International Conference Light at Extreme Intensities LEI' 09, Brasov, Romania.
[25] J. Jasapara, and W. Rudolph Opt. Lett. **24,** 777 (1999).
[26] W. Amir, T. A. Planchon, C. G. Durfee, J. A. Squier, P. Gabolde, R. Trebino, and M. Mueller, Opt. Lett. **31,** 2927 (2006).
[27] P. Bowlan, P. Gabolde, A. Schreenath, K. McGresham, and R. Trebino, Opt. Express **14,** 11892 (2006).
[28] P. Bowlan, P. Gabolde, R. Trebino, Opt. Express **15,** 10219 (2007).
[29] P. Bowlan, U. Fuchs, R. Trebino, U. D. Zeitner, Opt. Express **16,** 13663 (2008).
[30] P. Bowlan, P. Gabolde, M. A. Coughlan, R. Trebino, and R. J. Levis, J. Opt. Soc. Am. B **25,** A81 (2008).
[31] D.N. Fittinghoff, A. C. Millard, J. A. Squier, and M. Müller, IEEE J. Quantum Electron. **35,** 479 (1999).
[32] R. Chadwick, E. Spahr, J. A. Squier, C. G. Durfee, B. C. Walker, D. N. Fittinghoff, Opt. Lett. **31,** 3366 (2006).
[33] Z. L. Horváth, K. Osvay, Z. Bor, Opt. Commun. **111**, 478 (1994).
[34] Z. L. Horváth, Z. Bor, Phys. Rev. E **63,** 02661 (2001).
[35] Z. L. Horváth, J. Klebniczki, G. Kurdi, A. Kovács, Opt. Commun. **239**, 243 (2004).
[36] P. Saari, P.Bowlan, H. Valtna-Lukner, M. Lohmus, P. Piksarv, R. Trebino, Opt, Express **18,** 11083 (2010).
[37] O. Morice, Opt. Eng. **42**, 1530 (2003).
[38] http://www.lab2.de/
[39] http://www.opticasoftware.com/
[40] http://www.zemax.com

5.3 Diagnostics of Laser Parameters

5.3.1 Duration and spectral phase

There is a great demand of measurement of pulse duration and the accurate temporal intensity and phase in the generation, optimization and application of laser pulses. This chapter gives a brief overview about the most popular techniques. The continuously decreasing duration of ultra-short laser pulses, which are the shortest events in time ever created, made it necessary to develop various sophisticated temporal characterization techniques. Usual time-resolved measurements apply a much shorter event than a given process to sample it. Due to the shortness of laser pulses the only way is to sample them with themselves. In the measurement of ultra-short laser pulses a non-linear effect with a slow detector is typically involved.

There are numerous methods starting from the simplest second harmonic generation (SHG) intensity autocorrelation [1]. The input beam is split into two and the parts with a variable delay between them are sent – sometimes focused – into a non-linear medium – typically a non-linear optical crystal such as BBO. The generated second harmonic signal is measured as a function of the delay:

$$G^{(2)}(\tau) = \int_{-\infty}^{\infty} I(t)I(t-\tau)\,dt \tag{5.4}$$

An SHG autocorrelation does not accurately reflect the temporal shape of the pulses, but under certain assumptions for the pulse temporal profile, a good estimation can be obtained for the temporal full width at half maximum (FWHM) from the FWHM of the autocorrelation. SHG trace is always symmetric and thus has an ambiguity in shape -different temporal intensities lead to the same autocorrelation trace – and in the time direction – raising and trailing edges are not distinguishable. On the other hand, this symmetry provides an automatic self-consistency criterion. By measuring the laser spectrum a more correct ratio between the autocorrelation and the intensity can be determined – which is $\sqrt{2}$ for typically assumed Gaussian temporal pulse shape – in the case of a Fourier limited pulse. Other autocorrelators, for example based on third harmonic generation (THG) [2] – where $I^2(t)$ stands instead of $I(t)$ in the integrand in Eq. 5.4 – do not have time ambiguity, but still do not reflect the temporal shape of the laser pulses. Interferometric or fringe resolved autocorrelations [3] measure the non-linear signal after a collinear geometry and contain a background, but give some more information about the time structure – such as chirp – and are intrinsically calibrated in time.

To gain more insight into the temporal structure numerous versions of the frequency-resolved optical gating (FROG) technique [4], measuring the spectrogram of the pulse, have been developed. FROG is the most widespread pulse characterization approach and therefore it will be described in more detail. The first setup is based on an SHG autocorrelator [5], but instead the slow detector a spectrometer measures the spectrum of the generated second harmonic. In this way a 2D time-frequency distribution is obtained, which uniquely determines the temporal intensity and phase or alternatively the spectral intensity and phase of the pulses. Unfortunately, the SHG FROG still has the time direction ambiguity. However this can be eliminated by for example introducing a post pulse or a certain positive / negative chirp. To obtain the temporal intensity and phase an iterative retrieval algorithm is used, which depending on required accuracy and the initial guess might be slow enough to require an off-line evaluation. There are a certain number of versions of FROG [6] as by the autocorrelators based on SHG or a third order process including THG, polarization gate (PG), self-diffraction (SD) or transient grating (TG). The setup of these is similar using two pulse replicas – except the TG, which uses three – and generating the given non-linearity in a non-collinear geometry. For example the two input beam generates a sinusoidal beat pattern, which acts as a grating due to the non-linear index of refraction and scatters these input beams producing the SD signal. SD and PG provide an intuitive pattern, but PG needs a $\lambda/4$ plate and high quality polarizers and SD is not automatically

phase matched. The measured signals are given by:

$$I_{FROG}^{sig}(\omega,\tau) = \left| \int_{-\infty}^{\infty} E(t)\, g(t-\tau) \exp(-i\omega t)\, dt \right|^2$$
$$\text{and} \quad g(t-\tau) = \begin{cases} E(t-\tau) & \text{for} \quad SHG \\ E(t-\tau)^2 & \text{for} \quad THG \\ |E(t-\tau)|^2 & \text{for} \quad PG \\ E(t)\, E^*(t-\tau) & \text{for} \quad SD \end{cases} \tag{5.5}$$

The TG signal looks like the PG or the SD depending on the combination of the beams. Another less known advantage of a single-shot SHG FROG device is that it easily measures the spatial chirp and pulse front tilt – angular chirp. There are a large number of modified FROG setups. One of them is the GRENOUILLE [7], which has a very simple configuration allowing its almost alignment-free implementation down to about 10 fs duration.

An alternative technique is the spectral phase interferometry for direct electric-field reconstruction (SPIDER) [8], which is an interferometric measurement method using the spectral shearing interferometry in the frequency domain. Two replicas of the ultra-short laser pulse with a certain delay between them are mixed in a sum frequency generation crystal with a third significantly chirped and thus temporally stretched replica (longer than the original or the delay between the two pulses). In this way two “frequency doubled" replicas with a certain spectral shear – frequency shift – between them are generated and sent into a spectrometer. Due to the delay, the spectral shear and the spectral phase, a specific interference pattern will appear on the spectrum. After some basic transformations, the spectral phase of the initial pulse is obtained using simple algebraic procedure without any complex iterative algorithm. Measuring independently the spectral intensity a complete characterization is obtained and a Fourier transformation delivers the corresponding temporal profile. The SPIDER technique is internally single shot and experimentally simple and robust.

A relative new technique is the multiphoton intrapulse interference phase scan (MIIPS) [9], which is a fast way of characterization – and compression – using a pulse shaper. The pulses propagating through a temporal shaper (a 4-f line with a spatial light modulator in the Fourier plane or an acousto optic programmable dispersive filter, dubbed Dazzler) in the middle of the laser and after – further – amplification are frequency doubled at the end of the system. The SHG spectrum is measured as a function of an introduced reference function in the phase. This reference function can be a pure group delay dispersion (GDD). The SH signal at a given wavelength has its maximum when the second derivative of the spectral phase has the opposit sign and the same absolute value as the introduced GDD. So the MIIPS trace is very intuitive and in only a few iterations can optimize the pulse duration to reach the Fourier limit and characterize the spectral phase in the same time.

A brand new and promising pulse characterization method is the self-referencing spectral interferometry (SRSI) [10]. This technique involves cross polarized wave (XPW) generation [11], which is a third order non-linear process with automatic phase matching. In the XPW setup, a linearly polarized beam generates a perpendicularly polarized wave with a significantly smoothed spectral phase compared to the input pulse. In a first step the width of the spectrum of the XPW beam is optimized by a second order spectral phase scan with the pulse shaper. In a second step using this previously optimized GDD and an extra delay plate the spectral interference pattern between the original and the XPW pulse is obtained. This is similarly to SPIDER evaluated with a simple algorithm to obtain the spectral phase, which is then corrected by the shaper. In a few iterations the pulse possesses a flat phase. This heterodyne technique has very good measurement dynamics close to the main pulse reaching 4-5 orders of magnitude and thus it is the most sensitive approach in the vicinity of the pulse.

The measurement of few-cycle pulse duration is a real challenge even with the most powerful technique. The reasons for this are the required ultra-broad phase matching bandwidth, ideally all-reflective setup and minimal introduced dispersion by the generation of the non-linear signal. There are some versions of FROG as SHG [12] and TG [13] that under special conditions – such as few-μm thick non-linear medium – can support pulses with about a single optical cycle duration [14]. A much more complex, but even more detailed technique for sub-2-cycle pulses is based on the generation of a single XUV attosecond pulse and using the laser electric fields to shift the energy spectrum of free electrons produced by the XUV probe pulse. Measuring the electron spectrum as a function of the delay between the laser and the XUV pulse a so called "attosecond streaking" curve is obtained [15]. This determines the electric field of the laser and even the absolute phase or carrier envelope phase and the strength of the electric field in the point of measurement. Attosecond streaking belongs to the conventional approaches that to characterize a short pulse uses an even shorter pulse.

At the end of this brief overview the complete measurement of long pulse durations (100 ps–1 ns) with large time-bandwidth product (TBP) is discussed. It should be noted that a fast photodiode with an oscilloscope can measure the temporal intensity without the phase for these pulse durations – assuming there are no fast changes. This might be regular task in chirped pulse amplification systems to determine the temporal structure of the stretched pulse. A very simple, robust and linear technique is based on spectral interferometry. In this approach the pulses are split before stretching, one replica is stretched then the two pulses are combined with a variable delay between them and sent to a spectrometer. The spectrum will be obtained with an interference pattern at the wavelength, which arrives at the same time as the short pulse. This way the long stretched pulse is sampled and its group delay is determined as a function of the wavelength [16]. Recently, even spectral interferometry has been improved that it can measure long pulses with large TBP [17].

Bibliography

[1] Sala K. L., Kenney-Wallace G. A. and Hall G. E., IEEE Jour. Quant. Electr. **16**, 990 (1980.
Herrmann D., Tautz R., Tavella F., Krausz F. and Veisz L., Opt. Expr. **18**, 4170 (2010).

[2] Etchepare J., Grillon G. and Orszag A., IEEE Jour. Quant. Electr. **19**, 775 (1983.
Janszky J. and Corradi G., Opt. Commun. **60**, 251 (1986).

[3] Diels J. C. M. et al., Appl. Opt. **24**, 1270 (1985).

[4] Trebino R., Frequency-Resolved Optical Gating: The Measurement of Ultrashort Laser Pulses (Kluwer Academic Publishers, Norwell, USA, 2000;
http://www.physics.gatech.edu/frog/.

[5] DeLong K. W. et al., JOSA B **11**, 2206 (1994).

[6] Trebino R. et al., Rev. Sci. Instr. **68**, 3277 (1997).

[7] O'Shea P., Kimmel M., Gu X. and Trebino R., Opt. Lett. **26**, 932 (2001).

[8] Iaconis C. and Walmsley I. A., Opt. Lett. **23**, 792 (1998.
Iaconis C. and Walmsley I. A., IEEE Jour. Quant. Electr. **35**, 501 (1999).

[9] Lozovoy V. V., Pastirk I. and Dantus M., Opt. Lett. **29**, 775 (2004.
Xu B., Gunn J. M., Dela Cruz J. M., Lozovoy V. V., Dantus M., JOSA B **23**, 750 (2006).

[10] Oksenhendler T., Coudreau S., Forget N., Crozatier V., Grabielle S., Herzog R., Kaplan D. and Gobert O., App. Phys. B **99**, 7 (2010).

[11] Minkovski N., Petrov G. I., Saltiel S. M., Albert O. and Etchepare J., JOSA B **21**, 1659 (2004).

[12] Baltuska A., Pshenichnikov M. S. and Weirsma D. A., IEEE Jour. Quant. Electr. **35**, 459 (1999.
Baltuska A., Fuji T. and Kobayashi T., Opt. Lett. **27**, 306 (2002).

[13] Graf U., Fieß M., Schultze M., Kienberger R., Krausz F. and Goulielmakis E., Opt. Expr. **16**, 18956 (2009).
[14] Cavalieri A. L. et al, New J. Phys. **9**, 242 (2007).
[15] Goulielmakis E. et al., Science **305**, 1267 (2004).
[16] Dou T. H., Tautz R., Gu X., Marcus G., Feurer T., Krausz F. and Veisz L., Opt. Expr. **18**, 27900 (2010).
[17] Cohen J., Bowlan P., Chauhan V. and Trebino R., Opt. Expr. **18**, 6583 (2010)

5.3.2 CEP measurement and stabilization

The time dependence of the electric field of a laser pulse can be written as: $E(t) = E_0(t)\cos(\omega t + \varphi)$, where $E_0(t)$ is the envelope function of the field, ω is the angular frequency of the carrier wave, and φ is the Carrier-Envelope-Phase (CEP).

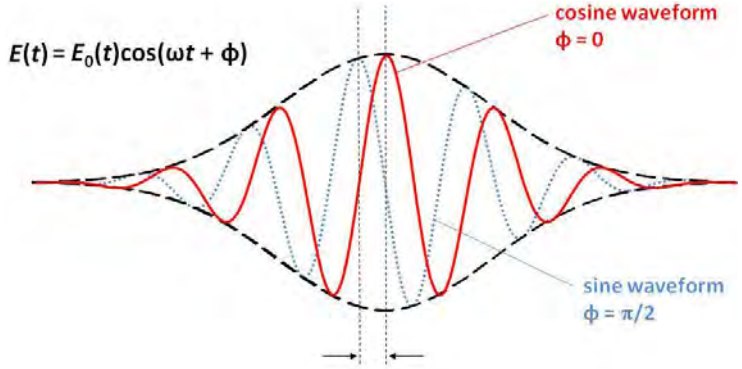

Figure 5.11: Influence of the CEP on the electric field of a few-cycle pulse; cosine waveform $\varphi = 0$ (red solid line), sine waveform $\varphi = \pi/2$ (blue dotted line).

It follows from this equation than only in the few-cycle regime (the pulse contains only few oscillations of the carrier wave of the field), the CEP plays a key role, as only when the pulse duration determined by the envelope is comparable to the period of the carrier wave, the electric field form is significantly affected by the CEP (see Fig. 5.11). The CEP, plays a fundamental role for extreme non-linear optics effects as these processes are driven by the precise electric field form rather than by the envelope as in conventional non-linear optics.

The reliable generation of isolated attosecond pulses requires the control of the CEP of ultrashort pulses as already demonstrated for high-order harmonic generated in gas [1]; the control of the CEP is expected to play a fundamental role also for the generation of isolated attosecond pulse on solid targets [2]. Application of isolated attosecond pulses for time resolved experiments, therefore, requires measurement and stabilization of the CEP. Several techniques have been proposed and experimentally applied to monitor and control this parameter. The techniques used for the determination of the CEP and the CEP drift will be discussed in the following sections devoted to the methods implemented to stabilize the CEP in amplified laser systems.

CEP measurement

In situ determination of the CEP requires an extreme nonlinear optics process whose outcome is directly linked to the precise electric field value. The process of Above-Threshold Ionization (ATI) and High-order Harmonic Generation (HHG) are ideal candidates to accomplish this task. The influence of the CEP on extreme nonlinear phenomena was first demonstrated on ATI in

2001 [3], and since then ATI based CEP measurement using a so called Stereo-ATI phase-meter evolved to a well established technique. Recently with such an apparatus it became possible to determine the CEP of single laser pulses consecutively up to several kHz repetition rates [4]. The method is based on the measurement in opposite directions (left-right or up-down) of the photoelectron spectra generated by re-scattering on the parent ion of the electrons freed by an intense laser field. The number and the energy of the electrons emitted in the left-right directions strongly depends on the maximum of the electric field pointing in that direction. As the CEP determines the ratio of the peak electric field in opposite directions, ATI is a well suited approach for the determination of the CEP of few-cycle pulses. For this purpose an asymmetry parameter, given by the difference of the numbers of electrons emitted in the two directions divided by the total number of electrons, can be introduced. The value of this parameter depends on the energy range of the photoelectrons. By proper choice of the energy ranges, each CEP value can be associated to two asymmetry parameters calculated in different energy ranges. Tagging the CEP of each single laser shot recently made possible the study of phase dependent phenomena at 3-kHz repetition rate without the need for phase stabilization [5]. Even though the envisaged ELI few-cycle lasers are planned to operate phase stabilized, CEP-tagging can be used as an alternative approach to perform CEP-dependent experiments.

The HHG process is also sensitive to the CEP; however due to phase matching effects, the harmonic spectra measured for different CEPs cannot be directly linked to the single atom response and extraction of the CEP from the experimental data can present additional difficulties. Nevertheless it has been demonstrated that, under proper conditions, this method can be used to determine the CEP of the driving pulse, even for relatively long ($\geq$10 fs) pulses; however always with a π phase ambiguity [6] as the HHG process is not influenced by a π change of the driving electric field. Other effects such as terahertz generation [7] and non-sequential double ionization [8] are affected by the CEP and could be implemented to determine its value. It is important to observe that due to intensity levels that will be reached by the laser system envisaged in ELI, the motion of the electron will be dominated by relativistic effects and therefore the characteristics of the HHG and ATI processes will be strongly modified. These methods can serve for monitoring the CEP of a low intensity leak from the main pulse, and thus determine the CEP with an offset ambiguity at the interaction; for the determination of the CEP in situ new effects and new approaches will be required, such as the angular distributions of photons emitted via multiphoton Compton scattering, as recently proposed [9].

For many applications, it is important to characterize the CEP drift, i.e. the change from pulse to pulse (or the change of the CEP over an ensemble of pulses) of the CEP, rather than the CEP value. For this purpose the most common approach is based on a nonlinear interferometer (f-2f interferometer) [10, 11]: a fraction of the energy of the pulses is focused in a nonlinear crystal (usually a sapphire plate) for generation of a white light continuum extending over more than an optical octave. The low frequency part of the continuum is frequency doubled in a second nonlinear crystal (for example BBO), cut in such a way that the frequency doubled radiation spectrally overlaps with the high frequency part of the white light. Due to the group delay dispersion introduced by the optical components and by the path in air between the generation of the white light and the frequency doubling, the two pulses in the high frequency region present a delay τ and give rise to an interference pattern in the spectral domain from which the CEP drift can be measured. This technique is currently used as detection of the CEP drift in commercially available laser systems and can work on a single shot basis up to several kHz repetition rate [12].

CEP stabilization

The control of the CEP in amplified laser systems is based on feedback loops to compensate for the CEP drift; the CEP value can be easily varied, for example, by moving into the beam

path a small amount of glass exploiting the difference between group and phase velocities in dispersive material (for example 52 μm of glass correspond to a variation of the CEP of 2π). The stabilization is usually divided in two steps: a first feedback operating on the oscillator, and a second one operating on the amplifier stages. The train of pulses delivered by an oscillator operating in mode-locking is characterized by a constant CEP drift that is determined by the difference between the group and the phase velocities in a round trip of the cavity. Moreover small intensity fluctuations of the pump laser induce different CEP drift due to the intensity-phase coupling inside the active medium. In order to stabilize the CEP drift, a feedback loop is usually implemented. A nonlinear interferometer, similar to the one outlined in the last section, is applied for the determination of the CEP drift; a modulation of the power of the pump laser via an acousto-optic modulator or the tilt of an end mirror of the cavity for prisms based oscillator, are usually used as actuators. Recently a new approach has been developed consisting in using a frequency shifter to shift the frequency comb of the train of the pulses delivered by the oscillator [13]. In the time domain this shift corresponds to a variation of the CEP drift. The main advantage of this technique is that the oscillator does not need to be CEP stabilized, but it is simply running in mode-locking; outside the cavity the CEP drift of the pulse train is then properly adjusted. This feedback loop holds the promise to achieve very long stabilization time.

The amplification process introduces additional CEP noise mainly due to mechanical instabilities in the stretcher-compressor setups, to beam pointing instabilities or to fluctuations of the power of the pump lasers. In order to compensate for such drifts, a second feedback loop is required. The CEP drift is usually detected using an f-2f interferometer after the final compression stage; several actuators have been proposed and experimentally demonstrated including adjustments of the grating separation distance [14], amount of glass in the beam path by moving a glass wedge [15], or acting on the power of the pump of the oscillator [1]. In the first two cases as massive moving mechanical parts are included in the loop, the feedback bandwidth is limited to few Hertz while in the last case, as two feedback loops (one for the oscillator and one for the amplifier) are acting on the same parameter, possible interference effects could be unavoidable. Recently a new method was proposed for the stabilization of the CEP of amplified pulses based on the use of a programmable acousto-optic dispersive filter (DAZZLER) inserted into the beam path [16]. Using a proper synchronization electronics, the acoustic wave in the DAZZLER can be synchronized with the pulse train delivered by the oscillator and the CEP phase drift can be compensated. The main advantage of such technique is the absence of moving parts, that could allow feedback bandwidths up to few tens of kHz.

All the methods outlined so far, are based on an active stabilization of the CEP. Passive stabilization can be achieved using a parametric effect referred to as difference frequency generation. Under suitable condition, the difference between two spectral regions of the spectrum of a pulse can be achieved inside a nonlinear crystal; as the two spectral regions stem from the same pulse, they will share the same CEP drift from pulse to pulse that therefore cancels in the difference output signal [17]. In this approach the difference frequency signal presents CEP drift equal to zero and all the pulses are characterized by the same CEP. Subsequent parametric amplification of such pulses preserves the CEP and is therefore particularly suitable for the generation of CEP stabilized laser pulses. However intensity fluctuations of the pump lasers, thermal drift and mechanical instabilities as well, introduce CEP fluctuations that need to be compensated for and require feedback loops similarly to the ones outlined before.

Bibliography

[1] Baltuška A., Udem Th., Uiberacker M., Hentschel M., Goulielmakis E., Gohle Ch., Holzwarth R., Yakovlev V. S., Scrinzi A., Hänsch T. W. and Krausz F., Nature **421,** 611 (2003).

[2] Tsakiris G. D., Eidmann K., Meyer-ter-Vehn J. and Krausz F., New J. Phys. **8,** 19 (2006).
[3] Paulus G. G., Grasbon F., Walther H., Villoresi P., Nisoli M., Stagira S., Priori E., De Silvestri S., Nature **414,** 182 (2001).
[4] Wittmann T., Horvath B., Helml W., Schätzel M. G., Gu X., Cavalieri A. L., Paulus G. G. and Kienberger R., Nature Physics **5,** 357 (2009).
[5] Johnson N. J., Herrwerth O., Bergues B., Wirth A., De S., Ben-Itzhak I., Lezius M., Krausz F., Kling M. F., Senftleben A., Schröter C. D., Moshammer R., Ullrich J., Betsch K. J., Jones R. R., Sayler A. M., Rathje T., Rü K., Mü W. and Paulus G. G. (in preparation).
[6] Haworth C. A., Chipperfield L. E., Robinson J. S., Knight P. L., Marangos J. P. and Tisch J. W. G., Nature Physics **3,** 52 (2007).
[7] Kreβ M., Löffler T., Thomson M. D., Dörner R., Gimpel H., Zrost K., Ergler T., Moshammer R., Morgner U., Ullrich J. and Roskos H. G., Nature Physics **2,** 327 (2006).
[8] Liu X., Rottke H., Eremina E., Sandner W., Goulielmakis E., Keeffe K. O., Lezius M., Krausz F., Lindner F., Schätzel M. G., Paulus G. G. and Walther H., Phys. Rev. Lett. **93,** 263001 (2004).
[9] Mackenroth F., Di Piazza A. and Keitel C. H., Phys. Rev. Lett. **105,** 063903 (2010).
[10] Mehendale M., Mitchell S. A., Likforman J.-P., Villeneuve D. M. and Corkum P. B., Opt. Lett. **25,** 1672 (2000).
[11] Kakehata M., Takada H., Kobayashi Y., Torizuka K., Fujihira Y., Homma T. and Takahashi H., Opt. Lett. **26,** 1436 (2001).
[12] Koke S., Grebing C., Manschwetus B. and Steinmeyer G., Opt. Lett. **33,** 2545 (2008).
[13] Koke S., Grebing C., Frei H., Anderson A., Assion A. and Steinmeyer G., Nature Photonics **4,** 462 (2010).
[14] Li C., Moon E., Mashiko H., Nakamura C. M., Ranitovic P., Maharjan C. M., Cocke C. L., Chang Z. and Paulus G. G., Opt. Express **14,** 11468 (2006).
[15] Schätzel M. G., Lindner F., Paulus G. G., Walther H., Goulielmakis E., Baltuška A., Lezius M. and Krausz F., App. Phys. B **79,** 1021 (2004).
[16] Forget N., Canova L., Chen X., Jullien A. and Lopez-Martens R., Opt. Lett. **34,** 3647 (2009).
[17] Baltuška A., Fuji T. And Kobayashi T., Phys. Rev. Lett. **88,** 133901 (2002).

5.3.3 Temporal contrast

Classification of temporal contrast

Besides pulse duration, spectral width and spectral phase, one of the most crucial properties of ultrashort high intensity laser pulses is their temporal contrast. It can be defined in a few ways. Intensity contrast, which is the ratio of the peak intensity to the pedestal and / or the nearest pre-pulses (Fig. 5.12). In some cases it may be practical to consider the energy contrast, which is the ratio of the energy in the main peak of the pulse and all the pedestals, mainly before the pulse. Since in most of the cases the intensity contrast has its highest importance, in the following we are dealing only with that.

Analyzing a typical (low) contrast measurement curve shown in Fig. 5.12, it is practical to divide it into three parts. The first can be called "nanosecond-scale" contrast which describes the situation well before the main pulse. The contrast degradation of this type stems from the use of nanosecond pumpe pulses in the (OP)CPA laser chain and primarily due to incoherent light like amplified spontaneous emission (ASE) or optical parametric superfluorescence (OPS). The second type of contrast degradation consist of pre-pulses originating from non-complete suppression of the typically MHz repetition rate pulse train from the femtosecond oscillator as well as spurious reflections on various optical elements. Since these pre-pulses come from the same (or subsequent) seed pulse, they are coherent to the main peak. Notably, as it has been

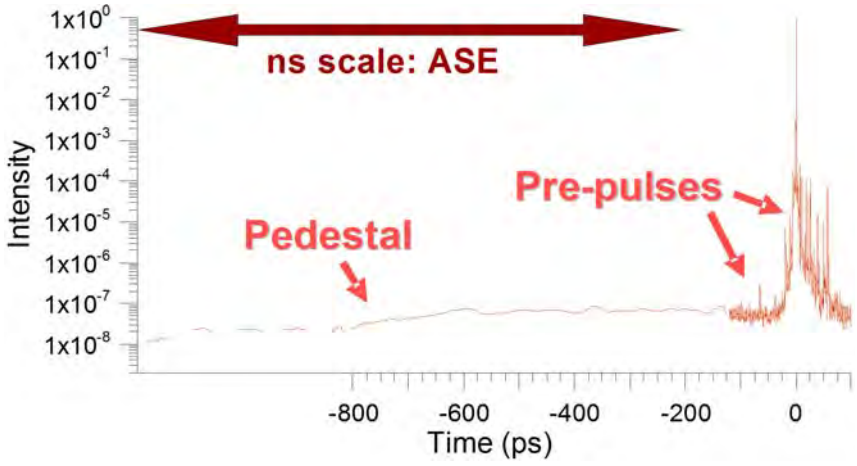

Figure 5.12: Part of the very first draft of the ELI-PP white book.

recently discussed, some of the pre-pulses stem from post-pulses, under the circumstances of considerable self phase modulation in the CPA laser chain [1].

The third, maybe less trivial origin of contrast degradation can be named as picosecond-scale or intrinsic contrast, and it manifests as sub-peaks temporally close (1–10 ps) to the main pulse. It is uniquely defined by the spectrum and the spectral phase shift (chirp) of the pulse as well as by the angular dispersion of the laser beam.

Efforts aiming to improve any of the three contrast types almost certainly affect the others. Hence, the improvement of a laser system requires several subsequent steps and often results in compromises as will be shown in the following sections.

Improve ASE contrast

One of the main directions of research and development of high intensity laser systems is to increase the pulse intensity on the target in laser-matter experiments, and to sufficiently suppress the level of pre-pulses and amplified spontaneous emission (ASE). One obvious solution satisfactory for both aims is to shorten the duration of the amplified pulses, that is, to broaden their bandwidth. As it became evident soon after the dawn of high power laser systems based on chirped pulse amplification (CPA), however, the broad emission spectrum of the amplifier medium (e.g. Ti:sapphire) is substantially narrowed upon high gain amplification [2]. This gain narrowing effect depends strongly on the total gain of the laser system. Hence, the higher is the energy of the amplified pulses the longer is their duration [3–5].

During the recent decade much effort has been made to develop techniques for overcoming the gain narrowing effect. An obvious approach is to feed the laser system with more energetic seed pulses, so that the total gain can be reduced [6–8]. Unfortunately, the construction of an appropriate laser oscillator is by far not evident. The early designs of cavity dumped laser oscillators [9–11] do not have sufficiently high temporal contrast [12–14]. Although they were used in some laser systems as a front end [15, 16] the robustness of their daily operation lagged behind that of the low energy Kerr-lens mode locked oscillators. Nowadays a new generation of high energy oscillators [17–18] is emerging, but their bandwidth is still narrow and temporal contrast has to be proven.

Shaping of the spectrum of the seed pulse prior to the amplifier chain was a reliable solution to increase the temporal contrast. However, these techniques based on acousto-optical crystals [19–21] or spatial light modulators [2] reduce substantially the energy of the seed pulse.

Consequently, to achieve the same level of multi-TW amplification, the Ti:sapphire amplifiers need to be driven harder, which would in turn increase the ASE level and hence decrease the temporal contrast. A further attempt of inserting etalons into the regenerative amplifier turned out to produce side peaks and, hence, also reduced the temporal contrast [22–23]. Shaping via deformable mirrors [24] does not give high enough spectral modulation for compensation of gain narrowing at high gain systems. Compensation for the gain narrowing with special dielectric coated mirrors is another method, which was successfully used for broadband amplification in Ti:Sa [25].

Another promising solution was the invention of optical parametric chirped pulse amplification (OPCPA) [27–28]. Since it offers a bandwidth over 200 nm even at high gain (10^6) operation, it has proved to be very successful during the last years [28–34]. However, there are still uncertainties regarding compensation of higher order phase distortions at the wings of the spectrum, and stability of operation. Moreover, the OPCPA technique at 800 nm runs into the inherent problem of temporal contrast when pulses with a duration shorter that 20 fs are to be amplified [7].

A fresh and brave approach was to design a double CPA system (DCPA) [35]. The pulses have been pre-amplified to a mJ level, then compressed to transform limited duration. With the use of a highly nonlinear process, the ASE pedestal and all the possible pre- and post-pulses have been diminished. A challenge was to find a suitable nonlinear process along with the suitable material. By now, the standard is the use of cross polarized wave generation in single or double configuration of BaF_2 crystals [36].

An alternative solution is the scheme of negatively and positively chirped pulse amplification (NPCPA), which is a variation of double chirped pulse amplification [37]. Here the first amplifier, where the femtosecond pulses are negatively chirped, acts as the necessary pulse shaper. By the second amplifier the sign of the chirp is changed, so that this combination offers significant broadening for the bandwidth of amplified femtosecond laser pulses.

Improve ps contrast

As it has been shown above, the CPA technique and its variations help to increase the ASE temporal contrast. However, due to the large stretch and compression factors, the origin of the substantial shoulder beneath the main peak is basically the non-compensated dispersion of the system, or with other words, some higher order distortion of the spectral phase. This latter may be attributed to mismatched stretcher-compressor performance, high level of self phase modulation, ripples on the surface of the optics, non-compensated angular dispersion in the beam, non-sufficient bandwidth of the optics, scattering on optical surfaces and inside of optical materials, non-sufficient size of the optics and also aberration of the (focusing) optics.

By now, commercial instruments are available for engineering of spectral phase, measurement of wave front distortions (aberrations) and angular dispersion. Compensation of spectral phase is a routine to the third order, can be challenging to the fourth order, and still lacking for reliable solutions to the higher than fourth orders.

Measurement of temporal contrast

Characterization of the leading edge of a short intense pulse on a nanosecond scale is relative straightforward, as it can be done with the use of ultrafast photodiodes on their own or in sequence (Fig. 5.13). Approaching the pedestal of the main pulse, however, the photodiodes becomes blind around half a nanosecond prior to the main peak.

In the picosecond regime only cross correlators could be used. There are basically two types. The traditional one is based on at least a third order processes like third harmonic generation in single or sequence of nonlinear conversion crystals or three photon ionization, etc. [39–43]. In these devices the main pulse is split into two. One replica is for instance frequency doubled,

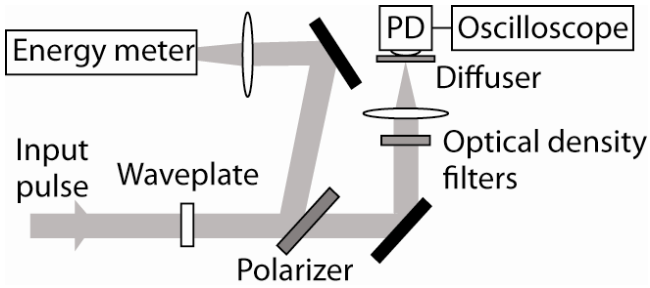

Figure 5.13: Measurement of temporal contrast on a high dynamic range with sequence of photodiodes [38].

and then this SH pulse is frequency mixed with the other replica of the main pulse in a third harmonic generator crystal. The amount of the resulting (usually UV) light, that is its energy is characteristics to the overlapping intensities and eventually the intensity contrast.

In a recent design [44] the philosophy has been changed, that is, not the main peak of the pulse is frequency converted, but in contrary, it is used for amplification of the wings in an optical parametric crystal. This type of optical parametric correlators are especiall useful for weak laser pulses [45].

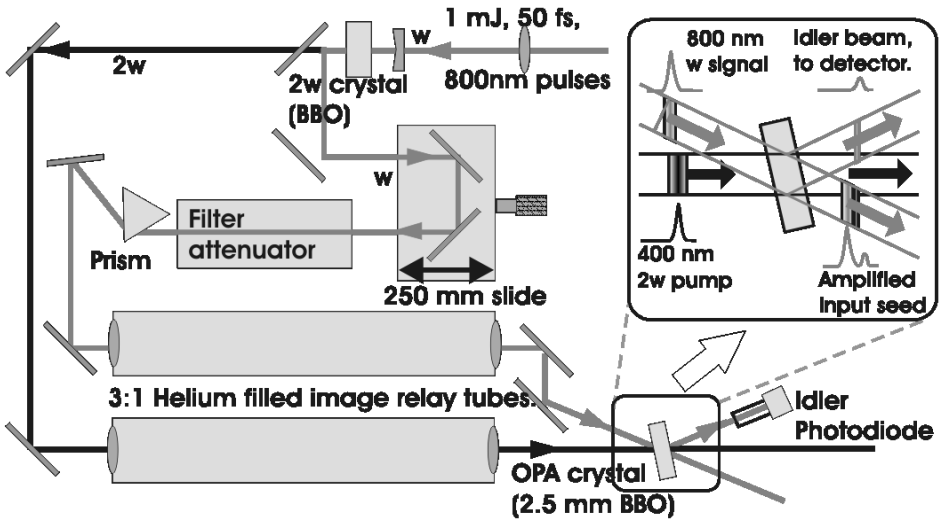

Figure 5.14: The first optical parametric amplification correlator [44].

Bibliography

[1] N.V. Didenko, A.V. Konyashchenko, A.P. Lutsenko, S. Yu. Tenyakov, Optics Express 16 (2008) 3178.
[2] S. Backus, C.G. Durfee III, M.M. Murnane, H.C. Kapteyn, Rev. Sci. Instr. **69** (1998) 1207.
[3] M. Aoyama, K. Yamakawa, Y. Akahane, J. Ma, N. Inoue, H. Ueda, H. Kiriyama, Opt. Lett. **28** (2003) 1594.
[4] S.-W. Bahk, P. Rousseau, T. A. Planchon, V. Chvykov, G. Kalintchenko, A. Maksimchuk, G. A. Mourou, V. Yanovsky, Opt. Lett. **29** (2004) 2837.

[5] J. Collier, O. Chekhlov, R. Clarke, E. Dival, E. Ertel, B. Fell, P. Foster, J. Govans, S. Hawkes, P. Holligan, C. Hooker, H. Hutchinson, S. Karsh, A. Langley, W. Lester, W. Martin, D. Neely, P. Norreys, M. Ritts, C. Reason, J. Smith, T. Winstone, R. Watt, B. Wyborn, RAL Report Nr. RAL-TR-2004-025, 182 (2004)
[6] J. Itatani, J. Faure, M. Nantel. G. Mourou, S. Watanabe, Opt. Commun. **148**, 70 (1998)
[7] K.Osvay, M.Csatári, I.N. Ross, A.Persson, C. G.Wahlström, Laser and Particle Beams **23,** 327 (2005)
[8] M.P. Kalashnikov, K. Osvay, SPIE **5975,** 125 (2006)
[9] A. Baltuška, Z.Wei, M.S. Pshenichnikov, D.A. Wiersma, R. Szipöcs, Appl. Phys. B **65** (1997) 175.
[10] Y.-H. Liau, A.N. Unterreiner, D.C. Arnett, N.F. Scherer, Appl. Opt. **38** (1999) 7386.
[11] N.W. Rimington, A. Cornea, A.J. Van Tassle, J. Santoro, W. A. Schroeder, Appl.Opt. **40** (2001) 4831.
[12] I.D. Jung, F.X. Kärtner, J. Henkmann, G. Zhang, U. Keller, Appl. Phys. B **65** (1997) 307.
[13] A. Kasper, K. J. Witte, J. Opt. Soc. Am. B **15** (1998) 2490.
[14] G. Cheriaux, T. Planchon, F. Auge, G. Mourou, J. P. Chambaret, in Proceedings of Ultrafast Optics 2001 (Springer-Verlag, Heidelberg, Germany, 2001), p. 16.
[15] Y. Jiang, T. Lee, W. Li, G. Ketwaroo, C.G. Rose-Petruck, Opt. Lett. **27** (2002) 963.
[16] N. Zhavoronkov, H. Maekawa, H. Okuno, K. Tominaga, J. Opt. Soc. B **22** (2005) 567.
[17] Y. Vidne, M. Rosenbluh, T.W. Hansch, Opt. Lett. **28** (2003) 2396.
[18] A. Fernandez, T. Fuji, A. Poppe, A. Furbach, F. Krausz, A. Apolonski, Opt. Lett. **29** (2004) 1366.
[19] P. Tournois, Optics Commun. **140** (1997) 245.
[20] Liu LQ, Peng HS, Wei XF, Zhu QH, Huang XJ, Wang XD, Zhou KN, Zeng XM, Wang X, Guo Y, Yuan XD, Peng ZT, Tang XD, Acta Physica Sinica **54** (2005) 2764.
[21] Pittman M, Ferre S, Rousseau JP, Notebaert L, Chambaret JP, Cheriaux G, Appl. Phys. B **74** (2002) 529.
[22] C. P. J. Barty, T. Guo, C. Le Blanc, F. Raksi, C. Rose-Petruck, J. Squier, K. R. Wilson, V. V. Yakovlev, K. Yamakawa, Opt. Lett. **21**, 668 (1996).
[23] K.Yamakawa, C. P. Barty, Opt. Lett. **28** (2003) 2402.
[24] X. Zhou, T. Kanai, D. Yoshitomi, T. Sekikawa, S. Watanabe, Appl. Phys. B **81** (2005) 13.
[25] H.Takada, M.Kakehata, K. Torizuka, Ultrafast Optics IV. Springer Series in Optical Science **95**, 87 (2003).
[26] A. Dubietis, G. Jonusauskas, A. Piskarskas, Opt. Commun. **88** (1992) 437.
[27] I. N. Ross, P. Matousek, M. Towrie, A. J. Langley, J. L. Collier, Opt. Commun. **144** (1997) 125.
[28] I.N. Ross, J.L. Collier, P.Matousek, C.N. Danson, D. Neely, R.M. Allott, D.A. Pepler, C. Hernandez-Gomez, K. Osvay, Appl. Opt. **39** (2000) 2422.
[29] I. Jovanovic, B.J. Comaskey, C.A. Ebbers, R.A. Bonner, D.M. Pennington, E.C. Morse, Appl. Opt. **41** (2002) 2923.
[30] X.D. Yang, Z.Z. Xu, Y.X. Leng, H.H. Lu, L.H. Lin, Z.Q. Zhang, R.X. Li, W.Q. Zhang, D.J. Yin, B. Tang, Opt. Lett. **27** (2002) 1135.
[31] H. Yoshida, E. Ishii, R. Kodama, H. Fujita, Y. Kitagawa, Y. Izawa, T. Yamanaka, Opt. Lett. **28** (2003) 257.
[32] V. Petrov, F. Noack, F. Rotermund, V. Pasiskevicius, A. Fragemann, F.Laurell, H. Hundertmark, P. Adel, C. Fallnich, Jap. J. Appl. Phys. **42** (2003) L1327.
[33] L.J. Waxer, V. Bagnoud, I.A. Begishev, M.J. Guardalben, J. Puth, J.D. Zuegel, Opt. Lett. **28** (2003) 1245.
[34] R.T. Zinkstok, S.Witte, W.Hogervorst, K.S.E. Eikema, Optics Letters **30** (2005) 78.
[35] M. P. Kalashnikov, E. Risse, H. Schönnagel, and W. Sandner, Optics Letters **30** (2005) 923.

[36] A. Jullien, O. Albert, F. Burgy, G. Hamoniaux, J.-P. Rousseau, J.-P. Chambaret, F. Augé-Rochereau, G. Chériaux, J. Etchepare, Optics Letters **30** (2005) 920.
[37] M. P. Kalashnikov, K. Osvay, I.M. Lachko, H. Schönnagel, W. Sandner, Appl. Phys. B **81** (2005) 1059.
[38] C. Dorrer, D. Irwin, A. Consentino, J. Qiao, ICUIL 2010, Watkins Glen, NY, 2010, paper ThO3.
[39] S. Luan, M. H. R. Hutchinson, R. A. Smith, F. Zhou, Meas. Sci. Technol. **4**, 1426 (1993).
[40] P.F. Curley, G. Darpentigny, G. Cheriaux, J.P. Chambaret, A. Antonetti: Opt. Commun. **120**, 71 (1995).
[41] I.D. Jung, F.X. Kaertner, J. Henkmann, G. Zhang, U. Keller, Appl. Phys. B **65**, 307 (1997).
[42] T. Feurer, S. Niedermeier, R. Sauerbrey, Appl. Phys. B **66**, 163 (1998).
[43] K. Osvay, I.N. Ross, J.M. D. Lister, C.J. Hooker, Appl. Phys. B **69,** 19 (1999).
[44] E.J. Divall, I.N. Ross, Opt.Lett. **29**, 2273 (2004).
[45] J. Bromage, C. Dorrer, J. D. Zuegel, ICUIL 2010, Watkins Glen, NY, 2010, paper MO2.

5.4 Pump sources

5.4.1 Flash-lamp pumped lasers.

Since the early 80's, most authors are considering that to enable high-average-power operation at the highest laser efficiency, it is necessary to replace flash-lamp pumped solid-state lasers with laser-diode pumped solid-state lasers. This assumption is based on the fact that diode pumping has many advantages compared to flash-lamp pumping that is seen as an old technology. Although it is very difficult to get true numbers, Diode Pumped Solid State Lasers nearby the kW level have a moderate efficiency (<<10%), much lower than expected. Flash lamp pumped fusion lasers are still in the run with a typical 1% efficiency but can access high beam quality and high harmonic generation efficiency.

Fifty years ago, Theodore Maiman was the first to use flash-lamp pumping for the early experiments with Ruby. Since that time, Neodymium doped solid state lasers have become the work horse of lasers. Neodymium doped YAG lasers are compact and cheap lasers that can be found in any laser laboratory all around the world. YAG lasers can access 10's of Hz repetition rate but are limited to the Joule level because the saturation fluence of Nd doped YAG is low. Neodymium doped glass lasers (Nd: glass) are by far the most widely used type of drivers in Inertial Confinement Fusion both in existing facilities and in the largest being built : the National Ignition Facility (NIF) in the USA and the Laser Megajoule (LMJ) in France. There are several good reasons for the preponderance of this type of laser material: one is because its saturation fluence is 4 to 5 J/cm^2, but the most important is its availability at large size because glass can be mould very easily.

Flash lamp pumped lasers have been widely studied in the past. Although lamp efficiencies are between 0.45 for Krypton arc lamp and 0.54 for Xenon arc lamp, the overall laser efficiency can hardly exceed 1% [1]. According to this percentage balance, NIF/LMJ total efficiency can be assessed in the range 0.5 to 1%. 0.66% efficiency has been published for NIF [2].

Laser design is a compromise solution somewhere between good beam quality, high electrical to optical efficiency and low cost of operation. Most of the time, repetition rate and wall-plug efficiency are discussed but the main issue to deal with is thermal loading in the laser amplifiers because the amplified beam quality is related to the laser material ability to dissipate heat.

If we discuss the possibility of extending solid-state laser technology to high-average-power and of improving the efficiency of such lasers, the critical elements of the laser design are [3]:

1. the thermal management (removing heat from the center of the solid with a cooling system at the end surfaces),
2. the thermal gradient control (minimizing optical wave front distortions),
3. the pump energy utilization (overall efficiency including absorption, stored energy, gain etc),
4. the efficient extraction (filling most of the pumped volume with extracting radiation and matching pump duration to the excited-state lifetime).

Although there are very efficient diode-pumped solid state lasers, it turns out that when looking through the beam quality (or M^2) point of view, only few systems can be considered as really efficient. The only highly efficient with the highest beam quality (i.e. M^2 close to 1) are CW lasers at cryogenic temperature [4–7]. Apart from multi kW-level lasers for military applications, Mercury is the only QCW laser that has been operated 3x10^5 shots but with a moderate efficiency (<<10%), lower than expected [8]. This is because QCW diode bars have a typical 1% duty cycle that makes them suitable for pumping ytterbium at 10 Hz (excited state lifetime is typically 1 ms in garnets). Using CW diodes means either CW operation or a few kHz repetition rates (this is true for both neodymium and ytterbium doped solid state hosts).

Moreover, learning curves [9] are telling us that diode bar prices are dropping with growing market but who knows how long we are going to wait for the market? The conclusion is that QCW diode bars are too expensive to be used in low rep-rate lasers (i.e. less than 10 Hz).

About fusion lasers and the way to improve repetition rate

There are engineering solutions to correct the wave front with deformable mirrors, pinholes and optical image relays. This configuration has been successfully tested in the last fusion lasers to correcting the wave front. Both NIF and LMJ prototype (LIL facility) have achieved more than 85% THG efficiency [10]. Both NIF and LMJ prototype (LIL facility) can fire every 2 hours (amplifier slabs are not cooled). LLE (OMEGA EP) while using this type of amplifier with water cooled lamps (but still un-cooled slabs) can fire every hour [11]. Disk amplifiers were developed for the 60-beam OMEGA and the four-beam OMEGA EP lasers. The 150-mm disk amplifier head, uses water-cooled flash lamps to facilitate operation at high storage efficiency with shot cycle times of 10-20 minutes. If cooling the slab surface is possible, the repetition rate can increase up to 1 shot per minute. This is because the heat flux or heat transfer ($\boldsymbol{h}$ in W/cm^2·K) is increased and the temperature drop across the cooling boundary is decreased. Typical $\boldsymbol{h}$ values are from 1 to 10 W/cm^2·K. This can be achieved with flow-cooled plates. This principle has been successfully tested on the Mercury laser with Helium gas [8].

What a flash-lamp pump laser could look like

The laser is based on a MOPA (Master Oscillator Power Amplifier) architecture.

As part of the front-end, the Pre-amplifier module (PAM) would incorporate a temporally shaped seed pulse and a beam shaping device to optimise both amplifier extraction and beam quality. A multi-pass disk amplifier system provides high-gain and high-energy output using a Q-switch and cavity-dump arrangement. Angular multiplexing is used to inject the input near the focal point of an input vacuum spatial filter (VSF) in a manner analogous to LMJ, NIF and OMEGA EP. Roundtrips inside the imaging multi-pass laser cavity can produce output pulse energies up to half the kJ at 1053 nm. The amplified pulse is cavity dumped by removing the Pockels cell drive voltage and directed to the second harmonic generation (SHG) stage by the output vacuum spatial filter. The SHG crystal is located at the final image plane of the beam shaper. KD*P or LBO crystals can be used to provide high SHG conversion efficiency ($\eta \sim 75$–80%) by optimizing the intensity and crystal length. The increased angular and temperature acceptance of LBO are attractive [12] but a well-designed laser system can effectively use KD*P.

For the purpose of pumping either large Ti:Sapphire crystals or OPCPA (Optical Parametric Chirped Pulse Amplifier) devices for the ELI project, we believe that considering a flash lamp pumped laser to delivering a few hundreds of Joule of green light makes sense as soon as the main amplifiers repetition rate does not exceed 1 shot per minute. Flash lamp pumped lasers are still in the run with a low efficiency but can access high beam quality and high harmonic generation at a reasonable repetition rate.

Bibliography

[1] W. Koechner, Solid-state laser engineering, 5^{th} ed. (Springer, Ed., 1999), pp. 393.
[2] J. Caird et al, Fusion Science and Technology **56**, 607 (2009).
[3] J. Emmett et al, UCRL53571, LLNL (1984).
[4] J. K. Brasseur et al, Proc. of SPIE **6952**, 69520L (2008).
[5] D. J. Ripin, Optics Letters, **29**, 2154 (2004).
[6] H. Furuse et al., Proc. of ASSP, WE6 (2009).
[7] T. Taira and M. Tsunekane, Proc. of SPIE **6216**, 621607 (2006).
[8] A. J. Bayramian et al., Fusion Science and Technology, **52**, 383-387 (2007); Fusion Science and Technology **56**, 295 (2009).
[9] C. Ebbers et al., Laser Focus World **43**, 3 (2009).
[10] C. Haynam et al., Applied Optics **46**, 3276 (2007); J. of Physics: Conference Series **112**, 032004 (2008).
[11] D. N. Maywar et al., J. of Physics: Conference Series **112**, 032007 (2008).
[12] G. Mennerat et al., Proc. of ASSP, MB26 (2009); Proc. of CLEO, CPDA1 (2008).

5.4.2 Diode pumped disk lasers

Producing isolated attosecond XUV pulses via high harmonic generation (HHG) requires high-energy, few cycle pulses preferably with kilohertz repetition rates (RR) for exploring hyperfast electronic phenomena [1–3]. Ultrashort pulses in the range of a few femtoseconds at $\sim$kHz RR have been demonstrated using a complex design consisting of an oscillator, a multipass chirped pulse amplifier and an additional nonlinear compression stage [4, 5]. However, it has been difficult to extend these systems to the multi-mJ level [6].

Optical parametric chirped pulse amplifiers (OPCPA) have emerged as a powerful alternative for creating broadband few-cycle pulses, and are the only method by which high-energy mulit-mJ few-cycle coherent light pulses have been generated [7, 8]. However, current OPCPA designs suffer from complex stretcher and compressor elements, necessitated by the pulse duration of pump laser pulses, which are currently several tens of picoseconds in duration or longer [9, 10]. Stretching the seed pulse to a significant fraction of the pump pulse duration is required for efficient energy extraction. Unfortunately, extensive stretching to tens of picoseconds requires highly dispersive prisms or grating components and consecutively complex adaptive dispersion management schemes for proper recompression [10, 11]. The use of shorter pump pulses in the range of a few picoseconds [12] would eliminate the need for such a large stretching and compression ratio. In this case, the seed pulse can be stretched by passing it through a few millimeter-long dispersive optical material and recompressed by a highly-efficient compressor consisting of a few chirped multilayer mirrors [13]. Furthermore, the threshold intensity for optical damage of transparent materials increases even faster than the $1/\tau^{1/2}$ for laser pulse durations below 20 ps [14]. As a consequence, pumping the nonlinear crystal with higher intensities allows the same OPA gain to be attained with a shorter crystal and hence over a broader bandwidth [15].

One aim of the European Extreme Light Infrastructure project are near infrared few-cycle OPCPAs with high repetition rates and pulse peak powers in the petawatt range. These light sources require high average power picosecond lasers especially tailored for pumping parametric amplifiers. Scaling a laser towards high repetition rates while still aiming for high energy picosecond pulses combines intensity-caused difficulties just like optical damage, self phase modulation and self focusing with exceedingly high thermal loads in the laser gain medium. Since the introduction of the thin disk laser in 1994 [16], no other laser concept has shown such a good scalability towards high average powers so far.

Energy and power scaling can be realized via area scaling of the disk while keeping peak temperature and mechanical stress profile of the gain media, optical peak intensity and beam divergence constant. Simultaneously the required pump beam brightness which is a main cost driver of diode pumped solid state laser systems, also remains constant [17]. Due to the efficient one dimensional heat removal a disk laser accepts extremely high pump densities of nearly 1 MW/cm^3 [18] while still keeping thermal induced distortions and lensing of the laser media low. This allows for good beam qualities even in multi pass arrangements. Another exciting aspect of a disk based laser is the small longitudinal extension of the gain medium allowing the amplification of short pulses without facing problems due to nonlinearities and large B-integral accumulation. Therefore high peak power are possible without cost intensive large gratings in stretcher and compressor setups by using chirped pulse amplification (CPA) setups [19] introducing only a small stretching to compression ratio. Fortunately, in the near infrared spectral range, CPA can be implemented with low loss owing to the availability of transmission or reflection gratings with diffraction efficiencies of >97% [20].

The disadvantage of low amplification in the thin disk gain media can be compensated in practice by the large possible pump densities and the feasibility of serial combination of several disks. In summary, the diode pumped disk laser concept allows to reach high wall plug efficiency, excellent beam quality, high average and peak power and high reliability of the laser at moderate

cost [17].

After the first demonstration of an one kW disk laser in 1999 by TRUMPF Laser [21] immense progress mainly due to improvement in the diode laser technology has been attained. Today, cw laser systems with 16 kW output power are commercially available [22] and more than 25 kW of output power was demonstrated [23]. As a quasi-three-level system, Yb:YAG requires a minimum pump intensity of 1.5 kW/cm^2. Since pump diodes with much higher intensity are available for the absorption bandwidth around 940 nm, Yb:YAG has become a popular laser medium for cw high power and even pulsed high energy lasers especially based on the thin disk technology. Yb:YAG exhibits a complete set of properties favorable for high-power diode-pumping [24]:

- low quantum defect (91% quantum efficiency)
- low fractional heating
- relatively broad absorption bands (10 nm @ 940 nm)
- high doping levels possible without quenching (>20%)
- no excited-state absorption or upconversion
- 940 nm pump wavelength, which enables the use of very reliable InGaAs diodes
- high thermal conductivity (6.6 Wm^{-1}K^{-1} @ 3% Yb doping)
- high tensile strength of the host material
- long lifetime of upper laser level ($\sim$ 1 ms)
- broad emission bands ($\sim$ 10 nm; $<$ 1 ps pulses possible)

Several other laser materials, for instance Yb:KGW or Yb-doped sesquioxides (Yb:Sc_2O_3; Yb:Lu_2O_3; Yb:Y_2O_3), could also be considered as laser media in high gain thin disk amplifiers impressing through higher quantum efficiency ($\sim$95%), higher heat conduction (up to 18 Wm^{-1}K^{-1}) and larger bandwidth (11.6–14.4 nm) than Yb:YAG [25].

Besides possible high pump power densities, diode pumping of high average power lasers offers additional benefits such as high electrical-to-optical efficiency, narrow optical bandwidth, long lifetime and compactness of the laser diodes. Nowadays, fiber coupled pump diodes are commercially available with powers of more than 13 kW [26] and could reach nearly 65 kW by combining the fibers of several 500 W modules to a fiber bundle [27]. Fiber coupled laser diodes as pump sources offer the great advantage of exchanging or upgrading them quickly. The supply units can be placed in a separate room, which saves space in the cost-intense laser hall while keeping away additional heat or vibrational sources from the laser setup.

All this advantages are combined in the thin disk based laser and amplifier heads [16] developed at the Institut für Strahlwerkzeuge (IFSW) at the Technical University Stuttgart. These heads are commercially available at the company Dausinger + Giesen GmbH. In these heads, the pump radiation of the laser diodes is first homogenized either by fiber coupling or by focusing into a quartz rod. Subsequently, it is imaged on the disk using collimation optics and the parabolic mirror inside the laser head. Since the disk is coated at the backside for reflecting the pump and signal wavelength, the unabsorbed part of the pump radiation is recollimated at the opposite side of the parabolic mirror and redirected via two mirrors to another part of the parabolic mirror, which refocuses it again on the disk. This re-imaging is repeated until the complete pump light is absorbed in the disk. This technically mature scheme can be used for 100 to 300 µm thin disks with a few millimeters in diameter attached to a water cooled substrate or up to a few millimeter thick free standing disks for 30 kW of pump light with several centimeters in diameter directly water cooled from the backside [28].

Using thin disk laser technology, the Ludwig-Maximilians-University München (LMU) in cooperation with the Max-Planck-Institute of Quantum Optics (MPQ) develops since 2007 high power pump sources especially designed for use in pumping efficient, high gain, high contrast, optical parametric chirped pulse amplifiers with a simplified stretcher-compressor system. The research area spans from femtosecond oscillators, which deliver 6 µJ pulse energy at 10 MHz [29], to picosecond regenerative thin disk laser amplifiers with kilohertz repetition rates [30]. Ap-

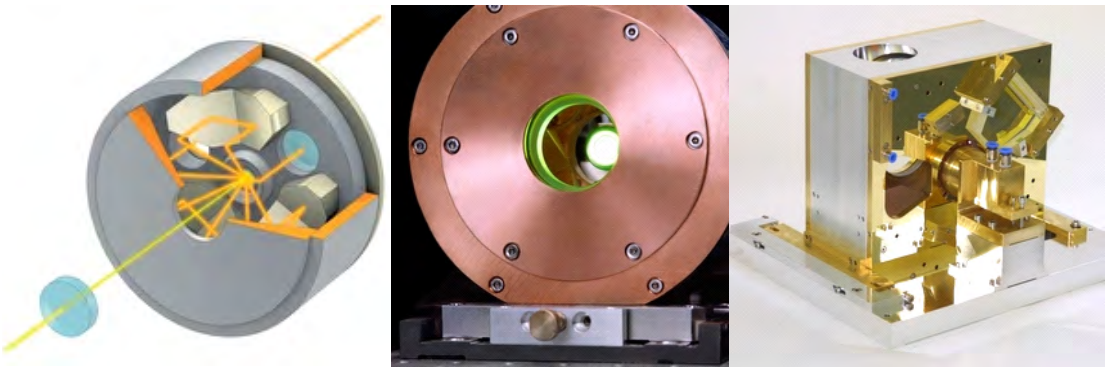

Figure 5.15: Principle of the disk laser and the pump light reimaging technique (left side), the 5 kW disk laser head by courtesy of TRUMPF Laser GmbH + Co. KG (center) and the TDM 10 disk laser head for 12 kW of pump light by courtesy of Dausinger + Giesen GmbH.

propriate amplifiers are necessary to generate short pulses with higher energy than typically produced with oscillators. Regenerative amplifiers are commonly used to strongly amplify individual selected low-energy pulses originating from mode-locked oscillators. An optical switch such as a Pockels Cell injects the selected pulses into the cavity, controls the number of round trips and ejects the amplified pulse usually when the gain is saturated. The pulse width is typically determined by the source of initial pulses and by gain narrowing in the amplifiying medium while in most cases the final amplitude of the pulse is only limited by the energy stored in the active medium.

The latest regenerative amplifier developed at the LMU/MPQ is based on an Yb:YAG thin-disk amplifier head from TRUMPF Laser GmbH + Co. KG. This laser system achieves an average output power of 75 W at $f_r = 3$ kHz with pulse energies exceeding 25 mJ, a pulse-to-pulse stability of $< 0.4\%$ (RMS), a pulse duration of 1.6 ps and a bandwidth of 1 nm (FWHM) at a center wavelength of 1030.2 nm in a near-diffraction-limited beam [31]. It consists of a seed laser, a stretcher, a fiber preamplifier, a pulse picker, an amplifier resonator and a compressor. The seed pulses are delivered by an ultra-broadband chirped-mirror Ti:sapphire oscillator (Rainbow, Femtolasers Produktions GmbH) covering the spectral range of 650-1100 nm [32]. This approach allows for nearly jitter-free optical synchronization between pump and signal pulses in the OPCPA as they are both derived from the same source [11, 33].

At present, a multipass amplifier based on the 5 kW disk laser head from TRUMPF Laser GmbH + Co. KG is under construction at the LMU/MPQ. Compared to the regen we plan to increase the pumped disk diameter by a factor of 3.3 and raise the pump power from currently 500 W to 5 kW by a factor of 10. To avoid air fluctuations in front of the pumped disk due to heat, the amplifier will be build in vacuum which allows for 2f-imaging of the multiple passes through the disk without optical breakthrough in air. Based on the simple scaling laws mentioned above, this setup should allow us to further amplify the pulse energy to > 150 mJ pulse energy at 3 kHz repetition rate.

At the Max-Born-Institute Berlin, the thin-disk laser group concentrates on producing high-energy pulses of $1 \ldots 5$ ps duration with a repetition rate between 100 and 200 Hz by optimizing various Yb:YAG thin disk amplifier setups.

The laser system developed at the MBI has the following architecture: A commercial Yb:YKGW oscillator generates the initial pulses which are subsequently stretched to 2 ns duration by a grating stretcher. After amplification to 1 mJ energy in a Yb:KGW regen, these pulses seed an Yb:YAG thin disk regenerative amplifier. This amplifier contains a thin-disk head from TRUMPF Laser GmbH + Co. KG pumped by up to four fiber-coupled diodes. Each of these

diodes produced by the Ferdinand Braun Institute in cooperation with Jenoptik Laserdiode GmbH, deliver a peak power of 1.0 kW at a pump pulse duration of 1 ms.

The output pulses of this regenerative amplifier have up to 300 mJ energy at 150 Hz maximum repetition rate. They are further amplified during eight round trips in a multipass amplifier to 450 mJ energy (status: summer 2010). This amplifier presently contains a thin-disk head from TRUMPF Laser GmbH + Co. KG of 17 mm disk diameter, which is pumped by eight fiber-coupled diodes. Finally, these pulses are recompressed by a grating compressor at the output of the laser.

The described system architecture is optimized for generating high-energy pulses at moderate repetition rates. The developed laser system will be used as a driver for a plasma X-ray laser in GRIP geometry [34, 35] and for pumping an OPCPA system for generation of few-cycle pulses.

At present, the MBI group concentrates on increasing the pulse energy of the final amplifier to several Joule by enlarging the diameter of the Yb:YAG thin disks to >25 mm. In addition, the group aims to raise the repetition rate to 200 Hz.

Amplified spontanious emission travelling between the two surfaces of the disk may limit the power scaling of larger disks [36]. In order to quantify this effect, Jochen Speiser conducted simulations at the German Aerospace Center [36, 37]. These simulations show that 8.3 J pulse energy can be extracted from a 0.89 mm thin disk that is pumped with 170 MW power in a spot diameter of 61.5 mm [37]. Quasi-cw pumping and undoped caps on top of the thin disks would increase the efficiency drastically [38]. This demonstrates that the development of a disk based amplifier requires a comprehensive design and should include the following parameters: Configuration of the pumped area, disk thickness, doping concentration, undoped cap, pump power density, pump duty cycle and the serial combination of disks. Following the scaling laws for thin disk lasers combined with a careful design and layout should provide the opportunity for a multijoule system at kHz repetition rate.

Bibliography

[1] R. Kienberger, E. Goulielmakis, M. Uiberacker, A. Baltuska, V. Yakovlev, F. Bammer, A. Scrinzi, T. Westerwalbesloh, U. Kleineberg, U. Heinzmann, M. Drescher, and F. Krausz, Nature **427**, 817 (2004).

[2] M. Schultze, E. Goulielmakis, M. Uiberacker, M. Hofstetter, J. Kim, D. Kim, F. Krausz, and U. Kleineberg, New J. Phys. **9**, 243 (2007).

[3] E. Goulielmakis, M. Schultze, M. Hofstetter, V. S. Yakovlev, J. Gagnon, M. Uiberacker, A. L. Aquila, E. M. Gullikson, D. T. Attwood, R. Kienberger, F. Krausz, and U. Kleineberg, Science **320**, 1614 (2008).

[4] S. Sartania, Z. Cheng, M. Lenzner, G. Tempea, Ch. Spielmann, F. Krausz, and K. Ferencz, Opt. Lett. **22**, 1562 (1997).

[5] M. Nisoli, S. De Silvestri, O. Svelto, R. Szipöcs, K. Ferencz, Ch. Spielmann, S. Sartania, and F. Krausz, Opt. Lett. **22**, 522 (1997).

[6] S. Backus, R. Bartels, S. Thompson, R. Dollinger, H. C. Kapteyn, and M. M. Murnane, Opt. Lett. **26**, 465 (2001).

[7] F. Tavella, A. Marcinkevièius, and F. Krausz, Opt. Expr. **14**, 12822 (2006).

[8] S. Witte, R. Th. Zinkstok, A. L. Wolf, W. Hogervorst, W. Ubachs, and K. S. E. Eikema, Opt. Express **14**, 8168 (2006).

[9] X. Gu, G. Marcus, Y. Deng, T. Metzger, C. Y. Teisset, N. Ishii, T. Fuji, A. Baltuška, R. Butkus, V. Pervak, H. Ishizuki, T. Taira, T. Kobayashi, R. Kienberger, and F. Krausz, Opt. Express **17**, 62 (2009).

[10] F. Tavella, Y. Nomura, L. Veisz, V. Pervak, A. Marcinkevièius, and F. Krausz, Opt. Lett. **32**, 2227 (2007).

[11] N. Ishii, C. Y. Teisset, T. Fuji, S. Köhler, K. Schmid, L. Veisz, A. Baltuška, and F. Krausz, IEEE. Sel. Top. Quantum Electron. **12**, 173 (2006).
[12] C. Dorrer, I. A. Begishev, A. V. Okishev, and J. D. Zuegel, Opt. Lett. **32**, 2143 (2007).
[13] R. Szipocs, K. Ferencz, C. Spielmann, and F. Krausz, Opt. Lett. **19**, 201 (1994).
[14] B. C. Stuart, M. D. Feit, S. Herman, A. M. Rubenchik, B. W. Shore, and M. D. Perry, Phys. Rev. B **53**, 1749 (1996).
[15] G. Cerullo and S. De Silvestri, Rev. Sci. Instrum. **74**, 1 (2003).
[16] A. Giesen, H. Hügel, A. Voss, K. Wittig, U. Brauch, and H. Opower, Appl. Phys. B **58**, 365 (1994).
[17] A. Killi, C. Stolzenburg, I. Zawischa, D. Sutter, J. Kleinbauer, S. Schad, R. Brockmann, S. Weiler, J. Neuhaus, S. Kalfhues, E. Mehner, D. Bauer, H. Schlueter, and C. Schmitz, Proc. SPIE **7193**, 71931T (2009).
[18] A. Giesen and J. Speiser, IEEE J. Sel. Top. Quantum Electron. **13**, 598 (2007).
[19] D. Strickland, and G. Mourou, Opt. Comm. **56**, 219 (1985).
[20] N. Destouches, A. Tishchenko, J. Pommier, S. Reynaud, O. Parriaux, S. Tonchev, and M. Ahmed, Opt. Express **13**, 3230 (2005).
[21] C. Schmitz, and A. Voss, Laser Munich (1999).
[22] TRUMPF Laser 18.08.2010 <http://www.trumpf-laser.com>.
[23] P. V. Avizonis, D. J. Bossert, M. S. Curtin, and A. Killi, Lasers and Electro-Optics, 2009 and 2009 Conference on Quantum electronics and Laser Science Conference. CLEO/QELS 1-2 (2009).
[24] T.Y. Fan, IEEE J. Quantum Electron. **29**, 1457 (1993).
[25] T. Südmeyer, C. Kränkel, C. R. E. Baer, O. H. Heckl, C. J. Saraceno, M. Golling, R. Peters, K. Petermann, G. Huber and U. Keller, Appl. Phys. B **97**, 281 (2009).
[26] Quotation from Laserline GmbH 02.03.2010 (2010).
[27] Information from nLIGHT Corporation 10.11.2009 (2009).
[28] Dausinger + Giesen GmbH 18.08.2010 <http://www.dausinger-giesen.de> (2010).
[29] C. Y. Teisset, H. Fattahi, A. Sugita, L. Turi, X. Gu, O. Pronin, V. Pervak, F. Krausz and A. Apolonski, Conference on ultrafast optics, Arcachon, France (2009).
[30] T. Metzger, C. Y. Teisset, and F. Krausz, Advanced Solid-State Photonics, OSA Technical Digest Series (CD) (Optical Society of America, 2008), paper TuA2. (2008).
[31] T. Metzger, A. Schwarz, C. Y. Teisset, D. Sutter, A. Killi, R. Kienberger, and F. Krausz, Opt. Lett. **34**, 2123 (2009).
[32] T. Fuji, A. Unterhuber, V. S. Yakovlev, G. Tempea, A. Stingl, F. Krausz, and W. Drexler, Appl. Phys. B **77**, 125 (2003).
[33] C. Y. Teisset, N. Ishii, T. Fuji, T. Metzger, S. Köhler, A. Baltuska, and Ferenc Krausz, in Conference on Lasers and Electro-Optics/Quantum Electronics and Laser Science and Photonic Applications Systems Technologies, Technical Digest (CD) (Optical Society of America, 2005), paper CMB3.
[34] R. Keenan, J. Dunn, P. K. Patel, D. F. Price, R. F. Smith, and V. N. Shlyaptsev, Phys. Rev. Lett. **94**, 103901/1 (2005).
[35] J. Tümmler, K. A. Janulewicz, G. Priebe, and P. V. Nickles, Physical Review E **72**, 037401/1 (2005).
[36] J. Speiser, Laser Physics **19**, 274 (2009).
[37] J. Speiser, J. Opt. Soc. Am. B **26**, 26 (2009).
[38] D. Kouznetsov, and J.-F. Bisson, J. Opt. Soc. Am. B **25**, 338 (2008).

5.4.3 Diode pumped slab lasers

The development of Petawatt-class lasers capable of delivering high-energy (10 to 50 J), short duration (sub-20 fs) pulses at high repetition rate (10 Hz) will provide an important tool for

studying ultra-high intensity light-matter interactions and novel applications, including particle acceleration and intense X-ray generation, as part of the Beamline Facility of ELI. Development of these lasers represents a significant technological challenge and one that is best met by diode pumped solid state laser (DPSSL) technology.

Efficient diode-pumped operation requires a gain material with a long fluorescence lifetime, to minimise the number of pump diodes required, and a reasonably high gain cross section to enable simple and efficient energy extraction. The material must exhibit good thermo-mechanical properties in order to handle the high average power and it must be available in large sizes, with good optical quality, in order to handle the high pulse energy. Several candidate materials exist, including Nd:Glass, Yb:SFAP, Yb:CaF_2 and ceramic Yb:YAG. Of these, glass-based materials have poor thermal characteristics, which limit the repetition rate of operation, crystalline SFAP and CaF_2 have limited availability in large apertures and Yb:CaF_2 suffers from a very high saturation fluence, which makes both pumping and efficient energy extraction while avoiding optical damage very difficult. This leaves ceramic YAG as the most promising candidate for high energy amplification at 1.03 μm.

Ceramic Yb:YAG has a respectable gain cross section and a reasonable fluorescence lifetime (of order 1 ms), whilst being available in large optical apertures (in excess of 10 cm). Although the required pump and extraction fluence levels for efficient operation are still quite high at room temperature, this can be overcome by cooling the medium to cryogenic temperatures of around 150 K. This has the effect of reducing ground-level population and hence minimising reabsorption losses and increasing the gain cross section, as well as improving thermo-mechanical and thermo-optical properties [1].

Two options exist for a diode-pumped Yb:YAG slab amplifier geometry that provide both a sufficiently high surface-to-volume ratio, to ensure heat can be removed efficiently, and ensure heat removal occurs in a direction parallel to the beam propagation axis, to minimise transverse temperature gradients that would otherwise introduce unwanted wave front distortions. Both options are based on a face-cooled thin-slab architecture, namely an active mirror (or thin-disk) or a gas-cooled slab-stack geometry.

In the active mirror concept a thin gain medium slab is conduction-cooled through one side only by a flowing liquid whilst pumping and energy extraction occur through the opposite side. This has proved very successful for cw and very high repetition rate operation where tremendous average power and efficiency levels have been achieved. However, in high energy, low repetition rate ($<$ 1 kHz) amplifiers this concept poses severe challenges related to amplified spontaneous emission (ASE) management; achieving sufficient gain and good optical-to-optical efficiency; identifying a suitable coolant for low temperature operation; and the intensity enhancement caused by the overlap between incoming and outgoing pulse, which leads to a greater risk of optical damage.

The gas-cooled slab-stack architecture was first demonstrated in the Mercury system [2] and consists of multiple thin slabs of gain medium each separated by a small gap and arranged sequentially in a stack formation. Each slab is cooled from both sides by a transverse stream of gas. Because the (overall) aspect ratio of the gain medium can be chosen freely without compromising cooling (by varying the number and thickness of slabs), this concept represents a flexible architecture that can easily be scaled for lower (10s of J) or higher (up to kJ) energy output from a single (or several) amplifier head(s). This is considered the best option for a high-energy diode-pumped Yb:YAG slab amplifier.

The basic structure of a cryogenically gas-cooled ceramic Yb:YAG slab amplifier is shown in Fig. 5.16a. Cold helium gas is forced through the gaps between the slabs for cooling. The amplifier is end or face-pumped from both sides. Employing slabs with increasing doping level towards the centre of the amplifier reduces the required overall thickness for a given maximum gain coefficient and also equalises the heat load for all slabs. Minimising amplifier thickness is particularly important for high intensity applications using YAG (as it has a high nonlinear

refractive index) to ensure the overall B-integral for the system is kept at a manageable level.

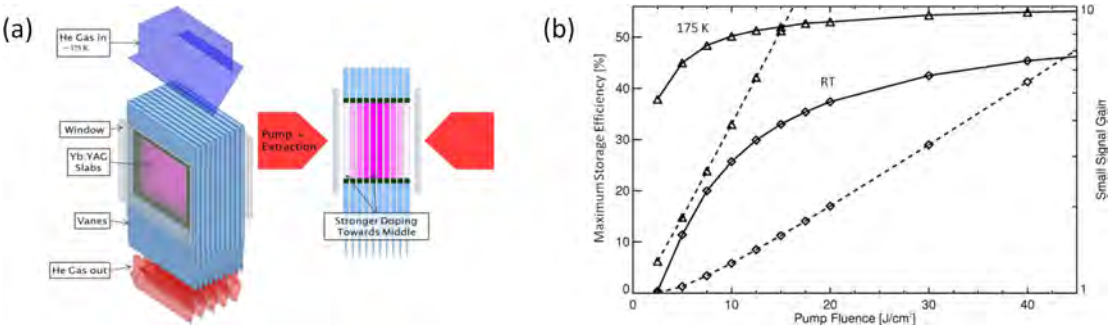

Figure 5.16: (a): Illustration of amplifier geometry: isometric (left) and side view (right). (b): Maximum storage efficiency (solid line) and small signal gain (dotted line) for amplifier operated at RT (diamonds) and 175 K (triangles).

The advantage of cryogenic cooling compared to room temperature operation can be seen in the increased storage efficiency and small signal gain predicted for the amplifier shown in Fig. 5.17b. These predictions have been obtained from a temporally and spectrally resolved 1D numerical model assuming a diode pump pulse duration of 1 ms and a 5 nm FWHM pump spectral width, centred at the optimum wavelength in the 940 nm Yb absorption band [3].

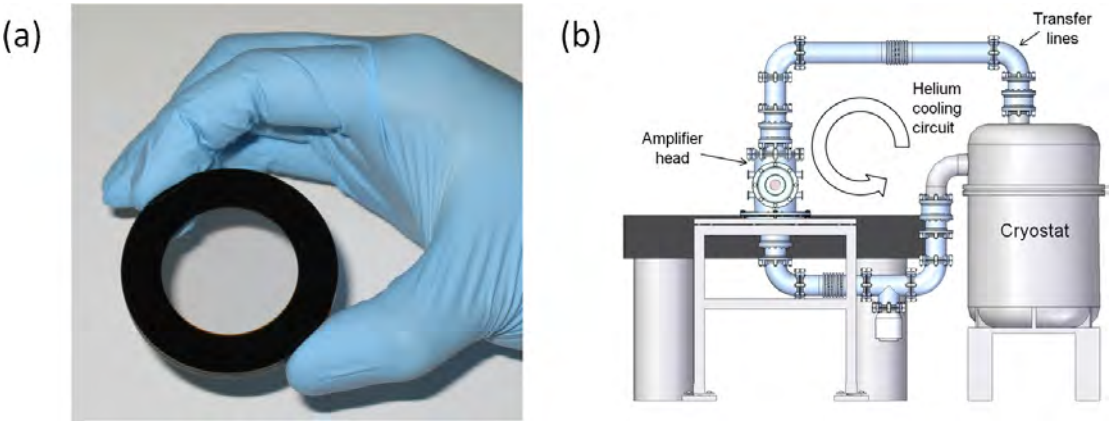

Figure 5.17: (a): Photograph of a polished co-sintered ceramic Cr:Yb:YAG disc supplied by Konoshima [4]. (b): Schematic of He gas cryocooler system.

The transverse dimensions and aspect ratio of the gain medium can be tailored to deliver the required amount of output energy from the amplifier. Model predictions indicate there is an optimum optical depth (product of Yb doping concentration and gain medium thickness) of 3.3% cm that leads to maximum energy storage potential. Table 5.1 gives an example of the amplifier gain medium dimensions for three different output energy scenarios and the corresponding average Yb doping concentration required for maximum energy storage. These figures assume a total pump fluence of 10 J/cm^2 (5 J/cm^2 from each side).

The amplifier dimensions given in Table 5.1 ensure the transverse gain-length product (g_0D), calculated along the diagonal across the square surface of the gain medium, is kept below 3 to minimise the risk of ASE. Furthermore, the use of ceramic YAG enables engineered composite slab designs to be employed to further reduce the impact of ASE. Fig. 5.17a shows a photograph

Table 5.1: Amplifier dimensions for various amplifier output energy scenarios.

Output energy	Transverse dimensions	Total Gain mediumthickness	AverageYb^{3+} doping
200 J	6.3 cm × 6.3 cm	4.5 cm (10 × 0.45 cm)	0.73 at.%
500 J	10 cm × 10 cm	7.0 cm (10 × 0.7 cm)	0.47 at.%
1 kJ	14 cm × 14 cm	10.0 cm (10 × 1 cm)	0.33 at.%

of a co-sintered ceramic YAG disc (55 mm in diameter, 5 mm thick) where the Yb-doped region (35 mm diameter) is surrounded by a 10 mm thick Cr^{4+} cladding to absorb unwanted transverse fluorescence that could otherwise lead to parasitic lasing. A test bed low-energy (10 J) laboratory prototype amplifier, based on four of these co-sintered ceramic YAG discs, is currently being built at the Central Laser Facility to confirm the potential of the diode-pumped cryogenic gas-cooled ceramic Yb:YAG amplifier concept. Fig. 5.17b shows a schematic of the helium cryocooler system currently under construction.

Amplifiers as described here are most suitable as the building blocks for the pump lasers for the 2 off, 10 Hz, 10 J and 2 off, 10 Hz, 50 J OPCPA beamlines proposed for the Beamline Facility. Assuming an optical-to-optical efficiency of 10 %, the four OPCPA beamlines will require a total of 1.2 kJ pump energy at 1 μm wavelength. This could be delivered by a single pump laser. Model predictions confirm that the heat load, B-integral and ASE levels are manageable for an amplifier of the required size. In practice it may be beneficial to use several smaller pump lasers with scaled-down amplifiers to provide a degree of redundancy and also to reduce the dimensions of amplifier and beamline optics, making them easier to manufacture, reducing the impact of non-linear effects and reducing the length of beam transport systems.

For a complete pump laser, other sub-systems required include a front-end laser delivering temporally shaped few-ns pulses and a multipass architecture to extract energy from the main amplifier. Neither should pose significant difficulties as they have already been successfully demonstrated on high-energy glass laser systems like Vulcan [5], NIF [6], and LIL/LMJ [7, 8]. Some optical components suitable for high repetition rate operation may, however, only be available in limited sizes, in particular Pockels cells and frequency doubling crystals. In this context it may again be beneficial to limit the pulse energy and therefore beam size of individual pump lasers.

Bibliography

[1] D. C. Brown et al., IEEE J. Sel. Top. in Quant. Electron. **11**, 587 (2005).
[2] A. Bayramian et al., Fusion Sci. Technology **52**, 383 (2007).
[3] K. Ertel et al., OSA Proc. of Advanced Solid State Photonics (ASSP) Conference, Paper AWB20 (2010).
[4] Konoshima Chemical Company Ltd, http://www.konoshima.co.jp/en/index.html.
[5] W. Shaikh et al., Central Laser Facility Annual report 2005–2006, 199, http://www.clf.rl.ac.uk/resources/PDF/ar05-06_s7_vulcan_dev_amplified_variable.pdf (2006).
[6] G. Miller et al., Optical Engineering **43**, 2841 (2004).
[7] P. Eyharts et al., Journal de Physique IV **133**, 727 (2006).
[8] M. Andre, Fusion Engineering and Design **44**, 43 (1999).

5.5 Nonlinear frequency conversion

5.5.1 Bandwidth broadening techniques

With a plethora of methods available for broadening the bandwidth of coherent light pulses, we have restricted this section to approaches proven, and practical, for the regimes of interest in ELI (bulk broadening, gas-filled capillary, filamentation in gas). All approaches, that we describe here, lend themselves to broadening of an input seed pulse spectrum for subsequent amplification and recompression. One or two methods have, in principle the (unproven) capability to coherently broaden but require coherent recombining of several beams to reach the desired output energy levels. Common to all of them is the fact that broadening relies on the nonlinear interaction, i.e. self-action, of laser radiation with the traversed medium. While they are simple to implement, the processes are mostly a complex interplay between several fundamental nonlinear effects; most important of them are self-phase modulation (SPM), four-wave mixing (FWM) and stimulated Raman scattering (SRS) in time, and their counterparts in space; self-focussing (SF), cross-focusing (CF) etc. It is just within the last few years that theoretical descriptions have advanced substantially and sophisticated models exist that take the full spatio/temporal field upon propagation into account. The interplay between different nonlinear effects affects broadening properties such as homogeneity and coherence and the interaction between different nonlinear processes is determined by the pumps' spectral locations and powers, and the nonlinear and dispersive characteristics of the medium. We add difference frequency generation (DFG) from broad band pulses as an additional method since it is a highly attractive method to 1. shift the wavelength for an OPCPA seed to longer wavelengths, 2. provide ultrabroad bandwidths, and 3. intrinsically stablize the carrier-to-envelope phase (CEP).

Table 5.2: Bandwidth broadening techniques.

	Bulk Broadening	DFG	Gas-filled capillary	Filamentation in gas
after oscillator	+++	+	–	—
after pre-amplifier	+	+++	+++	+++
shifting for synchronization	+++	-	++	++
self-compression	—	—	+	+++
preserves CEP	++	+++	+++	+++
stabilizes CEP	—	+++	—	—
ease of implementation	++	+	+	+++

Bulk Broadening

Spectral broadening and supercontinuum generation at oscillator energy levels is being used very successfully in optical fibers and bandgap structures such as photonic crystal fibers [1, 2]. Broadening and shifting was e.g. demonstrated to successfully optically derive a synchronization signal for OPCPA from a short pulse Ti:Sapphire oscillator with the typical center wavelength of 800 nm to reach 1064 nm, which was the center wavelength of the pump laser [3]. While fibers and bandgap structures are especially suitable for the lowest pulse energies of nanojoules, microjoule level energies are ideal for broadening in bulk materials [4] such as Sapphire, YAG and a variety of glasses [5]. A manifold of different combinations, e.g. whether the pulse up-

or down-shifts, at which energy and wavelength, chirp and so forth, are possible and make bulk broadening very attractive. The above mentioned methods are particularly interesting for deriving a synchonization signal between different laser branches. Contrast issues have to be carefully considered should the broadened output be used as direct seed for amplifier chains.

Hollow Fiber

With even higher energies available, i.e. near milijoule to multi milijoule levels, broadening is most readily achieved in noble gas filled hollow fibers [6] and with tens of femtosecond pulses. This technique is simple to implement and results not only in several octave wide spectra, but furthermore acts as extended spatial filter thereby cleaning the beam's spatial profile. The fibre ensures a long interaction length with the relatively low density gas, and energy efficiencies of up to 60% are possible. Spectral broadening and modulation typically requires some form of post compression and with some of the shortest pulses ever generated [7] it is one of the enabling techniques for attosecond pulse generation. Limitations stem from the fact that a high energy pulse has to be coupled very carefully into the hollow fiber which does not act by total internal reflection: i.e. the damage threshold of the material is one limiting factor together with plasma defocussing at the entrance. Some form of mitigation is possible with differential pumping, but maximum pulse energies lie in the ten milijoule range [8]. Extending the waveguide into one dimension seems to be the only viable approach to reach the several hundred milijoule range and possibly beyond [9].

Filamentation

An alternative technique [10] is to simply focus an ultrashort pulse into a gas-filled cell, where it self-acts and generates a filament which is signified by diffractionless propagation over several Rayleigh lengths. The pulse is typically confined to a region of high intensity by competing effects of self-focussing and diffraction, ensuring a long interaction length over which the spectral broadening occurs. Pulse requirements and geometries are very similar to the case of the gas-filled hollow fiber. The advantage of filamentation is that there is no fibre to damage, while some studies have shown that the pulse not only broadens but self-compresses during propagation [11]. However, the spatio-temporal structure of the broadened pulse is complex, and care must be taken to select the correct part of the pulse if few-cycle pulses are desired. Moreover, to generate a usable pulse and good spatial profile, the filament process should occur in a single filament mode so there is an upper limit on the energy that can be used before multiple filamentation occurs. Without the possibility to scale as with the rectangular waveguide, an alternative and interesting remedy could be the spatial arrangement of numerous filaments that nucleate next to each other, which are coupled through their terahertz emission. Studies have predicted that they are coherently coupled and possibly merge into a supermode with combined energy content [12]. Filamentation has also been demonstrated to preserve CEP with several octave wide bandwiths thereby giving easy access to CEP diagnostics as well as deriving various seed wavelengths.

DFG

DFG (if not driven strongly nonlinearly; i.e. into SPM) does not broaden any input bandwidth. We mention it in this section since it is extremely attractive to achieve similar effects for OPCPA. The DFG process mixes the frequencies of both pump and signal waves to broaden the bandwidth of the long wavelength idler pulse. I.e. if one uses moderately short seed and pump, the idler will be ultrabroadband and ideally provides self CEP stabilization [13]. For instance, mixing a 75 fs 1070 nm pulse and a 65 fs 1580 nm pulse from the same fibre oscillator has been shown to produce over one micron of bandwidth in the mid-IR at 3.2 microns [14], with a measured timing jitter in the same configuration corresponding to just 90 mrad of CEP phase noise comparable to

the best actively stabilised systems. The transform limit of the generated mid-IR bandwidth is just 33 fs or 3 cycles at 3.2 microns. If this pulse is amplified in an OPCPA chain, the large gain bandwidth means that high energy pulses can be generated while maintaining the ultrashort transform limit, removing the need for further bandwidth broadening at the end of the system. Further advantage is that the DFG center frequency is at longer wavelengths which is ideal for OPCPA and allows for easy optical synchronization and increased efficiency by pumping with the fundamental wavelength of 1 micron pump lasers such as Nd:YLF, Nd:YAG etc. We believe that this approach could be highly attractive, allowing construction short pulse OPCPA systems based on fibre front-ends and with DFG generating a phase stable signal between 1.2 and 1.8 microns.

Bibliography

[1] J. K. Ranka et al., Conference on Lasers and Electrooptics (CLEO '99), 1999, pp. CPD8/1–CPD8/2.
[2] J.K. Ranka et al., Opt. Lett. **25**, 25 (2000).
[3] C.Y. Teisset et al., Optics Express **13**, 6550 (2005).
[4] R.R. Alfano, S.L. Shapiro, Phys. Rev. Lett. **24**, 584 (1970).
[5] M. Bradler et al., Appl. Phys. B **97**, 561 (2009).
[6] M. Nisoli et al., Appl. Phys. Lett. **68**, 2793 (1996).
[7] B. Schenkel et al., Opt. Lett. **28**, 1987 (2003).
[8] A. Suda et al., Appl. Phys. Lett. **86**, 111116 (2005).
[9] C. L. Arnold et al., New Journal of Physics **12**, 073015 (2010).
[10] C. P. Hauri et al., Appl. Phys. B **79**, 673 (2004).
[11] A. Couairon et al., Opt. Lett. **30**, 2657 (2005).
[12] G. Mechain et al., Phys. Rev. Lett. **93**, 035003 (2004).
[13] A Baltuska et al., Phys. Rev. Lett. **88**, 133901 (2002).
[14] O. Chalus et al., Optics Express **17**, 3587 (2009).

5.5.2 XPW for pulse cleaning

Cross-polarized wave generation (XPW) is a novel technique for contrast enhancement of ultrashort pulses in high-energy laser systems. XPW is based on a degenerate four-wave mixing process governed by the anisotropy of the real part of a crystal's third-order nonlinearity tensor $[\chi^{(3)}]$, in which a new wave, polarized in the orthogonal direction, can be efficiently generated [1]. Implementation of XPW is quite straightforward: a linearly polarized laser pulse is focused into a crystal positioned in between two crossed polarizers:

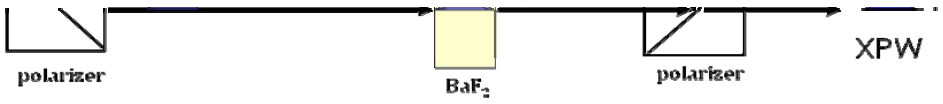

Figure 5.18: Implementation of cross-polarized wave generation (XPW).

Efficient conversion with XPW only occurs at high intensities. Weaker, unconverted pre- and post-pulses are thus rejected by the second polarizer, thereby improving the temporal contrast of

the pulse. Another interesting feature of XPW is that it permits spectral broadening of the pulse by at least a factor of $\sqrt{3}$ [2–5]. Moreover, further broadening occurs at high intensities and high conversion efficiencies due to the interplay between cross phase and self phase modulation of the fundamental and XPW pulses [4]. In line with obtaining high conversion efficiencies, XPW can be utilized as a tool not only for contrast enhancement but for spectral broadening as well. Preservation of the CEP in a single crystal XPW setup has recently been confirmed [6]. XPW is also an achromatic process that can therefore accommodate extremely short pulse durations down to a few optical cycles [7].

Despite its simplicity, XPW has several drawbacks especially in terms of simultaneously achieving high conversion efficiencies and output energies. Limitations in seeding the nonlinear filter with high energies arise from the upper intensity limit of white light generation ($<10^{13}$ W/cm^2) in the crystal, while high conversion efficiencies require excellent beam quality. For a simple, single crystal setup, multi-mJ input energies could be used either by utilizing long focal lengths (>10 m) or working out of focus. Both solutions have tradeoffs: the first resulting to a bulky, extended setup while the second may lead to hotspots in the incident beam profile which is unfavorable for XPW, thus limiting the internal conversion efficiency to the order of 10–15% [3, 4]. Dual crystal setups are capable of reaching efficiencies as high as 30% [3, 4] yet the separation between the two crystals also depends on the focusing. For multi-mJ pulses, the distance between the crystals lengthens to tens of meters, resulting in complicated and cumbersome configurations. Notwithstanding, dual-crystal setups are by nature more flexible than single-crystal configurations since they present the possibility of working at lower intensities at each crystal face. Moreover, they tend to feature pulse-to-pulse stabilities similar to that of the driving laser system [4].

The most promising approach for simultaneously having high energy and highly efficient XPW resides in improving the efficiency of the single crystal setup. Smooth, flat-top like beam profiles are preferable for high conversion efficiencies, theoretically reaching up to 37% with Z-cut crystallographic orientation crystals [3] and 45% with holographic-cut [4, 5]. In addition, higher energy transmission in the crystal is possible due to reduced self-focusing [4]. The conversion efficiency of a single crystal setup was improved to 28% for sub-mJ pulses with a sophisticated, nonlinear technique for beam shaping combined with pinhole filtering [4, 8]. Energy scalability is possible but not simple due to the complexity of the technique incorporating nonlinear beam shaping. Implementation of a simpler setup at the multi-mJ level, relying solely on pinhole filtering, proved to be insufficient for efficient XPW generation. With a pinhole alone, the excellent efficiency primarily due to beam shaping was unobtainable and decreased drastically to less than 10% [9]. Contrast enhancement via XPW in these multi-terawatt lasers has proven to be crucial in laser-driven particle acceleration and high-harmonic generation from solid targets [10–12].

Efficient XPW generation has been recently reported with high-energy input pulses up to 3.3 mJ [13]. The suggested configuration is based on a single BaF_2 crystal XPW stage and the use of a short length, hollow core waveguide as a spatial filter. This type of XPW setup is energy scalable, highly efficient, pulse shortening and carrier-envelope phase (CEP) stable. It is simple, compact and flexible as it allows contrast enhancement for a seed beam of a laser chain or the final stage of a multi-mJ laser [13]. This contrast filtering approach has also been recently validated on an ultra-broadband, CEP-stable seed laser system [14].

Bibliography

[1] A. Jullien, O. Albert, F. Burgy, G. Hamoniaux, J.P. Rousseau, J.P. Chambaret, F. Augé-Rochereau, G. Chériaux, J. Etchepare, N. Minkovski, and S.M. Saltiel, Optics Letters **30**, 920 (2005).

[2] L. Canova, O. Albert, N. Forget, B. Mercier, S. Kourtev, N. Minkovski, S.M. Saltiel, and R. Lopez Martens, Applied Physics B **93**, 443 (2008).
[3] A. Jullien, S. Kourtev, O. Albert, G. Chériaux, J. Etchepare, N. Minkovski, and S. Saltiel, Appl. Phys. B **84**, 409 (2006).
[4] A. Jullien, J.P. Rousseau, B. Mercier, L. Antonucci, O. Albert, G. Chériaux, S. Kourtev, N. Minkovski, and S.M. Saltiel, Optics Letters **33**, 2353 (2008).
[5] L. Canova, S. Kourtev, N. Minkovski, A. Jullien, O. Albert, R. Lopez Martens, S.M. Saltiel, Applied Physics Letters **92**, 231102 (2008).
[6] K. Osvay, L. Canova, C. Durfee, A.P. Kovács, Á. Börzsönyi, O. Albert, and R. Lopez-Martens, Optics Express **17**, 22358 (2009).
[7] A. Jullien, C.G. Durfee, A. Trisorio, L. Canova, J.-P. Rousseau, B. Mercier, L. Antonucci, G. Chériaux, O. Albert, R. Lopez-Martens, Applied Physics B **96**, 293 (2009).
[8] B. Mercier, J.P. Rousseau, A. Jullien, and L. Antonucci, Optics Communications **283**, 2900 (2010).
[9] P.M.E. Paul and L. Canova, Conference on Lasers and Electro-Optics (CTuK6), San Jose, CA, 16 May 2010.
[10] S. Bulanov, V. Chvykov, G. Kalinchenko, T. Matsuoka, P. Rousseau, S. Reed, V. Yanovsky, K. Krushelnick, A. Maksimchuk, A. Brantov, V.Y. Bychenkov and D.W. Litzenberg, Medical Physics **35**, 1770 (2008).
[11] A. Flacco, F. Sylla, M. Veltcheva, M. Carrie, R. Nuter, E. Lefebvre, D. Batani and V. Malka, Physical Review E **81**, 036405 (2010).
[12] P. Monot, G. Doumy, S. Dobosz, M. Perdrix, P. D'Oliveira, F. Quéré, F. Réau, P. Martin, P. Audebert, J.C. Gauthier, and J.P. Geindre, Optics Letters **29**, 893 (2004).
[13] L.P. Ramirez, D.N. Papadopoulos, A. Pellegrina, F. Druon, P. Georges, P. Monot, A. Ricci, A. Jullien, X. Chen, J.P. Rousseau, and R. Lopez-Martens, to be published in Optics Express.
[14] A. Jullien, X. Chen, A. Ricci, J.-P. Rousseau, R. Lopez-Martens, L.P. Ramirez, D. Papadopoulos, A. Pellegrina, F. Druon, P. Georges, Applied Physics B, DOI: 10.1007/s00340-010-4201-9.

5.5.3 SHG for pump lasers

The output energy delivered by the laser is directly linked to the pump laser one. All the parameters that allow an increase in terms of efficiency of pump energy have to be used. The second harmonic generation is one of these parameters that will allow obtaining efficient and cost effective laser system. The efficiency is driven by the intensity of the laser at the fundamental wavelength and by the non linear converter crystal. The importance of these two parameters is discussed in the next sub-chapters and an efficient solution for achieving high pump energy lasers is described.

Important parameters of the pump laser at the fundamental wavelength

As the amount of energy required for the ELI laser systems is very high, the use of large beams is necessary because of the limitation due to laser damage threshold. As a consequence the pumping lasers architecture is quite complex and numerous optical elements can lead to degrade the spatial and temporal characteristics of the infrared pulse. Nevertheless efforts have to be done in order to keep these characteristics high. Indeed the energy distribution, the wavefront and the temporal pulse shape are parameters that have a very strong impact on the second harmonic generation efficiency.

The energy distribution has to be as flat as possible in order to have an averaged intensity level constant and fully controlled onto the SHG crystal to maximize the efficiency. In the time domain, this is exactly the same, because it is also required a constant peak power during

the complete pulse. Thus a flat temporal profile is the best profile to enhance the conversion. The pulse duration is a parameter that is not very strict because the length of the crystal can be adjusted to fit with. Nevertheless long pulse duration is not desirable because the damage threshold concern occurs. A pulse duration in the range of 30 ns appears to be the best compromise between energy extraction in the laser gain medium and damage threshold issues.

The last point is the wavefront quality. The SHG in the crystal is requiring phase matching that implies a relation between the wave vector (k vector) of the laser beam and the optical axis of SHG crystal. As the wavefront distortions increase, the k vector directions are dispersed. This implies a phase mismatch in the laser beam, thus reducing conversion efficiency. Effort have to be done in the IR laser in order to keep the wavefront as flat as possible or to use a crystal that have reduced sensitivity to phase mismatch.

Importance of the non linear crystal: LBO crystal advantages

Many existing high energy lasers are commonly using KDP and KD*P as SHG crystal. A quite perfect laser has to be used to obtain high conversion efficiency with these crystals. Moreover these materials exhibit severe thermal and angular tolerances which are critical to the design and operation of large laser facilities, in particular regarding repetition rate, alignment and wavefront distortions.

In order to reduce the complexity of a pump laser, an interesting alternative is the use of LBO crystals. This crystal presents very interesting intrinsic thermo-optical properties compatible to high-average power frequency conversion that relaxes some constraint on the pump laser parameters. For example the angular acceptance of LBO is 9 times higher than in KDP.

Use of LBO was previously limited to low energy lasers because of its small available dimensions. Since 2 years R&D efforts have been done by ILE, CEA and Cristal Laser to increase the dimensions of this crystal. Nowadays diameter up to 65 mm is available. Experiments on “Alisé” Laser at CEA-CESTA in France have shown the possibility to obtain a conversion efficiency of 92% leading to have more than 200 joules in the green (Fig. 5.19).

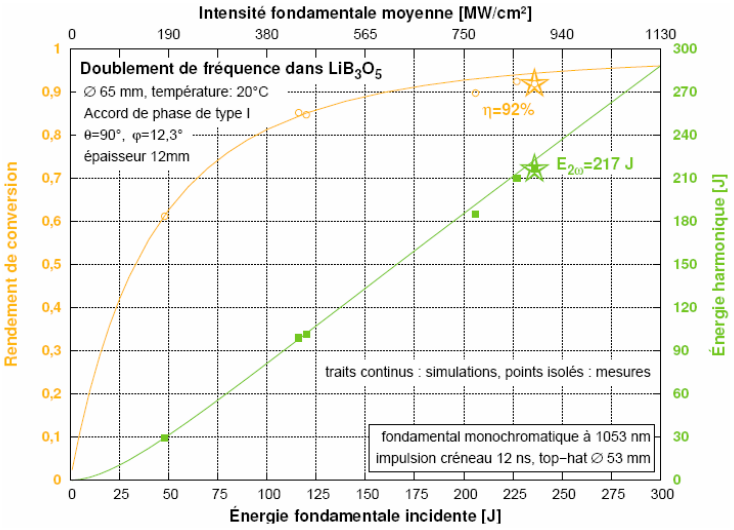

Figure 5.19: Conversion efficiencies and second harmonic energy in LBO crystal.

This tremendous value will allow reducing the number of amplifiers in the IR laser, thus reducing cost of purchase and maintenance, and also the footprint of the laser.

5.6 Materials and coatings

5.6.1 High damage threshold mirrors for broad bandwidth and dispersion control

Although the development of high-damage threshold optics has a 40-year history (see recent review [1]), most efforts have been spent on dielectric *periodic* quarterwave multilayer structures (also known as high reflectors). Such optics can usually support pulses around and longer than 20 fs and are available at several advanced optical companies. However, a high reflector has zero dispersion at its central wavelength and therefore cannot compensate for a material dispersion between the laser and the target. The problem of material dispersion becomes more severe for shorter pulses, which have a broader spectrum and therefore suffer from deviations of the material refractive index at the spectral wings from that at the central wavelength. Dispersion control over a broad spectral range became possible with the invention of periodic (or chirped, or dispersive) multilayer structures [2] shown in Fig. 5.20. Dispersive optics is the best choice for supporting sub-20 fs pulses in terms of broadband high reflectivity *and* the pulse phase control. Such optics is more vulnerable to the design and manufacturing errors because some layers can be of 10 nanometer thickness (roughly by a factor of 10 thinner than layers of a quarterwave periodic structure).

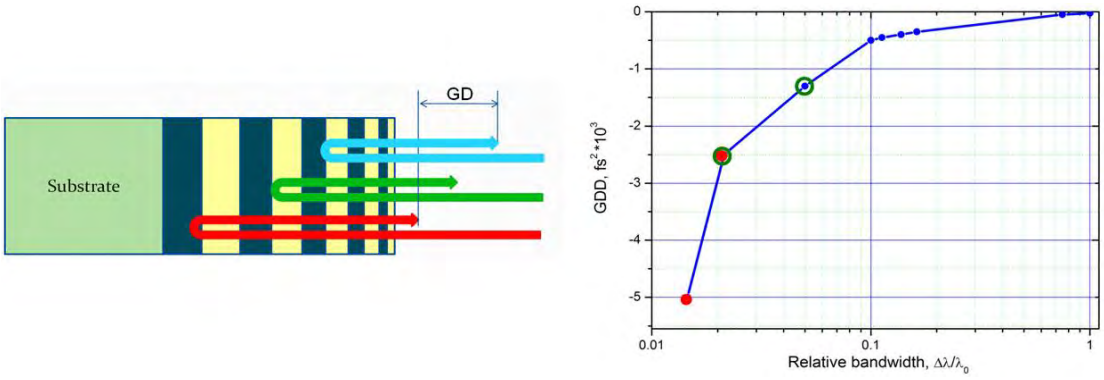

Figure 5.20: Left: the principle of operation of dispersive optics. Different spectral components entering the a-periodic multilayer simultaneously exit it with different group delays (GD). Right: the reference curve showing the maximal realized group delay dispersion (GDD, the second derivative of the spectral phase and the first derivative of GD with respect to frequency) vs. relative bandwidth $\Delta\lambda/\lambda_0$ (at the central wavelength $\lambda_0 \sim 1\,\mu$m) [3].

There is no high damage threshold dispersive optics (HDDO) available on the market now, for a simple reason: at the moment only a few people need it. However, several ultrahigh-intensity laser projects including ELI are entering their implementation phases within the next few years, and they will face lacking of such optics. Due to mostly technological bottlenecks, it will take several years to realize HDDO of the necessary damage threshold level. For instance, as a rule of thumb, we can consider the highest achievable HDDO damage level of the order of that for bulk fused silica, equal to 1 J/cm^2 for 10-fs pulses [4]. Next, let us assume we need to steer 10-fs, 100-J pulses. To operate a HDDO safely, the energy fluence at the mirror has to be roughly 5 times lower than the damage value, i.e. in our case 0.2 J/cm^2. This will correspond to a mirror surface of 500 cm^2, or 260-mm size optics. For 10-fs, 300-J pulses, optics of 450 mm size will be needed. In this estimation we did not take into account the effect of a decrease of the damage threshold at a larger laser spot. The main reason for that is the appearance of defects [5]. For 500-mm size optics such a factor of decrease can be between 5 and 50, if we take the damage threshold of a 100-μm spot as a reference.

An available magnetron sputtering machine at LMU (Helios, Leybold Optics) suitable for producing dispersive optics, has an upper limit of 100-mm size substrates. A bigger optics, up to 270 mm, can be produced with an electron-beam coating machine at LMU (Syrus, Leybold Optics). Unfortunately, at the present time, the deposition process at this machine is not stable enough for producing dispersive optics without any upgrade. The multilayer homogeneity across the large surface is another challenge for the developers of a new machine. At the moment, there is no clear understanding as to which deposition process will suit best the high demands of ELI. The state-of-the-art 1″ dispersive optics has a damage threshold of 0.1–0.2 J/cm^2 for 30–150-fs pulses.

The production of HDDO has four major steps, namely includes a robust design, a deposition technique, a proper substrate and coating materials. A choice of oxide materials with a high bandgap E_g necessary for suppressing ionization (a key element of the main damage mechanism), is very limited. The damage threshold in this case will be proportional to the product $E_g^{\alpha}\tau^{\beta}$, where τ is the pulse duration, and $\alpha \geq 1$ and β are coefficients depending on the model. A limited choice of materials will lead either to dispersion values not sufficient in comparison to the reference curve in Fig. 5.20 (right), or to a narrower bandwidth. In other words, the experimental points representing HDDOs will be shifted either downwards or to the left relative to the curve shown in the right panel. Other materials like fluorides with even higher E_g have to be also checked. Because of lower refractive indices of these materials, the bandwidth or/and reflectance of a corresponding multilayer will also be reduced.

As for the other optics necessary for the project, it has already been produced and successfully tested based on our achievements in the last 5 years of research. It includes a broadband (more than octave) dispersive optics (right points in the right panel of Fig. 5.20, with the GDD around -30 fs^2) [6], and highly dispersive optics necessary for all-mirror amplifier compressors and high-energy oscillators (left points in the right panel) [7]. The mirrors for the pump lasers will be based on high reflectors having the highest achievable damage threshold. A high reflector is robust against the design and manufacturing errors.

To make the preparatory stage for developing HDDO short and well directed, we will need an intense characterization research. Our first tests have already shown that even at fluence levels where no visible damage occurs, some properties of the coatings change. These changes need to be systematically investigated with the aim of reducing them.

Bibliography

[1] D. Ristau et al., Thin solid films **518**, 1607 (2009).
[2] R. Szipöcs et al., Opt. Lett. **19**, 201 (1994).
[3] V. Pervak et al., Opt. Express **16,** 10220 (2008).
[4] M. Lenzner et al., PRL **80,** 4076 (1998).
[5] S. Martin et al., Appl. Phys. A 77, 883 (2003).
[6] E. Goulielmakis et al., Science **317,** 769 (2007).
[7] V. Pervak et al., Opt. Express **17,** 19204 (2009).

5.6.2 Gratings

Diffraction gratings play a crucial role within the operation of high-energy chirped pulse amplification laser systems. They are used to increase the initial seed pulse length in a stretcher to enable further amplification without the onset of non-linear effects and then used to compress the pulse to as short duration as possible. These final gratings are exposed to extreme conditions with the pulse energy being at its highest and the pulse duration at its shortest. Table 5.3 highlights three of the principle specifications required of the gratings.

Table 5.3: Specification for the gratings required for the ELI beamline.

Property	Specification
Diffracted Bandwidth	>200nm
Diffraction Efficiency	>90%
Damage Threshold	>500mJ/cm^2

Pulses in the 15–20 fs regime requires bandwidths that are approaching 200 nm. This is especially true for the stretcher gratings where the bandwidth will be larger.

Delivery of the highest energy to the target requires that the pulse is compressed as efficiently as possible. This requires the gratings with as high diffraction efficiency as possible, since a typical 4 grating compressor consisting of gratings with a diffraction efficiency of 90% would have a transmission efficiency of 65% only.

To efficiently extract energy from amplifiers they shall be operated close to saturation fluence, which can be over 1 J/cm^2. To reduce the beam diameter after amplification requires the use of large expensive optics and off-axis parabolas. Therefore, a damage threshold comparable to this would have major benefits for the laser design.

At present, gold-coated diffraction gratings are the only ones available that can satisfy the bandwidth criteria. Figure 5.21 shows the diffraction efficiency for a gold-coated grating at 1480 l/mm. There has been significant development in the area of multilayer dielectric coatings to improve their bandwidth. All dielectric gratings have been reported with $\sim$ 50 nm bandwidth centered at 800 nm [1]. There has been some recent development of a combination of metal multi-layer dielectric gratings. In these structures a multilayer dielectric grating is generated on a metallic reflecting surface. Using a silver layer with a dielectric coating a bandwidth greater than 120 nm has demonstrated along with a diffraction efficiency >90% [1]. Optimization of the duty cycle, height and thickness of the dielectric layer may increase the performance >250 nm [2].

The diffraction efficiency for gold gratings is typically between 90–94% [3]. This has been demonstrated for the required bandwidth as shown in Fig. 5.21, which is the diffraction efficieny of a 1480-l/mm grating. Dielectric gratings have been demonstrated to have greater than 99% diffraction efficiency [4]. As mentioned above, developments in this area are being made to improve the bandwidth performance of these devices.

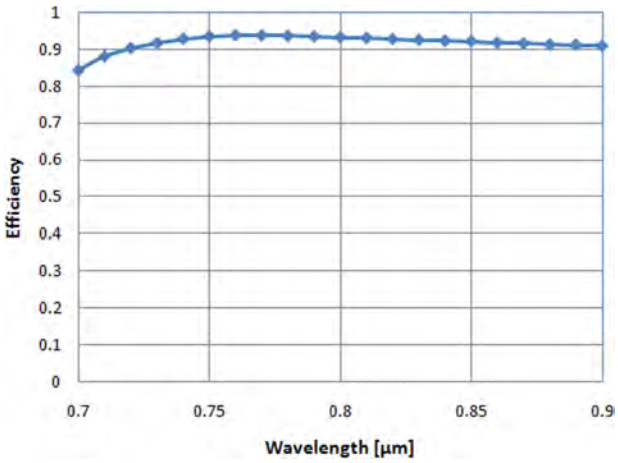

Figure 5.21: Diffraction efficiency for an optimized gold grating at 1480 l/mm.

Significant modifications to the laser system could be envisioned if the damage threshold of the gratings could be improved. Metallized gratings are limited to $\sim 200\,\mathrm{mJ/cm^2}$, which requires the beam diameter incident on the compressor to be increased, thereby adding to its cost and complexity. Results have been published [1] that show promising improvements in the damage threhsold for the dielectric grating structures, however, signifance work is still required to improve the repeatability of this performance.

Bibliography

[1] Canova et al., Opt. Exp. **15**, 15324 (2007).
[2] Wang et al., Appl. Opt. **49**, 2969 (2010).
[3] Boyd et al., Appl. Opt. **34**, 1697 (1995).
[4] Lu et al., Opt. Lett. **34**, 1708 (2009).

5.6.3 Optical metrology

From an optical point of view the specification of optical components is paramount to the successful operation of a high power laser system. Although very high quality specifications can be insisted upon, they are of no importance if they cannot be independent verified. As such it is recommended that the ELI facility has a relatively small, but well equipped, suite of Quality Assurance diagnostics. This will enable the verification of optics manufacturers meeting or, more usually, exceeding the specifications laid upon the respective optics.

Quality assurance – Characteristics

The types of characteristics vary between different optic types. A list is provided below for general reference:

Table 5.4: Types of characteristics of optics.

Characteristic	**To be determined**	**Instrument required**
Homogeneity	Variation of material homogeneity	Phase shift interferometer
Bubble/inclusion content	Number of and area of each within given volume	Travelling microscope with dark field capability
Internal defects	Number of and area of each within given volume	Travelling microscope with dark field capability
Surface finish	Quality and defects	Travelling microscope with dark field capability
Form	Deviation from prescribed surface shape	Stylus type profiler system
Figure/wavefront	Reflected wavefront, Reflected wavefront gradient	Phase shifted interferometer
Figure/transmitted wavefront	Transmitted wavefront, Transmitted wavefront gradient	Phase shifted interferometer

Frequency of defects	Power spectral density (PSD)	Phase shifted interferometer
Reflectivity	Centering of coatings, bandwidth and efficiency	Spectrophotometer
Diffraction efficiency	Efficiency of required diffracted order	Tunable CW laser and test bed
Coating scatter	Degree of scatter from the coating	Scatter measurement device
Coating defects	Number of and area of each within given area, crazing	Travelling microscope with dark field capability
Group velocity and higher order dispersion	Spectral phase shift and its derivatives	Spectrally and spatially resolved interferometer
Laser damage threshold	Survivability	Laser and assessment system
Cleaning	Survivability	Cleaning inspection system

Optical testing suite

Most of these characteristics can be measured with a relatively small metrology suite of specialist machines. This suite would need:

Phase shifted Interferometer – this can be used to measure the variation of the homogeneity of the glass, the figure or reflected wavefront of reflective optics, the transmitted wavefront of transmissive optics, the frequency of defects in the surface/transmitted/reflected wavefront.

Travelling microscope – This would enable the identification and measurement of bubble/inclusion content or internal defects within a volume of material. Also for the measurement of coating defects and coating crazing. This can be further enhanced with a dark field capability which enhances the contrast enabling the capture of images easier for measurement.

Stylus type profiler system – can be used to trace the minute deformations in the surface and the variation from the prescribed surface shape.

Spectrophotometer – measurement of the centering of coatings, coating bandwidth and reflectivity.

Tunable CW laser and test bed – this can be used to test the diffraction efficiency of gratings

Scatter measurement device – a device for the measurement of coating scatter

Group velocity and higher order dispersion device – measurement of the spectral phase shift of ultrabroadband laser pulses introduced by coatings.

Cleaning inspection system – Well cleaned optics can maintain the high Laser Damage Threshold of each optic. To obtain well cleaned optics a good cleaning and inspection station is required.

As well as this metrology suite it would be necessary to use semi-professional services at institutions such as the Vilnius University Laser Research Centre to conduct laser damage tests at required wavelengths, pulse durations and repetition rates.

Environmental conditions also need to be tested/assessed. If KDP is being used humidity controls would need to be added or alternatively a controlled micro-climate. Optics used in environments other than air need to be specified and assessed for crazing/delamination/other survivability characteristics. Survivability of coatings at short pulse lengths with high intensities under vacuum is a relatively little understood subject. The ability to test optic coatings in a vacuum/nitrogen chamber where high intensity lasers can be brought onto the surface would be used to determine survivability.

Dispersion measurement of optical elements by spectral interferometry

When an ultrashort pulse is reflected by or goes through an optical element, it becomes chirped and hence its temporal shape is affected. There are mirrors, in turn, designed especially for chirping the pulses by a certain amount (see 5.6.1). Hence, it is essential to measure the spectral phase $\varphi(\omega)$ function of all the optical elements used in a laser system. It is most common to determine not the entire $\varphi(\omega)$, but its Taylor coefficients only, up to the fourth order. The measurement techniques developed so far can be divided into two groups [1] depending on whether they work in the time domain (time of flight interferometry) or in the frequency domain (spectral interferometry, SI) [2, 3]. During the last two decades this latter has proved to be the simplest method, and was used for measuring the dispersion of chirped mirrors, laser crystals, stretcher-compressor systems and pulse shapers.

Spectral interferometry is based on the combination of a two-beam interferometer and a spectrograph (see Fig. 5.22(a)). The interferometer is illuminated by a broadband light source like a tungsten lamp or a femtosecond pulse. The optical element under test (sample) is inserted into one arm of the interferometer, and the other one serves as the reference arm. The spectrally resolved interference pattern is determined by not only the spectral phase of the sample but also the angle between the propagation direction of the sample and reference pulses. When the sample and reference pulses are propagating collinearly, the $\varphi(\omega)$ function of the sample is obtained from one line of the interferogram taken along the frequency axis.

The other type of the SI is the so-called spectrally and spatially resolved interferometry (SSRI) [4–7], where the phase fronts of the sample and reference pulses are tilted with an angle with respect to each other. The interference fringes formed by the temporally overlapping sample and reference pulses are imaged onto the input slit of the spectrograph. The two-dimensional image detected by a CCD camera is resolved spectrally (along the frequency or wavelength axes) and spatially (along the slit). One advantage of this method compared to the collinear method is that the precision is higher because the spectral phase at a given frequency is measured from a vertical slice of the interferogram [6, 7]. The other advantage is that the shape of the SSRI fringes follows the shape of the spectral phase function (apart from the linear term), hence it allows controlling the higher order dispersion of the sample visually [4, 5] (see Fig. 5.22(b)).

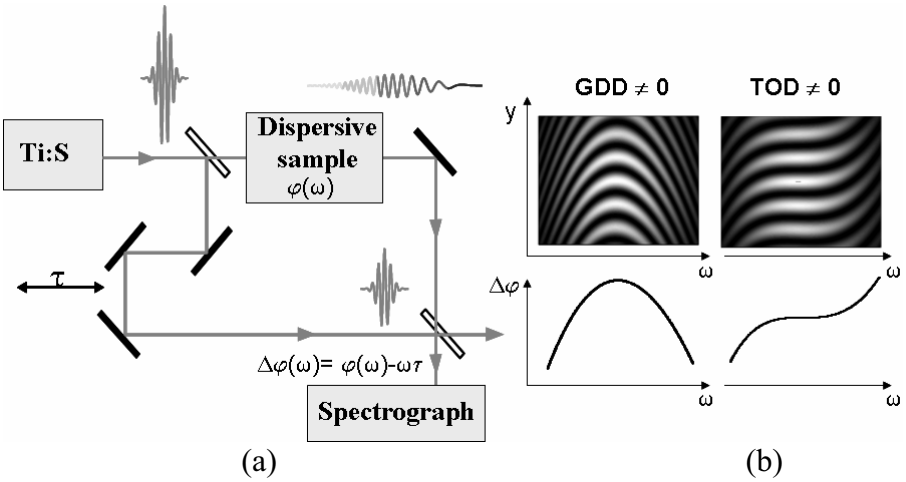

Figure 5.22: (a) Spectrally and spatially resolved interferometer. (b) The shape of the SSRI fringes follows the shape of the spectral phase of the dispersion element.

SSRI is capable of measuring not only the material dispersion but also the angular dispersion (or spectral chirp) [8]. This feature is especially important in cases when the laser beam

propagating in the sample arm becomes angularly dispersed due to the misalignment of the stretcher-compressor system of a CPA laser. Moreover, it has been also demonstrated that SSRI detects also the relative carrier envelope phase between the two arms [9].

Phase shifted interferometer

Interferometry is convenient and widely used methods for non-contact measurement of the wavefront distortion, surface analysis – flatness, micro-roughness measurement, quality control of optical elements, etc. In the developed instrument we combined advantages of different methods and implemented several novelties so the developed system has high resolution, wide measuring range and at the same time is a compact, reliable and easy to use system [10–12]. The measurement principle is based on phase-shifting Michelson interferometry where a high quality piezo translator is introduced in the reference arm for high precision controllable movement of the reference mirror. Using this translator a definite preprogrammed directional phase shift can be introduced in the interferometer which makes the determination of the 3D topography possible. When the phase shift introduced by the surface itself is $\Delta\varphi(x,y)$, using an additional phase shift introduced in 3 steps, we obtain 4 interferograms. After appropriate acquisition of the interferograms the (spatial) phase distortion can be reconstructed – or the topography of the surface can be defined.

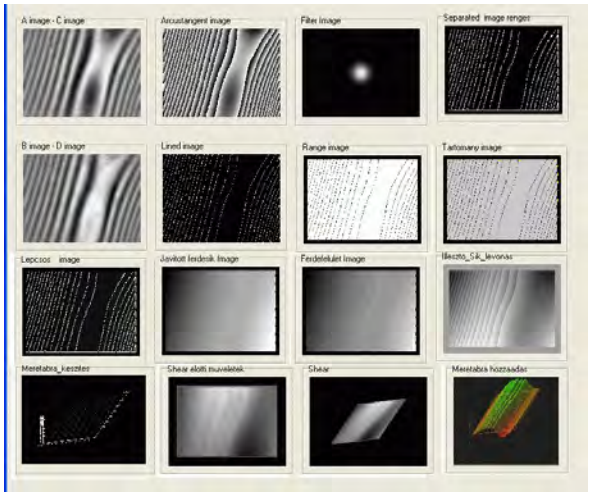

Figure 5.23: Main evaluation steps of phase shifted interferograms and 3D reconstruction of the optical surface.

It is worth mentioning that interferometric systems having long measuring arm and high resolution are also available for the vibration analysis of laser systems as well as for alignment control of the optical elements.

Bibliography

[1] I. Walmsley, L. Waxer, C. Dorrer, Rev. Sci. Inst. **72,** 1 (2001).
[2] Cl. Froehly, A. Lacourt, and J. Ch. Viénot, Nouv. Rev. Opt. Appl. **4,** 183 (1973).
[3] L. Lepetit, G. Chériaux, M. Joffre, J. Opt. Soc. Am. B **12,** 2467 (1995).
[4] A.P. Kovács, K. Osvay, Z. Bor, R. Szipõcs, Opt. Lett. **20,** 788 (1995).
[5] D. Meshulach, D. Yelin, Y. Siberberg, IEEE J. Quantum Electron. **33,** 1969 (1997).
[6] A. Börzsönyi, A.P. Kovács, M. Görbe, K. Osvay, Opt. Commun. **281,** 3051 (2008).

[7] P. Bowlan, P. Gabolde, A. Shreenath, K. McGresham, R. Trebino, S. Akturk, Opt. Express **14,** 11892 (2006).
[8] K. Varjú, A.P. Kovács, G. Kurdi, K. Osvay, Appl. Phys. B **74,** S259 (2002).
[9] K. Osvay, M. Görbe. C. Griebig, G. Steinmeyer, Opt. Lett. **32,** 3095 (2007).
[10] P. Gaál, P.Jani, A. Czitrovszky, Opt. Eng., 32, 2574, (1993).
[11] P. Jani, A. Nagy, Z. Lipp, A. Czitrovszky, J. Aeros.Sci. **31**, 390 (2000).
[12] P. Jani, Material Chem. Phys., **15**, 333 (1986).

5.7 Laser Control

5.7.1 Computer System and Network

Control System Overview

The ELI Laser Facilities, in line with other major science facilities around the world, such as the FAIR accelerator facility, GSI, Germany [1] and the Diamond Light Source, UK [2], will require a suite of complex control systems, which will provide and support a range of operational capabilities. The control system is likely to be comprised of multiple computers each of which will run a separate and dedicated application to monitor and drive a particular area or function of the facility and will interface with the "real-world" hardware to be controlled either through direct control of devices or through locally placed, chassis-mounted modules. Computerized controls are vital to the operability and flexibility of large-scale laser systems providing fundamental services, for example: automatic configuring of specialist hardware; monitoring large numbers of system status; motion control; firing shot sequences; enabling precision trigger distribution; pulsed beam calorimetry; vacuum monitoring and control; data acquisition and analysis. In fact, the only area where non computer based systems still enjoy a significant presence is in safety critical roles so that the integrity of the safety system is decoupled from that of the wider control system.

For many years this broad range of functions has successfully been provided by existing computer control systems. Using the experiences gained from existing large scale laser operations will enable control bottlenecks and unreliable components to be avoided, effectively cherry-picking the features and structures that have already proved most useful and reliable.

The ELI computer control system will employ the master/slave control structure, as used within many existing laser control systems. The majority of the distributed PCs will run applications which provide complete *local* control of equipment and in that sense they can be said to be a "master program". For example, a high-voltage capacitor bank control PC enables an engineer to locally and manually operate and test all amplifier and Faraday switch-gear, trigger amplifiers, interlocks, charging units etc., and for the main control PC to also remotely command the same functionality, thereby using the same application as a "slave program". This is simply achieved by writing the application in a modular fashion and providing two methods of executing a particular routine; first through an on screen click of a button control; second through the receipt of a specific networked command.

There is a distinct advantage in using these master/slave applications in that they are more modular and self-contained and it enables smaller sections of the controls to effectively be developed and tested separately before bringing them all together.

Network Considerations

Communications between the individual computer applications on the ELI control system and with instrumentation will be by standard ethernet TCP/IP or UDP protocols and where appropriate, to avoid signal degradation and electrical interference, should be by fibre optic transmission. Fibre coupling also avoids any problems that may arise from parts of the laser system being powered from separate electrical sub-stations which potentially could have different phasing or conductivity on their earths. Other peer-to-peer network communications that remain within the locale of the ELI control may be fibre-based or use standard Cat5e wired cable.

As systems have become increasingly computerized there has been a growing need to have laser data such as beam energies, temporal pulse-lengths and profiles, amplifier discharge waveforms, and 2D beam-profile images made available to engineers or users electronically. It is expected that the control and diagnostic systems, after capturing, saving and processing data

locally, will transfer it to a diagnostic data server. This is for the purposes of archiving and providing laser operators, staff and users of the facility external access to the data via a web-based data visualization application.

Alongside this, it is also a general recommendation that all PCs should periodically access both anti-virus and security patch updates so the control system needs to be able to see the "outside world" network level – securely via a network gateway or network address translator (NAT) device.

Bibliography

[1] "Controls, Commissioning and Operation of the Accelerators of FAIR", Technical Report, GSI 2005. http://bel.gsi.de/protokolle/dave/TR-Contr-DaVe-V1-zensiert.pdf
[2] http://www.diamond.ac.uk/Home/Technology/Controls.html

5.7.2 Laser Control and Alignment

The laser control system will allow fast switching between discrete laser operational modes varying from low power operation, to allow for alignment, testing and optimization of various stages in the laser system, to full power high intensity operation. This functionality encompasses the operation of the individual laser components as well as the necessary personal safety and hazard warning systems (interlocks, shutters and warning lights/displays).

In each operational mode the laser control system will coordinate and synchronize the operation of the various components of the laser system, including the master oscillator laser, various pump lasers and a variety of electro-optic devices such as Pockel's cells and Faraday rotators. This requires a cascade of electronic trigger signals to be distributed throughout the system with precisely controlled delays specific to the correct operation of the relevant component for a given operational mode. Similarly target area diagnostics will require such triggers 'slaved', i.e. with a fixed temporal relation, to the output of the master oscillator from which the high intensity pulse is derived. The relative sensitivity of each component to the arrival time of the trigger and the temporal jitter will determine the exact method of trigger signal delivery.

At a higher functional level the various diagnostics of laser performance will feed back real time information to the control system. This will allow on-line monitoring and automated or operator instigated manipulation of many critical aspects of the laser system. This feature will result in much greater stability in performance and will optimize data acquisition. Factors to be monitored will include the accurate pointing of the seed pulse through the fixed optical path of the laser amplifier chain to the final target interaction chamber; calorimetry of the pump and seed lasers throughout the various stages of amplification; the spectral shape and phase of the seed pulse as it undergoes amplification and the spatial uniformity of the pump and seed beams. To maintain optimal performance the control system will be automated to make real time corrections, for example by driving motorized pointing mirrors to stabilize beam transport, which may drift over time; adjusting current supplies and trigger delays to pump lasers where thermal effects and pump temporal profile affect the amplification and output spectrum; and controlling adaptive optics (deformable mirrors) to correct wavefront distortions imparted by the amplification media etc.

5.7.3 ELI Laser Safety Control

The laser safety system will be a part of the ELI Personnel Safety System, a standalone system of controls associated with each of the potential hazards of facility operation e.g. electrical safety and radiological risk management.

Design requirements of the Personnel Safety System

The Personnel Safety System will be directly controlled by a suite of hardwired logic circuits and/or safety programmable logic controllers (PLCs). These components will be chosen in accordance to European safety norms IEC61508 and IEC61511 and to the Laser safety and radiation safety officers' recommendations. The Personnel Safety System will be a standalone system separated from the other control systems i.e. that it's isolated and can work without the others. As such, the PSS should use dedicated safety networks as well. The PSS computers, PLCs and associated power supplies and network cabling will not be tasked with any functions other than those specifically related to the safety of facility personnel and use. Its operation will require interaction with other control systems, e.g. the access control system and interlocks.

Typically, each safety function is carried out by the combined action of input devices such as doors switches, a logic solver (hardwired logic or safety PLC) and actuators such as beam shutters. It is common practice to characterise the safety control system in terms of the System Integrity Level (SIL). A given SIL level requires that the system includes a certain level of redundancy, that certain cabling rules are applied and appropriate safety PLCs are used.

In similar laser facilities, such as Vulcan, Gemini (CLF, RAL, UK) and LULI2000, ELFIE (LULI, France) SIL 2 is needed for laser risk management. In accelerators and synchrotrons, usually, SIL 3 is needed to manage radiation risk. ELI can be considered as a mixed facility with laser and radiation risk.

The highest level of reliability is required for the PSS in the environments in which it operates. All safety critical subsystems will be positive security systems i.e. they will suppress the risks by default and when powered down.

Implementation, acceptance, periodic tests and evolution

To ensure SIL of safety loops, sensors and actuators should be certified with the required SIL.

Several companies such as Siemens, Pilz and Rockwell can supply reliable safety PLCs. The supplier will be chosen in a global approach taken into account all needs of PLC for the facility.

Installation, connections and tests should be made by skilled technicians using consistant, standardized cabling rules and best practices. Where high levels of electro-magnetic fields are present appropriate measures should be taken to avoid damage or errors caused by the induced currents in the cabling. Usually, safety networks use optical fibre for such a high electro-magnetic immunity level.

Programming of safety functions will be a major phase in the development process. All safety functions should be programmed and tested individually and in an integrated mode. IEC61511 gives guidelines for development of safety instruments systems.

Validation of the system is done thoroughly during the facility commissioning period. All tests must be performed in the presence of laser and radiation safety officers. Results will recorded in an acceptance book.

During the facility's operational lifetime, all changes in hardware or software must be thoroughly tested for intended function and for effects on other parts of the system. Periodic tests should be made every six months and after any hardware or software modification or evolution. All hardware and software modifications must be recorded throughout the lifetime of the facility.

6 Technological basis for the secondary sources

6.1 Attosecond pulse generation

Two types of sources have been foreseen und will be developed in the "Attosecond Science" beam-line, namely I) one based on large cross section higher order harmonic generation in gas targets and II) one based on surface plasma harmonic generation in solid targets. Sources based on harmonic emission from gases rely on rather mature technologies. Here physical mechanisms have been for many years studied and understood and source performance and specifications have been experimentally verified. Advancements in the framework of this project are expected and mainly rely on the improved characteristics of the driving laser. Harmonic emission from surface plasmas is a new highly promising field. It overcomes an intrinsic limitation that gas targets bring with, namely the depletion of the medium above certain driving intensity ranging somewhere between 10^{14}–10^{15} W/cm^2. During the interaction of ultra-intense femtosecond laser pulses with solid density plasmas, the entire available laser energy can be utilized at highest intensities, giving rise to high photon energies reaching the keV regime at unprecedented photon fluxes.

6.1.1 Source based on High Harmonic Generation in gases

Source specifications

The aim of this source is to convert in the most efficient way the radiation from a few-cycle high power NIR laser into the XUV / soft x-ray regime through high-harmonic-generation (HHG). In the design of an HHG source, one should take into consideration the coherence length and the absorption length of the interacting medium (usually a noble gas). Constant *et al.* has pointed out that the optimal conditions are $L_{med} > L_{abs}$ and $L_{coh} > L_{abs}$ [1] where L_{med} is the medium lenght, $L_{coh} = \pi/(k_q - qk_0)$ and L_{abs} is the length where the q^{th} harmonic is absorbed by a factor e^{-1}. From those conditions one can see that the optimum condition is different for different harmonic order and the design of the harmonic source should be flexible enough to allow of the optimization of different harmonics for different applications. It was also shown that when the coherence length is longer then both the absorption and medium lengths, the photon yield at the q^{th} harmonics is proportional to $(1-\eta)I_0^5 S_{spot}(PL_{med})^2$ [2,3] where P is the gas pressure, η is the ionization probability, I_0 and S_{spot} are the laser intensity and spot area at the interaction region. Three important conclusions can be derived from this formula. First, one should keep the ionization rate low enough to avoid depletion of the medium. For noble gases this condition limits the laser intensity to the range of 1×10^{14}–1×10^{15} W/cm^2 (depending on the specific atom and the pulse duration of the driving field). Second we observed that increasing the spot area will increase the photon yield. Last conclusion is that one can keep the product $(P \cdot L_{med})$ constant to have the same photon yield. This last condition gives some flexibility in the source design. The objective to use as high power laser as possible and the need to keep the intensity bellow a certain value force us to work in the loose focusing geometry. The 5 m focal length has produced at SACLAY XUV energies at the 1 μJ level. With the same focal length currently used at FORTH-IESL XUV intensities approaching 10^{15} W/cm^2 at the target have been achieved at central photon energies of 15 eV. In a recent collaborative initiative of FORTH-IESL with MPQ a focal lengths of 12 m are used, while the Attosecond Science and Technology Regional Partner Facility (see chapter 9.7) will operate a gas target source using 15 m focal lengths. Two kinds of gas targets come under consideration for the loose focusing geometry, a gas jet nozzle, or, a cell filled with gas and two pin holes to allow the laser going through the cell. Typical pressures and lengths for a static gas cell are 1–50 Torr and 3 mm–10 cm respectively (the large variation is due to different focusing condition and the need to optimize for different harmonics). Typical pressures and lengths for the gas jet are 10–500 Torr and 0.5–3 mm. To enhance the harmonics

yield even more, it is possible to adopt some quasi-phase-matching (QPM) techniques to counter the phase mismatch and increase the effective interaction length. Recently, Seres *et al.* showed QPM with a multi gas cell target [4]. Such a multi gas cell or multi gas jet target are ideal for the loose focusing geometry since the Rayleigh range is long and one can easily select and adjust the relative distances between the cells/nozzles. The drawback of this approach is the huge gas-load it puts on the vacuum system.

Figure 6.1: The loose focusing attosecond source operating at FORTH-IESL. Focused VUV/XUV (10–20 eV photons) intensities reach a level that allows comfortable exploitation of two-XUV-photon processes in attosecond pulse metrology (J. Kruse *et al.* Phys. Rev. A **82**, 021402(R) (2010)), time resolved XUV spectroscopy (see A. Peralta Conde *et al.* Phys. Rev. A**79** (R), 061405 (2009)), and XUV-pump-XUV-probe studies (ongoing experiment at FORTH). Applying IPG techniques 40 eV broad XUV quasi continua at 50 eV central photon energies and 0.5 µJ are currently generated.

Source design

As already mentioned in the previous section, HHG with high power laser lend itself to the loose focused geometry. Loose focusing geometry has many advantages such as low Gouy phase and a long Rayleigh range but it also has some drawbacks. The first consequence of the loose focusing geometry is a long beam line. Usually, in order to select the spectral region of interest and to separate the harmonics radiation from the fundamental, a thin metallic filter is placed after the generation chamber. To avoid damages to this filter, a long distance is needed to let the beam expand enough thus reducing the intensity. This distance is given by:

$$L = \frac{P_L}{\lambda\sqrt{I_0 I_{th}}} \tag{6.1}$$

where P_L is the average laser power, I_0 the average intensity at the focus, λ the laser wavelength and I_{th} is the damage threshold of the filter. To illustrate to which dimensions these considerations lead in an extreme case, let's consider a Gaussian beam with $M^2 = 1$, energy of 100 mJ, pulse duration of 10 fsec and keeping the average intensity on the gas target smaller

then 4×10^{14} W/cm^2. Assuming $I_{th} = 1 \times 10^{12}$ W/cm^2 we find L = 20 m. We also note from Eq. (6.1) that L is proportional to the laser power.

Nevertheless the separation of the fundamental from the harmonics may occur differently. For instance if the driving laser is an annular beam (formed by introducing a beam stop at the central part of the beam) the main separation is achieved using an iris blocking the IR and transmitting the harmonics. Residual IR radiation may then be absorbed by the filter. For photon energies up to 70 eV Si plates at Brewster angle for the XUV radiation can be used as separators. The laser beam is absorbed, while the XUV radiation is reflected to 60%. Thus even at the level of 1–5 J distances of the order of 10 m are sufficient. Expanding of the XUV is also required for a number of applications or for metrology purposes. The arrangement of the split mirror autocorrelator, described in sections “Specifications of temporal diagnostics" and “Design of temporal diagnostics", requires an XUV cross-section of few mm diameter. This fact already defines the required distances at loose focusing geometries.

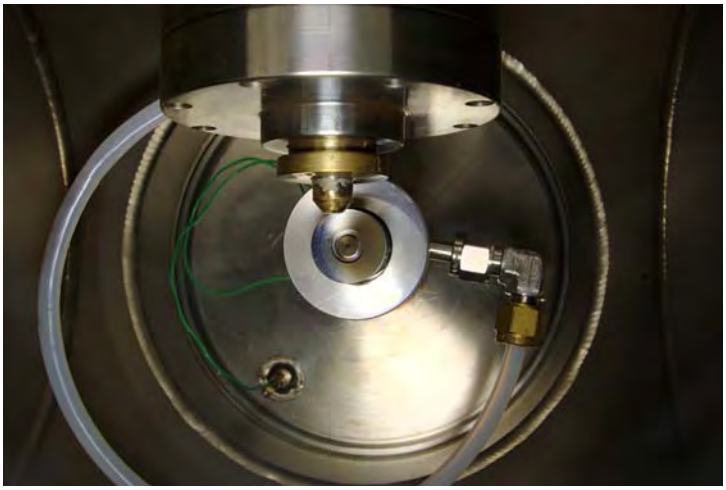

Figure 6.2: QPM arrangement used in a feasibility study at FORTH-IESL.

Another consequence of the loose focusing geometry is a large gas-load in the beam line. Using the above example, we can calculate the beam diameter at the focus to be $2\omega_0 = 2\sqrt{P_L/\pi I_0} = 1.7\,\text{mm}$. Due to the large focal spot, a gas jet with a large cross section is needed. Assuming a jet diameter of 2 mm with a pressure of 60 Torr [2] operating at repetition rate of 1 kHz, and assuming 30 μsec opening time of the pulsed nozzle, we can estimate a gas load of about 6 mbar·liter/sec. For a multi gas jet target, the gas load would be even larger and one should install few huge turbo pumps. It is also necessary to separate the interaction chamber from the rest of the beam-line with a differential pumping. It is possible to reduce the gas load by using a long cell of continuous flow with lower pressure instead of the gas jet nozzle, but that will limit the number of cells one can use for QPM.

Bibliography

[1] E. Constant, D. Garzella, P. Breger, E. Mevel, Ch. Dorrer, C. Le Blanc, F. Salin, P. Agostini, Phys. Rev. Lett. **82**, 1668 (1999).
[2] E.J. Takahashi, Y. Nabekawa, H. Mashiko, H. Hasegawa, A. Suda, K. Midorikawa, IEEE J. Sel. Top. in Q. Elec. **10**, 1315 (2004).
[3] J.L. Krause, K.J. Schafer, K.C. Kulander, Phys. Rev. A. **45**, 4998 (1992).

[4] J. Seres, V.S. Yakovlev, E. Seres, Ch. Streli, P. Wobrauschek, Ch. Spielmann, F. Krausz, Nat. Phys. **3**, 878 (2007).

6.1.2 Source based on surface harmonic

Source specifications

The generation of coherent high harmonics from the interaction of an ultra-intense laser pulse with a solid density plasma surface has the potential of overcoming the limitation of the medium depletion and producing attosecond pulses of unprecedented intensities [1] that could be applied for a wide range of experiments. The basic experimental configuration is rather simple and is illustrated in Fig. 6.3.

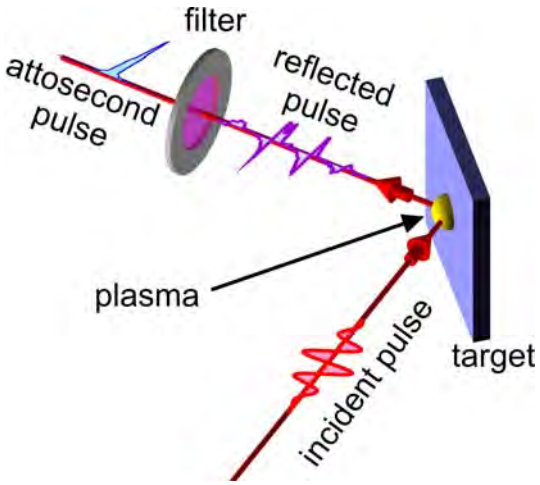

Figure 6.3: Schematic of solid target surface plasma harmonic generation. From G.D. Tsakiris *et al.*, New J. Phys. **8**, 19 (2006).

Two distinct mechanisms for plasma surface high harmonic generation (SHHG) have been identified. For relativistic laser intensities, i.e., when $I\lambda^2 > 1.38 \times 10^{18}$ Wcm$^{-2}\mu$m^2, the dominant process is the frequency up-shifting of the incident laser light due to the reflection off the relativistically oscillating electron density surface, the so called relativistic oscillating mirror (ROM) mechanism. This process is explained in detail by the theory of relativistic spikes of Baeva *et al.* [2]. For sub- and moderately relativistic intensities the dominant mechanism is the coherent wake emission (CWE) [3]. Both these mechanisms are predicted to generate coherent harmonics leading to temporal bunching and the generation of attosecond bursts of XUV radiation. While this has been experimentally demonstrated for the CWE mechanism [4,5] the ROM harmonic emission is predicted to produce attosecond pulses of superior specifications, some of which have already been verified. Thus in a series of measurements Dromey *et al.* have shown harmonic spectra extending up to the keV photon energy range (approximately the 2800^{th} order of the fundamental laser frequency [6]) and the generation of diffraction limited harmonic beams at 40 nm wavelength [7]. On this mechanism will be based both the initial user oriented attosecond source as well as the advanced source version to be developed later on.

The specifications of the source have been defined using simulated values resulted from 1D PIC simulations [1]. Input parameters have been, a phase stabilized, two-cycle ($\lambda_L = 0.8$ μm, $\tau_L \sim 5$ fs) laser pulse, with a Gaussian envelop and p-polarization focused at 45° on a planar target consisting of 80 times overdense plasma for the 0.8 μm laser wavelength. The normalized

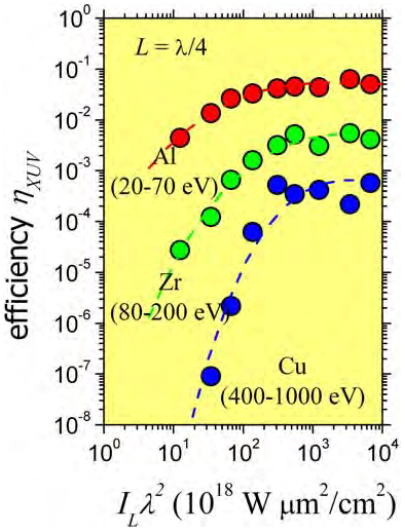

Figure 6.4: Variation of the XUV efficiency with the laser intensity for three different spectral ranges determined by the indicated thin filter used. From G.D. Tsakiris *et al.*, New J. Phys. **8**, 19 (2006).

Table 6.1: Source specifications.

Spectral range (eV)	Number of photons	Pulse duration (asec)
20–70	10^{16}	80
80–200	3×10^{14}	40
400–1000	2×10^{12}	5

vector potential was varied between $a_L = 3$–100 corresponding to a laser intensity range of 2×10^{19} to 2×10^{22} Wcm^{-2} [1]. Using realistic filters consisting of 0.2 μm thick Mg, Al, Zr or Cu metal foils the efficiency with which the attosecond XUV pulses are produced in the spectral regions (20–70 eV), (80–200 eV) and (400–1000 eV) respectively have been simulated as shown in Fig. 6.4. The efficiency depicts a steep rise with intensity and eventually saturates at remarkably high values. For low photon energies the conversion efficiency approaches 0.1, while even for 0.5–1 keV photons lies by $\sim 5 \cdot 10^{-4}$. Utilizing the above simulated conversion efficiencies and assuming a phase stabilized 5 fs, 1 J laser pulse focused down to a 10 μm diameter focal spot, the source specs (at the generation point) have been extracted and are shown in Table 6.1.

The source specifications very much depend upon the driving laser parameters. For an increased pulse energy up to 5 J possibly available at ELI and given that at saturation the photon number is linearly increasing with the driving intensity the numbers of the second column of Table 6.1 will be higher by a factor of 5. The numbers of Table 6.1 should be adjusted to take into account losses through beam transport, filter absorption and reflection for focusing. Recent studies have revealed that harmonics emitted by overdense plasmas exhibit high degree of spatial and temporal coherence. Spatial coherence has been studied at Saclay by observing the far field interference pattern of harmonics originating from three mutually coherent sources [8].

One decisive parameter for the source to posses the predicted specifications is the laser pulse contrast, i.e., the ratio of the peak to the pedestal or pre-pulse intensity. This is in order to avoid formation of pre-plasma with large scale length density gradient, when the main pulse impinges the surface, which turns off the coherent emission. In order to avoid formation of pre-

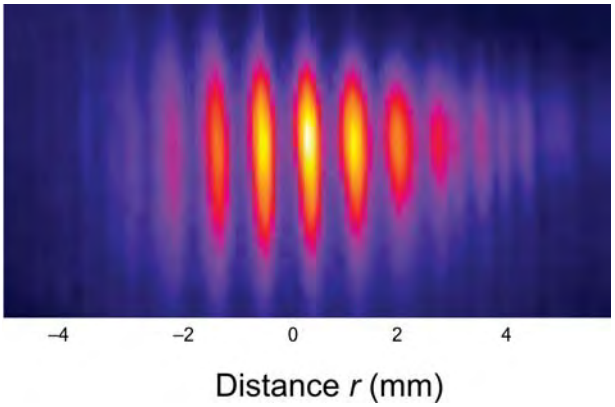

Figure 6.5: Single-shot far-field interference pattern of harmonics 8–10. The high fringe contrast evidence the excellent spatial coherence properties of the overdense plasma source. From C. Thaury *et al.* Nature Physics **4**, 631 (2008).

plasma, the pedestal intensity at the ps scale should not exceed $\sim 10^{10}$ W/cm^2, as the required contrast ratio is increasing linearly with the driving intensity. Without special measures this ratio reaches 10^8 in state of the art high peak power lasers. Relativistic intensities can then be reached straightforwardly. For intensities $\geq 10^{19}$ W/cm^2 additional pulse cleaning measures have to be taken the most successful one so far being the plasma mirrors [9].

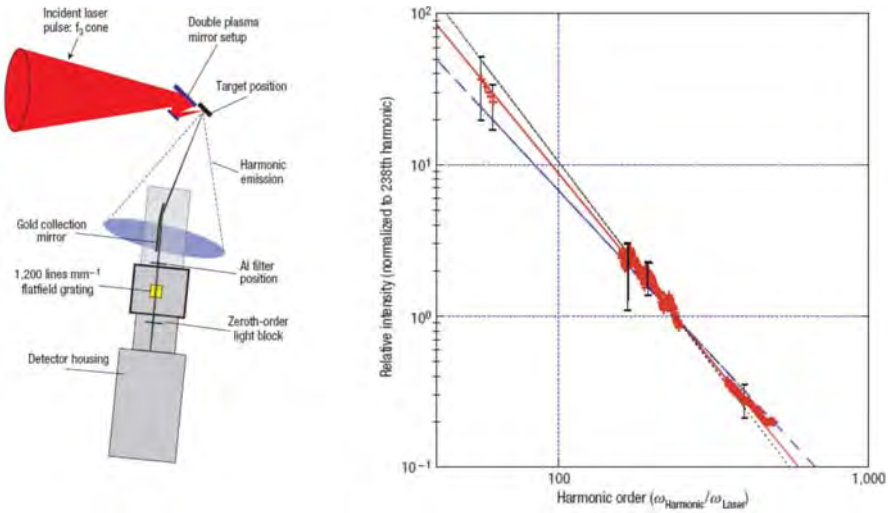

Figure 6.6: Double plasma mirror configuration (left). Demonstration of keV harmonics and verification of the harmonic emission power law. From B. Dromey *et al.*, Nature Phys. **2**, 456 (2006).

The technique relies on the fact that a surface starts to reflect when plasma is formed at the appropriate critical density. At proper intensity conditions plasma is formed by the leading part of the pedestal or by pre-pulses. The plasma reaches critical density when the actual pulse arrives at the vacuum-plasma interface. Thus unwanted radiation contributions before the main pulse are transmitted producing plasma, while the main pulse, cleaned from them, is reflected by the plasma mirror. Plasma mirrors are placed before the harmonic generation

target. Using a double plasma mirrors arrangement a contrast ration of 10^{12} has been recently achieved [10]. Of particular importance is the high contrast for ROM harmonics. In a recent experiment [11] in which the averaged focused intensity of the laser was 4×10^{18} W cm^{-2} in the $1/e^2$ radius and as high as 4×10^{19} W cm^{-2} in the peak, i.e., beyond the relativistic limit, surprisingly at first glance a distinct CWE cutoff was observed (see Fig. 6.7). In principle, the focused intensity was comparable to that achieved in other experiments (e.g. in [7]) where ROM harmonics were observed. The major difference between the two experiments is that the peak-to-prepulse contrast of the first one was roughly two orders of magnitude lower than in the other experiment owing to the fact that in the first experiment no plasma mirror was used (PM) for contrast enhancement. Instead it relied on the relatively high inherent contrast of 10^8 of the laser used.

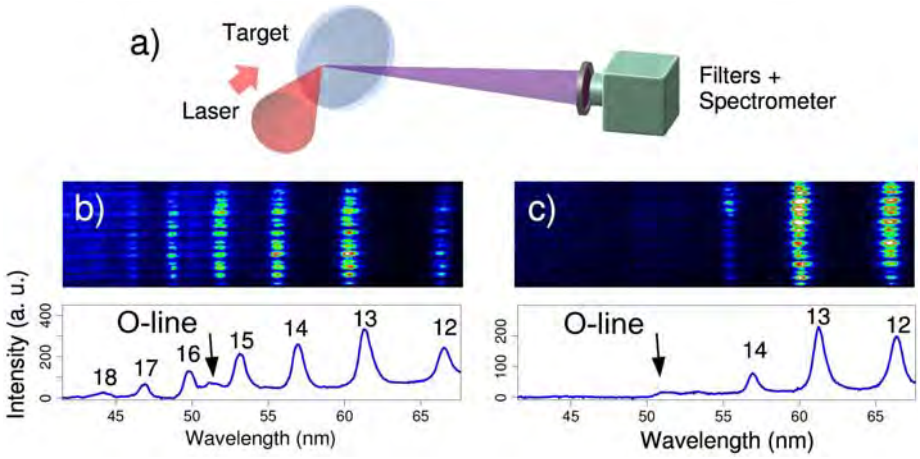

Figure 6.7: Sketch of the setup for surface harmonic generation and detection (a) and camera images and line-outs of measured harmonic spectra for two different target materials. The two spectra in this figure clearly show the difference in the emitted harmonic range for two different target materials. While the spectrum in (b) for a BK7-glass target (density ≈ 2.7 g cm^{-3}) extends up to the 18th harmonic, the PMMA target in (c) (density ≈ 1.2 g cm^{-3}) shows a clear CWE cutoff at the 14th. Both spectra were taken using an Al filter. The arrows mark the third order diffraction from an incoherent O_2 emission line at ≈ 18 nm. From R. Hörlein *et al.* Plasma Phys. and Contr. Fusion **50**, 1240002 (2008).

The laser intensity at the source target at the "attosecond science" secondary source of ELI is expected to exceed 10^{21} W/cm^2. Thus a contrast ratio higher than 10^{11} will be required and achieved unavoidably by using plasma mirrors.

Source design

The design of the source is along the lines of the today operational prototypes. One of those is that of MPQ Garching depicted in Fig. 6.8. The harmonic spectra are measured routinely using with an XUV/x-ray spectrometer as described in 4.8.

Focusing system

In the typical arrangement shown in Fig. 6.8 the laser beam is focused on the solid target with a large-aperture $f/2.5$ off-axis parabola. The same approach will be adopted in the source to be developed. A commercial autofocus set up will be employed for adjusting the parabola–target distance with a positioning accuracy of 1μm. The set up will monitor and if necessary correct this distance during the experiment. Since for the large photon energies ultra-low surface

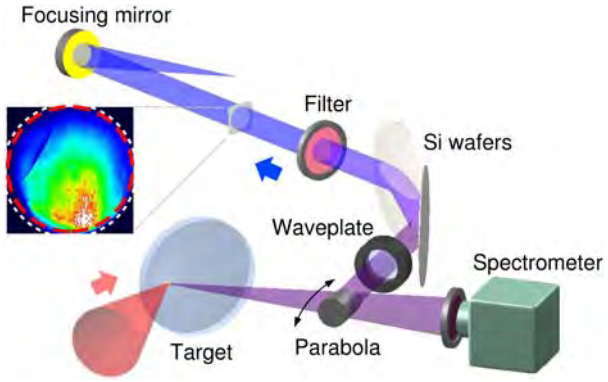

Figure 6.8: Schematic drawing of the setup used to produce, transport and refocus the XUV beam for an application. The laser is focused by an off axis parabola and the XUV beam is recollimated using a gold-coated off-axis parabola. Two silicon mirrors are used to efficiently suppress the residual IR and steer the beam that is subsequently filtered spectrally with a suitable metal filter and then refocused. The inlay shows a measured XUV beam profile (the dashed circle marks the size of the IR beam at the corresponding position of the setup). From R. Hörlein *et al.* Plasma Phys. Control. Fusion **5**, 124002, 13 (2008).

roughness grazing incidence reflective elements will be necessary, too large XUV/x-ray beam cross sections have to be avoided. Thus the XUV/x-ray beam divergence has to be kept low therefore parabolas with f ∼3-4 will have to be used.While in current experimental set-ups this is not possible because of the limited laser power the 1 PW driving laser beam at the ELI attosecond science source allows the use of rather large f numbers

Target

To meet the demands of pump–probe type experiments regarding the accumulation of shots in one measurement a special large-area target drive capable of holding 50 cm in diameter disc targets will be used. The discs will be rotated and translated, so that the laser focus spots will lie on a spiral. This allows taking several thousands of shots prior to the target replacement. The exact number of shots depends strongly on the target material and the laser energy, both of which influence the size of the damage spot on the target. For a shot to shot separation of 1 mm, for example, 120.000 shots can be taken. A target exchange set up will utilize 6 target holders, three of which will be introduced into the interaction chamber each time from an auxiliary target-introduction vacuum chamber separated from the interaction chamber by a vacuum valve. Thus the vacuum will be broken only in the auxiliary chamber in order to replace the used targets with fresh ones, while maintaining high vacuum in the interaction chamber at all times. Subsequently the auxiliary chamber will be evacuated reaching the required vacuum level for the introduction of the targets into the interaction chamber. The problem of the frequent target exchange may be solved by using liquid targets. Liquid targets in the form of a laminar flow sheet have been successfully used in photoelectron spectroscopy studies upon interaction with laser beams. Ultra low vapour pressure vacuum technology oils or metals with low melting point and ultra low vapour pressure (e.g. Indium) create laminar flow sheets with high degree of surface flatness and may be proven appropriate target media for harmonic generation. The option of using liquid targets has been considered. It must first be assessed and experiments of harmonic generation on liquid targets are currently in progress at MPQ showing encouraging results.

Beam transport

The key to the successful application of the coherent XUV/x-ray radiation routinely generated in the secondary source is a robust and efficient beam transport system. The setup has to fulfil a series of requirements such as collimating the XUV beam, spectral filtering and especially suppressing the residual IR light. At the same time it is necessary to keep the number of reflections in the system as low as possible to minimize the losses during beam transport allowing for high XUV energies in the interaction region. In Fig. 6.8. the harmonic beam generated from the target is recollimated using a 25 mm diameter 90° off-axis gold-coated parabola that can be removed from the beam to allow the measurement of the XUV spectrum. The IR fundamental laser radiation is strongly suppressed using two Brewster angle reflections on large-aperture silicon mirrors before the beam is spectrally filtered using thin metal foils. Finally the beam is focused for applications. If the pump–probe capability of the setup is desired, the focusing mirror can be replaced, for example, by a split mirror setup such as the one used in [12], acting as an XUV beam splitter.

IR-suppression

At the high laser energies used in the generation of the harmonics it is compulsory to suppress the IR radiation efficiently in order to prevent damage of the metal filter used for the spectral selection. It is also important to note that the method often employed in gas harmonic experiments of placing a beam block in the central part of the focusing laser and thus generating an annular IR beam after the target [13] that can in turn be blocked with a complementary mask does not work for surface harmonics because the generation mechanism itself behaves like an efficient spatial filter [14, 15]. A convenient solution to this problem for small photon energies up to 70 eV is the reflection of the beam from a Si surface under the Brewster angle for IR radiation [16]. Especially for Si the ratio between the XUV and IR reflectivity is very advantageous.

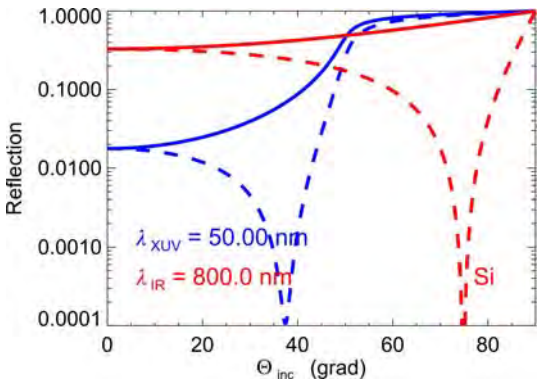

Figure 6.9: Reflectivity of a silicon surface as a function of the incident angle. The dashed curve is for p-polarization. From R. Hörlein *et al.* Plasma Phys. Control. Fusion **5**, 124002, 13 (2008).

At the same time large-aperture Si wafers are readily available because of their importance in chip production. However, due to their thinness, they are not adequately flat and thicker Si plates should be considered to maintain the focusing capability of the XUV beam. Figure 6.9 shows the reflectivity of Si for IR and XUV radiation as a function of the incidence angle and the polarization. Note the suppression of the fundamental for the 75° angle of incidence. While the calculation shown in Fig. 6.9 was done for a single wavelength it is important to point out that for a pulse of 30 nm spectral bandwidth the theoretically achievable suppression is still

better than 104:1 for a single reflection. In our experiment we implement the Si mirrors either in the configuration shown in Fig. 6.8 or in a separate IR suppression unit (image in Fig. 6.10.) that can be modularly inserted into any setup without altering the beam path. Also one is not restricted to silicon for IR suppression. Other elements like fused silica wedges can also be used for IR suppression. While the reflectivity for XUV is slightly lower in that case the main advantage lies in the fact that very high quality quartz surfaces are readily available due to their importance as mirror substrates.

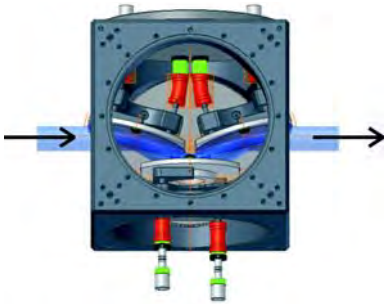

Figure 6.10: Technical drawing of a mobile IR suppression unit. It is fitted into a $50 \times 50 \times 50$ cm^3 vacuum cube that can be installed at various positions in the experimental set up. From R Hörlein *et al.* Plasma Phys. Control. Fusion **5**, 124002, 13 (2008).

For shorter XUV wavelengths, the suppression of the IR will be achieved using broad multilayer mirrors. The increase of the supported bandwidth maintaining sufficiently high reflectance is a current technological challenge that triggers continuous progress. In the soft x-ray region metal filters (or combination of filters and multilayer mirrors) of sufficient thickness as to avoid damage will block the IR radiation. It is worth noting that the collimation of the attosecond beam will be after the cross-section of the diverging beam has been substantially increased as to avoid catastrophic load on the filters.

Further developments

The XUV focal spot quality and the throughput of the beamline, are the two parameters that need to be improved for an optimized experimental setup. To improve the XUV/x-ray focusing departure from a spherical focusing optic to either parabolic or elliptical provides the best known solution. This not only improves the quality of the focus but it is also absolutely necessary for optimizing the throughput. For an increased reflectivity the angles of incidence have to be made as large as possible to take advantage of the inherently higher reflectivity for grazing-incidence reflections. This requires non-spherical surfaces in order to minimize aberrations, keeping the focal spot small. Optimized coatings (for example, multi-layers or certain metals) for the desired photon energy range will allow one to explore the full potential of the surface harmonics by minimizing the losses during beam transport.

In Fig. 6.11 optimized setups for two experimental scenarios are proposed. In Fig. 6.11(a) a set up utilizing two large angle of incidence off-axis parabolas for recollimation and subsequent aberration-free focusing is optimized for XUV-pump–XUV-probe type experiments using a split mirror. In Fig. 6.11(b) using an elliptical mirror for point-to-point imaging is ideal if a single XUV beam of maximum intensity is desired because the number of reflections is minimized in this scheme. In both setups the IR and the XUV beam are p polarized on all optics. The decision on the angles of incidence to be used, several factors have to be considered. On the one hand, for high reflectivity at short wavelengths as large as possible angle is required but, on the other hand, the feasible mirror sizes and beam diameters after collimation in scheme (a) are limited. Moreover the distance between the target and the mirror has to be sufficiently large so that the residual IR beam has expanded far enough to not damage the mirror coating. The decision also depends on the spectral region used since the divergence depends on that. In the end the decision has to be made for every range separately since it is based on many parameters

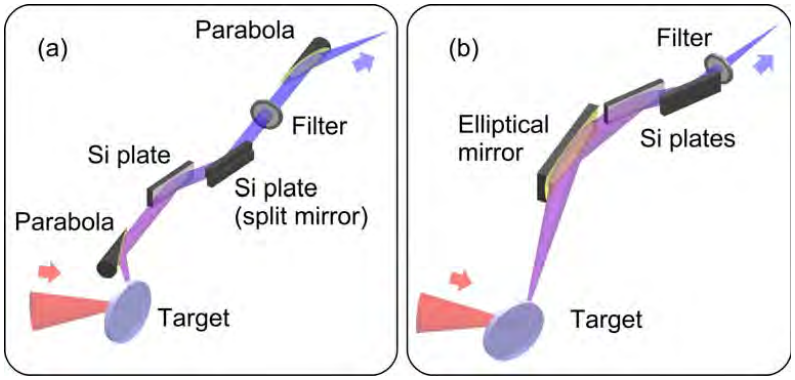

Figure 6.11: Two improved experimental setups for XUV beam. Setup (a) shows an optimized XUV-pump–XUV-probe experiment where a split mirror is needed to introduce a delay between two parts of the pulse. Setup (b) is designed for maximum XUV throughput by using an elliptical mirror for point-to-point imaging and minimizing the number of reflections in the beam path. From R. Hörlein *et al.* Plasma Phys. Control. Fusion **5**, 124002, 13 (2008).

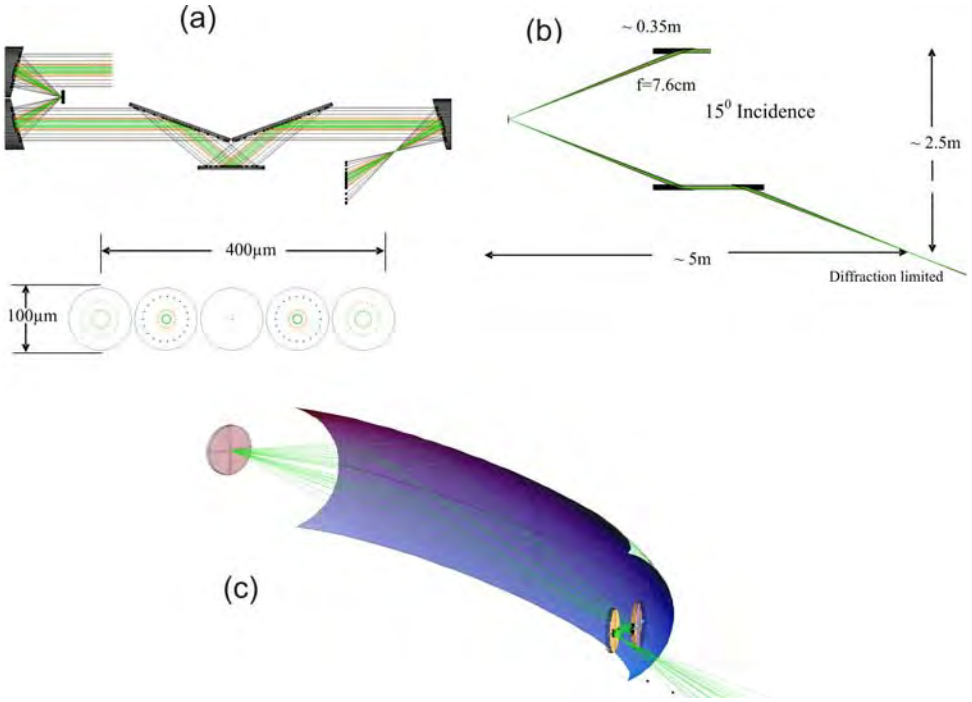

Figure 6.12: Ray tracing studies (Optica/Mathematica) of optimized focusing arrangements using parabolic and elliptical optics (performed at FO.R.T.H.).

of the specific experiment. In the soft x-ray region for wavelengths shorter than $\sim$ 20 nm, the Si wafers cannot be used. The IR suppression occurs through sufficiently thick filters at large enough distances from the source in order to avoid their damage and the split mirror has to be one of the parabolas or the elliptic mirror.

Figure 6.12 shows ray tracing studies (Optica/Mathematica), performed at FO.R.T.H., of optimized focusing arrangements using parabolic and elliptical optics. Fig. 6.12a illustrates an

arrangement using parabolic optics for on target focusing of the IR beam. The arrangement provides XUV collimation, IR-XUV separation, XUV wave front splitting and introduction of temporal delay in one of the two beam halves, XUV focusing on gas target, ideally leading to a diffraction limited focus. The flat mirrors are Si plates. The first or last Si plate can be omitted on the cost of a parallel shift of the out coming XUV beam. The arrangement can be used for pulse metrology and/or time resolved applications. Fig. 6.12b shows a set up based on small incidence off-axis parabolic mirrors, appropriate for short wavelengths. Si plates as in Fig. 6.12a can be introduced as well between the last two parabolas. Fig. 6.12c shows ray tracing modeling of an arrangement using an ellipsoidal element. The IR and XUV beams emerging from the solid target placed at the one focal point of the ellipsoidal are reflected by it and focused on the second focus. The two mirrors before the focus are Si plates acting as beam separators and/or delay line if the one of the plates is a split mirror.

Bibliography

[1] G.D. Tsakiris et al., New J. Phys. **8**, 19 (2006).
[2] T. Baeva et al., Phys. Rev. E **74**, 065401 (2006).
[3] F. Quéré et al., Phys. Rev. Lett. **96**, 125004 (2005).
[4] Y. Nomura et al., Nature Physics **5**, 124 (2009).
[5] R. Hörlein et al., New Journal of Physics **12**, 043020 (2010).
[6] B. Dromey et al., Phys. Rev. Lett. **99**, 085001 (2007).
[7] B. Dromey et al, Nature Physics **5**, 146 (2009).
[8] C. Thaury et al., Nature Physics **4**, 631 (2008).
[9] H. Kapteyn et al., Opt. Lett. **16,** 490 (1991).
[10] C. Thaury et al., Nature Physics **3**, 424 (2007).
[11] R. Hörlein et al., Plasma Phys. and Contr. Fusion **50**, 1240002 (2008).
[12] P. Tzallas et al., Nature **426**, 267 (2003).
[13] J. Peatross et al., Opt. Lett. **19**, 942 (1994).
[14] K. Moncur, Appl. Opt. **16**, 1449 (1977).
[15] R. Hörlein et al., New J. Phys. **10,** 083002 (2008).
[16] E. J. Takahashi et al., Opt. Lett. **29**, 507 (2004).

6.1.3 Source diagnostics

Specifications for photon diagnostics

Photon diagnostics are essential not only to fully understand and characterize the performance of the source during the development phase, but also to give to the users the necessary information on the experimental conditions. An ideal detector for ELI source has to cover the full dynamic range of gas and plasma harmonic sources, to be suitable for single-pulse measurements, to exhibit low degradation under radiant exposure in the extreme-ultraviolet (XUV) and soft X-ray region and to be ultra-high vacuum compatible and suitable for being assembled under clean room conditions. Furthermore, some experiments may require online diagnostics with minimum interference with the XUV beam: this means that the diagnostics should not block the XUV beam or alter some crucial beam properties such as coherence, temporal duration and intensity to an undesirable extent. The development of novel photon diagnostic techniques for the ELI facility may benefit from the large experience on the existing XUV free-electron-laser (FEL) facilities. In particular, on-line monitoring techniques are widely used to provide real-time information to the users about the spectrum and the intensity of FELs and may be applied also to high-order harmonic XUV radiation [1]. An example of a beamline for ultrashort sub-femtosecond pulses is shown in Fig. 6.13.

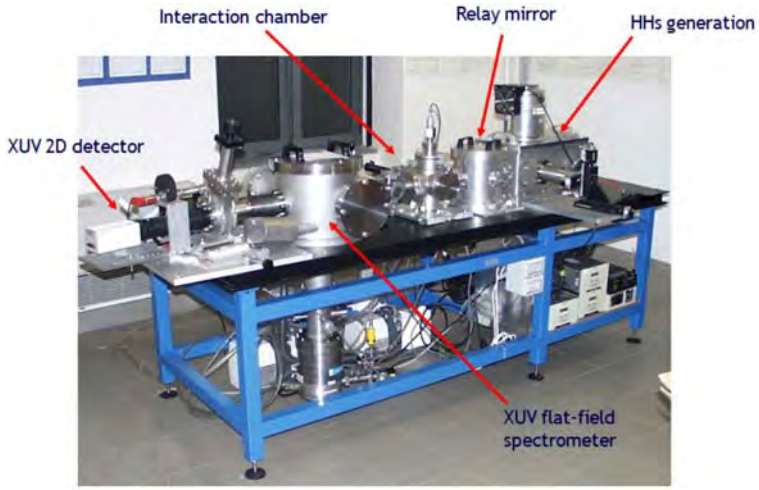

Figure 6.13: A typical beamline for ultrahort XUV pulses (presently at Politecnico Milano, Italy) L. Poletto *et al*, Rev. Sci. Inst. **75**, 4413 (2004).

The measurement of the spectrum is essential both to characterize the source during the development phase and to give to the users the necessary spectral information during the experiment. The use of flat-field grazing-incidence gratings gives the possibility of having single-shot spectrometers which acquire the spectrum on a broad-band with a 2D flat detector. This gives the possibility of measuring simultaneously the spectrum and the divergence of the source [2,3]. The sensitivity of the spectrometer should be as high to measure the single-shot spectrum with a spectral dispersion in the range 0.4–0.8 nm/mm in the 8-30 nm spectral region. In case of generation at low repetition rates with high laser pulse energies, the user may require the knowledge of the spectrum of the interacting radiation on-line. In such a case, the spectrum can be measured on-line without altering any of the properties of the photon beam but with a small reduction of the flux to the experiment, adopting the same solution as in the case of FELs [4].

Also the measurement of the intensity is of crucial importance both to optimize the photon flux through the control of the generation process and to give to the users the parameters of the experimental conditions. The intensity monitor has to cover the full XUV spectral range of the source. Several options are available; among them we can cite calibrated metallic photodiodes and MCP calibrated detectors. The users may require the on-line measurement of the intensity of the incoming radiation. In such a case, the method already developed and currently used for FELs, i.e., the gas ionization detector may be applied also to high-order harmonics [1,5].

However, the main issue that has to be solved and that is unique for high-harmonic generation is the co-propagation of the high-energy infrared pumping beam with the generated XUV radiation. This problem is very severe in terms of application of the harmonics: the high-intensity fundamental beam co-propagating with the harmonics may damage the XUV optics of the beamline or even destroy the sample if focused on it. The first optical element of the beamline, before any XUV photon diagnostics, is then a suitable system that separates the infrared fundamental beam and the XUV radiation. The main requirements for the separation are: high damage threshold, high attenuation of the pump pulse, high throughput in the XUV, no alteration of the pulse temporal structure. The study of such a system is of outmost importance in the definition of the elements of the beamline.

Even in the case of very high rejection efficiency of the separation system, the huge difference in intensity between the fundamental and the harmonics (that may be as high as 10^6–10^8) imposes normally the use of so-called solar-blind detectors, which are not sensitive at all to the

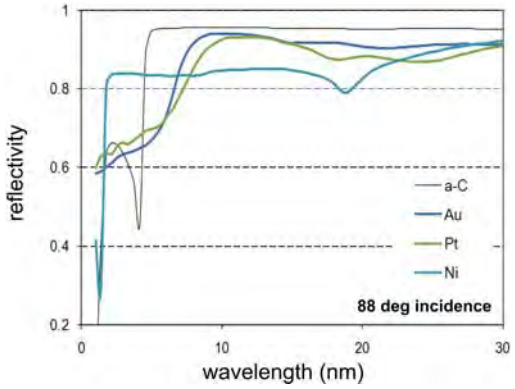

Figure 6.14: Reflectivity of some coatings at 88° in the 1–30 nm region.

visible and infrared radiation, e.g. channeltrons, microchannel-plates with suitable photocathodes or metallic photodiode. The use of solid-state detectors (typically silicon photodiodes or 2D CCD cameras) has to be carefully evaluated. In fact the efficiency of these detectors in the visible and near infrared is comparable or even higher than the efficiency in the XUV and the presence of some radiation in the infrared not completely eliminated by the separation system may add a substantial noise to the useful signal in the XUV and invalidate the measurement.

When defining the specifications of photon diagnostics, a strictly related issue is the transport of XUV radiation. Generally speaking, broad-band grazing-incidence optical elements are required to transport the beam from the source position to the experiment. The coating should be selected to have high and almost constant reflectivity on the whole spectral region of operation. Different coatings can be employed: metallic coatings such as gold, platinum or nickel have been widely used for laboratory experiments in the XUV. They exhibit good performance in terms of reflectivity and stability in time. Recently, highly-dense graphite has been used as coating for FEL beamlines, since it exhibit very high performances in the XUV region down to 5 nm. The reflectivity of some XUV coatings at grazing-incidence is shown in Fig. 6.14. Once the geometry of the beamline has been defined, the final choice of the coating and incidence angle depend on the spectral region of operation, the number of optical elements to be inserted and the requirements on the overall efficiency. Obviously, the smaller the grazing angle the larger the size of the optics for a given angular aperture. Since the energy density decreases as the sine of the grazing angle (95% decrease at 3 deg), the use of grazing-incidence elements as the front optics of the beamline gives much higher resistance to the damage by the fundamental laser beam. The photon handling made by mirrors with grazing-incidence broad-band coatings does not alter the temporal duration of the XUV pulse. Very small spot sizes can be achieved by using aspherical optics [6]. Also narrow-band multilayer-coated optics can be used at normal incidence to focus the XUV radiation in the experimental chamber. The operation at normal incidence minimizes the aberrations, then gives a smaller spot size [7, 8]. Depending on the experiment, the design of the beamline may require either the use of all-grazing-incidence elements or a proper combination of grazing-incidence optics to transport the radiation and normal-incidence optics to focus the beam.

Experiments on surface science require usually a monochromatized beam. The ideal monochromator for high-order harmonics should fulfill the following requirements: high transmission, tunability in the whole XUV range, no alteration of the pulse duration beyond the Fourier limit. This is crucial in order to have both high temporal resolution and high peak power. The simplest way to obtain the spectral selection with very modest time broadening is the use of a multilayer-coated mirror at normal incidence, which alters the pulse time duration up

to fractions of femtosecond and is moreover very efficient: in fact, the functions of selecting the harmonic and focusing it can be provided by a single concave optics, maximizing then the flux [7, 8]. The main drawback of the use of multilayer optics is the necessity of many different mirrors to have the tunability on a broad spectral region as the whole harmonic spectrum below 40 nm. The spectral selection can also be accomplished by an ordinary diffraction grating. In this case, the major mechanism that alters the time duration of the pulse is the difference in the lengths of the optical paths of the rays diffracted by different grating grooves. In fact, a single grating gives inevitably a time broadening of the ultrafast pulse because of the diffraction: the total difference in the optical paths of the rays diffracted at first order by N grooves illuminated by radiation at wavelength λ is Nλ. This effect is negligible in the picoseconds or longer scale, but is evident in the femtosecond scale. Let us consider a 200 gr/mm grating illuminated by radiation at 20 nm over a length of 10 mm; the total number of grooves involved in the diffraction is 2000, corresponding to a maximum delay in the first diffracted order of 40 μm, i.e., ≈ 130 fs. In case of an ultrashort pulse, this reduces dramatically both the time resolution capability and the peak intensity at the exit of the monochromator. Nevertheless, it is possible to realize time-delay compensated monochromators that do not alter the temporal duration of the ultrafast pulse in the femtosecond scale by using at least two gratings in a subtractive configuration: the second grating compensates for the temporal and spectral spread introduced by the first one [9, 10]. Such a configuration has been shown to be able to deliver intense output pulses in the few-femtoseconds time scale [11, 12]. The main drawbacks of using two- grating configurations are the lower efficiency of the monochromator with respect to the single-grating design and the higher complexity of the instrument. The choice between the single-grating or double-grating design has to be done as a trade-off process depending on the requirements from the users in terms of temporal resolution, tenability, spectral resolution and throughput.

Specifications of temporal diagnostics

Temporal diagnostics is a central issue for attosecond pulses as it is the ultra-short duration of these pulses that make them unique with respect to other XUV/x-ray sources. Most of the applications of the source to be developed target the study of ultrafast dynamics in all states of matter. It is thus essential to be able to accurately characterize the temporal properties of the pulses to be used, i.e., to be able to measure both the temporal pulse coherence as well as the pulse duration if not the temporal pulse profile.

Pulse duration – temporal profile measurements

For the measurement of the duration or the temporal profile of the pulses two basic approaches have been so far successfully implemented. The first relies on non-linear autocorrelation measurements, utilizing the recently developed non-linear XUV volume autocorrelator [13]. The approach has been so far implemented in both the intensity as well as in interferometric mode [14]. Furthermore frequency resolved non-linear autocorrelation measurements, already demonstrated for individual harmonics [15] as well as for harmonic superpositions [16], may be used for the retrieval of spectral phase distributions, which in combination with measured spectral amplitude distributions will give accurate temporal profiles of the pulses. Iterative approaches like those used in the FROG technique [17] may automate the procedure. Second order autocorrelation measurements have been recently implemented also at the FLASH free electron laser facility [18].

One of the obstacles that the non-linear autocorrelation method faces is the appropriate non-linear process it utilizes. So far a two-XUV-photon ionization of atoms has been the process to be used. Two-XUV-photon single ionization of helium was successfully employed for the characterization of XUV radiation up to the 15^{th} harmonic of the Ti:Sapph laser (23 eV). For shorter wavelengths two- photon direct double ionization or three-photon sequential ionization of He can be used. Two-photon direct double ionization has been observed in Kr, Ar and He using

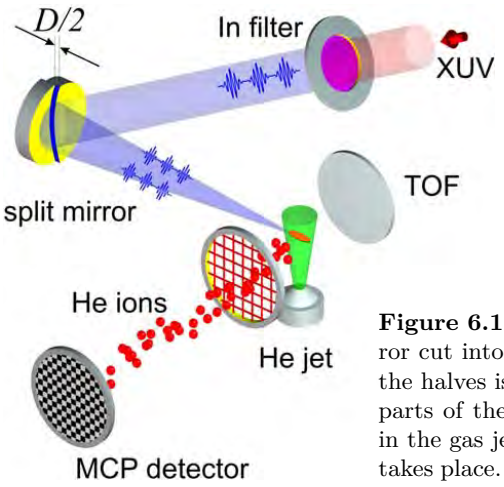

Figure 6.15: The wavefront splitting device. A gold spherical mirror cut into two halves is used to focus the XUV radiation. One of the halves is translated by a piezo-crystal translation unit. The two parts of the bisected XUV pulse are brought into a common focus in the gas jet produced by a nozzle where the non-linear interaction takes place. The ionization products are analysed by a time-of-flight (TOF) spectrometer.

harmonics [19,20] while three photon sequential ionization of He was used at FLASH in a second order autocorrelation measurement [18]. An alternative process is the two-photon ATI process with a higher in general cross section as the direct double ionization, but with the drawback of mandatory electron detection. For shorter wavelengths two photon multiple ionization (triple, etc.) will have to be employed, while in the soft x-ray region non-linear inner shell ionization is a possible candidate. The later is a fully unexplored research area that will be investigated once appropriate radiation specifications will be available. One crucial parameter is the pulse duration. For pulses with duration of some tens of fs non-linear inner shell ionization will always be obscured through outer shell ionization. In the attosecond regime and at intensities 10^{15}–10^{16} W/cm^2 the two-photon inner shell ionization has been estimated to become the dominant ionization process, before ionization saturation sets in, for specific atomic targets. It should be noted that this field is an active research field, reach in scientific and technological challenges, in which many new developments and breakthroughs are due. A second serious difficulty is the lack of beam splitters for the non-linear autocorrelator. A solution to this problem is the non-linear volume autocorrelator technique and its modifications that has been successfully used in pulse duration measurements of attosecond pulse trains, of individual harmonics and pulses of the FLASH FEL. The initial prototype is depicted in Fig. 6.15.

A wavefront splitting arrangement [13] consisting of a gold spherical mirror cut into two halves is used to focus the XUV radiation. One of these halves is mounted on a piezo-crystal translation unit and its positioning can be controlled with a resolution of 5 nm. The two parts of the bisected XUV pulse are brought into a common focus in the gas jet produced by a nozzle where the two photon absorption occurs. The ionization products are analysed by a time of-flight (TOF) ion mass- or electron spectrometer and detected by a micro-channel plate (MCP) detector. For the second-order AC, the ionization products are detected as a function of the delay corresponding to a total displacement D (twice the actual separation) between the two half mirrors. The focal spot produced by the split mirror exhibits an intricate pattern as a function of the relative displacement, but at a displacement of multiples of $\lambda/2$ the well-known Airy pattern is divided into two equal spots, each one having about half the maximum intensity. The pattern has been calculated for the fundamental frequency and it is shown for three displacements in Fig. 6.17 along with two measured one (insets) using the fundamental laser frequency. The double spot shape is used prior to an experimental run to adjust the orientation of the movable half of the mirror and position the fine travel in the middle of the extent of the laser pulse where the intensity is maximum. In addition, it provides the means of positioning the laser

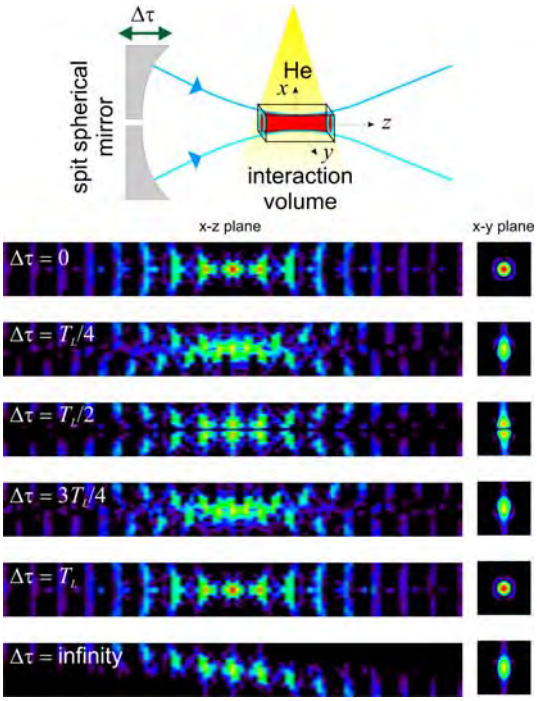

Figure 6.16: Three dimensional colour contours depicting in logarithmic scale over three decades the calculated intensity distribution at the interaction region of the volume autocorrelator for the indicated delays corresponding to a given mirror displacement. In the x-y plane, the Airy spot for zero delay becomes a double maximum distribution for $T_L/2$ delay corresponding to $D = \lambda/2$ displacement (T_L is the period of the laser. From P. Tzallas *et al*, J. of Mod. Opt. **52**, 321 (2005).

beam centrally within the spherical mirror aperture by adjusting the two spots to exhibit the same brightness. This ensures a 50% splitting of the incident laser beam. In case of a harmonic composition consisting of four harmonics with equal amplitude (7th, 9th, 11th, and 13th) the pattern becomes more complex and for various delays between the two halves of the split mirror is shown in Fig. 6.16. The second order autocorrelation approach can be further developed to be carried out in an energy resolved mode by using energy resolved electron detection instead of ion detection. In this case a FROG type retrieval of spectral phase and amplitude distributions is achievable and hence reconstruction of the pulse temporal profile is possible.

The second basic approach relies on a cross-correlation of the XUV/X-ray with the IR driving field. Attosecond streaking, RABITT or CRAB-FROG are versions of this basic approach. In the following will be discussed the Attosecond streak camera version of the cross correlation approach. In electron-optical chronoscopy realized by image-tube streak cameras, an electron "replica" of a light pulse, generated when the latter impinges on a photosensitive cathode, is deflected by a controlled electric field that projects its temporal structure on a screen. These techniques have permitted accurate characterization of sub-picosecond light pulses. Recently the extension of these ideas into the attosecond regime has been possible [22–24] by applying a key modification; the electric field of a laser pulse is used to streak electrons that are released within a small fraction its oscillation ($T_{laser} \sim 2.5$ fs) (Fig. 6.18a).

The field is applied along the direction of motion of the detected electrons and therefore does not result in deflection but rather in modification of their final kinetic energy. This capability renders possible the projection of the initial time-momentum distribution of the electron emission onto a series of different final (accurately measurable) momentum distributions. The idea, in its

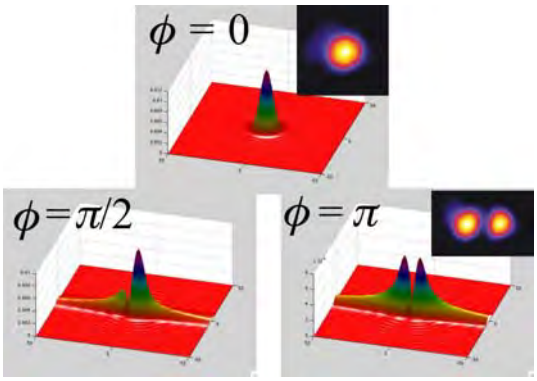

Figure 6.17: Calculated IR intensity distribution at the interaction region of the volume autocorrelator for three different displacements introducing o $\pi/2$ and π phase differences between the two wavefronts. The insets are measured images. From O. Faucher *et al.* Appl. Phys. B **97**, 505 (2009).

most generic case, where primary (photoionization) and secondary electron emission (e.g. Auger decay) can be temporally resolved is illustrated in Fig. 6.18b.

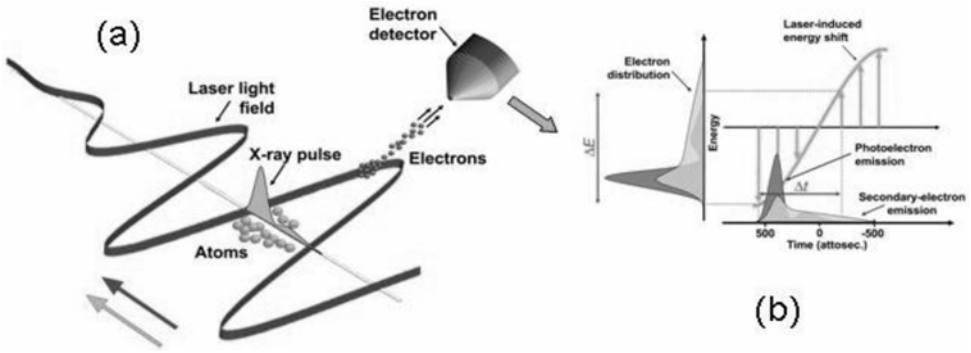

Figure 6.18: The Atomic Streak camera principle (a) Impulsive ionization of atoms by an XUV pulse releases its electron replica into a laser field. (b) Electrons detected along the laser polarization vector, suffer a strong transient shift of their momentum. A systematic variation of the timing of the electron release with respect to the laser streaking field, allows mapping of an initial time-momentum distribution onto a series of different final momentum distributions.

In its simplest incarnation, the technique can be used to characterize attosecond XUV pulses by interrogating the temporal structure of an electron replica that is generated by impulsive ionization of atoms, in the presence of the streaking field. Spectra accumulated at different delay settings between the streaking field and the attosecond pulse, can be put together to compose a spectrogram that resembles closely those generated in nonlinear pulse metrology techniques line.

Frequency Resolved Optical Gating (FROG) [25]. Here the electric field of light to provide a phase gate [26, 27]. Such an experimental spectrogram is shown in Fig. 6.19. Retrieval of the pulse can be realized utilizing reconstruction techniques developed over the last decades and that have been adapted to account for attosecond resolution. Reconstruction is not only possible for the attosecond pulse but for the gate (laser pulse) at the same time. In the latter case the attosecond pulse has the role of a sub-femtosecond sampler that tracks the oscillation of light waves (2). Figure 6.19 shows a measured and reconstructed spectrogram of a sub-100

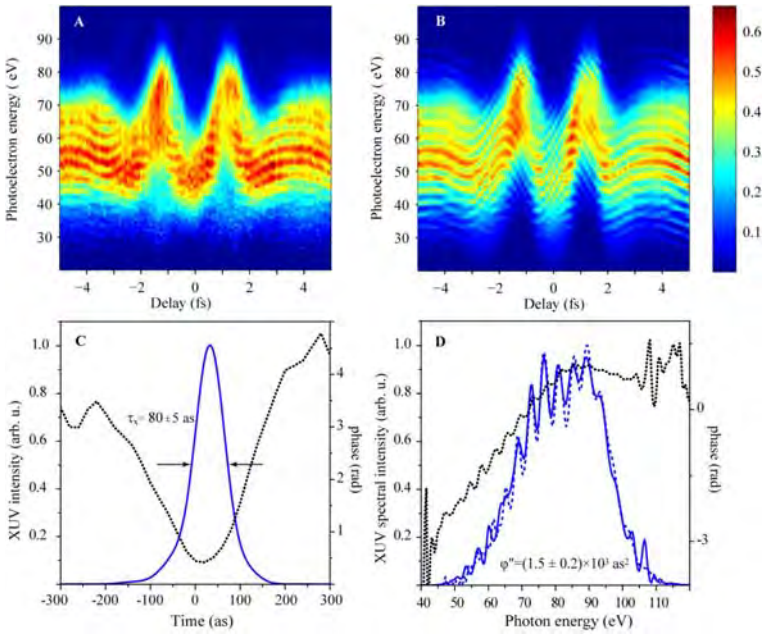

Figure 6.19: Characterization of sub-100 as soft x-ray pulses with the atomic streak camera technique From E. Goulielmakis *et al.*, Science **320**, 1614 (2008).

as soft x-ray and the temporal characteristics of the retrieved pulse [28].

As for the implementation of the technique and its specifications, Fig. 6.20 shows the experimental apparatus of an attosecond streak camera currently part of the AS-1 attosecond beamline in Garching. Laser pulses and attosecond pulses are focused into a gas (Ne or other noble gas) target by a double mirror assembly installed ~ 1.5 m downstream the source of the attosecond pulses. The inner part of the assembly is a multilayer mirror with $> 10\%$ reflectivity over several tens of eV bandwidth and therefore allows for the generation of pulses down to the sub-100 asec scale. The delay between the XUV and the laser pulse can be adjusted with high accuracy (better than 30 asec) using a piezo translational stage. Electron spectra will be recorded by a time of flight detector (TOF resolution > 0.5 eV) that collects electrons that are emitted along the direction of the laser polarization vector (see Fig. 6.18). The apparatus needs to be installed in a vacuum chamber with better than 10^{-6} Torr background pressure. Other diagnostics to be combined with this apparatus are discussed in other sections of this proposal.

To serve the key goals of the infrastructure, the proposed apparatus will be used for the characterization of attosecond pulses in the 30–150 eV energy range and with durations from 1 fs to 50 asec. The reflectivity and the central energy of modern multilayer mirrors (key component for this apparatus) can be tuned to a considerable extend and permit the applicability of the attosecond streak camera technique over a broad range of energies. The operation of the streak camera has been already tested in the lower energy regime 30 eV [24] as well as at the high energy 80–100 eV [23]. The technique requires laser pulses at kilohertz repetition rates and field reproducible waveforms from pulse to pulse. The apparatus can be realized to have a footprint <1 m^2 and therefore it can serve as a transportable diagnostic to different experimental areas of the infrastructure where characterization of attosecond pulses will be necessary. Between the two main approaches, i.e., XUV/x-ray autocorrelation and XUV/x-ray – IR cross correlation there has not been so far comparative studies. This is because the specifications of the so far operating attosecond sources do not allow a direct comparison. At the FLASH free electron facility both

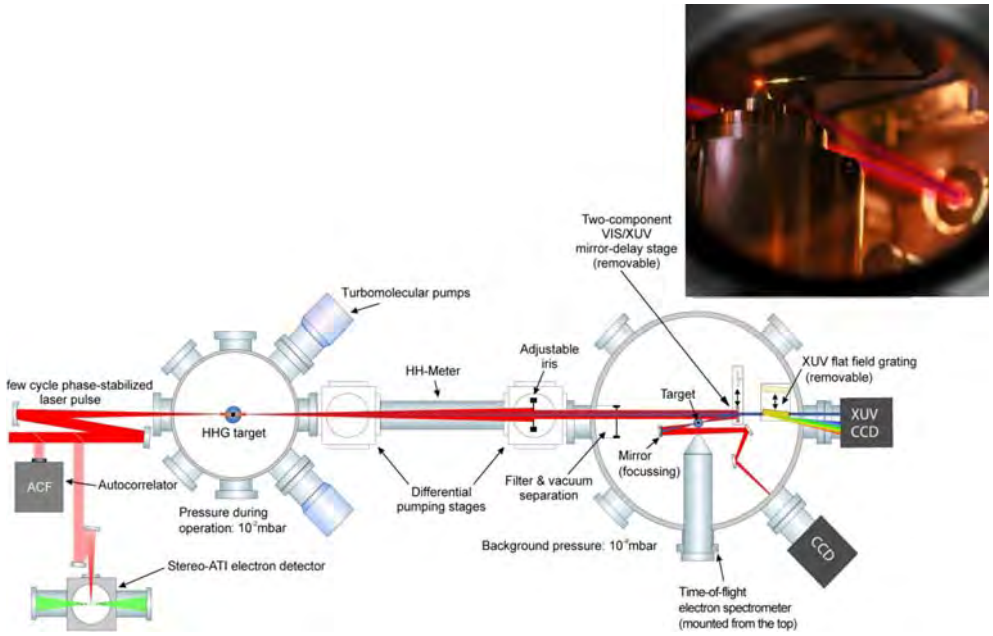

Figure 6.20: Attosecond streak camera apparatus in MPQ Garching (AS-1 beamline). Inset artistic representation of the two beams (red) laser pulses and (blue) the attosecond pulse, are focused by a two mirror assembly onto an atomic cloud emerging from a gas orifice.

approaches have been recently implemented giving similar results. The specifications of the attosecond science secondary source of the ELI will allow for such comparisons, while current developments in laser technology in some European laboratories may allow comparative studies prior to the operation of the ELI.

Since the estimated pulse duration in the attosecond science secondary source of the ELI ranges from 5 to 100 asec and the spectral range spans from 10 eV to 1 keV ulta-high accuracy positioning and translation stages, as well as ultra-high performance reflective or refractive optical elements are mandatory. To give some examples, the measurement of 50–100 asec long pulses requires a temporal resolution of at least 10 asec which translates to a translational step of 3 nm and mechanical decoupling from the environment that allows positioning stability better than 1 nm. The measurement of 5 asec duration requires sub asec temporal resolution which corresponds to optical paths of the order of 1 Å. Even for one order of magnitude higher translation steps at grazing incidence geometries this measurement becomes a technological challenge.

An important recent development in the attosecond pulse diagnostic area is the comparative study between the 2^{nd} order IVAC and the RABITT technique performed at FORTH-IESL for a superposition of gas harmonics 7^{th} -15^{th} (J. Kruse *et al.,* Phys. Rev. A **82**, 021402(R) (2010). The two techniques have produced diverging results. RABITT yielded attosecond beating in all three investigated focusing (phase matching) conditions, namely when the laser beam was focused before, at and after the gas jet. The 2^{nd} order IVAC in agreement with theory has produced attosecond beating only when the focus was before the gas jet. For the focus before the gas jet case the RABITT method resulted in pulse duration by a factor of two shorter than the one measured by the 2^{nd} order IVAC technique (J. Kruse *et al.,* Phys. Rev. A **82**, 021402(R) (2010). Similar but less pronounced behavior was found also for the cut off region. These results suggest that the metrology part of attosecond pulses is far from mature. Further

comparative studies are absolutely necessary in other wavelength regions and between all the temporal characterization techniques in order ELI to be able to provide reliable specs to its future users.

Temporal coherence

Temporal coherence can be determined by simply measuring the spectrum with well calibrated instrumentation for both the photon energy and the transmitted photon number per unit photon energy. The spectral coherence can then be extracted by an inverse Fourier transform of the corrected spectral amplitude distribution. An alternative and more direct approach is to perform a first order autocorrelation measurement of the pulse using flat spectral response or spectral throughput elements [29] or well calibrated elements so that corrections on the measured traces can be made. The attosecond radiation of the source will spectrally cover a wavelength range between 1 and 100 nm. For the temporal coherence measurements translation steps of the order of 1/10 of the central wavelength will be required, which for the XUV region is tractable. For the x-ray region the required sub-1 nm translational can be partially overcome in grazing incidence geometries where the spatial delay to be introduced is achieved by a translational movement of the optical component longer by a factor that depending on the incidence angle may reach a value of 10. Since this is still at the limit, the x-ray temporal coherence will easier be measured indirectly by measuring the spectrum.

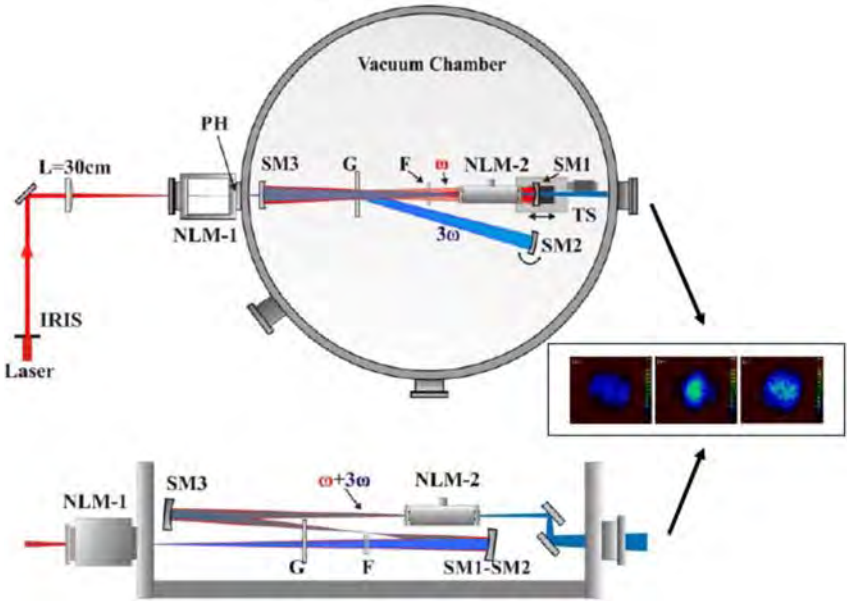

Figure 6.21: The grating auto- cross-corralator workstation of FORTH-IESL. A transmission grating splits the beam into the different diffraction orders. Beams are reflected back to and recombined at the grating. The device is almost dispersionless down to few attoseconds. From E. Papalazarou *et al.*, Phys. Rev. Lett. **96**, 163901 (2006).

Other relevant to temporal diagnostics beam steering and manipulation devices.

One of the chief obstacles in XUV beam steering and manipulation is the lack of XUV beam splitters. Beam splitters are indispensable elements for a number of operations, such us beam decoupling and recombining, autocorrelation and cross-correlation, interferometry. A versatile

component for all such devices is a free standing grating. The targeted splitting-recombining operation is occurring through diffraction into the different diffraction orders. The thus spatially dispersed radiation can be manipulated e.g. filtered, partially blocked, redirected, delayed, focused prior to be spatially "re-compressed". Transmission gratings have been exploited at FORTH-IESL (E. Goulielmakis *et al.*, Appl. Phys. B **74**, 197 (2002)) in auto- and cross-correlators performing 2^{nd} order autocorrelation measurements (N.A. Papadogiannis *et al.*, Opt. Lett. **27**, 1561 (2002)) and cross-correlation of low harmonics with IR radiation allowing full reconstruction of the harmonic waveforms (see E. Papalazarou *et al.*, Phys. Rev. Lett. **96**, 163901 (2006); P. Tzallas *et al.*, New J. of Phys. **9**, 232, (2007)). The auto- cross-correlator workstation of FORTH-IESL is depicted in Fig. 6.21. The set up can be further used as color separator and two or many color delay device for pump probe experiments.

Design for photon diagnostics

Some of the solutions presented in the previous paragraph are here briefly discussed in terms of optical and technical design.

6.1.4 Measurement of the spectrum

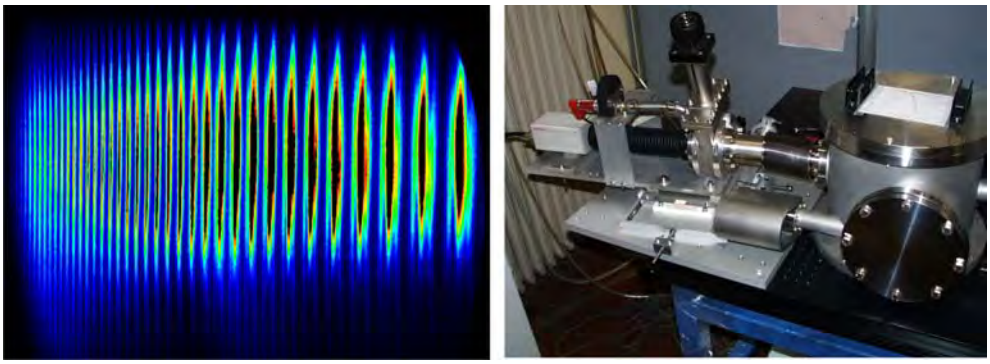

Figure 6.22: Left: high-order harmonic spectrum in Ne with sub-10 fs laser pulse, 6 to 35 nm; the wavelengths vary along the horizontal axis, the spatial distribution is displaced along the vertical axis. Right: picture of a flat-field spectrometer with MCP-based detector.

The XUV spectrum is usually measured by a grazing-incidence flat-field spectrometer. The flat field is achieved through the use of variable-line-spaced (VLS) gratings that disperse the spectrum on a flat surface where a 2D detector acquires the spectrum simultaneously. Either single- or multiple-shot acquisitions are possible. In addition, the use of a flat-field spectrometer gives simultaneously a measurement of the spectrum and of the divergence of the source. An example of a typical acquisition with a flat-field spectrometer is shown in Fig. 6.22 [1].

The use of VLS gratings allows also the in-line measurement of the spectrum. This solution is being realized in FEL facilities and can be considered also for some applications in high-order harmonics facilities [4]. The spectrum is measured by a grazing-incidence flat-field spectrometer equipped with a VLS plane grating. The polynomial law of variation of the groove density along the grating surface is selected to focus the diffracted radiation on an almost flat surface, where a plane detector acquires the spectrum. Since the length of the spectral curve is larger than the detector size, the latter is mounted on a linear stage and moved in the desired position to acquire the spectral interval of interest. At the grating plane, the radiation reflected at zero-order propagates unperturbed to the following sections, so no phase modifications on the ultrashort

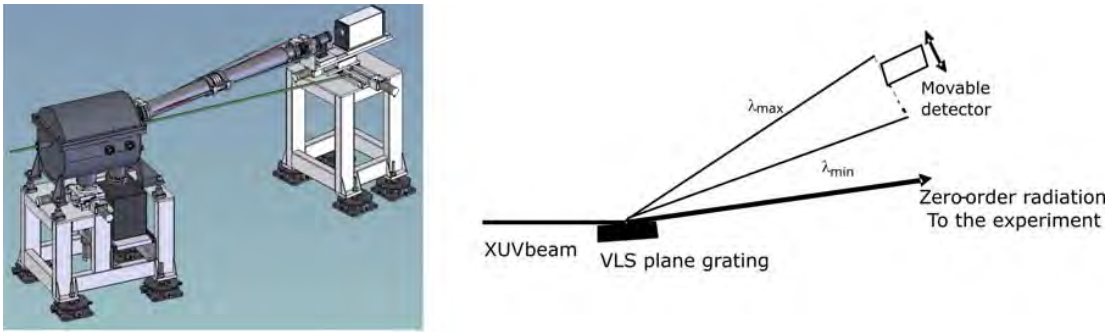

Figure 6.23: Left: schematic of the on-line spectrometer. Right: design of the on-line spectrometer for the FEL FERMI@ELETTRA (Trieste, Italy).

pulse are expected, but only a small decrease in intensity of the light that is transmitted ($\approx$ 85–90%) due to diffraction. A schematic of the concept is shown in Fig. 6.23.

6.1.5 On-line measurement of the intensity

It will be here briefly discussed a method to measure on-line the intensity of the XUV pulse, already used at the FEL FLASH facility in Hamburg [1, 5]. It consists of a gas ionization detector, i.e., an absolutely calibrated detector based on photoionisation of noble gases at a low target density and the detection of photoions and photoelectrons. The number of electrons/ions generated is proportional to the number of photons, to the target density, to the photoionisation cross section and to the length of the interaction volume. A schematic of the system adopted at the FLASH facility is shown in Fig. 6.24. This method has many advantages for the intensity measurement of ultrashort XUV pulses: 1) it is almost transparent to the beam and does not alter the beam properties; 2) it has a wide dynamic range; 3) it is independent from the beam position; 4) it has no saturation effects; 5) it can be absolutely calibrated within $\approx$ 10%.

Beam separator

Several methods to separate the IR laser beam from the XUV radiation have been proposed and realized: among them we can cite the use of a thin metal foil and the annular pumping beam geometry [31]. However, these methods do not perfectly satisfy the requirements indicated in the specifications section. For example, a thin metal foil consisting of a foil with thickness of few hundred nanometers deposited on a mesh is conventionally used as beam separator. The most used materials are aluminum, zirconium and palladium. Since the damage threshold is quite low, this method can be applied only for low-intensity pulses. In the case of the annular beam geometry, the center of the pump pulse is blocked before the focusing region creating a doughnut-shaped beam. After the focusing stage an aperture placed across the pump beam's axis blocks only the pump pulse and allows the HHs beam to pass through its center. However, some of the pump energy is still transmitted through the aperture because of diffraction at the edge of the beam blocker. Furthermore, a considerable portion of the pump energy is lost before focusing.

It has been recently demonstrated that high-throughput and high-damage-threshold beam separators can be realized by using two plane plates set at the Brewster angle with respect to the pump wavelength [32, 33]. The XUV light is reflected toward the experiment, while the IR pump pulse, that is linearly polarized, is attenuated. Both silicon plates and niobium nitride films have been used for XUV wavelengths respectively above 30 nm and between 10 and 30 nm. The beam splitters have been proved to have a damage threshold of at least 0.8 TW/cm^2 for

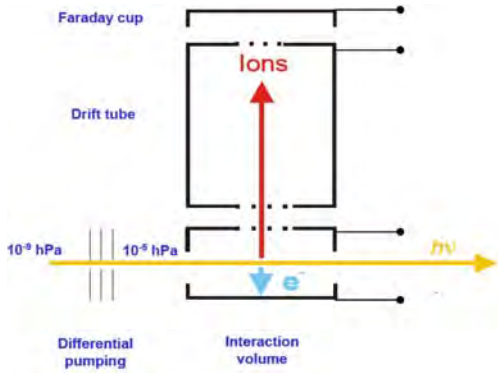

Figure 6.24: Schematic of the gas ionization detector adopted at FLASH (see TDR of the European XFEL).The device can be absolutely calibrated using synchrotron radiation at low photon intensities. The detector is typically operated with either nitrogen or a rare gas at low pressures of typically 10^{-5}–10^{-6} mbar.

a 30-fs pump pulse. The two-plate design is simple to be aligned, can be operated on a broad spectral region with high throughput and does not alter the phase of the XUV pulse. In addition, antireflection-coated mirrors especially designed to reject 800 nm Ti:Sa laser emission working at grazing incidence can be actually produced. They can be operated at 5°–6° grazing incidence and then have rather good reflectivity for radiation down to ≈ 6 nm.

As an alternative method for a beam separator able to work down to the water window, we can cite the use of two plane gratings [34]. The first grating acts as the beam separator: it diffracts the XUV light into the first order while reflects the visible and near-IR light into the zero order that can be stopped after the grating by a suitable light trap. The diffracted light goes on a second grating that is operated in a time-delay compensated configuration. The system can be designed for any wavelength in the 3–40 nm XUV region and is suitable to work at high laser energies. Unfortunately, it modifies the phase of the ultrashort pulse and can be used only for few-femtosecond narrow-band pulses. However, it is simple, tunable in a broad interval and efficient.

Monochromators

Some possible designs of monochromators for ultrashort pulses are discussed here.

i. Multilayer-based monochromators.

The simplest way to obtain the spectral selection of ultrashort pulses with very modest time broadening is the use of a single multilayer-coated mirror operated in normal incidence. The choice of the type of multilayer can be made among many couple of materials (i.e. the spacer and the absorber) to optimize the response in a given spectral region from the extreme vacuum ultraviolet down to the water window. The single-mirror configuration gives high throughput and high quality of the focal spot size because of the normal incidence operation [34, 35]. The main drawback of the single-mirror configuration is the lack of tunability, then the necessity of many different multilayers to work on a broad spectral region. As an alternative, tunable monochromators with two plane multilayer-coated mirrors have been proposed, with a design similar to double-crystal monochromators already used for synchrotron radiation [37]. A schematic of the configuration is shown in Fig. 6.25.

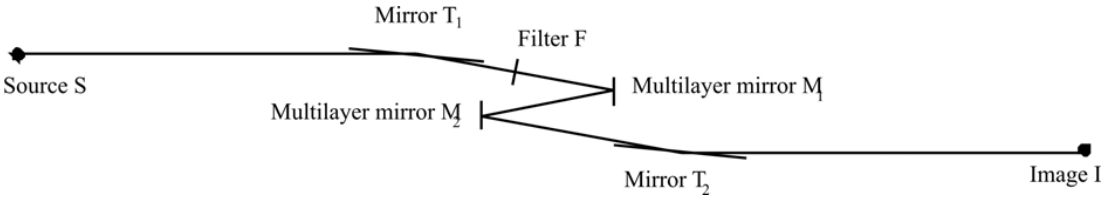

Figure 6.25: Schematic of a tunable monochromator with multilayer-coated optics. The tunability is achieved through a rotation of the plane mirrors and a linear translation of one of these.

ii. Single-grating monochromators.

If the users require high throughput and output pulses in the several femtosecond temporal scale, a single-grating design can be adopted. Recently, a new configuration for single-grating monochromators with minimum temporal broadening for ultrashort pulses has been introduced [38]. Strictly speaking this is not a time-delay compensated instrument; anyway the temporal broadening can be maintained in the 5–20 fs scale. The design adopts gratings in the off-plane geometry with low resolution (as that required for high-order harmonics), high efficiency and tunability in a broad spectral region, ranging from 5 to 70 nm. An example of such a monochromator is shown in Fig. 6.26.

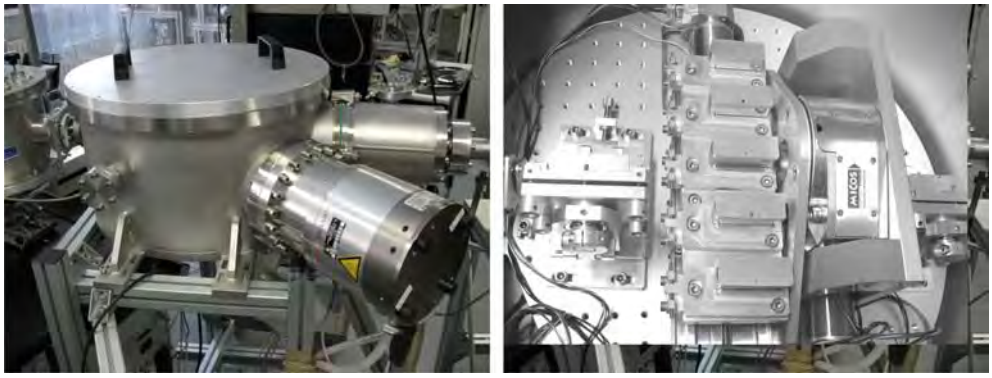

Figure 6.26: Grazing-incidence monochromator for high-order harmonics with gratings in the off-plane mount (presently at Rutherford Lab., UK). Left: external view of the instrument. Right: internal view of the optics.

iii. Time-delay compensated grating monochromators.

A single grating used to diffract the radiation gives inevitably a broadening of the ultrashort pulse because of diffraction. Nevertheless, it is possible to design grating monochromators that do not alter the duration of the pulse by using two gratings in a compensated configuration: the second grating compensates for the time and spectral spread introduced by the first one [9]. From the point of view of the ray paths, two are the conditions that the design must comply: 1) the differences that are caused by the first grating in the path lengths of rays with the same wavelength but with different entrance directions within the beam aperture must be compensated by the second grating, and 2) two rays at different wavelengths within the spectrum of the pulse to be selected have to be focused on the same point, i.e., the global spectral dispersion has to be zero. Both these conditions are satisfied by a scheme with two equal concave gratings mounted with opposite diffraction orders: the incidence angle on the second grating is equal to

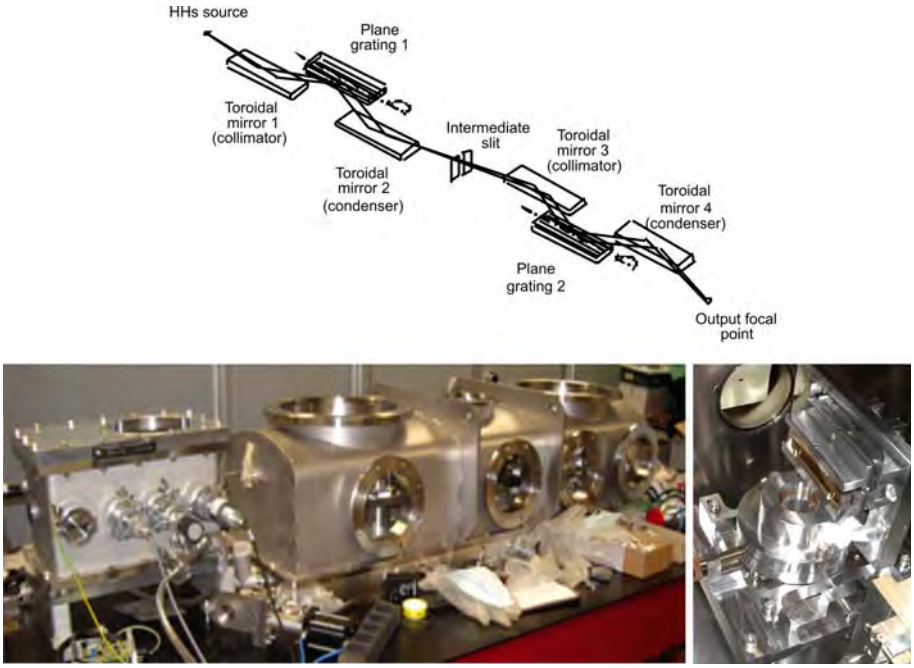

Figure 6.27: Time-delay compensated monochromator for high-order harmonics. Left: schematic of the configuration. Right: pictures of the instrument (presently at Politecnico Milano). From L. Poletto *et al.*, Appl. Opt. 45, 8577 (2006).

the diffraction angle of the first grating. The spectral selection is performed by a slit placed in an intermediate position between the gratings, where the radiation is focused after the diffraction from the first grating. This design has been recently extended to grazing-incidence configurations with plane gratings in the off-plane mount [10]. A time-delay compensated monochromator has been realized with high efficiency (18% at 30 nm) and tunability in the whole 15–60 nm region [11,12]. Output pulses of 7 fs have been measured at 35 nm [39]. Schematic and pictures of the instrument are shown in Fig. 6.27.

Design of temporal diagnostics

Different optimized set ups for the temporal diagnostics can be designed for the different wavelength regions for both the cross- and auto-correlation approaches. Three main wavelength ranges have to be considered: I) For long wavelengths in the range 50–160 nm Si wafers and close to normal incidence on metal coatings may be used. II) For wavelengths between 12 and 50 nm multilayer coatings can be used in normal incidence geometries, while III) for wavelengths between 2 and 20 nm grazing incidence on metal-coatings will be required and thus large dimension optics. However, novel more versatile designs, common for all three wavelengths regions, with close to optimal performance will be considered at the new source.

Temporal characterization through non-linear autocorrelation based approaches

Second order autocorrelation measurements in the ranges I) and II) can be performed using the classical set-up of Fig. 6.28 and gold coated or multilayer mirrors. At the high XUV photon fluxes of the new source this would be possible although the near normal incidence that is used in this arrangement substantially reduces the reflected photon flux. An alternative autocorrelator arrangement, based on grazing incidence reflection is illustrated in Fig. 6.28. It may be

introduced in the XUV/x-ray beam after removal of the IR radiation. Note that in Fig. 6.28 not grazing incidence angles are shown just for better visibility.

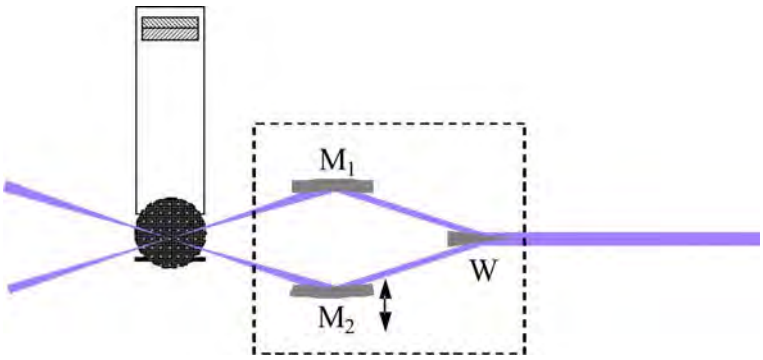

Figure 6.28: Second order autocorrelation set up. The wedge W splits the beam while the Parabolic Mirrors M_1 and M_2 bring the two beams to overlap in the interaction with the gas region. Variable delay is through the translation of M_2. Due to the grazing incidence the required step of the mirror translation is 10–30 times larger than the introduce delay path length. The overlapped beams two-photon ionize a gaseous medium and ions or electrons are detected with a TOF spectrometer (Design by FORTH-IESL).

As discussed below even unfocused beams would have sufficient intensities in order to safely perform a second order autocorrelation. The use of focused beams (parabolic instead of flat mirrors) here is because a sufficiently high contrast of a volume intensity autocorrelation trace requires small angle between the two beams and a focus in which the interference of diffraction limited beams form, depending on the delay, one or two, and not more, spatial fringes. Grazing incidence angles will ensure high throughput for all wavelength regions and are also required for the single shot operation described below.

An advanced version of the above arrangement can be used for long pulses, i.e., pulse duration of the order of 100 asec as a single shot autocorrelator without moving elements and utilizing flat instead parabolic mirrors. The principle is exactly the same as that of optical wavelength single shot second order autocorrelators. Instead of imaging the second harmonic profile onto the detector, the ionization pattern (ion spatial distribution) at the interaction volume has to be imaged onto the detector. Due to the high photon flux available in the new source, non focusing optical elements can now be used at grazing incidence angles. The imaging device, e.g. an ion-microscope, depicted with the dash cycle in Fig. 6.29 must now observe the plane defined by the two propagating beams. The required spatial resolution depends on the duration of the pulse and the angle between the two crossing beams. The width D of the ion distribution to be imaged is given by $D = 2d\frac{\cos(\varphi/2)}{\sin\varphi}$, d being the spatial width of the pulse and φ the crossing angle of the two beams. For a 30 nm wide pulse (100 asec), $\varphi = 4^\circ$ and 1 cm beam cross section, a $\sim$60 cm long, 2° wedge, 30 cm large mirrors will be required and the spatial width of the ion distribution at the interaction region would become $\sim$1000 nm. Thus the minimum required spatial resolution of the imaging device is $\sim$ 0.5 μm, while a resolution of 100 nm would allow a reliable duration measurement.

To give some estimation relevant to the applicability of the method with respect to the available XUV intensities, let us consider the spectral range between 10 and 80 eV. An emission of 10^{16} photons per pulse and pulses of 80 asec duration has been estimated [40] which corresponds to a power of 1 PW. After attenuation by a factor of 10^1–10^2 (depending on the specific wavelength interval) at the suppression of the IR and the beam splitter/combiner set up the remaining power is 10^{14}–10^{15} W, which for a beam diameter of 1cm would result to

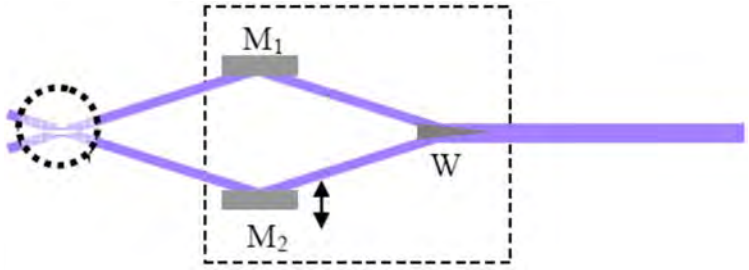

Figure 6.29: Single shot second order autocorrelation set up. The two flat Mirros M1 and M2 bring the two beams to overlap in the interaction with the gas region. Variable delay is through the translation of M2. The overlapped beams two-photon ionize a gaseous medium and ions are detected with an imaging ion-microscope depicted with the dash circle. (design by FORTH-IESL).

intensities of the order of 10^{14}–10^{15} W/cm^2. For the spectral region of 0.5–1 keV, according to the estimated photon numbers [40] the intensity at the overlap will be 10^{12}–10^{13} W/cm^2. At the 1 kHz repetition rate of the source these intensities will be sufficient for clean observation of a second order process and the recording of 2^{nd} order autocorrelation traces, given that even for low repetition rates (10 Hz) second order autocorrelation measurements have been performed at these or even lower intensities.

On line pulse duration measurements

The objective is a setup that will not affect the pulse to be characterized and the measured photoelectron spectra. For the non-linear autocorrelation based characterization part of the beam has to be decoupled and used for the characterization, without affecting the main beam.

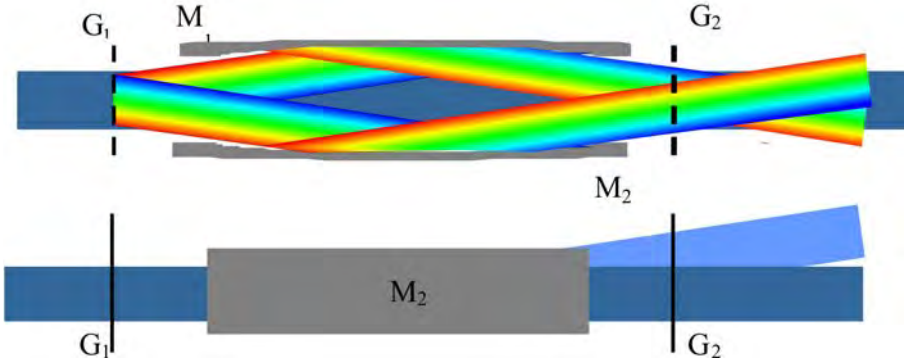

Figure 6.30: Top and side view of the decoupler–recombiner (design by FORTH-IESL).

This can be achieved through diffraction gratings. Since free standing transmission gratings have a constant spectral throughput for an extremely broad spectral range, a device utilizing such gratings will be considered here. The transmission gratings can be replaced by reflection ones dedicated to specific spectral regions. The decoupler–recombiner device as designed at FORTH-IESL is shown in Fig. 6.30. The grating G_1 disperses 10% of the incoming energy into the ± 1 order while the zero order diffracted beam continues propagating in the same direction. The ± 1 orders are impinging under grazing incidence the slightly tilted elliptical mirrors M_1 and M_2 and are reflected off plane. G_1 and G_2 are at the two foci of the ellipsoids so that G_1 is imaged on the G_2. Thus the system is dispersionless, apart from dispersion introduced

by the finite size of the beam. 10% of the ± 1 orders is first order diffracted by the G_2 and thus recombine propagating with a small off plane angle with respect to the main beam, the zero order diffraction of which at the G_2 maintains unaffected the initial propagation direction and may be used in the experiment. The splited and off plane propagating 1% of the beam energy can further be introduced into the non-linear autocorrelation device or into a device used for the characterization of the spatial or temporal coherence. Alternatively autocorrelation measurements can also be performed by translating one of the mirrors as in the similar set-up described in [41, 42]. The two additional outputs (zero order diffracted beams at G_2 of the ±1 order diffracted beams at the G_1, overlapped with the ±1 order diffracted beams at G_2 of the zero order diffracted beams at the G_1), also propagating off plane may be used for the spectral characterization of the radiation, simply by observing one of them on a position sensitive detector, as these beams are already spectrally dispersed.

Temporal coherence

The measurements of the temporal coherence is either indirectly through inverse Fourier transform of the spectrum measured as described in the previous section or in the section 6.1.3 or by performing a first order autocorrelation of the beam, i.e. using a linear ionization process instead of a non-linear one. The volume autocorrelator of Fig. 6.15 and 6.17 cannot be used for this purpose, unless the ion detection is spatially confined or the XUV/X-ray radiation power is detected with a linear diode. This is because the total energy in the interaction region does not depend on the delay between the two pulses and thus the spatially integrated signal is not modulated with the delay. The grating device shown in Fig. 6.30 can be straightforward used for a first order autocorrelation measurement by translating one of the mirrors. Single photon ionization of a gas induced by the spitted 1% of the beam can be detected as a function of the delay or the intensity of the radiation measured with a linear diode.

Bibliography

[1] R. Treusch, in HASYLAB Annual Report 2005, DESY (2005).
[2] L. Poletto et al., Rev. Sci. Inst. 75, 4413 (2004).
[3] L. Poletto et al., Opt. Eng. 40, 178 (2001).
[4] R. Reininger et al., AIP Conf. Proc. 705, 572 (2004).
[5] K. Tiedke, in HASYLAB Annual Report 2003, DESY (2003).
[6] H. Mashiko et al., Appl. Opt. 45, 573 (2006).
[7] M. Wieland et al., Appl. Phys. Lett. 81, 2520 (2002).
[8] H. Mashiko et al., Opt. Lett. 29, 1927 (2004).
[9] P. Villoresi, Appl. Opt. 38, 6040 (1999).
[10] L. Poletto, Appl. Phys. B 78, 1013 (2004).
[11] M. Pascolini et al., Appl. Opt. 45, 3253 (2006).
[12] L. Poletto et al., Appl. Opt. 45, 8577 (2006).
[13] P. Tzallas et al., Nature **426**, 267 (2003).
[14] P. Tzallas et al., J. of Mod. Opt. **52**, 321 (2005).
[15] Y. Nabekawa et al., Phys. Rev. Lett. **97**, 153904 (2006).
[16] T. Sekikawa et al., Phys. Rev. Lett. **83**, 2564 (1999).
[17] Y. Nabekawa et al., Phys. Rev. Lett. **96**, 083901 (2006).
[18] R. Trebino et al., Rev. Sci. Instrum. **68**, 3277 (1997).
[19] H. Zacharias et al., (private communication).
[20] T. Sekikawa, Phys. Rev. Lett. **83**, 2564 (1999).
[21] E. P. Benis et al., Phys. Rev. A **74**, 051402 (R) (2006).
[22] O. Faucher et al., Appl. Phys. B **97**, 505 (2009).
[23] R. Kienberger et al., Nature **427**, 817 (2004).

[24] E. Goulielmakis et al., Science **305,** 1267 (2004).
[25] G. Sansone et al., Science **314**, 443 (2006).
[26] R. Trebino and D. Kane, JOSA B, 1101 (1993).
[27] Y. Mairesse, F. Quere, Phys. Rev. A **71**, 011401(R) (2005).
[28] J. Gagnon et al., App. Phys. B **92**, 25 (2008).
[29] E. Goulielmakis et al., Science **320**, 1614 (2008).
[30] E. Papalazarou et al., Phys. Rev. Lett. **96**, 163901 (2006).
[31] P. Tzallas et al., New J. Phys. **9**, 232, (2007).
[32] R. Reininger et al., AIP Conf. Proc. **705**, 572 (2004).
[33] J. Peatross et al., Opt. Lett. **19**, 942 (1994).
[34] E. Takahashi et al., Opt. Lett. 29, 507 (2004).
[35] Y. Nagata et al., Opt. Lett. 31, 1316 (2006).
[36] F. Frassetto et al., JOSA A 25, 1104 (2008).
[37] M. Wieland et al., Appl. Phys. Lett. 81, 2520 (2002).
[38] H. Mashiko et al., Opt. Lett. 29, 1927 (2004).
[39] L. Poletto et al., Pure Appl. Opt. 3, 374 (2001).
[40] F. Frassetto et al., in SPIE Proc. 7077 (2008).
[41] L. Poletto et al., Opt. Lett. 32, 2897 (2007).
[42] G.D. Tsakiris et al., New J. Phys. **8**, 19 (2006).
[43] E. Goulielmakis et al., Appl. Phys. B **74**, 197 (2002).
[44] N.A. Papadogiannis et al., Opt. Lett. **27**, 1561 (2002).

6.2 Charged Particle Beamlines

6.2.1 Electron beamlines

Introduction

The initial motivation for the development of Laser-wakefield-Accelerators or Laser-Plasma Accelerators (LPA's) was the possibility of using plasmas as a medium to sustain relativistically moving waves carrying a longitudinal electric field that could be around 1 GeV/cm i. e. three orders of magnitude higher than in state-of-the-art RF-based accelerators. Therefore, in certain circumstances, LPA's have the potential to accelerate particles in 1/1000 of the length when compared with a conventional electron source. A convincing demonstration of the possibilities of this technology [1–3] with the generation of mono-energetic electron bunches, was only possible after 25 years of the publication of the original idea [4]. This delay was mainly due to the unavailability of adequate laser sources. Since 2007 we have scaling laws for LPA's [5] and we can use them as a general receipt to design efficient LPA's. Nevertheless, there are many possibilities for the fine tuning of the those sources to be made by experimental and numeric research. In this chapter we follow these scaling laws to sketch an electron LPA program for ELI.

In the next 5–10 years we expect important developments on LPA's with many large research programs worldwide as well as the increasing interest by plasma acceleration techniques by the conventional accelerator and high-energy-Physics communities. Therefore this program should be designed and executed with flexibility and redundancy in mind for adaptation to the fast developments in progress.

Rational for an ELI based research program on Laser-Plasma Electron Accelerators

Different factors play an important role on the definition of a research program on laser-plasma electron beams for ELI: 1) the source is new, i. e. there are a limited experience on its operation, the tested applications are very reduced and a community of users is reduced or inexistent, 2) the spectrum of possible parameters is to wide to cover with in a reasonable size facility, 3) there will be a considerable delay until the production of the first laser pulses (2015), 4) there will be other important laser-plasma electron beam research programs with potential to duplicate a program designed for ELI, 5) presently, commercial lasers reaching the 100 TW level start to be common.

By taking these factors in consideration it seams advisable that a program for ELI should be based on: 1) development of applications of the laser-plasma electron beams and 2) development of electron sources and related technologies and applications for energies clearly above the commercial level (20 J or 1 PW).

A brief comparison should also be made with other particle acceleration techniques: RF based conventional technology and new particle based plasma accelerators. Both technologies rely on well-proved and efficient RF linear acceleration stages. On large machines, where high repetition ratio is required, the electric efficiency of the acceleration technology is a key parameter. Radio-frequency acceleration technology can achieve electrical efficiencies above 10%. However, High-Energy Physics is requiring particles with energies above 1 TeV and distances of several kilometers are required to produce those energies. Particle-Plasma Wakefield Acceleration (PWFA), an emergent technology, uses high-energy particle beams to produce acceleration structures in plasmas in a similar way as in LPA's. In this way PWFA have the potential to produce high-energy particle beams in shorter distance (when compared with conventional RF) with the repetition rates and the efficiency of RF technology.

The laser to particle efficiency of LPA's can be estimated in 20%. However, the laser technology available for an LPA program presents two possibilities: Ti:Sapphire or OPCPA. Both laser technologies present electrical efficiencies below 5% (the 5% includes expected improvements

on tecnhology). Therefore the electrical efficiency of an LPA is smaller than 1%. A dramatic change in this situation will be only possible with a large laser system capable of delivering kJ pulses with durations around 300 fs with high repetition rate and an electric efficiency close to 50%.

Therefore, the interest of development of LPA technology for a complete high-energy physics machine is limited. However, LPA's have the potential to produce a compact front end for such a machine using its capability to produce high electric field gradients. This possibility becomes even more important if a short pulse of current is required such as for Free-Electron-Lasers.

As a conclusion, we are proposing to focus the LPA electron acceleration program on large experiments (> 20 J laser pulses) above the commercial lasers and direct the research program for new and existing applications that can take advantage of the unique properties of this source (high current, compactness, synchrony with lasers or other laser based sources).

Laser-plasma Electron beams for Applications

Laser-plasma accelerators are in the beginning of their use as particle sources for users. ELI will probably be the first facility providing beam time for pump-probe experiments using both moderately relativistic ultra-short electron beams and synchronized high-intensity lasers on a regular basis.

Therefore we present first a specification for the electron sources, based on current state-of-the-art that can be installed in the facility at an initial stage (this section) and a program for source development (next section).

We expect significant improvements on the state-of-the-art of electron accelerators. The sources parameters we are proposing for users are not yet demonstrated but they seem reasonable for a 6-year horizon. We also expect that a significant improvement on the source parameters related with the quality of the beam would be improved in future with multi-stage and all-optical injection techniques.

Design decisions

Laser beams

Number: up to 4

At this stage of the project we can foresee a maximum of two experiments running simultaneously using two beams each. With the development of the project an electron source can use up to 3 beams (electron injection plus two acceleration stages). Therefore these laboratories should be planned for up to 4 full energy beams. If budget constrain this number to less than 4, at least the basic infrastructure for 4 beams should be built. This includes space for the beams in vacuum chambers.

Energy: up to 50 J @ 10 Hz, if possible keep option of 100 Hz lower energy in two beams. If possible plan compatible with future energy up-grade.

Wavelength: although not critical, the wavelength should be known for detailed source design, so far we are using 800 nm. Possibility of using second harmonic to improve contrast or to extend the dephasing length of an electron accelerator should not be discarded as a future upgrade.

Pulse duration: pulse duration need to be finely tuned according to experimental needs from 20 to 150 fs, see Table 6.3, however, the use of shorter pulses may be beneficial for pump probe experiments and for future advanced injection schemes. Therefore, the compressor should be compatible with a future up-grade of at least one beam to the shortest pulse durations available at ELI.

Contrast: The maximum intensity on pre-pulses or pulse pedestal cannot disturb the plasma density. Therefore, we can set two contrast levels: ns contrast (prepulse) and ps contrast (pulse

pedestal). On ns time-scale we need to avoid the gas ionization (intensity below 10^{12} W/cm^2) while on ps-time scale we need at least to avoid bulk charge separation in the plasma (intensity below 10^{16} W/cm^2). We will consider two applications: blowout (intensities up to 10^{20} W/cm^2) and bubble (intensities up to 10^{22} W/cm^2) (see Table 6.3). We present the necessary contrast in Table 6.2.

Table 6.2: Electron sources for users – contrast required for pulses.

	ns contrast (pre-pulse)	ps contrast (pulse pedestal)
Bubble (one beam)	10^{10}	10^{6}
Blowout (other beams)	10^{8}	10^{4}

Table 6.3: Electron sources for users – experimental parameters. Electron sources for users. In this table we present the possible sources for the three main regimes: Blowout self-guiding, blowout external guiding and bubble. For each regime we present three laser energy levels. Parameters on red are considered very difficult to achieve in long term, parameters on orange are considered possible to achieve after a significant effort. Parameters green shaded are the proposed as sources for users on a early stage of the ELI project. Parameters orange shaded are the proposed as non-primary sources for users.

		Laser energy on target	100 mJ 1kHz	1.5 J 100 Hz	45 J 10 Hz
Blowout	Self guiding	τ [fs]	9.8	24.2	65.8
		W_0 [µm]	4.4	10.9	29.6
		$n_e[10^{18}\,cm^{-3}]$	23.2	3.83	0.63
		L [mm]	0.2	3.3	54.6
		Δ E[GeV]	0.1	0.62	4.59
		Q [nC]	0.13	0.31	1.04
	External guiding	τ [fs]	15.6	38.4	119.2
		W_0 [µm]	7.0	17.3	53.7
		$n_e[10^{18}\,cm^{-3}]$	4.62	0.76	0.08
		L [mm]	1.8	26.4	793.1
		Δ E[GeV]	0.26	1.56	15.06
		Q [nC]	0.1	0.25	0.78
Bubble		τ [fs]	6.6	12.2	26.8
		W_0 [µm]	2.0	3.7	8.1
		$n_e[10^{18}\,cm^{-3}]$	57.3	24.92	8.74
		L [mm]	0.03	0.2	1.8
		Δ E[GeV]	0.03	0.18	1.5
		Q [nC]	0.55	1.54	01.05.71

Organization of the laboratory

We propose a laboratory organization according to the scheme presented in Fig. 6.31. This arrangement allow to share the laser beams, pulse compressor, part of beam delivery and laser control by up to 3 experiments.

Since we expect that experiments may become temporarily activated during experiments at high repetition rate, the experimental stations should be isolated by thick walls in order to

allow the access to other experiments and laboratory common areas. In this way, it would be possible to use permanently the most expensive elements in the laboratory (pulse compressor, beam delivery).

The number of experimental stations should be at least 3. This number will allow installing three types of electron sources requiring different experimental configurations: blowout self-guided, blowout external guiding and bubble. More than 3 experiments may significantly increase the complexity of the operation and the cost of the shielding.

Figure 6.31: Electron sources for users – Schematic of electron source laboratory.

Room operation and radiation hazards

The proposed schematic for laboratory organization allow to maximize the use of the laser beams. Depending of the required laser beam configuration and beam time needed they can operate in parallel or sequentially. The room should allow a configurable setup disposition compatible with the radiation hazards from normal operation. Therefore an architectural solution should be found in order to allow the presence of an experimental team in the room when other experiment is operating. This is possible with the following approach:

1) The room should contain all the radiation inside
2) Each experimental station is separated by modular shielding blocks with capability to avoid that the radiation of on experimental station hit the next one or the common beam delivery area
3) Different experimental stations don't share the same access and it is not possible to circulate from one experimental station directly to other.
4) Experimental setup shielding should be designed in order to avoid the activation of the air in the room to a minimum. Nevertheless, the architectural solution should favor air separation between experimental stations
5) The radiation levels on each station should be measured permanently and temporary limits to circulation should be implemented whenever necessary.

Source specification

The specification of electron sources to be available for users in an early stage of the project are presented in Table 6.3. In this table we present three pulse energy levels possible at ELI at a repetition rate compatible with a source for users: 100 mJ–1 kHz, 1.5 J–100 Hz, and 45 J–10 Hz. We have calculated the laser and electron source main parameters for the three simple regimes: Blowout self guided, blowout external guiding and bubble. We also have identified the most

difficult laser and source parameters: red for the parameters difficult to attain in the medium term and orange for the parameters requiring a considerable effort to be attained.

Since we decided to have a conservative approach, the sources we are proposing for the initial stage of ELI, green shaded on the table, are those with parameters that are not requiring considerable scientific or technical effort.

At this point, there is no straight forward method to calculate electron beam properties, besides maximum energy and charge. Other important electron beam quantities, such as bunch energy dispersion, emittance and bunch length are very sensitive to experimental parameters and can only be anticipated by fully explicit three-dimensional heavy particle-in-cell simulations.

This source specification should be fine tuned before the construction phase since the state-of-the-art is in fast progress and new particle injection techniques may be include to improve the resulting electron beam parameters.

Source design

1. Laser target

Laser targets for electron accelerators are low atomic number gases (H_2 or He) or pre-formed highly ionized plasmas made of these gases.

These laser targets imply the introduction of significant amount of gas in the vacuum system. At ELI, these electron sources will operate for the first time at high repetition rate (10 Hz to 100 Hz). The amount of gas introduced in the vacuum system will increase significantly requiring: 1) reducing of the gas release per shot, 2) increase of the pumping speed and optimizing the geometry of the vacuum chambers including gas traps (taking advantage of the directionality of gas jets) , 3) use of differential pumping between sections of the vacuum system.

The gas is introduced in the interaction point by means of: 1) supersonic gas jets, 2) differential pumped gas cells, our 3) plasma sources.

Supersonic gas jets introduce a much higher amount of gas in the system than gas cells or discharge based plasma sources. However they can produce a gas target with much sharper gas-vacuum interface allowing for higher intensity on target. Supersonic nozzles with high Mach number also produce a highly directed gas jet making possible the efficient use of differential pumping schemes. Supersonic gas gets with diameters up to 1 cm have been used widely.

2. Laser beam delivery

Although fully in-vacuum beam delivery (prior to compression) is not required for the sources for users we are proposing. This may change in future with the introduction of advanced all-optical injection schemes or pump-probe experiments since this applications may require the use of highly synchronized pulses.

In this case, the level of synchronization do not need to resolve the laser wavelength (no beam combination) but should be better than 10% of the minimum pulse duration (2 fs or 0.6 micron). Due to the size of the installations this synchronization will require, besides vacuum beam delivery, a diagnostics and an active delay line between the beams. These equipments are not needed for the initial program now being proposed. However, the infrastructure need to be compatible with a future up-grade.

A laser beam alignment diagnostic and an alignment correction/shut-down is a crucial system to be installed since the radiation shielding may not be appropriated for accidental interaction of the laser with solids.

3. Laser beam metrology

Besides pulse synchronization and beam alignment (previous section), wavefront measurements, and full pulse characterization (FROG/SPIDER, energy, contrast, etc) are required for each beam, these diagnostics should be integrated with the beam delivery and the experimental room control.

Table 6.4: Electron sources for users – Focal distances for constant diameter beams.

	1.5 J	45 J
Blowout	$W_0 = 10.9\,\mu m$ $F = 8.6\,m$	$W_0 = 29.6\,\mu m$ $F = 23.2\,m$
	$W_0 = 17.3\,\mu m$ $F = 13.6\,m$	$W_0 = 53.7\,\mu m$ $F = 42.2\,m$
Bubble		$W_0 = 8.1\,\mu m$ $F = 6.4\,m$

4. Laser beam focusing
Laser beam focusing is achieved by off-axis-parabolic mirrors (OAP's). For larger lasers it is economical to use an active deformable mirror to improve the beam quality as well as strehl ratio coupled to a wavefront sensor. By using such a system it is possible to substitute the OPA by a spherical mirror since the deformable mirror can compensate for the aberrations. The spot size w_0 (for a Gaussian beam) result from the focal distance F and beam diameter D: $w_0 = 2\lambda F/(\pi D)$. Assuming a beam diameter of 0.4 m we got the following focal distances for the proposed sources.

Even if a correction factor resulting the fact that the beam is not gaussian the focal distances are still to long and we should consider non-conventional approaches to obtain the necessary focal spots with short focal distances.

The first possible method consists in the reduction of the laser beam diameter using the fact that when we require a larger laser spot size we also require a longer pulse duration. Therefore, it is possible to reduce the laser diameter before compression and reduce the focal distance by the same factor keeping the spot size constant. The following table contains the values of focal distances when we reduce the beam diameter according to the duration of the pulse ($D_{min} = 40$ cm$/(\tau$ [fs]$/20\,$fs$)^{1/2}/($Energy$/45$ J$)^{1/2}$).

Table 6.5: Electron sources for users – Minimum focal distances.

	1.5 J	45 J
Blowout	$W_0 = 10.9\,\mu m$ τ [fs] $= 24.2\,$fs $D_{min} = 6.6\,$cm $F_{min} = 1.4\,$m	$W_0 = 29.6\,\mu m$ τ [fs] $= 65.8\,$fs $D_{min} = 22\,$cm $F = 12.8\,$m
	$W_0 = 17.3\,\mu m$ τ [fs] $= 38.4\,$fs $D_{min} = 5.2\,$cm $F_{min} = 1.79\,$m	$W_0 = 53.7\,\mu m$ τ [fs] $= 119.2\,$fs $D_{min} = 16\,$cm $F = 17.3\,$m
Bubble		$W_0 = 8.1\ \mu m$ τ [fs] $= 26.8\,$fs $D_{min} = 34\,$cm $F = 5.5\,$m

The focal distances on Table 6.5 are the minimum focal to be used (for gaussian beams). Other techniques to further reduce this length should be developed. This includes the use of special optics or plasma lenses.

5. Laser beam dumping/electron charge collection
In a laser-plasma electron accelerator, a considerable part of the laser beam energy will the absorbed by the plasma and transferred to the electron beam. However, for a practical high repetition rate accelerator special care needs to be taken with the laser light transmitted by the plasma, specially if sensitive applications are ahead in the beam axis. One possibility to mitigate this problem consists in the inclusion of a short section of a high-Z gas (example Ar) and use it as a divergent lens for the laser light (due to ionization induced defocusing).

It is important to reduce the amount of electromagnet noise resulting from the ultra-fast rise-time pulsed currents in the accelerator. This noise strongly affects the electronic systems in the laboratory. This problem can be strongly mitigated if a collimator/beam dump consisting in a cylinder with a hole on the axis collect all the higher divergence (lower energy) electron ejected from the plasma. This collimator/beam dump will also concentrate most of the radiation in the target chamber reducing the activation of other elements.

This two elements need to be carefully designed and in order to maximize their efficiency in such a way that the electron beam properties did not came affected.

6. Electron beam optics/beam deflection
Current experiments are producing a significant amount of hard radiation due to betatron oscillations of the electron beam in the ion channel. This radiation may affect the electron beam experimental setup. Therefore the electron beam should have the possibility to be magnetically deflected from its original axis as well as to be imaged from the laser ion channel exit to the target.

Since the electron beams are to be used as a source for users we have to introduce some of the beamline concepts of conventional accelerators as well as diagnostics. The magnetic field used to deflect the beams out of the original axis should have the possibility to deflect it to at least two different axis: the experiment target beamline and a diagnostic beamline. This possibility is very important since the beam can be optimized and then sent to the experiment by changing only the magnetic field.

7. Electron beam diagnostics
Different electron beam diagnostics are necessary to measure and control the beam properties. These include:

Both beamlines:
FCT/ICT current transformers (commercial) (permanent)
Beam positioning (permanent)
Pepper-pot emittance diagnostic (insertable)
Beam shape OTR diagnostic (insertable)

Diagnostic beam line:
High-resolution magnetic electron spectrometer
Temporal bunch characterization (requires fs laser beam synchronized with the electron beam)

7. Electron beam target station
The target stations for electron beams should be flexible in order to accommodate multipurpose experiments. These can be from single electron beam experiments to complex pump-probe experiments involving the electron beam and multiple laser beams (synchronized with the electron beam).

Since at this point there are no pump-probe experiments planned in detail we provide only general remarks about this experimental space.

An 50 J/20 fs ELI laser beam can have a diameter up to 50 cm. Even if the experimental vacuum chambers in the electron beam target station are not initially designed to accommodate these large beams at least the space should allow a future up-grade. Therefore on designing the target station space for dealing with full power ELI beam should be considered. This space

includes not only the beam focusing (focal distances up to 10 meters) but also for the laser beam delay lines that may be necessary to synchronize the laser with the electron beam.

8. Electron beam dump
The electron beam must be absorbed in a material medium. Depending on the energy of the electron beam and on the atomic number of the material. The beam dump may require several meters to stop the electrons generated with ELI beams (up to 15 GeV/1 nC/10 Hz) on a single stage accelerator. A linear distance of up to 5 meters need to be reserved for beam dumping (distance to be confirmed by the work on WP6).

9. Vacuum system
Typical vacuum systems for laser-plasma interaction are high-vacuum systems ($\sim 10^{-4}$ mbar), while conventional accelerators are ultra-high-vacuum systems ($< 10^{-8}$ mbar). This is because the first ones release considerable quantities of gas and the later ones require ultra-high-vacuum to avoid damage by electrical disruption or cathode contamination.

At ELI we see no reason to improve the vacuum level except if specific experiments require it. However the particle sources may release considerable higher gas quantities for the vacuum system due to the high repetition rate (10 Hz and higher). This requires a clever design of the vacuum system in order to keep the high-vacuum necessary for high-intensity laser operation.

Since the entire vacuum system is communicating (from the laser system to the targets) dry vacuum should be used for protect sensitive diagnostics and laser elements.

10. Materials
High repetition rate laser-plasma electron accelerators will activate the materials in the experimental areas. The radiation protection is the subject at WP6. However we can anticipate, based on previous experience with smaller scale lasers, that operation of the rooms will be strongly affected by the activation of the room components if the materials in the room are not properly chosen.

The materials in contact with the primary as well as secondary radiation should have low atomic number and short decay lifetimes such as aluminum, plastics and carbon fiber. Materials as stainless steel, iron or cooper should be avoided since they have intermediate decay lifetimes when activated increasing the radiation levels in the room.

11. Target station space organization
We can foresee two types of target stations : 1) basic experiments without electron beamlines and 2) beamline experiments.

A possible generic setup for this target station is presented, in a simplified schematic, in the figure below.

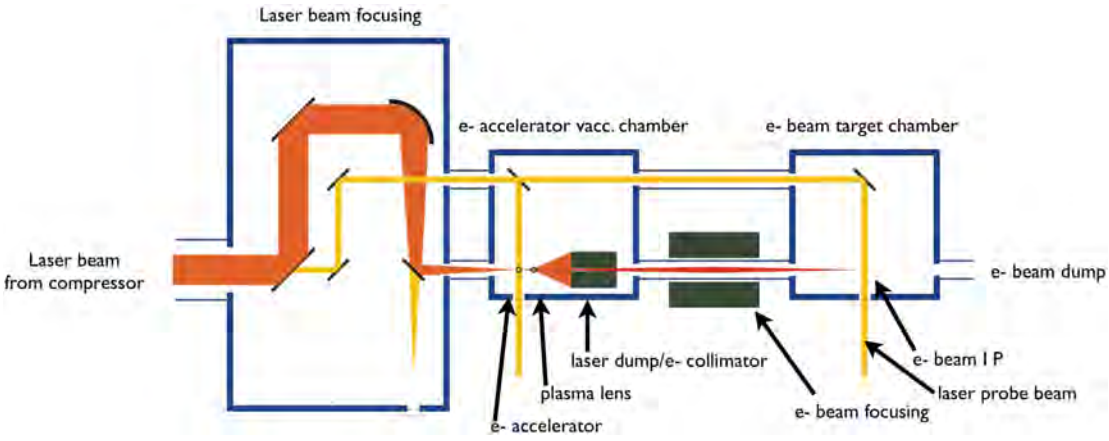

Figure 6.32: Generic setup for experiments without electron beamlines.

This first type can be contained in a space of $8 \times 20\,\mathrm{m}^2$.

The second type will require a larger area since the electron beam optics and diagnostics will require a considerable length.

In the next figure we can see a simple schematic of the second type of target station.

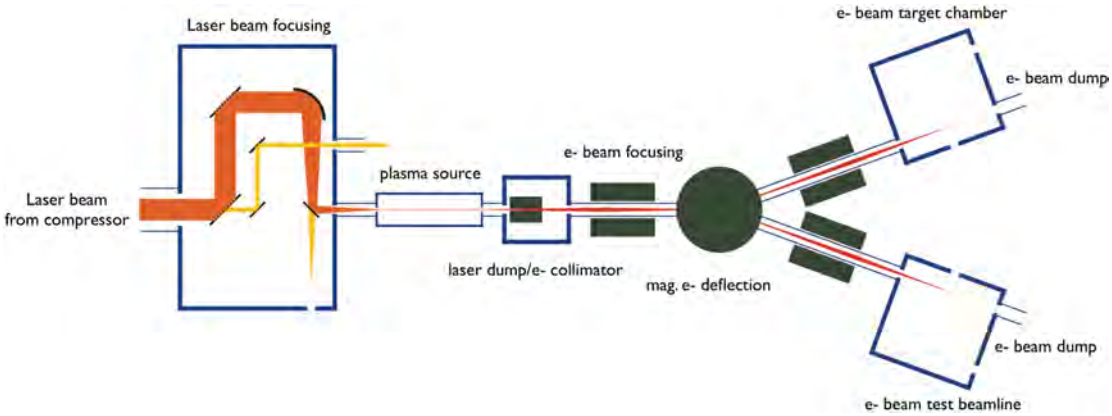

Figure 6.33: Generic setup for experiments with electron beamlines including electron beam optics and diagnostics.

The modularity of the experimental as well as the radiation shielding between target station room we are proposing are not compatible with a large gantry crane. However, lifting of heavy weight in all area is a fundamental requirement and should be planned from the beginning.

The heaviest items to be transported in the experimental area will be the shielding blocks. These blocks need to be moved when a setup change require the change of the shielding configuration or to allow the entrance of large setup elements such as optical tables, large vacuum vessels, etc. One possibility to move these heavy elements using air bearings. The use of air bearings in the laboratory should be planned from the beginning since the floor and the space organization need to be prepared for it.

12. Control room (for electron sources for users)

Each experimental area should have a control room for experiments, particle and radiation sources and laser beam delivery.

Like the corresponding experimental room, the control room should be flexible, configurable and should on each moment have the same functional organization as the control room.

The central, and permanent, element of the control room is the beam delivery and basic setup control, to be operated by facility staff. It should control the beam delivery to experiments, vacuum system of all experiments, gas injection in the experiments, and radiation safety. It supplies the triggers for data acquisition in the experiments. It controls the access to the experimental rooms by users (block access if activation radiation exceeds limits).

The secondary elements of the control room are the specific control of the sources (resident/permanent sources).

The tertiary elements of the control room are the specific control of the electron beam experiments.

The primary, secondary and tertiary control elements should have a special organization to promote communication between dependent elements. The space should also be configurable in order to produce acoustic isolation between elements since different teams can use the same space at different stages of work.

The basic triggers to be supplied by the primary control element, are (10Hz coincident with laser) and RF (oscillator or oscillator divided by 1 to 100). The combined use of both signals allows for the generation of long delay with sub-ns jitter required at experiments.

Some experimental modules will generate important electromagnetic noise (electron accelerators, plasma sources, and other elements using pulsed power). Therefore, all important triggers, and communications should be made by optical fiber. Plastic fiber optic and wireless communications should be used in all other signals in order to prevent failures in the control systems as well in other areas of the building.

Source upgradability

Future upgradability should result from
1) Source improvements (more charge – Improved injection, more energy double stage)
2) User needs (development should follow user needs: energy spectra, charge, repetition rate, beam quality)
3) Improvement on laser technology (more energy, higher damage threshold of optics, etc)

It was identified in this WP that the most important factors for electron source development and use where the repetition rate and stability. It seems possible now to use diode-pumping technology up to the 50 J/beam at ELI. This technology was not used, so far, at large scale and therefore an important up-grade in the energy level of the laser seems reasonable. The development of high-damage threshold dielectric gratings for pulse compression can also play an important role in the up-grade of the laser since they will allow to increase the pulse energy keeping the same beam diameter. This up-grade will be compatible with the pre-upgrade experimental facilities.

Interface with other sources/experiments

The sources to be developed at ELI can be used in complex experiments involving multiple sources and lasers beams. ELI will be the first facility to have this potential. Therefore, a effort to build the electron sources in a modular way so they can be reassembled in other experimental areas or transferred to other locations if they become obsolete on ELI due to laser up-grade.

Additional facilities for users

Besides space for users in the control room, additional space should be added to the experimental space for sample and target preparation and storage. Need to take into account that these materials may become radioactive.

Development program for electron beams

On this section we describe a development program for development of LPA electron beams for users in the medium/long term. Following the ideas on Sect. 6.2.1 we should focus this program on the source improvements in order to make it attractive for potential future applications. The main parameters to improve are (by order of importance): beam energy reproducibility, beam energy spread, beam emittance, bunch charge, beam repetition rate, possibility of multiple bunch acceleration and electric efficiency.

The most likely path to improve these parameters consists in de following development lines:
1) Improve the reproducibility, beam quality, pointing stability as well as diagnostics and metrology of the laser and laser delivery system on target
2) Develop the plasma channel technology in order to produce the adequate plasma target (for a first acceleration stage with electron bunch injection and for acceleration stages without injection)
3) Incorporate an electron bunch injection technique in the plasma channel of the first stage to produce precise injection of a an electron bunch aiming a low energy spread in the end of the acceleration stage

4) Develop beam optics and collimation for transport between acceleration stages and applications
5) Development of diagnostics for the electron beam and the plasma accelerator

Since LPA's are a fast developing field, these research lines should be reviewed with periodicity no longer than three years.

Improve the reproducibility, beam quality, pointing stability as well as diagnostics and metrology of the laser and laser delivery system on target

For most applications it is necessary to have a beam with good reproducibility (pointing, energy, shape, charge, etc). The reproducibility of an electron beam depends critically on the reproducibility of the laser beam and the plasma source. One of the potential problems that will affect the beam reproducibility will be the symmetry/asymmetry as well as the distance to the axis on the electron injection on the accelerating wakefield. These parameters will play an important role on the betatron motion (and radiation) of the accelerating bunch. To increase the efficiency and focusability of the beam the betatron motion should be reduced to the minimum. Although the fundamental issue will be the injection technique, a high quality and reproducibility focal spot with pointing stability better than 1/20 of the focal spot is necessary (since the electron bunch diameter is typically 1/5 to 1/10 of the laser spot size).

This degree of precision and reproducibility does not exist in current laser laboratories. Since the laser system will be larger than an optical table it will require that the facility (building and optical mounts) be stable enough (full range of vibrations frequency) in order to make possible an active system to compensate the remaining low frequency pointing drifts. The spot size beam quality can be obtained by adaptative optics (now available on main laser laboratories). The energy reproducibility of the laser shots is another factor where innovation is required. We can estimate that energy reproducibility better than 0.5% RMS will be required. Therefore, the lasers for beamlines are requiring the development of diode pump technology for high-energy amplifiers.

The effort to improve the primary source (the laser and the laser delivery) will require a parallel effort on the primary source metrology. The measure of all the relevant parameters should be permanent and at the necessary resolution. The results of this measurements should feed an active control system of the laser source and beam delivery system.

Develop the plasma channel technology in order to produce the adequate plasma target (for a first acceleration stage with electron bunch injection and for acceleration stages without injection)

As can be seen from Table 6.2, external guiding is necessary for maximize the energy of the accelerated electrons. Increasing the energy (and reducing the charge) of the accelerated bunches also improves the possibility of transport the beam to a next acceleration stage or to an application. Besides, the guiding of the laser beam may improve the pointing stability of the secondary source (the electron beam).

Current methods for creation of plasma channels rely on a laser beam or on high-power electric discharge to create a linear explosion of a plasma in the propagation axis. The expansion of the plasma lead to the creation of a close to parabolic radial density profile that can guide the laser beam as in a graded index optical fiber. Plasma channels as short as 3 cm have been used to produce electron bunches of 1 GeV. So far no technology was demonstrated to produce electron bunches in lengths longer than 3 cm.

The plasma channels for electron ELI parameters will require deeper channels (axial density around 5×10^{16} cm^{-3}–1×10^{17} cm^{-3} and and around 5–10 times higher at a 100 micron radius) and longer (0.5–1.0 meters long). This requires a significant progress on the plasma channeling technique from the current state-of-the-art. A possible solution to create the required plasma structure will use a massive ultra-short rise-time electric discharge (typical values 300 kV, 5 kA, rise-time <5 ns, duration 50 ns) on a preformed plasma. Such a scheme will require considerable

space on the laboratory, will constrain the design of the beam delivery and above all will produce an high level of electromagnetic noise.

Therefore, the use of plasma channels in ELI will require an initial planning of the whole laboratory (facility, beam delivery and all equipment) for the electromagnetic noise, radiation and electric hazard produced by the plasma channels.

Incorporate an electron bunch injection technique in the plasma channel of the first stage to produce precise injection of a an electron bunch aiming a low energy spread in the end of the acceleration stage

Pure external injection of a laser beam produced by conventional technology as a reduced interest since, for a reasonable charge and accelerator size, the length of the electron bunch will be much larger that the plasma wavelength (similar to the length of the acceleration structure) and would lead to an high energy dispersion making the beam impossible to transport and useless for most of the applications. Therefore, an injection scheme for an external guided laser-plasma accelerator will likely use a plasma that can radially confine the electron bunch to the propagation axis and present GeV/cm accelerating electric fields where making that bunch relativistic in a few millimeters. Nevertheless, once outside of the plasma such a beam would present a high perveance and would be hard to transport to the next stage.

The development of an injection scheme for a laser-plasma accelerator adequate for the ELI parameters should be a priority. The most promising research directions, (taking into account the present state-of-the-art) will include the use a counter-propagating beam to produce a precise charge injection in the entrance of a plasma channel on a setup with a complex geometry. It is possible that this injection technique can be enhanced by other effects: gas mixings, density ramps or other.

The charge injection in the plasma wakefield is currently a fast moving topic with an high impact on this source. Therefore the information in this item should be reviewed frequently.

Develop beam optics and collimation for transport between acceleration stages and applications

Beam transport and collimation should follow mainly the techniques developed for conventional accelerators. The main differences from conventional technology are that energy spread of the beams can be significantly higher on LPA's and more charge need to be collected at the collimators increasing the activation significantly. The beam transport should be designed for specific applications in order to increase the compactness a decrease the cost of the sources. Specific miniaturized optical elements for LPA's are in development and can be used on compact setups. Under certain conditions (low repetition rate, compact experiments, soft experimental constrains, etc) the philosophy beyond these devices can be extended to the design of the entire beamline resulting in a modular and easy to change setup adequate to the flexibility needed in this project.

Development of diagnostics for the electron beam and the plasma accelerator

Electron beam diagnostics for LPA's are not significantly different from conventional electron accelerator sources except on the measurement of the duration of electron bunches. Since the bunch duration can be smaller than 10 fs it will require an optical technique based in short laser-pulses synchronized with the electron beam. This techniques are being developed and used in different laboratories worldwide and will be available for ELI. The

The main diagnostics for the electron beam will be:

a) diagnostics for beam energy
   Imaging magnetic spectrometers for the relevant electron energies. The detection system should be made imaging a continuous detector with one or more CCD cameras.
b) diagnostics for beam emittance
   Pepper-pot method.

c) diagnostics for beam charge
Charge can be measured by a transformer (non-invasive), Faraday cups (invasive, possible some special resolution)
d) diagnostics for beam position
Beam position can be measured by transition radiation (invasive), florescent target (for low intensity beam) (invasive), movable solid wires or laser scattering (multiple shots required)
e) diagnostics for bunch duration
Techniques based on short pulse laser scattering.

The main diagnostics for the plasma will be
a) diagnostics for the plasma density
Interferometry of the plasma column in strategic places (measure the plasma density of the entire plasma column may not be possible by experimental constrains)
b) diagnostics for the plasma temperature (produced by discharge)
Plasma spectroscopy
c) diagnostics of the discharge (if one is used in to produce the channel)
current (fast transformer) and voltage (d-dot)
d) diagnostics for the acceleration structure
Plasma diagnostics based on advanced interferometry techniques are under development and may be used in this project. These diagnostics will require optical transverse access to the plasma.

Bibliography

[1] S.P.D. Mangles et al., Nature **431**, 535 (2004).
[2] C.G.R. Geddes et al., Nature **431**, 538 (2004).
[3] J. Faure et al., Nature **431**, 541 (2004).
[4] T. Tajima and J. M. Dawson, Phys. Rev. Lett. **43**, 267 (1979).
[5] W. Lu et al., Phys. Rev. ST Accel. Beams **10**, 061301 (2007).

6.2.2 Proton-ion beamlines

Specification of initial sources for users

Introduction

The initial sources specification is based on the assumption of 50 J laser pulses, corresponding to the second stage of ELI. The pulse duration is planned to be down to 15 fs. Assuming a diffraction-limited focal spot, the intensity could reach 10^{23} W.cm^{-2}. To relax a bit the constraints, one could base the specifications of the sources for the users taking a conservative estimate for the laser intensity of $\sim 10^{22}$ W.cm^{-2}. Based on the presently available projections for the production of proton and ions sources, with these parameters, the maximum energy could reach $\sim$200 MeV for protons and $\sim$50 MeV/nucleon for carbon ions, allowing one to project the range of possible applications.

Requirements from the users

Laser-plasma accelerators are in the beginning of their use as particle sources for users. ELI will probably be the first facility providing beam time for pump-probe experiments using both moderately relativistic ultra-short ion beams and synchronized high-intensity lasers, electron beams, X-ray sources or attosecond sources, all that could be combined on a regular basis with the ion source from the advantage of the users. What makes ELI additionally unique is the ability to vary all these different secondary sources independently as allowed by having independent

individual driving laser beams and adapting them optimal to the requirement of the specific experiment.

We present first a specification for the ions sources, based on current state-of-the-art and cautious anticipation of soon-to-be laser parameters, that can be installed in the facility at an initial stage (this section) and a program for source development (Sect. 2.1).

Source specification

Based on the present knowledge and know acceleration mechanisms, the source specifications would be

- 200 MeV for protons
- 50 MeV/nucleon for heavy ions
- $> 10^{12}$ ions/bunch
- $<$ ps duration at the source
- % ΔE/E
- µm virtual source size
- few degrees angular distribution
- kA current at the source

Source design

The source design follows from the fact that the dominant mechanism (TNSA) is currently well-known and optimal designs exist to exploit it. They however require a stringent temporal contrast for the laser (see below). Use of associated sophisticated targetry (ultra-thin target) is also required, not only in the prospect of exploiting TNSA, but also in order to possibly use as well the emerging RPA mechanism for increased efficiency and monochromaticity. In order to use the high repetition rate of the laser, one need also to consider all problems related to such "high-repetition" targetry, i. e. a flexible way of replacing the target once it has been shot by the laser. One possible option could be to use a "Film-target" such as a strip of metal or a very huge metallic surface. However, these solutions might not be adapted for very think target (nm scale) where a different type of targetry needs to be implemented (e.g. a series of independently mounted targets). A very general set-up delivering an ion beam is shown in the figure below. The probe beam can be used to diagnostic the electron population at the front side [1] (the auxiliary beam at the right side can generated protons that can be used for proton radiography of the rear surface field [2], the film behind the target can be used as detector for protons. The Spectrometer (spectro) and Thomson Parabola behind the target can be used as complementary diagnostic for detecting proton/ion energies.

Figure 6.34: Schematic of an experimental setup for generating laser-accelerated ions. OAP stands for off-axis parabola, T.P for Thomson parabola.

Source upgradability

The source upgradability will depend on a major part on the laser energy increase that could be provided by further laser amplification stages of ELI and the use of temporally stacked or phase-locked spatially overlapped laser beams to increase the on-target laser intensity. The source delivered dose will depend on the repetition rate that might be increased during the course of the construction. The ion source parameters that could then be envisioned are detailed in the next section "Source development program".

Diagnostics specification

The diagnostics should comprise:
- Spectrometer
- Emittance measurement
- Source size
- Divergence measurements
- Source duration
- Flux/charge

With the maximum energy that is planned for the initial ion source, most of these diagnostics, working adequately in the projected energy range, are already available as shown in Fig. 6.34.

Diagnostics design

These diagnostics have already been designed, calibrated and used extensively in several laboratories. They include: nuclear activation diagnostics, films, spectrometers for protons, electrons. For energy resolved beam profiling, new detectors are required to deal with the higher particle energies and fluxes. New detectors based on nuclear activation are currently developed, which could detect the much higher proton numbers, still provide excellent spatial and spectral resolution and can be absolutely calibrated. Compound detectors also will measure electron propagation inside solid density material using (γ,n) reactions with real and virtual photons. Those equipments will be used for the initial source as a pool and the expertise shared by several research teams. It is worth noting however that diagnostics for higher repetition rate with high spatial resolution will need further improvements. The sole diagnostic that is lacking at the moment is the source duration diagnostic towards which experimental teams are working on various schemes. However, a possible approach could be to use a RF-feeded dipole, as using on conventional accelerator facilities (e.g. SPARC).

Laser requirements

Based on the above source specifications, the following points will be required from ELI in order to be able to deliver the source:
- minimum two full power beams + lower power probe (non-harmonic preferably, possibility to be used chirped), all with their own compressors to vary the pulse duration
- un-compressed laser beams (at least two) are also needed to allow exploring the range of possible applications (e.g. HED physics requires the possibility to perform compression experiments.)
- Feedback control of synchronisation better than 10 fs
- temporally stacked pulses on the same beam to perform plasma conditioning
- Polarization control (Linear and Circular)
- Knowledge of pulse energy on target
- Laser parameters stability (better than 1%)
- tuneable temporal contrast with the possibility of having high temporal contrast (i.e. a laser pedestal with laser intensity $< 10^{10}\,\mathrm{W.cm^{-2}}$)

- frequency-doubling or plasma mirrors set-up will be required if laser temporal contrast does not meet requirements
- variable duration for the laser pulses and single shot control of the pulse shape
- Tighest focusing (with pointing better than 0.1 mrad)
- Focal spot shaping, wave front metrology and control
- Repetition rate: single pulse may be needed for specific applications

Interface with other sources/experiments

The interface with other sources represents a strong need to take advantage of unique synergies. For example, coupling with high-energy electron beam production would allow using the ion beams to probe the fields in the electron acceleration and thus to obtain a better understanding of the physical mechanisms. Coupling with X-ray sources would allow using them as a probing tool for warm dense matter produced by ion beams, thus measuring the plasma parameters and probing the atomic structure of the heated matter. This would allow for micron resolution radiography with highest temporal resolution of ELI experiments. Enough space needs also to be reserved to build an ion optical system for proton-irradiation experiments, which will benefit also from linking one target area to the other.

Additional facility for users

Besides a source for ultimate high particle energy (with reduced repetition rate) it should be possible to operate also a proton source with high repetition rate and a broad variability in the energy and flux, allowing also more technical relevant applications as well as studies on the coupling with common accelerator setups (seeding of cavities etc).

Source development program

Introduction

This section is intended to outline the program that is envisioned to push the development of the ions sources within ELI above the limit that is set by the first stage of ELI (i.e. up to 50 J laser pulses), and that has been addressed in the previous section. Based on the existing projections (see below), several hundred MeV up to a few GeV protons could be obtained with the ultimate ELI parameters, i.e. using laser intensities toward 10^{24} W.cm^{-2}. This would represent extremely significant improvements, compared to present state-of-the-art, or small extrapolations, of ion accelerators. The acceleration length can be as low as a few tens of microns, however with a downside associated with a non-guided process that is a higher beam emittance and divergence. These parameters have not been demonstrated because the required laser parameters are not available but, based on simulations, seem reasonable. It needs also to be demonstrated, but is equally expected from simulations, that the beam quality can be further improved (mostly in terms of divergence and monochromaticity, as the present ion sources are already extremely bright). This would also be a major achievement and would serve users with great benefit. One should add that at these intensities protons should reach the relativistic regime and in that regime different acceleration schemes than what mentioned above might occur. In this section we therefore focus on the acceleration schemes that have been currently identified and studied, knowing that this could be limiting our considerations.

Requirements from the developers

To obtain a highly performing ion source, we will need to address and optimize the following general issues: Maximum charge, energy spread, divergence, emittance, maximum energy. This will likely require some laser pulse shaping (uniform/flattop), the development of high repetition-rate capability (for the detectors, targets, etc), new detectors (potentially very large for GeV ions detection), and possibly some coupling to conventional technology for post-acceleration/focusing. A crucial point to address will be the source reproducibility (laser stability).

Design decisions for experimental setup(s)

We will need, along this source development program, to clarify the paths that are today envisioned from theoretical studies and that could lead to energy increase up to $> 200\,\mathrm{MeV}/1\,\mathrm{GeV}$. Such energy levels are extremely attractive to reach as they will open many new applications with high impact.

As mentioned above (in the ion beams state of the art section), a possible physical mechanism for ion acceleration that could be used to reach high ion energies would the radiation pressure in solids. There, the plasma electrons are pushed steadily by this force, and ions are accelerated in the strong electrostatic field forming a shock-like structure. The use of circularly polarized laser light might further improve the efficiency of such ponderomotive ion acceleration, avoiding strong electron overheating. It has been shown in simulations that it allows one to obtain a quasi-monoenergetic ion bunch in a homogeneous medium by adjusting the laser pulse and plasma parameters. Compared to TNSA, the ponderomotive mechanism allows a better control the ion energy distribution and acceleration of a much larger number of ions from a smaller target area. It will be also necessary to investigate in parallel the influence of radiation losses increasing with the intensity.

We have performed a series of PIC simulations to check the parameters that could be expected for the ion source at the 100 PW range. This analysis, made for WP6, focuses on specifying the source term for the most extreme conditions provided – 133 PW – assuming a beam energy of 2 kJ in a 15 fs duration. The experimental configurations that are here analysed are chosen to maximize the laser-particle energy transfer. The detailed study was made with the Osiris fully relativistic PIC code [3] in a series of runs for different target thicknesses. The targets are

Table 6.6: Summary of the input conditions for the Osiris simulations.

General	Type	Simulation PIC 2D fully relativistic code
Target	Type	Thin solid target
	Material	H
	Density [g.cm^{-3}]	0.088
	Thickness [μm]	1 ; 10 ; 20
Laser	Energy [J]	2000
	Pulse length [fs]	15
	Wavelength [nm]	800
	Intensity [W/cm^2]	1.6 10^{23}
	a_0	276
Layout	Focusing system (f/#)	f/10
	Beam waist [μm]	5.1 (1/e^2 intensity radius)
	Polarization	Circular
	Angle of incidence [$^\circ$]	0

modelled as solid hydrogen for faster simulation times. The 2D simulation series took a total of 18100 CPU hours at the IST cluster [4].

Particles with up to a few GeV can be generated with this setup (Table 6.7). But, unlike most data published in the literature, these spectra are resolved in direction, which is fundamental for a proper radiation shield planning, as required for WP6.

Table 6.7: The maximum energy and beam divergence for the different target thicknesses.

Target thickness (μm)	Peak energy (GeV)		Proton FWHM divergence (rad)
	Proton	Electron	
1	4.6	2.9	0.5
10	1.3	0.9	1.6
20	1.3	0.5	1.3

In the studied configurations the particle beams are not collimated. The divergence can be actually quite large, with denser side peaks of less energetic protons. It was also found a significant fraction of energetic protons travelling backwards. Thicker targets make a relatively uniform electron distribution in all the directions with some random spikes.

About the conversion efficiency, the 10 and 20 um thick targets reach lower peak energies but the proton yield is higher for the protons down to half the peak energy:

- 1 μm, [2-4] GeV range: $\sim 5 \times 10^5$ protons/(MeV.mrad.μm)
- 10 and 20 μm, [0.5-1] GeV range: $\sim 5 \times 10^6$ protons/(MeV.mrad.μm)

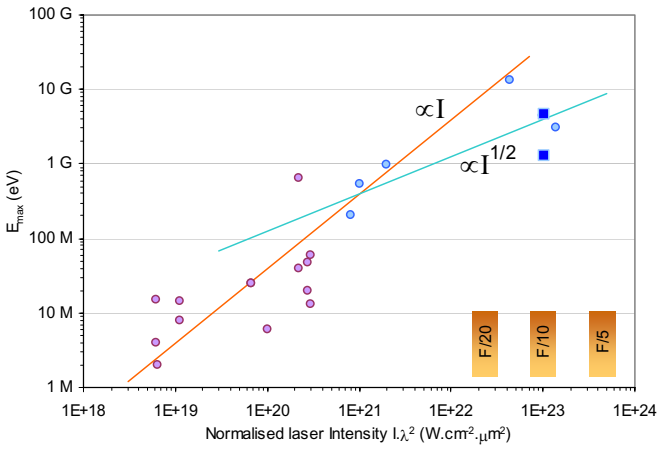

Figure 6.35: Maximum proton energy scaling with laser intensity. Purple dots are experimental values, blue are from simulations. The F/# rectangles show the intensity ranges achievable with the highest intensity ELI beam line using three different focal distances. The two darker blue squares at 1.0×10^{23} W.cm^{-2}.mm^2 show the results from the Osiris simulations on the 1 and 10 μm targets.

As shown in Fig. 6.35, the generated data aligns well with the known scaling laws [5] for particle acceleration. The estimation of the 3D particle distribution from the bi-dimensionally generated data can be accomplished by specifying a proper depth for the simulated target and considering the radial symmetry along the x_1 axis. For this particular set of data which used a laser spot diameter of 10.2 μm the simulation depth on x_3 is 6.4 μm, by applying the correction factor of $\sqrt{\pi/8}$ to preserve the laser energy in the 2- to 1D Gaussian shape conversion. Then, the particle density must normalised to the solid angle they correspond to, which, in first

approximation, is given by $\Delta\theta.2\pi g\sin(\theta)$ for $\theta g \neq \{0, \pi\}$, being θ the angle relative to the x_1 axis.

These numerical simulations foresee a one order of magnitude increase on the peak energy relative to the most energetic particles accelerated by today's operating lasers. They also show that for radio safety concerns, it will be important to optimise the configuration, namely by laser and/or target shaping, in order to improve the beam collimation and, eventually, create or reinforce its mono-energetic features. Further 3D simulations will be performed along the course of the ELI planning phase to accurate confirm the expected parameters of the future source.

Another potentially promising way to accelerate ions to high energies is to use underdense or near-critical density targets [6–8]. That approach has recently received a lot of attention [9–11]. Compared to solid targets where laser absorption is limited to the target surface, the laser pulse inside low density plasmas heats electrons on a large volume leading to higher laser absorption. This acceleration regime is also advantageous for applications as less debris are produced. It is more adapted for utilization with high repetition rate lasers. The laser contrast, which can be problematic with thin solid targets, is less detrimental as the gas jets are transparent for laser intensities below $10^{13}\,\mathrm{W/cm^2}$. The main acceleration processes in this low density regime are still being debated. It appears, using simulations, that acceleration processes depend strongly on the characteristics of the density gradient. We should also mention that, at extreme laser intensities that could be reached with the ultimate stage of ELI, using underdense targets also offers the potential for bubble regime acceleration at extreme $>$ GeV energies (proton acceleration using mixed ions).

The design strategy for the source development will therefore require first studying, in parallel, the various paths that can be pursued for ion energy increase. These include:

- simple laser intensity/energy increase
- use of ultrathin targets (requires very high contrast, circular polarization), production of protons and heavy ions
- use of small (mass-limited) targets (solids, μ droplets, spray)
- exploit/explore new mechanisms/regimes, other than TNSA, at higher intensities (e.g. shock acceleration, transparency regime, ponderomotive acceleration, etc). For this, the preplasma will have to be tuned at the target front, which will require an adjustable prepulse
- test the use of underdense targets (foam, gas, cluster, spray).

Various set-ups will be used to study these various aspects. This will be pursued in close consultation with Theory/Modeling WP for continuous source optimization. Once a route is chosen, based on the results obtained throughout the study, a final set-up will be chosen and implemented. For all set-ups used through the course of the study, the issue of target development will be addressed with consideration for repetition rate, and the study of the use either of structured solid targets (layered, pre-ionized, embedded dots, isolated targets, μ droplets of different size (enabling high repetition rate)) or of less than solid density where optimum prepulse will need to be adjusted.

We will have to take into consideration not only the maximum ion energy that will be reached through the various mechanisms that will be under study, but also the following parameters, in order to decide for the best suited for downstream applications:

- Laser to ions conversion efficiency
- Ability for beam handling & selection (either through target engineering or conventional solutions, e.g. quadrupoles)
- Ability for energy selection (with particular target/cylinder/capillary/others?)
- Ability for increased beam stability (energy distribution, particle numbers, emittance)
- Increased efficiency, even at modest energies

Experimental setup(s) design

The experimental setup designs will benefit from progress that will be accomplished en route to ELI, in partner laboratories, and also in the initial phase of ELI when the initial source will be delivered to users. The amount of work that will have been done at that time will allow to decide on the best experimental set-ups that will be most adequately suited to conduct the above mentioned design strategy for optimal source development.

Diagnostics specification

The diagnostic requirements are the same as for the initial source but specific issues will arise from the strong energy increase of the particles produced at extreme laser intensities. There will be an additional requirement of

- Pion, muon and neutrino beam detection.
- Neutron beam detection and transport.

As mentioned above, ELI, in its final phase, will likely be able to produce various kind of radiations (photons, particles) whose energy will range from MeV to GeV. Besides the number of particles per shot will be huge ($>10^{12}$ protons in the 5–6 GeV range). The characterization in energy and beam spreading of these particles will be a challenge since no unique detector can be used. This constitutes the specification for the diagnostics to be developed for the source development program.

Diagnostics design

Beyond 100 MeV and in the GeV range one must compose between the brightness of the radiation source and the variety of particles emitted together. Specific measures are required to plan for a beam stop of the bright proton/ion bunches. Nuclear high energy techniques could be considered, but they are huge equipments requiring very large experimental area.

Currently, a diagnostic working group that includes members of the ELI scientific community is active in France to elaborate adequate diagnostics for the PETAL high-energy-Petawatt (4 kJ, 1–10 ps) laser (in Bordeaux, France). This working group will work towards elaborating solutions that will be then used and duplicated for the ELI facility.

Laser requirements

Based on the above elaborated design strategy for the source development, the following points will be required from ELI in order to be able to perform the necessary studies for source development:

- Phasing for multiple beams when performing experiments in EW TA. Temporal stacked pulses on the same beam would also be necessary to optimize the plasma conditioning for optimum source production.
- Repetition rate: highest possible for applications (e.g. for laser-proton collisions at extreme intensities)
- different acceleration regimes can be explored depending on duration, as a consequence the laser pulse duration need to be varied (from the minium to a few ps)
- Also, some ion application experiments (HED physics) will require that the beam is allowed to be stretched significantly (up to tens of ps) to have both a high ion number and current but not a too high ion energy (i.e. not a too high laser intensity).
- Laser energy: Need to be controllable, more is good
- Polarization (Linear and Circular)

Interface with other sources/experiments

There is a strong need to be coupled to other beamlines of ELI to take advantage of unique synergies, as already outlined.

Additional facilities for source developers

This might become necessary if we can reach $> 200\,\mathrm{MeV}/1\,\mathrm{GeV}$, which opens the road to efficient sources of neutrons and "exotic" particle for which there will be a need for dedicated beamline (instrumentation, downstream chambers, etc).

Target area layout

The ELI facility is supposed to be built as central laser facility with different experimental stations that can be used and accessed independently, such as a Synchrotron Radiation Facility (e.g. ESRF). In order to define the infrastructure, the size and number of the experimental halls, it is important to specify the requirements in terms of size and auxiliary space that each experimental room will need. It is also necessary to define the interplay that will be needed between different experimental rooms.

The envisioned laser driven proton/ion source of huge particle energies (up to the GeV level) [12], in combination with other high-energy particle and radiation sources, requires a specific environment close to that of conventional accelerators. In contrast to the latter, which are planned for a dedicated energy range, the laser driven source is, according to the laser parameters that will be available on ELI and the projected parameters of the produced source, a "broadband" facility, which has to fulfill at least two aspects: 1. to explore the optimum mechanisms to create efficiently highest energy and flux accompanied by shaping the energy spectra with the available laser parameters, and 2. to use them for the envisioned scientific program and different other applications.

Therefore a high degree of variability of beam line steering and a flexibility of the experimental areas, in combination with adequate radio protection measures, are required. Whereas a lot of experiments for intermediate studies as well as applications could be arranged in radioprotected laboratories (thick walls of heavy concrete and local protection with lead bricks etc.) in the cellar of a central building to which the laser beams will be propagated (this will be studied in details by WP 7c), the ultimate experiments using the full ELI laser energy requires a special building offering more flexibility for the experiments and the radioprotection issues. This building should be erected in closest vicinity to the central building to reduce the costs for the laser beam propagation and should have enough space to accommodate all the necessary environment: full laser beam lines, target area, diagnostics, space for applications and flexible, stackable heavy concrete blocks movable by a crane. Such a building structure would ensure ELI operation also beyond the present day expectations and could in case of future necessity also experience an extension.

For the target area, there is a consensus on 3 rooms, 1 dedicated to ion source use with a fixed set-up and set parameters for users, and two for source development programs. These imply that there the users can change the set-ups for source studies, the justification of the two being that it allows optimal use, two teams can work in parallel. All these experimental rooms should have connection between them. A length of 30 m would allow room for irradiation station desirable for users, neuron generation and transport, and for potential two-stage acceleration studies.

Radioprotection considerations

Estimates of the number of shots per day in the "ion source for users" room are required to feed WP6. Consideration will then be done of whether a remote control and operation is required or not (which would however then be costly). There are three considered scenarios:

- 10 Hz, 8 hours of operation (for the "ion source for users" beamline → 3e5 shots/day
- 100 single shots/day
- An intermediate scenario with 1e3 shots/day

This with the assumption of 40 weeks of operation/year, the rest being for maintenance. These numbers will allow the WP6 to plan radioprotection and to estimate if these scenarii are realistic and was the incurred cost is.

Another important point is that consensus in the community shows that it is preferable to have more laser beams in the WP7B-ions rooms to reproduce there the desired radiations rather than to have connections with other ELI rooms to benefit from their radiations (electrons, X, as). The reason is that the first option saves the cost and complexity of beam transport lines (while requiring to duplicate set-ups of other rooms). This implies that we require **2 additional beams to be able to be transported in the "source development" rooms**. We need also then to **conceive beam dumps that can accommodate several kinds of radiation**.

For the source development program, one need to consider, as outlined above, that detectors could become very large, requiring the need for significant enlargement of the experimental area. Also, sufficient space needs to be reserved to build an ion optical system for proton-irradiation experiments, in order to explore the potential that these sources have in this area. For this, there will again be a strong benefit from linking ion target area to the areas of other radiation generation.

The high field chamber and experimental room will be also used for ion acceleration in order to access to the highest (EW) intensity available on ELI. In this case, we need either (i) all the 10 laser beams to be sent separately (for acceleration in a multi stage configuration) on various targets, or (ii) combined in one unique laser beam (with temporal and spatial phase locking).

Rather than having a fixed configuration building, mobile concrete walls, as in number of accelerators building, would be highly suited for experiments and to allow optimum coupling between the various synergistic sources of ELI. Flexibility will mean that a larger scientific program can be addressed. This will also allow using large-size detectors (e.g. as used by conventional accelerators) or perform particle-transport (postacceleration) experiments, as foreseen by the ELI scientific programme.

The infrastructure must be extensible to allow future development. This implies that there is a site around ELI which will allow a size increase compared to the initial plan. Also, this would suggest the idea of having the experimental site at the ground level (and not underground) to allow room for a possible extension, although this will substantially increase the costs for radioprotection.

Safety issues

ELI is a high intensity laser facility based on multi-laser beams scheme to obtain a tuneable energy and also an easier energy upgrade. Safety issues are at least of two kinds:

- issues relevant to any laser facility,
- issues relevant to radioprotection in any area where a laser beam can be focused at high intensity and produce radiations (photons, particle) in a wide scale in energy (keV to GeV).

Laser safety is usually well accounted for in laboratories driving laser facilities. Here driving several laser beams (10 in the final phase) will increase the requested controls. These issues will not be discussed here, but will be addressed in other WP.

As already said the energy range of the produced particles is extremely wide and to some extent there are unknown limits as the ELI facility enters a new domain of ultra high intensities.

The experimental area will be subject to various radioprotection controls depending on the specific zone: public area, controlled area and restricted area. These regulations will imply specific shielding of these areas; this will impact on the building design and then its cost. This radioprotection issues are specifically addressed in another WP (WP6).

Beam dumpers are already considered in WP6, these are hard for electrons but should not pose great problems for ions, even at the maximum level considered for the source development program, i.e. GeV

A general rule for room operation and radiation hazards could be as follows: depending of the required laser beam configuration and beam time, the experimental rooms could operate in parallel or sequentially. The room should allow a configurable setup disposition compatible with the radiation hazards from normal operation. Therefore an architectural solution should be found in order to allow the presence of an experimental team (e.g. setting up an experiment) in one room when other experiment is operating in the room besides. A possible approach to allow this would be:

1. The room should contain all the radiation inside
2. Each experimental station is separated by modular shielding blocks with capability to avoid that the radiation of on experimental station hit the next one or the common beam delivery area
3. Different experimental stations don't share the same access and it is not possible to circulate from one experimental station directly to other.
4. Experimental setup shieldings should be designed in order to avoid the activation of the air in the room to a minimum. Nevertheless, the architectural solution should favor air separation between experimental stations.

At this point the radiation yield resulting from secondary radiation and the activation of the room elements is not completely calculated. Therefore we can only provide qualitative design directions for radiation protection.

Finally during running operation of the ELI facility radioprotection issues will request a permanent position of a Radioprotection Competent Person for regular controls with various diagnostics of the experimental area. Upgrades of these diagnostics will be needed as the facility increases its performances (see also particle diagnostic section).

Power, cooling, vacuum and pressure requirements

All information regarding power, cooling, vacuum, pressure and temperature requirements are similar to those of general research facilities and accelerator infrastructure (e.g. SPARX). To ensure the necessary power supply a dedicated power station would be appropriated with backup; the cooling system should ensure a temperature of $\sim 20^\circ$ with stability $\pm 0.5^\circ$ in order to ensure a proper laser alignment. Pressure requirements are 10^{-7} Pa–10^{-8} Pa for the experimental stations and the overall vacuum system (these requirements are more stringent then for general laser-experiments but are necessary if one would like to couple laser-accelerated particles to conventional accelerating structures). Clean room conditions should be at least 10000 for the laser room. All auxiliary plants should be similar to what implemented in conventional accelerating facilities.

Interface with other source/experimental spaces

As outlined above, there is a strong need for synergies/coupling with other sources (i.e. other TAs).

Bibliography

[1] P. Antici et al., Phys. Rev. Lett. **101**, 105004 (2008).

[2] L. Romagnani et al., Phys. Rev. Lett. **95**, 195001 (2005).
[3] R. A. Fonseca et al., "OSIRIS: A Three-Dimensional, Fully Relativistic Particle in Cell Code for Modeling Plasma Based Accelerators", Lecture Notes in Computer Science 2331, pp. 342–351, Springer Berlin, Heidelberg (2002).
[4] https://istcluster3.ist.utl.pt/
[5] T. Esirkepov et al., Phys. Rev. Lett. **96**, 105001 (2006).
[6] T. Zh. Esirkepov et al., JETP Lett. **70**, 82 (1999).
[7] M. Yamagiwa et al., Phys. Rev. E **60**, 5987 (1999).
[8] Y. Sentoku et al., Phys. Rev. E **62**, 7271 (2000).
[9] L. Willingale et al., Phys. Rev. Lett. **96**, 245002 (2006).
[10] A. Yogo et al., Phys. Rev. E **77**, 016401 (2008).
[11] P. Antici et al., New J. Phys. **11**, 023038 (2009).
[12] T. Esirkepov et al., Phys. Rev. Lett. **92**, 175003 (2004).

6.3 A brilliant Neutron Beam produced via Neuton Halo Isomers with the ELI-NP γ-Beam

We propose to develop a brilliant, low-energy neutron beam from the γ beam of ELI-NP. In the paper [1], accepted by Appl. Phys. B, we describe in detail how low-energy neutrons will be released without moderation and without producing a broad range of fission fragments as in nuclear reactors, or a broad range of spallation products as in spallation neutron sources. Thus the new neutron facility has the advantage that it produces only small amounts of radioactivity and radioactive waste and thus requires only small efforts for radioprotection, therefore being very different from present reactor or spallation facilities. The new source can be operated as a multi-user neutron facility and could deliver several orders of magnitude more brilliant neutrons compared to the best existing neutron sources. When producing the neutrons, we envisage to use a two-step process: with the high-energy γ beam in a first step neutron halo isomers will be populated, while in a second step neutrons are released from the stopped neutron halo isomers by a second photon pulse.

For the realisation of such a neutron source we first plan to study the new neutron halo isomers in detail. We propose to search for neutron halo isomers populated via γ capture in stable nuclei with mass numbers of about A = 140–180 or A = 40–60, where the $4s_{1/2}$ or $3s_{1/2}$ neutron shell model states reach zero binding energy. These halo nuclei can be produced for the first time with the new γ-beams of high intensity and small band width ($\leq 0.1\%$), achievable via Compton back-scattering off brilliant electron beams. This production scheme thus offers a promising perspective to selectively populate these isomers with small separation energies of 1 eV to a few keV. Similar to single-neutron halo states for very light, extremely neutron-rich, radioactive nuclei [2], the low neutron separation energy and short-range nuclear force allows the neutron to tunnel far out into free space, much beyond the nuclear core radius. This results in prolonged half-lives of the isomers for the γ-decay back to the ground state in the 100 ps- μs range. Similar to the treatment of photodisintegration of the deuteron, the neutron release from a neutron halo isomer via a second, low-energy, intense photon beam has a known much larger cross section with a typical energy-threshold behavior. In the second step, the neutrons can be released as a low-energy, pulsed, polarized neutron beam of high intensity and high brilliance.

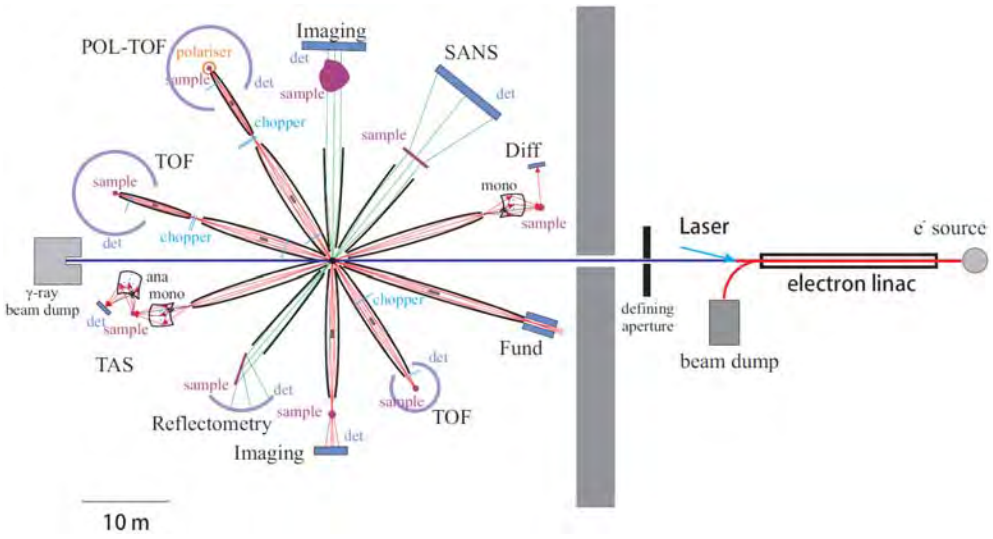

Figure 6.36: Schematic picture of a γ-beam-driven neutron facility.

In Fig. 6.36 we show the wide range of possibilities of neutron experiments with brilliant microneutron beams. The intense electron beam is shown in red. By Compton back-scattering of laser light, an intense γ beam is produced, which is shown in dark blue. The γ's populate the neutron halo isomers, from which a second photon beam releases the neutrons, which are guided by neutron mirrors. Exemplarily experiments are shown with TOF = Time of Flight, TAS = Triple Axis Spectrometer, SANS = Small Angle Neutron camera, DIF = Diffractometer, Fund = fundamental or nuclear physics.

Similarly as 30 years ago when synchrotron sources led to increases of the brilliance of x-ray beams by many orders of magnitude, the production of pulsed neutron beams with extremely high brilliance will lead to a dramatic leap in the field of neutron scattering. The well focused beams of highest intensity will allow the accurate determination of the structure of biological samples, heterostructures, and of new functional materials. These materials are often only available in small quantities. The exceptionally strong scattering of neutrons by hydrogen and other light materials will provide key information concerning the functionality of bio-materials, which cannot be easily obtained using synchrotron beams or existing neutron sources. In addition, the brilliant neutron beams will allow for the first time the investigation of collective excitations, i.e. magnons and phonons, and relaxation as well as diffusion processes in samples that are only available in smallest quantities. Moreover, the by orders of magnitude smaller width of the neutron pulses will allow the investigation of time dependent processes and the dynamics in systems far away from equilibrium. The new neutron beams will therefore open completely new scientific opportunities in the field from biology to hard condensed matter to geosciences and nuclear physics. In Ref. [1] many new possibilities are described in more detail.

Bibliography

[1] D. Habs, M. Gross, P. G. Thirolf, and P. Böni, arXiv 1008.5324v2[nucl-ex] 2010, accepted for publication in Appl. Phys. B.

[2] P.G. Hansen, A.S. Jensen, and B. Jonson, Annu. Rev. Nucl. Part. Sci. **45**, 591 (1995).

6.4 X-ray Generation

6.4.1 The ELI Plasma Wiggler Beamline

Since their discovery in 1896 [1], X-rays have fundamentally revolutionized science, medicine and technology. X-ray sources have seen a tremendous amount of development since the time of the original X-ray tubes. Each successive generation of X-ray machines has opened up new frontiers in science, such as the first radiographs and the determination of the structure of DNA. To further the progress in these fields, users need access to ever more powerful sources of higher quality X-rays. State-of-the-art X-ray sources can now produce *coherent* high-brightness beams of X-rays with energies greater than a kiloelectronvolt, which promise a new revolution in imaging complex systems on the nanometre and femtosecond scale. Despite these successes and the ensuing demand, only a few dedicated synchrotron facilities exist in the world, partly due to the size and cost of conventional particle accelerator facilities on which these sources are based [2]. Recent progress in laser-driven plasma accelerators now allows the accelerating high-charge electron beams to high energy in short distances [3–5], to produce directional, spatially coherent, intrinsically ultrafast beams of hard X-rays [6]. This reduces the size of the synchrotron source from the tens of metres to the centimetre scale, simultaneously accelerating and wiggling the electron beam.

Content

We introduce the theoretical framework of wakefield acceleration and plasma wiggler radiation generation in the "matched regime", give scaling laws and apply the scheme to laser scenarios planned for the ELI facilities. We compare the anticipated electron and X-ray beam parameters for ELI with previous experimental results. Depending on the ELI configuration used, X-rays from a plasma wiggler beamline (PWB) can be several orders of magnitude brighter than current betatron sources, and comparable to or better than 3^{rd} generation synchrotron facilities. We also discuss a basic layout of a PWB and motivate the ELI PWB with a wide range of unique usage scenarios, experiments and applications. An ELI PWB has the potential to facilitate a myriad of uses across the whole spectrum of light-source applications.

Novel Light Sources – Schemes and Recent Development

There are a number of proposals to use extreme nonlinear interactions of the latest generation of high-power ultrashort-pulse laser systems to produce beams of high-energy photons with high brightness and short pulse duration. For example, high-order harmonic generation from a flying [7, 8] or oscillating [9–13] plasma mirror promises (trains of) coherent attosecond pulses of unprecedented intensity [14], and Thomson and Compton scattering could extend photon energies into the X-ray and γ-regime [15–20]. An alternative proposal has been the use of compact laser–plasma accelerators to drive sources of undulating/wiggling radiation, either by coupling an electron beam from a laser wakefield accelerator into a conventional magnetic undulator [21, 22] or by using the plasma accelerator itself as the miniature wiggler [6, 23–25]. Both the conventional [26] and the plasma wiggler [27] may ultimately achieve gain, resulting in a compact free-electron laser.

The Plasma Bubble Wiggler – A Source of Betatron/Synchrotron Radiation

The concept of a plasma wiggler was discussed theoretically [23, 28], with the first experiments subsequently being carried out to characterize the beam divergence, keV energy range, broad spectral width [24], source size [29], detailed spectral shape [30, 31], betatron oscillation amplitude [32, 33] and pulse duration [34, 35]. Methods to influence the betatron spectrum by tuning the oscillation amplitude, at ultra-relativistic laser intensities (direct-laser-acceleration [25],

with density-tailored plasmas [36] and with laser profile shaping [37] have been discussed and experimentally implemented, demonstrating good control over the betatron mechanism. Recent progress in laser technology and laser-driven wakefield acceleration [3–5] in the blowout regime [38–41] has lead to stable [42] acceleration of high charge [43] electron beams to high energies [44], improving betatron source size, divergence, X-ray hardness, peak brightness and spatial coherence properties manifold [6, 45]. Theoretical, analytical and numerical modelling capabilities now allow (one-to-one) prediction of electron/X-ray beam parameters [6, 46–50].

In a recent experiment [6] carried out with the Hercules laser [51] at the Center for Ultrafast Optical Science at the University of Michigan, linearly polarized pulses with a central wavelength of $\lambda_0 = 800\,\mathrm{nm}$, a Gaussian FWHM pulse duration of $\tau = 32\,\mathrm{fs}$ and a maximum energy of 2.3 J were focused onto the front edge of a 3–10 mm supersonic helium gas jet, to a FWHM spot of 11 µm, peak intensity of $I = 4.7 \times 10^{19}\,\mathrm{W\,cm^{-2}}$ or normalized vector potential $a_0 = 4.7$ with an off-axis parabolic mirror of focal length f = 1 m and F-number of F = 10, yielding plasma electron densities of $4\text{–}22 \times 10^{18}\,\mathrm{cm^{-3}}$. For example, for an electron density of $8 \times 10^{18}\,\mathrm{cm^{-3}}$ on the 5 mm nozzle, electron beams of $\mathrm{W} = (230 \pm 70)\,\mathrm{MeV}$ with $\Delta\mathrm{W/W} = (25 \pm 10)\%$ energy spread at full-width at half-maximum (FWHM) were observed, with a root-mean-square (r.m.s.) divergence of $1.5 \times 1.8\,\mathrm{mrad^2}$ and r.m.s. pointing fluctuation of $4.8 \times 4.7\,\mathrm{mrad^2}$, with 100–300 pC of charge in the beam. A schematic of the setup is shown in Fig. 6.37a–b. With the electron beam deflected away from laser axis by a spectrometer magnet, a bright (undeviated) beam of X-rays was also observed co-propagating along the laser axis (Fig. 6.38a–c). The profile has a FWHM divergence of $\theta_x \times \theta_y = 4 \times 13\,\mathrm{mrad^2}$ giving a betatron strength parameter $\mathrm{K} = \theta\gamma_z$ of $\mathrm{K}_x = 1.8$ and $\mathrm{K}_y = 6$ for a simultaneously measured peak electron beam energy of 225 MeV ($\gamma = 440$). With $\mathrm{K} > 1$, the plasma wiggler operates in a mild wiggler regime. The X-ray beam resolves microscopic objects, as shown exemplarily by the radiographic image of a resolution test target with 3 µm features (Fig. 6.38d–f). Detailed analysis of the X-ray source size with penumbral imaging reveals that the $1/\mathrm{e}^2$ intensity source size can be as small as 1 µm, leading to the observation of Fresnel fringes (Fig. 6.39), a proof of the appreciable level of spatial coherence in the X-ray beam.

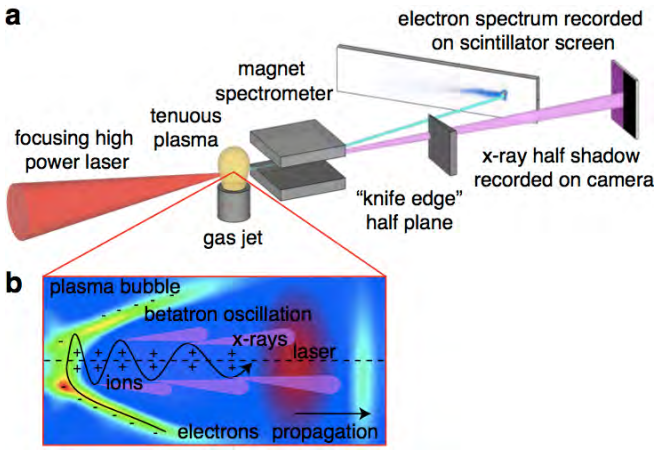

Figure 6.37: (a) Schematic of the experimental setup. A high intensity laser is focused into a supersonic gas jet, forming a tenuous plasma and driving a highly nonlinear plasma wave. (b) Electrons that are injected into the leading bubble-shaped plasma wave period are performing betatron oscillations whilst being accelerated along the laser propagation direction. (a) The betatron X-rays are diffracted by a knife edge to obtain the X-ray source size. The electron beam is dispersed with a permanent magnet to measure the spectrum and divergence.

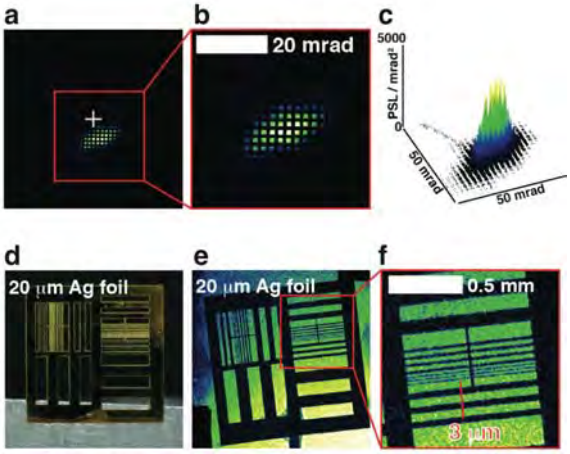

Figure 6.38: The quality of the X-ray beam is assessed by measuring its profile and imaging microscopic objects: (a–c) Single shot X-ray beam profile observed through a mesh of 60µm Ag wires, filtered with 13 µm Al foil and measured with imaging plate for a single shot at 65 TW on a 10 mm nozzle at 6.8×10^{18} cm^{-3} giving a monoenergetic beam at 225 MeV. The white plus signs indicate the direction of the laser. (d) Photograph of a 20 µm thick gold resolution test target. (e–f) Single shot radiograph of the resolution test target filtered with 2.4 µm Al foil and measured with an X-ray CCD for 66 TW on a 5 mm nozzle at 8.0×10^{18} cm^{-3}, giving a monoenergetic beam at 265 MeV.

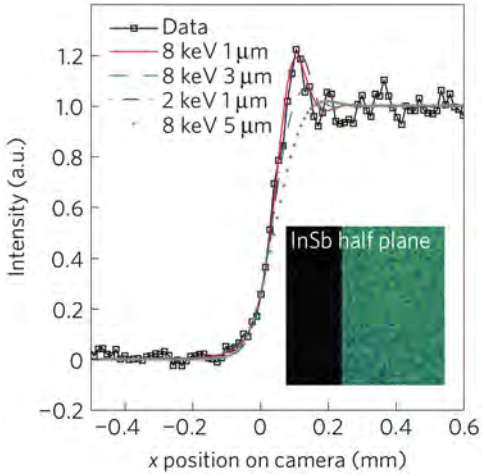

Figure 6.39: The X-ray source casts a shadow of a half-plane on the detector: Close-up of measured intensity distribution (black squares) integrated along the edge of the half-shadow (inset) and exemplary intensity distributions using Fresnel diffraction modelling, for a source with Gaussian intensity distribution and synchrotron spectrum E_{crit} /w$_x$ of 8 keV/1 µm (solid red), 8 keV/3 µm (dashed green), 2 keV/1 µm (dash–dotted blue) and 8 keV/5 µm (dotted grey).

Description of Theory

The plasma bubble wiggler is similar to an ion-channel wiggler [23] (and references therein), except for the strong longitudinal fields that mean that the electron beam is simultaneously both accelerated/decelerated while emitting radiation. This variation in electron energy implies that obtaining a monochromatic radiation source is more difficult, but for a broad-band source the combined accelerator/wiggler means that the source can be extremely compact.

The crucial parameters determining the radiation character emitted by a charged particle in a wiggler are the wavelength and amplitude of the oscillation, combined in the general definition of the scaled wiggler parameter $K = \gamma dx/\,dz|_{z=0} = \gamma k_0 x_0$ [52], where $\gamma = 1/\sqrt{1-\beta_0^2}$ is the Lorentz factor of an electron traveling at a fraction β_0 of the speed of light in the z direction, x_0 is the amplitude of oscillation and $k_0 = 2\pi/\lambda_0$ is the oscillation wave-number. For $K \gg 1$ the radiation is synchrotron-like, and for $K<1$ the radiation consists of one or more harmonics with a harmonic width determined by the number of wiggler periods and the properties of the charged particle bunch.

One key point when considering a plasma bubble wiggler is that both of these parameters, the wavelength and amplitude, depend on the Lorentz factor of the electron. In a plasma bubble we typically inject a bunch with some initial oscillation amplitude, but as the particle accelerates, its oscillation amplitude changes. This is because the particle motion is an adiabatic oscillator with some secular variation, analogous to a pendulum with a slowly varying length. Kostyukov *et al.* demonstrated adiabatic invariance for the system by formulating an effective 'transverse Hamiltonian' [39] for the oscillatory behavior in an idealized spherical bubble. The properties of the electron bunch at injection are therefore critical to determining the radiation that is produced. The simplest mechanism, and the one that occurs in almost all of the laser wakefield experiments to date, is trapping of electrons that form the sheath around the bubble. These electrons are pulled in to the center with a large transverse momentum, which results in a wiggler parameter that is large, $K \gg 1$ [49].

To examine the radiation scaling for a single stage plasma accelerator/wiggler with self-trapped electrons, Thomas [49] reformulated the equations of motion of an electron in a spherical bare ion cavity in a Lorentz boosted frame. These can be used to find the phase, amplitude and frequency of the oscillations at any point, from some approximate initial conditions calculated by assuming an electron follows the contours of the bubble before trapping (which is an elliptic trajectory in the boosted frame). Using the expression given in Lu *et al.* [41] for the matched bubble radius, $r_b = 2\sqrt{a_0}c/\omega_p$, this gave an initial transverse momentum at the point of injection of the electron of $p_{\perp 0} = (\pi/4)a_0 m_e c$. When accelerated in the bubble, the electrons gain a maximum energy of $E_{\max} = (2/3)a_0 n_c/n_p$, where n_c is the critical density, n_p is the plasma density and $a_0 = eE_0/m_e c\omega_0$ is the laser field strength parameter [41, 53].

In the laboratory frame, the radial equation of motion is [39, 53]:

$$\frac{d^2 r}{d\tau^2} = -\frac{1}{4}\gamma\omega_p^2 r\,(1+\beta_z)\,, \tag{6.2}$$

where τ is the proper time of the electron. Assuming that the electron acceleration time is long compared to the oscillation period, this results in simple harmonic motion with a slowly varying frequency in (proper) time, $\Omega_\tau = \omega_p\sqrt{\gamma/2}$. From classical mechanics, in a similar manner to the approach of Kostyukov *et al.* [39], for an adiabatically invariant hamiltonian $H_\perp$ of an oscillator, the action, $J = 2\pi H_\perp/\Omega_\tau$, is conserved. A Hamiltonian can be deduced a posteriori for the transverse dynamics of the electron, by analogy with the non-relativistic simple harmonic oscillator (substituting τ for t):

$$H_\perp = \frac{1}{2m_e}\left[p_\perp^2 + m_e^2\Omega_\tau^2 r^2\right]. \tag{6.3}$$

The solutions to the oscillator equation are [54]:

$$p_\perp \cong \sqrt{\frac{m_e J\Omega_\tau}{\pi}}\cos\left[\int \Omega_\tau d\tau\right], \tag{6.4}$$

$$r \cong \sqrt{\frac{J}{m_e\Omega_\tau\pi}}\sin\left[\int \Omega_\tau d\tau\right]. \tag{6.5}$$

$\Omega_\tau d\tau$ can be substituted for $\omega_\beta dt$, where $\omega_\beta = \omega_p/\sqrt{2\gamma}$, since $d\tau = \gamma dt$. Assuming that the electron oscillations are initiated close to the rear of the bubble, and on-axis with initial transverse momentum $p_{\perp 0}$ and energy γ_0, the oscillations are described by:

$$p_\perp \cong \left(\frac{\gamma(t)}{\gamma_0}\right)^{1/4} p_{\perp 0} \cos\left[\int \omega_\beta(t) dt\right], \tag{6.6}$$

$$r \cong \sqrt{\frac{2}{\gamma_0}} \left(\frac{\gamma_0}{\gamma(t)}\right)^{1/4} \left(\frac{p_{\perp 0}}{m_e c}\right) \frac{c}{\omega_p} \sin\left[\int \omega_\beta(t) dt\right]. \tag{6.7}$$

The wiggler parameter for this oscillator varies throughout the trajectory of the electron. From the fundamental definition, it is given by $K \approx (\pi/4)(\gamma(t)/\gamma_0)^{1/4} a_0$. To proceed with the scalings, since the wiggler parameter K for the plasma wiggler is large, a synchrotron-like spectrum results. We can assume that at each oscillation amplitude maximum, a synchrotron radiation spectrum is emitted. The sum of the contributions of the synchrotron spectra from different periods gives a spectrum:

$$\frac{d^2E}{d\omega d\Omega} = \frac{3e^2}{2\pi^3 \varepsilon_0 c} \gamma_{\max}^2 A\left(\frac{\omega}{\omega_{c\,\max}}\right) \tag{6.8}$$

where $\omega_{\mathrm{cmax}} = (3/2)\gamma_{\max}^3 \omega_\beta r_{\min}/c$ is the critical frequency for an electron orbit in an ion channel [23] corresponding to the maximum Lorentz factor $\gamma_{\max}$ and amplitude of oscillation at the maximum energy $r_{\min}$, and the spectrum function is [49]:

$$A(x) = x^2 \int_{-1}^{1} \frac{1}{(1-\mu^2)^{3/2}} K_{2/3}^2\left(\frac{x}{(1-\mu^2)^{7/4}}\right) d\mu. \tag{6.9}$$

Figure 6.40a shows this function (ii) calculated numerically, compared with (i) a synchrotron spectrum with a critical frequency corresponding to the maximum electron energy in the bubble and (iii) a synchrotron spectrum with a critical frequency so that the peak is comparable to that of (i). The spectral shape looks similar to a synchrotron spectrum, but has a hotter tail compared to a synchrotron with a similar peak frequency. The peak frequency is therefore reduced by a factor of approximately 0.57 compared with the peak energy that the electron obtains during the acceleration.

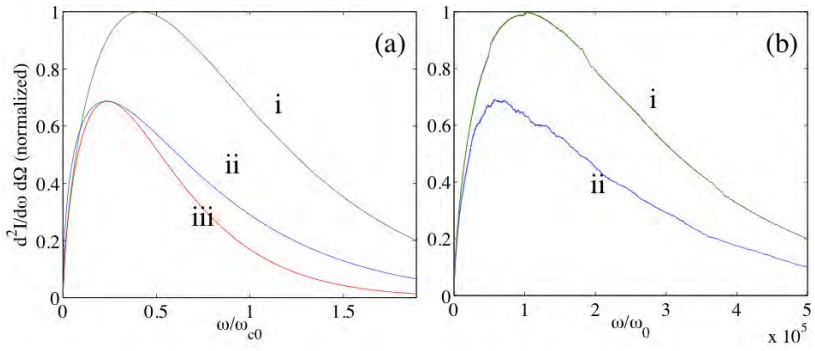

Figure 6.40: (a) Graph of the on-axis spectral intensity, $d^2E/d\omega d\Omega$ calculated from (i) the synchrotron-like spectrum, and (ii) equation 6.8 for a synchrotron spectrum emission by an electron with varying energy. (iii) shows a synchrotron-like spectrum with the same peak energy and amplitude as (ii), which a critical frequency $\omega_c = 0.57\omega_{\mathrm{cmax}}$ and an amplitude of 0.69 of (i). (b) Shows the spectra calculated using the code *RDTX* [55] from (i) 17.3 (i.e. γ_p) oscillations of an electron with Lorentz factor $\gamma = 3484$ and transverse momentum $p_y = 17.37 m_e c$ in a radial electric field and (ii) an electron accelerating in a bubble to maximum transverse oscillations and energy of $\gamma = 3484$, $p_\perp = 17.37 m_e c$. ω_0 is the frequency of the drive laser (reproduced from reference [49]).

ELI Betatron Beamline Parameters

The equations from the previous section can be used to derive scalings for the critical energy of the photons, $E_{\mathrm{crit}} = \hbar\omega_0 a_0^{5/2} (n_c/n_p)^{9/8}$ and peak spectral brightness from one electron, $S = \left(\frac{\omega_{\max}}{\sigma\tau_b}\right) \max\left(\frac{d^2E}{d\omega d\Omega}\right)$, where the source size (area) is σ, the duration of the radiation is τ_b and $\omega_{\max}$ is the frequency at the maximum of the spectral intensity. This can be expressed in terms of the photon flux, as in the synchrotron literature in units of (Photons) $\mathrm{s}^{-1}\,\mathrm{mrad}^{-2}\,\mathrm{mm}^{-2}/0.1\%\mathrm{BW}$. Using the maximum of the function A, $\alpha = e/c^4\pi\varepsilon_0$ the fine structure constant, an area of $\sigma = \pi y_{0\min} = \pi a_0 c^2/\gamma_p^{3/2}\omega_p^2$, a radiation temporal duration of $\tau_b = r_b/c$, the expressions derived for the maximum energy, and the number of oscillations γ_p , this becomes:

$$S\left(\frac{\text{Photons}}{\text{s mrad}^2\ \text{mm}^2\ 0.1\%\ \text{BW}}\right) \approx \frac{\alpha}{\pi^3}\frac{\omega_0^3}{10^{15}3^{9/4}c^2}a_0^{1/2}\left(\frac{n_c}{n_p}\right)^{7/4}. \tag{6.10}$$

We now use scalings for the electron bunch properties derived by Lu *et al.* [41] to express these parameters in a useful form as a function of plasma density and laser power. The field strength parameter a_0 can be expressed for a matched spot in terms of the laser power as $a_0 = 2(P/P_c)^{1/3}$, where $P_c = 17\times10^9 n_c/n_p$ is the critical power for self focusing. The size of the electron bunch is also given as $N_b = 3.1\times10^8\lambda_0\sqrt{P}$. In terms of the power, the electron bunch energy predicted is:

$$W_{\max}\,(\mathrm{MeV}) = 11.7\left(\frac{P}{100\ \mathrm{TW}}\right)^{1/3}\left(\frac{\lambda_0}{0.8\ \mu\mathrm{m}}\right)^{-4/3}\left(\frac{n_c}{n_p}\right)^{2/3}. \tag{6.11}$$

For a 0.8 µm laser driver, which is typical of current Ti:Sapphire high-power laser systems, the critical energy of the spectrum can therefore be expressed in keV for a laser with a matched spot with power P and taking into account the 0.57 factor for the varying electron energy, as:

$$E_{\mathrm{crit}}\,(\mathrm{keV}) = 6.8\left(\frac{P}{100\ \mathrm{TW}}\right)^{5/6}\left(\frac{n_c}{n_p}\right)^{7/24}. \tag{6.12}$$

Likewise, the peak spectral brightness from the bunch of electrons under ideal conditions, from the matched pulse given above can be expressed as:

$$S\left(\frac{\text{Photons}}{\text{s mrad}^2\ \text{mm}^2\ 0.1\%\ \text{BW}}\right) \approx 4.5\times10^{19}\left(\frac{\lambda_0}{0.8\ \mu\mathrm{m}}\right)\left(\frac{\mathrm{P}}{100\ \mathrm{TW}}\right)^{2/3}\left(\frac{n_c}{n_p}\right)^{19/12}. \tag{6.13}$$

Based on the formalism in equations 6.2–6.13, the laser focusing and plasma target requirements for a 10 TW, 100 TW, 1 PW and 10 PW laser are calculated and the electron and X-ray beam characteristics are predicted. This is summarized in Table 6.8. The three cases with the highest laser power in Table 6.8 represent various ELI laser scenarios and shall be referred to as ELI-100-TW-PWB, ELI-1-PW-PWB and ELI-10-PW-PWB from now on. Current experimental results fall between the 10 TW and 100 TW case, as comparison with Table 6.9 shows. The ELI-PWB cover the spectral range from soft X-rays to gamma-rays and extend the domain of existing 3^{rd} and 4^{th} generation light sources to highest brilliance at highest photon energy, as shown in Fig. 6.41.

Schematic of the ELI Plasma Wiggler Beamline

The ELI plasma wiggler beamline consists of a wakefield hutch, an optics hutch and an experimental hutch, as shown in Fig. 6.42.

The wakefield hutch includes:

a) laser focusing geometry

Table 6.8: Predicted radiation characteristics from the scalings for various laser parameters while maintaining $a_0 = 5$. *in units of Photons/(s mrad^2 mm^2 0.1%BW).

ELI Plasma Wiggler Beamline (PWB)		ELI-100-TW-PWB	ELI-1-PW-PWB	ELI-10-PW-PWB
Laser Power	10 TW	100 TW	1 PW	10 PW
Pulse duration	11.6 fs	37 fs	116 fs	368 fs
Spot Size	3.5 μm	11 μm	35 μm	110 μm
Plasma density	4.7×10^{19} cm^{-3}	4.7×10^{18} cm^{-3}	4.7×10^{17} cm^{-3}	4.7×10^{16} cm^{-3}
Plasma length	88 μm	2.8 mm	88 mm	2.8 m
Electron peak energy	61 MeV	610 MeV	6.1 GeV	61 GeV
Beam charge	0.13 nC	0.4 nC	1.3 nC	4 nC
X-ray critical energy	2.9 keV	38 keV	511 keV	6.8 MeV
Source size	1.3 μm	1.8 μm	2.4 μm	3.2 μm
Divergence	66 mrad	6.6 mrad	660 μrad	66 μrad
K parameter	6.9	9.2	12	16
X-ray peak brightness*	3×10^{21}	5.4×10^{23}	9.6×10^{25}	1.7×10^{28}
Photon number	1.5×10^{8}	2×10^{9}	2.6×10^{10}	3.5×10^{11}
Repetition rate	1 kHz	1 kHz	10 Hz	0.01 Hz
X-ray average brightness*	3×10^{10}	2×10^{13}	1×10^{14}	6×10^{15}

b) a plasma target (gas jet, gas cell or capillary waveguide) to generate the wakefield accelerator and plasma bubble wiggler for electron beam acceleration and radiation generation
c) electron beam diagnostics (beam profile monitor to measure the beam pointing, integrating current transformer (ICT) to measure the charge, optical transmission radiation diagnostic to measure the pulse duration, quadropole electron beam optics and dipole magnet spectrometer to measure the electron beam energy and energy spread, electron beam dump, radiation shielding walls, etc.)

The optics hutch includes

a) X-ray beam diagnostics (beam profile monitor to measure the beam pointing and divergence, spectrometer to measure the beam spectrum, calorimeter to measure the beam energy, etc.)
b) X-ray optics (slits, beam collimation, steering and focusing optics, etc.)
c) X-ray monochromator

1. beamline into the experimental hutch

The experimental hutch may include

a) further X-ray optics
b) sample handling capability
c) experimental diagnostics
d) others

depending on the specific requirements of the experiment.

In particular for the ELI-100-TW and ELI- 1-PW beam lines, due to the similarity of the

Table 6.9: Experimentally measured electron and radiation characteristics taken from [6]. *in units of Photons/(s mrad^2 mm^2 0.1%BW).

Laser Power	Hercules-70-TW [6]
Pulse duration	32 fs
Spot Size	11 µm
a_0	4.7
Plasma density	8×10^{18} cm^{-3}
Plasma length	5 mm
Electron energy/ temperature	$W_{max} = 230 \pm 70$ MeV
Beam charge	0.1–0.3 nC
X-ray energy	E_{crit}=29±13 keV
X-ray brightness*	10^{22}

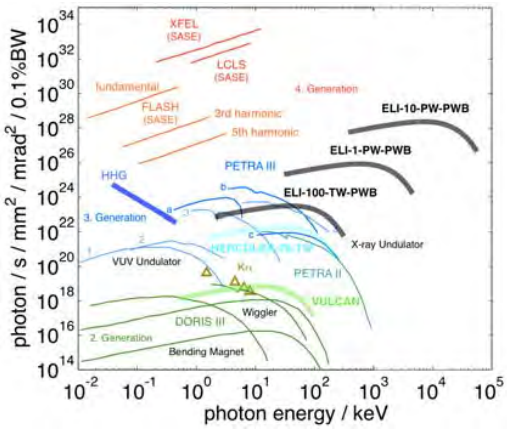

Figure 6.41: Peak brightness of ELI plasma wiggler beamlines, synchrotron, FEL and other novel light sources. Tuning curves of DORIS III sources are colored green including BW2 and BW3 wiggler and bending magnet. Tuning curve of PETRA II source is colored in cyan. Tuning curves of third generation PETRA III sources are colored in dark blue, with (a) soft X-ray undulator (4 m), (b) standard $K_{max} \simeq 2.2$ undulator (5 m), (c) hard X-ray $K_{max} \simeq 7.5$ wiggler (7.5 m). Tuning curves of other third generation sources are coloured in light blue, with (6.2) BESSY II U125, (6.3) ALS U5, (6.4) DIAMOND U46, (6.5) SPring-8 BL46. Betatron spectra from the experiments on the VULCAN and HERCULES laser are overlaid in fat green and blue lines, respectively. Upcoming 4th generation light sources LCLS, XFEL and recently commissioned soft X-ray FEL FLASH are given in red and orange, respectively. For comparison, peak brightness obtained from a laser solid target K_α [56] source and a laser solid target high harmonic source [11] is also included. All other curves taken from [57].

key X-ray beam parameters with existing, conventional synchrotron, wiggler and undulator sources, there will be significant synergy effects regarding layout and equipment of the optics hutch [57]. Similarly, target and electron beam diagnostics of the wakefield hutch can heavily draw from recent progress in laser wakefield acceleration [58]. Requirements of the wakefield and optics hutch for the ELI-10-PW beam line are to large extent beyond currently existing plasma acceleration and synchrotron technology, but may benefit from (Compton scattering) gamma-ray facilities [59]. Further research into aspects of the above list will be necessary before an ELI-10-PW beam line can be specified in greater detail.

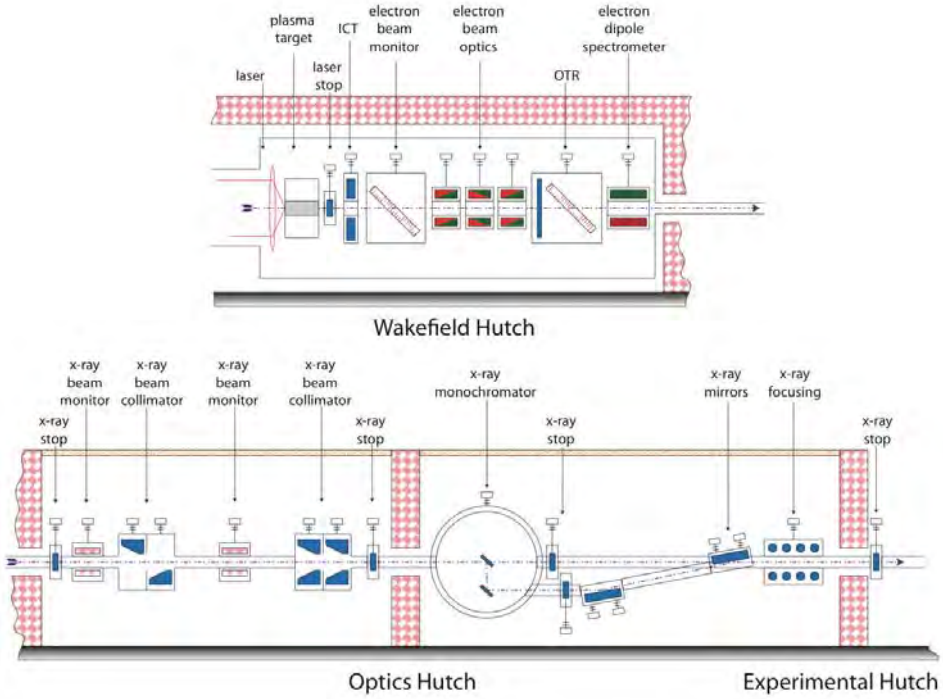

Figure 6.42: Schematic layout of the plasma wiggler beam line for the ELI-100-PW or ELI-1-PW laser.

Application Scenarios for the ELI Plasma Wiggler Beamlines

Due to the broad range of beam parameters covered (see Table 6.8), the ELI-PWBs are able to cater for a variety of experiments and applications. A unique advantage of each of the discussed ELI wiggler beam lines is their ability to be combined with each other and other optical lasers due to their all-optical and ultrafast nature and the laser portfolio offered by the ELI facility. This would allow for applications that require multiple optical and X-ray beams, such as pump probe experiments.

Synchrotron applications for the ELI-PWBs

With regard to photon energy range, pulse repetition rate, average and peak brightness, the ELI-100-TW-PWB (and ELI-1-PW-PWB to some extent) is similar to a conventional 3^{rd} generation Synchrotron wiggler beam line optimized for hard X-rays, with K-parameter $K \simeq 10$ (see Fig. 6.41). The ELI-PWB could therefore be fitted with various types of experimental stations for spectroscopy, diffraction and imaging experiments [57, 60].

Spectroscopic experiments allow researchers to reveal elemental composition [61, 62], chemical [61] and physical [62] properties of both inorganic material and biological systems. Scientists use X-rays to reveal characteristics of samples including biomedical specimen, condensed matter, engineering and magnetic materials that cannot be observed with infrared, UV or visible light.

When X-rays pass through a crystal they are reflected off the regular arrangement of planes of atoms that make up the crystal. Diffraction studies can be used to look at the structure of chemical compounds and composite materials, such as minerals, ceramics, biological samples and electronic and magnetic materials. Macromolecular crystallography for example yields the atomic structure of proteins, which, when crystallised, greatly reduce the X-ray fluence required

to measure a high-resolution diffraction patterns by coherent Bragg amplification. Polychromatic synchrotron radiation, as naturally available from the ELI-PWBs is necessary to record a Laue diffraction pattern with many diffraction spots, each of which correspond to the Fourier component (structure factor) of the electron density of the unit cell of the crystal. The method for example allows surveillance of the functioning of oxygen binding proteins (like haemoglobin) on the hundred picosecond timescale, as they grab and release carbon oxide in their catcher mitts [63].

Coherent imaging applications for the ELI-PWBs

Even when specimens do not crystallize, a similar computational technique can be used in a lensless imaging scheme [64] to infer the structure of a specimen from the diffraction pattern so long as the X-ray probe is (temporally and spatially) coherent and the spatial scale of interest is oversampled [65]. Lensless imaging is also the technique of choice for hard X-rays, where direct imaging methods are limited in resolution by the available X-ray optics [66].

Temporal coherence is inversely proportional to spectral width and can be achieved from the ELI-PWBs with suitable (crystal) monochromators as deployed at conventional synchrotrons. Spatial coherence increases proportionally with the distance from the source and with the inverse of the source size. This means conventional X-ray tubes and even synchrotron light sources must be apertured, which becomes difficult for hard X-rays, reduces the available photon flux and increases the required exposure time. Smaller source sizes can be obtained from high-harmonic sources, but their suitability for lensless imaging is limited to the relatively soft X-rays [67]. A unique advantage of the ELI plasma wiggler beam lines is therefore their micrometer source size for both soft and hard X-rays (see Table 6.8 and Section 3). This means their X-ray beams naturally possess an appreciable degree of spatial coherence.

Phase contrast imaging, which even works for white (spectrally broad) synchrotron radiation [68], can yield extra contrast from a specimen, not by absorption of X-rays but by bending of the wavefront. The huge potential of the technique for medical diagnostics is documented by numerous animal studies to visualize soft tissue such as cancerous liver or kidney lesions [69, 70] and for example by the first human transvenous coronary angiography, removing the need for a contrast agent [71]. Progress has been held back due to the lack of suitable X-ray sources with the necessary spatial coherence properties and/or due to the requirement for cumbersome imaging techniques [72].

The ELI-100-TW-PBB would not only facilitate phase contrast imaging, but due to its high repetition rate, three-dimensional phase or absorption contrast images using projections from multiple angles could be built up very fast. Absorption tomography has been used to reconstruct nanometer to micrometer resolution 3D images of biological samples such as butting yeast to study size, shape and distribution of its cell organelles [73] or trabecular vertabrae bones to assess age related bone decay in humans [74]. X-ray computed tomography can be extended to generate quantitative high-contrast three-dimensional electron density maps using a ptychographic coherent diffractive imaging approach [75, 76].

In addition to its suitability for these kinds of advanced imaging applications, the 10-100 times larger divergence angle of ELI-100-TW-PBW and ELI-1-PW-PBW when compared to conventional wiggler sources permits exposure of extended objects.

Ultrafast femtosecond applications for the ELI-PWBs

Additionally, the ultrashort pulse duration and peak brightness of the ELI-PWB could reduce the integration time required to obtain experimental data. Motion blur can be frozen on the millisecond timescale over which the sample may vibrate or move. Chemical reactions could be resolved on the femtosecond scale, as required for X-ray transient absorption spectroscopy [77].

Femtosecond X-ray pulse duration typically requires a 4^{th} generation light source (free-electron-laser) and peak brightness has to be traded for shortest pulse duration at conventional wiggler facilities [78].

Synchronized laser and X-ray beam applications for ELI

The following measurements require absolute synchronisation between an (optical) pump and (X-ray) probe pulse. Due to its unique portfolio of optical and X-ray beam capability, ELI could increase the scope of multiple-beam applications.

Time resolved X-ray diffraction using a laser solid target X-ray source has been used to measure non-destructively with subpicometer spatial and subpicosecond temporal resolution reversible changes in a nanostructure [79]. Point-projection K-shell absorption spectroscopy was used to infer the ionization and recombination dynamics of transient aluminum plasmas on a picosecond timescale [80]. Femtosecond time-resolved X-ray diffraction from laser-heated organic films has been demonstrated [81] and nonthermal melting of germanium was watched with ultrafast X-ray diffraction [82].

Gamma-ray Applications for the ELI-PWBs

ELI-1PW-PBW extends conventional synchrotron sources to higher brightness at harder energies. This could permit routine diagnosis of breast cancer from a single hair [83] or the discrimination of glass fragments for forensic analysis [84], which require photon energies in excess of 100 keV, not widely available from conventional synchrotrons. With even higher X-ray energies, ELI-1PW-PBW and ELI-10PW-PBW push into the gamma regime, where current sources are either radioisotopes (limiting the range of applications) or rely on Compton scattering (requiring large accelerator labs [59]). Gamma radiation has applications such as photofission and photodisintegration to transmute spent nuclear fuel, nuclear resonance fluorescence to study the nuclear structure or identify isotopes [19,59], gamma-ray radiography to scan cargo for homeland security and might open a way towards a gamma-gamma collider for high energy physics. [85] or pumping of a gamma laser [86].

Conclusions

In summary we have introduced laser driven plasma wigglers as a source of synchrotron-like radiation, presented a theoretical framework and reviewed the current state of the field. With the help of the framework, we have designed plasma wiggler beamlines, predicted their key performance parameters and outlined application scenarios for the 100 TW, 1 PW and 10 PW laser capability of the planned ELI facility. The ELI plasma wiggler beamlines extend the domain of existing 3^{rd} and 4^{th} generation light sources to highest brilliance at highest photon energy. The ELI-plasma wiggler beamlines will add X-ray and gamma-ray beam capability to the optical laser portfolio of ELI, making it a truly extreme light infrastructure.

Bibliography

[1] Roentgen, W. C., *Nature* **53**, 274 (1896).
[2] Bilderback, D. H., Elleaume, P. and Weckert, E., *J. Phys. B-At. Mol. Opt. Phys.* **38**, 773 (2005).
[3] Mangles, S. P. D. *et al.*, *Nature* **431**, 535 (2004).
[4] Geddes, C. G. R. *et al.*, *Nature* **431**, 538 (2004).
[5] Faure, J. *et al.*, *Nature* **431**, 541 (2004).
[6] Kneip, S. *et al., Nat. Phys.* **6**, 980, (2010).
[7] Kando, M. *et al.*, *Phys. Rev. Lett.* **99**, 135001 (2007).
[8] Kando, M. *et al.*, *Phys. Rev. Lett.* **103**, 235003-235004 (2009).

[9] Dromey, B. *et al.*, *Nat. Phys.* **5**, 146-152 (2009).
[10] Dromey, B. *et al.*, *Phys. Rev. Lett.* **99**, 085001 (2007).
[11] Dromey, B. *et al.*, *Nat. Phys.* **2**, 456 (2006).
[12] Nomura, Y. *et al.*, *Nat. Phys.* **5**, 124 (2009).
[13] Thaury, C. *et al.*, *Nat. Phys.* **3**, 424 (2007).
[14] Bulanov, S. V., Esirkepov, T. and Tajima, T., *Phys. Rev. Lett.* **91**, 085001 (2003).
[15] Esarey, E., Ride, S. K. and Sprangle, *Phys. Rev. E* **48**, 3003 (1993).
[16] Phuoc, K. T. *et al.*, *Phys. Rev. Lett.* **91**, 195001 (2003).
[17] Chen, S. Y., Maksimchuk, A. and Umstadter, D., *Nature* **396**, 653 (1998).
[18] Gibson, D. J. *et al.*, *Phys. Rev. Spec. Top.-Accel. Beams* **13**, 070703 (2010).
[19] Albert, F. *et al.*, *Phys. Rev. Spec. Top.-Accel. Beams* **13**, 070704 (2010).
[20] Schoenlein, R. W. *et al.*, *Science* **274**, 236 (1996).
[21] Fuchs, M. *et al.*, *Nat. Phys.* **5**, 826 (2009).
[22] Schlenvoigt, H. P. *et al.*, *Nat. Phys.* **4**, 130 (2008).
[23] Esarey, E., Shadwick, B. A., Catravas, P. and Leemans, W. P., *Phys. Rev. E* **65**, 056505 (2002).
[24] Rousse, A. *et al.*, *Phys. Rev. Lett.* **93**, 135005 (2004).
[25] Kneip, S. *et al.*, *Phys. Rev. Lett.* **100**, 105006 (2008).
[26] Gruner, F. *et al.*, *Appl. Phys. B-Lasers Opt.* **86**, 431 (2007).
[27] Whittum, D. H., Sessler, A. M. and Dawson, J. M., *Phys. Rev. Lett.* **64**, 2511 (1990).
[28] Kostyukov, I., Kiselev, S. and Pukhov, A., *Phys. Plasmas* **10**, 4818 (2003).
[29] Shah, R. C. *et al.*, *Phys. Rev. E* **74**, 045401 (2006).
[30] Albert, F. *et al.*, *Phys. Rev. E* **77**, 056402 (2008).
[31] Thorn, D. B. *et al.*, *Rev. Sci. Instrum.* **81**, 10E325 (2010).
[32] Phuoc, K. T. *et al.*, *Phys. Rev. Lett.* **97**, 225002 (2006).
[33] Glinec, Y. *et al.*, *European Physical Letters* **81**, 64001 (2008).
[34] Phuoc, K. T. *et al.*, *Phys. Plasmas* **14**, 080701 (2007).
[35] Debus, A. D. *et al.*, *Phys. Rev. Lett.* **104**, 084802 (2010).
[36] Phuoc, K. T. *et al.*, *Phys. Plasmas* **15**, 063102 (2008).
[37] Mangles, S. P. D. *et al.*, *Appl. Phys. Lett.* **95**, 181106 (2009).
[38] Pukhov, A. and Meyer-ter-Vehn, J., *Appl. Phys. B-Lasers Opt.* **74**, 355 (2002).
[39] Kostyukov, I., Pukhov, A. and Kiselev, S., *Phys. Plasmas* **11**, 5256 (2004).
[40] Lu, W., Huang, C., Zhou, M., Mori, W. B. and Katsouleas, T., *Phys. Rev. Lett.* **96**, 165002 (2006).
[41] Lu, W. *et al.*, *Phys. Rev. Spec. Top.-Accel. Beams* **10**, 061301 (2007).
[42] Faure, J. *et al.*, *Nature* **444**, 737 (2006).
[43] Kneip, S. *et al.*, *Phys. Rev. Lett.* **103**, 035002 (2009).
[44] Leemans, W. P. *et al.*, *Nat. Phys.* **2**, 696 (2006).
[45] Kneip, S. *et al.*, *AIP Conference Proceedings* **1299**, 185 (2010).
[46] Martins, S. F., Fonseca, R. A., Silva, L. O., Lu, W. and Mori, W. B., *Comput Phys Commun* **181**, 869 (2010).
[47] Martins, J. L., Martins, S. F., Fonseca, R. A. and Silva, L. O. in *Harnessing Relativistic Plasma Waves as Novel Radiation Sources from Terahertz to X-Rays and Beyond.*1 edn 73590V-73598 (SPIE).
[48] Martins, S. F., Fonseca, R. A., Lu, W., Mori, W. B. and Silva, L. O., *Nat. Phys.* **6**, 311 (2010).
[49] Thomas, A. G. R., *Phys. Plasmas* **17**, 056798 (2010).
[50] Thomas, A. G. R. and Krushelnick, K., *Phys. Plasmas* **16**, 103103 (2009).
[51] Yanovsky, V. *et al.*, *Opt. Express* **16**, 2109 (2008).
[52] Jackson, J. D., *Classical Electrodynamics.* 3 edn, (Wiley, 1999).
[53] Kostyukov, I., Nerush, E., Pukhov, A. and Seredov, V., *Phys. Rev. Lett.* **103**, 175003 (2009).

[54] Goldstein, H., Poole, C. P. and Safko, J. L. *Classical Mechanics*. 3rd edn, (Addison Wesley, Pearson PLC, 2001).
[55] Thomas, A. G. R., *Phys. Rev. Spec. Top.-Accel. Beams* **13**, 020702 (2010).
[56] Rousse, A., Phuoc, K. T., Shah, R., Fitour, R. and Albert, F., *Eur. Phys. J. D* **45**, 391 (2007).
[57] DESY. *PETRA III: A Low Emittance Synchrotron Radiation Source - Technical Design Report*, <http://petra3.desy.de/general/tdr/index_eng.html> (2004).
[58] Geddes, C. G. R., Clayton, C., Lu, W. and Thomas, A. G. R., *AIP Conference Proceedings* **1299**, 79 (2010).
[59] Weller, H. R. *et al.*, *Progress in Particle and Nuclear Physics* **62**, 257 (2009).
[60] Diamond. *The Diamond Light Source*, <http://www.diamond.ac.uk/> (2009).
[61] Taatjes, C. A. *et al.*, *The Journal of Physical Chemistry A* **110**, 3254 (2005).
[62] Ohta, T., Bostwick, A., Seyller, T., Horn, K. and Rotenberg, E., *Science* **313**, 951 (2006).
[63] Schotte, F. *et al.*, *Science* **300**, 1944 (2003).
[64] Miao, J. W., Charalambous, P., Kirz, J. and Sayre, D., *Nature* **400**, 342 (1999).
[65] Huang, X. *et al.*, *Phys. Rev. Lett.* **103**, 198101 (2009).
[66] Rodenburg, J. M. *et al.*, *Phys. Rev. Lett.* **98**, 034801 (2007).
[67] Sandberg, R. L. *et al.*, *Phys. Rev. Lett.* **99**, 098103 (2007).
[68] Wilkins, S. W., Gureyev, T. E., Gao, D., Pogany, A. and Stevenson, A. W., *Nature* **384**, 335 (1996).
[69] Momose, A., Takeda, T., Itai, Y. and Hirano, K., *Nat Med* **2**, 473 (1996).
[70] Wu, J. *et al.*, *Kidney Int* **75**, 945 (2009).
[71] Elleaume, H. *et al.*, *Phys. Med. Biol.* **45**, L39 (2000).
[72] Momose, A., *Jpn. J. Appl. Phys. Part 1 - Regul. Pap. Brief Commun. Rev. Pap.* **44**, 6355 (2005).
[73] Parkinson, D. Y., McDermott, G., Etkin, L. D., Le Gros, M. A. and Larabell, C. A., *J. Struct. Biol.* **162**, 380 (2008).
[74] Kinney, J. H., Stolken, J. S., Smith, T. S., Ryaby, J. T. and Lane, N. E., *Bone* **36**, 193 (2005).
[75] Dierolf, M. *et al.*, *Nature* **467**, 436 (2010).
[76] Chapman, H. N., *Nature* **467**, 409 (2010).
[77] Chen, L. X. *et al.*, *Science* **292**, 262 (2001).
[78] Schoenlein, R. W. *et al.*, *Appl. Phys. B-Lasers Opt.* **71**, 1 (2000).
[79] Bargheer, M. *et al.*, *Science* **306**, 1771 (2004).
[80] Audebert, P. *et al.*, *Phys. Rev. Lett.* **94**, 025004 (2005).
[81] Rischel, C. *et al.*, *Nature* **390**, 490 (1997).
[82] Siders, C. W. *et al.*, *Science* **286**, 1340 (1999).
[83] Corino, G. L. and French, P. W., *Int J Cancer* **122**, 847 (2008).
[84] Nishiwaki, Y., Nakanishi, T., Terada, Y., Ninomiya, T. and Nakai, I., *X-Ray Spectrom* **35**, 195 (2006).
[85] Kim, K.-J. and Sessler, A., *Beam Line* **26**, 16 (1996).
[86] Collins, C. B. and Carroll, J. J., *Hyperfine Interact.* **107**, 3 (1997).

6.4.2 XFEL-beamline

The grand goal is the setup of a fully operational laser-driven XFEL for various applications in ultrafast science and to organize it, in the long run, towards a future user facility within the framework of ELI. However, this is based upon a step-like approach from a first demonstration experiment over improved FEL-performance up to the full operation usable for user experiments.

Since the feasibility of any FEL depends crucially on the electron beam quality, novel diagnostic methods need to be developed for laser-plasma accelerator driven beams. They exhibit an

intrinsically short bunch length of few femtoseconds only, making measurements of local bunch parameters, such as the bunch profile, energy chirps, and the so-called slice energy spread and emittance, highly challenging. So far, no technique exists to probe a relativistic electron bunch on such time-scales. Therefore, we propose to advance in a two-fold step: since conventional accelerators at large-scale XFEL facilities (like LCLS in Stanford, USA, and the European-XFEL at DESY, Hamburg, Germany) also enter the few-femtosecond bunch length regime, it is certainly of mutual benefit, if one develops novel diagnostic regimes in a synergetic approach. The advantage of conventional accelerators is clearly seen in their well-defined and controllable beams with much less fluctuations than laser-driven beams. Hence, novel approaches are not complicated by beam instabilities, making their development more feasible. Therefore, in a first step, a beamline at DESY will be put up, where a high-power laser, situated at a conventional high-performance linac, is used for both novel diagnostic schemes and driving a laser-plasma accelerator for also testing the new methods with such beams. Once, these mandatory techniques are fully developed, they can be built up at Prague's ELI site with its much more powerful and more energetic diode pumped high repetition rate femtosecond driver lasers. ELI's effort in pushing accelerator physics to its limits is well advised when connecting it with a world-leading accelerator center in terms of an explicit and direct cooperation. With its planned maximum electron energy of up to 15 GeV at a repetition rate of 10 Hz the ELI-beamline facility will provide a broadely tunable source of seed electrons for XFEL research.

To speed up the process of developing a user facility we will use synergies with other European centers. For the ELI-beamline facility in Prague we plan as a first step to implement a full XFEL-beamline as already designed for a 5-keV-XFEL within the Munich CALA ("Centre for Advanced Laser Application"), which is closely linked to the already existing Cluster of Excellence MAP "Munich-Centre for Advanced Photonics", http://www.munich-photonics.de) project. This photon energy would allow addressing the majority of scientific cases, even up to single molecule imaging. In parallel, an extension to higher photon energies to the clinically relevant range of > 20 keV (e.g. mammography investigations) is envisioned using higher electron energies for LUX (Laser-driven Undulator X-ray source, generating spontaneous emission) available at the medical ELI-beamlines. The outline for the 5-keV-photon energy X-FEL is given in Fig. 6.43.

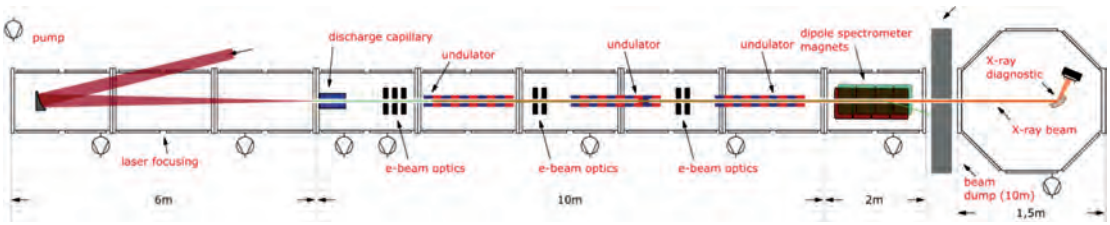

Figure 6.43: Outline of a 5-keV laser-driven XFEL beamline with all relevant elements and length figures.

The design is based upon a 3 PW laser, delivering 2 GeV electrons with a charge of 1 nC. The first 6 m are used for the laser focusing into a discharge capillary (200 µm diameter). The next section, 10 m long, consists of the actual XFEL: three undulator modules and beam optical elements in between. The last section holds a dipole magnet, serving as an electron spectrometer and bending the electrons away from the forward direction of the XFEL-radiation beam line into a beam dump (10 m long for absorbing up to 5 GeV electrons). Note that the LUX-beam line for medical imaging has about the same length, although it uses just one undulator, but due to the higher electron energy (above 3.5 GeV) the beam optics requires a larger distance. Since the XFEL- and LUX-operation is completely different, we propose the installation of two

separate beamlines, each of them dedicated for their specific use.

This setup was determined by full start-to-end simulations, yielding the optimum between compactness (note that comparable conventional XFELs would have kilometer length), electron beam optic, and FEL-performance. Within the funded CALA project we have estimated the total costs, including vacuum chambers, pumps, undulators, dipole magnets, capillary, and miniature quadrupole magnets, to amount to about 1.6 M€. Note that the beam dump is not included, as it is part of the shielding of the ELI building. Note also that the XFEL-length is realistic only, if the novel diagnostic techniques noted above allow the measurement and control of all FEL-relevant bunch parameters, else an increased saturation length would follow. This underlines again the necessity for an intense development work on novel diagnostic methods. These devices can be easily incorporated into the XFEL-beam line at ELI, once they are successfully developed and tested at DESY.

In summary a strong cooperation with other leading European facilities will enable and speed up the process of developing a compact laser driven high photon energy X-FEL within the rather short time frame given by the use of infrastructural funds. The higher power and energy as well as the increased repetition rate of the planned ELI laser drivers in comparison to university based laser systems will in the future considerably extend the available output parameters of compact laser driven X-FELs and LUX for the investigation of fundamental scientific problems and its use for medical and technological applications.

The laser driven compact XFEL development will be in direct cooperation with the electron accelerator working groups for enabling realistic assumptions of foreseeable electron beam quality. Novel diagnostic tools will enable us to control the FEL-relevant beam parameters. The goal is to establish a first FEL-demonstrator experiment and then a fully operational laser driven XFEL.

The group led by Prof. Dr. Florian Grüner will in the next ELI implementation phase realize first experimental setups at UHH/DESY (Hamburg). This will boost the development of the required novel diagnostic tools with a dedicated test beamline at DESY, which will be operated with conventional high-performance accelerators. This approach will speed up the development and realization of fully operational compact laser driven XFEL within the ELI beamline facilities.

6.4.3 Relativistic Flying Mirrors

The anticipated ELI laser technology will finally provide lasers of 200 PW power, which will result in light intensities up to $2 \times 10^{25}\,\mathrm{W/cm^2}$. Such high-intensity sources will allow studying principally new regimes of the electromagnetic radiation interaction with matter [1].

At light intensities of the order of or higher than $2 \times 10^{23}\,\mathrm{W/cm^2}$ (the first laser development stage 1–10 PW) we enter the regime when the radiation losses of the electrons quivering in the field of the electromagnetic wave (EMW) start to play a dominant role [2]. This intensity corresponds to the dimensionless amplitude of the laser pulse, $a_0 = eE_0/m_\mathrm{e}\omega_0 c$, given by

$$a_\mathrm{rad} = (3\lambda_0/4\pi r_\mathrm{e})^{1/3}. \tag{6.14}$$

It is equal to ≈ 400 for circularly polarized wave. Here, $r_\mathrm{e} = e^2/m_\mathrm{e}c^2 = 2.8 \times 10^{-13}\,\mathrm{cm}$ is the classical electron radius. In this regime the EMW energy is efficiently transformed into the energy of gamma-quanta emitted by the electrons, unlike the limit of relativistic ally strong but relatively moderate electromagnetic wave intensity, $10^{18}\,\mathrm{W/cm^2} < I < 10^{23}\,\mathrm{W/cm^2}$, when the energy is transformed into such coherent entities as the Langmuir waves, self-focusing channels, relativistic electromagnetic solitons, relativistic electron vortices and the associated quasistatic magnetic fields, and to the beams of fast electrons and ions. The emitted gamma-photon energy is of the order of

$$\hbar\omega_\gamma = \hbar\omega_0 a_\mathrm{rad}^3 = (3/2)m_\mathrm{e}c^2/\alpha, \tag{6.15}$$

where $\alpha = e^2/\hbar c \approx 1/137$ is the fine-structure constant. We see that the gamma-photon energy is approximately equal to 100 MeV. Studying of laser–matter interaction in the regime of dominant radiation losses will result, in particular, in the development of sources of high-power ultrashort gamma-ray pulses, which will open new horizons for the use of laser plasmas in various areas of fundamental sciences and technology.

At the next level, when the laser pulse intensity increases approximately by a factor of 50, i.e. reaches the level of $\approx 10^{25}$ W/cm^2, as is planned in the second stage of the ELI project, we shall meet regimes when the quantum electrodynamics effects completely change the scenarios of EMW propagation in media. The quantum electrodynamics threshold corresponds to the dimensionless amplitude of the laser light given by expression

$$a_{\mathrm{QM}} = 2e^2 m_{\mathrm{e}} c/3\hbar^2\omega_0 = 2\alpha m_{\mathrm{e}} c^2/3\hbar\omega_0, \tag{6.16}$$

i.e. it corresponds to a laser intensity $\approx 8\times 10^{24}$ W/cm^2. The first quantum effect is the recoil due to the photon emission, which leads to the "quantum diffusion" that is well known in accelerator physics. At this level of the laser pulse intensity the avalanche-type creation of the electron–positron pairs becomes possible, when the relatively low number of "seed" electrons in the strong laser field emit high-energy gamma photons. The gamma photons interacting with the laser light create "secondary" electron–positron pairs, which emit their gamma photons, and so on. Such an avalanche-type discharge will produce a high-density electron–positron plasma cloud embedded into the gamma-radiation background [3]. It will lead to a laser pulse decay and its energy transformation into the $e^-e^+\gamma$ plasma and high- and low-frequency electromagnetic radiation. The $e^-e^+\gamma$ plasma cloud expansion accompanied by the growth of the number of e^-e^+ pairs will produce an ultrashort flare of gamma rays and low-frequency radiation similarly to the electromagnetic radiation emission in the "fireball" scenario of the extragalactic gamma ray bursts. This phenomenon can be used for laboratory modeling with laser plasmas of such key importance for the relativistic astrophysics processes as the extragalactic gamma ray bursts.

The electromagnetic field strength is limited by the value given by the dimensionless amplitude

$$a_{\mathrm{QED}} = m_{\mathrm{e}} c^2/\hbar\omega_0, \tag{6.17}$$

which is of the order of $\approx 0.511 \times 10^6$. The electric field is the characteristic quantum electrodynamics field $E_{\mathrm{QED}} = m_{\mathrm{e}}^2 c^3/e\hbar$. This is also called the "Schwinger field." It corresponds to a light intensity of 3×10^{29} W/cm^2. This electric field over the distance of the Compton length $\lambda\!\!\!^{-}_{\mathrm{C}} = \hbar/m_{\mathrm{e}} c \approx 3.9 \times 10^{11}$ cm produces work equal to the electron rest mass energy. When the electric field approaches the Schwinger limit, the electron–positron pair creation from vacuum occurs. As a result, EMW decays transferring its energy to the produced $e^-e^+\gamma$ plasma. A detailed analysis of this process shows that the inhomogeneity of the electromagnetic pulses can reduce the light intensity required for electron–positron pair creation from vacuum by several orders of magnitude [4]. Studying of the electron–positron pair creation from vacuum under the laboratory conditions is of principal importance for contemporary theoretical physics because this process provides an example of the quantum-field phenomenon that cannot be described within the framework of perturbation theory. In high-energy physics it has an analogy to the Schwinger mechanism of the quark–gluon plasma generation in the relativistic heavy-ion collisions.

Other processes principally important for fundamental physics are related to the nonlinear vacuum polarization in a strong field due the vacuum response via virtual electron–positron pairs. In the limit of characteristic quantum electrodynamics field these processes will manifest themselves in the nonlinear interaction of electromagnetic waves with the cross-focusing, scattering and transformation of their frequency spectra.

Although the intensity limits of 2×10^{23} W/cm^2 and 8×10^{24} W/cm^2 are planned to be reached for the lasers with the ELI parameters, their realization in the first stage of the project

will not be easy for the extensive strategy of developing of the laser parameters, in particular in the case of laser pulse focusing into the region with a size substantially larger than the laser wavelength. The above-mentioned extensive strategy to increase the intensity implies increasing of the laser pulse energy only. The intensive strategy of the scientific concept contemplates novel approaches. Their use will make it possible to realize the conditions required for achieving the fields E_{QM} and E_{QED} at substantially lower laser system energy.

The methods of obtaining the electromagnetic pulses of extremely high power and extremely short duration are based on the relativistic mirror concept [5]. During propagation of high-intensity EMW in plasmas the nonlinear interaction naturally leads to the formation of strong modulations in the electron-density distribution, which propagate with a phase velocity close to the speed of light in vacuum. Reflection of the electromagnetic pulse at such relativistic electron shells results in the pulse longitudinal compression and its frequency upshifting due to the double Doppler effect. Focusing of the reflected wave in the region with the size determined by the shortened wavelength leads to an additional increase of intensity. The relativistic mirror formation in laser plasmas typically occurs due the nonlinear wave breaking obeying universal laws that describe the singularity formation in the electron-density distribution. The electrodynamics of EMW interaction with the singularities demonstrates a finiteness of the reflection coefficient that guarantees the realizability of the relativistic mirror effects under the conditions realistic for laboratory experiments.

Within the relativistic mirror concept a portion of the laser photons with energy $\hbar\omega_0$ is reflected from a relativistic electron mirror moving in the opposite direction with electron energy $m_{\mathrm{e}}c^2\gamma_{\mathrm{e}}$. The double Doppler effect boosts the reflected photon energy to $\approx 4\hbar\omega_0\gamma_{\mathrm{e}}^2$ [6]. When EMW interacts with the copropagating (receding) mirror, the reflected photon energy decreases and becomes equal to $\approx \hbar\omega_0/4\gamma_{\mathrm{e}}^2$, i.e. the electromagnetic pulse transfers its energy and momentum to the charged particles comprising the mirror. In the relativistic limit of the laser pulse interaction with a thin foil when the radiation pressure is dominant the efficiency of the laser energy transformation into the energy of relativistic ions is very high [7].

Compact, Intense, Brilliant X-Ray Source Based on the Flying Mirror Mechanism

The relativistic electron mirrors are made by utilizing nonlinear interaction of multiple high-power laser pulses in plasmas, as proposed in [5], where theoretical scaling and computer simulation are presented (Fig. 6.44).

In the flying mirror scheme in the wake behind the first laser pulse the plasma electrons form thin shells moving with a speed close to the speed of light in vacuum. The second, counter-propagating laser pulse is reflected coherently by the high-density relativistic electron shells (see Fig. 6.44). This process results in EMW frequency multiplication and in a wave intensification. The proof of principle of the flying mirror concept has been done in the experiments reported in [8], where the narrow band soft X-ray generation was demonstrated (Fig. 6.45).

Further development of the theory and results of the experiments with higher-energy lasers [9] have shown the way towards high efficiency and high frequency (in the hard X-ray photon energy range) regimes of the flying mirror source operation.

The relativistic mirror with a high enough reflection coefficient for the counterpropagating laser pulse can be formed during the breaking of the wake wave, that propagates in a plasma with phase velocity v_{ph} close to the speed of light in vacuum, which is equivalent to the relationship between the electron energy and phase velocity of the wave: $\gamma_{\mathrm{e}} = \gamma_{\mathrm{ph}} \equiv (1 - v_{\mathrm{ph}}^2/c^2)^{-1/2}$. At the break, a singularity is formed in the electron-density distribution, which breaks the geometrical optics approximation and leads to the reflection of a portion of the laser pulse in the backward direction and to the upshifting of the frequency of the reflected pulse [10]. The reflection coefficient in terms of reflected photon number scales as $\sim \gamma_{\mathrm{ph}}^{-3}$. Taking into account the volume change where the reflected laser pulse is localized we find that the intensity of the

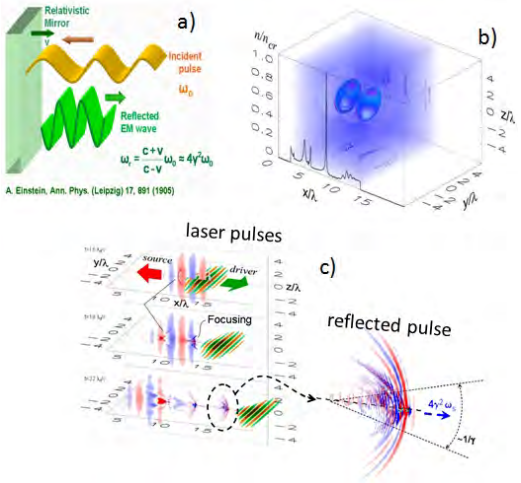

Figure 6.44: Flying mirror concept [5]. (a) Light reflection at the relativistic mirror. (b) Paraboloidal relativistic electron shells in the wake wave. (c) Interacting laser pulses. Inset: the reflected pulse is frequency upshifted and focused (3D PIC simulation).

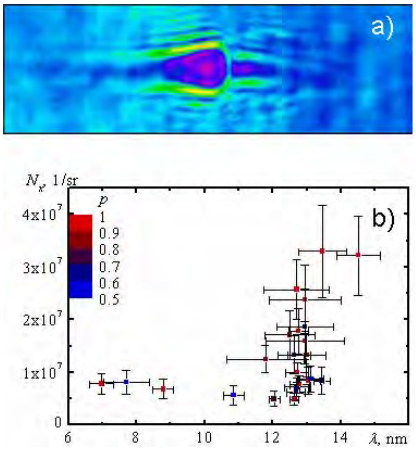

Figure 6.45: Experiment [8]. (a) Two colliding laser pulses on the shadowgraph. (b) The signals of the reflected radiation, detected in different shots.

reflected EMW increases is given by the factor

$$I_{\rm r} \approx 8 I_0 \left(D_0/\lambda_0\right)^2 \gamma_{\rm ph}^3, \tag{6.18}$$

with the reflected energy $\mathcal{E}_{\rm r} \approx \mathcal{E}_0/2\gamma_{\rm ph}$ and the power $\mathcal{P}_{\rm r} \approx 2\mathcal{P}_0\gamma_{\rm ph}$. As an example of laser pulse parameters required for approaching the Schwinger limit with the reflected wave, we consider the wakefield excitation in a gas of density at 10^{18} cm^{-3}, by EMW with amplitude $a_0 = 15$. The Lorentz factor associated with the phase velocity of the wakefield is of the order of 125, and the laser-pulse intensification is of the order of 450. The counterpropagating 1-μm laser pulse with intensity 2×10^{19} W/cm^2 is partially reflected and focused by the wakefield cusp. For a reflected beam diameter of $D_0 = 40\,\mu$m, the intensity in the focal spot is 5×10^{28} W/cm^2. The driver pulse intensity and its waist is assumed to be 4×10^{20} W/cm^2 and 40 μm. The driver and source have energies of 10 kJ and 30 J, respectively. We see that these parameters correspond to those of future ELI laser systems.

The nonlinear dependence of the vacuum susceptibilities on the electromagnetic field amplitude results in the birefringence of the vacuum, in the scattering of light by light, in the parametric four-wave processes, to soliton formation, and to the nonlinear phase shift of the counterpropagating electromagnetic waves. The Kerr constant, with the refraction index n as a function of the electric field $n = n_0 + \lambda_0 K|E|^2$, of the vacuum is given by

$$K = 7\alpha\lambda\!\!\!^{-3}_{\mathrm{C}}/90\pi m_{\mathrm{e}}c^2\lambda_0, \tag{6.19}$$

which for $\lambda_0 = 1$ μm is of the order of 10^{-27} cm^2/erg. In the QED nonlinear vacuum two counterpropagating electromagnetic waves mutually focus each other. The critical power $\mathcal{P}_{\mathrm{c}} = cE^2D_0^2/4\pi$, where D_0 is the laser beam waist, for the mutual focusing is equal to $\mathcal{P}_{\mathrm{c}} = (90/28)cE_{\mathrm{QED}}^2\lambda_0^2/\alpha$. For $\lambda \approx 1$ μm it yields $\mathcal{P}_{\mathrm{c}} \approx 2.5 \times 10^{24}$ W. Taking into account that the wavelength of the reflected and focused at the wake plasma wave the laser pulse becomes by a factor $4\gamma_{\mathrm{ph}}^2$ shorter and its power increases by a factor $2\gamma_{\mathrm{ph}}$ we find that the nonlinear QED vacuum polarization effects are expected to be observed for the 50 PW-laser at 1 μm, i.e. with the ELI laser it seems possible.

Here, we notice several other schemes for developing compact, intense, brilliant, tunable X-ray sources by using relativistic mirrors formed in nonlinear interactions in laser plasmas, whose realization with the ELI laser systems will open new ways in nonlinear electrodynamics of continuous media in the relativistic regime.

In [11] the interaction of regular nonlinear structures (such as subcycle solitons, electron vortices, and wake Langmuir waves) with a strong wake wave in a collisionless plasma has been proposed for exploitation in order to produce ultrashort electromagnetic pulses. The electromagnetic field of the nonlinear structure is partially reflected by the electron-density modulations of the incident wake wave and a single-cycle high-intensity electromagnetic pulse is formed. Due to the Doppler effect the length of this pulse is much shorter than that of the nonlinear structure.

Imperfect relativistic mirrors in the collective backscattering of intense laser radiation by energetic electron beams are considered in [12]. The collective backscattering process is proposed for the development of sources of ultrashort pulse radiation in the gamma-ray domain. It is shown that intense pulses of gamma rays, due to the double Doppler shift of the harmonics of the incident laser radiation, can be produced using the available technology, with durations less than one attosecond.

Dense laser-driven electron sheets accelerated by the laser pulse interacting with a thin plasma slab are considered as relativistic mirrors for coherent production of brilliant X-ray and gamma-ray beams [13].

Radiation-Pressure-Dominated Regime of Ion Acceleration in Light Interaction with a Receding Relativistic Mirror

Among the wide variety of ion-acceleration mechanisms realized in laser-plasma interaction, the radiation-pressure-dominated ion acceleration (RPDA) has the highest efficiency [7]. In the RPDA ion accelerator the laser pulse radiation pressure pushes forward the irradiated region of a thin foil as a whole. In the relativistic limit, when the electrons and ions move together with the same velocity due to a smallness of the electron to ion mass ratio, the ion kinetic energy is higher by a factor m_i/m_e times than the electron energy. In this case, the laser pulse interacts with an accelerated foil like with a relativistic copropagating (receding) mirror. The electromagnetic radiation reflected back by the relativistic mirror has negligible energy compared to the energy in the incident laser pulse, i.e. the laser energy is almost completely transformed into the energy of fast ions. In Fig. 6.46 we show results of 3D PIC simulations of this ion-acceleration regime. In the course of the interaction with a thin overdense plasma slab the multipetawatt laser pulse forms a cocoon confining the EMW energy, thus increasing the coupling of the EMW with the

target (see frame (a) and the 2D inset). The ions accelerated beyond the GeV energy level have a quasimonoenergetic spectrum (Fig. 6.46b). We notice that a combination of the RPDA mechanism with the use of double-layer targets can substantially increase the ion-acceleration efficiency as demonstrated in [14]. An indication on the RPDA regime of interaction is obtained in experimental studies of plasma jets ejected from the rear side of thin solid targets irradiated by ultraintense laser pulses [15].

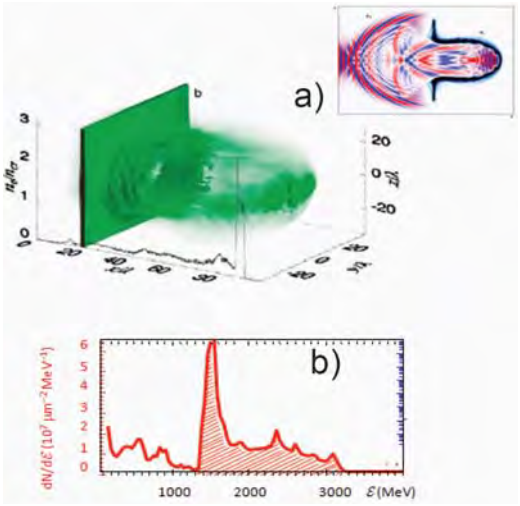

Figure 6.46: Results of 3D PIC simulations of the RPDA ion acceleration regime. (a) The electromagnetic pulse forms a cocoon confining the EMW energy. The right inset shows a cocoon seen in the plasma density and an EMW distribution obtained with the 2D PIC simulation. (b) Quasimonoenergetic ion spectrum.

When a planar foil is irradiated by a normally incident EMW, the ions achieve the energy $\mathcal{E}_\alpha = m_\alpha c^2 \left(1 + 2w^2/(1+2w)\right)$, where w is the normalized fluence, $w = \int_{-\infty}^{t-x/c} \left(\frac{E^2(\psi)}{2\pi n_0 l_0 m_\alpha c}\right) \mathrm{d}\psi$. The acceleration efficiency is $\kappa_{\mathrm{eff}} = m_\alpha c^2 2w/(1+2w)$, i.e. $\kappa_{\mathrm{eff}} \to 1$ in the limit $w \to \infty$ the resulting ion energy is equal to the ratio of the laser pulse energy, $\mathcal{E}_{\mathrm{las}}$, to the total number of accelerated ions, N_{tot}. The ion energy scaling in nonrelativistic (6.20) and ultrarelativistic (6.21) limits is given by the following expressions

$$\mathcal{E}_\alpha = 8 \left(10^{11}/N_{\mathrm{tot}}\right)^2 (m_{\mathrm{p}}/m_\alpha) \left(\mathcal{E}_{\mathrm{las}}/1\,J\right)^2 \ \mathrm{MeV}, \tag{6.20}$$

and

$$\mathcal{E}_\alpha = 62.5 \left(10^{11}/N_{\mathrm{tot}}\right) \left(\mathcal{E}_{\mathrm{las}}/10\,J\right) \ \mathrm{GeV}, \tag{6.21}$$

respectively. The ion-acceleration length in the limit $\mathcal{E}_\alpha/m_\alpha c^2 \to \infty$ is of the order of $l_{\mathrm{acc}} = l_{\mathrm{las}}/(1 - v_\alpha/c) \approx 2(\mathcal{E}_\alpha/m_\alpha c^2)^2 l_{\mathrm{las}}$, i.e. the acceleration length depends on the laser pulse duration, l_{las}/c, and on the final energy of accelerated ions, $\mathcal{E}_\alpha$. As an example, we consider a solid density foil, $n_0 = 10^{-24}$ cm^{-3}, of $l_0 = 1\,\mu$m thickness irradiated by a laser pulse with a transverse size of 100 μm. For a laser pulse energy of the order of 20 kJ and the pulse duration of 100 fs,we find that 10^{12} protons achieve an energy of about 100 GeV over the the acceleration length of the order of 60 cm. The ion energy of 100 GeV per nucleon is suitable for the quark–gluon plasma studies with the laser-based collider [7].

Relativistic High-Order Harmonics and Attosecond Pulse Generation

High-order harmonics generation (HOHG) during the interaction of high-intensity laser pulses with underdense and overdense plasmas presents a manifestation of one of the most basic non-

linear processes in physics. In addition to the key role they play in the theory of nonlinear waves, this radiation presents unique properties of coherence and pulse duration shortness.

The physical mechanisms of HOHG have much in common because they rely on the property of nonlinear systems to react in an anharmonical manner under the action of a periodic driving force. The specific realization of this property depends on the laser–matter interaction parameters, mainly on the laser intensity. At the subrelativistic intensity high-order harmonics occur due to the anharmonicity of the atom response on the finite amplitude oscillating electric field. When the laser radiation intensity reaches the relativistic level, the HOHG is due to the nonlinear dependence of the plasma refraction index on the electromagnetic wave amplitude.

High-order harmonics provide a way for generating attosecond light.

In underdense plasmas high harmonics are produced by the mechanism of parametric excitation by laser light of electromagnetic and electrostatic waves with different frequencies. The linearly polarized EMW in the underdense plasma has a transverse component which spectrum contains odd harmonics [16]

$$E_y = -E_0 \cos(\omega t - kx) - \frac{eE_0^3}{m_e^2 c^2} \frac{3(8\omega^2 + 3\omega_{pe}^2)}{8(4\omega^2 - \omega_{pe}^2)} \cos(3\omega t - 3kx) + \ldots, \tag{6.22}$$

and a longitudinal component with even harmonics

$$E_x = -\frac{k}{4\omega^2 - \omega_{pe}^2} \frac{e^2 E_0^2}{m_e} \sin(2\omega t - 2kx) + \ldots, \tag{6.23}$$

where the wave frequency depends on the wave number as $\omega = \sqrt{k^2 c^2 + \omega_{pe}^2}$. A finite duration laser pulse generates in a plasma a wake wave, which for a finite waist pulse has the form of a cavity moving with a velocity close to the speed of light in vacuum. Interaction of the laser light with the thin high-density walls of the cavity results in the HOHG.

When the high-intensity laser pulse interacts with overdense plasmas it induces a nonlinear electron motion at the plasma/vacuum interface, which in its turn results in formation of oscillating layers of the electron density. Depending on the laser pulse amplitude, the plasma density and the scale of the plasma inhomogeneity, we can see three main mechanisms of the HOHG [17] explained with: (a) the oscillating mirror model for HOHG [18]; (b) coherent wake emission [19]; (c) sliding mirror mechanism [20].

The oscillating mirror model [18] describes the case when the laser pulse interacts with the electron layer oscillating with the amplitude comparable to the light wavelength (see Fig. 6.47). As a result, the reflected wave frequency spectrum is enriched with the high-order harmonics: $\omega_0/4\gamma_e^2 < \omega < 4\gamma_e^2\omega_0$.

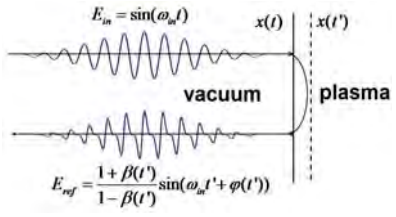

Figure 6.47: Oscillating mirror scheme.

In the coordinate space the reflected wave packet comprises extremely short (attosecond) pulses [21]. Generation of isolated attosecond pulses in the regime of tight focusing and ultrashort-pulse duration (λ^3 regime, [22]) in reflection from near-critical plasma, can be provided via relativistic deflection and compression of the electromagnetic wave by oscillating relativistic electron

layers. The smaller transversal size (λ^2) of the focal region reduces the instabilities and creates stronger slopes in the plasma density that separate subsequent half-cycles in the reflected radiation. The shorter pulse duration causes the electrons to move coherently, so that relativistic motion of electrons in the direction of the reflected pulse creates the Doppler compression forming attosecond pulses.

Figure 6.48 demonstrates these effects. On the plot of the reflected radiation one may observe deflection at each half-cycle of the pulse. With this technique of efficient generation of isolated attosecond pulses even shorter pulses could be produced for higher intensities. The target being shaped by the laser pulse at the moment of the attosecond pulse generation can focus these attosecond pulses simultaneously to much higher intensity [21]. The attosecond pulse width for optimal conditions scales with the laser pulse frequency and dimensionless amplitude a_0, as $\delta t_{\rm ap} = 1/\omega a_0 = 500/a_0$..

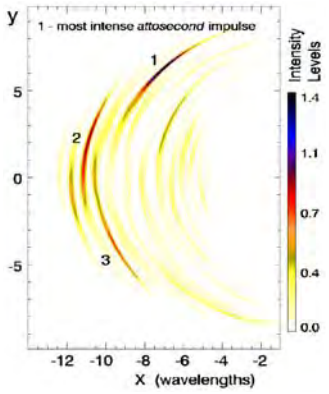

Figure 6.48: Attosecond pulses produced at the nonlinear reflection of EMW from the overdense plasma slab as seen in the electromagnetic energy-density distribution. Numbers 1, 2 and 3 indicate the most intense pulses in the reflected radiation [21].

The technique of high-order harmonic and attosecond pulse generation and focusing may enable us to reach extreme fields and approach the Schwinger limit with the ELI laser system.

High-order harmonic focusing by the reflection of a few-femtosecond laser pulse from a concave plasma surface was proposed in [23] as a mechanism of light intensification and as a way for achieving the Schwinger intensity.

As an example, we consider this mechanism using the scaling obtained within the framework of the sliding mirror model [20], when the laser pulse interacts with a thin foil target (see Fig. 6.49). The frequency spectrum scales as $S_n \approx 0.4(4\varepsilon_{\rm p}/n)^2$, where n is the harmonic number and $\varepsilon_{\rm p} = 2\pi e^2 n_0 l_0/m_{\rm e}\omega_0 c$ is the dimensionless parameter characterizing the foil target [24]. It is assumed that the condition $a_0 \geq \varepsilon_{\rm p}$ is fulfilled. The cutoff frequency of high-order harmonics produced by the sliding mirror is equal to $\omega_{\rm cr} = \omega_0 a_0$. If the $n_{\rm max} = \omega_{\rm cr}/\omega_0$ harmonic is focused to a spot with size $2\pi c/\omega_{\rm cr} = \lambda_0/a_0$, its intensity becomes of the order of

$$I_{\rm HOH} \approx 10^{18} a_0^4 (D_0/\lambda_0)^2 \,{\rm W/cm^2}. \tag{6.24}$$

It reaches the Schwinger limit at $a_0 \approx 560$, i.e. at the ELI intensity of $\approx 3 \times 10^{24}$ W/cm^2.

Boosted High Harmonics Pulse from a Double-Sided Relativistic Mirror

In [25] the concept of the accelerating double-sided mirror (Fig. 6.50) that efficiently reflects the counterpropagating relativistically strong EM radiation was formulated. The role of the mirror is played by a high-density plasma slab accelerated by an ultraintense laser pulse (the driver)

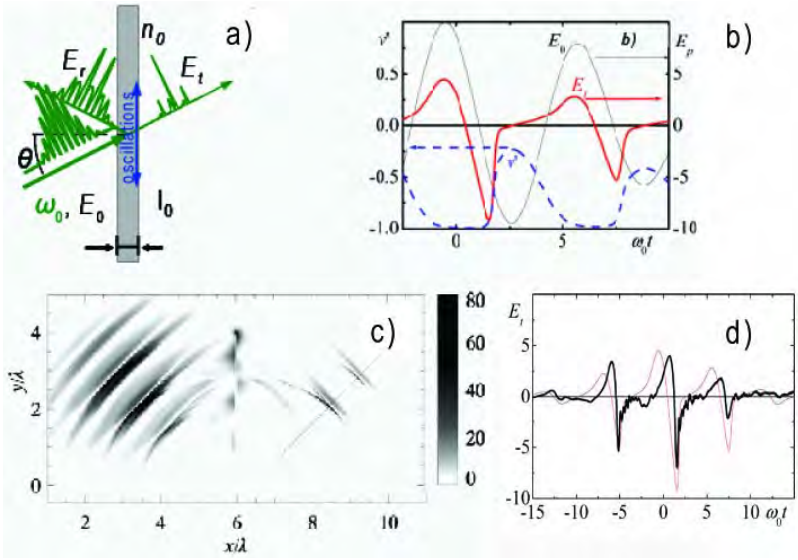

Figure 6.49: (a) Sliding mirror concept for HOHG [20]. (b) Trains of attosecond pulses generated by p-polarized incident pulses with $a_0 = 10$, dashed line, electron speed; thin and thick lines, the incident and the transmitted electric fields, respectively. (c) and (d) 2D PIC simulation results: distribution of the electric field squared after the interaction with the laser pulse and the transmitted electric field.

in the RPDA regime [7], when a thin plasma slab with the Lorentz factor $\gamma \gg 1$ reflects the copropagating driver, taking a substantial fraction of its energy, $\approx 1 - \gamma^{-2}$. The plasma slab acts as a mirror also for a counterpropagating relativistically strong EM radiation (the source), transferring the energy to the reflected light. The source pulse should be sufficiently weaker than the driver; nevertheless it can be relativistically strong. Exhibiting the properties of the sliding and oscillating mirrors, the plasma slab produces relativistic harmonics according to the oscillating or/and sliding mirror models [18, 20]. In the spectrum of the reflected radiation, the fundamental frequency of the incident radiation and the relativistic harmonics generated at the plasma slab are multiplied by the same factor, $\approx 4\gamma^2$.

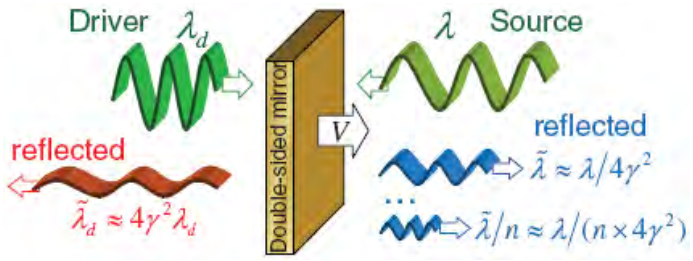

Figure 6.50: The accelerated double-sided mirror.

The particle-in-cell simulations show that in the interaction of the driver laser pulse with a thin foil target the driver makes a cocoon where it stays confined (Fig. 6.51a). The ions are accelerated, as seen from the ion-energy spectrum in Fig. 6.51b. The cocoon structure reveals itself as a loop-shaped pattern in the ion angular distribution, shown in grayscale in Fig. 6.51b where θ is an angle between the $x-$axis and the ion momentum. The accelerating plasma reflects the source pulse, which becomes chirped and compressed (Fig. 6.51a).

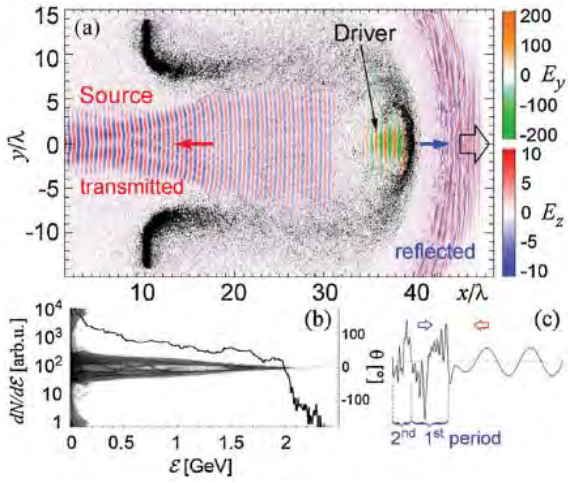

Figure 6.51: (a) The electric field y- and z-components representing driver and source pulses, respectively, and the ion density (black). According to the scheme in Fig. 6.50, the mirror accelerated by the driver reflects the counterpropagating source, boosting its frequency and harmonics. (b) The ion-energy spectrum (curve) and angular distribution (grayscale). (c) The electric field z-component: the first two reflected cycles overlapped with the source pulse.

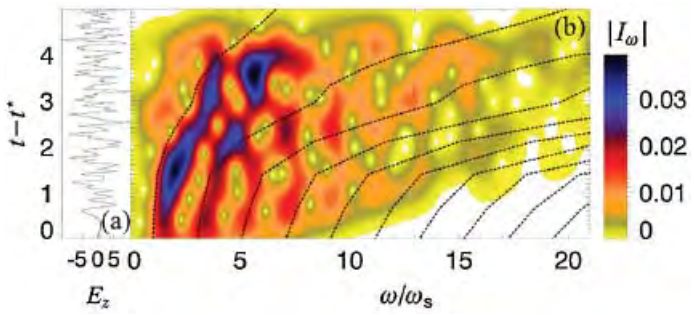

Figure 6.52: (a) The electric field component E_z along the x-axis representing the reflected radiation (emitted in the x-axis direction). (b) Color scale: the corresponding spectrum. Dashed curves: the odd harmonics frequency multiplied by the factor $(1+\beta)/(1-\beta)$ calculated from the fast-ion spectrum maximum.

As the mirror velocity, $c\beta$, increases, the reflected light frequency grows as $\omega_0(1+\beta)/(1-\beta)$; thus, the electric field profile along the x-axis becomes more and more jagged (Fig. 6.52a).

At the beginning, the magnitude of the reflected radiation is higher than that of the incident source, due to an enhancement of the reflectivity of the plasma slab compressed under the radiation pressure exerted by the driver and source pulses. In an instantaneous proper frame of the accelerating mirror, the frequency of the source pulse increases with time; thus, the mirror becomes more transparent. Correspondingly, the source starts to be transmitted through the plasma more efficiently, as seen in Fig. 6.51a. The reflected radiation has a complex structure of the spectrum. It contains not only the frequency-multiplied fundamental mode of the source pulse but also high-order harmonics. Figure 6.52b shows the modulus of the spectrum, $|I_\omega(t)|$, of the E_zE_z-component of the EM radiation emitted in the direction of the x-axis, taken for each moment of time.

In the double-sided mirror concept, a solid-density plasma slab, accelerated in the RPDA

regime, efficiently reflects a counterpropagating relativistically strong laser pulse. The reflected EM radiation consists of the fundamental mode and high harmonics, all multiplied by the factor $(1+\beta)/(1-\beta) \approx 4\gamma^2$, where the Lorentz factor of the plasma slab, γ, increases with time. In general, the reflected radiation is chirped due to the mirror acceleration. With a sufficiently short source pulse being sent with an appropriate delay to the accelerating mirror, one can obtain a high-intensity ultrashort X-ray pulse. For a mirror velocity above some threshold, in the mirror proper reference frame the average distance between electrons becomes greater than the incident wavelength. The reflection is no longer coherent, i.e. such that the reflected radiation power is proportional to the square of the number of electrons in the mirror. Instead, the reflected power becomes linearly proportional to the number of particles. Even with this scaling the interaction can provide efficient generation of X-ray pulses via backward (nonlinear) Thomson scattering due to a large number of electrons in a solid-density plasma. We estimate the reflected radiation brightness in two limiting cases. For $2\gamma < (n\lambda_s^3)^{1/6}$, the reflection is coherent and the corresponding brightness is

$$B_M \approx \mathcal{E}_s(\hbar\omega_r)^3\lambda_s\,/4\pi^5\hbar^4c^3, \tag{6.25}$$

where $\hbar\omega_r$ is the reflected photon energy and $\mathcal{E}_s$ is the source pulse energy. For larger γ, the interaction becomes incoherent in the above-mentioned sense. Assuming that the EM radiation is generated via the Thomson scattering, we obtain

$$B_T \approx a_d\mathcal{E}_s(\hbar\omega_r)^2r_e\lambda_s^2\,/8\pi^4\hbar^3c^2\lambda_d^3. \tag{6.26}$$

For example, if $\mathcal{E}_s$ =10 J, $\lambda_s = 0.8\,\mu$m, $\hbar\omega_r = 1$ keV ($\gamma = 13$), then $B_M \approx 0.8\times10^{40}$ photons/mm^2 mrad^2 s, which is orders of magnitude greater than any existing or proposed laboratory source [26]. For the same parameters of the source pulse and $\lambda_d = 0.8\,\mu$m, $\hbar\omega_r = 10$ keV, $a_d = 300$, i.e. $I \approx 10^{23}$ W/cm^2, $\hbar\omega_r = 1$ ($\gamma = 40$), we have $B_T \approx 3\times10^{32}$ photons/mm^2 mrad^2 s.

With the concept of the relativistic mirror, relatively compact and tunable extremely bright high-power sources of ultrashort pulses of X- and $\gamma\gamma$-rays and compact high-energy ion accelerators become realizable. This concept considerably expands the range of applications, requiring a large photon number in an ultrashort pulse and a short high-energy ion beam, and will create new applications and research fields, opening up new horizons of laboratory astrophysics [27], laser-driven nuclear physics [28], and fundamental science studies [7].

Bibliography

[1] G. Mourou, T. Tajima, and S. V. Bulanov, Rev. Mod. Phys. **78**, 309 (2006);
M. Marklund and P. Shukla, Rev. Mod. Phys. **78**, 591 (2006;
Y. I. Salamin, S. X. Hu, K. Z. Hatsagortsyan, and C. H. Keitel, Phys. Rep. **427**, 41 (2006).

[2] A.G. Zhidkov et al., Phys. Rev. Lett. **88**, 185002 (2002);
S. V. Bulanov, T. Z. Esirkepov, J. Koga, and T. Tajima, Plasma Phys. Rep. **30**, 196 (2004).

[3] A. R. Bell and J. G. Kirk, Phys. Rev. Lett. **101**, 200403 (2008);
G. Kirk, A. R. Bell, and I. Arka, Plasma Phys. Control Fusion **51**, 085008 (2009).

[4] N. B. Narozhny, S. S. Bulanov, V. D. Mur, and V. S. Popov, Phys. Lett. A **330**, 1 (2004);
S. Bulanov, N. B. Narozhny, V. D. Mur, and V. S. Popov JETP **102**, 9 (2006).

[5] S. V. Bulanov, T. Esirkepov, and T. Tajima, Phys. Rev. Lett. **91**, 085001 (2003).

[6] A. Einstein, Ann. Phys. (Leipzig) **17**, 891 (1905).

[7] T. Esirkepov, et al., Phys. Rev. Lett. **92**, 175003 (2004).

[8] M. Kando et al., Phys. Rev. Lett. **99**, 135001 (2007);
A. S. Pirozhkov et al., Phys. Plasmas **14**, 080904 (2007).

[9] M. Kando et al., Eur. Phys. J. D, **55**, 465 (2009).

[10] A. V. Panchenko et al., Phys. Rev. E **78**, 056402 (2008).

[11] S. S. Bulanov, T. Zh. Esirkepov, F. F. Kamenets, and F. Pegoraro, Phys. Rev. E **73**, 036408 (2006).
[12] J. T. Mendonca and A. Serbeto, Phys. Plasmas **15**, 113105 (2008).
[13] V.V. Kulagin et al., Phys. Plasmas 14, 113101 (2007);
D. Habs et al., Appl. Phys. B **93**, 349354 (2008);
J. Meyer-ter-Vehn and H.-C. Wu, Eur. Phys. J. D **55**, 433 (2009);
H.-C. Wu and J. Meyer-ter-Vehn, Eur. Phys. J. D **55**, 443 (2009).
[14] S. S. Bulanov et al., Phys. Rev. E **78**, 026412 (2008).
[15] S. Kar et al., Phys. Rev. Lett. **100**, 225004 (2008).
[16] A. I. Akhiezer and R. V. Polovin, Sov. Phys. JETP **30**, 915 (1956).
[17] A. Tarasevitch et al., Phys. Rev. Lett. **98**, 103902 (2007);
U. Teubner and P. Gibbon, Rev. Mod. Phys. **81**, 445 (2009);
A. Tarasevitch et al., J. Phys. B: At. Mol. Opt. Phys. **42**, 134006 (2009).
[18] S. V. Bulanov et al., Phys. Plasmas **1**, 745 (1994);
R. Lichters et al., ibid. **3**, 3425 (1996);
G. Tsakiris, K. Eidmann, J. Meyer-ter-Vehn, and F. Krausz, New J. Phys. **8**, 19 (2006).
[19] F. Quere et al., Phys. Rev. Lett. 96, 125004 (2006);
C. Thaury et al., Nature Phys. **3**, 424 (2007).
[20] A. S. Pirozhkov et al., Phys. Lett. A **349**, 256 (2006);
A. S. Pirozhkov et al., Phys. Plasmas **13**, 013107 (2006).
[21] N. M. Naumova et al., Phys. Rev. Lett. **92**, 063902 (2004).
[22] G. Mourou et al., Plasma Phys. Rep. **28**, 12 (2002).
[23] S. Gordienko, A. Pukhov, O. Shorokhov, and T. Baeva, Phys. Rev. Lett. **94**, 103903 (2005).
[24] V. A. Vshivkov et al., Phys. Plasmas **5**, 2752 (1998).
[25] T. Zh. Esirkepov, et al., Phys. Rev. Lett. **103**, 025002 (2009).
[26] F. V. Hartemann et al., Phys. Rev. Lett. **100**, 125001 (2008).
[27] S. V. Bulanov, T. Zh. Esirkepov, D. Habs, F. Pegoraro, and T. Tajima, Eur. Phys. J. D **55**, 483 (2009).
[28] D. Habs, B. M. Hegelish, J. Schreiber, and P. G. Thirolf, Eur. Phys. J. D **55**, 279 (2009).

6.5 Infrastructure Producing High Intensity Gamma Rays for ELI Nuclear Physics Pillar

6.5.1 Introduction

This report contains a description of the proposed infrastructure producing high intensity gamma rays, an important component of the Extreme Light Infrastructure – Nuclear Physics facility (ELI-NP). For simplicity reasons, we will call the infrastructure producing high intensity gamma rays "the γ source".

There are four main criteria for the comparison of high intensity γ ray sources, namely: the **energy of the γ beam**, the **total photon flux**, the **peak brilliance** and the **bandwidth**.

The **energy of the γ rays** range from a few keV to 100 MeV, although most radiation is in the range 50 keV – 6 MeV.
The **total photon flux** is measured in *photons/sec at 100%BW*.

The driving force behind the development of light sources is the optimization of their brilliance (or spectral brightness), which is the figure of merit of many experiments. Brilliance is defined as a function of frequency given by the number of photons emitted by the source in unit time in a unit solid angle, per unit surface of the source, and in a unit bandwidth of frequencies around the given one. The units in which it is usually expressed are *photons/s/mm^2/mrad^2/0.1%BW*, where 0.1%BW denotes a bandwidth $10^{-3}\omega$ centered around the frequency ω. As one can appreciate from the definition, brilliance puts a premium not only on the photon flux (photons per second in a given bandwidth), but also on the high phase space density of the photons, i.e. on being radiated out of a small area and with high directional collimation. Liouville's theorem ensures that brilliance is a property of the source and not of the optics of the beamline which delivers the photons to the experimental station. An ideal set of optical elements can only preserve the brilliance, a real one will always degrade brilliance (as some photons get lost on the way down the beamline). The **peak brilliance** is defined as the instantaneous peak value obtained at peaks of light pulses.

The γ beam bandwidth is the width of the range (or band) of frequencies in which the beam energy spectrum is concentrated.

The γ source will produce a very intense and brilliant γ beam ($E_\gamma = 1 - 13$ MeV for the beginning and $E_\gamma \leq 19.5$ MeV latter), which is obtained by incoherent Compton back scattering of direct laser light with a very brilliant and intense electron beam ($E_e \leq 0.6$ GeV). The experiments envisaged with the γ source suggests the parameters of the γ beam: bandwidth equal or lower than 10^{-3}, energy up to 19 MeV to access all GDR, total flux higher than 10^{13} photons/sec at 100%BW, peak brilliance higher than 10^{21} photons/mm^2/mrad^2/s/(0.1% BW). The high flux, narrow gamma-ray bandwidth and superb brilliance requires an excellent normalized emittance for the electron beam, in the range of 0.5 mm mrad. In addition, it is envisioned that the gamma source will be used in conjunction with the low repetition rate ELI-NP 10 PW laser beams for many experiments.

As for the implementation of ELI-NP γ source the following two principles were accepted as guideline:
1) a staged realization of the γ source
2) a flexible design of the γ source.

The first principle permits a sequential buildup of the facility according to the available resources. The first stage may target only the most basic physics topics and the basic facility components that need to be started immediately and may cover the period from 2011–2015. The second stage might start from 2016 for five years, including more ambitious programs. Subsequently the third stage might start from 2021 for maybe ten years. This stage might include the most ambitious and far reaching project.

The second principle requires that the first stage facility has to be flexible designed in such a way as to accommodate its future growth.

During the ELI-NP Executive Committee Meeting (April 12-13, 2010) three possible options for the γ source were presented: a storage ring, an energy recovery linac and a warm linac.

The storage ring is based on the ThomX project [1]. The ThomX machine is conceived to provide the maximum average flux in a fixed bandwidth. Consequently, the basic scheme takes into account a very important collision repetition frequency and therefore the possibility to have Compton interaction in a storage ring. Electron bunches are injected and stored in the ring and discarded in a beam dump after 20 ms. To increase the pulse power of the light pulse the high average power laser is injected into a passive optical resonator (Fabry Perot cavity). Here the laser pulse is stacked on the pulse circulating in the cavity up to its limit given by the cavity finesse. The two systems are synchronized in a way that every turn the electron beam interacts with a laser pulse.

The main difficulty of the ThomX machine comes from the fact that 50 MeV storage rings are not very stable since the electrons are not sufficiently relativistic and that in addition the electron is strongly affected by the dispersion introduced in the bunches by the laser and the Compton scattering. For applications in Nuclear Physics of interest to the ELI project, the photon energy range lies in the 1-16 MeV range. This will require electron energies between 250 MeV up to 1 GeV, since in Compton scattering, the photon energy rises quadratically with the electron energy. Preliminary simulations show a much stable ring dynamics therefore, besides the small inconvenient to have to build a somewhat larger ring (ThomX 50 MeV ring diameter is only 3 m, ELI machine's one should be around 35 m), the expected photon yield should be larger for the MeV photon source. Unfortunately the majority of the nuclear physics experiments proposed for ELI requires a better than 10^{-3} FWHM which can not be obtained by this storage ring proposal. More, a ring configuration cannot be upgraded after 2015 (due to the fix diameter of the ring).

The energy recovery linac [2] has excellent performance, in some respect better than the warm linac (e.g. the negligible parasite electron dump), but is in an earlier R&D stage which posses serious concerns regarding the 2015 ELI deadline. The estimated price is also the highest due to cryogenics technology. But upgrade to ERL after 2015 is possible using the warm linac configuration.

The warm linac is based on the MEGa-ray project [3]. It fulfils the requirements for the γ beam and has a well established technology.

In order to guarantee a reliable and timely available technological solution for the startup phase of ELI-NP, a "warm" linac was selected. This choice ensures that ELI-NP will be the world-leading gamma beam facility at the time of its start of operation. In the second stage, this facility could be upgraded with a 100 mA ERL.

6.5.2 First stage warm linac in X-band RF plus 532 nm laser

Description

The warm linac gamma source is based on technology developed for the MEGa-ray project [3]. This technology fulfils the requirements for the γ beam and is a well-established technology. This approach is based on the interaction of short pulse lasers with relativistic electrons, i.e. Compton scattering, to create ultra-bright Mono-Energetic Gamma-ray (MEGa-ray) beams. The scattered radiation is Doppler upshifted by more than 1,000,000 times and is forwardly-directed in a narrow, polarized, tunable, laser-like beam. The peak brilliance of an optimized MEGa-ray source is both revolutionary and transformative as in Fig. 6.53.

MEGa-ray is a third generation Compton machine following PEIADES [4] and T-REX [5] and has been optimized for peak brilliance and narrow bandwidth. The Thomson-Radiated

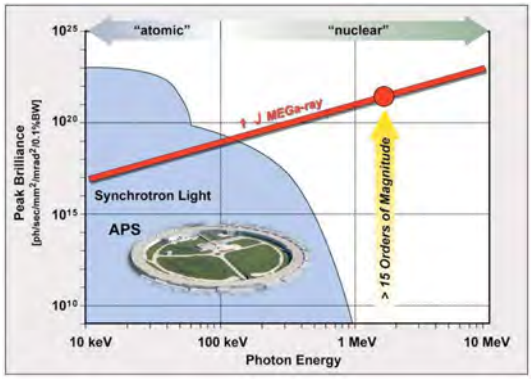

Figure 6.53: Peak brilliance for MEGa-ray.

Extreme X-ray Source (T-REX) project was the precursor project to MEGa-ray and produced monochromatic, highly collimated, tunable X-rays and gamma rays as a feasibility demonstration (see Fig. 6.54). With T-REX output researchers demonstrated an ability to use nuclear resonance flourescence to detect low density material (^{7}Li) shielded behind higher density materials (Al and Pb).

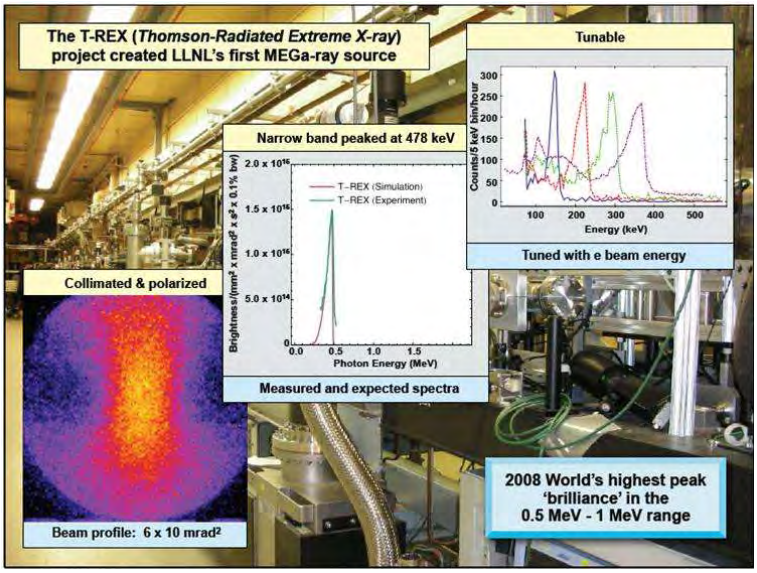

Figure 6.54: Feasibility of LLNL Thomson-Radiated Extreme X-ray.

The T-REX project used the S-band accelerator technology (~ 4 GHz and 10 MeV/m) for the accelerating structure. This technology could be easily scaled to higher energy (GeV scale) and work at higher flux and narrower bandwidth but is not compact and is relatively costly. One compact alternative is laser wakefield "acceleration" which can produce acceleration gradients of 10,000 MeV/m and can thus be extremely small. This technology however has relatively large energy spread and would produce gamma beams with >50% BW. Furthermore the lasers required for high flux wakefield acceleration would be very large, complicated and beyond the state of the art.

The best alternative is the high gradient X-band (~ 12 GHz) technology developed at the SLAC National Accelerator Lab which provides a path to future compact MEGa-ray machines with up to 180 MeV/m acceleration gradients. The accelerating section presented in Fig. 6.55 is

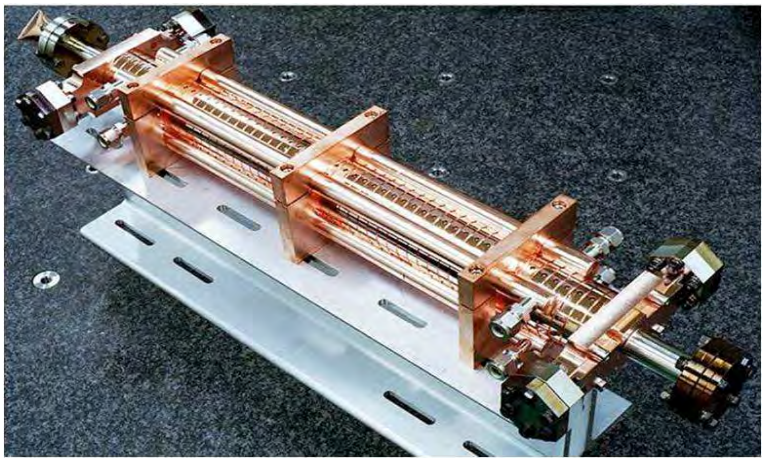

Figure 6.55: T53 accelerating structure.

capable of 120 MeV on aprox. 1 m length! The X-band accelerator technology was developped for the International Linear Colider competition and recently has been adopted for use by CLIC, the planned next generation high energy physics machine after LHC.

LLNL's planned Center for Gamma-ray Applied Science (CGrAS) will house the world's first '3rd Generation' MEGa-ray capability based on X-band accelerator and diode pumped laser technologies. CGrAS aims to develop compact and rapid, isotope-specific material detection, assay and imaging technologies and will house a gamma source with a brightness higher than 1.5×10^{21} for 2 MeV photons energy at 0.1% BW.

The goals of MEGa-ray (Mono-Energetic Gamma ray) source at CGrAS are four fold:

a) to increase gamma-ray source precision (2 orders of magnitude better banwidth than T-REX)
b) to increase peak brilliance (6 orders of magnitude relative to T-REX)
c) to increase gamma beam flux (5 orders of magnitude relative to T-REX)
d) to reduce gamma-ray source size.

The project is under development and implementation phase for the construction of a precision 250 MeV X-band Linac for a MeV-class Compton scattering light source and is scheduled to be fully operational and ready for users at the end of 2013.

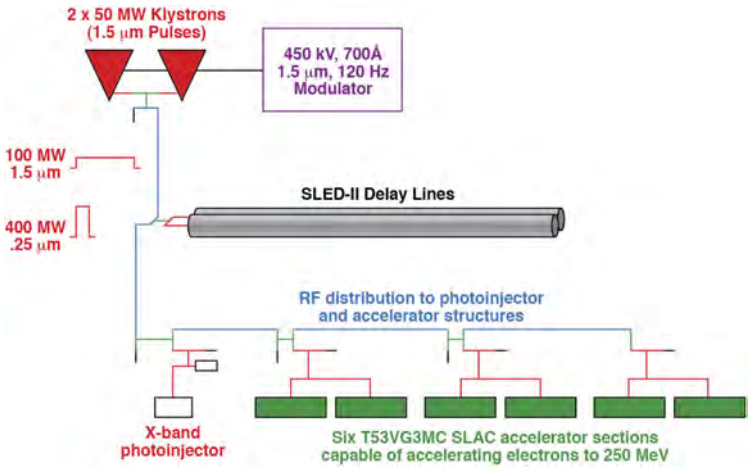

Figure 6.56: X-Band RF Power Distribution.

The linac is powered by a 400 MW, 11.424 GHz RF source and the requirements on rf phase and amplitude stability are very stringent as: 1° rf phase (243 fs), and 0.1% stability. The design includes ScandiNova solid-state modulators and SLAC XL-4 klystrons with SLED-II delay lines. The RF distribution is presented in Fig. 6.56.

Figure 6.57: The RF gun and the first accelerator stage.

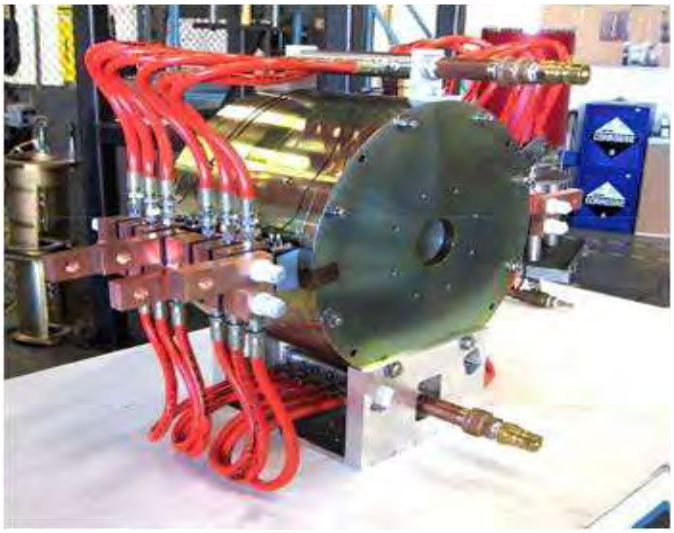

Figure 6.58: Solenoid Magnet (Anti-Helmholtz).

A very important subsystem is the 5.59 cell X-band RF gun (Fig. 6.57) which is a modified version of SLAC's (Arnold Vliek) original 5.49 cell X-band gun with the following optimized parameters:

- Cathode electric field: 200 MV/m
- Bunch duration: 10°, 2.5 ps
- Injection phase: optimized for each geometry; 20° for 5.59-cells
- Nominal charge: 250 pC
- Emittance: as low as 0.18 mm×mrad obtained for the DC photocathode using high acceleration voltage of 500 kV and 250 pC electron bunches
- Emittance compensation magnet: anti-Helmholtz pair, 7 kG (Fig. 6.58)

The linac main architecture is presented in Fig 6.59 and the timing of the laser and electron beam subsystems are given in Fig. 6.60.

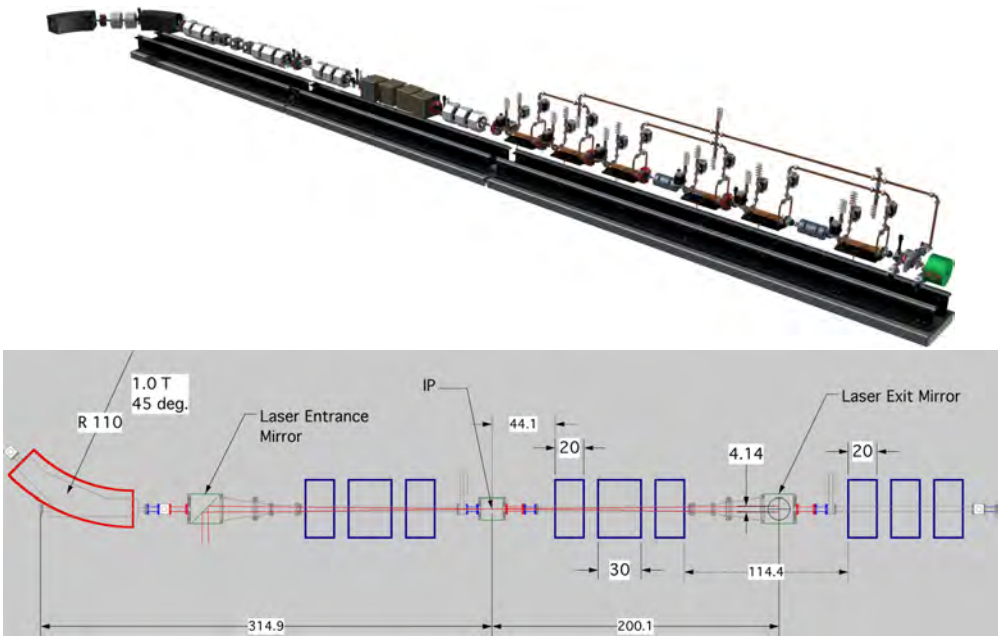

Figure 6.59: Architecture of 250 MeV X-Band Linac.

Table 6.10: Technical parameters for the MEGa-ray facility currently being constructed at LLNL.

Quantity	Value	Units
Peak gamma brilliance	1.5×10^{20}	Photons/sec/mm^2/mrad^2/(0.1% BW)
Effective Beam repetition	12,000	Hz (100 micro-bunches at 120 Hz rep rate)
Gammas per pulse	8×10^7	Photons at 100% BW
Spectral beam flux	10^6	Photons/sec/eV
Gamma pulse duration	2	Picoseconds
Gamma collimation	0.1	mrad at 0.1% BW
Gamma bandwidth	10^{-3}	ΔE/E
Gamma source size	10	microns
Electron beam energy	250	MeV
Laser pulse energy	0.15	Joules
Gamma-ray energy	0.5−2.3	MeV

A brief system overview is presented in Table 6.10 and the facility layout is described in Fig. 6.61. The interaction laser can run reliable at the high repetition rate of 120 Hz using diode pumping. By using a ring-down cavity for the laser pulse, within the macropulse of 120 Hz repetition rate, 100 micropulses can be realized, increasing the overall repetition rate to 12 kHz.

The predicted spectrum for the LLNL next MEGa-ray machine is shown in Fig. 6.62.

Specifications of the ELI-NP machine

The ELI-NP machine use identical X-band linac technology but extended from 250 MeV to 600 MeV, use identical state of the art 120 Hz diode pumped laser technology but extended from

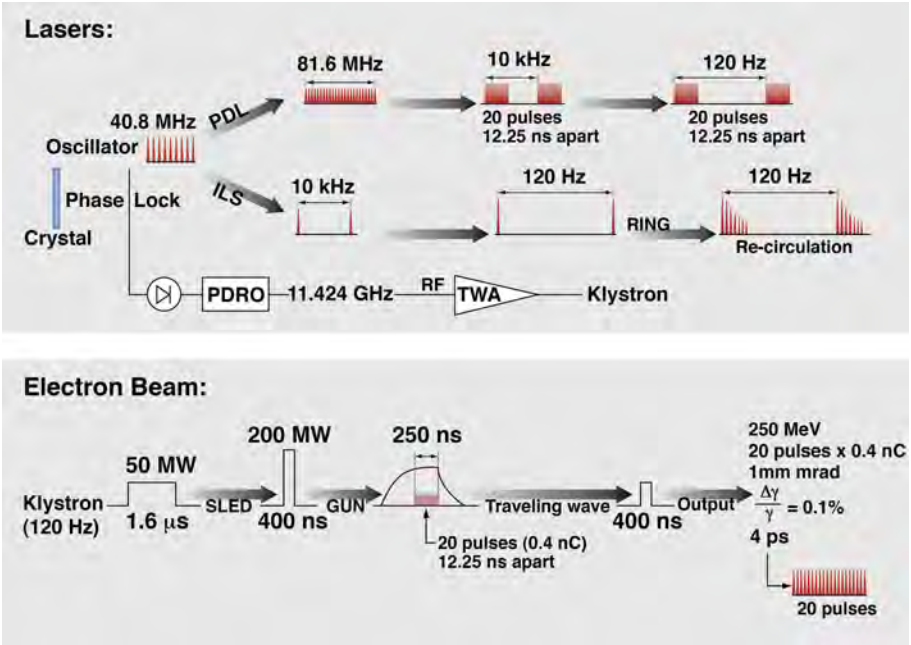

Figure 6.60: Sub-Picosecond Timing.

1 J to 10 J and duplicate as much as possible the controls systems and hardware being developed for the LLNL machine. The accelerator structure will be capable of 75 MeV/m in order to avoid higher breakdown rates and higher dark current signals. Specifications for the ELI-NP machine are listed in Table 6.11.

Table 6.11: The main specifications of the ELI-NP machine.

Quantity	**Value**	**Units**
Peak gamma brilliance	$>1.5\times10^{21}$	Photons/sec/mm^2/mrad^2/(0.1% BW)
Effective Beam repetition	12,000	Hz (100 micro-bunches at 120 Hz rep rate)
Gammas per pulse	8×10^8	Photons at 100% BW
Spectral beam flux	10^6	Photons/sec/eV
Gamma pulse duration	2	Picoseconds
Gamma collimation	0.1	mrad at 0.1% BW
Gamma bandwidth	10^{-3}	ΔE/E
Gamma source size	10	Microns
Electron beam energy	600	MeV
Laser pulse energy	1.5	Joules
Gamma-ray energy	1−13 (with 532 nm laser interaction)	MeV

This system will incorporate the latest in dark current noise mitigation and a fully documented and validated computer control system. It has to be stressed that 12,000 Hz is not the

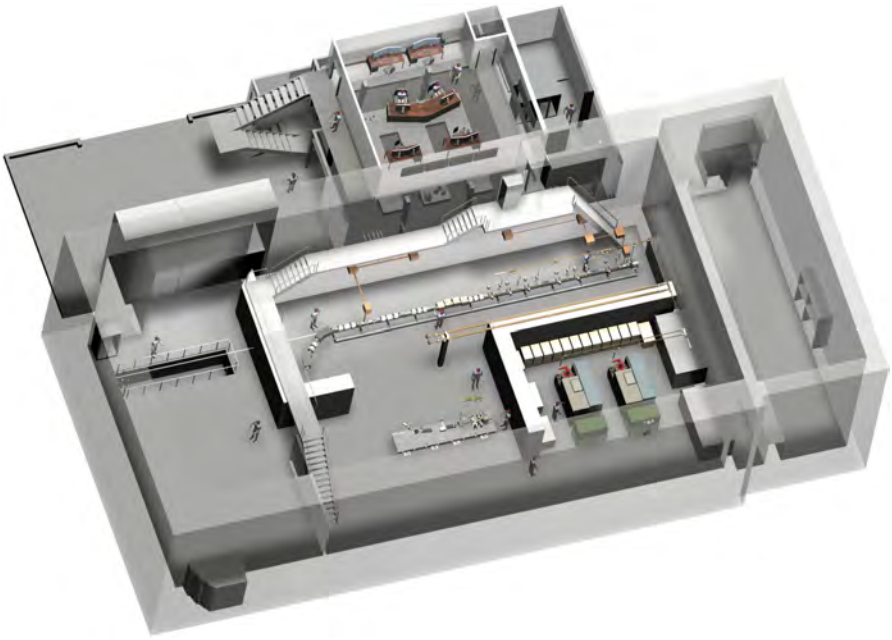

Figure 6.61: MEGa-ray Facility.

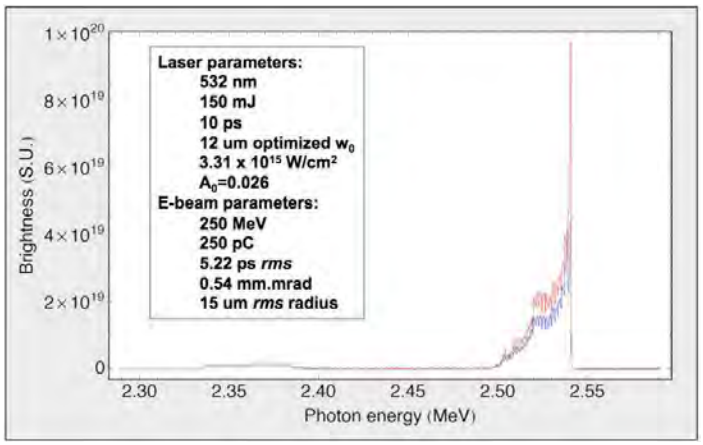

Figure 6.62: Predicted spectrum of an optimized MEGa-ray source at ~ 2.54 MeV.

upper limit on repetition rate for this system and that 10^{-3} is not the lower limit on bandwidth.

Going beyond these points however will require significant R&D that is not included in the estimates for the ELI-NP project.

Schematic of 600 MeV X-band linac and power distribution system for ELI-NP project is presented in Fig. 6.63 and an overall view of the proposed γ-source is presented in Fig. 6.64.

The proposed solution can be upgraded after 2015 as desired, e.g. by a 100 mA ERL. There is enough space to accommodate such an upgrade. Also, with a 355 nm laser instead of the 532 nm one, the γ output could be brought to 19.5 MeV. The upgrade is not trivial.

A number of significant activities are covered under this proposal. These include:

1) Development and test of a high energy laser and beam recirculation system which enables a gamma-ray flux that is 100× beyond LLNL's present machine.

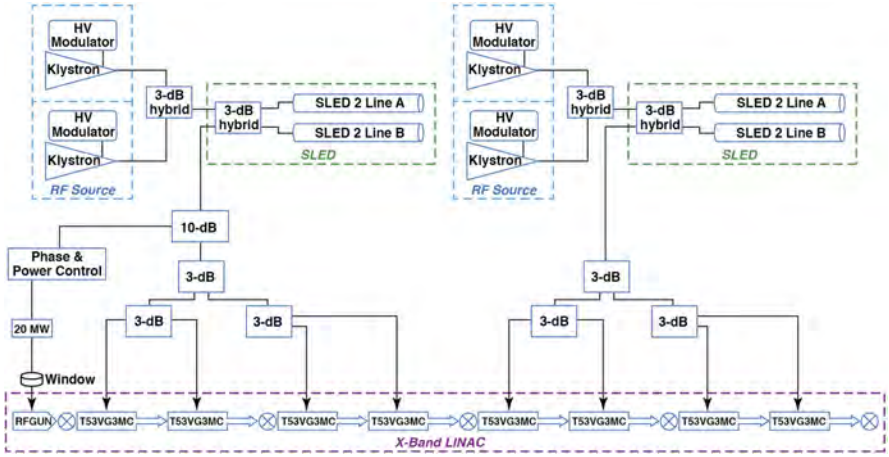

Figure 6.63: Schematic of 600 MeV X-band linac and power distribution system for ELI-NP project. SLAC XL-4 klystrons and T-53 linac sections are used.

a) Construction of a robust, femtosecond, fiber laser seed source that is synchronized to the linac X-band RF frequency.
b) Construction of a dispersion management system for narrowband chirped pulse amplification.
c) Construction of a 10 J-class interaction drive laser system with a base repetition rate of 120 Hz.
d) Construction and test of non-linear pulse recirculation hardware.
e) Construction and commissioning of a full suite of laser diagnostics.

2) Development of multi-bunch X-band linac technology and hardware for creation of high brightness 600 MeV electrons with an effective repetition rate of 12 kHz (see Fig.6.57).
a) Construction of an all fiber-laser-based photogun drive system synchronized to the linac X-band RF frequency.
b) Construction of a high brightness, multi-bunch compatible, high gradient X-band photogun.
c) Construction of 17 high gradient, X-band linac structures.
d) Construction of X-band power and power distribution system consisting of 8 klystrons and modulators.
e) Construction of X-band power pulse compressor for high gradient linac operation.
f) Construction of linac beam transport and dark current chicane.
g) Construction of laser-electron interaction region.
h) Construction and commissioning of a full suite of electron beam diagnostics.

3) Design, test and optimization of laser-electron interactions to maximize flux and/or minimize gamma-ray bandwidth.
4) Generation of an integrated computer control system for all components.
5) Generation of full construction, operation and maintenance documentation.

Four ELI-NP scientists should participate in the R&D, construction and test of the ELI-NP hardware at LLNL before it is shipped to Romania for installation there.

Possible upgrade in future

The proposed solution can be upgraded after 2015 as desired, e.g. by a 100 mA ERL. There is enough space to accommodate such an upgrade.

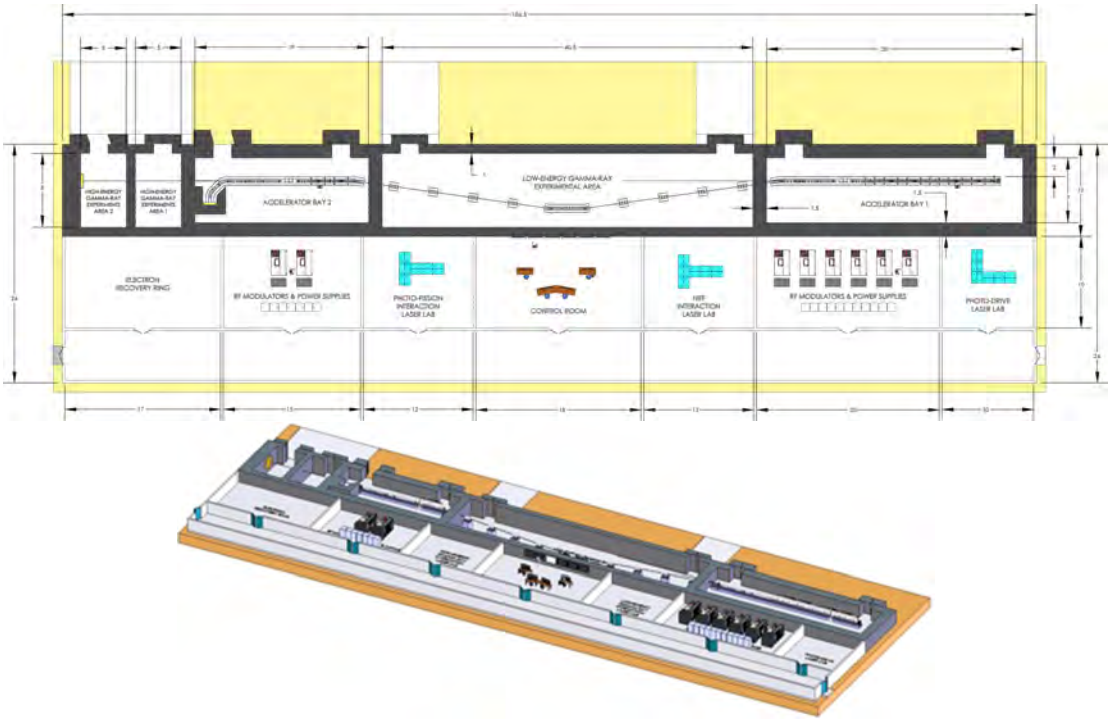

Figure 6.64: Overall view of the proposed ELI-NP γ source.

6.5.3 Second stage 100 mA Energy Recovery Linac

Energy-recovery linac (ERL) is a new class of accelerator which produces an electron beam of small-emittance and high-average current [6]. In an energy-recovery linac, an electron beam is accelerated by superconducting rf linac and the beam after use is decelerated in the same linac. Thus the electron energy is converted back into rf energy and recycled to accelerate succeeding electrons; this is "energy recovery".

This energy-recovery enables to accelerate an electron beam of high-average current with rf generators of small capacity. Moreover, the ERL is free from degradation of electron beam emittance caused by multiple recirculations of electrons, because an electron bunch in the ERL goes to a beam dump after deceleration and another fresh electron bunch is accelerated every turn.

The beam emittance of an ERL can be improved by adopting a small-emittance injector such as a photocathode electron gun. These features, generation of an electron beam with high-average current and small emittance, distinguish the ERL from other type of accelerators.

ERL has been developed for high-power free-electron lasers [7, 8] and now is considered as a platform for future X-ray light sources [9]. The ERL can also work for a high-flux and high-brilliance gamma-ray source in combination with laser Compton scattering as shown in Fig. 6.65 [10, 11]. A small-emittance electron beam from the ERL plays an essential role in the generation of high-flux and high-brilliance gamma-ray generation. In the high-brilliance mode, the electron beam, $\varepsilon_n = 0.1$ mm-mrad, is almost diffraction limited, and the on-axis gamma-ray bandwidth is dominated by monocromaticity of the electron beam and has a symmetric spectrum, while the bandwidth in the high-flux mode is dominated by electron beam emittance and has an anti-symmetric spectrum.

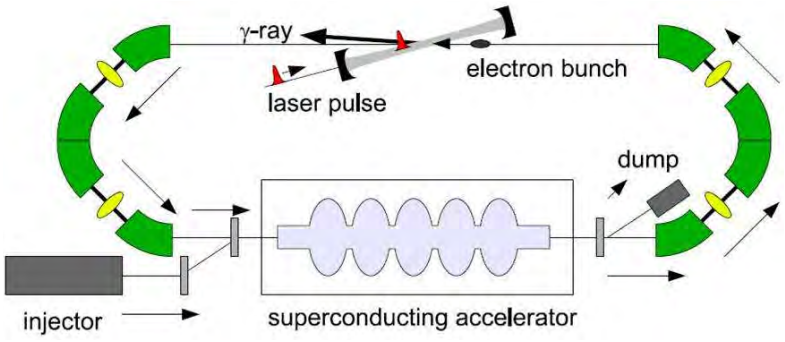

Figure 6.65: A schematic view of Compton gamma-ray source utilizing an energy-recovery linac (ERL).

Upgrade to 100-mA ERL can be made by adding superconducting ERL cavities under development in Japan [12]. After upgrade to 100-mA ERL, we can operate the gamma-ray source with parameters 80 pC, 130 MHz for the high-flux mode and 8 pC, 1.3 GHz for the high-brilliance mode. The flux and brilliance will be enhanced by 2 orders of magnitude.

6.5.4 Conclusions

Warm linac present and next future technology upgrades could provide for an affordable cost all requirements imposed by ELI. This facility is expected to be the best γ source worldwide, significantly better than the present best facility HIγS. By leveraging the LLNL activities it is believed that the working components for the ELI-NP machine could be constructed, tested and prepared for shipping to Romania in 3 years from the start of the project, i.e. receipt of funding.

Upgrade after 2015 is possible using the existing configuration. For example with 100 mA ERL current one can get a γ flux of 5×10^{15} ph/sec and an incredible bandwidth of 4×10^{-5}.

The development with time of the most important parameters of the gamma ray sources (Fig. 6.66) shows an exponential improvement with time. The planned ELI-NP facility will have the world-wide best gamma source parameters at the start of operation. In the long run with 100 mA ERL's one can reach a significantly better bandwidth and peak brilliance for the gamma-beams compared to the 2015 approach.

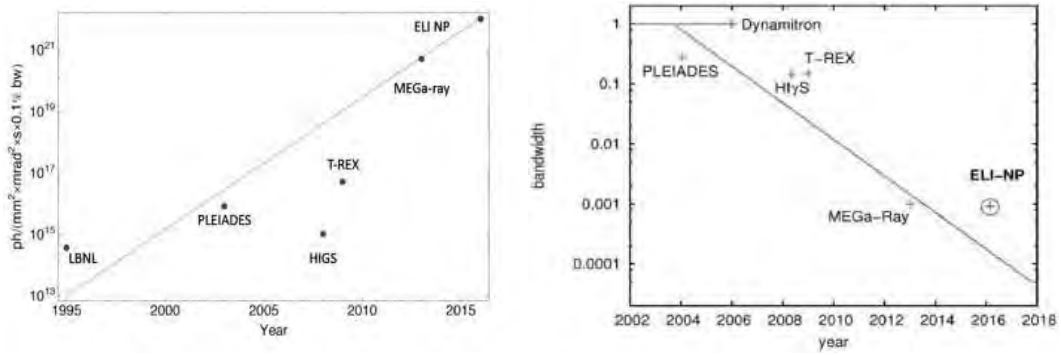

Figure 6.66: Development with time of the peak brilliance and bandwidth of the gamma ray sources, showing an exponential improvement with time.

Bibliography

[1] G. Wormser, Gamma Ray Source Working Group, http://www.eli-np.ro/documents/eli-excom-meeting/Wormser-Gamma-ray-source-working-group.pdf
[2] R. Hajima, High-Flux and High-Brightness g-ray Source Based on an Energy-Recovery Linac, http://www.eli-np.ro/executive-comittee-meeting-april-12-13.php; R. Hajima and N. Nishimori, private communication (2010).
[3] Ch. Barty, Development of MEGaRay technology at LLNL, http://www.eli-np.ro/executive-comittee-meeting-april-12-13.php and private communication (2010).
[4] W.J.Brown et al., "Experimental characterization of an ultrafast Thomson scattering X-ray source with three-dimensional time and frequency-domain analysis" Phys. Rev. ST-AB 7 0607021-1–060702-12 (2004).
[5] F.Albert et al., "Isotope specific detection of low-density materials with laser-based monoenergetic gamma-rays" Opt. Lett. 35, 354–356 (2010).
[6] R. Hajima, "Current status and future perspectives of energy-recovery linacs", in Proc. 2009 Particle Accelerator Conference (2009).
[7] G. R. Neil et al., "Sustained Kilowatt Lasing in a Free-Electron Laser with Same-Cell Energy Recovery", Phys. Rev. Lett. 84, 662–665 (2000).
[8] R. Hajima et al., "First demonstration of energy-recovery operation in the JAERI superconducting linac for a high-power free-electron laser", Nucl. Instr. Meth. A507, 115–119 (2003).
[9] S.M. Gruner et al., "Energy recovery linacs as synchrotron radiation source", Rev. Sci. Instr. 73, 1402–1406 (2002).
[10] R. Hajima et al., "Detection of radioactive isotopes by using laser Compton scattered γ-ray beams", Nucl. Instr. Meth. A608, S57–S61 (2009).
[11] V.N. Litvinenko et al., "Potential uses of ERL-based gamma-ray sources", IEEE Trans. Plasma Sci. 36, 1799–1807 (2008).
[12] R. Nagai et al., submitted.

Glossary

BW – Band Width;
CGrAS – Center for Gamma-ray Applied Science;
CLIC – Compact LInear Collider;
ELI-NP – Extreme Light Infrastructures – Nuclear Physics;
ERL – Energy-Recovery Linac;
FWHM – Full Width at Half Maximum;
HIγS – High Intensity γ (Gamma) Source;
LAL – Laboratoire de l'Accélérateur Linéaire;
LLNL – Lawrence Livermore National Laboratory;
LHC – Large Hadron Collider;
LINAC – LINear ACcelerator;
MEGa-ray – Mono-Energetic Gamma-ray;
PLEIADES – Picosecond Laser Electron Inter-Action for the Dynamic Evaluation of Structures;
RF – Radio Frequency;
R&D – Research and Development;
SLAC – Stanford Linear Accelerator Center;
SLED – SLAC Energy Doubler;
ThomX – Thomson X-ray Source;
T-REX – Thomson -Radiated Extreme X-ray Source.

6.6 Terahertz source

6.6.1 Introduction

The terahertz beamlines will provide a desirable radiation source for a wide range of researchers including physicists, chemists and biologists. ELI will enable access to a wholly new regime of THz generation with unprecedented pulse energies, orders of magnitude higher than existing sources. This THz facility will hold the key advantage of synchronicity with high power lasers and other intense secondary sources. We envision two THz beamlines. One source will be made by dedicating one of the relativistic electron beamlines to THz generation and will have similar specifications to current facilities such as FELIX [1] and FLASH [2]. The second source can be generated either through plasma mechanisms in a solid target or by optical rectification in a large aperture crystal providing high conversion efficiency and so high pulse energies.

Bibliography

[1] A. F. G. Van der Meer, Nucl. Instrum. Methods Phys. Res. Sect. A **528**, 8 (2004).
[2] S. Casalbuoni *et al.*, Phys. Rev. ST Accel. Beams **12**, 030705 (2009).

6.6.2 Source design

Optical rectification and difference-frequency generation

Optical rectification (OR) of intense femtosecond laser pulses offers a route to the generation of single-cycle THz pulses with extremely high intensity and field strength. Under optimum conditions the conversion efficiency should be as high as 10% [3]. If this can be scaled to petawatt-class pump beams using large crystal apertures we can expect to generate THz at the Joule level.

The spectral components of short optical pump pulses can generate low-frequency radiation in the THz spectral range by difference-frequency generation. The spectral content of the generated THz pulse depends on that of the pump pulse. The phase matching condition for this process can be formulated as a velocity-matching condition, $v(\Omega) = v_g(\omega_0)$, where $v(\Omega)$ is the phase velocity of the THz radiation and $v_g(\omega_0)$ is the group velocity of the optical pump pulse. When pumped at 800 nm wavelength velocity matching in collinear geometry is fulfilled in ZnTe for ~ 1 THz. However, at this pump wavelength ZnTe exhibits strong two-photon absorption which leads to free-carrier absorption and limits the useful pump intensity. One solution is to use large cross section beams. Ultrashort THz pulses with 1.5 μJ energy have been generated by using ZnTe wafers with 75 mm diameter [4]. Higher pump intensities can be used with ZnTe (and other low-bandgap semiconductors) if longer pump wavelengths are used [5], such that only higher-order multiphoton absorption becomes effective. However, high-energy THz pulse generation with this technique needs yet to be demonstrated.

Another possibility is to use nonlinear crystals with larger bandgap, such as $LiNbO_3$ (LN). LN has the advantage that its effective nonlinear coefficient is exceptionally large ($d_{\text{eff}} = 168$ pm/V at room temperature) [6]. However, due to the large difference in optical group index and THz refractive index, non-collinear geometry has to be used for phase matching. This can be accomplished by the tilted-pulse-front pumping (TPFP) scheme [7]. By using this technique (near) single-cycle THz pulses in the 1-THz frequency range (below phonon frequency) with energies up to 50 μJ were demonstrated [8, 9]. This resulted in focused electric field strengths approaching 1 MV/cm.

Ultrashort pulses with higher THz frequencies (above the phonon frequency) could be achieved by difference-frequency generation and optical parametric amplification in GaSe offering the advantage of birefringent phase matching [10, 11]. Phase-locked single-cycle transients with frequency components between 1 and 60 THz and peak fields of up to 12 MV/cm were generated

as the idler wave of a parametric amplifier [11]. Since this technique uses GaSe as the nonlinear material, its scalability to ultrahigh power levels might be limited.

THz generation by OR (using TPFP) has the advantage that it can be scaled up to ultrahigh-power lasers by increasing the pump spot size. However, this requires advanced source design technology. Our recent numerical study [3] shows that the output THz electric field strength in LN can be increased by at least one order of magnitude beyond the present experimental status by choosing optimal pump pulse duration and cryogenic temperatures (Fig. 6.67). The limitation of the pump spot size (and therefore of the pump energy) in commonly used TPFP setups containing imaging optics can be removed by using the contact grating technique [12]. With 500 fs pump pulses, 40 GW/cm^2 peak intensity and a beam diameter of 5 cm ($\sim$ 200 mJ pump energy) in LN at 10 K, 23 mJ THz energy (2.8 MV/cm electric field strength) is predicted. This will allow to achieve focused THz electric field strengths on the 100 MV/cm scale in the 1-THz frequency range [3]. The pump requirements are compatible with efficient diode-pumped solid-state laser technology available around 1 μm wavelength, which can also be easily synchronized to ELI lasers.

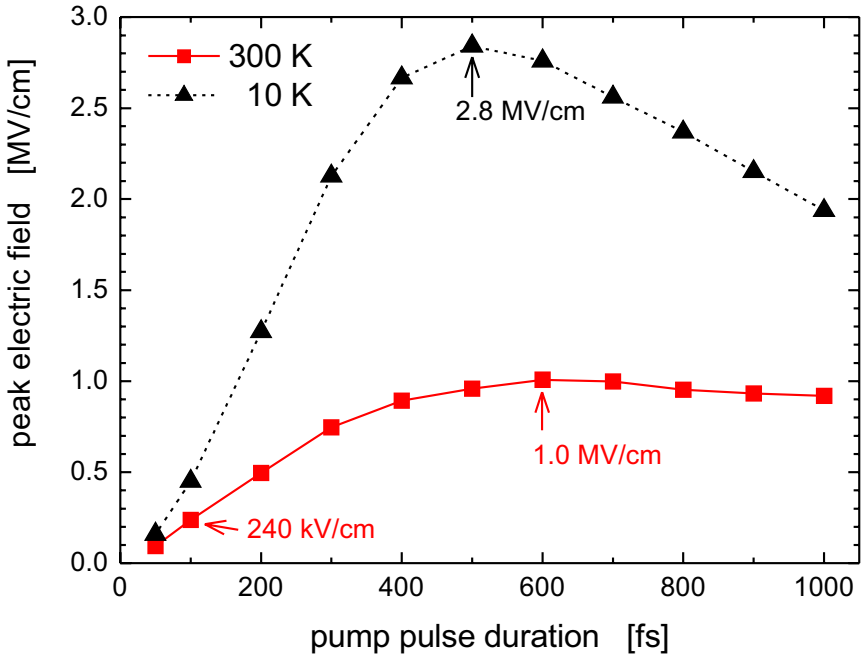

Figure 6.67: Peak electric field strength of the THz pulse versus the pump pulse duration at different temperatures in LN [3].

Surface plasma THz generation

Intense THz radiation can also be generated through interactions of ultrahigh (>10^{19} Wcm^{-2}) intensity lasers with solid density targets. There are two production mechanisms (see section 2.6) and it is not yet clear which one will be preferable. The ponderomotive process needs a controllable pulse shape to form a plasma density gradient whereas the antenna process is likely to be active with a steep density gradient. The latter is therefore more compatible with the requirements of the other secondary sources, such as harmonic generation, which use the best achievable laser contrast. It would be logical to use the same target station to produce several of the secondary sources which require high-contrast intense laser pulses irradiating

thin solid targets. It should thus be possible to combine terahertz generation with surface harmonic x-ray generation and ion acceleration. The terahertz emission from the interaction can be gathered with gold-coated mirrors covering the maximum possible collection angle in the specular reflection direction. It should be possible to operate the solid target source at 10 Hz and the pulse energy is expected to be >10 mJ with an output power of 10 GW for a single-cycle pulse. This could be focused to a spot $\sim$mm to generate intensities $\sim 10^{12}$ Wcm^{-2}.

THz from relativistic electron beams

Terahertz radiation can be harvested by using a dedicated electron beamline in a variety of ways. Perhaps the most convenient to employ are the coherent transition radiation (CTR) and the free-electron laser mechanisms. The construction of such a beamline can be based on the existing and well documented facilities such as FELIX [1] and FLASH [2]. In these systems the electron beam is directed on to a screen, such as silicon, to emit CTR or enters an undulator of length $\sim$3 m with period of order 1 cm. Characterization of the THz beam then has the added benefit of providing information about the quality of the electron beams. The expected performance of the electron-based THz source would be a 100 μJ pulse tuneable in wavelength from 30 μm to 1 mm at a repetition rate of at least 10 Hz. A single cycle pulse duration gives an output power of 100 MW.

THz generation in gas plasma

Another promising technique to obtain single-cycle THz pulses with high field strengths using femtosecond lasers is generation of THz pulses by nonlinear processes in gas plasmas [13]. THz generation in plasmas has the advantages that there is no damage threshold for the emitter since the gas target is continuously replenishable and that the available bandwidth of the THz pulses is essentially limited only by the duration of the pump laser pulse since no material absorption like optical phonons need to be considered. Conversely, air plasmas can also be used for detection of THz pulses [13]. When a femtosecond laser pulse is focused in gas, a plasma is generated when a threshold intensity on the order of GW/cm^2 is exceeded. This plasma emits a broad continuum of coherent and incoherent radiation. Mixing of femtosecond pulses with center frequency ω with their second harmonic at 2ω within the gas plasma [14], generation of ultrabroadband THz pulses with increased efficiency is possible. Kim et al. [15] reported on pump-to-THz conversion efficiencies exceeding 1×10^{-4}. By using 30-mJ pump pulses from a Ti:sapphire laser they generated ultra broadband (75 THz bandwidth) THz pulses with 5 μJ energy. However, the practical scalability of this method to ultrahigh-power lasers can be limited.

Bibliography

[1] A. F. G. Van der Meer, Nucl. Instrum. Methods Phys. Res. Sect. A **528**, 8 (2004).
[2] S. Casalbuoni *et al.*, Phys. Rev. ST Accel. Beams **12**, 030705 (2009).
[3] Fülöp J A, Pálfalvi L, Hoffmann M C, Almási G and Hebling J, in preparation (2010).
[4] Blanchard F, Razzari L, Bandulet H C, Sharma G, Morandotti R, Kieffer J C, Ozaki T, Reid M, Tiedje H F, Haugen H K and Hegmann F A, Opt. Express **15**, 13213 (2007).
[5] Fülöp J A, Pálfalvi L, Almási G and Hebling J, Opt. Express **18**, 12311 (2010).
[6] Hebling J, Yeh K-L, Hoffmann M C, Bartal B and Nelson K A, J. Opt. Soc. Am. B **25**, B6 (2008).
[7] Hebling J, Almasi G, Kozma I and Kuhl J, Opt. Express **10**, 1161 (2002).
[8] Yeh K L, Hoffmann M C, Hebling J and Nelson K A, Appl. Phys. Lett. **90**, 171121 (2007).
[9] Stepanov A G, Henin S, Petit Y, Bonacina L, Kasparian J and Wolf J P, Appl. Phys. B **101**, 11 (2010).
[10] Sell A, Leitenstorfer A and Huber R, Opt. Lett. **33**, 2767 (2008).

[11] F. Junginger, A. Sell, O. Schubert, B. Mayer, D. Brida, M. Marangoni, G. Cerullo, A. Leitenstorfer, and R. Huber, Opt. Lett. **35**, 2645 (2010).
[12] Pálfalvi L, Fülöp J A, Almási G and Hebling J, Appl. Phys. Lett. **92**, 171107 (2008).
[13] Karpowicz N, Lu X and Zhang X-C, J. Mod. Opt. **56**, 1137 (2009).
[14] Cook D J and Hochstrasser R M, Opt. Lett. **25**, 1210 (2000).
[15] Kim K Y, Taylor A J, Glownia J H and Rodriguez G, Nature Photon. **2**, 605 (2008).

6.6.3 Target area design

Beam transport

The target area will require a chamber dedicated to THz experiments including imaging, spectroscopy and material interactions. The availability of other secondary sources would be beneficial. This target station will be fed from two THz sources, a high repetition rate source driven by relativistic electron beams and a high energy source from either a solid target interaction or THz conversion through optical rectification. The THz beams can be transported either in vacuum pipes evacuated to better than 0.1 mbar or in nitrogen gas to avoid absorption in humid air. Gold-coated mirrors can be used for beam transport and focusing and the beam can pass between chambers through windows designed to preserve the broad bandwidth (diamond for example).

Beam diagnostics

The *beam profile* of the THz (near and far field) can be measured using pyroelectric array cameras which are sensitive from 1–3000 μm. A direct measurement of the *electric field* of the THz pulse can be obtained using electro-optic sampling [1] in case of sources with higher repetition rates (such as 10 Hz–10 kHz). Single shot technique is needed for the lower repetition rate sources. This requires a low energy chirped optical pulse to co-propagate through an electro-optic crystal (e.g. ZnTe) thus experiencing a polarisation rotation through the Pockels effect induced by the THz pulse. This can be performed as a single shot measurement by using a chirped [2–4] or tilted [5] probe pulse. Spectral analysis of the probe then yields the time-dependent electric field. The *spectrum* of the THz emission can be inferred by Fourier transforming the time-domain data or it can be measured directly using a grating spectrometer of the type used on the FLASH THz beamline [6]. This uses a reflecting grating and an array of pyroelectric detectors to build up a complete spectrum over a number of shots. The *energy* of the source can be measured with pyroelectric detectors. For added sensitivity a cryogenically cooled bolometer can be used. A discussion of material choices can be found in Ref. [7].

Safety considerations

Terahertz radiation is generally regarded as safe although there is no official standard [8]. Safety assessments can be based on those adopted by existing facilities such as FELIX and upcoming high power THz synchrotrons such as CIRCE [9]. However, at present there are no experimentally based skin exposure standards [10].

Bibliography

[1] Q. Wu and X.-C. Zhang, Appl. Phys. Lett. **68**, 1604 (1996)
[2] Y. Shen et al., Phys. Rev. Lett. **99**, 043901 (2007).
[3] J. van Tilborg et al., Opt. Lett. **33**, 1186 (2008).
[4] Z. Jiang and X.-C. Zhang, Appl. Phys. Lett. **72**, 1945 (1998).
[5] Y. Kawada, T. Yasuda, H. Takahashi and S. Aoshima, Opt. Lett. **33**, 180 (2008).

[6] H. Delsim-Hashemi et al., Proceedings of the 37th ICFA Beam Dynamics Workshop (FLS 2006), WG512.
[7] H.–W. Hübers et al., ICFA Beam Dynamics Newsletter, **35**, 117 (2004).
[8] www.teranova-ist.org.
[9] J. M. Byrd et al., ICFA Beam Dynamics Newsletter, **35,** 71 (2004).
[10] G. P. Williams, Rep. Prog. Phys. **69**, 301 (2006).

6.7 System Control

6.7.1 Computer System and Network

The control systems relating specifically to secondary sources of particles and radiation form a sub system of the overall facility control system and as such would consist of multiple computers and other hardware modules running local control applications, all connected via a secure network to allow remote operation by a master operator, typically in a centralized control room. The overall facility control system is discussed in Sect. 5.7. The vast majority of control functions necessary for the experiment would be remotely accessible from an isolated target area control room. Communication between all computers located in the vicinity of a high intensity target interaction area should be suitably resistant to electrical noise through the use of optical fibre cables, shielding and best practices.

6.7.2 Target Area Control Systems

Each ELI facility will require target areas specifically configured to most effectively support their respective experimental programmes. Many features of the target areas will vary between the different ELI facilities according to the specific laser system, repetition rate, secondary radiation and diagnostics employed. A common requirement will be that experimenters have at their disposal a single control system incorporating all of the varied experimental components. Though the target area controls may be operated independently of the main laser controls, the system will be connected to the main network and provide necessary information to the facility's operational data storage system.

Any control systems that are implemented must allow for automatic beam control, mirror alignment and target positioning. This is critical to a high repetition rate facility and will represent a departure from existing high power systems which operate at relatively low repetition rates, while current kilohertz repetition rate systems typically employ far smaller beam dimensions. This will require the precise control of a large number of motorized mechanical drives. The positional accuracy provided by the drive control system must be sufficient to ensure translational and angular accuracy of less than a micron and a microradian respectively. It is essential that the system is capable of recovering the calibrated drive positions if electrical power is lost. The ELI target areas are likely to be environments where high EMP's are experienced. This means that, in some cases, the target area motors must be robust and capable of surviving these EMPs and that the electronically encoded drive positions are not erased by EMPs. In addition to precise mechanical controls, the experimenters, where appropriate, should have local control of the target area vacuum systems. Other services such as gas or liquid supplies where gaseous or liquid targets are employed must also be controllable by the experimenters. A more comprehensive summary of the various controls necessary is given in table 6.12. Many of these systems will require fully automated modes of operation, for example to ensure stable high quality vacuum conditions during high power operation and to ensure personal safety in respect of radiation hazards.

In a high repetition rate system such as ELI, the amount of data generated during an experiment will be extremely large. It will be necessary to implement a system of automated data collection and storage and a method of real time data analysis, to deal with the vast quantity of data.

6.7.3 Data Acquisition System

During high power laser operation, the control systems will monitor and record a large range of data channels pertaining to the experimental interaction. The laser diagnostics are discussed in Sect. 5.3. Due to the high repetition rate, most if not all of the experimental data will be

Table 6.12: Summary of experimental components and utilities that require integration with the facility control system.

Component/utility	**Issues/Comments**
Laser manipulation and focusing optics	Feedback to laser control system for beam stability.
Secondary source beam optics	Where secondary sources are subsequently manipulated, e.g. gratings, curved crystals or charged particle optics.
Solid Laser target delivery/alignment	High repetition target delivery and auto alignment.
Gas/fluid flow rate monitoring	For high repetition gas cell/capillary/jet or liquid spray/droplet targets.
Target debris shielding (pellicles)	Debris shielding of sensitive optical surfaces degrades over time. Laser transmission through shielding monitored and pellicles cycled at appropriate times.
Vacuum pressure monitoring	Vacuum pressure critical to beam propagation and focusing - must not be compromised due to target debris or gas/fluid input. Real time response to changes in pressure.
In-chamber camera monitors	Where applicable to laser repetition rate and with filtering automated and linked to the power level.
Experimental Diagnostics	Require high speed data acquisition capability suitable for the given repetition rate. Multiple shot integration where appropriate. Capable of operation in high EMP strength environment.
Experimental data transfer/storage	EMP resistant data transfer and storage in shielded/isolated location.
Data manipulation/ processing	Function of the data acquisition and storage system. Appending metadata to data streams and running pre-programmed analysis routines.
On shot radiation monitoring	Real time monitoring of prompt radiation arising from primary and secondary source interaction with targets/samples/chamber walls.
Residual radiation monitoring	Nuclear activation or materials leading to various decay mechanisms.
Remote handling of activated materials	Integrated with safety systems to prevent exposure to ionizing radiation.
Personnel Safety System (PSS)	Target area specific components of facility wide PSS. Operated independently of other control systems for maximum reliability.
Laser interlocks and beam shutters	Target area relevant interlocks must be in operation whenever the laser is on and safety shutters must open and close in response to experimenter commands or safety shutdown.
Additional interlocks	E.g. high voltage power supplies operated under vacuum or residual radiation containment.
Hazard warning sirens/lights/displays	Operated as part of the laser control but the operation of which is monitored by the personnel safety system (PSS).

also be recorded electronically. The large volume of experimental data, due both to the high laser repetition rate and the number of experimental diagnostics, will require a dedicated data acquisition and storage system to adequately catalogue the experimental data and aid subsequent analysis.

The various computers associated with individual diagnostics should be networked to allow the data acquisition software to simultaneously access all the data channels. The software should collate the data and, where necessary, append additional metadata to the raw data, e.g. date; time; shot number or sequence; diagnostic type; and configuration parameters. This process will allow further routines to be applied to the data, aiding subsequent manipulation, analysis and visualization. This feature will also ensure common datatypes, file structures and metadata formats across various experimental areas and across the different ELI facilities, enhancing data value and archive viability. The final data will be stored in a dedicated repository in the same manner as the laser diagnostic data. This repository will be made accessible to experimenters throughout and subsequent to the experimental campaign via a web based interface. This interface will also feature analysis and visualization utilities. The data acquisition software may also be configured to conduct real time analysis and also meta-analysis of the various data streams to monitor secondary source performance.

Part IV

Implementation Strategy

7 Risks analysis and synergies with other projects

7.1 Risks and risk reduction

A detailed analysis of different risks factors and their influence on the successful finish of the project within the timeline and budget is given in the national applications of the three countries. As an example we have put it in a table with some important risk factors and their impacts as they have been established in the application to the EU of the Czech beam-line facility (see figure below). On the other side national and European high intensity laser development programs help to reduce considerably the risk connected with the development, building and exploitation of ELI. The estimated amount of money being spent over the next few years on this kind of laser research (not including ELI) in the UK, France, Germany, Czech Republic and Italy will exceed 160 Mio €. The developments being done within the European projects will include many technologically relevant components and setups necessary for ELI. Therefore the synergies with these projects are key elements for a successful realization of ELI. The Sect. 7.2 contains a detailed description of some of the relevant national projects. On the European level a close cooperation with Laserlab Europe, HIPER and the European XFEL (ESFRI-project), DESY Hamburg is planned to maximize synergies in high intensity laser developments, diode pumping and compact laser driven XFEL (Sect. 2.6 and Sect. 6.4).

Table 7.1

No.	Risk Description	Type	Probability (low to high)	Impact (low to high)	Inherent Risk	Residual risk (after mitigation)	Implications (H/M/L)	Mitigation Action
1	Implementation teams are not big enough to deal with all design and technical issues during design phase. Project may be delayed.	Organizational	4	5	20	10	H	Timely implementation of project teams by relevant specialists in all required fields, strong international cooperation.
2	Lack of definition of laser systems before completion of building design may result in remediation and rework during construction.	Project management	3	4	12	15	H	Early confirmation and approval of Technical Design Requirements
3	Radiation shielding requirements not fully defined. Further development of the scientific program may lead to changes in requirements.	Technical-Experimental	1	5	5	8	H	Early confirmation of Technical Design Requirements
4	Scope creep due to inadequately defined project requirements. Further development of the scientific program may lead to changes in requirements.	Project management	3	5	15	8	H	Early confirmation of Technical Design Requirements
5	Building designer is not able design full execution design of a complex project in time and required quality.	Technical-Functional	3	4	12	8	H	Appoint experienced company for execution design stage. Manage a detailed pre-qualification process with proposed designer.
6	Increased costs due to execution documentation and contractual documentation mistakes discovered during construction period and technology installation.	Technical-Functional	3	5	15	10	L	Ensure correct coordination between all parts of the project documentation and that the documentation matches Requirements.

Table 7.1: Continued.

7	Public procurement processes take longer than anticipated. Public prequalification and procurement processes may be constraining in time.	Financial	2	4	**8**	**6**	H	Quality of procurement strategy Stakeholder management, liaise with authorities, timely responses to questions and clarifications.
8	Failure of supply chain due to economic conditions. Current global economic conditions may lead to a suppliers failing, causing delays in delivery or loss of title to work in progress.	Commercial	2	5	**10**	**5**	H	Secure price quotations for total scope of supply, reflected in the estimate and within the bid submission timeframe. Suitable Terms and Conditions of contract to ensure title of goods.
9	Currency fluctuation £ or $ or Euro. Current global economic conditions will lead to market uncertainties resulting in greater than usual currency fluctuation.	External	3	3	**9**	**6**	M	Forward buying. Fix exchange rates with suppliers.
10	Materials inflation rises. Current global economic conditions will lead to market uncertainties resulting in higher than expected inflation.	External	3	3	**9**	**9**	M	Secure firm price quotations for total scope of supply, reflected in the estimate, and within the bid submission timeframe.
11	Delays in achieving building / statutory approvals. Local authority approvals and permits will be required before commencement of works.	External	2	5	**10**	**3**	H	Stakeholder management, liaise with local authorities
12	Discovery of archaeological remains may result in a delay of construction to allow for excavations and surveys.	Schedule	3	5	**15**	**10**	H	Advance negotiations with the funding authorities.
13	H&S accidents occur during construction period.	Health & Safety	2	5	**10**	**3**	M	General Contractor is to obey rules required in the design documentation and by local legislation. Provide Health & Safety coordinator.
14	Breach of quality or standard caused by General Building Contractor	Assurance	3	4	**12**	**4**	M	Continuously check the quality of performed work on site and will draw the attention if any deficiencies are discovered.
15	Discovery of unknown ground conditions or contamination may lead to delay and additional costs.	Schedule	2	3	**6**	**4**	M	Detailed surveys, boreholes etc.
16	Discovery of unknown underground services may lead to delay and additional costs.	Schedule	2	2	**4**	**4**	M	Detailed surveys, boreholes etc.
17	Delay to building schedule due to restricted access to construction site - heavy plant. Local planning or traffic constraint may limit access to site.	Schedule	2	3	**6**	**4**	M	Detailed planning. Liaison with local authorities
18	Delay in construction works or deliveries caused by insufficient performance of GC	Schedule	3	4	**12**	**4**	M	GL to provide a detailed time schedule with relevant milestones. Construction procedures to be initiated by GL to be contracted with GC.

Table 7.1: Continued.

19	Damage to installed equipment. Program constraints will lead to a large number of workers simultaneously working in a limited space resulting in the potential for accidental damage to installed equipment.	Technical-Functional	2	3	**6**	**4**	M	Detailed work plans and interface controls. Safe systems of work and permits.
20	Facility performs inadequately to justify the payment milestone. Delays in installation and commissioning may result in a failure to meet the acceptance criteria within the timeframe.	Technical-Functional	1	5	**5**	**5**	M	Define exact acceptance criteria. Schedule work to maximize time available for setting to work and acceptance testing.
21	Risk that the building performs satisfactorily at handover but subsequently fails when Installed Equipment is fitted out. The need to commission building services before final equipment installation may lead to imbalance in systems causing delays and rework.	Technical-Functional	2	5	**10**	**6**	L	Merge building design and Installed Equipment models. Specify suitable acceptance criteria and protocol
22	Equipment arriving in unclean condition. Failure to specify required conditions, or lack of quality control, may lead to additional work on receipt of components.	Technical-Functional	2	3	**6**	**4**	L	Careful Vendor selection and identification of requirements in specs.
23	Building/Installed equipment Interface causes delays for subcontractors/installation team. Lack of coordination of systems before completion of design may result in delays during construction.	Technical-Functional	2	5	**10**	**8**	M	Coordination of design. Preferred building contractor to appoint interface controller.
24	Interfaces between multiple sources of supply lead to problems in installation and setting to work. Lack of coordination of systems before completion of design may result in overlap or omissions in scope.	Technical-Functional	2	3	**6**	**4**	M	Technical monitoring and inspection of suppliers
25	Failure of identified suppliers to deliver on time. The specialist nature of the equipment limits the number of suitable suppliers. Requirements from other laser projects globally may increase demand over supply.	Schedule	3	4	**12**	**6**	M	More than one procurement resources, set manufacturing plans and milestones. Experience shows e.g. optics suppliers always deliver late.
26	Access to suitable state of-the-art equipment to enable project to proceed in time. The specialist nature of the equipment limits the number of suitable suppliers. Requirements from other laser projects globally may increase demand over supply.	Technical-Functional	2	5	**10**	**8**	H	Early engagement with suitable suppliers. Detailed prequalification process and selection of suppliers providing guarantees to supply equipment on time.

Table 7.1: Continued.

27	Incomplete security requirements leading to delays in the commissioning process.	Organizational	4	5	**20**	**8**	M	Early definition parallel with the Technical Design Requirements, liaison with authorities.
28	Unclear division of responsibilities within the project teams.	Organizational	3	3	**9**	**3**	M	The project charter, project organization and action plan are implemented with individual members responsible for the project areas.
29	Information obtained is not forwarded to the relevant project team members due to aggressive time schedule and overloaded Project Management.	Organizational	3	4	**12**	**4**	L	The project charter to define separate key areas. For each area the working group leader will be nominated, responsible for the tasks covered by the area.
30	Integrated Proposal is not supported by the associated countries and/or by ELI Steering Committee.	External	3	5	**15**	**4**	H	Organize working groups meetings to discuss Integrated Proposal draft and its parts.

7.2 National programmes

7.2.1 Apollon at Institute Lumiere Extreme (ILE), France

The French "single beamline" laser prototype, APOLLON, is presently under construction with the purpose of addressing all issues related to the flashlamp-pumped "Titanium Sapphire" approach. We will present here the developments under investigation to reach the expected specifications of laser pulses with 150 J/15 fs (10 PW) at a repetition rate of at least 1 shot per minute. The intensity on target is expected in the range of 10^{23} to 10^{24} W/cm^2.

Overview

The scheme of APOLLON is shown on Fig. 7.1. To seed the power amplifiers we need a well adapted Front End part delivering at high repetition rate Ultrashort pulses (5 to 10 fs) and with a very large bandwidth necessary to compensate the gain narrowing occurring through the power amplification process. For that we have developed an OPCPA front pumped by thin disk diode pumped lasers at 100 Hz, developed jointly with the Max Born Institute, Berlin, Germany.

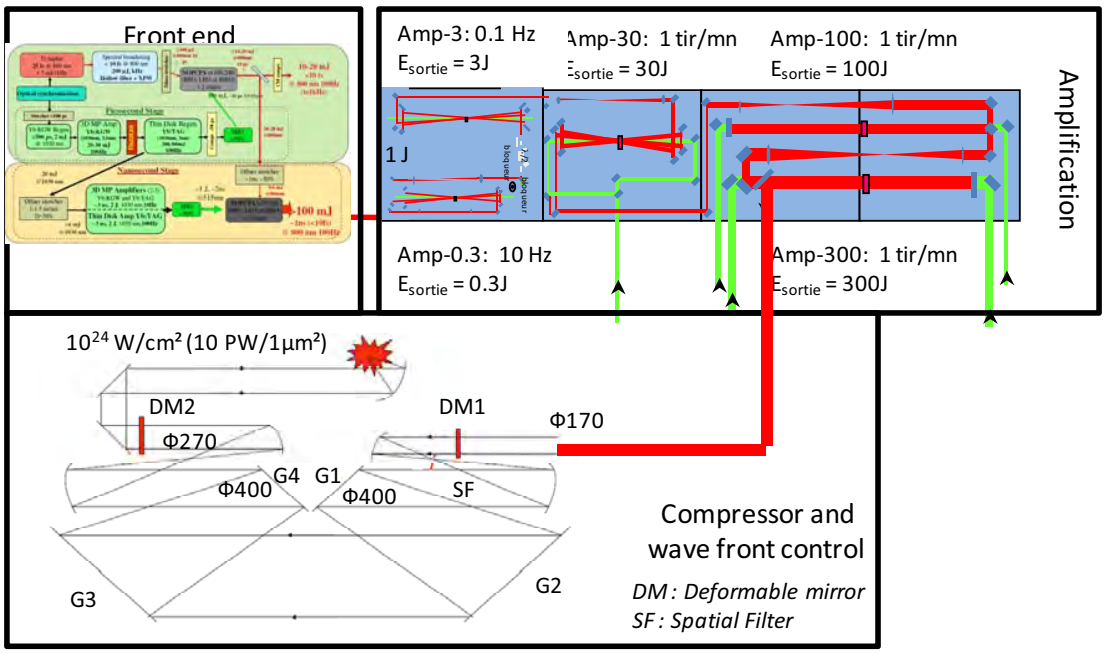

Figure 7.1: Schematics of the Apollon laser.

Pump laser must deliver on these crystals energy in the green as high as 600 to 800 J in nanosecond range, with a reasonable number of laser units avoiding the use of hundred of NdYag lasers delivering each few Joules at 532 nm. The development of new lasers systems delivering hundreds of Joules in the second harmonic must be studied, with the highest achievable repetition rates. Our lower limit was fixed at 1 shot per minute. To optimize the performances of such lasers, SHG conversion must be adapted to limit the required infrared energy, and the associated thermal load in the pump laser amplifiers. For that we are studying the availability of large size LBO crystals, which are very efficient to convert the infrared laser pulses, exhibit a high damage threshold, and a large angular acceptance.

Moreover, the pump fluency on the large TiSa is close to the damage threshold of the material and requires a good control of the spatial energy distribution to avoid hot spots which

could damage these expensive crystals. For smoothing these pump energy distribution we are developing new homogenizers based on Diffractive Optical Elements allowing to prevent the pumped crystal from any change in the pump energy distribution.

Scientific and technical bottlenecks

The weakest optical element in the Ultra intense CPA laser systems has always been the compression gratings. Those gratings must exhibit a broad spectral diffraction efficiency (200 nm centered around 800 nm) allowing recompression of pulses as short as 10–15 fs without spectral clipping effects. Only gold gratings could be used today for that reason, but these gratings present low damage threshold (below 200 mJ/cm^2), leading to the use of large and expensive off axis parabolic mirrors based beam expanders to extend the input beam to 40 cm in diameter. This huge beam diameter induces the need of extremely large gratings (on the meter size range). To overcome this problem we are presently investigating new schemes of diffraction gratings based on combination of metallic and dielectric layers we will present below in detail.

A main issue consists in the spatial quality of the beam and for that purpose we are working on developing new deformable mirrors with a broadband hard coating (700–900 nm) and with diameters as high as 200 mm. We plane to associated such Deformable Mirrors (DM) to high damage threshold grazing incidence dielectric spatial filters in order to remove high spatial frequencies wavefront distortions susceptible to generate hot spots on the compression gratings.

Finally we are also investigating new High Reflective, Broadband, High Damage Threshold mirror coatings allowing propagating hundreds of Joules of 10–15 fs pulses under vacuum from compressor to the experimental chambers.

7.2.2 Astra-Gemini at Central Laser Facility, RAL, U.K.

Overview

Astra Gemini is an upgrade of the existing Astra Ti:Sapphire (Ti:S) laser system. The general layout is illustrated in Fig. 7.1(a): the pulse from Astra with an energy of 1.5 J is split in two and each pulse is amplified in a separate four-pass Ti:S amplifier to an energy of 25 J and then compressed in a separate grating compressor. Each amplifier is pumped by up to 62 J of green light from a Nd:glass laser system operating at up to one shot per 20 s. The two re-compressed pulses (30 fs, 15 J, equiv. 0.5 PW) are delivered to an interaction chamber that is housed in a concrete bunker located underneath the laser room. This bunker with 1 m thick walls provides both radiation shielding and a very stable platform for the laser system, as shown in Fig. 7.1(b). With the chosen set-up, the two beams are synchronised, yet individually configurable in terms of energy, pulse duration and relative delay. This will enable a wide range of plasma physics experiments, e.g. pump-probe and backlighter configurations and the combination of a laser beam with a laser-generated particle or x-ray beam.

Beam transport

Great care has been taken to preserve a good beam quality by relay-imaging the beam all the way from the output of Astra to the grating compressors. This path is about 80 m long and contains six vacuum relay telescopes, three of which also act as beam expanders and the other three as spatial filters. Where necessary, the telescopes are chromatically corrected to avoid pulse front distortions [1]. We have devised a novel design for the final telescope that expands the beam from 50 mm to 150 mm. It contains a fused silica singlet output lens and a special doublet input lens that pre-compensates the chromatic error of the output lens, making the telescope achromatic as a whole. More detailed information can be found in [2].

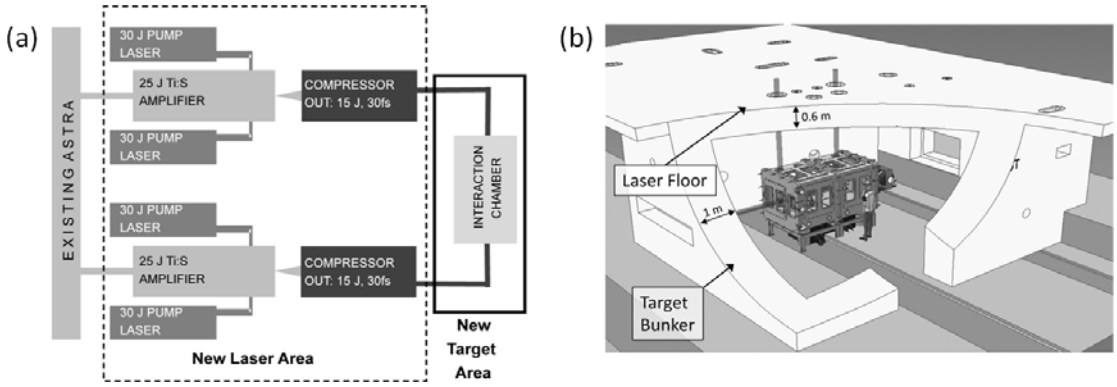

Figure 7.2: Schematic layout of Astra Gemini (a) and building layout (b).

Pulse amplification and compression

The two amplifiers each contain a 90 mm diameter Ti:S crystal, with the diameter of the pump end extraction beams being 50 mm. The extraction beam passes the crystal four times under different angles. The beam is spatially filtered after each of the first three passes. The crystal is pumped from both sides with up to 30 J each by pulses from a frequency doubled Nd:glass laser system (Quantel SA). The largest amplifier rods in the pump laser are 45 mm in diameter. Due to the high repetition rate of 1 shot per 20 s, the thermal stress in these rods is considerable, leading to a poor beam profile, as shown in Fig. 7.2(a). We have overcome this problem by employing diffractive optical elements (DOEs) for beam homogenisation. These DOEs (Silios Technologies) provide both a very uniform pump profile, as shown in Fig. 7.2(b) and very high diffraction efficiencies in excess of 93%.

Another serious challenge related to large aperture Ti:S amplifiers is amplified spontaneous emission (ASE) because of the very high gain-length product that is experienced by photons travelling perpendicular to the optical axis. To minimise ASE-related losses it is necessary to minimise this transverse gain and to suppress Fresnel reflections at the crystal surface in order to prevent parasitic lasing. We have minimised the transverse gain by choosing a weakly doped

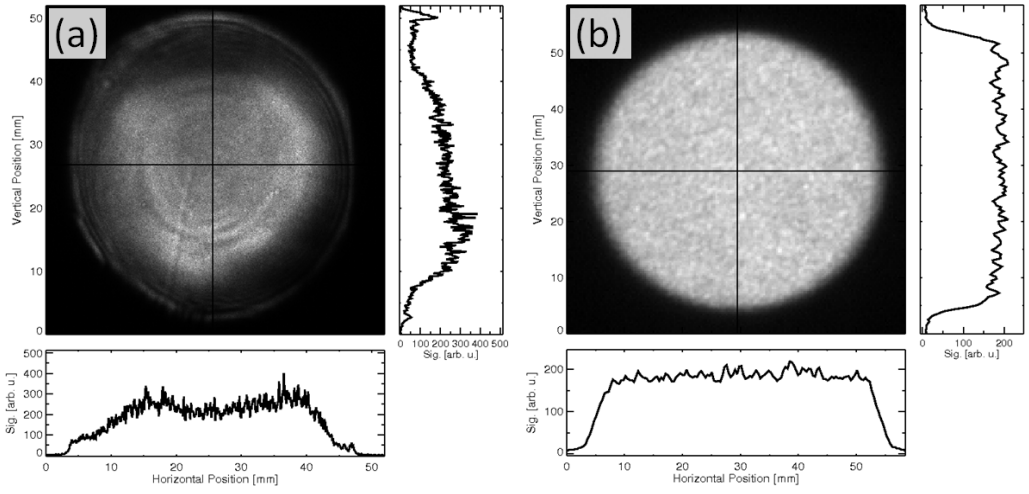

Figure 7.3: Pump beam profiles before (a) and after homogenisation (b).

Ti:S crystal and double-passing the pump beams through the crystal. The suppression of Fresnel reflections at the cylindrical face of the crystal and hence of parasitic lasing is provided by an index-matched absorber liquid. Detailed information on pump beam homogenisation, double-pass pumping and parasitic lasing suppression can be found in [3]. With pump homogenisation and ASE suppression in place, 26 J of amplified pulse energy were obtained with 62 J of pump energy.

After amplification, the beam is expanded to 150 mm diameter and pulses are recompressed in a vacuum compressor containing two large size gold-coated diffraction gratings in a double pass configuration. The shortest pulse duration measured so far was 40 fs.

First Plasma Physics Experiments

Since its commissioning, the Astra Gemini facility has played host to numerous user groups investigating a variety of high intensity laser plasma interactions, using both solid and gaseous targets. One highlight so far has been the acceleration of electrons in a free-space gas jet to nearly 1 GeV [4].

Bibliography

[1] Z. Bor, Opt. Lett. **14**, 119 (1989).
[2] O. Chekhlov et al., Central Laser Facility Annual Report 2006/2007, 165 (2007).
[3] K. Ertel et al., Opt. Express **16**, 8039 (2008).
[4] S. Kneip et al., Phys. Rev. Lett. **103**, 035002 (2009).

7.2.3 HiLASE: New lasers for industry and research

Summary

The main goal of the HiLASE project (High average power pulsed LASErs) is to create a national platform for development of new laser technologies having breakthrough technical parameters. In general, those lasers will be significantly more powerful and efficient, more compact, more stable and more easily maintained than the currently available flashlamp technology.

The HiLASE project focuses on development high-repetition lasers and laser systems that will find use in industry, in research laboratories, and particularly in large scale laser facilities such as ELI (Extreme Light Infrastructure) Beamlines planned to be realized in the Czech Republic. The project is specifically focused on diode pumped solid state laser systems (DPSSLs) and on the development of associated technologies. Two key technological concepts for DPSSLs will be explored within HiLASE:

1) thin-disk amplifiers to reach kW average output power, and
2) multi-slab amplifiers to reach high output pulse energy at 10 Hz scalable to kJ regime.

Laser systems with these technical parameters are not commercially available and thus will be unique not only in Czech Republic but also worldwide. The kW-class thin-disk laser is a perfect candidate as a pump source for booster amplifiers at the ELI Beamlines facility while the high-energy multi-slab laser is an ideal candidate as a pump source for power amplifiers at ELI which would otherwise have to be based on inefficient and low-repetition rate flashlamp technology.

Once commissioned in the HiLASE center these lasers will primarily enable:

– research relevant to testing of new dielectric optical components with high-damage threshold for high-energy and high average power laser systems, preparing new pumping lasers for OPCPA (optical parametric chirped pulse amplification) based laser systems which will be implemented

at the future large scale laser facilities such as ELI or HiPER, and driving high-repetition-rate/high-yield secondary photon sources, and

– industrial applications related to efficient processing of materials used in aircraft engines and turbines, gear components welding, ablative removal of thin layers from solar cells, car body soldering, cutting of optically transparent materials, antiques cleaning, laser peening and cutting, testing of efficient laser diodes and cooling systems.

There are 3 specific research programmes within HiLASE:

Research Programme 1 (RP-1): Development of multi-J, kW-class diode pumped solid state laser systems for industrial and scientific applications

Research Programme 2 (RP-2): Development of a 100 J/10 Hz class laser system to demonstrate scalability to kJ level

Research Programme 3 (RP-3): Development of key technologies for high repetition-rate amplifiers in partnership with industry

Scientific activities of the HiLASE project comprise of two major phases. Phase 1 (Implementation Phase) runs for four years from 2011 to the end of 2014. During this period, the technology of DPSSLs will be extended to new, hitherto inaccessible regimes of high pulse energy and high average power. At the end of this phase, prototype systems will be completed within the HiLASE facility and commissioned in readiness for Phase 2 of the programme. In Phase 2 (Operational Phase, from 2015), the facility will be operated for scientific and industrial users for an enduring programme of experiments and trials of new laser processing schemes. Both, the Implementation and Operational Phases of HiLASE are therefore considered as unique research and development. This programme will deliver new industrial and scientific results at all stages. These results will be carefully managed within HiLASE to ensure commercial and intellectual exploitation. RP-1 and RP-2 concern the development of the new laser capability and its delivery to the facility. These activities will be complete at the end of Phase 1 in 2014. RP-3 is a programme of associated technological development with runs throughout both the Implementation and Operational phases.

Development of multi-J, kW-class DPSSL system

The main thematic orientation of this research programme is the technological development and building of DPSSL prototypes with a high energy (J) and high repetition rates (kHz) based on the thin-disk technology and the establishment of such a capability in the HiLASE user facility for the industrial, scientific and medical applications. Work performed within RP-1 will comprise the scientific and engineering design of the laser system, its parts and subsystems, the development of selected components, the assembly, testing, and optimization of specific systems. Since the laser technologies of this kind are not yet commercially available, an international cooperation is going to play a key role. The laser system will be developed in close collaboration with other R&D institutions and/or commercial companies, and will be installed in the new HiLASE facility building. Among potential institutions that might cooperate on activities within RP-1 are, thanks to their expertise, e.g. Max-Born-Institute for Nonlinear Optics and Short Pulse Spectroscopy (MBI) and Max-Planck-Institute for Quantum Optics (MPQ) in Germany. The intellectual property protection and licensing rules will be applied to the outcomes of cooperation results taking into consideration their relevance and the participation of particular sides e.g. background intellectual property, in-kind contributions, matching funding, etc. that the collaborator brings to the project. The laser system of kW-class will be designed - recalling its great industrial potential – as a compact device with the smallest possible cost of ownership.

RP-1 embraces the development of two key technologies. The first one is the development of kW-class diode-pumped solid-state thin-disk laser operated at a repetition rate of 1–3 kHz

and delivering the pulse energy 100–300 mJ. The system design presumes a use of regenerative amplifier followed by a multipass power amplifier deployed in vacuum. Laser pulse duration will be of an order of a few ps at the central wavelength 1030 nm. The second area of interest is the development of DPSSL amplifier providing pulses with an energy of a few J at a repetition rate of about 100 Hz. The setup ought to be expandable to higher pulse energies using a regenerative amplifier with a large aperture architecture (LARA – Large Aperture Regenerative Amplifier) employing thin disks. An important research subject will be an optimization of high-energy and high-power laser system based on the thin-disk technology, in which it would be possible to raise the output power by tuning laser parameters. Additionally, testing of limitations of laser-diode pumping systems will be performed. After the optimization of the system and tests of alternative solutions the optimal configuration for realization of the 1–2 J/100 Hz prototype will be chosen. The prototype will be put into operation in the HiLASE centre for user experiments.

Developed laser system of the kW-class will constitute a basis for a long-term research and development plan in the HiLASE centre aimed at industrial and scientific users. Pulsed lasers reaching above the mentioned level of energy, repetition rate and power are not currently available on the market. Thus they will become a desirable tool for the industrial and scientific applications such as new generation of EUV lithography, optical parametric amplifiers pumping for ultraintense, extremely short pulses and the generation of secondary photon and particle sources with high luminance. It is going to be a tool e.g. for testing of laser electro-optical components from the providers who do not have access to laser devices of this type, i.e., with a high energy and a high average power. It is also expected to boost the international cooperation and lead to an upgrade of current technologies to higher power levels. The kW-class thin-disk laser developed within RP-1 will be an ideal candidate as a pump laser for booster amplifiers at the ELI Beamlines facility which would otherwise have to be based on current flashlamp technology.

Development of a 100 J/10 Hz class DPSSL system

The main objective of this research programme is an upgrade of pulsed DPSSLs by innovative solutions that will help to overcome current limitations in the high energy laser pulse generation. Such an upgrade will allow to obtain an energy level of about 100 J at 10 Hz and to increase it even further. To minimize the technological risks, RP-2 will be split into three phases. The Phase 1 (2011-2012) will advance 4 key technological tasks (see below). Results of the Phase 1 will be then utilized in the Phase 2 (2012–2013) to construct a technologically unique laser system producing optical pulses with an energy up to 100 J. This system, commissioned in Phase 3 (2014), will not only serve as a potentially new research tool, but will also prove the scalability of this technological concept into kJ/10 Hz range with the same level of technological risks.

It must be understood that RP-2 aims at a significant upscaling of current state-of-the-art laser technology and DPSSL system with similar parameters (100 J/10 Hz) is not yet commercially available. Therefore strong international cooperation towards delivery of laser system for RP-2 is going to play a key role. It will be developed in a collaboration with other R&D institutions and/or commercial companies, and will be installed in the new HiLASE facility building. Among potential institutions that might cooperate on activities within RP-2 is, thanks to their expertise, e.g. Rutherford Appleton Laboratory (RAL) in U.K. The intellectual property protection and licensing rules will be applied to the outcomes of cooperation results taking into consideration their relevance and the participation of particular sides, e.g. background intellectual property, in-kind contributions, matching funding, etc. that the collaborator brings to the project. After installation and commissioning of the system in the HiLASE building, the laser system will serve as a fundamental component of long-term research and development program. The program is aimed at the industrial and scientific users wanting to test the laser

and the opto-electronic components who have no access to other commercial high-energy laser pulse system with a high average power. As an additional benefit, the RP-2 will form a large group of scientists and engineers/technicians with specialized knowledge and qualification to run, maintain and further develop such a laser system. This group could then serve as a core of a team capable of construction of next-generation of the lasers, which will produce optical pulses with an energy of 1–10 kJ and a repetition rate of 10 Hz.

The Phase 1 of the RP-2 consists of 4 key technological tasks:

1) Development of efficient, and highly reliable system of pumping with laser diodes
2) Development of laser medium with adequate optical, mechanical, and thermal properties capable to sustain a high average power
3) Improvement of advanced cooling methods that will remove the heat from the laser amplifiers and maintain the necessary optical quality of laser beam in the laser chain
4) Development of the low-energy (1–10 J) front-end and pre-amplifier

The Phase 2 of RP-2 will make use of previous results to construct the 100 J class laser system with potential scalability to 1 kJ and beyond. Outcome of each task in the Phase 1 will be an assembly of summary documents that will include the results of outgoing research and the intellectual property created by HiLASE in cooperation with the involved institutions. For those results an international patent protection of intellectual property will be ensured. Outcome of the Phase 2 should be a functional prototype of the DPSSL delivering laser pulses with an energy reaching 100 J. However, the definite value of output energy will depend on the actual price of pumping laser diodes.

After commissioning in the HiLASE building, the laser system will serve as a development prototype, as a user-lab installation for testing the industrial electro-optical technologies and as a platform for validation of new technologies for laser machining and material processing that require high energy deposited on a large surface. The high-energy multi-slab laser system developed within RP-2 will be an ideal candidate as a pump laser for power amplifiers at the ELI facility which would otherwise have to be based on current flashlamp technology. The same is true for other planned laser fusion facilities such as HiPER and LIFE which will be fully based

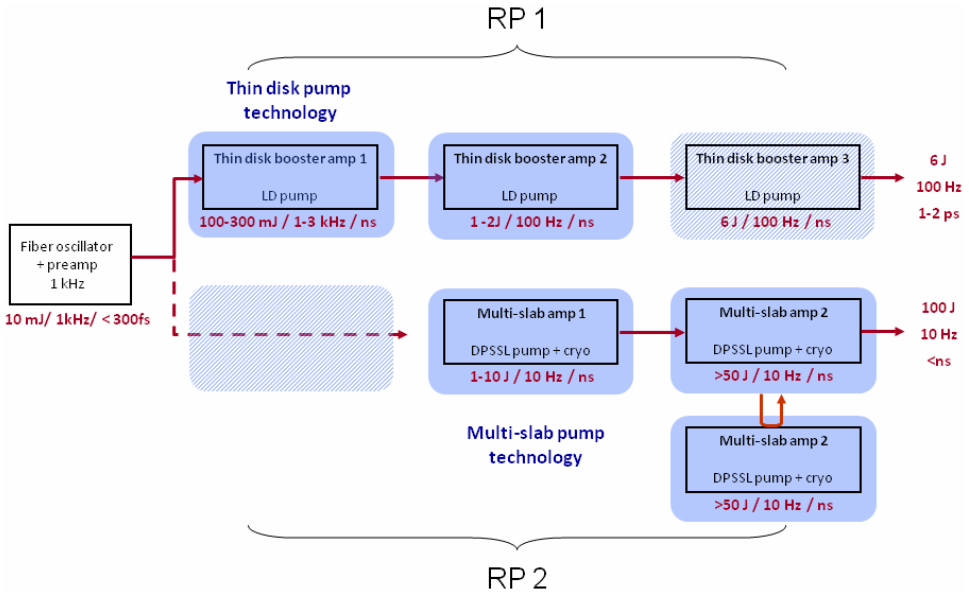

Figure 7.4: Conceptual layout of the DPSSL systems to be developed within HiLASE.

on DPSSL operating at few-kJ level – an upscaled version of laser system to be developed within RP-2 of HiLASE.

Development of key technologies for repetition-rate amplifiers

The objective of this auxiliary research programme is an identification of promising industrial applications and technologies using DPSSLs with a high repetition rate and a high average power that will be developed within RP-1 and RP-2. Laser systems deployed in the HiLASE facility shall be at a disposal of external users' for testing and development of versatile technologies. A key stone of RP-3 is a programmatic involvement and stimulation of industrial subjects that are related to DPSSL. The aim of this strategy is to increase their production capabilities, capacities and the market competitiveness. Within RP-3 training, know-how sharing, and setting up new links to the industry and research institutions will be supported.

During the implementation of the HiLASE project a significant progress in many fields is expected. Although, at this stage it is very difficult to specify exact outputs from the development of specific technologies, results are expected mainly in the following areas:

1. New laser materials, optical components and coatings development and testing
2. Diode-pumped fibre laser testbeds
3. Beam diagnostics for high-energy and high average power lasers

The work will be done making the lasers developed at HiLASE facility available, on user-fee basis, to companies for testing and tuning of the individual technologies. The individual technologies may include for instance: marking, micro machining, cutting and welding, coating removal, scribing, ablation, and surface shock wave modification of materials (laser peening).

Figure 7.5: Visualization of the HiLASE center.

Location of the HiLASE facility

As a location for the HiLASE center was selected village Dolní Běžany in Central Bohemia, situated southwards from Prague. This location offers environment that is highly appropriate for a research facility and/or technology centre with possibility of future expansion for additional technology park, spin-off companies or other research facilities. An important factor is the proximity of Prague where the required expertise in the given R&D field exists. The village is well connected with major motorways and Prague international airport Ruzyně is accessible within about 20 minutes. There is a very strong synergy with the ELI Beamlines Facility which is going to be built just next to HiLASE center.

The HiLASE building represents a highly specialized monolithic structure with specific and strict requirements on mechanical and thermal stability. Significant part of the building includes clean room facilities (classes ISO 100 to 10.000) for assembling and testing of the designed lasers, laboratories for optical metrology, facilities for testing of individual associated technologies, and for contractual user research. The supporting admistrative space will be capable to accommodate up to 50 people. The building is designed to provide adequate conditions for training students and includes a lecture hall for organizing workshops and conferences.

Additional information and update can be found at **www.hilase.cz**.

7.2.4 Petawatt Field Synthesizer at MPQ Garching, Germany

The Petawatt Field Synthesizer (PFS) project at the Max-Planck-Institut für Quantenoptik (MPQ) was started in 2005 in order to provide phase-stable few-cycle pulses at petawatt-class peak powers and high repetition rates for high-efficiency single attosecond pulse generation from solid surfaces and stable high-charge electron beams via bubble acceleration. The envisioned pulse parameters are 5 fs duration, 3 J energy and 10 Hz repetition rate.

General design principles

Presently the only realistic way of generating few-cycle pulses at energies above a few mJ seems to be non-collinear optical-parametric amplification (NOPA) using a three-wave mixing process inside a nonlinear crystal. Here, the amplification bandwidth is determined by the phase-matching properties and length of the chosen crystal. Broadband crystals such as BBO or LBO are still not readily available in sizes sufficient for petawatt peak powers. Therefore a modified approach was chosen for PFS, which offers several additional benefits and is schematically outlined in Fig. 7.6.

The main design idea is the use of short (few-mm) DKDP crystals for NOPA amplification, which in turn require high pump intensities in order to achieve sufficient gain over their short length. This necessitates the use of picosecond, high energy pump pulses, which are provided by a specially designed diode-pumped Yb:YAG CPA laser with a design output of 4×10 J at 1030 nm and 1 ps duration. Since there is no pump light outside this 1 ps temporal window, PFS is expected to reach an inherently high temporal contrast. The downside of this approach is the necessity for sub-100 fs synchronization between the pump pulses and the signal beam, which can only be achieved by an optical synchronization scheme. Since the pump light absorption in the NOPA crystals is almost negligible, it is expected that the PFS scheme can be scaled to high repetition rates for ELI by employing a suitable pump laser. Currently the PFS is in an advanced state of construction, and more details can be found in [1–5].

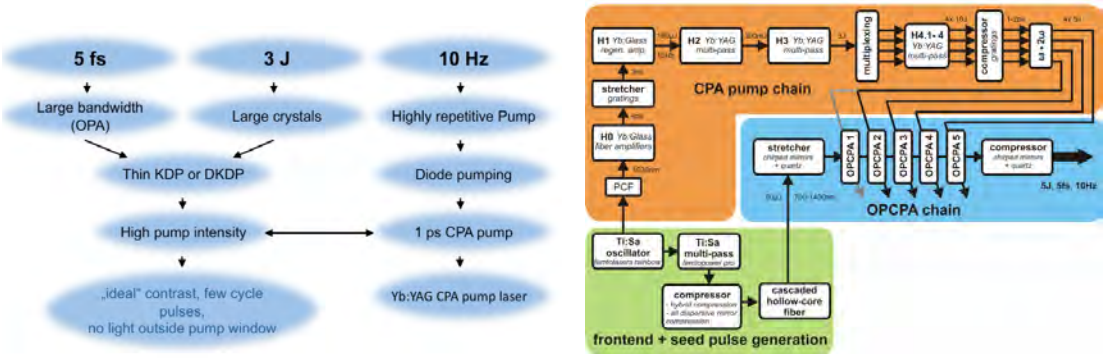

Figure 7.6: (left) PFS design philosophy, explaining the use of thin DKDP crystals for ps-pumped NOPA amplification driven by a diode-pumped Yb:YAG CPA laser. (right) schematic layout of PFS, detailing the frontend, pump-laser and NOPA-chain functional units.

Front end

The frontend provides the seed pulses for the pump laser and the NOPA chain in their respective spectral regions with few-10 fs synchronization. They are both derived for the output of an ultrabroadband, phase stabilized Ti:Sapphire oscillator. The seed pulses for the pump laser are split off and spectrally shifted to 1030 nm directly at the oscillator output, while the remainder is post-amplified to 2 mJ and compressed to 19 fs in a commercial Femtopower Ti:Sapphire amplifier. The pulses are spectrally broadened in a two-stage hollow-core fiber setup to yield a continuum ranging from 250 nm to 1400 nm. Its spectral phase was measured to be sufficiently smooth to be compensated by a combination of chirped mirrors and a Dazzler. These pulses are used as a seed for the demonstration of the first broadband NOPA stage, which will be described below.

Pump laser

The 1030 nm frequency-shifted output from the oscillator is fed into a two-stage Yb:glass fiber amplifier built by the Institute for Applied Physics (IAP) in Jena, which at its output provides 14 nJ pulses in a 10 nm spectral range. They are further stretched to 2 ns in a grating stretcher accepting a 3.5 nm spectral window, and subsequently pass through a second-zero dispersion stretcher with a spatial light modulator (SLM) in order to pre-compensate for spectral narrowing in the main Yb:YAG amplifiers. Without such spectral shaping gain narrowing in the amplification stages following the stretcher would lead to a final bandwidth of < 1 nm and thus require impractical dispersion values (i.e. grating separations) in the stretcher and compressor in order to maintain a safe, several-ns pulse duration during amplification. The SLM setup will be replaced by a Dazzler in the near future for more flexibility and higher throughput. After the stretcher the shaped pulses are amplified by approx. 100 passes in a 10 Hz, diode-pumped Yb:glass regenerative amplifier (regen) to 200 µJ without significant spectral modification. The regen is followed by the first diode pumped Yb:YAG 8-pass amplifier for a boost to 300 mJ energy at 10 Hz, keeping the full 3.5 nm bandwidth. At this stage, the pulses are currently passed into the compressor using multilayer-dielectric gratings with 6.5 m grating separation and compressed down to 1 ps duration with 200 mJ pulse energy. These pulses are frequency doubled to 515 nm using a DKDP crystal, currently providing up to 80 mJ, 1 ps pulses for the NOPA development.

In parallel to this, the development and optimization of the remaining Yb:YAG stages is ongoing. After having demonstrated up to 3 J pulses from an Yb:YAG amplifier in slab geometry

[2] at 1 Hz repetition rate, it became clear that a thick-disk approach will be better suited for reaching the repetition rate and efficiency goals of 10 Hz at PFS, since it will allow a multi-pass pumping scheme [6] and a more effective ratio of heat extraction surface and laser beam crossection. Therefore, both a new 500 mJ (instead of 300 mJ) amplifier and a subsequent 2 J stage are under construction, which have already demonstrated up to 1 J in a strongly simplified test setup. Depending on the experience with this novel design, the 10 J stages will be scaled up from this approach.

NOPA chain

The seed pulses for the NOPA chain are cut from the 250–1400 nm continuum delivered by the frontend and are stretched using a double prism pair setup to about 1.3 ps pulse duration. These pulses have a negative chirp and a spectral range of 700–1400 nm.

Before well-synchronized pump and seed pulses from PFS itself were available, short-pulse NOPA test experiments have been successfully conducted using a high-energy Ti:sapphire laser to investigate various critical aspects of short-pulse NOPA such as the verification of the predicted bandwidth and mode quality, and the necessity for pulse-front matching when two short laser pulses interact in the NOPA crystal at a non-zero angle [7]. These experiments confirmed the principal feasibility of scaling short-pulse NOPA to large beam diameters and confirmed the validity of the theoretical calculations.

Very recently, synchronized pump and seed pulses from PFS became available and preliminary OPCPA experiments confirm the predicted amplification bandwidth (see Fig. 7.7). The detailed results will be discussed elsewhere.

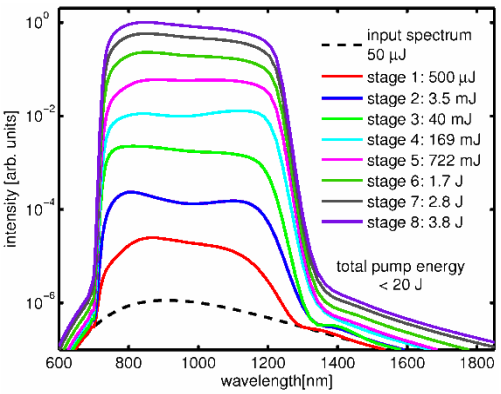

Figure 7.7: 1-dimensional design calculations for the PFS optical parametric amplification chain. The calculations shows that amplification to the Joule-level is possible in DKDP, while a sufficiently broad spectrum for a few-cycle pulse is also supported.

Bibliography

[1] C. Wandt, S. Klingebiel, M. Siebold, Zs. Major, J. Hein, F. Krausz, and S. Karsch, Opt. Lett. **33**, 1111 (2008).

[2] M. Siebold, J. Hein, C. Wandt, S. Klingebiel, F. Krausz, and S. Karsch, Optics Express **16**, 3675 (2008).

[3] I. Ahmad, S. A. Trushin, Zs. Major, C. Wandt, S. Klingebiel, T.-J. Wang, V. Pervak, A. Popp, M. Siebold, F. Krausz, S. Karsch, Appl. Phys. B **97**, 529 (2009).

[4] V. Pervak, I. Ahmad, S. A. Trushin, Zs. Major, A. Apolonski, S. Karsch, and F. Krausz, Opt. Exp. **17**, 19204 (2009).

[5] Zs. Major, S. Trushin, I. Ahmad, M. Siebold, C. Wandt, S. Klingebiel, T.-J. Wang, J. A. Fülöp, A. Henig, S. Kruber, R. Weingartner, A. Popp, J. Osterhoff, R. Hörlein, J. Hein, V. Pervak, A. Apolonski, F. Krausz, and S. Karsch, Review of Laser Engineering **37**, 431 (2009).
[6] M. Siebold, M. Loeser, U. Schramm, J. Koerner, M. Wolf, M. Hellwing, J. Hein, and K. Ertel, Opt. Exp. **17**, 19888 (2009).
[7] J. A. Fülöp, Zs. Major, A. Henig, S. Kruber, R. Weingartner, T. Clausnitzer, E.-B. Kley, A. Tünnermann, V. Pervak, A. Apolonski, J. Osterhoff, R. Hörlein, F. Krausz, and S. Karsch, New J. Phys. **9**, 438 (2007).

7.2.5 VULCAN 10 PW at Central Laser Facility, RAL, U.K.

The Vulcan 10 PW project aims to upgrade the Vulcan laser, located at the United Kingdoms' Central Laser Facility (CLF) to beyond the 10 PW power level and provide focussed intensities of greater than 10^{23} W/cm^2 to its UK and international user community. This will be achieved by generating pulses with energies of 300 J and with durations less than 30 fs. The upgrade will rely on OPCPA [1]. It has already been the subject of a great deal research over the last decade, including at the CLF [2–5].

Design principles

The design is based on a triple OPCPA amplification scheme with initial amplification occurring in the picosecond domain and subsequent amplification occurring in the nanosecond domain to guarantee a high contrast pulse. The project was divided into two phases, with phase one now completed. Phase two will commence in April 2010. A novel Front End has been developed during phase one to seed the remainder of the laser system [6]. This Front End comprises of a milli-Joule level broadband seed, a stretcher and an OPCPA Joule level amplifier based on LBO crystals. It delivers ultra-short pulses at 910 nm, with energies of up to 1 Joule and with a bandwidth of > 150 nm, sufficient to support a pulse duration of 30 fs or less.

The second phase will produce both a high energy amplified pulse and the associated compression/target interaction equipment to enable user experiments. The Joule level output from the Front End system will enter a final OPCPA system, based on two large aperture (DKDP) crystals, for amplification to the 500 J level. These two crystals will be pumped by ~ 3 ns duration beams from Vulcan. To achieve this level of energy two Vulcan high energy beam lines will be upgraded through the installation of additional Nd: glass 208 mm diameter amplifier chains. The amplified output beam will then be compressed in time and directed to one of two different interaction areas generating focussed intensities of greater than 10^{23} W/cm^2. In the first area, the 10 PW beam will be directed to the existing Target Area Petawatt (TAP) to be combined with the existing 1 PW beam from Vulcan in a 1+10 PW orthogonal configuration. In addition, the existing TAP area will been extended to enable a class of experiments that require the use of a long F#20 focussing optic. The 10 PW beam will also be directed to a new heavily shielded interaction area called the High Intensity Area (HIA) and with the aid of an F#0.7 focussing optic intensities 10^{23} W/cm^2 will be reached. A significant multi-floor extension to the existing Vulcan building will be required, the ground floor of which is shown in Fig. 7.8.

Diode pumped cryogenic kJ pump laser for VULCAN (DiPOLE)

Developing kJ-class diode pumped solid state lasers with multi-Hz repetition rate is pivotal for the future progress of ultra-high intensity science and its potential real-world applications. Here we present the conceptual design of a diode-pumped cryogenic kJ-class Yb:YAG amplifier as a potential pump source for multi-PW Ti:Sapphire or OPCPA systems.

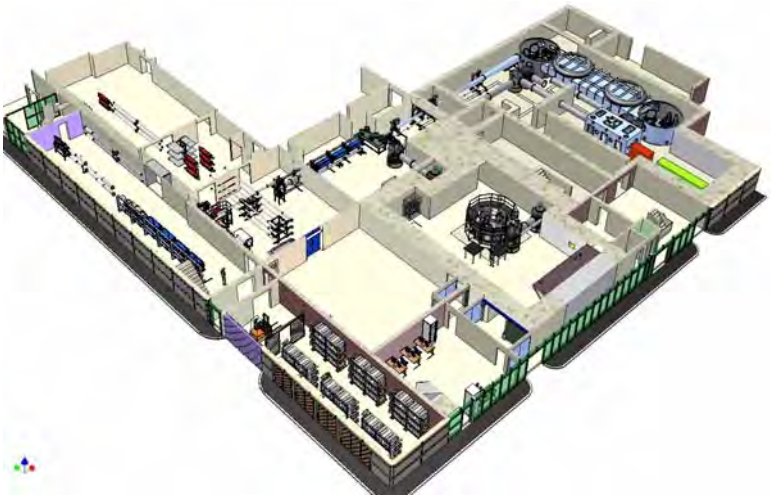

Figure 7.8: View of the ground floor of the building reconstructed for VULCAN 10 PW.

Choice of gain medium

As there is currently no gain material available that allows high-energy, ultra short (< 100 fs) pulse generation from a directly diode pumped laser, the best approach is to use a ns-pulse DPSSL for pumping large-aperture OPCPA or Ti:Sapphire amplifiers. The gain material for such a pump laser requires a long fluorescence lifetime in order to minimise the number of pump diodes required; good thermo-mechanical properties in order to handle the high average power; it must also be available in large sizes and good optical quality in order to handle the high pulse energy; and it should provide a reasonably high gain cross section to enable simple and efficient energy extraction.

Yb:YAG, in particular in ceramic form, fulfils all these requirements. However, at room temperature it exhibits a quasi-3-level nature and a still rather low gain cross section, necessitating very high fluence levels for efficient operation. The Boltzmann occupancy factor for the Stark sub-level of the 2F7/2 manifold for the peak transition at 1030 nm (612 cm^{-1}) is 4.6% at room temperature, reducing to 0.64% at 175 K. This reduction in lower laser level population leads to a more four-level-like behaviour with greatly reduced reabsorption losses. Also, low temperature operation leads to increased adsorption and gain cross sections and improved thermo-mechanical properties. The reduction in gain bandwidth at low temperature is no major drawback in this context.

Amplifier design and modelling

In order to determine amplifier design parameters, numerical modelling was carried out. In this model, the extractable storage efficiency was calculated for various parameters like pump fluence and pump pulse duration. The following results are calculated, unless stated otherwise, for an amplifier that is end-pumped from both sides with pump pulse duration of 1 ms, a 5 nm FWHM pump spectral width, centred at the optimum wavelength in the 940 nm absorption band. Spectrally resolved pump absorption cross sections were taken from [7]. First, calculations were carried out for room temperature operation shown by the square data points in Fig. 7.9. It becomes apparent that very strong pumping is required, firstly to overcome the high reabsorption losses and to achieve good efficiency and secondly to overcome the still rather low gain cross section to achieve reasonable gain. The required high pump and extraction fluences are difficult to achieve because of limited pump source brightness and limited laser damage threshold.

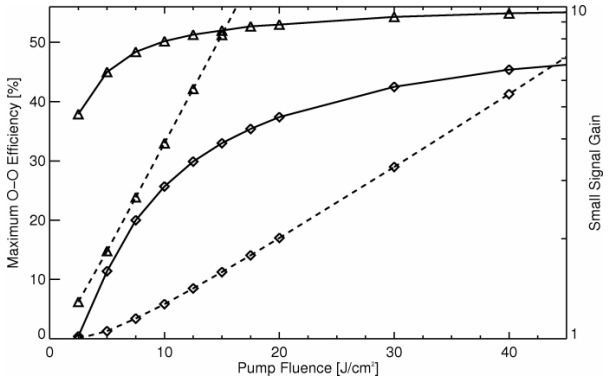

Figure 7.9: Maximum storage efficiency (solid line with square) and small signal gain (dotted line with square) for amplifier operated at room temperature. Corresponding maximum storage efficiency (solid line with triangle) and small signal gain (dotted line with triangle) as a function of pump fluence at 175 K operation.

Cooling the gain medium to 175 K drastically changes the situation, as illustrated in Fig. 7.9 (triangles). Reabsorption is reduced and the gain cross section increased, leading to greatly improved efficiency and gain, especially at moderate fluences. A pump fluence that is realistically achievable with today's laser diodes is 10 J/cm^2 (5 J/cm^2 from each side), yielding a storage efficiency of just over 50% (resulting in an extractable fluence of 5 J/cm^2) and a small signal gain of 3.8. This fluence is therefore chosen as the preliminary operating point for our amplifier.

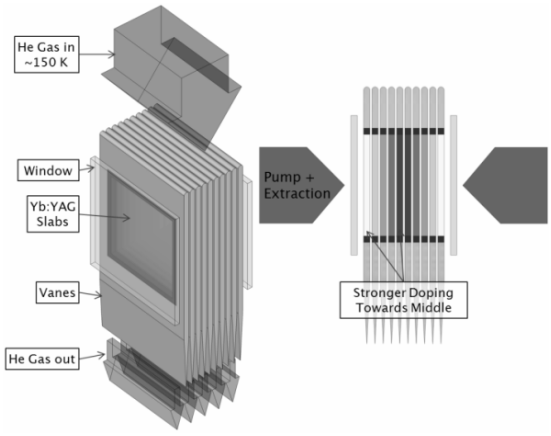

Figure 7.10: Illustration of amplifier geometry: isometric (left) and side view (right).

After determining operating temperature and pump fluence, the actual geometry of the amplifier needs to be defined. If the laser system is to yield an output energy of 1 kJ and the amplifier is to be operated at an output fluence of 5 J/cm^2, the aperture needs to be 200 cm^2 or 14×14 cm^2 if a square beam shape is adopted. The optimum area doping density $N \times l$ obtained from the numerical calculations is 3.15% cm, where N is the Yb-doping concentration in atomic% and l the geometrical thickness of the amplifier. The choice of N and consequently l is governed by ASE management considerations. If the gain-length product along the diagonal across the (square) surface of the amplifier is to be kept below 3, we require $N < 0.18\%$ and hence $l > 18$ cm. Such a thick amplifier requires distributed cooling, such as demonstrated

on the Mercury laser [8]. There, the gain medium is divided into a stack of thin slabs with He gas flowing through the gaps in between. The concept is illustrated in Fig. 7.10, where an amplifier consisting of 10 slabs is shown. If the criterion that the transverse gain-length product must not exceed a certain value is applied to each individual slab, one realises that the doping concentration can be increased towards the centre of the amplifier. The advantage is twofold: firstly, since the required overall $N \times l$ remains the same, the amplifier as a whole becomes thinner, facilitating pumping, saving material, and reducing the impact of nonlinear effects. Secondly the optical power absorbed in the individual slabs and hence the heat load is equalised.

Bibliography

[1] I. N. Ross et al., Opt. Commun. **144**, 125 (1997).
[2] I.N.Ross, J.L.Collier, P.Matousek, C.N.Danson, D.Neely, R.M.Allott, D.A.Pepler, C.Hernandez-Gomez, K.Osvay, Appl.Opt. **39,** 2422 (2000).
[3] J. Collier, C. Hernandez-Gomez, I.N. Ross, P. Matousek, C. Danson, J. Walczak, Appl. Opt. **38**, 7486 (1999).
[4] I.N.Ross, P.Matousek, G.H.C.New, K.Osvay, J. Opt. Soc. Am. B **19,** 2945 (2002).
[5] J.L.Collier et al., IFSA 2003, American Nuclear Society, Pub: Elsevier, 603-607, (2004).
[6] Y Tang et al., Opt.Lett. **33**, 2386 (2008).
[7] D. C. Brown, IEEE J Sel Top Quant. **11**, 587 (2005).
[8] A. Bayramian et al., Fusion Sci Technol **52**, 383 (2007).

7.2.6 Texas Petawatt Laser and 10 PW upgrade

This chapter describes a 10 PW laser technology based on OPCPA/Mixed laser glass architectures.

Overview

In this section we discuss the potential for reaching the 10 PW level in the ELI project by the use of a proven CPA configuration employing OPCPA amplification on the front end followed by final amplification to >1 kJ in Nd:glass. This approach has a number of major advantages in reaching the 10 PW level, perhaps the most important being that this approach uses technology that is already well proven. There are no significant technological bottlenecks in this approach; it simply requires the integration of technologies that are already proven at a number of labs around the world.

This approach is a natural evolution of CPA technology from the very first CPA laser at the University of Rochester, which was based on Nd:glass as well as the first Petawatt laser [1], which was also based on Nd:glass. That first CPA laser, along with most subsequent Nd:glass based lasers [2, 3], including the Petawatt laser at Lawrence Livermore, were limited to pulses of 500–1000 fs because of the limited bandwidth in phosphate-based Nd:glass that led to the gain narrowing associated with amplifying in the phosphate glass by factors of 10^5–10^8. Consequently, Ti:sapphire has become the gain material of choice for amplifying the shortest pulses. However, Nd:glass CPA lasers are still the highest energy lasers which can be constructed, limited principally by the gain narrowing that accompanies this high energy amplification.

The key advantage of Nd:glass is the high energy storage capability combined with the fact that high quality laser glass has the largest aperture of any solid state gain medium. The saturation fluence is sufficiently high for good energy storage and, at the same time, sufficiently below the damage fluence for efficient energy extraction with ns pulses. Petawatt lasers require 10 s–100 s of Joules in compressed pulses. Consequently to date ALL current petawatt lasers,

Nd:glass and Ti:sapphire, utilize Nd:glass as an energy storage material, either by amplifying chirped pulses directly in Nd:glass or by using Nd:glass in the pump lasers.

The concept presented here utilizes two major alterations to the architecture of the initial Nd:glass-based CPA lasers. These two elements allow the construction of a laser to the high energies (>1 kJ) that disk-type Nd:glass amplifiers allow but still retain the bandwidth needed to compress the amplified pulse to duration near 100 fs. A 10 PW laser, then, would operate with roughly 1.2 kJ of compressed pulse energy and a compressed pulse duration that is below 120 fs. Both major elements have been demonstrated in the lab up to the 1 PW level and the additional elements needed to scale the technology, such as phased, dielectric compression gratings, have also been demonstrated.

The first major element in this approach is to conduct the final high energy amplification in Nd:glass but limit gain in these amplifiers to ≤ 500. This takes advantage of the high saturation fluence of laser glass and the large aperture disk amplifiers that can be constructed from glass. In this way the gain narrowing in the final stages is lessened and bandwidths near 14 nm (FWHM) can be achieved. This technique requires substantial pre-amplification with a broadband gain technique at 1057 nm. This can be achieved with OPCPA operating at energies of up to and beyond 1 J [4]. With OPCPA, combined with the high quality spatially and temporally shaped Nd:YAG pump lasers that are now available, amplification of chirped 1μm pulses with bandwidth of over 30 nm to 1 J is easily done. Figure 7.11 illustrates the gain bandwidth that can be typically achieved in a BBO crystal pumped by 532 nm light. The operation of the OPCPA amp at near degeneracy gives a great insensitivity of the OPCPA amplifier bandwidth to crossing angle.

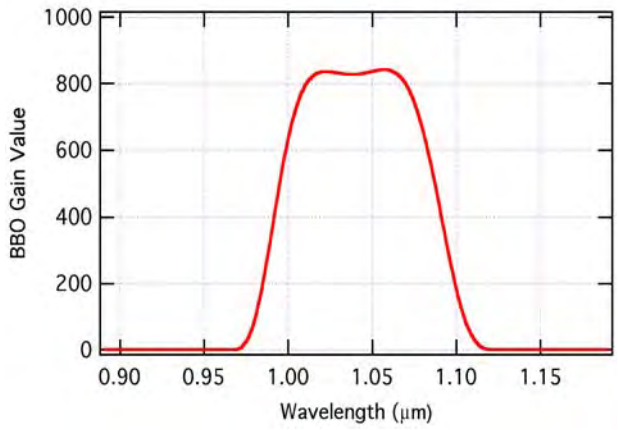

Figure 7.11: Calculated gain in a 1.2 cm long BBO crystal pumped by 350 MW/cm^2 with a 1° crossing angle.

The second major element needed in this approach is to further minimize gain narrowing in the Nd:glass stage of the amplifier chain by employing two kinds of laser glass, Nd:silicate and Nd:phosphate [5, 6]. The advantage of this mixed glass approach can be seen simply by comparing the center wavelengths of these two kinds of glasses, listed along with other relevant properties, a comparison presented in Table 7.2. Since the silicate has a center wavelength shifted by roughly 8 nm to the red side of the phosphate glass, combining their gain profiles in the amplifier chain results in a net gain profile which is broader than either glass alone. This is illustrated in Fig. 7.12 where the gain spectra of two common glasses, one phosphate the other silicate are plotted and summed. In practice, the order of the silicate and phosphate amplifiers is not important. Therefore, this mixing approach has the convenient advantage that the final, large aperture amplifier can be constructed from the more readily available phosphate glass.

With these elements, a hybrid OPCPA/mixed glass CPA laser otherwise takes on a familiar and straightforward architecture. Such a generic mixed glass layout is illustrated in Fig. 7.13. A 100 fs Ti:sapphire oscillator provides the see pulses which can be cleaned and then stretched in a typical diffraction grating stretcher. Because of the higher saturation fluence of Nd:glass it is desirable to stretch these pulses to >200 ps/nm resulting in pulses of 1–3 ns in the glass amplifiers. The majority of the gain ($\sim 10^9$) is performed in the OPCPA stages which can yield a seed bandwidth of >30 nm. Spectrally shaping can also be performed at this stage. This approach also has the proven advantage of the high contrast that is associated with an OPCPA front end [7].

Table 7.2:

Laser Glass Optical Properties

Optical Properties	Nd:Phosphate	Nd:Silicate
Peak-Fluorescence Wavelength (nm)	1053.9	1061
Line Width (nm) FWHM	27.8	28.5
Peak Stimulated Emission Cross-Section (cm^2)	3.4×10^{-20}	2.4×10^{-20}
Calculated Radiative Lifetime (μs)	370	406
Refractive Index at Peak Spectral Emission	1.537	1.558
Nonlinear Refractive Index (esu)	1.13×10^{-13}	1.49×10^{-13}*

*Calculated values fitted from data sheets provided by Lawrence Livermore National Laboratories.

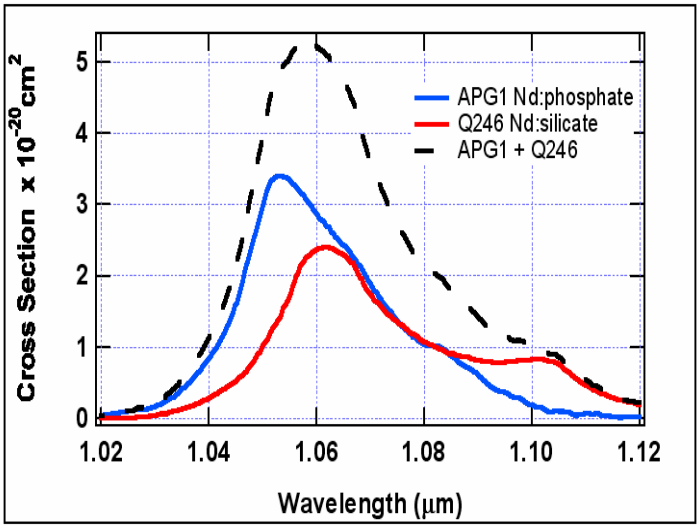

Figure 7.12: Gain spectra for two common glasses, one phosphate and one silicate. The dashed line is the sum of both gain cross section curves.

The pulse then traverses a combination of Nd:silicate glass and Nd:phosphate glass amplifiers which are flashlamp pumped. The gain in these two media are properly balanced to achieve the maximum output bandwidth, which can exceed 14 nm under optimum conditions. Then the

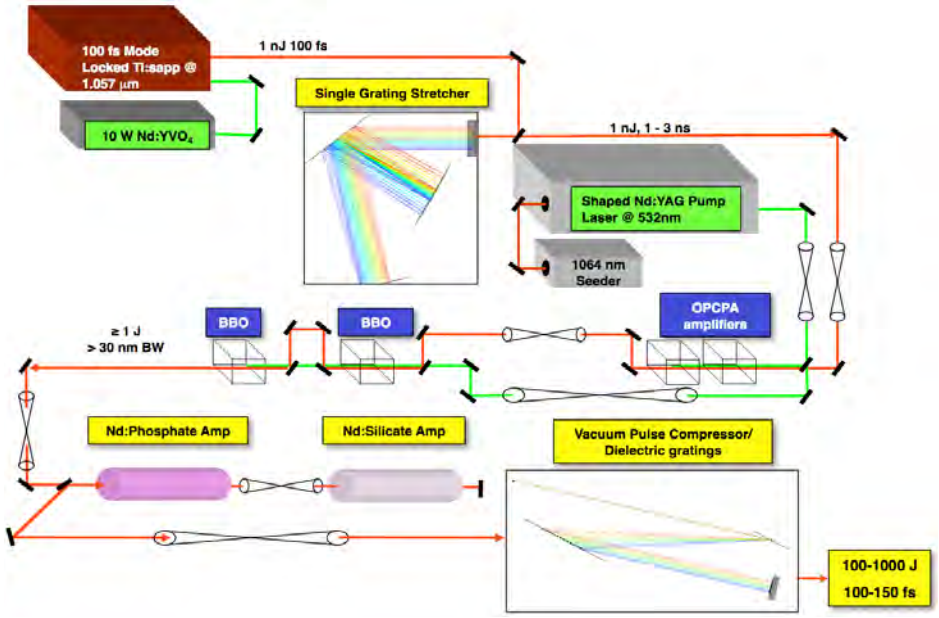

Figure 7.13: Generic design of a hybrid/mixed glass CPA laser.

pulses are then recompressed in a vacuum compressor employing dielectric gratings, which have a high diffraction efficiency and a resulting compressor throughput of nearly 90%.

With this approach, we propose that a straightforward path to 10 PW is to amplify 1μm pulses to 3 J in OPCPA followed by amplification in a series of silicate and phosphate disk amplifiers to 1.9 kJ. Recompression will then yield 1.5 kJ pulses with a duration of $\sim$ 130 fs giving a peak power of over 10 PW. Combining this technique with liquid cooled disk amplifiers a 10 PW laser firing at one shot a minute could be constructed within the next 4 years.

Advantages of the OPCPA/Mixed Laser Glass Concept

Our approach provides many advantages, enabling not only the feasibility of building a 10 PW laser within 4 years, but also ensuring its robust operability on a daily basis, as a scientific tool. It is also the most likely path to EW laser development over the next decade. Below, we list some of the explicit advantages of the approach described here.

1) **Nd:glass amplifiers are a well developed technology to achieve high energy laser pulses.** Nd:glass can be manufactured to very high quality at apertures of up to 40×80 cm (see photo in Fig. 7.14). Furthermore, laser glass has a saturation fluence of >4 J/cm^2 and is therefore an excellent energy storage medium. Using such disks in large aperture amplifiers is extremely well developed technology and is the basis for the large inertial confinement fusion lasers such as the NIF, LMJ, Omega and Gekko XII.

2) **Flashlamp pumped Nd:glass technology is a very robust, simple, and well developed technique.** Using Nd:glass as the final amplifier in a CPA chain eliminates the need for a high energy pump laser since the glass amplifiers are pumped directly by flashlamps. Flashlamps and their associated power conditioning technology is decades old and is exceedingly robust. This makes a 10 PW less expensive and more reliable.

3) **Operation of an OPCPA front end at 1μm permits easy near degenerate pumping at 532 nm.** OPCPA is becoming the widespread technique of choice in all high contrast CPA lasers. Operating an OPCPA front end at a wavelength of 1 μm enables pumping with the

Figure 7.14: Photo of a large aperture Nd:glass amplifier slab (photo courtesy of the Lawrence Livermore National Laboratory).

second harmonic of a Nd:YAG laser which is at the near degenerate point. So, unlike OPCPA at 800 nm, broad band amplification can be achieved without the need for a precise selection of the pump and seed crossing angle. This gives design flexibility and relaxes the difficulties in daily operation of the laser (e.g. maintaining the correct crossing angle to high precision).

4) **Compression of pulses at 1μm permits use of high damage threshold, high diffraction efficiency dielectric gratings.** Compressing pulses at 1 μm has the distinct advantage over other wavelengths like 800 nm because the technology of dielectric multi-layer (MLD) gratings is well developed at the 1 μm wavelength [8]. MLD gratings have excellent diffraction efficiency and somewhat higher damage threshold than gold gratings (around 1 J/cm^2 for $\sim$ 100 fs pulses). These advantages permit a compressor with nearly 90% throughput to be constructed at 1 μm.

5) **All elements of a 10 PW laser using the mixed glass approach have already been demonstrated in separate labs; integration into a laser at 10 PW is all that is presently needed.** In fact every element needed to reach 10 PW has already been demonstrated in one of a few lasers around the world. Integration into a full system is the straightforward next step, making this a low risk approach to achieving 10 PW in a few years. In particular, high energy OPCPA amplification of 1 μm pulses up to 1 J has been demonstrated as has compression of mixed glass amplified pulses down to 110 fs in Austin, Texas. Furthermore, the tiling of 43×47 cm^2 dielectric gratings and the compression of 2 kJ pulses has been demonstrated on the Omega EP laser in Rochester. High contrast OPCPA operation of 1 μm systems has been demonstrated in the UK, the US and Japan.

6) **The mixed glass approach is perhaps the only viable option to scale to a full 1 EW power laser in the foreseeable future.** With the development of new Nd:glasses, it might be possible to achieve higher gain factors in the Nd:glass stage of such a hybrid mixed glass laser along with shorter compressed pulses. This represents a very viable means to the 100 kJ/100 fs level and is likely the best path to a full exawatt laser on the 15 year time scale.

Recent Data on the Mixed Glass Approach at 1 PW

The mixed glass approach is based on solid experimental results at the 20 TW to 1 PW level in recent years. At the University of Texas two hybrid mixed glass lasers have been constructed and considerable data on their performance is now available. The optimum gain ratio between phosphate and silicate amplifiers in a hybrid chain was measured on a 20 TW system composed

of OPCPA up to the 20 mJ level and gain in mixed glass to 2.5 J. The measurement bandwidth from this system as a function of the ratio of total small signal gain in phosphate to total small signal gain in silicate while holding the total combined gain constant is plotted in Fig. 7.15. Typically about 1x to 4x gain in phosphate over gain in silicate is the optimum, yielding nearly 15 nm of bandwidth when a pre-shaped seed spectrum is injected into the chain.

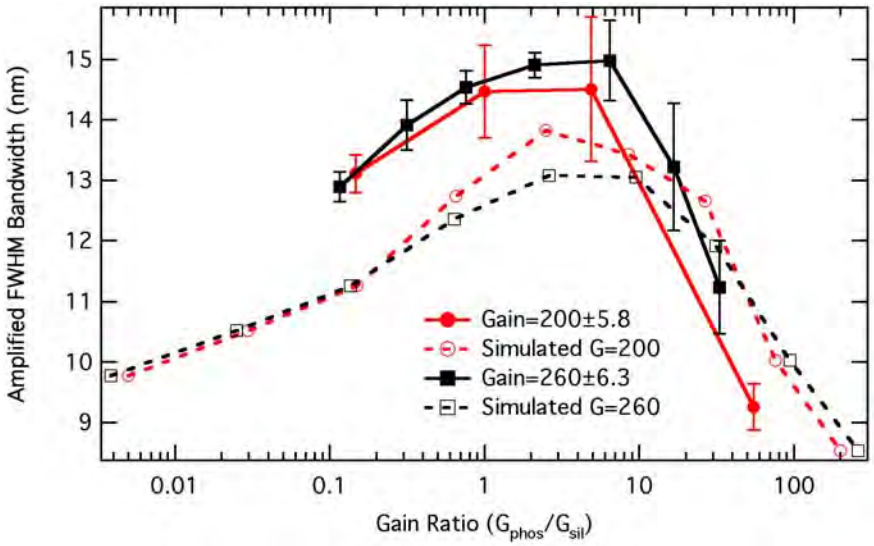

Figure 7.15: Measured and simulated amplified pulse bandwidth as a function of the ratio between gain in the phosphate and silicate glass keeping total gain in the glass constant at $\sim 200\times$.

Figure 7.16a shows the spectra before and after amplification in the mixed glass section, showing the resulting 14.9 nm of bandwidth. Figure 7.16b then illustrates the compressed pulse at 2.5 J which was just under 110 fs FWHM.

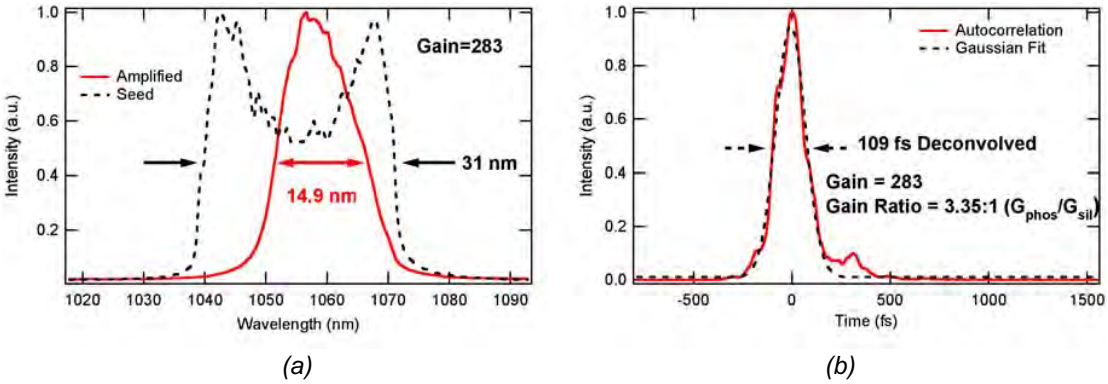

Figure 7.16: Measured spectrum before and after mixed Nd:glass amplification (a) and the resulting compressed pulse duration from a 20 TW, 2.5 J hybrid mixed glass laser.

This hybrid mixed glass technique was scaled to the 1 PW level in the Texas Petawatt laser [9], whose optical layout is illustrated in Fig. 7.17. In this laser 1µm pulses were stretched to over 1 ns and amplified in an OPCPA stage to 0.8 J. These pulses are then passed 8 times through a flashlamp pumped 64 mm Nd:silicate glass rod (see Fig. 7.18a) and then passed 4

Figure 7.17: Layout of the Texas Petawatt laser system.

times through a Nd:phosphate 31 cm disk amplifier (Fig. 7.18b). A two-grating compressor employing 40×80 cm MLD gratings delivers pulses which are compressed to 130 fs with energy up to 185 J.

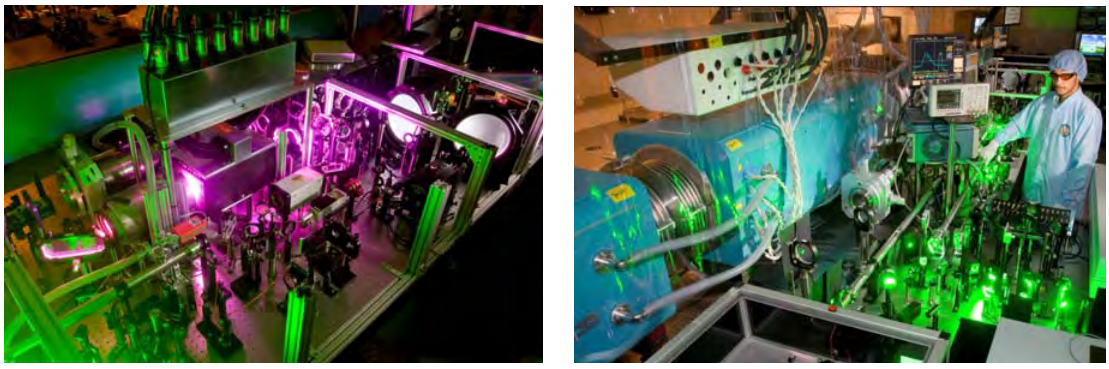

(a) *(b)*

Figure 7.18: Photos of the texas Petawatt Laser including the silicate rod amplifier (a) and the 31 cm Phosphate disk amplifier (b).

Architecture of a 10 PW Mixed Glass Laser

With recent data like those shown here, it is possible to make concrete statements of how a 10 PW laser design would look. The basic architecture of a 10 PW system would have the elements illustrated in Fig. 7.19. This figure also details some of the design considerations that would need to go into a detailed engineering design of such a system.

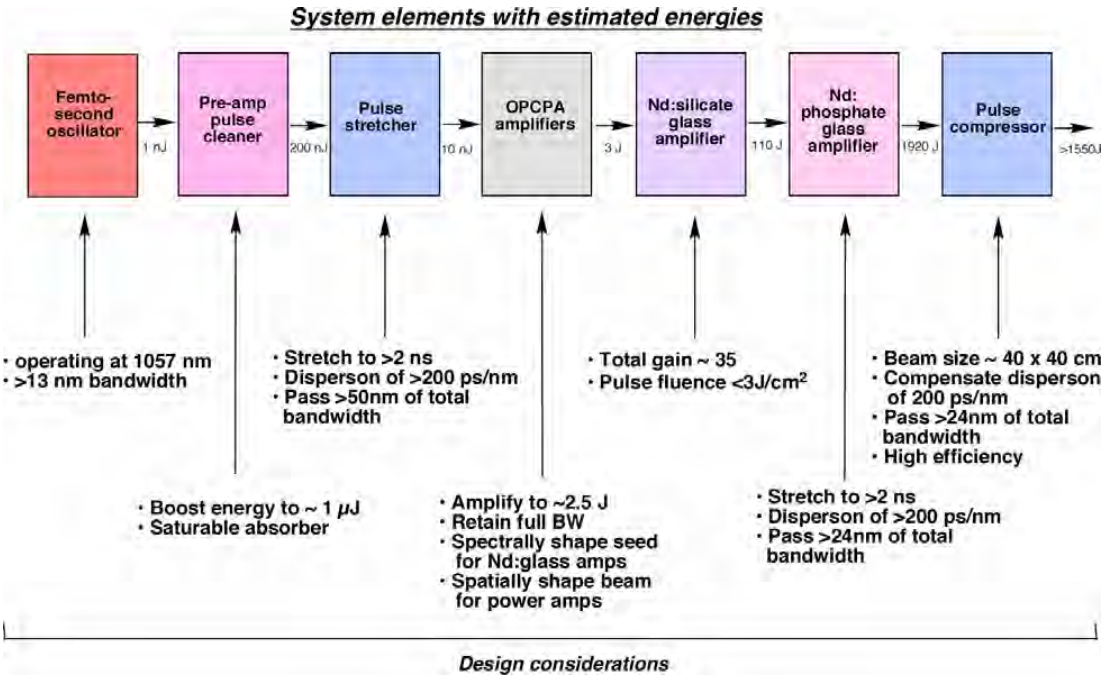

Figure 7.19: Design block diagram of the 10 PW mixed glass laser with design considerations listed for each sub component.

Figure 7.20: Optical schematic of a 10 PW mixed glass laser.

One such potential 10 PW mixed glass architecture is illustrated in Fig. 7.20. The front end is very similar to that employed in the operating Texas Petawatt, though additional pre-pulse cleaning elements would likely be needed for the higher intensities anticipated with the 10 PW laser. A single grating stretcher imparting about 220 ps/nm of chirp on the pulse would be constructed, followed by OPCPA amplification.

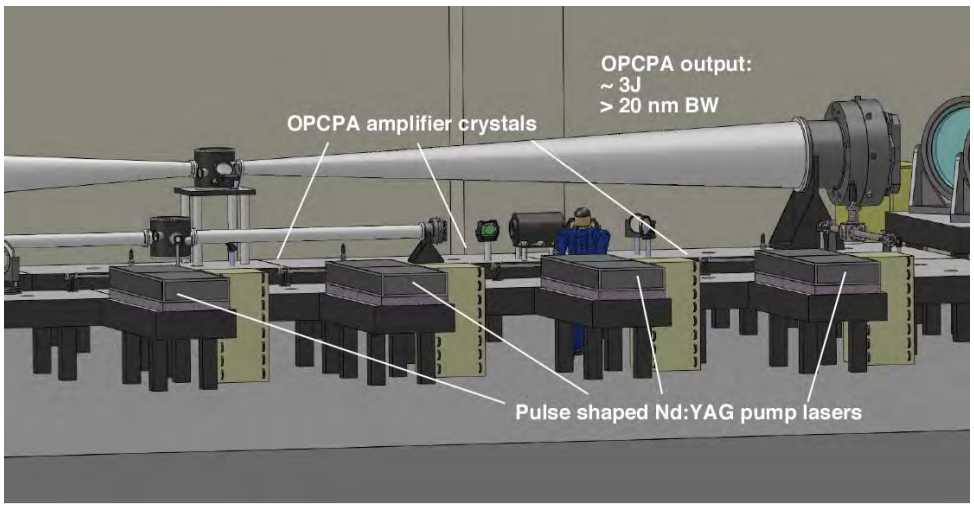

Figure 7.21: The OPCPA section of the 10 PW laser.

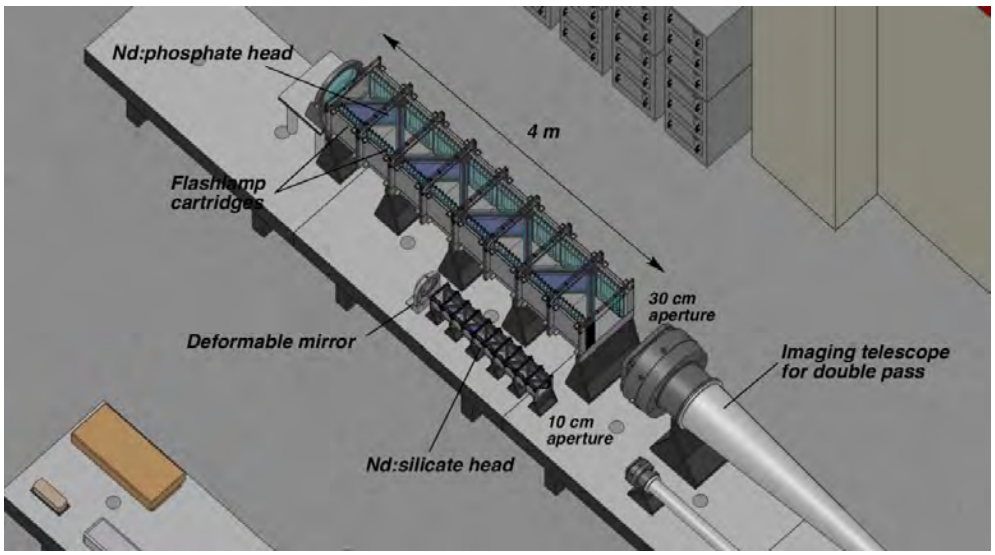

Figure 7.22: The mixed glass section of the 10 PW laser.

The OPCPA amplifiers would utilize in their pump lasers the pulse shaping technology which has been explicitly developed for OPCPA pumping by Continuum Lasers. The OPCPA section will need to boost the energy to ~ 3 J, which can be achieved in 4 stages. The first will employ a sequence of modest sized BBO crystals. The final three stages are power amplifiers and would require larger aperture ($\geq 2 \times 2$ cm) KDP or YCOB crystals [10], each pumped by its own 5 J

Figure 7.23: Split disk concept for cooling the glass slab amplifiers in the 10 PW laser chain.

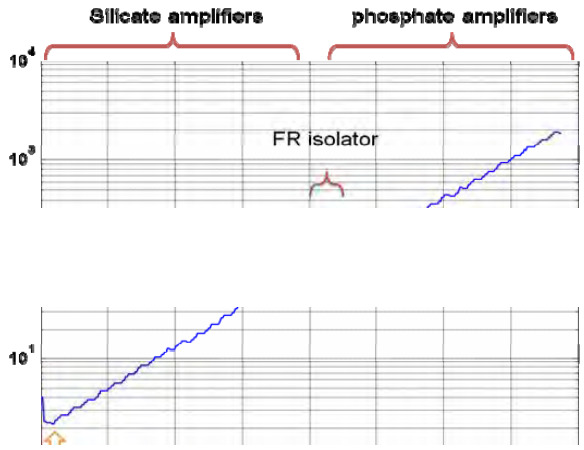

Figure 7.24: Energetics modeling of the glass amplifier chain. Element number refers to each of the optics transmitted including each of the individual Nd:glass slabs.

pulse shaped Nd:YAG laser operating at $\sim 2\,\mathrm{Hz}$. Spectral shaping will likely be necessary here as well to precompensate for the gain narrowing in the subsequent Nd:glass amplifiers. The layout of such an OPCPA stage is presented in Fig. 7.21.

The 3 J pulses from the OPCPA stage would be relay imaged into first, a double-passed disk amplifier utilizing Nd:silicate slabs and then a double-passed Nd:phosphate amplifier. The first amplifier would operate with a clear aperture of roughly 10 cm, which is well matched to the current technology for pouring silicate laser glass. The final amplifier would require a clear aperture of about 30×30 cm. This size is comparable to the Nd:phosphate slab amplifiers employed in the Texas Petawatt and Omega EP systems. A sense of the layout of the Nd:glass section is illustrated in Fig. 7.22.

Liquid cooling of the Nd:glass slabs is a distinct possibility which means that they could be rep-rated perhaps as high as one shot per minute. The glass slabs would be pumped with standard flashlamp technology by a collection of flashlamp cartridges (illustrated in Fig. 7.22). One concept for increasing the repetition rate of the large amplifiers would involve liquid cooling

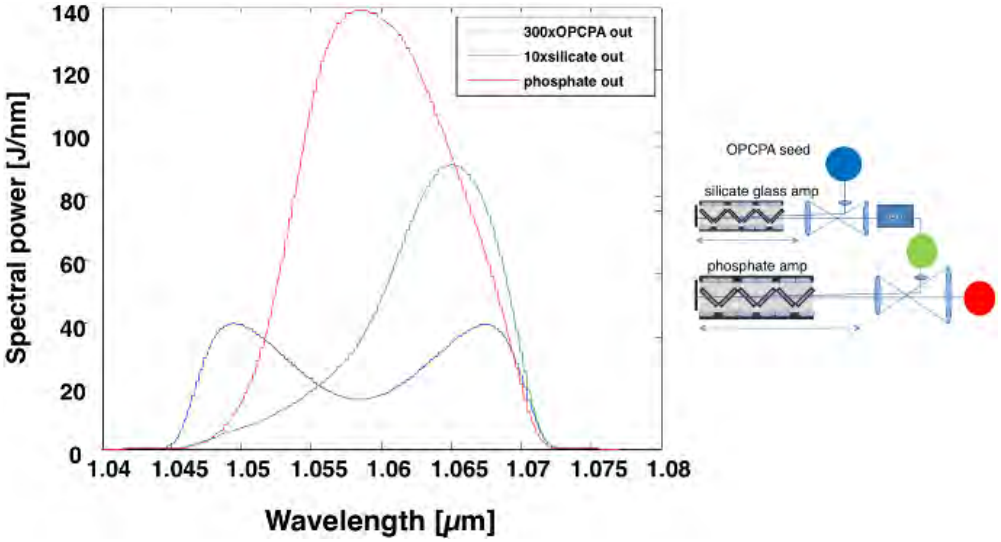

Figure 7.25: Calculated spectrum into the Nd:glass chain, after the silicate stage and after the phosphate stage.

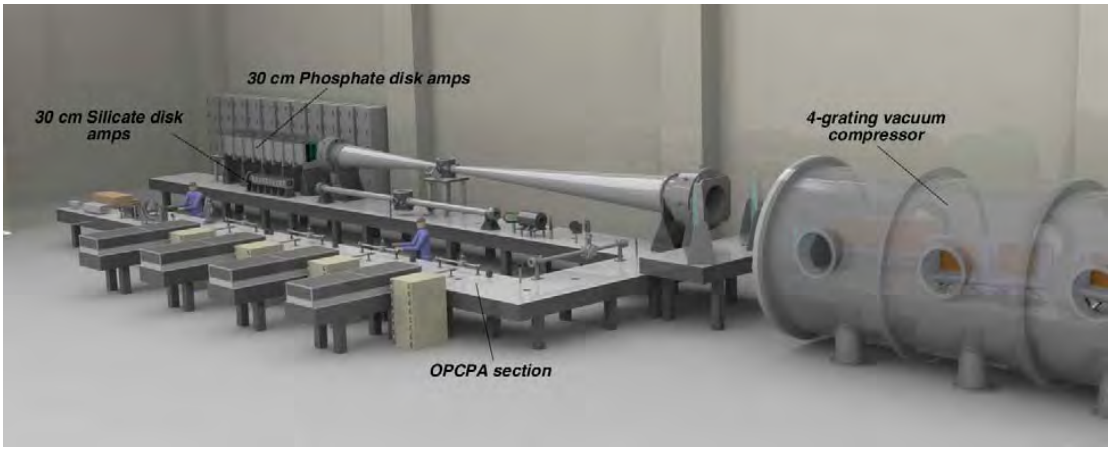

Figure 7.26: The entire 10 PW mixed glass laser.

the faces of the slabs in a configuration like that illustrated in Fig. 7.23. This kind of geometry would permit cooling gradients of as small as 1 cm in the glass while maintaining large beam apertures. With near term development of such liquid cooled slab amplifiers,

Energetics modeling of such a glass amplifier chain is shown in Fig. 7.24. The silicate stage would raise the pulse energy to $\sim$ 100 J and the phosphate stage will further amplify to roughly 1900 J for a total gain in glass of about 700×.

The shape of the seed pulse spectrum at each stage of the amplifier chain as calculated using standard saturated gain models is shown in Fig. 7.25. The initial spectrum will need some shaping coming from the OPCPA stage. However, the gain in the two laser glass stages reduce the bandwidth to between 13 and 14 nm FWHM. These pulses can then be compressed to $\leq$ 130 fs in a vacuum compressor. One potential configuration would be to employ a 4 grating design, with each grating composed of two optics phased with mechanical controls. The final beam size in the compressor would need to be about 40×40 cm, which would allow the

use of two 50 × 90 cm gratings placed end to end in each of the 4 grating hit locations. The final compressed energy could be in excess of 1.5 kJ which implies a final compressed power of 10–12 PW.

Such a 10 PW laser would be surprisingly compact. A potential layout is illustrated in Fig. 7.26. The total footprint of such a laser, including the pulsed power supplies, could be 15 × 40 m.

Toward an Exawatt laser with the Mixed Glass Approach

One of the attractions of pursuing the mixed glass approach in the context of ELI is that this technique could be scaled to the exawatt level in the near future [11]. This possibility exists by combining the mixed glass technique with new kinds of laser glass, that exhibit different peak wavelengths and bandwidths. Table 7.3 lists the properties of two glasses which were investigated 30 years ago by Lawrence Livermore and its industry partners. Both glasses have bandwidth which exceeds silicate glass and center wavelengths further to the red than silicate. This is illustrated in the spectra plotted in Fig. 7.27.

Using a combination of such glasses would permit amplification in glass by greater gain factors, perhaps as much as $10^6\times$, so that much higher laser pulse energies could be achieved without the need for exceedingly large OPCPA amplifiers. As illustrated in ref. [11], using existing technology, such as NIF-size phosphate amplifiers and phasing an array of gratings, it is possible with laser glasses such as those shown in Table 7.3 to amplify pulses up to 15 kJ in a single beamline and recompress them to under 100 fs.

The availability of such glasses is dependent on the development of them by glass manufacturers. Schott North America presently has a program to develop such glasses including new laser glasses with properties that are more conducive to manufacturing.

Table 7.3:

Broad Spectrum Laser Glass Optical Properties

Optical Properties	K-824 Silicate	L-65 Aluminate
Peak-Fluorescence Wavelength (nm)	1064.5	1067
Line Width (nm) FWHM	38.2	41.23
Peak Stimulated Emission Cross-Section (cm^2)	2.4×10^{-20}	1.8×10^{-20}
Saturation Fluence (J/cm^2) at peak emission wavelength	7.0	10.0
Nonlinear Refractive Index (esu)	3.44×10^{-13}*	2.92×10^{-13}*

*Measured and calculated values listed from data sheets provided by Lawrence Livermore National Laboratories.

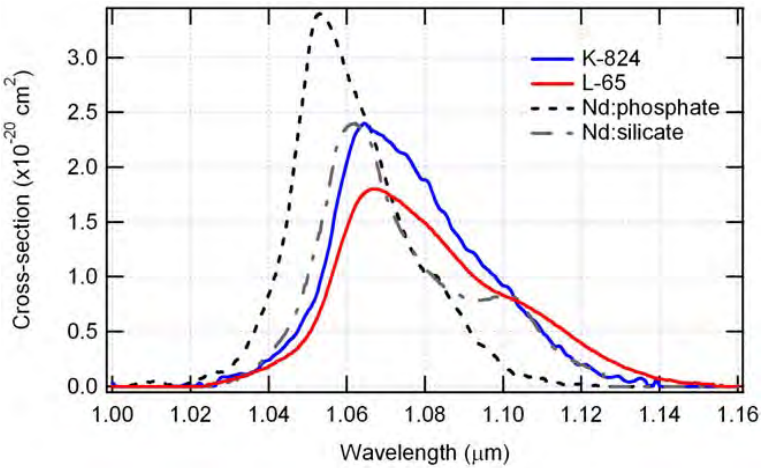

Figure 7.27: Gain cross section spectra for two promising alternative glasses suitable for Exawatt pulse production.

Conclusion and Summary of Next Steps

In summary, the hybrid mixed glass approach represents a straightforward way to reach 10 PW in a 4 year time scale. With modest R&D over the next year, all the components for constructing a laser delivering 1.5 kJ in 130 fs will exist. This approach has a number of advantages over alternate schemes to reach 10 PW, including low risk and low cost. With the development of liquid cooled amplifier slab lasers, even good repetition rate from such a laser will be possible.

With this goal in mind, it seems that the fastest path forward on such a laser is to pursue three near term research and develop goals (on the one year time scale) in parallel with a longer term R&D program to work toward an exawatt laser.

Next R&D Steps:
1. Work on the development of liquid cooled slab amplifiers at the 10 cm and 30 cm size
2. Work on developing a 3 J OPCPA front end with pulse shaping and pre-pulse control
3. Develop an engineering design for the 4-grating compressor
4. Push development of new glasses with displaced peak wavelengths

Bibliography

[1] M.D. Perry, D. Pennington, B.C. Stuart, G. Tietbohl, J.A. Britten, et al., Opt. Lett. **24**, 160 (1999).
[2] C. N. Danson et al., Laser Part. Beams **23**, 87 (2005).
[3] Y. Kitagawa, H. Fujita, et al., IEEE Journal of Quantum Electronics **40**, 281, (2004).
[4] I. N. Ross et al., Opt. Commun. **144**, 125 (1997).
[5] Ian N. Ross, Mark Trentelman, and Colin N. Danson, App. Opt. **36**, 9348 (1997).
[6] Blanchot et al., Opt. Lett. **20**, 395 (1995).
[7] H. Kiriyama et al., Opt. Lett. **35**, 1497 (2010).
[8] H. T. Nguyen, J.A. Britten, et al., Proc. of SPIE Vol. **5991**, 59911M (2005).
[9] E. W. Gaul et al., Appl. Opt. **49**, 1676 (2010).
[10] Zhi M. Liao, Igor Jovanovic, Chris A. Ebbers,Yiting Fei and Bruce Chai, Opt Lett. **31**, 1380, (2006).
[11] G Hays, E Gaul, M Martinez, T Ditmire, Appl. Opt. **46**, 4813 (2007).

7.3 European Programmes

7.3.1 The European X-ray Free-Electron Laser Facility in Hamburg

In the world, a number of projects are under way to generate extremely brilliant (peak brilliance $\sim 10^{33}$ photons/s/mm^2/mrad^2/0.1%BW) and ultra-short ($\sim$ 10–100 fs) pulses of transversely coherent X-rays with very short wavelengths (down to ~ 0.05 nm). The goal is to exploit these X-rays for revolutionary scientific experiments in a variety of disciplines, including physics, chemistry, materials science, and biology.

In the US and Japan, free-electron lasers (FELs) are being developed that are based on room-temperature linear accelerators (linacs). The US project, the Linac Coherent Light Source (LCLS) at Stanford University, which is based on the SLAC Linac, started operation in 2009. The Japanese project, SPring-8 Compact SASE Source (SCSS), is expected to produce its first light in 2011.

In Europe, the superconducting linear accelerator technology that was developed at the Deutsches Elektronen-Synchrotron (DESY) as part of the TESLA project, was successfully applied to produce laser-like radiation down to the 4.5 nm range at the DESY Free-Electron Laser in Hamburg (FLASH) facility. It is now being adopted at the European X-ray Free Electron Laser (XFEL) facility currently under construction.

The most important advantage of the superconducting technology is the very large number of pulses per second, in the case of the European XFEL, up to 27,000 pulses per second. It is foreseen that electron bunches will be accelerated to high energies (14 to 17.5 GeV) in a $\sim$ 2 km linac and then passed through (up to 200 m long) undulators, where they will generate bursts of coherent X-rays through the self-amplified spontaneous emission (SASE) process. Commissioning, with the first beam of the facility, is expected to start in 2014. Initially, 3 beamlines and 6 instruments will be built. Eventually, 5 photon beamlines and 10 experimental stations will enable experiments that exploit the high intensity, coherence, and time structure of the new source.

Some expected scientific benefits:

- Studying molecular configuration rearrangements during chemical reactions down to the sub-ps scale
- Observing the dynamics of fluctuations on unprecedented time and length scales
- Providing experimental access to regions of the phase diagram of materials currently found only in astrophysical environments or under conditions unfavorable for accurate experiments

A fascinating benefit is the chance to investigate the structure of macromolecules down to atomic resolution, without the need for crystallization. The feasibility depends on whether single ultra-short and ultra-intense pulses can obtain diffraction patterns of sufficient quality in a time that is shorter than that in which distortion of the molecular structure occurs because of ionization and subsequent damage processes. Results using 25-fs soft X-ray pulses at the FLASH facility demonstrate the feasibility of imaging single particles with less than a few times 10 nm resolution.

The new facility is organized as a limited liability company (European XFEL GmbH) under German law, according to the terms established by an intergovernmental Convention that has to date been signed by 11 countries (Denmark, France, Germany, Greece, Hungary, Italy, Poland, Russia, Slovakia, Sweden, and Switzerland). Construction costs (investment, personnel, and commissioning) are in the range of 1.1 billion euros. Operation costs per year are estimated at 80 million euros (at 2005 price levels). Civil construction started in early 2009. The actual boring of the tunnels started in July 2010.

Possible upgrades – which are not included in the baseline design, but may be implemented in the short to medium term, after the start of operations – include seeding schemes for improving the longitudinal coherence (monochromaticity) of the hard X-ray beams. The baseline design

of the European XFEL foresees the generation of coherent X-rays by the SASE process, which provides little longitudinal coherence and limited pulse-to-pulse reproducibility.

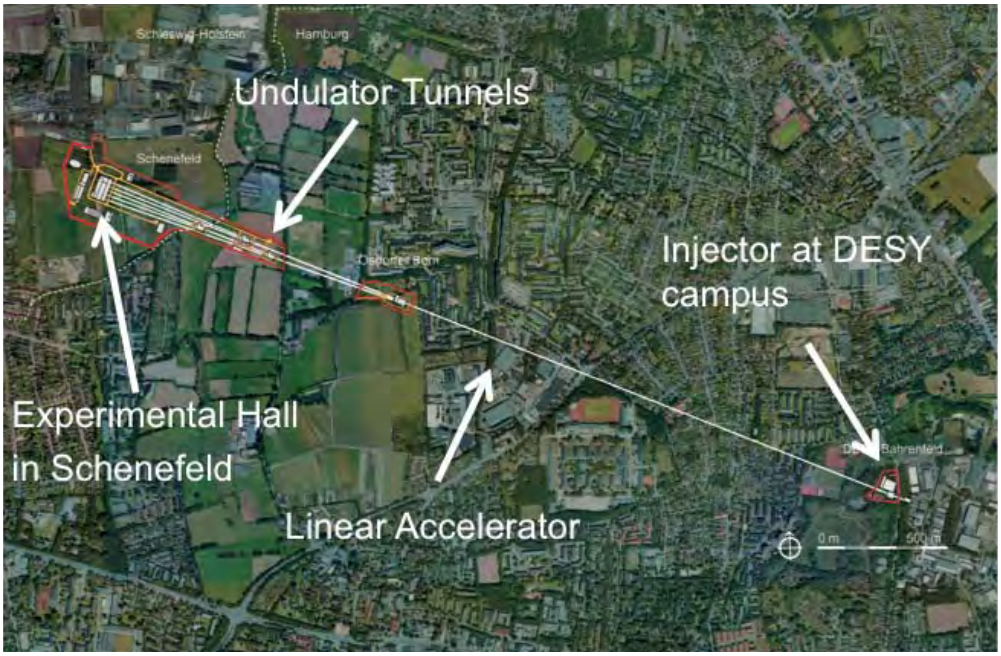

Figure 7.28: Layout of the European XFEL facility superposed on the map of part of the city of Hamburg and the neighboring federal State of Schleswig-Holstein.

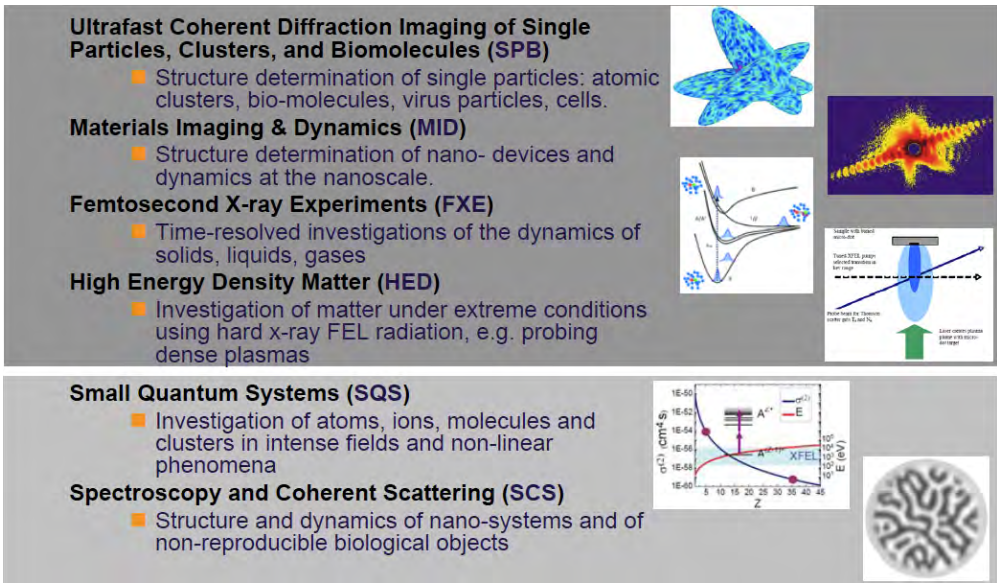

Figure 7.29: Schematic description of the six priority experimental stations (two for each of the three SASE undulators). Top: the four hard x-ray instruments; bottom: the two soft X-ray instruments.

7.3.2 ELI-Beamlines Synergy with the HiPER Project

The HiPER project seeks to develop laser driven fusion for energy production on the 2030 timescale. Currently in its Preparatory Phase, the project has received funding for technical work from UK and Czech Republic Governments, funding for management and co-ordination activities from E.C., and "in-kind" contribution from other nations. The Preparatory Phase Project, due to end in April 2011, is being extended to April 2013, to enable participating nations to seek national funding for the next phase, and to maintain the profile of the project up to, and beyond, the time during which ignition is anticipated at the National Ignition Facility (NIF) at Lawrence Livermore Laboratory, California.

The prospect of ignition and burn with net energy gain within the next 18 to 24 months, represents an important opportunity for Europe to raise the profile of inertial fusion energy and to build a compelling business case for national support of the Technology Development Phase of the HiPER project.

During the Preparatory Phase, the Executive Board of HiPER made a down-selection decision for the laser driver to diode pumped, solid state laser (DPSSL) technology. DPSSLs offer the essential, twin benefits high overall efficiency ($\sim 10\%$) and high repetition rate (10–20 Hz). A significant activity during the Technology Development Phase will be the construction of a series of DPSSL prototypes and demonstrators, starting from an initial 10J unit and then scaling the technology progressively to 100 J, 1 kJ and thence to 10 kJ, the basic HiPER "beamline unit".

The decision to base the laser technology of the ELI-Beamlines on DPSSLs represents a singular opportunity for synergistic development between the two projects. The energy requirement for the ELI-beamlines facility is at the 500 J level, at a repetition rate of 10Hz, entirely consistent with the development track of the HiPER laser driver. Thus the ELI-beamlines laser development project will effectively de-risk the first and intermediate level of laser development for HiPER, leaving just the final scale-up to the 10 kJ level.

There are important additional benefits to HiPER which accrue from the ELI-Beamlines project. ELI-Beamlines, and the associated smaller prototypes, will act as an invaluable test-bed for assessing the performance of DPSSL technology operated for extended periods at high repetition rate. Ultimately, the realisation of laser energy requires the laser driver to operate without significant intervention or unplanned maintenance for 10^9 to 10^{10} pulses. The ability to gain operational experience of DPSSL systems over an extended period will inform design decisions for the 10 kJ HiPER beamline prototype. Behaviour of the system, understanding of the operational envelope, the maintenance regime, failure modes, diode lifetime and susceptibility to damage will enable any further development to be identified and targeted in the most critical areas.

Furthermore, the requirements for laser control and safety systems architecture will be very similar between the two projects and early development for ELI-beamlines will result in significant cost savings for HiPER. The requirements for environmental control, beamline enclosures and performance monitoring are further areas of synergy and an opportunity to avoid duplication. Engagement with the supply chain will be an important aspect of the next phase of HiPER, and much can be done jointly between the two projects.

The timing of the start of the ELI-Beamlines project is extremely fortuitous. It is anticipated that the Technology Development Phase of HiPER will run from the present until the later part of this decade, entirely consistent with the 2015 completion date of ELI-Beamlines.

In conclusion, the investment in advanced DPSSL laser technology represented by ELI-Beamlines will bring substantial benefit to the HiPER project. It will also bring opportunities to European industry which will be incentivised to gear up for high volume production of DPSSL laser systems. This will put Europe in a strong position to benefit from laser energy projects world-wide and to exploit DPSSL technology in other market sectors.

8 Safety

8.1 Laser and other hazards

8.1.1 Laser safety

In order to establish the laser-related hazards to be faced in any ELI facility, the safety code [1] of the Rutherford Appleton Laboratory will be used as reference.

Lasers emit beams of non-ionising radiation at wavelengths spanning the ultraviolet to the far infrared. The skin and eyes are at risk of injury; thermal burns from visible or infrared laser beams or photochemical burns from ultraviolet laser beams. For lasers in the visible or near infrared part of the spectrum there is a particular risk of damage to the retina of the eye, resulting in permanent visual impairment. The power of laser beams, particularly pulsed lasers, can be so high that not only the main beam but also weak reflections and diffusely scattered radiation can be hazardous.

Lasers are flexible research tools, which enjoy wide use across all disciplines. For lasers whose output presents a significant risk of harm, this flexibility and breadth of use combined with continuing evolution (*e.g.* higher output from physically smaller devices) creates unique challenges to the control of the laser hazard, in many cases preventing a rigid prescriptive approach to laser safety and relying instead on detailed risk assessment, a mix of engineering and administrative control, and laser safety eyewear to address residual risks.

There are no health and safety regulations specific to the safe use of lasers, but there is an international user guide "Safety of laser products: Part 14 – A user's guide, TR 60825-14" [2], which sets out current best practices. TR 60825-14 as well as other safety codes such as Ref. [3], which translates its general guidance into specific requirements and defines the responsibilities of those persons appointed to carry out specific laser safety duties, can be adopted as the basis for the laser safety procedures in the ELI facilities. It is important to point that the ELI lasers are within the categories analyzed in those reports (High Risk, Low Risk, and Embedded Laser Products) and do not represent a special or different case from the laser safety point of view.

These documents deal principally with the beam hazards of using lasers and refer to but do not deal with associated (non-beam) hazards of laser use (Sect. 8.1.2). For completeness, we can now briefly describe these beam hazards.

Injury mechanisms

There are three principal types of tissue-damage mechanisms for laser radiation: thermal, photochemical and thermo-mechanical. The predominant injury mechanism is determined principally by the laser wavelength, the duration and the irradiance of tissue exposure.

Ocular injuries

The biological effects on the eyes for different wavelengths are:

	Wavelength range	Primary tissue at risk of damage
Ultraviolet	180 nm–400 nm	Cornea or lens (302–315 nm)
Visible near infra-red	400 nm–1.4 μm	Retina
Medium & far infra-red	1.4 μm–1 mm	Cornea or lens (1.4–3.0 μm)

Retinal eye damage from laser radiation can occur at very low power levels due to the focusing effect of the cornea and lens of the eye and the coherence of laser radiation.

In a research laboratory there may be lasers operating at different wavelengths, fixed and variable, from the UV to the visible and IR. What may seem to be a steady beam may be a pulsed laser operating at a high pulse repetition rate with peak powers in the individual pulses

that are more than a million times the average power of the beam. Apparently weak blue or red beams may be operating at wavelengths at the extreme of the visual response range of the eye where its sensitivity is several thousand times below its peak sensitivity (yellow light). UV and IR beams cannot be seen at all.

The Maximum Permissible Exposure (MPE) represents a safe level of exposure to laser radiation; it varies with the wavelength range and the duration of the exposure. For example, for a 30000 s exposure (a working day of approximately 8 hours) the MPE for intrabeam viewing of laser radiation is 10 Wm^{-2} in the range 315–400 nm where the UV light is absorbed by the lens of the eye. In the visible region where the lens of the eye brings the radiation to a focus on the retina, the MPE is much lower, *e.g.* 0.01 Wm^{-2} in the range 400–550 nm; this arises because the eye can focus such a radiation to a spot with a diameter so small as 20 μm on the retina, corresponding to an increase in power density of 10^5–10^6.

Damage to the eye can arise from different mechanisms depending on the duration of the exposure to the light. In particular, for very short exposures ($<10^{-6}$ s), damage arises from thermo-acoustic transients. Simple heating effects predominate in the range 100 ms–10 s and for exposures longer than 100 s photochemical effects can predominate for wavelengths less than 600 nm. These different processes make the determination of safe radiation levels for pulsed lasers a complicated task that requires a detailed study of the MPE tables.

Injuries to the skin

The biological effects of skin exposure to laser radiation are simpler to assess than those for the eye. The injury is surface burning, which may occur following an acute exposure to cw laser beams. This can occur in a fraction of a second for a beam of 0.5 W or more; or over a prolonged period for photochemical burns from ultraviolet-laser beams. Unlike retinal eye burns, skin burns may easily be treated. They are sterile and generally heal quickly.

In the visible and near infrared wavelength range, the MPE for >10 s skin exposure is 1000 Wm^{-2}, similar to the solar constant of 1400 Wm^{-2}. In the UV the MPE for skin exposure is identical to that for eye exposure.

Skin damaged by laser is similar to thermal burns for visible or infra-red laser radiation or photochemical burns for UV exposure namely, reddening, blistering and charring.

Bibliography

[1] STFC Safety Code Nº 1, Rev 3 (2008).
[2] IEC Technical Report 60825 (2008).
[3] Science & Technology Facilities Council STFC Safety code Nº 1 (2008).

8.1.2 Non-laser-related hazards

There could be a variety of potential risks not related to the laser or radioactive emission during the operation of ELI facilities. The potential risks could be brought into the following groups: chemical hazards (dermal contact, inhalation, ingestion, spills, explosives, etc.), biological hazards, electricity-related risks, confined spaces risks, burns (cryogenic and fire-related) and accidents of different origin (machine-shop, elevator, vacuum and high-pressure equipment related, hot or very cold surfaces, etc.).

Chemical hazards

The chemical hazards depend on the used materials. At the moment, it is difficult to identify which specific chemicals/materials will be used at ELI facilities (solvents, liquid nitrogen, helium, acids, etc.). Exposure to certain chemicals can cause illness or other health problems. This includes chemicals that are toxic, corrosive (*e.g.* acids), cause harm to skin, internal organs or nervous system or cause allergic reactions after a repeated exposure via dermal contact, inhalation or ingestion.

All chemicals coming from manufacturers must be labelled properly. The labels on all chemical containers in a workplace should carry the following information: 1) the name of the chemical or a list of chemical ingredients if the product contains more than one chemical; 2) a warning of the hazards associated with the product in written and/or symbolic forms; 3) contact information of the manufacturer or importer.

Additionally, chemical manufacturers should provide Material Safety Data Sheets (MSDS), which contain information concerning the safe use of a product. The MSDSs should be kept in the workplace for each chemical used.

Depending on the provider, MSDSs usually contain the following information:

- name of the chemical product, including the chemical formula;
- physical and chemical properties;
- fire and explosion data;
- health hazard data and necessary procedures in the case of emergency;
- safe handling procedures and recommended protective equipment;
- information on proper disposal.

People who will work with certain chemicals are supposed to be familiar with MSDSs and dealing with potential hazards. If not, they should be trained to work safely with those chemicals. Depending on the country that will host an ELI facility, there could also be a requirement to have a special document defining general procedures of safe work, training, waste utilization, etc. Depending on the types and quantities of chemicals that will be used in the ELI facility, there should be appropriate personal protective equipment, such as gloves (available in a variety of materials), chemical splash goggles along with face shields, splash aprons and respirators. In most cases, unexpected contact with chemicals results in skin/eye irritation or burns and can be assisted by first-aid. Therefore, first-aid kits, safety glasses and water supply should be installed in places where usage of chemicals is anticipated. While it is true that certain chemicals in the workplace may be hazardous, it is possible to minimize the potential risks following these recommendations:

- substitution of toxic materials with less toxic ones whenever possible;
- installation and use of appropriate engineering controls such as ventilation;
- maintaining the workplace clean and orderly;
- use of necessary safety equipment;
- labelling containers with the identity of their contents and appropriate hazard warnings;
- storing incompatible chemicals in separate areas;
- limiting the volume of volatile or flammable material to the minimum needed.

If there is a threat of asphyxiation due to frequent usage, for instance, of liquid nitrogen in a closed room, a ventilation system with gas detectors and valves could be considered and emergency wired telephone (or a button/switch) could also be installed in some critical places.

There may be risks of accidental spills of chemicals. The laboratory personnel working with chemicals should be prepared to contain and clean-up a “minor” spill since they are expected to be familiar with this and similar hazards of the chemicals that they normally handle. A spill can be regarded as “minor” if it does not pose a significant safety or health hazard to employees in the immediate vicinity and it does not have the potential to become an emergency within a short time frame. It is not expected that large amounts of chemicals will be used in the ELI facility,

thus there should not happen "major" spills. If there has been a release to the environment, an appropriate national agency must be contacted immediately. However, improper clean-up of even a "minor" chemical spill may result in injury, illness, fire or property damage. In case of a chemical spill, the floor drains or other means for environmental release should be protected by special materials depending on the type of chemical (*e.g.* different materials have to be used for mercury).

The assessment for the need of spill control materials should be done and appropriate types and quantities of spill control materials shall be provided. They should be placed in easily accessible locations close to the areas where the use of chemicals is anticipated along with necessary personal protective equipment, such as gloves, safety goggles, face protection or respirators.

Biological hazards

Biological hazards can occur from the improper use of certain biological agents in laboratories. Although it is not known for the moment what kind of biological agents will be used in ELI laboratories, some biological experiments will most likely be performed and therefore some precautions have to be taken to avoid unnecessary accidents. Infectious biological agents are classified into four risk groups [1]:

Group 1: agents that unlikely cause human diseases (*asporogenic Bacillus subtilis or Bacillus licheniformis*, etc.).
Group 2: agents that can cause human diseases and might be a hazard to workers. They unlikely spread to the community and there is usually effective prophylaxis or treatment available (*hepatitis A, B, C, D, and E viruses*, etc.).
Group 3: agents that can cause severe human diseases and present serious hazards to workers. They may present a risk of spreading to the community, but there is usually effective prophylaxis or treatment available (*Rabies virus, Yellow fever virus,* etc.).
Group 4: agents that cause severe human diseases and are serious hazards to workers. They may present a high risk of spreading to the community; there is usually no effective prophylaxis or treatment available (*Ebola virus,* etc.).

It is unlikely that biological agents from groups 3 and 4 may be used at ELI for experiments. There are several global organizations committed to improve the knowledge and understanding of biological safety issues, seeking to influence and support emerging legislation and standards in the areas of biological safety, biosecurity, biotechnology, transport and associated activities. Those organizations are the World Health Organization (WHO), European Biosafety Association (EBSA), European Committee for Standardization (CEN) and some others. The WHO has released a "Laboratory Biosecurity Guidance" [2], which contains useful information on biorisk management in laboratories. The CEN, which seeks to provide a platform for the development of European Standards, has developed a "Laboratory Biorisk Management Standard" through a CEN Workshop Agreement. The objective of this CEN Workshop was to develop and promote the adoption of recognized standards for the management of biological risks. It is appreciated that, although this is a wide field, commonly shared biorisk principles and practices apply. The proposed standard is not intended to replace any national or subnational regulatory requirements that may apply to the laboratory/facility [3].

These documents provide enough information on safe handling of biological agents in laboratory environment including disposal, procedures in case of spillage, animal handling (if relevant), storage techniques, transport, clothing and Personal Protective Equipment (PPE), training, authorized access, visitors, and emergency plans. The management body of an ELI site shall ensure suitable methodologies for the allocation of actions resulting from risk assessments, including time lines, responsible persons and associated reporting mechanisms are identified, implemented and maintained. As for the equipment needed for containment of biological agents, assuming

that only agents from groups 1 and 2 could potentially be used on site, an installation of autoclave and wash hand basin on site should appear as sufficient safety measures.

Electricity-related risks

It is known that even relatively low (220 V) electricity can potentially cause burns, severe injuries or death and there will be some equipment on the ELI facility that will require even higher voltages. Normally this equipment will be maintained by qualified personnel who are aware of the potential risks, know how to completely turn-on/off and plug/unplug certain devices and are trained to utilize electrically-rated tools and protective equipment. The installation or reparation of power lines and connectors should be performed by qualified electrical workers only who are familiar with safe work practice when dealing with electricity.

Should there be devices that require high-voltage electricity but are supposed to be maintained by some of the local staff, appropriate assisting measures have to be available on site as well. Electrically-rated protective equipment (gloves, face-shields, safety glasses, electrically rated steel-toed boots, head-protection, etc.) and needed tools should be labelled with the amount of voltage for which they are approved and stored in special places along with insulating materials, such as non-conductive matting and insulated blankets. Safety signs and tags must also be used to warn employees of possible electrical hazards.

Risks of confined spaces

Depending on the design of the ELI facility and the equipment used, there may be some risks associated with confined spaces. Briefly, an area can be defined as a confined space if it meets the following three criteria:
1) limited openings for entry and exit;
2) the space is not intended for continuous human occupancy;
3) the space is large enough for human beings to enter and conduct work.

The person aiming to perform certain work in a confined space may encounter either atmospheric of physical hazards. Atmospheric hazards usually associated with confined spaces are:

1) oxygen deficiency;
2) oxygen displacement;
3) flammable atmospheres;
4) toxic gases.

Physical hazards can be detected through human senses (touch, sight). Hot, very cold or wet surfaces may also possess serious risks.

Before entering a confined space that may possess an atmospheric hazard, a multi-gas meter should be used to determine levels of oxygen, carbon monoxide, hydrogen sulfide, and the concentration of combustible gas. If needed, other types of meters and sensors could be used to detect concentration of specific gases (chlorine, sulphur dioxide, etc.). A blower motor could be used to ventilate the space before entering it and additional equipment (communication, lightning, etc.) helping to conduct safe work may be necessary. If the above mentioned assistance measures will not be available and a confined space will be recognized as possessing a safety hazard, the professionals should be called in to perform needed tasks.

Prevention from accidents should include standardized procedures for authorized access to machine-shop, vacuum, cryogenic, high-pressure equipment, etc. If periodical servicing/maintenance jobs are anticipated (*e.g.* opening the chamber lid), appropriate procedures should be developed to minimize probability of an accident.

First-aid kits and fire-extinguishers have to be distributed accordingly to the local safety regulations (country-wise) and should help if any kind of accidents or burns would happen. In

case of serious emergency situations, professional medical help will be needed and if it could not be available in a reasonably short time from outside the ELI site, it would be useful to have a medical emergency room inside the ELI with permanent assistance dealing with intoxication, burns, injuries and some kinds of sickness (of permanent staff and visitors). It could also deal with possible biological issues by performing testing and/or vaccination if applicable.

Bibliography

[1] Directive 2000/54EC of 18 September 2000 (O.J. L 262, 17.10.2000, p.21).
[2] World Health Organization Laboratory Biosecurity Guidance (2006).
[3] CEN, The Laboratory Biorisk Management Standard CWA 15793 (2008).

8.1.3 Impact of non-radiation risks on the environment

The ELI facility is not expected to be a substantial air, water, vibration and noise pollutant.

The amount of chemicals used on the ELI in liquid form is anticipated to be relatively low, however, there could accidentally happen certain leakage of chemicals during either operation or dismantling procedures of the ELI facility. Old and expired chemicals should be periodically cleaned-out by a specialized company/agency.

In some cases glass containers that are contaminated with certain chemical waste cannot be disposed. Such glass must be thoroughly rinsed prior to disposal in the glass container, and all rinse must be disposed of as hazardous waste. Only then cleaned empty glass containers and/or broken glass should be disposed in broken glass boxes.

8.2 Radioprotection safety

Few years ago, it was demonstrated both theoretically and experimentally that ionizing particles (mainly electrons, protons and ions) and radiation sources (X-rays) can be produced and accelerated by lasers, opening a new era in different fields of science. Since then, all practices concerning the use of such lasers have been regarded as practices with radiation risks and consequently treated. A list of what must be considered regarding radiosafety is presented below:

- Prompt, high-energy photon radiation produced from high-intensity solid target interactions.
- High-energy, quasi-mono-energetic electron beams generated from long focal length interactions in gas jets and capillary targets.
- High-energy proton emission from solid targets
- Neutron production from high-energy proton spallation in secondary materials.
- Synchrotron radiation generated within electron spectrometers.
- Photon, neutron, proton, pion and muon radiation emitted from relativistic particle cascades in shielding materials, primarily within the electron "get lost tube".
- Activation induced by protons, neutrons and photons of the materials of the interaction areas/chambers. This may include both air and water activation.
- Activated target debris released through pump exhaust systems.

8.2.1 Pre-definition of the radiation source term for 1 PW, 10 PW and 100 PW lasers

The crucial data required for the radio safety and design of the shielding of a facility is the radiological source term. While on an accelerator facility the source term is quite well known, on a high power laser facility it is an open question.

In this field, even measuring the source term on existing facilities is not an easy task, and most of the measurements are limited to dosimetric evaluations. Lack of a global database from this kind of data makes the task more complex.

At this stage, we can provide a preliminary source term for three different power levels: 1 PW, 10 PW and above 100 PW suitable for radioprotection purposes.

Database of source terms and dosimetry data

In order to design the future shielding and the radioprotection of the ELI facilities, in the preparatory phase, we have collected all data available from the existing facilities and calculations in the high-intensity regime in a new database. The database has been built by the Salamanca University and is located in:

http://eli6.fis.usal.es

We define a radiation source term as the entire number of particles emitted from the target during the interaction with the laser. It includes x-rays, gamma rays, electrons and protons emitted and/or accelerated by the plasma. However, it does not include all other secondary particles generated by scattering of the primary radiation on the equipment inside or outside the interaction chamber or on the target.

We have defined a standard format for all the data. In this way, it will be easier to compare different sources and provide the data to different parts of the project and/or to the community.

The standard form can be divided into thermal components, quasi-monochromatic components and, if required, an energy cut-off. For each thermal component i, we ask for the total number of particles per steradiant N_i^T, and the temperature T_i in MeV. For the quasi-monochromatic components, we will consider a Gaussian shape, asking for the number of the particles per steradiant N_j^G, the central energy E_j^G in MeV and the FWHM ΔE_j^G in MeV. In

case of an energy cut-off, we just ask for the energy value E^{MAX} in MeV. Within this scheme, the spectrum is represented by this formula:

$$N(x) = \begin{cases} 0 & \text{for } x \geq E^{MAX} \\ \sum_i \frac{N_i^T}{T_i} \exp\left(-\frac{x}{T_i}\right) + \sum_j \frac{N_j^G}{\Delta E_j^G} \sqrt{\frac{\ln 2}{\pi}} \exp\left[-4 \ln 2 \left(-\frac{x - E_j^G}{\Delta E_j^G}\right)^2\right] & \text{for } x < E^{MAX} \end{cases} \tag{8.1}$$

If T_i is not provided, it is supposed to be infinity, and N_i^T will become the number of protons per steradiant and per MeV. In case of a beam, we ask for three angles (in degrees): the divergence δ, the direction respect to the laser α, and/or the direction respect to the normal from the back surface of the target β. For no-collimated radiation, only α and/or β are required.

Radiation source term for 1 PW lasers

Vulcan Data

The main objective is to obtain information about the spectra and the angular distribution of the different types of radiation. Figures 8.1 and 8.2 show experimental data from the Vulcan facility at 1 PW, for protons and gamma rays in solid targets and electrons in a He gas jet.

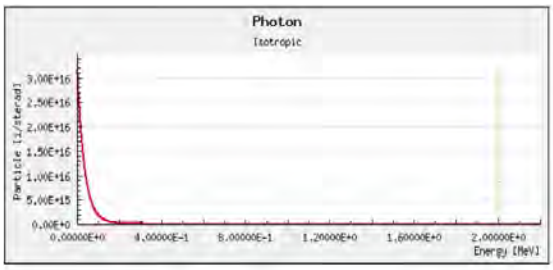

$$N(x) = \begin{cases} 0 & \text{for } x \geq E^{MAX} \\ \sum_i \frac{N_i^T}{T_i} \exp\left(-\frac{x}{T_i}\right) + \sum_j 2 \frac{N_j^G}{\Delta E_j^G} \sqrt{\frac{\ln 2}{\pi}} \exp\left[-4 \ln 2 \left(\frac{x - E_j^G}{\Delta E_j^G}\right)^2\right] & \text{for } x < E^{MAX} \end{cases}$$

Experiment	Experiment: Vulcan-001.	
Target	Al Foil, 4.0E+23 gm/cm^3.	
Pulse	1.0E+21 W/cm^2, 600 fs, 300 J, 1053 nm, Polarization p.	
Particle, instrument	Photon, Scintillation counter.	
Cut-off (E^{MAX})	2 MeV	
Angular distribution	Isotropic	
Thermal Components		
Temperature (T_i) [MeV]	Particle number (N^T_i) [1/sterad]	Plot
0.035	1.1E+15	
0.58	1.0E+14	
8.8	900000000000	

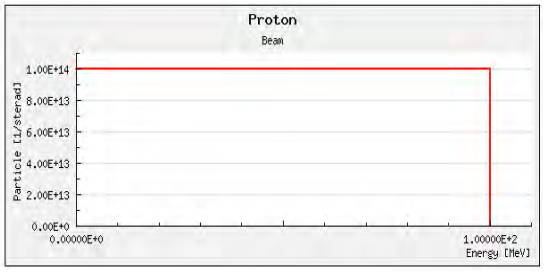

$$N(x) = \begin{cases} 0 & \text{for } x \geq E^{MAX} \\ \sum_i \frac{N_i^T}{T_i} \exp\left(-\frac{x}{T_i}\right) + \sum_j 2 \frac{N_j^G}{\Delta E_j^G} \sqrt{\frac{\ln 2}{\pi}} \exp\left[-4 \ln 2 \left(\frac{x - E_j^G}{\Delta E_j^G}\right)^2\right] & \text{for } x < E^{MAX} \end{cases}$$

Experiment	Experiment: Vulcan-000.
Target	Al Foil, 4.0E+23 gm/cm^3.
Pulse	1.0E+21 W/cm^2, 600 fs, 300 J, 1053 nm, Polarization p.
Particle, instrument	Proton, Scintillation counter.
Cut-off (E^{MAX})	100 MeV
Angular distribution	Beam [α= °, β = 0°, δ = 40°]
Offset distribution	
Particle number [1/sterad]	1.0E+14

Figure 8.1: Photon (left) and proton (right) energy spectra from Vulcan measurements in experiments with an Aluminium target foil are displayed. The maximum intensity is $I = 10^{21}$ Wcm^{-2}.

Estimations for ELI

As all the collected data correspond to a pulse length different to the one expected for ELI, it is necessary to scale them to the required pulse length. From the dosimetric data obtained at different facilities, it is reasonable to scale the number of the particles with the energy of the

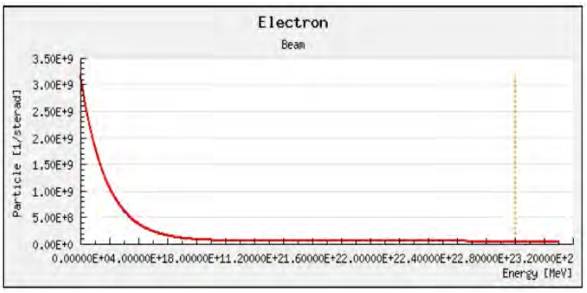

$$N(x) = \begin{cases} 0 & \text{for } x \geq E^{MAX} \\ \left(\sum_i \frac{N_i^T}{T_i} \exp\left(-\frac{x}{T_i}\right) + \sum_j 2\frac{N_j^G}{\Delta E_j^G} \sqrt{\frac{\ln 2}{\pi}} \exp\left[-4\ln 2\left(\frac{x - E_j^G}{\Delta E_j^G}\right)^2\right] \right. & \text{for } x < E^{MAX} \end{cases}$$

Experiment	Experiment: Vulcan-002.	
Target	He Gas jet, 10000000000 gm/cm^3.	
Pulse	1.0E+21 W/cm^2, 600 fs, 300 J, 1053 nm, Polarization p.	
Particle, instrument	Electron, Scintillation counter.	
Cut-off (E^{MAX})	300 MeV	
Angular distribution	Beam [α= 0°, β = °, δ = 2.9°]	
Thermal Components		
Temperature (T_i) [MeV]	**Particle number (N^T_i) [1/sterad]**	**Plot**
17.6	55000000000	
3500	200000000000	

Figure 8.2: Electron spectrum measured in Vulcan in a Helium gas jet. The maximum intensity is $I = 10^{21}$ Wcm^{-2}.

Table 8.1: Equivalent doses outside (third column) and inside (second column) the interaction chamber are presented for different intensities. Approximate scaling is denoted by an asterisk.

I (W/cm^2)	Full spectrum dose (mSv/J @ 1m)	Dose >300 KeV (approx.) (mSv/J @ 1 m)
10^{20}	0.1	0.02
10^{21}	0.5	0.1
10^{22} *	1	0.3
10^{23}*	5	1

laser pulse. Assuming a pulse of 15 fs and 15 J and a wavelength of 800 nm for ELI, we obtain the results shown in Figs. 8.3 and 8.4.

Estimations for 10 PW lasers

Even if there are no facilities at this power level, it is possible to extrapolate the data from the 1 PW case and/or use some simulation codes.

Regarding the production of gamma rays, it is reasonable to assume the same spectrum and divergence as in the 1 PW case. To obtain the total number of particles, we can use the dosimetric data collected from all the community and scale them up with the intensity. The results are summarized in Table 8.1.

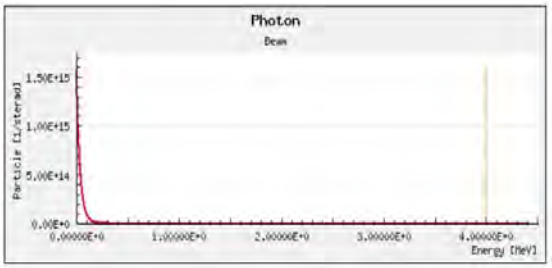

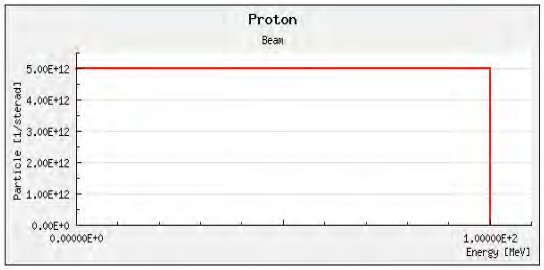

$$N(x) = \begin{cases} 0 & \text{for } x \geq E^{MAX} \\ \sum_i \frac{N_i^T}{T_i} \exp\left(-\frac{x}{T_i}\right) + \sum_j 2\frac{N_j^G}{\Delta E_j^G}\sqrt{\frac{\ln 2}{\pi}} \exp\left[-4\ln 2\left(\frac{x-E_j^G}{\Delta E_j^G}\right)^2\right] & \text{for } x < E^{MAX} \end{cases}$$

Experiment	Estimate: ELI Estimate 1PW.	
Target	Al Foil, 4.0E+23 gm/cm^3.	
Pulse	1.0E+21 W/cm^2, 15 fs, 15 J, 800 nm, Polarization p.	
Particle, instrument	Photon, Scintillation counter.	
Cut-off (E^{MAX})	4 MeV	
Angular distribution	Beam [α= 0°, β = °, δ = 40°]	
Thermal Components		
Temperature (T_i) [MeV]	Particle number (N^T_i) [1/sterad]	Plot
0.035	55000000000000	
0.58	5000000000000	
8.8	45000000000	

$$N(x) = \begin{cases} 0 & \text{for } x \geq E^{MAX} \\ \sum_i \frac{N_i^T}{T_i} \exp\left(-\frac{x}{T_i}\right) + \sum_j 2\frac{N_j^G}{\Delta E_j^G}\sqrt{\frac{\ln 2}{\pi}} \exp\left[-4\ln 2\left(\frac{x-E_j^G}{\Delta E_j^G}\right)^2\right] & \text{for } x < E^{MAX} \end{cases}$$

Experiment	Estimate: ELI Estimate 1PW.
Target	Al Foil, 4.0E+23 gm/cm^3.
Pulse	1.0E+21 W/cm^2, 15 fs, 15 J, 800 nm, Polarization p.
Particle, instrument	Proton, Scintillation counter.
Cut-off (E^{MAX})	100 MeV
Angular distribution	Beam [α= °, β = 0°, δ = 40°]
Offset distribution	
Particle number [1/sterad]	5000000000000

Figure 8.3: Estimations of ELI source terms for 1 PW, using 15 J and 15 fs pulses. Photon (left) and proton (right) energy spectra with an Aluminium target foil are displayed. The maximum intensity is $I = 10^{21}$ Wcm^{-2}.

Table 8.2: Properties of the 10 PW laser.

Laser	Energy [J]	150
	Pulse length [fs]	15
	Intensity [W/cm^2]	10^{22} (or smaller, for electrons)

Scaling from 10^{21} to 10^{22} W/cm^2, a factor 2 (approx.) is obtained. If we also take into account the increased energy, we end up with a total factor of 20. For the proton radiation, both numerical simulations and modelling suggest the presence of a tail at high energies (up to $\sim$2 GeV), with total proton numbers of about 10^{10} in this energy region. For the less energetic protons, we can scale the numbers as we have done for the gamma rays above. For the electron production, it is extremely important to determine the maximum acceleration length available into the target area, which directly determines the maximum acceleration energy of the electrons. Supposing an available length of 4 m, the maximum energy will be around 38 GeV [1], for a bunch around 3.5 nC [2]. The divergence will be less than 1 deg. The information given above is summarized in Table 8.2 and Figs. 8.5–8.6.

Estimations for lasers above 100 PW

In this region, the only way to have an indication about the source term is to use a numerical simulation. Even so, not all the physical processes involved are well known and included in the existing codes.

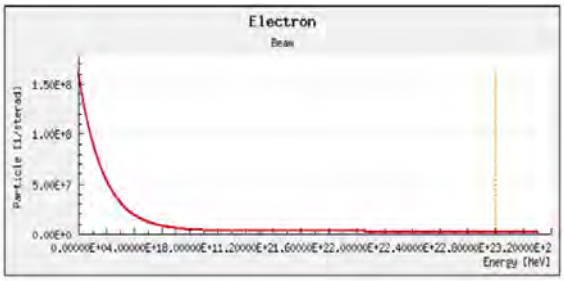

$$N(x) = \begin{cases} 0 & \text{for } x \geq E^{MAX} \\ \left(\sum_i \frac{N_i^T}{T_i} \exp\left(-\frac{x}{T_i}\right) + \sum_j 2\frac{N_j^0}{\Delta E_j^0} \sqrt{\frac{\ln 2}{\pi}} \exp\left[-4\ln 2 \left(\frac{x - E_j^0}{\Delta E_j^0}\right)^2\right] \right. & \text{for } x < E^{MAX} \end{cases}$$

Experiment	Estimate: ELI Estimate 1PW.	
Target	Al Foil, 4.0E+23 gm/cm^3.	
Pulse	1.0E+21 W/cm^2, 15 fs, 15 J, 800 nm, Polarization p.	
Particle, instrument	Electron, Scintillation counter.	
Cut-off (E^{MAX})	300 MeV	
Angular distribution	Beam [α= 0°, β = °, δ = 2.9°]	
Thermal Components		
Temperature (T_i) [MeV]	**Particle number (N^T_i) [1/sterad]**	**Plot**
17.6	2800000000	
3500	10000000000	

Figure 8.4: Estimations of ELI source terms for 1 PW, using 15 J and 15 fs pulses. Electron spectrum from a Helium gas jet is represented. The maximum intensity is $I = 10^{21}$ Wcm^{-2}.

Table 8.3: Characteristics of the laser and target used for the calculations above 100 PW are shown. These calculations were done for electrons in a plasma channel guide and only one acceleration stage was considered.

General	Type	Analytical estimation based on scaling laws
Target	Type	Plasma channel guide
	Density [cm^{-3}]	3.0×10^{16}
	Lenght [m]	4.0
Laser	Energy [J]	2000
	Pulse length [fs]	194
	Wavelength [nm]	800
	Intensity [W/cm^2]	1.7×10^{19}
	Beam waist [μm]	281 (diameter)

The results that will be presented here are based on a 2D PIC [3] code and analytic estimations. It is worth pointing that no QED effects were taken into account.

Electrons in a plasma channel guide

The easiest source term is connected with the accelerated electrons. In this case, higher pulse energies could only be used to have higher electron numbers, just increasing the beam size, or higher energies, stacking more amplification stages. This second option will require very long

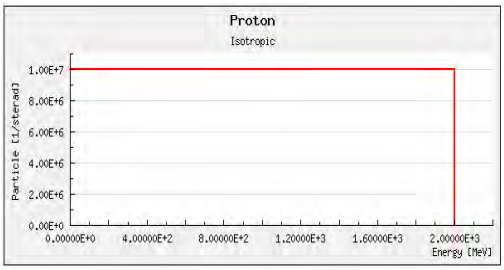

$$N(x) = \begin{cases} 0 & \text{for } x \geq E^{MAX} \\ \sum_i \frac{N_i^T}{T_i} \exp\left(-\frac{x}{T_i}\right) + \sum_j 2\frac{N_j^G}{\Delta E_j^G}\sqrt{\frac{\ln 2}{\pi}} \exp\left[-4\ln 2\left(\frac{x-E_j^G}{\Delta E_j^G}\right)^2\right] & \text{for } x < E^{MAX} \end{cases}$$

Experiment	Estimate: ELI Estimate 10PW - 001.
Target	Al Foil, 4.0E+23 gm/cm^3.
Pulse	1.0E+22 W/cm^2, 15 fs, 150 J, 800 nm, Polarization p.
Particle, instrument	Proton, Scintillation counter.
Cut-off (E^{MAX})	2000 MeV
Angular distribution	Isotropic
Offset distribution	
Particle number [1/sterad]	10000000

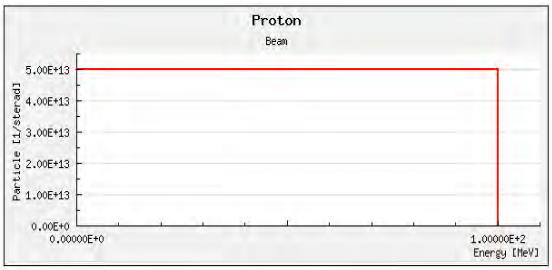

$$N(x) = \begin{cases} 0 & \text{for } x \geq E^{MAX} \\ \sum_i \frac{N_i^T}{T_i} \exp\left(-\frac{x}{T_i}\right) + \sum_j 2\frac{N_j^G}{\Delta E_j^G}\sqrt{\frac{\ln 2}{\pi}} \exp\left[-4\ln 2\left(\frac{x-E_j^G}{\Delta E_j^G}\right)^2\right] & \text{for } x < E^{MAX} \end{cases}$$

Experiment	Estimate: ELI Estimate 10PW - 001.
Target	Al Foil, 4.0E+23 gm/cm^3.
Pulse	1.0E+22 W/cm^2, 15 fs, 150 J, 800 nm, Polarization p.
Particle, instrument	Proton, Scintillation counter.
Cut-off (E^{MAX})	100 MeV
Angular distribution	Beam [α= °, β = 0°, δ = 40°]
Offset distribution	
Particle number [1/sterad]	50000000000000

Figure 8.5: Estimations for the 10 PW laser of ELI from Vulcan measurements. Proton spectra in a solid target are displayed. Two intensities are considered: $I = 10^{22}$ Wcm^{-2} (left), and $I = 10^{23}$ Wcm^{-2} (right).

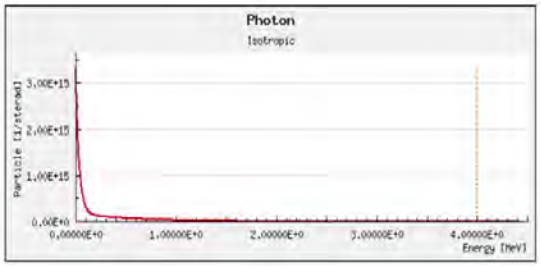

$$N(x) = \begin{cases} 0 & \text{for } x \geq E^{MAX} \\ \sum_i \frac{N_i^T}{T_i} \exp\left(-\frac{x}{T_i}\right) + \sum_j 2\frac{N_j^G}{\Delta E_j^G}\sqrt{\frac{\ln 2}{\pi}} \exp\left[-4\ln 2\left(\frac{x-E_j^G}{\Delta E_j^G}\right)^2\right] & \text{for } x < E^{MAX} \end{cases}$$

Experiment	Estimate: ELI Estimate 10PW - 001.		
Target	Al Foil, 4.0E+23 gm/cm^3.		
Pulse	1.0E+22 W/cm^2, 15 fs, 150 J, 800 nm, Polarization p.		
Particle, instrument	Photon, Solid state detector.		
Cut-off (E^{MAX})	4 MeV		
Angular distribution	Isotropic		
Thermal Components			
Temperature (T_i) [MeV]	Particle number (N^T_i) [1/sterad]	Plot	
0.035	1.1E+14		
0.58	1.0E+14		
8.8	900000000000		

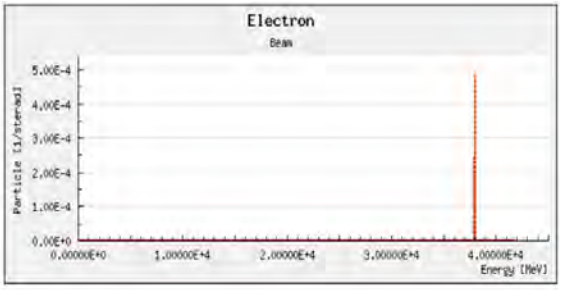

$$N(x) = \begin{cases} 0 & \text{for } x \geq E^{MAX} \\ \sum_i \frac{N_i^T}{T_i} \exp\left(-\frac{x}{T_i}\right) + \sum_j 2\frac{N_j^G}{\Delta E_j^G}\sqrt{\frac{\ln 2}{\pi}} \exp\left[-4\ln 2\left(\frac{x-E_j^G}{\Delta E_j^G}\right)^2\right] & \text{for } x < E^{MAX} \end{cases}$$

Experiment	Estimate: ELI Estimate 10PW Channel - 001.			
Target	H Composite, -1 gm/cm^3.			
Pulse	1.0E+22 W/cm^2, 15 fs, 150 J, 800 nm, Polarization p.			
Particle, instrument	Electron, Scintillation counter.			
Cut-off (E^{MAX})	38000 MeV			
Angular distribution	Beam [α= 0°, β = °, δ = °]			
Quasi-monochromatic Components				
Energy (E^G_j) [MeV]	FWHM (ΔE^G_j) [MeV]	Particle number (N^G_j) [1/sterad]	Plot	
38000	1	90000000000000		

Figure 8.6: Estimations for the 10 PW laser of ELI from Vulcan measurements. Photon spectrum in a solid target, $I = 10^{22}$ Wcm^{-2} (left), and electron spectrum in a plasma channel, $I = 10^{22}$ Wcm^{-2} (right).

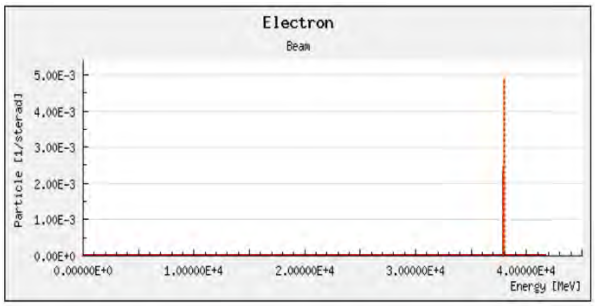

$$N(x) = \begin{cases} 0 & \text{for } x \geq E^{MAX} \\ \sum_i \frac{N_i^T}{T_i} \exp\left(-\frac{x}{T_i}\right) + \sum_j 2\frac{N_j^G}{\Delta E_j^G}\sqrt{\frac{\ln 2}{\pi}} \exp\left[-4\ln 2\left(\frac{x-E_j^G}{\Delta E_j^G}\right)^2\right] & \text{for } x < E^{MAX} \end{cases}$$

Experiment		Estimate: ELI Estimate 100PW Channel.	
Target		H Composite, 3.0E+16 gm/cm^3.	
Pulse		1.7E+19 W/cm^2, 194 fs, 2000 J, 800 nm, Polarization p.	
Particle, instrument		Electron, Scintillation counter.	
Cut-off (E^{MAX})		38000 MeV	
Angular distribution		Beam [α= 0°, β = °, δ = °]	
Quasi-monochromatic Components			
Energy (E^G_j) [MeV]	**FWHM (ΔE^G_j) [MeV]**	**Particle number (N^G_j) [1/sterad]**	**Plot**
38000	1	9.0E+14	

Figure 8.7: Electron spectrum in a plasma channel guide, $I = 1.7\times10^{19}$ Wcm^{-2}. Only one acceleration stage was considered.

Table 8.4: Characteristics of the laser and target used for the calculations above 100 PW are shown. These calculations were done for electrons in a plasma channel guide and ten acceleration stages were considered.

General	Type	Analytical estimation based on scaling laws
Target	Type	Plasma channel guide
	Density [cm^{-3}]	3.0×10^{16}
	Lenght [m]	4.0
Laser	Energy [J]	200 (per stage)
	Pulse length [fs]	194
	Wavelength [nm]	800
	Intensity [W/cm^2]	1.7×10^{19}
	a_0	4 (peak)
Layout	Focusing system (f/#)	f/87
	Beam waist [μm]	89 (diameter)
	Number of stages	10

Table 8.5: Characteristics of the laser and target used for the calculations above 100 PW are shown. These calculations were done to determine proton and electron source terms for experiments with solid targets of different thicknesses.

General	Type	Simulation PIC 2D fully relativistic code
Target	Type	Thin solid target
	Material	H
	Density [g cm^{-3}]	0.088
	Thickness [μm]	1; 5; 10; 20
Laser	Energy [J]	2000
	Pulse length [fs]	15
	Wavelength [nm]	800
	Intensity [W/cm^2]	1.6×10^{23}
	a_0	276
Layout	Focusing system (f/#)	f/10
	Beam waist [μm]	5.1($1/e^2$ intensity radius)
	Polarization (p, s, circle)	Circular
	Angle of incidence [deg]	0°

distances. Supposing 10 stages like the one of 10 PW, the maximum energy will be 380 GeV (theoretically), with a total acceleration length of 40 m. However, multi-stage acceleration has not been done at the moment. Tables 8.3–8.4 and Figs. 8.7–8.8 summarize the results obtained in both situations.

Protons and electrons

This study was made with the Osiris fully relativistic PIC code [3] in series of runs for different target thicknesses. The targets were modelled as solid Hydrogen in order to increase the simulation speed. The 2D simulation series took a total time of 21000 CPU hours at the IST cluster [4].

The estimation of the 3D particle distribution from the bi-dimensionally generated data is accomplished by specifying a proper depth for the simulated target and considering radial symmetry along the x_1 axis. For this particular set of data, which assumed a laser spot diameter of 10.2 μm, the simulation depth on x_3 is 6.4 μm, by applying the correction factor of $\sqrt{\frac{\pi}{8}}$ to preserve the laser energy in the 2 to 1D Gaussian-shape conversion. Then, the particle density must be normalised to the corresponding solid angle, which, in first approximation, is given by $2\pi\Delta\theta \sin\theta$ for $\theta \neq \{0, \pi\}$, where θ is the angle respect to the x_1 axis.

Table 8.5 shows the details of the simulations carried out, where proton and electron source terms were calculated for different target thicknesses. Figs. 8.8 and 8.10 show an example of the results obtained for protons and electrons, respectively.

Bibliography

[1] W. Lu et al., Phys. Rev. S.T. Accelerators and Beams **10**, 061301 (2007).
[2] M. Tzoufras et al., Phys. Rev. Lett. **101**, 145002 (2008).
[3] R. A. Fonseca et al., Lecture Notes in Computer Science **2331**, 342 (2002).
[4] https://istcluster3.ist.utl.pt.

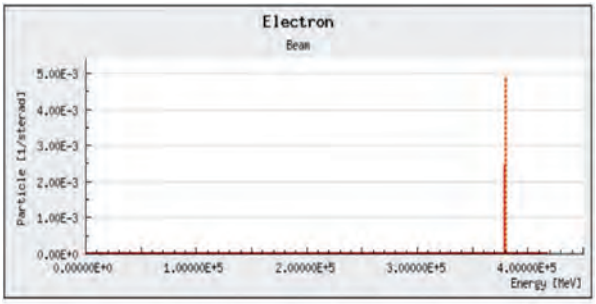

$$N(x) = \begin{cases} 0 & \text{for } x \geq E^{MAX} \\ \left(\sum_i \frac{N_i^T}{T_i} \exp\left(-\frac{x}{T_i}\right) + \sum_j 2\frac{N_j^G}{\Delta E_j^G} \sqrt{\frac{\ln 2}{\pi}} \exp\left[-4\ln 2 \left(\frac{x - E_j^G}{\Delta E_j^G}\right)^2\right] \right) & \text{for } x < E^{MAX} \end{cases}$$

Experiment		Estimate: ELI Estimate 100PW Channel - 002.	
Target		H Composite, 3.0E+16 gm/cm^3.	
Pulse		1.7E+19 W/cm^2, 194 fs, 200 J, 800 nm, Polarization p.	
Particle, instrument		Electron, Scintillation counter.	
Cut-off (E^{MAX})		380000 MeV	
Angular distribution		Beam [α= 0°, β = °, δ = °]	
Quasi-monochromatic Components			
Energy (E^G_j) [MeV]	**FWHM (ΔE^G_j) [MeV]**	**Particle number (N^G_j) [1/sterad]**	**Plot**
380000	1	9.0E+14	

Figure 8.8: Electron spectrum in a plasma channel guide, $I = 1.7 \times 10^{19}$ Wcm^{-2}. Ten acceleration stages can lead to 380 GeV electrons.

8.2.2 Shielding

The shielding of the ELI facilities should be designed taking into account the particularities of each specific case. In the following, a first preliminary report about the shielding for the electron acceleration area in the facility of the Czech Republic is presented as an example.

As first step the radiation beams that are produced in laser-matter interactions have been characterized both for the electron and the proton case. Then these "source terms" have been inserted in a full simulation with the FLUKA Monte Carlo code [1,2], version 2008.3c: a key point for this choice has been the possibility to calculate in the same simulation the development of the electromagnetic and hadronic showers in the whole energy range of interest and the neutron production and transport until the thermal energies, as well as the ambient dose equivalent, that is due to all the radiation field components.

The source terms

As we mentioned above, unlike a standard accelerator facility, the definition of a source term case for the ELI laser-acceleration beamline facility is a tangled issue. In fact, this facility will allow laser-matter interaction experiments in a new regime of laser intensity, the so-called ultra-relativistic regime ($I_L > 10^{23}$ W/cm^2), and will use ultra-short pulse (few tens of femtoseconds): hence, there are no experimental data in literature reporting the spectral range of the produced ionizing radiation in those conditions, as well as the correspondent ambient dose equivalent. The only way to define a source term is to use analytical estimations, numerical simulations and sometimes scaling laws. In addition, various configurations for the future experiments have been

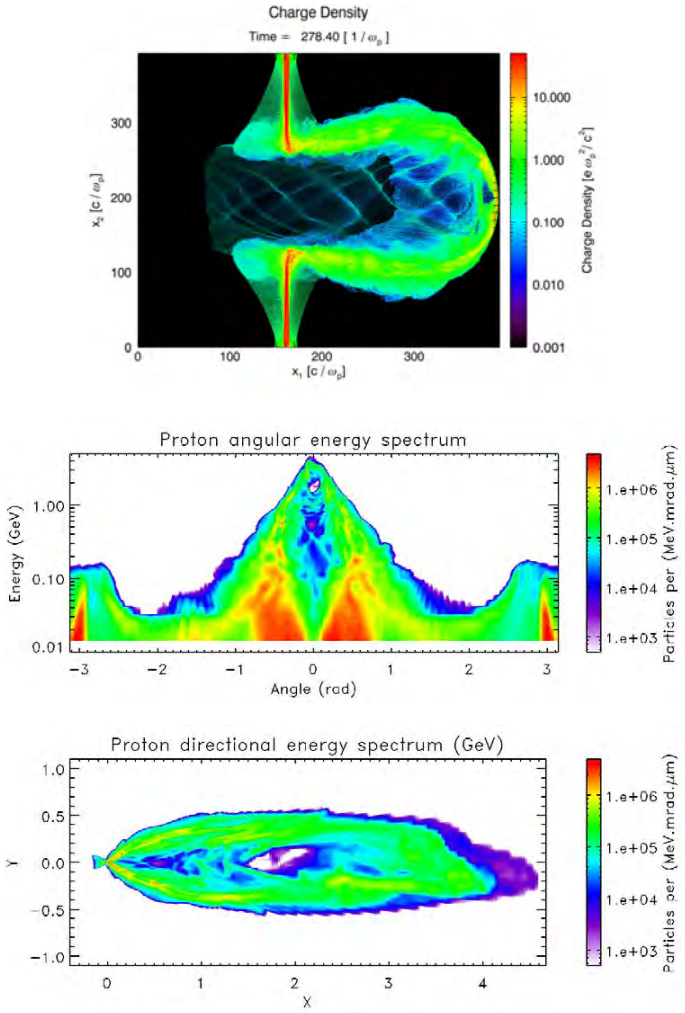

Figure 8.9: Simulation results for the proton source term, using a 1 μm thick target. The proton density is given in normalized simulation units. The laser propagates along the x_1 direction, coming from the left. (Top) charge density. (Middle) angular energy spectrum. (Bottom) directional energy spectrum.

proposed by several scientists: our general criterion has been, therefore, to set the laser-target interaction conditions by considering the "worst" scenario in terms of radiation protection issues.

Even if the ELI pillar in the Czech Republic will provide several beamlines at different laser energy/power and repetition rates, we will take into account two general cases: experiments with the highest energy/power laser beamline at 0.1 Hz and experiments at 10 Hz with the highest repetition rate but relatively low energy/power laser beamline that is compatible with this repetition rate. The former can be considered a "hazard" because of the ultra-high energy range of the associated emitted radiation, while the latter can provide higher secondary particle fluences at a comparable working time. Moreover, we classified the possible experiments that are planned at the Particle Accelerator Target Area into two main classes: Electron Acceleration and Particle Acceleration experiments, which will occur in different experimental rooms, as reported in the sketch of Fig. 8.11.

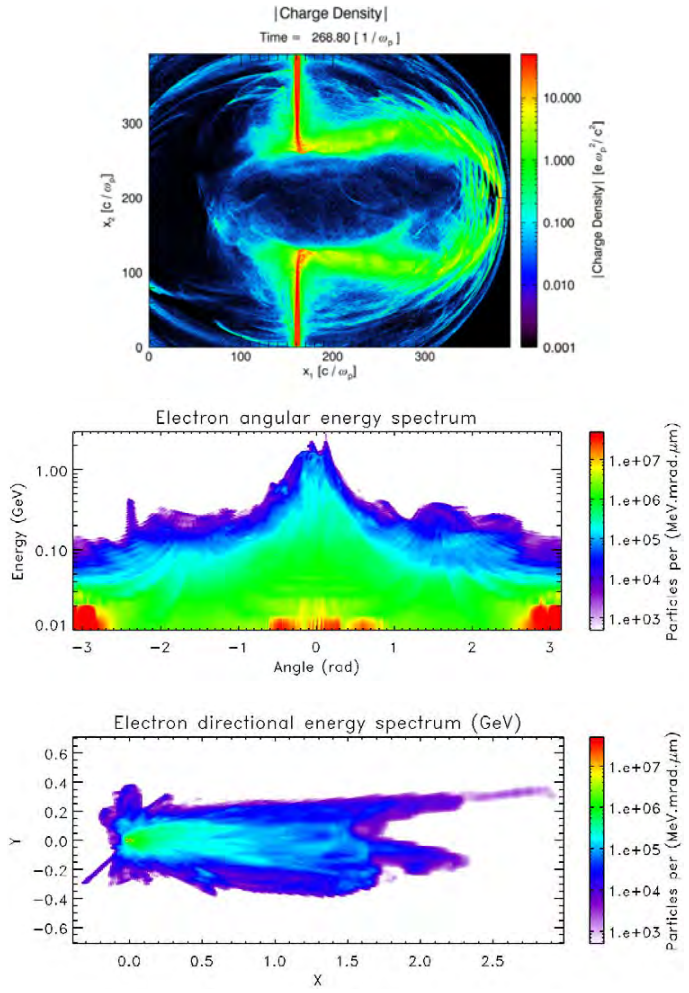

Figure 8.10: Simulation results for the electron source term, using a 1 μm thick target. The proton density is given in normalized simulation units. The laser propagates along the x_1 direction, coming from the left. (Top) charge density. (Middle) Angular energy spectrum. (Bottom) Directional energy.

Electron Acceleration

In this target area only experiments where the laser beam interacts with gas-targets will take place. The non-linear interactions will accelerate electron beams with different energies and charge, depending on the studied scheme.

The most hazardous scheme in terms of maximum electron beam energy seems to be the blowout regime (external injection) where the 300 J, 0.1 Hz laser beamline will be focused and channelled through many Rayleigh lengths of tenuous plasma (plasma density, laser pulse length and spot size have to be chosen properly) creating a plasma wave wake on which electrons can surf and reach a very high energy. Analytical formulas [3] allowed us to estimate that the electron beam can be accelerated with a mean energy of about 50 GeV and a total charge of about 1.5 nC (nominally 41 GeV and 1.3 nC, respectively) within a distance of about 5 m. The electron beam used as input for the FLUKA simulations was supposed to have a Gaussian energy distribution with a spread of 10% and a divergence of 1 deg.

The second electron acceleration configuration which has been considered is the one where

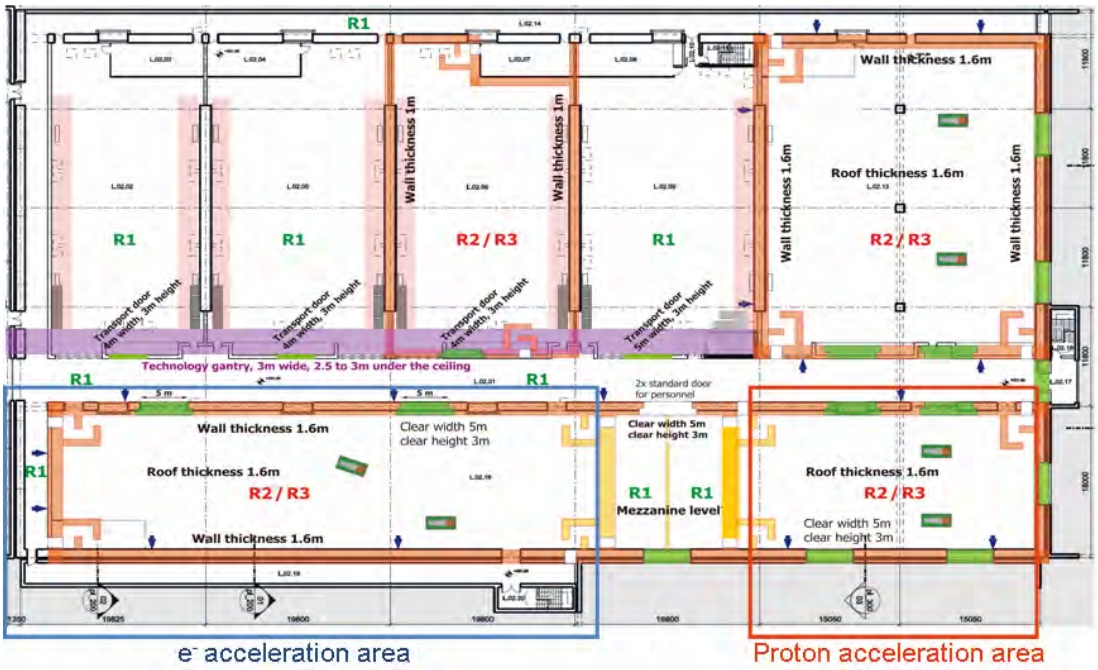

Figure 8.11: Sketch of the experimental areas at the ELI beamline facility in Czech Republic. The electron acceleration area and the proton acceleration area are in evidence. The R1/R2/R3 classification is related to the radiation protection requirements in these areas: <7.5 μSv/h in R1, <25 μSv/h in R2 and >25 μSv/h in R3.

the 50 J, 10 Hz laser beamline will be used in the blowout regime (self-injection), in order to accelerate electrons at 5 GeV (nominally 4 GeV) with a total charge of about 1 nC within several centimetres. Also in this case the electron beam was supposed to have a Gaussian energy distribution with a spread of 10% and a divergence of 1 deg.

Proton acceleration

In the target area dedicated to proton/ion acceleration various experiments where different laser beamlines focused onto thin solid targets at very high intensities will be performed. In this case the main literature data, that report scaling laws and numerical simulations at similar laser irradiation conditions, have been used to define the source term [4–6].

Table 8.6: Main properties of the source term in the electron beam case.

Laser properties				Accel. regime	Electron beam properties					
					Nominal		Used in FLUKA simulations			
Energy (J)	Width (fs)	R. rate (Hz)	Pow. (PW)		e- Energy (GeV)	Charge (nC)	Sim. e- Energy (GeV)	Sim. charge (nC)	ΔE/E (FWHM)	Beam divergence
300	280	0.1	~ 1	blowout ext. inj.	41	1.3	50	1.5	10%	1°
50	80	10	~ 0.6	blowout self inj.	3.7	1	5	1	10%	1°

Table 8.7: Main properties of the source term in the proton beam case.

Laser properties					Proton beam properties				
					Nominal	Assumptions for FLUKA simulations			
Energy (J)	Width (fs)	R. rate (Hz)	Power (PW)	Intensity (W/cm^2)	Energy cut-off (GeV)	Sim. energy, rectangular (GeV)	Sim. p/pulse	ΔE/E (GeV)	Beam divergence
150 (5 × 300)	30	0.1	~ 50	$5{\cdot}10^{23}$	3.7	3	$6{\cdot}10^{11}$	0.3	40°
50	20	10	~ 2.5	10^{21}÷10^{22}	0.2 ÷ 0.3	0.2	10^{12}	0.01	4°

To reduce the degree of freedom in our estimations of the maximum proton energy and the total proton current, which depend on many parameters (as laser intensity, pulse duration, target thickness, target material and so on), we set some experimental configuration. Thus we considered numerical simulations with "ideal" 1 μm thick hydrogen targets [5,6] or scaling laws based on experimental results where proton beams were accelerated from hydrogen impurities on the target surface [4].

The highest energy ionizing radiation is again generated at the 300 J, 0.1 Hz laser beamline which in principle could reach a maximum intensity on the target surface of about 5×10^{23} W/cm^2 if a future upgrading of the system at 50 PW (5 beamlines at 300 J, 10 PW) is assumed. For this source term we considered a proton beam with a mean energy of 3 GeV and a total yield of 6×10^{11}/pulse (conversion efficiency of about 20%), in agreement with literature data [5]. For simplicity the proton beam is supposed to have a rectangular energy distribution with a spread of 10% and a divergence of 40 deg.

The source term at 50 J, 10 Hz (2.5 PW, 10^{22} W/cm^2) laser beamline was estimated to be able to generate proton beams with the following specifications: 200 MeV, 10^{12}/pulse, 50% efficiency, 5% energy spread, 4 deg divergence. Those estimations are in agreement with literature data in the hypothesis of very thin target (few hundreds of nm) and circularly polarized laser pulses, the so-called radiation pressure acceleration regime [6].

Moreover, another ionizing radiation source, that is intrinsically associated with the proton one, has to be considered: a part of the electrons in the target material are accelerated at high energies, as confirmed by particle-in-cell simulations. Specifications of associated electron beams for the two considered cases are: 1.5 GeV, 2×10^{11}/pulse, 40 deg of divergence (3% efficiency) at 50 PW, 0.1 Hz, and 100 MeV, 2×10^{11}/pulse, 40 deg of divergence (8% efficiency) at 2.5 PW, 10 Hz laser beamline.

Shielding optimization in the electron case

To have a realistic description of the irradiation in the electron case, the source has been considered inside a typical chamber, to take into account also the secondary radiation that is generated through the interaction of the accelerated electron beam with the materials around. A standard chamber model for the ASTRA-GEMINI [7] project at RAL has been considered: a rectangular chamber in aluminium, 6 cm thick, with external dimensions 150 cm × 200 cm × 185 cm. A pipe in stainless steel (the composition of the AISI-316L has been assumed), 2 cm thick, comes out from the chamber for a length of 2 m, and is closed at the end by 1 cm of stainless steel. Moreover, in order to establish an operation time of the facility we assumed some preliminary limits reported in Table 8.8. As it will be shown from the FLUKA simulation results reported below the first assumption for the operation time limits can be largely increased especially in the case of electron acceleration.

As a first step we have studied the longitudinal shielding by using a simple high-Z one-material dump. Four different materials have been studied: lead, stainless steel AISI-316L, iron and copper. Several meters of shielding are expected due to the fact that the most penetrating radiation is given by high energy muons that are generated both by direct pair production and

Table 8.8: Preliminary operation times for the two most critical electron beamlines.

Repetition rate (Hz)	Shots/day
0.1	100
10	6000

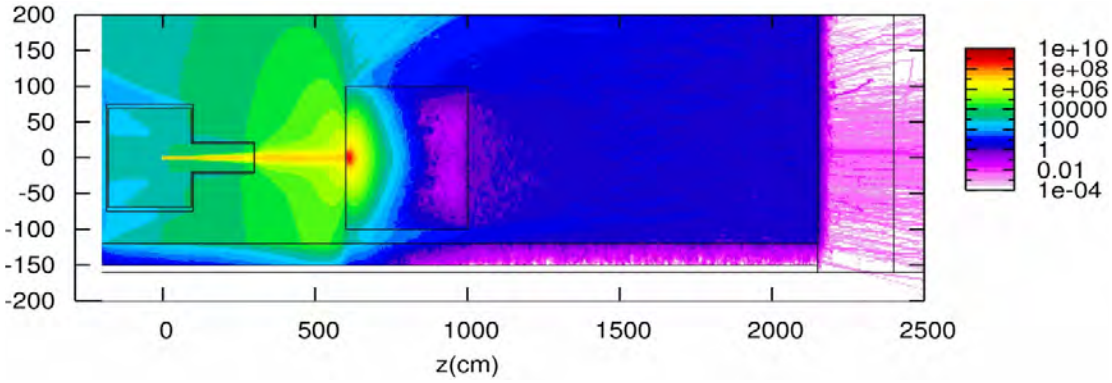

Figure 8.12: H*(10) rate (in μSv/day) in the case of the 50 GeV electron beam, 0.1 Hz, impinging on a mono-material dump in AISI-316L. From the left to the right are visible the electron source inside the vacuum chamber, the beam pipe that comes out from the chamber, the beam dump and the final heavy concrete wall.

by pion and kaon decay, together with high energy spallation neutrons and a less critical fast neutron spectrum coming from photoproduction processes on the high-Z material. Figs. 8.12 and 8.13 show the ambient dose equivalent integrated over a day of operation for the two most critical cases, in energy and in beam intensity, according with the operation times reported in Table 8.8. The two two-dimensional vertical projections (plane z-y) are calculated averaging along the horizontal direction, x, perpendicular to the beam direction, over a symmetric volume 20 cm deep around the beamline, and using a step of 5 cm in z and 2.5 in y (see [8] for the FLUKA graphical interface). Very similar results, in terms of shielding capability, have been obtained for the four used materials. Fig. 8.12 shows that for the 50 GeV electron beam a high-Z dump 4 m long, associated with a final heavy concrete wall 2.5 m thick, guarantees an optimal residual radiation level of around 10 nSv/day beyond the shielding wall. Fig. 8.13 shows, on the other hand, that the higher intensity/lower energy beamline is not at all a critical case: the high energy muons reach the end of their range already in the first 50 cm of the final shielding wall and the secondary neutron radiation is fully absorbed in the very first part of the concrete as well. Thus we are confident that a good solution for the 50 GeV beamline will automatically satisfy the shielding requirement for the 5 GeV/10 Hz beamline.

A one-material dump solution appears, however, to be not optimal for two main reasons, both related to the neutron secondary radiation. The first one is the huge amount of backscattered radiation due to the fact that in this case the maximum intensity of both the electromagnetic and the hadronic cascades are located in the very first part of the high-Z material dump. As consequence, a huge amount of radiation, which is mainly due to neutrons coming from spallation processes and from evaporation of nuclei in inelastic interactions, is travelling in air in backward direction, being potentially dangerous both for the lateral/backward containment of the radiation and as source of background in the experimental area inside the vacuum cham-

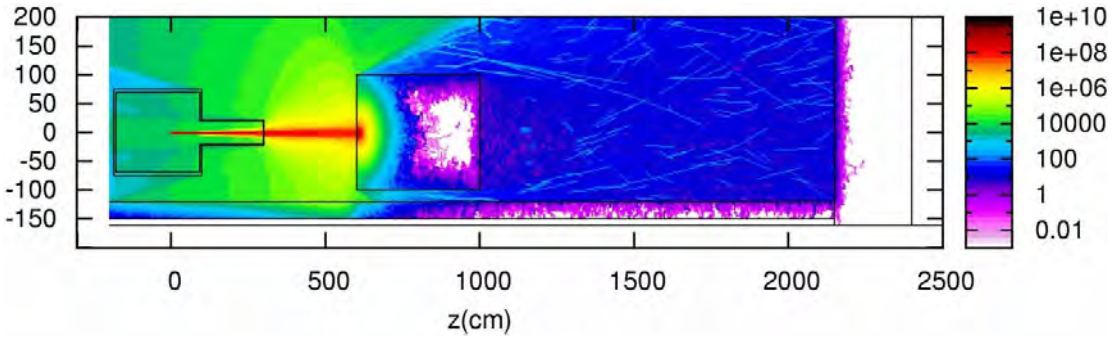

Figure 8.13: H*(10) rate (in μSv/day) in the case of the 5 GeV electron beam, 10 Hz, impinging on a mono-material dump in copper.

ber. This can be observed in Fig. 8.14, where the neutron fluence for the higher energy case is drawn (the vertical projection is the same as in the previous pictures). The second reason appears evident looking at the same picture: the longitudinal containment of neutrons, even if fully satisfactory in terms of doses beyond the final heavy concrete wall, is not total, the main reason being the fact that the secondary neutrons are not moderated with a suitable material. A solution to this problem will be the choice of a multi-material structure and will be discussed in the last section.

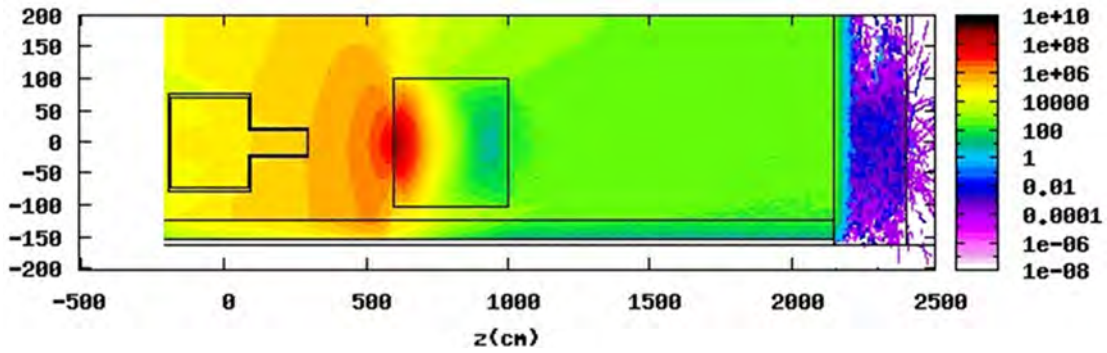

Figure 8.14: Neutron fluence rate (neutrons cm^{-2} s^{-1}) in the case of the 50 GeV electron beam, 0.1 Hz, with a mono-material dump in AISI-316L.

The choice of the high-Z material as main absorber (material activation)

The choice of the high-Z material to be used as main absorber in the dump structure has been done via a study of the induced radioactivity and is explained carefully in Sect. 8.2.3. The results justify the election of stainless steel as the main absorber material.

The 3-material dump structure

An optimal solution to the problem of the backscattered radiation which also allows for a better general shielding is to place a "soft" core in a low-Z material with moderation properties in the first part of the dump. Due to the softness of the material, the electromagnetic and the hadronic cascades develop more deeply in the dump, with the effect that the first part of the dump can properly shield against the backward radiation. If the low-Z material is a good moderator (a very

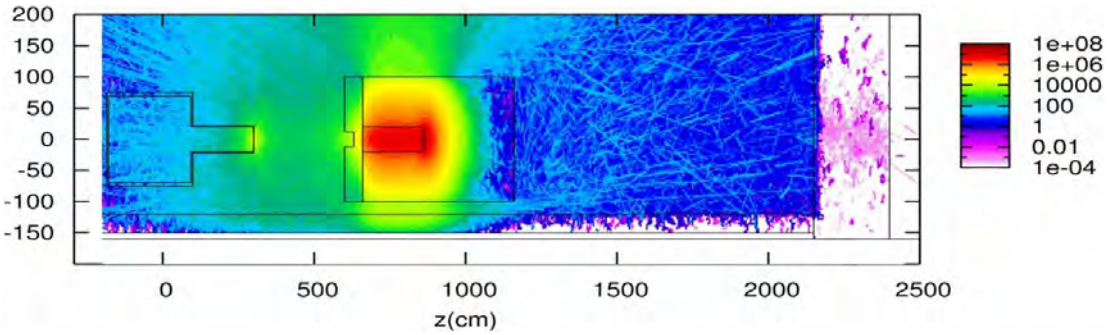

Figure 8.15: Neutron fluence rate (neutrons $cm^{-2}\,s^{-1}$) in the case of the 50 GeV electron beam, 0.1 Hz, with a 3-material dump structure in borated polyethylene, high density carbon fibres and AISI-316L.

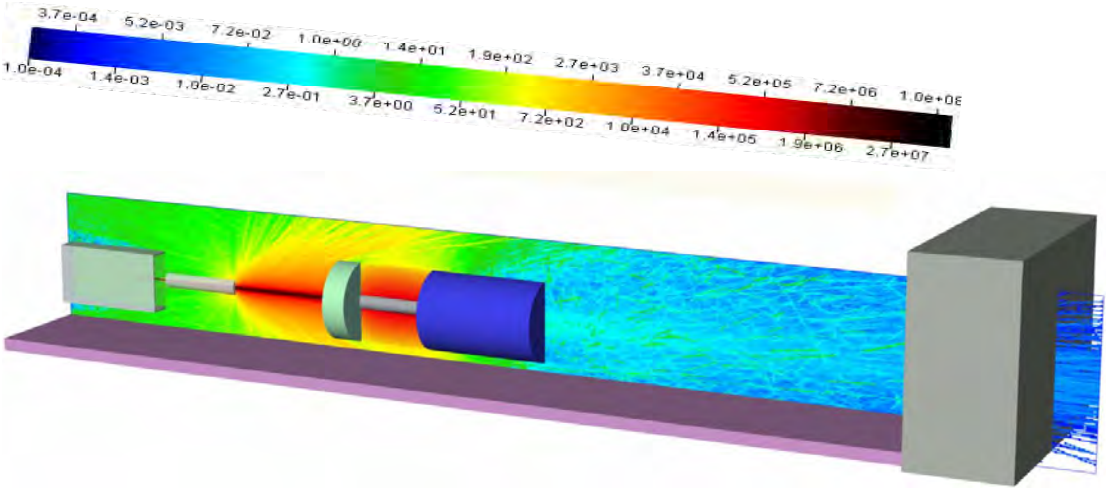

Figure 8.16: H*(10) rate (μSv/day) in the case of the 50 GeV electron beam, 0.1 Hz, impinging on the 3-material dump structure.

effective choice is given by high density carbon fibres, with typical densities of 1.9 g/cm^3) the produced secondary neutrons will be slowed down along the moderator, increasing the shielding properties of the part of the dump in stainless steel.

Finally, the addition of a first layer made of absorber material for low energy neutrons will significantly increase the containment of the backscattered neutron radiation. Fig. 8.15 shows an example of this 3-material dump: 60 cm of borated polyethylene are followed by a cylinder, 2 m long, in high density carbon fibres, surrounded and followed by the AISI-316L material, which acts as main absorber. 3 m of stainless steel after the carbon cylinder guarantee an optimal longitudinal behaviour of the neutron fluence. In Fig. 8.16 the behaviour of the ambient dose equivalent rate, integrated over a day of operation time, is shown: the residual prompt radiation after the final shielding wall, basically due to the survived attenuated muons, is at the very satisfactory level of 10 nSv/day, as it can be observed in the longitudinal profile of Fig. 8.17. Even imaging to increase in the future the number of shots per day by a factor 10, reaching the value of 1000 shots/day, the radiation beyond the shielding would remain at the absolutely safe level of 100 nSv/day.

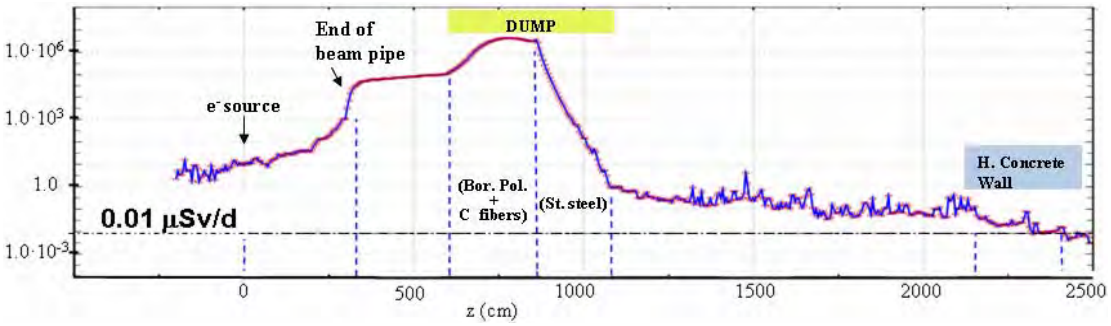

Figure 8.17: Longitudinal profile of the ambient dose equivalent rate showed in Fig. 8.18, obtained by averaging the H*(10) rate in the vertical coordinate y, in a small volume 20 cm large around the beamline.

Shielding optimization in the proton case

In the proton acceleration case, the source has been considered inside a similar interaction chamber than the one described above for the electron case. However, due to the high proton divergence, the pipe in stainless steel was removed and replaced by a circular flange, 50 cm in diameter and closed at the end by 0.5 cm stainless steel (this size has been chosen in order to fit with a source distance of 50 cm). The assumed operation time is the same reported in Table 8.8. Nevertheless, it is worth to mention that also in this case all the estimated radiation dose values will fit with the our planned dose limit restrictions even if an increase of a factor 10 in the operation times is assumed.

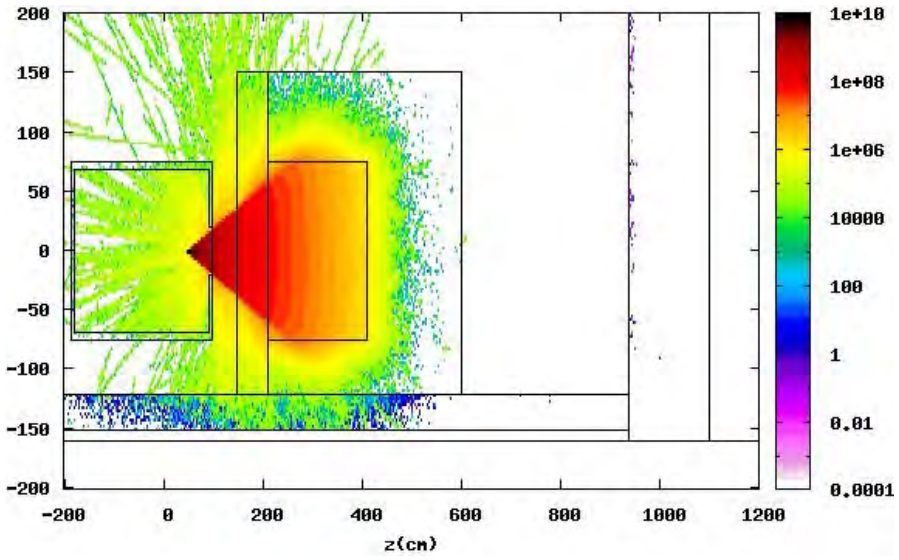

Figure 8.18: Proton fluence rate (protons cm^{-2} per shot) in the case of the 3 GeV proton beam, 0.1 Hz, with a 3-material dump structure in borated polyethylene, high density carbon fibres and AISI-316L.

The philosophy of the dump geometry is similar to the one used for the shielding of the electron acceleration case. In fact, the secondary radiation which deeply propagates when the primary protons strike the dump is essentially constituted by spallation neutrons. This radiation exhibits the higher rate of inelastic isotropic reaction in the high-Z material that is the basic

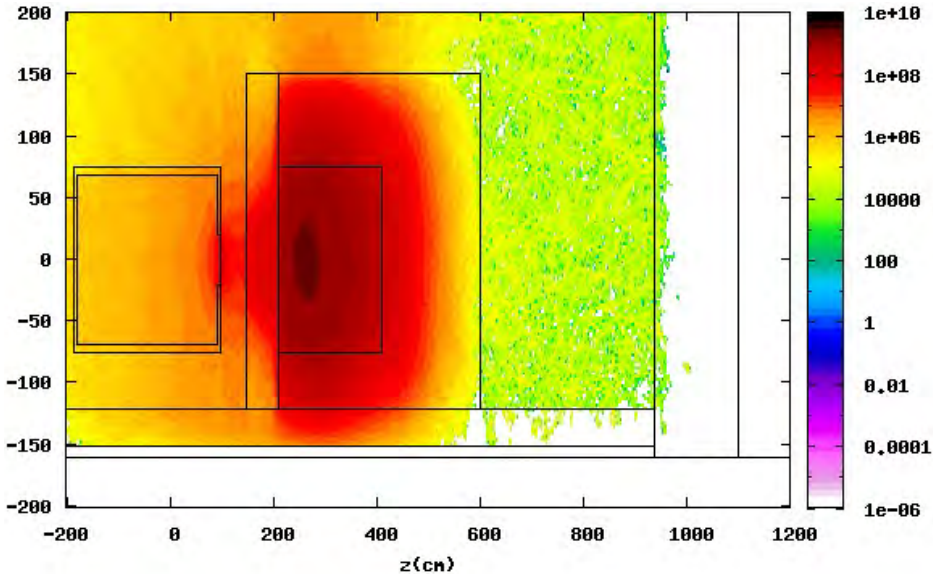

Figure 8.19: Neutron fluence rate (neutrons cm^{-2} per shot) in the case of the 3 GeV proton beam, 0.1 Hz, with a 3-material dump structure in borated polyethylene, high density carbon fibres and AISI-316L.

component of any shielding structure. A 3-material dump solution has been chosen, constituted by: a low-energy neutron absorber (borated polyethylene), a "soft" core (high density carbon fibres) and finally a surrounding high-Z material with good shielding properties (stainless steel). The use of a low-Z core is essential for three reasons: a reasonably low spallation neutron yield, a shift of the maximum rate of inelastic processes into the inner part of the dump structure and an efficient moderation of the backscattered neutrons.

Fig. 8.18 shows the proton fluence rate (protons cm^{-2} per shot) for a 3 GeV, 40° divergent proton beam. The optimal transversal size of the inner graphite cylinder fitting with the solid angle covered by the impinging proton beam is 150 cm in diameters. The surrounding stainless steel cylinder has a transversal size of 270 cm. The longitudinal size of the graphite moderator is 200 cm followed by further 200 cm of stainless steel. This dump length ensures not only a full shielding of the primary radiation but also a very satisfactory containment of the secondary neutrons (see Fig. 8.19). Once moderated, the backscattered neutron radiation is absorbed by a borated polyethylene slab (60 cm thick) placed at the beginning of the dump structure. The Fig. 8.20 shows the simulation results for the ambient dose equivalent (H*(10)) rate: the longitudinal shielding is fully accomplished, while a satisfactory containment of the transversal radiation can be reached by slightly increasing the dump radius or by covering the lateral structure with a few tens of centimetre thick concrete layer.

Prompt target radiation

The prompt radiation from the laser target has been studied for the last few years, and Fig. 8.21 (and additional data) shows the collated data from eight international facilities over the last 5 years, with additional data being added on a continual basis. These facilities vary in both energy and pulse length, and have been shown to generate the same dose per Joule of laser energy with similar target conditions when firing at comparative intensities. This data spans systems operating in the few J region with 10's of fs pulses up to several hundred Joules systems operating in the few ps regime. The majority of the data is collated from experiments at the

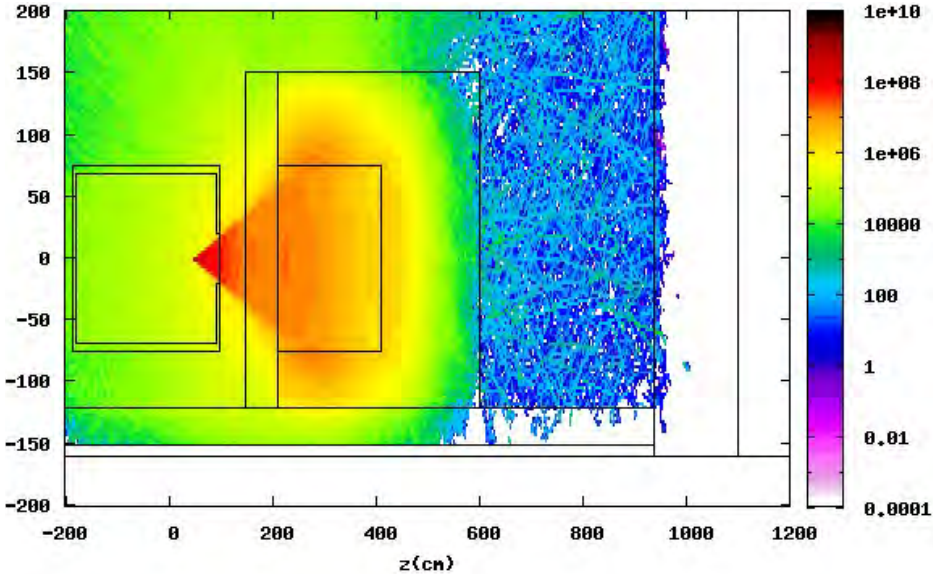

Figure 8.20: H*(10) rate (μSv/day) in the case of the 3 GeV proton beam, 0.1 Hz, with a 3-material dump structure in borated polyethylene, high density carbon fibres and AISI-316L.

UK's Central Laser Facility (CLF) which is part of the UK's Science and Technology Research Council (STFC).

Extrapolation of the presented data allows us to estimate the maximum dose (Black data) expected from a 10 PW beamline, operating at up to 10^{23} W/cm^2. This data is shown in the table below:

Table 8.9: Maximum unshielded doses for prompt target radiation for various laser intensities and target types.

Beam intensity	Target type	Unshielded dose per J @ 1 m	Unshielded dose per shot @ 1 m (300 J)
10^{21} W/cm^2	Thick	0.6 mSv	180 mSv
	Thin	20 μSv	6 mSv
10^{22} W/cm^2	Thick	5 mSv	1.5 Sv
	Thin	40 μSv	12 mSv
10^{23} W/cm^2	Thick	20 mSv	6 Sv
	Thin	100 μSv	30 mSv

Gamma radiation exiting from the chamber is typically 4 times lower due to the spectral cut-off below $\sim$ 300 keV (Red data). The thin target data escaping from the chamber (Blue data) is typical of shots with targets $<$ 200 μm thick, though the emitted dose drops quickly as target thicknesses decreases. This thin target data sees the same attenuation as the "Red" doses measuring $>$ 300 keV energies.

The primary dose emission from all these shots has been seen to be in the direction of laser propagation, with doses outside of this cone being $>$ 10 times lower. The spectral shape of the emitted radiation has been studied on both of the CLF's High Power facilities (Vulcan and

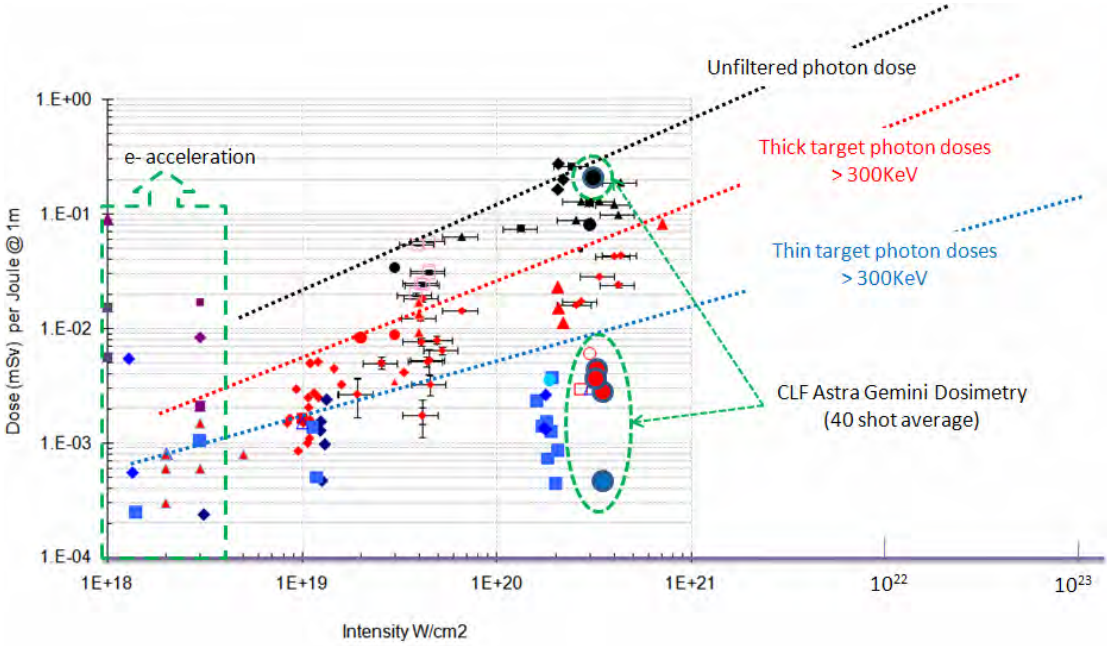

Figure 8.21: Dosimetry data from international high-power laser facilities collated over the last 5 years.

Astra), investigating both high power and ultra-short pulses. Published data [9] from Vulcan TAP (1 PW) shows the normalised spectral shapes of generated photons in the forward and side directions and is plotted in Fig. 8.22.

Comparing direct dosimetry data from Vulcan TAP and Astra Gemini, taken during 2009–2010, plotted as a function of photon dose per Joule of laser energy (shot averaging for the Gemini data) can be seen in Fig. 8.23, with doted curves representative of TAP shots and solid curves for Gemini shots. The two data sets are taken at comparable intensities.

For both data sets, the TLD filtering set-up was similar, and the plot shows the raw photon dose per Joule against linear density of the filtering, the transmission of which is directly related to the photon energies. The TAP shots produce higher doses in the high-energy spectral region (high linear density) than those of Astra Gemini, which could be representative of the shot averaging on Gemini (campaigns were run to an integrated energy of 400 J at $\sim$ 10 J per shot). Extending the latest data set to higher linear densities and trying to de-convolve the incident photon spectrum and referencing against Fluka modelling is ongoing.

The discussed data has been used to generate a full spectrum dose, based on the integral of the curve being equivalent to the total dose anticipated for the specific laser and targets and from the direct data in Fig. 8.22. Doses are obviously dominated by the thick target shots at the highest intensities. A cross check using the data in Fig. 8.23 derives the same shielded dose calculations when using the 30 g/cm^2 figure of 1×10^{-2} mSv/J @ 1m and factoring this for laser energy, number of shots, distance and Tenth Value Thickness (TVT) of concrete, since almost all spectral modification has taken place within the first 10's of cm of concrete. These figures agree to within 20% and hence order of magnitude shielding estimates can be made using TVT values for concrete (30 cm of concrete at 2.2–2.4 g/cm^3 is $\sim$ 1 order of magnitude attenuation) provided at least 2 TVT's are in place to ensure the full spectral modification of the emitted photon radiation from the target interaction.

Shot numbers for low yield target shots (using thin targets) need to be considered as part of

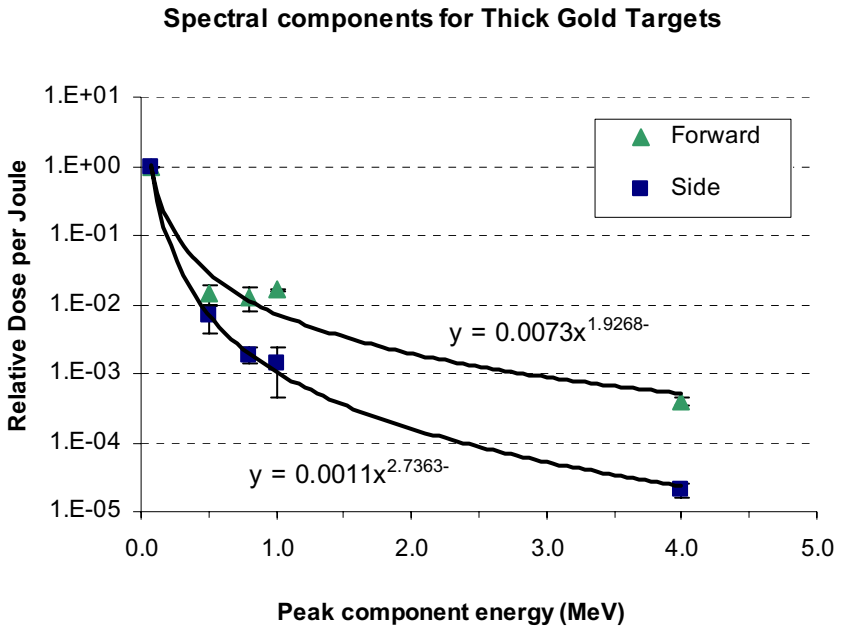

Figure 8.22: Spectral components of the radiation emitted from thick targets [9].

the radiation shielding if they exceed $\sim$ 2 orders of magnitude greater shot numbers than the thick target shots. Below this level, the shielding is dominated only by the thick target yields since the generated radiation from the low yield experiments is much softer. In addition, the potential for failed shots must also be considered since thin targets are likely to be mounted to thick substrates, and at high shot rates, a large number of effective thick target shots could be delivered accidentally by improper target alignment.

The facility commission plan will require dedicated shots for radiation shielding tests, with controlled ramp up of delivered laser energy to target, target thickness and target z. This commissioning period must be monitored and controlled by the local Radiation Protection Supervisor (RPS) in with full consultation with the site Radiation Protection Advisor (RPA).

Bibliography

[1] G. Battistoni et al., Proceeding of the Hadronic Shower Simulation Workshop 2006, AIP Conference Proceeding **896**, 31 (2007).
[2] A. Fasso, A. Ferrari, J. Ranft and P. R. Sala, CERN-2005-10 (2005), INFN/TC_05/11, SLAC-R-773.
[3] W. Lu et al., Phys. Rev. ST Accel. and Beams **10**, 061301 (2007).
[4] J. Fuchs et al., C. R. Physique **10**, 176 (2009).
[5] J. Davis and G. M. Petrov, Physics of Plasmas **16**, 023105 (2009).
[6] B. Qiao et al., Phys. Rev. Lett. **102**, 145002 (2009).
[7] C. J. Hooker et al., J. Phys. IV France **133**, 673 (2009).
[8] V. Vlachoudis Proceeding of the International Conference on Mathematics, Computational Methods & Reactor Physics (2009).
[9] R. J. Clarke et al., J. Radiol. Prot. **26**, 277 (2006).

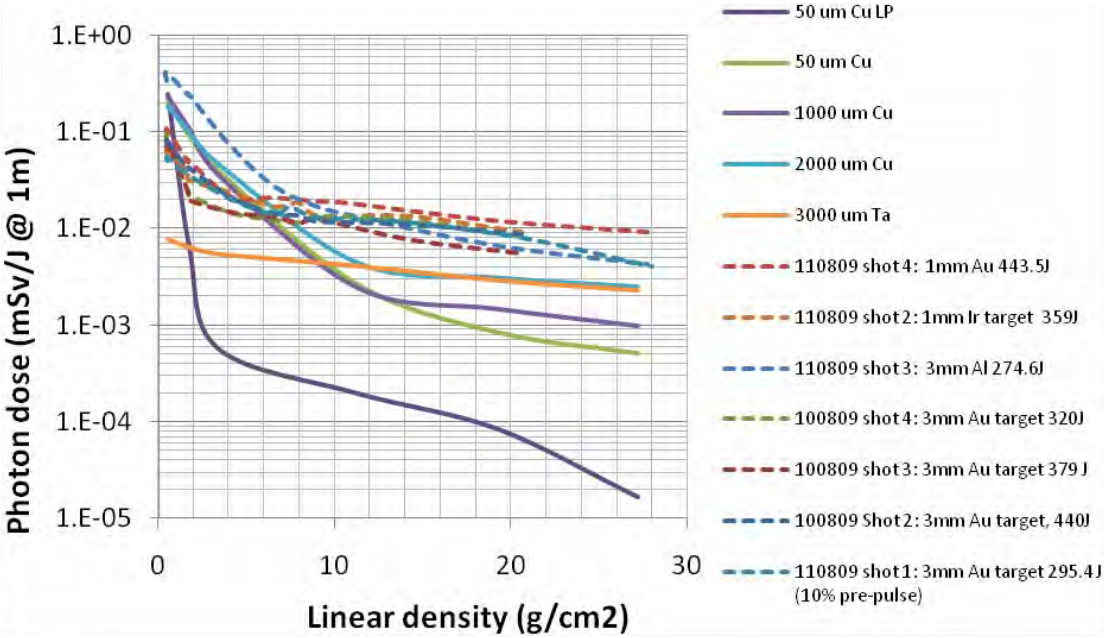

Figure 8.23: Filtered dosimetry data from TAP and Gemini as a function of linear density of filtration.

8.2.3 Activation

Activation studies were carried out in order to determine the high-Z material that should be used as main absorber in the dump of the electron acceleration area. Different samples of the four candidate materials (lead, stainless steel AISI-316L, iron and copper) have been simulated with a simple geometry: a cylinder 50 cm long and with a radius of 20 cm. With the aim to evaluate both the short-time effects, very important for the protection of the workers, and the effect of long irradiation periods, which are mostly related with decommissioning problems, two irradiation patterns with the 50 GeV electron beam have been considered: a 1-day irradiation period (100 shots/day considered as continuous), followed by an analysis of the residual radiation at cooling times that go from few minutes to several hours, and a 1-year irradiation period, followed by an analysis at longer cooling times. In Fig. 8.24 the results for the residual H*(10) distribution due to the induced radioactivity 10 minutes after the end of a daily irradiation is shown for the most and the less activated samples: the copper sample, which shows a specific activity of 2830 Bq/g, gives a dose rate at the level of 10 μSv/h at 1 m, while the sample in stainless steel, which shows the considerably lower specific activity of 134 Bq/g, gives a dose rate well below 1 μSv/h. The behaviour of the stainless steel after the 1-year irradiation has been found satisfactory as well, especially in comparison with the lead: the specific activity after one day of cooling for the AISI-316L has been estimated 364 Bq/g, to be compared with the value of 3925 Bq/g found for the lead. In Fig. 8.25 the distribution of the specific activity for the stainless steel sample after the long term irradiation is presented in the A–Z plane. These results have moved the choice of the absorber on the stainless steel.

8.2.4 Monitoring

The peculiarities of ELI experiments, different from standard accelerator, have to be taken into account. Accordingly to these peculiarities, main design criteria for choosing the features of

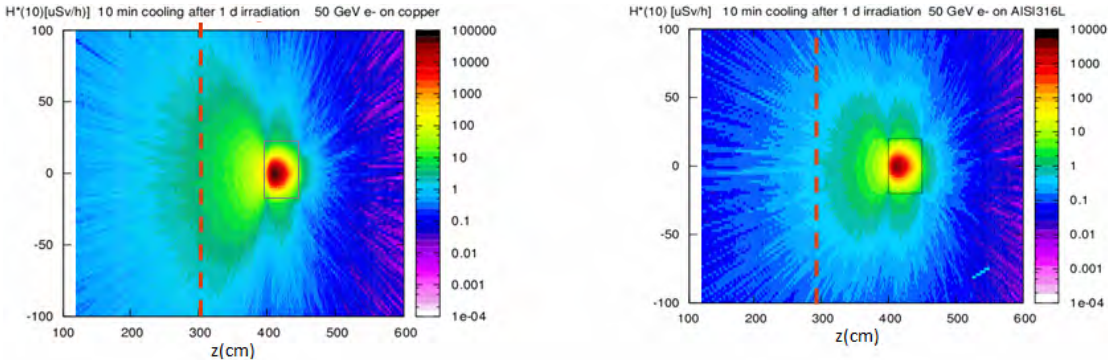

Figure 8.24: Residual Ambient dose equivalent (μSv/h) due to the induced radioactivity in two different high-Z samples (left: copper; right: AISI-316L), irradiated by the 50 GeV electron beam for 1 day operation time, 10 minutes after the end of the irradiation.

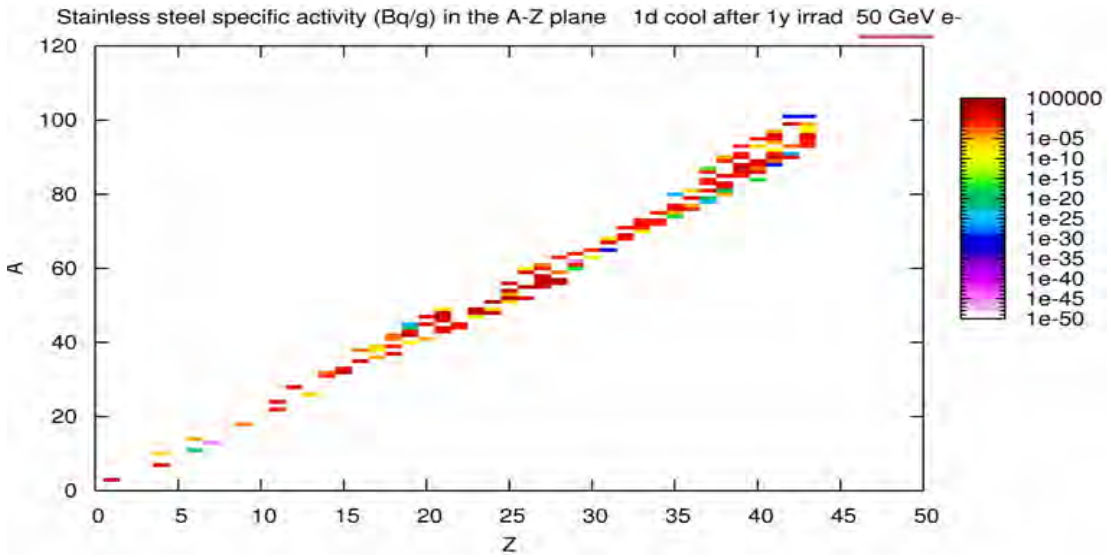

Figure 8.25: Distribution of the specific activity in the A–Z plane for the AISI-316L sample, after an irradiation of one year with the 50 GeV electron beam and a cooling time of 24 hours.

monitors to be used in and around ELI facilities are:

- Good efficiency to prompt radiation, taking into account a length of radiation pulse up to 20 fs;
- wide measurement range;
- sensitivity sufficiently high to detect a small fractions of the recommended limits;
- dose response curve in agreement with ICRP dose response curve, for neutron detectors;
- use of scintillation detectors for radioactive gas measurements;
- complete independence between monitors network and PC used for measure recording;
- fail safe;

8.3 Law

In this section, we delineate those aspects of major importance in the operation of particle-accelerator installations and provide design guidelines for radiation protection. These guidelines are necessary to prepare the licensing application in order to obtain the authorization for the operation of a facility.

8.3.1 Advisory Agencies

At the international level, three organizations are extremely important:
- The International Atomic Energy Agency (IAEA).
- The International Commission on Radiological Protection (ICRP).
- The International Commission on Radiation Units and Measurements (ICRU).

IAEA

The IAEA is the world centre for cooperation in the nuclear field and its work is guided by the interests and needs of the member states. Three main areas are considered:
- safety [1] and security;
- science and technology;
- safeguards and verification.

The IAEA has issued three reports, which deal with radiological operation of electron accelerators [2], proton accelerators [3] and neutron generators.

ICRP

The ICRP provides recommendations and guidance on all aspects of protection against ionizing radiation. The basic considerations of radiation protection were stated in Publication 26. [4] and reiterated in Publications 60 and 103 [5,6]. The following topics are treated in detail:
- definition of a source;
- types of exposure situations;
- categories of exposure;
- identification of exposed individuals;
- levels of radiological protection
- the principles of radiological protection: justification, optimization of protection and dose limits;
- dose constraints and reference levels;
- protection of environment;
- quantities used in radiological protection;

ICRU

The ICRU develops and promulgates the internationally accepted recommendations on radiation quantities and units, terminology, measurement procedures, and reference data for the safe and efficient application of ionizing radiation to medical diagnosis and therapy, radiation science, technology, and radiation protection. The ICRU has issued reports on basic aspects of high energy-particle interactions and radiation dosimetry, as well as on fundamental quantities and units for ionizing radiation [7].

Bibliography

[1] IAEA Safety series N° 115-I (1994).
[2] IAEA Technical Report Series N°188 (1979).
[3] IAEA Technical Report Series N°283 (1988).
[4] ICRP Annals of ICRP Publication 26 (1977).
[5] ICRP Annals of ICRP Publication 60 (1991).
[6] ICRP Annals of ICRP Publication 103 (2007).
[7] ICRU Journal of the ICRU Report 28 (1978).
ICRU Journal of the ICRU Report 33 (1980).
ICRU Journal of the ICRU Report 39 (1985).
ICRU Journal of the ICRU Report 47 (1992).
ICRU Journal of the ICRU Report 51 (1993).
ICRU Journal of the ICRU Report 60 (1998).

8.3.2 Regulatory Agency

The Council of the European Union, considering the treaty that establishes the European Energy Community (articles 2b, 30, 31, 32 and 33), has adopted the Directive 96/29/Euratom of 13 May 1996 [1]. This Directive lays down basic safety standards for the protection of workers and general public against the danger arising from ionizing radiation, taking into account the recommendations of International Advisory Agencies. The title X of Directive 96/29/Euratom establishes: "the basic safety standards for protection of the health of workers and general public against the danger arising from ionizing radiation with the aim of the uniform implementation by member states".

In addition, "If a member state is to adopt dose limits which are stricter than those laid down in this directive, it shall inform the commission and member states".

All member states should comply with this directive.

Bibliography

[1] Council Directive 96/29/Euratom of 13 May 1996.

8.3.3 ELI license

An exhaustive list of the general needs to prepare the licensing application, following the laws in force in the European Union, is reported below. On the basis of this list, it is possible to prepare a set of documents, which will be sent to the licensing authorities that will decide whether to authorize the commencement of a practice.

Description of the ELI project

Firstly, a general description, including the scientific motivations as well as the scientific case, has to be written.

Sitting and layout

Secondly, the geographic location of the ELI facility has to be detailed:

- A general description of the site where ELI will be constructed; information on site geography, seismology meteorology, hydrogeology, demography;
- a site map;
- a description of the border areas;
- a description of the activities outside the site;

- information on adjacent facilities that may affect the accelerator safety or may be affected by the accelerator operation.

Several factors play an important role in determining the optimum location of a radiological facility. The ELI infrastructure should be totally assimilated to an accelerator complex facility and the following factors should be considered by ELI management: radiological protection limits (workers and general public), environmental impact, accessibility and availability of existing buildings. It is important to select an appropriate location for any new facility. Sometimes, the cost of a radiological system such as the shielding for a big installation may represent a significant fraction of the total cost. It is advisable to develop a close collaboration between the responsible for the facility design and the responsible for the safety feature.

Radiological impact

Finally, we have to understand the radiological impact of the facility. This implies the following steps:

1. Specification of design parameters: type of particles accelerated, beam characteristics, maximum energy and current, duty cycle.
2. Specification of assumptions on expected operation: operation time per year and occupational factor for different buildings and locations.
3. Determination of radiation protection goals: assessment of the radiological risk for workers and general public under normal working and accident conditions.
4. Estimation of the radiation source strength.
   - Production of primary particles (electrons, protons, ions). Physical information concerning fluence, energy and angular distributions is needed.
   - Production of prompt radiation: bremssstrahlung, neutrons, muons, pions, kaons, and any other particle (charged particles, ions, nuclear fragments and delayed radiation).

At large distances, the radiation field due to the accelerator operation comprises two components: direct and scattered radiation. The term "skyshine" refers to all radiation scattered by the ground, air or neighbouring buildings:

- Neutron skyshine.
- Photon skyshine.

Induced radioactivity:

- Radionuclides produced in solid materials: accelerator structures and their ancillary components, shielding materials.
- Radionuclides produced in cooling water.
- Radionuclides produced in air: radionuclides produced directly in air and radionuclides produced in dust.
- Radionuclides produced in earth shielding and groundwater.
- Environmental impact and exposure of members of the public due to the prompt radiation field, included skyshine component, and to the residual radioactivity, mainly airborne and groundwater radionuclides.
- Noxious gas production.
- Radiation damage.

5) Specification of shield-walls and roof thicknesses, beam line dimensions, distances between facilities, and site features are required to accommodate the necessary measures for radiological protection.

6) Characterization and quantification of conventional hazards: non ionizing radiation, electrical, vacuum and pressure, magnetic fields, cryogenic, chemical, mechanical, noxious gases.

7) Description of other sources of radiation: several auxiliary systems are potential sources of ionizing radiation, including high-voltage systems, microwave power systems and cooling systems.

8) Ventilation of the buildings that house the facility and/or the target.

9) Commissioning program, including special and not routine operation.

10) Decommissioning program, including the monitoring and control of radioactive material and guidance for clearance.

11) Fire-prevention system.

8.4 Operative rules

8.4.1 Basic concepts of the laser safety procedure at ELI

In this section, we introduce some basic operation rules related to laser safety in ELI facilities.

All persons on ELI site should carry a badge

The badge should include selective access to individual labs (Staff – picture ID, User – picture ID, Visitor – temporary, no photo). It may also include a personal dosimeter, which should be RFID (Radio-Frequency Identification) based to allow permanent surveillance, at least inside NHZ (defined below). It should be provided at the reception desk.

Safety training procedure

1. User (validity 1–2 years)

Before arrival (through ELI website):

- registration (personal data, project info);
- self-study of general safety rules (laser, radiation, electrical, chemical, cryogens, first aid, other hazards) according to IEC standards [1];
- exam (multiple attempts possible)

After arrival to ELI:

- long (30 min.) video presentation showing specific rules on ELI site;-
- ELI orientation: visit to the experimental rooms with escort to show the actual operation regime in reality;
- Safety Certification will be issued by ELI and signed by the user.

1. Visitor (1 day validity)

- short (10 min.) video describing the facility;
- guided visit, always with escort (no safety training);
- for groups of more than 5 people (max. 20 per group), a list including personal data (name, ID/passport, address) must be sent in advance.

2. Staff

- detailed safety course;
- exam;
- periodic re-training every year, and updates by email whenever necessary;
- new examination after accident involvement if culpable. After relapsing twice no permission to enter NHZ

Medical surveillance (1 year validity)

1. Staff: regular complete medical check provided by ELI.
2. User: only for users who directly manipulate laser beams:
   - Ophthalmological certificate (visual acuity for each eye, visual field test, retinal fundus examination) before arrival, using ELI form;
   - after an experimental campaign, the user should sign a declaration of good eyesight (if not, a medical check can be provided by ELI after user request).
3. Visitor: no medical certificate needed.

Generic laser-safety procedures

1) Visitors must be always accompanied by an escort who has completed the safety training. Escort is directly responsible for the safety of the visitor and must stay with him/her all the time inside the ELI facility.
2) Other responsibilities of the escort: check that the laser is not operating while using the gallery (however, there should be an interlock); check that all the visitors have the badge; direct the visitors to the nearest exit in case of alarm.
3) Visitors must be registered in the "ELI Guest Book" (name, address, ID/passport).
4) Visitors can only access safe zones (outside NHZ).
5) Visits inside the experimental areas can be arranged on special request only.
6) Each experimental room and laser bay will have an observation gallery for visitors (including shutter, radiation shield and interlock) and few LCD screens to see details of on-going experiments.
7) Access to any experimental room is controlled by a card key (badge) system.
8) Light signals on each lab door (LASER OFF = green = free entry, LASER ALIGNMENT = orange = limited access (laser class 2), LASER ON = red = no entry).
9) Video cameras for NHZ monitoring.
10) Video displays at the entrance of NHZ with daily schedule and responsibilities.
11) Only authorized personnel may operate lasers. Authorization is received from the Laser Safety Officer (LSO) after training.
12) Design of laser beam paths, following the Standard Operation Procedures (SOP).
13) Avoid positions where the eyes approach the axis of a laser beam (even with eye protection on).
14) Keep beam paths below or above the standing or sitting eye levels. Do not direct them towards other people.
15) Do not damage laser protective housings, or defeat the interlocks on these housings.
16) Eliminate all reflective material from the vicinity of the beam paths.
17) Never use viewing instruments to look directly into a laser beam or its specular reflection. If this is necessary, install an appropriate filter into the optical element assembly.
18) Keep ambient light levels as high as operations permit.
19) Do not work alone when performing high-power laser operations.
20) Doors must be closed and locked during laser operations. The warning light on the top of the doors (internal side) must be on during operations. A light will indicate when the laser is not operating (OFF). An additional light will show when the laser is powered up (STAND BY) but not operating. Finally, a flashing light will indicate when the laser is operating (LASER ON).
21) Door windows, lab windows, open portals, etc. must be covered to prevent the escape of a laser beam, unless an interlocked laser beam path enclosure is provided.
22) Prior to shooting, perform a "countdown" or make an acoustic announcement to warn others that you are about to shoot.
23) In each experimental room, the presence of people will be automatically checked (RFID – radio-frequency identification).
24) An enclosure that surrounds the area of the laser focusing optics and encloses the immediate area of the workstation must be used.
25) During periods of beam access such as setup maintenance activities, protective equipment (eye protection, temporary barriers, clothing and/or gloves, respirators, etc.) should be used.
26) Laser protective eyewear must be worn whenever you are within the NHZ. Goggles (only one type for everybody) available near the door before entering. Special goggles for particular wavelengths might be used in addition by laser staff only.

27) Eyewear must have the correct optical density and offer protection at the wavelength(s) of the laser(s) being used.
28) LSO is in charge of the periodical inspection and replacing of damaged or defective individual protective equipment, i.e. eyewear, clothing, etc.
29) Appropriate wear for skin and eye protection during alignment operations must be used.
30) Use a low-power laser for alignments. If this is not possible, adjust your laser to minimum power levels and/or use a filter to bring down the power to safe levels.
31) Use viewers or viewing cards to sight where an invisible beam is. To sight where a visible beam is, use lower optical density laser protective eyewear or sight beams with a non-specular, dark coloured viewing card.
32) Terminate laser beams at the end of their useful path with immovable, non-specular, fire-retardant beam stops or targets.
33) During maintenance procedures, set up a temporary controlled area that restricts access to the nominal hazard zone. Remove only the minimum number of protective housings required to do the work.
34) In case of an emergency, call a special number for assistance. Emergency response personnel will be directed to you. An emergency power-off button is located in the lab to shut down power in the lab.
35) The laser-room doors shall allow both rapid entrance and exit under all conditions.
36) People unnecessary for the laser operation should be kept outside.
37) Class IV lasers [1] and laser systems require a master switch control. The switch can be operated by a key or a computer code. When disabled (key or code removed), the laser is not capable of operation. Only authorized system operators will have access to the key or the code.
38) Whenever possible, the laser system should be fired and monitored only from remote positions.
39) A laser warning sign shall be posted both inside and outside the laser controlled area.
40) Monitoring of the laser interaction rooms and laser bay via video cameras with zoom.
41) Access interlocks, active laser guarding, laser radiation monitoring devices, security video-cameras and laser threat warning system will be controlled from a Laser Safety Desk.

Definitions

Staff : ELI employees (permanent, contractual) or temporary workers (*e.g.* installing some device).

Escort : staff/user after the required training.

User : experimentalist.

Visitor : non-ELI employee, guest, staff/user before completing training.

NHZ (Nominal Hazard Zone): area where the laser-beam power exceeds the maximum permissible exposure levels. It is determined through the following characteristics: power or energy output, beam diameter, beam divergence, pulse-repetition frequency, wavelength, beam path including reflections, beam profile, maximum anticipated exposure duration. During maintenance or alignment operations, the NHZ extends to the entire lab or to the partitioned laser used area. Once the laser beam path is well defined and contained in a specific area, the NHZ may be reduced in size to the area where the experiment is taking place.

LSO (Laser Safety Officer): is the person who has the authority to monitor and enforce the control of laser hazards and perform the knowledgeable evaluation. The LSO administers the overall laser safety program, where the duties include items such as confirming the classification of lasers, evaluate NHZ, assuring that the proper control measures are in place and approving substitute controls, approving SOP's, recommend and/or approve eyewear and other protective

equipment, special appropriate signs and labels, approve overall facility controls, effect proper laser safety training as needed, effect medical surveillance and designate the laser personnel categories. For ELI, LSO must be a full time assignment.

Bibliography

[1] IEC Technical Report 60825 (2008).

8.4.2 The laser-based accelerator safety system

Design criteria

The purpose of the Operational Safety System program is to avoid life-threatening exposure and/or to minimize inadvertent, but potentially significant, exposure to personnel. A personnel protection system can be considered as divided into two main parts: an access control system and a radiation alarm system. The access control system is intended to prevent any unauthorised or accidental entry into radiation areas.

The access control system is composed by physical barriers (doors, shields and hutches), signs, closed TV circuit, flashing lights, audible warning devices (including associated interlock systems) and a body of administrative procedures that define conditions when entry is safe. The radiation alarm system includes radiation monitors, which measure radiation field directly giving an interlock signal when the alarm level is reached.

Interlock design and features

The objective of a safety interlock is to prevent injury or damage from radiation. To achieve this goal, the interlock must operate with a high degree of reliability. All components should be of high grade for dependability, long life and radiation resistant. All circuits and components must be fail safe (relay technology preferably).

To reduce the likelihood of accidental damage or deliberate tampering, all cables must run in separate conduits and all logic equipment must be mounted in locked racks.

Two independent chains of interlocks must be foreseen, each interlock consisting of two micro switches in series and each micro switches consisting of two contacts.

Emergency-off buttons must be clearly visible in the darkness and readily accessible. The reset of emergency-off buttons must be done locally.

Emergency exit mechanisms must be provided at all doors.

Warning lights must be flashing and audible warnings must be given inside radiation areas before the accelerator is turned on.

Before starting the accelerator, a radiation area search must be initiated by the activation of a “search start" button. “Search confirmation" buttons mounted along the search path must also be provided. A “Search complete" button at the exit point must also be set.

Restarting of the accelerator must be avoided if the search is not performed in the right order or if time expires.

The interlock system must prevent beams from being turned on until the audible and visual warning cycle has ended.

Any violation of the radiation areas must cause the interlocks system to render the area safe.

Restarting must be impossible before a new search. Procedures to control and keep account of access to accelerator vaults or tunnels must be implemented.

Radiation alarm system

The radiation alarm system should be composed by a network of gamma, neutron and radioactive gas monitors connected to a PC to record date. Each monitor in fact operates independently from the PC. The alarm triggers the interlock if the radiation level measured is greater than the prearranged level for the prearranged length (of time).

Data recording

The data acquisition and recording should be composed by a PC connected (in stellar model) to a monitors network. The PC records each shot or minutes in case of 10 Hz operation in ASCII TEXT format, the data or the data averaged on one minute of each monitor. The date and the time of the acquisition are also recorded together with the state of operation of the monitor (alarm or alert). In a separate file, only the alarm and the alert state are recorded with the corresponding values.

8.4.3 Access to experimental areas and material-transportation rules

The operating rules concerning personnel access to the experimental areas and material transportation to/from ELI sites will have to be established as well. While local site-specific operating rules will be implemented, they will have to comply with appropriate national and international rules and practices.

Depending on the host country, there are or will be national regulations defining the procedures for dealing with ionizing radiation. As an example, the UK facilities dealing with ionizing radiation follow four legislation acts: Ionizing Radiation Regulations (IRR 1999), Radioactive Substance Act (RSA 1993), Radiation (Emergency Preparedness and Public Information) Regulations (REPRIR 2001) and Carriage of Dangerous Goods & use of Portable Pressure Equipment Regulations (CDA 2009). These acts are available to the public and delineate general principles and procedures of dealing and transportation of radioactive objects such as:

- prior risk assessment;
- contingency plans;
- designation and monitoring of controlled areas;
- designation of classified persons;
- dose limits, assessment and recording;
- personal protective equipment;
- accounting, keeping and moving of radioactive substances;
- maintenance and examination of engineering controls;
- etc.

Finally, there will have to be local, site-specific rules established complying with certain national and international legislations. Local rules will define responsibilities and procedures related to the management and transportation of radioactive substances on a particular ELI-site. The STFC Safety Codes [1] in UK can serve as an example. Two documents (STFCSC 27 – Carriage of dangerous goods and STFCSC 29 – Management of ionizing radiation at work) define the responsibilities of the Safety team, regular staff, users and visitors. The designation and signing of controlled areas, monitoring of designated areas, access with permissions, maintenance of engineering controls and personal protective equipment, dose recording and training requirements are also considered. As for transportation of radioactive substances, the legal ways for road/air transport and packaging guidelines of dangerous goods are provided. Dangerous Goods Dispatch pro formas are depicted and completion and checking procedures of logistic documents are defined.

If a new kind of experiment is proposed, every effort must be made to identify potential hazards associated with the planned research activity. The unchecked materials cannot be brought to ELI site(s) without authorization of responsible safety personnel.

Bibliography

[1] http://www.shepublic.stfc.ac.uk/Codes/STFC/STFC.aspx.

9 ELI Facilities

9.1 Site decision process

On October 1st, 2009, in Prague, the Steering Committee of the ELI Preparatory Phase Consortium decided on a multi-site implementation of the Extreme Light Infrastructure. It gave the mandate to the Czech Republic, Hungary and Romania to jointly implement the ELI project through the construction of three facilities, each being dedicated to a specific dimension of ELI's scientific case. This outcome represents the result of an internal process of debate and evaluation on the best conditions of implementation of the Project. This section of the White Book provides information on how this decision was taken and on how the various options of implementation were screened. In conclusion, we briefly present the three sites chosen for the construction of the three first ELI facilities.

9.1.1 Organisation of the site decision process

The final decision on the implementation of ELI is the result of a long process initiated in at the beginning of 2008. A "Site Choice Committee" (SCC) was formed in order to define a procedure and a working plan. The role of the SCC was to favour the site implementation studies in order to identify suitable locations of the future ELI facility. In addition, in order to support the evaluation of the SCC, an external Expert Panel was appointed. The role of the Panel was not to point out the site to be chosen, but to provide recommendations according to the scientific and managerial experience of its members. The support from the Expert Panel proved very helpful to the SCC in order to define a scenario of suitable sites to locate ELI. The Panel members were selected amongst scientists involved in large-scale infrastructures or research agencies.

The composition of the SCC and Expert Panel was as follows:

- **ELI Site Choice Committee**
  - Rytis Butkus, University of Vilnius (Lithuania)
  - Dimitrios Charalambidis, FORTH (Crete, Greece)
  - Sandro De Silvestri, Politecnico di Milano and CNR-INFM (Italy), Chairman
  - Luis Roso, University of Salamanca (Spain)
  - Solomon Saltiel, University of Sofia (Bulgaria)
- **Expert Panel**
  - Mario Calvetti, Director of INFN National Laboratory (Frascati, Italy)
  - Jerome Hastings, "Photon Science" Faculty and Project Director at SLAC (Stanford, USA)
  - Jürgen Mlynek, President of Helmholtz Association (Berlin, Germany)
  - Sune Svanberg, Director of Lund Laser Centre (Lund, Sweden)

A call for site proposals was issued in February 2008 on the basis of a template application form listing the various characteristics of the proposed site to be considered and developed by the bidders. The form included in particular: (i) *Location of ELI; (ii) Rationale for hosting ELI; (iii) Quality of the region/country and impact; (iv) Level of the surrounding civil infrastructures; (v) Environment of ELI site; (vi) Accommodation of permanent and non-permanent staff; (vii) Financial aspects; (viii) Legal aspects and management.* Five applications were submitted, namely from Czech Republic, France, Romania, Hungary and United Kingdom.

The evaluation conducted by the SCC and the Expert Panel was based on a set of minimum requirements for hosting a large scale infrastructure as ELI, namely:

- *Quality and size of the scientific community relevant to ELI.*
  - Research Institutes with activities on high power lasers and related applications
  - Research teams in Universities on high power lasers and related applications
  - Research in optics in general and laser plasma physics
  - International visibility (e.g. participation to European projects and/or networks)

- *Quality and size of the industries relevant to ELI*
  - Small and medium enterprises in lasers and/or optical components
  - Small and medium enterprises in related construction needs as for example fine mechanical components, high vacuum technology, etc.
- *Synergy within existing and planned scientific initiatives*
  - National research programs on laser development or related aspects (past, present and future)
  - National programs on large scale infrastructures
- *Financial aspects*
  - Level of financial commitment
  - Regional/National funding capacity
  - Expected level of structural funds
  - Level of involvement in the running costs

An evaluation session was held on April 17–18th 2009 in Stresa (Italy) in the presence of the SCC, the Expert Panel and the bidders. Each proposal was judged through the identification of strong and weak points with respect to the criteria listed above. The Chairman of the SCC issued the report resulting from this evaluation session on April 28th.

9.1.2 Terms and milestones of the decision on the conditions of implementation of ELI

The report of the SCC served as a reference framework to the subsequent discussions on the implementation of ELI held within the Steering Committee of the ELI-PP Consortium. On May 20th, 2009 in Paris, the Czech Republic was mandated by the Steering Committee to start negotiations with other members of the ELI-PP Consortium on an "Integrated Proposal" offering sufficient guarantees for the successful implementation of the Project from a financial, governance, scientific and technical point of view, according as following:

1. ELI should be a multi-site infrastructure placed under a single governance
2. The Integrated Proposal should encompass the whole scientific case of ELI including the ultra-high-intensity “pillar” of the project.

Czech Republic, Hungary and Romania were involved in the join negotiations and work on an Integrated Proposal complying with the above principles.

On October 1st, 2009, the Steering Committee approved the Integrated Proposal presented by the three countries. The funding agencies of the 13 countries involved in the ELI-PP Consortium gave the mandate to the three countries to jointly implement ELI as a distributed infrastructure through the construction by end 2015 of three research facilities specialised in the attosecond, high-energy beam and nuclear physics applications of the Project. It was also decided that a fourth “pillar”, dedicated to the emblematic ultra-high field applications of ELI, would be implemented later on under conditions to be decided in 2012 on the basis of a review of the performance and readiness of the various technological options. This last pillar will be the result of an incremental development of the laser sources with unprecedented peak power performance, from tens of petawatts up to a fraction of exawatt. The location of this pillar will be decided after validation of the technology.

The unity of the Project and the interdependence of its components will be pursued by jointly operating within a single pan-European Consortium established under the legal form of an ERIC (European Research Infrastructure Consortium). In order to coordinate their efforts during the implementation of the Project, the three countries complied with the resolutions of the Steering Committee and signed a Memorandum of Understanding on April 16th 2010, whereby an interim structure – the *ELI Delivery Consortium* – is established. Its purpose is twofold:

- Defining a single, robust technical delivery plan encompassing the whole Project and optimising the use of the financial, technological and human capacities available in Europe
- Defining the Statutes, Governance model and Financial and Contribution Plan of the ELI-ERIC, as well as coordinating the completion of all proceedings related to the establishment of this Consortium.

As detailed in Chapter 10 of the White Book, the three founding countries have invited all the other partners involved in the Preparatory Phase to join the ELI Delivery Consortium.

9.1.3 Rationale of the distributed implementation of ELI

The decision of the Steering Committee on the conditions of implementation of ELI takes into account a variety of motivations. However, the scientific and technical requirements of the Project were considered in the place.

The detailed definition of the scientific case of ELI represented one of the main objectives of the Preparatory Phase. This task resulted in a significant expansion of the scope of the Project with the identification of a large variety of research opportunities which had not originally been identified. Eventually, the scientific ambition of the Project was depicted through the image of a four-pillar structure with the first following three "Grand Challenges" supporting a fourth one:

- **High Energy beam facility and X-rays:** ultra-short energetic particles (> 10 GeV) and radiation (up to few MeV) beams produced from compact laser plasma accelerators
- **Attosecond science:** snap-shot in the attosecond scale of the electron dynamics in atoms, molecules, plasmas and solids
- **Laser-based Nuclear Physics:** radiation and beam particles with high energy suited to nuclear process studies
- **Ultra-high field Science:** access the ultra-relativistic regime. Investigations in particle physics, gravitational physics, non-linear field theory, ultrahigh pressure physics, astrophysics and cosmology (at intensities exceeding 10^{24} W/cm^2).

In the report issued in May 2009, the ELI-PP Scientific Advisory Committee acknowledged this approach: "*We believe that this broad and yet deep and layered science goals with multiple pillars are what ELI is really unique about among the contemporary large and acute science projects, where too often the projects are nearly single-purposed and too narrowly (or too 'precisely') defined.*" Their conclusion was: "*With this philosophy of ELI understood, we praise the choice of four pillars*".

Based on these scientific grounds, the decision of the Steering Committee represents an attempt to make the best use of the political support and financial resources available among the countries involved in the Project, with the objective of enabling the swift materialisation of ELI within acceptable risk.

- On the one hand, indeed, in a context where the interest in high intensity laser science is booming at global level, the swift development of ELI is considered a priority for Europe's scientific competitiveness. The availability of structural funding in the three hosting countries, in addition to a strong political support, was analysed as a unique opportunity to gather sufficient funding and materialise the first phase of the project. The impossibility of pooling structural funds stemming from different countries due to the conditions applying to the use of this kind of funding supported the scientific and technical arguments in favour of a multi-site implementation.
- On the other hand, from a political point of view, establishing a large-scale Research Infrastructure of the magnitude of ELI in three new Member States appeared as a major opportunity to support the development of the European Research Area (ERA), the cornerstone of EU's research objectives. ELI will indeed represent a significant contribution to a better balance in the distribution of Research Infrastructures in Europe (there is no other Research Infrastructure of such a scale in the new Member States). Finally, the three ELI

facilities, forming a single infrastructure, will have the potential for promoting mobility of researchers while preventing brain drain, a curse that has long affected Central and East European countries.

9.1.4 Elements on the sites of the three first ELI facilities

In Czech Republic the ELI pillar will focus on providing ultra-short energetic particle (above 10 GeV) and radiation (up to few MeV) beams produced from compact laser plasma accelerators at enhanced repetition rates. In Hungary the ELI pillar will be dedicated to extremely fast dynamics by taking snap-shots in the attosecond scale (10^{-18} s) of the electron dynamics in atoms, molecules, plasmas and solids. In Romania the ELI pillar will focus on laser-based nuclear physics. Atomic processes are well suited to the visible or near visible laser radiation: ELI will make possible radiation and beam particles with much higher energy suited to nuclear process studies.

- **ELI Beamlines Facility in the Czech Republic**
  The ELI facility will be located in a small town called Dolní Břežany, in the immediate Southern vicinity of Prague in the Central Bohemia Region. The location is in close proximity to the nearly completed Prague motorway ring, which directly connects to the European motorway network and to the International Airport (see Sect. 9.2).
- **Attosecond Pulse Light Source Facility in Hungary**
  The city of Szeged is located in the south part of Hungary very close to the Serbian (12 km) and Romanian (48 km) border. Szeged can be reached from Budapest via motorway M5 in 1.5–2 hours (170 km). The proposed site is within a distance of 1 km from the Szeged North junction of M5. The construction of the M43 expressway started in 2008, and is to be opened in 2010 improving accessibility towards Serbia, Montenegro, and Romania.
- **ELI Nuclear Physics Facility in Romania**
  The ELI Nuclear Physics Facility will be located in the campus of Magurele, which is located in the Bucharest metropolitan area. Magurele can be easily reached from both inside Romania and abroad, in particular thanks to two international airports situated within 30 and 20 km distance from Magurele. The construction of a third airport of a significantly larger capacity to be located 15 km from Magurele is scheduled by 2015 (see Sect. 9.4).

9.2 ELI-Beamlines in the Czech Republic

The ELI-Beamlines will be a modern, cutting-edge laser facility enabling many research and application projects involving interaction of light with matter at intensities that are more than 100 times greater than the values achieved at present. ELI-Beamlines will be delivering ultrashort laser pulses lasting typically a few femtoseconds (10^{-15} s) and is upgradeable to attain peak intensities of up to 200 PW.

The primary mission of the ELI Beamline Facility will consist of producing an entirely new generation of secondary sources driven by ultra-intense lasers. These secondary sources will produce pulses of radiation and particles such as flashes of X-rays and gamma-rays, bunches of accelerated electrons, protons and ions, etc., exploitable as unprecedented research tools in many research disciplines and in the development of new technologies.

The research agenda using the ultrashort and ultra intense pulses delivered by the ELI laser will focus on the following main activities: X-ray sources driven by ultrashort laser pulses, particle acceleration by lasers, applications in molecular, biomedical, and material sciences, physics of plasmas, physics of high energy densities and of warm dense matter and exotic and frontier physics.

The establishment of a favourable environment for the development of advanced cutting-edge technologies will strengthen the research, development and innovation potential of the Czech Republic of course, but the ELI Beamlines facility, jointly with the other ELI facilities, will also represent a major contribution to Europe's competitiveness in the field of laser research.

This section provides details on the beamline scheme projected for the facility, and indications on the site, the design of the building, the financial requirements and implementation schedule.

9.2.1 Beamline scheme

Laser Layout

The schematic layout of the ELI Beamlines facility is shown in the below figure.

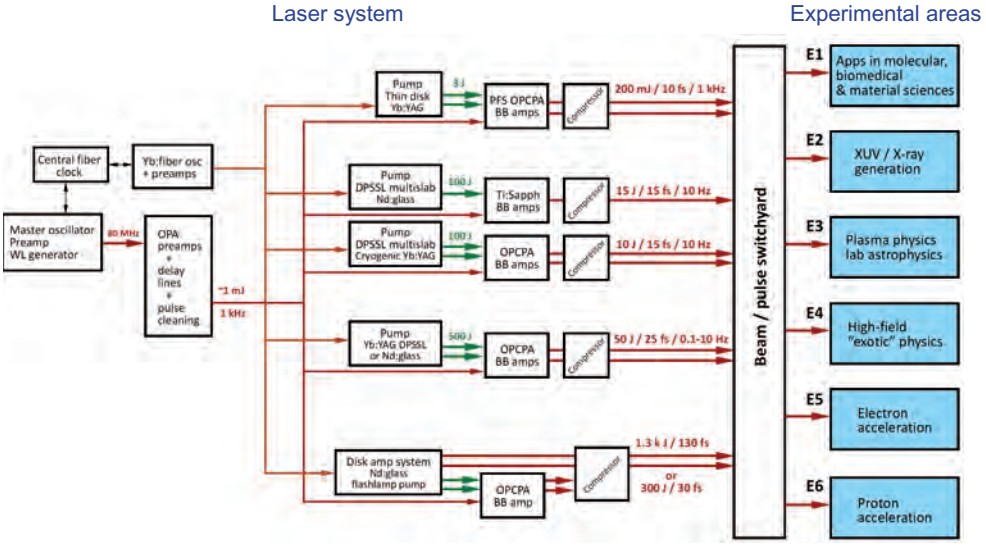

Figure 9.1a: Schematic layout of laser chains of ELI-Beamlines. Its primary mission will be to deliver repetition-rate ultrashort pulses with up to 50 J of energy, and contribute to development of the high-intensity systems. The two 10-PW laser blocks will serve to development and testing of selected technologies (OPCPA and/or Ti:Sapphire). Pulse compressors are not represented.

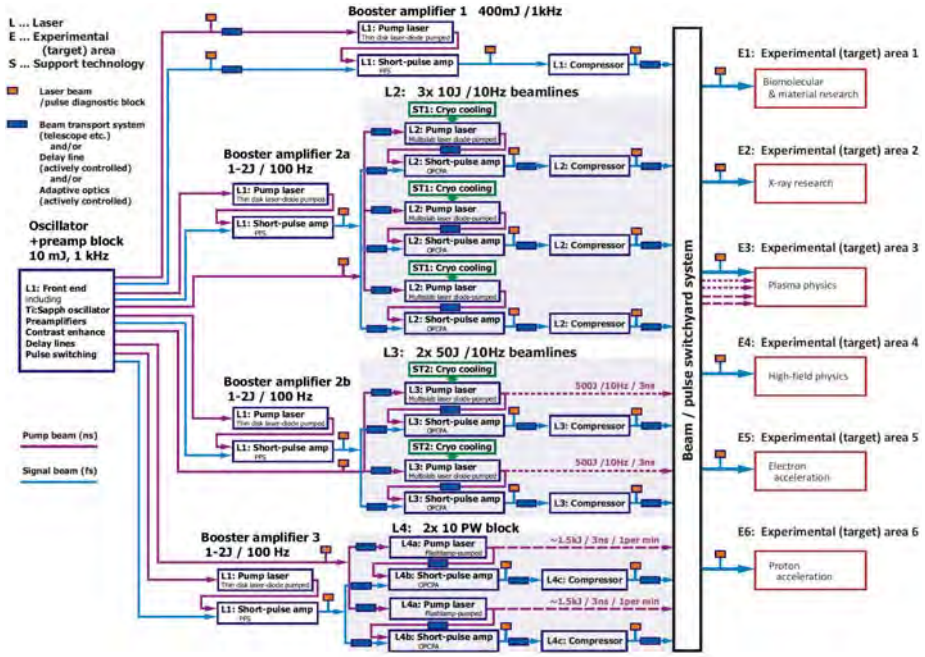

Figure 9.1b: System layout of laser chains of ELI-Beamlines, indicating the pump lasers.

The laser consists of:

- Front end including the oscillator section and the three booster amplifiers;
- Beamlines with output energy 10 J, including pulse compressors;
- Beamlines with output energy 50 J, including pulse compressors;
- High intensity 2×10 PW section, including pulse compressors.

i. Front-end: Oscillators, OPCPA

The laser front end will consist of the oscillator section (three optically synchronized identical oscillators) delivering ~ 5 fs pulses with > 200 nm equivalent bandwidth, pre-amplified by the PFS technique to approximately 10 mJ level. The front end will supply pulses into booster repetition-rate amplifiers based on the PFS technique and pumped by thin disk lasers currently prototyped at the Max-Planck Institute for Quantum Optics (MPQ) in Garching and at the Max-Born Institute (MBI) in Berlin. The system will involve two types of the booster amplifiers: the first type running at 1 kHz and providing equivalent energy of 200 mJ in the compressed pulse, the second type running at 100 Hz and delivering equivalent energy of about 1 J in the compressed pulse. The first type will deliver pulses directly to the experimental areas, whereas the second type will feed the beamline power amplifiers and the 10-PW test laser blocks.

ii. High-Power Amplifiers OPCPA, Ti:Sapphire

The beamline power amplifiers will be based on the OPCPA technique, driven by repetition rate diode pumped solid-state lasers (DPSSL) at a frequency of 10 Hz. The OPCPA technique is preferred as nominal solution due to its large bandwidth and a possibility to provide high output energy at a significant repetition rate. The DPSSL pump systems for the beamline power amplifiers will be a critical component for successful delivery of this Research Activity. These pump systems will be based on a multi-slab cryogenic amplifiers and will represent today's cutting-edge technology. Development and optimization of these lasers and associated technologies is to be accomplished, partially within this project.

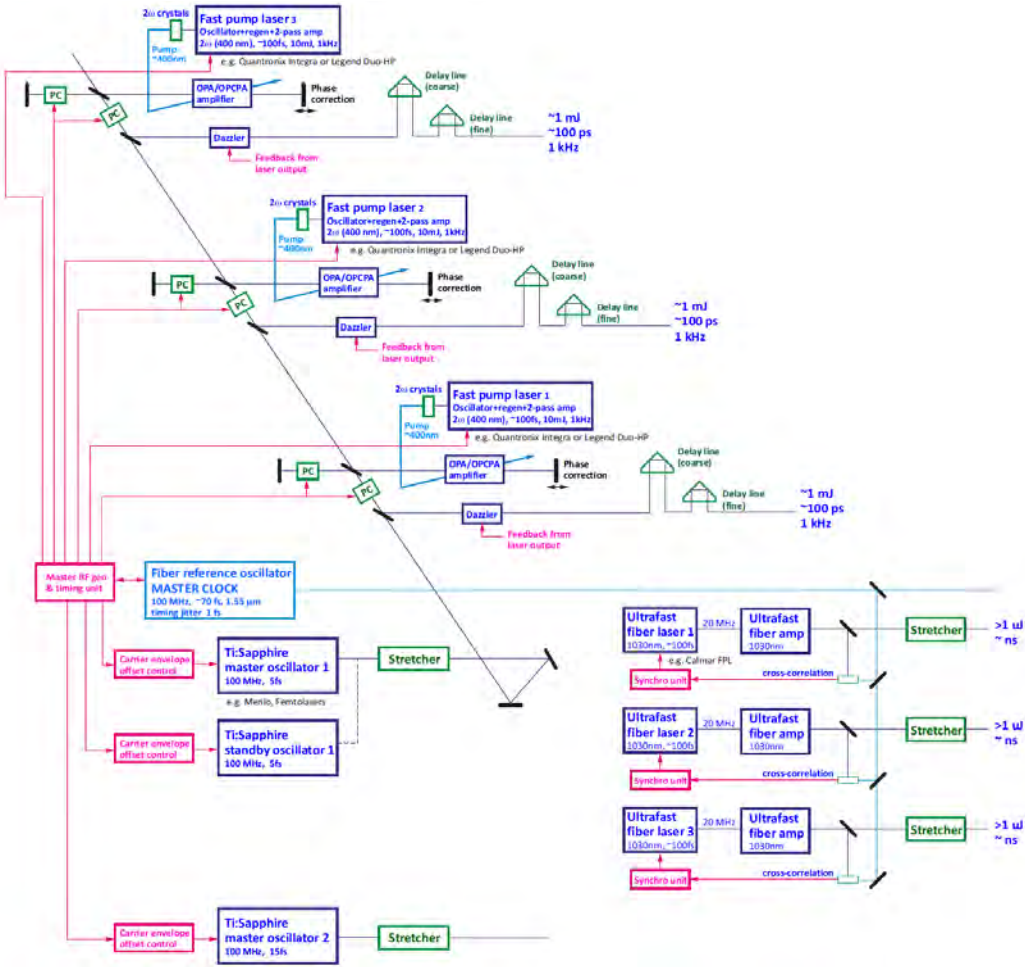

Figure 9.2: Proposed scheme of the ELI-Beamlines front end.

The designed laser system will involve two types of repetition-rate beamline power amplifiers, both operating at 10 Hz. Two identical beamlines of each type will be installed in the facility. The first type will deliver approximately 10 J of compressed energy, implying requirement for $\sim$100 J (at the fundamental wavelength 1 μm) pump pulses. The second type will provide about 50 J of compressed energy and will thus require $\sim$500 J pump pulses. One 10 J and one 50 J beamline will be dedicated to the target area for electron and acceleration, and will be compressed to provide flexible pulse lengths between about 50 and 200 fs.

The fallback solution for the beamline power amplifiers will be Ti:Sapphire technology using as pump systems conventional Nd:YAG flashlamp lasers, at repetition rate of 0.1 Hz.

iii. Pump lasers

The front-end systems of the ELI-Beamline will extensively use thin disk pump lasers providing 1–2 ps long pulses. These thin disk pump lasers for repetition rates 100 Hz to 1 kHz will be based on the architecture currently developed at the Max Planck Institute in Garching and at the Max Born Institute in Berlin, constituting today's cutting-edge technology; collaboration on prototyping and optimization of these lasers will also be the subject of activities covered by ELI-Beamlines.

The laser design involves two types of repetition beamlines, providing respectively 10 J and 50 J in the compressed pulse, both at repetition rate 10 Hz. The amplification technique will be OPCPA. The most critical element of the beamlines will be DPSSL pump systems providing respectively 100 J and 500 J at the fundamental harmonics (1.05 microns for Yb:YAG ceramic). These pump lasers have been conceptually designed at the Rutherford Appleton Laboratory (UK), based on the technology demonstrated by the Mercury laser at the Lawrence Livermore National Laboratory (60 J with 10 Hz rep-rate). The architecture uses a stack of variably doped cryo-cooled Yb:YAG ceramic slabs, face-pumped by laser diode arrays. Extensive international collaboration, especially with the Rutherford Appleton Laboratory, on prototyping and optimization of these pump lasers will be one of key research topics of this project.

The fallback solution for the beamline power amplifiers will be Ti:Sapphire technology using as pump systems conventional Nd:YAG flashlamp lasers. This technology is matured and commercially available. If used here, the beamlines will provide repetition rate of 1 shot per minute (= 0.016 Hz).

iv. Stretchers and Compressors

The compressors of the 10 PW beamlines are based on the design considered for the 10 PW facility at the Rutherford Appleton Laboratory. The current proposal is based upon Au gratings however it is envisioned that with the development of the MLD gratings that they might have achieved sufficient maturity to provide a better solution. Although in the short pulse duration laser induced damage threshold gold and MLD gratings demonstrate similar damage threshold levels.

The design envisions availability of gratings will become with a size of 920×530 mm. This should allow an approximately 70% increase in the amount of energy that the compressor is capable of withstanding. If a MLD or hybrid MLD/Gold grating solution can be found then the efficiency of the throughput of the compressor could be increased as well. If we assume 98% diffraction efficiency for the MLD gratings then the throughput will increase to 92%.

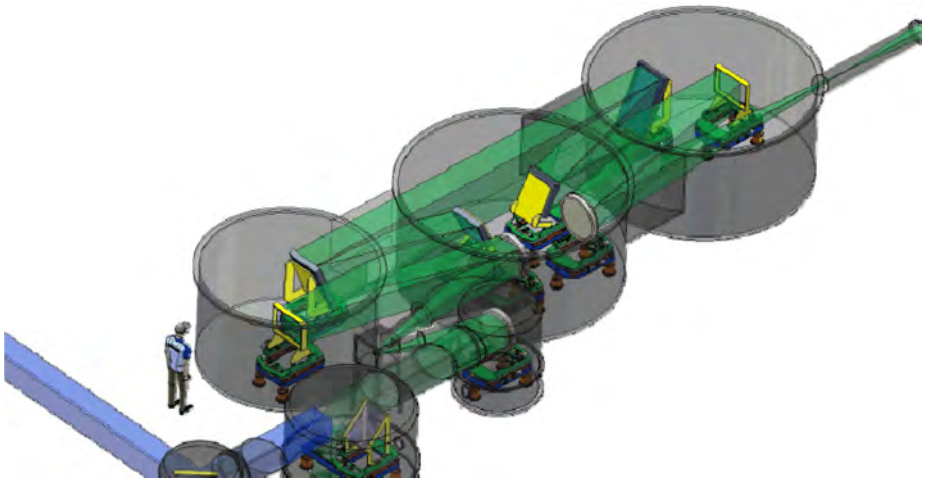

Figure 9.3: Visualization of the 10-PW compressor design that will be built at as a part of the 10 PW Vulcan project at the Rutherford Appleton Laboratory. The compressor is designed for 900 lines/mm gratings and for out-of diffraction plane Littrow configuration (courtesy of J. Collier, RAL).

v. Beam distribution system

The figure below shows the preliminary layout of the beam delivery architecture. Two beam/pulse switchyards will be located along the ground floor, while one switchyard system to distribute additionally large-energy pulses will be located in the underground experimental floor. This pulse delivery is one the facility systems that will be remotely controlled and fully automated, and will integrate fundamental beam diagnostic systems.

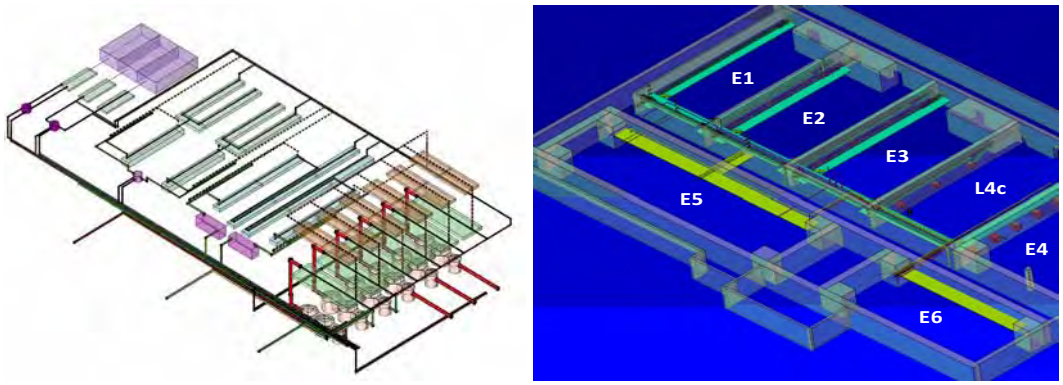

Figure 9.4: Designed beam delivery implementation of the ELI facility. On left, overall scheme is indicated. On right, servicing gantries along the beam distribution lines are shown.

System control

The ELI Beamlines systems will be based on robust industrial controllers using modular PLC systems and distributed input-output peripheral systems (most likely based on PLC Siemens industrial standard); similar systems are now used in cutting-edge automotive and aerospace applications. The baseline scheme of the control system is displayed in Fig. 9.5 below. The core of the system consists of an array of PLCs (programmable logic controllers). The master PLC and the slave PLCs are linked by a robust, interference-resistant, system bus (e. g. Profibus). Each PLC is located near a specific technological unit/node (e. g. amplifier head, pulse compressor, cryogenic unit, vacuum chamber, etc.) that has to be individually controlled. The PLC units provide hardware warning signals, which ensures maximum robustness and operation reliability.

The PLC units will be equipped with HMI (human-machine interface, e. g. touchscreens, keyboards) for local manual control, and will also make use of e. g. Labview for data visualization. The local manual control (local peripheries) will be exploited especially for the start-up period, system testing, and maintenance purposes. The local peripheries are linked to the local PLC by means of standard I/O links or standard interfaces. The sensors and actuators (e. g. beam sensors, valve coils, position sensors, limit switches) of the monitored and/or controlled components are linked to the local PLC via distributed I/O units and local bus. This concept ensures robustness of the system and resistance to interferences, minimizes the need of cabling, and allows for expansion of the system. All important data (configuration, working stages, faults, accesses, etc.) are stored in the main data storage unit.

The whole control system will be entirely separated from other local control subsystems, LANs, personal computers, etc., and will have a dedicated UPS power backup. This will ensure maximum operational reliability of the control system. In order to facilitate interaction with the control of particular experiments, privileged users will be able to enter the system through a sole external access point. This exclusive access point/gate using dedicated HW and SW tools will protect the control system against external environment.

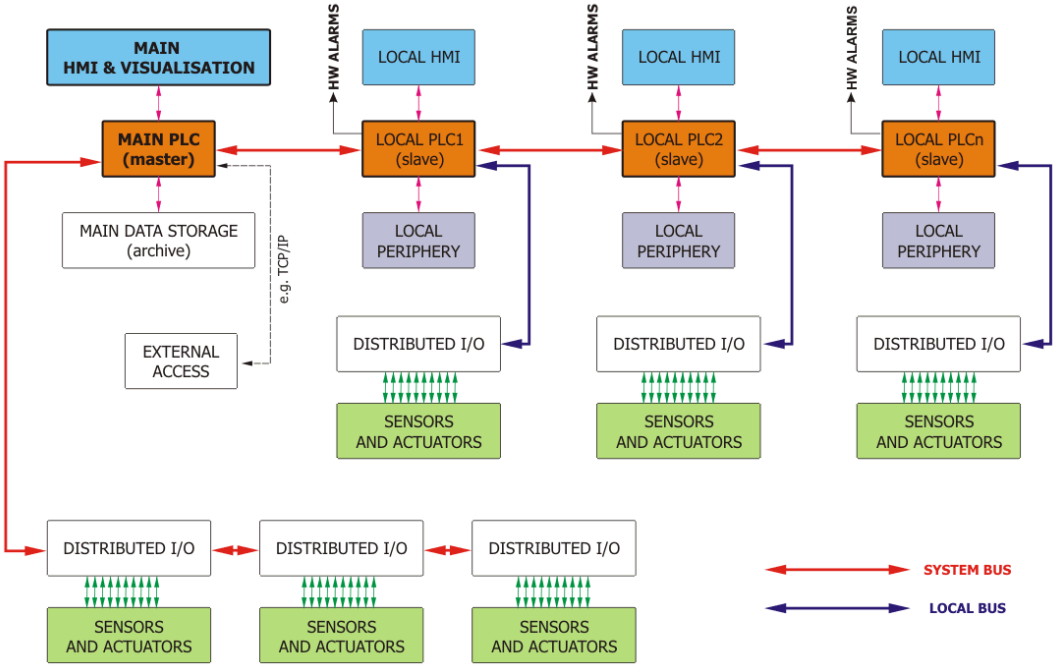

Figure 9.5: Preliminary concept of a system for the control of the laser chains and of pulse distribution into the experimental areas at the ELI-Beamlines facility. It is based on robust, state-of-the-art, modular PLC units and distributed input-output peripheral systems ensuring transmission of individual signals to the PLC via interference-resistant serial bus. The system is expandable; selected components can be commanded remotely by e. g. TCP/IP communication.

9.2.2 Site and building

The ELI Research Center complex consists of two main units: an administrative building and a laser research building; together the complex of buildings is able to accommodate approximately 300 people[1]. The two buildings and their respective sub-building wings are physically interlinked and easily communicate with each other, thereby creating within the complex the atmosphere of an academic campus.

The campus style buildings and their wings have been located in accordance with the regulation study provided by local authorities. Based upon the town's planning guidelines, the laser research building has been located at the southern part of the site with the administrative functions and publicly accessible facilities being located adjacently to the North. Equally important when setting the placement of the building functions was the configuration of the existing terrain.

The administrative building consists of offices, supported by a series of multifunctional spaces; these are connected via an atrium space. The building's East/West orientation allows natural ventilation by means of a structured ventricular system. Offices are located in the western part of the building next to the representative lobby. It calculates with the minimum of 80 offices, including 20 offices, each for one manager, 40 offices for 2 people and 20 offices for 3 people. Furthermore within building, there are three designated areas addressed as freely available, so-called "open space": each is able to accommodate 10 people and five development laboratories. The administrative building further includes a classroom for 40 students, three

[1] Maximum utilization capacity of the building in headcounts.

meeting room/lounges, each for 20 people, a lecture hall for 150 students, a library and reading room.

The monolithic structure, housing the highly sensitive laser equipment, will be isolated from the general structure and designed to withstand a vibration frequency of 30 Hz, which is resistant to external vibration (vehicle traffic, etc.), air-conditioned and heat stabilized. The laboratories will be located to the West of the laser adjoining the isolated 'box'. There are included laboratory testing and metrology laboratories (5 rooms, each min. 20 m^2), the assembly rooms (3 rooms, each min. 30 m^2), mechanical and optical workrooms (5 rooms, each min. 30 m^2), laser control rooms and experimental units (4 rooms, each min. 20 m^2), and ancillary office/analytical spaces for 75 people (approx. 15 rooms).

Figure 9.6: Visualization of the entire technology park.

Characteristics of the site of ELI-Beamlines facility

i. Overview of the site

The ELI facility will be located in a small town called Dolní Břežany, in the immediate Southern vicinity of Prague in the Central Bohemia Region. The location is in close proximity to the nearly completed Prague motorway ring, which directly connects to the European motorway network and to the International Airport.

The town of Dolní Břežany is located immediately beyond Prague's Southern administrative border. It is a progressive, developing community with a clear and coherent concept of local and regional development. This is evidenced by the town's public school and its newly completed commercial centre/ town square, where one finds a complex of buildings for residential and commercial-administrative-business use, and a new 3.5 hectare public park with lake.

Peripheral to the town centre, there are residential areas, sports facilities and areas for production. Near the new centre is a Baroque chateau, which is in the list of national cultural heritage; it is anticipated that this chateau will within the next few years be reconstructed for use as a four star hotel with restaurant. Land lying between the chateau and the town's

municipal house is to be upgraded to become a new administrative pedestrian square that will also serve as a front door to the technology park.

These architectural alterations shall result in the creation of a representative urban axis connecting the new commercial centre, the new pedestrian zone in front of the chateau and the municipal house and the new technology campus to be comprised of ELI buildings. This representative, science and technology park will offer employees a pleasant working environment with sufficient support services and opportunities for relaxation, leisure and other outside activities.

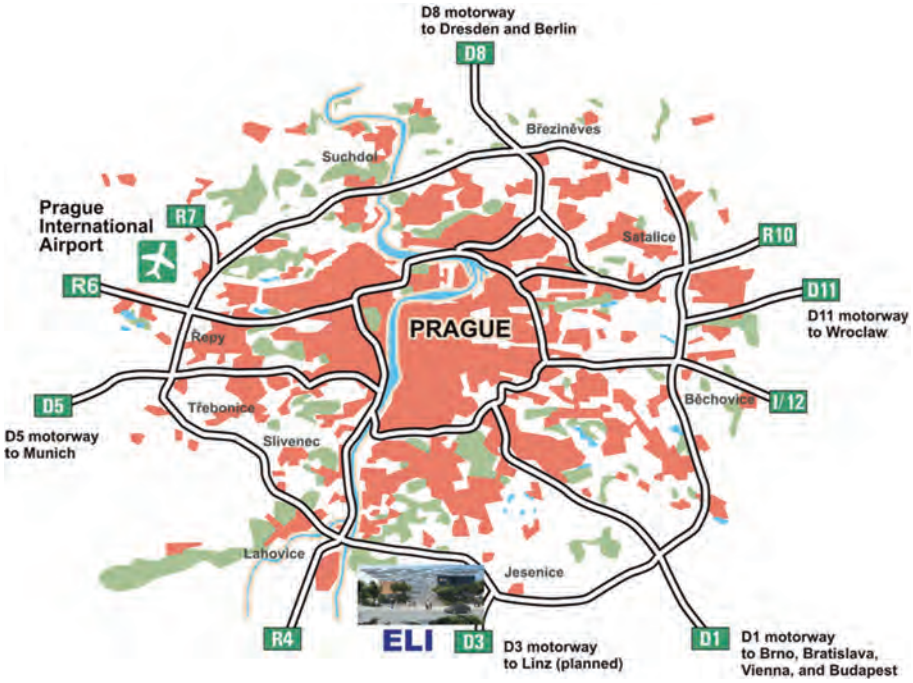

Figure 9.7: Town Dolní Břežany – location.

The ELI building is to occupy the brown-field site adjacent to the chateau. Nowadays, the brown-field site is used for agriculture, storage, production facilities and garages. According to the town's master plan ratified in September 2009 by the municipal assembly, this area has been zoned for civic amenities/ science and research. The land area designated for these functions provides sufficient area for the project itself and for other projects with similar function. An area for further, similar development is located immediately to the south of this existing brown-field site.

Regarding the demographic situation, Dolní Břežany exceeded in the thirties of the twentieth century to 1000 people. In the postwar period, the development of the population basically stagnated and even dropped ine eighties. However, there has been a significant increase since 2000. Currently, the population of Dolní Břežany is 2911. In the future a further increase in population of approximately 4000 can be expected. Mainly due to proximity of the City of Prague and related trends in migration in the territory.

ii. Main raisons supporting the choice of the site

Four main considerations have driven the choice of this site: its adaptation to the technical requirements of the facility, especially in terms of security and stability, the possibility for future expansion, its connection to required infrastructures and utilities and its accessibility.

Figure 9.8: Town Dolní Břežany – overview of town's important places.

- The building plot contracted for the ELI Facility includes protective buffer zones on its west, south and east sides. The positioning of the ELI Facility was based on the geometry of the land in an effort to minimize impacts of any surrounding vibrations on the laser building, and the laser and technological systems placed within. Eliminating the impacts of all surrounding vibrations on the laser systems is the essential key factor for the successful completion of the

entire project.
Measurements of the residential vibrations at the site of the future laser hall as well as calculations of the transmission of such vibrations on the construction of the monolithic laser building have therefore become a part of the Project Preparation Phase. Resulting data have shown that in the existing vibrations environment the proposed building meets the positional stability requirements (variance < 10 micrometers), while two essential factors must be maintained at all times: preserving the distance set from the westerly situated road (Ke Zvoli Rd.), and the absence of additional tremors from vibration sources in the immediate vicinity of the laser building. That is why the presence of the buffer zone around the entire laser building is of such essential importance in securing the future operation of the ELI Facility.

- The arrangement of the ELI Beamlines buildings on the site and the structural design of the Laser Building in particular, allow the possibility of an upgrade that would provide space for the 4th pillar of ELI. This would require construction of additional underground experimental halls to the south and east and extending the laser system.

Future expansion could also include other facilities such as a technology incubator park on the lot of land extending to the south. The diagram below shows the layout of the currently projected ELI-Beamlines Laser Building (blue) and its possible future expansion area (red).

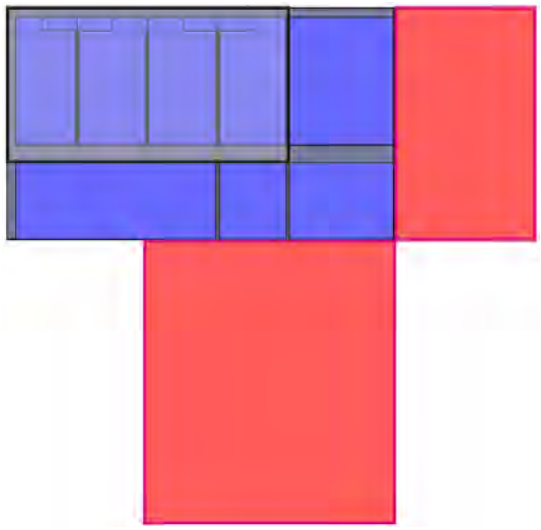

Figure 9.9: Schematic concept of future expansion of the ELI-Beamline facility (in red).

Construction features will be included in the base-build design that will facilitate future expansion. In particular, fully framed openings will be formed in the basement walls at access points to the extension areas. These openings will be filled with concrete blocks and waterproofed as necessary. Stub walls and slabs containing sufficient length of starter bars will be provided where structurally necessary to ensure stability of the future building extensions.

- ELI's proposed complex of buildings will be connected with all existing engineering networks today located along 5.Kvìtna Street. Regarding utilities, ELI building shall be connected to new infrastructure to be built by the village pursuant to the project TECHNOLOGY CENTER Dolní Břežany – Phase I engineering network. This project calls for building a new water main, sewer lines, gas lines, electrical cable distribution, distribution of public lighting and communication lines. A new electric transformer station within the project boundaries is to be built by ČEZ.

- Dolní Břežany village is connected to Prague's broader public transportation by regular bus service running to Budìjovická in Prague 4, where there is direct link to the metro line C and the city's tram network. The Prague ring road "R1," now in its later stages of realization, is to be completed on November 2010. When finished, it will connect the village with all motorways; traveling to Prague airport Ruzynì by car will require 20 minutes. According to Prague's overall city master plan, a new metro line D is to be constructed (present projected date of completion is the year 2017) that shall extend metro service to the southern limits of the city and shall terminate in Písnice, 3 km distant from Dolní Břežany.

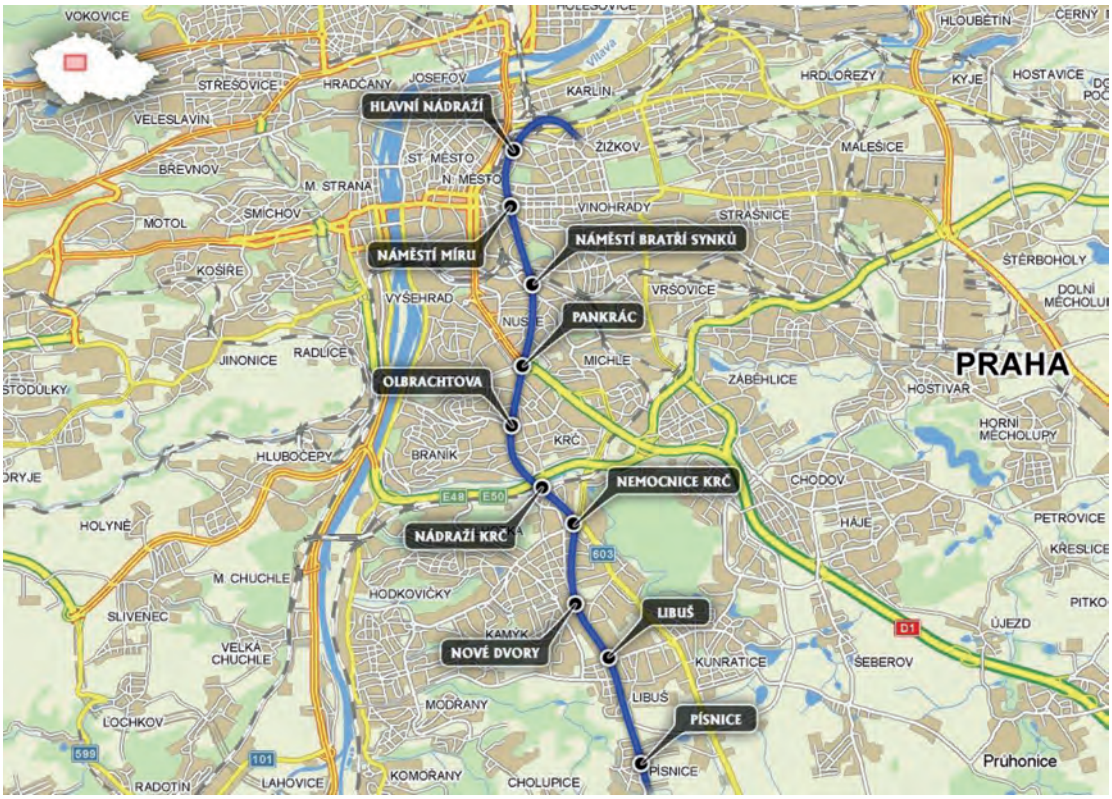

Figure 9.10: New metro line D to Pìsnice.

Layout of the building, shielding and security policy

i. Overview of the facility

The facility is designed features six Experimental Halls (E1 to E6). These experimental halls are supplied with laser beams generated by the laser systems L1 to L4.

Laser systems L1 (oscillator and booster amplifiers), L2 (diode-pumped 10 J/10 Hz beamlines) and L3 (diode-pumped 50 J/10 Hz beamlines) are placed in the ground floor, whereas the 10-PW laser units spreads over the three floors (pump system on the first floor (4a), broadband amplifiers on the ground floor (4b) and optical compressors in the basement(4c)).

Support technology systems located in the first floor include heat exchangers of the cryogenic circuits, capacitor banks, and power supplies for the diode-pumped repetition laser blocks L2 and L3.

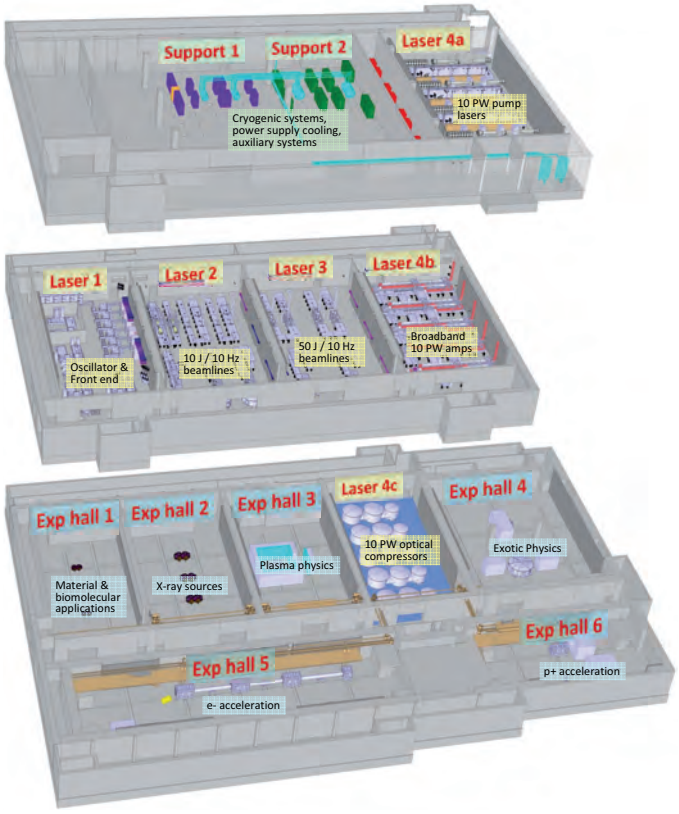

Figure 9.11a: Proposed layout of the internal structure of ELI-Beamlines facility.

-

Figure 9.11b: Elements of master structural design of the ELI-Beamlines facility: in blue is monolithic structure of the laser and experimental halls, in red are adjacent technology areas.

ii. Shielding of ionizing radiation sources

The general principle is to locate shielding material as close as practicable to the radiation source. This means that the primary shielding of radiation will be by means of shielding blocks of appropriate material built around the target / beam dump locations as part of the experimental set-up. This primary shielding will impose local floor loads of several tons per square meter. However, all the relevant locations are on the basement floor slab so this should not cause significant problems for structural support.

It will not be practicable to make a perfect primary shield around the target/beam dump and there will be unavoidable leakage of prompt ionizing radiation when laser shots are being fired. Also, parts of the target, the primary shield and other surrounding materials will become continuously radioactive as a result of neutron induced transmutation. In some of the experimental halls, material choices will be limited due to the effects of activation. These issues shall be carefully explored in respect of all equipment considered to be at risk of activation. Inappropriate selection of materials could lead to a very considerably reduced availability of the facility target areas for experimentation.

It is a design intent in ELI-Beamlines that the areas adjacent to a given Experimental Hall (e. g. corridors and control rooms) should be capable of continuous normal occupation even whilst laser shots are being fired. It will therefore be necessary for the walls and roof of the experimental halls also to provide shielding.

This is specified to be 1.6 m of void-free ordinary concrete (density 2300 kg/m^3) for all walls around Experimental Halls 4, 5 and 6 and 1.6 m void-free thickness for the roofs of the same areas. The thickness of walls and ceiling surrounding Experimental Hall 3 is 1 m but with 1.3 m thickness for the wall to Control Room 3. The basement floor thickness is not determined by shielding requirements.

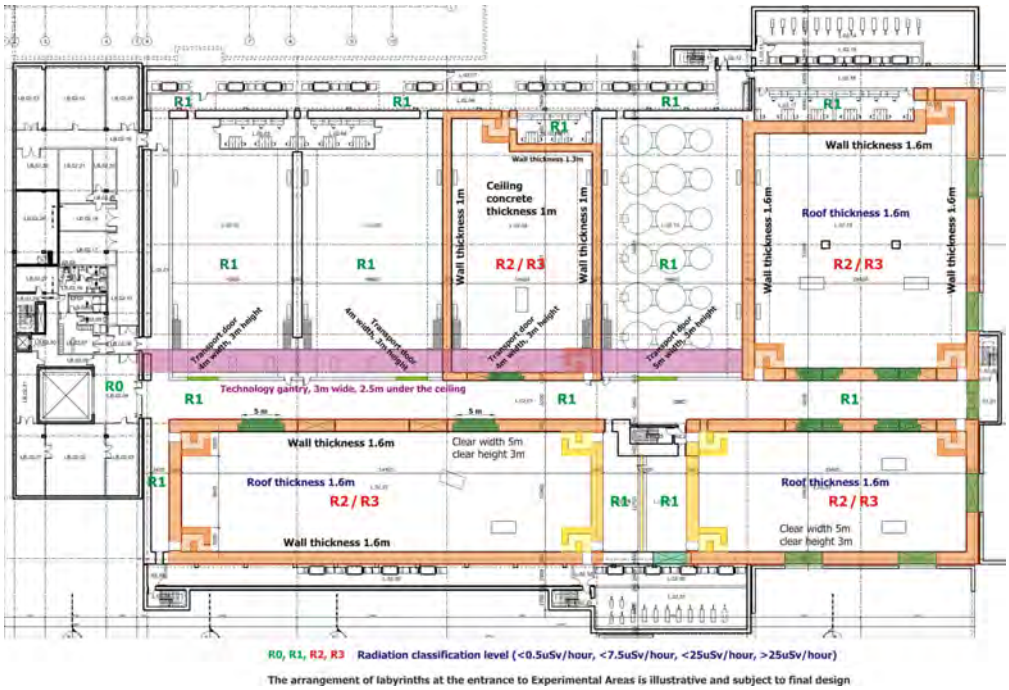

Figure 9.12: Shielding of ionising radiation in laser building.

iii. Health and safety requirements

Directive 92/57/EEC (OJ No L245, 26.8.92) on the implementation of minimum safety and health requirements at temporary or mobile construction sites requires the production of a Health and Safety File which is contributed to by all designers. The role of the designer is clearly explained in these regulations and it is more extensive than personnel contributing to the project often realize.

iv. Security philosophy

A system of physical and administrative security will be implemented on the ELI Beamlines site so as to control access by members of the public and the staff to different parts of the site. The security system will be one part of the arrangements to ensure the safety of all persons on the ELI Beamlines site and for the necessary protection of physical and intellectual assets.

The security system will comprise physical barriers (e. g. fences, walls and controlled access points) and administrative means (security personnel, security procedures).

The overall philosophy is to divide the site into concentric Security Zones of increasingly restricted access:

Zone 0

- Designated External Areas, Entrance Foyer and Cafeteria

These pedestrian areas will be freely accessible during normal working hours to members of the public, unaccompanied and without prior arrangement. Outside normal working hours these areas will be closed to the public and accessible only to authorized persons by passing a card access turnstile adjacent to the Security Post.

The Designated External Areas are located between the outer and inner security fences. This area will include visitor car parking accessed through a vehicle barrier controlled by Security Staff from the Security Post. Parking permit holders will also be able to operate this barrier by means of an access card.

Zone I

- Underground parking
  Underground parking will be reserved for parking permit holders only. Access will be by operation of a card access controlled vehicle barrier.
- Atrium Office Suite, Lecture Room and Visitors Gallery (Laser Hall)
  These areas will be accessible on foot by means of card access turnstiles to persons with appropriate access rights. Access to visitors will be granted by issue of time-limited (e. g. daily) temporary access cards.
- External Areas within Inner Security Fence
  The Zone I external areas will be accessible to appropriately authorised pedestrians directly from the Office Suite or through card access turnstiles from Zone 0.
  Vehicle access to the Zone I external areas will be through normally locked gates controlled by Security Staff. Note: for security purposes the Industrial Gases Compound will also be treated as a Zone I external area.

Zone II

- Laboratories
  Access to the Laboratories (outside the Laser Hall) will be by means of card access turnstiles to persons with appropriate access rights. Not all persons able to access Zone I will necessarily be permitted to enter Zone II. Visitors to the Laboratories will be issued with a time-limited (e. g. daily) temporary access card. For safety reasons, Visitors to the Laboratories must be accompanied at all times by a permanent pass holder. Permanent pass holders to the Laboratories must have successfully completed a safety/security induction course.

Zone III

- Laser Halls
  Access to the Laser Hall (excluding Visitors Gallery) will be by means of card access turnstiles to persons with appropriate access rights. Not all persons able to access Zones I and II will necessarily be permitted to enter the Laser Hall (Zone III). Visitors to the Laser Hall will be issued with a time-limited (e. g. daily) temporary access card. For safety reasons, Visitors to the Laser Hall must be accompanied at all times by a permanent pass holder. Permanent

pass holders to the Laser Hall must have successfully completed an extensive safety/security induction course. Visitors to the Laser Hall must have received a safety/security briefing before issue of a temporary pass.
Within the Laser Hall there will be further control of access to various areas for the purpose of laser, electrical and radiological safety. The security system may need to interface with the safety access control system but without compromise to the requirements of either system.

v. Commissionning considerations

A fully detailed base-build commissioning plan will be required which permits finalization of clean rooms at times when they will not be at risk of re-contaminated with dirt. A phased handover of the building is expected. The acceptance criteria for building handover need to be fully detailed and understood by all parties as will the devolvement of responsibility for areas of the building.

A separate plan will be produced for the Technology Installation Phase, which will require assembly of sensitive optical components in the building after the ELI building commissioning is completed. This can be a major logistical exercise as clean room conditions of up to Class 100 will be required for the assembly of beamline components which reside in the high vacuum environment. The logistics of procurement, assembly and integration of the laser and target area components will require appropriate batch packaging and storage facilities.

9.2.3 Budget and timeline

Implementation budget

The table below shows the implementation budget of the ELI Beamlines facility as submitted to the European Commission in June 2010 by the Institute of Physics of the Academy of Sciences of the Czech Republic. The Institute will be the legal entity in charge of the implementation of the ELI Beamlines project. A final version of this budget will be included in the grant agreement that will be signed shortly after the approval of the application for funds by the European Commission. This approval is expected in the course of February or March 2011.

The figures displayed in the table are based on a detailed budget containing more than 700 items and covering both preparation costs (additional to those already covered by the European Commission grant to the Preparatory Phase of ELI), investment costs and start-up costs (mainly personnel costs, travels and some services). All items have been collected by the team or by external specialists on the basis of market surveys or, in relevant cases, risk-assessed best estimates. A value engineering exercise has been performed on the basis of the initial building design as well as quantitative and qualitative risk analyses (Monte-Carlo analysis in particular).

As indicated in Chapter 10, the implementation phase will be funded with structural funds of the European Regional Development Fund under the Czech Operational Programme "Research and Development for Innovations". Structural funds will cover approximately 85% of the implementation budget, the rest being funded with national institutional resources.

Operational costs

The operational costs shown in the table below represent the annual average required for the operational of the ELI Beamlines facility. Re-investment costs have also be included since technological upgrades will be required to preserve ELI's and this particular facility's competitiveness. The current strategy is based on the assumption of a massive re-investment taking place in 2020, 2021 and 2022. The figure indicated in the table below represents the average re-investment per annum over the whole operational period (2016–2030).

Table 9.1: Operational budget (based on the detailed budget submitted to the European Commission in June 2010).

	Implementation phase budget	ELI-Beamlines
1	Planning / Design fees	5.6
2	Land purchase	10.4
3	Building and construction	54.7
4	Plant and machinery	141.2
5	Contingencies	5.7
6	Technical assistance / start-up grant	32.5
T1	TOTAL (excluding VAT)	250.1
	VAT	40.2
T2	TOTAL (including VAT)	290.3

Operational costs are currently under detailed estimation in the three host countries. This evaluation is done in parallel with the detailed definition of the operational model of the future infrastructure. A detailed consolidated operational budget covering the first three ELI facilities is expected by the end of 2011.

Table 9.2: Operational budget (based on the detailed budget submitted to the European Commission in June 2010).

	Implementation phase budget	ELI-Beamlines
1	Planning / Design fees	5.6
2	Land purchase	10.4
3	Building and construction	54.7
4	Plant and machinery	141.2
5	Contingencies	5.7
6	Technical assistance / start-up grant	32.5
T1	TOTAL (excluding VAT)	250.1
	VAT	40.2
T2	TOTAL (including VAT)	290.3

Implementation timeline

The implementation of the ELI Beamlines facility is expected to be completed by end 2015 in compliance with the legislation pertaining to the use of ERDF resources. The timeline below provides a summary of the schedule of the implementation tasks since mid-2010. In practice, preparation activities started in the first quarter of 2009 with the negotiations on the future land purchase and design activities. The second half of 2015 will be dedicating to testing the technology and prepare the transition to the operational phase.

Table 9.3: Draft time schedule of the implementation of the ELI beamline facility.

ID	Task Name
1	1 ELI - DRAFT MASTER PROGRAMME - working version
2	1.1 STATUTARY & LEGAL & STRATEGY
12	1.2 PLANNING PROCESS
15	1.3 PROJECT BRIEF COMPLETION
19	1.4 DESIGN PROCESS
20	1.4.1 Value engineering design
29	1.4.2 Execution design
65	1.4.3 Tender design
72	1.5 COST PLANNING & COST CONTROL
95	1.6 SITE INVESTIGATION
110	1.7 PREPARATORY PHASE PROCESS
111	1.7.1 Procurement process of preparatory phase
147	1.7.2 Preparatory phase on site
175	1.8 MAIN CONSTRUCTION PHASE PROCESS
176	1.8.1 Procurement process of construction phase
212	1.8.2 Buildings
213	1.8.2.1 Site handover
214	1.8.2.2 Contractor mobilization
215	1.8.2.3 Shop drawings - reinforcement
216	1.8.2.4 Laser Building
296	1.8.2.5 Laboratories
359	1.8.2.6 Office Building
418	1.8.2.7 Multifunction Building
466	1.8.2.8 Atrium
472	1.8.3 External works - external parking, connections, landscaping
478	1.8.4 Finish of the construction process
479	1.8.5 Enabling works for laser services
480	1.9 LASER TECHNOLOGY INSTALLATION

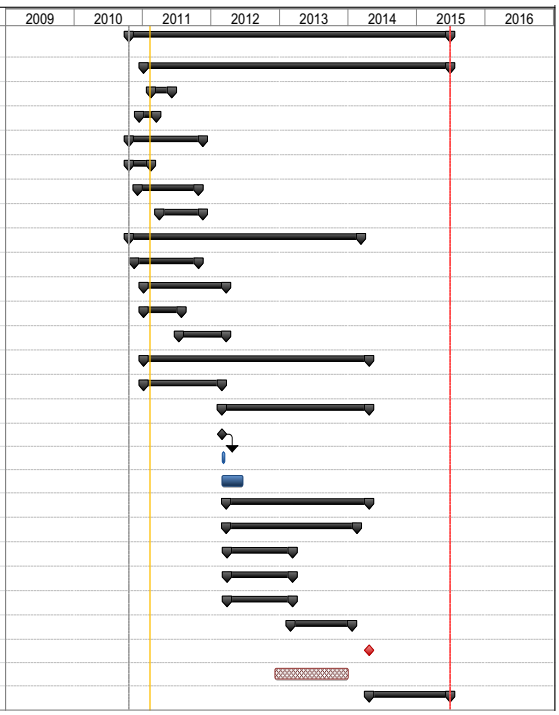

9.3 ELI-ALPS in Hungary

Hungary is traditionally known of its very high level of education system and strong support of science, which may be evident looking at the number of Nobel laureates with Hungarian origin and education as well as the high number of scientific publications pro inhabitants. As it is, Hungary has been long waiting for an opportunity to host a European Large scale research Infrastructure.

The Hungarian scientific community has been very pleased with the decision of the ELI-PP Steering Committee on 1st October, 2009, granting Hungary the possibility to host one of the ELI pillars. Due to the national elections and the consequential change of the Hungarian government in May, 2010 as well as other organisational issues, the preparation of the ELI-ALPS on national level has been delayed by more than half a year with respect to the initial planning. The Hungarian project company (ELI-Hu Kft.) responsible for the implementation of ELI-ALPS will do its best to catch up and make up for the lost time.

9.3.1 Beamline scheme

The primary mission of the Extreme Light Infrastructure Attosecond Light Pulse Source (ELI-ALPS) Research Infrastructure is to provide the international scientific community with a broad range of ultrafast light sources, especially with coherent XUV and X-ray radiation, including single attosecond pulses. The secondary purpose is to contribute to the scientific and technological developments towards generating 200 PW pulses, being the ultimate goal of the ELI project. ELI-ALPS to be built in Szeged, Hungary will be operated partially as a user facility and hence serve basic and applied research in physical, chemical, material and biomedical sciences as well as industrial applications.

In the following a brief summary is given on the current status of planning ELI-ALPS beamlines (Fig. 9.13), which also incorporates the proposals of the ELI ALPS 1st Scientific Workshop held in July 2010 in Budapest, and the contributions from colleagues working for laboratories participating ELI-PP, especially from CLF (RAL), MPQ, MBI, ILE-ENSTA, CUSBO, and FORTH. Due to the relatively late start explained above, the layout will be fixed by the end of 2010 and validated by the Scientific Advisory Committee of ELI-PP.

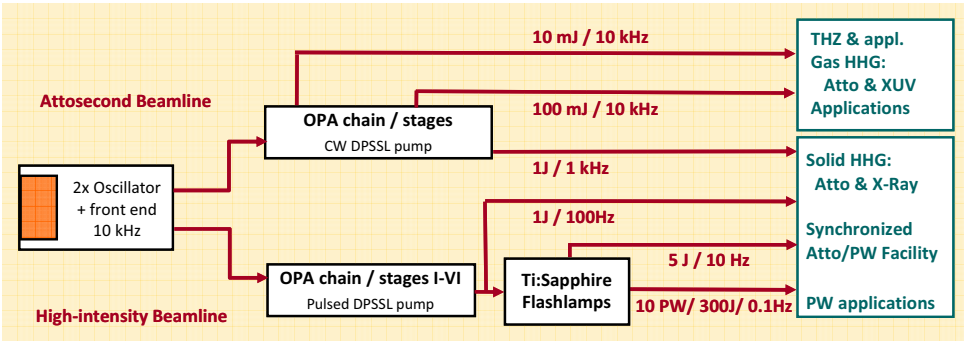

Figure 9.13: Current schematics of the laser systems of the ELI-ALPS Research Infrastructure with a list of secondary sources and applications.

Attosecond beamlines

To fulfill the primary mission of ELI-ALPS, PW class driving lasers providing few cycle, CEP stabilised laser pules are necessary to operate at unprecedentedly high repetition rate. These pulses enable the utilization of all known methods of attosecond pulse generation.

i) The well-established high harmonic generation in rare gases (GHHG) will be pushed to its ultimate limits by a loose focusing geometry, aiming at producing attosecond pulses with tens of μJ pulse energy.
ii) It is anticipated that much more energetic and probably shorter attosecond pulses can be generated in plasma formed on surfaces of solids reaching the X-ray domain (SHHG). This method is not yet fully explored, so research will be also directed for the full exploitation of the technique. These two methods are offering complementary parameters to deliver a versatile atto-source for users.
iii) Finally, new methods of attosecond pulse generation utilizing field enhancement at nanostructured surfaces or dc-like external fields will be tested to enhance the generation process of atto pulses. Partly for this purpose, intense, synchronized THz pulses will be generated and their use for atto generation will be implemented.

The Attosecond Beamlines of ELI-ALPS will thus offer a unique combination of various photon sources for multi-colour pump-probe experiments: spanning the spectrum from the THz to the X-ray range, with ultrashort pulse durations down to few cycles. The planned laser system will also provide a record breaking photon flux in attosecond pulses, as well as the shortest wavelengths and pulse durations for attoscience applications.

The Attosecond Beamline will partly serve as a user facilty. In this frame a well-establised and reliable source has to be provided, i.e. GHHG pulses will be offered to users directly from the beginning and SHHG pulses shall follow with the improvement of corresponding technologies. ELI ALPS will offer both broadband, isolated attosecond pulses, using temporal or spectral gating techniques and quasi-monochromatic, strong femtosecond XUV pulses (isolated from the broad spectrum). A number of user stations will supplement the facility equipped for a set of spectroscopic and time-resolved experiments. The beamlines will open sequentially from 2015 on, starting with the GHHG beamline.

The HHG sources will be driven by primary laser pulses with different characteristics. For GHHG, loose focusing and high repetition rates are desirable. We propose a driver beamline that will run at up to 10 kHz with pulses of 5 fs and up to 100 mJ. These sources (first run at moderate pulse energy) will operate as a facility for users continuously improved with the advance of technology. SHHG will operate according to the results of a technology assessment procedure to be carried out in 2012. Depending on the state of the art in 2015, this will either start immediately as a user facility, or as a test beamline. This beamline will be driven by laser pulses at 10 Hz. . . 1 kHz with the highest pulse energies from the laser sources.

User applications of the femto- and attosecond X-ray pulses, produced via high harmonic generation, scan a wide range including fundamental time-resolved and structural studies, Coulomb explosion imaging of large molecules and clusters, attosecond metrology, attosecond and ultrafast X-ray spectroscopy as well as diffraction imaging. These sources will provide tools to probe electron dynamics in atoms, molecules, and solids with sub-femtosecond temporal resolution, or will be used in plasma diagnostics and single molecule imaging in time-resolved microscopic studies.

High-Intensity Beamline

To meet all the missions of ELI-ALPS, another laser chain is planned at a peak power of around 10 PW at a moderate repetition rate of 0.1 Hz. Besides the research on different amplification schemes, coherent beam combination experiments will be carried out to assess technologies for the final ELI goal of a 200 PW facility.

Once this High Intensity Beamline is established, independent experimental studies are also planned directly with the laser pulses or indirectly via generation of other secondary sources. Moreover, synchronisation with the Attosecond beamline would offer the possibility of combination of any primary and secondary light pulses in both beamlines. The applications will exploit

the unprecedented flexibility offered by the laser and secondary source parameters in terms of repetition rate, wavelength (spanning the spectral range from THz to X-rays), pulse duration (from femtosecond to attosecond) etc.

The design criteria for the high intensity target areas are the following. i) synchronized input from both laser beamlines should be possible. ii) the layout of the target areas should offer the highest degree of modularity in terms of secondary source and user station layout and further extendability (vacuum ports and chamber extensions, movable shielding etc.) iii) time-resolved pump-probe-type studies with various radiation and particle sources should be made possible iv) user access source units and source development units should be separated to allow effective technology developments.

Laser pulses of various energy level and repetition rate will be coupled out after each major amplification stage of the high-intensity, 10 PW laser chain, and steered towards the target areas. Since only a few split-outs in the chain require separate laser pulse vacuum compressor, the exact outcoupling positions will be determined in due course according to the given application and user/industry requirements.

In details, (i) femto- and attosecond X-ray pulses will be generated via solid high harmonic generation (SHHG) to enable experiments detailed in the Section above. (ii) Ultrafast particles (electrons, protons and ions) will be generated to serve fundamental and applied research as well as biomedical applications. (iii) The focused ultrahigh-intensity laser pulses will also be available for fundamental (partially time-resolved) studies of laser plasma interactions and exotic physics applications. The goals here will be partly technological since novel focusing and coherent beam combination methods will also be investigated in order to exploit the full power of the 10 PW beam to produce the highest focused intensities.

The distribution of the target areas will offer unique possibilies for the combination of laser beams from all parts of the facility. Hence, a versatile beam delivery matrix is to be designed in order to maximize functionality and flexibility for unique experiments with multi-source inputs. Ongoing discussions with experts and potential users will clarify the desired parameters of secondary sources of high-energy particle beams and ultrashort pulsed electromagnetic radiation spanning the THz to X-ray spectral range. The specifications will include the necessary laser parameters for each secondary source (intensity, pulse shape and length, contrast, repetition rate etc.) as well as the feasible secondary source parameters.

Primary light sources – laser chains

In order to satisfy all the design criteria driven by application of laser pulses, the scheme in Fig. 9.13 has been recently drafted. The two laser beamlines will have identical early front ends, consisting of a commercial laser system working at 800 nm and with 10 kHz repetition rate. This architecture makes also possible synchronised running of both laser chains with the use of either of the front ends only.

The DPSSL pump lasers at 1.03 μm as well as a 1.5 μm satellite amplifier for THz generation will be fed by a part of the 5 mJ, sub-30 fs laser pulses. The seed pulses for both the attosecond driver chain at 900 nm central wavelength and for the 10-PW chain at 800 nm will be generated from the largest part of the commercial system through spectral broadening and subsequent XPW filtering, so that few cycle, high temporal contrast laser pulses enter the OPCPA stages.

The repetition rate and bandwidth of the pulses in the attosecond driver chain are to be kept initially at 10 kHz and >300 nm, respectively. For the higher pulse energy amplifier stages, the repetition rate is reduced to 1 kHz. The pump sources are based on diode pumped solid state laser (DPSSL) technology, using cw diode lasers. The generated pulses at various energy levels are to be provided for HHG and attosecond generation and application. This part of the Research Infrastructure is designed to enable user facility operations from the opening in 2015.

The first OPCPA stages of the High Intensity Beamline will operate at 100 Hz repetition rate and pumped by pulsed diode based thin disk pump lasers. The subsequent power amplifiers are to utilize Ti:Sapphire technology and are likely to be pumped by flashlamp-pumped Nd:YAG and Nd:Glass lasers, providing higher pulse energies but limited to a lower repetition rate. We have to mention that this scenario is held assuming that the development rate of DPSSL technology remains the same as today. However, if DPSSL technology speeds up likely offerring high energy pulses at higher repetition rate and lower cost, then it might happen that DPSSL lasers will be applied right from the start of implementation, instead of flashlamp pumped lasers.

Having regarded all the bottlenecks and challenges above and also keeping in mind the uniqueness of the laser system based on repetition rate, a revised scheme has been recently proposed (Fig. 9.14).

Here a separate, user facility channel would be devoted to GHHG generation at 100 kHz level, which we believe would attract not only fundamental physics but industrial R&D applications, as well. This system may have a carrier wavelength close to the rest of the system, which may provide an obvious possibility of synchronisation (noted by dashed line). However, it may also make sense to build this 100 kHz part operating in mid-IR. Although the possibility of synchronisation between the beamlines would be less obvious, the community may gain from the attractive light source at a different spectral range.

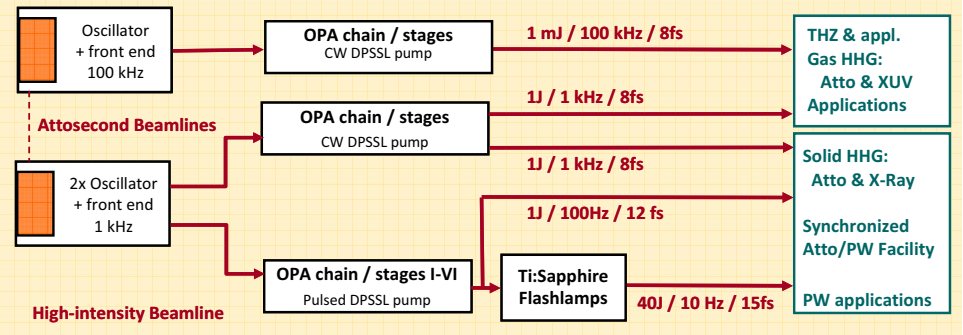

Figure 9.14: The "second generation" scheme of the laser systems of the ELI-ALPS Research Infrastructure. Synchronisation between the two types of front ends is possible – it depends on the wavelength range chosen for the 100 kHz arm.

The concept of dual laser system with common and synchonised front ends is still held on. There would be, however, two outputs of the kHz system. One is devoted for facility operations, while the other is for developmental work and pilot experiments.

Concerning the high intensity branch, the separate 100 Hz output would be still available at somewhat longer pulse durations, which can be devoted to ion acceleration experiments and related applications, too. The peak power of the highest intensity part is traded in for repetition rate. That is, now laser pulses at 3 PW level would be available at 10 Hz repetition rate.

Most of the major bottlenecks in laser technology have been identified. Among these the industrial ones are the availability and price of (i) kW class pump lasers at high repetition rate; (ii) optical coatings with suitable bandwidth and laser damage threshold; and (iii) dielectric diffraction gratings for pulse compression with suitable bandwidth and laser damage threshold. Besides these, considerable research efforts have to be aimed to achieve laser pulses on the target with a temporal contrast of 12 orders of magnitude, to maintain carrier envelope phase stabilization and to compress the high intensity laser pulses down to 8 fs. Solving these challenges during developments in the prototype projects of ELI is a prerequisite for the success of the ELI ALPS facility.

9.3.2 Site and building

The European region of the Southern Great Plain is located in the South-East part of the country, in the east and south bordered by Romania and Serbia, respectively. The capital of the region, Szeged, the fourth largest city of Hungary is located in the southern part of Hungary very close to the Serbian (12 km) and Romanian (48 km) borders. The second largest river of Hungary, the River Tisza intersects the city, and the mouth of the River Maros is also here.

Geographically Szeged is located at the intersection of national and international transport corridors. The city can be accessed by the basic infrastructure of all four means of transport – by road, by rail, by air and by water. Namely, Szeged can be reached from Budapest via motorway M5 in 1,5 hours (170 km). This route provides access from Serbia and Montenegro. The construction of the M43 expressway started in 2008, and is to be opened in the Fall of 2010 improving accessibility towards Romania. Szeged has good railway connections to Budapest and the neighbouring cities, as well as to Romania, Serbia and Montenegro. Port of Szeged is one of the six river ports of national importance, the River Tisza is navigable by 1,500 ton ships.

Regarding air traffic, the country's largest airport Ferihegy can be reached via the motorway within 1.5 hours. There are trains in each hour between Budapest and Szeged, having a stop direct at the arport, too. Szeged has also a small scale airport with a 1.8 km runway, available for middle-size airplanes.

Characteristics of the site of ELI (Öthalom University Site) [1]

The site is located at a distance of 1 km from the Szeged-North junction of the M5 motorway (Fig. 9.15). Furthermore, we must point out the vicinity of the M43 expressway (1 km), to be finished in 2010, making this site a favourable location in terms of transport.

Figure 9.15: Aerial view of the site of ELI-ALPS in the sub-urban region of Szeged, close to the motorways.

Morphology: The area of Öthalom is in a transitional zone between the Danube-Tisza area and Tiszántúl (area beyond the River Tisza) in terms of structure and morphology alike. In terms of ground stage it is located on the Pleistocene terrace and the floodless ground surface.

In the west and in the north it is surrounded by Aeolian sand hills, while in the east, north and south it is surrounded by Holocene flood plains.

Geomorphologically it is located on the elevated part of the alluvial plain, on a Pleistocene loessal mud base. The south-east shore of Lake Fehér is lined with dunes. The drift-sand covered area of the Danube-Tisza area begins 5 km to the west. In the east there lies the low floodplain of the River Tisza.

Surface movements: The movement of Aeolian sandhills located at the northern boundary of the area was halted by planting acacias and poplars, wherefore there are no surface movements in the area. There are no surface movements in the alluvial formations on the surface or near the surface of the site either. This is especially true for the area of over 6 hectares covered with concrete.

Subsurface geology. The Paleozoic granitoids that form the basement at the bottom of the Pannonian basin were explored through the exploration wells at a depth of 2,550 to 3,000 m in the area of Szeged. In this region this formation forms the foot of macroporous Triassic dolomite. In the Sarmatian and then the Pannonian sea the floor was then covered with a 1,000 m thick, mostly clayey layer. Then, in the Upper Pannonian period, the rivers coming from the surrounding mountains deposited a mixed, 1,500 m thick layer (clayey aquifuges, sandy pervious layers). At a depth of 400 to 500 m quaternary layers can be found, which are also off alluvial origin and typically contain large amounts of aquifers.

The geology of near-surface formations. The surface forming activity of the river in the Holocene and Pleistocene periods affected the entirety of the area. The alluvium covering the surface was deposited at the times of floods, and contains alternating formations of clay and fine-grained sand. In the Holocene period the River Tisza deposited granular sediments – finer than sand – onto floodplains lying farther off from the river bed. These formations are 3 to 6 m thick, under which we can find more compact clay due to alkalisation.

Regional hydrogeological characteristics: The near-surface formations have a high imhibition value and are aquifers. The initial water table of the groundwater can be found at a depth of 1 to 3 m on average. Groundwater is recharged from the infiltrating precipitation water. Apart from evaporation it is drained towards the River Tisza, wherefore the slope of the watertable is in that direction, too. The description of the near-surface formations points out that the first free surface water reservoir is missing, and the wells open a subsurface aquifer under mild pressure, wherefore the difference between the initial watertable and the watertable discovered in the formation can be as much as 0.5 m. However, this can also be caused – in part – by the fact that the groundwater is found in the network of cracks of the muddy and clayey formations, and therefore it raises the water level in the borehole only slowly, by seeping into the borehole. Based on the monthly average data of many years, the annual fluctuation of the groundwater table does not exceed 2 metres. The fluctuation of the groundwater level correlates with the amount of precipitation, albeit with a smaller amplitude, since the near-surface clayey formation may swell after the infiltration of water from the surface, and may even become an aquifuge.

R&D activity and higher education

In Hungary there are several laser research groups, with many-decade-long traditions, in Budapest since 1963, in Szeged since 1968, in Pécs since 1983. These universities and research institutes [2–6] work in close cooperation with each other forming a well organized research community with a network of permanent cooperations (e.g. Committee of Laser Physics and Spectroscopy of Hungarian Academy of Sciences; Quantum Electronics Group of Roland Eötvös Physical Socity). The Hungarian laser community is well embedded into the laser science of the World, and that of the EU, which are highlighted by the following representative facts: Center of Excellence in FP5; participation in LaserLAB Europe and EuLASNet, as well as in more than 20 FP6 and FP7 research projects.

This laser community has achieved significant scientific results, many times at the leading edge of basic and applied research, and in some areas directly related to ELI as well. Graduate, postgraduate students, researchers and technical specialists are in the field of laser technology and quantum optics trained at high standard.

The R&D expenditures of Szeged and its region spent on scientific and technological developments exceed 1.7% of the GDP which is well above the national average of 1%. (A higher rate is achieved only in Budapest in Hungary.)

The R&D potential of Szeged is currently provided by four R&D organisations that dominate the life of the city (University of Szeged; Biological Research Centre of the Hungarian Academy of Sciences; Research Institute for Biotechnology of the Bay Zoltán Foundation for Applied Research; Cereal Research Non-Profit Company). These organisations employ around 2,000 (FTE) R&D professionals and researchers. Nearly 50% of these people are qualified researchers, including habilitated researchers representing 20% of the staff. The four organisations – which are engaged in research and development, and higher education, too – have an R&D output of around HUF 5–10 billion (EUR 20–40 million) annually. This output is utilised directly by the economy, which makes the city's R&D activity inspiring and significant in the development of the economy, too.

In terms of the level of education of the labour market participants, Szeged is one of the most qualified regions of Hungary. Higher education degree holders account for nearly 25% of the labour market of Szeged, and quality labour supply can be ensured with graduates from the University of Szeged. The University of Szeged releases around 6,000 graduates to the labour market each year. In relation to the output of graduates, the release of physics graduates is outstanding, accounting for 20% of the higher level physics education in the country. The Physics PhD school of the University is traditionally the strongest in Hungary concerning optics and laser physics. The number and distribution of graduates that enter the labour market each year ensures the development of the R&D potential of the city and the enhancement of knowledge intensive activities. Laser physics R&D has a synergic effect, and provides services in cooperation with other research groups for businesses engaged in the processing industry; trade; repair services; vehicle and fuel trade; economic services and healthcare.

Infrastructure and environment of the site

The infrastructure of the proposed area is designed to serve industrial companies, its expansion is not hindered by any foreseeable obstacles. Facilities in the immediate vicinity of the site: rubber factory, dairy company, the industrial site of a construction company, as well as Praktiker, Cora and Metro stores (Fig. 9.16).

Construction environments. No specific construction rules apply to the proposed site. The construction is governed by the categorisation of the area pursuant to the Decree on the Construction Regulations of Szeged: The total area is 47 hectares, of which 1/8 of the entire site is special institutional zone: established architectural character; maximum built-up ratio: 30–55%; construction height of built facilities: 8–12.5 m; 7/8 of the site is categorized as other industrial economic zone; not yet established architectural characteristics; maximum built-up ratio: 30%; types of buildings to be erected: detached.

Construction of ELI as a research infrastructure is governed basically by the general construction rules. Obtaining the appropriate authorization is a prerequisite for starting the construction. This process is governed first of all local regulation of the municipalities of the city of Szeged.

Building

A draft of the first conceptual design and the neighbourhood are shown on Figure 9.17. Inside the common circular structure there are three separate buildings. The middle one would host

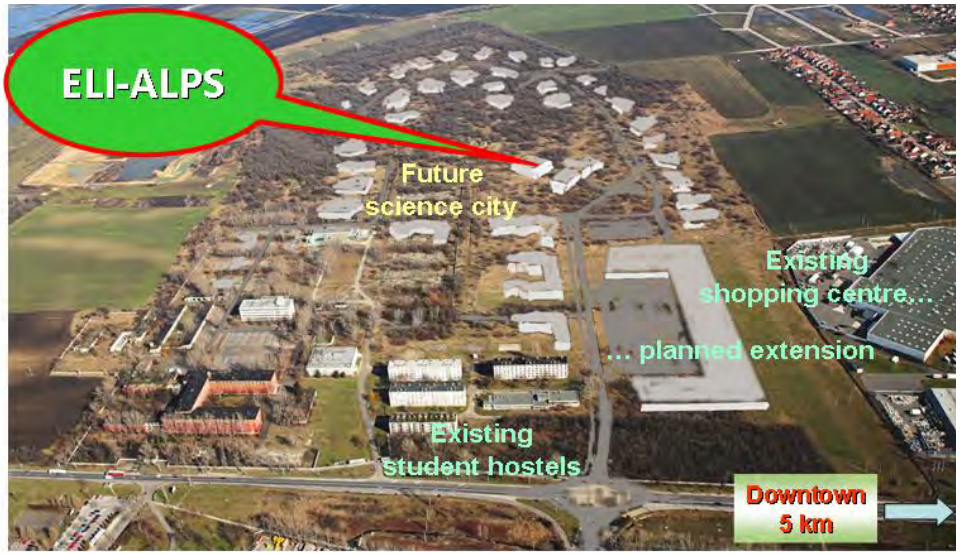

Figure 9.16: Site plan of ELI-ALPS [7].

the laser and the secondary sources, and would have a considerable underground part. The two side buldings are to host the administrative and scientific staff, conference rooms, service blocks and amenities. Once this (or maybe, a new) concept is confirmed, a more detailed design including vibration analysis etc. is to follow by early of 2011.

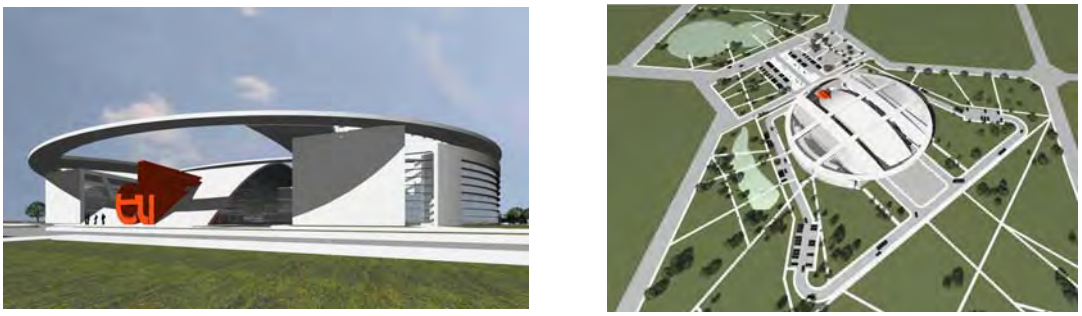

Figure 9.17: Conceptual building plan and the close neighbourhood [8].

Bibliography

[1] Limit Tanácsadó és Vagyonértékelõ Kft., 2010.
[2] Research Institute for Solid State Physics and Optics: www.szfki.hu
[3] Research Institute for Particle and Nuclear Physics: www.rmki.kfki.hu
[4] Institute of Physics, University of Pécs: physics.ttk.pte.hu/english/home/index.shtml
[5] Departments of Physics, University of Szeged: www.physx.u-szeged.hu
[6] Institute of Physics, Technical University of Budapest: www.phy.bme.hu
[7] Kiss és Tsa Mûépítész KKT, 2010.
[8] Lázár Antal, BMGE, 2010.

9.3.3 Budget and timeline

The total cost of the implementation is close to 250 M€, including the infrastructure, the lasers and experimental equipment as well as salaries (Table 9.4). During the implementation phase the number of employees would exceed 200 by 2015 from the planned initial 10 in early 2011. The distribution of the gross budget is likely to be changed as soon as the laser system and the secondary sources are fixed.

The financial source of the implementation would be 85% of the Structural Funds of the European Union, while 15% is provided by Hungary. Large part of the Hungarian contribution would be sourced from national public funds and project funds, while small contribution from the private companies may also be expected.

Table 9.4: Estimated gross budget of the implementation phase of ELI-ALPS [1].

Implementation	€m
Site acquisition	1,8
Building cost	57,0
Oscillators and front-end	2,5
Boosters and final amplifiers	35,0
High-intensity systems	83,2
Beam delivery and diagnostics	7,5
Experimental facilities, prototyping	26,7
Services	7,2
Personnel	20,0
Others, Overheads	2,8
TOTAL	**244,7**

During the operational phase the annual budget is estimated around 25 M€. About half of it (50%) is to be spent on the salaries of the 250–300 employees.

The preliminary timeline of the implementation is already getting very strict (Table 9.5). This schedule counts with a starting date of December 2010, and an average speed of the official and burocratic administration, permission and licensing processes. It also leaves very small margin for any error of the management and the Authorities, so that a duplication of any work phase may endanger the implementation. Even at this schedule, the building is planned to be handled over for installation and comissioning of the technology in early 2015. Since it is unrealistic that a year would be sufficient to install and build up all the lasers etc., it is likely that an extra space equipped with proper air conditioning and clean room services shall be hired close to the site, where most of the pre-assembly and installations would start from late 2013.

Bibliography

[1] NKTH ELI Project Office, 2009.
[2] Céh Inc., 2010.

Table 9.5: Draft time schedule of the implementation ELI-ALPS [1].

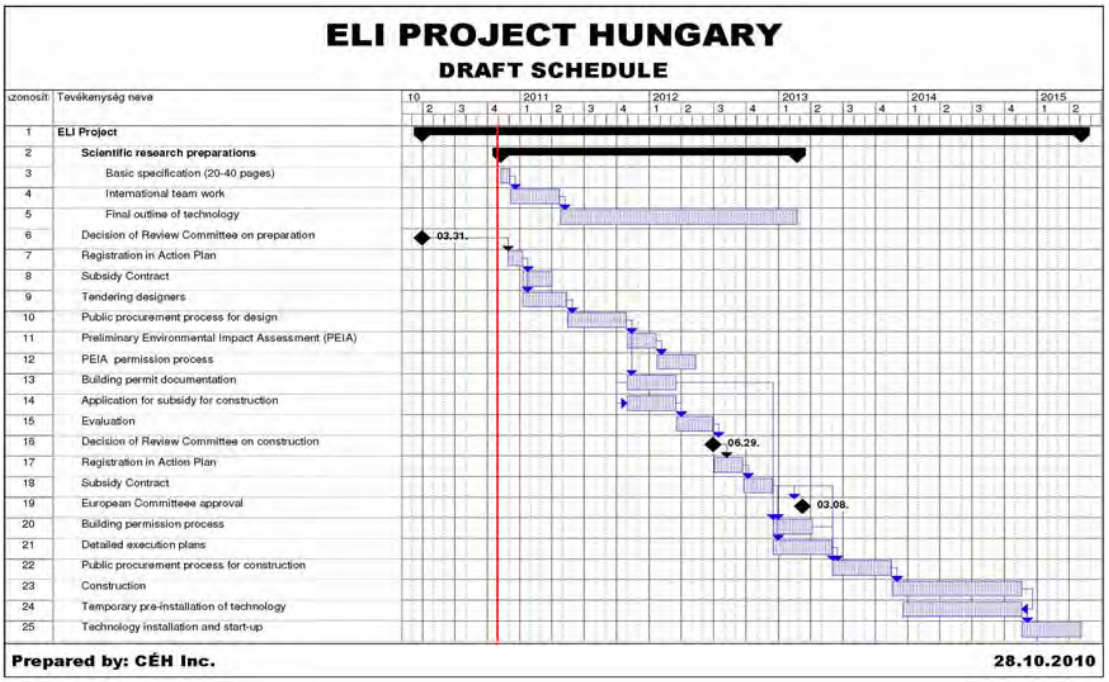

9.4 ELI-NP in Romania

The ELI-NP facility will generate particle beams with high energies and brilliances suited to studies of nuclear and fundamental processes. The core of the facility is a high-power laser system. In order to perform cutting edge photo-nuclear physics experiments, a complementary highly brilliant gamma beam, with energies in the 15 MeV range, will be generated via the laser interaction with a brilliant bunched electron beam. Thus ELI-NP will allow either combined experiments using the high power laser and the γ beam or stand-alone experiments. The design of the facility is modular, reserving the space for further extension of the laser system and allowing the extension later of the experimental area, according to the needs.

The basic objectives of the ELI-RO Nuclear Physics (NP) pillar are:

- to proceed to a precise diagnosis of the laser beam interaction with matter with techniques specific to Nuclear Physics.
- to use photonuclear reactions and laser accelerated particles for nuclear structure studies and for applications

9.4.1 Beamlines Scheme

For the ELI-RO NP facility two new central instruments are planned:

- a very high intensity laser beam, where two multi-PW Apollon-type lasers are coherently added to the high intensity of 10^{23}–10^{24} W/cm^2 or electrical fields of 10^{15} V/m.
- a very intense, brilliant, very low bandwidth, high-energy γ beam, which is obtained by incoherent Compton back scattering of a laser light on a very brilliant, intense, classical electron beam.

The core of the facility is a laser system using Ti:Sapphire technology. The conceptual design is presesented in the Figure 9.18. It will use OPCPA technology at the front-end and Ti:Sapphire high-energy amplification stages, similar to the ones developed at the APOLLON laser system. The ELI-NP laser facility will have two front-ends. They will temporally stretch and amplify initial ultrashort pulses with 800 nm central wavelength to the 100 mJ level, preserving the needed large bandwidth of the 15 fs laser pulses and the temporal contrast of the pulses in the range of 10^{-12}. Due to the complexity of such OPCPA system, the alignment and maintenance time for one front-end is long. To avoid such dead-times, one front-end is planned to operate at a time, the second one being used during the maintenance of the other front-end, significantly increasing the available beam-time of the laser facility.

The pulses after the front end are split and distributed to further laser amplifiers, reaching few Joules of energy at 10 Hz repetition rate and few tens of Joules at a repetition period of the order of few seconds. At these energy levels, the pulses can be extracted from the laser amplification chain and recompressed to shortest duration in vacuum compressors. Subsequently, they are distributed to the high repetition rate experimental areas.

Alternatively, the laser pulses are further amplified in the amplification chains to energies of the order of 200 J. The repetition rate of the pump lasers will restrict the repetition period of the high energy pulses to the minutes range. Adaptive optics and optical isolation of the pulses will be implemented before the optical compressors.

The ultrashort pulses will be distributed to the high energy experimental areas, where stand-alone experiments or combined nuclear physics experiments using the highly brilliant γ beam will be performed.

Coherent combination of the high power ultrashort pulses with the ultraintense and ultrashort pulses from the parallel amplification chains is envisaged, in order to reach intensities of the order of 10^{23} W cm^{-2} and above. The operation of the experiments will take place in parallel, the laser pulses being delivered to different experimental areas on request.

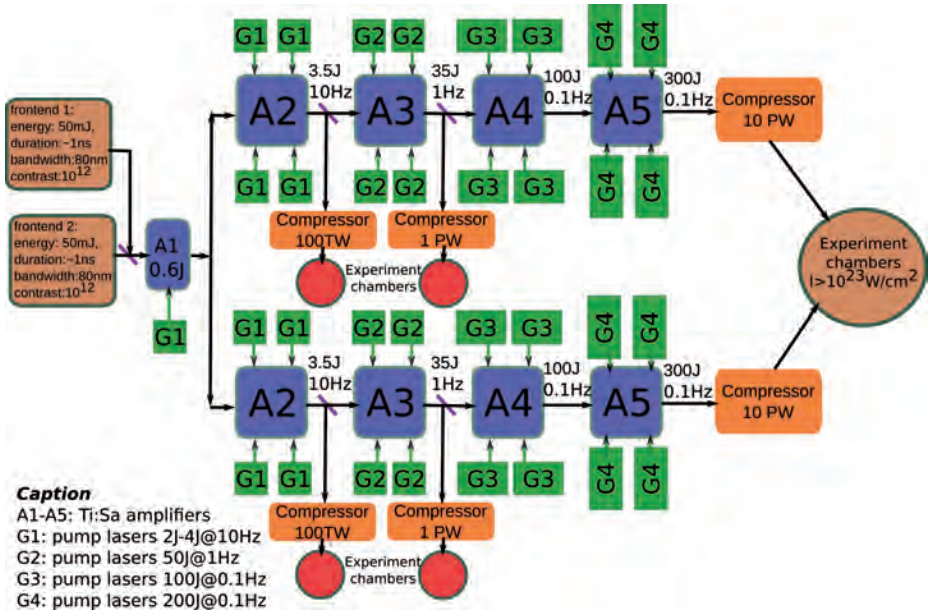

Figure 9.18: The ELI-NP multi-PW laser system conceptual design: FE1, FE2 – Font-End based on OPCPA. A1–A5 – Ti:sapphire amplifiers.

As concerns the gamma beam part, there are four main criteria for a high intensity γ ray sources, namely: the energy of the γ beam, the total photon flux, the peak brilliance and the bandwidth. In order to guarantee a reliable and timely available technological solution the scientific community decided that the gamma beam should be generated by a X-band 'warm' LINAC. This choice ensures that ELI-NP will be the world-leading gamma beam facility at the time of its start of operation.

The ELI-NP machine will use the X-band linac technology developed at LLNL for MEGa-ray but extended from 250 MeV to 600 MeV, the identical state of the art 120 Hz diode pumped laser technology but extended from 1 J to 10 J and duplicate as much as possible the controls systems and hardware being developed for the LLNL machine. The schematic view of the ELI-NP gamma source is presented below in Figure 9.19. A laser pulse recirculation system synchronized to a train of electron bunches allows to increase by a factor of 100 the effective gamma pulse rate up to 12 kHz. The characteristics of these systems are adapted to produce gamma beams with variable energy up to 19 MeV, 10^{-3} energetic width, 10^{13} photons/second total flux and a peak brilliance larger than 10^{21} photons/sec/mm^2/mrad^2/0.1%BW. After a first stage of acceleration up to 400 MeV, a similar laser-electrons interaction system is installed such that intermediary energies gamma beams are available in two additional experimental halls increasing the experiments preparation flexibility and, consequently, the total beam time effectively used.

Compared to other facilities that produce gamma beams (for example HIGS at Duke University – USA) the one envisaged for ELI-NP will have a much narrower energetic width allowing the improvement of the experimental sensitivity and new applications.

Coupling a high power laser with a gamma beam will confer ELI-NP facility a truly unique character in the world. Indeed, none of the many existing new projects, lasers with powers similar to those proposed for ELI-NP, will not be able to benefit from the gamma beams synergy proposed here. Technically the temporal and spatial superposition of ultra-short laser and gamma pulses will be for the first time implemented and demonstrated at ELI-NP.

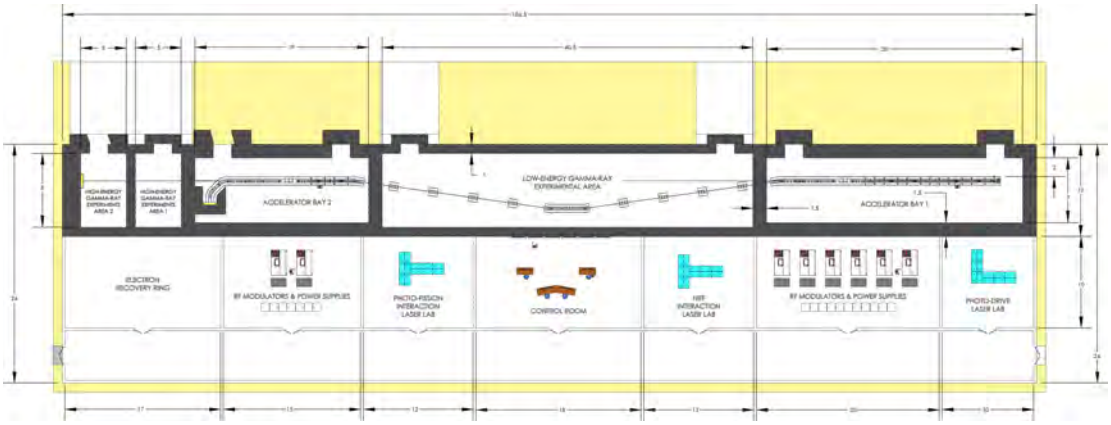

Figure 9.19: Schematic view of ELI-NP high-brilliance gamma source.

The experimental program of the ELI-NP facility addresses both fundamental science research and application-oriented developments in a wide range of fields. Fundamental physics of perturbative and non-perturbative high-field QED, high resolution nuclear spectroscopy and astrophysics-related studies of r-, s-, and p- processes in nucleosynthesis are included in the basic scientific research. The emerging applications are mainly related to the use of nuclear resonance fluorescence (NRF) reactions for radioactive materials and radioactive waste management and of brilliant γ, X, n, e+, e- microbeams in material science and life science. The following list described briefly the role of main experimental equipments needed for such studies:

- The **Spectrometers** are selection and analysis devices for the various types of radiation produced in the interaction of the high-intensity laser beam with the targets. The **Thomson spectrometers for electrons** are compact devices with parallel electric and magnetic fields that allow analyzing of the electron spectrum according to velocity. The version of **Thomson spectrometers for heavy ions** is larger in size and analyzes the heavy ion distribution according to velocity and charge state. The **electron spectrometers** are devices that provide high-resolution information about the energy distribution of the electrons. The **Wien filters** are selection devices, which allow the passage of a narrow band of the total velocity distribution of the ions using perpendicular electric and magnetic fields. The **quadrupole mass filters** are magnetic selection devices, which allow the passage of selected mass ranges from the integral incident ion flux. The **TOF and A/q spectrometers** are charged-particle analyzing devices based on the measurement of the time of flight and mass-over-charge state respectively. The **optical spectrometers** provide high-resolution spectral information about the photon spectra around visible wavelength domain.
- The **Radiation detectors** are radiation sensitive devices, which transform the energy deposited by the incident radiation in electronic signals. The electronic signals are further processed by dedicated electronics and finally digitized and stored for offline analysis. The radiation detectors foreseen for the present section will be used as final stage for the radiation selected or analyzed by spectrometers, or in stand-alone mode.
- The **HPGe detectors** are high-resolution gamma ray detection devices using high-purity Germanium crystals. In the **multi-crystal configuration** the detector normally accommodates four HPGe crystals and provide higher detection efficiency and granularity. The HPGe detectors are used with dedicated electronics, specially designed to preserve their good energy resolution. A **LN2 (liquid nitrogen) filling** system is required for the use of HPGe detectors, since these are functioning only cooled at very low temperatures. In order to reduce the background and increase the peak-to-total ration, the HPGe detectors can be used together

with **BGO anti-Compton shields**, which are low-resolution, high-efficiency scintillation-based detectors covering the sides of the HPGe detector and providing a veto signal in case of Compton scattering.
- The **LEPS** (low-energy photon spectrometers) are thin HPGe detectors transparent for $\sim$MeV photons and efficient for $\sim$100 keV energy domain.
- The **liquid scintillators** are the most effective detectors for neutrons and can be constructed in various sizes and configurations according to experimental requirements. These detectors have poor energy resolution but good time response and need dedicated electronics to separate signals generated by neutrons from the signals generated by gamma rays using pulse-shape discrimination.
- The **neutron spectrometers** are high-resolution analysis devices for the neutron energy distribution. The high resolution is achieved through the measurement of the time-of-flight of the neutrons over suitable distances.
- The **charged-particle detectors** are compact detectors made from Silicon crystals, CsI or other dedicated materials. The charged particles are identified either according to the energy deposition in successive detection layers or by pulse-shape discrimination. These detectors have good energy and timing resolution, but are limited in size. The charged-particle detectors are normally placed under vacuum inside the reaction chamber, in the configuration defined by the experimental requirements.
- The **ionization chambers** are gas-filled detectors for heavy ions, with response proportional to the energy deposition inside them. They can be constructed in large-volume configurations and with reasonably good energy resolution, but with limited timing capabilities.
- The **Time Projection Chambers** are gaseous detectors able to track the path of charged particles through collection of ions generated in gas on a high granularity cathode (proving bidimensional projection of the track while the third dimension is extracted from timing signals, related to the arrival moment of ions cloud on the concerned pad).
- The **Penning trap** is a complex device that allows trapping and accumulation of ions using strong external fields. The **charge breeding** system is used to increase the charge state of temporarily trapped ions.
- The **Reaction chambers for high-intensity lasers** are large volume containers (**frames**) under **vacuum**, specially designed to contain focusing mirrors and other equipment needed for the delivery of the laser beam as requested by the experiments. Furthermore, the reactions chambers must accommodate inside part of the radiation detectors, to allow connections to spectrometers under proper vacuum conditions and to be provided with low-absorption windows to allow gamma and X radiation detection with detectors placed outside the chamber. For the optimal use of the beam-time and also for radioprotection reasons, a **remote target handling** system must be installed in each reaction chamber for high-intensity lasers.
- The **Cryogenic target** systems are needed when the material for the target is gaseous at room temperature, as for instance the Neon. The cryogenic target system allows the cooling of the material up to temperatures when becomes solid, using liquid He.

Fully equipped Optical, Targets, Detectors and Electronics, Dosimetry and Gamma Spectroscopy Laboratories together with Mechanical workshops will assure the maintenance, repairs of the equipments and provide specific support for experiments.

The experimental halls are located efficiently in between the high-power laser and high-brilliance gamma systems. A total of eight experimental halls were proposed, denoted E1–E8, having main primarily thematic assignment as follows:
- E1 – laser induced nuclear reactions;
- E2 – nuclear resonance fluorescence and applications;
- E3 – positrons source and experiments;
- E4/E5 – accelerated beams induced by high repetition laser beams of 1 PW and 100 TW pulse power;

- E6 – intense electron and gamma beams induced by high power laser beams;
- E7 – experiments with combined laser and gamma beams;
- E8 – nuclear reactions induced by high energy gamma beams.

Up to three of these halls are supposed to be used simultaneously: one of them receiving multi-PW laser pulses, the second one – 100 TW/1 PW, high repetition rate pulses, and the third one – the gamma beam. Meanwhile the other halls are available for preparation of next experiments. The use of movable concrete blocks for walls and ceiling allows reconfiguring the experimental area according to the needs expected to evolve very fast in the emerging field of laser driven nuclear physics addressed by ELI-NP facility.

9.4.2 Site and building

ELI-NP will be built at Magurele, Ilfov County, on the premises of the "Horia Hulubei" National Institute of Research and Development in Physics and Nuclear Engineering (IFIN-HH). The site is situated Southwest of Bucharest, at 15 km from the centre of the town. A circular forest with a radius of 800 meters forms the sanitary protection area for the nuclear activities being performed on the site as shown in Figure 9.20.

Figure 9.20: Satellite view of the site and forest ring (Google).

The main reason for choosing Magurele as building site for the ELI-NP facility is its long tradition as a pole of excellence in Physics, the only site in Romania and in all South-East Europe with such a large concentration of research, educational and technological facilities in all major fields of Physics and related domains.

The ELI-NP research infrastructure consists of a major buildings group, which forms the functional and compositional core of the architectural concept, and several adjacent buildings imperatively necessary to sustain the main purpose from technical and functional point of view.

The main buildings assembly shown in the Figure 9.21 is divided into three areas: "Laser Building", "Gamma Beam and Experiments Building" and "Laboratories and Workshops Building". The main adjacent buildings area consists of offices building for research and administrative staff, restaurant, guest-house and the gate access building. All together they amount to about 33 500 m^2 of total built area.

The two arms of the multi-PW ELI-NP laser system are placed in an area of approximately 42×34 m^2. A 50×50 m^2 area will be available for further extensions of the laser system and experimental rooms. The laser system is installed in a 10.000 class clean room, thermally stabilized within approx. 0.5 K, and controlled humidity of 30–50%. The required very low vibration level is maintained installing all sensitive components on thick concrete slab isolated from the walls and suspended form the basement by a matrix of spring and dampers.

Figure 9.21: ELI-NP facility main buildings.

The "Gamma Beam and Experiments Building" will have an external light structure of industrial type and will be equiped with a large crane able to move the concrete blocks defining the experimental rooms and other heavy equipments. The conditions related to temperature, humidity and cleanness are less demanding for this building. Instead, the vibrations has to maintained at the same low level for an even larger area and with much higher load due to the thick biological radioprotection walls defining the various experimental halls. The same technology will be used with a much dense matrix of spring and dampers. It will assure also highly effective antiseismic protection for all the equipments, the building itself being througly design taking account the seismic risk according to national relevant regulations and classification of the region where the facility will be built.

The needs of heating/cooling power for all buildings and equipments may achieve maxima of about 4 MW. A large geo-thermal system is foreseen consisting in about 260 km close-loop liquid circuit (installed in 1000 pits of 130 m each) eliminating completely the gas consumption and compensating rapidly the higher investment cost as compared to a classical system.

9.4.3 Planned budget and timeline

The construction of ELI-NP is scheduled to last approximately 60 months (including the tendering processes). The total value of the investment is 280,000,000 Euro including manpower and excluding VAT. The European Regional Development Fund (85%) and the Romanian public budget (15%) are the addressed financial sources. The budget breakdown is shown in Table 9.6.

Table 9.6: ELI-NP implementation cost breakdown.

Item	Budget (M€)
Planning/Design fees	2,7
Land purchase	0,0
Building and construction	62,8
Plant and machinery	169,3
Laser systems	*80,2*
Gamma beam	*59,6*
Experimental equipments	*23,3*
Workshops and laboratories	*4,3*
Furniture and Fixtures	*0,8*
Intangibles	*1,0*
Contingences	14,0
Technical Assistance – Start-up Grant	30,6
Consultancy	*1,0*
Commissions, taxes	*0,8*
Payroll	*23,0*
Travels	*2,9*
Invited researchers	*0,9*
Others	*0,6*
Overheads	*1,4*
Publicity	0,2
Supervision during construction	0,4
TOTAL excl. VAT	**280,0**

The building and utilities grids cost about 63 MEuro and have an estimated duration of construction of 36 months including design phase and tendering. Thus, the last 24 months of the project will be devoted to installation of specific equipments (high-power laser system, gamma beam source and experimental instrumentation) that will be actually designed and then manufactured on components starting from the very beginning of the project. The personnel is expected to evolve gradually from about 40 part-time employees in 2011 to about 250 full-time employees in 2015. The above budget includes not only their salaries (payroll) but also significant financial resources for their travels to collaborating laboratories as well as for invitation of external experts, organization of workshops and conferences, dissemination of results and publicity.

The draft time schedule of the ELI NP implementation is given in Table 9.7.

Table 9.7: ELI-NP Implementation draft time schedule.

9.5 Regional facilities

The Ecosystem of EU embraces three types of research installations: The European Research Infrastructures, the Regional Facilities and the National Facilities. National Facilities can operate as Regional Facilities as well. EU envisages action integrating all three types and establishing close links, networking and synergy. In this spirit Annex 1 of the Grant Agreement of the ELI preparatory phase (ELI-PP) has foreseen and later the preparatory phase has elaborated on the scheme of Regional Partner Facility (RPF) complimenting the landscape of the ELI pillars. RPFs facilitate optimal integration and exploitation of existing Pan-European expertise in the ELI project. They make active involvement of institutions and scientists in ELI more attractive and long term; promote regional development; support and serve simultaneously European, Regional and National needs and enhance synergy with existing European Research Facilities operating in other locations than the ELI pillars hosting regions.

RPFs are auxiliary facilities of the three (four) ELI pillars, located in other countries (or regions) and providing on demand long term support and services to the ELI pillars. They are small and flexible operational units integrated in the - through them - strengthened operation of the ELI pillars. RPFs operate under the label the central ELI. Upon establishment of the planned ELI-ERIC they operate as part of it.

Their mission is:

- To fill gaps and provide, on demand, transfer of knowledge, training, support and services of any kind, such as technical, technological, scientific, computational, managerial and educational, to the ELI pillars.
- To act as facilities in which methods, technologies and special instrumentation to be exploited by the ELI pillars will be designed and/or developed.
- To act as facilities for testing instrumentation and devices to be used at the ELI pillars, or for feasibility studies of experiments to be implemented at the ELI pillars.
- To act as an incubator of the ELI pillars, in which a number of technological and technical problems may be defined and/or solved.
- To possibly prepare and foster future experiments to be conducted in the main ELI.
- To act as training sites of personnel and users of the ELI pillars.

All costs related to the RPFs are considered to be covered regionally and thus they may act as National Facilities. The investment of the hosting country towards the operation of the established facility as an RPF can be accounted, if requested by the hosting country, as part of the country's contribution to the ELI-ERIC. The ELI pillars may sub-contract the RPF to realize specific projects. The management of the RPFs will be on local basis in collaboration with the central ELI management. Before the establishment of the ELI-ERIC they will operate under national law. The governance of the RPFs will be part of the ELI governance scheme.

During the ELI PP three institutions have expressed their interest in hosting an RPF:

- **CLPU, Salamanca:** The Petawatt laser Science and Technology training RPF.
- **IST, Lisbon:** The High Field Computational Sciences RPF.
- **FORTH-IESL, Heraklion:** The Attosecond Science and Technology RPF.

The ELI preparatory phase has endorsed the development of these three RPFs and has handed the issue out to the delivery consortium thus becoming part of the negotiations between funding agencies and ELI towards the establishment of the ELI-ERIC. Upon establishment of the ELI-ERIC, it may invite in the future other facilities to become an RPF. The three RPFs considered by the ELI-PP are described in the following sections.

9.5.1 The Attosecond science and technology RPF, Greece

I. Location of the Attosecond science and technology RPF

The attosecond science and technology RPF has been proposed by and is considered to be hosted in the premises of the Institute of Electronic Structure and Lasers (I.E.S.L.) of the Foundation for Research and Technology Hellas (FO.R.T.H.) in the campus of the Science and Technology Park of Crete (STEP-C), in Heraklion Crete.

Address: N. Plastira 100, Vassilika Vouton, P/O/ Box 70013, Heraklion, Crete Greece

The infrastructure will not require new buildings but only modifications, redistribution and upgrades of the existing constructions. Its size will be of the order of 500 m^2 including lab and secondary support spaces.

II. Description of, scope and rationale for hosting the Attosecond Science and Technology RPF

The infrastructure will be based on a conventional driving laser source that will be an upgrade of the 3 TW, 40 fs Ti:Sa laser system currently operating at FORTH-IESL. The upgraded system will be a multiple amplification stage, low repetition rate, 70 TW (1.4 J, 20 fs, 10 Hz) Ti:Sa system. Phase stabilization of the system is subject to the success of recently initiated research developments. The RPF will run two XUV/soft-x-ray sources, one based on frequency up-conversion in gaseous media and one based on harmonic emission from surface plasma.

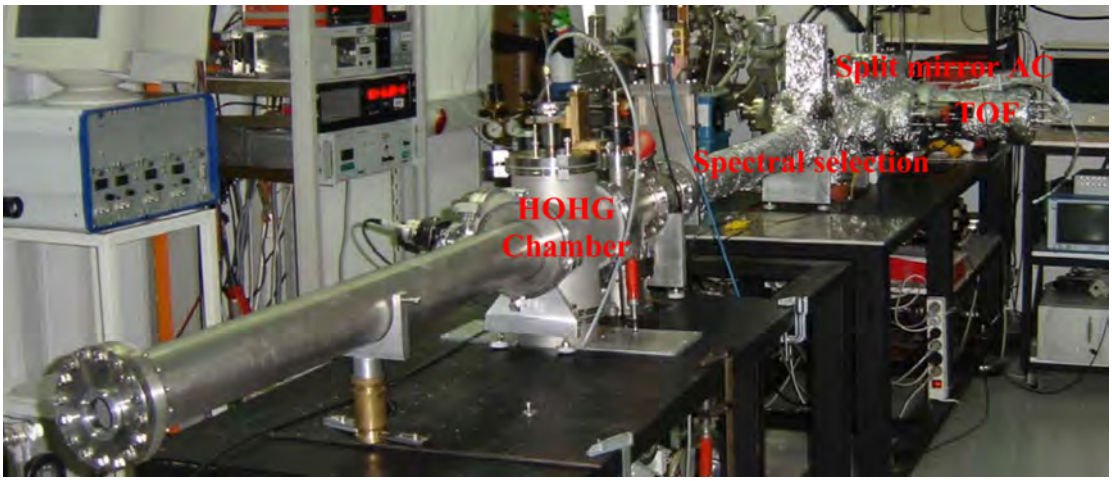

Figure 9.22: Workstation for atomic gas harmonic generation operating at FORTH-IESL. Loose focusing (f = 3 m) leads to intense coherent XUV emission The workstation includes the interaction chamber, spectral region selection and beam delivery unit, split spherical mirror autocorrelator (nominal resolution 6 asec) and XUV ion mass/electron time of flight spectrometer.

The gaseous target source will exploit lose focusing conditions and quasi-phase matching. Increasing the focal length from the current 3 m to 15 m and applying multi-stage quasi phase matching an improvement of the current XUV power of the FORTH-IESL source by three orders of magnitude has been estimated, leading to a GW range XUV power for low harmonics and MW for soft x-rays at the source. While the 20 fs long pulses will generate trains of attosecond pulses, isolated attosecond bursts will be available applying advanced Interferometric Polarization Gating (IPG) techniques, successfully implemented at FORTH-IESL (see [1] and [2]).

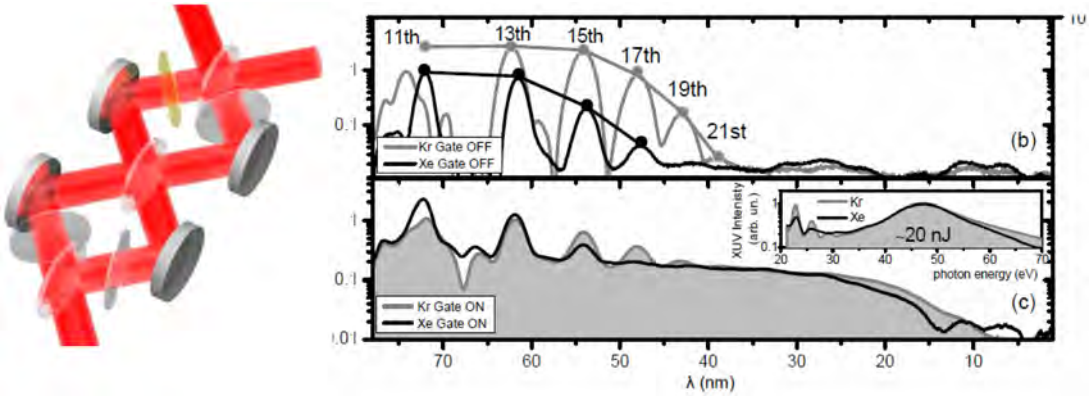

Figure 9.23: Generation of intense broad XUV continua through interferometric polarization gating (see P. Tzallas et al. Nature Phys. 3, 846 (2007)). 30 eV broad continua (central photon energy ∼50eV) produced at FORTH-IESL with an energy content >20 nJ [2], the highest so far generated energy in an isolated broad band pulse, most likely in the attosecond temporal regime.

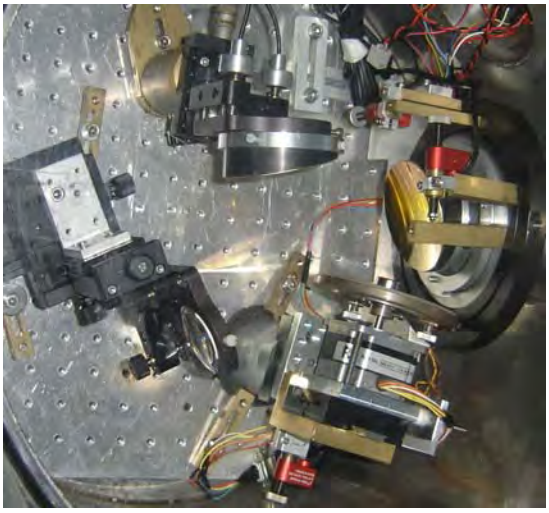

Figure 9.24: Detail from the workstation for surface plasma harmonic generation operating at FORTH-IESL. The first parabola focuses the laser on to the rotating and translationally moving target. The second parabola collimates the XUV radiation.

The recently through IPG achieved sub-100 nJ pulse energy in a several tens of eV broad XUV continuum at central photon energy of about 50 eV is estimated to reach the level of few hundreds of μJ in the new RPF source, allowing the development and tests of non-linear XUV metrology approaches with single asec pulse.

The solid target source based on harmonic emission from surface plasma is estimated to produce pulses of 300–30 asec duration, with 10^{15}–10^{12} photons per pulse at the source, and 20 eV–0.6 keV photon energy respectively.

It should be noted that the above given powers or pulse energies will be reduced by one to three orders of magnitude at the target depending on the wavelength region of the radiation.

The RPF will operate an attosecond radiation source providing unique specs for an intermediate period until the central up-scaled ELI attosecond science beamline will be operational. The RPF specs will be such as to allow realization of a number of developments relevant and

beneficial to the central ELI and in particular the Hungarian pillar. The RPF will develop and test methods, equipment and devices that can be used at the central ELI.

Prototypes of instrumentation to be developed that upon demand can be copied and/or transferred for use in the central ELI include:

Source diagnostics (feasibility studies, design, construction, testing)
A) Temporal
A1) VUV-XUV-x ray non-linear auto-correlators
A1a) 2^{nd} order IVAC
A1b) single shot 2^{nd} order IVAC (not yet demonstrated, ongoing project)
A1c) VUV-XUV FROG (not yet demonstrated, ongoing project)
A2) IR-VUV-XUV cross-correlators

B) Spectral
B1) VUV-XUV spectrometers
B2) Ion–Electron spectrometers

C) Spatial
C1) VUV-XUV beam imaging systems (beam profilers)
C2) Spatial coherence devices (Spatial interferometers)

Source components (feasibility studies, design, construction, testing)
A) Targets – generators
A1) Gas-jet targets (synchronization) – quasi static cells – quasi phase matching arrangements.
A2) Solid state targets (Surface targets) – multitarget arrangements (under development).
A3) Efficient/compact polarization gating setups for intense isolated attosecond pulse generation

B) Beam manipulation-delivery set-ups
B1) Beam delivery stages (collimators-focusing systems)
B2) Spectral range selecting set-ups-beam separators
B3) VUV-XUV spatial modulators (not yet demonstrated)
B4) Compressors
B5) Multi color multi beam lines for time resolved experiments
B5a) Multi color (IR-VUV-XUV) delivering devices with variable relative delays.
B5b) VUV, XUV, X-ray time resolved spectroscopy workstations
B5c) VUV-XUV pump – VUV-XUV probe spectroscopy workstations
The RPF will be further available for testing of new XUV and X-ray optics to be used at the central ELI.

Some of the above items are conventional equipment, some are already operational at FORTH-IESL, some others need further development, while few of the above require demanding research that ideally should be conducted in joint research projects of the RPF, the Hungarian pillar and/or other ELI partners.

Highly relevant to the development of instrumentation is the progress in development and evaluation of methods. Here research in extending non-linear processes to shorter XUV wavelengths and X-rays will be conducted. These processes are highly pertinent to attosecond pulse metrology, based on non-linear autocorrelation approaches. In this framework, the so far unexplored territory of inner shell non-linear processes becomes relevant and will be part of the RPFs research program. Furthermore comparative studies between different approaches are becoming important in order to reach reliable metrology tools. A recent comparison between the 2^{nd} order IVAC and the RABITT approach performed at FORTH-IESL has given significantly different results between the two approaches [3].

This experiment alarms the quest for the continuation of this type of studies in different spectral regions and also be conducted for other approaches as well. Such investigations are

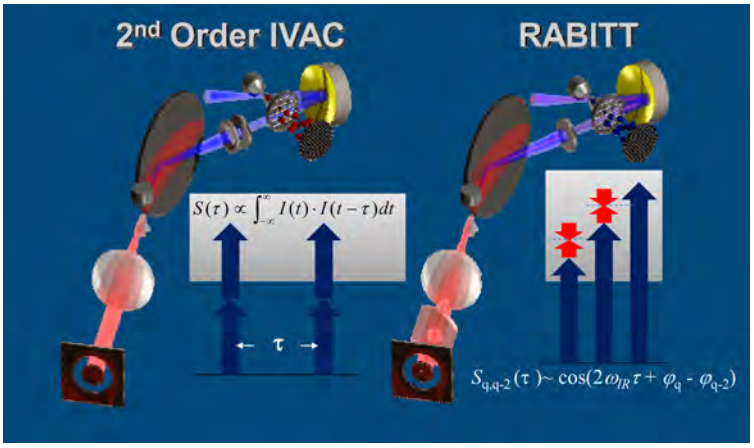

Figure 9.25: The experimental set-ups used in the comparative study between the 2^{nd} order IVAC and the RABITT technique [3]. The set ups are almost identical. The split mirror has been used as wave front divider in the 2^{nd} order IVAC and as a mirror in the RABITT.

in FORTH-IESL's research priorities and will be also included in the research program of the RPF. The RPF will preferably conduct them in collaboration with the research personnel of the Hungarian pillar, initially at the RPF and later on, for verification, at site of the pillar. The recently initiated at FORTH-IESL broad band XUV Fourier Transform Spectroscopy (see [4], time resolved XUV spectroscopy [5]) and the currently under development XUV-pump-XUV-probe (two-XUV-color) spectroscopy are further research topics of the RPF, which can be integrated in a common research program with the central ELI, through which the RPF will further provide training to collaborators of the central ELI.

After the central ELI will be delivered the regional infrastructure will continue serving on demand needs of and support the operational central ELI. It will further be used as an instrument for innovative developments to be integrated in the central ELI attosecond beam line, as well as a test unit for components and set ups to be used in ELI

III. The hosting region and impact

The hosting of an attosecond regional infrastructure of ELI by FORTH-IESL serves strategic purposes of the project. The region of Crete has a long standing successful presence in the landscape of European RIs and received several excellent assessment reports. FORTH-IESL operating as a European Research Infrastructure since 1990, has provided more than 2000 days of access to European researchers from 25 countries dedicated to more than 350 research projects. An international scientific environment is well established. Numerous research collaborations exist with universities, research and cultural centres around the world in the framework of EU funded projects, as well as on international programmes and on bilateral basis, while links with industry and technology companies have been established in the framework of technology oriented projects. IESL is also active in training, operating as a Marie Curie Training Site supporting European PhD candidates.

The existing human expertise in the field at the host, part of its today operating advanced equipment (3 TW laser system, the intense XUV attosecond radiation workstation, diagnostics and related material) will form a substantial basis of the regional infrastructure, thus reducing its construction costs.

As for the regional and national impact initiatives to which synergies of the infrastructure will be developed are contained in the National Roadmap for Research Infrastructures, with

additional commitments by the RI plan of the region of Crete. The infrastructure will promote regional development and act as a national and regional infrastructure, serving besides ELI the recently established relevant Greek network of 11 institutions. Finally the infrastructure in synergy with the European Laser Facility, operating at FORTH in the framework of LaserLab Europe, will form a Regional Research Complex at the periphery of Europe and the region of eastern Mediterranean basin enhancing innovative R&T initiatives in the region.

IV. Environment of the site

Since the infrastructure will be hosted in the exciting operational buildings all relevant issues and regulations had been adhered to, such as seismic issues and construction considerations. Special building upgrades with respect to the interferometric stability of instrumentation and lab environment cleanliness are foreseen and included in the financial breakdown.

The safety and radioprotection framework of the infrastructure will be established through the Safety Plan that is currently worked out by the subcontracting institution of FORTH, namely the Technical University of Chania (TUC) within the ELI preparatory phase program.

V. Financial aspects

An indicative cost of the construction of the infrastructure is 5 MEuro, with running costs per year of the order of 300 kEuro. These costs are considered to be covered by the hosting country and institution. Part of this cost will be valued as establishment cost of the RPF, which will be accounted as in kind contribution of the hosting country to the ELI-ERIC.

VI. Legal aspects and management

Prior to the establishment of the ELI-ERIC, the RPF will operate under national low and later on under the ERIC legal scheme. The management of the infrastructure will be by a local management team, which will be in close collaboration with the ELI management and within the ELI governance framework.

Bibliography

[1] P. Tzallas et al. Nature Phys. **3**, 846 (2007)
[2] P. Tzallas et al. Opt. Lett. 34, 1732 (2009)
[3] J. Kruse *et al.* Phys. Rev. A 82, 021402(R) (2010)
[4] E. Skantzakis et. al. Phys. Rev. Lett. **105**, 043902 (2010)
[5] A. Peralta Conde PRA **79** 061405(R) (2009)

9.5.2 High Field Computational Sciences RPF, Portugal

Context and Rationale

ELI will open new and exciting avenues for research in high field science with ultra high laser intensities, where traditionally there has always been a strong interplay and link between experiments, theory and simulations. While there are many theoretical and computational initiatives in individual EU countries addressing high field science, the large scale nature of ELI and the corresponding scientific challenges require common strategies and foster the need to federate these initiatives, since simulation and computational techniques are a critical enabling tool to unravel all the potential of ELI. Therefore, it is important to establish coordinated efforts in order to build up critical mass and to perform advanced training to support the development of ELI and the associated communities at EU level. While it is likely that some of the critical simulation and theoretical aspects will be directly supported at the level of the ELI pillars, there is an obvious need to further support ELI in terms of High Field Computational Sciences.

Goal

The main goal of the High Field Computational Sciences RPF is to be the hub and focal point for a collaborative network of research teams on theory and modeling of high field physics with ultra high laser intensities.

The High Field Computational Sciences RPF will assume the format of a "collaboratorium" through dedicated workshops, mini-courses, a visitors' program (senior scientists), students and post-docs, and by hosting of workgroups on Computational Science topics directly relevant for ELI with dedicated access to the relevant infrastructures (office space, meeting rooms, and videoconference facilities) and tools (high performance computing, numerical codes, visualization tools), thus minimizing permanent costs but providing the enabling conditions for successful collaboration in Computational Sciences. We envision that the High Field Computational Sciences RPF will be hosted by Portugal.

By providing a a hub for collaboration in theory and modeling of high field physics, and working as a common platform between HiPER and ELI in theory and simulations, it will foster coordinated actions in Computational Sciences between the ELI pillars to support numerical and theoretical developments in the field of high field physics with ultra high laser intensities.

The activities of the High Field Computational Sciences RPF will also leverage on the connection with other activities of the ESFRI projects HiPER (on laser fusion) and PRACE (on supercomputing), while providing a direct gate to global initiatives in EU Information and Communication Technologies R&D and Training programs.

The High Field Computational Sciences RPF will be the forefront of the european joint effort in High Field Computational Sciences and a partner and enabler to its most advanced experimental facilities.

9.5.3 Ultrashort, Ultraintense Pulsed Laser Center, Spain

The Ultrashort, Ultraintense Pulsed Laser Centre (CLPU) is a new research facility that has been created as a Consortium of the Spanish Ministry of Science and Innovation, the Regional Government of Castilla y León and the University of Salamanca, as part of the implementation of the Spanish Scientific Infrastructures Roadmap. The Consortium headquarters are located in Salamanca, Spain. The Consortium was created on December 14th, 2007. The objectives of the Consortium, as stated at the starting document, are to build and operate a Petawatt Laser in Salamanca, to develop ultra-short-pulse technology in Spain, to make significant advances in intense, compact laser technology, to promote the use of such technology in several fields: Physics, Engineering, Chemistry, Biology, Medicine, Energy, etc., and to open the facility to the domestic and international scientific community. CLPU is the reference center in Spain for Ultraintense Lasers.

CLPU main equipments will be a 200 TW/30 fs laser with a repetition rate of 10 Hz and a one PW/30 fs system at one shot per second. Both systems will be open to ELI users and also will be open to help in the construction of ELI for checking ideas/parts of the construction. CLPU is building also an attosecond beam line that can be relevant for the additional interaction with one of the ELI pillars.

One strength of CLPU, and of the University of Salamanca, is high level training. CLPU and the University offer a Master and Ph.D. Program on Lasers specifically devoted to the TW and PW technology. Through this program, or variations of it, a training for future PW users is specifically foreseen. Since multi-PW experiments are very demanding and very expensive, in certain cases and for non laser-expert users training on the possiblities of such lasers and preliminary proofs-of-concept can de done at PW facilities al lower price and lower risk. Users having a clear experimental evidence that a PW is not enough for their needs are the ideal users of multi-PW facilities.

Also CLPU is setting the Spanish laser radioprotection standards. CLPU experience in this point is opened to the three ELI sites to design their own radioprotection plans.

Being CLPU the Spanish National Center for this kind of technology, it will convey and organize the efforts of many other Spanish institutions in relation to ELI, both from the point of view of universities and research centers and from the point of view of Spanish companies involved in laser technology or in auxiliary technologies relevant for the ELI sites. Moreover, CLPU will be operative before any of the ELI sites.

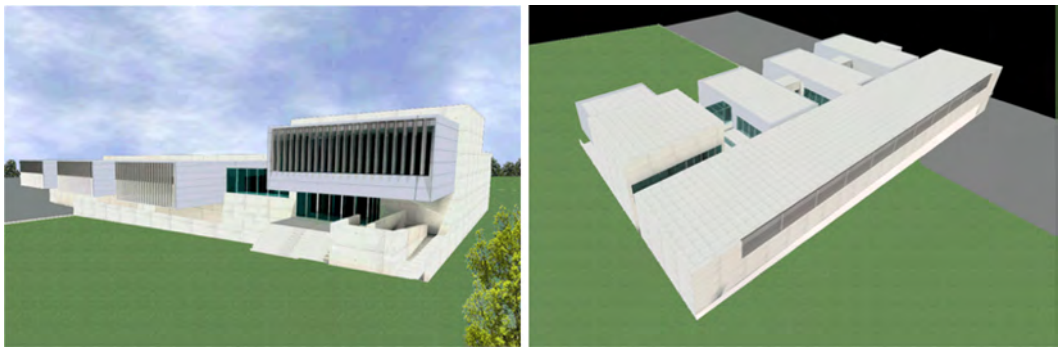

CLPU, Salamanca: The Petawatt laser Science and Technology training RPF.

10 Institutional and legal implementation of ELI

This chapter provides details on the legal and organizational arrangements envisaged for the implementation and subsequent operation of the Extreme-Light-Infrastructure.

On October 1st 2009, in Prague, the Steering Committee of the ELI Preparatory Phase Consortium (ELI-PP) – which consists of the representatives of the funding agencies of the 13 EU countries involved in ELI-PP – gave the mandate to the Czech Republic, Hungary and Romania to jointly implement the project through the construction of three facilities with respective mission in the beamline, attosecond and photonuclear applications of ELI, three of the four Grand Challenges identified in the scientific case of the project and described in this White Book.

The three host countries are committed to invest nearly 800 million euros from structural funds to build, commission and open ELI to users by end 2015. This investment also covers their participation in the technological developments necessary for the fourth Grand Challenge of ELI – the ultra-high field facility – in international coordination and cooperation with the other ongoing prototyping initiatives. The location of this fourth emblematic "pillar" should be decided in 2012 on the basis of a review of the performance and readiness of the various technological options.

The decision to implement ELI as a multi-site research infrastructure is the result of a thorough analysis conducted within the Preparatory Phase, both at the scientific and political levels. The scientific and technical terms of this debate are detailed in the previous chapters of this White Book. However, financial and strategic elements were also taken into account when reviewing the potential options for implementation.

On the one hand, in a context where the interest in high intensity laser science is booming at global level, the swift materialisation of ELI is considered a priority for Europe's scientific competitiveness. The availability of structural funding in the three host countries, in addition to a strong political support, was therefore analysed as a unique opportunity to gather sufficient funding and materialise swiftly the first phase of the project. The impossibility of pooling structural funds from different countries due to the conditions applying to this kind of funding supported the scientific and technical arguments in favour of a multi-site implementation.

On the other hand, from a political point of view, establishing a large-scale Research Infrastructure of the magnitude of ELI in three new Member States appeared as a major opportunity to support the development of the European Research Area (ERA), the cornerstone of EU's research objectives. ELI will indeed represent a significant contribution to a better balance in the distribution of Research Infrastructures in Europe (there is no other Research Infrastructure of such a scale in the new Member States). Finally, thanks to appropriate HR schemes, the three ELI facilities, forming a single infrastructure, will have the potential for promoting mobility of researchers and preventing brain drain, a curse that has long affected Central and East European countries.

In its resolutions, the Steering Committee provided precisions on the legal conditions that should govern this mutli-site implementation of the Project:

- The mandate granted to the three host countries concerns the development of an "integrated" infrastructure, i.e. of an infrastructure placed under the coordination of a single governance structure
- The three nations have the responsibility to establish a pan-European consortium to deliver ELI
- The hosts should sign as soon as possible a Memorandum of Understanding leading to an ERIC, followed by the countries "ready and willing to contribute to the realisation of ELI".

The latter three resolutions were based on a preliminary legal analysis conducted within the Work Package "Legal" of the ELI Preparatory Phase. Participants in this working group had

reviewed various possible legal forms and concluded that the newly established "European Research Infrastructure Consortium" represented the most appropriate one given its flexibility, its recognition and validity in all EU Member States, and its privileges and exemptions (see elements of understanding on the ERIC legal form in section 4 of this chapter). It was also perceived as the most convenient structure to preserve the inclusive and pan-European nature of the Project and allow for the involvement and contribution of other partners.

Since October 2009, the Work Package "Legal" and the three host countries have studied in depth under which conditions the resolutions of the Steering Committee could be legally implemented. The main objective of this analysis was to define more precisely, under which legal arrangements the establishment of the ELI-ERIC could be feasible, especially given the constraints pertaining to the use of structural funds by the three host countries.

It results from this analysis that the legal organisation of the project will be based on two main phases:

- During the implementation of the project (2010-2015), the three host countries will apply for funding and conduct all activities linked to the construction, research and development, setting-up, assembling, testing and commissioning of the three ELI facilities by the proxy of local legal entities (already existing or specifically created for the Project). These entities will be placed under the coordination of a Consortium – the *ELI Delivery Consortium* – the tasks of which will be to ensure the best use of available technological and human resources within the European scientific community and the accomplishment of all steps required for the establishment of the ELI-ERIC.
- In due time, when all required conditions will be satisfied and when negotiations will be completed, the application for establishing the ELI-ERIC will be submitted to the European Commission for approval. The main task of the ELI-ERIC will be to establish ELI as a single research infrastructure by pooling the three facilities and organise their joint operation. The establishment of the ELI-ERIC is therefore targeted no later than the end of 2014 in order to organise efficiently the opening of the infrastructure to users by January 2016.

This chapter consists of 4 sections:

- The first section reminds the steps that led to the approval of the multi-site implementation and details the resolutions adopted on 1 October 2009 by the Steering Committee of ELI-PP
- The second section briefly introduces the institutional arrangements adopted at national level by the three host countries to carry out the implementation activities related to the Project
- In the third section, we detail the rationale, objectives and organisation of the ELI Delivery Consortium as well as the steps leading to the establish of the ELI-ERIC
- Finally, the fourth section provides elements of understanding on the ERIC legal form and introduces the organisational structure considered at this stage for the operation of ELI. It details in particular the distribution of tasks between the ELI-ERIC and the local ELI entities located in the three host countries.

10.1 Genesis and terms of the decision on the implementation of ELI

10.1.1 Path to the decision

The decision on the location and conditions of implementation of ELI is the result of a long process initiated in the second half of 2008 with the launch of a call for site proposals, and concluded on 1 October 2009 with the resolutions of the Steering Committee detailed below. This process involved official discussions, under the aegis of the Site Choice Committee of the Preparatory Phase and of the Steering Committee, but also informal discussions between the Czech, Hungarian and Romanian representatives, with the strong support of other parties involved in the Preparatory Phase. We summarize below the main steps of this process.

- Following a call, five countries (the Czech Republic, France, Hungary, Romania, and the United Kingdom) submitted a proposal for hosting ELI in October 2008. On 17 April 2009, the five countries presented and defended their proposals in Stresa (Italy) before the Site Choice Committee of ELI-PP advised by a panel of four international experts from Germany, Italy, Sweden and the USA. They reviewed and evaluated the proposals on the basis of four criteria: quality and size of the scientific community relevant to ELI in the country, quality and size of the industries relevant to ELI, synergy with existing and planned scientific initiatives, and financial aspects.
- On 20 May 2009 in Paris, the Czech Republic was mandated by the ELI Steering Committee to take the lead of negotiations with other members of the ELI-PP Consortium on an “Integrated Proposal" for the implementation of the ELI project.
- A first version of a Czech-Hungarian Integrated Proposal was presented to the Steering Committee in Budapest on 17 July 2009. It was agreed on that occasion that both countries should invite Romania to join negotiations and work on an Integrated Proposal complying with the following principles:
  1. ELI should be a multi-site infrastructure placed under a single governance.
  2. The Integrated Proposal should encompass the whole scientific case of ELI including the ultra-high-intensity “pillar" of the project.
- On 5 August 2009, Romania issued a written proposal whereby it offered to contribute to the implementation of ELI through the establishment of a laser-induced photonuclear physics facility in Magurele (Romania) by end 2015. It was agreed by the three negotiating parties to submit the Romanian proposal to experts from France, Germany and the UK for evaluation.
- After two months of negotiations and following the review of the Romanian proposal by the experts, the Steering Committee met in Prague on 1 October 2009 and approved the Integrated Proposal presented by the three countries. This decision was fully supported by the European Commission, represented at this meeting by Robert-Jan Smits, Director of Directorate B (The European Research Area: Research Programmes and Capacity) and representative of the European Commission within the European Strategic Forum on Research Infrastructures (ESFRI).
- The three host countries presented the Integrated Proposal and proclaimed their readiness to accept the mandate given to them by the Steering Committee on the occasion of a meeting of the Competitiveness Council, in Brussels, on 3 December 2009. Figure 10.1 below details the main steps of the negotiation process.

10.1.2 Resolutions of the ELI-PP Steering Committee on the implementation of ELI

Here, we reproduce the content of the resolutions of the Steering Committee of the ELI Preparatory Phase, as adopted on 1 October 2009 in Prague. These resolutions represent for the three host countries and their future partners a binding framework for action since they are, up to now, the only document on the implementation of ELI formally approved by the Funding Agencies.

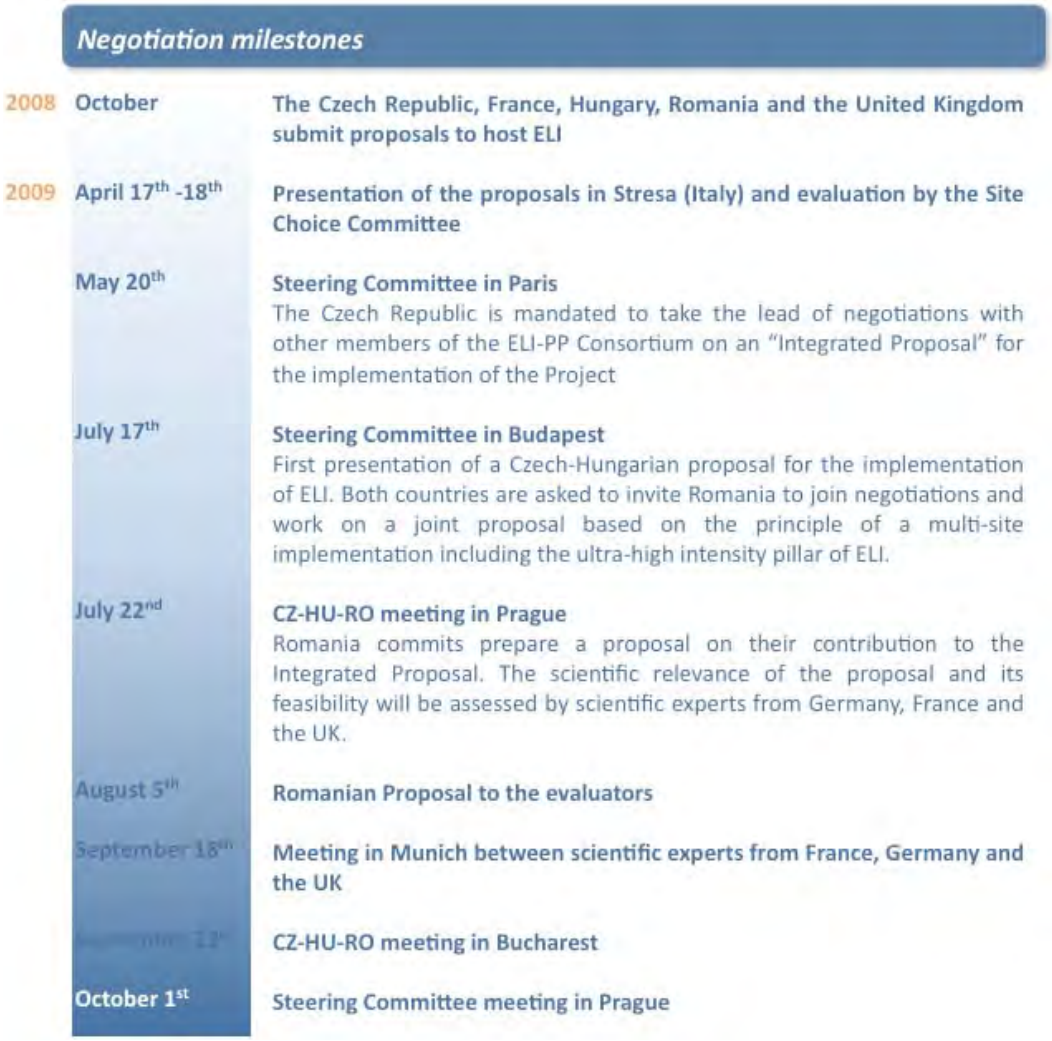

Figure 10.1: Main steps of the negotiation process.

The Steering Committee of ELI-PP declares:

- It is very satisfied with the progress made by the ELI PP consortium and the formation of an integrated proposal by the Czech Republic, Hungary, and Romania.
- The three candidate host nations (Czech Republic, Hungary, Romania) have the mandate to continue their development of an integrated ELI infrastructure. The three have equal status.
- The existing ELI-PP consortium should provide full ongoing support and help ensure a smooth transition to the new structure.
- The three nations take the responsibility to establish a pan-European consortium to deliver ELI. Every effort should be made to be as inclusive as possible in forming this delivery consortium.
- The hosts' responsibility encompasses:
  - Establishment of the appropriate legal, governance and financial solutions.
  - Establishment of a single, robust technical delivery plan that encompasses the whole ELI project, consistent with the constraints imposed by the funding agencies and the technical

capacity and capability of the partners

- The three hosts should aim to declare their leadership and forward plan at the European Competitiveness Council on 3rd December 2009.
- A Memorandum of Understanding leading to an ERIC should be signed as soon as possible by the host nations, followed by those nations ready and willing to contribute to the realisation of ELI.
- The option of including other nations at a later date should be kept fully open.
- The relationship between the ELI ERIC and Regional Partner Facilities should be defined on the same timescale as the formation of the ERIC.

10.2 Institutional arrangements in the three host countries

10.2.1 Elements on the EU Regional Policy

The facilities located in the three host countries will be funded by means of structural funds. This type of funding is the main instrument of the Regional Policy of the European Union, the aim of which is, among others, to promote growth-enhancing conditions and factors leading to real convergence for the least-developed Member States and regions of the Union.

Although the Structural Funds are part of the Community budget, the way they are spent is based on a system of shared responsibility between the European Commission and Member State authorities:

- The Commission negotiates and approves the development programmes ("Operational Programmes") proposed by the eligible Member States and allocates resources.
- The Member States and their regions manage the programmes, implement them by selecting projects, control and assess them.
- The Commission is involved in programme monitoring, commits and pays out approved expenditure and verifies the control systems of the national competent authorities.

For each Operational Programme, the Member State appoints a managing authority (a national, regional or local public authority or public/private body to manage the operational programme), a certification body (a national, regional or local public authority or body to certify the statement of expenditure and the payment applications before their transmission to the Commission), and an auditing body (a national, regional or local public authority or body for each operational programme to oversee the efficient running of the management and monitoring system).

10.2.2 Application process in the three host countries

The three facilities located in the Czech Republic, Hungary and Romania will therefore be funded under three different Operational Programmes co-funded by the European Regional Development Fund (ERDF)[1]:

- The Operational Programme "Research and Development for Innovations" in the Czech Republic
- The Operational Programme "Economic Development" in Hungary
- The Operational Programme "Increase of Economic Competitiveness" in Romania.

A specific evaluation process organised by the relevant national Managing Authority decides on the allocation of funding in each of these Operational Programmes. Given the level of funding – over € 50 million –, the three facilities are considered *major projects* and have to be approved by the European Commission.

As most policies of the European Union, Regional Policy is defined and organised according to the budgetary timeframe of the EU, i.e. by Framework Programmes (FPs). The ongoing Seventh Framework Programme covers the 2007–2013 period. However, to facilitate their adaptation and integration, a two-year extension is granted to new Member States in some instances. This will apply to the three ELI grants, and the deadline conditioning the eligibility of funds is therefore 31 December 2015.

The rules of the three Operational Programmes exclude the possibility of having a non-national entity as the applicant for funding or beneficiary of the grant. This precluded in particular having an international Consortium or even the ELI-ERIC as the applicant or direct beneficiary of the funds. In the three host countries, national entities – existing entities or ad-hoc legal vehicles – will be in charge of preparing the application and managing all activities related to the implementation of the ELI Project (all activities linked to the construction, research and

[1] In all three countries, part of the investment is co-funded by national financial resources (approximately 15% in the three countries).

development, setting-up, assembling, testing and commissioning of the three ELI facilities until December 2015):

- The Institute of Physics of the Academy of Sciences in the Czech Republic
- The ELI-Hungary limited liability company in Hungary, an ad-hoc not-for-profit public company owned by the town of Szeged and the State
- The Horia Hulubei National Institute of Physics and Nuclear Engineering, in Romania, in partnership with two other Institutes located in Magurele, namely the National Institute for Laser, Plasma and Radiation Physics and the National Institute for Research and Development for Material Physics.

The application for the funding of the ELI Beamlines facility located in the Czech Republic has been submitted to the European Commission on 30 June 2010. It is expected that it will be approved by the end of the same year. The application for the ELI Nuclear Physics facility located in Romania should be submitted to the European Commission by the end of 2010. The submission of the application for ELI Attosecond facility located in Hungary is scheduled in March 2011.

The three applicants and beneficiaries mentioned above will be solely accountable to their respective national Managing Authority for the due execution of the activities described in the grant agreements. This individual responsibility will not affect the consistency of the project. All three grant applications comply entirely with the decisions taken within the ELI Preparatory Phase and with the terms of this White Book. In addition, the three facilities will be placed under the coordination of the ELI Delivery Consortium the task of which will be, among others, to ensure the consistency of ELI as a single Research Infrastructure.

10.3 Objectives and organisation of the ELI Delivery Consortium

10.3.1 Establishment and missions of the ELI Delivery Consortium

As requested by the ELI-PP Steering Committee in its resolutions of 1 October 2009, the three host countries negotiated a Memorandum of Understanding enshrining their official commitment to work jointly on the implementation of ELI in full accordance with the terms of the Steering Committee's resolutions (see above). This document was signed on 16 April 2010 and is reproduced in the annex to this chapter.

In order to manage efficiently the transition between the ELI Preparatory Phase and the future ELI-ERIC, the Memorandum of Understanding establishes a new organisation, the ELI Delivery Consortium. Structured in the same spirit of an ERIC, this Consortium is designed so as to enable the coordination of the local project teams of the three host countries and involve and connect efficiently all stakeholders interested in participating in the implementation of the project.

The ELI Delivery Consortium will be entrusted with two essential tasks:

- Definition of a robust and comprehensive delivery plan: on the basis of a precise assessment of the human resources and expertise available in Europe, the delivery plan should set the conditions for an implementation of ELI on time, to budget and to formulate the necessary specifications, consistently with the constraints of the funding agencies and within acceptable risk
- Establishment of the ELI-ERIC: the ELI Delivery Consortium will initiate and coordinate all activities required for the establishment of the ELI-ERIC, including the definition of the Statutes, governance model, and consolidated budget (Cost Book for implementation and operation of ELI) as well as all negotiations within the Steering Board of the new Consortium between funding agencies willing to contribute.

Both the definition of this delivery plan and the preparation of the application for establishing the ELI-ERIC represent an opportunity for an optimal coordination of all existing and projected activities potentially useful for the implementation of ELI. Given the magnitude of the project and the tight time constraints imposed by the use of structural funds (see previous section), the objective of the ELI Delivery Consortium is to define the conditions of an optimal use of the available resources and maximise the chance of success of ELI by defining strategically the rules governing the participation of funding agencies and partner institutions.

10.3.2 Organisation of the ELI Delivery Consortium

The ELI Delivery Consortium will consist of three types of organs: a Steering Board, a Project Management Board and Task Groups.

- The ELI Delivery Steering Board will be the supervising body of the ELI Delivery Consortium. It will approve the final delivery plan attached to the Statutes of the ELI-ERIC, approve the reports of the Management Board on the activities of the Delivery Consortium and enable the members of the Consortium to decide and commit on matters required for the establishment of the ELI-ERIC and especially on contributions. The Steering Board will aim at taking decisions unanimously (meaning in particular that no decision can be taken against the national interests of the Parties involved in the Consortium).
- The ELI Delivery Management Board will be the management body of the ELI Delivery Consortium at operative level acting according to the decisions of the Steering Board. Its main tasks include in particular the coordination and control of the activities of the Task Groups and reporting on progress to the Steering Board. The Management Board shall consist of at least one representative of each member country appointed by its respective ELI plenipotentiary.

- The Management Board will establish specialised Task Groups in charge of carrying out the tasks of the Consortium, such as technical and scientific coordination, financial and legal issues, industrial aspects, etc. The Management Board will define an action plan and deliverables for each of the Task Groups.

An Expert Group shall be established by the Managing Board and entrusted with the mission to produce a "Resourced Project Assessment" (see Article 2(4) of the Memorandum of Understanding reproduced in the annex). This assessment shall identify in particular the human resource capacities and expertise available at the European level for the implementation of the Project and review the funding capacities and time constraints. On the basis of this assessment, the Expert Group shall provide the Steering Board of the ELI Delivery Consortium with recommendations on the establishment of a consistent and single delivery plan for the overall project.

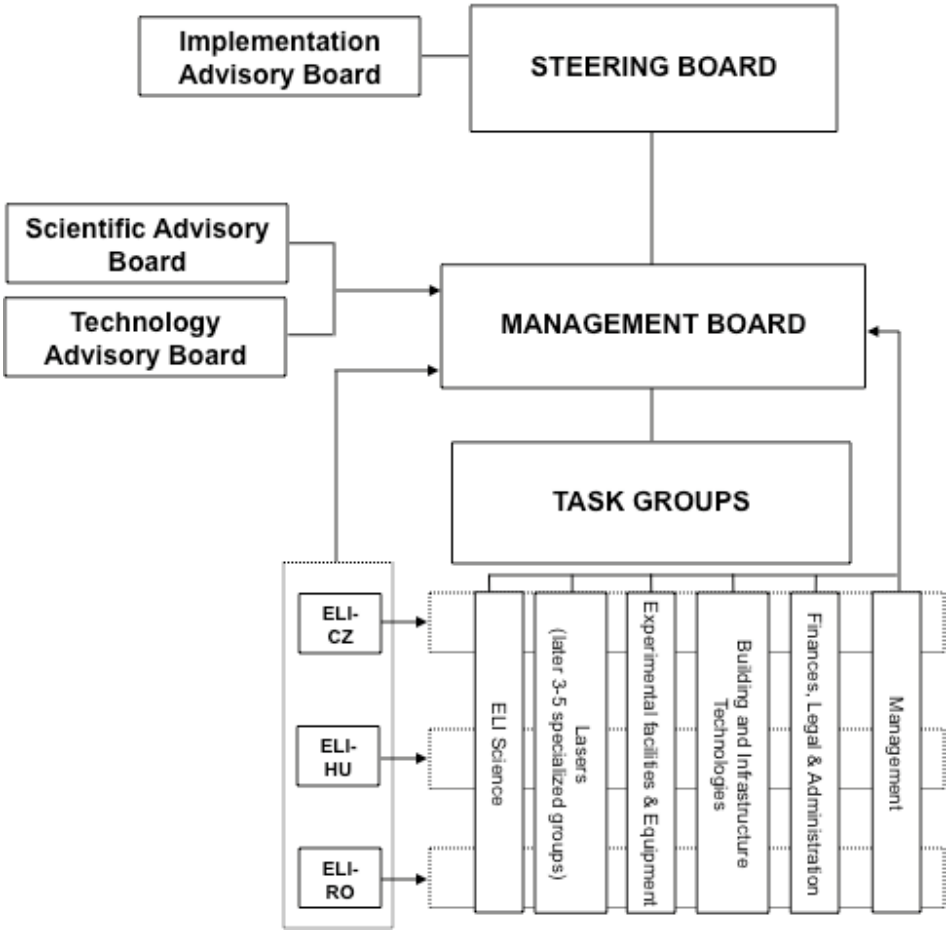

Figure 10.2: Organisational structure of the ELI Delivery Consortium.

As shown on Figure 10.2, some longer-term advisory bodies are envisaged such as a Technology Advisory Board and a Scientific Advisory Board. An Implementation Advisory Board shall also review the progress of the implementation activities carried out on site and report to the Steering Board of the ELI Delivery Consortium.

10.3.3 Work plan of the ELI Delivery Consortium

At this early stage, the following milestones are foreseen:

- Invitation of other funding agencies to join the ELI Delivery Consortium: an invitation letter was jointly sent by the Czech, Hungarian and Romanian plenipotentiaries for ELI to the 10 other funding agencies involved in the Preparatory Phase. This letter invites all countries interested in participating in the negotiations on the establishment of the ELI-ERIC to join the ELI Delivery Consortium
- Negotiations of the terms of accession between the three host countries and the countries willing to join the ELI Delivery Consortium
- Definition of the terms of reference and internal regulations of the ELI Delivery Consortium
- Appointment of an Expert Group in charge of producing a "Resourced Plan Assessment" of the human resource capacities and expertise available at European level for the implementation of the project on the basis of the implementation plans and project documentation prepared and provided for by the three local ELI teams
- Definition of a single and robust delivery plan of the project on the basis of the Resourced Plan Assessment
- Definition of a "Cost Book" and of rules for contributions to the ELI-ERIC
- Negotiations on the establishment of the ELI-ERIC.

10.4 Prospective structure and missions of the ELI European Research Infrastructure Consortium (ELI-ERIC)

One of the deliverables of the Work Package "Legal" within the ELI Preparatory Phase consisted in reviewing the possible legal vehicles for the future infrastructure and on deciding on the most appropriate one. The newly formed ERIC is the one that was favoured by most participants and further approved by the ELI-PP Steering Committee.

10.4.1 Elements of understanding on the ERIC legal form

Creating an appropriate Community legal framework for the development of pan-European research infrastructures has been one of the key initiatives taken by the European Commission to reinforce the European Research Area over the past four years. Until now, the absence of an adequate legal framework allowing the creation of appropriate partnerships with partners from different countries has been a major difficulty for Member States in setting up large-scale Research Infrastructures. The resulting lack of legal and fiscal clarity caused delays in investment and construction.

This is why, in July 2008, the European Commission presented a proposal for a Council regulation on a Community legal framework for European Research Infrastructures. The Council of the European Union reached a political agreement on the draft regulation on 29th May 2009. Published on 28 August 2009, Regulation (EC) 723/2009 establishes this new Community legal framework for a European Research Infrastructure Consortium (ERIC). It is the result of a 2-year consultation involving experts and stakeholders.

This legal framework addresses five essential needs:

- It provides a legal personality recognised in all Member States
- Its universal recognition at European level makes it a genuine European venture
- It has enough flexibility to adapt to the requirements of specific infrastructures
- This legal entity is provided with some of the privileges and exemptions allowed at a national level to intergovernmental organisations
- This tailor-made legal framework will offer the opportunity to cut down significantly the time and legal complexity necessary for setting up European research infrastructures and is therefore expected to facilitate the implementation of the ESFRI Roadmap.

Objective and missions of an ERIC

Article 3.1 of Council Regulation (EC) No 723/2009 of 25 June 2009 on the Community Legal Framework for a European Research Infrastructure Consortium (ERIC) states that the principal task of an ERIC shall be "to establish and operate a research infrastructure". The latest version of the Practical Guidelines on the ERIC Regulation[2], issued in April 2010 by the Directorate-General for Research, provides some interpretation of this provision (page 12) by indicating that Article 3.1 "does not hinder the setting-up of an ERIC in order to manage an existing research infrastructure".

It results from this interpretation that the task of "establishing a research infrastructure" shall not be understood as referring strictly to the construction of the facility itself, but that "establishing a research infrastructure" has the broader meaning of providing the scientific community with facilities, resources and related services necessary to conduct a certain type of research.

As a consequence, "establishing" the Extreme-Light-Infrastructure can be understood, within the meaning of Article 3.1, as the definition of the legal and institutional arrangements organising the "efficient coordinated operations of [the] distributed facilities" (Practical Guidelines of

[2] Available on http://ec.europa.eu/research/infrastructures/index_en.cfm?pg=eric

the ERIC Regulation, page 12) and does not therefore necessarily need to include the activities related to the construction and implementation of the latter facilities. Given the distributed nature of ELI, the pooling of the three facilities will materialise the condition for the "establishment" of the infrastructure. Article 2(1) of the Memorandum of Understanding on the Establishment and Operation of the Extreme-Light-Infrastructure signed on 16 April 2010 by the plenipotentiaries for ELI of the Czech Republic, Hungary and Romania, which stipulates that the "principal task of the ELI-ERIC shall be to establish and operate full scope of the Extreme-Light-Infrastructure", should be understood within the same.

In addition, ERICs should operate on a non-economic basis. They may only carry out some limited economic activities in order to promote innovation and knowledge and technology transfer, but these activities should not jeopardize the main purpose of the infrastructure.

Finally, each future infrastructure applying for the status of ERIC should fulfil five conditions connected with the objective of the European Research Area (ERA):

- The infrastructure should be necessary for European research activities, including Community programmes;
- It should provide open and effective access for the European research community (Member States + Associated countries);
- It should represented an added value in the development of the ERA and a significant improvement in relevant S&T fields at international level;
- It should contribute to the dissemination and optimisation of the results of the activities, and;
- It should contribute to the mobility of knowledge and researchers within the ERA for an increased use of intellectual potential throughout Europe.

Membership

The ERIC Regulation states that only States or intergovernmental organisations are eligible for being members of an ERIC. The Regulation defines three categories of members:

- Member States of the European Union;
- Third countries (including associated countries);
- Specialized intergovernmental organizations.

It should be noted that the members of an ERIC may be represented by one or more public entities exercising the rights and discharging the obligations of the member. The representatives shall not be considered as formal members. They shall only act on behalf of the State member of an ERIC (this is a condition for the ERIC to be regarded as an international body and thereby exempted from some taxes and duties).

In order to be established, an ERIC shall have at least 3 Member States as members. The statutory seat shall be established within the territory of a Member State of the EU or an associated country. In any case, EU Member States shall jointly hold the majority of the voting rights within the Assembly of members. Further membership for other States should be possible at any time on fair and reasonable conditions set in the Statutes. Members may be accepted as full members (with voting rights) or only observers (with no voting rights).

Establishment of an ERIC

In order to establish an ERIC, the contracting parties have to submit an application to the European Commission. This application shall include a formal request, the proposed Statutes of the legal body, a technical and scientific description of the Research Infrastructure, a declaration of the host Member State recognising the ERIC as an international body or organisation in the sense of the European directives on VAT, excise duties, and procurement. The ELI Delivery Consortium will be in charge of coordinating the preparation of this application documentation.

The Directorate General Research of the European Commission assisted by several committees and independent experts assesses the application. One of these committees is formed with representatives of the EU Member States.

The decision is communicated to the applicants, who have the opportunity, if required, to complete or amend their application within a reasonable time.

After the establishment, the European Commission remains an essential actor. It approves most amendments to the Statutes adopted by the Assembly of Members of the ERIC and examines the scientific, financial and operational reporting reports submitted annually by the Consortium.

Exemption from VAT, excise duties and public procurement rules

In order to be approved by the European Commission and established, any ERIC has to be regarded by the contracting parties as:

- An international body within the meaning of Article 151 (1) (b) of Directive 2006/112/EC;
- An international organisation within the meaning of the second indent of Article 23 (1) of Directive 92/12/EEC and Article 15, point c) of Directive 2004/18/EC.

It shall thus be exempted from VAT and excise duties and does not have to apply the European directive on public procurement rules (2004/18/EC). It shall only respect the principles of transparency, non-discrimination and competition. The members of the ERIC agree on the limits and conditions of the exemptions regarding the procedures of public procurement.

10.4.2 Prospective structure of the ELI-ERIC

The ERIC Regulation defines two mandatory bodies:

- **Assembly of members**, with full decision-making power (including on the adoption of the budget), formed by the members or by their representatives
- **Director of Board of directors:** executive body and legal representative appointed by the Assembly of members.

Provided that the Statutes include the two aforementioned bodies, the Members of the ERIC remain free to define a governance and institutional model tailored to the needs of the infrastructure. In particular, they have the possibility to establish relevant advisory committees.

Figure 10.3 below displays the organisational framework envisaged for the future ELI-ERIC. It is based on the principle of single governance. In compliance with the ERIC Regulation, the two main central bodies of the Consortium will be the Assembly of Members and the Board of directors.

The former will gather representatives of the Member Countries and will decide on fundamental strategies and orientations for the infrastructure, such as the definition and conditions of implementation of the access policy and quality policy, the definition of the overall scientific and research strategy, the development of common standards, the training and dissemination policy, etc.

The Board of directors will be the executive body of the infrastructure in charge of daily management. It will be especially in charge of ensuring the efficient coordination and consistency between the three sites (and maybe four at a later stage).

A Beam Allocation Board will be in charge of review of the proposals submitted by users. This Board will consist of independent international experts in the scientific and research fields covered by the infrastructure as well as representatives of the application sphere. The practical organisation of access for users selected by the Beam Allocation Board will be managed at the level of each ELI facility, in coordination with the Management Board of the ELI-ERIC.

Additional advisory bodies, such as an International Scientific Committee and a Facility Users' Council, will enable due representation of the users of the facility and independent recommendations on the scientific and financial management of the ERIC.

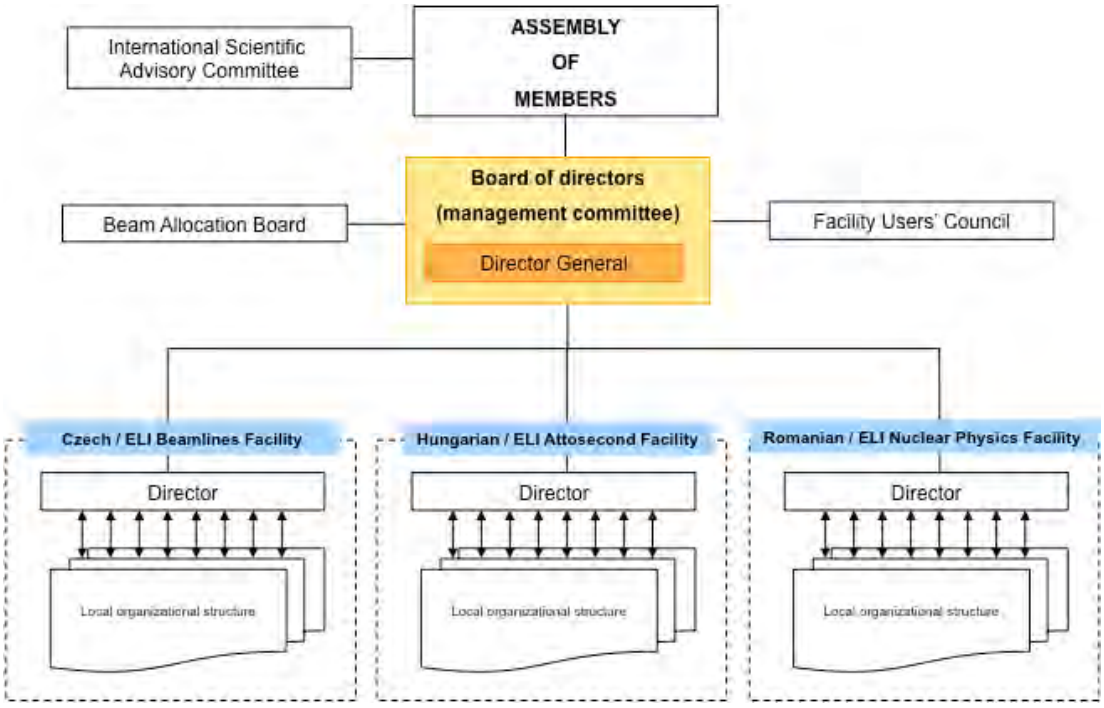

Figure 10.3: Prospective structure of the ELI-ERIC.

10.4.3 Distribution of tasks between the ELI-ERIC and the local ELI facilities

On the basis of the interpretation of Article 3.1 of Council Regulation (EC) No 723/2009 which interprets what "establishing a Research Infrastructure" means, the plenipotentiaries have agreed on the following organisation of the implementation and operational phases:

- In each of the three host countries, the existing or ad-hoc legal entities described in section 2 of this chapter will be in charge of applying for funding within the relevant national Operational Programmes and will be responsible for the implementation activities described in their respective Grant Agreement.
- The ELI Delivery Consortium will coordinate the involvement of other partners in the delivery of the project, in order to ensure an optimal use of the human resources and know-how available in the European scientific community.
- Negotiations on the establishment of the ELI-ERIC will be organised and coordinated by the ELI Delivery Consortium.
- The ELI-ERIC will have no responsibility in carrying out implementation activities. In compliance with the Practical Guidelines on the ERIC Regulation, the ELI-ERIC should have "clear and significant responsibility for the operation of the infrastructure", including the following tasks: definition of access policy and joint peer-reviewed evaluation of the proposals of users, provision and support of the effective and quality based access to the infrastructure, definition of the overall scientific and research strategy, definition of common standards, joint training and technology-transfer activities.
- The three local beneficiaries will retain ownership of the facilities even during operation. The beneficiaries will grant the right of use and operation (without any charges) to the ELI-ERIC.

10.4.4 Memorandum of Understanding on the Establishment and Operation of the Extreme Light Infrastructure (ELI)

The Ministry of Education, Youth and Sports of the Czech Republic,
duly represented by Prof. Vlastimil RŮŽIČKA, Vice Minister for Research and Higher Education, Plenipotentiary for the ELI Project in the Czech Republic

The National Office for Research and Technology of Hungary,
duly represented by Dr. Tivadar LIPPÉNYI, CEO of ELI-HU Ltd., Plenipotentiary for the ELI Project in Hungary

The National Authority for Scientific Research of Romania,
duly represented by Prof. Dr. Nicolae-Victor ZAMFIR, General Director of the National Institute for Nuclear Physics and Engineering, Plenipotentiary for the ELI Project in Romania

Hereinafter referred as "the Undersigning Parties",

- Recognizing that the ambition of ELI to establish and operate the first Research Infrastructure in the world dedicated to the investigation and applications of laser-matter interaction in the unprecedented ultra-relativistic regime corresponds to one of the major scientific needs of Europe, as identified by the European Strategic Forum on Research Infrastructures in its Roadmap issued in October 2006 and updated in December 2008;
- Desiring the establishment of ELI as a highly multidisciplinary international platform granting effective access to researchers and users from the European Union, associated countries and third countries;
- Recognizing that ELI represents an added value in the strengthening and structuring of the European Research Area (ERA) by contributing to the mobility of knowledge and researchers;
- Desiring that ELI will foster significant scientific and technological improvements in the field of laser science and beyond at international level and will increase the use of intellectual potential throughout Europe through their dissemination;
- Acknowledging the results achieved within the ELI Preparatory Phase and the conclusions reached on October 1^{st}, 2009 by the ELI Preparatory Phase Steering Committee on the Integrated Proposal presented by the Czech Republic, Hungary and Romania with the strong support of the representatives of the European Commission.

Have agreed as follows:

Article 1 – Cooperation on the establishment of the ELI-ERIC

(1) The Undersigning Parties are willing to cooperate on the establishment of a European Research Infrastructure Consortium, with the name "Extreme Light European Research Infrastructure Consortium" (hereinafter referred to as "ELI-ERIC" or "ERIC"), according to rules set in Council Regulation EC 723/2009[3] and as requested in the resolutions of the Steering Committee meeting of the ELI Preparatory Phase Consortium held on October 1^{st}, 2009.

(2) The ELI-ERIC shall be established for an unlimited period or for a period ending not earlier than five years after the beginning of the operational phase, in compliance with Council Regulation (EC) 1083/2006[4].

(3) The Undersigning Parties shall comply with the obligation set in Council Regulation EC 723/2009 of recognising ELI-ERIC as an international body, in the sense of Article 151 (1)(b) of

[3] EC 723/2009, Community legal framework for a European Research Infrastructure Consortium (ERIC) (OJ L206, 08/08/2009).

[4] EC 1083/2006, Laying down general provisions on the European Regional Development Fund, the European Social Fund and the Cohesion Fund and repealing Regulation EC 1260/1999 (OJ L210, 31/07/2006).

Directive 2006/112/EC[5], and as an international organization in the sense of the second indent of Article 23 (1) of Directive 92/12/EEC[6] and Article 15, point (c) of Directive 2004/18/EC[7]. The limits and conditions of the exemptions provided for in these provisions shall be laid down in the Statutes of the ERIC between the Parties founding the ERIC.

(4) The ELI-ERIC shall have its registered office on the territory of a Member State or a country associated to a community research, technological development and demonstration programme in accordance with the Council Regulation 723/2009 Article 8, paragraph (1).

(5) The ELI-ERIC and its facilities will be designed and used exclusively for civilian research. It shall pursue its activities on a non-economic basis, as defined and in the conditions described in Article 3 of Council Regulation EC 723/2009. The ELI-ERIC may carry out limited economic activities, provided that they are closely related to the principal task to establish and operate the Extreme-Light-Infrastructure and do not jeopardize its mission.

(6) The Statutes of the ELI-ERIC shall be established in accordance with the conditions of the Czech-Hungarian-Romanian Integrated Proposal approved on October 1^{st}, 2009 by the Steering Committee of the ELI Preparatory Phase Consortium.

Article 2 – Tasks and Scope of the future ELI-ERIC

(1) The principal task of the ELI-ERIC shall be to establish and operate full scope of the Extreme-Light-Infrastructure.

(2) The Undersigning Parties shall implement and commission, with highest priority, by December 31^{st}, 2015 at the latest, a facility with primary mission in beamline generation of secondary sources for science and applications in Dolní Bøežany near Prague (Czech Republic), a facility with primary mission in attosecond science and applications, in Szeged (Hungary), and a facility with primary mission in ELI nuclear physics in Mãgurele, near Bucharest (Romania). Development of technologies, necessary for building the ultra-high intensity facility, will also be carried out at the three sites by the ELI-ERIC through coordinated and complementary programmes.

(3) The three Undersigning Parties hosting a facility shall have equal status as ELI hosts.

(4) Within the framework of the ELI Delivery Consortium defined in Article 4 of the present Memorandum, the Undersigning Parties shall establish an Expert Group entrusted with the mission to produce a Resourced Project Assessment which shall detail the tasks to be performed to deliver the Extreme-Light-Infrastructure on the basis of the human resources capacities and expertise available within Europe. The assessment shall be consistent with the constraints of the funding capacity and timescales, and within acceptable risk to the funding agencies. This Expert Group shall include representatives from all members of the ELI Delivery Consortium, in particular from the hosting countries, and from France, Germany and the United Kingdom.

(5) On the basis of a review of the performance and readiness of the various technological options, the Assembly of Members of the ELI-ERIC will decide on the location of the ultra-high-intensity facility by 2012, for a timely delivery of the latter facility, ideally by end 2015 but no later than 2018. All members of the ELI Delivery Consortium shall be eligible for bidding to host the ultra-high-Intensity facility.

(6) The Undersigning Parties expect strong, highly dedicated support in particular from France, Germany and the United Kingdom in the realisation of the aforementioned facilities and the pursuit of all related goals in the form of expertise, know-how and technology transfer.

[5]EC Directive 2006/112/EC, On the common system of value added tax (OJ L347, 11/12/2006).

[6]EC Directive 92/12/EEC, On the general arrangements for products subject to excise duty and on the holding, movement and monitoring of such products (OJ L076, 23/03/1992).

[7]EP-EC Directive 2004/18/EC, On the coordination of procedures for the award of public works contracts, public supply contracts and public service contracts (OJ L134, 30/04/2004).

(7) The Undersigning Parties acknowledge that the present Memorandum does not entail any binding commitment regarding their level of future contribution to the ELI-ERIC.

Article 3 – Organs of the ELI-ERIC

(1) The ELI-ERIC shall operate as a distributed infrastructure with single centralized decision-making and governing bodies.

(2) Pursuant with Article 12 of Council Regulation EC 723/2009, the organs of the ELI-ERIC shall be the Assembly of Members and the Board of Directors.

(3) The Assembly of Members shall be granted with full decision-making powers, including on the adoption of the budget, the definition of the general orientations of the research strategy and international cooperation strategy, the appointment of the Board of Directors, the adoption of amendments to the Statutes. The Assembly of Members shall comprise the contributing Parties with voting rights and non-contributing Parties, attending as Observers with no voting rights.

(4) The Board of Directors shall be the executive body and the legal representative of the ELI-ERIC. It will be chaired by a Director General and several Directors with specialized attributions appointed by the Assembly of Members. The Board will be responsible for the implementation of the research and international cooperation strategy, for communication at global level, and for the daily management of the infrastructure. It shall be jointly accountable for its action before the Assembly of Members.

(5) The Assembly of Members shall be assisted by a Facility Users' Council. The Board of Directors shall be assisted by an Advisory Board and, during the implementation phase, by an Implementation Committee. The Statutes and the bylaws shall define the conditions of their intervention.

(6) The Members of the ELI-ERIC shall make sure that the Statutes create the conditions for each contributing party to comply with national and EU legislations regarding the execution and use of their financial commitment.

Article 4 – Establishment of an ELI Delivery Consortium

(1) By virtue of the present Memorandum, an ELI Delivery Consortium is established by the Undersigning Parties as soon as all three Undersigning Parties have attached signatures of their entitled representatives.

(2) The main goal of the ELI Delivery Consortium is the establishment of the ELI-ERIC and the detailed definition of the implementation plan. The tasks and responsibilities of the ELI Delivery Consortium are in particular:

- The definition of a single and robust technical delivery plan of the entire ELI project in line with the TDR (technical design report) currently being finalized within the ELI Preparatory Phase Consortium, with the conditions defined in Article 2 of the present Memorandum, and with the Resourced Project Assessment produced by the Expert Group, as mentioned in Article 2, paragraph (4), and based on the resolutions taken by the ELI Steering Committee on October 1^{st}, 2009. When establishing the delivery plan, it should be ensured that unnecessary duplications are avoided and that economies of scale are exploited;
- The definition of the Statutes, Governance model and Financial and Contribution plan of the ELI-ERIC, as well as the coordinated completion of all proceedings related to its establishment and definition of processes ensuring its efficient operation.

(3) The ELI Delivery Consortium on its own has no legal personality, and does not entail any financial commitment or contribution for the Undersigning Parties. Each party to the ELI Delivery Consortium bears on its own the expenditures linked to its participation in the activities of the Consortium.

Article 5 – Organs and operation of the ELI Delivery Consortium

(1) The organs of the ELI Delivery Consortium shall be: the Steering Board, the Project Management Board and the Task Groups. The creation of additional organs may be decided by the Steering Board depending on the needs of the ELI Delivery Consortium.

(2) The ELI Delivery Steering Board (hereinafter "Steering Board") shall be the supervising body of the ELI Delivery Consortium. It shall approve the final delivery plan attached to the Statutes of the ELI-ERIC, approve the reports of the ELI Delivery Management Board on the activities of the Delivery Consortium and enable the Undersigning Parties to decide and commit on matters required for the establishment of the ELI-ERIC. Initially, the Steering Board will consist of one representative of each of the Undersigning Parties. The Steering Board will invite other countries to join the Steering Board. The Steering Board will aim at taking decisions unanimously. No decision can be taken against the national interests of the Undersigning Parties.

(3) The ELI Delivery Management Board (hereinafter "Management Board") shall be the management body of the ELI Delivery Consortium at operative level acting according to the decisions of the Steering Board. Its main tasks include in particular the coordination and control of the activities of the Task Groups and reporting on progress to the Steering Board. The Management Board shall consist of at least one representative of each Undersigning Country appointed by its respective ELI plenipotentiary. Unresolved issues – with relation to legal, governance and financial matters in particular – can be escalated to the Steering Board at any time.

(4) After the entry into force of the present Memorandum, the Management Board shall establish specialised Task Groups in charge of carrying out the tasks described in Article 4(2). The Management Board shall define the action plan and deliverables of the Task Groups. Their composition will be agreed on by the Management Board on the basis of the conditions established in the Internal Regulations of the ELI Delivery Consortium.

(5) An Expert Group shall be established by the Managing Board as soon as possible after the entry into force of the present Memorandum and entrusted with the mission to produce the Resourced Project Assessment referred to in Article 2(4). The Expert Group shall identify in particular the human resource capacities and expertise available at European level for the implementation of the project and review the funding capacities and time constraints. On the basis of this assessment, the Expert Group shall provide the Steering Board with recommendations on the establishment of the delivery plan which should comply with the provisions of the Integrated Proposal presented by the Czech Republic, Hungary and Romania.

(6) The Terms of Reference and the Internal Regulations of the ELI Delivery Consortium will be elaborated by the Undersigning Parties, and agreed on by the ELI Delivery Steering Board following the entry into force of the present Memorandum. The activities shall be organised so as to ensure efficiency, cooperation and fair representation of all interests.

Article 6 – Language

All dealings under this Memorandum of Understanding shall be done in the English language.

Article 7 – Disputes

The Undersigning Parties shall endeavour to settle by negotiations any dispute concerning the interpretation or application of the present Memorandum of Understanding.

Article 8 – Entry into force

This Memorandum of Understanding shall enter into force as soon as all three Undersigning Parties have attached signatures of their entitled representatives.

Article 9 – Accession

After the entry into force of this Memorandum of Understanding, and having set up the ELI Delivery Consortium, the three Undersigning Parties shall invite members of the ELI Preparatory Phase Consortium and other countries to join the ELI Delivery Consortium. Any competent authority of any State already a member of the ELI Preparatory Phase Consortium and willing to contribute to the establishment of the ELI-ERIC and to the implementation of the tasks defined in Article 2 of the present Memorandum, may accede to the ELI Delivery Consortium. The conditions of accession shall be the subject of an agreement between the acceding authorities and the ELI Delivery Consortium.

Article 10 – Amendments to this Memorandum of Understanding

Any amendment to this Memorandum of Understanding shall be decided upon consensus among all Undersigning Parties, and shall not undermine or jeopardize ELI's scientific and technological goals as well as their achievement as outlined in this Memorandum of Understanding and defined by the ELI Delivery Consortium. The amended Memorandum of Understanding shall enter into force as soon as all Undersigning Parties have attached signatures of their entitled representatives to the amended version. The dealings related to the amendment processes and/or signatures shall not delay the project or compromise the activities of the Undersigning Parties.

Article 11 – Termination and withdrawal

(1) The Memorandum of Understanding is concluded for an indefinite period. The conditions stipulated in this Memorandum of Understanding shall govern the relationships between the Undersigning Parties within the ELI Delivery Consortium until the ELI-ERIC is established.

(2) The Undersigning Parties may withdraw from this Memorandum of Understanding by notifying their decision to the ELI Delivery Steering Board convoked for this specific purpose. The withdrawal will become effective only six months after notification to the ELI Delivery Steering Board to allow negotiations on the decision to withdraw between the Undersigning Parties and on the appropriate reorganization of the ELI Delivery Consortium. During this six-month period, the Undersigning Party willing to withdraw shall attend the meetings of the ELI Delivery Steering Board, but shall not take part into decisions. Withdrawal shall not entitle the withdrawing Undersigning Party to any reimbursement of the expenses incurred under this Memorandum.

Article 12 – Signature

The present Memorandum of Understanding was established in the English language and signed in six copies by the Undersigning Parties.

EUROPEAN UNION
EUROPEAN REGIONAL DEVELOPMENT FUND
INVESTING IN YOUR FUTURE

OP Research and
Development for Innovation